Springer Water

Kim Dan Nguyen
Sylvain Guillou
Philippe Gourbesville
Jérôme Thiébot *Editors*

Estuaries and Coastal Zones in Times of Global Change

Proceedings of ICEC-2018

Springer

Springer Water

Series Editor

Andrey G. Kostianoy, Russian Academy of Sciences, P.P. Shirshov Institute of Oceanology, Moscow, Russia

The book series Springer Water comprises a broad portfolio of multi- and interdisciplinary scientific books, aiming at researchers, students, and everyone interested in water-related science. The series includes peer-reviewed monographs, edited volumes, textbooks, and conference proceedings. Its volumes combine all kinds of water-related research areas, such as: the movement, distribution and quality of freshwater; water resources; the quality and pollution of water and its influence on health; the water industry including drinking water, wastewater, and desalination services and technologies; water history; as well as water management and the governmental, political, developmental, and ethical aspects of water.

More information about this series at http://www.springer.com/series/13419

Kim Dan Nguyen · Sylvain Guillou ·
Philippe Gourbesville · Jérôme Thiébot
Editors

Estuaries and Coastal Zones in Times of Global Change

Proceedings of ICEC-2018

Springer

Editors
Kim Dan Nguyen
Laboratoire d'Hydraulique Saint-Venant
Paris, France

Philippe Gourbesville
Ecole Polytechnique
University of Nice-Sophia Antipolis
Nice, France

Sylvain Guillou
LUSAC
University of Caen-Normandy
Cherbourg-en-Cotentin, France

Jérôme Thiébot
LUSAC
University of Caen-Normandy
Cherbourg-en-Cotentin, France

ISSN 2364-6934 ISSN 2364-8198 (electronic)
Springer Water
ISBN 978-981-15-2080-8 ISBN 978-981-15-2081-5 (eBook)
https://doi.org/10.1007/978-981-15-2081-5

This Springer imprint is published by the registered company Springer Nature Singapore Pte Ltd.
The registered company address is: 152 Beach Road, #21-01/04 Gateway East, Singapore 189721, Singapore

Preface

This book compiles 48 chapters organised in seven parts with a brief introduction to each chapter. These chapters were selected among a total of 110 manuscripts from 15 countries presented and discussed at the 6th International Conference on Estuaries and Coasts (ICEC-2018) which was held from 20 to 23 August 2018 in Caen, France. Using this opportunity, we would like to acknowledge the numerous reviewers (see Reviewers) for their thorough evaluation which was fundamental for this selection and for the overall quality of this book (two reviewers/paper). Though only 46% of the papers are selected, the scope of this book is kept deliberately as broad and interdisciplinary as for the ICEC-2018 conference, encompassing the latest advances and the most innovative developments related to the respective conference topics which might be viewed in the context of global change.

Previous ICEC conferences were held in 2003 in Hangzhou/China (1st), 2006 in Guangzhou/China (2nd), 2009 in Sendai/Japan (3rd), 2012 in Hanoi/Vietnam (4th) and 2015 in Muscat/Oman (5th). This conferences series aims to bring together leading academic scientists, researchers and practitioners to share their results, the solutions adopted and the challenges encountered in diverse topics related to estuarine, deltaic and coastal environments.

The 6th ICEC-2018 has been jointly organised by GIS HED^2 (Groupement d'Intérêt Scientific "Hydraulique pour l'Environnement et le Développement Durable", France), University of Caen-Normandy and IRTCES (International Research and Training Centre on Erosion and Sedimentation). GIS HEDD includes 34 (i.e. almost all) French national research institutions in hydraulic engineering and university laboratories. GIS HED^2 has been recognised and supported by French Ministries (Ministry of Research and Ministry of Ecology and Sustainable Development).

As such, the ICEC conference series represents an ideal interdisciplinary platform for the presentation and discussion of the state-of-the art and the most recent innovations, trends and future challenges in estuaries and coasts.

As reflected by the table of contents and by the number of chapters of different parts, a wide range of topics is covered with a clear focus on sediment transport and morphological changes in estuaries and coasts. Each part is briefly introduced by an overall comment on the contextual relevance or/and content of the chapter followed by a very short outline of the constitutive chapters.

In the first part with seven chapters, both modelling and monitoring of different aspects of saline intrusion in estuaries and other water bodies are addressed with a particular focus on case studies from China, France, France, Italy and Egypt.

Overall, this part illustrates the high complexity of the processes associated with saline intrusion and its impacts on ecosystems and human activities, implying inter alia that combined modelling and monitoring may represent the only viable approach to cope with such complexity and the ensuing challenges.

Second part with seven chapters is focused on CFD modelling of marine renewable energy (MRE) systems and their interactions with currents, sediments on the bed of the water body and the associated ecosystems. This includes seawater pumped storage power stations (SPPS), oscillating water columns (OWC), tidal energy converters (TEC) and offshore wind turbines (OWT).

As an overall conclusion which might be tentatively drawn from these contributions, it is worth mentioning that the interactions between MRE systems/farms, currents, sediments and ecosystems are generally in two way, implying that integrated modelling approaches and more efficient coupling of different models (e.g. hydrodynamic, geo-morphodynamic and ecological large-scale models) are necessary to cope with such complex interactions.

In the third part with ten chapters, the prime focus is the modelling of sediment transport and geo-morphological changes in estuaries and deltas, particularly including the effects of human activities on these changes. The chapters encompass a broad spectrum of diverse modelling approaches and processes, also including management tools for estuarine environments such as mapping and geo-ecological indicators. Besides the applications of common hydro-morphodynamic codes such as Delft3D and MIKE21 for the study of the effect of river flooding on morphological changes, and the study of tidal currents and sediment transport processes in estuaries and bays, these also include other modelling approaches. Among the latter, it is worth to mention a 3D multi-class modelling of sediment flux to implement dredging and dumping processes, a 3D non-hydrostatic model for coherent flow structures and the associated scour until equilibrium, a two-phase Eulerian approach for CFD modelling of sediment plumes, a 3D advanced CFD model coupled with a multi-layered mixed sediment (sand + mud) model for the study of sediment exchanges between estuary and sea as well as the associated uncertainties.

Among the lessons learned from this part, it should be underlined that generally there is no model readily available to resolve at local and regional scales the diverse processes/interactions associated with sediment transport and geo-morphological changes in estuaries and deltas; i.e. from local to regional scales and short to long term. Therefore, the first step is a proper selection of (i) the CFD models and/or the

geo-morphodynamic models (including grid resolutions) and (ii) the coupling approaches which are most appropriate to the problem under study. After a proper calibration/validation of the proper model system, it is fundamental, before the ultimate application of the validated model system, to use it for systematic sensitivity analysis of the most relevant parameters within their uncertainty ranges. Though an exact quantification of the uncertainties of the simulation results is generally hardly possible, an approximate uncertainty assessment is required for the latter to be practically useful.

In the fourth part with twelve chapters, various coastal processes associated with waves, current and sediment transport using numerical tools, laboratory experiments, field surveys and remote sensing imagery are addressed with a focus on engineering applications. The thirteen chapters may be subdivided in three groups depending on their focus: (i) Application of aerial/satellite imagery and/or field surveys for the study of shoreline changes (First four chapters), (ii) Numerical modelling of the interactions between waves, currents and sediment transport with a focus on engineering problems (Next four chapters) and (iii) Mitigating measures (Five last chapters). The applications in the first group of papers encompass diverse types of coasts (mud, sand, mixed sand-gravel) and diverse effects on shoreline evolution (coastal structures, ports, river sediment supply, mangroves and aquaculture development). The second group also covers modelling studies of diverse impacts and processes, such as the effects of changes in wave regimes and river discharges on sediment fluxes to estuaries and in adjacent beaches, the effects of current–wave interactions at inlets on boating operations, the effect of storms on cohesive and non-cohesive sediment transport/deposition and morphodynamic changes in waterways and the impact of engineering works on suspended sediment transport near critical infrastructures. In the third group, the focus is rather on nature-based solutions (e.g. eco-geosystems) and soft solutions (e.g. groyne like net systems) to reduce coastal erosion as well as on wave transformation and conditions triggering co-oscillating tides for the improvement of predictions and warning systems.

Overall, the contributions show that most of the lessons learned in the third part for the modelling in estuaries and deltas (see above) also generally apply for coastal environments. In addition, they show implicitly that the efficient management of future coastal risks requires a full understanding of the evolution of the coastal environment and the underlying processes/interactions, which can very often only be achieved through a synergetic combination of numerical modelling, laboratory experiments, field surveys and remote sensing techniques such as airborne/satellite imagery. They also show that the trend to mitigate coastal risks in the context of global change is clearly towards nature-based solutions.

Fifth part with four chapters deals with experimental studies related to various effects related to sediment transport and flow, such as (i) the effect of sediment availability/supply on the characteristics of bed forms (dunes and ripples), horizontal coherent flow structures in compound vegetated channels as well as their

effect on transverse exchange processes and the importance of the latter for engineering applications related to mitigation measures, such as forests and river bank protection, (ii) the effects of sediment size/concentration and concentration of other minerals and organic matter on sediment flocculation and settlement, (iii) the effects of abrupt changes in river flow discharge and sediment supply on the short-term response of alluvial fans and (iv) the effects of rough and smooth ice covers on bed scour around pile groups.

Altogether, these five chapters represent an opportune confirmation of the necessity and value of physical modelling for the improvement of process understanding. The latter, besides the validation of numerical models, is crucial, particularly in the study of highly complex processes, such as fan formation and evolution in deltas and other geosystems where computational modelling supported by airborne/satellite imagery still dominates and where physical modelling has been experiencing a revival in recent years.

In the sixth part with four chapters focusing on the impacts of human activities on sediment transport and the morphological evolution of estuaries and coastlines. Various activities such ports, waterways, river damming (e.g. hydropower dams), sand mining, river narrowing, navigation infrastructures and dredging are considered by using different approaches, such as monitoring data analysis, diverse numerical models or their combination.

Overall, these studies support the results of previous studies, showing among others that human activities are responsible for the reductions in sediment flux in rivers and in sediment fluxes from rivers to the ocean, and confirm the range of the reported relative contributions of the different types of human activities to these reductions.

Seventh part with four chapters is dedicated to monitoring with a focus on remote sensing and satellite image analysis, generally supported by field surveys. The applications cover different processes and purposes in highly complex estuarine and deltaic environments, such as (i) the analysis of sediment dynamics (e.g. erosion/progradation, morphological changes) to provide synoptic maps of biophysical characteristics of sediments, (ii) the study of seasonal and spatial variations to provide maps with high spatial resolution for potential sediment transport trends and (iii) the analyses of historical hourly water level data in rivers and deltaic coasts to provide long-term hydrological data for the planning and management purposes.

Overall, the results well illustrate the recent advances in the applications of diverse remote sensing techniques and the potential of their combination as well as that of their deployment together with in situ measurement techniques.

Finally, we would also like to thank the authors for their contributions and nice collaboration in the revision process, the members of the Local Organisation Committee for their devotement and contribution to the very successful

organisation of the conference, the sponsors IAHR, SHF and the Regional Council of Normandy for all their support and last but not least the editorial team for their support and the opportunity to publish these selected ICEC 2018 papers as a Springer book.

Kim Dan Nguyen
(Chairman of ICCE-2018)
Executive Director of GIS HED^2
Paris, France

Hocine Oumeraci
TU Braunscheig
Braunscheig, Germany

Sylvain Guillou
LUSAC, University of Caen-Normandy
Cherbourg-en-Cotentin, France

Jérôme Thiébot
LUSAC, University of Caen-Normandy
Cherbourg-en-Cotentin, France

Philippe Gourbesville
Ecole Polytechnique, University of Nice
Nice, France

Reviewers

Iskander Abroug, University of Caen, France
María Aranda García, University of Cadiz, Spain
Gubash Azhikodan, Tokyo Metropolitan University, Japan
Mustapha Benaouicha, Segula, France
Butsawan Bidorn, Chulalongkorn University, Thaïlande
Joan Cecilia Casila, University of the Philippines, Philippines
Bruno Castelle, University of Bordeaux, France
Julie Castiglione, IFREMER, France
Ning Chan Shu, Hong Kong University of Science and Technology, Hong Kong
Julien Chauchat, University of Grenoble, France
Nicolò Colombani, UNIFE, Italy
Alexandra Coynel, University of Bordeaux, France
Philippe Cugier, IFREMER, France
Liu Guangdong Da, Research Institute of Water Resources and Hydropower, China
Pierre-Luc Delafin, University of Caen, France
Frederic Dias, University College, Dublin, Ireland
Lei Ding, NHRI, China
Uwe Dornbusch, Environment Agency, UK
Xi-Ping Dou, NHRI, China
Xiaotao Du, SINA, China
Mohamed Elshemy, Tanta University, Egypt
Xi Feng, Hohai University, China
Lucille Furgerot, University of Caen, France
Régis Gallon, CNAM, France
Dixon Gevana, University of the Philippines, Philippines
Florent Grasso, IFREMER, France
Nicolas Guillou, CEREMA, France
Sylvain Guillou, University of Caen, France
Chuansheng Guo, China Institute of Water Resources and Hydropower Research, China
Scott Hagen, Louisiana State University, USA

Arnaud Hequette, University of Littoral, France
Olajumoke Jejelola, Federal University of Technology, Nigeria
Jian Jiao, NHRI, China
Kavyavu Kambale, Université de Conservation de la Nature et de Développement de kasugho, Congo
Manoni Kodua, Georgian Technical University, Georgia
Philippe Larroude, INP Grenoble, France
Jean Philippe Lemoine, GIP Seine-Aval, France
Sandric Lesourd, University of Caen, France
Honghai Li, U.S. Army Corps of Engineers, USA
Ti-Lai Li, NHRI, China
Yuting Li, NHRI, China
Chen Lu, Pearl River Hydraulic Research Institute, China
Claire Marion, CNAM, France
Baptiste Mengual, IFREMER, France
Li Mingchang, Tianjin Research Institute of Water Transport Engineering, China
Meii Mohamad-Norizam, University Malaysia Terengganu, Malaysia
Antoine Mury, EPHE, France
Simon Neill, Bangor University, UK
Kim Dan Nguyen, Laboratory for Hydraulics Saint-Venant, France
Sylvain Orseau, University of Compiègne, France
Hocine Oumeraci, Technische Universität Braunschweig, Germany
Gaële Perret, University of Le Havre, France
Damien Pham Van Bang, Saint-Venant Laboratory for Hydraulics, France
Hung Phan, Delft University of Technology, Netherlands
Yves Plancke, Flemish Government, Belgium
Daniel Potter, Lancaster University, UK
Wang Qiushun, ZIHE, China
Dano Roelvink, IHE Delft Institute for Water Education, Netherlands
Alina Santa Cruz, University of Caen, France
Sabine Schmidt, University of Bordeaux, France
Franck Schoefs, University of Nantes, France
Holger Schüttrumpf, RWTH Aachen University, Germany
Alexei Sentchev, University of Littoral, France
Philippe Sergent, CEREMA, France
Honglin Song, Tongji University, China
Aldo Sottolichio, University of Bordeaux, France
Pierre Stephan, University of Brest, France
Hitoshi Tanaka, Tohoku University, Japan
Jérôme Thiébot, University of Caen, France
Rodger Tomlinson, Griffith University, Australia
Anne Vallette, ARGANS, France
Romaric Verney, IFREMER, France
Charles Verpoorter, University of Littoral, France

Chonghao Wang, China Institute of Water Resources and Hydropower Research, China
Yanhong Wang, NHRI, China
Weiming Wu, Clarkson University, USA
Gao Xiangyu, NHRI, China
Shi Ying-Biao, ZIHE, China
Katsuhide Yokoyama, Tokyo Metropolitan University, Japan
Han Yufang, NHRI, China
Barbara Zanuttigh, Bologna University, Italy
Miguel Zapata, Centro de Investigación en Matemáticas, Mexico
Jingxin Zhang, SJTU, China
Jinshan Zhang, NHRI, China
Jinqiong Zhao, Changjiang River Scientific Research Institute, China
Lei Zhu, Wuhan University, China

Contents

Wave Transformation and Morphological Changes in Coastal Zones

Saline Intrusion and Impacts: Modelling and Monitoring Case Studies

Saline intrusion within coastal rivers and hydro-environments is a complex process that may generate significant impacts on natural ecosystems and human activities. In order to assess in a detailed way potential consequences, monitoring strategies are developed in sensitive coastal areas and are frequently combined with modelling approaches. The current part is dedicated to various operational approaches covering both aspects for monitoring and modelling and implemented in different coastal contexts and especially in major estuaries.

The first chapter by Sabine Schmidt addresses the situation of one of the largest European estuary: the Gironde. Over 14 years, since 2004, a multi-sites and high-frequency monitoring system (MAGEST) have been set up, and four physico-chemical parameters, including salinity, are recorded with the objective to establish a reference database of water quality of this large fluvio-estuarine system, in order to address current and future water quality issues, including saline intrusion. Sabine Schmidt presents in details the 14-year time series of salinity along the Garonne–Gironde continuum. Not surprisingly, there are large differences among the instrumented stations depending on their localization. High-frequency salinity chronic at Bordeaux is used to assess the occurrence of saline intrusion in the Tidal Garonne River, revealing marked inter-annual variability in marine intrusion depending on fluvial discharge. The ongoing regional changes suggest an increase in salinity in the Tidal Garonne River in the next decades.

In the second chapter, Veerapaga et al. have developed a numerical analysis with a 3D hydrodynamic model on a conceptual estuary in order to discuss the variation of salinity intrusion and mixing types in terms of estuary length, width, depth and bathymetry. The obtained results will allow readers and researchers to understand how those variables may affect the saline intrusion and what could be the different expected mixing conditions.

The third and fourth chapters by Ding Lei et al. are dedicated to the response of saline intrusion within the Yangtze Estuary in China. The impact of saline intrusion may strongly affects the water supply conditions of the city of Shanghai that relies up to 70% on the Yangtse for water services. A modelling approach based on a 3D model is used to assess the interest to block the saline intrusion and to maximize freshwater within the North Branch of the estuary. The results demonstrate the efficiency of the concept that requests further developments to reach the operational state. The model

is also used to investigate the potential risk of salt intrusion on the Dongfengxisha reservoir that was created in 2014 and dedicated to provide freshwater resources to estuary residents. The authors demonstrate the interest to implement a tidal gate on the North branch within the Yangste estuary.

In the fifth chapter, Shi et al. present the case of the Qiantang Estuary in China. Strong tidal bore, high sediment concentration, severe erosion/deposition and human activities characterize this estuary. The authors propose the law of interaction among runoff, channel volume and salinity by means of the analysis of the long-term hydrological and measured salinity data. A 2D salinity movable bed mathematical model considering water flow, sediment salinity transport and riverbed deformation and other multiple factor couplings has been established. The actually measured water flow, sediment, salinity and other data are used to verify the salinity transport process, and the model established can reflect the actual transport law of water flow, sediment and salinity in the Qiantang Estuary. The study shows that riverbed scouring and silting have a large effect on the salinity transport for the medium and long term at the Qiantang Estuary. The best results are obtained with a movable bed model for salinity forecast. This movable riverbed model has been successfully applied to predict the saltwater intrusion in the protection process against salt tide to guarantee the safety of water supply in Hangzhou City.

The last two chapters by Mastrocicco et al. and by Shalby et al. address the situation of wetlands and coastal lagoons in Italy and in Egypt. Direct evaporation from surface water bodies like lakes, wetlands and lagoons will increase due to temperature increase leading to salt accumulation. To understand the hydrological exchanges between the transitional coastal wetlands of the Variconi oasis, the unconfined aquifer of the Volturno River Delta and the Tyrrhenian Sea, the contributions of various processes were monitored and assessed. Physical–chemical parameters like salinity, pH, Eh and temperature were monitored. The results show that the permanent wetlands fed by both the Volturno River and the Tyrrhenian Sea show a smoothed salinity peak during the summer season; while the ephemeral wetlands hydraulically disconnected from the aquifer show high salinity peaks during the summer season due to evapo-concentration processes. The projected increase in salinity of these wetlands due to coastal erosion, augmented evapotranspiration rates and sea-level rise could be of serious concern for the biodiversity. Lake Burullus, the second largest coastal lagoon in Egypt, has a great economic situation which is vulnerable to climate change threats. The authors have used MIKE 21 to develop an eco-hydrodynamic model for the lake. Based on a regional climate model (RCM) and meteorological data extracted for one Representative Concentration Pathways (RCPs) scenario, the results show that the water depths in the lake will increase; waters will be warmer and more saline. These processes will significantly affect the water quality status of the lake and its economic situation. In both cases, the authors underline the interest to implement urgently monitoring and management strategies in order to preserve those fragile environments.

Philippe Gourbesville
Ecole Polytechnique, University of Nice, France

A 14-Year Multi-sites and High-Frequency Monitoring of Salinity in the Tidal Garonne River (S-W France) Reveals Marked Inter-annual Variability in Marine Intrusion

Sabine Schmidt

Abstract With its 625 km^2, the Gironde estuary (S-W France) is one of the largest European estuaries. The tidal Garonne and Dordogne Rivers, whose confluence is located at about 75 km from the mouth, form its fluvial section. The Tidal Garonne River (TGR) represents about 2/3 of the freshwater inputs to the Gironde. For a long time it has been accepted the limit of saline intrusion, identified by a salinity higher than 0.5, was nearly at the confluence. In the last decades, there has been a significant decrease of the annual mean TGR discharge, likely to influence marine intrusion. It is often difficult to establish changes in marine intrusion in estuaries due to the limited available data set. This work presents the interest of a multi-sites and high frequency monitoring system, called MAGEST, that records since 2004 four physico-chemical parameters, including salinity, to establish a reference database of water-quality of this large fluvio-estuarine system, in order to address current and future water-quality issues, including saline intrusion. This work presents in details the 14-year time series of salinity along the Garonne-Gironde continuum. Not surprisingly, there are large differences among the instrumented stations depending on their localization. High-frequency salinity chronic at Bordeaux is used to assess the occurrence of saline intrusion in the Tidal Garonne River, revealing marked inter-annual variability in marine intrusion depending of fluvial discharge. The ongoing regional changes suggest an increase of salinity in TGR in the next decades.

Keywords Gironde estuary · Salinity · Monitoring · High-frequency · Fluvial discharge · Variability

S. Schmidt (✉)
UMR5805 EPOC, CNRS, OASU, Université de Bordeaux, 33615 Pessac, France
e-mail: icec-2018@sciencesconf.org; sabine.schmidt@u-bordeaux.fr

K. D. Nguyen et al. (eds.), *Estuaries and Coastal Zones in Times of Global Change*, Springer Water,
https://doi.org/10.1007/978-981-15-2081-5_1

1 Introduction

Estuaries form a natural interface in which rivers and oceans meet, mixing both fresh and salt waters. Thus, salinity presents large spatial and seasonal variations, depending of the degree of water mixing (Savenije 1993; Uncles and Stephens 2011). The balance between the landward transport of salt by tidal processes and its seaward return by freshwater discharges determines the limit of salinity intrusion along an estuary. The main factor that affects the upstream limit of saline intrusion is freshwater inflow. In a context of global change, salinity intrusion in estuaries is expected to increase due to the cumulative effect of decrease in freshwater flows (changes in rain rate, increase of water abstraction in the watershed) and to sea level rise. At present, it is still difficult to establish changes in marine intrusion in estuaries due to the limited available data set.

The Gironde estuary (S-W France) and its tributaries, the tidal Garonne and Dordogne Rivers, constitute one of the largest European estuaries (Fig. 1). It has long been recognized that the limit of saline intrusion (salinity > 0.5) was to about 75 km from the mouth, at the Garonne-Dordogne confluence during low fluvial discharge

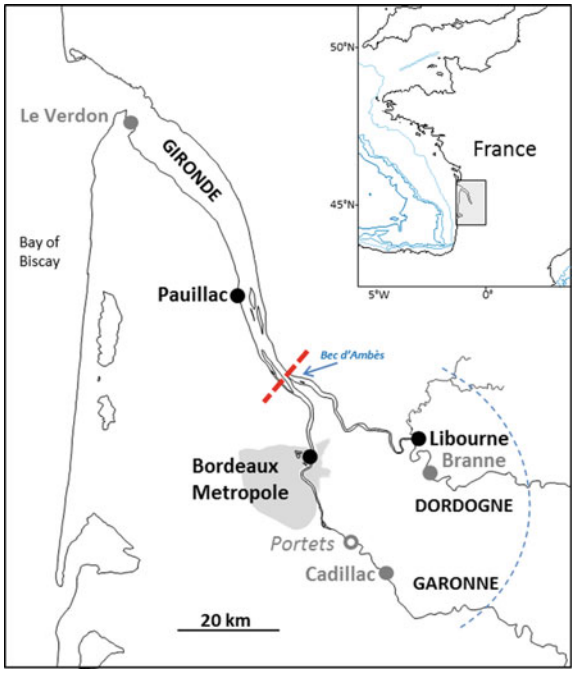

Fig. 1 The Gironde fluvio-estuarine system. The dotted arc shows the upstream limit of the tidal influence. The red dashed line highlights the historical limit of saline intrusion. The sites of the MAGEST network are also indicated: the four first instrumented stations (in dark) and the three new stations (in grey) started in 2017

periods, with incursions upstream Bordeaux (about 100 km of the mouth) at high tide (Allen 1972). By contrast, the upstream limit of tidal influence extends about 100 km more landward. What about 40 years later, considering the local hydro-morphological evolution. The Garonne mean annual discharge has decreased by 31% since the last six decades (Jalón-Rojas et al. 2015) and the duration of low-water periods increased (Schmidt et al. 2017). Both climate change and increase in water abstraction in the watershed (hydropower dams and agriculture) explain these changes. It is now established the cumulative impact of changes in hydrology and morphology (upstream shift of accretion zone, gravel extractions) have also enhanced tidal range in the Tidal Garonne River (TGR) (Jalón-Rojas et al. 2018). Therefore, one could speculate these discharge and tide changes may have led to a landward extension of the saltwater intrusion beyond its historical limit.

This work presents a 14-years continuous time series of salinity in surface waters at Bordeaux in the Tidal Garonne River. This multi-year salinity chronic enables to illustrate the variability of salinity at different timescales, and to assess the occurrences of saline intrusion. These results demonstrate the interest of long-term monitoring to better understand inter-annual salinity dynamic and to produce reliable records essential for the identification of saline intrusions in estuaries.

2 Study Site and the MAGEST Network

The macrotidal and highly-turbid Gironde fluvio-estuarine system is located in the South-West France and drains daily about 684 $m^3\ s^{-1}$ (104–6048; 2005–2014) to the Bay of Biscay (Jalón-Rojas et al. 2018). Tides at the mouth are semidiurnal, with a tidal range varying from about 2.5–5 m on mean neap/spring tides. The Tidal Garonne River represents about 2/3 of the freshwater inputs to the Gironde. The mean annual Garonne discharge is 597 m for the period 1913–2018 (data from http://www.hydro.eaufrance.fr/stations/O9000010 station Tonneins). However, since 2004, the year a high-frequency monitoring network was established, mean annual discharges were usually below this level. Years 2005, 2011 and 2017 were particularly dry (347, 311, 340 $m^3\ s^{-1}$, respectively); only the years 2013 (748 $m^3\ s^{-1}$) and 2014 (634 $m^3\ s^{-1}$) were above the reference mean.

Since 2004, a real-time, multi-sites and high frequency monitoring network, called MAGEST, records four selected parameters, including salinity, to establish a reference database of water-quality of this large fluvio-estuarine system and to address current and future water-quality issues (Etcheber et al. 2011). A consortium of local water authorities (research laboratories, water and river basin agencies, port and energy operators) have joined in the effort to develop this network, which is operated by the laboratory EPOC (University Bordeaux, CNRS). This project started in 2004–2005 with four stations: in the central estuary (Pauillac) and in the Tidal Garonne (Bordeaux, Portets) and Dordogne (Libourne) Rivers (Fig. 1). Today, this network encompasses the whole estuary from the mouth (Le Verdon) to the upper tidal rivers

(Cadillac, Branne). The first sites were equipped of automated systems that measured temperature, salinity, turbidity and dissolved oxygen every 10 min (Etcheber et al. 2011). These systems, installed on floating pontoons, pumped water 1 m below the surface; estuarine waters circulated next thought a measurement chamber. The automated stations needed power supply, and the maintenance was expensive and complicate. Thanks for the technological development, there are now performant multi-sensor probes that simplify fieldwork. Since 2017, all sites of the MAGEST network are equipped by SAMBAT probes (NKE Instrument), which measure the same parameters. To optimize battery life, the measurement frequency is now 20 min. The two systems send data via GSM transmission.

3 Salinity Variability at Different Timescales

Large amplitude tidal waves propagate in the Gironde-Garonne system, with an amplification from the mouth to the upper tidal Garonne River. The tides reach their maximum amplitude (up to 6.3 in spring tides) and current velocities at about Cadillac (Fig. 1) (Bonneton et al. 2015). The strong tidal currents create an intense mixing and salinity profiles are rather homogeneous through the water column in TGR (personal data). Then, only the site localization and the daily tidal range determine salinity.

The neap-spring-neap (NSN) cycle in the second half of August 2017 gives a good illustration of the salinity range along the Gironde-Garonne continuum (Fig. 2)

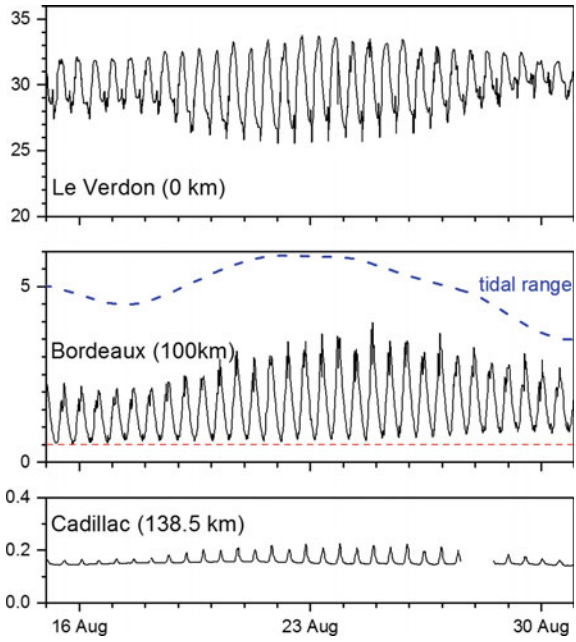

Fig. 2 High-frequency salinity record (every 20 min) at Le Verdon, Bordeaux and at Cadillac during a neap–spring—neap cycle, from August, 14–31, 2017. The dashed curve in the middle panel shows the daily tidal range (in meter). The red line underlines the threshold of salinity intrusion. Numbers in brackets correspond to the distance from the mouth

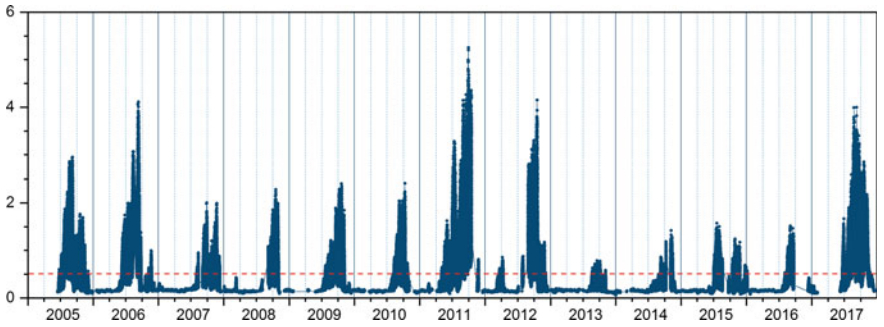

Fig. 3 Multi-annual chronic of salinity, measured every 10 min, at Bordeaux from 2005 to 2017. The red line underlines the threshold of salinity intrusion

during a dry period. At the mouth (Le Verdon), not surprisingly salinity is the highest: raw values are comprised between 25.5 and 33.8. Daily-average salinity varies a little, between 29.5 and 30.8. But the amplitude during a semi-diurnal tide cycle increases from 3.0 m at neap tide to 8.2 at spring tide. At Bordeaux, located 100 km from the mouth, the NSN cycle is always obvious on salinity variability (Fig. 2). But, salinities recorded at Bordeaux are much lower compared to Le Verdon, which is not surprising considering the distance from the mouth. Salinities range between 0.53 and 3.99, depending of tidal range. As a result, daily-mean values (1.19–1.91) are systematically higher to 0.5. At Cadillac, 38.5 km upstream Bordeaux (138.5 km from the mouth), minimum salinity is about 0.14, which corresponds to the baseline of the Garonne River. There is a weak imprint of tidal cycle, with values reaching 0.22 at high tide. These results indicate that the limit of salinity intrusion is probably located between 110 and 130 km from the mouth for this period, which recorded the highest salinities in 2017 whereas the Garonne discharge was below 100 $m^3\ s^{-1}$ over 15 consecutive days.

The MAGEST salinity chronic gives the opportunity to investigate the occurrence of salinity intrusion in the Tidal Garonne River (Fig. 3). There is a clear seasonal pattern in salinity, the lowest values (around 0.14) are always observed during winter. Then, there is usually a progressive increase of salinity from spring to summer, when the highest values are reached annually. The annual salinity maximum may vary from year to year: from 0.78 in 2013 to 5.25 in 2011. Depending of the year, the period during which salinity exceeds 0.5 may last from 2 to 5–6 months.

An atypical feature is the occurrence of salinity peaks beyond the Garonne baseline (0.14) during dry winters (2008, 2011, 2012). Jalón-Rojas et al. (2015) have also reported a concomitant presence of turbidity maximum zone in the Tidal Garonne River during the same periods. Winter events are less frequents and more limited in intensity and duration compared to the summer salt intrusion. However, the winter 2012 is remarkable with salinity exceeding the threshold of 0.5 from March to mid-April.

4 Salinity and Fluvial Discharge

A zoom on the two extreme years, the driest 2013 and the wettest 2011 of the period 2005–2017, is now detailed. As the changes in salinity during a semi-diurnal tide cycle are large (Fig. 2), salinity higher to 0.5 could be only the result of a brief salt incursion at high tides. To assess effective salinity intrusion, the choice in the following figures is to use daily-mean salinity (next salinity*; Fig. 4) to better evidence the link between fluvial discharge and salinity at Bordeaux. In 2011, following two weak floods, fluvial discharge reached early in the season the levels usually observed in summer. As a result, the onset of salinity* above the Garonne baseline occurred also very soon, compared to the other years (Fig. 3). The first saline incursions were measured late May. Then there is a gradual increase of salinity* up to 2.1 following the decrease in discharge and the rhythm of neap-spring tide cycles. This trend is only disrupt during a brief wet event late July. Despite missing data, it is obvious salt

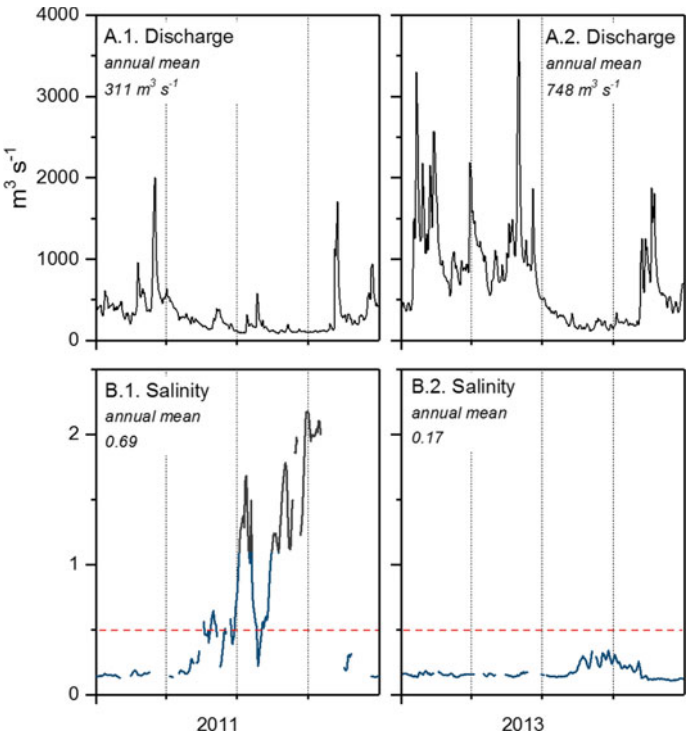

Fig. 4 Comparison of daily mean Garonne discharge (1) and salinity* (2) during 2011 (A) and 2013 (B). Daily mean salinities were calculated based on the MAGEST high-frequency measurements in surface waters. The red line underlines the threshold of salinity intrusion. Numbers in italic correspond to the annual means of discharge and of salinity for 2011 and 2013

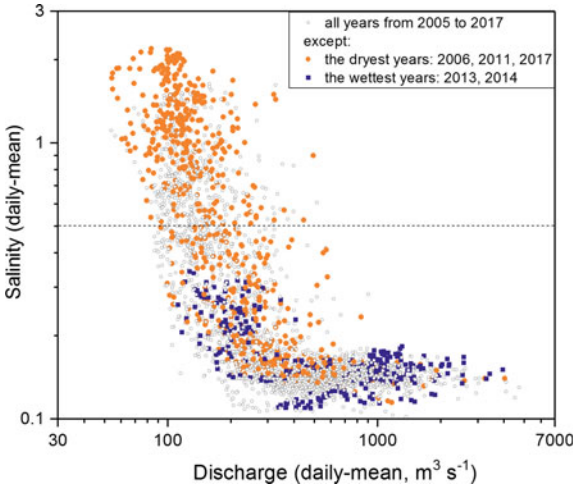

Fig. 5 Salinity* against daily mean Garonne discharge at Bordeaux. Daily mean salinities (salinity*) were calculated based on the MAGEST high-frequency measurements in surface waters. All years are plotted from 2005 to 2017. The wettest years (2013, 2014) are represented by orange circles; the driest (2006, 2011, 2017) by blue squares

was flushed away from the Tidal Garonne River in October 2011 when the Garonne discharge increased durably.

The salinity* record in 2013 is readily different. The first 2013 semester is particularly wet, forbidding the intrusion of saline waters. With the summer decrease of fluvial discharge, there is a slight increase in salinity*. However the combination of this late arrival and of rather high summer flow limits the rise in salinity* at a maximum value of 0.34 at spring tides. The first autumnal flood evacuated almost immediately extra salt.

The comparison of years 2011 and 2013 illustrates the link between discharge and salinity. To precise this relationship, salinity* was plotted against daily mean discharge (Fig. 5). For fluvial discharge higher to 1000 $m^3\ s^{-1}$, salinity* is systematically below 0.16, which corresponds to the baseline level of the Tidal Garonne River. Between 300 and 1000 $m^3\ s^{-1}$, salinity* presents some variability, but most values remain below 0.5. For example, during the wettest years, summer fluvial discharges always stayed above 110–120 $m^3\ s^{-1}$, and salinity* was rather low, never exceeding 0.4. Then, when fluvial discharge decrease from 300 $m^3\ s^{-1}$ to very dry conditions, salinity* rapidly increase above the threshold of 0.5, up to 2.2. This indicates a limit of saline intrusion clearly upstream Bordeaux these years.

5 Occurrence of Saline Intrusion

During the period 2005–2017, wet summers did not favour salt intrusion in the Tidal Garonne River. Salinity* remains always below the limit of 0.5 (Figs. 5 and 6). This may correspond roughly to the past observations. On the opposite, dry summers are associated with a marked presence of salt. In summers 2006 and 2011, salinities*

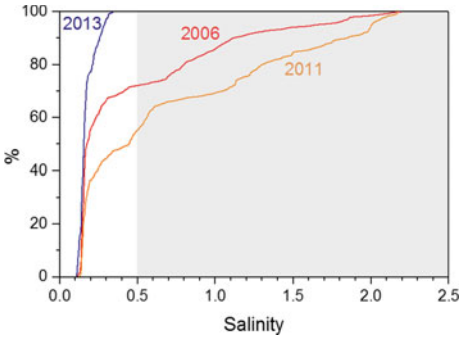

Fig. 6 Cumulative distribution function plot of summer salinity* in 2006, 2011 and 2013. Summer salinity* correspond to data acquired during July, August and September of each considered year

higher than 0.5 represent 29% and 44.5%, respectively, of data acquired from July to September (Fig. 6).

Statistics on summer salinity record shows that, except the two wettest years 2013 and 2014, each year since 2005 has registered salinity intrusion. One could speculate the historical limits of saline intrusion is no more relevant. However, such a conclusion could be hazardous. Indeed the multi-year salinity record at Bordeaux testifies of a large salinity variability during semi-diurnal and neap-spring tide cycles. In addition a brief wet event as observed in 2011 could also temporary reduce salinity to levels below 0.5. Therefore, concluding on a change of the limit of the saline intrusion since early 70s is not possible due to the limited dataset available at that time (Fig. 7).

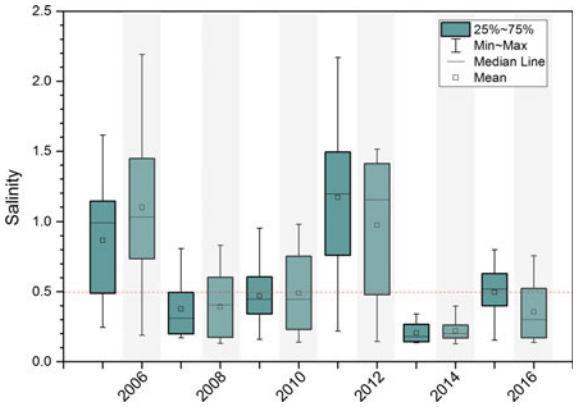

Fig. 7 Box plot of summer salinity*. Summer salinity* correspond to data acquired during July, August and September of each considered year

6 Conclusions

The 14-year multi-sites and high frequency monitoring of salinity along the Gironde-Garonne continuum shows large difference among the instrumented stations depending on their localization. In addition, the time-series highlights strong inter-annual variability in marine intrusion in the Tidal Garonne River. Whereas in winter and spring, daily mean salinity is usually low, summer fluvial discharges usually promote salinity intrusion, amplified by spring tides. In the coming decades, the projected regional decrease in fluvial discharges and sea level rise suggests an increased presence of salt waters in the Tidal Garonne River, at least in summer.

Acknowledgements This network is funded by the following organisms: AEAG (Agence de l'Eau Adour-Garonne), SMIDDEST (Syndicat MIxte pour le Développement Durable de l'ESTuaire de la Gironde), SMEAG (Syndicat Mixte d'Etudes et d'Aménagement de la Garonne), EPIDOR (Etablissement Public Interdépartemental de la Dordogne), EDF, GPMB (Grand Port Maritime de Bordeaux), BORDEAUX METROPOLE, Conseil Régional Aquitaine, Conseil Général de Gironde, IRSTEA, CNRS, and Université de Bordeaux.

References

Allen, G. P. (1972). Etude des processus sédimentaires dans l'estuaire de la Gironde, Thèse Doctorat es Sciences, Université de Bordeaux I, No. 353, 314pp.

Bonneton, P., Bonneton, N., Parisot, J.-P., & Castelle, B. (2015). Tidal bore dynamicus in funnel-shaped estuaries. *Journal of Geophysical Research – Oceans*, #2014JC010267.

Etcheber, H., Schmidt, S., Sottolichio, A., Maneux, E., Chabaud, G., Escalier, J.-M., et al. (2011). Monitoring water quality in estuarine environments: lessons from the MAGEST monitoring program in the Gironde fluvial-estuarine system. *Hydrological and Earth System Sciences, 15*, 831–840.

Jalón-Rojas, I., Schmidt, S., & Sottolichio, A. (2015). Turbidity in the fluvial Gironde Estuary (S.-W. France) based on 10-year continuous monitoring: sensitivity to hydrological conditions. *Hydrological and Earth System Sciences, 19*, 2805–2819.

Jalón-Rojas, I., Sottolichio, A., Hanquiez, V., Fort, A., & Schmidt S. (2018). To what extent multidecadal changes in morphology and fluvial discharge impact tide in a convergent (turbid) tidal river. *Journal of Geophysical Research – Oceans*, #2017JC013466RR.

Savenije, H. H. (1993). Composition and driving mechanisms of longitudinal tidal average salinity dispersion in estuaries. *Journal of Hydrology, 144*, 127–141.

Schmidt, S., Bernard, C., Escalier, J.-M., Etcheber, H., & Lamouroux, M. (2017). Assessing and managing the risks of hypoxia in transitional waters: a case study in the tidal Garonne River (South-West France). *Environmental Science and Pollution Research, 24*, 3251–3259.

Uncles, R. J., & Stephens, J. A. (2011). The effects of wind, runoff and tides on salinity in a strongly tidal sub-estuary. *Estuaries and Coast, 24*, 758–774.

Study on Salinity Intrusion and Mixing Types in a Conceptual Estuary Using 3-D Hydrodynamic Simulation: Effects of Length, Width, Depth, and Bathymetry

Nagendram Veerapaga, Tetsuya Shintani, Gubash Azhikodan and Katsuhide Yokoyama

Abstract In order to discuss the variation of salinity intrusion and mixing types in terms of estuary length, width, depth, and bathymetry, a total of 31 numerical experiments were carried out with a conceptual estuary by using a three-dimensional hydrodynamic simulator, Fantom-Refined. Since sand bars are formed in a river channel, and cyclic variation of the river bed height is found in longitudinal direction, sinusoidal wavy shapes were considered for rough bottom cases to represent the river bed with four different wave amplitudes (0.1, 0.2, 0.3 and 0.4 m) and wavelengths (350, 700, 1400 and 2800 m). In the cases of constant tidal range and discharge with the flat bottom, salinity intrusion length was decreased with increase in estuary length, and mixing condition was changed from salt wedge to well mixed type. On the other hand, salinity intrusion length was increased with increase in width of the channel under constant discharge. Further, the salinity mixing condition was changed from well mixed to salt wedge with the increase in depth of the channel. The salinity intrusion length was increased in the case of funnel shaped estuary when compared with the rectangular shaped estuary. Wavy bottom of the channel had less intrusion length compared with the flat bottom of the constant tidal range and discharge as the bottom friction reduced the velocity of the gravitational flow as well as enhanced vertical mixing. For the constant wavelength, the salinity intrusion length was decreased with increase in wave amplitude. On the other hand, for constant wave amplitude, the salinity intrusion length was increased with increase in wavelength.

N. Veerapaga (✉) · T. Shintani · G. Azhikodan · K. Yokoyama
Department of Civil and Environmental Engineering, Tokyo Metropolitan University, Tokyo, Japan
e-mail: vnagendra@tmu.ac.jp

T. Shintani
e-mail: shintani@tmu.ac.jp

G. Azhikodan
e-mail: gubash@tmu.ac.jp

K. Yokoyama
e-mail: k-yoko@tmu.ac.jp

K. D. Nguyen et al. (eds.), *Estuaries and Coastal Zones in Times of Global Change*, Springer Water,
https://doi.org/10.1007/978-981-15-2081-5_2

Keywords Salinity intrusion · Mixing types · Wavy bottom · Conceptual estuary · Numerical simulation · Fantom-Refined

1 Introduction

Salinity intrusion and mixing are the major factors which influence the existence and distribution of the organisms in estuaries. Azhikodan and Yokoyama (2014) investigated the effect of salinity mixing and estuarine turbidity maximum (ETM) on the state of phytoplankton. They found that the growth of phytoplankton was high during the neap tide when the estuary was salt wedge and low ETM. Therefore, understanding the mechanism that governs the tidal circulation and salinity transport is of great importance for coastal engineering, aquaculture, and water security (Xing et al. 2012). The spatial and temporal distribution of salinity can significantly affects the residual transport of sediments, pollutants and waterborne materials through gravitational and tidal circulation (Wei et al. 2016). Salinity stratification will lead to the bottom water hypoxia in shallow estuaries, which causes the unavailability of dissolved oxygen for the living organisms. Accurate prediction of the salinity stratification is essential to estimate the bottom water hypoxia in the shallow estuaries (Xu et al. 2008).

The salinity intrusion and mixing type in the estuary are mainly affected by the tidal range and freshwater discharge. The estuaries are classified into well mixed, partially mixed and salt wedge/stratified depending on the vertical distribution of salinity along the estuary. They are also classified into microtidal, mesotidal, macrotidal, and hypertidal depending on the tidal range. An estuary with strong tidal flow and weak freshwater discharge tend to the well mixed type, whereas the estuary with weak tidal flow and strong freshwater discharge tend to the salt wedge type. The partially mixed estuary is the transition between the well mixed and salt wedge estuaries. In addition, the mixing types in the estuaries can be classified using the empirical equations such as the stratification number (Prandle 1985) and the Froude number (Jay and Smith 1988). However, these classifications mainly derived for narrow and shallow estuaries, it is difficult classify the estuaries based on these simple classifications.

The estuary length, width, depth, and bathymetry also have significant effect on the salinity intrusion and mixing. Hence, it is important to understand the effect of these features on salinity intrusion and mixing condition of an estuary. In order to understand the behavior of salinity intrusion and mixing types, many field investigations (New et al. 1986; Schroder and Siedler 1989; Nepf and Geyer 1996; Geyer et al. 2000; Schoellhamer 2000; Bowen and Geyer 2003; Azhikodan and Yokoyama 2015, 2018), analytical models (Stigebrandt 1981; Prandle 1985; Brockway et al. 2006; Zhang et al. 2010; Zhang et al. 2011) and numerical models (Hamilton 1975; Oey et al. 1985; Kurup et al. 1998; Warner et al. 2005; Xu et al. 2008; Li and Li 2011; Barcena et al. 2016; Wan and Wang 2017) were employed in real estuaries.

New et al. (1986) predicted the generation and propagation of internal waves and mixing in a partially stratified estuary using field measurements. Nepf and Geyer

(1996) investigated the intra–tidal variations in stratification and mixing in the Hudson estuary using field observations. Schoellhamer (2000) investigated the effect of salinity, bottom topography, and tides on location of estuarine turbidity maximum (ETM) in northern San Francisco Bay, California using the field measurements. Azhikodan and Yokoyama (2015, 2018) carried out intensive field measurements in macrotidal Chikugo River estuary, Japan to understand the upward movement of suspended sediment transport and formation of fluid mud layer. Although field investigations are effective methods to understand the behavior of salinity intrusion and mixing condition, they are time consuming, expensive and labor intensive.

Stigebrandt (1981) developed an analytical model for the estuarine circulation in deep, strongly stratified Fjords. Prandle (1985) developed an analytical solution to find out the salinity intrusion and stratification patterns in narrow tidal estuaries. Brockway et al. (2006) developed an analytical solution for the salt intrusion in a well mixed, funnel–shaped estuary whose cross sectional area decreases exponentially with distance in—land and applied it to the Incomati estuary, Mozambique. Zhang et al. (2010) developed an analytical solution to find the relationship between the discharge and salinity intrusion in Modaomen waterway, Pearl River estuary, China. Sometimes, the analytical modelling becomes very complex due to the non-linearity of the model.

Numerical models are the most effective tools due to its capability to reproduce different phenomenon with high spatial and temporal resolution. Xu et al. (2008) investigated the variation of current circulation, salt intrusion, and wind conditions in the Pamlico River estuary, North Carolina, USA using a three–dimensional numerical model. Li and Li (2011) investigated the effect of axial winds on stratification and circulation in partially mixed estuary of Chesapeake Bay, North America using a three–dimensional hydrodynamic model. Barcena et al. (2016) developed a methodology to determine the spatial and temporal evolution of stratification in estuaries driven by astronomical tides and river discharges using a three–dimensional hydrodynamic model in the Suances estuary, Spain. However, their results include a combination of several factors such as geometric effects, freshwater inflow, tidal variation, and weather forcing affecting the behavior of the salinity intrusion. Veerapaga et al. (2018) investigated the effect of discharge and tidal flux on salinity intrusion and mixing types in a conceptual estuary using three—dimensional hydrodynamic model. So far, there are few studies focused on the individual effect of estuary length, width, depth, and bathymetry on salinity intrusion and mixing types in more generic environments. Hence, it is essential to understand the effect of basic features (estuary length, width, depth, and bathymetry) of an estuary on salinity intrusion and mixing types.

In the previous study (Veerapaga et al. 2018) investigated the effect of discharge and tidal range on salinity intrusion and mixing condition. In this study, a simple conceptual estuary was constructed to investigate the effect of the estuary length, width, depth, and bathymetry on the mixing and salinity intrusion by using a numerical model. First, the computational methods, conditions, and important parameters were explained initially. Second, the salinity intrusion length (SIL) as a function of the Estuary length, width, and depth was quantified. Additionally, the effect of the

channel shape and sinusoidal bathymetry on salinity intrusion and mixing type was investigated.

2 Methodology

(1) Model Description

Numerical investigation was carried out using a three–dimensional hydrodynamic simulator, Fantom–Refined (Shintani 2017). Basic equations utilized in the model are the equation of continuity,

$$\frac{\partial u}{\partial x}+\frac{\partial v}{\partial y}+\frac{\partial w}{\partial z}=0 \tag{1}$$

where, u, v and w are the velocities in x, y and z directions.

The three–dimensional Navier–Stokes equations with incompressible and Boussinesq approximations,

$$\frac{\partial u}{\partial t}+u\frac{\partial u}{\partial x}+v\frac{\partial u}{\partial y}+w\frac{\partial u}{\partial z}-fu=-\frac{1}{\rho_0}\frac{\partial p}{\partial x}+\frac{\partial}{\partial x}\left(v_H\frac{\partial u}{\partial x}\right)+\frac{\partial}{\partial y}\left(v_H\frac{\partial u}{\partial y}\right)+\frac{\partial}{\partial z}\left(v_V\frac{\partial u}{\partial z}\right) \tag{2.1}$$

$$\frac{\partial v}{\partial t}+u\frac{\partial v}{\partial x}+v\frac{\partial v}{\partial y}+w\frac{\partial v}{\partial z}+fv=-\frac{1}{\rho_0}\frac{\partial p}{\partial y}+\frac{\partial}{\partial x}\left(v_H\frac{\partial v}{\partial x}\right)+\frac{\partial}{\partial y}\left(v_H\frac{\partial v}{\partial y}\right)+\frac{\partial}{\partial z}\left(v_V\frac{\partial v}{\partial z}\right) \tag{2.2}$$

$$\frac{\partial w}{\partial t}+u\frac{\partial w}{\partial x}+v\frac{\partial w}{\partial y}+w\frac{\partial w}{\partial z}=-\frac{1}{\rho_0}\frac{\partial p}{\partial z}+\frac{\partial}{\partial x}\left(v_H\frac{\partial w}{\partial x}\right)+\frac{\partial}{\partial y}\left(v_H\frac{\partial w}{\partial y}\right)+\frac{\partial}{\partial z}\left(v_V\frac{\partial w}{\partial z}\right)-\frac{g}{\rho_0}(\rho_0+\rho) \tag{2.3}$$

where, ρ_0 is the reference density, $\rho_0+\rho$ is the density, $f = 2\omega sin\varphi$: is the Coriolis coefficient, φ is the latitude, ω is the angular velocity, v_H is the horizontal eddy viscosity coefficient and v_V is the vertical eddy viscosity coefficient.

The transport equations for salinity and temperature,

$$\frac{\partial S}{\partial t}+u\frac{\partial S}{\partial x}+v\frac{\partial S}{\partial y}+w\frac{\partial S}{\partial z}=\frac{\partial}{\partial x}K_x\left(\frac{\partial S}{\partial x}\right)+\frac{\partial}{\partial y}K_y\left(\frac{\partial S}{\partial y}\right)+\frac{\partial}{\partial z}K_z\left(\frac{\partial S}{\partial z}\right) \tag{2.4}$$

$$\frac{\partial T}{\partial t} + u\frac{\partial T}{\partial x} + v\frac{\partial T}{\partial y} + w\frac{\partial T}{\partial z} = \frac{\partial}{\partial x}K_x\left(\frac{\partial T}{\partial x}\right) + \frac{\partial}{\partial y}K_y\left(\frac{\partial T}{\partial y}\right) + \frac{\partial}{\partial z}K_z\left(\frac{\partial T}{\partial z}\right) \tag{2.5}$$

where, S is the salinity, T is the temperature, K_x, K_y and K_z are the diffusion coefficients.

The governing equations were discretized based on a collocated finite volume method. Temporal derivatives were discretized using the second–order Adams–Bashforth method for explicit terms. Surface elevation and vertical diffusion was computed using the second–order theta–method. The advection terms were discretized by third–order ULTIMATE–QUICKEST scheme. The hydrostatic components of the simulator were used in this study. The GLS turbulence closure model was used for the calculation of vertical eddy viscosity and diffusion coefficients (Shintani 2016). Bottom friction was computed by Drag law with a drag coefficient of 0.0026. The partial step method proposed by Adcroft et al. (1997) was used to represent the sub grid scale bed topography.

This model was used by Matsumura et al. (2017) in earlier study to investigate the salinity intrusion and freshwater dispersion in the Chikugo River estuary and the Ariake sea inter–tidal mudflat. A good agreement was found between the measured and computed data.

(2) **Analysis**

(a) **Mixing types**

There are several methods to classify the mixing types with varying salinity in an estuary. In this study, salinity interface gradient (*SIG*), which is defined as the slope of the 10 isohaline was used to classify the mixing conditions in the estuary (Azhikodan et al. 2014; Azhikodan and Yokoyama 2015).

$$SIG = \frac{H}{X_b - X_s} \tag{3}$$

where, H is the water depth near the area where salinity is 10, X_b is the distance from the mouth of the estuary to the position where the bottom salinity is 10, and X_s is the distance from the estuary mouth to the position where the surface salinity is 10 (Fig. 1).

When $H = 5$ m, if $SIG \geq 0.005$, then the condition was defined as well mixed. If $0.005 > SIG \geq 0.001$, then the condition was defined as partially mixed. $SIG < 0.001$ was defined as salt wedge/stratified.

(b) **Salinity intrusion length (SIL)**

In this study, salinity intrusion length (SIL) was defined as the distance from the estuary mouth to the tip of the salt wedge at which the salinity has reached 10 at the bottom (Azhikodan et al. 2014) (Fig. 1).

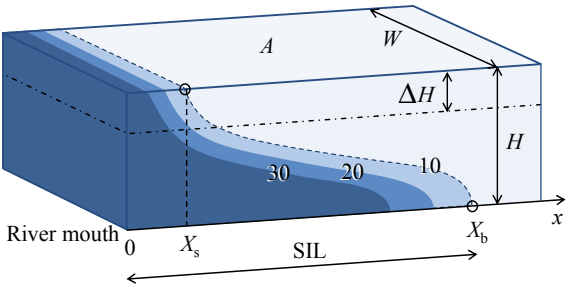

Fig. 1 Schematic representation of salinity distribution in an estuary

(3) Conceptual Estuary Model

The Chikugo River estuary, which has a length of 23 km and the effective ocean width of 20 km, was taken as a reference area to construct the conceptual estuary model. Hence, the conceptual estuary model was constructed with a simple straight channel length of 24 km and the ocean width of 24 km. Length of the ocean boundary from the river mouth was analysed (Veerapaga et al. 2018) and finally it was taken as 24 km.

A minimum grid size of 20 m was considered for the simulations in the estuary area (Fig. 2). From the estuary mouth, the grid size was changed to 20, 40, 80, and 160 m for every 320 m up to 1.28 km towards the ocean. Outside of their grids, the grid size was changed to 320 m up to the 6 km, 640 m up to the 9 km and 1280 m up to the ocean boundary. A non–uniform grid size of 0.25 to 1 m was taken in the

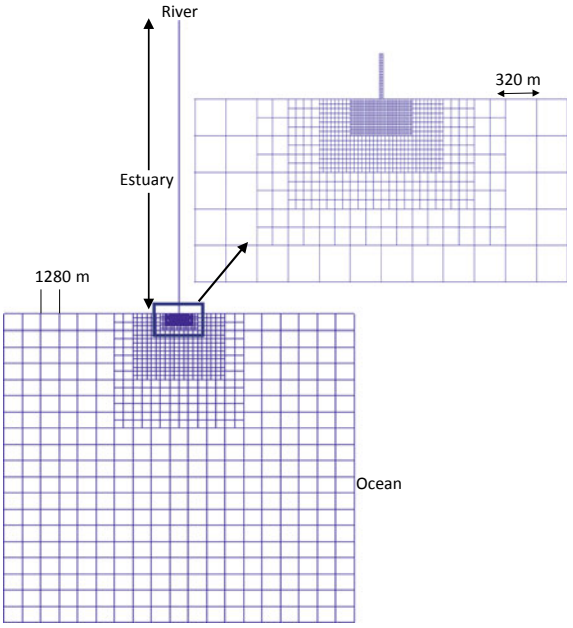

Fig. 2 Grid resolution at the mouth of the conceptual estuary

vertical direction. The total number of vertical grids was 40 and the number of active grids depends on the water depth.

The boundary conditions used in the system were open ocean boundary and river boundary. At the open ocean boundary, the tidal elevation and salinity of 30 were specified as the boundary condition. For the initial condition, the ocean salinity was taken as 30. The salinity from the estuary mouth to the 600 m upstream linearly varied from 30 to 0 and the rest of the estuary taken as 0. The temperature of the ocean and the estuary was set to 25 °C. The numerical experiments always start from the rest (zero velocity).

(4) Computational Cases

Numerical experiments were conducted with different combinations of the estuary length (12, 24, 36, and 48 km), width (40, 80, and 160 m), and depth (2–7 m) for a constant river discharge and tidal range for a duration of five days (Table 1). Since sand bars are formed in a river channel, and cyclic variation of the river bed height is found in longitudinal direction, sinusoidal wavy shapes were considered for rough bottom cases to represent the river bed with four different wave amplitudes and wavelengths. Further, the effect of channel shape on salinity intrusion and mixing type was investigated with (i) constant width of 1000 m (rectangular shape) and (ii) varied width from 2000 to 40 m from river mouth to the upstream (V/funnel shape) as shown in Fig. 3.

Table 1 Description of computational cases for the conceptual estuary

Case	Width (m)	Length (km)	Depth (m)	Discharge (m^3/s)	Tidal range (m)	Sinusoidal wavy bottom	
						Wavelength (m)	Amplitude (m)
1	40	12, 24, 36, 48	4	25	1	–	–
2	40, 80, 160	24	4	25	1	–	–
3	40	24	2, 3, 4, 5, 6, 7	25	1	–	–
4	1000	24	4	25	1	–	–
5	40–2000	24	4	25	1	–	–
6	40	24	4	25	1	350	0.1, 0.2, 0.3, 0.4
7	40	24	4	25	1	700	0.1, 0.2, 0.3, 0.4
8	40	24	4	25	1	1400	0.1, 0.2, 0.3, 0.4
9	40	24	4	25	1	2800	0.1, 0.2, 0.3, 0.4

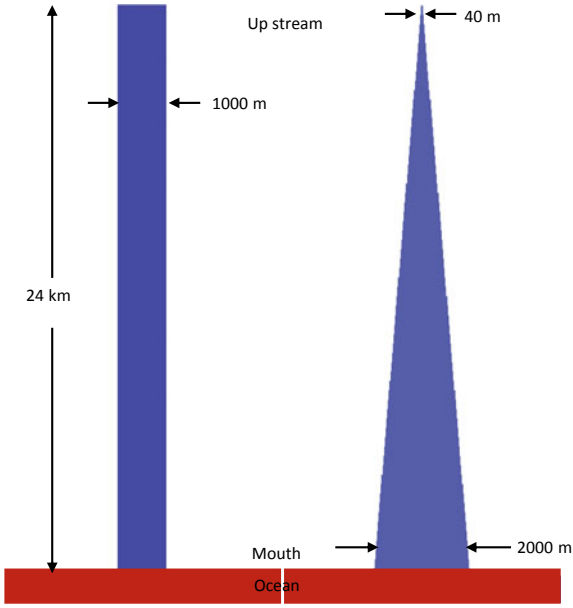

Fig. 3 Comparison of variation of channel shape for conceptual estuary

3 Results and Discussion

(1) Effect of Estuary Length

Estuary length has considerable effect on the salinity intrusion as well as mixing types. With increase in estuary length, salinity intrusion was reduced and mixing condition was changed from salt wedge to the well mixed. Figure 4a–d shows the relationship between the estuary lengths, salinity intrusion, and mixing types for a constant discharge of 25 m^3/s and tidal range of 1 m. For the estuary of 12 km length, salinity intrusion was reached to the upstream and mixing condition was salt wedge type (Fig. 4a). Salinity intrusion was reached to 12 km from estuary mouth in the case of 24 km estuary length and it was partially mixed type (Fig. 4b). For 36 km estuary length, salinity intrusion was reduced to 10.5 km and mixing condition was well mixed type (Fig. 4c). For 48 km estuary length, SIL was reached to 7.5 km (Fig. 4d) and it was well mixed type.

The influence of freshwater became stronger with increase in length of the estuary than the tidal and gravitational circulation due to increase in freshwater volume. It reduced the salinity intrusion as well as enhanced the vertical mixing. Hence, when constructing a dam or barrage in lower reaches of river, the distance from the ocean must be considered to avoid the salinity intrusion to the upstream.

(2) Effect of Estuary Width

Figure 5a–c shows the effect of estuary width on salinity intrusion and mixing types for a constant discharge and tidal range. For a constant discharge of 25 m^3/s and tidal

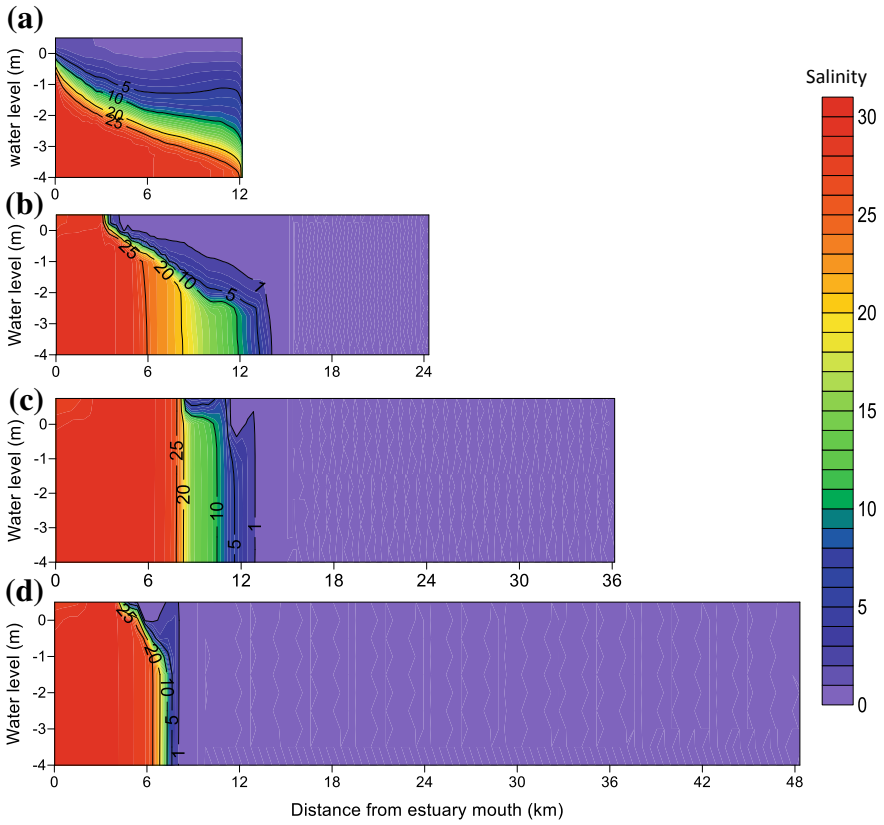

Fig. 4 Vertical distribution of salinity for **a** 12 **b** 24, **c** 36 and **c** 48 km estuary length

range of 1 m, the salinity intrusion was reached to 12 km for the 40 m width of the channel and it was partially mixed type (Fig. 5a). The SIL reached to 22 km for the 80 m estuary width and the mixing condition changed to salt wedge. For 160 m width of the channel, salinity intrusion was reached to the upstream and mixing condition was highly stratified (Fig. 5b, c).

Salinity intrusion was increased and mixing condition changed from partially mixed to salt wedge with increase in width of the estuary. The strength of the freshwater decreased with increase in estuary width as it decreased the discharge per unit width. There was not enough turbulance to mix the salinity in the water column. The gravitational flux relatively become dominant than the freshwater and lead to the two–layered flow that extended the length of salinity intrusion. Hence, proper management of the river banks is necessary to avoid the excessive salinity intrusion.

(3) **Effect of Estuary Depth**

The variation of salinity intrusion for different average depths of channel (2–7 m) with a constant discharge of 25 m^3/s and tidal range of 1 m was shown in Fig. 6a–f.

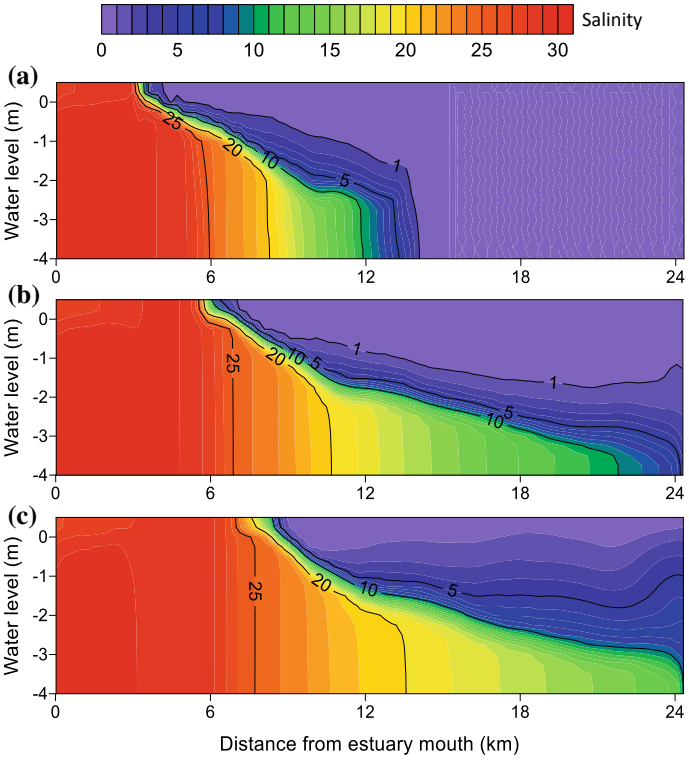

Fig. 5 Vertical distribution of salinity for **a** 40 **b** 80 and **c** 160 m width of estuary

The salinity intrusion was reached to 5 km from the estuary mouth for depth of 2 m and it was well mixed type (Fig. 6a). The salinity intrusion was increased to 7 km for the depth of 3 m. However, the mixing condition did not change (Fig. 6b). For the depth of 4 m, the salinity intrusion was reached to the 12 km and the mixing condition changed to the partially mixed type (Fig. 6c). For 5 m deep, the salinity intrusion was reached to the upstream and it was completely salt wedge type (Fig. 6d). For the 6 and 7 m depth of estuary, the salinity was reached to the upstream and started to re-circulate by mixing with the fresh water and the estuary was highly stratified (Fig. 6e, f). It was clear that, the salinity intrusion was increased and the mixing condition was changed from well mixed to the salt wedge with increase in depth of the estuary.

The salinity intrusion was reached steady state in case of 2, 3, and 4 m depths of the estuary (Fig. 6a–c). Whereas for the 5, 6, and 7 m depths of the estuary, salinity intrusion did not reached the steady state and it was progressing. For the 5 m deep, SIL reached upstream and progressing (Fig. 6d) and salinity was started re–circulation by mixing with the fresh water in case of 6 and 7 m depths of the estuary (Fig. 6e, f).

The relative strength of the freshwater and tidal flow became small with increase in depth of the estuary. There was not enough turbulence to mix the salinity in the water

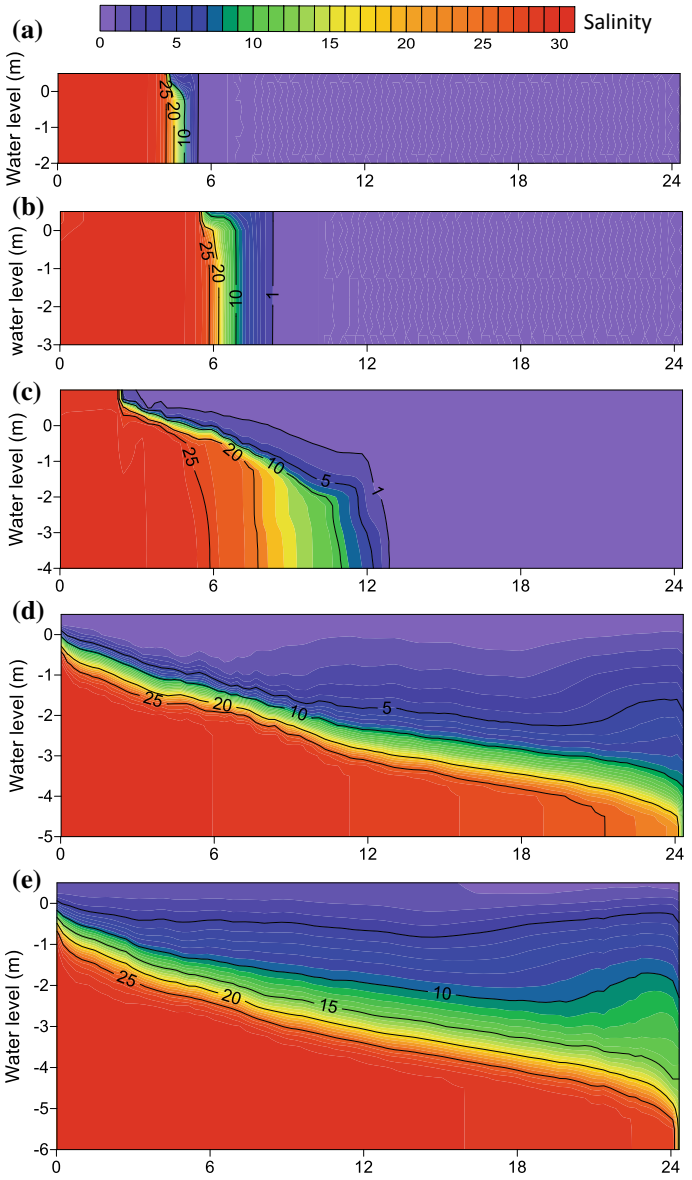

Fig. 6 Vertical distribution of salinity for **a** 2 **b** 3 **c** 4 **d** 5 **e** 6 and **f** 7 m depth of estuary

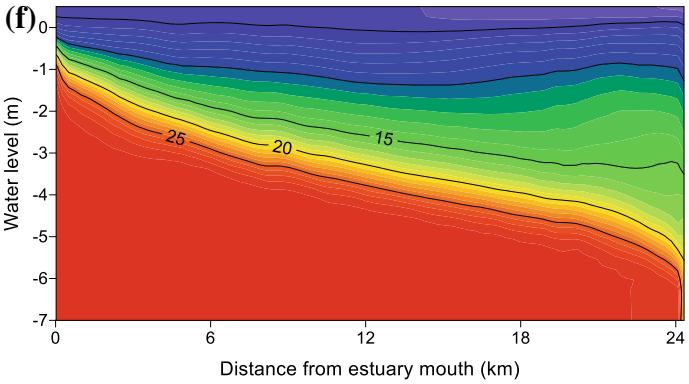

Fig. 6 (continued)

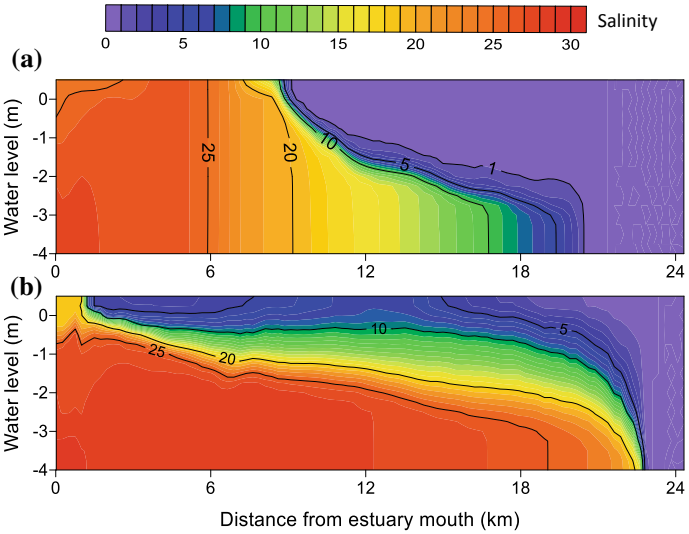

Fig. 7 Vertical distribution of salinity for **a** rectangle, and **b** V/funnel shaped estuary

column that created the density gradient in the estuary. So that the gravitational flux became dominant, which created the two–layered flow and lead to the stratification. Hence, it is important to know the effect of the depth on salinity intrusion, so that the dredging of the channel can be carried out effectively.

(4) **Effect of Channel Shape**

Rectangular and V/funnel shaped estuaries were considered in order to understand the effect of shape of the estuary on salinity intrusion and mixing condition. Figure 7a, b shows the effect of estuary shape on salinity intrusion and mixing type for a constant discharge and tidal range. For a constant discharge 250 m^3/s and tidal range of 1 m,

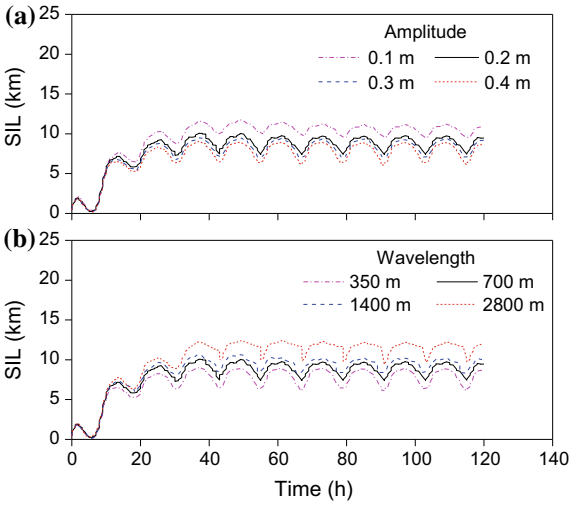

Fig. 8 Temporal variation of salinity intrusion length for **a** wavelength of 350 m, and **b** wave amplitude of 0.4 m

rectangular shaped estuary has the salinity intrusion of 20 km and mixing condition was salt wedge (Fig. 7a). The salinity intrusion was reached to the upstream (24 km) and mixing condition was highly stratified in the case of V/funnel shaped estuary (Fig. 7b). Even though, both the estuaries have the same estuary volume, the salinity intrusion and mixing condition was different. The rectangular shaped estuaries have less salinity intrusion compared with the funnel shaped estuaries.

The discharge per unit width is constant along the estuary for rectangular shaped estuary. Whereas for the funnel shaped estuary, the discharge per unit width decreases towards the mouth of the estuary compared to the upstream due to increase in cross–sectional area. There was more salinity intrusion at the mouth and less at the upstream, which lead to increase in gravitational flux (density driven flow) at downstream side of the estuary and created two–layered flow that made the estuary highly stratified and the salinity intrusion longer.

(5) Effect of Sinusoidal Wavy Bottom

Sinusoidal wave with different wave amplitudes and wavelengths was considered to understand the effect of bathymetry of the estuary on salinity intrusion and mixing types. Salinity intrusion and mixing condition for 350 m wavelength with four different wave amplitudes (0.1–0.4 m) was shown in Figs. 8a and 9. The salinity intrusion was decreased with increase in wave amplitude from 0.1 to 0.4 m, salinity intrusion was reached to 11 km for 0.1 m, whereas SIL was around 8.5 km for 0.4 m (Fig. 8a). With increase in wave amplitude, the bottom friction increased that reduced the salinity intrusion. There was not much change in the mixing condition, it was partially mixed for 0.1 m wave amplitude and it changed a little towards well mixed for the 0.4 m wave amplitude (Fig. 9).

Salinity intrusion and mixing condition for 0.4 m wave amplitude with four different wavelengths (350, 700, 1400 and 2800 m) was shown in Figs. 8b and 10. The

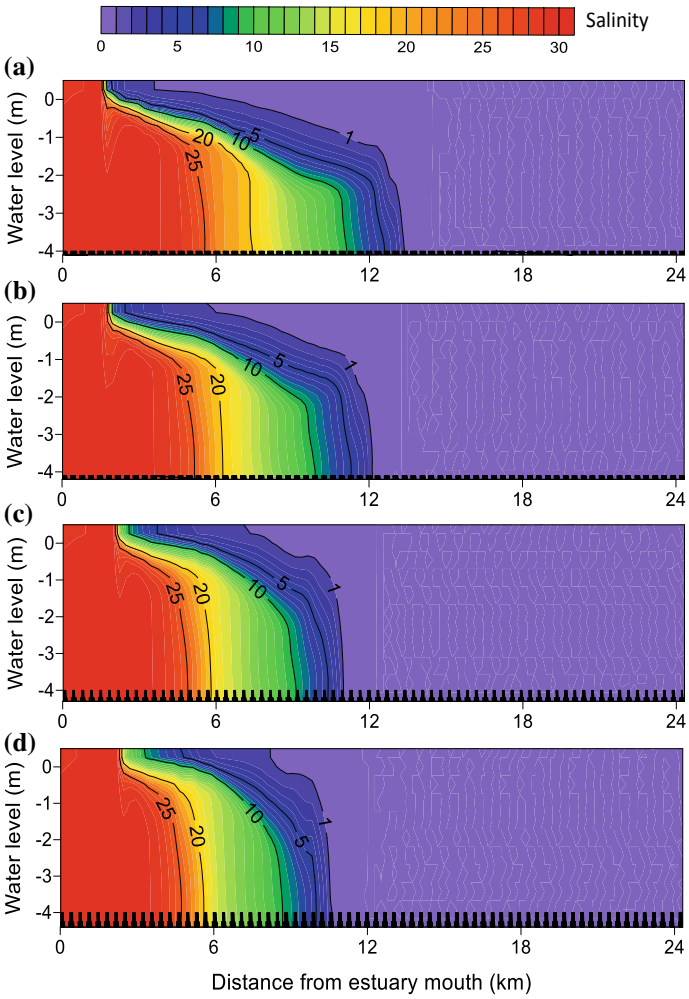

Fig. 9 Vertical distribution of salinity for **a** 0.1 **b** 0.2 **c** 0.3 and **d** 0.4 m wave amplitude for 350 m of wavelength of estuary

salinity intrusion was increased with increase in wavelength from 350 to 2800 m, SIL was around 8.5 km for 350 m, whereas it was reached to 13 km for 2800 m wave length (Fig. 8b). With increase in wavelength, the bottom friction was reduced that contributed to increase in salinity intrusion. The mixing condition was changed from partially mixed for 350 m to salt wedge for the 2800 m (Fig. 10).

The wavy bottom has less salinity intrusion as compared with the flat bottom of the estuary. The bottom friction reduced the velocity of the gravitational flow as well as enhanced vertical mixing for the wavy bottom. There was salinity tapping in the bottom hollows of the estuary during the ebb tide which contributed to the

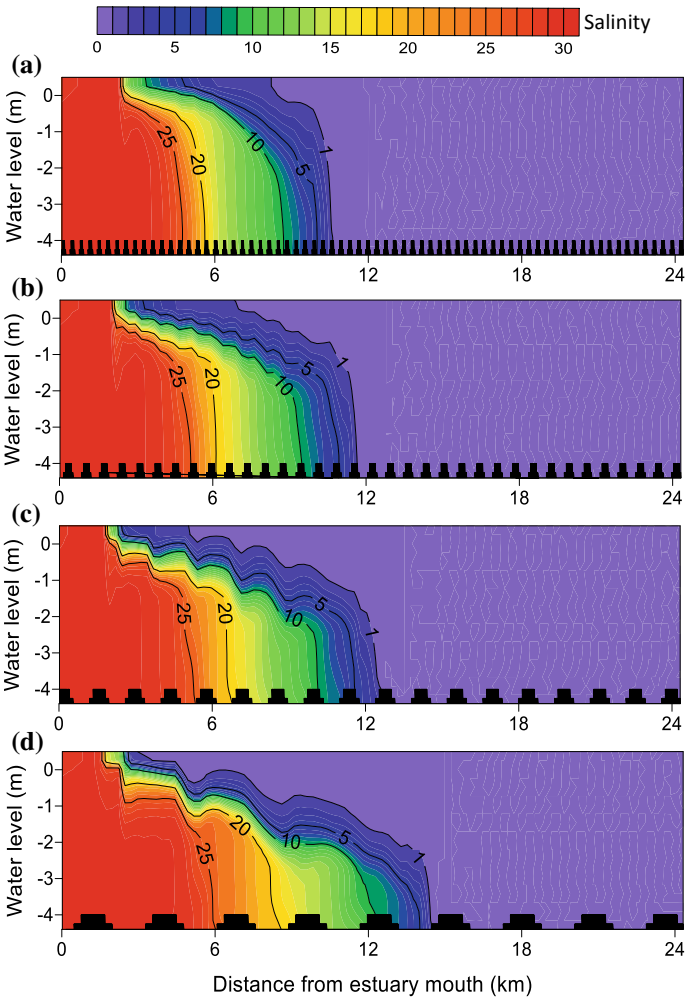

Fig. 10 Vertical distribution of salinity for **a** 350 **b** 700 **c** 1400 and **d** 2800 m wavelength for 0.4 m wave amplitude of estuary

vertical mixing. The bathymetry of the estuary has significant effect on the salinity intrusion and mixing. Hence, it is important to consider the bathymetry for numerical simulations.

4 Conclusions

Effect of the estuary length, width, depth, and bathymetry on the salinity intrusion and mixing type were carried to using the numerical model. For the cases of constant discharge and tidal range with the flat bottom, salinity intrusion length was decreased with increase in length, and mixing condition was changed from salt wedge at 12 km to well mixed type at 48 km length of the estuary. On the other hand, salinity intrusion length was increased with increase in width of the channel and the mixing condition was changed from partially mixed for 40 m width to the highly stratified for 160 m width.

The salinity intrusion length was increased with increase in depth of the channel and mixing condition was changed from well mixed to salt wedge with the increase in depth of the channel. The salinity intrusion length was increased in the case of funnel–shaped estuary compared to the rectangular shaped estuary. The mixing condition was salt wedge for the funnel–shaped estuary and it was partially mixed for the rectangular shaped estuary.

Wavy bottom of the channel had less salinity intrusion length compared with the flat bottom of the constant tidal range and discharge as the bottom friction reduced the velocity of the gravitational flow as well as enhanced vertical mixing. In the case of the wavy bottom, there was salinity tapping in the bottom hollows of the estuary during the ebb tide. For the constant wavelength, the salinity intrusion length was decreased with increase in wave amplitude. On the other hand, for constant wave amplitude, the salinity intrusion length was increased with increase in wavelength.

This study explored the effect of the each basic feature of the estuary on salinity intrusion and mixing conditions with the simple conceptual estuary. Even though the effects of estuary length, width, depth, and bathymetry were explored in this study, there are other predominant factors such as meandering of the channel and weather forcing, which influence the salinity intrusion and mixing in the estuary and that will be explored in the future studies.

Acknowledgements This research was supported in part by the River Fund of the River Foundation, Japan and the project entitled: "Study on guerrilla rainstorm, flood, and water pollution in megacity urban watersheds–Countermeasures against megacity urban water–related disasters bipolarized by climate change" funded by the Tokyo Metropolitan Government. The authors express special gratitude to the Tokyo Metropolitan Government for supporting Ph.D. study of Nagendram Veerapaga by the Tokyo Human Resource Fund for City Diplomacy Scholarship.

References

Adcroft, A., Hill, C., & Marshall, J. (1997). Representation of topography by shaved cells in a height coordinate ocean model. *Monthly Weather Review, 125,* 2293–2315.

Azhikodan, G., & Yokoyama, K. (2014). Estuarine mixing and spatial distribution of phytoplankton in the Chikugo river estuary. *Journal of Japan Society of Civil Engineers, Ser. B2 (Coastal Engineering), 70*(2), 1081–1085.

Azhikodan, G., & Yokoyama, K. (2015). Temporal and spatial variation of mixing and movement of suspended sediment in the macrotidal Chikugo River estuary. *Journal of Coastal Research, 31*(3), 680–689.

Azhikodan, G., & Yokoyama, K. (2018). Sediment transport and fluid mud layer formation in the macro-tidal Chikugo river estuary during a fortnightly tidal cycle. *Estuarine Coastal and Shelf Science, 202,* 232–245.

Azhikodan, G., Yokoyama, K., & Morimura, Y. (2014). Effect of mixing on turbidity maximum movement during semilunar tidal cycle in the Chikugo River estuary. *Journal of Japan Society of Civil Engineers, Ser. B1 (Hydraulic Engineering), 70*(4), 37–42.

Barcena, J. F., Garcia-Alba, J., Garcia, A., & Alvarez, C. (2016). Analysis of stratification patterns in river-influenced mesotidal and macrotidal estuaries using 3D hydrodynamic modelling and K-means clustering. *Estuarine Coastal and Shelf Science, 181,* 1–13.

Bowen, M. M., & Geyer, W. R. (2003). Salt transport aand the time-dependent salt balance of a partially stratified estuary. *Journal of Geophysical Research, 108*(C5), 3158. https://doi.org/10.1029/2001JC001231.

Brockway, R., Bowers, D., Hoguane, A., Dove, V., & Vassele, V. (2006). A note on salt intrusion in funnel-shaped estuaries: Application to the Incomati estuary, Mozambique. *Estuarine Coastal and Shelf Science, 66,* 1–5.

Geyer, W. R., Trowbride, J. H., & Bowen, M. M. (2000). The dynamics of a partially mixed estuary. *Journal of Physical Oceanography, 30,* 2035–2048.

Hamilton, P. (1975). A numerical model of the vertical circulation of tidal estuaries and its application to the Rotterdam waterway. *Geophysical Journal of Royal Astronomical Society, 40,* 1–21.

Jay, D. A., & Smith, J. D. (1988). Residual circulation in and classification of shallow, stratified estuaries. In J. Dronkers & W. van Leussen (Eds.), *Physical processes in Estuaries* (pp. 21–41). Berlin: Springer.

Kurup, G. R., Hamilton, D. P., & Patterson, J. C. (1998). Modelling the E ect of seasonal flow variations on the position of salt wedge in a microtidal estuary. *Estuarine Coastal and Shelf Science, 47,* 191–208.

Li, Y., & Li, M. (2011). Effects of winds on stratification and circulation in a partially mixed estuary. *Journal of Geophysical Research, 116,* C12012.

Matsumura, K., Morimura, Y., Shintani, T., & Yokoyama, K. (2017). Three-dimensional numerical simulation of salinity intrusion in Chikugo river estuary. *Journal of Japan Society of Civil Engineers, Ser. B1 (Hydraulic Engineering), 73*(4), 1039–1044.

Nepf, H. M., & Geyer, W. R. (1996). Intratidal variations in stratification and mixing in the Hudson estuary. *Journal of Geophysical Research, 101*(C5), 12079–12086.

New, A. L., Dyer, K. R., & Lewis, R. E. (1986). Predictions of the generation and propagation of internal waves and mixing in a partially stratified estuary. *Estuarine Coastal and Shelf Science, 22,* 199–214.

Oey, L. Y., Mellor, G. L., & Hires, R. I. (1985). A three-dimensional simulation of the Hudson-Raritan estuary. Part I: Description of the model and model simulations. *Journal of Physical Oceanography, 15,* 1676–1692.

Prandle, D. (1985). On salinity regimes and the vertical structure of residual flows in narrow tidal estuaries. *Estuarine Coastal and Shelf Science, 20,* 615–635.

Schoellhamer, D. H. (2000). Influence of salinity, bottom topography, and tides on locations of estuarine turbidity maxima in northern San Francisco Bay. *Proceedings in Marine Science, 3,* 343–357.

Schroder, M., & Siedler, G. (1989). Turbulent momentum and salt transport in the mixing zone of the Elbe estuary. *Estuarine Coastal and Shelf Science, 28,* 615–638.

Shintani, T. (2016). Performance of GLS turbulence closure model implemented in 3D unstructured hydrodynamic simulator. *Journal of Japan Society of Civil Engineers Ser. B1 (Hydraulic Engineering), 72*(4), 667–672.

Shintani, T. (2017). An unstructured-Cartesian hydrodynamic simulator with local mesh refinement technique. *Journal of Japan Society of Civil Engineers, Ser. B1 (Hydraulic Engineering), 73*(4), 967–972.

Stigebrandt, A. (1981). A mechanism governing the estuarine circulation in deep, strongly stratified fjords. *Estuarine Coastal and Shelf Science, 13,* 197–211.

Veerapaga, N., Shintani, T., Azhikodan, A., & Yokoyama, K. (2018). Numerical investigation on effects of discharge, tidal range and bathymetry of estuary on type and length of salinity intrusion. *Journal of Japan Society of Civil Engineers, Ser. B1 (Hydraulic Engineering), 74*(4), 781–786.

Wan, Y., & Wang, Li. (2017). Numerical investigation of the factors influencing the vertical profiles of current, salinity, and SSC within a turbidity maximum zone. *International Journal of Sediment Research, 32,* 20–33.

Warner, J. C., Geyer, W. R. and Lerczak, J. A. (2005). Numerical modelling of an estuary: A comprehensive skill assessment. *Journal of Geophysical Research*, *110* (C05001). https://doi.org/10.1029/2004jc002691.

Wei, X., Schramkowski, G. P., & Schuttelaars, H. M. (2016). Salt dynamics in well-mixed estuaries: Importance of advection by tides. *Journal of Physical Oceanography, 46,* 1457–1475.

Xing, Y., Ai, C., & Jin, S. (2012). A three-dimensional hydrodynamic and salt transport model of estuarine circulation with an application to a macrotidal estuary. *Applied Ocean Research, 39,* 53–71.

Xu, H., Lin, J., & Wang, D. (2008). Numerical study on salinity stratification in the Pamilco river estuary. *Estuarine Coastal and Shelf Science, 80,* 74–84.

Zhang, Z., Cui, B., Zhao, H., Fan, X., & Zhang, H. (2010). Discharge – salinity relationships in Modaomen waterway, Pearl River estuary. *Procedia Environmental Sciences, 2,* 1235–1245.

Zhang, E., Savenje, H. H. G., Wu, H., Kong, Y., & Zhu, J. (2011). Analytical solution for salt intrusion in the Yangtze estuary, China. *Estuarine Coastal and Shelf Science, 91,* 492–501.

Response of Salinity Intrusion to the Fictitious Blockade of the North Branch in the Yangtze Estuary, China

Ding Lei, Dou Xiping, Gao Xiangyu, Jiao Jian and Hu Jing

Abstract The Yangtze Estuary plays an important role in the economic development in the Yangtze River Basin, China. Shanghai is a megalopolis, and more than 70% of its water is supplied from the Yangtze Estuary. Salinity intrusion has become the most restrictive factor for water supply in nature, while the North Branch is the most serious branch compared to others where the salt water in water sources mainly comes from. If the North Branch is properly blocked, construction of tidal gate for example, may alleviate the salinity intrusion. In this chapter, a numerical model is established to study the fresh water distribution characteristic and the impact of the salinity intrusion on the water sources after the North Branch is fictitious blocked. The study shows that salinity intrusion in the Yangtze Estuary is the most serious in January, during which the safety of water sources is likely to be threatened by salt water. The salinity would be greatly reduced in the water sources intake with the North Branch blocked. The salinity of the water intake in the Dongfengxisha Reservoir and Chenhang Reservoir would be close to 0 in any condition while the Qingcaosha Reservoir is still threatened by salt water when continuous northerly wind happens. This study could provide a reference for the discovery of measures for the water source safety in the Yangtze Estuary.

Keywords The Yangtze Estuary · Water source · Fictitious blockade · Salinity intrusion · North wind

Estuary plays an important role in human history, where 2/3 large cities are located in. The fresh water from the upper stream of the river and the high concentration of salt water from the sea meet at the estuary, mixing together under the turbulence and the molecular diffusion. The Yangtze Estuary is China's largest estuary of about 182 km long with its upper reach starting from Xuliujing. It is located in the subtropical

D. Lei (✉) · D. Xiping · G. Xiangyu · J. Jian
Key Laboratory of Port, Waterway and Sedimentation Engineering of the Ministry of Transport, Nanjing Hydraulic Research Institute, Nanjing 210029, China
e-mail: lding@nhri.cn

H. Jing
Nanjing Water Planning and Designing Institute CO. Ltd., Nanjing 210006, China

K. D. Nguyen et al. (eds.), *Estuaries and Coastal Zones in Times of Global Change*, Springer Water,
https://doi.org/10.1007/978-981-15-2081-5_3

Fig. 1 The location of the water sources in the Yangtze Estuary

monsoon climate zone, the northern wind prevails in winter and the southern wind prevails in summer (Dai and Zhu 2015). Its reaches are fan-shaped in plane and in the pattern of three-order bifurcations and four outlets into the sea(Fig. 1).

Chongming island divides the estuary into the North Branch and the South Branch. Changxing Island and Hengsha Island divide the South Branch into the North Channel and the South Channel. Jiuduan Shore divides the South Channel into the North Passage and the South Passage. The water runs through the North Branch, the North Channel, the North Passage and the South Passage into the sea. The Yangtze Estuary is the start of "the Marine Silk Road", which proposed by the Chinese government to communicate deeply with the world in many fields like culture, economy and so on. The Yangtze Delta is densely populated, economically developed and convenient for transportation with a tremendous strategic status in the economic and social development in China. The Yangtze River provides abundant fresh water resource for the development of the region. More than 70% municipal water supply for megacity—Shanghai comes from the three major water sources in the Yangtze Estuary: Chenhang Reservoir (1992), Qingcaosha Reservoir (2010) and Dongfengxisha Reservoir (2014). For geographical reason, salinity intrusion has become the most restrictive factor for water use in nature (Ding et al. 2015).

Many scholars have done research on salinity intrusion in the Yangtze Estuary since 1980s. It has begun to be concerned as the potential impacts of the South to North Water Transfer Project and the Three Gorges Dam (Shen and Huang 1987; Hu 1989). More attention has been paid since the site selection of the water sources and the safety after the its construction (Tao 1991; Huang and Xu 1996). The salinity intrusion in the Yangtze Estuary is characterized by the fact that the lower reach of the South Branch is not only affected by the frontal intrusion from the outer sea but also the salt water spilled over from the North Branch, which is relevant to the river regime in the North Branch. The upper stream of the North Branch is almost

in straight angle with South Branch. The lower reach of the North Branch shows the shape of a bell mouth (Ding et al. 2016). That result in the small runoff distribution ratio and the strong tidal power (Tang et al. 2011). The salt water in the South Branch is mainly spilled over from the North Branch, which means the water supply in the Chenhang Reservoir and Dongfengxisha Reservoir whose intakes are located in the South Branch are mainly threatened by salinity intrusion in the North Branch.

Sun et al. (2017) found the connection between the tide range and the lunar calendar. Only knowing the runoff of Dationg Station, a method to rapidly estimate the salinity of the specific areas in the South Branch has been proposed. Mao and Shen found that before the construction of the Qingcaosha Reservoir, the salt water in Qingcaosha Reservoir is from both the frontal intrusion and salinity spilling over from the North Branch. However, Gu et al. (2003) thought that the salinity intrusion through the North Passage and the South Passage is not a threat to water source safety of Chenhang Reservoir which is already built and the Qingcaosha Reservoir which is on planning at that time. Li (2011) found that the area of Qingcaosha Reservoir is affected by the salinity spilling over from the North Branch before its construction, and is affected by the salt water directly from the outer sea after its construction during the spring tide. Through numerical simulation, Chen and Zhu (2014) found that the salt water in Qingcaosha Reservoir comes from the North Branch for most of the time, but more and more salt water directly from the sea intrude with the help of northerly wind (Wang and Zhu 2015).

Therefore, if the salinity spilling over from the North Branch can be effectively controlled, the water source safety of the Yangtze Estuary will be improved. This chapter puts forward the idea of blocking the North Branch by engineering measures and intercepting the sea water into the North Branch, such as building a tidal gate in the North Branch. Numerical simulation is carried out to study the effect of the blocking on the improvement of the water source safety. Considering the north wind would aggravate the frontal intrusion, the water source safety under the unfavorable factor-continuous north wind after the blocking is also researched. The results would provide a reference for the safety measures of the water source in the Yangtze Estuary.

1 Introduction of the Research Area

1.1 Hydrological Conditions in the Yangtze Estuary

The total amount of water resource in the Yangtze Estuary is 4.233 billion m^3, of which the amount of surface water resource is 3.8 billion m^3. The annual variation of water into the sea is obvious in the Yangtze River. Runoff in the flood season (May–October) is large, and that in the dry season (November to the next April) is small. Datong Hydrological Station is more than 600 km from the Yangtze Estuary. It is the nearest hydrological station in the lower reaches from the estuary, and not influenced by the tidal dynamic.

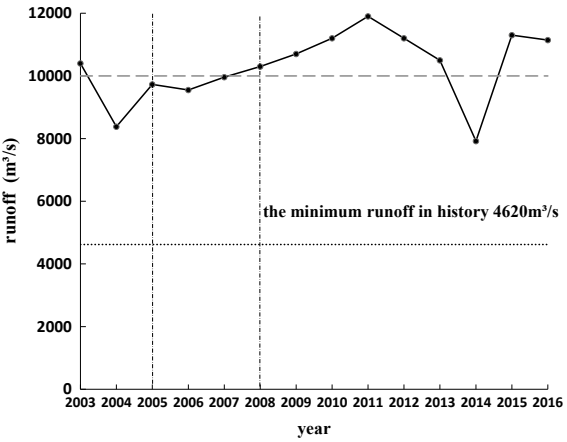

Fig. 2 Annual minimum runoff of Datong Station

According to data statistics of Datong from the year 1950 to 2016, the average annual runoff of Datong station is 28,300 m^3/s, the maximum is 92,600 m^3/s appearing on August 1st, 1954, the minimum is 4620 m^3/s appearing on January 31st, 1979. The Three Gorges Dam changes the annual distribution, and the runoff in the dry season increases in general. The annual minimum runoff after the impoundment of the Three Gorges Dam in 2003 is shown in Fig. 2. The minimum runoff has never been less than 5000 m^3/s. During the Experimental Impoundment Period (after 2008), only in the year 2014 the annual runoff is less than 10,000 m^3/s.

The tidal range of the Yangtze Estuary is medium sized, with the average annual range for 2.66 m and the maximum for 4.62 m in the ZhongJun Station. The total tide prism at the estuary is from 1.3 billion m^3 (dry season neap tide) to 5.3 billion m^3 (flood season spring tide). The tides are controlled by the external tidal waves, and regular semidiurnal tides in the sea while that in the mouth are shallow irregular semidiurnal tides. In this region, tide is dominated by M2 tide from East China Sea's forward wave system and it is also influenced by the rotary tidal wave in the Yellow Sea, which is marked by the K1 and O1 tides. After tidal waves enter the Yangtze Estuary, the tidal waves would deform under the influence of boundary conditions and upstream runoff. The waves are neither the typical progressive waves nor the typical standing waves.

1.2 The Construction of Water Sources in the Yangtze Estuary.

At present, there are three major water sources in the Yangtze Estuary, namely Chenhang Reservoir, the Qingcaosha Reservoir and the Dongfengxisha Reservoir (Table 1). Some of the water supply in Shanghai was taken from the Chenhang Reservoir since 1992. The Qingcaosha Reservoir was built on June 5th, 2007, and the water

Table 1 The designed features of the main reservoirs of Shanghai in the Yangtze Estuary

	Chen-hang	Qingcao-sha	Dongfe-ngxisha
Maximum impounded level (m)	8.10	7.00	5.65
Ordinary water level (m)	3.4–7.4	2.0–4.0	3.0–4.0
Dead water level (m)	3.4	−1.5	1.0
Total capacity (10^3 m^3)	9500	527,000	9762
Effective capacity (10^3 m^3)	8330	438,000	8902
Water supply scale (10^3 m^3/d)	1660	7190	400
Water supply population (10^3)	4000	13,000	650
Safe days of water supply (day)	6	68 (designed), 35 (now)	26

supply was connected to the water supply pipelines on October 2010. On January 17th, 2014, Dongfengxisha Reservoir has formally provided water to Chongming Island. After the completion of Qingcaosha Reservoir in 2010, Shanghai completed the water sources transfer from the Huangpu River to the Yangtze River, forming the water source structure of "two rivers simultaneously and the Yangtze River based". The water supply of the Yangtze Estuary has reached about 70% in Shanghai's water supply, and its safety has played a key role. As for the designed safe water supply days, the number for Chenhang Reservoir is 6, for Qingcaosha Reservoir is 68 (35 days for actual operation), for Dongfengxisha Reservoir is 26.

2 The Establishment and Verification of Mathematical Model

The mixed type of salt and fresh water in most regions of the Yangtze Estuary is partially-mixed type in dry season, while in the North Branch is well-mixed, and there is almost no weakly-mixed type (Jin and Sun 1992; Yao and Zhu 2017). Therefore, the saltwater wedge and the difference of the salinity vertical distribution is not obvious in the dry season. The two-dimensional mathematical model could be used to simulate the salinity transport. The Chinese scholars have done many related researches (Luo and Chen 2005; Kuang et al. 2012). The runoff module in Delft-3D which is an international software is used to establish a two horizontal dimensional mathematical model of the tidal current and salinity in the Yangtze Estuary to study the salinity transport process. The calculation range which includes the Yangtze Estuary, Hangzhou Bay and adjacent waters is shown in Fig. 3, together with the calculation grid.

The north boundary is at 34.67° N; the south boundary is at 29.33° N; the farthest east boundary is at 124.24° E. The open boundary is controlled by water level and is gained through the harmonic analysis of the constituent tide. The upstream boundary

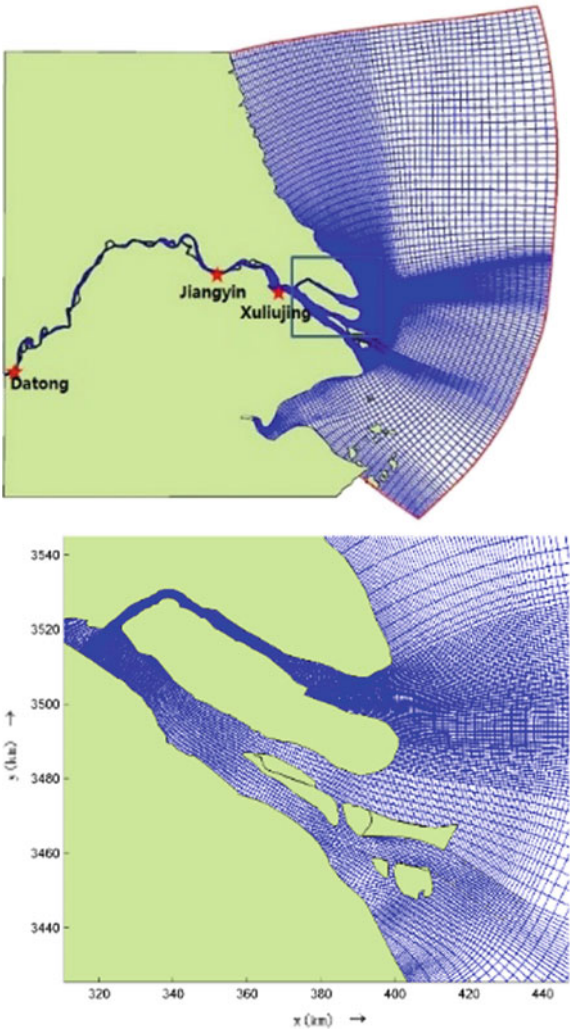

Fig. 3 The integral grid of the model and the local grid of the Yangtze Estuary

is taken in Datong, which is controlled by runoff. The hourly measured runoff at Datong Station is used for Verification. The model grids are body-fitted orthogonal grids, with 1431 elements horizontally and 163 vertically. The grid size in the open sea is large, reaching up to 2 km × 2 km and the grids are locally densified in the Yangtze Estuary, with the minimum size of 70 m × 60 m.

The terrain from Jiangyin to the Yangtze Estuary is measured in 2011 and local terrain is updated according to the Xincunsha reclamation project and the land formation project of Hengsha East Shore. The terrain from Jiangyin to Datong is measured in 2006. The terrain of the sea is digitalized by the nautical chart. The time step is set at 15 s. The roughness of the model is provided by Chezy coefficient, and the value

varies from 80 to 200 $m^{1/2}/s$ according to the terrain. The initial flow velocity is set to 0, and the initial water level is set to 0 m. The salinity at the open sea boundary is 35‰, and the salinity of the Datong boundary is set to 0‰. The data in the estuary is interpolated according to the field data, and the salinity from Datong to XuliuJing is obtained by linear interpolation. The average salinity diffusion coefficient is 250 m^2/s. The wind field can be specified pursuant to the measured wind speed. When the wind speed is equal to or more than 4 m/s, the drag coefficient is 0.0021. The drag coefficient is 0.0012 when the wind speed is 0 m/s. When the wind speed is at 0–4 m/s, the drag coefficient is linearly related to the wind speed. After simulating for 2 months, the initial field is got.

The model used the large-scale full-tide simultaneous hydrological survey in the Yangtze Estuary in January 2016 to conduct the Verification of hydrodynamic force and salinity and validated the water level, velocity, flow direction and salinity at each measuring point. Due to limited space, only the Verification results of the spring tide at the measuring point near the entrance of the North Branch and near Qingcaosha Reservoir were given. As indicated by Fig. 4, the model can well simulate the hydrodynamic force and saltwater transport in the Yangtze Estuary (Ding et al. 2017a, b).

3 Model Calculation and Analysis

3.1 Influence of the North Branch Blocking on the Distribution of Fresh Water

The Pearson type III curve analysis was made for the Datong daily runoff each month, and the 50% frequency can indicate the general situation of the monthly runoff (normal condition). The steady flow is selected as the upstream boundary. The spring tide and the neap tide occur alternatively, which is obvious in one month. The tidal level process in dry season of the year from 2006 to 2014 of the open sea boundary is obtained by harmonic analysis. The tidal range of each semi-monthly cycle is calculated. And the maximum tidal range of semi-monthly cycle is analyzed. When the maximum tidal range is closed to 50% frequency of the tidal range, it can represent the dry season in general. The water level of the complete semilunar tidal cycle is used as the level boundary of the water level. The analysis period starts from the 4 days before the maximum tidal range, and ends at the 4 days after the minimum tidal range with the total semilunar cycle of 16 days. According to the Chinese standard, the content of chloride in water source should be no more than 250 mg/L, which means salinity is less than 0.45‰. The fresh water is defined with salinity less than 0.45‰.

In January, the runoff is relatively the smallest which at 50% frequency is 12,384 m^3/s. The fresh water distribution of four typical moments in semi-monthly cycle is shown at Fig. 5. They are the flood and ebb slacks of spring tide and the

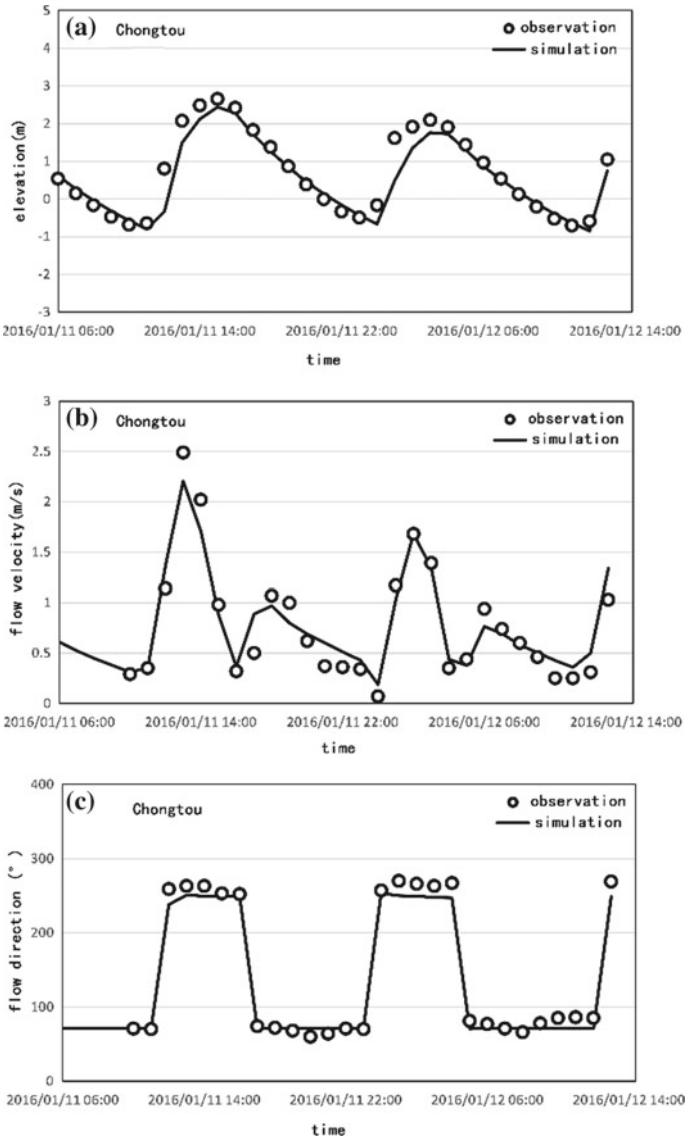

Fig. 4 The verification results **a**–**d** is water level, flow velocity, flow direction and salinity of Chongtou; **e** and **f** is water level, flow velocity, flow direction and salinity of Qingcaosha)

flood and ebb slacks of neap tide. Light blue in the picture indicates fresh water areas. Due to the large range of the Yangtze Estuary, there are variations in the flood and ebb phases in different regions. The flood and ebb slacks mentioned in this chapter refer to the state of Chongtou. At the flood slack of spring tide, 0.45‰ isohaline has crossed bifurcation of the North Branch and the South Branch. The Yangtze Estuary

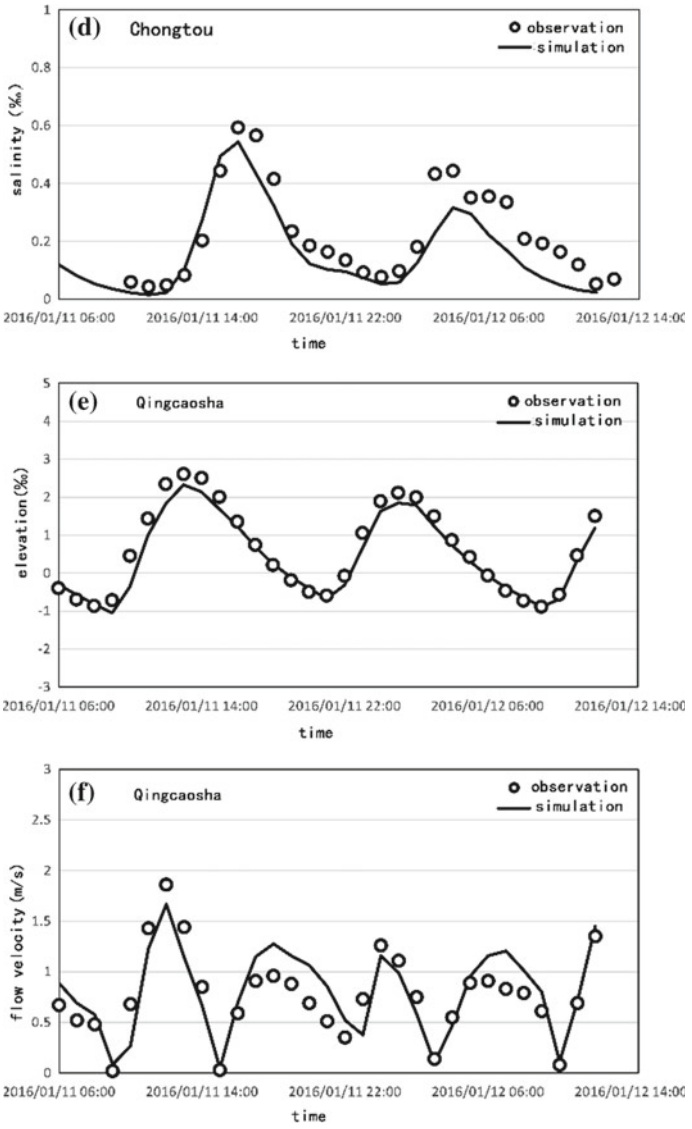

Fig. 4 (continued)

is occupied by saltwater. At the ebb slack of spring tide, the isohaline moves towards the lower reaches and appears in the downstream of Baimao Estuary. The whole Yangtze Estuary is still basically occupied by saltwater. The freshwater distribution area during neap tide is larger than that during spring tide. At the flood slack of neap tide, the isohaline of the South Branch appears at about 7 km in the upper reaches of Liuhe Estuary. Fresh water has already appeared in the Dongfengxisha Reservoir

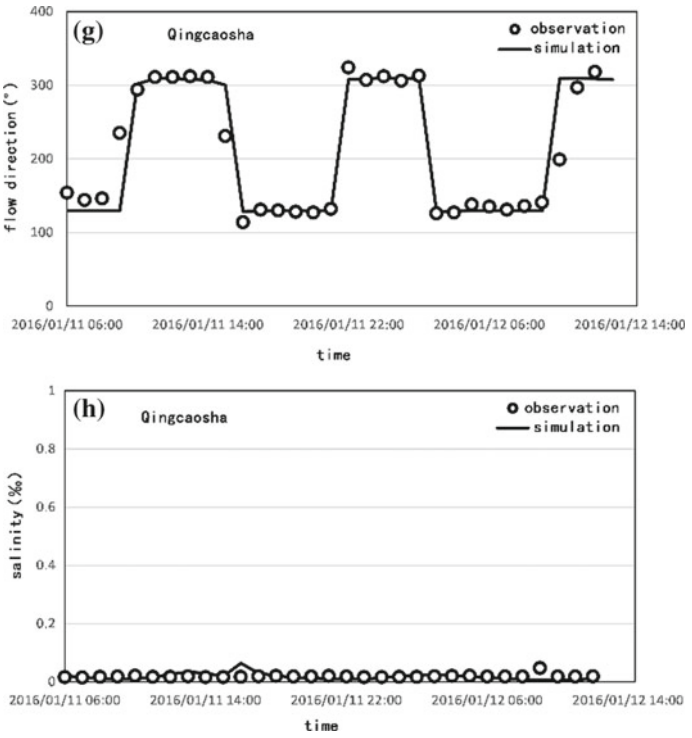

Fig. 4 (continued)

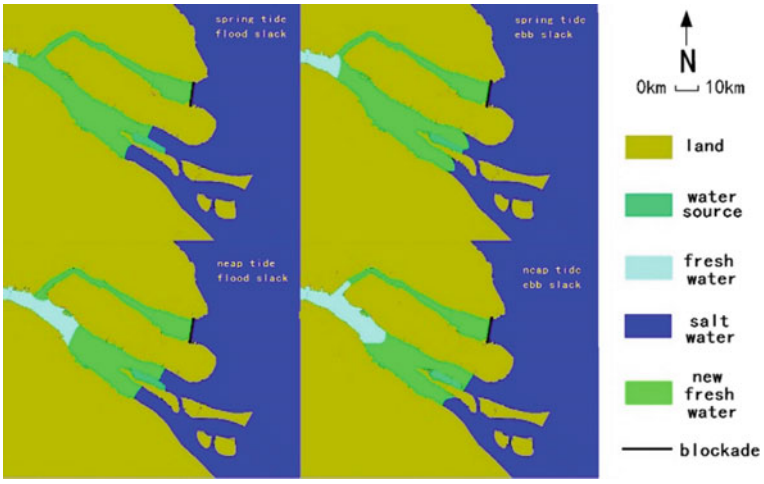

Fig. 5 Distribution of fresh water resources before and after blockade

intake and North Branch is still full of saltwater. At the ebb slack of spring tide, the isohaline is near the Liuhe Estuary and the isohaline of the North Branch is near Chongtou. In January, the salt water intrusion is serious in the normal year. Fresh water appears in the upper and middle reaches of the South Branch only in case of neap tide. The whole Yangtze Estuary is full of salt water in spring tide.

The numerical simulation of salinity intrusion in the Yangtze Estuary after the blockade of the North Branch is carried out. After the completion of the Three Gorges Dam, the impoundment of the Three Gorges Reservoir would advance the salinity intrusion in the Yangtze Estuary, which may occur in October. The area of freshwater in the Yangtze Estuary is greatly increased under the same runoff (Fig. 5). The North Branch is diluted by fresh water and form a freshwater pool. The South Branch is also occupied by fresh water. The North and South Channel are affected by frontal salinity intrusion. The 0.45‰ isohaline move as the tidal dynamic change in one day and in a semi-monthly cycle.

3.2 Effect of the North Branch Blocking on the Salinity Around Water Source Intakes

As shown in Fig. 6a, salinity in the water intakes around every water source may exceeds the standard value in the current situation (without the North Branch blocking). The longest unsuitable water drawing days is an important index to evaluate the water sources safety. When number of the unsuitable water drawing days is larger than the number of water safe supply days, the safety of the water source will be threatened. Therefore, in the semi-monthly period of the simulation, the longest unsuitable water drawing days for the Dongfengxisha Reservoir, the Chenhang Reservoir and the Qingcaosha Reservoir are 11 days, 8 days and 16 days (all of the analyzing time) respectively. The longest unsuitable water drawing day in the Chenhang Reservoir is more than the number of water safe supply days, indicating that the safety of the water source is not guaranteed. It is unable to take water from the Qingcaosha Reservoir during the analysis period, which should also be paid attention to. After the North Branch is blocked, the salinity of the water intake of each water source would be greatly reduced (Fig. 6b). The salinity of the water intake from the water source of Dongfengxisha Reservoir and Chenhang Reservoir is close to 0. The salinity process of the water intake from Qingcaosha Reservoir has obvious fluctuation, but the highest salinity is also lower than 0.45‰. Water could be taken from the three water sources at any time.

The prevailing north wind would aggravate salinity intrusion in the North Channel. Therefore, on the basis of previous research, further study would focus on the water source safety under the influence of the severe frontal intrusion caused by north wind after the North Branch blocking. The change of the water source intake salinity effected by different wind speeds is explored. The wind direction in the model is set as positive north wind, and the wind speed is 5 m/s, 10 m/s and 15 m/s respectively. The

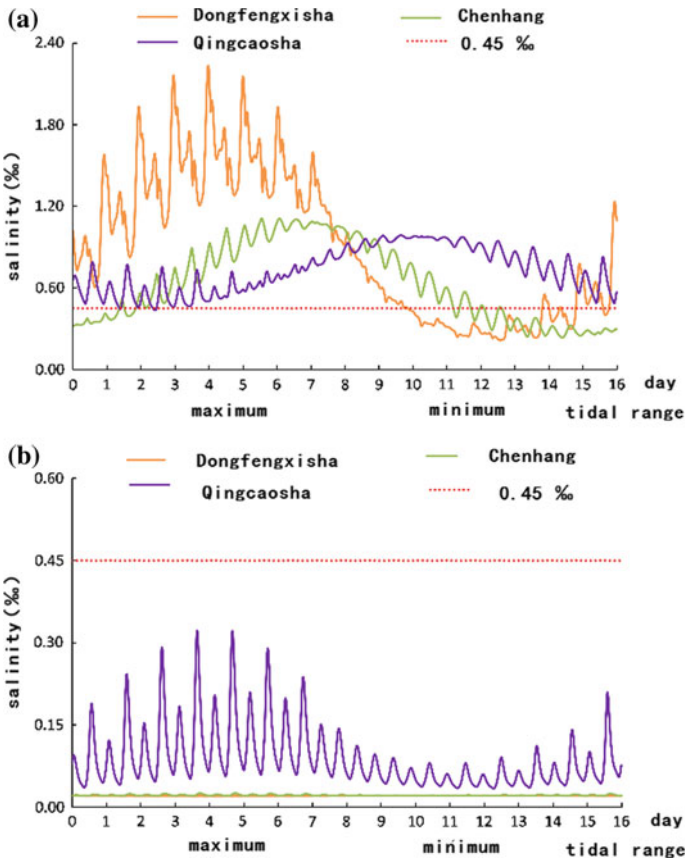

Fig. 6 Semi-monthly salinity process of the water source intakes before and after the north branch blocking (**a** is before the blocking; **b** is after the blocking)

salinity of Dongfengxisha Reservoir intake is still close to 0 under the influence of different wind speeds, and the process lines are almost completely coincided (Fig. 7a). It shows that although the frontal salinity intrusion is aggravated by the north wind, Dongfengxisha Reservoir wouldn't be affected. The salinity of the water intake in Chenhang Reservoir is shown in Fig. 7b. When the wind speed is less than 5 m/s, the salinity is almost 0, and when the wind speed is 10 m/s, the salinity fluctuates with the tide fluctuation. When the wind speed reaches 15 m/s, the salinity fluctuates obviously and the salinity exceeds the standard value at some time. However, because the exceeding duration is short, the water source safety would not be affected. The salinity around Qingcaosha Reservoir intake is significantly affected by the front salinity intrusion in the North Channel, as shown in Fig. 7c. When the wind speed reaches 5 m/s, the highest semi-monthly salinity is around 0.45‰. When the wind speed is 10 m/s, salinity has already exceeded the standard value for most of the time. When the wind speed reaches 15 m/s, the lowest salinity in half a month is 5 times of

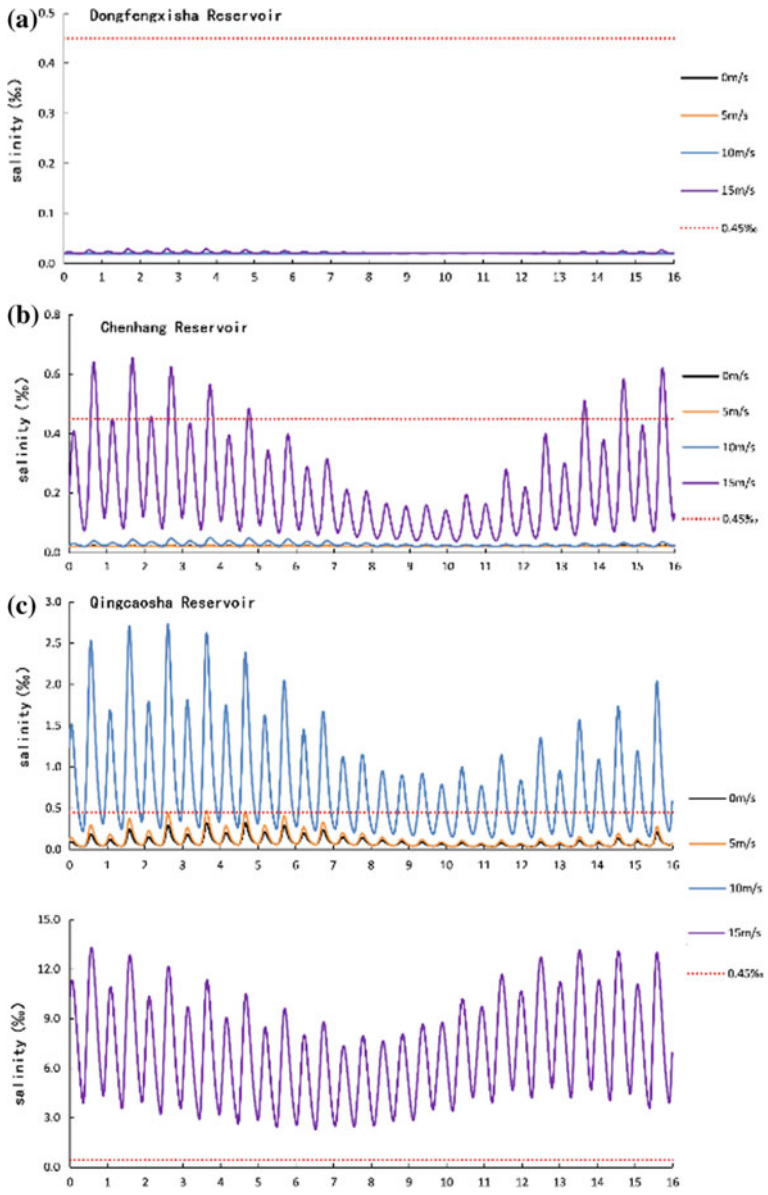

Fig. 7 Semi-monthly Salinity Process of the Water source intake before and after the north branch blocking under the influence of different wind speed (**a** is Dongfengxisha reservoir; **b** is Chenhang reservoir; **c** is Qingcaosha reservoir)

the standard value. Therefore, after the blocking, the salinity around Dongfengxisha Reservoir intake is almost unaffected by the north wind. Chenhang Reservoir would be affected and the salinity may exceed the standard value but the safety of the water source would still be guaranteed. The salinity of Qingcaosha Reservoir would be significantly increased by the north wind. Even if there is no salinity from the North Branch, the frontal salinity intrusion through the North Channel would threat the water source safety.

4 Conclusion

In this chapter, the idea of blocking the North Branch is put forward based on the present situation of which the water source safety of the Yangtze Estuary in Shanghai is affected by the North Branch salinity intrusion in dry season. A mathematical model is used to explore the safety of the water sources before and after the fictitious blockade. Continuous unsuitable water drawing days is considered as the index to evaluate the water source safety. The safety would be threatened by salinity intrusion when the runoff is small in present situation. The North Branch blocking is beneficial to the salinity reduction of the water source intake, and the water source safety would be greatly improved. Continuous strong north wind would aggravate frontal intrusion. The water source safety in Qingcaosha Reservoir would be threatened by the salinity intrusion while Dongfengxisha Reservoir and Chenhang Reservoir would not be affected. Therefore, besides the fictitious blockade, other measures should be combined, in order to solve the water sources safety of Qingcaosha Reservoir.

Acknowledgements This work is supported by the National Key R&D Program of China (2017YFC0405400), the National Natural Science Foundation of China (51479122), the Fundamental Research Fund of Nanjing Hydraulic Research Institute (Y217010), the Follow-up Subject VI of the Three Gorges Dam by the Ministry of Water Resources (12610100000018J129-06).

References

Chen, J., & Zhu, J. R. (2014). Source for saltwater intrusion at the water intake of Qingcaosha Reservoir in the Changjiang Estuary. *Acta Oceanologica Sinica, 36*, 131–141.

Dai, R., & Zhu, J. R. (2015). Statistical analysis of the wind at the Chongming Eastern Beach. *Journal of East China Normal University(Natural Science), 4*, 17–25.

Ding, L., Dou, X. P., Gao, X. Y., et al. (2015). A review on salt water intrusion in Yangtze Estuary, China. In *17th China marine (Offshore) engineering symposium*, China.

Ding, L., Dou, X. P., Gao, X. Y., Hai-Dong, X. U., & Jiao, J. (2016). Analysis of saltwater intrusion into Yangtze Estuary during dry seasons of 2013 and 2014. *Hydro-Science and Engineering, 4*, 47–53.

Ding, L., Dou, X. P., Gao, X. Y., et al. (2017a). Response of salinity intrusion to winds in the Yangtze Estuary. In *5th international conference on hydraulic engineering hydraulic engineering V of P.R. China*, Shanghai.

Ding, L., Gao, X. Y., Dou, X. P., et al. (2017b). Research of the influence of salinity intrusion on Qingcaosha water source. In *5th IAHR WORLD CONGRESS-managing water for sustainable development, learning from the past for the future*, Malaysia.

Gu, Y. L., Wu, S. P., & Le, Q. (2003). Impact of intruded saline water via north branch of the Yangtze river on water source areas in the estuary area. *Yangtze River, 34*, 1–3.

Hu, C. X. (1989). Research on evaluation method of the Yangtze Estuary salinity intrusion. *Water Resources Protection, 4*, 34–37.

Huang, J. X., & Xu, J. Y. (1996). Research of the address of the second water source in Shanghai. *Water Resources Planning and Design, 1*, 15–20.

Jin, Y. H., & Sun, Z. L. (1992). Mixing characteristics of salt water and fresh water in Chinese Estuarie. *Acta Geographica Sinica, 2*, 165–173.

Kuang, C. P., Huang, J., Chen, S. Y., et al. (2012). A saltwater intrusion model based on semi-implicit Eulerian-Lagrangian finite-volume method. *Journal of Tongji University (Natural Science), 40*, 38–44.

Le, Q., et al. (2009). Study on location of water intake and water drawing method in QingCaoSha reservoir. *Water & Wastewater Engineering, 35*, 46–51.

Li, L. (2011). *Spatial-temporal dynamic characteristics of saltwater intrusion in the Changjiang Estuary*. ShangHai: East China Normal University.

Luo, X. F., & Chen, Z. C. (2005). Numerical simulation study of effect of runoff and tide on the Changjiang river mouth saltwater intrusion. *Coastal Engineering, 3*, 1–6.

Shen, H. S., & Huang, Y. L. (1987). Primary study of the three Gorges Dam influence's on salinity intrusion in Yangtze Estuary. *Yangtze River, 10*, 30–33.

Sun, Z. H., Yan, X., Xie, C. S., & Li, Q. (2017). An empirical predictive model for saltwater intrusion in the south branch influenced by tidal flow from the north branch in the Yangtze River Estuary. *Advances in Water Science, 28*, 213–222.

Tang, J. H., Xu, J. Y., Zhao, K. W., & Liu, W. W. (2011). Research on saltwater intrusion of the south branch of the Changjiang Estuary based on the measure data. *Resources and Environment in the Yangtze Basin, 06*, 677–684.

Tao, X. W. (1991). Primary study of the address for the water intake at second water source (the Yangtze Estuary) in Shanghai. *Ocean Development and Management, 3*, 69–74.

Wang, S. X., & Zhu, J. R. (2015). Saltwater intrusion sources at the water intake of Qingcaosha Reservoir in different tidal pattern and wind case. *Journal of East China Normal University (Natural Science), 4*, 65–76.

Yao, Y. M., & Zhu, Y. L. (2017). The fresh and salt water mixing analysis of Yangtze River estuary based on lamination factor and mixing ratio method. *Port & Waterway Engineering, 4*, 60–65.

Influence of the Salinity Intrusion on Island Water Source Safety: A Case Study of the Chongming Island, China

Lei Ding and Jing Hu

Abstract The estuary is a junction of river and sea and is also where freshwater and saltwater meet together. Salinity intrusion may happen when the runoff is relatively weaker or the tidal dynamic is relatively stronger. The Yangtze Estuary is the largest estuary in China. There are some water sources in the estuary to store and provide freshwater. The Dongfengxisha Reservoir is one of these water sources and is constructed in 2014 to provide drinking water for the islanders in the Chongming Island. The water source safety of major islands is most often suffer from the high salinity content of water. For The Dongfengxisha Reservoir, saltwater spilling over from the North Branch is a major threat under natural conditions. To research into how salinity intrusion influence on the water source safety, A two-dimensional tidal-salinity numerical model of the Yangtze Estuary is established to study the relationship between the salinity and the runoff process of the water intake in Dongfengxisha Reservoir. Salinity intrusion in the Yangtze Estuary is the most severe in January and because of its short duration, the water sources safety can be guaranteed. The northeast and northerly wind would increase the salinity of the water intake and northeast wind has a greater influence. The northwest wind would reduce the salinity of the water intake. The sustained north wind would aggravate the intrusion below the South Branch, but it would not affect the water source area. This research can provide reference for the construction of water sources in other islands.

Keywords The Yangtze Estuary · The Chongming Island · Salinity intrusion · Northerly wind

The Chongming Island (Fig. 1) is the third largest island in China and located in the Yangtze Estuary, which is the start of "the Marine Silk Road", that proposed by the Chinese government to communicate deeply with the world in many fields

L. Ding (✉)
Key Laboratory of Port, Waterway and Sedimentation Engineering of the Ministry of Transport, Nanjing Hydraulic Research Institute, Nanjing 210029, China
e-mail: lding@nhri.cn

J. Hu
Nanjing Water Planning and Designing Institute Co. Ltd., Nanjing 210006, China

K. D. Nguyen et al. (eds.), *Estuaries and Coastal Zones in Times of Global Change*, Springer Water,
https://doi.org/10.1007/978-981-15-2081-5_4

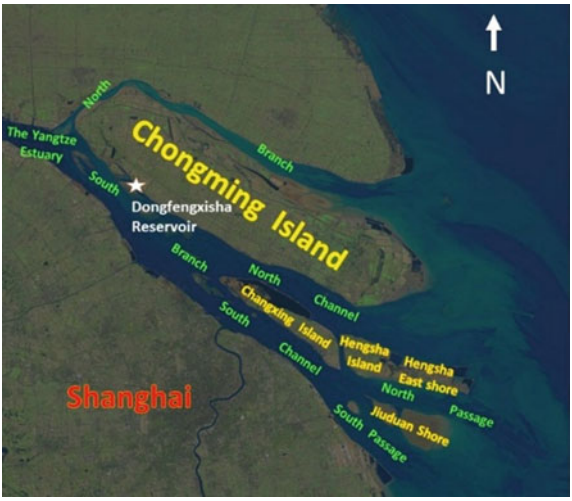

Fig. 1 The location of the Chongming Island and its water source—Dongfengxisha Reservoir

like culture, economy and so on. The Yangtze Estuary is in the pattern of 'three-order bifurcations and four outlets into the sea' and the first bifurcation is conducted by the Chongming Island. The Chongming Island divides the Yangtze Estuary into the North Branch and the South Branch. Before 2014, the drinking water in this island is taken decentralized. To improve the water quality supplied to the island, Dongfengxisha Water Source (Fig. 1) has provided freshwater since June, 2014, with the function of avoiding saltwater and storing freshwater. Thus central water supply bas been realized.

In this chapter, the construction details of the Dongfengxisha Reservoir are introduced. The salinity intrusion of the Yangtze Estuary is simulated by a two horizontal dimensional numerical model. The salt water source and salinity duration characteristic of the Dongfengxisha Reservoir intake is analyzed and the water source safety is also researched. This research can also provide reference for the construction of water sources in other islands.

1 Introduction of the Research Area

1.1 Natural Conditions of the Chongming Island

The Chongming Island is in the area of subtropical monsoon climate with four distinct seasons. The summer is hot and wet, and the leading wind direction is southeast; the winter is cold and dry, and prevails northerly wind (Dai and Zhu 2015). The annual average temperature is 15.3 °C. The rainwater is abundant and annual average amount of precipitation is 1117.1 mm (Wang and Jia 2018). The Chongming Island is 3.5–4.5 m above the sea level and the area is over 1000 km^2, with a history of more

Table 1 Average runoff of each month in dry season of Datong station (unit: m^3/s)

Period	1950–2002	2003–2016
January	10,987	12,491
February	11,711	13,817
March	15,960	19,262
April	24,115	22,094
November	23,366	18,884
December	14,328	14,125

than 1300 years. The area of the island is still increasing for natural siltation and reclamation project.

1.2 The Hydrological Situation of the Yangtze Estuary

1.2.1 Runoff

Datong Hydrological Station in Anhui Province is more than 600 km in the upper reaches of the Yangtze Estuary. It is the nearest hydrological station in the lower reaches of the Yangtze River from the estuary, but not influenced by the tidal dynamic. According to the statistical data of Datong from 1950 to 2016, the annual runoff is 28,300 m^3/s; the maximum runoff was 92,600 m^3/s and appeared in August 1st, 1954; the minimum runoff was 4620 m^3/s and appeared in January 31st, 1979.

After the operation of the Three Gorges Project in 2003, the runoff volume distribution in a year is changed. Table 1 shows the average runoff of each month before and after 2003. The runoff volume in January and February is smaller than that in the other month and this character has not been changed, but the runoff in these two months are added by nearly 200 m^3/s for the impoundment of the Three Gorges Project.

1.2.2 Tide

The annual average tidal range (Zhongjun Station) is 2.66 m, and the extreme tidal range is 4.62 m. The total tidal influx at the entrance of the estuary ranges from 1.3 billion m^3 (neap tide in dry seasons) to 5.3 billion m^3 (spring tide in flood seasons). Tides outside the estuary are regular semi-diurnal tides, and tides within the estuary are irregular half-day shallow sea tides.

1.3 The Construction of the Dongfengxisha Reservoir

The usage of Dongfengxisha Reservoir meets the demand of 0.7 million residents in the Chongming Island and is tremendous meaningful for improve the drinking water quality. It sits in the southwest of the Chongming Island and takes water from the South Branch. The total area is nearly 3.88 km^2. The effective storage capacity is 8.9 million m^3. The recent water supply scale is 215 thousand m^3/d, while that planned in the future is 400 thousand m^3/d. The designed water supply days was 26 days. According to the feasibility study report of Dongfengxisha Reservoir, the designed water level is from 1.0 to 5.65 m. On the basis of the relationship between water level and storage volume after the operation, the reservoir can supply water for 6.9–18.7 days recently and 3.7–22.3 days in the future (Table 2).

The site of Dongfengxisha Reservoir is chosen at the southwest side of Chongming Island. Because there is a deep trough between the Dongfengxisha Island and Chongming Island, the construction engineering quantity can be greatly saved. The site selection is also related to the salt water intrusion characteristics of the Yangtze Estuary. The pattern of 'three-order bifurcations and four outlets into the sea' makes the rule of salinity intrusion in the Yangtze Estuary more complicated than other single estuaries.

The lower reaches of the North Branch shows the shape of a bell mouth while the upper reaches are almost in a right angle with the South Branch. Thus the runoff into the North Branch is less than 4% of the total Yangtze River runoff, while the tidal volume into the North Branch is about 25% of all. Therefore, salinity intrusion in the North Branch is the severest. Thus it is more suitable to take the South Branch as the water source to avoid salt and store fresh water. When the runoff is small and the tidal power is strong, the high concentration salt water from the outer sea would intrude to the Chongtou as the rising tide of the North Branch, then spill over into the South Branch, thus the salinity of the upper reaches of the South Branch rises. The saltwater in the Dongfengxisha Reservoir only comes from the North Branch and it is not affected by the frontal intrusion down the South Branch generally. In recent years, studies have shown that sustained north wind would aggravate the frontal

Table 2 The relation between water lever and storage capacity

Water level/m	Storage capacity/10^6 m^3	Water supply days	
		Now	Future
1.00	0.86	0.0	0.0
2.50	2.35	6.9	3.7
3.00	2.93	9.6	5.2
3.50	3.65	13.0	7.0
4.00	4.88	18.7	10.1
5.65	9.76	41.4	22.3

salinity intrusion. Therefore, it is also worthwhile to research whether and how the Dongfengxisha Reservoir is affected by the frontal salinity intrusion.

2 The Establishment and Verification of Numerical Model

2.1 Model Establishment

The numerical model is one of the main methods to simulate and analyze the salinity intrusion. The mixing type of most area in the Yangtze Estuary in dry season is partial mixing and North Branch is well-mixed (Yao and Zhu 2017). Which means the difference in a vertical line is not obvious. Therefore, a two-dimensional horizontal numerical model can simulate the salinity intrusion well in the Yangtze Estuary, and Chinese scholars have relatively successful experience (Luo and Chen 2005).

The Flow module in Delft-3D is used to establish the two-dimensional numerical model of the tidal current and salinity transport in the Yangtze Estuary to carry out simulation research of the salinity transport process.

The north boundary is at 34.67°N, the south boundary is at 29.33°N, the farthest east boundary is at 124.24°E. The open boundary is controlled by water level and is gained through the harmonic analysis of the constituent tide. The upstream boundary is taken in Datong, which is controlled by runoff. The hourly measured runoff at Datong Station is used for validation. The model grids are body-fitted orthogonal grids, with 1431 elements horizontally and 163 vertically. The grid size in the open sea is large, reaching up to 2 km × 2 km and the grids are locally densified in the Yangtze Estuary, with the minimum size of 70 m × 60 m (Fig. 2).

The terrain from Jiangyin down to the Yangtze Estuary is measured in 2011 and local terrain is updated according to the Xincunsha reclamation project and the land

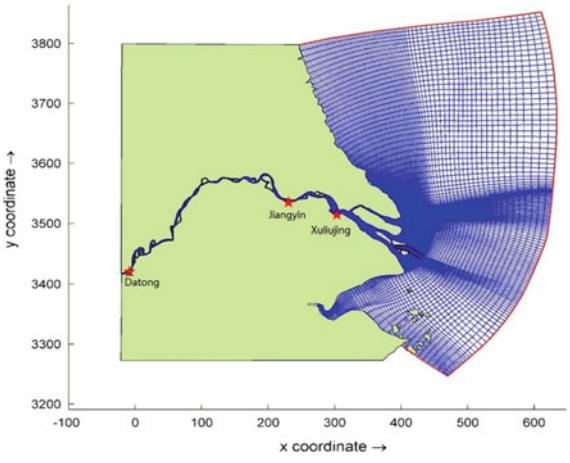

Fig. 2 The integral grid of the model and the local grid of the Yangtze Estuary

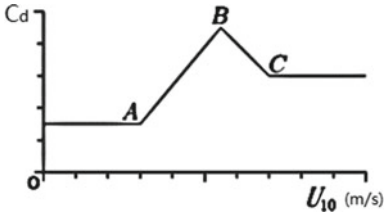

Fig. 3 The relation of wind speed and wind drag coefficient

formation project of Hengsha East Beach. The terrain from Jiangyin to Datong is measured in 2006. The terrain of the sea is digitalized by the nautical chart. The time step is set at 15 s. The roughness of the model is provided by Chezy coefficient, and the value varies from 80 to 200 $m^{1/2}/s$ according to the terrain. The initial flow velocity is set to 0, and the initial water level is set to 0 m. The salinity at the open sea boundary is 35‰, and the salinity of the Datong boundary is set to 0‰. The data in the estuary is interpolated according to the field data, and the salinity from Datong to XuliuJing is obtained by linear interpolation. The average salinity diffusion coefficient is 250 m^2/s.

The effect of wind is expressed by wind stress τ_w on the water surface in this model. For the flow in 2D numerical model:

$$\overrightarrow{\tau_w} = \rho_a C_d \overrightarrow{U_{10}} \left| \overrightarrow{U_{10}} \right| \tag{1}$$

where ρ_a is air density, C_d is the drag coefficient of winds, U_{10} is the wind speed 10 m above the free surface. C_d is influenced by U_{10} shown in Fig. 3. The wind field can be specified pursuant to the measured wind speed. According the wind field above the Yangtze Estuary and adjacent sea, in this model, when wind is 0 m/s the C_d is 0.0012; when wind is 4 m/s the C_d is 0.0021.; when wind is during 0–4 m/s, they are primary function related.

During model calculation, the field after running for 2 months is taken as the initial field, and then the plans are simulated.

2.2 Model Verification

The model used the large-scale full-tide simultaneous hydrological survey in the Yangtze Estuary in January 2016 to conduct the validation of hydrodynamic force and salinity and validated the water level, velocity, flow direction and salinity at each measuring point. Due to limited space, only the validation results of the spring tide at the measuring point near the entrance of the North Branch and near Dongfengxisha Reservoir were given. As indicated by Fig. 4, the model can well simulate the hydrodynamic force and saltwater transport in the Yangtze Estuary (Ding et al. 2016).

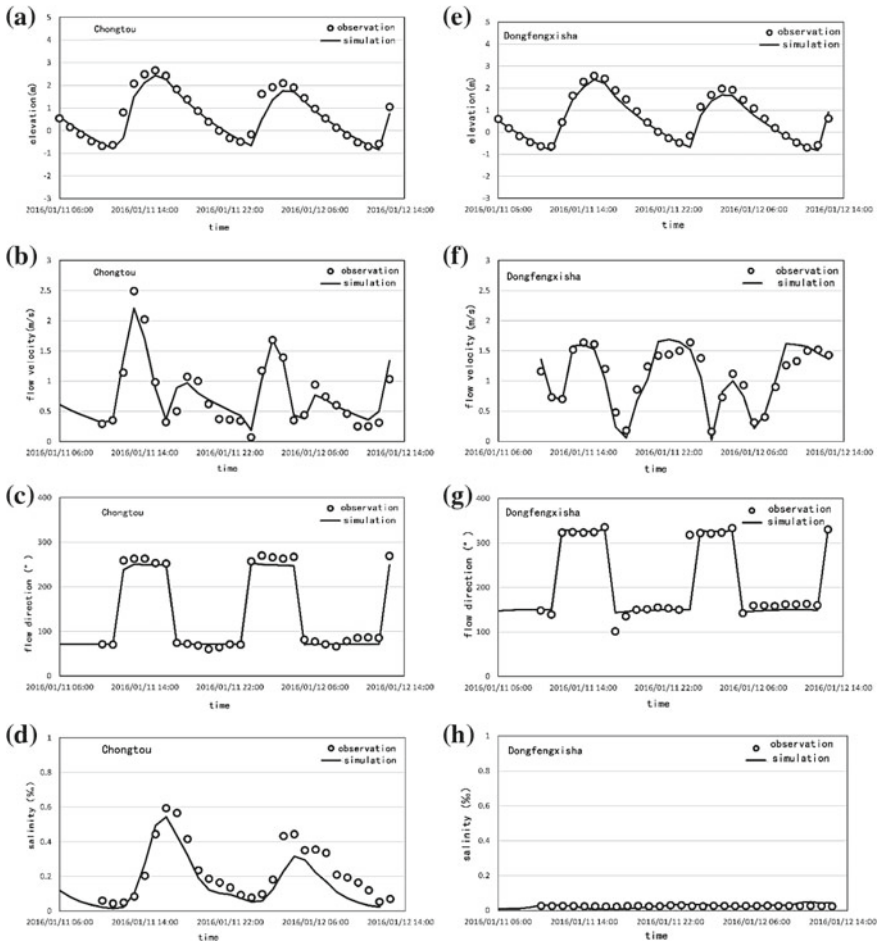

Fig. 4 The validation results **a**–**d** is water level, flow velocity, flow direction and salinity of Chongtou; **e**–**f** is water level, flow velocity, flow direction and salinity of Qingcaosha

3 Calculation and Analysis

3.1 Boundary Conditions

The steady flow is used as the upstream condition in the model. In terms of tide, the calculation of closed cycle for a complete semimonthly period is taken. The analysis time is 16 days, including a complete semimonthly period, from the 4th days before the maximum tidal range, to the 4th day after the minimum tidal range. The wind speed and direction remain constant throughout the simulation range and period.

The salinity of water source intake in the Yangtze Estuary changes with the tide. If the salt water is derived from the upstream of the water intake, which means is affected by the salinity intrusion in the North Branch. Salinity increases as the ebb tide and decreases as the flood tide. If the salt water is derived from the downstream of the water intake, which means it is affected by the frontal intrusion and the saltwater mass traced back as the flood current from the downstream of the water intake. Salinity increases as the flood tide and decreases as the ebb tide. Under different runoff, the salinity of water intake is different, but the change characteristic of the salinity process is similar. In this chapter, the averaged runoff volume (12,491 m^3/s) in Datong after the construction of the Three Gorges Dam is taken as the example to analyze the characteristics of salinity process in the Dongfengxisha Reservoir.

The relationship between the salinity process and the water level process shows two different characteristics according to the tidal range during semimonthly cycle of Dongfengxisha Reservoir Fig. 5a: Character I: 4 global maximum salinity values may appear in one day when tidal range is large. The salinity rises at flood tide

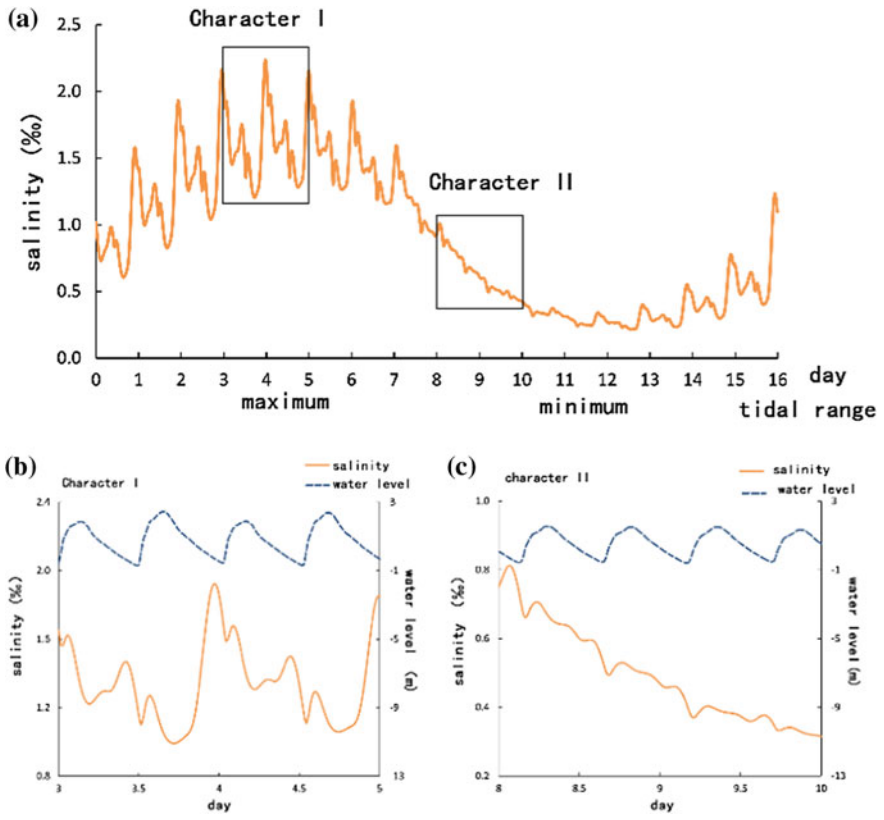

Fig. 5 Salinity and water level process at the intake of Dongfengxisha Reservoir (**a** is the salinity process; **b** and **c** are the detail of Character I and Character II respectively)

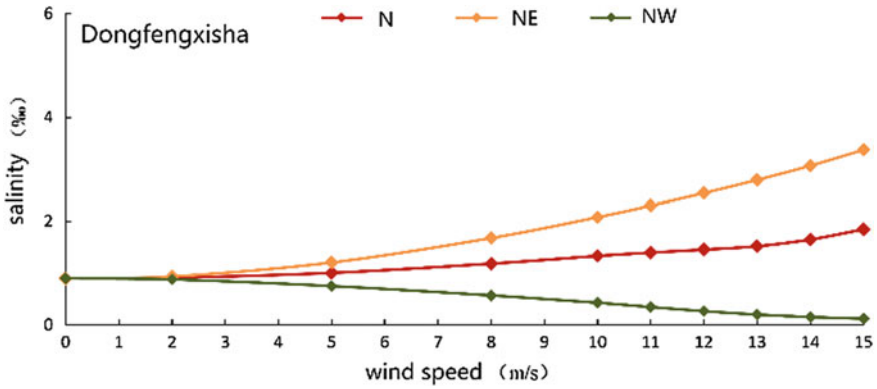

Fig. 6 Influence of different wind speed and direction on intake salinity

and rises again after a transient fall at ebb tide. The salinity maxima in the ebb tide is much larger than that in the flood tide (Fig. 5b). Character II: The salinity process has a downward trend with the tidal range decrease. The salinity maxima may disappear when the tidal range depress to a certain extent. The salinity generally shows a downward trend in addition to a smaller rise during tide ebb (Fig. 5c). After the neap tide, salinity maxima at the ebb tide begins to emerge gradually, as shown in Fig. 5b.

The above analysis shows that the salinity intrusion from the North Branch has an important influence on the Dongfengxisha Reservoir. The influence of the frontal salinity intrusion below the South Branch is also worth considering. The serious frontal intrusion of the Yangtze Estuary, such as February 2014, is usually accompanied by severe sustained northerly wind. The wind sensitivity is analyzed and the water intake salinity is illustrated. Salinity increases with the increase of northeast wind and north wind speed and decreases with the increase of northwest wind speed (Fig. 6). If the North Branch is blocked, numerical simulation shows that the intake salinity of the Dongfengxisha Reservoir is close to 0 at all levels of wind speed (Fig. 7). It means that even if the north wind aggravates the salinity intrusion below the South Branch, it would not affect Dongfengxisha Reservoir.

The daily average salinity is calculated and the maximum daily salinity in semi-monthly period is found on the day of the flood tide. The higher salinity continues to the moderate tide after the flood tide. The raising time of daily average salinity is slightly higher than that of the falling time. It takes one day for the salt water mass to move from the North Branch to the Dongfengxisha Reservoir.

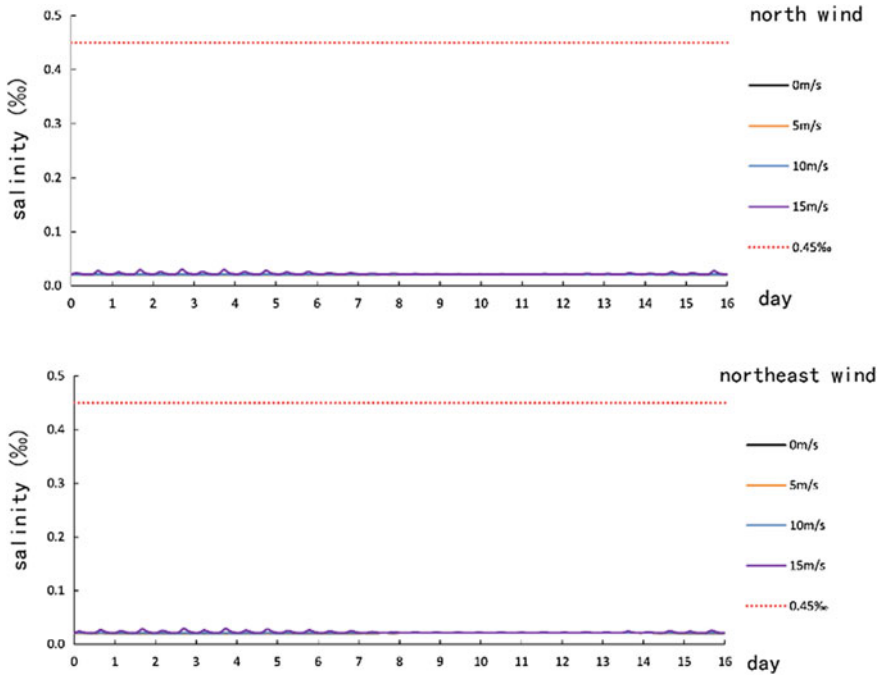

Fig. 7 The salinity process of the Dongfengxisha Reservoir intake affected by the Northery wind after the north branch blocking

3.2 Water Source Safety Assessment

Water source safety for every month in dry season affected by the salinity intrusion is evaluated under the normal situation. During the simulation, the average monthly runoff of 2003–2016 is taken for the upstream boundary. The monthly mean wind speed and direction of Chongming East Shore in recent years are obtained as the wind boundary (Table 3). The tide level boundary is consistent with the previous scheme. The maximum, minimum and average values of salinity in the analysis cycle are shown in Table 4. The numerical simulation results show that in the 6 months of

Table 3 The average wind condition of each month in dry season

Month	Wind direction	Wind speed (m/s)
January	N	4.2
February	NE	4.6
March	NE	4.9
April	SE	4.9
November	N	4.1
December	N	4.3

Table 4 The characteristic value of salinity in each month

Month	Salinity		
	Maximum	Minimum	Average
January	2.31	0.23	0.93
February	2.1	0.18	0.81
March	0.65	0.03	0.19
April	0.15	0.02	0.05
November	0.56	0.03	0.16
December	1.84	0.13	0.66

the dry season, only the salinity of April is all below 0.45‰ and the salinity in other months exceeds the standard for time. January is the most severe month. The maximum salinity is 2.31‰, which is 5 times higher than the standard limit value and the average salinity is 2 times more than the standard limit. Followed by February, the highest salinity and average salinity are 2.10‰ and 0.81‰ respectively. Then followed by December, the highest salinity and average salinity are 1.84‰ and 0.66‰ respectively. The salinity exceeding time for the previous three months (December, January and February) mainly focus on the moderate tide after the neap tide, spring tide and the moderate tide after the spring tide. The exceeding time is between 10 and 12 days.

The average salinity of November and March is far below the standard drinking water limit. Salinity exceeds the standard only for few times in spring tide and the highest salinity is 0.65‰ and 0.56‰ respectively. The analysis shows that the salt water would appear in the intake of Dongfengxisha Reservoir for 5 months in a year, but even in the January whose intrusion is severest, there would be at least 4 days of water drawing favorable during the analysis cycle. It indicates that as long as the water level in the reservoir reaches a certain level before the saltwater comes, the normal water supply in Chongming Island would be guaranteed and the residents' life on the island would not be affected by salinity intrusion.

4 Conclusions

Chongming Island is the third largest island in China, located in the Yangtze Estuary. In 2014, the completion of Dongfengxisha Reservoir provided the 700 thousand island residents with excellent quality water. Salinity intrusion is an important threat to the safety of the water source. A two-dimensional mathematical model of the Yangtze Estuary is established to simulate the salinity intrusion and the salinity process of the water intake with the next conclusions:

(1) The salt water around the Dongfengxisha Reservoir is spilled over from the North Branch. The northeast and northerly wind would increase the salinity of the water intake and northeast wind has a greater influence. The northwest wind

would reduce the salinity of the water intake. The sustained north wind would aggravate the intrusion below the South Branch, but it would not affect the water source area.

(2) In the Yangtze Estuary, January is the month suffered the severest saltwater intrusion. During the semimonthly period, the greatest impact for Dongfengxisha Reservoir is in the spring tide, with the maximum salinity of 2.31‰. but there are still at least 4 days available for drawing water.

(3) According to the reservoir designed capacity, as long as water level of the reservoir reaches a certain water level before the intrusion, the water supply in Chongming Island could be ensured and the island inhabitants would not be affected by the salt water.

Acknowledgements This work is supported by the National Key R&D Program of China (2017YFC0405400), The Follow-up Subject VI of the Three Gorges Dam by the Ministry of Water Resources (12610100000018J129-06).

References

Dai, R., & Zhu, J. R. (2015). Statistical analysis of the wind at the Chongming Eastern Beach. *Journal of East China Normal University (Natural Science), 4*, 17–25.

Ding, L., Dou, X. P., & Gao, X. Y. (2016). Analysis of saltwater intrusion into Yangtze estuary during dry seasons of 2013 and 2014. *Hydro-Science and Engineering, 4*, 47–53.

Luo, X. F., & Chen, Z. C. (2005). Numerical simulation study of effect of runoff and tide on the Changjiang River mouth saltwater intrusion. *Coastal Engineering, 3*, 1–6.

Wang, D. D., & Jia, W. X. (2018). Retrieving coastal soil saline based on landsat image in Chongming Dongtan. *Journal of Agricultural Science and Technology, 20*, 55–63.

Yao, Y. M., & Zhu, Y. L. (2017). The fresh and salt water mixing analysis of Yangtze River estuary based on lamination factor and mixing ratio method. *Port & Waterway Engineering, 4*, 60–65.

Law of Salt Tide Intrusion of the Qiantang Estuary and Its Numerical Simulation

Ying-biao Shi and Wen-long Cheng

Abstract The Qiantang Estuary is characterized by strong tidal bore, high sediment concentration, severe erosion/deposition and frequent human activities. The law of saltwater intrusion is different from other general tidal estuary. This chapter reveals the law of interaction among runoff, channel volume and salinity by means of the analysis of the long-term hydrological and measured salinity data of the Qiantang Estuary. Based on the concept of water, sand and salt mixture density, the muddy water control equations have been derived, and the mathematical model coupling with strong tidal bore-sediment-salinity has been developed as a result, and the model has also been verified, which shows that the result adopting movable-bed numerical simulation model in calculation agrees more with the actual condition.

Keywords Qiantang estuary · Salt tide intrusion · Movable bed simulation · Interaction of runoff-channel volume-salinity

1 Introduction

The Qiantang Estuary has such characteristics as strong tide, high sediment concentration, fierce sediment erosion/deposition and frequent human activities. It is a typical strong mixing estuary (Fig. 1).

Therefore, the intensity and length of the salt tide intrusion in the Qiantang Estuary are much larger than those of the general tidal estuary. Under the conditions of low water runoff, the salty tide of the Qiantang Estuary can be traced back beyond Wenyan 207 km from the mouth of Hangzhou Bay. The water quality of the water intake is affected by the salt tide intrusion to varied extent, and when the chlorinity of the river water exceeds the standard, the water supply stoppage may occur from time to time; therefore, it is required to take engineering and non-engineering measures

Y. Shi (✉) · W. Cheng
Key Laboratory of Estuarine and Coast of Zhejiang Province, Hangzhou 310016, China
e-mail: shiyb@zjwater.gov.cn

Y. Shi
Marine College of Zhejiang University, Hangzhou 310054, China

K. D. Nguyen et al. (eds.), *Estuaries and Coastal Zones in Times of Global Change*, Springer Water,
https://doi.org/10.1007/978-981-15-2081-5_5

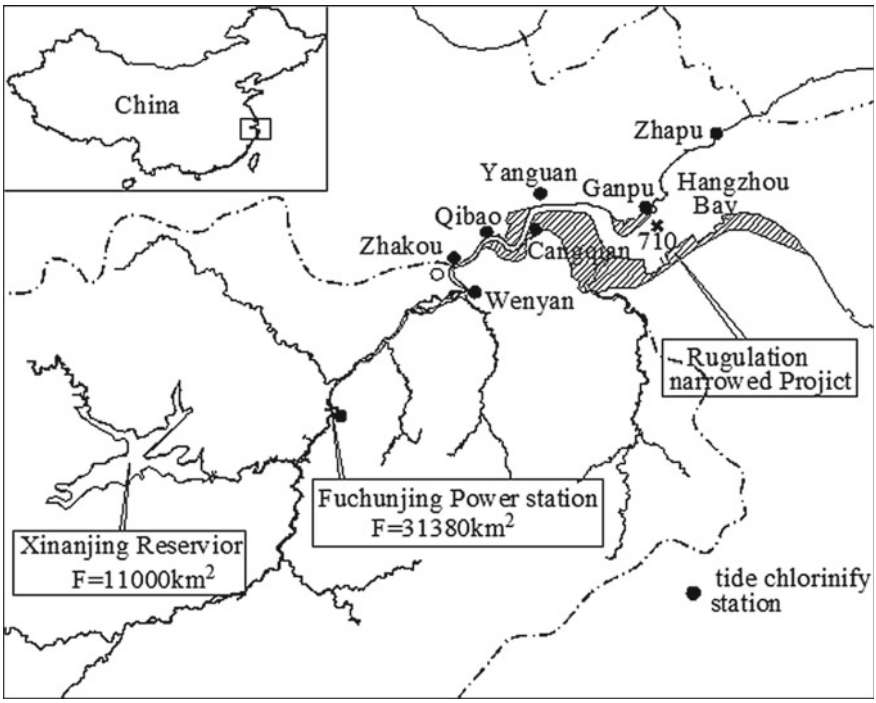

Fig. 1 Layout of Qiantang Estuary

to protect the water safety in the estuary area. Salt tide forecast is one of the non-engineering measures, which can provide important basis for the decision-making in the fighting against salt tide. In addition, the intrusion of salt tide has an effect on estuarine hydrodynamics, sediment erosion/deposition, and material transport and diffusion. Therefore, the study of estuarine tide invasion has all along been one of the important contents of estuarine research, and is also the hot topic at present.

As early as in the 1960s, many researchers had carried out the study of the characteristics of salt tide intrusion in the Qiantang Estuary. Mao (1964) used the monthly mean salinity along the Qiantang Estuary to verify the analytic solution of the vertical distribution of salinity; Han et al. (2003) developed relations that the tidal coefficient is directly proportional to runoff and river channel volume and inversely proportional to the tidal range, and subsequently established the 1D tidal flow salinity mathematical model and studied the law of salt tide intrusion in the Qiantang Estuary, and systematically analyzed the impact of the Xin'anjiang reservoir and estuary narrowing on the salt tide intrusion in the Qiantang Estuary(Han et al. 2002); in the 1990s and thereafter, Han et al. (2012) and Shi et al. (2015) established the mid-term and long-term numerical prediction model for the saltwater intrusion in the Qiantang Estuary taking into account the action of river bed erosion/deposition and applied it to the study and practical application of the Fuchunjiang reservoir in restraining the

salinity in dry season each year; Pan et al. (2014) established the salinity mathematical model under the action of tidal bore, and studied the influence of tidal bore on salinity using the actually measured data and mathematical model. Shi et al. (2012) established the numerical model of 2D saltwater intrusion and explored the law of salt tide intrusion.

Similar to the law of salt tide intrusion in the Yangtze River estuary and the Pearl River estuary etc. (Savenije 2005; Shen et al. 2003; Bao et al. 2009), runoff and tide are the important factors affecting the salt tide invasion of the Qiantang Estuary. However, as the Qiantang Estuary is the alluvial one with strong tide, strong erosion/deposition and its bed is composed of fine silt that can be easily eroded/deposed, the runoff is more sensitive to the river bed erosion/deposition; the erosion of river bed by the runoff leads to the enlargement of river volume and the significant enhancement of tidal dynamics, which have strengthened the intrusion of salt tide. The law of the interaction among runoff-channel volume-salt tide salinity is the characteristic of salt tide intrusion in the Qiantang Estuary, which has rarely been studied and reported and almost not involved by other people. Based on the analysis of hydrological and salinity data of Qiantang Estuary, this chapter has analyzed the law of interaction among runoff-channel volume-salt tide salinity. On the basis of the water, salt and muddy water control equation, this chapter has established the movable riverbed mathematical model coupling the strong tidal bore-sediment-salinity, the verification result of which shows that it can be used to study the law of salt tide intrusion in the Qiantang Estuary.

2 Law of Salt Tide Intrusion in Qiantang Estuary

Through the observation of the continuous salinity of the river water in the Qiantang Estuary for as long as about 60 years as well as the topographic surveying and mapping of river channel and the observation of runoff and tidal level in April, July and November each year, we have a profound understanding of the law of salt tide intrusion in the Qiantang Estuary; as with the law of salt tide intrusion in ordinary tidal estuary, runoff and tide are the main factors affecting the intrusion of salt tide, but the erosion or deposition of river bed in the Qiantang Estuary has a significant impact on the intrusion of salt tide

2.1 Impact of Runoff on Salt Tide Intrusion

The runoff has a very obvious impact on the end reach of the salt tide intrusion in the Qiantang Estuary, which mainly manifests the obvious cyclic changes of the salt tide intrusion within the season, month and half a month. The dry season of the spring tide from August to November each year is the period when there is obvious impact of salt tide intrusion; in the wet season from April to July, as the runoff is large, the

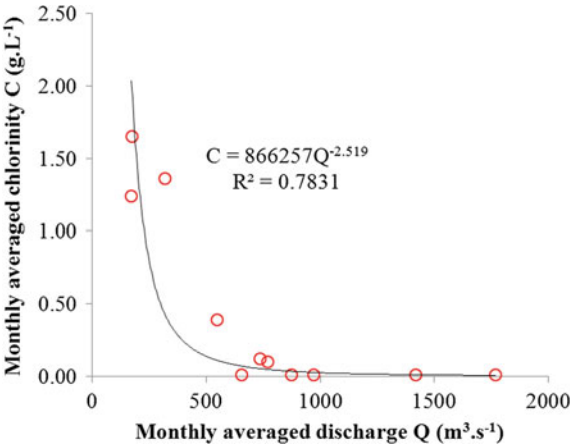

Fig. 2 The relationship between monthly average chlorinity and monthly average discharge

reach of the river up beyond Qibao has less impact of salt tide intrusion; the period from December to March in the following year is the dry season, which, however, impact of salt tide intrusion is generally not obvious because of riverbed deposit and small tide dynamics. Figure 2 shows the relation diagram between monthly mean discharge (Q) at Fuchunjiang Power Station and the monthly mean chlorinity (C) at Qibao station in 2003, from which we can see that chlorinity and runoff are in the exponential relationship that the greater the runoff is, the lower the chlorinity is. When the runoff discharge is larger than 900 m^3/s, the chlorinity at Qibao is close to zero; when the discharge is less than 600 m^3/s, the chlorinity will increase rapidly with the decrease of runoff, which is the direct effect of runoff on salt tide intrusion. When the discharge is less than 300 m^3/s, the actually measured points are relatively discrete and the impact of tide on chlorinity increases.

However, for the long time scale (several months), salinity changes subject to the combined effects of various factors such as runoff, tides and riverbed terrain etc. become very complicated. Figure 3 shows the relation between the yearly average chlorinity at Qibao station and the average discharge at Fuchunjiang Power Station from 1994 to 2012. From the figure, we can see that the points between the two are scattered and very poor in correlation with almost no rules to follow. The reason is mainly due to the interaction of unique runoff-channel volume-tidal dynamics in the Qiantang Estuary. Under certain sediment inflow conditions, the riverbed terrain is the result of the interaction between runoff and tidal currents, which in turn affects the tidal dynamics in the upper reach of the estuary. The runoff volume in wet period each year determines the riverbed terrain. The larger runoff volume is, the larger riverbed volume is and then, the larger tidal dynamics in the upper section of the estuary in the second half of the year. Meanwhile, the second half of the year is of the dry period; under the joint action of low water and the tide, the salt tide intrusion at this time is most serious. This is the indirect effect of runoff on salinity. The runoff scours the riverbed terrain in wet season, and then the feedback change causes the

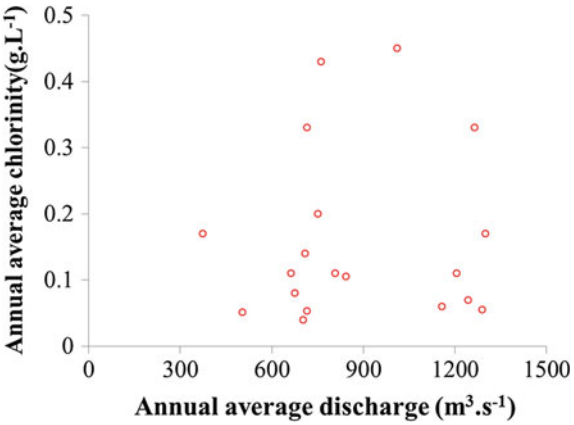

Fig. 3 The relationship between annual average discharge and chlorinity at Qibao station

strengthening of tidal dynamics in the upper estuary, which indirectly affects the salt tide intrusion with a certain delay in time.

2.2 Effect of River Channel Volume on Salt Tide Invasion

River channel volume is the internal boundary condition of runoff and tidal dynamics. As the Qiantang Estuary is a strongly wandering and large scouring/silting estuary, in addition to the fluctuations of tidal range caused by astronomical tide on the daily and monthly bases, the wet season (from April 1 to July 15) accounts for 60–70% of the annual runoff, in which period, the river channel is often scoured deep with increased tidal range; the period from July to November is the spring tide and dry season, in which period, river channel is silted again with reduced tidal range. Table 1 shows the maximum four tidal range values in August and January in the wet year (2010) and the dry year (2008) at Qibao station, from which we can see that the average tidal range values of large tide is 8 times larger than those of neap tides. As the tidal range at Qibao station is small in winter, the Hangzhou section is rarely threatened by the intrusion of salt tide in winter; because the tidal range of neap tide in August is also very small, there will not be continuous standard-exceeding for more than

Table 1 The tidal range of spring, middle, neap tide at Qibao station (m)

Time	Spring	Middle	Neap
	① ~ ④	① ~ ④	① ~ ④
August in 2010	3.08 ~ 3.28	1.8 ~ 2.44	0.04 ~ 0.82
January in 2010	1.55 ~ 1.81	1.01 ~ 1.18	0.01 ~ 0.32
August in 2008	1.33 ~ 1.48	0.86 ~ 0.94	0.09 ~ 0.18
January in 2008	0.23 ~ 0.30	0.12 ~ 0.15	0.05 ~ 0.08

10 days except that there are continuous dry months. The main reason is that runoff causes different length and volume of river channel in wet and dry seasons, which then makes big difference between tidal range and tidal volume through feedback. It can be seen that the runoff-channel volume-tidal dynamics of Qiantang Estuary has a significant interaction effect, which in turn causes the impact of salt tide intrusion.

Figure 4 shows the relationship between the average annual discharge in the wet year, medium year and dry year and the average monthly tidal range and the average maximum chlorinity.

According to the comparison among the wet year, dry year and medium year, the runoff discharge is large in the wet year, the river bed volume is large (river bed volume in July is 2.1 times that in the dry year), and the tide is strong (the maximum monthly average tidal range is 2.9 times that in the dry year and 1.8 times that in medium year); in the wet period, the salinity of the river water is very low, but the salinity of the river is higher in the autumn of the year, which shows the large changes of the salinity of the river in the year. The monthly maximum range of chlorinity change is 0.01–1.718 g/L; the maximum value is 172 times the minimum value; the annual average maximum value is 0.532 g/L, about 1 times higher than that in dry period; in the dry year, the runoff discharge is small, bed volume is small, the tide is weak, and salinity changes of the river water is relatively small with the monthly average maximum chlorine range of 0.02–0.56 g/L (the maximum value is 28 times the minimum value)

2.3 Relationship Between Runoff-Channel Volume-Salinity

In view of the characteristics of the large scouring and large silting of the river bed of the Qiantang Estuary and its characteristic of the severe feedback of salt tide intrusion, the river channel volume is introduced as an important parameter. First, the diversified and correlated relationship between the time exceeding salinity standard of river water at the water intake and runoff ($\triangle Q$), tidal range ($\triangle Z$) at Qibao station is established (Fig. 5a); then the correlated relationship between the river channel volume (V_7) in the Qiantang Estuary and the maximum monthly tidal range at Qibao (Fig. 5b) is used to reveal the interaction between the runoff-channel volume- salinity of salt tide of the Qiantang Estuary, and reflect that the effect of runoff on the salinity of salt tide is not only instantaneous, but also has lagging effect through the interaction between water flow, sediment transport and river bed, which is the unique law of salt tide intrusion in the Qiantang Estuary.

2.4 2D Salinity Movable Bed Mathematical Model

Although the Qiantang Estuary is the one of strong mixed type, there are still differences for salinity on the plane due to the facts that there's the existence of the main

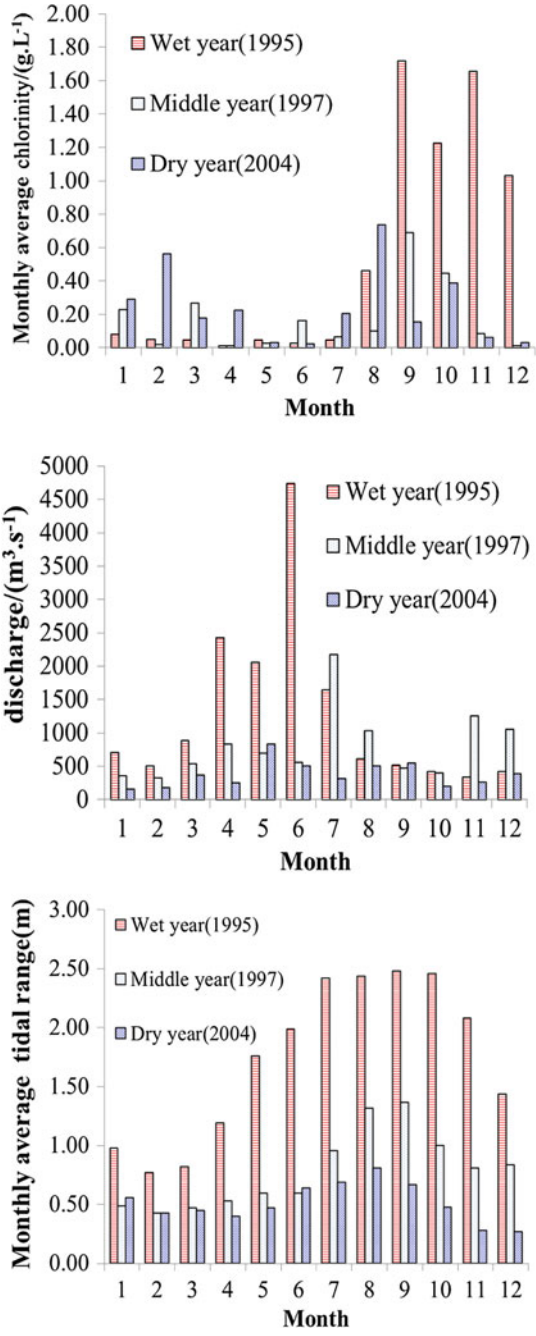

Fig. 4 The relationship between monthly average chlorinity, discharge and tidal range

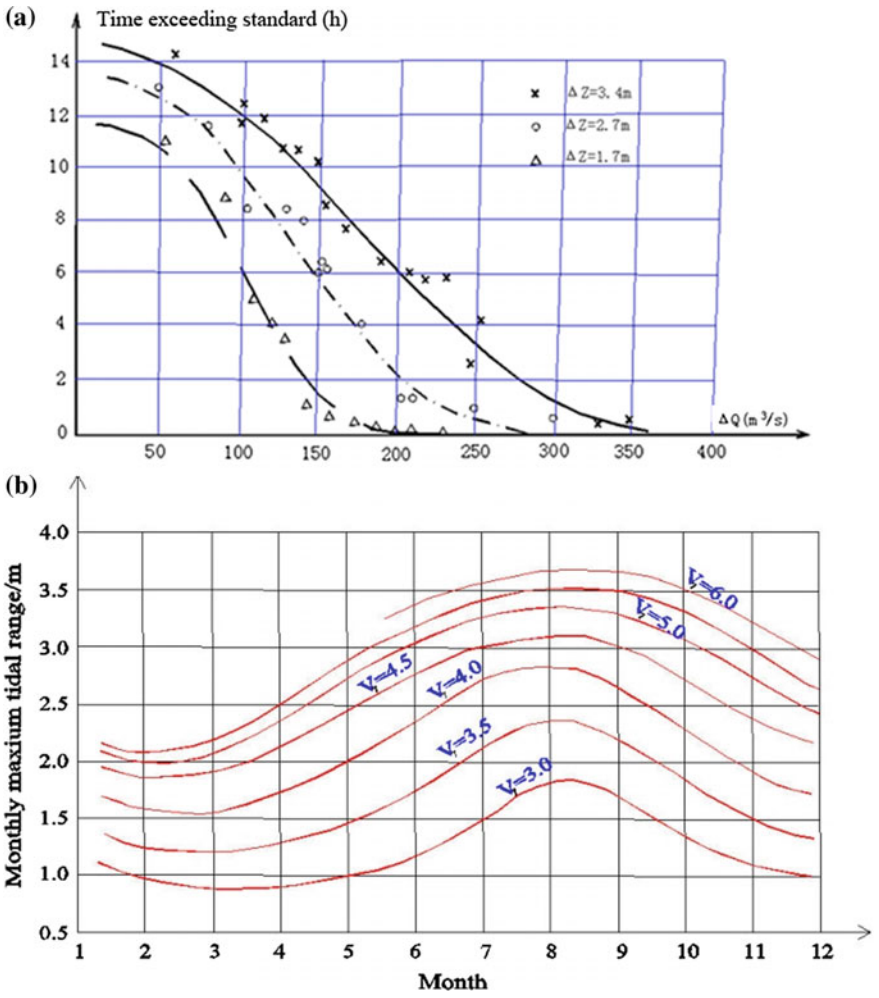

Fig. 5 **a** Relationship between salinity standard exceeding time and runoff, tidal range **b** relationship between monthly maximum tidal range and river channel volume

channel and side beach, and the difference of water depth and flow rate of beach channel on the section. As mentioned aforesaid, the Qiantang Estuary is different from the general tidal estuary in that on the one hand, the existence of water level and sudden change of flow speed bring great difficulties to the numerical simulation. On the other hand, as the Qiantang Estuary is the strong alluvial one with strong tide, high sediment concentration and riverbed erosion/deposition, the sediment transport of tide is unbalanced, the sediment brought by the flood tides cannot be tide of the tide cannot be brought out by ebb current, which transports net sediment to the upstream,

resulting in sediment deposition from up to down. The long-term prediction of salinity is required to consider the impact of interaction between water and sand and river bed on tidal dynamics and salt tide intrusion.

The salinity numerical prediction taking the erosion and deposition of river bed into consideration shall also, in addition to water volume, momentum, salt quantity and other conservation equations, include the unbalanced sediment transport and river bed deformation equation etc. to carry out coupled solution. Based on the concept of the mixture density of water, sediment, salinity etc., the control equation of the model system is deduced as follows

$$\frac{\partial \boldsymbol{U}}{\partial t} + \frac{\partial F(\boldsymbol{U})}{\partial x} + \frac{\partial G(\boldsymbol{U})}{\partial y} = S(\boldsymbol{U}) \tag{1}$$

where: $U = \left(\boldsymbol{\rho_m h}, \boldsymbol{\rho_m hu}, \boldsymbol{\rho_m hv}, \boldsymbol{hs}, \boldsymbol{hc}, z_0\right)^T$ are water current, sediment, salinity and other variables, the interface flux F, G and equation source S are expressed as follows:

$$\boldsymbol{F} = \begin{bmatrix} \rho_m \boldsymbol{hu} \\ \rho_m \boldsymbol{hu}^2 + \frac{1}{2}\rho_m \boldsymbol{gh}^2 - 2\boldsymbol{h}\rho_m \nu_t \frac{\partial \boldsymbol{u}}{\partial \boldsymbol{x}} \\ \rho_m \boldsymbol{huv} - \boldsymbol{h}\rho_m \nu_t \left(\frac{\partial \boldsymbol{u}}{\partial \boldsymbol{y}} + \frac{\partial \boldsymbol{v}}{\partial \boldsymbol{x}}\right) \\ \boldsymbol{hus} - \boldsymbol{E}_{sx}\boldsymbol{h}\frac{\partial \boldsymbol{s}}{\partial \boldsymbol{x}} \\ \boldsymbol{huc} - \boldsymbol{E}_{cx}\boldsymbol{h}\frac{\partial \boldsymbol{c}}{\partial \boldsymbol{x}} \\ 0 \end{bmatrix}$$

$$\boldsymbol{G} = \begin{bmatrix} \rho_m \boldsymbol{hv} \\ \rho_m \boldsymbol{huv} - \boldsymbol{h}\rho_m \nu_t \left(\frac{\partial \boldsymbol{u}}{\partial \boldsymbol{y}} + \frac{\partial \boldsymbol{v}}{\partial \boldsymbol{x}}\right) \\ \rho_m \boldsymbol{hv}^2 + \frac{1}{2}\rho_m \boldsymbol{gh}^2 - 2\boldsymbol{h}\rho_m \nu_t \frac{\partial \boldsymbol{v}}{\partial \boldsymbol{y}} \\ \boldsymbol{hvs} - \boldsymbol{E}_{sy}\boldsymbol{h}\frac{\partial \boldsymbol{s}}{\partial \boldsymbol{y}} \\ \boldsymbol{hvc} - \boldsymbol{E}_{cy}\boldsymbol{h}\frac{\partial \boldsymbol{c}}{\partial \boldsymbol{x}} \\ 0 \end{bmatrix}$$

$$S = \begin{bmatrix} Q_s \rho_m / A \\ -\rho_m g h \left(\frac{\partial z_0}{\partial x} + \frac{u\sqrt{u^2+v^2}}{C_z^2 h} \right) + f \rho_m h v + Q_s \rho_m u \cos(\theta) / A \\ -\rho_m g h \left(\frac{\partial z_0}{\partial y} + \frac{v\sqrt{u^2+v^2}}{C_z^2 h} \right) - f \rho_m h u + Q_s \rho_m v \sin(\theta) / A \\ E - D \\ Q_s C_s / A \\ (D - E) / \gamma_s' \end{bmatrix}$$

where: h is the water depth; u, v are respectively the flow rates in x, y directions; c is salinity; s is sediment concentration in water; g is gravitational acceleration; z_0 is the river bottom elevation; C_z is Chezy coefficient; f is the Coriolis coefficient; ν_t is the eddy viscosity coefficient determined by Smagorinsky empirical formula (Smagorinsky 1963);

$\rho_{m=}\rho_0 + \alpha c + s(\rho_s\text{-}\rho_0)/\rho_s$ is the muddy water density; ρ_0 is the fresh water density; E_{sx}, E_{sy} are the turbulence diffusion coefficient of sediment in x and y directions respectively; E_{cx}, E_{cy} are the turbulence diffusion coefficient of salinity in x and y directions respectively; Q_s and C_s are the flow rate and chlorinity concentration at the water intake and outlet; and A is the area of control body.

The initial and boundary conditions for the above equations are as followings:

$$\begin{aligned} &\mathbf{z}(\mathbf{x}, \mathbf{y})|_{\mathbf{t}=0} = \mathbf{z}_0(\mathbf{x}, \mathbf{y}) \quad \mathbf{u}(\mathbf{x}, \mathbf{y})|_{\mathbf{t}=0} = \mathbf{u}_0(\mathbf{x}, \mathbf{y}) \\ &\mathbf{v}(\mathbf{x}, \mathbf{y})|_{\mathbf{t}=0} = \mathbf{v}_0(\mathbf{x}, \mathbf{y})| \quad \mathbf{c}(\mathbf{x}, \mathbf{y})||_{\mathbf{t}=0} = \mathbf{c}_0(\mathbf{x}, \mathbf{y})|; \\ &\mathbf{s}(\mathbf{x}, \mathbf{y})||_{\mathbf{t}=0} = \mathrm{s}_0(\mathbf{x}, \mathbf{y})| \end{aligned}$$

Water Boundary conditions:

$$z(x, y, t) = z^*(x, y, t), c(x, y, t) = c^*(x, y, t),$$

Flow into the computational domain:

$$\frac{\partial(Hc)}{\partial t} + \frac{\partial(Huc)}{\partial x} + \frac{\partial(Hvc)}{\partial y} = 0$$

Land boundary: $\vec{V}_n = 0$

flow rate in normal direction is zero, $\frac{\partial c}{\partial n} = 0$

Numerical solution Eq. (1) has already had many mature methods (MacCormack and Paullay 1972), but considering the influx of the Qiantang Estuary which has a high requirement for the conservation, intermittent capture and the source item processing of the numerical calculation format (Cun-hong and Kun 2006), this chapter uses the conservation variable to carry out finite volume method discretion on the Eq. (1) and avoids using h, hu and hv as the conservation variables to solve the water flow equation, which may result in the new baroclinic item, riverbed erosion and sedimentation and other source items discrete difficulties. As limited by the length of this chapter, the derivation of the numerical format is omitted.

2.5 Model Validation

2.5.1 Salinity Convection Diffusion Model Test

The convective transport in a square area uniform flow field of a circular distribution concentration is used as an example to test the model to verify the rationality of programming and mathematical processing. Computational domain is 2 × 2 m in area, the flow rate in the domain is steady uniform flow with the flow velocity of u = v = 0.8 m/s, and the distribution equation of the initial concentration is:

$$c(x, y, 0) = e^{-\left(\frac{(x-0.5)^2}{0.01}+\frac{(y-0.5)^2}{0.01}\right)},$$

the chlorinity diffusion coefficient is: $E_{cx} = E_{cy} = 0$

There are 22,992 computational domain triangular elements, and the number of triangular nodes is 11,667, and the time step is 0.001 s. In theory, the concentration distribution remains constant during transport, which will neither calm nor oscillate. The simulative result is as shown in Fig. 6.

From the figure, the distribution result of the circular density of the second-order precision calculation flowing in the direction along square diagonal of the model is similar to the theoretical value in the flow direction of the along the square line at 1.25 s after the transport is basically in line with the theoretical value except for the slight numerical diffusion; the calculation error of the maximum value is 1%, and the concentration in the calculation process does not appear negative. But the corresponding first-order precision calculation format appears to be calming, and the area with larger concentration gradient of the larger areas shows negative concentration.

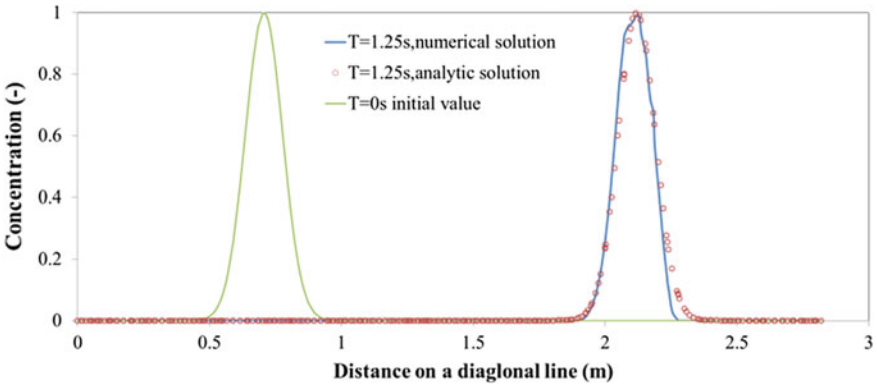

Fig. 6 Transport of circular concentration distribution in a uniform flow field

2.5.2 Salinity Verification in the Qiantang Estuary

The established 2D salinity movable bed numerical simulation is used in the numerical simulation of salinity transport process of Qiantang Estuary for more than half a year. The numerical calculation area and the hydrological verification points are as shown in Fig. 1. The upper boundary of the model is at the Fuchunjiang hydropower station, and the lower boundary is at the Ganpu section of the Qiantang Estuary with the computational domain of 790 km^2. The computational grid adopts the unstructured triangular element, and is intensified appropriately near the water intake and outlet of the key area; the computational grid totally arranges 11,710 triangular elements and 6973 nodes; the minimum triangular element is about 100 m in length with the time step length of 60 s. The upper boundary condition adopts the daily discharge of the power station and the constant chlorine content of 0.01 g/L, and the lower boundary adopts the actually measured tide level and the chlorinity process at Ganpu station. The water, sediment and salt process of the Qiantang Estuary from July to December in 2007 have been verified; Shi et al. (2012, 2015) adopts respectively 1D movable bed and 2D fixed-bed mathematical model to perform the calculation, and in this chapter, 2D salinity movable bed model is used to calculate. As limited by the length of this chapter, this chapter has focused on listing the chlorinity process validation result in August and September at Qibao station. Such two models as moving bed and fixed bed are respectively used to carry out simulated calculation.

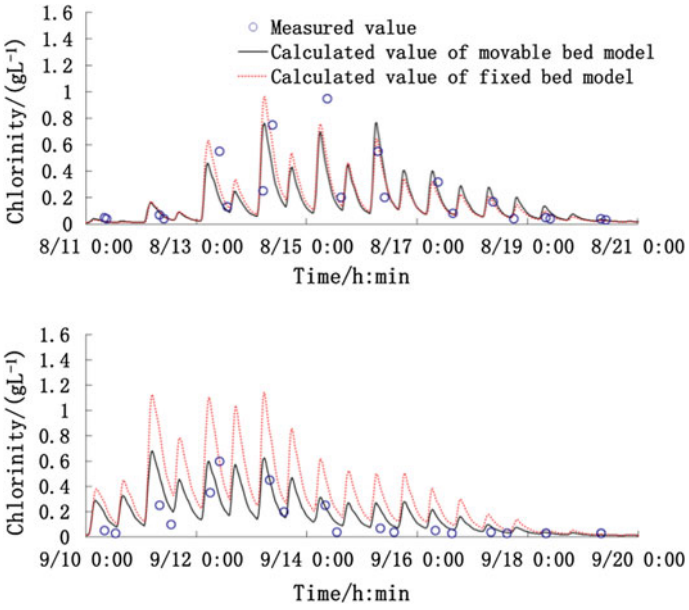

Fig. 7 Comparison of calculated and measured values of chlorinity in August and September, 2007

Figure 7 is the comparison between the calculation and the actually measured values in the spring tide period from August to September at Qibao station.

From Fig. 7, it is obvious to see the difference between the movable bed and the fixed-bed calculation of long-term chlorinity; in the first month (as in August), the difference between the movable bed and the fixed bed is not yet apparent, but the second month (e.g., September), the difference between movable bed and fixed bed is very significant; according to the movable bed calculation, the maximum chlorinity is about 0.6 g/L, which is close to the actually measured values, while the corresponding value of fixed bed calculation can reach up to 1.15 g/L, a difference of about one times. The reason is that the Qiantang Estuary is a strong alluvial estuary, and the silt of its river bed is easy to scour and silt. The variation of runoff is very sensitive to the erosion/siltation of the river bed. The tidal volume and tidal range decrease due to the obvious siltation of the river bed in the middle and late stage of the dry water and spring tide season, which leads to the weakening of salt water intrusion and the decrease of chlorinity. While the fixed bed model is completely unable to reflect this kind of feedback effect on the tidal dynamics and salinity, so that the simulation error is great for the fixed bed salinity mathematical model.

The error analysis formula (van Rijn et al. 2003) was used to evaluate Brier skill score (BSS) of the movable bed and fixed bed salinity forecast models. BSS of the movable bed model is 0.8, which is excellent, and the fixed bed model score is 0.5, which is fair. Therefore, it is necessary to adopt the movable bed model for salinity prediction in the medium or long-term (more than half a year) for the Qiantang Estuary.

2.6 Model Application

2.6.1 Impact of Runoff and Tide on Saline Water Intrusion Distance

A quantitative study is made on the change about the distance from the upper bound of chlorinity line (0.25 g/L) to Ganpu in the estuary using the verified 2D chlorinity mathematical model (as shown in Fig. 8). It shows that under the identical discharge, the distance of saline water intrusion is further with stronger tide. E.g. as the discharge is 400 m^3/s, with 4.0 m tidal range, the upper bound of saline water intrusion is about 130 km away from Ganpu; with 2.8 m tidal range, the upper bound approaches 109 km; with 1.5 m tidal range, the upper bound is at 85 km. The distance of saline water intrusion may differ by 24–45 km with different tidal ranges.

The intensity of saline water intrusion is correlated with the size of runoff. It is visible in the Fig. 8 that as the upstream discharge is 5 m^3/s, the furthest distance from the upper bound of saline water intrusion to Ganpu is about 150 km, 146 km and 135 km respectively, when the tide range of Qibao station is at 4.0, 2.8 and 1.5 m. As the runoff discharge is 1000 m^3/s, the furthest distance is about 106, 94 and 70 km, when the tide range of Qibao is at 4.0 m, 2.8 m and 1.5 m. Evidently, the upper bound of saline water intrusion in the Qiantang Estuary is basically beside

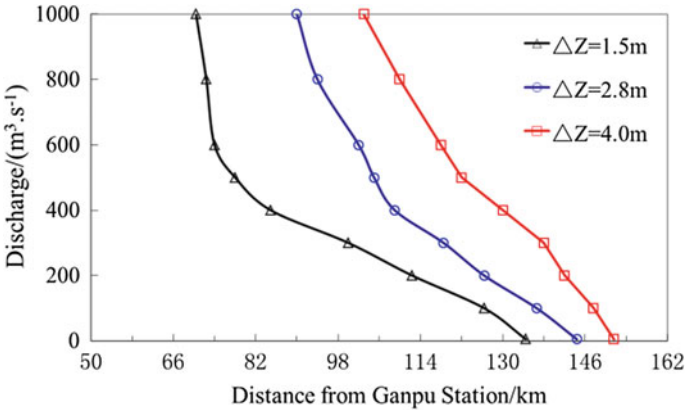

Fig. 8 Impact of discharge and tide range on saline water intrusion distance

Fuyang under extremely low water, and under the condition of the average discharge of 350–400 m^3/s and the tide range of 2.0–3.0 m during spring tide, it is, by and large, nearby the place from Shanhusha to Qibao. This is fully identical with the layout of main water intakes in Hangzhou City at present.

Under the same tidal range, as the discharged runoff at Fuchunjiang Hydropower Station decreases, the distance of saline water intrusion increases. Furthermore, with the same decrease of flow, the intrusion distance increases significantly with smaller flow. For the discharge >500–600 m^3/s, the increase of the same flow has a weakened inhibiting effect on saline water intrusion. For the discharge <500–600 m^3/s, flow increase may significantly reduce saline water intrusion. This conclusion is consistent with the conclusion of chlorinity control and operation in recent 40 years. It implies that infinite increase of discharged runoff to inhibit saline water intrusion has a slight impact on increasing the utilization efficiency of water resource at the Qiantang Estuary.

2.6.2 Impact of Runoff and Tide on Over-Standard Time of Chlorinity at the Water Intake

Table 2 shows the statistical result of the continuous over-standard time of chlorinity at the river water of spring tide (15d) under different discharge (Q) and tide range (△Z). Apparently, runoff and tide may impact the over-standard time of chlorinity at the water intake. As the maximum tidal range in Qibao reaches 2.8 m and the discharged runoff is smaller than 200 m^3/s in a spring tide, the over-standard time of chlorinity at the water intake may be as long as above 6.4d. While the discharge is greater than 300 m^3/s, the continuous over-standard time is within 0.3d. With 1.5 m tidal range, the discharge with standard chlorinity at the water intake is about

Table 2 Statistics on the continuous over-standard time of chlorinity (d)

	△Z = 4.0 m	△Z = 2.8 m	△Z = 1.5 m
Q = 5 m^3/s	12.0	12.0	11.8
Q = 100 m^3/s	11.3	9.6	8.8
Q = 200 m^3/s	8.8	6.4	0.35
Q = 300 m^3/s	4.4	0.3	0.0
Q = 400 m^3/s	0.4	0.1	0.0
Q = 500 m^3/s	0.2	0.0	0.0

300 m^3/s. These results calculated are all consistent with the data observed under the same conditions in recent 40 years.

2.6.3 Planar Distribution of Chlorinity at the River Bend

The lateral distribution of chlorinity isoline is significantly affected by the morphology of the river section, and the lateral distribution of chlorinity shows remarkable differences in different reaches, due to different plane modalities of riverbed. In the straight reach, the lateral distribution of chlorinity is relatively uniform due to U-shaped section morphology and can be simulated with 1D model; while the swale varies significantly in water of depth at the section of river bend, the lateral distribution of chlorinity shows obvious non-uniformity. Figure 9 shows the planar distribution of chlorinity at steep rise of Qige Bend and Laoyancang Bend.

Apparently, the chlorinity isoline presents an uneven lateral distribution, and chlorinity at the concave-bank deep channel is smaller than that at convex-bank beach on the whole. This is mainly because that the rising time of tide at the bottomland is earlier than that at the concave-bank deep channel, the tidewater with high salinity may reach the convex-bank beach first, while the fresh water with lower salinity may discharge from the main channel generally, showing slightly lower chlorinity. However, this lateral variation of chlorinity will decrease gradually with the rise of the tidal level.

3 Conclusions

The main factors affecting the intrusion of saltwater in the Qiantang Estuary are runoff, tide and river channel terrain. The effect of runoff on the salinity of Qiantang Estuary is both direct and indirect. The indirect effect of runoff on saltwater intrusion in Qiantang Estuary is mainly through runoff erosion and scouring, which increases tidal dynamics after wet season and indirectly affects salt tide intrusion.

In view of the characteristics of severe erosion/deposition of the Qiantang Estuary and its characteristic of the obvious feedback effect of erosion/sedimentation on saltwater intrusion, the river channel volume is introduced as an important parameter

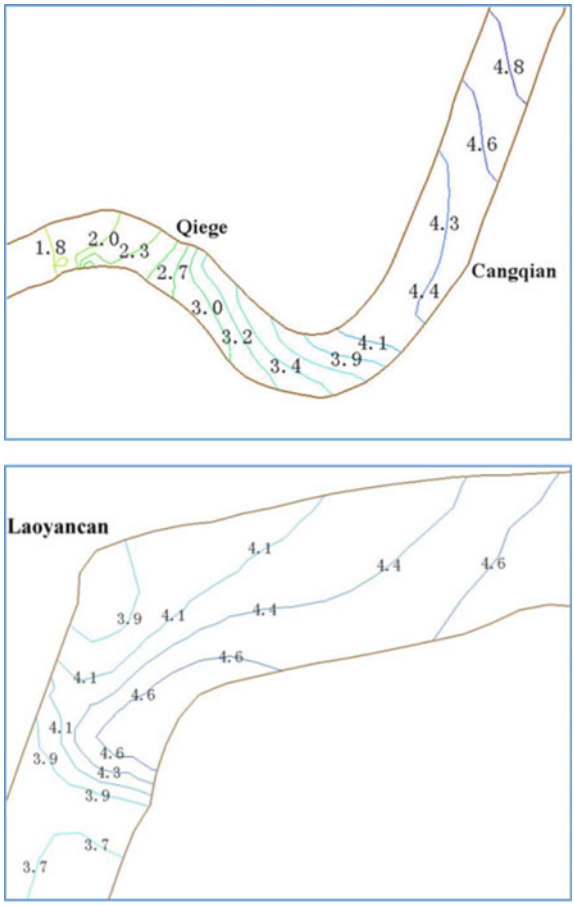

Fig. 9 Planar distribution of chlorinity (g/L)

to establish the interactive relationship among runoff, channel volume and salinity, which reflect that the effect of runoff on the salinity is not only instantaneous, but also shows the lagging effect through the interaction between hydro-sediment dynamics and riverbed. It can be used to forecast the time of excessive salinity at the water intake.

The 2D salinity movable bed mathematical model considering water flow, sediment salinity transport and river bed deformation and other multiple factor couplings has been established. The actually measured water flow, sediment, salinity and other data are used to verify the salinity transport process and the model established can reflect the actual transport law of water flow, sediment, and salinity in the Qiantang Estuary. The study shows that riverbed scouring and silting have large effect on the salinity transport for the medium and long term at the Qiantang Estuary and it is imperative to use movable bed model for salinity forecast. This movable riverbed

model has been successfully applied to predict the saltwater intrusion in the fighting against salt tide to guarantee the safety of water supply in Hangzhou City.

Acknowledgements The research reported in this chapter was supported by the special Project of Zhejiang Province Scientific Research Institute (No. 2016F50018).

References

Bao, Y., Liu, J. B., Ren, J., et al. (2009). Research of law and dynamic mechanism for strong saline water intrusion in Modaomen waterway. *China Science G, 39*(10), 1527–1534.

Cun-hong, P., & Kun, X. (2006). Kinetic flux vector splitting scheme for solving 2-D shallow water equations with triangular mesh. *Chinese Journal of Hydraulic Engineering, 37*(7), 858–864.

Han, Z. C., Cheng, H. P., & Shi, Y. B. (2012). Long term forecast of salt water intrusion at the Qiantang Estuary. *Chinese Journal of Hydraulic Engineering, 43*(2), 232–240.

Han, Z. C., Dai, Z. H., & Li, G. B. (2003). *Management and development of Qiantang Estuary*. Beijing: China Water Resources and Hydropower Press.

Han, Z. C., Pan, C. H., & Shi, Y. B. (2002). Effects of human activities on saltwater intrusion in estuaries. *Advances of Water Science, 13*(3), 333–339.

MacCormack, R. W., Paullay, A. (1972). Computational efficiency achieved by time split ting of finite difference operators. *AIAA Paper*, 72–154.

Mao, H. L. (1964). Preliminary study on mixed tide of Hangzhou Bay. *Oceanology ET Limnologia Sinica, 6*(2).

Pan, C. H., Zhang, S. Y., Shi, Y. B., et al. (2014). Study on saltwater intrusion in Qiantang Estuary affected by tidal bore. *Chinese Journal of Hydraulic Engineering, 45*(11), 1301–1308.

Savenije, H. H. G. (2005). *Salinity and tides in alluvial estuaries*. Amsterdam: Elsevier Press.

Shen, F., Mao, Z., & Zhu, J. (2003). *The saltwater intrusion of the Changjiang Estuary*. Beijing: The Ocean Publish.

Shi, Y. B., Li, R. H., & Yao, G. H. (2015). 1D Movable bed numerical forecast model of salinity of the Qiantang Estuarine reach and its application. *Advances of Water Science (chinese), 26*(2), 212–220.

Shi, Y. B., Pan, C. H., Cheng, W. L., et al. (2012). Temporal spatial variation and numerical forecast model of salt water intrusion of the Qiantang Estuarine reach. *Advances in Water Science (Chinese), 23*(3), 419–428.

Smagorinsky, J. (1963). General circulation experiment with the primitive equations. *Monthly Weather Review, 91*(3), 99–164.

van Rijn, L. C., Walstra, D. J. R., Grasmeijer, B., et al. (2003). The predictability of cross-shore bed evolution of sandy beaches at the time scale of storms and season using process-based profile models. *Coastal Engineering, 47,* 295–327.

Seasonal Salinity Variations in a Coastal Wetland Induced by Complex Interactions Between Sea, River and Evapoconcentration Processes

Micòl Mastrocicco, Gianluigi Busico, Nicolò Colombani, Alessio Usai and Daniela Ruberti

Abstract Deltaic coastal areas are often formed by a piecemeal of transitional wetland environments. These environments consist of wetland-aquifer systems, which commonly react rapidly to climate changes. Direct evaporation from surface water bodies like lakes, wetlands and lagoons will increase due to temperature increase leading to salt accumulation. To understand the hydrological exchanges between the transitional coastal wetlands of the Variconi oasis, the unconfined aquifer of the Volturno River Delta and the Tyrrenian Sea, the contributions of various processes were monitored and assessed. Physical-chemical parameters like salinity, pH, Eh and temperature were monitored during the hydrological year 2016–2017 on a monthly basis. Moreover, the use of groundwater and surface water equivalent freshwater heads, along with hydraulic conductivity tests and the geological architecture, permitted to connect the salinity variations in the wetlands with the degree of the hydraulic connection between the wetlands, the Volturno River, the Tyrrenian Sea and the coastal aquifer. The results show that the permanent wetlands fed by both the Volturno River and the Tyrrenian Sea, show a smoothed salinity peak during the summer season; while the ephemeral wetlands hydraulically disconnected from the aquifer show high salinity peaks during the summer season due to evapoconcentration processes. Spatial mapping of salinity and other measured parameters, highlighted an elevated heterogeneity of environments (from saline to freshwater

M. Mastrocicco · G. Busico
DiSTABiF—Department of Environmental, Biological and Pharmaceutical Sciences and Technologies, University of Campania "Luigi Vanvitelli", Via Vivaldi 43, 81100 Caserta, Italy

N. Colombani (✉)
SIMAU—Department of Materials, Environmental Sciences and Urban Planning, Polytechnic University of Marche, Via Brecce Bianche 12, 60131 Ancona, Italy
e-mail: n.colombani@univpm.it

A. Usai
Ente Riserve Naturali Regionali "Foce Volturno-Costa Di Licola" E "Lago Falciano", Via Giotto, 13, 81030 Castel Volturno Caserta, Italy

D. Ruberti
DiCDEA—Department of Civil Engineering, Buildings Design and Environment, University of Campania "Luigi Vanvitelli", via Roma 29, 81031 Aversa Caserta, Italy

K. D. Nguyen et al. (eds.), *Estuaries and Coastal Zones in Times of Global Change*, Springer Water,
https://doi.org/10.1007/978-981-15-2081-5_6

environments) enclosed in the Variconi oasis. This in turn, induced a large biodiversity of both autochthonous and migratory species. Despite of this, the projected increase in salinity of these wetlands due to coastal erosion, augmented evapotranspiration rates and sea level rise, could be of serious concern for the above-mentioned biodiversity, thus monitoring and management strategies are urgently required to preserve this and other oasis in the Mediterranean area that are key sites employed as stop-over along migratory routes.

Keywords Transitional environments · Groundwater salinization · Hydrological cycle · Environmental monitoring

1 Introduction

Coastal wetlands are important ecotones and usually host a variety of sedentary and migratory species (Childers 2006; Holland et al. 1990). These environments are more and more frequently threatened by the growing and unmanaged urbanization (Lee et al. 2006), which influences the functionality of coastal wetlands affecting the hydrological cycle, and consequently the nutrients and contaminants fluxes (McGrane 2016). Coastal wetlands are characterized by elevated variety in salinity; in fact, they can be brackish, saline or hypersaline depending on their geographical location (Webster 2010). Coastal wetlands may be connected to surface water bodies such as rivers, and/or to aquifers (Golden et al. 2014). In addition, wetland-aquifer systems can be hydraulically managed by pumping stations for land reclamation in polders (Colombani et al. 2017; Yu et al. 2018). Given that in coastal wetlands salts accretion may induce an alteration from species-rich freshwater biota to species-poor salt tolerant biota (Nielsen and Brock 2009), understanding the key factors that drive salinity shifts in coastal wetlands in highly anthropized areas is a priority.

To achieve this target, the geological architecture that permits or inhibits water fluxes between surface and groundwater bodies must be known in detail (Kløve et al. 2011). The Variconi oasis was selected for the present study because a precise stratigraphic and sedimentary information is available (Amorosi et al. 2012), and land use changes over the last century have been recorded and mapped (Ruberti et al. 2017). Thus, a reconstruction of the past and actual zones where groundwater and surface water actively exchange was obtained. Besides, it has been demonstrated that here direct evaporation from coastal wetlands and lagoons will increase leading to salt accumulation (Werner et al. 2013; Havens and Steinman 2015), due to climate change effects, like sea level rise and changes in evapotranspiration/recharge rates. Moreover, according to Lambeck et al. (2011) predictions, the Tyrrenian Sea level rise in the proximity of the Volturno River mouth will produce a relative sea level rise for the next century ranging from approximately 0.22–1.44 m. Therefore, it is necessary to study the mutual interplay between the coastal wetlands and the coastal aquifer. For this reason, in the presented work, a dataset collected during a hydrological year was studied to estimate the processes that drive the salinity variations within the

Variconi oasis coastal wetlands. The geological architecture and hydrogeological information were both employed to constrain the conceptual model.

2 Study Area

The study area is situated in the coastal floodplain pertaining to the Volturno River mouth, in the Campania Plain (Southern Italy) at a latitude of 41.02° and a longitude of 13.93° (Fig. 1). The Variconi oasis, included in the Ramsar Wetland convention, is an area considered significant for both its environmental and ecological value although it has been subjected to frequent land use changes (Ruberti and Vigliotti 2017). Since this is a low-lying area, with mean ground elevation above sea level (a.s.l.) of approximately 1.0 m, precipitations accumulate to form semi-permanent water bodies. The coastal aquifer is formed by sandy dune sediments (16–18 m thick) interbedded with silt lenses (0.5–1.0 m thick), which locally generate semi-confined conditions. At approximately a depth of −16 m a.s.l., a clay prodelta wedge forms the saline aquiclude. The water table depth is generally shallow, between 0.5 and 1.5 m below ground level (b.g.l.). The groundwater flow is converging towards the coastal wetlands and the Tyrrenian Sea, since the Volturno River behaves as a groundwater divide that feeds the aquifer (Busico et al. 2018). This hydrogeological pattern could trigger upcoming conditions from the saline groundwater hosted below the wetlands. Within this composite hydrogeological context, the coastal wetlands of the Variconi oasis have been monitored to recognise their connections with the shallow aquifer.

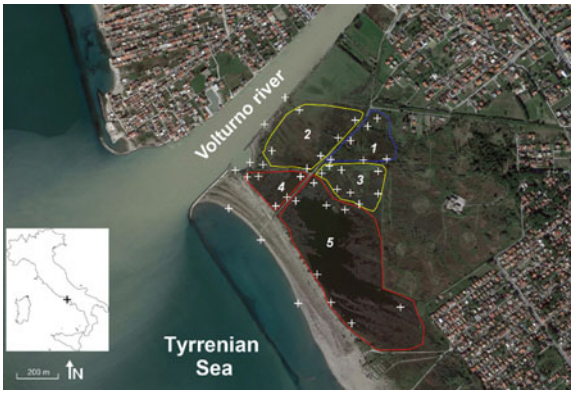

Fig. 1 Location of the Variconi oasis, with sampling points (white crosses) and wetlands maximum extension. Red polygons 4 and 5 are characterized by polyhaline water, yellow polygons 2 and 3 by mesohaline water and blue polygon 1 by oligohaline water

3 Materials and Methods

Thirty-one surface water monitoring stations and ten shallow auger holes down to −2 m b.g.l. were used to map surface water and groundwater quality and level. The selected monitoring stations are located within the main surface water bodies to characterize their spatial heterogeneities (Fig. 1).

The groundwater was sampled in a sampling campaign in May 2017 from the auger-drilled cores. A 60 ml syringe was used for low flow purging and groundwater collection. Temperature, pH, redox potential (Eh) and salinity were determined at the end of purging using a multi-parameter probe (Hydrolab MS-5). The measurements were converted into equivalent freshwater heads to take into account the variable density effect (Post et al. 2007). The temperature, pH, Eh and salinity data for surface waters were collected from the same stations in nine sampling campaigns from October 2016 to September 2017. The climatic data were found on a database available online (MIPAAF 2018). Actual evaporation rates from the wetlands were calculated using the Penman–Monteith equation by multiplying reference evapotranspiration for short grass with the crop coefficients suggested by Allen et al. (2007). The data of Tyrrenian Sea level were sourced from the database available online at the ISPRA web portal (ISPRA 2018).

4 Results and Discussion

Table 1 shows the monthly and cumulative precipitation and evapotranspiration trends in the Variconi oasis during the hydrological year 2016/2017 and for the climatic average. The difference between the cumulated precipitations in the hydrological year 2016/2017 and the climatic average are elevated, since 2017 has been recorded as one of the hottest years over the last century, with a reduction of approximately 25% of precipitations and a slight increase of evapotranspiration.

Figure 2 compares the mean monthly surplus (precipitation minus evapotranspiration) versus the 2016/2017 monthly surplus. The surplus estimation is considered reliable since the run-off at the site is negligible and irrigation has never been applied. Given that the mean surplus is nearly balanced, with only −77 mm/year of annual deficit, the equilibrium between water losses and gain is reached in the historical mean climatic record. While, during the monitored period an annual deficit of −339 mm/year was recorded. This was due to the lack of precipitations and the high temperatures recorded during the summer period (Table 1). Although, the year 2017 was an outlier respect to the historical mean, a constant increase in mean annual atmospheric temperatures has been recorded in this area over the last 15 years (Mastrocicco et al. 2018). Thus, this peculiar year could offer a window on the response of such oasis if stressed by warming conditions. Namely, the lack of recharge could increase salinity especially in the brackish and freshwater ponds due to evapoconcentration processes. Thus, the effects on salinity, pH and Eh recorded in the Variconi

Table 1 Monthly and cumulative precipitation and evapotranspiration rates for the hydrological year 2016/2017 and for climatic mean

Date	Prec. 2016/2017 (mm)	Prec. mean (mm)	EVT 2016/2017 (mm)	EVT mean (mm)
Oct-16	169.6	120.6	54	63.9
Nov-16	101.8	140.4	33.1	36.7
Dec-16	18.5	104.5	31.2	33.4
Jan-17	80.7	86.6	32.3	31.7
Feb-17	38.2	82.4	34.2	40.9
Mar-17	29.8	71.1	69.4	60
Apr-17	22	70.6	82.2	78.6
May-17	17.2	44.5	117.4	113
Jun-17	26.2	31	144.5	133.5
Jul-17	14.7	26.4	169.5	154.5
Aug-17	3.2	26.5	148.2	128.3
Sep-17	132.4	74.8	77.1	82.6
Cumulative	654.3	879.4	993.1	957.1

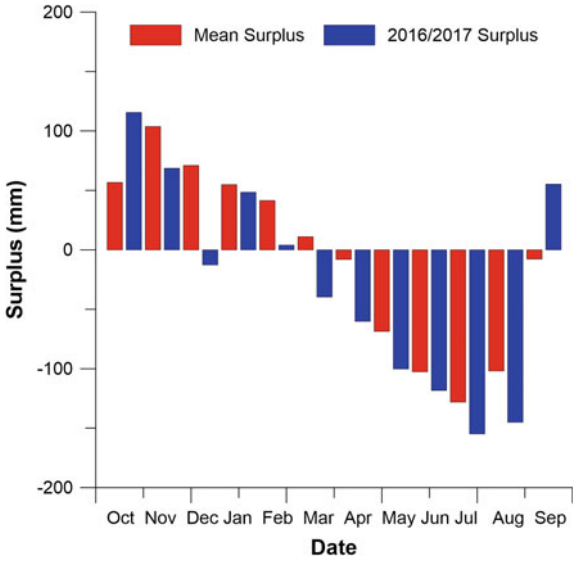

Fig. 2 Temporal trends of surplus in the Variconi oasis, calculated for the historical mean and for the monitored period

oasis during the hydrological year 2016/2017 can give some insights on the near future climate changes.

Figure 3 shows the salinity trends in the different ponds of the Variconi oasis during the hydrological year 2016/2017. It can be noticed that salinity shows a clear seasonal fluctuation in all the ponds due to the alternation of desiccation during the

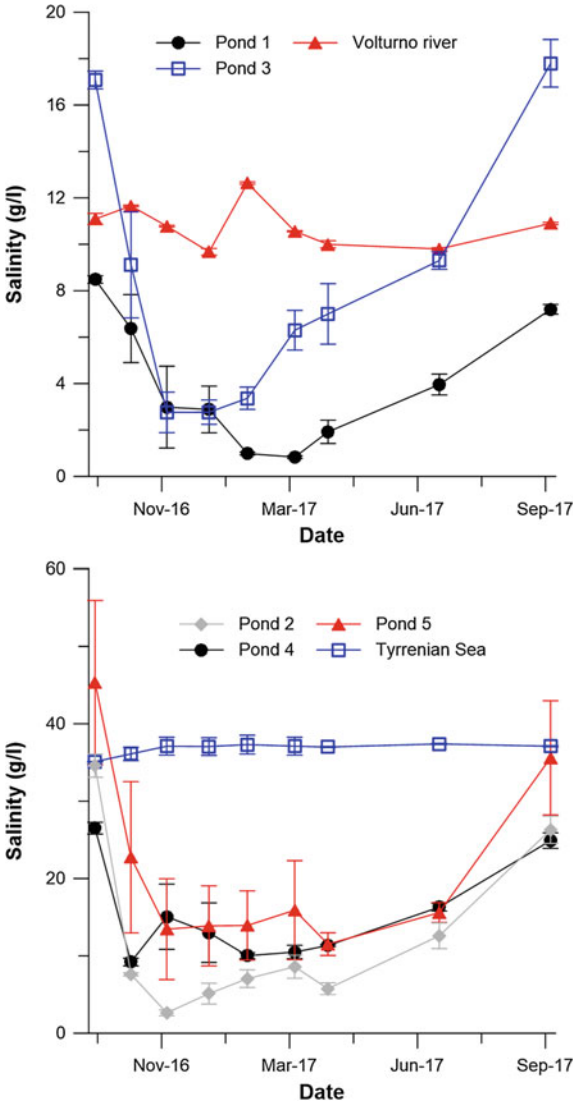

Fig. 3 Temporal trends of salinity in the Variconi oasis; refer to Fig. 1 for ponds' location. The error bars represent the standard deviations

late summer/early autumn period and recharge during winter/spring. This trend is not present in the Volturno River and the Tyrrenian Sea plots, both exhibiting stable values. Despite the increase of salinity in all the ponds during the summer time, the ponds 4 and 5 maintained a higher salinity also in wintertime since they are well connected with the Tyrrenian Sea via the sand dunes. This connection is more pronounced in the pond 5, while in pond 4 silty sediments at the bottom of the pond partially prevent groundwater fluxes.

The groundwater levels monitored via auger holes showed that the Volturno River is continuously recharging the shallow aquifer and the groundwater salinity (nearly the same of the Volturno River) confirmed this hypothesis. The pond 2 has only limited exchange with the shallow aquifer, since most of the area is confined by a lens of silty clay sediments.

Figure 4 shows the monitored central Tyrrenian Sea level variations during the study period. The graph shows that the tidal oscillations are not very pronounced, usually in the order of 0.4–0.5 m. The average value is −0.05 m a.s.l. with minimum and maximum of −0.36 and 0.41 m a.s.l. Although the variations of the sea level were not large during the monitored period, the data show a marked sea level decrease in December 2016 due to anomalous high atmospheric pressure in that period. While, from February to September 2017 the sea level slowly recovered towards positive values. Since the water level in the ponds of the Variconi oasis was always higher than 0.5 m a.s.l., saltwater intrusion is unlikely to occur at elevated rates. In fact, as shown by Fig. 3, seasonal variations of salinity in the freshwater and brackish ponds are more likely triggered by precipitation and evapotranspiration processes. Although, a density dependent numerical model should be employed to accurately quantify the water and salt exchange between the pond 4 and 5 (see Fig. 1 for location) and the Tyrrenian Sea. Besides, given the very low head gradients present in this flat area, the projected Tyrrenian Sea level rise (Lambeck et al. 2011), could severely impact the salinization of the ponds on a mid and long-term perspective.

Figure 5 shows the pH trends in the different ponds of the Variconi oasis during the hydrological year 2016/2017. Also for this parameter, a clear seasonal trend is recorded, with alkaline conditions during the summer/autumn period and slightly acidic conditions during the winter/spring period. The pH decrease of two orders of

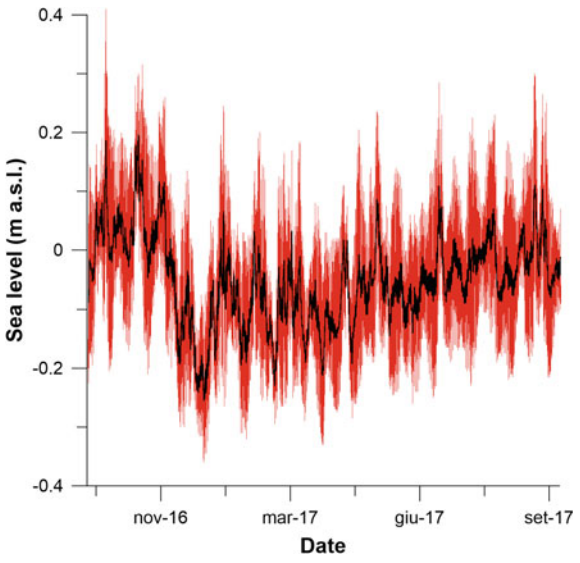

Fig. 4 Continuous measurements (very 10 min) of the central Tyrrenian Sea level (red line); in black is also plotted the running average every 12 h

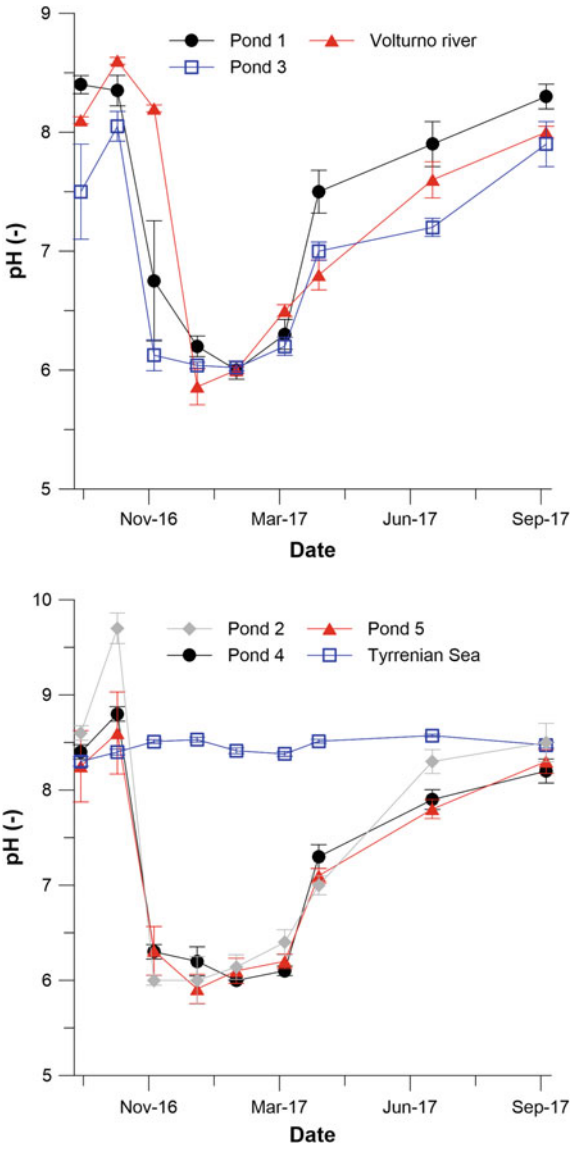

Fig. 5 Temporal trends of pH in the Variconi oasis; refer to Fig. 1 for ponds' location. The error bars represent the standard deviations

magnitude is due to precipitations that usually have slightly acidic composition in the Campania Plain (Arienzo et al. 2001). This trend is not applicable to the Tyrrenian Sea, while the Volturno River exhibits variable values also induced by rainfall events. In this case, pH is not a good proxy of the surface waters-groundwater interaction, since it is much affected by precipitations due to the lack of buffering capacity of these coastal wetlands.

Figure 6 shows the Eh trends for the different ponds of the Variconi oasis during the hydrological year 2016/2017. In this case, there is not a clear seasonal trend, nor in the ponds nor in the river and in the sea. The waters are all in oxic conditions, especially in winter when low temperatures and recharge from rainfalls promote oxygen dissolution in surface waters; only few samples collected in pond 2, where buffalos usually graze, show sub oxic conditions.

In general, the reported changes in climate as highlighted by the chart bars of Fig. 2 and consequently in water chemistry, together with human-induced coastal

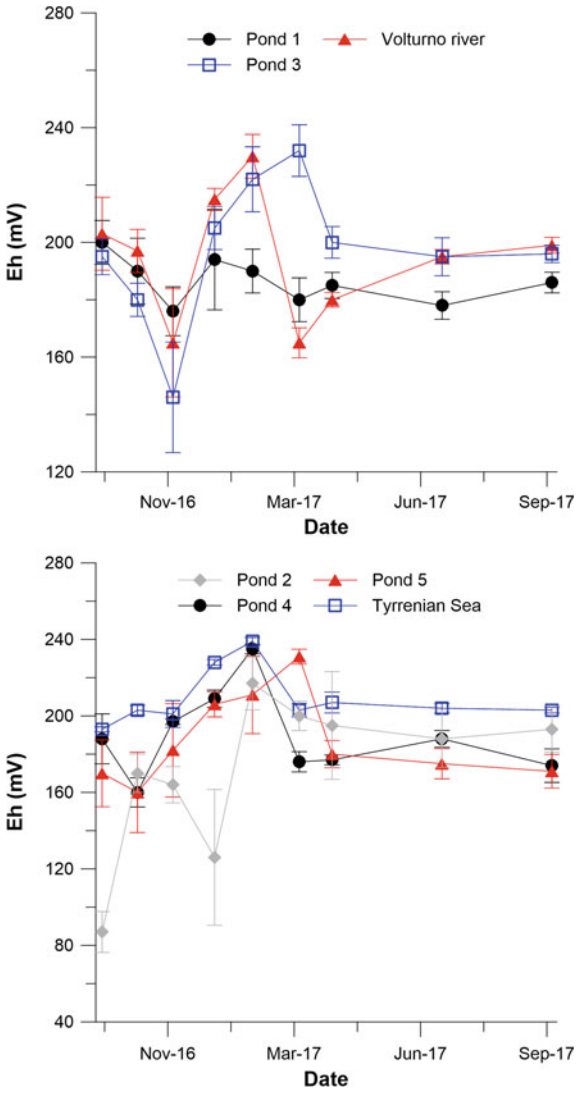

Fig. 6 Temporal trends of Eh in the Variconi oasis; refer to Fig. 1 for ponds' location. The error bars represent the standard deviations

erosion that has been demonstrated to be one of the major drivers of the local fluvial dynamics (Ruberti et al. 2017), may endanger the Variconi oasis biodiversity.

In fact, results of a study focusing on the preferences of migratory duck species over 11 wetland areas in Campania region (Giustino et al. 2017) showed that the most popular wetland resulted to be the Variconi coastal ponds, which were chosen by 9 out of 10 duck species. In particular, the Variconi oasis is one of the wetlands that hosts more wintering ducks throughout the whole nation; for instance, in wintertime it hosts more than 1% of the Gadwalls present on the Italian territory (Fraissinet et al. 2014). Moreover, it is a strategic site for at least two duck species, in fact more than 90% of Gadwall and Shoveler present in the Caserta province are concentrated here during the wintertime (Fraissinet et al. 2014).

In addition to ducks, many other bird species are present, e.g. the fan-tailed warbler, the blackcap, the chestnut warbler, the eye-catcher, the robin, the stonechat, the heron and the river nightingale. Besides, these coastal wetlands host a variety of plants like: reed beds, tamarisk groves, rush and glasswort marshlands.

Given the crucial importance of this site it is considered essential to intensify the monitoring of any possible impact attributable to climate change on this coastal wetland, also because the first signs of negative impacts have already been found: a slight decrease in the number of wintering ducks in the last 2 years and the appearance of alien species, like *Cotula coronopifolia*, recently recognized and registered in the Variconi oasis (Provincia di Caserta 2012).

5 Conclusions

The results show that the permanent wetlands are fed by both the Volturno River and the Tyrrenian Sea waters showing a smoothed salinity peak during the summer season, while ephemeral wetlands hydraulically disconnected from the aquifer show high salinity peaks during the summer season due to evapoconcentration processes. Spatial mapping of salinity and other measured parameters, highlighted an elevated heterogeneities of environments (from saline to freshwater environments) enclosed in the Variconi oasis. This in turn, induced a large biodiversity of both autochthonous and migratory species. Despite of this, the projected increase in salinity of wetlands due to coastal erosion, augmented evapotranspiration rates and sea level rise could be of serious concern in the near future for the above-mentioned biodiversity, thus monitoring and management strategies are urgently required to preserve this and others similar oasis in the Mediterranean area that are key sites employed as stop-over along migratory routes.

Acknowledgements The authors wish to acknowledge all the voluntary personnel working at the Variconi oasis for the tireless help in conserving this precious environment.

References

Allen, R. G., Wright, J. L., Pruitt, W. O., Pereira, L. S., & Jensen, M. E. (2007). Water requirements. In *Design and operation of farm irrigation systems* (2nd ed., pp. 208–288). Michigan, USA: American Society of Agricultural and Biological Engineers.

Amorosi, A., Pacifico, A., Rossi, V., & Ruberti, D. (2012). Late quaternary incision and deposition in an active volcanic setting: The Volturno valley fill, Southern Italy. *Sedimentary Geology, 282*, 307–320.

Arienzo, M., Adamo, P., Bianco, M. R., & Violante, P. (2001). Chemical, mineralogical and morphological characterization of wet and dry deposition in Campania Region (Southwest Italy). *Toxicological & Environmental Chemistry, 79*(3–4), 137–156.

Busico, G., Cuoco, E., Kazakis, N., Colombani, N., Mastrocicco, M., Tedesco, D., et al. (2018). Multivariate statistical analysis to characterize/discriminate between anthropogenic and geogenic trace elements occurrence in the Campania Plain, Southern Italy. *Environmental Pollution, 234*, 260–269.

Childers, D. L. (2006). A synthesis of long-term research by the Florida Coastal Everglades LTER Program. *Hydrobiologia, 569*(1), 531–544.

Colombani, N., Giambastiani, B. M., & Mastrocicco, M. (2017). Impact of climate variability on the salinization of the coastal wetland-aquifer system of the Po Delta, Italy. *Journal of Water Supply: Research and Technology-Aqua, 66*(7), 430–441.

Fraissinet, M., Bruschini, M., Esse, E., Grimaldi, S., Giustino, S., Mastronardi, D., et al. (2014). Andamenti delle anatre svernanti nelle zone umide della Provincia di Caserta nel periodo 2003–2014. *Picus, 40*, 109–118.

Giustino, S., Bruschini, M., Esse, E., Grimaldi, S., Mastronardi, D., Capasso, S., et al. (2017). Wetland selection, niche breadth and overlap in 10 duck species wintering in northern Campania (Italy). *Research in Ornithology, 87*(2), 3–8.

Golden, H. E., Lane, C. R., Amatya, D. M., Bandilla, K. W., Kiperwas, H. R., Knightes, C. D., et al. (2014). Hydrologic connectivity between geographically isolated wetlands and surface water systems: A review of select modeling methods. *Environmental Modelling & Software, 53*, 190–206.

Havens, K. E., & Steinman, A. D. (2015). Ecological responses of a large shallow lake (Okeechobee, Florida) to climate change and potential future hydrologic regimes. *Environmental management, 55*(4), 763–775.

Holland, M. M., Whigham, D. F., & Gopal, B. (1990). The characteristics of wetland ecotones. In *The ecology and management of aquatic-terrestrial ecotones* (pp. 171–198).

ISPRA. (2018). Marine National Tide Gauge Network Online Database. https://mareografico.it/.

Kløve, B., Ala-aho, P., Bertrand, G., Boukalova, Z., Ertürk, A., Goldscheider, N., et al. (2011). Groundwater dependent ecosystems. Part I: Hydroecological status and trends. *Environmental Science & Policy, 14*(7), 770–781.

Lambeck, K., Antonioli, F., Anzidei, M., Ferranti, L., Leoni, G., Scicchitano, G., et al. (2011). Sea level change along the Italian coast during the Holocene and projections for the future. *Quaternary International, 232*, 250–257.

Lee, S. Y., Dunn, R. J. K., Young, R. A., Connolly, R. M., Dale, P. E. R., Dehayr, R., et al. (2006). Impact of urbanization on coastal wetland structure and function. *Austral Ecology, 31*(2), 149–163.

Mastrocicco, M., Busico, G., & Colombani, N. (2018). Groundwater temperature trend as a proxy for climate variability. In *E-Proceedings of the 3rd EWaS International Conference—Insights on the Water-Energy-Food Nexus* (pp. 498–503).

McGrane, S. J. (2016). Impacts of urbanisation on hydrological and water quality dynamics, and urban water management: A review. *Hydrological Sciences Journal, 61*(13), 2295–2311.

MIPAAF. (2018). Agrometeorological Online Database. https://www.politicheagricole.it/flex/cm/pages/ServeBLOB.php/L/IT/IDPagina/7012.

Nielsen, D. L., & Brock, M. A. (2009). Modified water regime and salinity as a consequence of climate change: Prospects for wetlands of Southern Australia. *Climatic Change, 95*(3–4), 523–533.

Post, V., Kooi, H., & Simmons, C. (2007). Using hydraulic head measurements in variable-density ground water flow analyses. *Ground Water, 45*(6), 664–671.

Provincia di Caserta. (2012). Valutazione dell'incidenza del Ptcp sui siti Natura 2000. In *Piano territoriale di coordinamento provinciale* (p. 158).

Ruberti, D., & Vigliotti, M. (2017). Land use and landscape pattern changes driven by land reclamation in a coastal area: The case of Volturno delta plain, Campania Region, Southern Italy. *Environmental Earth Sciences, 76*(20), 694.

Ruberti, D., Vigliotti, M., Di Mauro, A., Chieffi, R., & Di Natale, M. (2017). Human influence over 150 years of coastal evolution in the Volturno delta system (Southern Italy). *Journal of Coastal Conservation*, 1–21.

Webster, I. T. (2010). The hydrodynamics and salinity regime of a coastal lagoon—The Coorong, Australia-Seasonal to multi-decadal timescales. *Estuarine, Coastal and Shelf Science, 90*(4), 264–274.

Werner, A. D., Bakker, M., Post, V. E. A., Vandenbohede, A., Lu, C., Ataie-Ashtiani, B., et al. (2013). Seawater intrusion processes, investigation and management: Recent advances and future challenges. *Advances in Water Resources, 51*, 3–26.

Yu, L., Rozemeijer, J., van Breukelen, B. M., Ouboter, M., van der Vlugt, C., & Broers, H. P. (2018). Groundwater impacts on surface water quality and nutrient loads in lowland polder catchments: Monitoring the greater Amsterdam area 2. *Hydrology and Earth System Sciences, 22*(1), 487–508.

Water Quality Mitigation Scenarios for Burullus Coastal Lake, Egypt

M. Elshemy, B. A. Zeidan and W. Assar

Abstract Lake Burullus is the second largest coastal lagoon in Egypt, its ecosystem has been deteriorated, due to its central location inside the Nile Delta. The lake receives most of the drainage water of the Nile Delta region through eight agricultural drains. The drainage water which discharged into the lake is mostly nutrient-rich fresh water, polluted with agricultural fertilizer and heavy metals from industry. Lake Burullus is classified as hypereutrophic with bad to very bad environmental conditions. The main objective of this study is to investigate the feasibility of applying different water quality management scenarios to improve the lake ecosystem. A calibrated hydrodynamic and water quality model for the lake was developed using a two-dimensional, vertically averaged, finite difference hydrodynamic and ecological code, MIKE21. This developed model was calibrated with measured field data collected during the period (June 2010–July 2011). Three hydrodynamic parameters and five water quality parameters of the lake were chosen to present the study results. These parameters are: water levels, water temperature, salinity, dissolved oxygen, biochemical oxygen demand, nitrate, Ammonia and ortho-phosphate. Three enhancing water quality scenarios for the lake were investigated: an additional artificial outlet, treatment plants for drains discharge and constructing of radial channels in lake bed. The study results verified that, economically, treatment plants scenario for the two most polluted drains is highly recommended. Constructing of an additional outlet will increase the average lake salinity and is considered as the most effective scenario for enhancing the DO concentrations in the lake. A water quality management strategy is urgently required for the lake ecosystem.

Keywords Lake burullus · MIKE 21 · Nile delta · Ecology

M. Elshemy (✉) · B. A. Zeidan · W. Assar
Faculty of Engineering, Tanta University, Tanta, Egypt
e-mail: m.elshemy@f-eng.tanta.edu.eg

M. Elshemy
Faculty of Engineering, Al-Baha University, Al-Baha, KSA, Saudi Arabia

K. D. Nguyen et al. (eds.), *Estuaries and Coastal Zones in Times of Global Change*, Springer Water,
https://doi.org/10.1007/978-981-15-2081-5_7

Abbreviations

AME	Absolute Mean Error
BOD	Biochemical Oxygen Demand
COD	Chemical Oxygen Demand
DO	Dissolved Oxygen
GIS	Geographical Information System
NH_4	Ammonium
NO_3	Nitrates
PO_4	Phosphate
RMS	Root Mean Square Errors
Sc.n	Scenarios No. n
Sn	Station No. n

1 Introduction

Pollution of the River Nile and freshwater lakes in Egypt reduces the availability of fresh water resources. Egyptian coastal lakes are five lakes, namely (from east to west); Lake Bardawil, Lake Manzalah, Lake Burullus, Edko and Maryut. These lakes were contributing by more than 50% of Egypt total fish production (Mehanna et al. 2014) but now their contribution is decreased to be about 11% (2004–2013) and to be about 9.96% in 2013 (GAFRD 2014). Egyptian coastal lakes have been highly contaminated in the last few decades, due to the high effluents loads of municipal, industrial and agricultural waste water (Elghobashy et al. 2001). Lake Burullus has been selected as a case study for this work because of its great economic importance; it is considered as one of the most productive lakes in Egypt and contributed by about 45% (2004-2013) and, unfortunately decreased to about 34% in 2013 from the total annual production of the northern Delta lakes (GAFRD 2014). The lake is considered as a very important resource for the local people (Zingstra 2013). Youness and Nafea (2012) reported that Lake Burullus is an important site for the migration and rest of birds, which should be conserved and protected. In 1998, Lake Burullus was declared as a national protected area, and added to RAMSAR sites (Shaltout and Al-Sodany 2008). In 2012, Youness and Nafea declared that the environmental conditions of the lake have been impacted by the discharge of agricultural wastes into the water body. The authors reported that continuous release of wastewater from the southern drains is much greater than seawater discharge into the lagoon. The lake has been converted from a brackish water lake into a fresh water lake due to the absence of the seawater inflow (Zingstra 2013). Zingstra (2013) concluded that the deteriorating quality of the lake (as aquatic environment) is mainly caused by conflicting management and lack of law enforcement. The author reported that there is no sense to elaborate a new management plan as long as the sharing of responsibilities is not clarified. This chapter addressed some pressures on the lake such as water pollution, climate change and the

lake area decreasing. The detection of lake area is caused by turning parts of the lake into either agricultural lands or aqua culture ponds. The author reported that during his study, the aqua culture ponds were still being built in the lake and the sand dunes and the salt marshes were still being reclaimed for agricultural purposes. The lake water pollution is mainly caused by: inflow of untreated domestic wastewater, effluent from the aqua culture ponds along the shoreline and the inflow of irrigated lands. Nutrients and heavy metals are recorded at increasing levels (Zingstra 2013). Several studies have recently discussed the ecosystem of Lake Burullus and assessed its biological status (Abou-Elela and Ghanem 2005; Al Sayes et al. 2007; Karajeh et al. 2011; Alsayes 2005; Eid et al. 2012, 2014; Nafea and Zyada 2015; Okbah 2005; Radwan 2005; Shakweer and Radwan 2004; Shaltout 2007, 2017; Yassin and Mahmoud 2016; Younis and Nafea 2012). In 2011, the trophic status index was used to investigate the trophic status of the lake (Karajeh et al. 2011). Lake Burullus was classified as hypereutrophic with bad to very bad environmental conditions. Obtained results showed that Lake Burullus has been severely deteriorated over the last two decades. Applying of remote sensing technique to study the lake change detection and water quality monitoring are addressed in some other publications (Mohsen et al. 2016; Hossen and Negm 2016; Hereher et al. 2010; Farag and El-Gamal 2011; El-Zeiny and El-Kafrawy 2017; El-Asmar et al. 2013; Donia and Farag 2012; Dewidar and Khedr 2005). The spatiotemporal changes of Lake Burullus in the period 1972–2015 were detected using twelve Landsat imageries and two water indices (Mohsen et al. 2016). Results revealed a significant decrease in the water area of the lake by about (49%) of its surface area. In 2017, El-Zeiny and El-Kafrawy (2017) explored the use of Landsat data and GIS for assessing the water pollution of Lake Burullus. The results showed that the lake is subjected to pollution from different sources; particularly domestic and agricultural drains. The south western and north eastern parts of the lake are the most polluted parts. The authors concluded that the lake is extensively subjected to interrupting human activities which negatively affect its water quality status. Investigation of Lake Burullus sediment state can be found in some published works (Appleby et al. 2001; Chen et al. 2010; El-Reefy et al. 2014; Khalil et al. 2007; Masoud et al. 2011; Nafea and Zyada 2015; Saeed and Shaker 2008; Shalaby et al. 2017; Younis et al. 2014). Chen et al (2010) stated that the pollution and eutrophication are increasingly threatening the ecosystems of the region of the Nile Delta. This study highlighted the increase of toxic heavy metals in the lake in recent years. The authors addressed the need for action to decrease pollution through run off from agricultural lands and from the effluent from aqua ponds in order to maintain the lake as a healthy and productive. Developing of a water quality model for the lake is a very difficult task which are addressed in limited publications (Akl et al. 2017; El-Adawy et al. 2013a, b, 2014; Soliman and Ushijima 2013; Soliman et al. 2013). In 2013, the impacts of two climate change scenarios on the salinity distribution in Lake Burullus were (Soliman and Ushijima 2013; Soliman et al. 2013). The results showed that an increase in the salinity values to about double of the current values is expected. Delft-3D model was utilized to develop a hydrodynamic model to investigate the impacts of climate change on evaporation rates and the spatial distribution of salinity in Lake

Burullus (El-Adawy et al. 2013a; El-Adawy et al. 2013b). In 2014, the authors developed the proposed model to include the water quality module of Delft-3D (WAQ). The feasibility of adding an additional artificial outlet or diversion of some connected drains to the west branch of the Nile to control the pollution in the lake were investigated (El-Adawy et al. 2014). The results revealed that the construction of a new outlet will increase the salinity in the lake, particularly in the area around the existing outlet, due to increased exchange rates between the lake and the Mediterranean Sea. While in the case of the drains diversion, DO will have an average increase of approximately 1 mg/l. In 2017, The Surface Water Modeling System (SMS) model was used to develop a hydrodynamic and water quality model for Lake Burullus to investigate the potential and effects of several factors on the developed model (Akl et al. 2017). Three parameters were simulated; water temperature, salinity and DO. Based on the literature review, it can be noticed that, Lake Burullus is exposed to large amounts of pollutants from the agricultural drains of the Delta region, so the lake ecosystem has been environmentally deteriorated. Moreover, this lake is expected to have great impacts on its water quality status due to future climate change, due to expected increase in air temperature and sea level rise. For that, feasible enhancing scenarios should be investigated to help decision makers to study and apply water quality management strategies. The objective of this study is investigating the feasibility of applying different water quality management scenarios for the lake using MIKE21 Code.

2 Study Area

Lake Burullus is a coastal lagoon which is connected to the Mediterranean Sea by a small natural outlet (Boughaz), about 44 m width. It lies between longitude 30° 30′ E and 31° 10′ E and latitude 31° 21′ N and 31° 35′ N in the Nile Delta, Egypt, between the two main Nile River branches: Rosetta and Damietta, The coastal length of the lake is about 65 km, with a varying width between 6 and 16 Kms, with an average of about 11 km (El-Adawy et al. 2013a). The main basin of Lake Burullus is classified to three sectors: eastern, middle and western, each of them has some sort of homogeneity in the geomorphological, hydrological and biological characteristics (Younis and Nafea 2012).The eastern sector of the lake is the shallowest with depth of the lake ranges between 0.42 and 2.07 m an average depth of 0.8 m (El-Shinnawy 2003). The Lake receives most of the drainage waters from cultivated areas through eight agricultural drains in addition to fresh irrigation water from Brimbal Canal at the western part of the lake, Fig. 1. El-Shinnawy (2004), characterized the hydrological situation of Lake Burullus, which collects agricultural drainage water from about 4000 km^2. He reported that, under its original natural conditions the water level of Lake Burullus ranged from 0 to 26 cm below sea level, allowing clean sea water to enter the lake. However, due to the continuous inflow of drainage water, the inflow to the lake is now greater than its outflow and consequently, its water level now ranged between 0 and 0.61 m above mean sea level, and therefore the lake water is in continuous movement toward the sea. The author indicated that, by applying

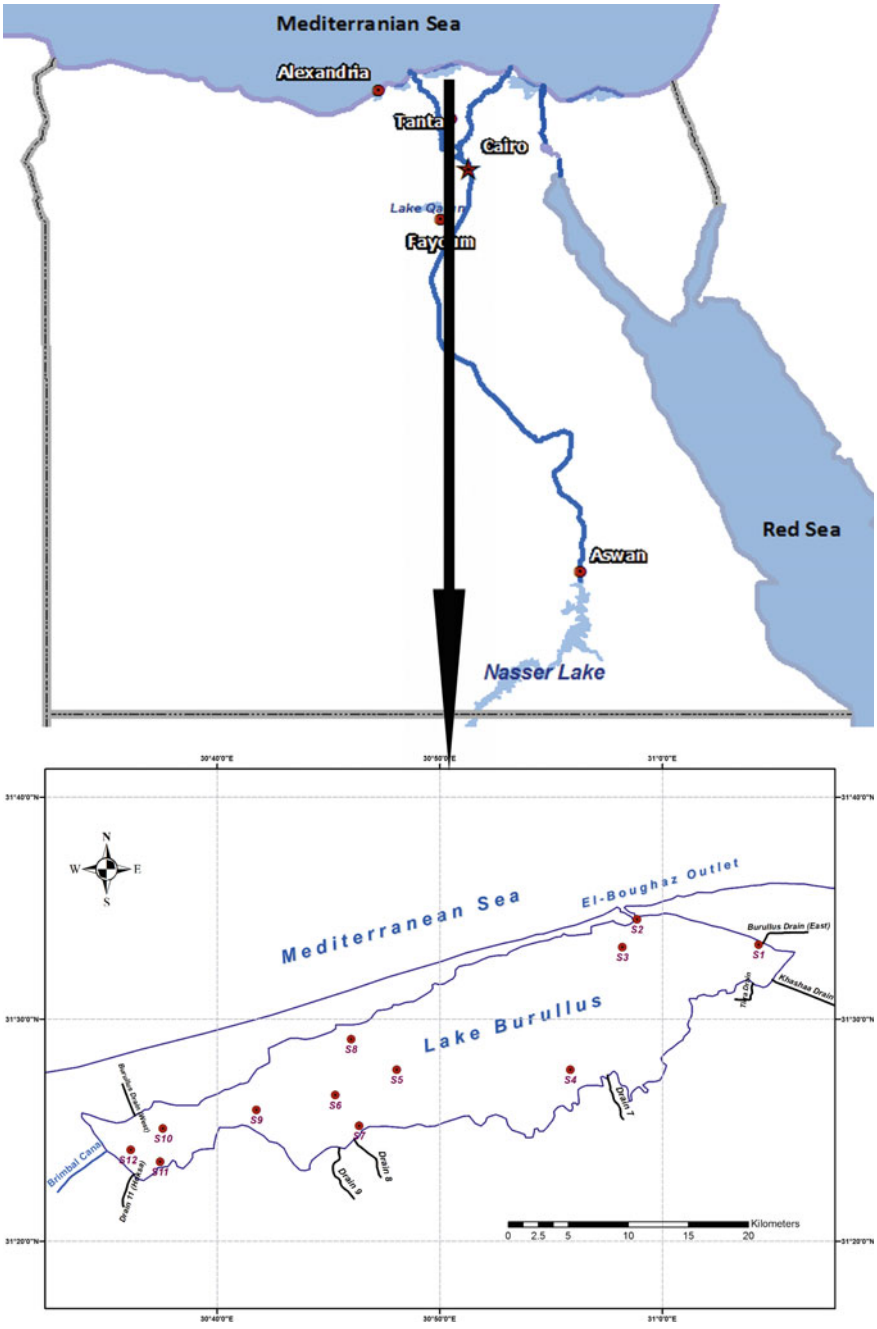

Fig. 1 Study area layout showing the connected drains, the outlet and the field records stations

a winter (January) lock policy, the water level would decrease to about (−0.26) m below sea level, allowing sea water to move into the lake again. It is estimated that 70–80% of municipal sewage and 90–95% of industrial waste waters of the Delta region surrounding the lake are disposed of into the drainage system (Karajeh et al. 2011). The drainage water which discharged into the lake is mostly nutrient-rich fresh water, polluted with agricultural fertilizer and heavy metals from industry.

3 Materials and Methods

To investigate a water quality management strategy for Lake Burullus, including the investigating of some feasible water quality enhancing scenarios, developing of a hydrodynamic and water quality model for the lake are required. In the following sections, the characteristics of the developed model and the suggested water quality enhancing scenarios are presented.

3.1 Lake Burullus Hydrodynamic and Water Quality Model

Assar et al. (2015) have developed a two-dimensional (vertically averaged) hydrodynamic and ecological model for Lake Burullus. The developed model was based on a two-dimensional hydrodynamic and ecological modeling system (code), MIKE21. This code includes three modules, hydrodynamic, advection-dispersion and ECO Lab and has a wide range of engineering and environmental applications in coastal hydraulics, oceanography, wave dynamics, harbors, rivers, lakes, environmental hydraulics and sediment processes (DHI 2012). This model computes water surface elevation, horizontal and vertical velocities, water temperature, salinity and other water quality parameters such as DO and nutrients. The basic input data for the model include: lake topography (bathymetry), drains and outlets stream flow, water quality records (physical, chemical and biological), meteorological conditions, as well as model initial and boundary conditions. The lake bathymetry was established using a finite difference grid of 48,000 cells, each one is a square of 150 m width, Fig. 2. Discharges and water surface elevations were specified as monthly and daily average values, respectively. Water levels were collected two times a day by Coastal Research Institute (CORI), Egypt, using stage boarder at different stations, Fig. 3, typical water level records for one year at different stations can be seen in Fig. 4. The required meteorological data, such as tidal variations, wind vectors, relative humidity and water temperature were obtained for the nearby local meteorological station eight times per day. Figure 5 shows the 2010–2011 distribution of air temperature at the nearest station to Burullus Lake, as an example. Water quality records, including DO, BOD, PO_4, NO_3 and NH_4, were collected from twelve stations in the lake (Fig. 1), four times per year, by the Egyptian Environmental Affairs Agency (EEAA) monitoring program for Egyptian lakes. The model boundary conditions

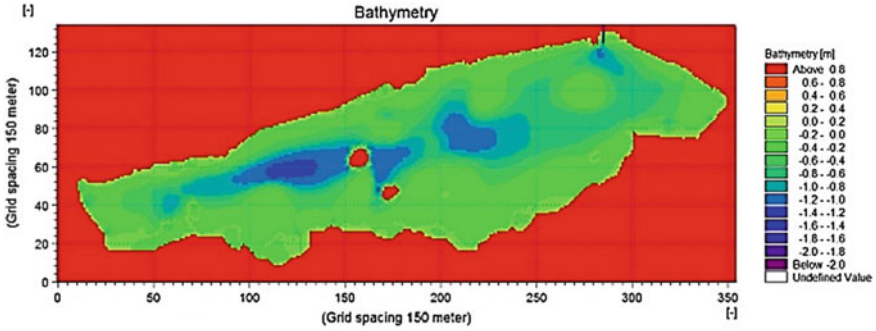

Fig. 2 Lake Burullus model Bathymetry

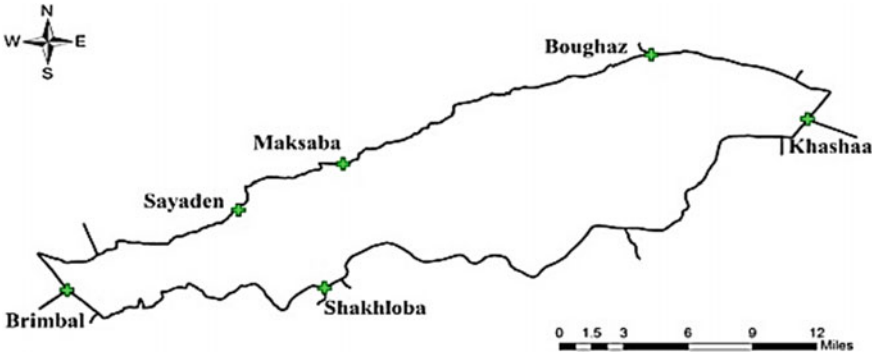

Fig. 3 Lake Burullus water level recording stations

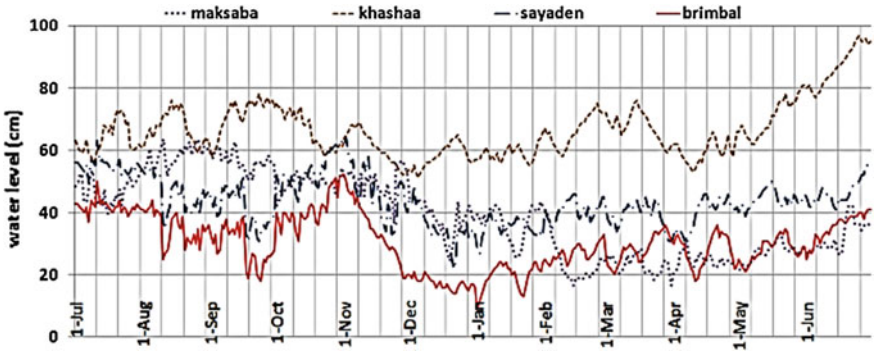

Fig. 4 Typical water levels for one year at different stations in Lake Burullus

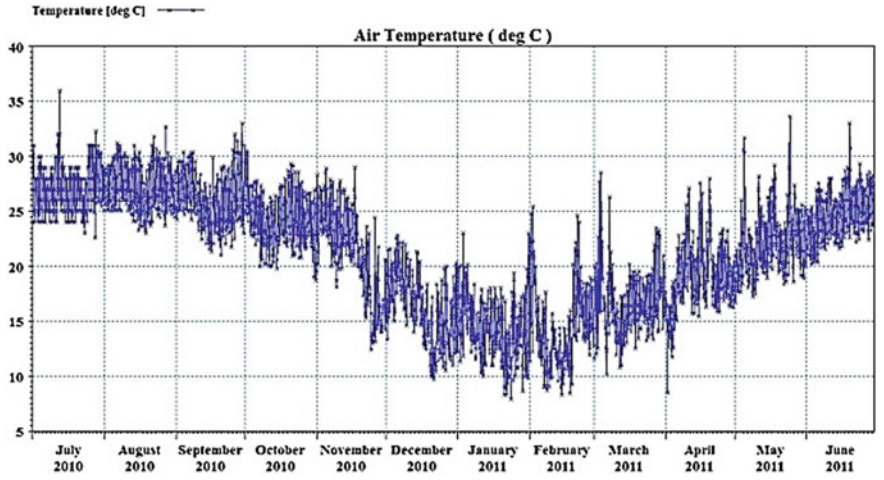

Fig. 5 Air temperature records (2010–2011) for Lake Burullus, Egypt

include the discharges and water quality records for the lake outlet, Brimbal Canal and the eight drains during the simulation period (June 2010–July 2011). While the model initial conditions include the water levels and the water quality records for the lake at the simulation start (1st June 2010, 9:00 AM). GIS was used, as an integral model, to generate missing observed data at drains outlets, such as water levels and water quality parameters.

The proposed model was calibrated using hydrodynamic and water quality records for one year (June 2010–July 2011), by modifying some model coefficients to give the smallest error between measured and simulated records of the lake. Some of the modified coefficients were: eddy viscosity coefficient (set as a time-varying function of the local gradients in the velocity field and Smagorinsky factor is equal to 0.25), Chezy number (set as 50 $m^{1/2}/s$) and wind friction coefficient (set as varying with wind speed and equals to 0.0016). Two statistics are used to evaluate the model performance, AME and RMS, which are computed according to the following equations:

$$\text{AME} = \frac{\sum|\text{Simulated value} - \text{Observed value}|}{\text{Number of Observations}} \tag{1}$$

$$\text{RMS} = \sqrt{\frac{\sum(\text{Simulated value} - \text{Observed value})^2}{\text{Number of Observations}}} \tag{2}$$

The calibrated model showed a good agreement between measured and simulated records, acceptable values of AME and RMS can be noticed in Fig. 6a, b. The average error values [AME & RMS] were as following: [0.11 & 0.13 m] for water levels, [1.14 & 1.43 °C] for water temperature, [0.64 & 0.77 ppt] for salinity, [1.45 & 1.86 mg/l] for DO, [1.86 & 2.38 mg/l] for BOD, [0.70 & 0.79 mg/l] for NO_3, [0.46 & 0.54 mg/l] for NH_3 and [0.11 & 0.13 mg/l] for PO_4.

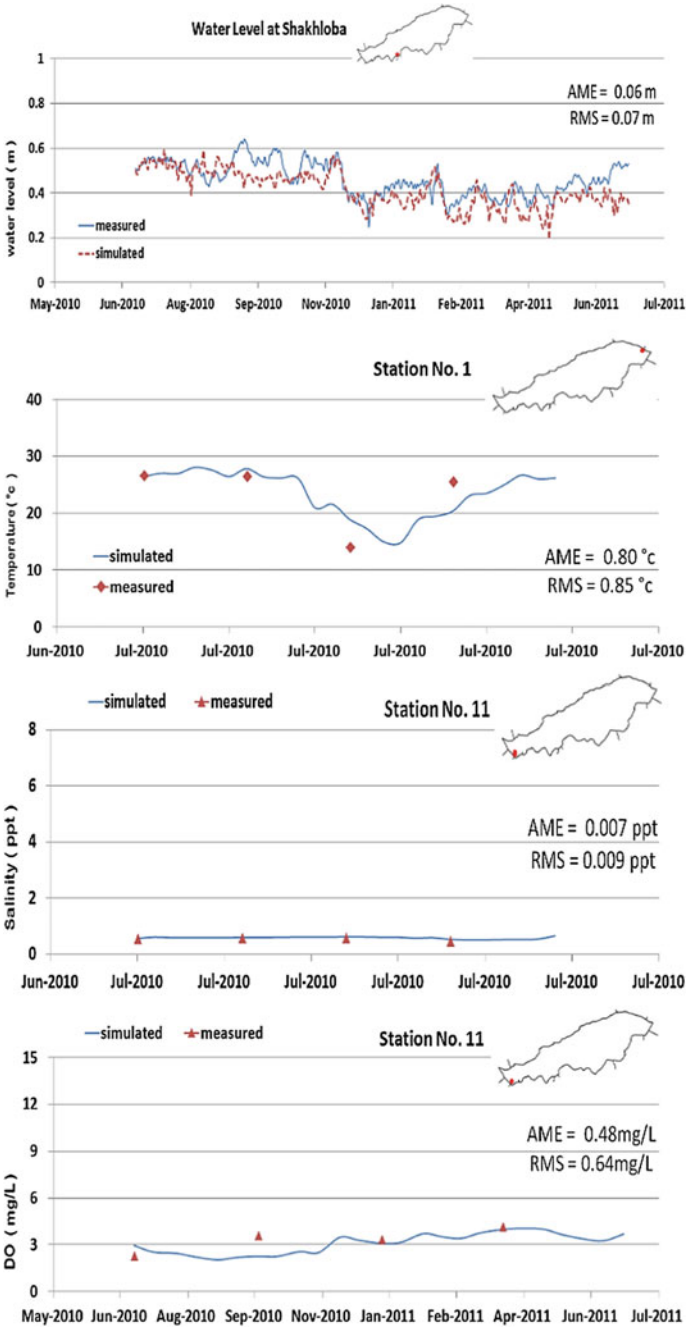

Fig. 6 **a**, **b** Lake Burullus hydrodynamic and water quality model calibration results at different stations (2010–2011)

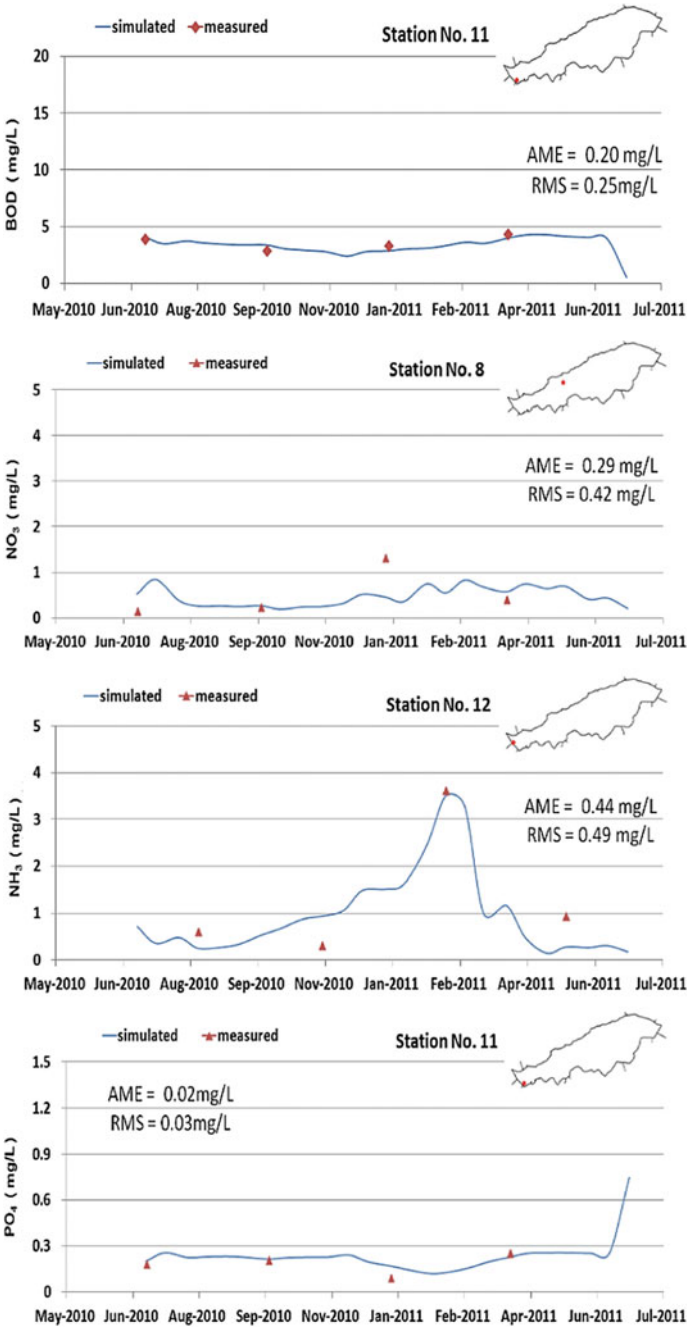

Fig. 6 (continued)

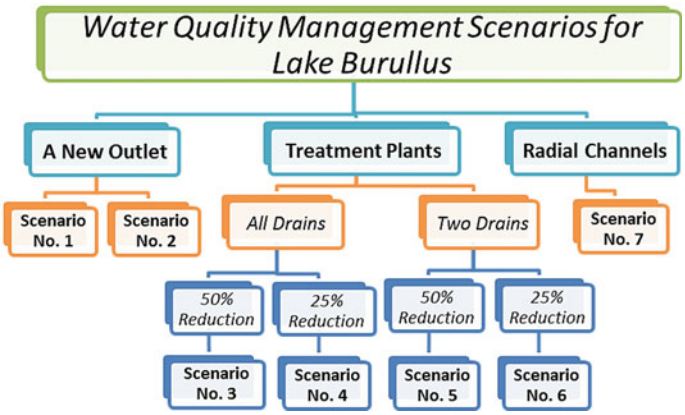

Fig. 7 Schematic representation for Lake Burullus water quality management scenarios

3.2 Management Scenarios of the Lake Water Quality

The calibrated model has been used to examine applying of some water quality enhancement scenarios for the lake to obtain a better eco-system of the lake. There are three main suggested scenarios: constructing of a new artificial outlet for the lake, installing water quality treatment plants for the drains and constructing radial channels in the lake. Figure 7 gives a schematic representation for the suggested Lake Burullus water quality enhancement scenarios.

3.2.1 Added Artificial Outlet

Thinking for making a new artificial outlet is one of the solutions to remediate water quality of Lake Burullus by increasing the interaction between the lake and the sea. In the case of creating a new artificial outlet, there are two suggested positions for this outlet. One outlet is suggested to be constructed close to the existing outlet "El-Boughaz" by about 3 km to study the effect of the two outlets on salinity and water quality parameters (Sc.1). While the other outlet position is suggested to be constructed far away from El-Boughaz by about 13 km to investigate how may the impact of the distance between the outlets affect the water quality parameters of the lake (Sc.2). Figure 8 shows the suggested locations for the two scenarios.

3.2.2 Drains Treatment Plants

Drains Treatment plants are considered also as one of the solutions to remediate water quality, by setting treatment plants (or using water quality treatment techniques or practices) on the outlets of all drains (Sc.3 & Sc.4). Or, as an economic solution,

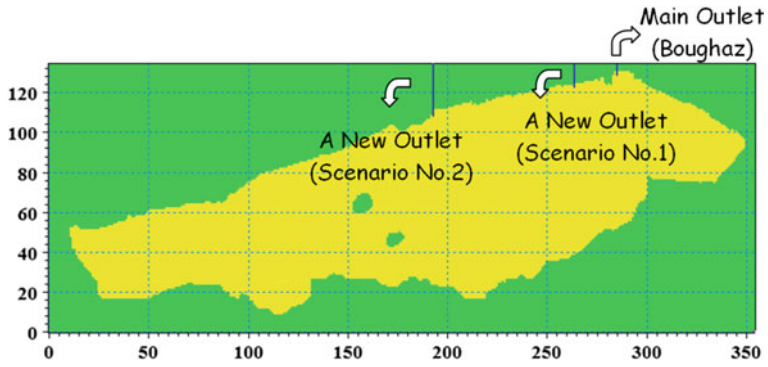

Fig. 8 New outlets suggested locations for Lake Burullus (Sc.1& Sc.2)

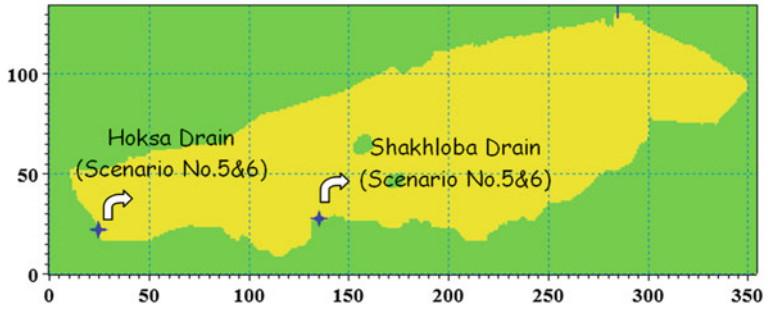

Fig. 9 Locations of suggested treatment plants for the Shakhloba and Hoksa Drains (Sc.5 & Sc.6)

treatment plants are placed on the outlets of the most polluted drains (Sc.5 & Sc.6). Where from observed data, S7 (Shakhloba or Drain 9) and S11 (Hoksa Drain) are estimated as the most polluted stations, Fig. 9. The treatment involved a reduction of nutrients effluent by 25% (Sc.3 & Sc.5) and 50% (Sc.4 & Sc.6).

3.2.3 Drains Radial Channels

Constructing drains passes, which are connected to the sea via the lake outlets, is considered an innovative management scenario, which allows the drains effluents to be directly drained to the sea. This scenario should be accompanied by an assessment and monitoring program for the sea close to the outlet to keep its water quality status into the permissible limits. These radial channels can be constructed by lowering the lake bed starting from the outlets of the most polluted drains to the lake outlet. Figure 10 shows the suggested radial channels for Lake Burullus.

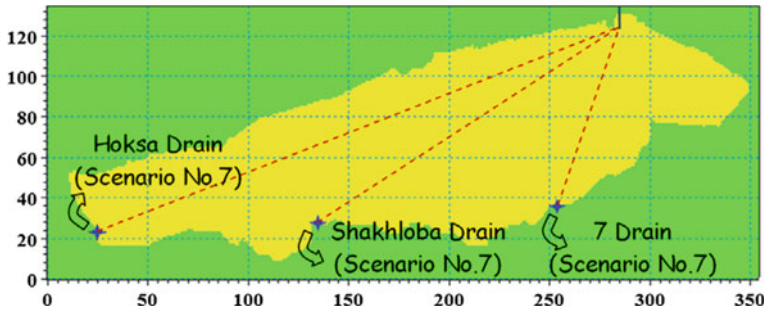

Fig. 10 Suggested radial channels locations for Lake Burullus (Sc.7)

4 Results and Discussion

The calibrated hydrodynamic and water quality model for Lake Burullus has been modified according to the suggested water quality management scenarios, to investigate the effectiveness of these scenarios. Four indicators [salinity, DO, PO_4 and NO_3] have been chosen to study the effect of the suggested scenarios at the three different zones of the lake [the Eastern zone (S1 to S3), the Middle zone (S5 to S8) and the Western zone (S10 to S12)]. The calibrated model results were considered as the referenced concentrations for the four studied indicators. Salinity has been influenced only by the applying of the two new artificial outlets scenarios, so salinity profiles will be studied to recognize the effect of the suggested scenarios Sc.1 & Sc.2. The change in parameters referenced concentrations is calculated at each considered station (for each scenario and indicator) using the following equation:

$$\mathbf{\Delta} = [(\mathbf{P_{sc}} - \mathbf{P_{ref}})/\mathbf{P_{ref}}] * \mathbf{100} \tag{3}$$

Where

Δ Change in reference value (%).
P_{sc} Parameter value due to applied scenario.
P_{ref} Parameter reference value (calibrated model).

Figure 11 shows the boxplot representations for the averages changes in indicators referenced concentrations at all stations due to applying of the management scenarios. Boxplot charts are used to present the minimum, the maximum, the median, the 1st quartile and the 3rd quartile of the changes. While the average changes in indicators referenced concentrations due to the management scenarios for the whole lake (Av.) and at the different lake zones (west, middle (mid.) and east.) are presented in Fig. 12. Figure 13 represents the spatial distribution of the average changes at the studied stations for different indicators and scenarios. A comparison between DO referenced and modified profiles at S12 due to applying scenario No. 2 (New outlet 2), as an example, can be seen in Fig. 14.

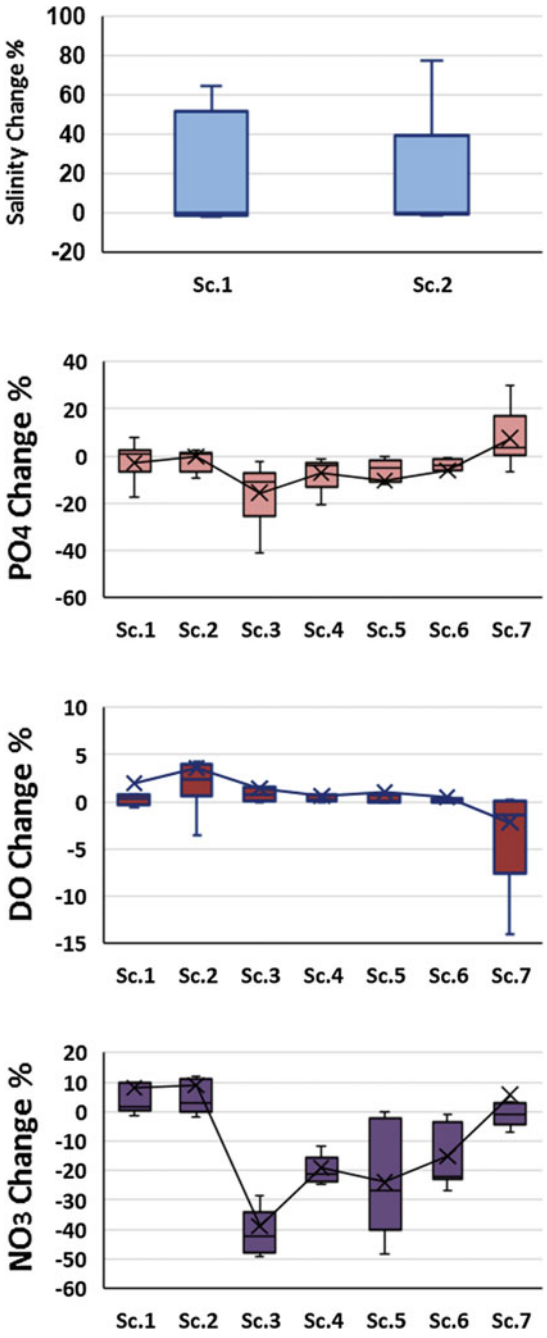

Fig. 11 Concentrations changes (%) of different water quality indicators in Lake Burullus due to different management scenarios

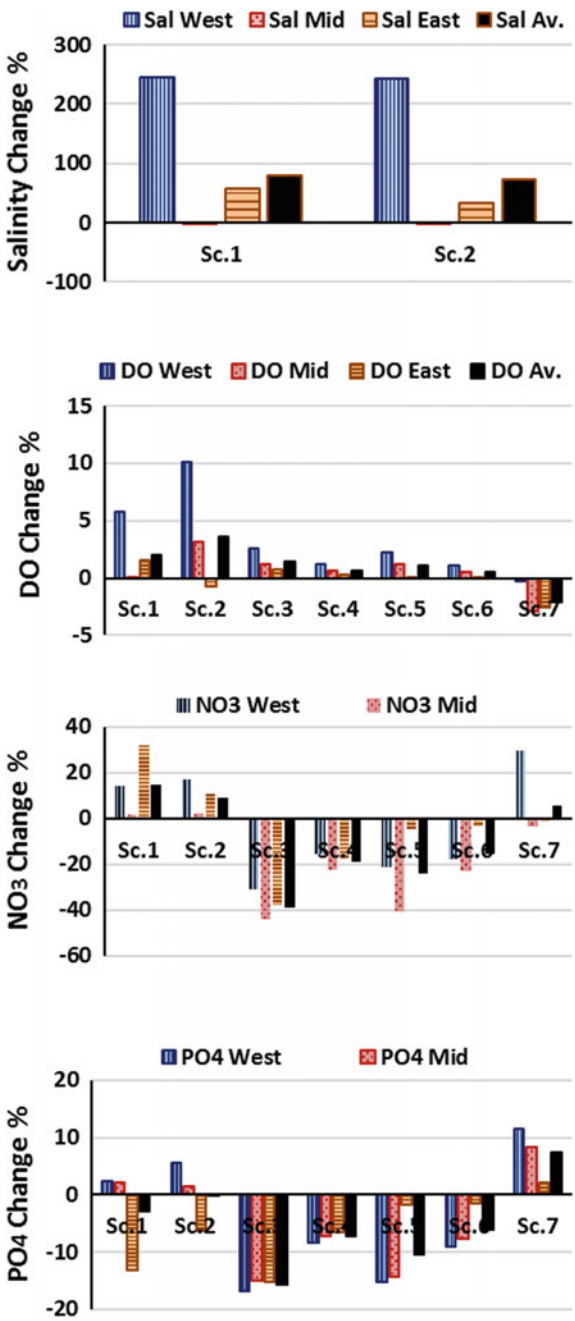

Fig. 12 Average concentrations changes (%) of different water quality indicators at different zones in Lake Burullus due to different management scenarios

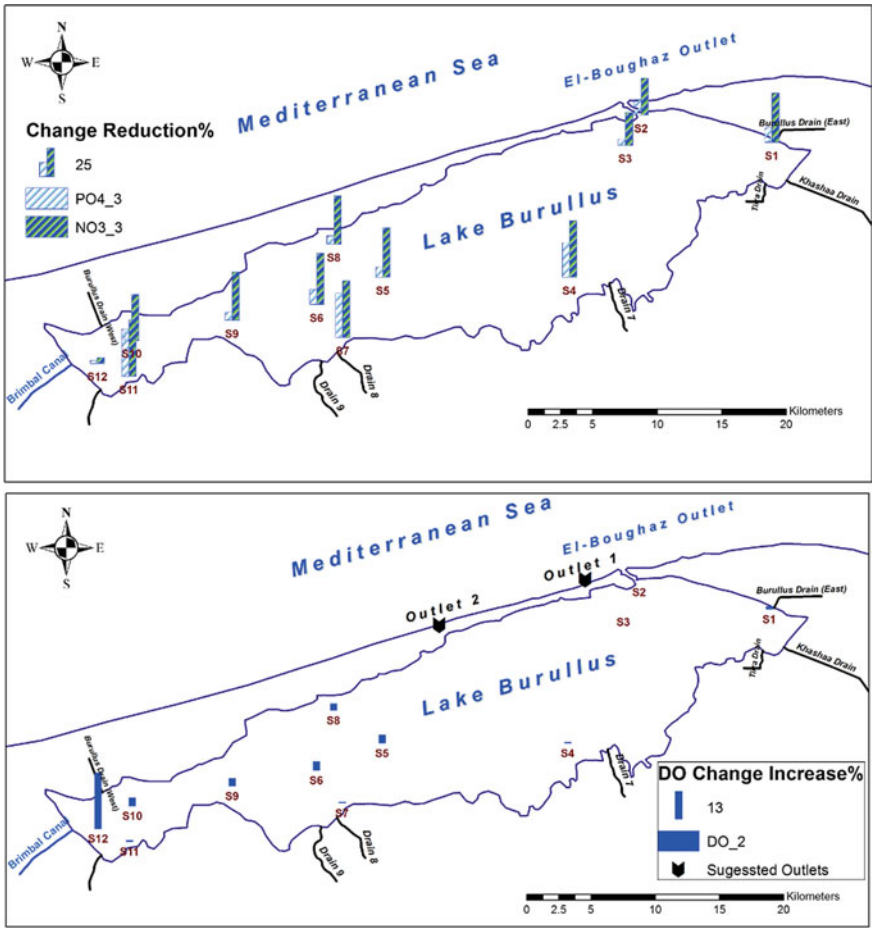

Fig. 13 Spatial distribution of concentrations changes (%) of phosphate, nitrate and dissolved oxygen indicators in Lake Burullus due to different management scenarios

For salinity, applying of the first two suggested scenarios (Sc.1 & Sc.2) significantly affects the lake salinity concentrations, the average changes (increases) are about 79.7% and 72%, for Sc.1 and Sc.2, respectively. The significant impacts of these scenarios can be clearly noticed in the eastern and western zones of the lake due to the existing lake outlet "Boughaz" (seawater source) at the eastern zone and the Brimbal Canal (freshwater source) at the western zone. For the eastern zone, the average changes are about 58% and 34% for Sc.1 and Sc.2, respectively. The significant changes (increase) are noticed at S2 and S3 stations (close to the lake outlet), the average changes are about 152.5% and 65%, respectively, for scenario Sc.1 and 77.5% and 50%, respectively, for scenario Sc.2. While for the western zone, the average changes are about 244% for both scenarios. The significant changes (increases)

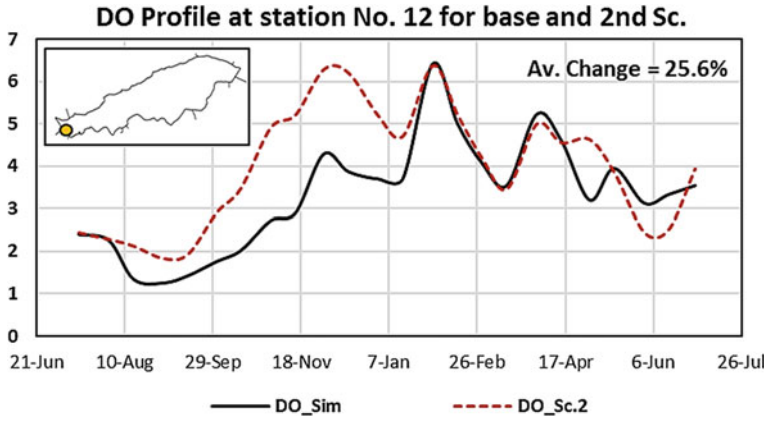

Fig. 14 A comparison between dissolved oxygen profiles for the simulated referenced case and the management scenario Sc.2 at S12 in Lake Burullus

are noticed at S12 station (close to the Brimbal Canal, the average salinity referenced concentration is about 0.75 ppt), the average change was about 734% and 732% for Sc.1 and Sc.2 scenarios, respectively.

For dissolved oxygen, the new outlet scenarios (Sc.1 & Sc.2) are the most effective scenarios for enhancing the DO concentrations in the lake. The second scenario (outlet 2) has a better impact than the first one, due to its location (in the middle zone, Figs. 8 and 13), except for the eastern zone (Fig. 12). The averages DO changes for the whole lake are about 3.6% and 2% for Sc.2 and Sc.1, respectively. The western zone of the lake is the most impacted zone; increases in the DO concentrations by about 10% and 5.8% for Sc.2 and Sc.1, respectively, are noticed. This mainly returns to the effect of Brimbal Canal (freshwater source) at S12 station, which is located in front of it (Fig. 1). This effect become clearer due to the construction of new outlets which enables more intrusion for the Brimbal Canal, particularly for the period from August to January, see Fig. 14. The referenced DO concentration at S12 is about 3.3 mg/l, increasing by about 25.6% and 17.2% for Sc.2 and Sc.1, respectively, is noticed. No change has been noticed for DO concentrations in the middle zone of the lake for Sc.1, due to its location; it is so closed to the existing outlet (Boughaz) and both are located in the eastern zone. While for Sc.2, the middle zone has the best impact among all studied scenarios (Fig. 12), due to the construction of the new outlet (outlet 2) in the same zone, an increase by about 3.15% in the DO concentrations of this zone is noticed. The change in the lake water circulation and the sea-lake water exchange, due to the construction of new outlets (Sc.1 and Sc.2), significantly affect the DO concentrations in the eastern zone of the lake. The averages changes in DO concentrations are an increase by about 1.6% and a decrease by about 0.7% can be noticed for Sc.1 and Sc.2, respectively. For Sc.1, a good effect on DO concentrations at S2 station (which is located in front of the existing outlet, Fig. 1) occurs; the average DO increase is about 8.5%. While S3 station has the worst impact due to

Sc.1 and Sc.2, the average DO decrease is about 3.5%. For Sc.2, an average decrease by about 1.4% is recorded at S2. This mainly returns to the hydraulic impacts of a new outlet construction on the existing outlet.

For treatment plants scenarios (Sc.3 to Sc.6), it can be reported that Sc.3 (a 50% nutrient reduction for all drains) is the best scenario which enhances the DO concentrations, compared to the other scenarios (Figs. 11 and 12). The averages increase in DO concentrations are about 1.4, 0.7, 1 and 0.5% for Sc.3, Sc.4, Sc.5 and Sc.6, respectively. A slight difference in DO change between Sc.3 and Sc.5 (a 50% nutrient reduction for two specific drains) for the western and the eastern zones (Fig. 12); the averages Sc.3 DO increases are about 2.5 and 1.2%, while the averages Sc.5 DO increases are about 2.2 and 1.2%, for the western and the middle zones, respectively. While the eastern zone is not impacted for both scenarios, Sc.5 and Sc.6, as both treated drains are far away from this zone. For Sc.3 and Sc.4, the averages increases are about 0.8 and 0.3%, respectively.

The seventh scenario (Sc.7) is the only one which has negative impacts on the all lake zones, regarding to DO concentrations (Fig. 12). The average decrease is about 2.2%, while the maximum decrease is about 3% at the middle zone. Mainly this reduction in DO concentrations returns to the limited sea water exchange due to the directing of three main drains inflow to the outlet.

For investigated nutrients (NO_3 and PO_4), treatment plants scenarios (Sc.3 to Sc.6) are the best effective scenarios to reduce the nutrients concentrations in the lake (Fig. 12). The averages reductions are about 39, 19, 24 and 15% for Sc.3, Sc.4, Sc.5 and Sc.6, respectively. It can be clearly noticed that Sc.5 (a 50% nutrient reduction for two specific drains) has a better impact on the lake nutrients concentrations than Sc.4 (a 25% nutrient reduction for all drains), due to the heavy pollution loads of these drains. Moreover, the middle zone of the lake is the most impacted zone by the nutrients reduction; the averages reductions are about 44% and 41% (NO_3) for Sc.3 and Sc.5, respectively. For PO_4 the averages reductions are about 15% and 14% for Sc.3 and Sc.5, respectively. As the averages referenced PO_4 concentrations for the middle and the western zones are about 0.79 mg/l and 0.36 mg/l, respectively.

As mentioned before in the discussion of DO impacts, construction of new outlets significantly affects the water circulation and generally the hydraulics activities in the lake. This in turn affects the concentrations of all water quality parameters in the lake. For nutrients, Sc.1 (and Sc.2 with a smaller scale) causes an increase by about 15% in NO_3 concentrations and a decrease by about 3% in PO_4 concentrations.

The western zone of the lake has the significant impacts due to these scenarios; about an average increase by about 32% in NO_3 and an average decrease by about 13% in PO_4 for Sc.1 are noticed. Sc.7, as well as, has negative impacts on the lake, regarding to the nutrient concentrations (and DO concentrations as explained before). The averages increase in NO_3 and PO_4 concentrations are about 6% and 8% (Fig. 12), respectively.

5 Conclusions

Typical Some enhancement feasible scenarios for the lake water quality of Lake Burullus are applied: (i) creating a new artificial outlet, one outlet is suggested to be set near El-Boughaz by about 3 km (Scenario No.1), while the other outlet is suggested to be set far from El-Boughaz by about 13 km, (ii) setting treatment plants on all drains to reduce nutrients concentrations by a 50% or 25% (Scenarios No. 3&4), or as an economic solution, treatment plants are placed on the most polluted drains (Scenarios No. 5&6) and (iii) constructing of radial channels by lowering the lake's bed from the most polluted drains to the lake outlet, an assessment and monitoring program for the sea close to the outlet should be implemented for this scenario to keep the sea water quality status into the permissible limits. Based on the presented results, it can be concluded the following:

- For salinity, unfortunately, constructing of new outlets (Sc.1 and Sc.2) will increase the salinity concentrations in the lake, particularly at the western zone. The average increase for the lake is about 80% (Sc.1) compared to the referenced concentration, while the average increase for the western zone is about 244% for both scenarios.
- For DO, the new outlet scenarios are the most effective scenarios for enhancing the DO concentrations in the lake, the second scenario (outlet 2) has a better impact than the first one; the average DO increase for the whole lake is about 3.6% compared to the referenced concentration. The western zone of the lake is the most impacted zone by this scenario; the average increase is about 10%. Treatment plants scenarios (Sc. 3 to Sc.6), as well as, have significant enhancement impacts on DO concentrations in the lake. The averages increases are about 1.4% and 1% for Sc.3 (a 50% nutrient reduction for all drains) and Sc.5 (a 50% nutrient reduction for two specific drains out of eight drains), respectively. For that, Sc.5 is recommended as an effective and economic scenario. Radial channels scenario (Sc.7) is the only one which has negative impacts on the all lake zones, regarding to DO concentrations; an average decrease is about 2.2%.
- For nutrients (NO_3 and PO_4), treatment plants scenarios (Sc.3 to Sc.6) are the best effective scenarios to reduce the nutrients concentrations in the lake; the averages reductions are about 39% and 24% for Sc.3 and Sc.5, respectively. It can be clearly noticed that Sc.5 (a 50% nutrient reduction for two specific drains) has a better impact on the lake nutrients concentrations than Sc.4 (a 25% nutrient reduction for all drains). Moreover, the middle zone of the lake is the most impacted zone by the nutrients reduction. For PO_4 the averages reductions are about 15% and 14% for Sc.3 and Sc.5, respectively. New outlet scenarios, Sc.1 and Sc.2, cause an average increase by about 15% (Sc.1) in NO_3 concentrations and a decrease by about 3% (Sc.1) in PO_4 concentrations. The western zone of the lake is the most impacted zone due to these scenarios. Sc.7, as well as, has negative impacts on the nutrient concentrations in the lake; the averages increase in NO_3 and PO_4 concentrations are about 6% and 8%, respectively. Economically, scenario No. 5, which is constructing treatment stations for the most polluted drains (9 Drain and Hoksa) by a reduction of nutrients by 50%, is be considered as the most

economic and effective scenario to reduce nutrients concentrations. As well as, it significantly enhances the DO concentrations in the lake. The impacts due to coupling of some significant management scenarios on the hydrodynamic and water quality conditions of the lake should be investigated. This study should can be used as a guide for decision makers for applying water quality management plans for Lake Burullus.

Acknowledgements The authors extremely thank Prof. Dr. Ibrahim El-Shinnawy, the former Director of Coastal Research Institute (CORI), Egypt, and the Egyptian Environmental Affairs Agency (EEAA) for providing field records for Lake Burullus. Sincere thanks must go to the reviewers who participated in enhancing of the quality of this chapter.

References

Abou-Elela, G., & Ghanem, N. (2005). Phenotypic characterization and numerical taxonomy of some actinomycetes strains isolated from Burullos Lake. *Egyptian Journal of Aquatic Research, 31*(2), 125–144.

Akl, F., El-Azizy, I., Azeem, M. A., & Nasser, G. A. (2017). Environmental hydrodynamics mitigation and water quality modelling, case study El-Burullus Lake in Egypt—using SMS 12.1. *International Journal of Recent Advances in Multidisciplinary Research, 4*(1), 2200–2208.

Al Sayes, A., Radwan, A., & Shakweer, L. (2007). Impact of drainage water inflow on the environmental conditions and fishery resources of Lake Borollus. *Egyptian Journal of Aquatic Research, 33*(1), 312–321.

Alsayes, A. (2005). Environmental and fishery investigation on Lake Borollus, 5—Fishing gears and methods used at Lake Borollus—Their effects on fish populations at the lake. *Egyptian Journal of Aquatic Research, 31,* 410–446.

Appleby, P., Birks, H. H., Flower, R. J., Rose, N., Peglar, S. M., Ramdani, M., et al. (2001). Radiometrically determined dates and sedimentation rates for recent sediments in nine North African wetland lakes (the CASSARINA Project). *Aquatic Ecology, 35*(3), 347–367.

Assar, W., Elshemy, M., Zeidan, B. (2015). Water quality modeling for Lake Burullus, Egypt, Part I: Model Calibration. *Mansoura Engineering Journal, 40*(2).

Chen, Z., Salem, A., Xu, Z., & Zhang, W. (2010). Ecological implications of heavy metal concentrations in the sediments of Burullus Lagoon of Nile Delta, Egypt. *Estuarine Coastal and Shelf Science, 86*(3), 491–498.

Dewidar, K., & Khedr, A. (2005). Remote sensing of water quality for Burullus Lake, Egypt. *Geocarto International, 20*(3), 43–49.

DHI. (2012). Mike21 Flow Model: User Guide. http://www.mikebydhi.com/products/mike-21.

Donia, N. S., Farag, H. (2012). *Monitoring Burullus lake using remote sensing techniques*. Paper presented at the Sixteenth International Water Technology Conference, Istanbul, Turkey.

Eid, E. M., Shaltout, K. H., & Asaeda, T. (2012). Modeling growth dynamics of Typha domingensis (Pers.) Poir. ex Steud. in Lake Burullus. *Egyptian Ecological Modelling, 243,* 63–72.

Eid, E. M., Shaltout, K. H., & Asaeda, T. (2014). Growth dynamics of Potamogeton pectinatus L. in Lake Burullus, Egypt: A modelling approach. *African Journal of Ecology, 52*(4), 414–426.

El-Adawy, A., Negm, A., Elzeir, M., Saavedra, O., El-Shinnawy, I., & Nadaoka, K. (2013a). Modeling the hydrodynamics and salinity of el-burullus lake (nile delta, Northern Egypt). *Journal of Clean Energy Technologies, 1*(2), 157–163.

El-Adawy, A., Negm, A., Saavedra, O., Nadaoka, K., & El-Shinnawy, I. (2014). Coupled hydrodynamic-water quality model for pollution control scenarios in El-Burullus Lake (Nile delta, Egypt). *American Journal of Environmental Sciences, 10*(6), 546.

El-Adawy, A., Negm, A. M., Valeriano, O. C. S., El-Shinawy, I. (2013b). Assessment of climate change impacts on El-Burullus Lake, Egypt, based on hydrodynamic modeling. *International Water Technology Journal, 3*(4).

El-Asmar, H. M., Hereher, M. E., & El Kafrawy, S. B. (2013). Surface area change detection of the Burullus Lagoon, north of the Nile Delta, Egypt, using water indices: A remote sensing approach. *The Egyptian Journal of Remote Sensing and Space Science, 16*(1), 119–123.

Elghobashy, H. A., Zaghloul, K. H., & Metwally, M. (2001). Effect of some water pollutants on the Nile tilapia Oreochromis niloticus collected from the river Nile and some Egyptian Lakes. *Egyptian Journal of Aquatic Biology and Fisheries, 5*(4), 251–279.

El-Reefy, H., Badran, H., Sharshar, T., Hilal, M., & Elnimr, T. (2014). Factors affecting the distribution of natural and anthropogenic radionuclides in the coastal Burullus Lake. *Journal of Environmental Radioactivity, 134,* 35–42.

El-Shinnawy, I. (2003). Water budget estimate for environmental management at Al-Burullus Lake, Egypt. In *Proceedings of 4th International Conference and Exhibition for Environmental Technologies Environment*.

El-Shinnawy, I. (2004). Impact of the agricultural drainage on hydrological environment of Al-Burullus Lake. In *First African Regional Conference on Drainage (ARCOD)*.

El-Zeiny, A., & El-Kafrawy, S. (2017). Assessment of water pollution induced by human activities in Burullus Lake using Landsat 8 operational land imager and GIS. *The Egyptian Journal of Remote Sensing and Space Science, 20,* S49–S56.

Farag, H., & El-Gamal, A. (2011). Assessment of the eutrophic status of Lake Burullus (Egypt) using remote sensing. *International Journal of Environmental Science and Engineering, 2,* 61–74.

General Authority for Fish Resources Development (GAFRD). (2014). *Fish Statistics Yearbook* 2013. Cairo, Egypt.

Hereher, M., Salem, M., & Darwish, D. (2010). Mapping water quality of Burullus Lagoon using remote sensing and geographic information system. *Journal of American Science, 7*(1), 138–143.

Hossen, H., & Negm, A. (2016). Change detection in the water bodies of Burullus Lake, Northern Nile Delta, Egypt, using RS/GIS. *Procedia Engineering, 154,* 951–958.

Karajeh, F., Oweis, T., Swelam, A., El-Gindy, A., El-Quosy, D., Khalifa, H., El-Kholy, M., El-Hafez, S. A. (2011). *Water and agriculture in Egypt.* Technical paper based on the Egypt-Australia-ICARDA Workshop On-farm Water-use Efficiency. Egypt: International Center for Agricultural Research in the Dry Areas (ICARDA).

Khalil, M. K., Radwan, A., & El-Moselhy, K. M. (2007). Distribution of phosphorus fractions and some of heavy metals in surface sediments of Burullus lagoon and adjacent Mediterranean Sea. *Egyptian Journal of Aquatic Research, 33*(1), 277–289.

Masoud, M. S., Fahmy, M. A., Ali, A. E., & Mohamed, E. A. (2011). Heavy metal speciation and their accumulation in sediments of Lake Burullus, Egypt. *African Journal of Environmental Science and Technology, 5*(4), 280–298.

Mehanna, S. F., Shaker, I. M., Farouk, A. E. (2014). Impacts of excessive fishing effort and heavy metals pollution on the tilapia production from Lake Manzalah. In *4th Conference of Central Laboratory for Aquaculture Research* (pp. 57–74).

Mohsen, A., Elshemy, M., Zeidan, B. (2016). Change detection for Lake Burullus, Egypt using remote sensing and GIS approaches. *Environmental Science and Pollution Research*, 1–9.

Nafea, E. M. A., & Zyada, M. A. (2015). Biomonitoring of heavy metals pollution in Lake Burrullas, Northern Delta, Egypt. *African Journal of Environmental Science and Technology, 9*(1), 1–7.

Okbah, M. (2005). Nitrogen and phosphorus species of Lake Burullus water (Egypt). *Egyptian Journal of Aquatic Research, 31*(1), 186–198.

Radwan, A. (2005). Some factors affecting the primary production of phytoplankton in Lake Burullus. *Egyptian Journal of Aquatic Research, 31*(2), 72–88.

Saeed, S. M., Shaker, I. M. (2008). Assessment of heavy metals pollution in water and sediments and their effect on Oreochromis niloticus in the northern delta lakes, Egypt. In *8th International Symposium on Tilapia in Aquaculture* (pp. 475–490).

Shakweer, L., & Radwan, A. (2004). Environmental and fishery investigation on Lake Burullus. 2. B. Rates of trace elements accumulation in the marine macrophytes and Fish at lake Burullus. *Egyptian Journal of Aquatic Research, 30,* 49–120.

Shalaby, B., Samy, Y. M., Mashaly, A. O., El Hefnawy, M. (2017). Comparative geochemical assessment of heavy metal pollutants among the mediterranean Deltaic Lakes sediments (Edku, Burullus and Manzala), Egypt. Egyptian Journal of Chemistry, *60*(3), 361–378.

Shaltout, K. H. (2007). Towards mainstreaming Lake Burullus biodiversity, Egypt. *UNDP-GEF-SFA*, *183*.

Shaltout, K. H. (2017). Reed products from Lake Burullus, Egypt. In: Al. CMFe (Ed.), *The Wetland Book*. Springer Science+Business Media B.V. https://doi.org/10.1007/978-94-007-6172-8_211-8.

Shaltout, K. H., & Al-Sodany, Y. M. (2008). Vegetation analysis of Burullus Wetland: A RAMSAR site in Egypt. *Wetlands Ecology and Management, 16*(5), 421–439.

Soliman, M., & Ushijima, S. (2013). Climate change impact on El-Burullus lake salinizaton process. *Journal of Japan Society of Civil Engineers, Ser B1 (Hydraulic Engineering), 69*(4), I_253–I_258.

Soliman, M., Ushijima, S., & El-Shinawy, I. (2013). Re-originate Burullus coastal lake's ecosystem using salinity dynamics as a management tool. *Ocean and Coastal Management, 85,* 7–18.

Yassin, E.-K. H., & Mahmoud, G. S. (2016). Studies on Spatio-temporal dynamics of phytoplankton in Burullus Lagoon, Southern Mediterranean Coast, Egypt. *The Egyptian Journal of Experimental Biology (Botany), 12*(2), 255–266.

Younis, A. M., El-Zokm, G. M., & Okbah, M. A. (2014). Spatial variation of acid-volatile sulfide and simultaneously extracted metals in Egyptian Mediterranean sea lagoon sediments. *Environmental Monitoring and Assessment, 186*(6), 3567–3579.

Younis, A., & Nafea, E. (2012). Impact of environmental conditions on the biodiversity of Mediterranean Sea lagoon, Burullus protected area, Egypt. *World Applied Sciences Journal, 19*(10), 1423–1430.

Zingstra, H. (2013). *Lake Burullus: Local Food Security and Biodiversity Under Pressure* (Final Report). Wageningen UR: Centre for Development Innovation.

Renewable Energies in the Sea and in Tidal Rivers: CFD Modelling and Impacts

The awareness rising about the greenhouse effects and their consequences on climate change led the nations to promote non-fossil energies. Oceans constitute a tremendous energy reservoir and several projects are running to developed Marine Renewable Energies (MRE). Among MRE systems, the more developed ones are the offshore wind turbines and tidal turbines. Wave energy converter like oscillating water column is in the test also. Moreover, the great difference between the sea level and some coastlines could be used to develop seawater pumped-storage power stations, which store non-permanent energies, like wind turbines, and provide electricity later when necessary. This part includes seven chapters relative to Marine Renewable Energy and its interaction with environment.

The first chapter by Huang et al. concerns the seawater pumped-storage power stations (SPPS). SPPS are currently used to store electricity energies for long periods. They will pump water up to a reservoir, from which electricity could be produced by hydro-turbines. Location of such a system is limited by the topography, whereas the necessity of energy storage is growing with the increase in the renewable energies. Seawaters offer the opportunity to increase the capacity of energy storage. The subject of the chapter is to study SPPS, for which the level between the upper reservoir and the lower one is smaller than SPPS capacity. The authors propose a schematic diagram of SPPS and a mathematic modelling. In particular, they study the use of chambers in order to save the tailrace tunnel placed between the turbine and the lower reservoir.

The second chapter by Niquil et al. studies the potential effect of an offshore wind turbine on the ecosystem. Offshore wind farm, as an alternative to fossil energy, is planned to be installed in France. The chapter presents the main methods and results of the ANR TROPHIK project. The main objective of this project is to develop an integrated ecosystem approach using several modelling tools. The potential impacts associated with the development of the offshore wind farm of Courseulle-sur-mer (Normandy, France) have been investigated. A model of food web has been proposed to investigate the use of Ecological Network Analysis (ENA). The model shows an increase in the biomass of bivalves after the installation of the wind farm, which is a reef effect. Then, a spatial model has been developed at the scale of the Baie de Seine to evaluate the impact of several parameters (climate change, offshore wind,

fisheries) on the ecosystem. Finally, a combined food web/social network modelling has been proposed.

The third chapter is by Rameliarison et al. concerns the interaction between sediment bottom and the functioning of an oscillating water column (OWC). An OWC is a system built in coastal zones to extract the energy from the waves. It consists of a semi-immersed chamber in contact with the sea and the atmosphere. When the free water surface goes up and down following the waves, aboe air is forced to go through a turbine and product energy. The approach developed by the authors is to use a two-phase (air–water) CFD modelling to study the fluid dynamic outside and inside the chamber. The direct numerical simulations have been done without turbines, and the effect of the geometry is studied. Finally, the first estimations of the sediment processes and morphology evolution are provided by considering the bottom friction stress.

The fourth chapter by Furgerot et al. is related to the measurement of velocity variability in a tidal energy site. Tidal energy converter (TEC) or tidal turbines will be installed in the sites like the Raz Blanchard. The knowledge of the resource assessment is a major importance to the installation of such a device. The chapter presents some results of the ANR HYD2M concerning the velocity measurements at three locations in the area dedicated to the pilot TEC farm. Acoustic Doppler current metre profilers were deployed in the Raz Blanchard area for more than one year. The mean velocity profile has been studied, and a power law is proposed with an α coefficient of 6.6. They observed a strong variability of the average velocity along the vertical axis.

The fifth chapter by Clary et al. presents the development of a simplified model representing a vertical-axis stream turbine. The best model that represents a turbine is the blade resolved model. It permits the simulation of the load on blades and of the wake effect. Nevertheless, this kind of modelling is time-consuming and is difficult to use in the framework of a farm composed of tens of turbines. The objective of the authors is to propose a simplified model by introducing a source term, which is built based on the blade element momentum (BEM). The source term is calibrated with flume measurements. Such a model could lead to the prediction of the velocities in a TEC farm and then of the TEC array arrangement.

The sixth chapter by Potter et al. concerns the impact of row of tidal stream turbines on the overtides of the lunar constituent. Installing tidal energy converter (TEC) along the coast will have an impact on the natural flow. As it was studied in the literature, the extraction of energy by reducing the velocity or increasing the vorticity could have an impact at regional scale on the transport of elements (transport, transport of food, waste, species). The question addressed by the authors is the impact of a large TEC's farm on the tidal asymmetry. Tidal asymmetry is a difference in term of magnitude and duration of the rise and the fall of the tide. The authors have used a shallow water model where the turbines are represented by a friction force based on the actuator disc theory. They have explored the impact on the M2, M4 and M6 constituents on a period of three days. They found that, as an example, the alteration to M4 tidal harmonic reduces as the blockage ratio increases.

The seventh chapter by Guillou and Chapalain proposes an evaluation of the influence of a tidal farm on residual currents in an area with strong potential. Residual currents are responsible for the large-scale circulation and transport, and the question of the influence of the extraction of current energy by tidal farm could be of tremendous importance. The authors propose to evaluate the tidal circulation in the Fromveur Strait due to the lunar semi-diurnal constituent M2 (Western Brittany) with a two-dimensional shallow water model and the global action of the tidal farm by adding a bed friction sink term. The Lagrangian residual circulation is estimated by the Lagrangian barycentric method. They show that the tidal farm modifies the Lagrangian circulation (amplitude and direction) along the axis of the strait and then could affect the seabed morphology.

Sylvain S. Guillou
LUSAC, University of Caen-Normandy, France

Research on the Setting Condition of Tailrace Surge Chambers for Seawater Pumped-Storage Power Stations with Long Tailrace Tunnels

Wei Huang, Kailin Yang, Xinlei Guo, Yongxin Guo, Tao Wang, Hui Fu and Jiazhen Li

Abstract Seawater pumped-storage power station (SPPS), as an efficient large-scale energy storage facility for marine renewable energies, has been incorporated into the key research tasks in the "13th Five-Year Plan" of hydropower development in China. The tailrace surge chamber is very important for the operation safety of the SPPS with a long tailrace tunnel. To determine the conditions under which a SPPS requires a tailrace surge chamber and to account for the time sequence superposition of water hammer vacuum, velocity head vacuum and head loss vacuum, a new setting criterion using the rigid water hammer theory was derived. Then, comparisons among several setting criteria of tailrace surge chambers are conducted. Ultimately, the new setting criterion is investigated and validated by 1D numerical simulation of the hydraulic transient process for a certain pumped-storage power station. The discriminant result obtained by the new setting criterion is consistent with the actual setting condition, and it can be applied as a preliminary setting criterion of tailrace surge chambers for SPPSs and can provide guidance for preliminary engineering design.

Keywords Seawater pumped-storage power station · Tailrace surge chamber · Hydraulic transient · Head loss · Draft tube

Nomenclature

SPPS	Seawater Pumped-Storage Power Station
PPS	Pumped-storage Power Station
CLTS	Critical Length of the Tailrace System, m

W. Huang · K. Yang · X. Guo (✉) · Y. Guo · T. Wang · H. Fu · J. Li
State Key Laboratory of Simulation and Regulation of Water Cycle in River Basin, China Institute of Water Resources and Hydropower Research, Beijing 100038, People's Republic of China
e-mail: guoxinlei@163.com

W. Huang
State Key Laboratory of Hydroscience and Engineering, Department of Hydraulic Engineering, Tsinghua University, Beijing 100084, People's Republic of China

K. D. Nguyen et al. (eds.), *Estuaries and Coastal Zones in Times of Global Change*, Springer Water,
https://doi.org/10.1007/978-981-15-2081-5_8

WHV	Water Hammer Vacuum, m
VHV	Velocity Head Vacuum, m
HLV	Head Loss Vacuum, m
A	Cross-sectional area, m^2
c	Wave speed, m/s
D	Diameter of the pipe or tunnel, m
f	Machine type modification factor
g	Gravitational acceleration, m/s^2
H	Pump turbine working head, m
H_0	Initial head, m
H_S	Draft head, m
H_r	Rated head, m
h_{wu}	Head loss of the headrace system, m
h_{ww}	Head loss of the tailrace system, m
k_s	Relative head loss coefficient
L	Pipe or tunnel length, m
L_w	Actual length of the tailrace system, m
$[L_w]$	Critical length of the tailrace system, m
m	Water hammer phase number
n_r	Rated speed, rpm
P_r	Rated output, MW
P	Cross-sectional average pressure, Pa
Q	Diversion flow rate, m^3/s
Q_0	Initial discharge, m^3/s
Q_r	Rated discharge, m^3/s
q	Relative discharge
S	Total head loss coefficient
T_S	Effective closing time of the guide vane, s
T_Z	Total closing time of the guide vane, s
T_c	Lag time of adjustment, s
T_k	Buffer time, s
T_{ws}	Water inertia time constant of the tailrace system, s
$[T_{ws}]$	Allowable value of T_{ws}, s
V	Cross-sectional average velocity, m/s
V_{w0}	Average velocity in the pressure tailrace tunnel, m/s
Z	Relative elevation, m
α	Kinetic energy correction coefficient
γ	Specific weight of water, N/m^3
λ	Coefficient of the frictional head loss
ζ	Coefficient of the local head loss
σ	Characteristic coefficient of the pipeline
ϕ	Relative opening degree of the guide vane
ξ	Pressure change rate
∇	Setting elevation of the pump turbine, m
N_{11}	Unit speed, rpm

Q_{11}	Unit discharge, m^3/s
T_{11}	Unit torque, N·m
D_{ref}	Runner diameter, m
n	Rotational speed, rpm
T	Torque, N·m
GD^2	Moment of inertia, $t \cdot m^2$

Subscripts and Superscripts

1	Upstream reservoir section
2	Pump turbine inlet section
3	Draft tube inlet section
4	Downstream reservoir section
u	Headrace system (penstock)
w	Tailrace system (pressure tailrace tunnel, draft tube extension and draft tube)
d	Downstream reservoir
min	Minimum value
max	Maximum value
nor	Normal value

1 Introduction

Seawater pumped-storage power station (SPPS), as an efficient large-scale energy storage facility for marine renewable energies, has been incorporated into the key research tasks in the "13th Five-Year Plan" of hydropower development in China. With the development of new energy such as nuclear power, offshore wind energy, tidal energy, and solar energy in the coastal areas of China, the supporting construction of SPPSs can not only meet the demand for electricity and optimize the power supply structure in the coastal and island areas with insufficient energy resources, but also play an important role in building a safe, stable, economical and clean energy supply system in these areas (National Energy Administration 2016). Nowadays, China is promoting the construction of demonstration projects of SPPSs to accelerate the formation of a multi-energy complementary and comprehensively integrated energy utilization mode for islands.

However, due to the limitation of topographic and geological conditions, the water conveyance system of a SPPS tends to have a long tailrace tunnel, leading to a significant pressure drop in the draft tube during the load rejection. Once the pressure in the draft tube drops to the saturated vapour pressure, water column separation would happen, which could cause significant pressure pulsation and structure damage for the whole plant (Mei 2000; Bergant et al. 2006; Fang and Koutnik 2012; Berlin and

Murav'ev 2014). Setting up the tailrace surge chamber is one of the most effective engineering measures to solve the above problems. The chamber can reduce the amplitude of pressure pulsations by reflecting the incoming water hammer waves and can break the vacuum by providing water, thereby inhibiting water column separation and ensuring the safe operation of the system (Pejovic et al. 2011; Murav'ev 2011; Kendir and Ozdamar 2013). However, a large quantity of excavation and lining are necessary in the construction of surge chambers, leading to high investment. Therefore, in the context of promoting the construction of SPPSs in China (Zhang et al. 2017; Qian 2017), it is important to determine whether a tailrace surge chamber is required.

Currently, the critical length of tailrace system (CLTS) is often used to estimate the risk of water column separation. When the actual length of the tailrace system is longer than CLTS, water column separation is thought to occur in the draft tube, and a tailrace surge chamber is considered to be established. Krivchenko (1981) and Gubin (1983) independently proposed an empirical formula of CLTS using the direct water hammer assumption. Zhao (1986) and Ji and Liu (1991) thought that the direct water hammer hardly ever occurs in plants; therefore the tailrace surge chamber setting conditions should be relaxed. A formula based on the last-phase water hammer assumption was recommended according to Chinese early specification (Ministry of power industry of the People's Republic of China 1997) and has been widely used in the preliminary design of conventional hydropower stations in China. However, these previous studies treated the velocity head at the draft tube inlet as a constant, and little attention was paid to the phase interval between the maximum water hammer vacuum (WHV) and the maximum velocity head vacuum (VHV). To address this issue, a mixed function that describes the dynamic process of WHV and VHV was developed by Zhao et al. (2004); however, the simple assumption that turbine discharge changed linearly during load rejection is not realistic for pumped-storage power stations (PPSs). In accordance with the designs of PPSs with long tailrace tunnels in Japan, Sugishita (2000) presented an empirical formula related to the water inertia time constant of the tailrace system, which indicates the ratio of the instantaneous pressure change to the submerged depth of the pump-turbines. Based on a case study, Zhang et al. (2004, 2008) discussed certain influencing factors of the minimum pressure in the draft tube and indicated that the recommended formula for hydropower stations in the specifications is not appropriate for PPSs. Bao et al. (2014) believe that the minimum pressure in the draft tube often occurs in the flow fast decreasing phase, and the duration of this phase should be used instead of the guide vane closing time to modify the discriminant in the early specification. Chinese revised specification (National Energy Administration 2014) recommended the Japanese empirical formula proposed by Sugishita (2000) as the setting criterion for PPSs and also introduced the American empirical formula. These previous studies are beneficial discussions on the setting criterion of tailrace surge chambers for PPSs; nevertheless, none of these studies treat head loss as an influencing factor, even if the water conveyance system is long. In practice, the pressure conduits of PPSs are usually much longer than that of hydropower stations, leading to larger head loss vacuum (HLV); thus, ignoring the head loss may introduce substantial errors.

Therefore, this chapter aims to overcome the above limitations and to theoretically derive a new setting criterion of tailrace surge chambers for PPSs that considers the head loss and the time sequence superposition of the WHV caused by the inertia of tailrace system, the VHV at the draft tube inlet and the HLV of the water conveyance system. Since the SPPS is one type of PPS, this new criterion is also applicable to the SPPS.

2 Mathematical Model

Hydraulic transients in pressure conduits are generally investigated using two different theories: rigid water hammer theory and the elastic water hammer theory. Krivchenko (1981) and Chang (2005) noted that when the water hammer phase number of penstock (m_u) was greater than 8, the elasticity of flow and tube wall have less impact on the water hammer pressure value, can usually be ignored. Note that the water hammer phase number of penstock and tailrace tunnel are $m_u = cT_Z/2L_u$ and $m_d = cT_Z/2L_w$, where c is the wave speed (m/s), T_Z is the closing time of guide vane (s), and L_u and L_w are the length of penstock and tailrace tunnel (m), respectively. Because the guide vane adjustment time of the PPSs is generally longer than that of conventional hydropower plants during load rejection, its water hammer phase number is large, as listed in Table 1. Thus, the dynamic process of the unsteady flow in PPSs is analysed using the rigid water hammer theory in this chapter.

2.1 Water Hammer Equations

According to the schematic diagram of a PPS shown in Fig. 1, using the draft tube inlet section as the benchmark section, the pump-turbine working head can be expressed as the gross head difference between the pump-turbine inlet Section 2-2 and the draft tube inlet Section 3-3 (Yang 1987; Jain et al. 2015) as follows:

$$H = H_2 - H_3 = \left(Z_2 + \frac{P_2}{\gamma} + \frac{\alpha_2 Q^2}{2gA_2^2}\right) - \left(Z_3 + \frac{P_3}{\gamma} + \frac{\alpha_3 Q^2}{2gA_3^2}\right) \quad (1)$$

where

subscripts 2 and 3	pump-turbine inlet section and the draft tube inlet section, respectively;
H	pump-turbine working head, m;
Z	elevation relative to the benchmark section, m;
P	cross-sectional average pressure, Pa;
Γ	specific weight of water, N/m^3;

Table 1 Water hammer phase number of penstock and tailrace tunnel for the main Chinese conventional PPSs

Serial number	PPS projects	T_Z (s)	m_u	m_d
1	Xilongchi	46.8	20.89	53.18
2	Jixi	22.0	11.17	8.63
3	Tianhuangping	13.5	5.77	29.35
4	Baoquan	25.0	8.31	14.12
5	Shisanling	23.0	13.45	11.39
6	Xianju	36.4	14.56	17.67
7	Xianyou	25.0	12.25	9.54
8	Huanggou	30.0	16.39	11.41
9	Yixing	38.2	19.10	10.73
10	Pushihe	46.0	21.90	16.49
11	Zhanghewan	28.3	20.21	72.56
12	Heimifeng	36.6	16.79	32.39
13	Tongbai	22.3	15.70	19.39
14	Taian	13.0	11.02	4.38
15	Bailianhe	36.5	43.45	42.94
16	Xiangshuijian	21.7	22.14	26.14
17	Langyashan	33.4	42.28	15.53

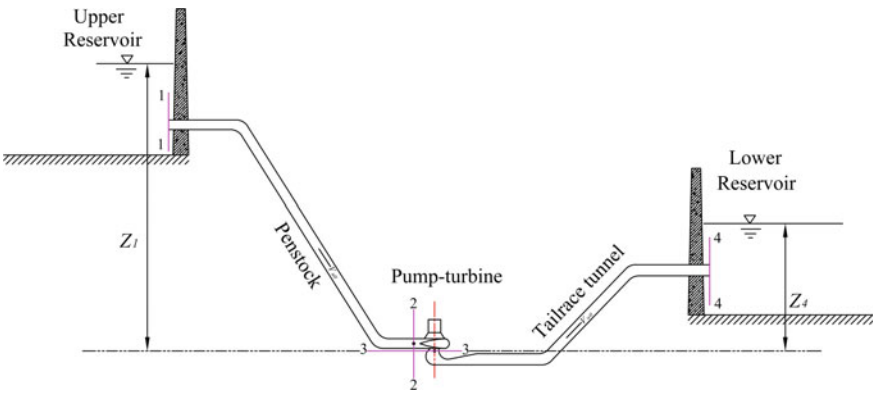

Fig. 1 Schematic diagram of a PPS or a SPPS

A kinetic energy correction coefficient, which is generally similar to 1;
Q diversion flow rate, m^3/s;
A cross-sectional area, m^2;
g gravitational acceleration, m/s^2.

To obtain the gross head of Sections 2-2 and 3-3, Bernoulli's energy equation can be established between the upstream reservoir Section 1-1 and the pump-turbine inlet Section 2-2:

$$Z_2 + \frac{P_2}{\gamma} + \frac{\alpha_2 Q^2}{2gA_2^2} = Z_1 + \frac{P_1}{\gamma} + \frac{\alpha_1 Q^2}{2gA_1^2} - \frac{L_u}{gA_u}\frac{\mathrm{d}Q}{\mathrm{d}t} - h_{wu} \tag{2}$$

Bernoulli's energy equation between the draft tube inlet Section 3-3 and the downstream reservoir Section 4-4 is as follows:

$$Z_3 + \frac{P_3}{\gamma} + \frac{\alpha_3 Q^2}{2gA_3^2} = Z_4 + \frac{P_4}{\gamma} + \frac{\alpha_4 Q^2}{2gA_4^2} + \frac{L_w}{gA_w}\frac{dQ}{dt} + h_{ww} \tag{3}$$

where

subscripts 1 and 4	upstream reservoir section and the downstream reservoir section, respectively;
subscripts u and w	the headrace system (penstock) and the tailrace system (pressure tailrace tunnel, draft tube extension, and draft tube), respectively;
	$\alpha Q^2 / (2gA^2)$ = velocity head, m;
	$L\mathrm{d}Q / (gA\mathrm{d}t)$ = water hammer pressure, m;
L	pipe or tunnel length, m;
	$h_{wu} = S_u Q\|Q\|$ = is the head loss of the headrace system, m;
	$h_{ww} = S_w Q\|Q\|$ = is the head loss of the tailrace system, m;
	$S_u = (\lambda_u L_u / D_u + \sum \zeta_u) / (2gA_u^2)$;
	$S_w = (\lambda_w L_w / D_w + \sum \zeta_w) / (2gA_w^2)$;
λ	coefficient of the frictional head loss;
$\sum\zeta$	coefficient of the local head loss;
D	diameter of the pipe or tunnel, m.

P_1 and P_4 are the surface atmospheric pressure of the upper reservoir and the lower reservoir, respectively; and they are approximately equal. Comparatively speaking, the near velocities V_1 and V_4 are much smaller than the flow velocity in the pipeline and can be neglected. Substituting Eq. (2) and Eq. (3) into Eq. (1) yields the following equation as the guide vane opening changes linearly:

$$H = Z_1 - Z_4 + \sigma H_0 \frac{\mathrm{d}q}{\mathrm{d}\phi} - SQ_0^2 q|q| \tag{4}$$

where

$\sigma = L_u Q_0 / (gA_u H_0 T_S) + L_w Q_0 / (gA_w H_0 T_S)$ is the characteristic coefficient of the penstock and the tailrace tunnel;

$H_0 = Z_1 - Z_4 - SQ_0^2$ is the initial working head of units, m; T_S = effective closing time of guide vane, i.e., the line segment closing time in Fig. 2 is generally

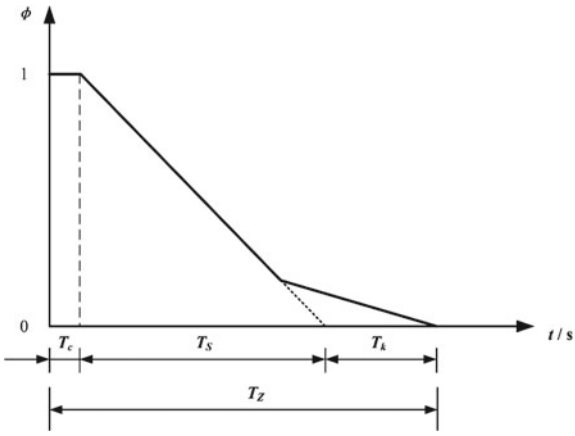

Fig. 2 Schematic diagram of T_S

in the range of 5–10 s, and for large capacity units, it can be up to 15 s or even longer (National Energy Administration 2014), s;

T_c	lag time of adjustment, s;
T_k	buffer time, s;
T_Z	total closing time of the guide vane, s;
$q = Q/Q_0$	relative discharge;
Q_0	initial discharge of units, m^3/s;
$\phi = 1 - t/T_S$	is the relative opening of guide vane under the linear closure law;
$S = S_u + S_w$	is the total head loss coefficient;
SQ_0^2	total head loss in pipeline under steady flow, m.

Introducing a dimensionless pressure change rate ξ, Eq. (4) can be converted as follows:

$$\xi = \sigma \frac{\mathrm{d}q}{\mathrm{d}\phi} + k_s - k_s q|q| \tag{5}$$

where

$\xi = (H - H_0)/H_0$;

$k_s = SQ_0^2/H_0$ is the relative head loss coefficient.

2.2 Derivation of the CLTS

Because the turbine is a rigid component, it can be approximately considered as a type of valve to simplify the mathematical derivation (Choo et al. 2008; Zeng et al. 2010, 2013; Nanaware et al. 2012; Sarasúa et al. 2015); however, the water hammer pressure obtained by this method should be multiplied by a machine type correction coefficient f. As a result, the flow law of the units can be expressed as follows:

$$q = \phi\sqrt{1+\xi} \tag{6}$$

Because we are concerned about the pressure drop process of the draft tube during load rejection, the flow rate is generally positive in the process. Therefore, the absolute value symbol of the item $k_s q|q|$ in the Eq. (5) can be removed. Then, substituting Eq. (5) into (6), taking the square of both sides, and then transposing items, we obtain

$$\frac{q^2}{\phi^2}\left(1+k_s\phi^2\right) = 1 + k_s + \sigma\frac{\mathrm{d}q}{\mathrm{d}\phi} \tag{7}$$

Taking the square root on both sides of the equal sign, Eq. (7) can be rewritten as

$$\frac{q}{\phi}\sqrt{1+k_s\phi^2} = \sqrt{1+k_s+\sigma\frac{\mathrm{d}q}{\mathrm{d}\phi}} \tag{8}$$

As $k_s\phi^2$ is often small, we have $\sqrt{1+k_s\phi^2} \approx 1+k_s\phi^2/2$; in addition, when the pressure rising rate ξ is under 50%, $\sqrt{1+k_s+\sigma\mathrm{d}q/\mathrm{d}\phi} \approx 1+k_s/2+\sigma\mathrm{d}q/2\mathrm{d}\phi$ (Taniguchi 1981; Shen 2008). As a result, the above formula can be simplified as

$$\frac{\mathrm{d}q}{\mathrm{d}\phi} - \left(\frac{2}{\sigma\phi} + \frac{k_s\phi}{\sigma}\right)q = -\frac{2+k_s}{\sigma} \tag{9}$$

Equation (9) is a first-order non-homogeneous differential equation, and its general solution is

$$q = \left[C - \frac{2+k_s}{\sigma}\int \phi^{-\frac{2}{\sigma}}\exp\left(-\frac{k_s}{2\sigma}\phi^2\right)\mathrm{d}\phi\right]\phi^{\frac{2}{\sigma}}\exp\left(\frac{k_s}{2\sigma}\phi^2\right) \tag{10}$$

where

C Integral constant.

Expanding $\exp(-k_s\phi^2/2\sigma)$ into a power series of ϕ, and integrating, Thus, we can get the approximate solution of q by ignoring the third order and above terms and substituting the initial condition $q|_{\phi=1} = 1$ into Eq. (10):

$$q = -\frac{\sigma+k_s}{2-\sigma}\phi^{\frac{2}{\sigma}} + \frac{2+k_s}{2-\sigma}\phi \tag{11}$$

Then, according to Eq. (3) and considering the machine type correction, the draft tube inlet pressure head can be obtained via transposition of terms:

$$\frac{P_3}{\gamma} = -H_S + \underbrace{\left(-f\frac{L_w V_{w0}}{gT_S}\frac{\mathrm{d}q}{\mathrm{d}\phi}\right)}_{\text{(I)}} + \underbrace{\left(-\frac{\alpha_3 Q_0^2}{2gA_3^2}q^2\right)}_{\text{(II)}} + \underbrace{S_w Q_0^2 q^2}_{\text{(III)}} \tag{12}$$

where

(I), (II), and (III)	WHV, VHV, and HLV, m;
$H_S = Z_3 - Z_4$	is the draft head of units, m;
f	machine type correction coefficient;
L_w	actual length of the tailrace system, m;
$V_{w0} = Q_0 / A_w$	is the average flow velocity in the pressure tailrace tunnel on the steady-state operation, m/s;
A_w	cross-sectional average area of the tailrace system, m^2;
A_3	cross-sectional area of the draft tube inlet, m^2.

Thus, the above problem is converted into the problem of solving the minimum value of function $U(\phi)$ in $\phi = [0, 1]$, where $U(\phi) = P_3 / \gamma$, $U_1(\phi) = -f L_w V_{w0} \mathrm{d}q / (g T_S \mathrm{d}\phi)$ and $U_2(\phi) = [S_w - \alpha_3 / (2gA_3^2)] Q_0^2 q^2$. Ultimately, the minimum of $g(\phi)$ can be obtained at $\phi = 0$ (Huang et al. 2018), i.e.,

$$\min\left(\frac{P_3}{\gamma}\right) = \left.\frac{P_3}{\gamma}\right|_{\phi=0} = -H_S - (2 + k_s) f \frac{L_w V_{w0}}{(2 - \sigma) g T_S} \tag{13}$$

To inhibit water column separation, the maximum vacuum at the draft tube inlet (i.e., the maximum vacuum in the tailrace system) as a design requirement, should be less than 8.0 m (National Development and Reform Commission 2004), and in a high altitude area, we also need to correct the vacuum limit value, i.e., $\min(P_3 / \gamma) \geq -(8 - \nabla / 900)$; thus, a formula of CLTS for PPSs is given as follows:

$$[L_w] = (2 - \sigma) K \frac{g T_S}{(2 + k_s) V_{w0}} \left(8 - \frac{\nabla}{900} - H_S\right) \tag{14}$$

where

$[L_w]$	CLTS, m;
∇	Setting elevation of the pump-turbine, m;
$K = f^{-1}$	and generally, $K = 0.6 \sim 0.7$.

Depending on the operating condition (i.e., a sudden full load rejection occurs under rated condition and guide vane closes linearly) and by using rigid water hammer theory and considering the time sequence superposition of the three terms including the WHV caused by the inertia of tailrace system, the VHV at the draft tube inlet and the HLV of the water conveyance system, Eq. (14), representing the setting criterion of tailrace surge chamber in a PPS, is proposed. Routinely, a tailrace surge chamber should be set up when $L_w > [L_w]$.

The setting criterion of tailrace surge chamber in conventional hydropower station recommended by Chinese early specification is as follows:

$$[L_w] = \frac{5 T_Z}{V_{w0}} \left(8 - \frac{\nabla}{900} - \frac{V_3^2}{2g} - H_S\right) \tag{15}$$

Due to the performance limitation of the governor and the influence of the dynamic discharge characteristics of the turbines, Chinese revised specification uses the effective closing time of guide vane (T_S) instead of the total closing time of the guide vane (T_Z), i.e.,

$$[L_w] = \frac{5T_S}{V_{w0}}\left(8 - \frac{\nabla}{900} - \frac{V_3^2}{2g} - H_S\right) \tag{16}$$

Moreover, Chinese revised specification introduces the American empirical discriminant and the Japanese empirical discriminant as follows:

$$\sum L_{wi} V_{wi} > 1800 \tag{17}$$

$$T_{ws} = \frac{\sum L_{wi} V_{wi}}{g(-H_S)}; \quad [T_{ws}] = 4 \sim 6\text{s} \tag{18}$$

where

L_{wi} Each segment length of tailrace system, m;
V_{wi} Average flow velocity in the corresponding tailrace pipe segment, m/s;
T_{ws} Actual water inertia time constant of tailrace system, s;
$[T_{ws}]$ Allowable value of T_{ws}, which is usually in the range of 4 ~ 6 s.
$[T_{ws}]$ Allowable value of T_{ws}, which is usually in the range of 4 ~ 6 s.

When ignoring the diameter changes of the tailrace tunnel, Eqs. (17) and (18) can be rewritten as follows:

$$[L_w] = \frac{1800}{V_{w0}} \tag{19}$$

$$[L_w] = \frac{[T_{ws}]g(-H_S)}{V_{w0}} \tag{20}$$

According to the American empirical discriminant, if the actual length of the tailrace system L_w is longer than the CLTS ($[L_w]$) obtained by Eq. (19), it is necessary to set up a tailrace surge chamber; according to the Japanese empirical discriminant, when $T_{ws} \leq 4$s, the tailrace surge chamber is unnecessary; when $T_{ws} \geq 6$s, a tailrace surge chamber needs to be set up; and when 4s $< T_{ws} <$ 6s, a detailed numerical simulation and investment analysis must be conducted to determine whether to set up a tailrace surge chamber.

3 Case Study

3.1 Analysis with Different Discriminants

Okinawa Yanbaru SPPS, the world's first experimental SPPS operated in Okinawa, Japan and was decommissioned in 2016. Because its tailrace tunnel is only 205 m in length, there is no need to set up a tailrace surge chamber (Hiratsuka et al. 1993). To verify the validity of the new setting criterion, five large PPSs with long tailrace tunnels in China were selected. The basic design parameters of these PPSs are listed in Table 2, where H_r, Q_r, n_r and P_r represent the rated head, discharge, rotational speed and output power of a single turbine; T_Z is obtained by the actual guide vane closure law; according to Chinese specification, T_S can be taken as 10 s in the preliminary design stage, and the characteristic coefficient of the pipeline σ can be taken as 0.5 to ensure the safety of the project; the relative head loss coefficient k_s is determined by the layout of water conveyance system.

The values of CLTS are calculated using different discriminants, as shown in Table 3. The Chinese specification discriminant gives the calculated results corresponding to Eqs. (15) and (16); The Japanese empirical discriminant gives the calculated CLTS corresponding to $T_{ws} = 4$ s and $T_{ws} = 6$ s; the coefficient K in Eq. (14) is set as 0.7 according to the specification. The measured pressure head at the draft tube inlet during 100% load rejection are also shown in Table 3.

Table 2 Basic design parameters of five Chinese conventional PPSs

Design parameters	PPS projects				
	Langyashan	Bailianhe	Tongbai	Heimifeng	Xianju
H_r (m)	126	195	244	300	447
Q_r ($m^3 \cdot s^{-1}$)	102.1	171.2	142.3	118.3	96.6
n_r ($r \cdot min^{-1}$)	230.8	250.0	300.0	300.0	375.0
P_r MW	153.0	306.0	306.0	306.0	382.7
T_S (s)	10.0	10.0	10.0	10.0	10.0
T_Z (s)	33.4	36.5	22.3	36.6	36.4
∇(m)	-10	41	52	15	107
H_S (m)	-32	-63	-58	-50	-71
σ	0.50	0.5	0.5	0.5	0.5
k_s	0.023	0.035	0.017	0.014	0.026
V_3 ($m \cdot s^{-1}$)	11.76	16.94	18.22	20.67	19.07
V_{w0} ($m \cdot s^{-1}$)	3.36	4.36	3.70	4.19	4.49
L_w (m)	1077.0	425.7	571.4	563.9	1031.0
Actual setting condition of tailrace surge chambers (Yes or No)	Yes	No	No	No	Yes

Table 3 Calculated results of CLTS with different discriminants

Different discriminants		Calculated CLTS [L_w] (m)				
		Langyashan	Bailianhe	Tongbai	Heimifeng	Xianju
Chinese discriminant	T_Z	1638.3	2357.8	1477.3	1581.4	2446.1
	T_S	490.5	646.0	662.5	432.1	672.0
American discriminant		535.7	412.8	486.5	429.6	400.9
Japanese discriminant	$T_{ws} = 4$ s	373.7	567.0	615.1	468.3	620.5
	$T_{ws} = 6$ s	560.6	850.5	922.7	702.4	930.8
New discriminant Eq. (14)		606.3	823.7	910.2	707.8	893.2
Measured minimum pressure head at draft tube inlet during 100% load rejection		11.6	26.8	32.1	9.1	37.5

From Table 3, the following results are summarized:

(1) The values of CLTS calculated by the Chinese early discriminant given by Eq. (15) are all much longer than the actual length of the tailrace system, i.e., for these five PPSs, the tailrace surge chambers are not necessary according to this criterion. However, in fact, tailrace surge chambers are set up in Langyashan and Xianju PPS after the detailed numerical simulation of the hydraulic transient process. It indicates that taking Eq. (15) as the setting criterion of tailrace surge chambers for PPSs or SPPSs may have an adverse impact on their safe operation. The reason for this result is that Eq. (15) is mainly aimed at early small-capacity conventional hydropower stations, where the total closing time of guide vane (T_Z) during the load rejection is generally short. So it can be considered that T_Z is approximately equal to the effective closing time T_S. However, for large-capacity PPSs or SPPSs, the guide vane closes for a long time, and sometimes even up to 40 s or more. Here, the change time of discharge that affects the minimum pressure in the draft tube is much smaller than T_Z. Therefore, if we still use T_Z to calculate the CLTS, the result will be much larger, which is obviously inappropriate.

When using T_S instead of T_Z, the value of CLTS of Heimifeng PPS calculated by Eq. (16) is less than its actual length of the tailrace system. According to its viewpoint, the tailrace surge chamber needs to be set up. However, without tailrace surge chambers, the measured minimum pressure head at the draft tube inlet of Heimifeng PPS at 100% load rejection is 9.1 m, with large safety margins. That is because Eq. (16) assumes that the velocity head at the draft tube inlet is a constant during the load rejection, and ignores the phase interval between the maximum water hammer vacuum (WHV) and the maximum velocity head vacuum (VHV) of the draft tube inlet.

(2) Because the calculated CLTS obtained by American empirical discriminant given by Eq. (19) are much smaller than the actual length of the tailrace tunnel, the tailrace surge chambers should be set up for these five PPSs when we take it

as the criterion. However, as we know, the on-site load rejection test shows that the draft tube and the tailrace system of Bailianhe, Tongbai and Heimifeng PPSs are still safe without the tailrace surge chambers. This indicates that Eq. (19) is conservative and may cause a significant increase in investment. In addition, the CLTS in Eq. (19) is only related to V_{w0}. When the V_{w0} of high, medium and low head PPSs or SPPSs are close, the CLTS calculated by Eq. (19) are almost identical, which is not practical.

(3) The Japanese empirical discriminant given by Eq. (20) provides a wide range of CLTS. Since the actual length of tailrace system of Heimifeng PPS is between the upper and lower bound of $[L_w]$ obtained by Eq. (20), it is necessary to conduct a detailed numerical simulation and investment analysis to determine whether to set up a tailrace surge chamber. This may delay the preliminary design progress of the PPSs. For Xianju PPS, because its actual length of the tailrace tunnel is 1031.0 m and it exceeds the CLTS (930.8 m) when $T_{ws} = 6$ s, it is necessary to set up a tailrace surge chamber according to the Japanese empirical discriminant. The discriminant result is in accordance with the actual setting condition of Xianju PPS.

(4) The calculated results achieved by the new discriminant given by Eq. (14), which are all consistent with the actual setting conditions of tailrace surge chambers of the five PPSs. Different from Eqs. (15) and (16), the new discriminant Eq. (14) considers the time sequence superposition of WHV, VHV and HLV. In addition, since the guide vane closing law can significantly affect the flow change rate ($\mathrm{d}Q/\mathrm{d}t$), and then affect the pressure at the draft tube inlet, it is more realistic to incorporate T_S and k_s into the influencing factors compared to other empirical discriminants.

3.2 Numerical Simulations

Note that the above discriminants are just rough criteria, and the purpose is to avoid large changes in the later period of the design, such as the cancellation and the addition of the tailrace surge chambers, thereby speeding up the design progress of the project. Certainly, whether the tailrace surge chamber needs to be set up in the final scheme should be determined after the detailed numerical simulation of the hydraulic transient process and comparative analysis of technology and economy for multiple schemes based on the known design parameters of the water conveyance system and the units.

Taking Xianju PPS as an example, the hydraulic transient process is performing by using SIMSEN-Hydro software (Nicolet 2007) in the case of setting and not setting the tailrace surge chamber to evaluate its function and verify the preliminary design scheme. The complete characteristic curves of Xianju pump-turbine are shown in Fig. 3, in which N_{11}, Q_{11} and T_{11} are defined as follows:

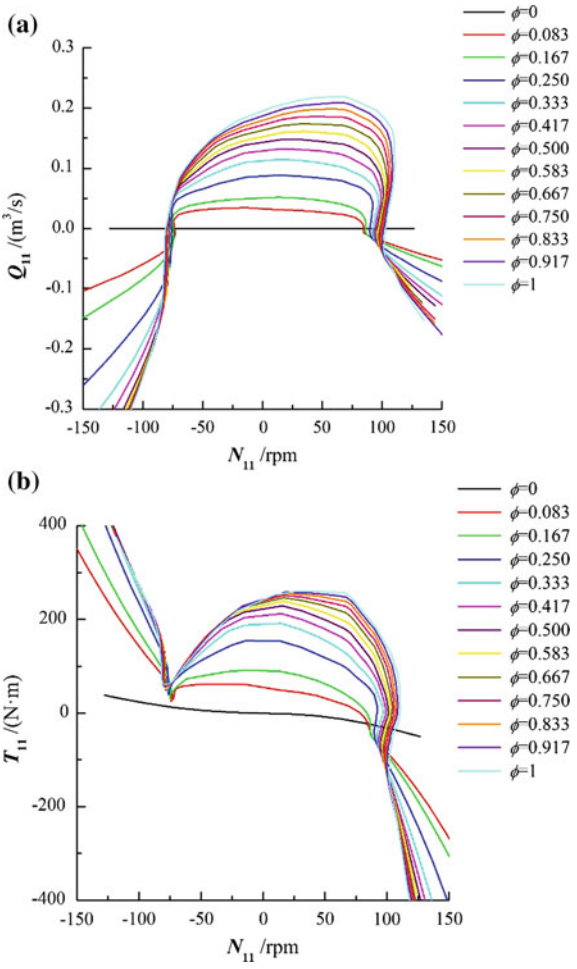

Fig. 3 Complete characteristic curves of Xianju pump-turbine. **a** N_{11}–Q_{11} characteristics; **b** N_{11}–T_{11} characteristics

$$N_{11} = \frac{nD_{ref}}{\sqrt{H}}, Q_{11} = \frac{Q}{D_{ref}^2\sqrt{H}}, T_{11} = \frac{T}{D_{ref}^3 H} \tag{21}$$

where

N_{11} unit speed, rpm;
Q_{11} unit discharge, m^3/s;
T_{11} unit torque, N·m;
D_{ref} runner diameter, m;
H water head, m;
N rotational speed, rpm;
Q discharge, m^3/s;
T torque, N·m.

And the layout of Xianju PPS is presented in Fig. 4. A water conservancy system of Xianju PPS is made of an upstream reservoir, a 90 m long pressure headrace tunnel, a common penstock of about 1125 m long and 6.2 m of diameter connected to two 375 MW pump-turbines, connected to the tailrace surge chamber by a common draft tube extension of 278 m long, and a pressure tailrace tunnel of about 758 m long and 7.4 m of diameter. The main characteristics of Xianju PPS are presented in Table 4.

According to the tentative calculations of multiple working conditions, the most critical load case for the minimum pressure in the draft tube was found, i.e., Unit 1 with 2 s delay rejects after the load rejection of Unit 2. Figure 5 presents the guide vane closure law in generating mode.

To evaluate the effect of the tailrace surge chamber and to verify the preliminary design scheme, the hydraulic transient process is simulated with and without setting the tailrace surge chamber, and the transient results of the worst case are shown in Fig. 6 in case of the load rejection of Unit 2 occurring at $t = 10$ s. Both the water level of upstream reservoirs and downstream reservoirs are normal water level and dead water level, respectively. Table 5 presents the comparison of the maximum rotational speed, the maximum pressure at the spiral case inlet and the minimum pressure at the draft tube inlet.

It can be noticed that the maximum rotational speed of the unit is reduced by 7%, the maximum pressure at the spiral case inlet is reduced by 2.5%, and the minimum pressure at the draft tube inlet is increased by 7.6 m after setting the tailrace surge chamber. Considering that the simulated pressure is the average cross-sectional pressure and the pressure pulsation have a significant effect on the pressure at the

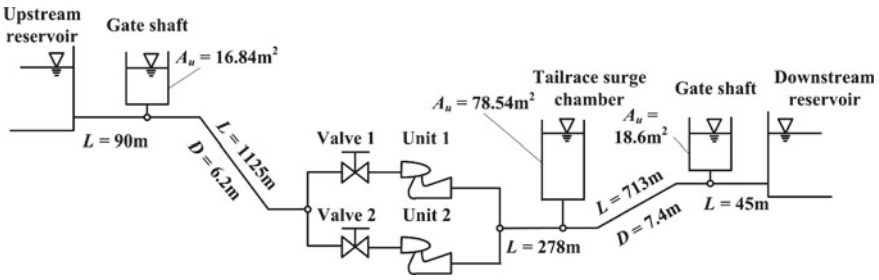

Fig. 4 The layout of Xianju PPS

Table 4 Main characteristics of Xianju PPS

Upstream reservoir	Downstream reservoir	Unit parameters
$H_{u\max} = 676.8$ m $H_{u\text{nor}} = 675.0$ m $H_{u\min} = 641.0$ m	$H_{d\max} = 213.9$ m $H_{d\text{nor}} = 208.0$ m $H_{d\min} = 178.0$ m	$H_r = 447$ m $Q_r = 96.6$ m^3/s $n_r = 375$ rpm $P_r = 382.7$ MW $GD^2 = 9515$ t·m^2 $D_{ref} = 4.86$ m

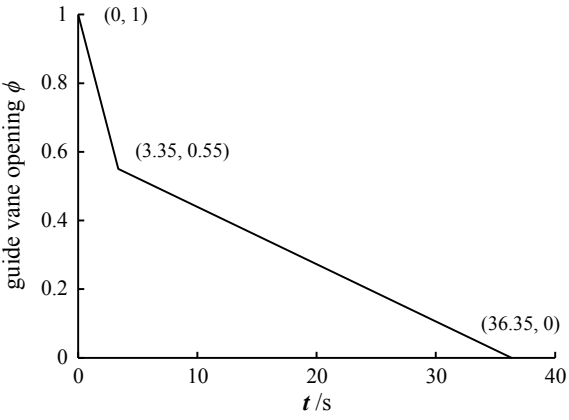

Fig. 5 Guide vane closure law

draft tube inlet, the simulated pressure at the draft tube inlet needs to be corrected. Normally, we can take 2% of the net head of the unit (491.39 m) before the load rejection as the correction value. Thus, the pressures at the draft tube inlet with and without a tailrace surge chamber are corrected as 2.16 m and −5.44 m, respectively. Obviously, without the tailrace surge chamber, a large negative pressure is generated in the draft tube, which may cause the water column separation and threaten the safe operation of the PPS. Therefore, the tailrace surge chamber is necessary for Xianju PPS, and this is consistent with the result obtained by the new setting criterion.

4 Conclusion

In contrast to the existing discriminants, the new setting criterion of tailrace surge chambers proposed in this study considers the dynamic head loss and the time sequence superposition of WHV, VHV and HLV. Through performing a comparative analysis, the following conclusions are drawn:

(1) Directly applying the setting criterion Eq. (15) for the tailrace surge chambers of conventional hydropower plants into PPSs and SPPSs will have an adverse impact on the safe operation; the American empirical discriminant Eq. (19) tends to be conservative on setting up tailrace surge chambers, may resulting in unnecessary waste; the Japanese empirical discriminant Eq. (20) is difficult to judge for the situation where T_{ws} is between 4 and 6. This may delay the preliminary design progress of the PPSs and SPPSs.

(2) Relatively speaking, taking more comprehensive influencing factors into account, the new setting criterion Eq. (14) proposed in this chapter can effectively reflect the influence of head loss and guide vane closing law on CLTS. The results obtained by the new setting criterion are in good agreement with

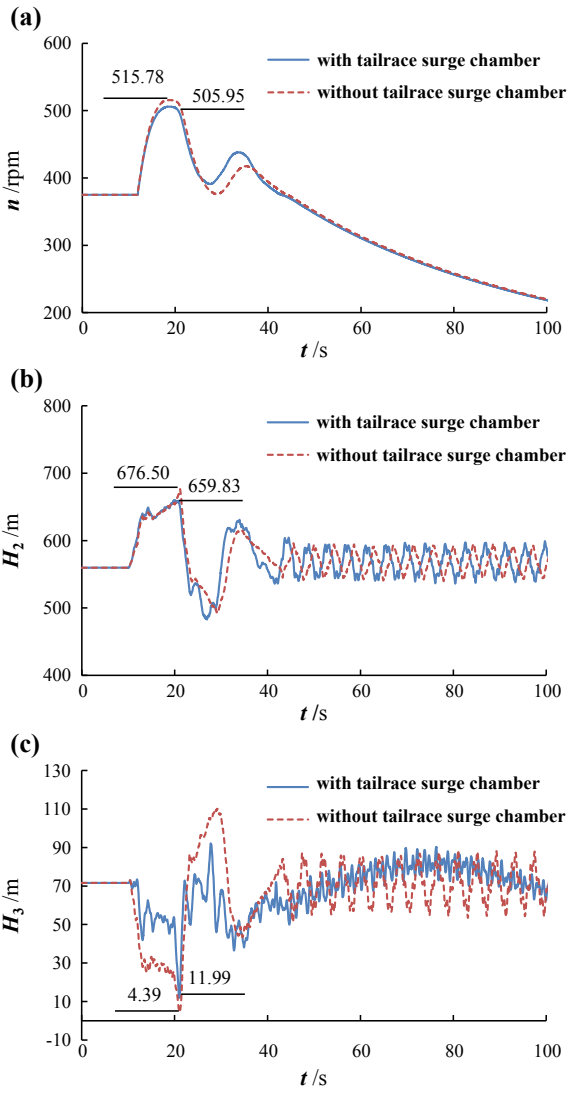

Fig. 6 Transient results of the worst case with and without the tailrace surge chamber. **a** rotational speed; **b** pressure at the spiral case inlet; **c** pressure at the draft tube inlet

Table 5 Transient conditions with and without tailrace surge chamber

Simulation results	Max. Speed rise (%)	Max. Head at spiral case inlet (m)	Min. Head at draft tube inlet (m)
With tailrace surge chamber	34.9	659.83	11.99
Without tailrace surge chamber	37.5	676.50	4.39

the actual setting condition. Thus, the new setting criterion is valid as a preliminary judgment standard for setting up a tailrace surge chamber in a PPS or a SPPS and provides guidance for the preliminary design of the project. Certainly, whether the tailrace surge chamber needs to be set up in the final scheme should be determined after a detailed numerical simulation of the hydraulic transient process or a physical model test to verify the preliminary plan.

In this study, a CLTS is derived under the conditions of linear guide vane closure. The impact of nonlinear closing law on CLTS are matters of interest for future research.

Acknowledgements This work was supported by the National Key Research and Development Program of China (Grant No. 2016YFC0401808), National Science & Technology Pillar Program during the Twelfth Five year Plan Period (Grant No. 2015BAD24B02), National Natural Science Foundation of China (Grant Nos. 51379099 and 51609265) and Beijing Natural Science Foundation (Grant No. 9152010).

References

Bergant, A., Simpson, A. R., & Tijsseling, A. S. (2006). Water hammer with column separation: a historical review. *Journal of Fluids and Structures, 22*(2), 135–171.

Berlin, V. V., & Murav'ev, O. A. (2014). Load drops at high-head pumped-storage power plants with branched conduits. *Power Technology and Engineering, 48*(1), 23–28.

Bao, H. Y., Fu, L., & Yang, J. D. (2014). Discussion on setting condition of tailrace surge tank of pumped storage hydropower station. *Journal of Hydroelectric Engineering, 33*(1), 95–101. (in Chinese).

Chang, J. S. (2005). *Transients of hydraulic machine installations*. Beijing: Higher Education Press. (in Chinese).

Choo, Y. C., Muttaqi, K. M., & Negnevitsky, M. (2008). Modelling of hydraulic governor-turbine for control stabilization. *Australian and New Zealand Industrial and Applied Mathematics Journal, 49,* 681–698.

Fang, Y. J., Koutnik, J. (2012). The numerical simulation of the delayed load rejection of a pump-turbine powerplant. In *IOP Conference Series: Earth and Environmental Science 26th IAHR symposium on Hydraulic Machinery and Systems* (Vol. 15, p. 022018).

Gubin, F. F. (1983). *Hydropower station*. (R. Xu, Trans.). Beijing: Water Resources and Electric Power Press (in Chinese).

Huang, W., Yang, K. L., Ma, J. M., Xu, Y. W., Guo, X. L., & Wang, J. (2018). A new setting criterion of tailrace surge chambers for pumped-storage power plants. *Renewable Energy, 116,* 194–201.

Hiratsuka, A., Arai, T., & Yoshimura, T. (1993). Seawater pumped-storage power plant in Okinawa island, Japan. *Engineering Geology, 35*(3), 237–246.

Ji, K., & Liu, W. L. (1991). Discussion on the condition for setting tailrace surge chamber. *Journal of Zhengzhou Institute of Technology, 12*(4), 17–21. (in Chinese).

Jain, S. V., Swarnkar, A., Motwani, K. H., & Patel, R. N. (2015). Effects of impeller diameter and rotational speed on performance of pump running in turbine mode. *Energy Conversion and Management, 89,* 808–824.

Kendir, T. E., & Ozdamar, A. (2013). Numerical and experimental investigation of optimum surge tank forms in hydroelectric power plants. *Renewable Energy, 60,* 323–331.

Krivchenko, G. I. (1981). *Transient process of power installation of hydropower station*. (Z. T. Chang, Trans.). Beijing: Water Conservancy Press (in Chinese).

Mei, Z. Y. (2000). *Pumped storage power generation technology*. Beijing: Machinery Industry Press. (in Chinese).

Murav'ev, O. A. (2011). Effect of turbine-operating regime and adjustment of automated control system on stability and critical area of surge tanks at HPP. *Power Technology and Engineering, 45*(1), 6–11.

Ministry of power industry of the People's Republic of China. (1997). *Specifications for design of surge chamber of hydropower stations*. Beijing: China Power Press. Standard ID: DL/T 5058-1996 (in Chinese).

National Energy Administration. (2016). *13th Five-Year Plan of hydropower development*. http://www.nea.gov.cn/2016-11/29/c_135867663.htm. (in Chinese).

National Energy Administration. (2014). *Design code for surge chamber of hydropower stations*. Beijing: China Electric Power Press. Standard ID: NB/T 35021-2014 (in Chinese).

Nanaware, R. A., Sawant, S. R. and Jadhav, B. T. (2012). Modeling of hydraulic turbine and governor for dynamic studies of HPP. In *IJCA Proceedings on International Conference on Recent Trends in Information Technology and Computer Science* (pp. 6–11).

National Development and Reform Commission. (2004). *Electrical-mechanical design code of hydropower plant.* Beijing: China Electric Power Press. Standard ID: DL/T 5186-2004 (in Chinese).

Nicolet, C. (2007). *Hydroacoustic modelling and numerical simulation of unsteady operation of hydroelectric systems* (Ph.D. thesis). Lausanne: EPFL.

Pejovic, S., Zhang, Q. F., Karney, B., and Gajic, A. (2011). Analysis of pump-turbine S instability and reverse waterhammer incidents in hydropower systems. In *4th International Meeting on Cavitation and Dynamic Problems in Hydraulic Machinery and Systems*. Belgrade, Serbia. October 26–28 2011.

Qian, G. L. (2017). Brief introduction of Chinese seawater pumped storage power station's resources. *Hydropower and Pumped Storage, 3*(05), 1–6.

Sugishita, K. (2000). Experimental study to eliminate a surge chamber from long tailrace tunnels of high head pumped storage power plants. *In The World Bank and Jiangsu Provincial Electric Power Company. Proceeding of Pumped Storage International Workshop* (Vol. 11(9), pp. 555–557). Nanjing, China.

Sarasúa, J. I., Pérez-Díaz, J. I., Wilhelmi, J. R., & Sánchez-Fernández, J. Á. (2015). Dynamic response and governor tuning of a long penstock pumped-storage hydropower plant equipped with a pump-turbine and a doubly fed induction generator. *Energy Conversion and Management, 106,* 151–164.

Shen, Z. Y. (2008). *Turbine regulation*. Beijing: China Water Conservancy and Hydropower Press. (in Chinese).

Taniguchi, H. (1981). *Water hammer and pressure fluctuation* (P. F. Zhi, Trans.). Beijing: Electric Power Industry Press (in Chinese).

Yang, K. L. (1987). The optimum computation approach for the transients caused by pump-turbine load rejection. *Journal of Hydraulic Engineering, 11,* 29–36. (in Chinese).

Zhang, J., & Suo, L. S. (2008). Study on tailrace surge chamber installation and hydraulic transients at pumped-storage plant. *Water Resources and Power, 26*(3), 83–87. (in Chinese).

Zhang, J., Zhang, W., Jiang, Z. J., & Xu, Y. M. (2004). Special considerations for removing a tailwater surge chamber from the waterway system in a pumped-storage plant. *Water Resources and Hydropower Engineering, 35*(8), 116–118.

Zhang, H. T., Wu, S. D., Rui, D. F., & Zhang, D. (2017). Study on selection and development of demonstration project of seawater pumped storage power station in China. *Hydropower and Pumped Storage, 3*(05), 7–10.

Zhao, Q. (1986). *Research on the condition for setting surge chamber* (Master thesis). Wuhan College of Hydraulic and Electric Engineering, Wuhan (in Chinese).

Zhao, G. L., Yang, J. D., Xu, Y. J., & Li, J. P. (2004). Research on the condition to set a tailrace surge tank. *Journal of Hydrodynamics, Ser. B, 16*(4), 486–491.

Zeng, Y., Zhang, L. X., Xu, T. M., Dong, H. K. (2010). Building and analysis of hydro turbine dynamic model with elastic water column. In *Asia-Pacific Power and Energy Engineering Conference*, Chengdu, China, March 28–31 2010.

Zeng, Y., Guo, Y. K., Zhang, L. X., Xu, T. M., & Dong, H. K. (2013). Nonlinear hydro turbine model having a surge tank. *Mathematical Modelling of Systems, 19*(1), 12–28.

Toward an Ecosystem Approach of Marine Renewable Energy: The Case of the Offshore Wind Farm of Courseulles-sur-Mer in the Bay of Seine

Nathalie Niquil, Aurore Raoux, Matilda Haraldsson, Emma Araignous, Ghassen Halouani, Boris Leroy, Georges Safi, Quentin Noguès, Karine Grangeré, Jean-Claude Dauvin, Fabien Riera, Camille Mazé, François Le Loc'h, M. Ching Villanueva, Tarek Hattab, Pierre Bourdaud, Juliette Champagnat and Frida Ben Rais Lasram

Abstract Environmental impact assessment (EIA) studies for offshore wind farm projects endeavour to consider the sensitivity of ecological compartments (benthos, fish, birds and marine mammals) to potential pressures/changes occurring in the ecosystem structure and functioning. EIA is expected to be conducted considering an integrated ecosystem approach, which is still a target to reach. In this context, and as a complementary approach to the traditional impact assessments, the objective of the ANR TROPHIK project is to develop an integrated ecosystem approach using several modelling tools for a holistic consideration of the food web. Here, we take into account the case of the Courseulles-sur-Mer offshore wind farm project located in the Bay of Seine. In this project, the potential impacts associated with this planned offshore wind farm are modelled. A model of the food web at the site of the construction was built to test possible reef- and reserve-effects, and to investigate the usefulness of Ecological Network Analysis (ENA) indices in the assessment of

N. Niquil (✉) · A. Raoux · M. Haraldsson · E. Araignous · G. Halouani · B. Leroy · G. Safi · Q. Noguès · K. Grangeré
Normandie University, UMR BOREA, CNRS/MNHN/Université de Caen Normandie/Université Des Antilles/IRD/Sorbonne Université, Caen, Paris, France
e-mail: nathalie.niquil@unicaen.fr

A. Raoux · J.-C. Dauvin
Normandie University, UMR M2C, CNRS/Université de Caen Normandie/Université de Rouen Normandie, Caen, France

F. Riera · C. Mazé · F. Le Loc'h
UMR LEMAR, UBO, CNRS, IRD, Ifremer, IUEM, Brest, France

G. Halouani · M. Ching Villanueva
Ifremer, LBH-STH, Plouzané, France

T. Hattab · P. Bourdaud · J. Champagnat · F. B. R. Lasram
CNRS, UMR 8187, LOG, Laboratoire D'Océanologie et de Géosciences, University Littoral Cote D'Opale, University Lille, Wimereux, France

K. D. Nguyen et al. (eds.), *Estuaries and Coastal Zones in Times of Global Change*, Springer Water,
https://doi.org/10.1007/978-981-15-2081-5_9

ecosystem health state. After the installation of the wind farm, our model showed that the ecosystem witnessed a change in its functioning mainly due to the important increase of the biomass of bivalves with the reef effect related to the installation of hard structures for the OWF. To go further into the integration of these results, we enlarged the description of the ecosystem functioning from a local to a larger spatial scale, where the initial zone was extended to the whole Bay of Seine using a spatial model. Different scenarios were built to test how the association of cumulative impacts, from climate change to fisheries, could affect the ecosystem. Finally, we propose a combined food-web and social network modelling approach to the Courseulles-sur-Mer model. The objectives of this latter analysis are to construct a decision-making process focusing on the network of actors involved, and to couple these social and ecological networks into a qualitative common model for a better understanding of the social-ecological system. Our approach aims to contribute to sustainable development through the analysis of interactions between the different categories of stakeholders groups, and can be applied in other offshore wind farm implementation in European waters.

Keywords Ecosystem · Food-web model · Ecological network analysis · Socio-ecological system · Cumulative impacts · Global change

1 Introduction

The development of Marine Renewable Energy (MRE) projects has grown considerably in recent years. Operational offshore wind farms in France are not yet fully implemented but should be in the coming years in spite of numerous administrative procedures (Pezy et al. in press). The integration of such infrastructures in complex and fragile coastal marine environments is a challenge for developers from technical, legal, societal and environmental points of view. These MREs will have to be implemented in ecosystems already subjected to numerous and growing natural and anthropic disturbances. These can cause changes in ecosystem functioning, impacting their resilience which may cause them to shift from one state to another (Knowlton 1992, 2004). Understanding the behaviour of these complex systems is essential in order to anticipate state changes (Hughes et al. 2005) and facilitate the implementation of conservation actions with sustainable development scopes (Hosack et al. 2009). In order to do so, integrative approaches such as food web models are needed. The quantification of the energetic flows between all living organisms in the ecosystem can allow the calculation of numerical indices necessary for the characterization of a system's functional properties (ENA, Ecological Network Analysis indices).

The objective of the ANR TROPHIK project is to model the food web of the area intended for wind farm constructions at Courseulles-sur-Mer (Fig. 1) in order to improve the current knowledge of the system and to characterize its present ecological properties. Firstly, a sensitivity study of the model, based on different types of impacts characterized from the literature on the exploitation of wind farms, was carried out in

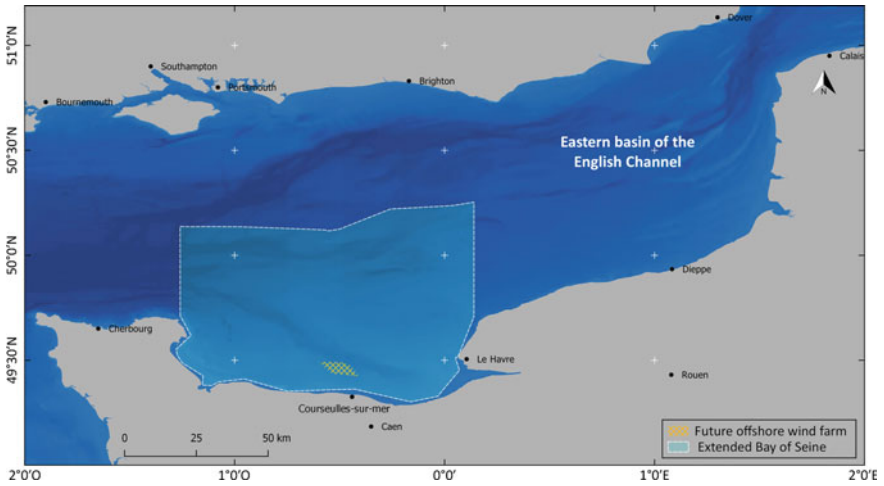

Fig. 1 Map of the Eastern basin of the English Channel, between France and UK. Here, "Local ecosystem modelling" (yellow zone) concerns only the future construction site of the offshore wind farm while the "Spatial ecosystem modelling" includes the whole Bay of Seine (light blue) until the France-UK ZEE limit

order to predict the possible effects of the construction and exploitation phases on the organization and functioning properties of the food web. Then, cumulative impacts on the food web were studied based on simulation studies that takes into account both the MRE interactions with the fisheries and species' distribution changes due to climate change. The cumulative impacts were studied both at a local, and larger spatial scales. To do so, the initial Courseulles-sur-mer model was extended to a spatial model, covering the extended Bay of Seine (Fig. 1). Last but not least, the collaboration with anthropologists allowed to go further in the consideration of the effects of the offshore wind farm on the social-ecological system. With the aim of integrating this ecosystem overview into a balanced framework of the socio-ecological system, a holistic model is built where human and environmental network interactions are described at approximately the same level of detail.

2 Local Ecosystem Modelling

The first modelling exercise was a zero dimension approach of the complete food web in the future site of the offshore wind farm in Courseulles-sur-mer, completed under different scenarios of the effects of its presence on the ecosystem. For this, the modelling tool Ecopath with Ecosim (EwE) was used. This modelling approach was developed to evaluate ecosystem-based management of fisheries (Walters et al. 1997). The species of the ecosystem were gathered within 37 compartments of similar trophic behaviour (same preys and same predators). Special attention was given

for commercial species by positioning them in monospecific compartments. Three scenarios were also modelled: (1) the reef effect due to the new presence of a hard substrate in a zone of coarse sands and pebbles, (2) the reserve effect associated with an optimized strategy of authorising the fisheries along the turbine axes and with fishing restrictions at 15% of the farm area surface, and (3) the combination of both effects (Fig. 2) (for more details see Raoux et al. 2017 and in press). For each model (Before Offshore Wind Farm = BOWF and the three scenarios described above), energetic flows were quantified before and 30 years after the offshore wind farm construction building using EwE, and then the food web was characterised based on the ENA indices. These indices, which are of multidisciplinary origin, allow the characterisation of emergent properties of the trophic network functioning. These indices enable the characterization of the recycling, the redundancy of the flows, the omnivory, or the mean trophic levels in an ecosystem (Latham 2006). Such indices have been recently proposed as ecosystem health indicators for describing the food web functioning in different contexts (Niquil et al. 2014), including the implementation of the Marine Strategy Framework Directive in Europe.

Furthermore, the uncertainty associated with the estimations of energetic flows and ENA properties was quantified. Firstly, the confidence interval for each ENA indices of each model was characterised using the numerical tool ENATool (Guesnet et al. 2015), which is based on a semi-quantitative approach of uncertainty. Secondly, the confidence intervals were more precisely quantified using an alternative

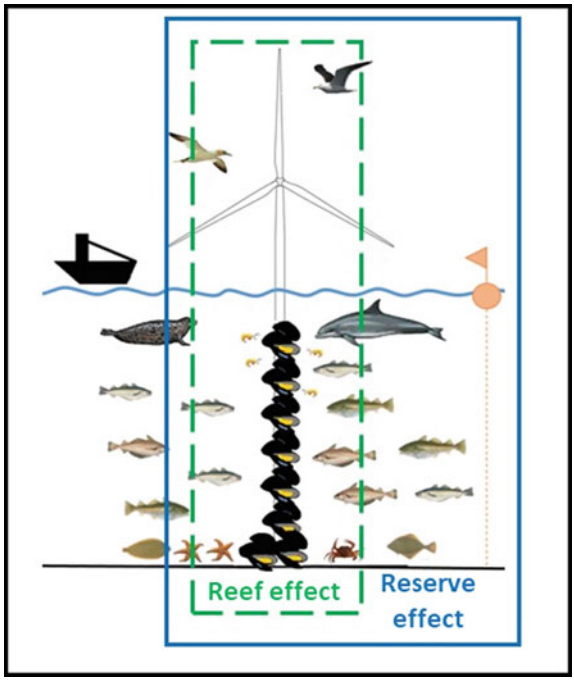

Fig. 2 Modelled scenarios of the offshore wind farm exploitation effects on the food web functioning (Raoux et al. 2019)

modelling method, Linear Inverse Model-Monte Carlo Markov Chain (LIM-MCMC, Kones et al. 2009), traditionally used for the quantification of flows within microbial food webs. This method was applied to the whole ecosystem, but with the re-aggregation of the 37 initial compartments into 19, based on trophic behaviour similarities (Raoux 2017; Noguès 2018). The LIM-MCMC was applied to compare the present situation with the situation with reef effect based on the wind farm, but also with the consequences of climate change on the distribution of the biomass of the most present species.

In order to do so, the potential impacts of climate change on the distribution of 75 species was characterized with correlative species distribution models (Ben Rais Lasram et al. in prep). We applied a two-scale approach (see Hattab et al. 2014): we modelled the climatic niche of species (temperature and salinity) at a large spatial scale (global extent, 1/12° resolution) and their habitat (bathymetry, slope, substrate) at a fine spatial scale (French coast, 250 m resolution). We applied multiple modelling algorithms and combined all outputs in average and uncertainty maps with an ensemble modelling approach (Araujo and New 2007). We projected future distributions maps on the basis of two climate change scenarios (RCP 2.6 and RCP 8.5) and three general circulation models. We integrated the predicted changes in species distributions in LIM-MCMC models with the method developed by Chaalali et al. (2015).

The main conclusion of this multi-modelling work is that the food web in Courseulles-sur-mer is characterised by a control of the food web by the intermediate trophic level (Raoux et al. 2017), opposed to a classical bottom-up or top-down control observed in other zones (Cury et al. 2003; Lassalle et al. 2011). This is because the main keystone species is the pouting (*Trisopterus luscus*), a fish positioned at an intermediate trophic level, indicating that this trophic level dominates the control of the food web. Furthermore, the analyses of the 3 model scenarios reveal that the dominating effect of the offshore wind farm is the reef effect due to the massive arrival of blue mussels and associated species on the hard substrate. This anticipated mussel biomass increase after the offshore wind farm construction is predicted to lead to a detritivory-dominated food web (Raoux et al. 2017), which is in line with Norling and Kautsky (2008) hypothesis. An increase in benthic invertebrate and benthos-feeding fish biomasses in response to this reef effect is predicted to attract apex predators, as hypothesized by Lindeboom et al. (2011) and Henkel et al. (2014).

Our results based on the ENA indices analyses revealed a combination of changes in the ecosystem structure and functioning. After the installation of the Offshore Wind Farm (OWF), the ecosystem is expected to increase not only detritivorous but also omnivorous species, with a higher level of recycling (Raoux et al. 2019), due to the reef effect, and especially to the action of filter feeders. Moreover, our study highlighted that the small size of the fisheries restriction area is not expected to have an impact on the ecosystem structure and functioning. However, the different indices gave opposite results on system maturity level analyses when system functioning was associated with the ENA indices [according to ecological theories developed by Odum (1969, 1971), and Ulanowicz (1986)]. The most sensitive biological compartment (fish benthos feeders, including the pouting) to climate change was also the

one of highest keystoneness (as defined by Libralato et al. 2006). These results indicate the interest of using a large set of ENA indices to characterise different trophic functioning attributes, essential for a complete view of the induced changes (Raoux et al. 2019; Noguès 2018).

3 Spatial Ecosystem Modelling

The second objective of our project was to obtain a spatial view of the cumulative impact at the larger scale (Fig. 1). A grid of cells of one nautical mile length was applied and the food web based on 42 compartments was modelled within each of these squares. Here we used Ecospace, the spatial module of EwE. This model is detailed in Halouani et al. (in prep). The Ecospace model simulates the trophic functioning of the ecosystem by projecting the temporal dynamics of the Ecosim models onto a two-dimensional grid of square cells of the same size. Implementing an Ecospace model requires the definition of the base map and the different types of habitats that will determine the distribution of trophic groups according to their habitat preferences, their response to environmental parameters, their dispersion rates and their foraging behaviour. The intensity of the fishing effort is distributed over the entire map according to a "gravity model" which assigns a fishing effort to a cell according to its profitability in terms of catches (Christensen et al. 2008). Thus, the fishing effort is distributed so that the effort applied in a cell: (1) is proportional to its profitability, (2) possibly depends on the distribution of the different fleets, and (3) could be sensitive to navigation costs. These features allows the fishing effort to be distributed in a more realistic way by predicting the behaviour of the fishing fleets.

Prior to analysing the scenarios of impact, a technical feature had to be developed. As the food-web functioning (flow values) of the different cells of the grid was characterised, we needed an algorithm to calculate ENA indices within each cell of the grid and for each year of the simulation. In collaboration with the EwE development team (Joe Buszowski and Jeroen Steenbeek), a new plug-in (Araignous et al. in prep) has been developed which allows the results from the Ecospace model to be exported as a set of files (one for each cell and for each year of the simulation) in the SCOR format adopted by the Scientific Committee for Oceanic Research (UNESCO) Working Group73. Then, an R script was built to allow the use, on each file, of the package enaR (Borrett and Lau 2014). This allows the realizations of maps for each simulation, each time step, and each ENA index. As an example, Fig. 3 presents the map, in the present situation, of the recycling, quantified by the Finn Cycling Index (Finn 1980).

For the moment, only the model representing the present state of the ecosystem, depicting the ecosystem before the offshore wind farm construction, has been established. The scenarios for future pressures are currently being implemented. They will represent the reef and reserve effects, following the same scenarios as in Raoux et al. (2017, in press). The climate change effect will be applied spatially, according to the results obtain using the ensemble modelling of various niche models and

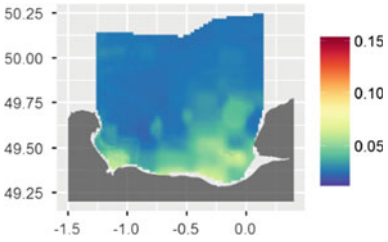

Fig. 3 Map of the ENA index called the Finn Cycling Index (0.15 means that 15% of the organic matter is flowing within cyclic pathways in the food wed of the cell). It is based on a calculation derived from the outputs of the Ecospace model of the extended Bay of Seine, in the present situation (before the Offshore Wind Farm building). The scale of colours is given on the right. Latitudes and longitudes are given on the map

according to the different IPCC scenarios (Ben Rais Lasram et al. in prep; Bourdaud et al. in prep). These scenarios will be completed by scenarios of fisheries spatial management (Champagnat et al. in prep).

4 Social-ecological System Modelling

Social-ecological system models have been suggested as a tool to understand human-nature relationships (Österblom et al. 2013). These models have commonly been used in a context were the system was mainly composed of human actors (Tiller et al. 2013; Tiller and Richards 2016), or was mainly composed of environmental variables (Fulton 2010; Lassalle et al. 2014). In the ANR TROPHIK project, our aim is to acknowledge the importance of both categories of actors in a social-ecological system by including a similar number of social and ecological variables. This is done in order to give a balanced description of the potential cascading effects in the system (Figs. 4 and 5). Behind this background, the social-ecological system affected by the Courseulles-sur-mer's wind farm construction was modelled using a qualitative modelling technique. The technique involves the use of oriented di-graphs (as in Fig. 5), where networks of variables and their positive and negative interactions are built, without attempting to quantify the strength of these interactions. Based on the analyses of feedback cycles within these networks, press (constant) perturbation analyses can be done using Bayesian Belief Networks (BBN). BBN are used to derive predictions of the probability of change for all actors or variables in the network, given one or several perturbations in the system. If one actor or pressure is increased, the BBN gives the probability for all other variables to an increase, decrease or if it will stay unchanged.

Cumulative impacts can be assessed, and the tests can then be used to address questions related to indirect effects of social-ecological impacts, and potential cascading effects through the ecosystem represented by its food web. A first approach

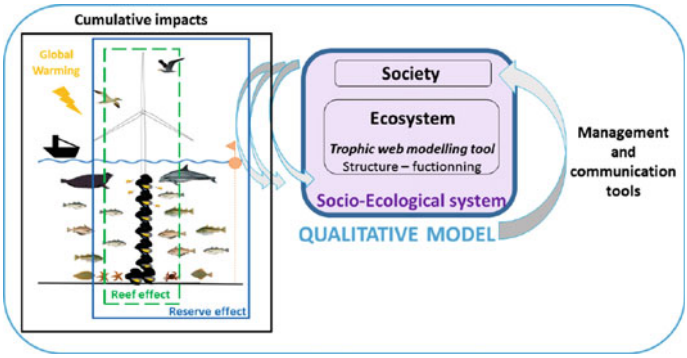

Fig. 4 Conceptual schema representing the relative position of the quantitative (on the left) and qualitative models (also called signed di-graph, on the right) used in the project to study the socio-ecological system responses to cumulative impacts (Raoux et al. 2018)

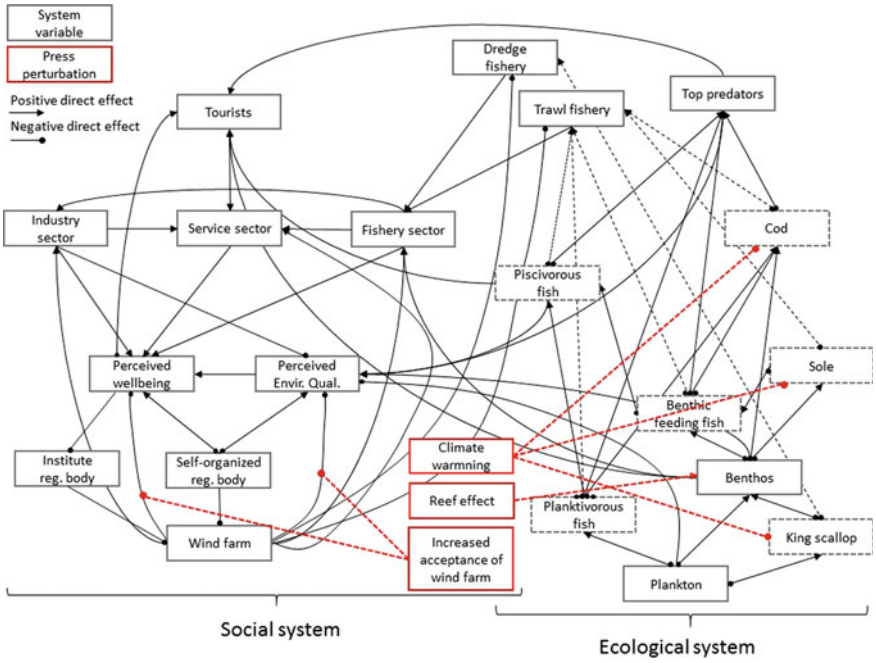

Fig. 5 Social-ecological system of the Courseulles-sur-mer offshore wind farm project, modelled using signed digraph within the ANR TROPHIK Project. Links ending in an arrow signal a positive direct effect while those ending in a circle indicate a negative direct effect (more details in Haraldsson et al. submitted)

was based on the Courseulles-sur-mer Ecopath model previously described and analysed under the cumulative impacts of fisheries, climate change, and the offshore wind farm (Raoux et al. 2018), which has been extended to include important social actors in the system (Fig. 5, Haraldsson et al. submitted). This type of combined models represents a promising tool to enlighten the direct or indirect effects on local population or actors and help overcome residual environmental concerns, social conflicts and potentially increase acceptance.

5 Conclusion

The project aimed to study potential impacts of an offshore wind farm, on the ecosystem, at both small (Courseulles-sur-mer) and larger (extended Bay of Seine) scales, in order to emphasize all direct and indirect impacts. The use of different modelling methods at different dimensions provided a holistic approach necessary for a global understanding of marine renewable energies (MRE) effects in a multiple pressures context and simultaneously considering the social aspects. Here, we propose a set of combined methods for a complementary understanding of the socio-ecological aspects of MRE effects and of cumulated impacts. The modelling approaches used include EwE, LIM-MCMC, ENA indices, and qualitative modelling by oriented digraphs of the socio-ecological network associated with BBN analysis.

Our modelling analyses showed that cumulative perturbations on the ecosystems studied can possibly lead to the re-organization of its biological components and the overall functioning of the system, thus, modifying in the future the system's response, resilience and stability as well as the services they provide. The ENA indices appeared essential and complementary numerical tools to describe these changes in emergent properties.

As no wind farms exist along the metropolitan French coast our global approach is based on several potential scenarios taking into account the existing results acquired on other European wind farm especially in the North Sea. Our modelling approach can be applied in other offshore wind farm implementations in European waters. It underlined also the need to have detailed biomass data on a maximum of biological compartment useful to the modelling of food webs. To do that, it is necessary to persuade the wind farm developers to ensure a long-term monitoring of the impact of new infrastructures on the coastal ecosystem taking into account a maximum of biological compartments, from microbial items to top-predators and from benthos to pelagos.

Acknowledgements This work is supported by France Energies Marines (www.france-energies-marines.org). It is part of the project TROPHIK co-funded by the ANR (Agence Nationale de la Recherche), under the program "Investissements d'avenir" (ANR/FEM EMR-ITE 2015 number ANR-10-IEED-0006-12). It is also funded, in support of A Raoux's Ph.D., by the Normandie Region and by the company "Eoliennes Offshore du Calvados" (EOC). We also acknowledge, the Centre Régional Informatique et d'Applications Numériques de Normandie, CRIANN for running

the ENAtool and LIM-MCMC calculations and especially Béatrice Charton and Benoist Gaston for their help.

References

Araignous, E., Buszowski, J., Steenbeek, J., Bourdaud, P., Lasram, F., & Niquil, N. (in prep). Preliminary title: Spatialization of ecological network analysis indicators: The enaR software plug-in for Ecopath with Ecosim models. Planned submission to *Environmental modelling and software.*

Araújo, M. B., & New, M. (2007). Ensemble forecasting of species distributions. *Trends in Ecology and Evolution, 22*(1), 42–47.

Ben Rais Lasram, F., Hattab, T., Noguès, Q., Beaugrand, G., Dauvin, J.C., Halouani, G., et al. (in prep). A ready-to-use R script for projecting future patterns of marine species distributions at the local scale. Submitted to Ecological Informatics.

Borrett, S. R., & Lau, M. K. (2014). enaR: An R package for ecosystem network analysis. *Methods in Ecology and Evolution, 5*(11), 1206–1213.

Bourdaud, P., Araignous, E., Champagnat, J., Ben Rais Lasram, F., Halouani, G., Hattab, T., et al. (in prep). Preliminary title: Impact of climate change on the Bay of Seine ecosystem: Approach by forcing of niche models on a spatio-temporal trophic model. Planned submission *ICES Journal of Marine Science*.

Chaalali, A., Saint-Béat, B., Lassalle, G., Le Loc'h, F., Tecchio, S., Safi, G., et al. (2015). A new modeling approach to define marine ecosystems food-web status with uncertainty assessment. *Progress in Oceanography, 135,* 37–47.

Champagnat, J., Araignous, E., Bourdaud, P., Ben Rais Lasram, F., Halouani, G., Niquil, N. (in prep). Preliminary title Assessing the sensitivity of ecosystemic indicators to fishing: A trophic modelling of the Bay of Seine. Planned submission to *Ecological Indicators*.

Christensen, V., Walters, C. J., Ahrens, R., Alder, J., Buszowski, J., Christensen, L. B., et al. (2008). Models of the world's large marine ecosystems. GEF/LME global project promoting ecosystem-based approaches to fisheries conservation and large marine ecosystems.

Cury, P., Shannon, L., & Shin, Y. J. (2003). The functioning of marine ecosystems: A fisheries perspective. *Responsible Fisheries in the Marine Ecosystem,* 103–123.

Finn, J. T. (1980). Flow analysis of models of the Hubbard Brook ecosystem. *Ecology, 61*(3), 562–571.

Fulton, E. A. (2010). Approaches to end-to-end ecosystem models. *Journal of Marine Systems, 81*(1–2), 171–183.

Guesnet, V., Lassalle, G., Chaalali, A., Kearney, K., Saint-Béat, B., Karimi, B., et al. (2015). Incorporating food-web parameter uncertainty into Ecopath-derived ecological network indicators. *Ecological Modelling, 313,* 29–40.

Halouani, G., Villanueva, M. C., Raoux, A., Dauvin, J. C, Ben Rais Lasram, F., Foucher, E., et al. (in prep). Preliminary title: A spatial food web model to investigate potential effects of an offshore wind farm. Planned submission to *Journal of Marine Systems*.

Haraldsson, M., Raoux, A., Riera, F., Hay, J., Dambacher, Niquil, N. (submitted). How to model Social-Ecological Systems?—A case study on the effects of a future offshore windfarm on the local society and ecosystem, and whether social compensation matters. Submitted to Marine Policy (under revision).

Hattab, T., Albouy, C., Lasram, F. B. R., Somot, S., Loc'h, L., & Leprieur, F. (2014). Towards a better understanding of potential impacts of climate change on marine species distribution: A multiscale modelling approach. *Global Ecology and Biogeography, 23*(12), 1417–1429.

Henkel, S. K., Suryan, R. M., & Lagerquist, B. A. (2014). Marine renewable energy and environmental interactions: Baseline Assessments of Seabirds, Marine Mammals, Sea Turtles and

Benthic Communities on the Oregon Shelf. In M. A. Shields, A. Payne (Eds.),*Marine renewable energy technology and environmental interactions* (176 pp.). Springer Sciences.

Hosack, G. R., Li, H. W., & Rossignol, P. A. (2009). Sensitivity of system stability to model structure. *Ecological Modelling., 220*, 1054–1062.

Hughes, T. P., Bellwood, D. R., Folke, C., Steneck, R. S., & Wilson, J. (2005). New paradigms for supporting the resilience of marine ecosystems. *Trends in Ecology & Evolution, 20*, 380–386.

Knowlton, N. (1992). Thresholds and multiple stable states in coral reef community dynamics. *American Zoologist, 32*, 674–682.

Knowlton, N. (2004). Multiple stable states and the conservation of marine ecosystems. *Progress in Oceanography, 60*, 387–396.

Kones, J. K., Soetaert, K., van Oevelen, D., & Owino, J. O. (2009). Are network indices robust indicators of food web functioning? A Monte Carlo approach. *Ecological Modelling, 220*, 370–382.

Latham, L. G. (2006). Network flow analysis algorithms. *Ecological Modelling, 192*, 586–600.

Lassalle, G., Lobry, J., Le Loc'h, F., Bustamante, P., Certain, G., Delmas, D., et al. (2011). Lower trophic levels and detrital biomass control the Bay of Biscay continental shelf food web: Implications for ecosystem management. *Progress in Oceanography, 91*(4), 561–575.

Lassalle, G., Chouvelon, T., Bustamante, P., & Niquil, N. (2014). An assessment of the trophic structure of the Bay of Biscay continental shelf food web: Comparing estimates derived from an ecosystem model and isotopic data. *Progress in Oceanography, 120*, 205–215.

Libralato, S., Christensen, V., & Pauly, D. (2006). A method for identifying keystone species in food web models. *Ecological Modelling, 195*, 153–171.

Lindeboom, H. J., Kouwenhoven, H. J., Bergman, M. J. N., Bouma, S., Brasseur, S., Daan, R., et al. (2011). Short term ecological effects of an offshore wind farm in the Dutch coastal zone; A compilation. *Environmental Research Letters, 6,* 1–13.

Niquil, N., Le Loc'h, F., Tecchio, S., Chaalali, A., Vouriot, P., Mialet, B., et al. (2014). Ongoing research on ecosystem health indicators for food webs in the MSFD context. In *Trans-Channel forum Proceedings "Science and Governance of the Channel Marine Ecosystem"* (pp. 14–15), Caen, France.

Noguès, Q. (2018). Analyse de sensibilité du cumul de l'effet récif et de l'effet du changement climatique, sur différents indices ENA: Le cas du parc éolien offshore de Courseulles-sur-Mer. Université de Bordeaux - Master 2, mention Sciences de la Mer, parcours Biologie et écologie marines (45 pp.).

Norling, P., & Kautsky, N. (2008). Patches of the mussel *Mytilus* sp. are islands of high biodiversity in subtidal sediment habitats in the Baltic Sea. *Aquatic Biololy, 4*, 75–87.

Odum, E. P. (1969). The strategy of ecosystem development. *Science,164*, 262–270.

Odum, E. P. (1971). *Fundamentals of ecology* (574 pp.). Philadelphia, USA: W. B. Saunders Co.

Österblom, H., Merrie, A., Metian, M., Boonstra, W. J., Blenckner, T., Watson, J. R., et al. (2013). Modeling social-ecological scenarios in marine systems. *Bioscience, 63,* 735–744.

Pezy, J. P., Raoux, A., Niquil, N., Dauvin, J. C. (in press). Offshore renewable energy development in France with an emphasis on the eastern part of the English Channel: State at the end of 2017. In *Proceedings of the Conference on Wind Energy and Wildlife Impacts*, Estoril, September 2017.

Raoux, A. (2017). Approche écosystémique des Energies Marines Renouvelables: étude de l'impact sur le réseau trophique de la construction du parc éolien au large de Courseulles-sur-mer et du cumul d'impacts. Thèse de Doctorat, Université de Caen Normandie, France (293 pp.).

Raoux, A., Tecchio, S., Pezy, J. P., Degraer, S., Wilhelmsson, D., Cachera, M., et al. (2017). Benthic and fish aggregation inside an offshore wind farm: Which effects on the trophic web functioning? *Ecological Indicators,72,* 33–46.

Raoux, A., Dambacher, J. M., Pezy, J. P., Mazé, C., Dauvin, J. C., & Niquil, N. (2018). Assessing cumulative socio-ecological impacts of offshore wind farm development in the Bay of Seine (English Channel). *Marine Policy, 89*, 11–20.

Raoux, A., Lassalle, G., Pezy, J. P., Tecchio, S., Safi, G., Ernande, B., et al. (2019). Measuring sensitivity of two Ospar indicators for a coastal food web model under Offshore Wind Farm construction. *Ecological Indicators, 96*, 728–738.

Tiller, R., Gentry, R., & Richards, R. (2013). Stakeholder driven future scenarios as an element of interdisciplinary management tools; The case of future offshore aquaculture development and the potential effects on fishermen in Santa Barbara, California. *Ocean & Coastal Management, 73*, 127–135.

Tiller, R., & Richards, R. (2016). Once bitten, twice shy: Aquaculture, stakeholder adaptive capacity, and policy implications of iterative stakeholder workshops; the case of Frøya, Norway. *Ocean & Coastal Management, 118*, 98–109.

Ulanowicz, R. E. (1986). *Growth and development: Ecosystems phenomenology* (166 pp.). New York: Springer.

Walters, C. J., Christensen, V., & Pauly, D. (1997). Structuring dynamic models of exploited ecosystems from trophic mass-balance assessments. *Reviews in Fish Biology and Fisheries, 7*, 139–172.

Velocity Profile Variabilities at a Tidal-Stream Energy Site Facing Open Sea (Raz Blanchard, France)

Lucille Furgerot, Pascal Bailly du Bois, Mehdi Morillon, Yann Méar and Emmanuel Poizot

Abstract The Alderney Race is one of the most powerful current in Europe (up to 5 m/s during spring tide). Considering these important currents, this site has been identified to extract energy from the tide with installation of tidal turbines. However, this area is facing open sea to the west and thus strong wind can generate significant wave height interplaying with the tidal currents, which is a critical point for the dimensioning of the tidal turbines. This chapter deals with in situ measurements of waves and currents in Alderney Race.

Keywords Wave-current interactions · Alderney race · ADCP measurements · Velocity vertical profiles

1 Introduction

The Alderney Race (French Raz Blanchard) current occurring between Normandy (France) and the Channel Sea Islands (UK) is one of the most powerful current in Europe (5 $m.s^{-1}$ during spring tide). This current, give opportunity to extract energy from the tide with installation of tidal turbines (Bahaj and Myers, 2004). However, as the Alderney Race area is facing open sea to the west, strong wind can generate significant wave height (*Hs*) interplaying with the tidal currents. The HYD2M project aims to improve the tidal energy estimation by combining an original dataset of in-situ measurements with the development of 3D numerical model including wind and waves effects. We have carried out 5 campaigns in the Alderney Race with water level, current, waves and wind measurements (from April 2017 to July 2018). The high temporal resolution of our dataset (up to 2 Hz, for most of the campaigns

L. Furgerot (✉)
LUSAC Laboratory, University of Caen Normandy, Cherbourg en Cotentin, France
e-mail: lucille.furgerot@hotmail.fr

P. Bailly du Bois · M. Morillon
IRSN-LRC, Cherbourg en Cotentin, France

Y. Méar · E. Poizot
CNAM Intechmer, Cherbourg en Cotentin, France

K. D. Nguyen et al. (eds.), *Estuaries and Coastal Zones in Times of Global Change*, Springer Water,
https://doi.org/10.1007/978-981-15-2081-5_10

and devices) allows the study of the interactions between waves and tidal currents. Since measurements are still in progress, this chapter focuses on preliminary results, including (i) a description of meteorological and dominant waves conditions, (ii) a description of the tidal currents dynamic, (iii) a study of averaged vertical profiles variability, and (iv) a preliminary discussion concerning the influence of the waves on the vertical profiles, mainly dominated by tidal currents.

2 Study Site: Alderney Race

The Alderney Race tidal current is located in the northern part of the Normandy-Brittany Gulf (France) between the Alderney Island and the La Hague Cape (Fig. 1).

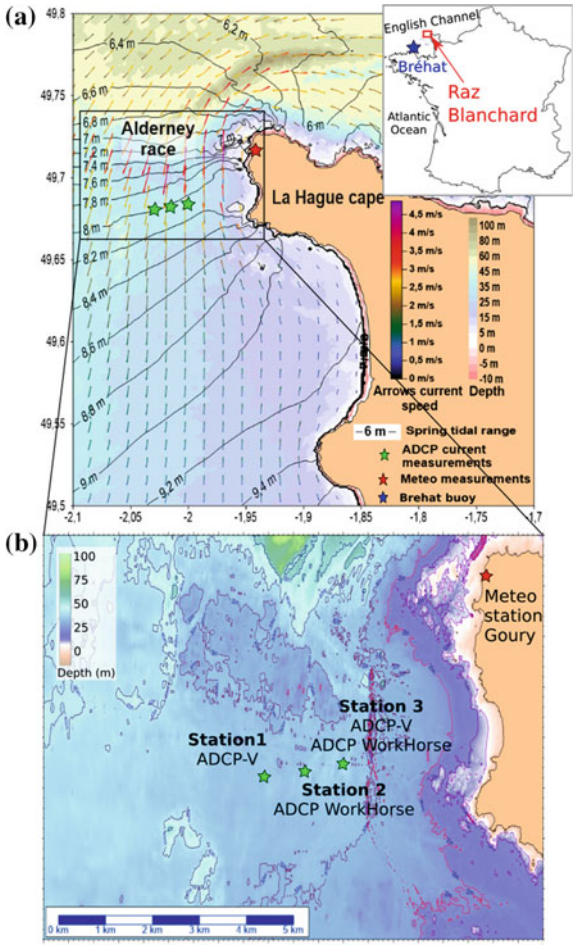

Fig. 1 **a** Location map with simulated tidal amplitude (spring tide), direction of maximum currents, as well as current-measurement locations; **b** Zoom on the measurement area showing the location of 3 ADCP stations and the meteorological station

Currents are related to the tidal wave coming from the Atlantic Ocean. The tidal wave amplitude increases when it crosses the continental shelf (500 km westward) and subsequently when this wave is reflected by the Cotentin Peninsula, acting as a barrier. This creates a significant tidal range (more than 14 m near the Mont Saint Michel bay) in the Normandy-Brittany Gulf causing strong tidal currents. From North to South of the La Hague Cape, the maximum tidal range varies from 6 m to 11 m (5 km apart). This leads to a significant slope of the water (black contours—Fig. 1) that generates the strong currents. In addition, the shallow depth (<50 m, colors Fig. 1) and the presence of the Alderney island creates a funnel effect, increasing the flow (arrows on Fig. 1). Previous studies mainly focus on numerical models (Bailly du Bois and Dumas 2005; Neill et al. 2011; Coles et al. 2017), validated by local and punctual measurements using in situ current meters. They have identified an area with maximum currents velocities (Bailly du Bois et al. 2012), located between the La Hague Cape and the Alderney Island (red arrows Fig. 1). In this area, the current magnitude (U_{mag}) can reach 5 m.s^{-1} during the high spring tides. The tide is commonly described as an asymmetric tide, dominated by a NNE-directed flow current, estimated to be 3% stronger than the SSW-directed ebb current (Thiébot et al. 2015). The current inversion during the transition between the ebb and the flood is relatively fast, around 15 min. Because of strong in situ technical constrains for instrumentation (strong currents, short time window with relatively low currents during the inversion, etc) only few studies have been carried out over long periods.

3 Materials and Methods

Since the 21th April, 2017, we have carried out 5 campaigns on the Thalia and Côtes de la Manche research vessel (CNRS-INSU, France) that allowed the measurement of water level and currents along vertical profiles, at three different stations (Fig. 1). These stations are located along an E-W profile and are named respectively stations 1, 2 and 3 (from West to East). They are located south of the strongest current zone for technical constraints, particularly the difficulty to find plane areas (rocks with one meter mean size in the north). We deployed on the bottom (made of boulders and blocks) one structure for each station, where ADCP (Acoustic Doppler Current Profiler) have been fixed. These structures have been designed specifically to resist to strong currents and to protect the sensors from possible impacts of pebbles or other particles, moving close to the bottom (bottom mainly consists of sand and pebble (Foveau et al. 2017 confirmed by photos). The maximum immersion depth was around 40 m. Technical problems occurred related to the recovery of the structures with an automatized remote buoy. Despite the technical issues, a huge amount of data has been recorded (up to 240 days of data corresponding to ~20 million entries in the database). We have also collected meteorological (Goury semaphore, Météo

Table 1 ADCP configurations for the three measurements station (stations located in Fig. 1)

	April	*June*	*September*	*October*	*February*
Station 1	ADCP-V 2Hz (burst of 20 min every each hour)				
Station 2	ADCP Workhorse Average data of 1Hz over 5min		ADCP Workhorse Continuous 1Hz measurements		ADCP Workhorse 1Hz (burst of 2min every each 5min)
Station 3	No data		ADCP Workhorse Continuous 1Hz measurements		ADCP-V Continuous 2Hz measurements

France) and wave parameters (French buoy network Candhis) in open access sources in order to complete our database.

Tidal Currents and Elevation

Pressure sensors from the ADCP allow the measurement of the surface variations above each offshore structure.

Measurements of currents along vertical profiles using ADCP have been carried out simultaneously for the three structures in the three locations (Fig. 1). During a typical campaign at sea, we have recovered the structures, collected the data and re-immersed the structures. During each data recovery, we checked if the ADCPs were still operating. The measurement cells size is 1 m high and the first cell is located from 1.5 to 2 m above the sea floor.

We used two different types of ADCP models from RDI®: (i) an ADCP-V 500 kHz and (ii) an ADCP Workhorse 600 kHz. The model of ADCP deployed in each station and their acquisition frequency varies through time because of one accidental lost and adjustment of the acquisition frequency according to the batteries and memory capacity (Table 1).

Because of the lost and other problems in station 3 during the first period, in this chapter, we present only the data from stations 1 and 2.

Each ADCP measures the current velocity along three axes, directed north-south (V, positive values northward), east-west (U, positive values eastward) and vertically (W, positive values upward) for each point, along vertical profiles. The two main velocity components (U and V) allow the calculation of the velocity vectors (U_{mag}). The direction ranges from 0 to 360°, with 0° northward. The data were averaged over a period of 5 min ($\overline{U_{mag}}$) to allow easy viewing and to study the velocity evolution during tidal cycles (Fig. 3). High-frequency raw data (1 Hz and 2 Hz) are presented at the end of this chapter (Fig. 5). After a general analysis, the vertical velocity profiles have been compared for eight cases of U_{mag} averaged on the water column to study the variability of profiles (Lewis et al. 2017). This analysis of profile shape has been made by using the equation:

$$V(z) = V_0\left(\frac{z}{d}\right)^{1/\alpha} \tag{1}$$

which allows to analyzed the variability of the α coefficient. V_0 corresponds to the surface velocity, d represent the depth of the water column and z the distance from the bottom for each point. The use of this method could be discussed, as the higher measuring cell of the ADCPs is located at 3 m below the surface. The α coefficient have been tested for a range of values from 1 to 15, for each intervals of 0,1 and the best coefficient have been estimated from linear regression fit of Log Log representation of velocity. This analysis takes into account the velocity variations in the boundary layer for important depths. According to Thiébault and Sentchev (2017) and Soulsby (1977), the boundary layer may extend over tens of meters in high hydrodynamic conditions.

Waves Data

For the wave analyses, we have collected open source data from the buoy located 20 km North of Bréhat (Candhis network). The ADCP-V (initially station 1 and 3 and then only station 1—Fig. 1), allowed the calculation of the main waves parameters, using different methods: *Hs* (significant height), *Ts* (significant period) and *Dp* (main peak direction). We chose the orbital velocities method. According Wiberg and Sherwood (2008), this method is assumed to be reliable, especially when the free surface spectral analyses cannot be done, which is the case in the present chapter, due to pressure sensor problems.

Wind Intensity and Direction

The wind data used in this study are measured by the Météo-France at semaphore in Goury (Fig. 1). Each data corresponds to an average over a period of 6 min, at an altitude of 10 m. The wind direction has been measured with a resolution of 10°.

4 Preliminary Results

General Meteorological and Waves Climates During Campaigns

One main wave regime has been identified from both Bréhat and our data set (Fig. 2a), with waves coming from the West (N280° to N290°).

A secondary wave regime has been found in the Bréhat data (Fig. 2a), from the north and on our data (Fig. 2a) coming from the northeast but is negligible compared to the main regime. The dominant wind comes from the southwest (from N180° to N270°) and less frequently from the east (Fig. 2a). The waves from the principal regime come from the Atlantic Ocean where the fetch length is very large. In the other directions, the fetch length is not enough important to generate measurable significant swell waves. The directions show a more important dispersion from the southwest to northwest compared with Bréhat. This could be due to wave refraction on the islands or due to shallower depth. During the acquisition campaigns, five neap/spring tide cycles have been recorded. The tidal range fluctuated between 1.8 m and 7.8 m

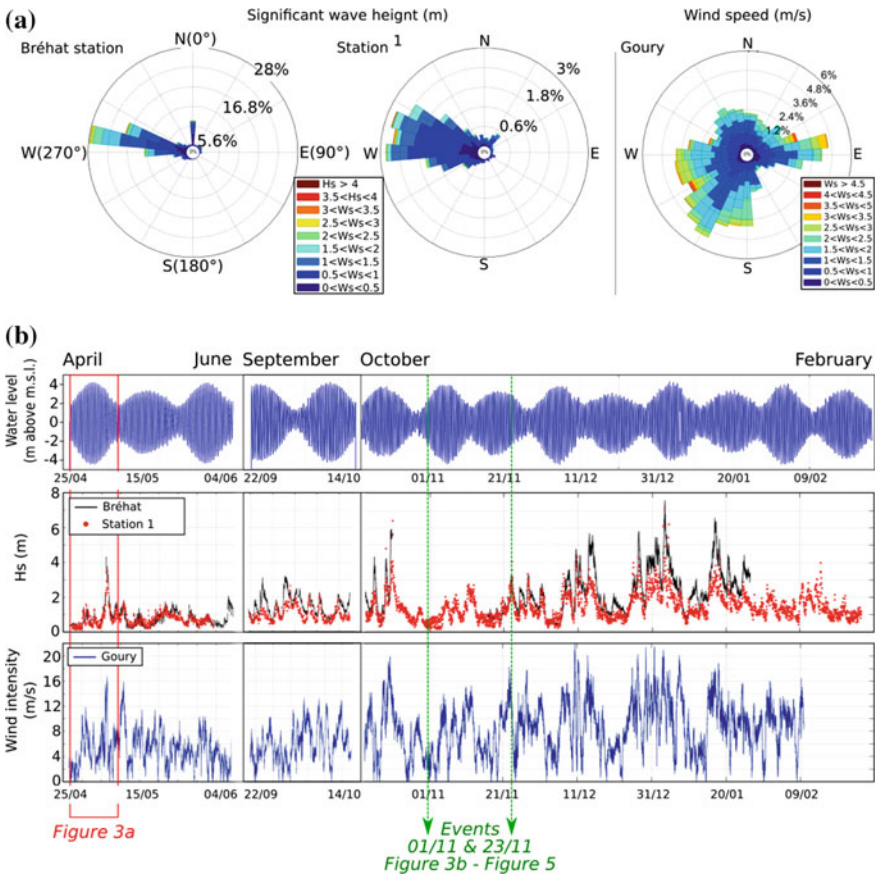

Fig. 2 Waves and wind climates during the field works: **a** waves origin according to the significant height (*Hs*) for the Bréhat station (~110 km Southwest of Alderney Race) and for the station 1 (location Fig. 1) and Wind origin from the Météo-France measurements in Goury semaphore; **b** times series of the conditions evolution during the field work: top, water level evolution (m.s.l.: mean sea level); middle, significant wave height (Hs, Bréhat station and ADCP-V data; station 1) and bottom, wind intensity in Goury

(Fig. 2b), the peak wind reached 23 m.s^{-1} and the maximum *Hs* was 4.3 m in Bréhat and 3.5 m in our study area (Fig. 2b).

Current Evolution During a Typical Tidal Cycle

The evolution of current velocities in the Alderney Race area follows a progressive tidal wave regime. The maximum velocities are recorded during the high and low tide and not during the flood and ebb (Fig. 3a). One typical tidal cycle is showed in Fig. 3b.

A first current velocity peak is registered during the high tide with an averaged direction toward the NNE (~N20°) for the three stations Subsequently, the velocity

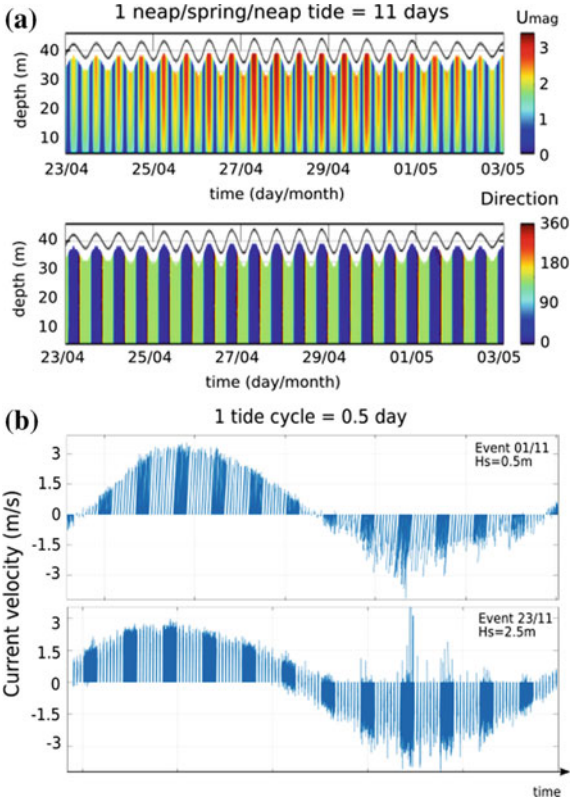

Fig. 3 **a** Spatial-temporal diagrams of the Umag (top) and direction (bottom) during the first neap/spring tide (April/May 2017); **b** Fishbone diagram of measured current vectors at station 2 during two events: 01 and 23 November 2017

decreases during the first half of the ebb until it reaches a value close to 0.1 m.s^{-1} (Fig. 3b). Current velocities increase again progressively in the opposite direction, toward the SSW (N190°) until the low tide, when a second velocity peak is recorded. Then the current velocities decrease until the half flood and a new tidal cycle start. The current inversions in the tide cycle is characterized by quasi-instantaneous clockwise current rotation. The maximal mean U_{mag} recorded are correlated with the tidal range (Fig. 3a). In the area, the highest measured of mean U_{mag} over the water column reaches 3 m.s^{-1} during the high tide with the higher tidal range of 7.8 m (data averaged for 5 min). In neap tide conditions (tidal range < 1.8 m), the velocities during the high tide are relatively lower, around 1.8 m.s^{-1}. As shown in Fig. 1, the measurement site is located to the south of the maximal current zone of Alderney Race. However, during the acquisition period, and for all winds, waves and tides conditions, U_{mag} during high and low tide is always higher than 1 m.s^{-1}.

Vertical Profile Variations During Different Tide Phases

Firstly, the α coefficient have been calculated, using five minutes averaged data windows. However, when U_{mag} is lower than 0.5 m.s^{-1} for all the water column, the associated profiles are relatively linear and this induces high values for the α

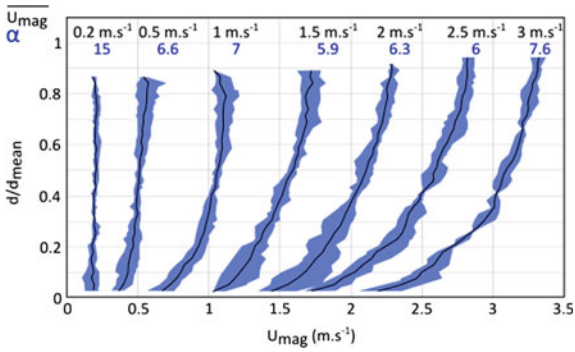

Fig. 4 Graph shows seven vertical profiles corresponding to mean velocity (from 0.2 to 3 $m.s^{-1}$). The blue values correspond to the estimated alpha

coefficient (for 0.2 $m.s^{-1}$ the α coefficient is up to 15, Fig. 4). Therefore, we removed all the profiles when U_{mag} is lower than 0.5 $m.s^{-1}$ for the calculation of the average of the α coefficient. This gives an average value equals to 6.6 ranging from 4 to 12, as in the study of Gooch et al. (2009).

Secondly, we have studied the relationships between the shape of the vertical profiles and the averaged velocity in the water column. We chose eight different cases for seven different averaged velocities (0.2; 0.5; 1; 1.5; 2; 2.5 and 3 $m.s^{-1}$, Fig. 4). The selection criteria in Fig. 4 where the U_{mag} averaged equal to the defined velocity at more and less 3% (blue envelop). Then, all the profiles have been merged and the α coefficient have been calculated (Fig. 4). The graph in Fig. 4 shows that for a given averaged velocity, all the profiles display a relatively similar shape, but the variability of α is too important to infer a correlation. In addition, there is no direct apparent relationship between the α coefficient and the increase of U_{mag} (Fig. 4).

Thirdly, we calculated the average for the α coefficient only in windows of 15 min during the different tide phases and specially around the velocity peak during high and low tide. This gives a value of 7.4 for the coefficient during high tides and value of 8.3 for the low tides. This difference between the α values indicates a more bended profile and a more developed boundary layer for high tides compared with low tides. Such tendency is corroborated by the analyses of the velocity gradients between the sea bed and the surface, showing stronger gradient during high tide and more generally, when the velocity increases.

Preliminary Observations on the Waves/Current Interaction

Two cases are presented here: the 01st and 23rd November 2017 cases showing a tidal range of 5.5 m and 5 m (see Table 2 and Fig. 2b). These events have been chosen because their tidal ranges are similar. They occurred close to each other in time and the difference between their *Hs* is significant. Other interesting events have been identified but the associated data are still in processing.

During the first case, the significant wave height reaches only 0.5 m, while *Hs* reaches 2.5 m during the second event (Table 2). For these two events, waves are coming from the northwest (N290°). For each case, we have selected two periods of 5 min showing two different current velocity situations, with averaged velocities

Table 2 Characterization of events described and presented Fig. 5

Events (2017)	Tidal range (m)	*Hs* (m)	Waves origin (°)	Current velocity $\overline{U_{mag}}$ (m.s^{-1})	Tide phase (current direction)
01/11	5.5	0.5	N290	0.36	Flood (NNE)
				2.25	Flood (NNE)
23/11	5	2.5	N290	0.36	Inversion (SSE)
				2.25	Flood (NNE)

$\overline{U_{mag}}$ of 0.36 m.s^{-1} and 2.25 m.s^{-1}. Three chosen events correspond to high tide phases with a main current direction toward the NNE (between N20° and N42° in average) and one event during the current inversion with a mean current direction toward the SE (case 23/11 with $\overline{U_{mag}}$ of 0.36 m.s^{-1}). This selection of four events allows the comparison of different wave heights (0.5 m and 2.5 m) for the same current situation (for 0.36 m.s^{-1} or for 2.25 m.s^{-1}) (Table 2). Figure 5 summarizes the U_{mag} and direction evolutions using spatial-temporal diagrams (during 5 min) for the four selected events. The velocity distribution using histograms at four selected depth (33 m, 23 m, 13 m and 3 m above the sea floor) is also represented for each event, the blue and red histograms correspond to low (0.5 m) and high (2.5 m) *Hs*, respectively.

For the low current velocity events ($\overline{U_{mag}} = 0.36$ m.s^{-1}), the mean velocity profiles at 0.2 and 0.5 m.s^{-1} (Fig. 4) shows that $\overline{U_{mag}}$ only slightly varies in the water column. However, in details, the wave effect is clearly highlighted by U_{mag} variations in the almost whole water column (Fig. 5a) for the event with high *Hs* (2.5 m). In this case, U_{mag} vary from 0.01 to 1.5 m.s^{-1} within a few seconds in the upper part of water column. The increase of U_{mag} (> 1 m.s^{-1}) in this part is related to the wave propagation. The direction variations (Fig. 5a) are very significant for this case with an evolution from N50° (NE), followed by a current directed to N180° (S) up to N300° (NW) between profiles separated by few seconds. These oscillations reach the bottom. The mean flow direction is toward the SSE but some local and brutal changes related with the waves occur. A period of 6–6.5 s can be calculated and the structures related with the waves are well defined. In these environmental conditions, waves have an important impact on the current. For the event with small *Hs* (0.5 m), the U_{mag} variation is lower with recorded variations of about 0.5 m.s^{-1} in a few seconds. However, some oscillation structures are still visible in the first meters below the surface, meaning that the impact of waves in the water column for *Hs* of 0.5 m is not negligible when the mean tidal current is low (0.2 m.s^{-1}) in the upper part of water column. These observations are confirmed by the distribution of current velocity on the histogram (Fig. 5a). The histogram distribution near surface 33 m above the bottom is wider than at 23, 13 and 3 m above the bottom (blue curve for *Hs* = 0.5 m). For the event with high *Hs* (red curve) the distribution near surface is very spread out compared with low *Hs* (from 0 to 2 m.s^{-1}). This spreading decreases with

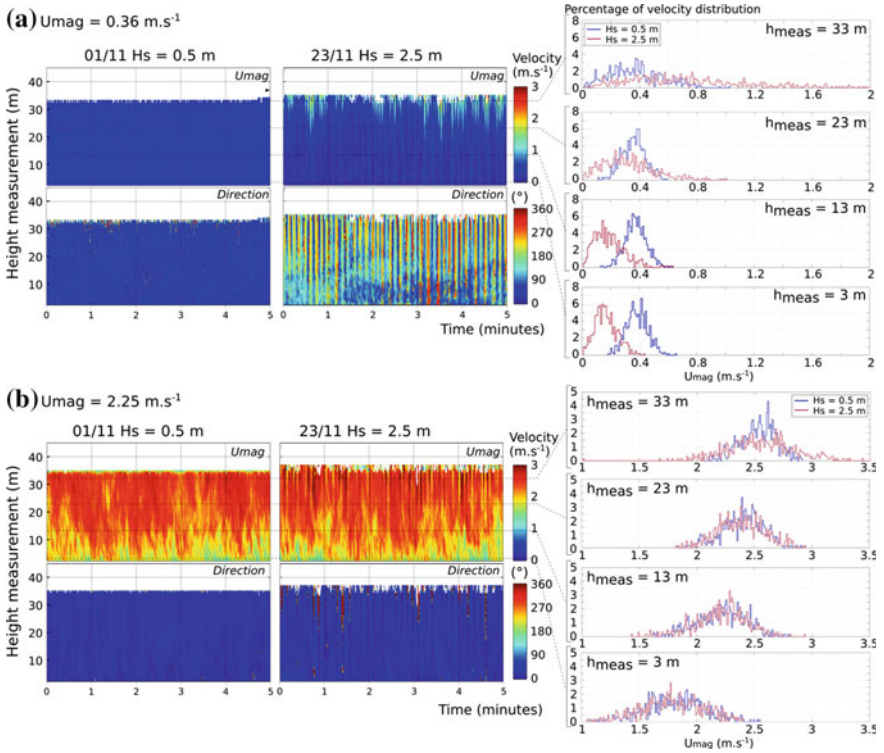

Fig. 5 Data for the four studied cases: two events with different current velocity situations are selected during 5 min: **a** $\overline{U_{mag}} = 0.36$ and **b** 2.25 m.s^{-1}. For each case, two moderates waves climate ($Hs = 0.5$ m and $Hs = 2.5$ m) are presented. The spatio-temporal diagrams on the top of Fig. 5a, b are the U_{mag} and the direction on the sea bottom. On the right, histograms with velocity distribution at 33, 23, 13 and 3 m above the sea bed (h_{meas})

depth and the distribution becomes more focused on the mean velocity. This mean velocity evolves in the water column from 0.3 m.s^{-1} at 23 m to 0.15 m.s^{-1} near the bottom, while it is expected to be centered on 0.36 m.s^{-1}. It may be explained by the fact that the mean velocity calculated at 0.36 m.s^{-1} take account the high velocity variation for waves propagation in the upper part of water column (Groeneweg and Klopman 1998).

For the high current velocities events (Fig. 5b $\overline{U_{mag}} = 2.25$ m.s^{-1}), the structures related with the waves propagation are relatively well defined when Hs is high (2.5 m case) in the upper part of water column and are absent when Hs is low (0.5 m case). For the low Hs (0.5 m), the current direction displays any dispersion compared with the events with low current velocities (0.36 m.s^{-1} events), with only a direction variation of 15° (N15°–N30°, toward the NNE). When Hs is high, U_{mag} vary from 0 to 1 m.s^{-1} in few seconds in the upper part of water column. These variations are lower than the low current case. The period of the oscillations has been estimated at 6 s. The direction slightly varies between NNW (N350°) and NNE (N40°). In both

cases with low (0.5 m) and high (2.5 m) *Hs*, the low direction variation means that the current directions mainly reflect the tidal influence and not the wave effects, as the tidal currents during the high tide are focused toward the NNE. In addition, the histogram distributions are centered on mean velocity values that decrease with depth, following a power law, as shown in Fig. 4 in both cases. The histogram distribution of the upper measuring ADCP cell, near the surface is relatively wider (red curve) when *Hs* is high compared with the case of low *Hs*. This shows that waves with a height of 2.5 m are able to affected the upper water column, even when the tidal current are high (2.25 $m.s^{-1}$).

5 Conclusion and Perspectives

Three ADCP have been deployed in the Alderney Race area during thirteen neap/spring tide cycles. These data, which cover a long-time period allow the study of the current evolution at 1 or 2 Hz for several cycles. This chapter describes preliminary results concerning:

(i) An estimation of the α coefficient of 6.6 for all periods of measurement with a difference between the high and low tide phases. This value is close to the α coefficient recommended in the literature (Frost et al. 2014).
(ii) An important variability for the average velocity along vertical profiles (variations of U_{mag} from 0.7 to 2.1 $m.s^{-1}$ in few seconds) that may be attributed to the tidal range, to the stage of tide, to the roughness of the sea floor, to the wind or the waves.
(iii) A preliminary description of four events showing two different types of structures: an oscillation of the water particles linked with the waves in the upper part of the water column (but sometimes reaching the bottom) and turbulent structures probably linked with the roughness of the sea floor.

In a future work, we will quantify the influence of the waves on the tidal currents and the influence of the tidal currents on the orbital velocity of waves mainly in the cases of high currents and high waves. The important database collected allows us to study these processes for many events that will be presented in the future. In addition, the influence of the wind intensity and direction on the current characteristics will be also developed in future studies.

Acknowledgements Authors are supported by the HYD2M project (ANR-10-IEED-0006-07) funded by the program called "Investissements d'avenir" for the building of France Energies Marines. Authors acknowledge the crews of the ocean research vessels the CNRS vessels "Thalia" and "Côtes de la Manche".

References

Bahaj, A. S., & Myers, L. E. (2004). Analytical estimates of the energy yield potential from the Alderney Race (Channel Islands), using marine current energy converters. *Renewable Energy, 29,* 1931–1945.

Bailly du Bois, P., & Dumas, F. (2005). Fast hydrodynamic model for medium- and long-term dispersion in seawater in the English Channel and southern North Sea, qualitative and quantitative validation by radionuclide tracers. *Ocean Modelling, 9,* 169–210.

Bailly du Bois, P., Dumas, F., Solier, L., & Voiseux, C. (2012). In-situ database toolbox for short-term dispersion model validation in macro-tidal seas, application for 2D-model. *Continental Shelf Research, 36,* 63–82.

Coles, D. S., Blunden, L. S., & Bahaj, A. S. (2017). Assessment of the energy extraction potential at tidal sites around the Channel Islands. *Energy, 124,* 171–186.

Foveau, A., Haquin, S., & Dauvin, J. (2017). Using underwater imagery as a complementary tool for benthos sampling in an area with high-energy hydrodynamic conditions. *Journal of Marine Biology Oceanography, 6,* 1–7.

Frost, C., Evans, P. S., Morris, C. E., Mason-Jones, A., O'Doherty, T., & O'Doherty, D. (2014). The effect of axial flow misalignment on tidal turbine performance. In *Proceedings of 1st International Conference on Renewable Energies Offshore*.

Gooch, S., Thomson, J., Polagye, B., & Meggitt, D. (2009). Site characterization for tidal power. In *OCEANS 2009, MTS/IEEE Biloxi-Marine Technology for Our Future: Global and Local Challenges*.

Groeneweg, J., & Klopman, G. (1998). Changes of the mean velocity profiles in the combined wave—current motion described in a GLM formulation. *Journal of Fluid Mechanics, 370,* 271–296.

Lewis, M., Neill, S., Robins, P., Hashemi, M., & Ward, S. (2017). Characteristics of the velocity profile at tidal-stream energy sites. *Renewable Energy, 114,* 258–272.

Neill, S. P., Jordan, J. R., & Couch, S. J. (2011). *Impact of tidal stream turbines on sand bank dynamics* (pp. 2238–2245). Linköping, Sweden: World Renewable Energy Congress.

Soulsby, R. L. (1977). Similarity scaling of turbulence spectra in marine and atmospheric boundary layers. *Journal of Physical Oceanography, 7*(6), 934–937.

Thièbault, M., & Sentchev, A. (2017). Asymmetry of tidal currents off W. Brittany coast and assessment of tidal energy resource around Ushant Island. *Renewable Energy, 105,* 735–747.

Thiébot, J., Bailly du Bois, P., & Guillou, S. (2015). Numerical modeling of the effect of tidal stream turbines on the hydrodynamics and the sediment transport—Application to the Alderney Race (Raz Blanchard), France. *Renewable Energy, 75,* 356–365.

Wiberg, P. L., & Sherwood, C. R. (2008). Calculating wave-generated bottom orbital velocities from surface wave parameters. *Computers & Geosciences, 34*(10), 1243–1262.

Navier-Stokes Modelling of Fluid Flow and Related Sediment Transport in the Near Field of an Oscillating Water Column Wave Energy Converter

Valérie Rameliarison, Dominique Astruc and Georges Chapalain

Abstract The fluid dynamics around and inside an OWC-type wave energy device is studied using Direct Numerical Simulations of the multiphase air-water two-dimensional vertical Navier-Stokes equations. A schematic rectangular shaped OWC device placed against the vertical ending wall of the numerical rectilinear wave flume is considered. Owing to numerical constraints, reduced scale simulations are carried out with a focus on the near field of the device over a couple of wavelengths. The power take-off system is simply modelled by an opening through the roof of the device. A parametric study on incident wave period is performed to determine the fluid-structure interactions. Beyond the efficiency predictions, which agree fairly well with different values found in the literature, specific behaviours related with an enhancement of free-surface non-linearities around the resonance frequency are observed. Water flow vorticity is found mainly produced in the vicinity of the end of the semi-immersed frontal wall of the device. Significant energy dissipation results from shear-layer and vorticity associated with the air flow passing through the turbine opening. A one-dimensional vertical analytical model is used to compute the instantaneous bottom shear stress and the induced-bedload sediment transport rate which appears impacted by OWC device.

Keywords Marine renewable energy · Direct numerical simulation · Fluid-structure interactions · Device efficiency · Sea bed impact

V. Rameliarison (✉) · G. Chapalain
Cerema Eau Mer et Fleuves, Laboratoire de Génie Côtier et Environnement, Technopôle Brest Iroise, 155 Rue Pierre Bouguer, Plouzané 29280, France
e-mail: valerie.rameliarison@cerema.fr

V. Rameliarison · D. Astruc
Institut de Mécanique des Fluides de Toulouse, IMFT, Université de Toulouse, CNRS, Allée Du Prof. Camille Soula, Toulouse 31400, France

K. D. Nguyen et al. (eds.), *Estuaries and Coastal Zones in Times of Global Change*, Springer Water,
https://doi.org/10.1007/978-981-15-2081-5_11

1 Introduction

The challenge of Marine Renewable Energy exploitation is currently tackled by different means. Among them, the wave energy conversion is the one that offers the widest diversity of technologies (Wave Energy Converters, WEC) depending on their location and the way they extract wave energy (de Falcao 2010). Onshore Oscillating Water Column (OWC) is one of the most studied WEC (de Falcao and Henriques 2016). Among the various technologies for wave energy extraction, the OWC offers an original concept. Waves move a volume of air contained in a semi-immersed chamber. Air mechanical energy is converted into electric energy with a power take off (PTO) device. The PTO device is a turbine whose characteristics depends on the air flow through the turbine and the pressure drop between the atmosphere and the chamber. In the literature, the pressure drop is also usually referred as the turbine induced damping coefficient. Most of works have dealt with chamber geometry and/or damping coefficient optimisation to increase OWC performance. Works include both analytical (Evans and Porter 1995; Martins-Rivas and Mei 2009; Rezanejad et al. 2013; Sarmento and Falcao 1985) and numerical studies based on potential theory as well as CFD models. The former, from basic linear frequency domain (Delauré and Lewis 2003) solvers to more sophisticated time domain solvers (Josset and Clément 2007) give an overall of the main OWC features and implement control strategies in order to improve the OWC efficiency. They are practical design tools or to estimate the OWC energy production for a given sea state. The latter focus on detailed fluid flow modelling using Navier-Stokes equations. Both air and water phases are modelled to describe the flows as precisely as possible (Iturrioz et al. 2015; Teixeira et al. 2013). CFD models have been used first to compare the OWC performance depending on geometric parameters with estimations given by potential models. Although resource consuming they turn out more accurate than potential models to calculate the efficiency (Zhang et al. 2012). Usually RANS equations are chosen to reduce computation time. Optimal power, damping coefficient and pressure drop were also put forward through turbine damping optimisation (Kamath et al. 2015; Lopez et al. 2014). Yet, some efforts still have to be made to analyse in detail the flow field and to relate it to the OWC efficiency. Furthermore another major aspect of the OWC dynamics is related to sediment transport, as these devices are likely to be implemented in coastal zones where key sedimentary processes occur. Currently WEC impacts on sediment motion is poorly documented. In this context, our perspective is first to analyse the OWC flows dynamics and relate it to OWC efficiency. So as to carry out the detailed analysis in the vicinity of the device and inside of the OWC chamber we choose to resort to Direct Numerical Simulation of Navier-Stokes equations. Wave propagation, wave-structure interaction, air and water flows are investigated. The present work makes an effort to relate OWC efficiency to flow dynamics. Then we intend to assess the influence of these devices on local hydrodynamics, including bottom boundary layer. We make preliminary

calculations to evaluate sedimentary processes, and possibly morphological evolution, related to OWC device. To this aim, we study a 2D vertical schematic OWC configuration.

2 Numerical Model

a. Navier-Stokes solver

The numerical model is based on a Navier-Stokes equations resolution module on orthogonal grids. An additional module for mobile interface monitoring based on a Volume Of Fluid (VOF) method for fluid-fluid interfaces and an Immersed Boundary Method (IBM) for fluid-solid interfaces is used to model respectively the free surface and the OWC structure. In the VOF method (Hirt and Nichols 1981), the two incompressible fluids are modelled by a single equivalent fluid. The fluid flow is governed by mass and momentum conservation equations and by a transport equation of the volemic fraction of one of the phases C:

$$\frac{\partial \rho}{\partial t} + \nabla.(\rho u) = 0 \tag{1}$$

$$\frac{\partial u}{\partial t} + \nabla.(uu) = -\frac{1}{\rho}\nabla p + g + \mu \Delta u \tag{2}$$

$$\frac{\partial C}{\partial t} + \nabla.(uC) = 0 \tag{3}$$

x and z are the horizontal and vertical coordinates, t is the time, $u = (u, w)$ is the 2D velocity vector, p is the pressure field and g is the gravity constant. The equivalent fluid density ρ and viscosity μ are defined as:

$$\begin{aligned} \mu &= C\mu_w + (1 - C)\mu_a \\ \rho &= C\rho_w + (1 - C)\rho_a \end{aligned} \tag{4}$$

where μ_w, ρ_w, μ_a, ρ_a are respectively the dynamical viscosity and density of water and air.

The Immersed Boundary Method implemented in the model (Gsell et al. 2016) takes into account the solid obstacle by adding an extra forcing $\boldsymbol{f}$ in the momentum equation which is equivalent to impose a no-slip boundary condition at the fluid-solid interface. α_{ibm} is the solid presence rate, equal to 1 in solid cells and 0 in fluid cells. The solid boundary has a thickness of a few cells. It is used to adjust the forcing value near the boundary (Bigot et al. 2014).

$$\frac{\partial u}{\partial t} + \nabla.(uu) = -\frac{1}{\rho}\nabla p + g + \mu \Delta u + f \tag{5}$$

Table 1 Wave and geometric parameters for the different computed cases

Case	A	B	C	D	E	F
T (s)	2.3	1.924	1.67	1.25	1.09	0.909
f_0 (Hz)	0.43	0.52	0.6	0.8	0.92	1.1
λ (m)	6.07	4.81	3.9	2.4	1.8	1.3
b/λ	0.11	0.13	0.16	0.27	0.36	0.49

with: $f = \alpha_{ibm} \frac{u}{\Delta t}$

The equations are solved in Direct Numerical Simulation (DNS). They are discretized on a staggered grid by a second order finite volume method (Calmet and Magnaudet 1997). Advection terms, pressure and exterior forces are computed using a third order Runge-Kutta method. The viscous term is treated with an implicit Crank-Nicholson scheme. The incompressibility condition is satisfied with a projection method.

b. Model configuration

The dimensional computation domain is chosen to be close to a laboratory scale model. The length scale is 1/12.5, similarly to other existing models in the literature. At such a reduced scale air incompressibility is usually assumed. A T-periodic linear progressive wave of amplitude a_0 is used to prescribe the free surface elevation and the velocity profile at the upstream boundary of the numerical flume. The wave propagates in mean water depth D. The resulting wavelength λ is given by the linear Airy theory. Wave amplitude a_0 and mean water depth D are kept constant at $a_0 = 0.04$ m and $D = 0.92$ m. The different values of the wave period T and related parameters namely the frequency $f_0 = 1/T$ and the wavelength λ are given in Table 1. The dimensions of the OWC device (Fig. 1) are its length $b = 0.64$ m, the emergent part $hc = 0.415$ m, the front wall thickness $\delta = 0.04$ m and the front wall immersion depth $a = 0.15$ m. The inducing pressure drop PTO system is modelled with a 5 mm opening in the center of the top wall. The computational domain is horizontally restricted to three times the wavelength λ plus the OWC chamber length b. The domain height is three times the height of the OWC (hc + D) to reduce the confinement effect. The origin of the coordinate system is situated at the crossing between the middle of the front wall ($x = 0$) and the undisturbed free-surface ($z = 0$). x increases along the flume and z increases towards the top of the flume.

To reproduce accurately the processes at work dimensionless numbers observed in real size situations should be conserved in the computations. Froude number, defined as the ratio between inertia and gravity forces, should be conserved for the wave propagation to be similar as in nature scale. Froude number is comprised between 0.04 and 0.09. However Reynolds number cannot be conserved in particular for model stability reasons. Then air and water viscosities are chosen ten times greater than real viscosities leading to Reynolds numbers around 1000, i.e. 450 times smaller than real ones.

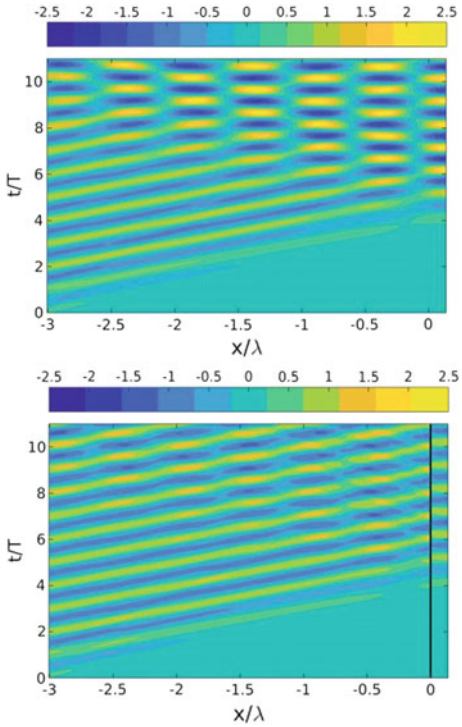

Fig. 1 Time evolution of non-dimensional free surface elevation ζ/a0 along the flume without OWC (top) and with the OWC for case B (bottom). The vertical line marks the front wall position

The computational mesh is irregular in both x and z directions. The domain is divided into several areas requiring a specific meshing, in particular free-surface, chamber walls boundary layers, air chamber and orifice. Near the free surface, the vertical grid spacing is refined to $\Delta z = a_0/20$. IBM boundaries are refined to $\Delta x = \Delta z = 2$ mm. In the air chamber, the flow may be very strong or rotational so the mesh is refined to $\Delta x = \Delta z = 5$ mm. Finally, a $\Delta x = 1$ mm horizontal grid spacing is adopted across the opening. Outside these critical areas, the horizontal step is $\Delta x = \lambda/200$ and the vertical step is $\Delta z = 1$ cm. The maximum time step is $\Delta t = 2.10^{-4}$ s. In the numerical computation the bottom is hydraulically smooth. A no-slip condition is imposed at the bottom boundary. An open boundary condition is imposed at the top of the domain, with the pressure and the velocity gradient equal to zero, so that the fluid can come in and out of the domain.

3 OWC Efficiency

The mean power available for the turbine P_{owc} is defined as the period averaged product of pressure and air flow in the opening:

$$P_{owc} = \frac{1}{T} \int_T p(t)w(t)bdt \tag{6}$$

The OWC efficiency η is then calculated as the ratio of P_{owc} to the incident wave power $P_{inc} = \frac{1}{2}\rho_w g a_0^2 u_g$, where u_g is the wave group velocity equal to $u_g = \frac{d\omega}{dk}$.

Figure 2 compares the efficiency values with various results from the literature. They are plotted against a water depth parameter $\frac{\omega^2 D}{g}$ where ω is the wave pulsation. They include experimental (Morris-Thomas et al. 2007), analytical (Evans and Porter 1995), and numerical values (Kamath et al. 2015; Zhang et al. 2012). The geometric configuration is the same in particular the immersion depth (a/D = 0.16) and the chamber length to depth ratio (b/D = 0.70). In all studies the turbine is modelled with a 5 mm opening except for Kamath et al (2015) who chose a porous media whose permeability coefficient is varied. We plotted the extreme efficiency values they found (subscripts 1 and 2). Besides the wave amplitude a_0 for Kamath experiments is 25% lower than in other investigated studies, including present study. The efficiency estimated in the present study follow the same trend as the others values from the literature. The highest efficiency values (59%) are reached at expected frequencies (case B and C). While intermediate efficiency value (case A $\frac{\omega^2 D}{g} = 0.7$ and case D $\frac{\omega^2 D}{g} = 2.4$) closely match experimental values even better than other models do, we can discern that maximum values are underestimated by 25% (with Kamath results) to 35% (with Zhang results). The disparity with Kamath results can be first explained with the lower wave amplitude. Kamath et al. (2015) themselves showed the decreasing OWC efficiency with wave amplitude. Zhang et al. (2012) noticeably overestimate experimental results at optimal and highest frequencies. They suggested this behaviour could be a consequence of large pressure gradients close to resonance. This matter is not a unique case. Wang et al. (2002) numerical model also underestimated optimal efficiencies compared with experimental values. They attributed it to significant nonlinearities at resonance. In this frequency range a finer mesh in the chamber and orifice regions may be needed to get more accurate results. In the present study, another explanation could be the chosen low Reynolds number.

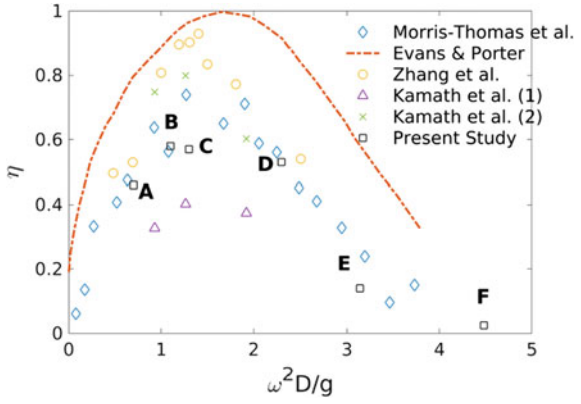

Fig. 2 Present study computed efficiency η plotted with existing estimated values in the literature

4 Free-Surface Dynamics

a. Outside the OWC

We first focus on the free surface dynamics upstream of the OWC. Figure 3 depicts time and space free surface evolution in the flume without OWC (Fig. 3 top) and with an OWC for case B (Fig. 3 bottom). Without OWC there is a visible change in wave amplitude pattern coinciding with the evolution from wave propagation regime (continuous long crests) to wave reflexion regime (short crests) on the OWC wall. With the OWC, the transition between the two regimes is less obvious. The maximal amplitude is lowered. The long crests put forward the reduced wave reflexion. The wave envelope for case B, corresponding to minimal and maximal free surface positions (ζ_{min} and ζ_{max}) of the waves propagating along the flume, is extracted and plotted in Fig. 4 for the first nine waves. The first two waves amplitudes are quickly attenuated along the flume. They correspond to the propagation regime setting up. The third wave reaches the target amplitude a_0 and reflects on the back wall. As it approaches the wall the wave amplitude increases and interacts with the previous wave which has just reflected. A standing wave begins to form. From the fifth to tenth wave the standing wave seems to have converged at least in the close vicinity of the OWC (one wavelength in front of the wall). The reflexion regime is established. The convergence of the standing wave then evolves up to the upstream boundary at phase velocity. Contrary to a wave reflecting against a simple wall, the reflection on the OWC front wall is only partial and so is the standing wave. Beyond the tenth wave secondary reflections on the upstream boundary take place in the flume and are overlaid on the established standing wave. For these reasons, in the following of the work, only the time period between t = 6T and t = 10T will be considered.

Furthermore wave irregularities are visible on the wave envelope, showing secondary extrema. A first explanation is the nonlinear evolution of the wave that cannot be neglected in the model in shallow water depth (Rameliarison et al. 2015). Besides, wave reflection on the wall generates continuous distortion and extra nonlinearities. Finally, the shortness of the flume could prevent from optimal standing wave. Despite the establishment of the reflexion regime, the wave shape evolution and distorsion should be taken in account in the following.

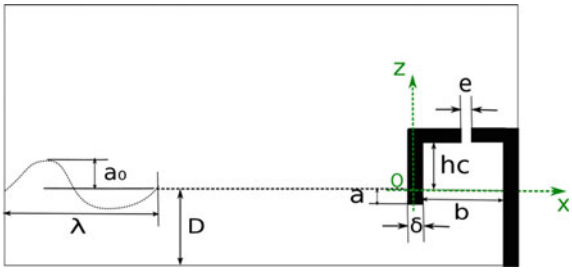

Fig. 3 Definition of wave and geometrical parameters of the numerical domain (the sketch is not to scale)

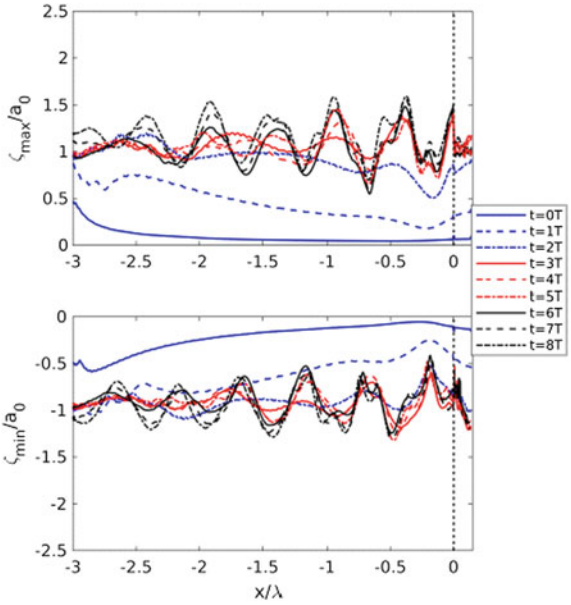

Fig. 4 Non dimensional free-surface envelope for successive waves. The legend indicates the initial time of wave generation at the boundary

b. Inside the OWC

The Fig. 5 shows the spatial distribution across the OWC device of the amplitude of the first three harmonic components (f_0, $2f_0$, $3f_0$) of the free-surface elevation for cases A, B, D and F. The maximum amplitude is obtained for the fundamental

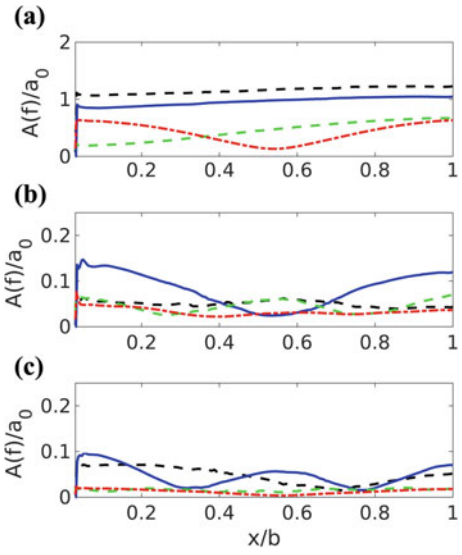

Fig. 5 Spatial distribution of normalised amplitude free-surface harmonic components (**a**:f = f0, **b**:f = 2f0 , **c**:f = 3f0) along the OWC device. Case A: black dash, case B: blue plain, case D: green dash, case : red dash-dot

and does not exceed $2a_0$ (amplitude of the standing wave). Three different spatial distributions of free-surface Fourier fundamental mode can be observed. For cases A and B the amplitude is quasi constant along the chamber. For case D the amplitude is higher at the back of the chamber where it reaches 0.6 a_0 than at the front of the chamber (only 0.2 a_0). For case F the amplitude is high at the two ends of the chamber and is almost zero at the center. The free-surface behaviour is related to the relative chamber length b/λ compared with the first node position of the standing wave, situated a quarter of wavelength from the back wall. For long waves only the antinode is captured in the chamber. As b/λ decreases (cases D and E), the front wall gets closer to the node position. Consequently for case D, the free surface level decreases from the back to the front of the chamber. In the same way for case F, the wavelength is twice the chamber length so the node is situated in the middle of the chamber. In the case F, the sloshing mode is excited leading to large asymmetric motion in the chamber. Because of the spatial disparity of free surface elevation, the OWC efficiency is very low.

As a consequence of the PTO damping effect on the OWC, the maximum amplitude does not exceed $2a_0$ (amplitude of the standing wave without OWC). The fundamental mode amplitude is the highest for case A, for which the wave is the longest. The amplitude reaches $1.2a_0$. For case D, the maximum amplitude is twice less. The damping effect decreases with the wave period. Despite the non uniformity of the free surface level, the efficiency is higher for case D than for case A. We can highlight that maximum efficiency is reached when the inner free-surface elevation equals the incident amplitude a_0 (case B). Case B is then named the optimal OWC regime. Furthermore, at case B higher order harmonics ($2f_0$ and $3f_0$) can reach up to 10% of the maximal amplitude in the chamber. The spatial distribution displays nodes and antinodes at these frequencies revealing that higher chamber modes are also excited. The OWC chamber behaviour is highly nonlinear at resonance frequency. OWC functioning regimes are distinguished through the free-surface Fourier modes distribution along the chamber: the optimal regime (case B) where the inner free-surface elevation equals a_0, the underdamped regime (case A) where the inner free-surface elevation exceeds a_0, the overdamped regime (case D) where the inner free-surface elevation is smaller than a_0 and the sloshing mode where antisymmetric motion occur in the chamber.

5 Flow Inside the OWC

a. Water flow

For the chosen PTO modelling value, the flow mechanics is similar for most of cases (A to D). The major difference are related with the incident velocity intensity and free-surface elevation. To describe the water flow we then focus on the optimal OWC functioning (case B). Figure 6 describes the horizontal and vertical velocities at different locations in the OWC chamber. At the entrance of the chamber (Fig. 6a) the

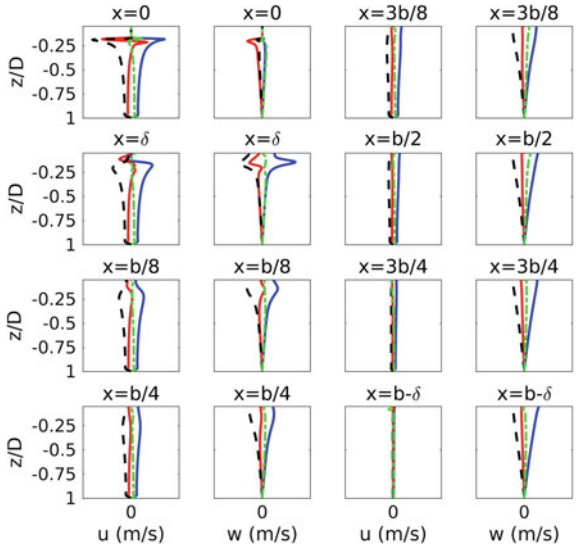

Fig. 6 Horizontal and vertical velocity profiles at different locations in the chamber, and at different wave period instants: t = 0 (blue plain), t = T/4 (red plain), t = T/2 (black dash) and t = 3T/4 (green dash-dot)

horizontal velocity u is 0.095 m/s in the water column (at z/D = 0.5). Then u gradually decreases up to u = 0 at the end of the chamber (Fig. 6l). In the meantime the vertical velocities w show a uniform profile in almost all the chamber (from x = b/4 to x = b, Fig. 6h and Fig. 6m–p). At z = −a/D (the immersion depth), w in the chamber is around 0.11 m/s. It seems that the oscillating horizontal movement at the entrance of the chamber is entirely converted into an oscillating vertical movement inside the chamber, which is consistent with the first Fourier mode distribution (Fig. 5a). Moreover, the narrowing created by the front wall accelerates the flow (Fig. 6a–d). The maximum incoming horizontal velocity u reaches 0.35 m/s at x = 0. A shear zone is forming which extends vertically along a distance equal to 0.07D from the end of the front wall, and horizontally in the lee of the front wall between x = 0 and x = b/4. The shear zone is also visible on vertical velocities (Fig. 6e–h). Consequently there is a recirculation evolving at the chamber entrance.

Figure 7 (left) shows the evolution of the water vorticity field at different instants of the wave period. Vorticity is generated at the end of the front wall. A counter clockwise (positive) vortex is generated with the incoming flow in the chamber (Fig. 7a). It moves up along the front wall in the chamber (Fig. 7b). As the flow is reversing, the vortex magnitude decays and the vortex is advected out of the chamber. A clockwise (negative) vortex is generated with the out coming flow (Fig. 7c). The pair of vortices is then advected upwards (Fig. 7d). The positive vortex stays confined within the free surface whereas the negative one is dissipated during the following wave period. The vortices trajectories are restricted to the close vicinity of the wall. At this regime functioning, vortices dynamics does not take part in the global water flow dynamics. They would rather be an energy dissipation mechanism that could explain the very small difference of mean free-surface elevation between the front (lower elevation) and the back (higher elevation) in the chamber.

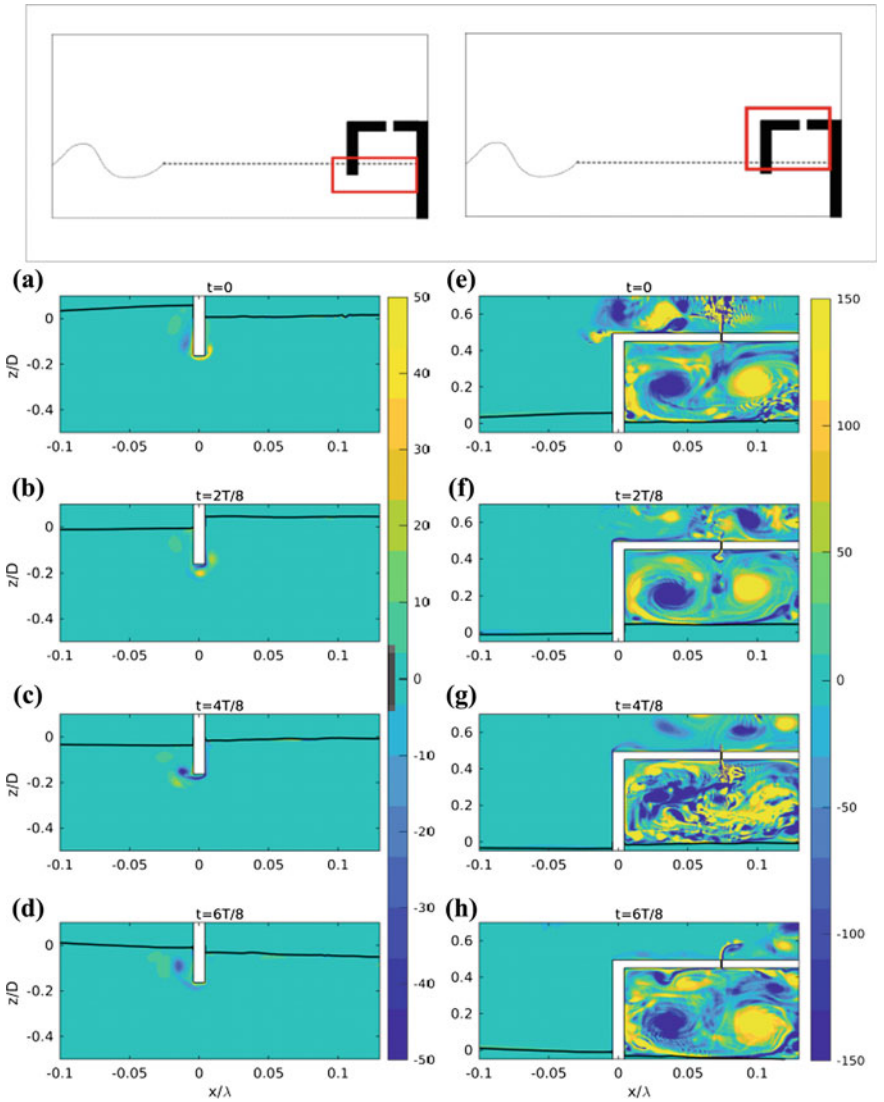

Fig. 7 Water (left) and air (right) vorticity fields (s-1) in the OWC chamber at different wave period instants for case B

b. Air flow

The air flow dynamics in the chamber is controlled both by the free-surface dynamics running the air flow and the pressure drop through the orifice. Figure 8 displays air vertical velocities and pressure both in the orifice and in the chamber for different cases. The longest waves (cases A and B) give the highest air pressure in the chamber (Fig. 8c) and in the orifice (Fig. 8d). The maximum pressure in the chamber

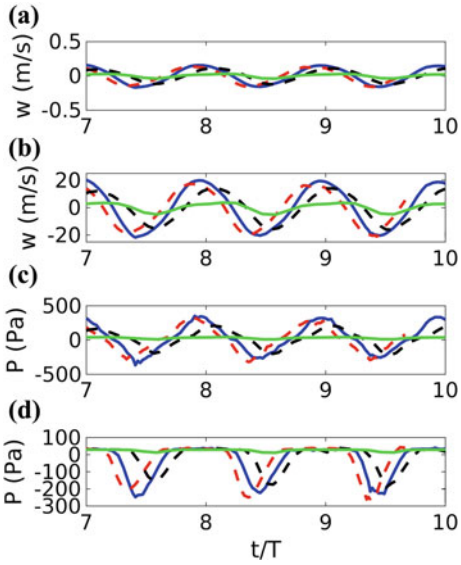

Fig. 8 Comparison of air velocities (**a**: in the chamber, **b**: in the orifice) an air pressure (**c**: in the chamber, **d**: in the orifice). Case A (red dash), case B (blue plain), case D (black dash), case F (green plain)

is measured for case B (320 Pa). We can observe a 25% difference between the positive and negative pressure maxima in the chamber at optimal functioning. The pressure signal asymmetry is a probable manifestation of non linearities occurring at resonance. Air pressure and velocities are 12% higher for optimal regime (case B) than for underdamped regime (case A). Despite the relatively high chamber pressure at underdamped regime (case A), the pressure drop is still insufficient to constrain the inner motion (mean free-surface elevation 20% greater than the optimal one, Sect. 4b) and reach an optimal efficiency. For the overdamped regime (case D) air pressure and velocities in the chamber are 20% less than at optimal regime. Despite the low pressure in the chamber (210 Pa) at this frequency the pressure drop is still too important to reach the optimal efficiency. As the air dynamics seems more easily damped at high frequencies less energy is naturally needed at these frequencies to get closer to the optimal regime. This may be a reason why overdamped regimes at high frequency can supply a better efficiency than underdamped regimes at low frequencies.

An example of air flow dynamics in the chamber is shown on Fig. 7 (right) for the optimal regime (case B). High velocities through the orifice lead to large shear zones on the air jet edges. Vortices are generated. Large opposite circulations are formed at each side of the central jet. The vorticies are advected all over the chamber and are not dissipated within the wave period. The persistence of the vorticity field in the chamber could possibly explain the underestimation of efficiency at optimal regime.

6 Sediment Transport in the Vicinity of the OWC

The interactions between the OWC and a bottom made of mobile solid particles are addressed through the computation of the shearing stress acting on the bottom. In the present reduced scale modelling, a reduced density of 1105 kg/m^3 is adopted. So the Shields number θ which controls incipient sediment motion is conserved. Instead of performing a DNS, which would yield prohibitive computational costs, a 1-D vertical analytical model based on the time invariant Myrhaug (1989) viscosity profile is applied. The model is driven by instantaneous near-bottom free-stream velocities $u_b(t)$ formerly computed with the Navier-Stokes model. The instantaneous bottom shear stress expresses as:

$$\tau_b(t) = \frac{1}{2}\rho f_w(t) u_b(t)|u_b(t)| \tag{7}$$

where the time-varying friction factor $f_w(t)$ is given by the implicit formula of Myrhaug (1989). This formula is valid for a large range of turbulent and transitional hydraulic regimes. The threshold Shield parameter θ_{cr} is given by Soulsby and Whitehouse (1997). The bedload sediment transport rate is finally calculated using the formula of Ribberink (1998):

$$\phi = \begin{cases} 11 \times (\theta - \theta_{cr})^{1,65} & \text{if} |\theta| > \theta_{cr} \\ 0 & \text{if} |\theta| < \theta_{cr} \end{cases} \tag{8}$$

Only the optimal OWC regime (case B, f_0= 0.52 Hz) is analysed in the following. According to the previous free-surface analysis, this sedimentary study only focuses on the wavelength in front and inside the OWC, to insure a well established reflection regime. The residual bedload flux is calculated as the averaged instantaneous bedload flux from a chosen initial calculation time t_0 over a wave period. The evolution of the residual is then monitored over the wave cycles following t_0. OWC impact on sediment transport is evaluated in comparison with a reference situation where the wave propagates towards a vertical wall, without OWC device. Figure 9 depicts residual bedload flux and residual orbital velocity. Both residual velocity and residual bedload flux follow a similar trend, which is consistent with the free-surface enveloppe extrema too. Outside from velocity nodes where the residual naturally vanishes, the residual bedload flux is mainly positive, i.e. onshore directed. It reaches up to 18% of the mean bedload flux. Differences are noticed from one period to an other but the trend is the same overall. The same differences can be observed in the residual velocities. They may be attributed to free-surface non-linearities noticed in Sect. 4a. Similar observations can be made on the residuals patterns when the OWC is functioning at optimal regime (Fig. 10). However the residual bedload flux is three times reduced just in front of the device and up to six times on the rest of the studied domain. The closest peak to the OWC is relatively more important regarding the average amount of instantaneous flux. The OWC optimal regime can

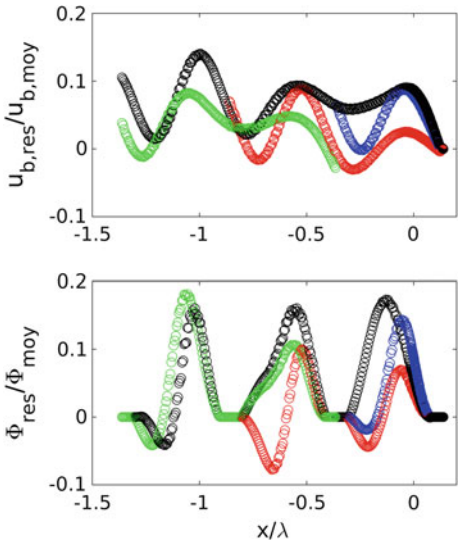

Fig. 9 Spatial evolution of the residual fluid velocity (top) and the residual bedload flux (bottom). The colours refer to the wave over which the residual has been calculated, and defined with the initial calculation time t0 (blue t0 = 6.5T; red: t0 = 7.5T; black: t0 = 8.5T; green t0 = 9.5T. Reference case without OWC

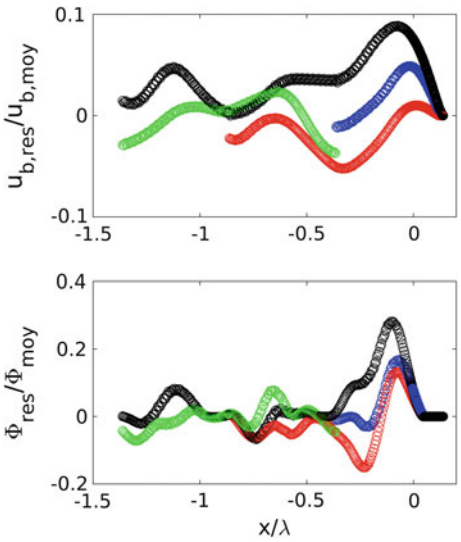

Fig. 10 Horizontal and vertical velocity profiles at different locations in the chamber, and at different wave period instants: t = 0 (blue plain), t = T/4 (red plain), t = T/2 (black dash) and t = 3T/4 (green dash-dot)

provoke an accumulation of sediment at the entrance of the device. According to the amount of available sediment, this could trigger a reduction of the aperture under the semi-immersed wall or a filling of the OWC chamber.

7 Conclusions

A numerical model using DNS of Navier-Stokes equations has been used to study the dynamics of an OWC device and then evaluate analytically its impacts on sediment motion, focusing on the near field of the OWC. It has been shown that:

(i) Computed efficiencies turn out close to the literature existing results, especially experimental and numerical ones, although the deliberate choice of low Reynolds number tends to underestimate optimal values.
(ii) Optimal, under damped, over damped and sloshing regimes were put forward through an analysis of free-surface dynamics.
(iii) Air and water flow dynamics were described: vortices generation is enhanced leading to possible energy dissipation.
(iv) Nonlinearities are noticed at optimal regime making that regime dynamics more difficult to model.
(v) The optimal OWC regime has an impact on the amount of residual bedload flux, engendering possible accretion at the OWC entrance.

Acknowledgements The authors acknowledge Annaïg Pedrono and Thomas Bonometti for their help with JADIM use and programming. This work was granted access to the HPC resources of CALMIP supercomputing center under the allocation 2014-[p1438].

References

Bigot, B., Bonometti, T., Lacaze, L., & Thual, O. (2014). A simple immersed-boundary method for solid-fluid interaction in constant and stratified density flows. *Computers & Fluids, 97,* 126–142.

Calmet, I., & Magnaudet, J. (1997). Large-eddy simulation of high-schmidt number mass transfer in a turbulent channel flow. *Physics of Fluids, 9,* 438–455.

de Falcao, A. F. O. (2010). Wave energy utilization: A review of the technologies. *Renewable and Sustainable Energy Reviews, 14,* 899–918.

de Falcao, A. F. O., & Henriques, J. C. C. (2016). Oscillating-water-column wave energy converters and air turbines: A review. *Renewable Energy, 85,* 1391–1424.

Delauré, Y. M., & Lewis, A. (2003). 3D hydrodynamic modelling of fixed oscillating water column wave power plant by a boundary element methods. *Ocean Engineering, 30,* 309–330.

Evans, D. V., & Porter, R. (1995). Hydrodynamic characteristics of an oscillating water column device. *Applied Ocean Research, 17,* 155–164.

Gsell, S., Bonometti, T., & Astruc, D. (2016). A coupled volume-of-fluid/immersed-boundary method for the study of propagating waves over complex-shaped bottom: Application to the solitary wave. *Computers & Fluids, 131,* 56–65.

Hirt, C. W., & Nichols, B. D. (1981). Volume of Fluid (VOF) Method for the Dynamics of Free Boundaries. *Journal of Computational Physics, 39,* 201–225.

Iturrioz, A., Guanche, R., Lara, J. L., Vidal, C., & Losada, I. J. (2015). Validation of OpenFOAM for oscillating water column three-dimensional modeling. *Ocean Engineering, 107,* 222–236.

Josset, C., & Clément, A. H. (2007). A time-domain numerical simulator for oscillating water column wave power plants. *Renewable Energy, 32,* 1379–1402.

Kamath, A., Bihs, H., & Arnsten, O. A. (2015). Numerical modeling of power take-off damping in an oscillating water column device. *International Journal of Marine Energy, 10,* 1–16.

Lopez, I., Pereiras, B., Castro, F., & Iglesias, G. (2014). Optimisation of turbine-induced damping for an OWC wave energy converter using a RANS-VOF numerical model. *Applied Energy, 127,* 105–114.

Martins-Rivas, H., & Mei, C. C. (2009). Wave power extraction from an oscillating water column at the tip of a breakwater. *Journal of Fluid Mechanics, 626,* 395–414.

Morris-Thomas, M. T., Irvin, R. J., & Thiagarajan, K. P. (2007). An investigation into the hydrodynamic efficiency of an oscillating water column. *Journal of Offshore Mechanics and Arctic Engineering, 129*(4), 273–278.

Myrhaug, D. (1989). A rational approach to wave friction coefficient for rough, smooth and transitional turbulent flow. *Coastal Engineering, 24,* 259–273.

Rameliarison, V., Astruc, D., & Chapalain, G. (2015). Assessment of Navier-Stokes modelling of an oscillating water column wave energy converter. In *Proceedings of the 11th European Wave and Tidal Energy Conference*, Nantes.

Rezanejad, K., Bhattacharjee, J., & Guedes Soares, C. (2013). Stepped sea bottom effects on the efficiency of nearshore oscillating water column device. *Ocean Engineering, 70,* 25–38.

Ribberink, J. S. (1998). Bed-load transport for steady flows and unsteady oscillatory flows. *Coastal Engineering, 34,* 59–82.

Sarmento, A. J. N., & de Falcao, A. F. O. (1985). Wave generation by an oscillating surface-pressure and its application in wave-energy extraction. *Journal of Fluid Mechanics, 150,* 467–485.

Soulsby, R. L., & Whitehouse, R. J. S. (1997). Threshold of sediment motion in coastal environments. In *Pacific Coasts and Ports' 97: Proceedings of the 13th Australasian Coastal and Ocean Engineering Conference and the 6th Australasian Port and Harbour Conference*, vol. 1. Centre for Advanced Engineering, University of Canterbury.

Teixeira, P. R., Davyt, D. P., Didier, E., & Ramalhais, R. (2013). Numerical simulation of an oscillating water column device using a code based on Navier-Stokes equations. *Energy, 61,* 513–530.

Wang, D. J., Katory, M., & LI, Y. S. (2002). Analytical and experimental investigation on the hydrodynamic performance of onshore wave-power devices. *Ocean Engineering, 29,* 871–885.

Zhang, Y., Zou, Q. P., & Greaves, D. (2012). Air-water two phase flow modelling of hydrodynamic performance of an oscillating water column device. *Renewable Energy, 41,* 159–170.

A Simple 3D River/Tidal Turbine Model for Farm Computation—Comparison with Experiments

Vincent Clary, Thibault Oudart, Thierry Maitre, Joel Sommeria, Wassim Zeidan, Luis A. Morocho, Ali Makhour, Philippe Larroudé, Tristan Vandenberghe, Laure Vignal, Michel Riondet, Florence Joussellin, Mathieu Rodriguez, Khoa Borzeix, Olivier Bertrand and Julien Schaguene

Abstract A simple CFD modeling using force source terms in the momentum equation is implemented, with the aim of computing the performance of a Darrieus turbine in its exploitation area and simulating the wake created behind the turbine. It uses the RANS solution method to reproduce ambient turbulent flow conditions with relatively low computational costs. The force distribution used is three-dimensional and has been calculated prior to implementation using a single URANS simulation of the flow through the real geometry of the turbine. To take into account the velocity and turbulent conditions of the flow impacting the turbine, forces can be corrected by the total forces obtained experimentally on a reduced-scale model for different flow cases. The impact on the turbine of upstream turbulence generated by a grid is studied experimentally. The power coefficient, drag force and transverse component of the force on the turbine are studied, as well as the shape and extension of its wake using Particle Imaging Velocimetry. Simplified models with different levels of detail are compared to the experimental data. The results turn out to be in good agreement in the far-wake, with an underestimation of the flow deficit in the near-wake.

Keywords Array power production · Turbine wake · Cross-flow hydrokinetic turbine · Vertical axis stream turbine

V. Clary (✉) · T. Oudart · T. Maitre · J. Sommeria · W. Zeidan · L. A. Morocho · A. Makhour · P. Larroudé · T. Vandenberghe · L. Vignal · M. Riondet · F. Joussellin
Université Grenoble Alpes, Grenoble INP (Grenoble Institute of Engineering), LEGI, 38000 Grenoble, France
e-mail: vincent.clary@univ-grenoble-alpes.fr

T. Maitre
e-mail: thierry.maitre@legi.grenoble-inp.fr

M. Rodriguez · K. Borzeix
CERG, 38800 Le Pont-de-Claix, France

O. Bertrand · J. Schaguene
Artelia Eau & Environnement, 38130 Echirolles, France

K. D. Nguyen et al. (eds.), *Estuaries and Coastal Zones in Times of Global Change*, Springer Water,
https://doi.org/10.1007/978-981-15-2081-5_12

Nomenclature

Symbol	Name (Unit)
C	Correction factor (-)
c	Chord length of hydrofoil (m)
Cp	Power coefficient (-)
Cx	Axial force coefficient (-)
Cy	Transverse force coefficient (-)
D	Diameter of the turbine (m)
Fx	Axial total force on the turbine (N)
Fy	Transverse total force on the turbine (N)
g	Gravity constant (m/s^2)
I_{turb}	Turbulence intensity (-)
k	Turbulent kinetic energy (m^2/s^2)
n	Blade number of the turbine (-)
S	Projected area of the turbine (m^2)
T	Torque of the flow on the turbine (Nm)
Ux	X-component of velocity (m/s)
Uy	Y-component of velocity (m/s)
Uz	Z-component of velocity (m/s)
u'^2	Averaged square of x-velocity fluctuation (m^2/s^2)
v'^2	Averaged square of x-velocity fluctuation (m^2/s^2)
w'^2	Averaged square of x-velocity fluctuation (m^2/s^2)
λ	Tip speed ratio (-)
Ω	Rotational speed of the turbine (rad/s)
ω	Omega turbulence parameter (s^{-1})
ρ	Water density (kg/m^3)

1 Introduction

Tidal or river stream turbine technology is currently undergoing rapid progress. The first prototypes have been installed and tested in oceans as well as in rivers. In a site with high potential (i.e. high tidal or river currents), the position of turbines related to each other has to be calculated, for the optimization of their efficiency and impact studies. The turbine performance and the size of the wake must be computed efficiently. Two main generic turbine shapes exist nowadays: vertical axis turbines, for example the Darrieus model tested at LEGI by Maître et al. (2013), and horizontal axis turbines like the model tested in Southampton by Myers and Bahaj (2006). The method presented here aims at developing a simple 3D turbine model for farm computations by means of experimental studies and numerical developments. It can be applied to any kind of turbine, but results are presented in this work for a vertical axis turbine.

Various studies have been undertaken recently to develop models of stream turbine arrays. For axial turbines, analytical methods based on the Betz-Joukowsky law (the Actuator Disk method) have been improved to take into account confinement of stream turbines under water, due to the presence of the bathymetry, free surface and the other adjacent turbines (Garett and Cummins 2007; Whelan et al. 2009). The models were extended to an array of tidal stream turbines by Vennell (2013) or Draper and Nishino (2014).

Detailed CFD simulations of different turbines have been performed, taking into account the impact of the local velocity of the flow on a turbine. RANS simulations of a farm containing 4 axial tidal stream turbines, have been performed by Nuernberg and Tao (2018) with relevant results but relatively high computational costs. Concerning vertical axis turbines, efficient unsteady RANS simulations using a SST turbulence closure model were carried out by Kinsey and Dumas (2017), yet without studying the far-wake.

To properly model all the eddies characterizing the wake of a turbine in operating conditions, LES simulations of a single turbine can be performed with a turbulent inlet velocity profile. Posa et al. (2016) conducted LES simulations of vertical axis wind turbines, and the wake structure was found to be in good agreement with experiments. Concerning the modelling of axial tidal stream turbine arrays, interactions between 3 turbines in tri-frame configuration were simulated using the LES method by Chawdhary et al. (2017).

The aforementioned simulations have a high computational cost, therefore simplified CFD models are being developed in an industrial context. Using them, it is possible to consider many turbines at real sites and provide a practical tool for the optimization of the turbine positions. At the oceanic scale, large domains and long durations are computed thanks to 2D models, in order to simulate properly the effects of the tides at a potential site all along the year. Two different approaches exist to compute the effect of a tidal turbine: it can be modeled by a friction force on the bottom (Vogel et al. 2017), or by adding a force source term in the momentum equations (De Dominicis et al. 2017), with significantly the same results. Three-dimensional simulations might be useful to take into account the bathymetry more precisely. Wimshurst and Willden (2016) showed using an Actuator Disk (AD) approach that a turbine at a location where water depth is diminishing (in the current direction) produces less power than the same turbine at a location with increasing water depth. This is due to modifications in the boundary layer, as turbines are often placed in elevations that are still impacted by the velocity reduction in the bed boundary layer. Using the 3D AD method is simple enough to simulate large turbine arrays, whilst also taking turbulence into account using RANS turbulence models (Harrison et al. 2009; Roc et al. 2013). For the axial turbine, different turbulence models (K-Epsilon, K-Epsilon Realizable, RSM, K-Omega-SST) have been tested by Nguyen et al. (2016) and produced different results. The authors proposed to add a source term in the turbulence equations to improve the results but the value must be chosen properly. In another study, van der Laan (2014) modified the K-Epsilon equations to get accurate results for wind turbine farms computation.

For cross-flow stream turbines, Gebreslassie et al. (2016) used an improved Actuator Cylinder approach, which is a modification to the AD method, applying rotating forces depending on the blade positions. Forces are applied to the hollow cylindrical zone swept by the blades. A very accurate description of the wake of a single turbine was obtained by setting the total force value, which had to be determined precisely. It led to an interesting model of a whole farm of cross-flow tidal turbines (Gebreslassie et al. 2015).

In the Actuator Disk or Actuator Cylinder methods, results are very sensitive to the force (distribution and magnitude) representing the turbine. To determine the lift and drag force values exerted on the blades of a turbine, the Blade Element Momentum (BEM) approach can be used for the different types of turbines. Such methods were performed in 2D to model a vertical axis stream turbine (Dominguez et al. 2016). On this basis, a 3D model of a vertical axis turbine array has been computed in TELEMAC by Bertrand et al. (2015) and needs comparison with experiments.

The natural turbulence conditions of the flow impacting a turbine have also an influence that is still difficult to obtain numerically. Experiments of a reduced scale axial stream turbine in a free-surface channel showed that the length of the wake was more than two times shorter with a strong inlet turbulence intensity (15%) than with a low inlet turbulence intensity (3%) (Mycek et al. 2014). Still no study to our knowledge has addressed the influence of inlet turbulence intensity on vertical axis turbines. This point will be addressed in this work.

Turbulence also reduces the delivered power. Loads on the turbine can be affected significantly by the ambient turbulence properties. Shives and Crawford (2015) presented an axial turbine model using a non-uniform force distribution applied in the volume swept by the blades that also takes into account local velocity and free-stream turbulence. The force distribution is computed for different conditions with a 3D BEM method. Experimental data is used to correct the total force values, to take into account the Reynolds effects as well as the turbulence and inlet velocity conditions of the flow impacting the turbine in each case. Total force values are interpolated from the experimental data to correspond to the ambient flow conditions experienced in an operational site. This method provides good results with a few cells in the domain (9 per diameter of the turbine) and two turbines in a row have been computed.

In the present work, we investigate results of a 3D RANS simulation with a detailed force source field added in the momentum equation, including components in the three dimensions. It is demonstrated using a cross-flow turbine model already tested at LEGI. Experimental measurements are carried out at CERG hydrodynamic tunnel in order to examine the influence of upstream turbulence and velocity on the turbine loadings, efficiency and wake. The mean torque is measured, as well as forces in the streamwise and transverse directions. Inlet conditions are controlled by choosing to use a turbulence grid or not, and a characterization of the flow is performed in each case without the turbine, using Laser Doppler Velocimetry (LDV) measurements.

To analyze the results of the present simplified turbine model, a comparison with Particle Imaging Velocimetry (PIV) measurements of the wake of the cross-flow turbine is made. Various force distributions, ranging from the classical Actuator

Cylinder model to a detailed 3D force distribution including force terms in the arm area are compared for the simplified model.

The model is also implemented in TELEMAC, using the 3D non-hydrostatic solver with the K-Epsilon turbulence model, to check the ability of an oceanic code to reproduce the correct wake.

2 Experimental Setup

The CERG hydrodynamic tunnel TH2 is used for the experiments. It is a closed loop where water is pumped by a propeller pump at velocities up to 6 m/s. Dimensions of the test section are 2.5 m long, 0.60 m wide and 0.55 m high, and it is preceded by a half-convergent in the bottom of the channel (Fig. 1). At the end of the convergent section, a regular turbulence grid can be added 0.91 m upstream of the axis of the turbine. Positions are defined with a reference frame (x, y, z), with x streamwise, y lateral and z vertical. The axis origin lies on the turbine axis, at mid-height of the turbine.

To characterize the ambient flow, a first lateral window allows LDV-measurements of the velocity fluctuations without any turbine. Two cases are investigated: without any grid and with a regular turbulence grid whose bars are 12.5 mm thick with a mesh of 50 mm (Fig. 3b). The laser-2-focus technique is used, with two sets of two beams emitted, enabling measurements in x (streamwise) and z (vertical) directions. 2000 points are taken for each measurement, to obtain mean velocities and mean fluctuations of the velocity. The profile in the streamwise direction is measured in the middle of the channel, from 130 mm downstream of the turbine axis to 720 mm downstream of the axis. Profiles are presented in Fig. 2 for the cases with and without the regular turbulence grid.

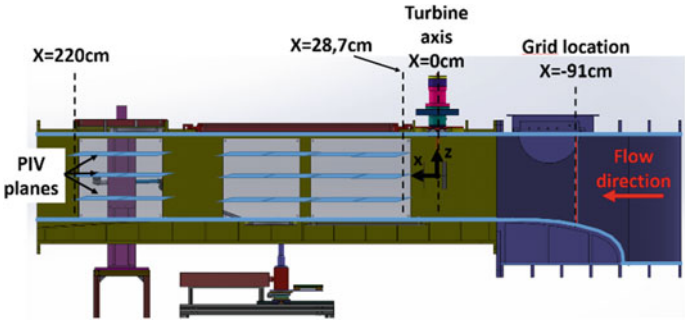

Fig. 1 CAD view of the CERG hydrodynamic tunnel test section, with turbine, grid position, and PIV planes positions

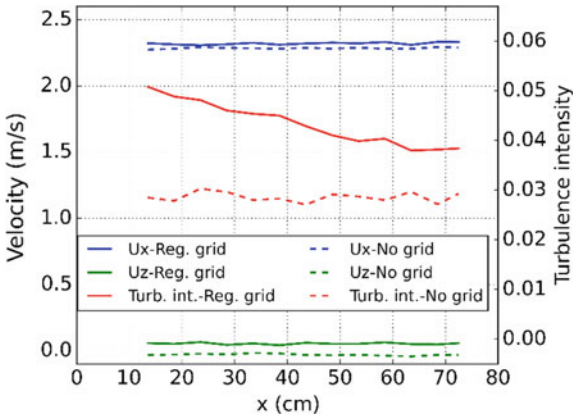

Fig. 2 x-profile of measured mean x and z components of velocity, and turbulence intensity compared for the cases with and without the regular turbulence grid

For measuring the level of turbulence, turbulence intensity is calculated using an assumption for v', the third component of the velocity fluctuation (y-component) that could not be measured.

The following assumption was made:

$$v'^2 = \frac{u'^2 + w'^2}{2} \Rightarrow$$

$$Iturb \equiv \frac{\sqrt{\frac{1}{3}\left(u'^2 + v'^2 + w'^2\right)}}{\sqrt{U_x^2 + U_y^2 + U_z^2}} = \frac{\sqrt{\frac{1}{2}\left(u'^2 + w'^2\right)}}{\sqrt{U_x^2}} \tag{1}$$

Similar profiles were measured in the transverse directions. The velocity proves to be constant throughout most of the channel section, and the boundary layers extend up to 10 cm from the channel walls, guarantying that they do not influence the flow in the turbine area. However the turbulence intensity is not uniform in the z direction in the case without turbulence grid, even far from the channel walls. This is due to the shape of the asymmetric convergent section that creates more turbulence in the bottom. The turbulence intensity measured in Fig. 2 is about 2.9%. But values in other altitudes range from 2.0 to 3.0%, therefore the value of 2.5% is chosen for the simulations. In the case of the turbulence grid, this problem does not appear because the grid is smoothing the turbulence intensity profile. A turbulence decay is observed. The turbulence intensity is extrapolated to find the value of 5.5% in the zone of the channel where the turbine can be placed.

The water velocity in the channel is controlled with a Prandtl probe, located approximately 170 cm upstream of the beginning of the convergent section. It was calibrated before the measurements using the LDV-results. The turbine used is a vertical axis water turbine with n = 3 straight blades, with a diameter D = 175 mm and a height of 175 mm (Fig. 3a). The blades are NACA0018 profiles, with a camber

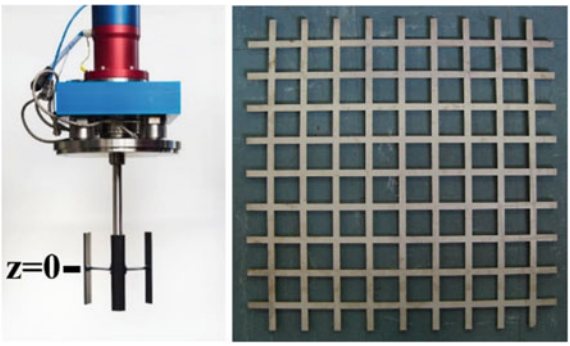

Fig. 3 **a** (left): Darrieus turbine used during the experiments with its shaft, motor and measurement system, **b** (right): Regular turbulence grid used

following a rotating circle of diameter 175 mm. Its chord value is c = 32 mm, leading to a solidity $\frac{2nc}{D} = 1.1$.

The turbine is centered in z-direction, and situated 5 cm to the right of the center of the channel in y-direction. Its rotational speed is controlled by an electric motor placed above the channel. The turbine is connected to the motor by a 22 mm diameter shaft. The regulation and measurement system is detailed in previous work (Aumelas 2011). Piezoelectric sensors measure the instantaneous x and y force components applied to the whole turbine, with an absolute error estimated to be ±3 N due essentially to a time drift. For each measurement, 4800 points are acquired with a frequency corresponding to one point per 3° travelled by the turbine, which ensures an averaging time corresponding to 40 revolutions.

In the case with turbulence grid, the forces are measured for different channel velocities to observe the influence of Reynolds number. They are compared to forces obtained in the case without turbulence grid, for a channel velocity of 2.3 m/s, in Fig. 4. A dimensional force coefficients are plotted, defined as

$$Cx = \frac{Fx}{\frac{1}{2}\rho S U_x^2}; Cy = \frac{Fy}{\frac{1}{2}\rho S U_x^2} \tag{2}$$

In (Eq. 2), the velocity Ux is measured via the Prandtl probe, and is time-averaged over 5 min to remove a non-negligible noise due to the probe.

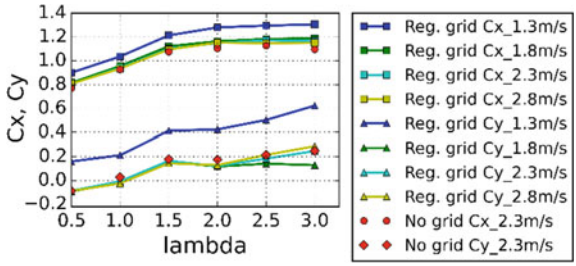

Fig. 4 Cx and Cy experimental measurements versus λ for different inlet flow cases

The force coefficients are found not to be dependent on the Reynolds number anymore for inlet velocities equal to or higher than 2 m/s. Moreover, the turbulence grid has no significant influence for those velocities, therefore a sole value of the total forces will be used in the simplified model simulations for both turbulence cases.

The instantaneous total torque is obtained via the current measurement of the motor. Measured values are averaged over at least 5 revolutions of the turbine. The motor torque, T, varies linearly with the current intensity, with a coefficient equal to -1.38 Nm/A given by the manufacturer. It enables one to calculate the power coefficient Cp in each case, defined as:

$$Cp = \frac{T\Omega}{\frac{1}{2}\rho S(U_x)^3} \tag{3}$$

The measured torque includes the mechanical friction of the bearings and the rubber seal, the latter having a large friction torque. Measurements of the friction torque are carried out 5 times without the turbine for different rotational speeds. The torque occurs to be approximately constant and equal to -0.2 Nm. This value is subtracted to the measured torque to obtain a power coefficient of the turbine itself, independent of the mechanical components.

The turbine wake is measured with PIV. An injecting tube is placed approximately 1.2 m upstream of the turbulence grid position, with a variable injection height. 30 μm diameter polyamide particles are used and are distributed regularly throughout the whole channel thanks to the turbulent dispersion. Horizontal planes, starting 0.29 m up to a maximum of 2.20 m downstream of the turbine (depending on the planes), allow to get measurements up to a maximum of 12 diameters downstream of the turbine. Plane 0 is located little above the mid-height of the turbine (z = 1 cm with $\pm$0.5 cm uncertainty regarding this position), then 5 planes are spaced above plane 0 with +4 cm increment in z direction each time, and 5 planes are spaced the same way under plane 0. Only the x and y velocity components are caught in the measurements.

One thousand pairs of images are taken for each measurement, and are synchronized with the key blade being in the most downstream position. This position is detected by a trigger, so that one image pair is taken each turbine revolution. The chosen time interval for an image pair is 600 μs, in order to capture the small velocities in the near wake, as well as higher velocities. For the far wake, a time interval of 800 μs is used.

PIV results are post-treated with the UVMAT software, available in the internet page http://servforge.legi.grenoble-inp.fr/projects/soft-uvmat.

3 Numerical Modelling

The aim of the whole study is to get an accurate simplified CFD model in order to simulate the wake of a vertical axis stream turbine. In the simplified model, the geometry of the turbine is not modeled. Instead, force terms are added in the 3

components of the momentum equations for all cells included in the volume swept by the turbine. Simplified model simulations are stationary, and a time-averaged force distribution is used in this volume, depending on the position of each cell. This force distribution has to be known. Shives and Crawford (2015) used a BEM method to get the force distribution for various flow velocities and turbulence conditions. In our case, we obtain a detailed force distribution for a unique case, and a correction is then applied to take into account flow velocity and turbulence conditions if they differ.

Full geometry URANS simulation to obtain the load distribution on the turbine
To compute this force distribution, a unique full-geometry URANS simulation of the flow through the turbine is performed, with a chosen inlet flow velocity of 2.3 m/s and a turbulence intensity of 2.5%. This simulation is done with OpenFoam. The dimensions of the simulation domain correspond to the experimental dimensions with a section of 0.60 m wide, 0.55 m high and 2.5 m in the direction of flow (0.5 m upstream, 2 m downstream of the turbine). To reduce the number of cells, a symmetry is used on the median plane ($z = 0$). A RANS turbulence closure model is used with the k-Omega Shear Stress Transport linear eddy viscosity equations (Menter 1994; Menter et al. 2003). This model has two equations on k and ω, and allows to capture correctly the flow separation. To capture the boundary layer flow near the turbine, a dimensionless wall distance y+ less than 5 (corresponding to a cell height of 2.0×10^{-5} m near the wall) is used and extended within 10 layers. The turbine rotation is taken into account using a dynamic mesh interface between the tunnel and a cylinder containing the turbine. These specifics lead to a full mesh composed of 16 million cells.

The pimpleDyMFoam solver is used to get accurate results in acceptable time. It is a large time-step transient solver for incompressible, turbulent flow, using the PIMPLE (merged PISO-SIMPLE) algorithm and with the ability to take into account dynamic mesh. The numerical schemes used are second order (backward) for the time, and second order for pressure, velocity, k and omega (Gauss linear) with a limiter for k and omega. At $\lambda = 2$, the time step is chosen to correspond to a rotation of 1° of the turbine with a maximum of 30 subiterations each time step. A lower time step is chosen for lower lambda values. Results are extracted only once 15 revolutions of the turbine have been completed.

To obtain a representative distribution of the turbine forces exerted on the flow, a time-averaged force field is extracted on a new cylindrical mesh. Its cells are the basic volume elements of a cylindrical coordinate system which does not rotate with the turbine (Fig. 5). The decomposition is done here for the half of the turbine simulated, and will be extended later by symmetry to the whole turbine. The zone where blade forces are present is decomposed into one cell in the radial direction, 10 cells in z-direction and 72 cells along the 360° of θ ($d\theta = 5°$). For the arms, forces are extracted in a domain that contains 10 cells in the radial direction, 1 cell in z-direction, with $d\theta = 5°$.

During the 15th revolution of the turbine, both arms and blades forces are extracted for every cells of this cylindrical referential, for each time step equivalent to 1°

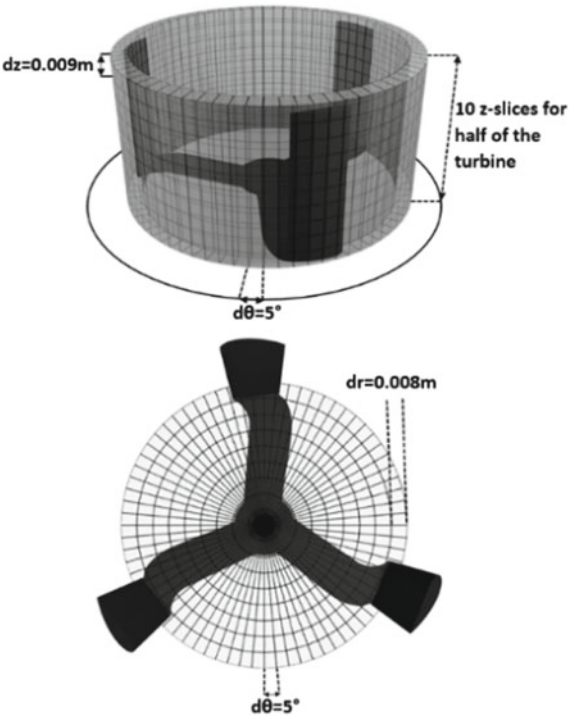

Fig. 5 Cylindrical mesh used to compute the time-averaged forces to be used in the simplified model simulations

rotation. This referential being fixed, at each time step, cells of the cylindrical mesh witness either a part of the blades or arms (in this case corresponding forces are extracted) or only fluid (no forces are extracted). At last, a time-averaging of those force distributions during the whole revolution is performed for each cell to obtain a stationary spatial distribution of the forces.

Simulations were done on a Xeon DELL C6320 with 20 cores and lasted 30 days for 15 revolutions.

Experimental correction for each inlet flow condition

To take into account ambient flow conditions and have turbine performances conform to the experiment, the force distribution obtained with simulations is multiplied by a corrector C, so that the total forces are equal to the total forces measured along x and y axis for each experimental case. The total force along z should be null due to the symmetry, and no correction is applied in that direction. In the simplified model, for each zone i of the decomposed domain, the x-component of force applied is

$$F_{x,i}^{corrected} = \frac{F_{x,tot}^{measured}}{\sum_i F_{x,i}^{not\ corrected}} * F_{x,i}^{not\ corrected}$$

$$F_{x,i}^{corrected} = C\left(I_{turb}, \lambda^*\right) * F_{x,i}^{notcorrected} \quad (4)$$

where C depends on the advance parameter (or tip speed ratio) λ, and I_{turb} is the ambient turbulence intensity. We have seen before that turbulence intensity plays no role in the total x and y-forces, so that C only depends on λ here. The y-component of the force is corrected the same way.

In the future, it will be necessary to discuss how to choose the local velocity to compute the λ parameter for each turbine of a farm.

Simplified simulation setup

The simplified model uses the RANS solution method, and has been coded both in OpenFoam and TELEMAC3D software. Only the case with the regular turbulence grid (corresponding to 5.5% turbulence intensity at turbine position) is presented here, for which the inlet turbulence properties are well controlled.

The OpenFoam simulation is done using the SimpleFoam solver. A classical resolution of the steady-state RANS equations is performed, and both K-Epsilon and K-Omega-SST turbulence models are used in the simulations.

Telemac3D is a free surface software with a moving mesh following the free surface. The non-hydrostatic version of the code is used, solving the RANS equations in the three directions, plus adding a step for the free surface calculation in z-direction. Therefore the horizontal components and the vertical component are computed separately. The K-Epsilon turbulence model is used here in both the horizontal and vertical directions. The program uses a time-step resolution, even if a steady-state is simulated here.

The simulation domain is faithful to the tunnel size for the OpenFoam simulation, with a 3 m long domain with 0.6 m breadth and 0.55 m height. The domain starts 0.37 m upstream of the turbine to assure that the inlet uniform velocity condition does not affect the turbine calculation. The outlet condition used is of the InletOutlet type, and gives the same results as a simulation using a longer calculation domain.

For the TELEMAC simulation, the domain could not respect the experimental setup geometry. Indeed for a water height of 0.55 m, the Froude number is 0.99, leading to a transitional regime. Therefore the water height was increased to 2 m. This does not introduce a significant error as the confinement is very low (section area of the tunnel is 10 times bigger than the turbine projected area). A channel length of 4.5 m is used to be sure that the outlet pressure condition has no influence on the wake computation. The inlet flowrate condition and outlet altitude condition (i.e. a hydrostatic pressure condition) are chosen. Due to the bottom friction, a small difference in altitude is observed, creating a velocity deficit in the inlet section. The velocity at inlet is therefore found to be 2.23 m/s instead of 2.3 m/s.

In both cases, the mesh is refined near the walls. In the whole wake domain, the mesh is uniform and has cubic cells with sides of length 0.01 m. This domain comprises at least 20 cm on each side of the turbine center in y and z directions, starts at inlet and continues until outlet in x direction. A cell size $dx = 0.01$ m enables one to have 17 cells along the diameter of the turbine.

In both codes, turbulence has to be set properly at the inlet. With the turbulence grid, turbulent kinetic energy and Epsilon or Omega values have to be set to obtain the correct turbulence intensity value at the turbine position, and the correct turbulence

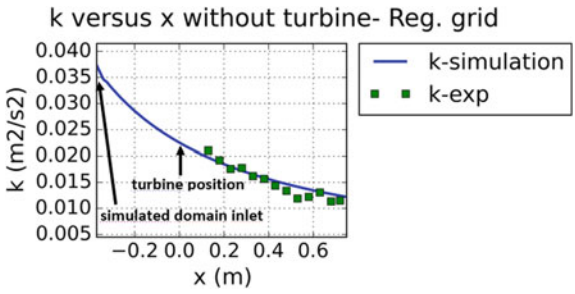

Fig. 6 Experimental and simulated turbulent kinetic energy (k) decay along x, in the center of the channel, without turbine

decay. Several iterations of simulations of the flow in the channel without any turbine were performed to properly set both values, and the final simulated turbulence decay at the channel center fits the experimental measurements (Fig. 6). Both software give the same results. The TELEMAC code was implemented to impose properly inlet turbulence conditions.

The different simplified models used

Different levels of simplification have been tested. As simulation times were far lower for the OpenFoam simulations, all models were implemented in that code whereas only model 2 was implemented in TELEMAC3D for comparison.

- Model 1 is the most detailed, with a non-uniform force distribution depending on the 3 directions all along the blade area and the arm area. Fx, Fy and Fz are considered in this model.
- Model 2 is a 2 dimensional detailed force distribution in the blades area only, depending on the angle but not on the altitude. Fz is not considered.
- Model 3 is a uniform distribution in the cylinder formed by the whole area swept by the turbine. Fz is not considered.

4 Results

The power coefficient curves versus λ proved to have a certain variability across the measurements. This might be explained by fluctuations of the velocity impacting the turbine. Therefore 5 curves were plotted each time, and the colored envelopes of the maximum and minimum values measured each time are shown in Fig. 7, for various flow conditions. The cases with and without the regular grid are considered. We observe that the variability is larger for the case without the grid, where turbulence is less controlled. A strong Reynolds number influence is noticeable for the case without the grid at velocities under 2.3 m/s. This velocity is therefore chosen for future measurements. In both cases, the maximum Cp observed is close to 0.25 for $\lambda = 1.75$ It has to be compared to the maximum Cp obtained for the full-geometry

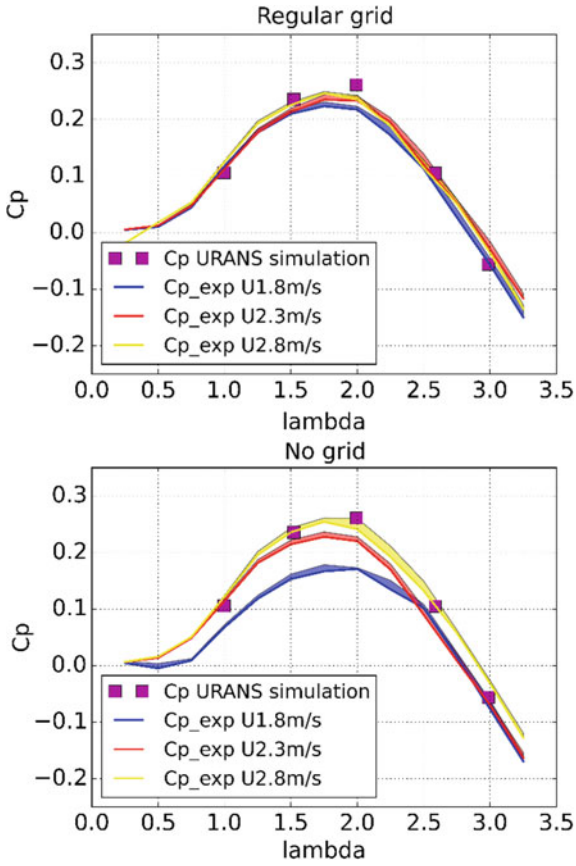

Fig. 7 Experimental results at different channel speeds and URANS full geometry results for Cp versus λ

URANS simulation, which is 0.26 for $\lambda = 2$. The simulated values are in good agreement with the experimental values.

The Cx and Cy experimental measurements have already been presented in Fig. 4. To determine the forces applied on the turbine without including its shaft, as done in the simulations, the drag exerted on the shaft must be subtracted. It is estimated using the drag coefficient formulae for an infinite cylinder. At the channel velocity of 2.3 m/s, the Reynolds number order is 10^4, giving a drag coefficient value of 1.0 (corresponding to the turbulent area on the Cd curve). The calculated drag value is $Fx_{shaft} = 12.3$ N. The forces are compared to the URANS full-geometry simulation results in Table 1. A lift component should also be calculated, as the shaft is rotating. A first estimation referring to the work of Badalamenti and Prince (2008) gives an estimation of -3 N that has not been considered here.

At $\lambda = 2$, the simulated total forces are close to the experimental total forces measured, and the URANS simulation is in good agreement with the experiment. For lower and higher λ, the x-component of force is correctly computed but the y-component presents errors. Further investigations are needed to compare URANS

Table 1 Total experimental forces compared to the total forces computed with URANS simulation

	λ = 1		λ = 2		λ = 3	
U = 2.3 m/s	Fx(N)	Fy(N)	Fx(N)	Fy(N)	Fx(N)	Fy(N)
Experimental forces without shaft correction	74.7	−0.6	91.2	9.6	92.4	19.6
Shaft force corrections	12.3	0	12.3	0	12.3	0
Experimental forces with shaft correction	**62.4**	**−0.6**	**78.9**	**9.6**	**80.1**	**19.6**
URANS computed forces	58.3	−9.8	79.9	6.6	82.1	13.4

Bold values are the force values used in the simplified model simulations

results to experiments. It might appear that URANS simulations are sufficient to obtain the force distributions, saving a lot of instrumentation efforts.

Concerning the wakes, the PIV images taken for the cases with and without turbulence grid, at λ = 2, present few differences. Plots of the mean velocity in the transverse direction at plane 0 (z = 0 cm) are presented in Fig. 8 for both cases. The plots are presented for different positions downstream of the turbine (2 diameters downstream, 4 diameters downstream…). The velocity deficit is slightly larger in the near-wake for the case with the low turbulence level (without grid), and then tends to recover faster. But the curves are really close. The two ambient turbulence levels studied here are close (2–3% and 5.5%) and explain the proximity of the results. Other measurements with a higher ambient turbulence intensity are needed to determine if this parameter impacts the wake as much as for axial turbines.

A comparison was made between the wakes obtained with experiments, with the 3 simplified models implemented in OpenFoam, and with the simplified model implemented in TELEMAC. The OpenFoam simulations results are shown only with the K-Omega-SST model, but results proved to be the same with the K-Epsilon model for the cell sizes used in the simulations. Figure 9a shows the axial mean velocities for all cases in a horizontal cross-section at the altitude of plane 1 (corresponding to the middle of the upper part of the blades). This is done at different positions downstream of the turbine (2 diameters downstream, 4 diameters downstream…).

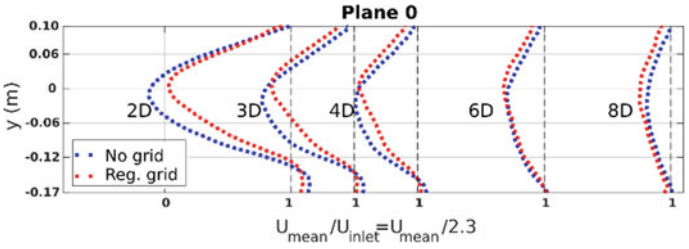

Fig. 8 Comparison of the transverse profiles of mean velocity obtained by PIV in plane 0 for the cases λ = 2

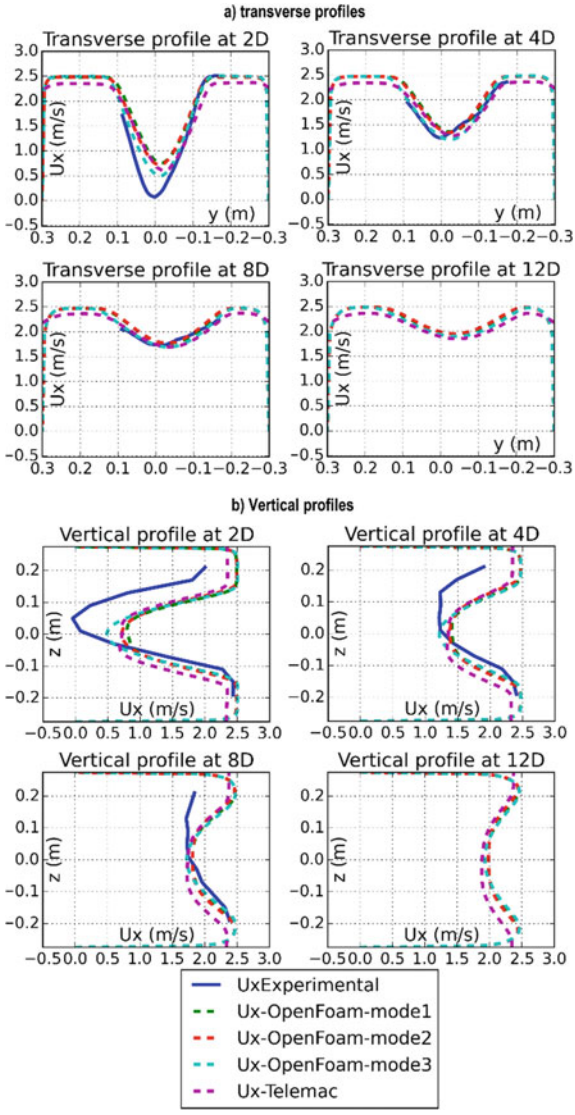

Fig. 9 Transverse and vertical Ux profiles compared between the experiment, the three OpenFoam simulations and the TELEMAC simulation

Vertical plots at y = 0 are also compared at the same positions downstream of the turbine on Fig. 9b.

The position of the maximum experimental velocity deficit is about 4 cm above the simulated ones. The asymmetric convergence at inlet might explain this drift by creating a global deviation of the flow towards the ceiling. Figure 2 shows a slightly positive z-velocity in the turbine area, supporting this theory.

All simulations tend to underestimate the velocity deficit in the near wake. However simplified models are not representing the flow exactly, as forces applied reduce

the velocity locally but do not stop the flow totally like the faces of the blades do. It is normal that they present errors in the near-wake.

In the far-wake at x = 8D, relative errors on the velocity profiles are lower but the wake tends to recover slower in the simulations.

In all cases, the wake expansion is bigger in the z-direction than in the y-direction. This phenomena still has to be analyzed.

Comparing the different simulation models, one sees almost no difference between model 1 (detailed force distribution in 3 dimensions) and model 2 (force distribution in 2 dimensions depending on the angle but not the altitude). A slight difference exists with model 3 (uniform force distribution) but it is negligible. Therefore a uniform force distribution gives correct results in the far-wake for the case $\lambda = 2$. However, results might be different, especially for lower λ, where eddies on the blade might have three-dimensional characteristics. The TELEMAC simulation presents a velocity offset of approximately 0.2 m/s. It can be explained in part by the inlet velocity offset present during the simulation, and by the slightly different confinement configuration. It is in good agreement with the OpenFoam simulation using the same model (model 2) considering the approximations made.

The root mean square values of the fluctuating velocities are obtained via PIV for the x and y components, for the case with regular turbulence grid. To make a comparison with simulations, the numerical u'^{2} value is calculated according to the turbulent kinetic energy definition, knowing that the turbulence is isotropic in the model:

$$\mathrm{k} = \frac{1}{2}\left(u'^2 + v'^2 + w'^2\right) = \frac{3}{2}u'^2 \Rightarrow u'^2 = \frac{2}{3}\mathrm{k} \tag{5}$$

Figure 10 presents the compared transverse profiles for u'^{2} at the same positions as before in plane 1.

Turbulence is not isotropic in the measurements. Still, the simulated values lay between the two components measured or close to them. It allows one to state that isotropic RANS turbulence models are accurate to model the turbine wake.

5 Conclusion

A simplified CFD model of a Darrieus turbine using the RANS solution method has been developed. The turbine was modeled by force source terms added to the momentum equations. The force distribution was obtained with a unique URANS full geometry simulation of the flow through the turbine. The simulated performances fitted well with those of a reduced scale Darrieus turbine tested in a hydrodynamic tunnel. A set of experimental total force curves for different ambient flow conditions impacting the turbine can be useful to correct the total forces used in the simplified model, in order to take into account flow conditions in this model. However, at the

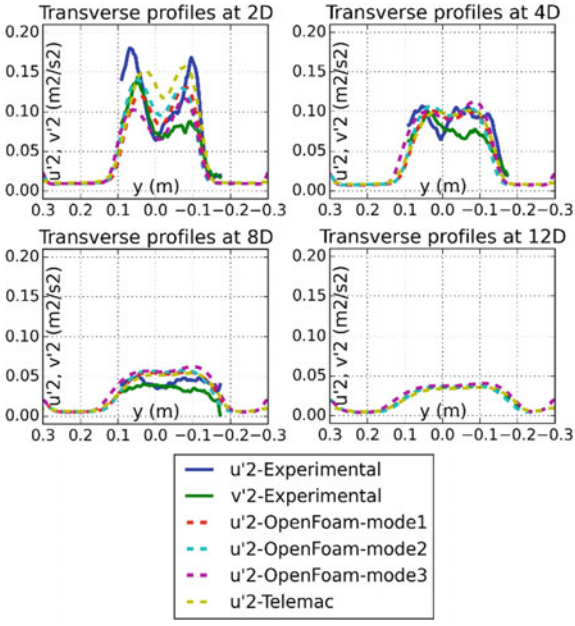

Fig. 10 Transverse u'^2 and v'^2 profiles compared between the experiment, the three OpenFoam simulations and the TELEMAC simulation

optimal operating point, the URANS simulated forces are very close to the measured ones and no correction of force is needed in the simplified model.

Measurements of the power coefficient, the axial and transverse forces applied on the turbine, and PIV-images of its wake were obtained for two different turbulence cases, with turbulence intensities of 2–3% and 5.5% respectively. For channel velocities of 2.3 and 2.8 m/s, no significant differences could be found between the two cases for the power output and forces. A small influence on the wake was observed, the velocity deficit near the machine being higher without grid. Other differences were found without turbulence grid, for a lower velocity of 1.8 m/s. It seems that the regular grid limited sensitivity to the Reynolds number. Further studies are needed with higher turbulence levels corresponding to in situ river or tidal conditions, in order to attest the influence of a turbulent flow on a Darrieus turbine.

Different simplified models were simulated with OpenFoam and compared to measurements. At the optimal operating point ($\lambda = 2$), all models gave sensibly the same results. The forces were not dependent on the z direction and the experimental flow might have no component in that direction when flowing around the hydrofoil profiles of the blade. Smaller λ might result in a 3-dimensional flow on the hydrofoil walls and require a higher-resolution model. All simplified models underestimated the velocity just behind the turbine, but were in good agreement in the area between 4 diameters and 8 diameters behind the turbine, with only a slight overestimation of the velocity deficit in the far-wake.

Finally, a simplified model simulation conducted with TELEMAC3D proved to be in good agreement with the OpenFoam simulations, even if the channel geometry could not be respected.

In the future, it is planned that the same approach will be applied on a horizontal axis tidal turbine to strengthen the methodology developed.

Acknowledgements This work is part of the ANR 3DMMTA project financed by the french 'Agence nationale de la recherche'.

References

Aumelas, V. (2011). *Modélisation des hydroliennes à axe vertical libres ou carénées: développement d'un moyen expérimental et d'un moyen numérique pour l'étude de la cavitation*. PhD thesis, Grenoble-INP.

Badalamenti, C., & Prince, S. A. (2008) The effects of endplates on a rotating cylinder in crossflow. In *26th AIAA Applied Aerodynamics Conference*, Honolulu, Hawaii.

Bertrand, O., Rebai, A., & Girard, C. (2015, 13–16 October). Development of a three-dimensional model of a vertical-axis and transverse-flow hydrokinetic turbine. In *22nd Telemac & Mascaret User Club*, STFC Daresbury Laboratory, UK.

Chawdhary, S., Hill, C., Yang, X., Guala, M., Corren, D., Colby, J., & Sotiropoulos, F. (2017). Wake characteristics of a TriFrame of axial-flow hydrokinetic turbines. *Renewable Energy, 109*, 332–345.

De Dominicis, M., O'Hara, Murray R., & Wolf, J. (2017). Multi-scale ocean response to a large tidal stream turbine array. *Renewable Energy, 114,* 1160–1179.

Dominguez, F., Achard, J.-L., Zanette, J., & Corre, C. (2016). Fast power output prediction for a single row of ducted cross-flow water turbines using a BEM-RANS approach. *Renewable Energy, 89,* 658–670.

Draper, S., & Nishino, T. (2014). Centred and staggered arrangements of tidal turbines. *Journal of Fluid Mechanics, 739,* 72–93.

Garett, C., & Cummins, P. (2007). The efficiency of a turbine in a tidal channel. *Journal of Fluid Mechanics, 588,* 243–251.

Gebreslassie, M. G., Sanchez, S. O., Tabor, G. R., Belmont, M. R., Bruce, T., Payne, G. S., et al. (2016). Experimental and CFD analysis of the wake characteristics of tidal turbines. *International Journal of Marine Energy, 16,* 209–219.

Gebreslassie, M. G., Tabor, G. R., & Belmont, M. R. (2015). Investigation of the performance of a staggered configuration of tidal turbines using CFD. *Renewable Energy, 80,* 690–698.

Harrison, M. E., Batten, W. M. J., Myers, L. E., & Bahaj, A. S. (2009). A comparison between CFD simulations and experiments for predicting the far wake of horizontal axis tidal turbines. In *Proceedings of the 8th European Wave and Tidal Energy Conference*, Uppsala, Sweden.

Kinsey, T., & Dumas, G. (2017). Impact of channel blockage on the performance of axial and cross-flow hydrokinetic turbines. *Renewable Energy, 103,* 239–254.

Maître, T., Amet, E., & Pellone, C. (2013). Modeling of the flow in a Darrieus water turbine: Wall grid refinement analysis and comparison with experiments. *Renewable Energy, 51,* 497–512.

Menter, F. R. (1994). Two-equation Eddy-viscosity turbulence models for engineering applications. *AIAA Journal, 32*(8), 1598–1605.

Menter, F. R., Kuntz, M., & Langtry, R. (2003). Ten years of industrial experience with the SST turbulence model. In *Proceedings of the fourth international symposium on turbulence, heat and mass transfer* (pp. 625–632), Antalya, Turkey: Begell House.

Mycek, P., Gaurier, B., Germain, G., Pinon, G., & Rivoalen, E. (2014). Experimental study of the turbulence intensity effects on marine current turbines behaviour. Part I: One single turbine. *Renewable Energy, 66,* 729–746.

Myers, L., & Bahaj, A. S. (2006). Power output performance characteristics of a horizontal axis marine current turbine. *Renewable Energy, 31,* 197–208.

Nguyen, V. T., Guillou, S. S., Thiebot, J., & Santa Cruz, A. (2016). Modelling turbulence with an Actuator Disk representing a tidal turbine. *Renewable Energy, 97,* 625–635.

Nuernberg, M., & Tao, L. (2018). Three dimensional tidal turbine array simulations using OpenFOAM with dynamic mesh. *Ocean Engineering, 147,* 629–646.

Posa, A., Parker, C. M., Leftwich, M. C., & Balaras, E. (2016). Wake structure of a single vertical axis wind turbine. *International Journal of Heat and Fluid Flow, 61,* 75–84.

Roc, T., Conley, D. C., & Greaves, D. (2013). Methodology for tidal turbine representation in ocean circulation model. *Renewable Energy, 51,* 448–464.

Shives, M., & Crawford, C. (2015). Validation of a practical CFD method for predicting hydrokinetic turbine performance in wake shadow. In *Proceedings of the 11th European wave and tidal energy conference*, September 6–11, 2015, Nantes, France.

van der Laan, P. (2014). Efficient turbulence modelling for CFD wake simulation, PHD report, DTU Wind Energy.

Vennell, R. (2013). Exceeding the Betz limit with tidal turbines. *Renewable Energy, 55,* 277–285.

Vogel, C. R., Willden, R. H. J., & Houlsby, G. T. (2017). Power available from a depth-averaged simulation of a tidal turbine array. *Renewable Energy, 114,* 513–524.

Whelan, J. I., Graham, J. M. R., & Peir'o, J. (2009). A free-surface and blockage correction for tidal turbines. *Journal of Fluid Mechanics, 624,* 281–291.

Wimshurst, A., & Willden, R. (2016). Tidal power extraction on a streamwise bed slope. *Ocean Engineering, 125,* 70–81.

Assessing the Impact of Rows of Tidal-Stream Turbines on the Overtides of the M_2

D. Potter, S. Ilić and A. Folkard

Abstract Flood-ebb asymmetry of a tidal flow has important implications for net sediment transport and the potential extractable resource. The asymmetry of the tide in U.K. waters may be understood through the interaction of the M_2 (principal lunar) and M_4 (first even overtide of the M_2) tidal constituents. The interaction of the M_2 tide with a tidal-stream turbine will alter the M_4 tide, both augmenting and reducing the M_4 amplitude, leading to an alteration of flood-ebb asymmetry. In this chapter the impact of a row of tidal-stream turbines on the overtides of the M_2 has been investigated through a numerical modelling study. Further, the way that additional turbines alter the way the turbines impact the shallow-water tides individually is explored. The results of the modelling show that when deployed in a row, on average, the *peak* velocity deficit and change to the current magnitude asymmetry (CMA) per turbine was less than were it deployed alone. The difference between the per turbine impact of turbines in a row and that of an individual turbine grew as the number of turbines in the row, and therefore the row blockage, increased. Additionally, the total area of the model domain experiencing a change to the M_2 current and CMA > 1% increased with the addition of turbines to the row, for a row blockage >~10%, but remained similar to the single turbine case for lower blockage values. The implication of the change to the CMA by a turbine in a row for the asymmetry in energy conversion for its lateral neighbours was small as the turbines do not lie within the area of effect of their neighbours. However, the per turbine energy conversion increased as the number of turbines and row blockage increased, in line with theory.

Keywords Tidal-Stream turbines · Tidal asymmetry · Tidal-Stream array · Physical environment impact

D. Potter (✉) · S. Ilić · A. Folkard
Lancaster Environment Centre, Lancaster University, Lancaster, UK
e-mail: d.potter1@lancaster.ac.uk

K. D. Nguyen et al. (eds.), *Estuaries and Coastal Zones in Times of Global Change*, Springer Water,
https://doi.org/10.1007/978-981-15-2081-5_13

1 Introduction

The removal of kinetic energy from tidal flows will alter the nature of the flow local to turbines (e.g. Stallard et al. 2013), and for larger arrays of turbines, at the regional scale also (De Dominicis et al. 2017).

Locally, the velocity of the fluid passing through the turbine(s) will be reduced, and the vorticity of the flow will be increased, by the very presence of the device (Tritton 1988). This downstream flow region is known as the wake. The rotation of the turbine blades will add additional rotation to this wake (Chen and Lam 2014) and the turbine(s) will also present a blockage to the flow, resulting in some acceleration of flow around the turbine(s) (Masters et al. 2013).

Regionally, the removal of energy by turbines also results in reduced flow speeds and changes to tidal amplitudes (Ahmadian et al. 2012; O'Hara-Murray and Gallego 2017; De Dominicis et al. 2017). The blockage presented by the turbines also interferes with the tidal regime, altering the times of high and low tide and bay/estuarine flushing (Nash et al. 2014).

These alterations to the flow environment will have implications for; sediment transport and coastal morphodynamics (Neill et al. 2009, 2012; Robins et al. 2014), turbidity and water quality (Ahmadian et al. 2012), sessile species, dependent on the flows for the transport of food, waste and propagules and the propagation of odour, impacting species dependent on olfaction (Shields et al. 2011). At the regional-scale, the large-scale extraction of tidal energy may also impact on seasonal stratification, with knock-on effects for marine ecosystem dynamics and species behaviour (De Dominicis et al. 2017).

A further hydrodynamic alteration that has received less attention is the change to tidal asymmetry resulting from the deployment of tidal-stream turbines. Tidal asymmetry is an asymmetry between either the magnitude or duration of the rise and fall of the tide, or the flood and ebb tidal currents (Dronkers 1986; Wang et al. 1999). Asymmetry in the tide results from non-linear processes (Parker 1991) which grow in importance in shallower waters. For example, when the water depth (h) is shallow enough that the difference in water depth between high and low tide is non-negligible, i.e. $\eta/h \ll 1$ (where η is the water surface elevation) is no-longer true, frictional attenuation of momentum per unit volume will be greater at low tide than at high tide (Parker 1991), by virtue of the differing volumes of fluid under the tidal wave. Similarly, flood-ebb asymmetric attenuation of currents by tidal-stream turbines, will lead to changes to the flood-ebb asymmetry of tidal currents (Potter 2019).

The significance of this alteration to the flood-ebb asymmetry of the tidal current, by a turbine, lies in its consequences for other processes. For example, flood-ebb asymmetry of tidal currents plays an important role in sediment transport (Pingree and Griffiths 1979; Dronkers 1986; Wang et al. 1999). Also, asymmetry in currents also effects the technically exploitable resource (Bruder and Haas 2014; Neill et al. 2014; Robins et al. 2015). Thus, alterations to the asymmetry by the turbines may,

(a) alter local, possibly regional, sediment transport, and (b) effect the power-production of their neighbouring turbines. On this first point, changes to sediment transport as a result of tidal turbines have already been identified by Neill et al. (2009, 2012) and others.

With the changes to flood-ebb (tidal) current magnitude asymmetry (CMA) resulting from a single turbine having been explored in Potter 2019, this chapter will look to extend that work by exploring how this effect scales up to an array of turbines. Additionally, with multiple turbines present, it will also be possible to explore how the changes to the asymmetry will alter the power production of the turbines.

2 Experimental Approach

The approach taken in this study was to simulate the impact of the turbines numerically. This was done using the MIKE21 FM modelling system (DHI 2016). The MIKE21 code solves the depth-averaged, Reynolds-averaged Navier-Stokes equations, under the Boussinesq and hydrostatic pressure assumptions. The model geometry and mesh used in this study was the same as that of Potter (2019), an 80 km long, 1.08 km wide, 36 m deep, uniform rectangular channel. Fitted with a multi-scale unstructured mesh, with element sizes ranging from 30 to 40 m in a high-resolution region at the channel centre, where the turbines are to be deployed, to ~ 240 m near the boundaries. Figure 1 illustrates the model geometry and mesh.

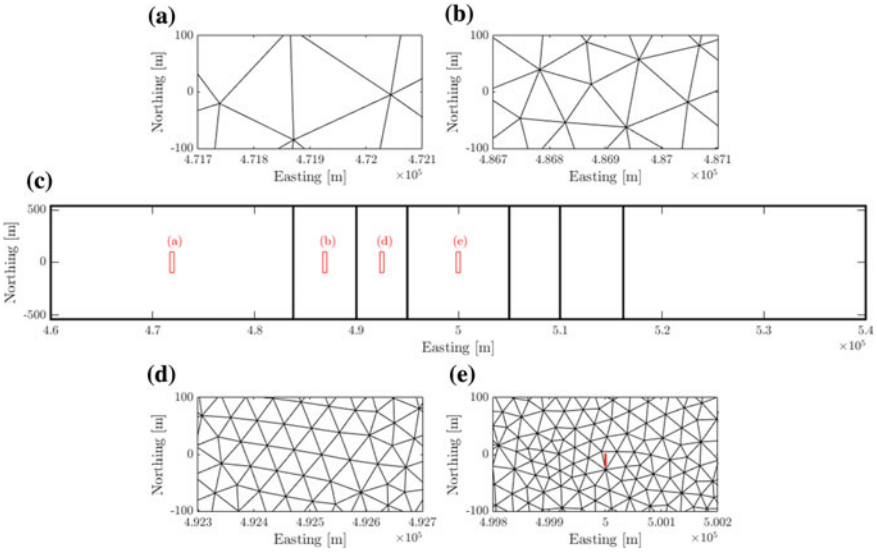

Fig. 1 Snapshots of model mesh (**a**, **b**, **d**, **e**) and outline of model geometry (**c**)

The model was forced at the two boundaries by only the M_2 tide,[1] with an amplitude of 5 m at both boundaries and a phase difference of 100° between the two boundaries, which introduces the head difference required to drive a flow through the channel. As a result of this elevation forcing, currents of up to 4.5 m/s were seen in the channel (Potter 2019). The model was run for a total of 4 days, which included a 24-hour spin-up period. The remaining 3 days was more than sufficient to identify the M_2, M_4 and M_6 harmonics of the surface elevation and current, by harmonic analysis, using the *t_tide*- MATLAB script (Pawlowicz et al. 2002).

In total, the experiment consisted of 6 model runs, the first (Run-1) ran the model with the channel unoccupied, the second (Run-2) with 9 turbines deployed in a single row, with an inter-turbine/turbine-wall spacing of 5*D*, where *D* is the turbine diameter. Further runs deployed additional turbines in the row so that the spacing reduced to 4*D* (Run-3), 3*D* (Run-4), 2*D* (Run-5) and 1*D* (Run-6). Corresponding to single rows of 9, 10, 13, 17 and 26 turbines respectively. The locations of the turbines in the mesh are illustrated in Fig. 2.

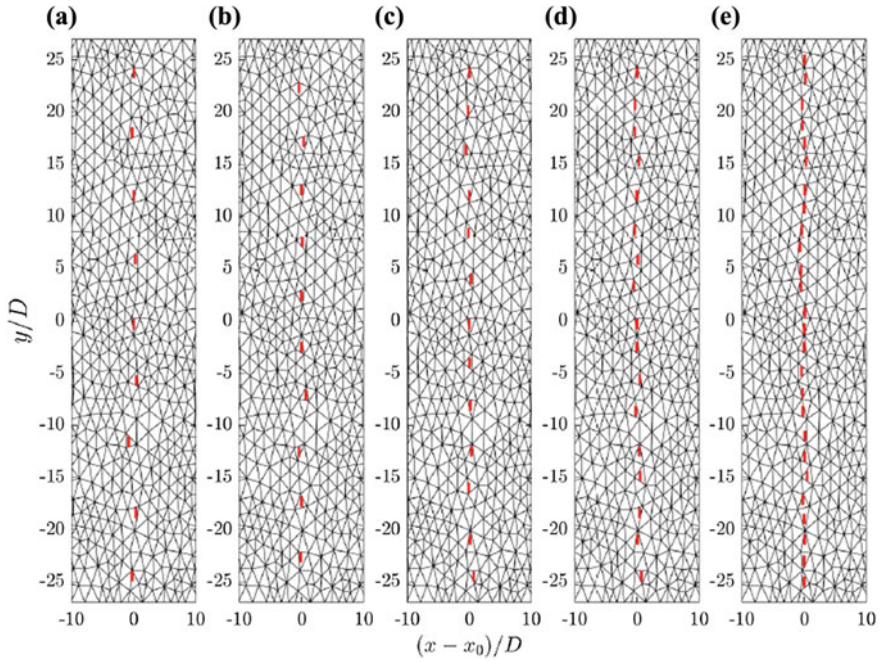

Fig. 2 Local mesh and turbine locations for; **a** 5*D* (9-turbine), **b** 4*D* (10-turbine), **c** 3*D* (13-turbine), **d** 2*D* (17-turbine) and **e** 1*D* (26-turbine), spaced row runs

[1]When simulating a real-world site, better representation of the harmonic generation within the model domain will be obtained by supplying the harmonic tides at the boundaries of the model (Le Provost and Fornerino 1985). As only an idealised case is considered in this work any choice of harmonics supplied at the boundaries would be somewhat arbitrary. Therefore, the simplest case was considered. The case of undistorted tides at either boundary, i.e. M_2 tide with negligible harmonics.

The turbines were simulated using MIKE21's in-built sub-grid turbine representation. Turbines were represented as sink terms in the momentum equations, based on actuator disk theory (DHI 2016). The sink term representing the turbine is given by:

$$F_T = \frac{1}{2}\rho_0 \alpha C_T A_T \vec{V}_0^2 \tag{1}$$

where ρ_0 is the water density, $A_T = \pi D^2/4$ is the turbine swept area, $D = 20$ m is the turbine diameter, $\vec{V}_0 = (u_0, v_0)$ is the undisturbed tidal current, u_0 and v_0 are its x- and y-components, α is a correction term given by Kramer et al. (2014) and C_T is the turbine thrust coefficient. In these experiments a fixed value of $C_T = 0.85$ is used based on the generic turbine thrust coefficient curve given by Baston et al. (2014).

Turbines were added such that each turbine only occupied a single mesh element, and each element only contained a single turbine. This was done in order to localize the turbine sink term as much as possible, and to ensure each sink represented just a single turbine, with view to better representation of reality.

Harmonic analysis of the currents in each model element was carried out for each of the runs, and the differences in the amplitudes and phases of each constituent calculated. The CMA in the current velocity time series was calculated, following Neill et al. (2014), using:

$$A_S = \frac{u_f - |u_e|}{\langle |u| \rangle} \tag{2}$$

where $u_{f,e}$ are the flood and ebb peak currents and $\langle\ \rangle$ denotes the mean over a tidal cycle. The change to this parameter, along with the changes to the M_2, M_4 and M_6 constituents of the tidal current resulting from the addition of the above rows of turbines to the channel will be explored and compared to the results of Potter (2019).

3 Results

3.1 Change to M_2, Overtides and Asymmetry

Potter (2019) used profiles running the channel length, through the turbine, to present the change to the harmonic parameters due to a single turbine. Rather than plotting 9–26 profiles per experiment, the mean across all profiles, at each point, i, along the profile, was calculated as follows:

$$\overline{\Delta X}(i,k) = \frac{1}{n}\sum_{j=1}^{n} \Delta X(i,j,k) \tag{3}$$

where n is the number of turbines in the row, ΔX is the change in parameter $X = u_{M2}, \psi_{M2}, \ldots, A_S$ between Run-1 and Run-k, where $k = 2, 3, 4, 5, 6$. For A_S and ψ_{M2} etc.:

$$\Delta X = X_1 - X_k \tag{4}$$

and for u_{M2} etc.:

$$\Delta X = \frac{X_1 - X_k}{X_1} \tag{5}$$

These single mean profiles, along with envelopes, given by the maximum, $\max_{d2}(\Delta X(i, j))$, where $\max_{d\delta}(X)$ is the maximum value of X across dimension δ) and minimum values across all profiles, $\min_{d2}(\Delta X(i, j))$, at point i along the profile, are plotted in Figs. 3, 4, 5 and 6. These figures show the change to the amplitude (Figs. 3 and 5) and phase (Figs. 4 and 6) of the M_2, M_4 and M_6 constituents resulting from the $5D$ (Figs. 3 and 4) and $1D$ (Figs. 5 and 6) spaced rows. In a similar fashion, the associated CMA change profiles are plotted in Fig. 7.

In the single turbine runs there was an ~ 8% reduction to the M_2 and M_6 current amplitudes local to the turbine, dying off moving away in either direction. For the M_4 current amplitude, there was augmentation of ~ 40% to the west, and reduction of ~ 10% to the east of the turbine. There was little change to the phase of the M_2 and M_6 currents (up to ~ 0.15° and ~ 1° respectively) seen with the addition of the

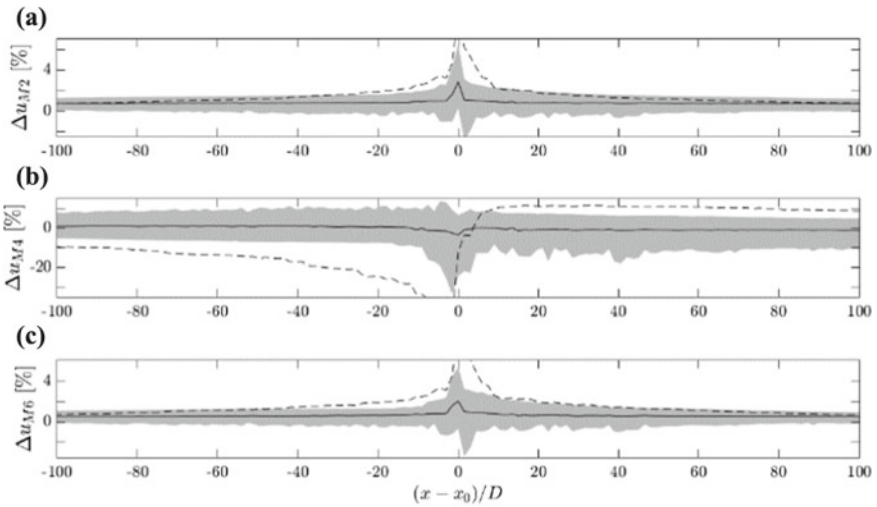

Fig. 3 Change to the amplitude of the M_2 (**a**), M_4 (**b**) and M_6 (**c**) current constituents, resulting from the $1D$ spaced row (Fig. 2e). Represented by the mean across all profiles (solid black line), and envelope given by maximum and minimum values across all profiles (shaded area). For comparison the single-turbine change-profile, from Potter (2019), is also plotted (dashed line)

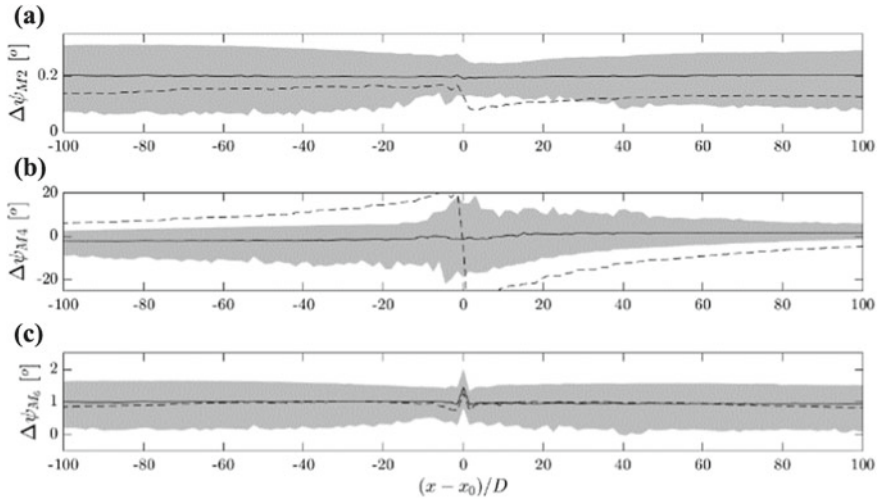

Fig. 4 Change to phase of the M_2 (**a**), M_4 (**b**) and M_6 (**c**) current constituents. Presented as described in Fig. 3

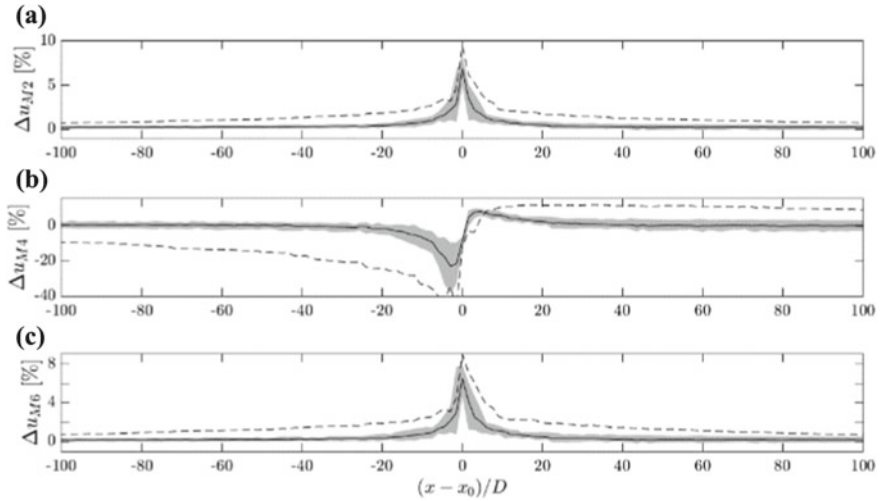

Fig. 5 As described in Fig. 3, but for the 5*D* row (Fig. 2a)

turbine. For the M_4 phase, there was a decrease of ~ 20° to the west of the turbine, and an increase of ~ 50° to the east.

For the 5*D* row (Figs. 5 and 6) the pattern of change that was seen for the single turbine deployment was again seen (e.g. Figure 5). However, the magnitude of the changes to all harmonic amplitudes and the M_4 phase was reduced. The same pattern, with reduced magnitudes of change, was seen for the 4*D* and 3*D* rows (not shown),

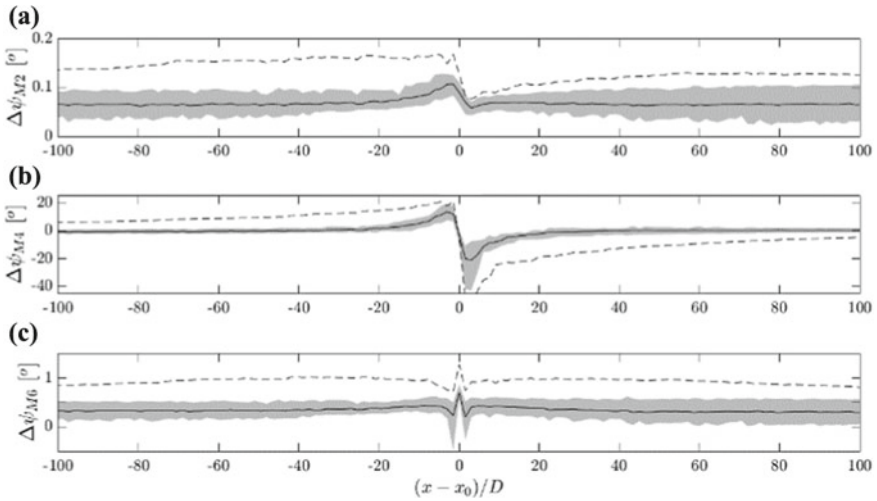

Fig. 6 As described in Fig. 4, but for the 5*D* row (Fig. 2a)

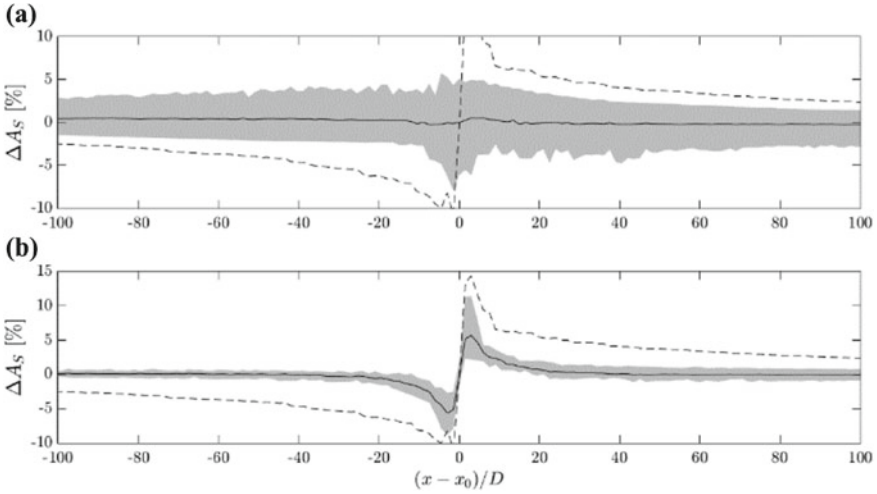

Fig. 7 Change to CMA due to 1*D* (**a**) and 5*D* (**b**) rows. Presented as described in Fig. 3

with the difference between the array and single turbine deployments growing with the addition of turbines to the row. However, the difference in the magnitude of the changes to the M_2 and M_6 phase between the row and single turbine deployments reduced with the addition of turbines to the row. For the 2*D* (not shown) and the 1*D* rows (Figs. 3 and 4), the single-turbine pattern of change was far less clear in the mean row profile. The magnitude of the changes were again much smaller for the amplitude of all tides and the phase of the M_4. For the M_2 phase the magnitude of the

changes were larger in the row deployment than for a single turbine (e.g. Figure 4a) and for the M_6 phase, the magnitude of the changes were similar (e.g. Figure 4c).

The change to the CMA resulting from the turbine row deployments again displays the same pattern of change to all parameters as was seen in the single turbine deployment, up to the $2D$ row, where the pattern is less clear. The magnitude of the changes to the CMA is always smaller in the row runs than the single turbine run (Fig. 7).

In summary; (i) the magnitude of the changes, *per turbine*, are smaller in an array than in the case of a single turbine (with the exception of the M_2 and M_6 phase), (ii) the difference increases with the number of turbines deployed in the row, and (iii) the variability across the profiles increases with more turbines added to the row (evidenced by the wider envelopes).

As the turbines were deployed so that they occupied just a single element, with more turbines occupying the row, it became harder to maintain both, a constant inter-turbine spacing, and along channel turbine position (see Fig. 2). It is therefore supposed that the greater variability in the turbine position is the cause of the increased variability of the profiles for the denser row runs, coupled with the variability of the size of the elements the turbines are deployed in.

To explore point (ii) above (and by extension point (i)), Fig. 8 plots the average of peak values across all profiles, for each of the row runs. The peak values were calculated by:

$$\overline{\Delta X_p}(k) = \frac{1}{n}\sum_{j=1}^{n} \max_{d1}(\Delta X(i, j, k)) \tag{6}$$

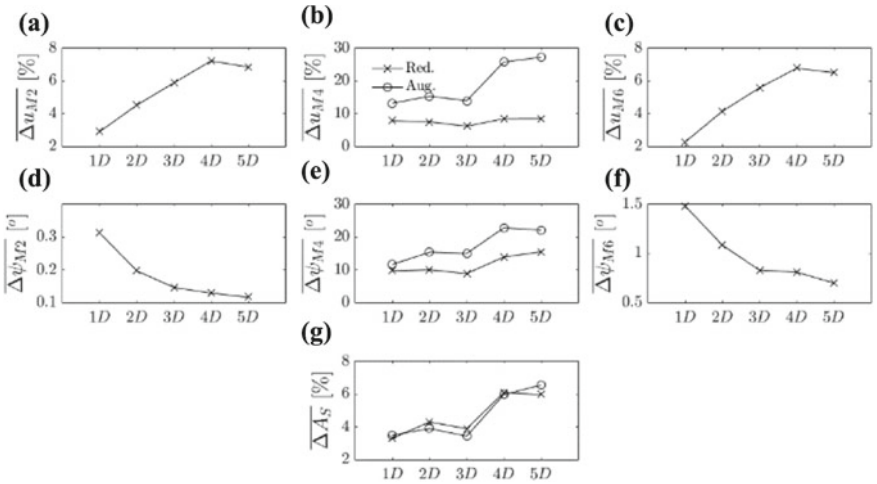

Fig. 8 Average peak values (augmentation: circles, reduction: crosses) across all profiles for each row. (**a**–**c**): current amplitude, (**d**–**f**): current phase, (**g**): CMA, (**a**) & (**d**): M_2, (**b**) & (**e**): M_4 and (**c**) & (**f**): M_6

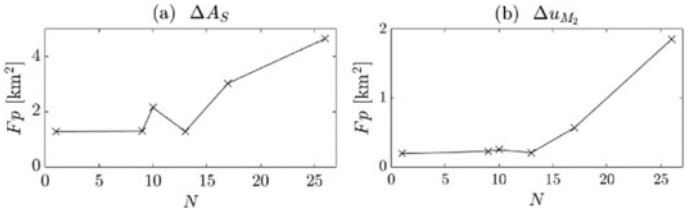

Fig. 9 Footprints of 5 rows mentioned above and single turbine from Potter (2019) on A_S (**a**), and u_{M2} (b). Here the rows are given by the number of turbines, N

The peak values of the augmentation (negative) peaks were calculated using (6) with $\max_{d1}(\,)$ replaced with $\min_{d1}(\,)$. From this figure one can see, as suspected from examination of Figs. 3, 4, 5, 6 and 7, that indeed, the average peak change per-turbine decreases with more turbines added to the row, in all but the cases of the M_2 and M_6 current phase.

As Fig. 8 only looks at the average peak values, it does not give the full picture. With more turbines in the row, one expects changes over a wider area. To explore this, the total areas where the absolute change to the M_2 amplitude (Δu_{M2}) and CMA ($|\Delta A_S|$) was $> 1\%$ were calculated. Henceforth these areas will be referred to as the array *footprint*, Fp. The footprint of the 5 rows, and the single turbine from Potter (2019), on the CMA and M_2 current amplitude are plotted in Fig. 9a, b respectively. In both cases, broadly speaking, the array footprint on both parameters changes little with further turbines added to the row, up to 13 turbines (corresponding to an inter-turbine spacing of $3D$ and a channel blockage at zero elevation of $\varepsilon_0 = NA_T/E \cong 0.1$, where E is the channel cross-sectional area) and is comparable to the footprint of a single turbine. Beyond this the footprint on both parameters increases sharply with additional turbines.

This perhaps hints at a balance between the reduced *per turbine* impact on the flow and the overall impact of the array due to the addition of turbines. A balance that is tipped beyond 13 turbines, or $\varepsilon_0 \cong 0.1$. A few things to note before drawing such a conclusion however. First, the plots in Fig. 9 are based on just 6 data-points. Trends and outliers would be clearer if the experiment was extended so that turbines were added to the channel one-by-one, giving more data-points. Second, the threshold of 1% was used, but it was arbitrarily chosen. However, what constitutes an appropriate threshold of change to u_{M2} or A_S is unknown and is likely to be site specific. This lies beyond the scope of this work as a thorough examination of the environmental consequences of various levels of change would be required.

As a quantitative examination of the knock-on environmental consequences of the changes to the hydrodynamics will not be considered here, the footprints from Fig. 9a, b will be re-expressed in Figs. 10 and 11. The total areas experiencing changes to u_{M2} and A_S lying within single percentage bins have been calculated, and this data presented as bar charts for ΔA_S and Δu_{M2} in Figs. 10 and 11 respectively. Thus, the choice of threshold, i.e. the level beyond which change is considered, e.g. $> 1\%$ used for Fig. 9, does not matter when presented this way, and a reader with a threshold

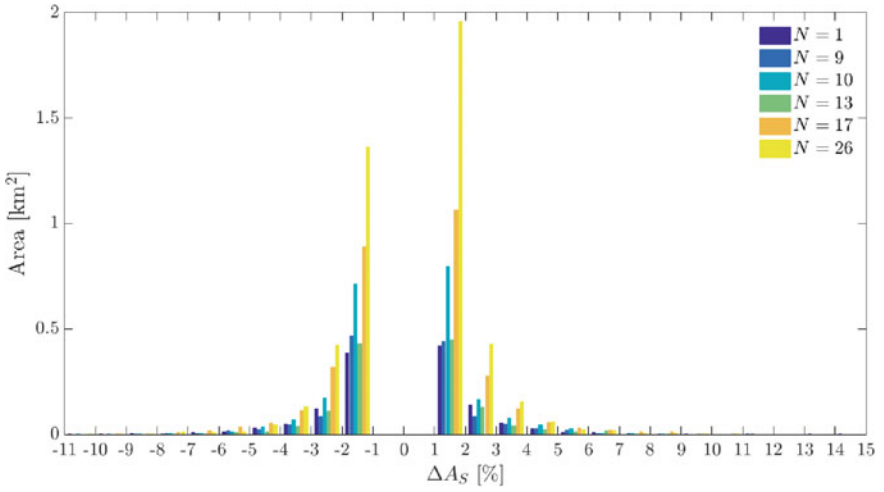

Fig. 10 Breakdown of row (and single turbine) footprints on CMA (A_S) into single percentage bins

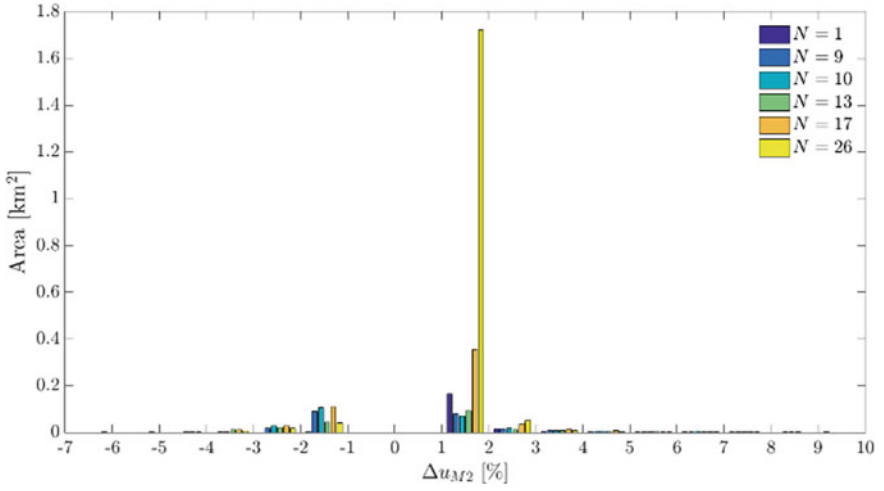

Fig. 11 Breakdown of row (and single turbine) footprints on the tidal current (u_{M2}: proxy) into single percentage bins

in mind may only consider the footprint beyond their chosen threshold. In Figs. 10 and 11, the −1 to 0% and 0 to 1% bins are not plotted, as in the majority of the channel there is no change, thus these bars dwarf all others, masking their pattern on a standard y-axis. For completeness, the footprints for all percentage bins are presented in Tables 1 and 2. In these tables, the absolute changes have been presented

Table 1 Breakdown of row (and single turbine) footprints (δFp) on the CMA (A_S) into single percentage bins. (Recall Fp_A defined for $|\Delta A_S| > 1\%$, so 0–1% row not included in summation for Fp)

N	1	9	10	13	17	26	$\delta Fp\times$
$\lvert\Delta A_S\rvert$	δFp (m^2)						
0–1%	8.51	8.51	8.42	8.51	8.34	8.17	$\times 10^7$
1–2%	0.81	0.91	1.51	0.88	1.95	3.32	$\times 10^6$
2–3%	2.60	1.72	3.41	2.41	5.94	8.50	$\times 10^5$
3–4%	1.02	0.97	1.49	0.77	2.36	2.88	$\times 10^5$
4–5%	0.56	0.52	0.82	0.36	1.11	1.05	$\times 10^5$
5–6%	2.41	3.82	4.15	2.38	6.54	3.98	$\times 10^4$
6–7%	1.59	1.01	1.38	1.87	3.63	2.61	$\times 10^4$
7–8%	0.35	0.75	0.81	0.28	2.22	1.73	$\times 10^4$
8–9%	3.72	2.27	1.70	0.58	14.80	5.79	$\times 10^3$
9–10%	2.56	0	2.04	0.70	1.89	2.10	$\times 10^3$
10–11%	1.08	0	0.40	0	0.35	0.76	$\times 10^3$
11–12%	0.92	1.02	0	0	0	0	$\times 10^3$
12–13%	0	0	0	0	0	0	–
13–14%	3.94	0	0	0	0	0	$\times 10^4$
14–15%	6.29	0	0	0	0	0	$\times 10^2$
$Fp\left(\text{m}^2\right)$	1.28	1.29	2.15	1.28	3.04	4.66	$\times 10^6$

Table 2 Breakdown of row (and single turbine) footprints (δFp) on the tidal current (u_{M2}: proxy) into single percentage bins. (Recall Fp_U defined for $|\Delta u_{M2}| > 1\%$, so 0–1% row not included in summation for Fp)

N	1	9	10	13	17	26	$\delta Fp\times$
$\lvert\Delta u_{M2}\rvert$	δFp (m^2)						
0–1%	8.62	8.62	8.62	8.62	8.58	8.45	$\times 10^7$
1–2%	1.65	1.69	1.77	1.40	4.65	17.60	$\times 10^5$
2–3%	1.59	3.33	4.51	3.20	6.03	6.95	$\times 10^4$
3–4%	0.43	0.88	0.88	1.79	2.55	1.03	$\times 10^4$
4–5%	1.28	5.41	6.12	6.64	12.60	5.23	$\times 10^3$
5–6%	1.12	2.89	2.49	4.94	1.35	2.22	$\times 10^3$
6–7%	0.39	2.95	3.61	0.92	0.49	1.13	$\times 10^3$
7–8%	0.93	1.03	1.46	1.28	1.32	0	$\times 10^3$
8–9%	0	9.02	8.17	4.88	0	0	$\times 10^2$
9–10%	4.36	0	0	0	0	0	$\times 10^2$
$Fp\left(\text{m}^2\right)$	1.89	2.24	2.45	2.04	5.67	18.50	$\times 10^5$

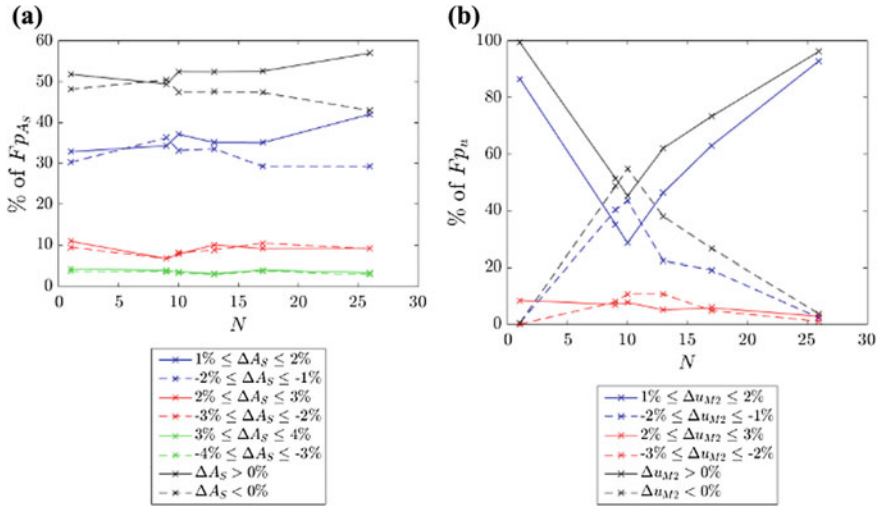

Fig. 12 Percentages of the total array footprint on the CMA (**a**) and M_2 current (**b**) falling in the 1–2% (blue), 2–3% (red) or 3–4% (green) range, with dashed lines indicating augmentation and solid lines reduction. Also plotted are the percentages of the total array footprint where augmentation (dashed black line) and reduction (solid black line) is seen

in the interest of brevity. However, the positive negative split can be approximately determined from Figs. 10 and 11.

For the *single turbine the area experiencing increased* currents ($\Delta u_{M2} < 0\%$), indicating accelerated bypass flow, was ~ 0% of Fp_u (Fig. 11), where Fp_u is the Fp of the turbine(s) on u_{M2}. For the 5D row the areas where $\Delta u_{M2} \leq -1\%$, $Fp_u^{<0}$, was approximately the same as the area where $\Delta u_{M2} \geq 1\%$, $Fp_u^{>0}$ (~ 49% and ~ 51% respectively). For the 4D row, $Fp_u^{<0}$ is larger than $Fp_u^{>0}$, i.e. currents are increased over a greater area than they are reduced. This can be seen in Fig. 11, but is illustrated more clearly in Fig. 12b. Up to this point with the addition of turbines to the row the area of bypass flow increases, and the area of flow reduction reduces. This is reversed for the 3D and 2D rows, and there was again a greater area experiencing reduced currents than augmented currents. Finally, for the 1D row the area experiencing augmented current is negligible compared to the area experiencing reduced currents, similar to the single turbine. For the CMA the positive/negative split of Fp_{A_S} remained similar across all rows (Fig. 12a).

The distribution of the absolute change to the CMA and current into the percentage bins remains similar across 5 row runs and the single turbine run (Fig. 13). In the case of the current, there is a small skewing of Fp_u towards higher percentage bins with the addition of turbines up to $N = 13$. Although it should be noted that with more turbines the very highest percentage changes are no longer seen (e.g. Table 2). Beyond $N = 13$ there is a small skewing of Fp_u towards the lower percentage changes, with > 90% of Fp_u in the $1\% \leq |\Delta u_{M2}| \leq 2\%$ range for the $N = 26$ (1D) row.

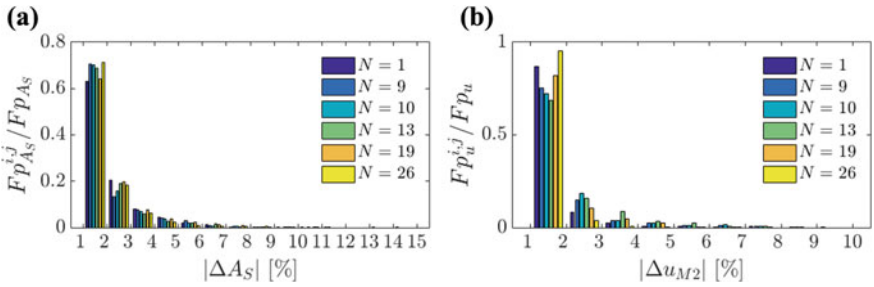

Fig. 13 Distribution of CMA (**a**) and current (**b**) footprints into absolute percentage bins. Areas in range $i\% \leq |\Delta X| \leq j\%$, $Fp_X^{i,j}$, normalised by overall footprint, Fp_X ($X = A_S, u_{M2}$)

3.2 Change to Turbine Power Production

Finally, the power production of the turbines was explored. This information is readily available from MIKE, as time-series of the turbine power are output by the model. The power time-series for a full M_2 period outside of the model spin-up period were used to calculate the turbine energy conversion per tidal cycle, $E_{t.c.}$, and the flood-ebb asymmetry in energy conversion, ΔE. These parameters were calculated as follows:

$$E_{f,e} = \int_{f,e} P dt \tag{7}$$

$$E_{t.c.} = E_f + E_e \tag{8}$$

$$\Delta E = 100 \times \frac{E_f - E_e}{E_f} \tag{9}$$

where f and e are the flood and ebb phases of the tidal cycle. $E_{t.c.}$ and ΔE were calculated for each turbine, in each row run. The mean and envelope of $E_{t.c.}$ and ΔE are presented in Fig. 14a, b respectively.

In Fig. 14, one can see that with more turbines added to the channel each turbine in the row on average converted more energy than a single turbine operating alone in the channel. This is despite the decreasing per turbine velocity reduction with additional turbines.

The (flood-ebb) asymmetry in the energy conversion, remained at a similar level, ~ 27–31%, on average, even with additional turbines added to the channel. However, for the denser rows the variability in the asymmetry across the turbines in the row increased. This is expected to, in a large part, be due to the increased variability in the turbines position, in terms of inter-turbine spacing and along channel position, with more turbines in the channel. The change to the asymmetry resulting from the turbine occurs mostly in the along channel direction, the two-dimensional structure is a familiar wake structure. Therefore, when the along channel position of the turbines is

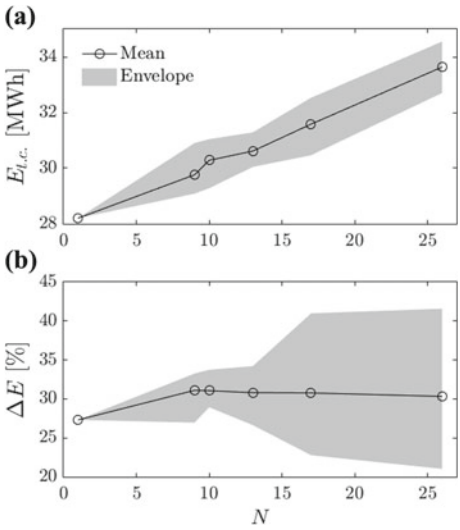

Fig. 14 Per-turbine energy conversion per tidal cycle, $E_{l.c.}$ (**a**), and per-turbine flood-ebb asymmetry in energy conversion, ΔE (**b**). Values plotted for rows 1, 9, 10, 13, 17 and 26 turbines, corresponding to blockage ratios of $\varepsilon_0 = 0.008$, 0.073, 0.081, 0.105, 0.137 and 0.210 respectively

varied in conjunction with the turbines being located closer together, some interaction of the turbines and wakes may occur, resulting in the varied effect seen.

4 Discussion

The goal of this numerical investigation was to explore how the change to the CMA resulting from tidal-stream turbine operation, identified by Potter (2019), scales up with multiple turbines. Despite the use of the inter-turbine spacing in the definition of the rows, this study *does not* give any conclusive statement about the effect of the inter-turbine spacing on the change to CMA. This is due to the changing number of turbines, and therefore changing blockage ratio. Therefore, the results will henceforth be discussed in the context of changing blockage. To look at the effect of spacing specifically, further runs would be required, where the spacing between turbines is reduced whilst keeping the total number of turbines, N, fixed.

It was seen that with increased row blockage the peak per-turbine change to the CMA actually decreased. The reason for this lies in the fact that it is the turbine wake that is of central importance to the changes to the CMA resulting from turbine operation, as discussed by Potter (2019). Potter (2019) concluded that it was the temporal variability in the spatial distribution of current attenuation by the turbine that leads to the change to the CMA. The current is attenuated downstream of the turbine, and what is downstream of the turbine changes on the flood and ebb of the

tide as the direction of the current changes. Therefore, in some regions the flood current is attenuated, and in others the ebb current is attenuated, which alters the CMA. Thus, both the spatial extent and magnitude of the change to the CMA is intrinsically linked to the extent and magnitude of the current attenuation (wake).

The change to the spatial extent of CMA change with the addition of turbines to the row (Fig. 9a) follows the same pattern as the change to the spatial extent of the current deficit with the addition of turbine to the row (Fig. 9b). The footprint of the array is similar for a single turbine, up to 13 turbines, with a blockage of $\varepsilon_0 \cong 0.1$. However, for the CMA footprint the distribution of area across the bins remains approximately the same for each of the row deployments. This is not the case for the current footprint, Fp_u. For Fp_u with the addition of turbines up to 13 turbines ($\varepsilon_0 \cong 0.1$) there is a skewing of the distribution of area towards the higher percentage bins. This reverses beyond $N = 13$ ($3D$ row) and for $N = 19$, 26 ($2D$ and $1D$ rows respectively) the distribution is similar to that of the single turbine.

Another interesting feature of the Fp_u distribution is the change in (percentage) share of Fp_u where augmentation/reduction to the current was seen (Fig. 12b). Adding turbines to the row up to $N = 10$, less and less of Fp_u is reduction to u_{M2} and more and more is augmentation. With a greater share of Fp_u indicating accelerated bypass flow, than reduced wake flow for $N = 10$ ($4D$ row). With additional turbines there will be greater constriction of the flow through the gaps, and more gaps, thus flow acceleration over a greater area.

This then reverses for additional turbines beyond $N = 10$, and for $N = 26$ ($5D$ row), the augmentation share of Fp_u is negligible compared to the reduction share. Stallard et al. 2013 identified wake merging downstream of rows of turbines when they were deployed with spacings of $2D$ or less. This coupled with the model resolution may explain drop-off in the share of the footprint where augmentation to the current was seen. In the near turbine region the element face length was similar to the turbine diameter. Therefore, for the more densely packed rows the resolution of the model may not be sufficient to fully resolve the shrinking regions of flow acceleration between the turbine gaps and the merging wakes.

The similar size of Fp with the addition of turbines implies that each turbines wake has a smaller spatial extent. The magnitude of the peak velocity deficit in the wake (or surplus in the case of the M_4 current) was also seen to reduce with additional turbines added to the channel (beyond $N = 10$ at least) (Fig. 8). This pattern was seen for the M_4 phase also (Fig. 8). Conversely, the peak, *per turbine*, change to the phase of the M_2 and M_6 increased with turbines added to the row (Fig. 8).

The trend of increased phase lag to the M_2, a proxy for the total tidal current, follows physical intuition. The turbines impede the flow, leading to a phase lag, the more turbines, the greater the impediment, the greater the induced phase lag.

The decreasing reduction to the current amplitude with additional turbines can be understood together with the increasing phase lag. The increased impediment to the flow leads to the build-up of a head difference across the row. As such the turbine energy conversion comes from both head-loss and momentum reduction, leading to smaller momentum reduction by the turbines (Vennell 2012, 2013). Also, further turbines in the row means greater thrust imparted on the flow through the channel, and

therefore a reduced upstream velocity (Garrett and Cummins 2007; Vennell 2010), implying reduced velocity through the turbines. The force exerted onto the flow by the turbines depends on the inflow speed and thus will also be reduced, which will also decrease the velocity reduction by the turbines.

Despite the reduced, *per turbine*, peak M_2 velocity deficit the *per turbine* energy conversion increased as turbines were added to the row. This is linked to the above discussion. With the more turbines added to the row the turbines convert energy from the increased head difference across the row as well as from the current. Also, at higher blockage of the channel, the turbines will convert energy more efficiently as there is less energy loss due to downstream mixing of the wake and bypass flow (Garrett and Cummins 2007; Vennell 2010).

The change to the blockage appears to have little bearing on the asymmetry of energy conversion, despite the reduced change to CMA with increased blockage. The physical explanation for this requires further consideration. It may be that in our idealised, rectilinear case, changes to the CMA are restricted to the along channel direction, and for the inter-turbine spacings considered, these changes have little bearing on the asymmetry of the incident flow for across-channel neighbours. We also note the large variability in the calculated asymmetry in energy conversion for the higher blockage rows.

The importance of the wake for the change to the CMA raises the issue of accurate simulation of the turbine wake. In MIKE the turbine is represented as a sink term in the 2D momentum equations, based on actuator disk theory (DHI 2016). More accurate representation of the turbine wake can be achieved by also adding source and sink terms to the model's turbulence closure scheme (Roc et al. 2013, 2014). The actuator-disk representation itself may be improved on by using an actuator line representation (e.g. Churchfield et al. 2011) or blade element momentum (BEM) theory (e.g. Masters et al. 2013). These latter two representations incur a much greater computational cost. In coastal scale models, such as MIKE, the turbines are represented as sub-grid scale objects, in actuator line and BEM representations many elements span the swept area of the turbine. For this project the increased computational cost for these more detailed simulations was prohibitive. Also, the variation of surface elevation plays an essential role in the generation of the shallow-water tidal constituents (Parker 1991; Le Provost 1991) which favored the choice of coastal model, and therefore sub-grid scale turbine representation.

The experiment presented here requires expansion to (i) consider the effect of inter-turbine, for fixed blockage, on the turbine wakes, (ii) consider a wider range of N values, e.g. $N = 1, 2, \ldots 26$, and (iii) refine the model mesh. On this latter point it is suggested that in future work the mesh is designed so that the size of the elements that the turbines are deployed in are identical. In MIKE, this may be achieved by using N square elements for the turbines and triangular elements elsewhere. This method also has the advantage that the resolution between turbines may be increased allowing for increased resolution of the turbine wakes and bypass flow.

5 Conclusion

The scaling up of alteration to the CMA by a tidal-stream turbine was explored in this work using a highly idealised model geometry, and a regional coastal modelling system (MIKE21). It was found that:

(1) The peak alteration (both augmentation and reduction) to the M_4 tidal harmonic (amplitude and phase) by the turbine reduced as the row blockage was increased.
(2) The peak reduction to the M_2 and M_6 amplitude also reduced with increased row blockage. However, the peak imparted phase lag increased for both constituents.
(3) These changes (1 & 2) resulted in reduced peak alteration (both augmentation and reduction) to the CMA with increased blockage.
(4) The overall spatial extend of the (absolute) change (> 1%, to A_S or u_{M2}) increased as the blockage of the row increased. However, this result is sensitive to the choice of change threshold, and significant increase is only seen for $\varepsilon_0 \gtrsim 0.1$/inter-turbine spacings $\lesssim 2D$.
(5) Despite the changes to the CMA, the asymmetry in the *average per-turbine* energy conversion in the row varied little. However, there was a large variability in the energy conversion asymmetry across the turbines in the row, which grew with increased blockage (and therefore more turbines). This expected to be partially a numeric effect, and partial related to the experimental set-up.

Points 1 and 2, and by extension 3, are in accordance with analytical work (Garrett and Cummins 2007; Vennell 2010). Increased blockage reduces the velocity deficit in the turbine wakes, which has implications for the change to the M_4 constituent, and therefore CMA. The apparent lack of implication of changes to the CMA for the asymmetry in turbine energy conversion is suspected to be due to the turbines lying outside the area of effect of each other.

Acknowledgements This work was funded by a Natural Environment Research Council studentship, part of the ENVISON Doctoral Training Program, awarded to the lead author. Thanks also goes to DHI UK for providing a student licence for MIKE, allowing this work to be undertaken.

References

Ahmadian, R., Falconer, R., & Bockelmann-Evans, B. (2012). Far-field modelling of the hydro-environmental impact of tidal stream turbines. *Renewable Energy, 38,* 107–116.

Baston, S., Waldman, S., & Side, J. (2014). Modelling energy extraction in tidal flows. In *TerraWatt Position Papers* (p. 102). MASTS.

Bruder, B., & Haas, K. (2014). Tidal distortion as pertains to hydrokinetic turbine selection and resource assessment. In *Proceedings of the 2nd Marine Energy Technology Symposium*, METS2014, 15–18 April, 2014, Seattle, WA.

Chen, L., & Lam, W. (2014). Slipstream between marine current turbine and seabed. *Energy, 68,* 801–810.

Churchfield, M., Li, Y., & Moriarty, P. (2011). A large-eddy simulation study of wake propagation and power production in an array of tidal-current turbines. In *Proceedings of EWTEC 2011*, Southampton.

De Dominicis, M., O'Hara-Murray, R., & Wolf, J. (2017). Multi-scale ocean response to a large tidal-stream turbine array. *Renewable Energy, 114,* 1160–1179.

DHI. (2016). *MIKE 21 & MIKE 3 flow model FM, hydrodynamic and transport module, scientific documentation*.

Dronkers, J. (1986). Tidal asymmetry and estuarine morphology. *Netherlands Journal of Sea Research, 20,* 119–131.

Garrett, C., & Cummins, P. (2007). The efficiency of a turbine in a tidal channel. *Journal of Fluid Mechanics, 588,* 243–251.

Kramer, S., Piggott, M., Hill, J., Kregting, L., Pritchard, D., & Elsaesser, B. (2014). The modelling of tidal turbine farms using multi-scale, unstructured mesh models. In *Proceedings of the 2nd International Conference on Environmental Interactions of Marine Renewable Energy Technologies (EMIR 2014)*. Stornoway, Scotland.

Le Provost, C. (1991). Generation of overtides and compound tides (review). In B. Parker (Ed.), *Tidal hydrodynamics*. New York: Wiley.

Le Provost, C., & Fornerino, M. (1985). Tidal spectroscopy of the English Channel with a numerical model. *Journal of Physical Oceanography, 15,* 1009–1031.

Masters, I., Malki, R., Williams, A., & Croft, T. (2013). The influence of flow acceleration on tidal stream turbine wake dynamics: A numerical study using a coupled BEM-CFD model. *Applied Mathematical Modelling, 37,* 7905–7918.

Nash, S., O'Brien, N., Olbert, A., & Hartnett, M. (2014). Modelling the far field hydro-environmental impacts of tidal farms—A focus on tidal regime, inter-tidal zones and flushing. *Computers & Geoscience, 71,* 20–27.

Neill, S., Litt, E., Couch, S., & Davies, A. (2009). The impact of tidal stream turbines on large scale sediment dynamics. *Renewable Energy, 34,* 2803–2812.

Neill, S., Jordan, J., & Couch, S. (2012). Impact of tidal energy converter (TEC) arrays on the dynamics of headland sand banks. *Renewable Energy, 37,* 387–397.

Neill, S., Hashemi, M., & Lewis, M. (2014). The role of asymmetry in characterizing the tidal resource of Orkney. *Renewable Energy, 68,* 337–350.

O'Hara-Murray, R., & Gallego, A. (2017). A modelling study of the tidal stream resource of the Pentland Firth, Scotland. *Renewable Energy, 102,* 326–340.

Parker, B. (1991). The relative importance of the various nonlinear mechanisms in a wide range of tidal interactions (review). In B. Parker (Ed.), *Tidal hydrodynamics*. New York: Wiley.

Pawlowicz, R., Beardsley, B., & Lentz, S. (2002). Classical tidal harmonic analysis including error estimates in MATLAB using *t_tide*. *Computers & Geoscience, 28,* 929–937.

Potter, D. (2019). *Alteration to the shallow-water tides and tidal asymmetry by tidal-stream turbines*. Ph.D. thesis, Lancaster University.

Pingree, R., & Griffiths, D. (1979). Sand transport pathways around the British Isles resulting from the M2 and M4 tidal interactions. *Journal of the Marine Biological Association of the United Kingdom, 59*, 497–513.

Robins, P., Neill, S., & Lewis, M. (2014). Impact of tidal-stream arrays in relation to the natural variability of sedimentary processes. *Renewable Energy, 72,* 311–321.

Robins, P., Neill, S., Lewis, M., & Ward, S. (2015). Characterising the spatial and temporal variability of the tidal-stream energy resource over the northwest European shelf seas. *Applied Energy, 147,* 510–522.

Roc, T., Conley, D., & Greaves, D. (2013). Methodology for tidal turbine representation in ocean circulation model. *Renewable Energy, 51,* 448–464.

Roc, T., Greaves, D., Thyng, K., & Conley, D. (2014). Tidal turbine representation in an ocean circulation model: Towards realistic applications. *Ocean Engineering, 78,* 95–111.

Shields, M., Woolf, D., Grist, E., Kerr, S., Jackson, A., Harris, R., et al. (2011). Marine renewable energy: The ecological implications of altering the hydrodynamics of the marine environment. *Ocean and Coastal Management, 54,* 2–9.

Stallard, T., Collings, R., Feng, T., & Whelan, J. (2013). Interactions between tidal turbine wakes: Experimental study of a group of three-bladed rotors. *Philosophical Transactions of the Royal Society A: Mathematical, Physical and Engineering Sciences, 371,* 20120159.

Tritton, D. (1988). *Physical fluid dynamics* (2nd ed.). London: Clarendon Press.

Vennell, R. (2010). Tuning tidal turbines in a channel. *Journal of Fluid Mechanics, 663,* 253–267.

Vennell, R. (2012). Realizing the potential of tidal currents and the efficiency of turbine farms in a channel. *Renewable Energy, 47,* 95–102.

Vennell, R. (2013). Exceeding the Betz limit with tidal turbines. *Renewable Energy, 55,* 277–285.

Wang, Z., Jeuken, C., & de Vriend, H. (1999). *Tidal asymmetry and residual sediment transport in estuaries.* Technical Report Z2749, WL Delft Hydraulics, Delft, Netherlands.

Evaluating the Effects of Tidal Turbines on Water-Mass Transport with the Lagrangian Barycentric Method

Nicolas Guillou and Georges Chapalain

Abstract Characterising circulation pathways in tidal stream energy sites is fundamental to evaluate the effects of turbines power extraction on the transport of water-mass and associated particles. The Lagrangian residual currents are commonly considered to assess the displacement of water particles over the tidal period. The associated circulation is, however, characterised by a strong dispersion as water particles may follow different trajectories depending on the release time during a tidal cycle. In order to obtain a synthetic cartography of the Lagrangian Residual Circulation (LRC), Salomon et al. (1988) proposed an original method allocating the residual currents at the barycentre of particle trajectories. This Lagrangian barycentric method was here applied to the Fromveur Strait (western Brittany)—a region with strong potential for turbine farm implementation along the coast of France. A high-resolution depth-averaged numerical model computed the tidal circulation driven by the principal lunar semi-diurnal constituent M_2. The initial particle positions were taken at the 14,026 nodes of the unstructured computational grid surrounding the area of interest with a spatial resolution below 50 m. In the strait, the LRC was characterised by a strong asymmetry between (i) a prominent north-eastern pathway with residual currents up to 0.45 ms^{-1} and (ii) a southward circulation. Both upstream and downstream of the strait, we exhibited furthermore prominent cyclonic and anti-cyclonic recirculations. A close correlation was found between the north eddy and a prominent sand bank. We simulated finally the forces induced by a series of horizontal-axis turbines as an additional bed friction sink term at the scale of the tidal farm. The extraction of tidal stream energy modified the magnitude and direction of the LRC along the current stream emerging from the strait with (i) a tendency for surrounding eddies to get closer to the tidal stream energy site and (ii) potential effects on nearby sandbanks.

Keywords Water particles · Lagrangian residual current · Numerical modelling · Telemac · Fromveur strait

N. Guillou (✉) · G. Chapalain
Cerema, DtecEMF, ER, Laboratoire de Génie Côtier et Environnement, 155 rue Pierre Bouguer, Technopôle Brest-Iroise, BP 5, 29280 Plouzané, France
e-mail: nicolas.guillou@cerema.fr

K. D. Nguyen et al. (eds.), *Estuaries and Coastal Zones in Times of Global Change*, Springer Water,
https://doi.org/10.1007/978-981-15-2081-5_14

1 Introduction

The evaluation of water-mass transport in tidal stream energy sites is of great ecological interest in assessing water-quality changes induced by turbines power extraction. This includes effects on trapping and dispersion of fish eggs, larvae, nutrients, and suspended sediments (Edwards et al. 2006). But it may also serve specific objectives like transport predictions of (i) drifters potentially harmful to structures' blades or (ii) polluting substances accidentally released by devices (Sanderson and Redden 2015). Transport studies in stream energy sites were, however, primarily dedicated to changes induced by turbines on sediment transport (e.g., Neill et al. 2012; Fairley et al. 2015; Thiébot et al. 2015). Shapiro (2011) conducted a preliminary numerical evaluation of turbines' effects on passive tracer pathways in the Celtic Sea, north of Cornwall (the United-Kingdom). Nevertheless, simulations operated a single release of floats disregarding the influence of the initial drop time on particle trajectories.

In this study, we investigated the impacts of tidal stream power extraction on the long-term displacement of water particles by exhibiting changes induced on the Lagrangian Residual Circulation (LRC). As water particles may follow different trajectories depending on the release time during a tidal cycle, residual currents are characterised by a strong dispersion and are difficult to define in a single synoptic view. We thus relied on an original method, proposed by Salomon et al. (1988), to map the LRC in the English Channel and western Brittany. This technique, denominated as the Lagrangian barycentric method, was applied for a tidal circulation driven by a single tidal harmonic, such as the principal lunar semi-diurnal component M_2 along the Atlantic coast of Europe. It provided furthermore a first overview of long-term transport pathways in north-western European shelf seas while significantly reducing the computational time (Orbi and Salomon 1988; Salomon and Breton 1993; Breton and Salomon 1995).

In this study, this method was applied to the tidal stream energy site of the Fromveur Strait, off western Brittany (France, Fig. 1). This strait, with a width of 2 km and a mean water depth of 50 m, separates Ushant island from the Molène archipelago, a series of island extending from the landmass. This location was identified, with the Alderney Race in the English Channel, as one of the largest tidal stream energy resources along the coast of France (Guillou et al. 2018). The French government thus delimited a restricted area of 4 km^2 within the strait for the implementation of tidal stream arrays. A series of numerical investigations were conducted in this site to refine the predictions of available tidal kinetic energy and evaluate the short-term hydrodynamic effects induced by tidal stream power extraction (Guillou et al. 2016; Guillou and Thiébot 2016a, b; Guillou 2017). Nevertheless, no modelling study was dedicated to capture of, at high-spatial resolutions (~ 50 to 100 m), (i) the tide-induced circulation pathways in this strait and (ii) the changes associated with tidal stream power extraction.

An original approach was adopted to couple the Lagrangian barycentric method (Sect. 2.1) with numerical predictions of particle tracking obtained at high-spatial

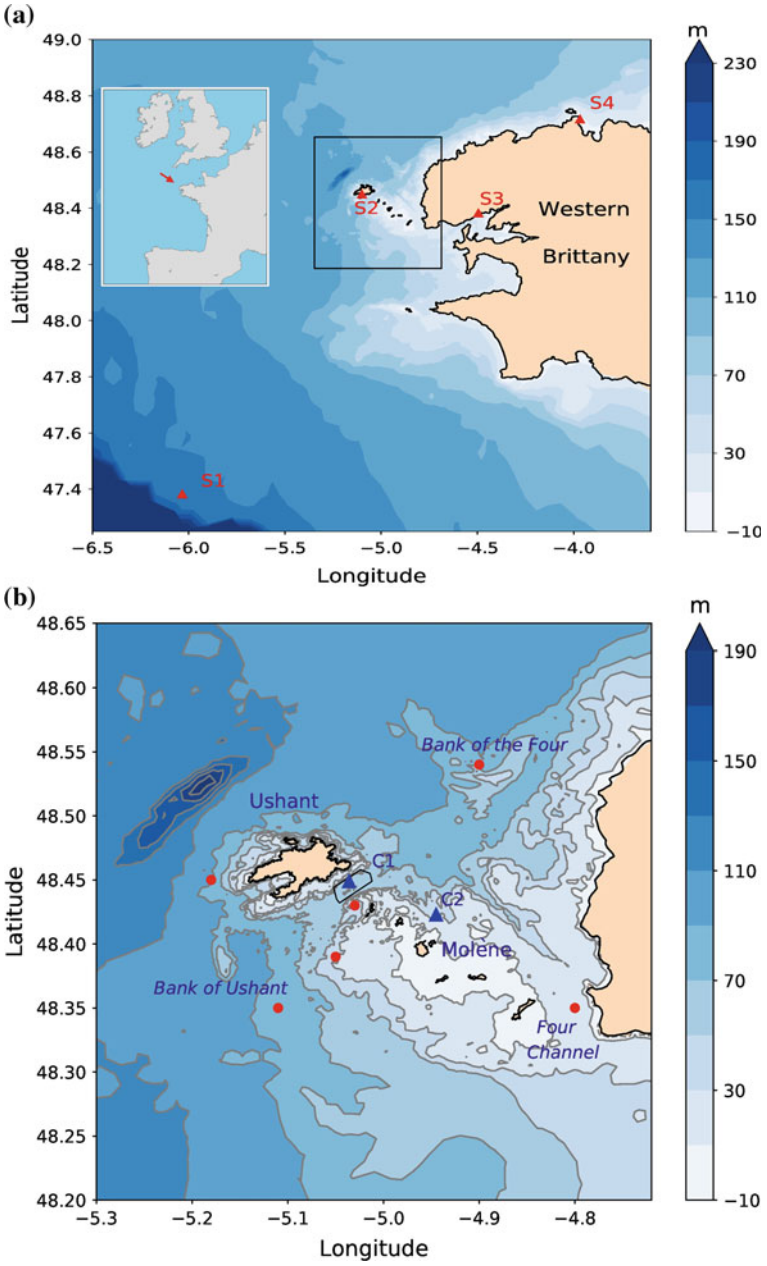

Fig. 1 Bathymetry of the Ushant-Molène archipelago with locations of available tidal gauges S1-S4 (red triangles), current meters C1 and C2 (blue triangles) and initial positions of floats for assessing long-term particles trajectories (red circles). The black line delimits the area of interest for turbine implementation in the Fromveur Strait. Water depth is relative to mean sea level

resolution in the strait (Sect. 2.2). Predictions were assessed against available measurements of current magnitude and direction at two locations in the area of interest (Sect. 3.1). LRC patterns were interpreted in relation to the tidal-current asymmetry and recirculations in the area of interest (Sect. 3.2). This investigation was completed by an analysis of long-term particle trajectories (Sect. 3.3). Changes induced by a series of horizontal-axis turbines, varying in numbers, were finally evaluated (Sect. 3.4).

2 Materials and Methods

2.1 Lagrangian Barycentric Method

The different steps of the Lagrangian barycentric method are briefly detailed hereafter. Further information can be found in Salomon et al. (1988), Orbi and Salomon (1988), and Salomon and Breton (1993).

The first step is to compute, based on a particle-tracking numerical method, the trajectories of drifters released at hourly intervals during a tidal cycle. The circulation model is driven by a mono-frequency tide to emphasise the single period that characterises the long-term displacements of water particles. The dominant semi-diurnal constituent M_2 is usually retained along the European Atlantic coast. The initial particle positions have to be spread over the area of interest while covering, with a refined spatial resolution, shoals and coastal irregularities that may impact the tidal circulation.

The second step is to compute the Lagrangian residual currents defined as the displacements of water particles over the tidal period considered (Zimmerman 1979). For a given initial position, a series of Lagrangian residual currents is thus obtained, the total number matching with the number of particles released during a tidal cycle. The computed vector field presents, however, a strong dispersion that exhibits the influence of the release time on particle trajectories (Fig. 2). At a given position, this is characterised by a beam of Lagrangian velocities that is very difficult to analyse and interpret. In order to reduce the dispersion of the vector field, residual currents are allocated at the barycentre of computed trajectories, considered to be more representative of particle displacements.

The non-divergence of the velocity field is finally evaluated. The result is a single Lagrangian residual velocity field that can be exploited to identify and depict the major patterns of tide-induced particle transport.

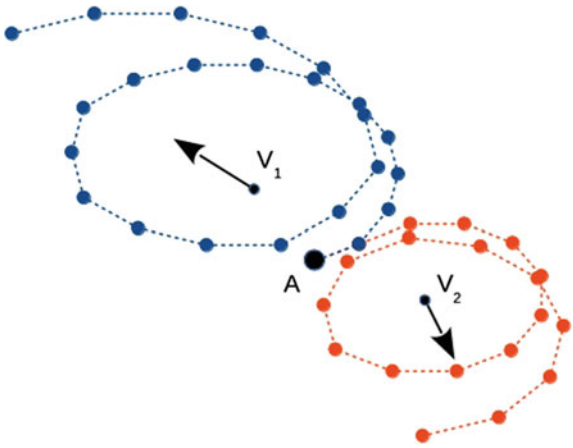

Fig. 2 Schematic representation of the barycentric system

2.2 *Numerical Modelling*

The application of the Lagrangian barycentric method in the Fromveur Strait relied on numerical simulations of tidal currents conducted by Guillou and Thiébot (2016a, b). The depth-averaged model Telemac 2D (version v6p3; Hervouet 2007) was implemented on an unstructured computational grid covering the western extend of Brittany with a spatial resolution of 10 km at offshore sea boundaries to less than 50 m in the strait. Whereas the area of interest may be subjected to storm wave conditions liable to impact tidal currents (e.g., Guillou and Chapalain 2015; Guillou et al. 2016), these effects were disregarded driving simulations with the dominant M_2 component and its quarter-diurnal generated harmonic M_4. Integrating the M_4 forcings was found to improve its generation from M_2 in the numerical model, in particular at open boundaries close to landmass (Pingree and Maddock 1978; Guillou and Chapalain 2010). A series of major harmonic components was furthermore considered to assess model's performances with respect to in situ currents measurements. The harmonic components were extracted from the TPXO7-atlas 2011 database that covers the area of interest with a spatial resolution of 1/12° (Egbert and Erofeeva 2002).

Particle trajectories were computed with the transport module of Telemac 2D (EDF R&D 2013; Joly et al. 2014). The initial particle positions were taken at the 14,026 nodes of the computational grid surrounding the Ushant-Molène archipelago (Fig. 3). Particles were released at a hourly interval during a M_2 tidal cycle, resulting in a field of 182,338 ($= 13 \times 14{,}026$) Lagrangian residual vectors. The velocity field was allocated at the barycentre of particle trajectories and finally, its non-divergence was evaluated.

In the numerical model, the effect of tidal stream power extraction on the tidal circulation was integrated as an additional bed friction sink term in the momentum equations. This sink term was computed by averaging the turbines' thrust and

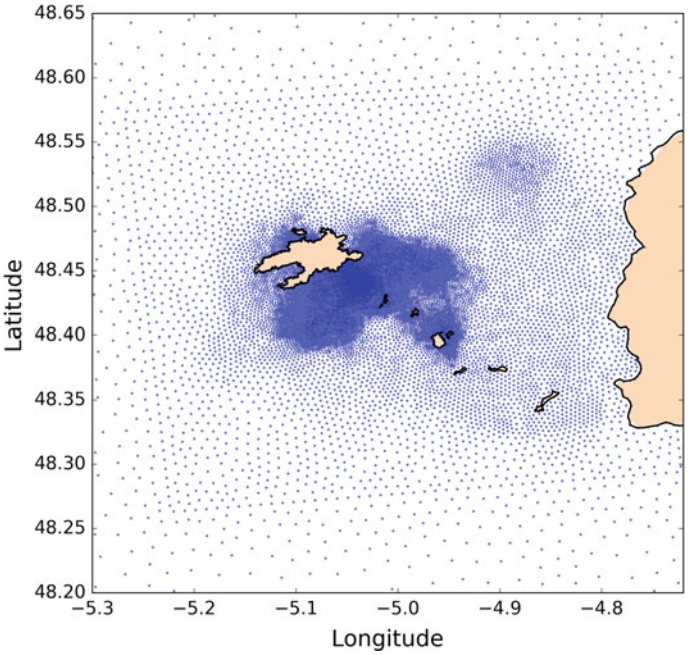

Fig. 3 Spatial distribution of computational nodes around the Ushant-Molène archipelago. This distribution displays the initial particle positions

structural drag forces over the 4 km^2 area covered by the proposed array (Plew and Stevens 2013). Further details about this numerical approach are available in Guillou and Thiébot (2016a). The investigation considered horizontal-axis turbines with a blade diameter of 18.6 m and maximum power output of 1 MW (Plew and Stevens 2013; Guillou and Thiébot 2016a). Finally, simulations integrated five tidal farm configurations varying in the number of turbines: 10, 50, 100, 150, and 207 devices. The number of 207 turbines was obtained by retaining a density of 50 machines per km^2 over the area identified for the implementation of tidal stream arrays in the Fromveur Strait (Thiébot et al. 2015).

3 Results and Discussion

3.1 Evaluation of Model Predictions

Attention was first directed to the evaluation of model's ability to reproduce tidal harmonic components. This was then followed by a comparison of predicted currents against observed currents.

Predicted magnitudes and phases of the M_2 and M_4 harmonic components were computed with a simple Fourier analyses of predicted sea-surface elevations. The results were compared to values derived from tidal-gauge observations at four locations in western Brittany, corresponding to stations (i) S1 in offshore waters ($\lambda = 6.033°$ W, $\varphi = 47.383°$ N), (ii) S2 near Ushant island ($\lambda = 5.100°$ W, $\varphi = 48.450°$ N), (iii) S3 in the harbor of Brest ($\lambda = 4.495°$ W, $\varphi = 48.383°$ N), and (iv) S4 in the harbor of Roscoff ($\lambda = 3.967°$ W, $\varphi = 48.717°$ N) (Fig. 1a, Tables 1 and 2). The observations were extracted from the compilations established by Sinha and Pingree (1997) and Pouvreau (2008). The numerical results reproduced the magnitudes and phases of the harmonic components, and the northwards increase of the M_2 magnitude with differences restricted to 1%. Greater differences were obtained for M_4 at point S4. These results were, however, consistent with the numerical estimations of Sinha and Pingree (1997), both models integrating lower spatial resolution around the islands and shoals of north-eastern Brittany. Finally, the predicted spatial distributions of the magnitudes and phases of M_2 and M_4 were consistent with maps published by Sinha and Pingree (1997) and Pineau-Guillou (2013) at the scale of the European shelf seas. These comparisons confirm the model's ability to assess tide-induced vertical variations of the water surface within the area of interest.

Evaluation of model's performances was completed by a comparison of predictions with measurements of current magnitude and direction, performed by the French navy SHOM ("Service Hydrographique et Océanographique de la Marine"), at two locations, in the Fromveur Strait (point C1, $\lambda = 5.036°$ W, $\varphi = 48.449°$ N) and north of Molène island (point C2, $\lambda = 4.945°$ W, $\varphi = 48.423°$ N) (Figs. 1b,

Table 1 Observed and predicted magnitudes A and phases G (relative to Greenwich) for M_2 harmonic constituent at locations S1, S2, S3 and S4

Station number	Observed		Modelled	
	A (m)	G (deg.)	A (m)	G (deg.)
S1 (offshore)	1.36	99.7	1.35	90.9
S2 (Ushant)	2.07	111.0	2.09	99.9
S3 (Brest)	2.05	–	2.06	–
S4 (Roscoff)	2.70	142.8	2.69	133.1

Table 2 Observed and predicted magnitudes A and phases G (relative to Greenwich) for M_4 harmonic constituent at locations S1, S2, S3 and S4

Station number	Observed		Modelled	
	A (m)	G (deg.)	A (m)	G (deg.)
S1 (offshore)	1.2×10^{-2}	296.5	1.2×10^{-2}	290.3
S2 (Ushant)	–	–	–	–
S3 (Brest)	5.4×10^{-2}	–	6.8×10^{-2}	–
S4 (Roscoff)	5.4×10^{-2}	143.4	9.1×10^{-2}	120.0

4, and 5). Measurements periods covered spring to neap tidal conditions between (i) 19 March and 2 April 1993 at point C1 and (ii) 14 May and 11 June 1993 at point C2. Assuming vertical logarithmic velocity profiles, the comparison was conducted 10 m above the bed, matching the operating height of horizontal-axis turbines in the strait (Guillou et al. 2016). The agreement between predictions and observations was

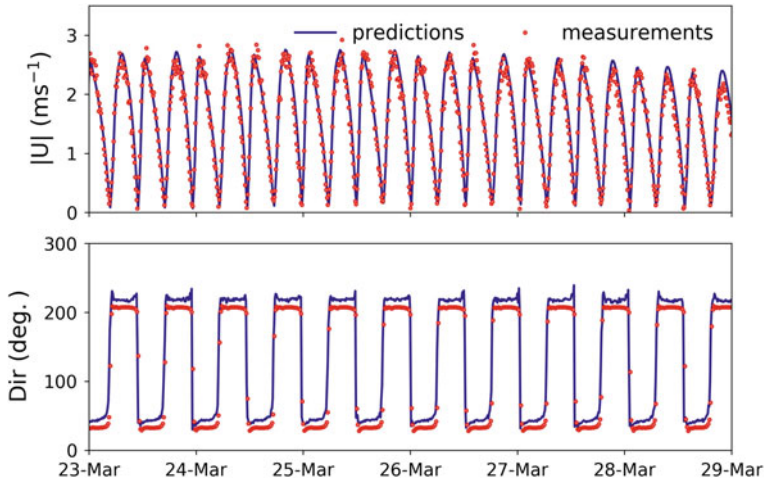

Fig. 4 Measured and computed time series of the magnitude and direction (anticlockwise convention from the East) of the current, 10 m above the bed, at point C1 (Fig. 1) in March 1993

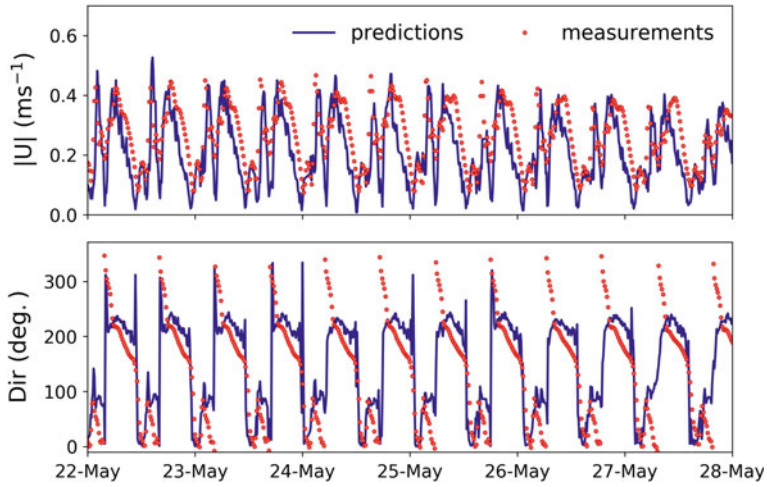

Fig. 5 Measured and computed time series of the magnitude and direction (anticlockwise convention from the East) of the current, 10 m above the bed, at point C2 (Fig. 1) in May–June 1993

particularly noticeable in the Fromveur Strait. Numerical results approached the evolution of current magnitude seen in the observations, with a mean relative difference of 0.06 ms^{-1}, and Pearson's correlation coefficient of 0.96. Greater differences were seen to the north of Molène, a region characterised by complex hydrodynamics recirculations, impacted by shoals and islands. The numerical results reproduce, however, the pronounced observed asymmetry of spring tidal currents with (i) strong and short north-eastern components and (ii) reduced, long-lasting south-western velocities. In both cases, the model simulated furthermore the abrupt changes observed between south-west and north-east directions.

3.2 Lagrangian Circulation Pathways

In the Fromveur Strait, the predicted LRC exhibited a central divergence area between (i) a prominent north-eastern pathway with residual currents up to 0.45 ms^{-1}, and (ii) a southward circulation with Lagrangian currents restricted to 0.20 ms^{-1} (Fig. 6). This Lagrangian pattern was partly associated with the asymmetry of tidal currents in the strait, characterised by (i) a north-eastern flood-dominated sector in the north, and (ii) a south-western ebb-dominated region in the south (Guillou and Thiébot 2016a, b; Fig. 7).

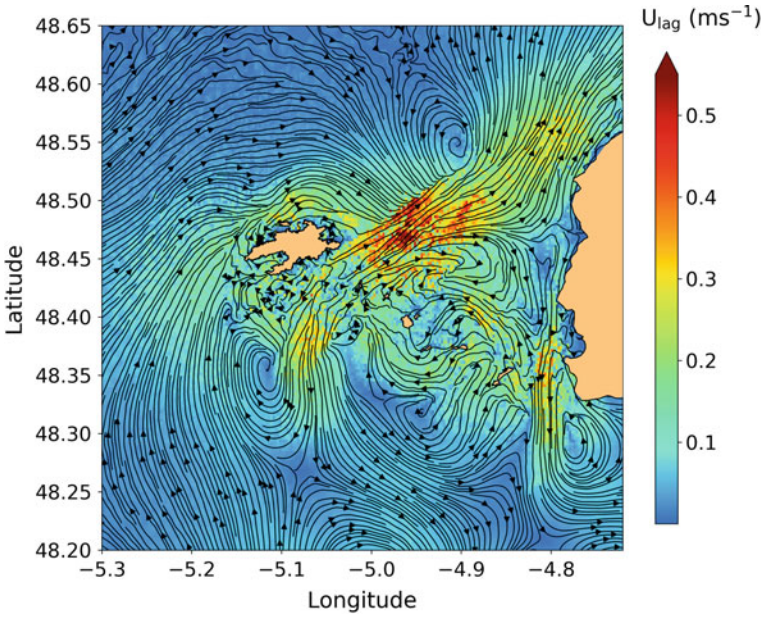

Fig. 6 Streamlines from tidal residual Lagrangian currents without effects of stream power extraction (adapted from Guillou and Chapalain 2017a)

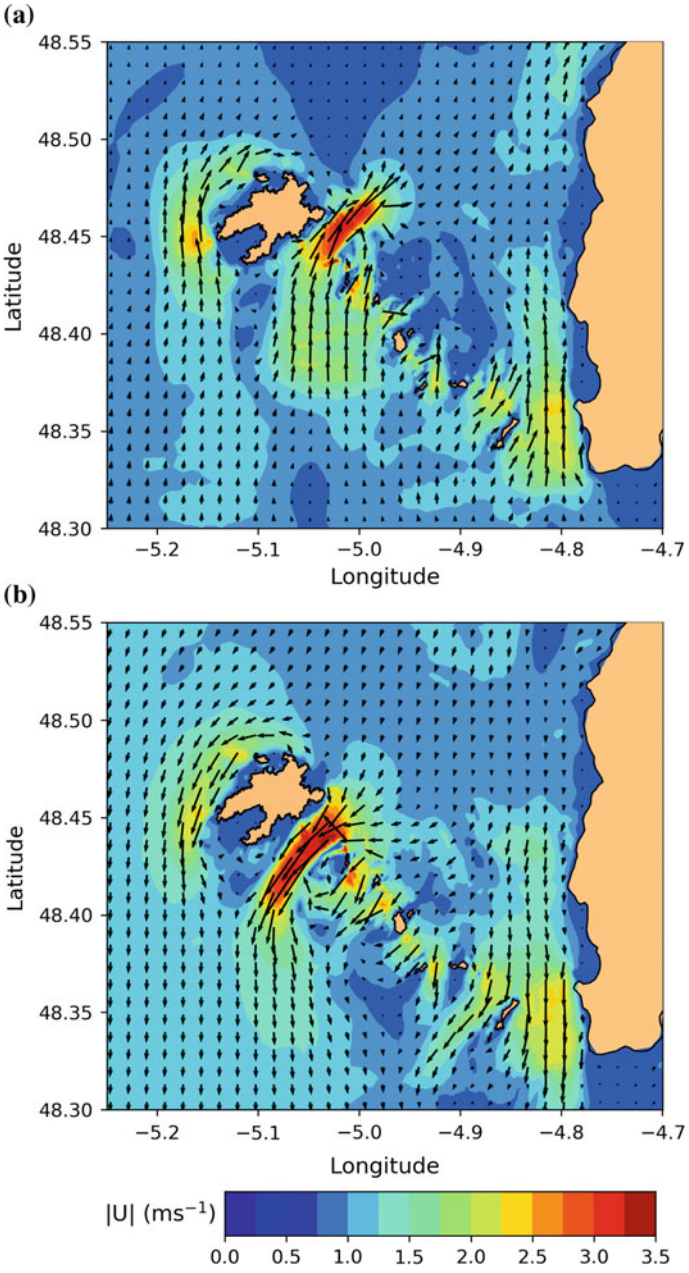

Fig. 7 Depth-averaged tidal currents without turbines at times of **a** flood and **b** ebb peaks of a M_2 tidal cycle in the Fromveur Strait

As revealed by a series of numerical investigations (Neill et al. 2014; Guillou and Chapalain 2017b; Guillou et al. 2018), such asymmetry is typical of tidal strait dynamics and arises from the phase relationship between M_2 and M_4. The central divergence area of tidal straits is thus primarily targeted for the development of tidal farm projects as it is characterised by reduced current asymmetry allowing thus balanced energy production between flood and ebb.

Away from the strait, computed streamlines were consistent with the regional investigation conducted, in western Brittany, by Salomon et al. (1988) and based on the Lagrangian barycentric method. The residual currents thus exhibited a prominent northward pathway deflecting towards the east around Ushant and connecting to the circulation emerging from the Fromveur Strait.

Both upstream and downstream the strait, prominent cyclonic and anti-cyclonic recirculations, with diameters of around 8 km, were seen. The LRC placed these eddies to the south and north-east of Ushant island, respectively. The location of the northern eddy differed, however, from previous regional investigations conducted at the scale of western Brittany. Salomon et al. (1988) located this Lagrangian structure to the north of Ushant island by applying the Lagrangian barycentric method to regional tidal predictions. Muller et al. (2009) positioned it further west by relying on High-Frequency Radar (HFR) observations of the surface circulation in calm weather conditions. Nevertheless, the eddy, identified to the north-east of Ushant island, was closely correlated with the Bank of the Four, which confirmed its position (Figs. 1 and 6). It was thus centred at the edge of the corner formed by the bank while extending to its southern and eastern limits. Following Neill and Scourse (2009) and Guillou and Chapalain (2011), a possible relationship may exist between this prominent sandbank and the tide-induced Lagrangian structure.

Further simulations showed that this residual eddy resulted from recirculations that appeared on the western edge of the flow emerging from the Fromveur Strait (Fig. 8). The residual Lagrangian structure was thus still present if the sandbank was removed from the bathymetry. It seems therefore that a refined spatial resolution is required to resolve the residual circulation emerging from the strait and the associated recirculations. Previous studies in this area (Salomon et al., 1988; Muller et al., 2009) were conducted at spatial resolutions between 650 m and 1.5 km, whilst the numerical model adopted here used a mesh size of 50 m in the strait. This may explain the differences in the reported LRC around the Ushant-Molène archipelago.

3.3 Particle Trajectories

The investigation was completed with an analysis of float trajectories as validation of the Lagrangian barycentric method, and confirmation of the major features of the computed LRC. The initial particle positions were selected at six locations of interest in and around the Ushant-Molène archipelago, including the positions of surrounding sandbanks (Fig. 1). Predictions exhibited the dispersion of particle pathways with respect to the initial time of release during the tidal cycle (Fig. 9). Drifters released in

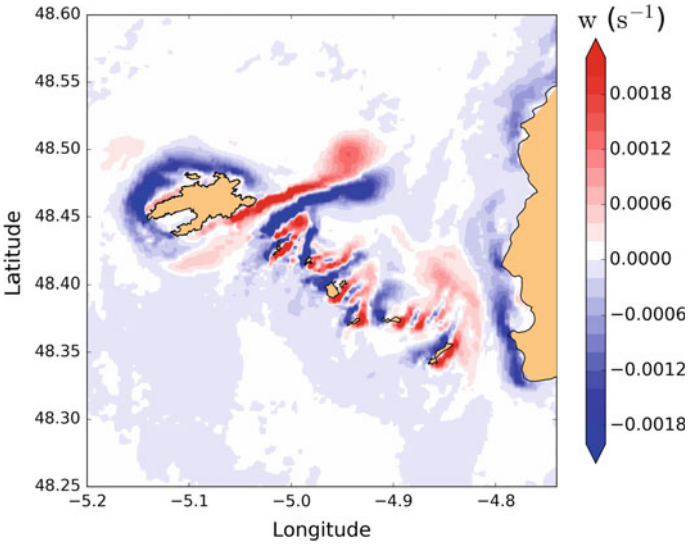

Fig. 8 Spatial distribution of the vorticity of depth-averaged tidal currents during the flood period in the Fromveur Strait

the south-western part of the Fromveur Strait may thus (i) flow towards the English Channel following the prominent north-eastern circulation, (ii) flow around the western side of Ushant, another prominent pathway, or (iii) be driven towards the southern boundary (Fig. 9b). The computed LRC (Fig. 6) was, however, consistent with these trajectories, reproducing the pathways' variability. Particle trajectories confirmed, in particular, (i) the asymmetry of residual currents in the strait and (ii) surrounding recirculations. The initial release in the Four Channel displayed the cyclonic recirculation identified above the Bank of the Four (Fig. 9c). Finally, the area of interest was characterised by short residence times. Whereas localised trapping areas may be identified in the nearshore waters of the Molène archipelago, particles released in the vicinity of the Fromveur Strait were characterised by short residence times, being evacuated from the area of interest, on average, in less than three days.

3.4 Effects of Tidal Stream Power Extraction

The extraction of tidal stream power impacted mainly (i) the magnitude and direction of the residual currents emerging from the Fromveur Strait and (ii) the locations of surroundings eddies (Figs. 10 and 11). The southward Lagrangian pathway was thus found to deviate westwards, modifying the anti-cyclonic recirculation identified in the vicinity of the Bank of Ushant. The north-eastern Lagrangian pathway, emerging from the strait, was characterised by a reduced magnitude, which displaced south-westwards the location of the cyclonic eddy to the northeast of Ushant. For

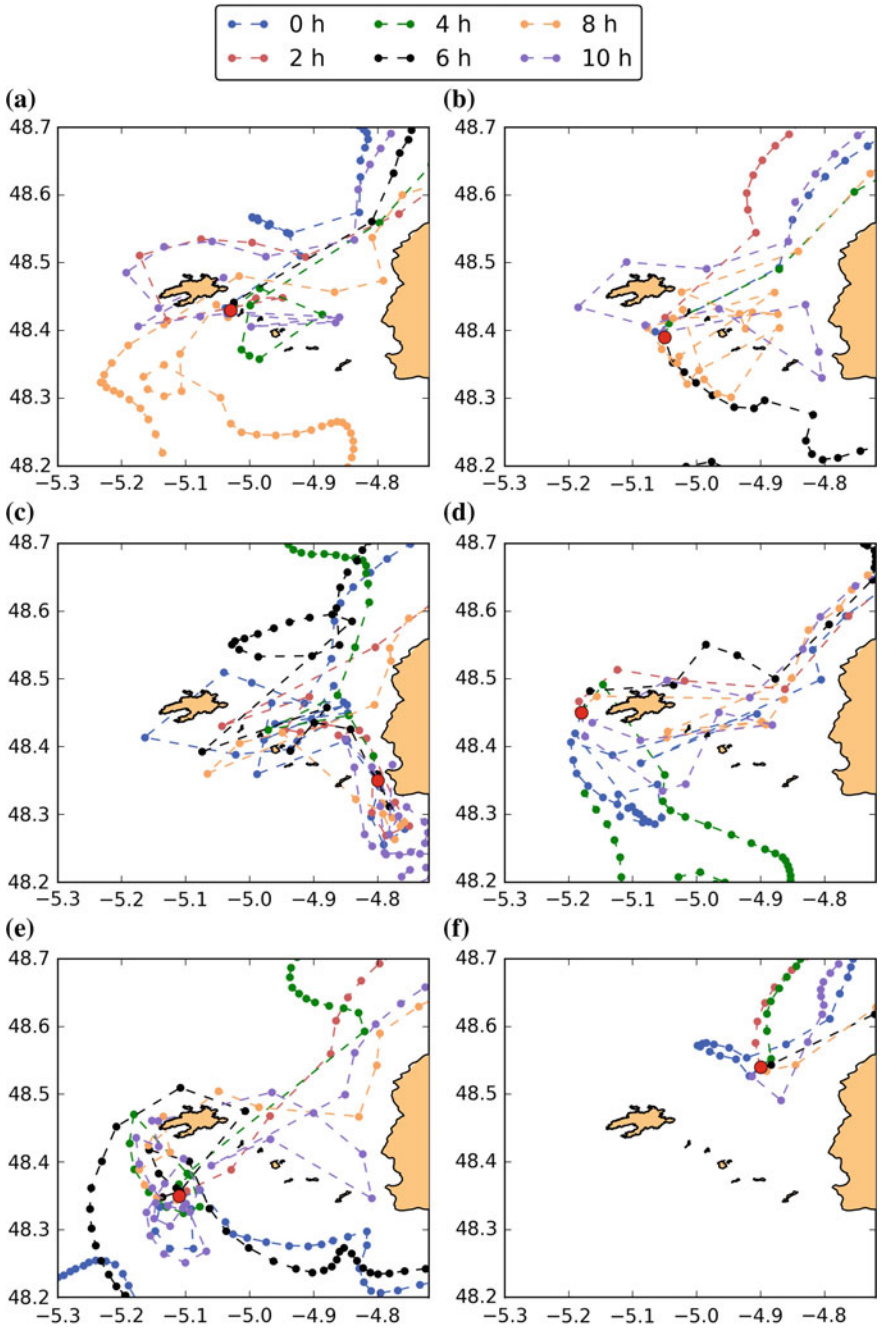

Fig. 9 Long-term trajectories resulting from the release of floats, with a time step of 2 h, during a M_2 tidal cycle. The initial positions of floats are indicated with red circles. Particles positions are displayed every 12 h to facilitate the interpretation of trajectories (adapted from Guillou and Chapalain 2017a)

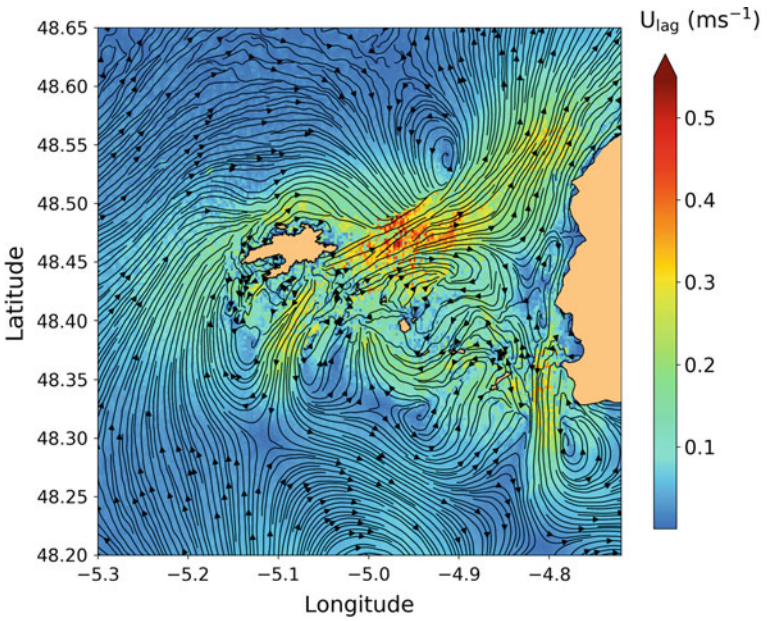

Fig. 10 Streamlines from tidal residual Lagrangian currents with effects of stream power extraction from a series of 207 devices in the Fromveur Strait

the extreme array configuration that incorporated 207 turbines, the positions of the southern and northern eddies were modified by 3 and 1.7 km, respectively. These modifications may have possible implications on the evolutions of sandbanks. This may impact mainly the Bank of the Four, whose location correlated strongly with the northern eddy (Sect. 3.2). As the southern eddy was closer to the strait than the northern eddy, changes induced by tidal stream power extraction were more noticeable for this recirculation. For the 50 device array configuration, the centre of the southern eddy moved by 820 m whilst the displacement of the northern recirculation was restricted to 220 m. Furthermore, the induced modifications followed a non-linear evolution, evolving in stages, with respect to the number of turbines.

4 Conclusions

The Lagrangian barycentric method was coupled with predictions from the high-resolution depth-averaged circulation model Telemac 2D to assess the LRC in the tidal stream energy site of the Fromveur Strait (Western Brittany, France). The main outcomes of the present investigation are as follows:

1. Results obtained refined the definition of the LRC in the Ushant-Molène archipelago exhibiting prominent transport pathways and recirculations liable to

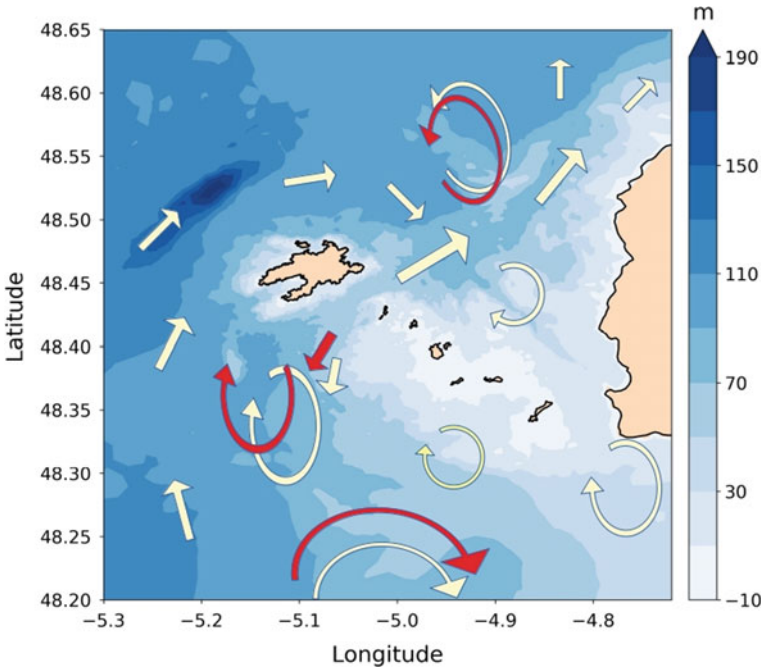

Fig. 11 Interpretation of major features of residual Lagrangian currents patterns without (yellow lines) and with (red lines) a tidal farm of 207 turbines in the Fromveur Strait (adapted from Guillou and Chapalain 2017a)

trap water particles. The strait was characterised by a strong asymmetry between (i) a prominent north-eastern pathway with residual currents up to 0.45 ms^{-1} and (ii) a southward circulation. Both upstream and downstream of the strait, the computed LRC identified cyclonic and anti-cyclonic recirculations.

2. A close correlation was exhibited between the north cyclonic eddy and the Bank of the Four. The investigation of current vorticity highlighted that this residual eddy was generated from recirculations on the western edge of the flow emerging from the strait. Refined spatial resolutions are thus required to reproduce this recirculation, which explains differences between this result and previous regional investigations.
3. The extraction of tidal stream power modified the magnitude and direction of residual currents emerging from the strait, and the positions of the surrounding eddies. These recirculations moved closer to the tidal stream energy site as the number of turbines increased. For the extreme configurations that integrated 207 devices, the displacements of the eddy centres exceeded 1.5 km, with potential effects on the evolution of nearby seabed features.

The Lagrangian barycentric method provided a synthetic overview of water particle trajectories exhibiting the major patterns of the complex circulation at the tidal

stream energy site of the Fromveur Strait. However, further in situ observations of drifters trajectories are required to refine the assessment of the particle-tracking method retained here. Three-dimensional numerical modelling may furthermore be conducted to include the influences of meteorological forcings, in particular the wind-driven circulation.

Acknowledgements The authors warmly thank Jean-Michel Hervouet (EDF R&D) for his support in applying the particle transport module of Telemac 2D. Simulations were performed with the HPC facilities DATARMOR of "Pôle de Calcul et de Données pour la Mer" (PCDM). The present chapter is a contribution to the research program DIADEME ("Design et InterActions des Dispositifs d'extraction d'Energies Marines avec l'Environnement") of the Laboratory of Coastal Engineering and Environment (Cerema, http://www.cerema.fr).

References

Breton, M., & Salomon, J. C. (1995). A 2D long-term advection-dispersion model for the Channel and southern North Sea. Part A: Validation through comparison with artificial radionuclides. *Journal of Marine Systems, 6*(5–6), 495–514.

EDF R&D. (2013). *TELEMAC modelling system—TELEMAC-3D software – release 6.2*. Technical report, EDF.

Edwards, K., Hare, J., Werner, F., & Blanton, B. (2006). Lagrangian circulation on the Southeast US Continental Shelf: Implications for larval dispersal and retention. *Continental Shelf Research, 26,* 1375–1394.

Egbert, G., & Erofeeva, S. Y. (2002). Efficient inverse modeling of barotropic ocean tides. *Journal of Atmospheric and Oceanic Technology, 19,* 183–204.

Fairley, I., Masters, I., & Karunarathna, H. (2015). The cumulative impact of tidal stream turbine arrays on sediment transport in the Pentland Firth. *Renewable Energy, 80,* 755–769.

Guillou, N., & Chapalain, G. (2010). Numerical simulation of tide-induced transport of heterogeneous sediments in the English Channel. *Continental Shelf Research, 30,* 806–819.

Guillou, N., & Chapalain, G. (2011). Effects of waves on the initiation of headland-associated sandbanks. *Continental Shelf Research, 31,* 1202–1213.

Guillou, N., & Chapalain, G. (2015). Numerical modelling of nearshore wave energy resource in the Sea of Iroise. *Renewable Energy, 83,* 942–953.

Guillou, N., & Thiébot, J. (2016a). The impact of seabed rock roughness on tidal stream power extraction. *Energy, 112,* 762–773.

Guillou, N., & Thiébot, J. (2016b). *Environmental impact of a tidal stream farm: predictions sensitivity to bottom roughness*. 15èmes Journées de l'Hydrodynamique, Brest.

Guillou, N., Chapalain, G., & Neill, S. P. (2016). The influence of waves on the tidal kinetic energy resource at a tidal stream energy site. *Applied Energy, 180,* 402–415.

Guillou, N. (2017). Modelling effects of tidal currents on waves at a tidal stream energy site. *Renewable Energy, 114,* 180–190.

Guillou, N., & Chapalain, G. (2017a). Assessing the impact of tidal stream energy extraction on the Lagrangian circulation. *Applied Energy, 203,* 321–332.

Guillou, N., & Chapalain, G. (2017b). Tidal Turbines' layout in a stream with asymmetry and misalignment. *Energies, 10,* 1892.

Guillou, N., Neill, S. P., & Robins, P. E. (2018). Characterising the tidal stream power resource around France using a high-resolution harmonic database. *Renewable Energy, 123,* 706–718.

Hervouet, J. M. (2007). *Hydrodynamics of free surface flows, modelling with the finite element method*. Cambridge: Cambridge University Press.

Joly, A., Goeury, C., & Hervouet, J. M. (2014). *Adding a particle transport module to Telemac-2D with applications to algae blooms and oil spills.* Technical report, EDF R&D.

Muller, H., Blanke, B., Dumas, F., Lekien, F., & Mariette, V. (2009). Estimating the Lagrangian residual circulation in the Iroise Sea. *Journal of Marine Systems, 78,* S17–S36.

Neill, S. P., Jordan, J. R., & Couch, S. J. (2012). Impact of tidal energy convertor (TEC) arrays on the dynamics of headland sand banks. *Renewable Energy, 37,* 387–397.

Neill, S. P., Hashemi, R., & Lewis, M. (2014). The role of tidal asymmetry in characterizing the tidal energy resource of Orkney. *Renewable Energy, 68,* 337–350.

Neill, S. P., & Scourse, J. D. (2009). The formation of headland/island sandbanks. *Continental Shelf Research, 29,* 2167–2177.

Orbi, A., & Salomon, J. C. (1988). Dynamique de marée dans le Golfe Normand-Breton. *Oceanologica Acta, 11*(1), 55–64.

Pingree, R., & Maddock, L. (1978). The M_4 tide in the English Channel derived from a non-linear numerical model of the M_2 tide. *Deep-Sea Research, 25,* 53–63.

Pineau-Guillou, L. (2013). *PREVIMER Validation des atlas de composantes harmoniques de hauteurs et courants de marée*. Technical report, Ifremer.

Plew, D., & Stevens, C. (2013). Numerical modelling of the effects of turbines on currents in a tidal channel—Tory Channel, New Zealand. *Renewable Energy, 57,* 269–282.

Pouvreau N. (2008). *Trois cents ans de mesures marégraphiques en France: outils, méthodes et tendances des composantes du niveau de la mer au port de Brest.* Ph.D. thesis. Université de La Rochelle.

Salomon, J. C., Guéguéniat, P., Orbi, A., & Baron, Y. (1988). A Lagrangian model for long-term tidally induced transport and mixing. Verification by artificial radionuclide concentrations. In J. Guary, & P. Guéguéniat (Eds.), *Radionuclides: A tool for oceanography* (pp. 384–394). London, New York: Elsevier Applied Science Publishers.

Salomon, J. C., & Breton, M. (1993). An atlas of long-term currents in the channel. *Oceanologica Acta, 16*(5–6), 439–448.

Sanderson, B., & Redden, A. (2015). Perspective on the risk that sediment-laden ice poses to in-stream tidal turbines in Minas Passage, Bay of Fundy. *International Journal of Marine Energy, 10,* 52–69.

Shapiro, G. I. (2011). Effect of tidal stream power generation on the region-wide circulation in a shallow sea. *Ocean Science, 7,* 165–174.

Sinha, B., & Pingree, R. D. (1997). The principal lunar semidiurnal tide and its harmonics: baseline solutions for M_2 and M_4 constituents on the North-West European Continental Shelf. *Continental Shelf Research, 1*(11), 1321–1365.

Thiébot, J., Bailly du Bois, P., & Guillou, S. (2015). Numerical modeling of the effect of tidal stream turbines on the hydrodynamics and the sediment transport—Application to the Alderney Race (Raz Blanchard), France. *Renewable Energy, 75,* 356–365.

Zimmermann, J. T. F. (1979). On the Euler-Lagrangian transformation and the Stokes drift in the presence of oscillatory and residual currents. *Deep-Sea Research, 26 A*, 505–520.

Modeling of Sediment Transport and Morphological Evolution in Estuaries

Introduction

Nowadays, climate change and sea-level rise essentially modify morphological evolution in rivers and estuaries. This evolution has been aggravated by changes in anthropogenic activities. As an example, the Mekong Delta is still undergoing a slow dead not only due to climate change impacts but also to the hydro-power developments in the upper Mekong Basin. These changes induce an essential reduction in the sediment budget in the Mekong Delta and cause fundamental modifications of the morphology of the entire delta both in mainland and in adjacent coastal zones. Therefore, improvement, extension and deepening of our knowledge, methodologies and experiences in this area are more than necessary.

This part includes ten chapters to the modeling of sediment transport and morphology evolution in estuaries.

The first chapter by Lemoine et al. aims to (i) understand and model the contributions of dredging to the characteristics of estuarine turbidity maximum (ETM), to sediment fluxes, and (ii) compare natural fluxes with the anthropogenic fluxes related to dredging. In the Seine Estuary, maintenance dredging is operated continuously, and yearly dredged volumes have the same order of magnitude as natural sediment fluxes at the mouth of the estuary. Their approach relies on a 3D multi-class hydro-sedimentary model validated by Grasso et al. (2018), in which dredging and dumping processes were implemented with respect to the rules defined by port authorities of Rouen and Le Havre. Model results are evaluated first regarding the temporal and spatial variability of dredging in the Seine Estuary, and secondly, regarding the stability of dumping sites. In order to track the fate of dredged materials, the latter are numerically marked by assigning them to specific state variables that respect the particle characteristics (gravel, sands or mud). The corresponding concentrations of these new variables can be computed either in the water column (suspensions) or in the layered sediment. Their contributions to the total suspended sediment mass of the estuary and to the siltation rate are evaluated. Results show that most of the dredged material remains in the proximity of the dumping site, but the rest contributes to the turbidity and to the siltation pattern in the estuary. The similitude between the global

siltation pattern and the distribution of redeposited dredged material reveals a strong mixing of the latter within the whole estuary mouth.

In the second chapter, Uh Zapata et al. propose a numerical method for fast-evolving flows governed by the two-dimensional shallow water equations semi-coupled with the Exner sediment balance equation for bed evolutions. The method is based on Chorin's projection, which combines the momentum and continuity equations in order to establish a Poisson-type equation for the water surface level including the bed evolution. The equations are discretized using an unstructured finite-volume technique. In the model, a second-order upwind scheme combined with a local extremum diminishing method is developed to handle convection terms. A comparison with quasi-analytical and existing numerical results are done to test the performance of the used scheme, including the modeling of a dam break on a mobile bed.

The third chapter by Zhang et al. talks on The Jiao (Ling) River, which is a typical mountainous macro-tidal river. The tidal current and runoff jointly guide sediment gathering in a specific section to form the turbidity maximum zone and develop fluid mud. This plays an important role in riverbed evolution. The construction of sluice in the mainstream of the Jiang (Ling) River will greatly change the original flow and sediment movement characteristics of the river channel, forming siltation downstream sluice and producing a big influence on flood control and drainage and navigation. The flow and sediment movement characteristics of Jiang (Ling) River are analyzed and the influence of fine-grained cohesive sediment movement characteristics and salinity considered. A flow and sediment mathematical model for sluice construction in the Jiang (Ling) River is established to simulate the hydrodynamic change and the temporal and spatial distribution characteristics of sedimentation after the sluice construction. The research results show that the sluice construction has an influence on the entire channel downstream of the sluice. The closer to the sluice site, the bigger the influence will be. At the initial stage of sluice construction, sediment is mainly deposited in a deep trench of 10 kilometers downstream of the sluice. The siltation downstream of the sluice will elevate the flood level and lower water levels, thus affecting flood controls and drainages. It will also decrease the water depth of the channel, thus reducing the navigation capacity of the Jiao (Ling) River.

The fourth chapter by Aranda et al. proposes as methodology the combination of different detailed maps to identify links between morpho-sedimentary systems and related EU habitats of community interest. Indeed, characterizing the functionality of an estuary is a key element to develop adequate management tools for estuarine environments. Unfortunately, only very few studies have focused on the connectivity among their elements, mostly overlooking the derived interactions inherent to them. As an example, San Vicente de la Barquera Estuary (Cantabria, Spain) has been selected for this first approach**.** The combination of these types of detailed maps allows to draw up a table of equivalences to relate morpho-sedimentary units and habitat characteristics from a geographical point of view. In a second phase of this approach, physical processes related to morphological systems (i.e., river discharges, water mixing, tidal currents, dynamo-sedimentary models) and biological processes

related to ecological systems (i.e., presence and variation of plant communities) are identified. Additionally, induced anthropogenic processes are considered as driving forces acting directly on the previous ones. With the aim of evaluating the global dynamic of the estuary, a set of geo-ecological indicators are proposed to describe the processes and the connectivity established between their subsystems.

The fifth chapter by Azhikodan et al. investigates the spatial and temporal dynamics of bed morphology in relation to semidiurnal and fortnightly tidal variations, the magnitude and movement of the *estuarine* turbidity maximum (ETM) and seasonal variations in river discharge in a meandering estuarine channel. Intensive field surveys (longitudinal and transverse) in the upper region of the Chikugo River Estuary (12–14.6 km landward from the river mouth), in Japan, were carried out in every three or four months during 2009–2011 using a digital sonar system equipped with a differential global positioning system. The results reveal that the estuary was dominated by tidal discharges for most of the year, except for rainy season, in which river flow dominates. During the low flow season (September to May), fine sediment was deposited near the inner bank during every semidiurnal tidal cycle and the depth of the inner bank diminished. On the contrary, the outer bank was heavily eroded and steepened. As a result, ETM developed at the upstream of the estuary and the channel capacity reduced gradually during this period. However, in the rainy season (June to August), large flood events led to the breakdown of ETM and export the sediment in the upper reach of the estuary to the downstream tidal flat. The seasonal cyclic pattern of erosion and deposition processes was evident at the upstream meander. This cycle of morphological evolution of river bed continues based on the upstream sediment transport by the fortnightly tidal cycles and downstream sediment transport by the river discharge. Hysteretic effects between shear stress and SSC due to the asymmetrical flood and ebb tides as well as the seasonal variations in river discharge are the dominant factors that cause sediment transport and morphological changes in tide-dominated estuaries.

The sixth chapter by Wang et al. presents two mathematical models for sediment transport and currents using MIKE21. The large model covers the whole Bohai Bay. This model is calibrated by the harmonic tidal components of observation data. Based on the open boundary conditions given by the large model, the tidal currents and sediment transport processes in the Yellow River Estuary are simulated by a small model with finer grids. The computational results show that three high tidal current zones exist with maximum speed reaches at 1.7 m/s. The alongshore current from Bohai Bay to Laizhou Bay is the dominant driver of transport sediment. The analysis and calculated results show that net fluxes of sediments crossing both sides of 10 km width and into the open sea at the routes of Diaokou River, Old Channel, current Qing Route, Maxinhe Route, Beicha Route and Shibahu Router are of about 51.04, 39.27, 29.94,17.75, 12.96 and 7.22%, comparing with the amount of sediment in the Lijin station, respectively. In the planning of the available flow route, the DiaoKouhe Route has the largest sediment transport capacity.

In the seventh chapter, Diaz et al. develop a 3D realistic hydrodynamic model of the Gironde Estuary (South-West France) and the continental shelf seaward coupled with a multi-layer process-based sediment model, accounting for sand and mud

mixtures. In order to better understand the sediment dynamics between the estuary and the continental shelf, the objective is to provide a quantification of suspended sediment mass uncertainties associated with sediment transport parameters. The sensitivity analysis is conducted considering the changes in the key sediment transport parameters, such as the settling velocity of the mud class and the sediment initial distribution. A better understanding of the uncertainties associated with simulated sediment transport will enhance the degree of confidence that can be placed in the quantification of the estuarine sediment exchanges with the sea. Such a quantification provides knowledge about the intra-estuarine exchanges with lateral intertidal mudflats, as well as sediment export to the sea, possible trapping in the subtidal muddy areas seaward of the mouth (e.g., the West Gironde Mud Patch) and dispersion along the adjacent coasts.

In the eighth chapter, Phan et al. use a two-dimensional, barotropic numerical model to investigate the dynamics of tidal wave propagation in the South China Sea with a particular interest for its characteristics along the Mekong deltaic coast under wind monsoon climate. The results reveal that wind monsoon climate could cause damped or amplified tidal amplitudes around Mekong deltaic coast approximately 2–3 cm due to the changing atmospheric pressure, the tangential stress of wind over the water surface and wind enhanced bottom friction. The monsoon climate strongly affects the M2 semidiurnal tide system in the eastern Mekong deltaic coast, while the monsoon climate controls K1 diurnal tide in the western region of Mekong delta.

The ninth chapter by Lu et al. is based on the analysis of hydrodynamic and sediment transport at the Pearl River Estuary, to detect key points and methods for modeling sediment motion with physical model. Especially, the key technologies of sediment selection and automatic sediment adding device are developed. By characterizing the sediment transport and key technical issues in the region, simulations and verifications of currents, waves and sediments are carried out. Furthermore, the physical model for sediment transport is applied to the Hong Kong-Zhuhai-Macao Bridge project. The results indicate that the model can satisfy the similarity of flow movement and sediment siltation, which provides an important technical support for project construction.

The tenth chapter by Chan et al. presents a CFD modeling of sediment plumes in a non-stratified stagnant ambient using the two-phase Eulerian approach. The axisymmetric two-phase continuity and momentum equations are solved with the drag force term accounting for the interaction between phases. The standard k-ε model is used for turbulence closure for sediment–water mixture. The radial turbulent dispersion of particles is modeled by a drift velocity term related to the concentration gradient of the particle phase. The model prediction is validated against experiments of a companion work and independent investigations, with a wide range of particle sizes (68–1500 μm) and initial plume sediment volume fraction (maximum of 60%). The model predicted cross-sectional distribution of sediment concentration, plume fluid velocity and the slip velocity of particle to fluid can be well described by Gaussian profiles. The reduction in plume spreading rate with increasing particle size and settling velocity is also well predicted by the model. The CFD model results

shed light on the development of a simple integral model for predicting the mixing of sediment plumes.

Kim Dan Nguyen
Laboratory for Hydraulics Saint-Venant, Université de Paris-Est, France

Numerical Study of Sediment Transport in the Seine Estuary: Contribution of Dredging

Jean-Philippe Lemoine, Pierre Le Hir and Florent Grasso

Abstract In the Seine estuary, maintenance dredging is operated continuously and yearly dredged volumes have the same order of magnitude as natural sediment fluxes at the mouth of the estuary. Prior to 2017, the main dumping site was in the vicinity of the estuarine turbidity maximum (ETM), therefore impacting sediment dynamics in the area. In this context, the aim of our research is to understand and model the contributions of maintenance dredging to the ETM characteristics and to sediment fluxes, and to compare natural fluxes to the anthropogenic ones related to these activities. Our approach relies on a 3D multi-class hydro-sedimentary model validated by (Grasso et al. in J Geophys Res: Oceans 12(3):558–577, 2018), in which dredging and dumping were implemented as processes following rules defined by port authorities of Rouen and Le Havre. Model results are first evaluated regarding the temporal and spatial variability of dredging in the Seine Estuary, and secondly regarding the stability of dumping sites. In order to follow the fate of dredged materials, the latter are numerically marked by assigning them to specific state variables of the model that respect the particle characteristics (gravel, sands or mud). The corresponding concentrations of these new variables can be computed either in the water column (suspensions) or in the layered sediment. Their contributions to the total suspended sediment mass of the estuary and to the siltation rate are evaluated. Results show that most of the dredged material remains in the proximity of the dumping site but the rest contributes to the turbidity and to the siltation pattern in the estuary. The similitude between the global siltation pattern and the distribution of re-deposited dredged material reveals a strong mixing of the latter within the whole estuary mouth. After 3 years of marking, the contribution of dredged sediment to the ETM can be estimated around 1%.

J.-P. Lemoine (✉)
GIP Seine-Aval, Hangar C - Espace des Marégraphes, Quai de Boisguilbert, 76000 Rouen, France
e-mail: jplemoine@seine-aval.fr

P. Le Hir · F. Grasso
IFREMER, Laboratory DYNECO/DHYSED, Centre de Bretagne, CS 10070,
29820 Plouzané, France

K. D. Nguyen et al. (eds.), *Estuaries and Coastal Zones in Times of Global Change*, Springer Water,
https://doi.org/10.1007/978-981-15-2081-5_15

Keywords Estuary · Sediment transport · Mixed sediment · Numerical tracing · Maintenance dredging

1 Introduction: Importance of Dredging in the Seine Estuary

The Seine estuary, located in the Northern part of France can be classified as a tide dominated estuary (Dalrymple et al. 1992) with a tidal range reaching 8 m at Le Havre. It is 170 km long from the mouth up to the upper limit of the tidal propagation, artificially limited by a weir, at Poses. It is the outlet of a low slope 79,000 km^2 catchment area exposed to an oceanic climate, characterized by a mean river discharge of 440 m^3/s with minimum below 100 m^3/s and maximum around 2500 m^3/s. Salinity gradients and the Estuarine Turbidity Maximum zone (ETM) are located in the lower 50 km of the estuary (area represented on Fig. 1). The ETM position and mass are mainly driven by the spring/neap tidal cycles, its mass can reach 250,000 t during spring tide (e.g. Grasso et al. 2018).

As many estuaries worldwide, The Seine estuary was shaped by engineering works to improve its accessibility to marine vessel (Avoine 1981; Lesourd 2000; Delsinne 2005). In particular, two submersible dikes, almost 10 km each, were built in the 1960's (Fig. 1). These dikes were designed to enhance ebb currents and thus to limit siltation in the navigation channel.

Navigation channels of both Rouen and Le Havre harbours were significantly deepened, which has induced extensive maintenance dredging in order to maintain a constant nautical depth in both fairways. Rouen Harbour stretches along 110 km from Honfleur to Rouen, but 85% of its total maintenance dredging activity is located in the lower 30 km of the estuary. This area which corresponds to the ETM location

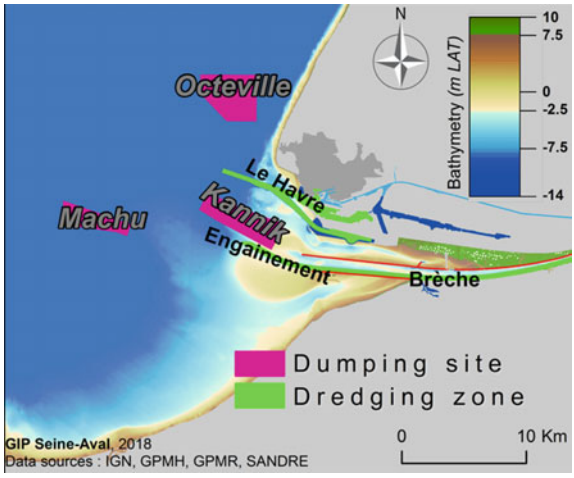

Fig. 1 Bathymetry, dykes in red and dredging (green) and dumping areas (pink)

experiences strong tidal currents (2 m/s). Nevertheless, siltation in this part of the navigation channel of Rouen Harbor is around 4 million tons per year and is mainly muddy (65% in weight). Dredging of Rouen harbour is operated continuously by at least one trailer suction hopper dredger. Prior to 2017, these sediments were released on a disposal site called Kannik, located just at the mouth in a very dynamic area. Now these sediments are dumped on Machu site, located more offshore. Le Havre harbour is dredging an annual volume of around 2 million tons in its basins and navigation fairways. As tidal currents are low in these areas, and waves remain moderate in the deep navigation channels, sediment dredged is mainly muddy (90% of mud). These sediments are released on the disposal site of Octeville located north from the mouth of the estuary (cf. Fig. 1).

Analysing the actual sediment budget of the Seine estuary and confronting natural sediment inputs to the annually dredged masses shows that the 6 million m^3 dredged volume are of the same order of magnitude as the sum of continental (1million ton per year) and marine natural sediment input (4 million tons per year) (Lemoine et al. 2016).

Previous studies have shown that estuarine sediment processes and morphodynamics could be sensitive to dredging and dumping strategies (Jeuken and Wang 2010; Hibma 2008; Monge-Ganuzas et al. 2013; Dam et al. 2013). Nevertheless, most of these studies were conducted in sandy environments, and often addressed systems where natural ebb and flood channels can be distinguished. These characters are not applicable to the Seine estuary where the ETM is located nearby the dredged zone.

In this context, it appears essential to investigate the role of maintenance dredging and associated dumping on the sediment dynamics of the Seine estuary and furthermore on its morphological evolutions. Currently this scientific problematic is getting more and more interest at the scale of the Seine estuary as Rouen harbour has just revisited its dredging strategy with a new disposal site located in a calmer and deeper area, outside the estuary mouth.

In this chapter, we will focus on the methodology we are setting up to determine the contribution of maintenance dredging to sediment dynamics (Sect. 2) and on preliminary results in Sect. 3.

2 Material and Methods

2.1 Model Set-Up

Our approach relies on the use of the hydrodynamic model MARS-3D (Lazure and Dumas 2008), coupled to the process based morpho-sedimentologic model of Le Hir et al. (2011). The model uses a curvilinear non-orthogonal mesh to limit the computation time and to fit the funnel shape of the estuarine morphology (Khojasteh Pour Fard 2015). Grid resolution ranges from 2×2 km^2 in the bay of Seine to 30

$\times$ 100 m^2 in the area of interest: the estuarine mouth. The 10 $\times$ 10 m bathymetric data of 2010 provided by port authorities of Rouen and Le Havre were interpolated on this grid.

The hydrodynamic model is forced by the main tidal components from the CST France database at his northern open boundary (Service Hydrographique et Océanographique de la Marine, SHOM). Diurnal Seine river discharged is imposed at the upstream limit. Meteorological forcings, wind and pressure gradients are derived from the Meteo-France model ARPEGE. Waves forcing are extracted from dedicated WaveWatch III® simulations forced by the same wind information locally and a large-scale model of the Atlantic Ocean considering free surface elevation and current velocities provided by MARS-3D. The wave model runs on the same curvilinear computational grid and accounts for free surface elevation and current velocities provided by MARS-3D (Roland and Ardhuin 2014). This model has been validated in hydrodynamics by Kervella et al. (2012).

Suspended sediment transport is simulated by solving an advection/diffusion equation for different sediment types ranging from mud to fine and medium sand (Le Hir et al. 2011). For mud, flocculation processes are accounted for by a variation of the settling velocity according to the mud concentration and turbulent intensities, following Van Leussen (1994). A multi-layered bed model is associated to the 3D hydrodynamics model, with the same computational grid. The vertical discretization of the sediment enables to account for sediment distribution and consolidation. Consolidation of sand and mud mixtures is solved according to a modified Gibson equation (Grasso et al. 2015). Layers thickness varies according to erosion and deposition events, typically between 1 and 5 mm. The maximum number of layers is 100, so that in case of excess deposition, a buffer layer with not limited thickness is constituted at the basis of the sediment. 5 class of sediment are considered: 1 mud, 3 sands (100, 210 and 800 μm) and 1 gravel (10 mm). Initial sediment conditions are derived from the Seine estuary facies map made by Lesourd et al. (2015).

Continental sediment supply is set as a source term at the upstream limit of the model considering relations between river discharge and suspended solids concentration (SSC), based on Avoine (1981). A constant and uniform concentration of mud equal to 2 mg/L is imposed at the ocean open boundary, qualitatively in agreement with observations in the English Channel in accordance with Blanpain (2009). Further details about the sediment model and its validation can be found in Grasso et al. (2018).

Considering the importance of dredging induced sediment fluxes, the model is considering the dredging and dumping activity of both Rouen and Le Havre Harbour. To analyse the impact of dredging and its possible feedbacks on the global dynamic of the system, dredged quantities of any class of particles are not imposed but are computed by the model, in specific areas where a maximum bed elevation is imposed. Based on the approach described in Waeles and Le Hir (2006), sediment is removed from the sea bed of dredged area when the bed elevation (which accounts for sedimentation, consolidation and erosion) exceeds the level specified by port authorities. Then in coherence with results from Boutin (1999) and Nguyen

et al. (2012) sediment are released in the bottom layer of the water column above the dumping sites.

Taking into account dredging as a result of the morphodynamic model enables the study of the dredging strategy feedbacks on the global functioning and especially on dredged quantities themselves. It is then possible to evaluate the mid to long term implication of a dredging strategy on the annually dredged volume. This approach also implies that there is no additional calibration, so that dredged quantities and their nature are dependent on the overall validation of the sediment transport model.

2.2 Model Validation

Results of the dredging procedure are stored as time series of dredged masses of each type of sediment per dredging area. This information enables us to compare numerical dredging with in-situ data gathered by dredging vessels. Considering the human induced variabilities in in-situ data, comparisons were made on a yearly basis. These analyses mainly focus on 3 indicators which are (i) the yearly dredged volume for 3 dredging areas, (ii) the ratio of sand and mud mass fractions of dredged sediment (Lemoine et al. 2017) and (iii) the stability of dumping sites. Dumping site stability is calculated as the ratio of the dumped sediment mass on the disposal site versus the dumped sediment mass remaining on the seabed site and its close surrounding. Dumping site stability are only shown for Kannik and Octeville because we don't have the same long term information for the new site of Macchu.

As there is no specific fitting parameters in the dredging procedure, dredging results do not require any specific calibration phase and can only be validated. If validation is not satisfying, then the hydro sedimentary parameterization of the model has to be revisited, which considerably complicated the exercise: indeed, dredging results have to be considered as data for comparison between model results and observations, as well as suspended sediment concentrations, erosion/deposition patterns and changes in surficial sediment composition.

An exception can be made for the indicator iii relative to the stability of dumping sites. Our modelling assumes that all materials are released as suspension in the lower computation cell of the water column above the dumping site, considering that settling velocity is large enough to imply actual deposition. For mud, deposition is likely to be underestimated as the actual dredged muddy material may look like more or less fluid mud, more than suspension.

Comparison presented in Table 1, shows similar tendencies between numerical and in-situ data. Despite some important difference in term of dredged mass in Le Havre harbor and mud ratio on the dredging site of "Engainement", we propose to use our model in its present calibration for a preliminary qualitative analysis of the contribution of dredging to the Seine estuary functioning.

Table 1 Dredging validation indicators

Validation indicators	Dredging areas	In-situ values	Model results
Dredged masses (10^6 t/year)	Brèche	1.6	2.1
	Engainement	2.3	3.3
	Le Havre	2	4.5
Mud mass fraction (%)	Brèche	50	38
	Engainement	65	12
	Le Havre	85	75
Dumping site stability (mass %)	Kannik	±60%	70%
	Octeville	<10%	10%

2.3 Numerical Tracing of Sediment

In order to follow the fate of specific sediment materials in the model, the latter are numerically traced. Sediment can be marked when introduced in the domain from a specific source or after a specific sediment process. Tracers are dealt with as specific state variables of the model, and marking process is achieved by transferring the corresponding sediment mass in such a new state variable. These tracing state variables have exactly the same properties as the 5 classes of the model (gravel, sands or mud), so that each sediment class has to be distinguished. The corresponding concentrations of these new variables can be computed either in the water column (suspensions) or in the layered surficial sediment. Thus, the contribution of the traced sediment to the global estuarine sediment dynamic can be easily evaluated.

This technique can be used to trace natural and anthropogenous sediment process, and especially dredging. In this case, when a mass of non-marked sediment is dredged, it is marked when it is released on the dumping site, and then it can be transported in suspension or deposited and possibly reworked again. Eventually, the traced sediments may be transported into the dredged areas under natural processes, and be dredged again. In this case, (i) corresponding mass will be added to the stock of dredged material as a mass of already dredged material, (ii) there won't be any new transfer in another state variable. This gives us information on the potential return of some sediment from the disposal sites to the navigational channels.

This tracing technique constitutes an interesting analog to the in-situ technique of tracing based on the use of radionuclides, exotic particles, rare earth elements or fingerprinting (Kimoto et al. 2008). Artificial Radionuclides tracing techniques were used in the 80s in the Seine estuary by Hoslin et al. (1989) to follow dredged sand. The specificities of these experiments make quantitative comparisons with our model difficult. Indeed, estuarine morphology evolved a lot since 1989 and also the way Hoslin injected its sandy tracers is hardly reproducible with our model. Nevertheless, qualitatively sand dispersion directions of both model and Hoslin experiments have similar amplitude and are both mainly directed towards the estuary.

2.4 Studied Cases

To characterize the weight of the dredging activity in the global estuarine sediment dynamic, we set up two different types of tracing simulations. In the first one only dredged materials were traced: sediment were marked before being released on dumping site. This was done for two configurations that can be distinguished by the dumping site of material dredged for Rouen access (Kannik) and Le Havre (Octeville). In a second simulation, the whole "mobile" sediment was traced. "Mobile" sediment addresses any material that has been eroded from the seabed (at least once). To do so, sediment is marked since it is eroded and remains marked for the rest of the simulation.

In addition, in order to compare the fate of dredged sediment to the ones from other sources, the 3 different "natural" sources of sediment in the model were traced: initial seafloor sediment, offshore and continental inputs.

3 Results

3.1 Hydrodynamic Induced Variabilities

In-situ data collected on dredging vessels by port authorities of Rouen and Le Havre do not show any clear relation between hydrodynamics forcings and dredging. In fact, dredging activity is submitted to different operational constraints. Dredging vessels have limited capacities in term of daily dredged mass and also in term of daily dredged surface. Dredging is also submitted to operative constraints, for example maintenance operations. It appears that these constraints conceal the natural variabilities of the siltation in fairways. Indeed, it is known that during a high river discharge period or after a storm, it takes several weeks for dredgers to completely clear the navigational channels, and yet in-situ data do not show the corresponding increase in dredging activity. In fact, it appears that most of the time during and after a huge siltation event, dredging cannot maintain the nautical depth all along the fairways.

On the contrary, the model results can highlight clear tendencies and linkages between hydrodynamics forcings and dredging. For instance, Fig. 2a, c illustrates the relation between mud dredging in Le Havre harbour and waterways and storms occurrence, especially during winter 2009. On Fig. 2b the evolution of dredged quantities on the dredged zone called "Brèche" shows a relationship with both fluvial and tidal forcing. Dredging requirements increase with the river discharge as the ETM is closer to the dredged zone. On the site "Brèche" there is also a relation with the tidal range. In fact, the ETM position oscillates with tidal range variations around this site (kilometric point 350). ETM position shifts downstream during the neap to spring phase and upstream during spring to neap phase (Grasso et al. 2018). These results enhance the knowledge of port authorities and can help them in planning their maintenance dredging campaign. For example, they can anticipate a dredging

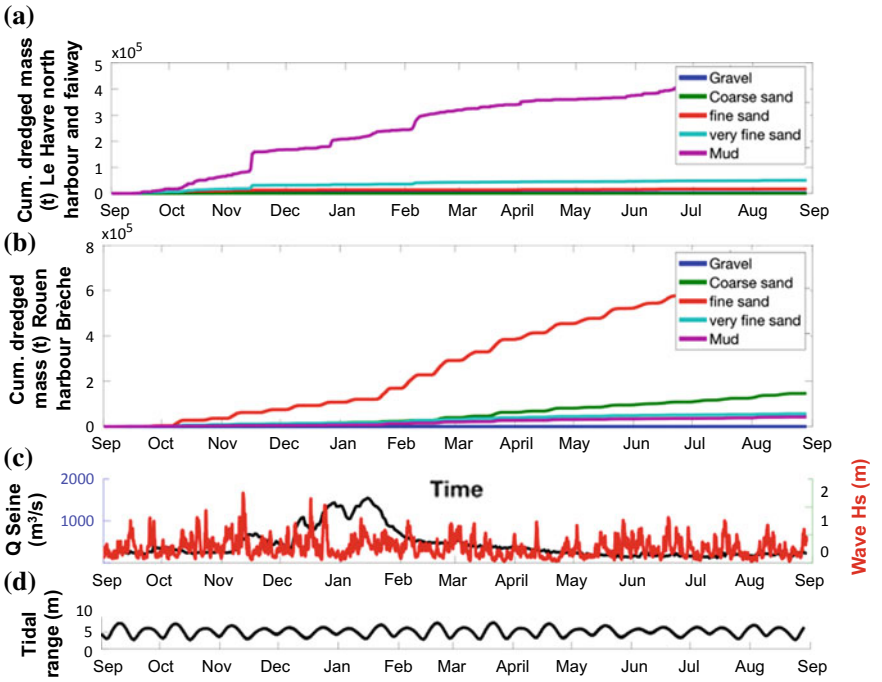

Fig. 2 Temporal variability of dredging (**a** and **b**) in two areas: **a** Le Havre harbor and fairways and **b** one breach in the Rouen waterway, called Brèche; simultaneous variation of hydrodynamic forcings: river discharge and waves Hs (**c**) and tidal range (**d**). On **a** and **b**, curve colours indicate the sediment class (mud, sands or gravel)

campaign after periods of high siltation as during a neap or spring tidal phase where Le Havre harbour (resp. Rouen) will dredge muddy sediment (resp. sandy sediment).

Also, considering the fact that the dredging capacity is limited, and to be more realistic on the modelling of some operational scenarios, a daily limitation of the dredged masses has been tested in our model. As observed in situ, this operative constraint tends to blur the high frequency variabilities due to storms and spring/neap tidal cycles.

3.2 Contribution of the Dredging and of the Different Sediment Sources to the Total SPM

Tracing the different sediment sources (seabed, continental and offshore) combined with the tracing of dredging enables us to analyse the contribution of dredging to the estuarine turbidity. These simulations show that 2 years after the beginning of dredged materials tracing, dredging is responsible of around 1% of the ETM mass

in average, while the riverine sediment source contributes for 0.1% and the sediment input at the sea boundary of the computational grid (where a concentration of 2 mg/l is imposed when water is entering) contributes for 0.25% (Fig. 3). Naturally, these latter contributions are likely to increase with time, unlike the dredging contribution which seems not to increase. On the other hand, even if these results are interesting, they remain hard to exploit because they are really dependant of the duration of the tracing period.

Further analysis and longer simulations are needed to appreciate the contribution of dredging to estuarine turbidity. Indeed, it takes a non-negligible period for the offshore and the continental sediment to substantially feed the estuary. If we focus on the quantity of dredged material within the domain or within the estuary, we notice that marked sediment quantities are continuously increasing during the simulation even if suspended quantities are stable. This leads us to the question "is it possible to reach a steady state with an almost stable marked sediment quantity in the model? And in suspension?".

3.3 Dispersion of Dumped Sediments on the Seabed

Figure 4 illustrates the distinctive dispersion in sediment after one month of non-cohesive (designated as sands) and mud dredged in the Rouen waterway and dumped on the disposal site of Kannik. These results show that as expected sands dynamic is much slower and lower than mud dynamic. In fact, after one month, a part of mud dumped on kannik is advected along the coast in the northern direction under the influence of the so-called Verhaule current which is linked to the flood current in the English Channel (Le Hir et al. 1985). The other part of the dumped mud can be found on mudflats located almost 30 km upstream while sand remains close to the dumping site within a 5 km radius. These features are mainly induced by the much larger settling velocity of sands, more than by any change in the erodability of deposited material.

The distribution in sediment of marked material after 3 years, either the sediment dredged in the Rouen waterway and dumped at Kannik site, or any sediment eroded by waves and/or currents, is represented on Fig. 5a, b, respectively. Their respective patterns are remarkably similar, except a relative increase of dredged sediment in the vicinity of the dumping site. This result illustrates that dumped sediment contributes to the global siltation observed in the estuary. However, at the studied time scale (3 years) the contribution of dumped sediment to the siltation appears to be more important in proximity of the disposal site.

Tracing the fate of sediment dumped by Le Havre harbor on the highly dispersive disposal site of Octeville highlights the baroclinic circulation in the area between Octeville and Le Havre navigational fairways (Schulz et al. 2018). Dredged Mud and sands dispersions after 3 years of dumping on the disposal site of Octeville are very contrasted (Fig. 6). In fact, dredged non-cohesive particles are mainly transported northward probably in agreement with a dominance of northern component (Verhaule

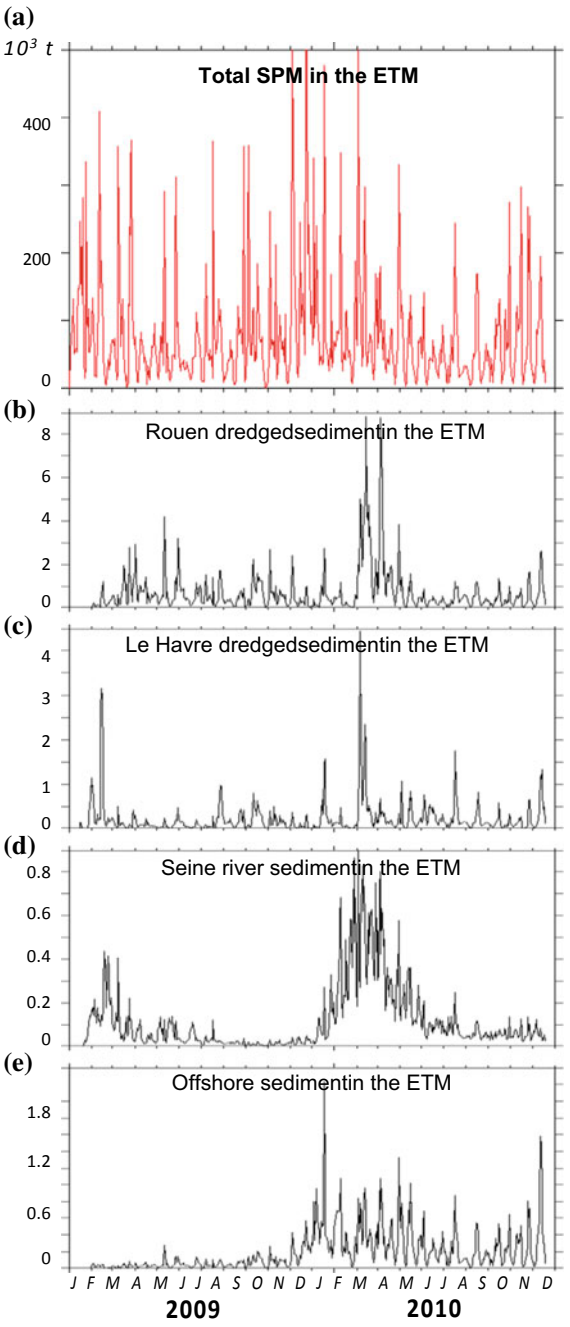

Fig. 3 Contribution of the dredging of the different sediment sources to the total SPM in the estuarine turbidity maximum zone in 10^3 t. **a** Total suspended mass in the ETM, **b** and **c** dredged sediment of Rouen and Le Havre, **d** and **e** Seine river and offshore sediment

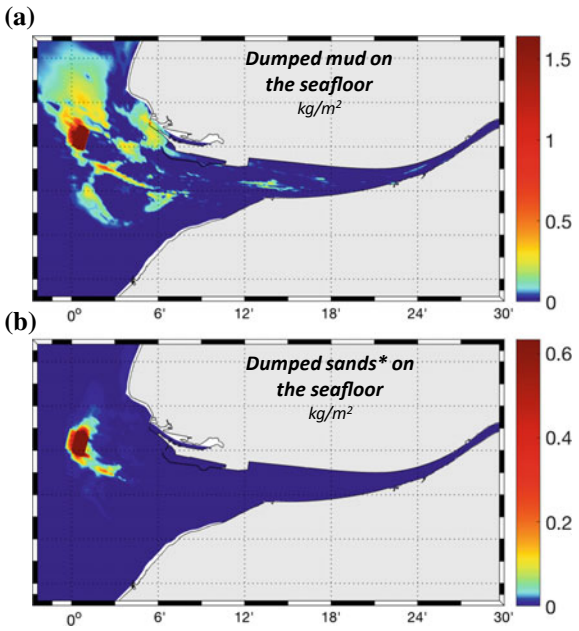

Fig. 4 Dispersion after one month of mud (**a**) and sands (**b**) dredged in the Rouen waterway and dumped on the disposal site of Kannik (*sands represents the sum of the 4 non-cohesive classes considered by the model)

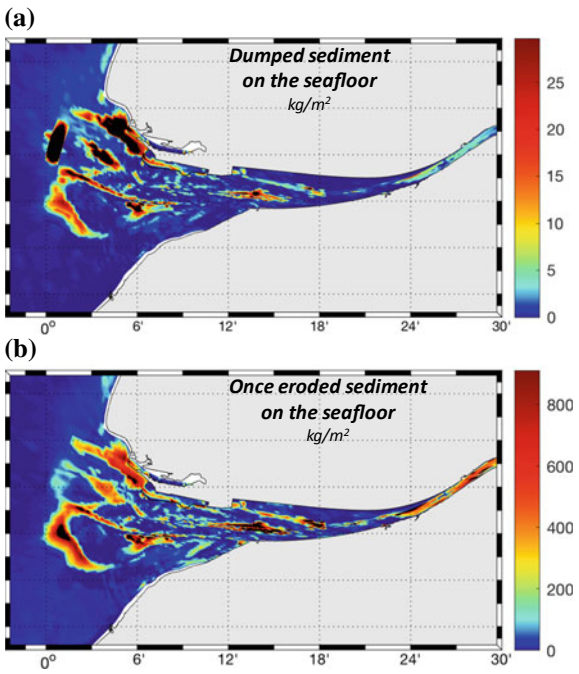

Fig. 5 Distribution in sediment of marked material after 3 years: **a** tracing affects dredged material in the Rouen waterway, **b** tracing affects any eroded sediment

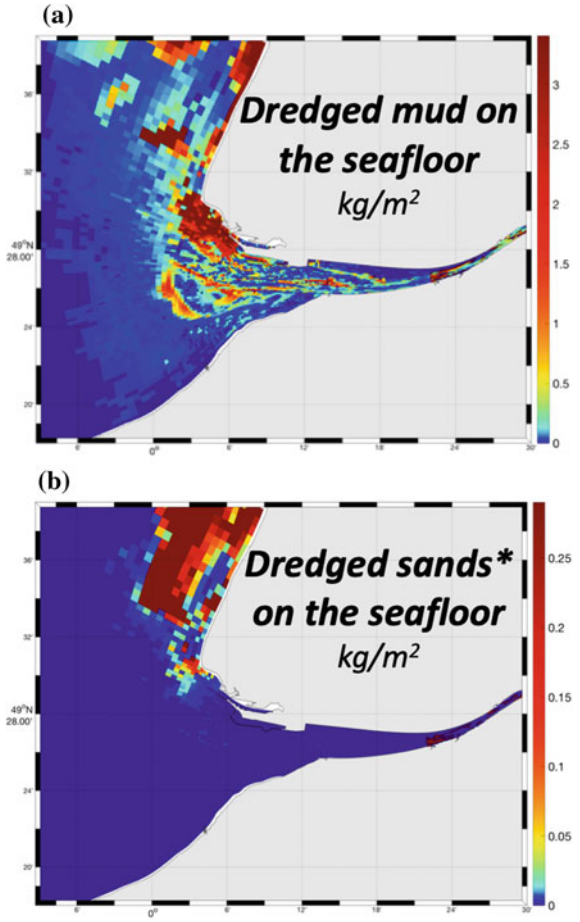

Fig. 6 Comparison of the siltation of mud (**a**) and sand (**b**) after three years of tracing Le Havre harbor dredging material (*sands represents the sum of the 4 non-cohesive classes considered by the model)

current) at the location of the dumping site. Dredged mud is also transported by the residual bottom flow induced by the baroclinic circulation towards the estuary with a relatively significant return in Le Havre navigational fairways.

4 Discussions and Perspectives

Modelling the dredging of sand and mud mixtures in estuarine navigation fairways appears to be a really difficult exercise. In fact, considering dredging as a process implies that the model is able to well reproduce both sand and mud dynamic as excess deposition in dredged areas is an integrative result of all estuarine sediment processes. With this approach of dredging, the calibration and validation of the model is dependent of the whole parameterization of the hydro-sedimentary processes as

there is no dredging specific fitting parameters. This is all the more sensitive since we should not compromise the model validation (water-level, currents, salinity, SPM, etc.) in order to be able to study the interactions of dredging activities with the global dynamic of the system.

Numerical tracing of sediment dynamic by using dedicated state variables is a powerful method to understand the importance or the role of different sediment sources and processes in the global functioning of a system. However, this method needs to be used wisely as its results appear to be time dependent, because the quantity of traced sediment in the domain can fluctuate with the duration of the simulation. In our case, numerical tracing constitutes a powerful method to quantify the implication of dredging on the natural sediment dynamics. For stakeholders, it may become an essential tool for assessing the impact of dredging activities.

Our perspectives are to model alternative scenarios to better understand the actual dynamic and its main drivers, and also to describe how dredging and natural functioning are interacting. These alternative sediment management scenarios will also be instructive to determine optimal dredging strategies which will make dredging quantities decrease overtime or which will induce positive morphologic evolutions for both the navigation and the ecological functioning. Indeed, the final objective of our study is to understand these interactions to be able to assess the impact of dredging strategies on estuarine physiotope, and thus to evaluate its implications on the estuarine ecology.

Acknowledgements This work is part of the IFREMER and GIP Seine-Aval collaborative project MEANDRES funded by the Seine-Aval research program. Data were provided by port authorities of Rouen (GPMR) and Le Havre (GPMH).

References

Avoine, J. (1981). Estuaire de la Seine : sédiments et dynamique sédimentaire. Thèse Doct. Sci., Université de Caen, 236 p.

Blanpain, O. (2009). Dynamique sédimentaire multiclasse : de l'étude des processus à la modélisation en Manche. Ph.D. Thesis, Université de Rouen. https://archimer.ifremer.fr/doc/00003/11426/.

Boutin, R. (1999). Amélioration des connaissances sur le comportement des rejets en mer de produits de dragage de type vase - Phénomènes à court terme et dans le champ proche. Thèse de doctorat de l'Institut National des Sciences Appliquées de Lyon, 527 p.

Dalrymple, R. W., Zaitlin, B. A., & Boyd, R. (1992). Estuarine facies models: Conceptual basis and stratigraphic implications. *Journal of Sedimentary Petrology, 62*(6), 1130–1146.

Dam, G., Poortman, S. E., Bliek, A. J., & Plancke, Y. (2013). Long-term modeling of the impact of dredging strategies on morpho- and hydrodynamic developments in the Western Scheldt. In *20th World Dredging Congress and Exhibition 2013 (WODCON XX)* (p. 739), Art Dredging Brussels, Belgium, 3–7 June 2013.

Delsinne, N. (2005). Evolution pluri-millenaire à pluri-annuelle du prisme sédimentaire d'embouchure de la Seine. Facteurs de contrôle naturels et d'origine anthropique. Thèse de 3ème cycle, Université de Caen. 179 p.

Jeuken, M. C. J. L., & Wang, Z. B. (2010). Impact of dredging and dumping on the stability of ebb-flood channel systems. *Coastal Engineering, 57*(6), 553–566. https://doi.org/10.1016/j.coastaleng.2009.12.004.

Grasso, F., Le Hir, P., & Bassoullet, P. (2015). Numerical modelling of mixed-sediment consolidation. *Ocean Dynamics, 65*(4), 607–616.

Grasso, F., Verney, R., Le Hir, P., Thouvenin, B., Schulz, E., Kervella, Y., et al. (2018). Suspended sediment dynamics in the macrotidal Seine Estuary (France): 1. Numerical modeling of turbidity maximum dynamics. *Journal of Geophysical Research: Oceans, 123*, 558–577. https://doi.org/10.1002/2017JC01318510.1002/2017JC013185

Hibma, A., Wang, Z. B., Stive, M. J. F., & De Vriend, H. J. (2008). Modelling impact of dredging and dumping in ebb-flood channel systems. *Transactions of Tianjin University, 15*(1), 70–74. https://doi.org/10.1007/s12209.

Hoslin, R., Brisset, P., Massias, J., Pogi, A., & Sannie, G. (1989). Etude, au moyen de traceurs radioactifs, de l'évolution des dépôts de dragage situés dans l'estuaire de la Seine – Zone de dépôt intermédiaire et du vidage aval. Rapport d'étude du Commissariat à l'Energie Atomique.

Kervella, Y., Khojasteh Pour Fard, I., Le Hir, P., Renault, E., & Lemoine, J.-P. (2012). Modélisation hydrodynamique tridimensionnelle en coordonnées curvilignes non-orthogonales de l'estuaire de la Seine. Proc. XIIèmes Journées nationales Génie Côtier-Génie Civil, Cherbourg, 12–14 juin 2012.

Khojasteh Pour Fard, I. (2015). Modélisation des échanges dissous entre l'estuaire de la Loire et les baies côtières adjacentes. Thèse de 3ème cycle, Université de Bordeaux. 258 p.

Kimoto, A., Fares, A., & Polyakov, V. (2008). Chapter 3 Sediment tracing techniques and their application to coastal watersheds. In: *WIT transactions on state of the art in science and engineering* (Vol. 33). WIT Press. https://doi.org/10.2495/978-1-84564-091-0/03.

Lazure, P., & Dumas, F. (2008). An external-internal mode coupling for a 3D hydrodynamical model for applications at regional scale (MARS). *Advances in Water Resources, 31*(2), 233–250. https://dx.doi.org/10.1016/j.advwatres.2007.06.010.

Le Hir, P., Salomon, J., Leprovost, C., Chabertd'Hieres, G., Mauvais, J. (1985). Approche de la circulation residuelle en Baie de Seine. Actes de colloques. Ifremer. Brest [ACTES COLLOQ. IFREMER.]. https://archimer.ifremer.fr/doc/00000/1263/.

Le Hir, P., Cayocca, F., & Waeles, B. (2011). Dynamics of sand and mud mixtures: A multiprocess-based modelling strategy. *Continental Shelf Research, 31*(10), S135–S149. Publisher's official version: https://dx.doi.org/10.1016/j.csr.2010.12.009, Open Access version: https://archimer.ifremer.fr/doc/00028/13952/.

Lemoine, J. P., Verney, R., Le Hir, P., & Grasso, F. (2016). Bilan sédimentaire de l'estuaire de la Seine : état des connaissances. Acte du colloque SHF: Gestion des sites à forte sédimentation.

Lemoine, J. P., Le Hir, P., & Grasso, F. (2017). Impact of maintenance dredging on suspended sediment dynamics in the Seine estuary. In: *INTERCOH Conference*, Montevideo, 13–17 November 2017.

Lesourd, S. (2000). Processus d'envasement d'un estuaire macrotidal: zoom temporel du siècle à l'heure; application à l'estuaire de la Seine. Thèse de 3ème cycle, Université de Caen. 290 p.

Lesourd, S., Lesueur, P., Fisson, C., & Dauvin, J.-C. (2015). Sediment evolution in the mouth of the Seine estuary (France): A long-term monitoring during the last 150years. Comptes Rendus Geoscience.

Monge-Ganuzas, M., Cearreta, A., & Evans, G. (2013). Morphodynamic consequences of dredging and dumping activities along the lower Oka estuary (Urdaibai Biosphere Reserve, Southeastern Bay of Biscay, Spain). *Ocean and Coastal Management, 2013*(77), 40–49. https://doi.org/10.1016/j.ocecoaman.2012.02.006.

Nguyen, D. H., Levy, F., PhamVan Bang, D., Guillou, S., Nguyen, K. D., & Chauchat, J. (2012). Simulation of dredged sediment releases into homogeneous water using a two-phase model. *Advances in Water Resources, 48*, 102–112.

Roland, A., & Ardhuin, F. (2014). On the developments of spectral wave models: Numerics and parameterizations for the coastal ocean. *Ocean Dynamics, 64*(6), 833–846.

Schulz, E., Grasso, F., Le Hir, R., Verney, B., & Thouvenin, B. (2018). Suspended sediment dynamics in the macrotidal Seine Estuary (France): 2. Numerical modeling of sediment fluxes and budgets under typical hydrological and meteorological conditions. *Journal of Geophysical Research: Oceans, 123*(1), 578–600.

Van Leussen, W. (1994). Estuarine macroflocs and their role in fine-grained sediment transport. Ministry of Transport, Public Works and Water Management, National Institute for Coastal and Marine Management (RIKZ).

Waeles, B., & Le Hir, P. (2006). Simulation des activités de dragage et de leur impact sédimentaire à l'aide d'une modélisation morphodynamique de l'embouchure de la Seine, 471–481. https://doi.org/10.5150/jngcgc.2006.046-W.

A Semi-coupled Projection Model for the Morphodynamics of Fast Evolving Flows Based on an Unstructured Finite-Volume Method

Miguel Uh Zapata and Kim Dan Nguyen

Abstract The aim of this work is to present a numerical method for fast evolving flows governed by the two-dimensional shallow water equations semi-coupled with the Exner sediment balance equation for bed evolutions. The method is based on Chorin's projection, which combines the momentum and continuity equations in order to establish a Poisson-type equation for the water surface level including the bed evolution. The equations are discretized using an unstructured finite-volume technique. In the model, a second-order upwind scheme combined with a Local Extremum Diminishing method is developed to handle convection terms. A comparison with quasi-analytical and existing numerical results are done to test the performance of the used scheme, including the modeling of a dam-break on a mobile bed.

Keywords Sediment transport · Exner equation · Shallow-water equations · Unstructured finite-volume method · Projection method · Dam-break

1 Introduction

The present study aims to show the numerical capacities of a model based on the projection technique for fast evolving flows and sediment transport. In more detail, we show that for dam-break events, the proposed formulation performs similar to ones with more sophisticated solvers. This work is focused on the cases where the influence of the suspended load is negligible. The morphodynamic process is described by the Exner equation.

M. Uh Zapata (✉)
CONACYT - Centro de Investigación en Matemáticas A.C, CIMAT-Mérida, 97302 Mérida, México
e-mail: angeluh@cimat.mx

K. D. Nguyen
Laboratory for Hydraulics Saint-Venant, Université Paris-Est, ENPC-EDF-CEREMA, 78400 Chatou, France

K. D. Nguyen et al. (eds.), *Estuaries and Coastal Zones in Times of Global Change*, Springer Water,
https://doi.org/10.1007/978-981-15-2081-5_16

Several numerical formulations have been proposed in the literature to solved this problem. The suitable numerical strategy depends on the physical and mathematical nature of the problem (Garegnani et al. 2011). A coupled approach is preferable for simulating the cases with rapidly-varies flows such as dam-break over mobile beds. On the other hand, the uncoupled approach is mainly used for slowly bed evolution over a long time.

Many numerical methods, coupled and uncoupled, are used to solve the Saint-Venant-Exner system (Hudson and Sweby 2005; Castro Díaz et al. 2009; Murillo and García-Navarro 2010; Bilanceri et al. 2012; Liu and Beljadid 2017; Bladé et al. 2014). In general, the coupled strategy has shown to be more stable than the uncoupled method. However, it has the inconvenience of theoretical complexities due to the nature of the implementation, high numerical cost and excessive diffusion in the evolution of the bed. Semi-coupled methods can be a preferred option. These methods have many of the advantages of uncoupled methods with more stability, a better response to high dependence fluid-sediment and also to super-critical fluids (Kassem and Chaydhry 1998; Wu 2004; Juez et al. 2014). In this chapter, the formulation is based on a semi-coupled approach.

Although many works have been done using structured elements, the use of unstructured meshes is necessary for real applications. There are different numerical formulations using a finite volume method on unstructured grids. Recently, the authors have proposed a semi-coupled projection technique (Uh Zapata et al. 2019) using an unstructured finite volume method (UFVM) originally developed by Nguyen et al. (2006); Shi et al. (2013). However, only slow varying flows are already analyzed. Thus, the purpose of this chapter is to present a semi-coupled numerical method for the solution of Saint-Venant-Exner equations for fast evolving flows.

In the present model, the continuity and momentum equations of the Saint-Venant equations are combined to establish a water surface Poisson-type equation including the bed evolution. Then the Exner equation is solved. A second-order upwind scheme is introduced to handle convection terms. In order to preserve the monotonicity of the variables, the Local Extremum Diminishing (LED) technique proposed by Vidović et al. (2006) is used here. To the best of the present authors' knowledge, previous works considering the same formulation to simulate fast evolving flows are not found in the existing literature.

The organization of this chapter is as follows. Section 2 introduces the governing equations of the problem. In Sect. 3, the projection method is described. In Sect. 4, the unstructured finite volume method is presented. In Sect. 5, numerical experiments are conducted to show the efficiency and the effectiveness of the present model. Finally, conclusions are given in the Sect. 6.

2 The Governing Equations

In this chapter, the hydrodynamic component is governed by the Saint-Venant equations (Saint-Venant 1871). Continuity and momentum equations are

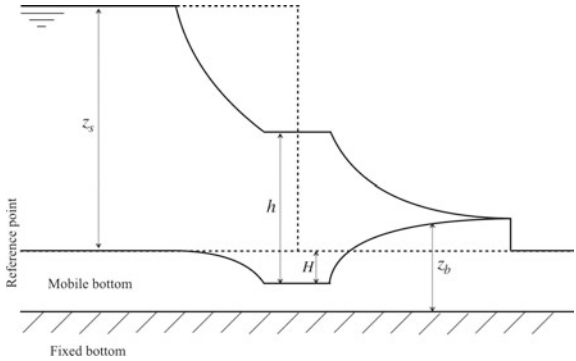

Fig. 1 Sketch of the flow variables and initial conditions of the dam-break on a mobile bed

$$\frac{\partial h}{\partial t} + \frac{\partial q_x}{\partial x} + \frac{\partial q_y}{\partial y} = 0, \tag{1}$$

$$\frac{\partial q_x}{\partial t} + \frac{\partial u q_x}{\partial x} + \frac{\partial v q_x}{\partial y} = -gh\frac{\partial z_s}{\partial x} - \frac{\tau_{bx}}{\rho} + f q_y, \tag{2}$$

$$\frac{\partial q_y}{\partial t} + \frac{\partial u q_y}{\partial x} + \frac{\partial v q_y}{\partial y} = -gh\frac{\partial z_s}{\partial y} - \frac{\tau_{by}}{\rho} - f q_x, \tag{3}$$

where $h(\mathbf{x}, t) = H + z_s$ represents the total water depth, z_s is the water surface elevation, and H is the bottom depth measured from a fixed level of reference, see Fig. 1. The unit discharges are denoted as

$$\mathbf{q} = (q_x, q_y) = (hu, hv),$$

where u and v are the depth-averaged velocity components in x- and y-direction, respectively; g is the gravity acceleration; f is the Coriolis parameter and ρ denotes the water density. In the equations, $\boldsymbol{\tau}_b = (\tau_{bx}, \tau_{by})$ is the bed shear stress due to steady flow, and it can be expressed by using the Chézy's formula as follows

$$\frac{1}{\rho}\boldsymbol{\tau}_b = \left(\frac{\tau_{bx}}{\rho}, \frac{\tau_{by}}{\rho}\right) = (F q_x, F q_y),$$

where

$$F = \frac{g}{h^2 C_h^2}||\mathbf{q}||,$$

and the Chézy coefficient is given by

$$C_h = h^{1/6}/n,$$

with n as the Manning's coefficient of the bed.

The morphodynamic process is described by the Exner equation. Let $z_b(\mathbf{x}, t)$ be the bed thickness laying on a non-erodible bottom; the sediment layer motion due to bed load transport is given by

$$\frac{\partial z_b}{\partial t} + \xi \frac{\partial q_{bx}}{\partial x} + \xi \frac{\partial q_{by}}{\partial y} = 0 \tag{4}$$

where $\xi = (1 - \sigma)^{-1}$ with $\sigma \in (0, 1)$ being the porosity of the bed material and $\mathbf{q_b}$ is the sediment transport discharge. In this work we consider the formulation proposed by Grass (1981) for the solid transport discharge, which considers $\mathbf{q}_b$ as a function of the flow velocity and a constant coefficient. Thus, the solid transport discharges in (4) is given as

$$\mathbf{q}_b = (q_{b_x}, q_{b_y}) = A_g \|\mathbf{u}\|^2 (u, v), \tag{5}$$

where $A_g \in (0, 1]$ (s^2/m) takes into account the grain diameter and the kinematic viscosity and is directly related to the strength of the interaction between the water flow and the bed load.

3 The Semi-coupled Projection Method

In this chapter, we consider a semi-coupled approach to solve the system of equations (1)–(4). This is not an uncoupled approach because the projection method includes the change of the sediment bed in the hydrodynamic approximation as described in this section.

Although Saint-Venant equations only consider the hydrostatic pressure, the projection method suggested by Chorin (1968) can be applied to split up the fluid components and water surface elevation separately. The projection method consist of three steps: the convection-diffusion equations, a water surface Poisson equation and a velocity correction.

First, the momentum equations (2) and (3) are split into two parts:

$$\begin{aligned} \frac{q_x^* - q_x^n}{\Delta t} + \frac{\partial (u q_x^*)}{\partial x} + \frac{\partial (v q_y^*)}{\partial y} &= 0, \\ \frac{q_y^* - q_y^n}{\Delta t} + \frac{\partial (u q_y^*)}{\partial x} + \frac{\partial (v q_y^*)}{\partial y} &= 0. \end{aligned} \tag{6}$$

and

$$\begin{aligned} \frac{q_x^{n+1} - q_x^*}{\Delta t} &= -gh \frac{\partial z_s}{\partial x} - F q_x^n + f q_y^n, \\ \frac{q_y^{n+1} - q_y^*}{\Delta t} &= -gh \frac{\partial z_s}{\partial y} - F q_y^n - f q_x^n. \end{aligned} \tag{7}$$

Note that the first set of equations do not include the water surface elevation term z_s. This yields an approximation of the velocity field field, which is in general not divergence free. A correction with water elevation terms is applied to the velocity field using (PMstep2). Subscript $(*)$ is purely symbolic to design values of q_x and q_y, obtained after this step.

A divergence free velocity field is produced by taking the divergence of the momentum equations and employing the continuity equation. However to overcome time-step restriction, a full-implicit scheme is considered. Thus, all space derivatives are evaluated in the new time step. The combination of the continuity and momentum equations without convection and diffusion terms allows us to get a Poisson-type equation for only water surface levels

$$\delta_z = z_s^{n+1} - z_s^n, \tag{8}$$

as unknowns. Thus in the second step, we solve

$$\left[1 - \frac{gh}{\alpha}\left(\frac{\partial^2}{\partial x^2} + \frac{\partial^2}{\partial y^2}\right)\right]\delta_z = f_\delta, \tag{9}$$

where the right-hand side f_δ is given by

$$f_\delta = \frac{\beta}{\alpha} - \Delta t \frac{\partial H}{\partial t}, \tag{10}$$

with

$$\alpha = \frac{1}{\Delta t}\left(\frac{1}{\Delta t} + F\right), \tag{11}$$

$$\beta = gh\left(\frac{\partial^2 z_s^n}{\partial x^2} + \frac{\partial^2 z_s^n}{\partial y^2}\right) - \frac{\partial f q_y^n}{\partial x} + \frac{\partial f q_x^n}{\partial y} - \frac{1}{\Delta t}\left(\frac{\partial q_x^*}{\partial x} + \frac{\partial q_y^*}{\partial y}\right). \tag{12}$$

It is important to remark that term $\Delta t \frac{\partial H}{\partial t}$ at the right-hand side of equation (10) includes the changed of sediment bed z_b which has not been considered in previous works only simulating the shallow water flows (Nguyen et al. 2006; Shi et al. 2013). We now must introduce this term to take into consideration the changing bottom at each time step; particularly for fast evolving flows.

Finally, the unit discharges are corrected using (7). Once unknowns q_x, q_y and z_s are solved, the bed elevation z_b is updated by

$$\frac{z_b^{n+1} - z_b^n}{\Delta t} + \xi\left(\frac{\partial q_{bx}^{n+1}}{\partial x} + \frac{\partial q_{by}^{n+1}}{\partial y}\right) = 0. \tag{13}$$

The equations will be discretized on unstructured grids by a finite-volume method as described in the next section.

4 Unstructured Finite Volume Method

The idea of the finite volume scheme is to find an approximation of the solution of equations (6)–(7), (9) and (13) by setting up a system of discrete equations for the values in control volumes. The two-dimensional domain is discretized into triangular cells. The index i indicates its position in the horizontal. Thus each triangular-shaped control volume V_i has 3 edges L_j ($j = 1, 2, 3$). The cell centered node of each triangle is denoted by $\mathbf{x}_i$. A schematic plot of the discretization is shown in Fig. 2. We define the unknowns at the cell-centered point of the triangles. In the following sections, we briefly described the discretization for the momentum, Poisson and Exner equations.

4.1 Discretization of the Momentum Equation

Following the idea of the finite volume framework, momentum equations are integrated over each control volume V_i. By applying Green's theorem, we get

$$m(V_i)\frac{\phi_i - \phi_i^n}{\Delta t} + \sum_{j=1}^{3} \int_{L_j} \phi\,(u, v) \cdot \mathbf{n}_j dL = 0, \tag{14}$$

where ϕ can denote either q_x or q_y, $m(V_i)$ indicates the area of V_i, and $\mathbf{n}_j$ is the normal unit vector at each edge L_j.

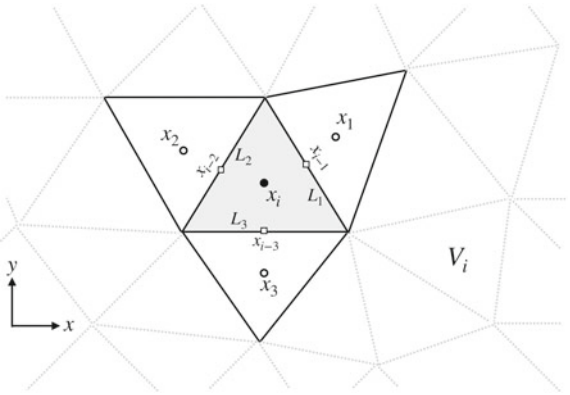

Fig. 2 Discretization in triangular elements of a two-dimensional domain. Control volume V_i, cell-centered point x_i and neighbors x_j ($j = 1, 2, 3$), triangular edges L_j and middle edge points x_{i-j}

To avoid stability problems, the fluxes are approximated using an upwind scheme. Thus, a finite volume discretization of the convection term is given by

$$\int_{L_j} \phi\,(u, v) \approx \phi_{i-j} U_{i-j}, \tag{15}$$

where ϕ_{i-j} accounts for the variable ϕ at the middle edge point x_{i-j} of L_j. The values U_{i-j} represent the mass flux crossing the edge and it is approximated as follows

$$U_{i-j} \approx (u, v)_{i-j} \cdot \mathbf{n}_j \Delta L_j, \tag{16}$$

where ΔL_i is the length of the edge L_j. The edge velocity components $(u, v)_{i-j}$ are evaluated using an space average value of u and v over the control volume V_i and V_j. Finally, a second-order accuracy scheme is obtained by using a Taylor expansion around x_{i-j} as follows

$$\phi_{i-j} = \begin{cases} \phi_i + \psi_i \nabla\phi_i \cdot \mathbf{r}_i & U_{i-j} \geq 0, \\ \phi_j + \psi_j \nabla\phi_j \cdot \mathbf{r}_j & U_{i-j} < 0, \end{cases} \tag{17}$$

where $\mathbf{r}$ is the position vector from the cell-center to the edge. In order to eliminate non-desirable oscillations and to improve the stability of the numerical results, Eq. (17) is modified by introducing ψ_i and ψ_j as flux limiters. We apply the Local Extremum Diminishing (LED) technique proposed by Vidović et al. (2006). It is determined such that

$$\min_j(\phi_i, \phi_j) = \phi_{\min} \leq \phi_{i-j} \leq \phi_{\max} = \max_j(\phi_i, \phi_j)$$

where the minimum and the maximum are taken over V_i and the three surrounding cells V_j. A unique value of the flux limiter per control volume V_i is determined as

$$\psi_i = \min_j(\psi_{i-j}), \tag{18}$$

where

$$\psi_{i-j} = \begin{cases} \min\left(1, \frac{\phi_{\max} - \phi_j}{\Theta_i}\right), & \Theta_e > 0 \\ \min\left(1, \frac{\phi_{\min} - \phi_j}{\Theta_i}\right), & \Theta_e < 0 \\ 1 & \Theta_e = 0 \end{cases}, \tag{19}$$

and

$$\Theta_i = \nabla\phi_i \cdot \mathbf{r}_i. \tag{20}$$

This technique ensures that local maximum cannot increase and local minimum cannot decrease. Note that gradient approximations are needed which is determined by a least square technique (Kobayashi et al. 1999).

4.2 Discretization of the Poisson Equation

Poisson equation (9) is discretized as follows

$$m(V_i)\delta_z - \frac{gh}{\alpha}\sum_{j=1}^{3}\int_{L_j}\nabla\delta_z\cdot\mathbf{n}_j dL = \int_{V_i} f_\delta dA. \tag{21}$$

The diffusive term is approximated by the sum of numerical diffusive flux approximations as follows

$$\int_{L_j}\nabla\delta_z\cdot\mathbf{n}_j dL \approx (\nabla\delta_z)_{i-j}\,\mathbf{n}_j\Delta L_j, \tag{22}$$

where the gradient approximation is given by

$$(\nabla\delta_z)_{i-j} \approx \frac{1}{m(V_{i-j})}\left[\sum_{s=1}^{4}\int_{L_s}\delta_z\,\mathbf{n}_{L_s}dS\right]. \tag{23}$$

In this equation, V_{i-j} represents the 2D region delimitated by the two cell-centers and the vertices of the interface. Each region V_{i-j} is delimitaded by four faces L_s with $\mathbf{n}_{L_s}$ as unit normal and $m(V_{i-j})$ as the corresponding area. The final integrals at equation (23) are approximated using the trapezoidal rule. The discretization of the diffusion term involves the knowlegde of the values at the vertex points which are obtained by averaging over all surrounding cell-centered nodal values. The readers can be referred to (Shi et al. 2013) for more details of these techniques.

4.3 Discretization of the Exner Equation

In this section, we apply the finite volume discretization of Exner equation by considering the function

$$\phi = \xi A_g\|\mathbf{u}\|^2. \tag{24}$$

Equation (13) is integrated on each prism control volume V_i. After application of Green's theorem, the integral of the second term becomes

$$m(V_i)\frac{z_{b_i}^{n+1}-z_{b_i}^{n}}{\Delta t}+\sum_{j=1}^{3}\int_{L_j}\phi(u,v)\cdot\mathbf{n}_j dL=0, \tag{25}$$

Thus, a finite volume discretization of the Exner equation is given by

$$z_{b_i}^{n+1}=z_{b_i}^{n}-\frac{\Delta t}{m(V_i)}\sum_{j=1}^{3}\phi_{i-j}^{(n+1)}U_{i-j}^{(n+1)}, \tag{26}$$

where ϕ_{i-j}^{n+1} accounts for the discretization of variable at the control volume edges and $U_{i-j}^{(n+1)}$ for the discretization of the mass flux. These values are also computed with an adequate upwind scheme and flux limiter (17).

5 Numerical Results

In this section, the semi-coupled projection formulation is tested by several examples. Linear systems are solved using the Gauss-Seidel method with a tolerance value of $\varepsilon = 10^{-5}$. Unstructured meshes have been generated using the free software BlueKenue developed by the Canadian Hydraulics Centre. In the case of structured meshes, the domain is firstly divided into uniform rectangles and then each rectangle is split into two right-angled triangles. In this work, we denote Δx as the length of the side of the uniform rectangle for structured meshes or as the mean interior edge length for unstructured meshes.

5.1 Bed Load Transport of a Sediment Layer with Lintel Form

For the first example, let us consider a sediment layer of lintel form in a frictionless rectangular channel. The motivation for considering this problem is to analyze the proposed model with a slowly varying bed. The computational domain consists of a channel of length 1000 m × 100 m. The bottom is initially described by

$$z_b=\begin{cases}0.1+\sin^2\left(\frac{\pi(x-300)}{200}\right) & 300\le x\le 500,\\ 0.1 & \text{otherwise},\end{cases}$$

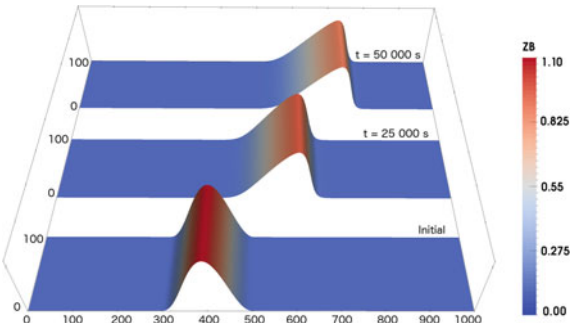

Fig. 3 Numerical solution of the bed load transport of a sediment layer with lintel form at different times using an unstructured mesh of 12,165 triangular cells

and the initial conditions are given by

$$
\begin{aligned}
h(x, y, 0) &= 10.1 - z_b(x, y, 0), \\
q_x(x, y, 0) &= 10 \text{ m}^2/\text{s}, \\
q_y(x, y, 0) &= 0.
\end{aligned}
$$

The discharge $\mathbf{q} = (10, 0)$ and the sediment thickness $z_b = 0.1$ are imposed at $x = 0$ and a free boundary condition is imposed at $x = 1000$ m. Slip boundary conditions are imposed at the lateral walls $y = 0$, $y = 100$. Finally, the model is based on Grass formula with $A_g = 0.01$ and sediment porosity $\sigma = 0.4$.

Figure 3 shows the bed load sediment transport at the initial and two simulated time stages using an unstructured mesh of 12,165 triangular elements with a mean interior edge length of 4.4 m. The numerical solution is obtained using $\Delta t = 0.1$ as a time step. As expected, numerical results shows that the bed load are accurately resolved.

Figure 4 shows the bed elevation at the main horizontal cross section ($y = 50$ m) at $t = 50,000$ s. Figure 4a compares the proposed UFVM with the one-dimensional quasi-analytical solution proposed by Hudson and Sweby (2003) and the numerical solution based on a Roe method (*HOS2-Rec2*) presented by Castro Díaz et al. (2009). For a better comparison, only the central part of the computational domain is illustrated. Note that the numerical results are in good agreement with the quasi-analytic solution. Moreover, the present finite volume formulation shows similar results to those obtained with more sophisticated second-order solvers.

The coupling between the hydrodynamics and the bed evolution is given by the incorporation of the term $\frac{\partial H}{\partial t}$ in Poisson equation (9). If we consider a slowly varying bed, then the derivative is close to zero and uncoupled discretization is recovered. The effect of the lack of this term is analyzed in Fig. 4b. As expected, both solutions, with and without the term $\frac{\partial H}{\partial t}$, are almost identical. However, this is not the case of the modelling of the fast evolution of mobile beds, as we will discuss next.

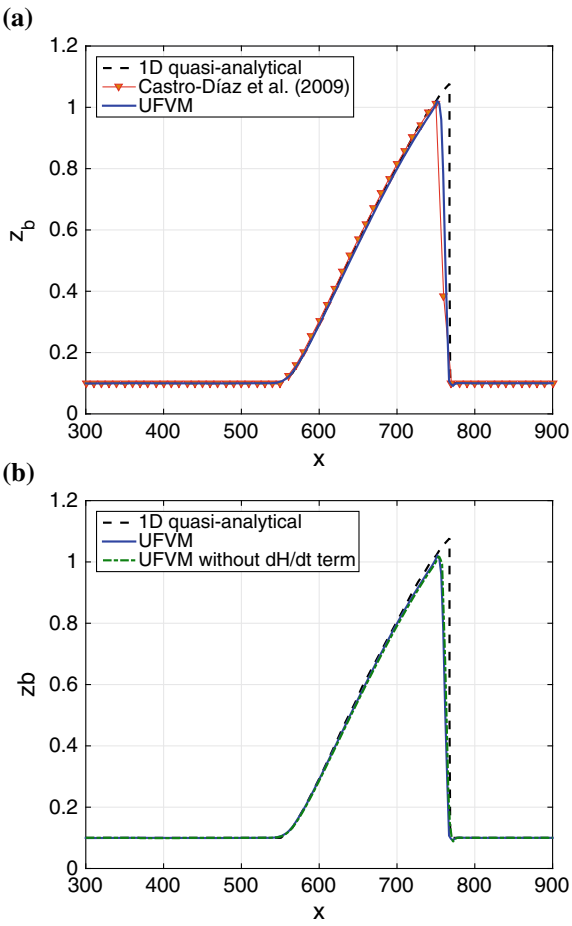

Fig. 4 Bed level at $t = 50,000$ s of the sediment layer with lintel form problem at reference point $y = 50$ m using different numerical models

5.2 *Dam-Break Flow over a Fixed Bed*

The accuracy of the proposed numerical model is now tested for an idealized dam-break flow over a horizontal frictionless and fixed bed, for which the exact solution is known (Fraccarollo and Toro 1995). This problem is ideal to know the limit of the UFVM in capturing shock waves and simulating unsteady flows with the presence of discontinuity of velocity and water-level profiles. This problem is also chosen to know the appropriate spatial resolution for the given initial water depths.

This example consists of the dam-break problem in a rectangular channel $[-1, 0.6] \times [0, 0.1]$ with a bottom assumed to be flat. The initial depth is given by

$$h = \begin{cases} h_1 \; x \leq 0, \\ h_2 \; x > 0. \end{cases} \tag{27}$$

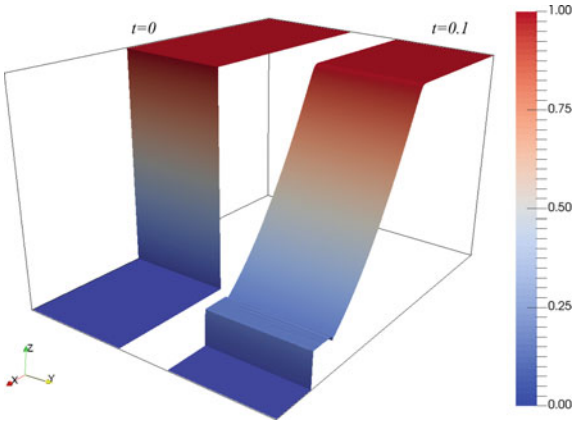

Fig. 5 Water elevation profile using $h = 0.01$ for the dam-break flow over a fixed bed at $t = 0$ and 0.1 s

The dam suddenly collapses at $t = 0$ and the simulation evolves until $t = 0.1$ s, as shown in Fig. 5. The computational domain is discretized by 51,200 triangles ($\Delta x = 0.0025$ m). The simulating time uses the time steps of $\Delta t = 10^{-4}$.

Figure 6 presents the analytical and numerical results obtained by the UFVM using $h_2 = 0.1$ m, 0.05 m, and 0.01 m, respectively. A simple inspection of these results shows that the water elevation and the velocity profiles are accurately resolved for $h_2 = 0.1$ and 0.05. For $h_2 = 0.01$, the numerical still predicts the general features of the analytical solution. However, the present model is not good enough in capturing discontinuous waves when the problem becomes more hyperbolic dominant ($h_2 < 0.01$). It is important to remark that the current UFVM results shows more precision compared to the numerical simulations presented by Nguyen et al. (2006) without a flux limiter formulation. Moreover, stable solution for smaller values of h_2 can now be simulated.

Figure 7 shows the water elevation and velocity at times $t = 0.1$ s using 52,200, 12,800, 3200 and 0.02 triangular elements corresponding to structured meshes of $\Delta x = 0.0025$, 0.005, 0.01 and 0.02, respectively. Note that for a better comparison, only parts of the computational domain are illustrated. Even for coarse meshes, results shows an overall agreement between the analytical and numerical solution of the water elevation and velocity profiles. Thus, the UFVM is also suitable to model the evolution of a coarse-water elevation in the presence of a fast varying flow.

5.3 Dam Break Flow over an Erodible Bed

Dam-break over mobile beds provides a unique case to gain enhanced insight into the interaction between flow, sediment transport, and morphological evolution, which is so magnified to identify (Cao et al. 2004). For the mobile bed case, we consider the Grass model for $\mathbf{q}_b$ with condition $A_g = 0.004$ s^2/m and sediment porosity $\sigma = 0.4$.

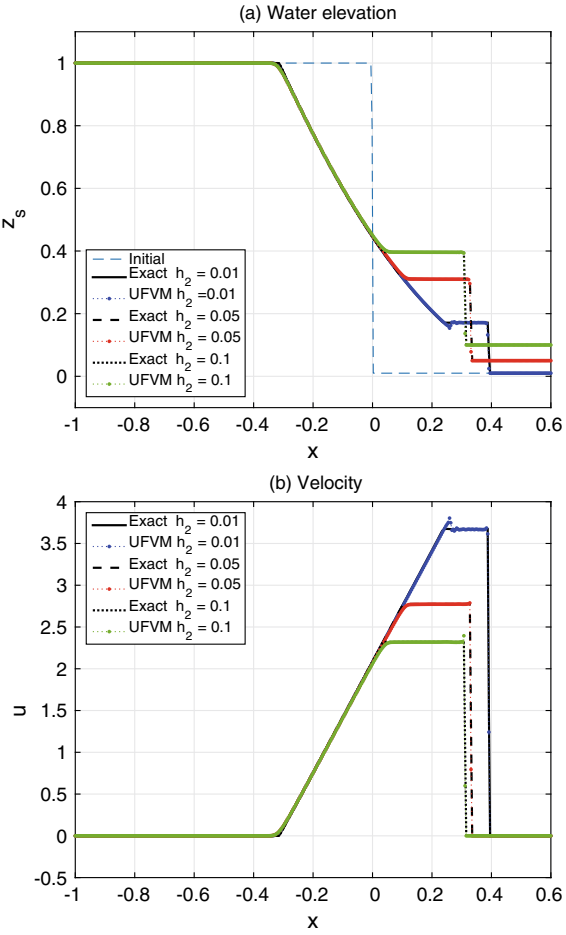

Fig. 6 **a** Water elevation and **b** velocity for different h_2 values at $t = 0.1$ s

In this case, the channel is 20 m long with the width of 0.1 m. The dam is initially located at the middle of the channel ($x = 0$). The initial depth is given by Eq. (27). In all the tests considered in this section, the mesh corresponds to a structured triangular mesh using different values Δx. The time step is $\Delta t = \times 10^{-5}$ which is considerably smaller that the fixed bed test case.

Figure 8 shows the water elevation and bed profiles for the initial condition and at $t = 1$ using $h_2 = 10^{-3}$ m. The computational domain is discretized by 40,000 triangles. The size of triangles is generated using $\Delta x = 0.02$ m. It is important to remark that the numerical solution is unstable if we do not include the term $\frac{\partial H}{\partial t}$ in the right-hand side of the Poisson equation (9).

Figure 9 shows a comparison between the quasi-analytical (Kelly 2009) and the unstructured finite volume solution for the water elevation, velocity and bed profiles using $\Delta x = 0.02$ m. We also plot the one-dimensional computed solution presented

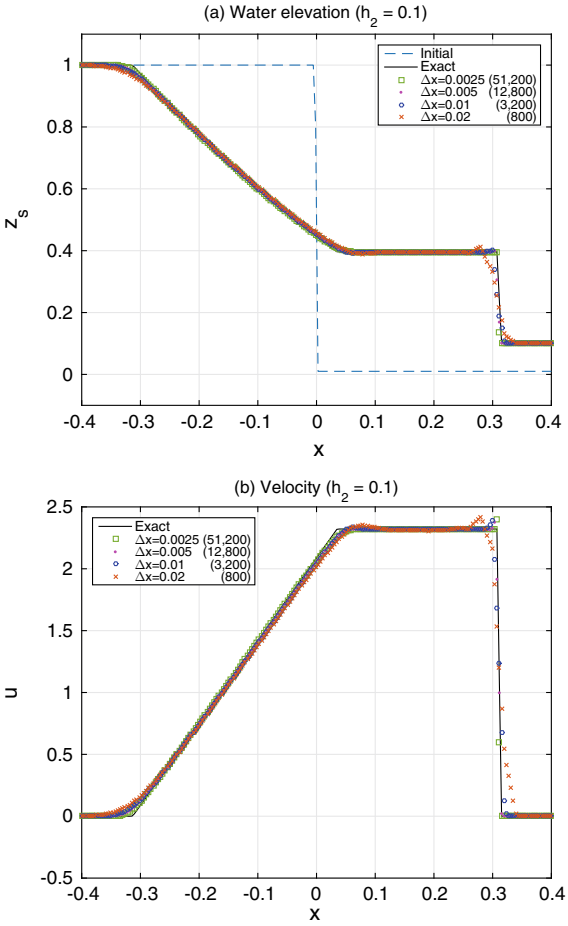

Fig. 7 **a** Water elevation and **b** velocity for $h_2 = 0.1$ m at $t = 0.1$ s using different mesh resolutions. The number between parenthesis corresponds to the total number of triangular cells used for each simulation

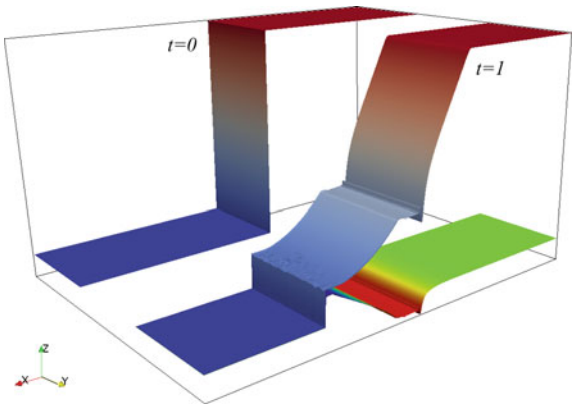

Fig. 8 Water elevation and sediment bed profiles for the dam-break flow over a mobile bed at $t = 0$ and 1 s using a mesh of resolution of $\Delta x = 0.01$ and $h_2 = 10^{-3}$

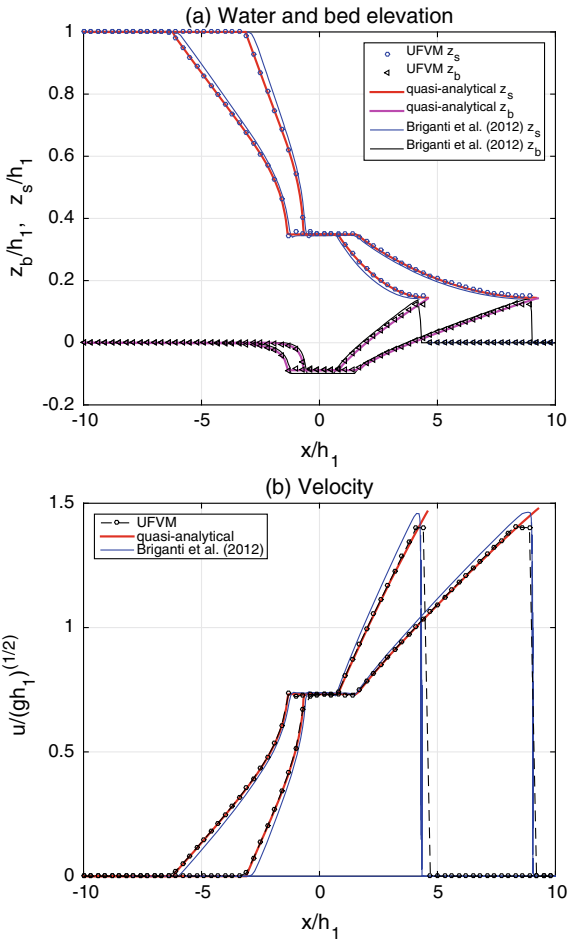

Fig. 9 Numerical results for the dam-break on a mobile bed at $t = 1$ and 2 s using $\Delta x = 0.02$ and $h_2 = 10^{-3}$. Dimensionless **a** water, bed elevation and **b** velocity. Solid lines correspond to the quasi-analytical solution (red and magenta) and the numerically predicted (blue and black) by Briganti et al. (2012)

by Briganti et al. (2012) based on a coupled approach. Note that the UFVM numerical results agree well with the quasi-analytical. Moreover, the proposed method is closer to the quasi-analytical than the computed results using the TVD-MacCormack scheme proposed at (Briganti et al. 2012). However, the our method shows small instabilities close to the discontinuities.

Figure 10 shows the water elevation, sediment bed and velocity at time $t = 1$ s using different mesh resolutions. Results shows an overall agreement between the quasi-analytical and numerical solution. However, the numerical solution using this coarse mesh seem to be deteriorated by excessive numerical diffusion. This effect is more visible at the late stages of the simulation times.

Finally, we examine the effect of the minimum depth by comparing the numerical results using $h_2 = 10^{-2}$ and $h_2 = 10^{-3}$. Figure 11 shows the numerical results at times $t = 1$ s. A simple inspection of these results shows that the accuracy of all

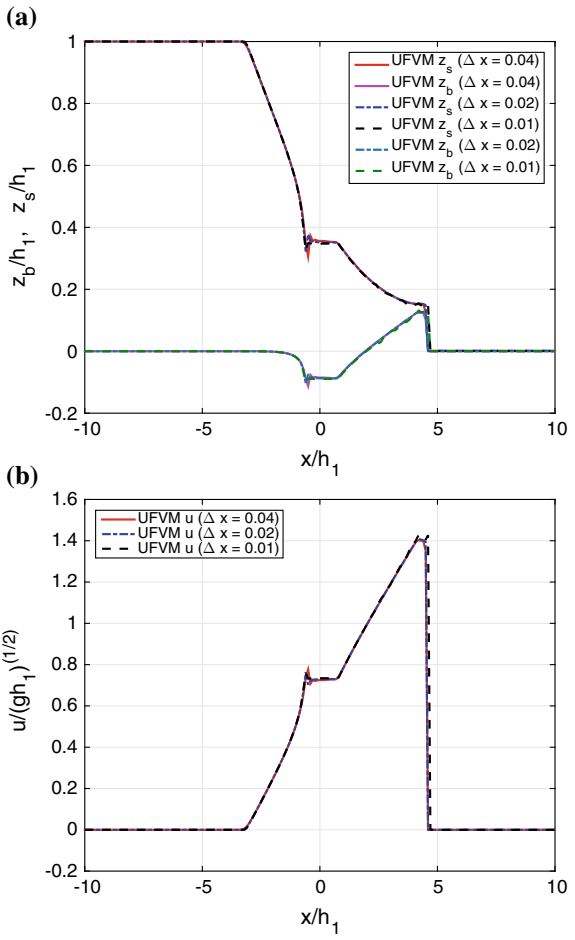

Fig. 10 Dimensionless **a** water elevation, sediment bed and **b** velocity profiles for $h_2 = 0.001$ m at $t = 1$ s using different mesh resolutions

variables are significantly affected by the selection of this value. For the dam break over mobile beds, value $h_2 = 10^{-3}$ m is the minimum that will still preserve stability of the proposed model. However, note that h_2 is smaller than the values already tested in the previous section.

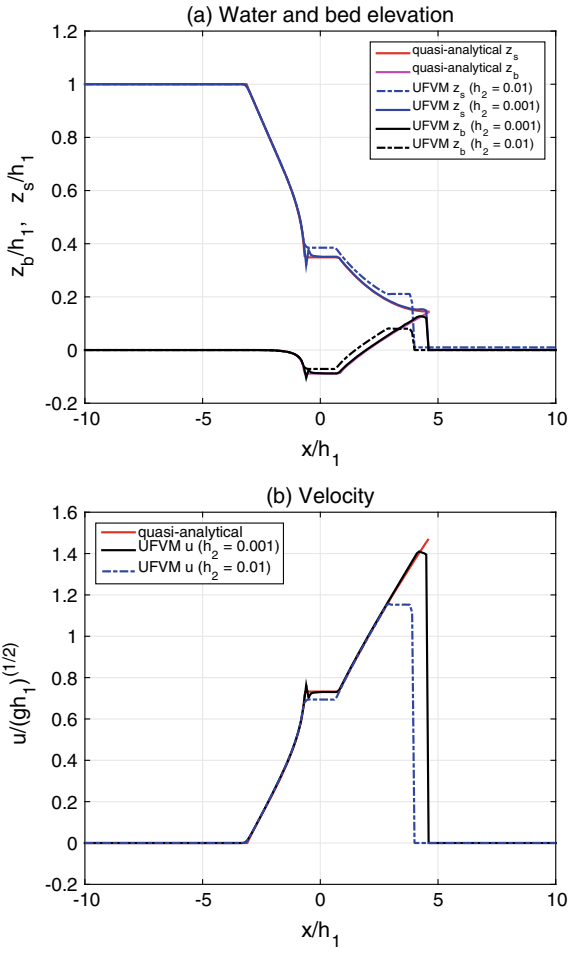

Fig. 11 Dimensionless **a** water elevation, sediment bed and **b** velocity profiles for $h_2 = 10^{-3}$ m and $h_2 = 10^{-2}$ at $t = 1$ s using $\Delta x = 0.02$

6 Conclusions

In this chapter, we present a finite-volume method for solving a semi-coupled model of bed load transport in shallow-water fast evolving flows. The proposed method solves the Saint-Venant-Exner system by a projection technique. To increase the accuracy and stability of the scheme, a flux limiter technique is incorporated in the approximation of nonlinear terms. Validation of the proposed method is carried out using the break dam over fixed and mobile bottoms. The method exhibited good shape, high accuracy and stability behavior for the water elevation, sediment bed and velocity components. The presented results demonstrate the capability of the unstructured finite-volume method that can provide insight to complex bed load transport in shallow-water flows.

Acknowledgements This work was partially supported by a Mexican Council of Science and Technology, CONACYT Grant CB No. 256252.

References

Bilanceri, M., Beux, F., Elmahi, I., Guillard, H., & Salvetti, M. V. (2012). Linearized implicit time advancing and defect correction applied to sediment transport simulations. *Computers & Fluids*, *63*, 82–104.

Bladé, E., Cea, L., Corestein, G., Escolano, E., Puertas, J., Vázquez-Cendón, E., et al. (2014). Iber: herramienta de simulacin numérica del flujo en ríos. *Revista Internacional de Métodos Numéricos para Cálculo y Diseño en Ingeniería*, *30*(1), 1–10.

Briganti, R., Dodd, N., Kelly, D., & Pokrajac, D. (2012). An efficient and flexible solver for the simulation of the morphodynamics of fast evolving flows on coarse sediment beaches. *International Journal for Numerical Methods in Fluids*, *69*(4), 859–877.

Cao, Z., Pender, G., Wallis, S., & Carling, P. (2004). Computational dam-break hydraulics over erodible sediment bed. *Journal of Hydraulic Engineering*, *130*(7), 689–703.

Castro Díaz, M. J., Fernández-Nieto, E. D., Ferreiro, A. M., & Parés, C. (2009). Two-dimensional sediment transport models in shallow water equations. A second order finite volume approach on unstructured meshes. *Computer Methods in Applied Mechanics and Engineering*, *198*(33–36), 2520–2538.

Chorin, A. J. (1968). Numerical solution of the Navier-Stokes equations. *Mathematics of Computation*, *22*(104), 745–762.

De Vriend, H. J. (1987). 2DH mathematical modelling of morphological evolutions in shallow water. *Coastal Engineering*, *11*(1), 1–27.

Fraccarollo, L., & Toro, E. F. (1995). Experimental and numerical assessment of the shallow water model for two-dimensional dambreak type problems. *Journal of Hydraulic Research*, *33*(6), 843–864.

Garegnani, G., Rosatti, G., & Bonaventura, L. (2011). Free surface flows over mobile bed: Mathematical analysis and numerical modeling of coupled and decoupled approaches. *Communications in Applied and Industrial Mathematics*, *2*(1).

Grass, A. (1981). *Sediments transport by waves and currents*, SERC London Cent. Mar. Technol., Report No. FL29.

Hudson, J., & Sweby, P. K. (2003). Formulations for numerically approximating hyperbolic systems governing sediment transport. *Journal of Scientific Computing*, *19*, 225–252.

Hudson, J., & Sweby, P. K. (2005). A high-resolution scheme for the equations governing 2D bedload sediment transport. *International Journal for Numerical Methods in Fluids*, *47*, 1085–1091.

Juez, C., Murillo, J., & García-Navarro, P. (2014). A 2D weakly-coupled and efficient numerical model for transient shallow flow and movable bed. *Advances in Water Resources*, *71*, 93–109.

Kassem, A., & Chaydhry, M. H. (1998). Comparison of coupled and semicoupled numerical models for alluvial channels. *Journal of Hydraulic Engineering*, *124*(8), 794–802.

Kelly, D. M. (2009). *Bore-driven swash on a mobile beach*. Doctoral dissertation, University of Nottingham.

Kobayashi, M. H., Pereira, J. M. C., & Pereira, J. C. F. (1999). A conservative finite-volume second-order accurate projection method on hybrid unstructured grids. *Journal of Computational Physics*, *150*(1), 40–75.

Liu, X., & Beljadid, A. (2017). A coupled numerical model for water flow, sediment transport and bed erosion. *Computers & Fluids*, *154*, 273–284.

Murillo, J., & García-Navarro, P. (2010). An Exner-based coupled model for two-dimensional transient flow over erodible bed. *Journal of Computational Physics*, *229*(23), 8704–8732.

Nguyen, D. K., Shi, Y. E., Wang, S. S., & Nguyen, T. H. (2006). 2-D Shallow-Water Models using unstructured finite-volumes methods. *Journal of Hydraulic Engineering*, *132*(3), 258–269.

Saint-Venant, A. D. (1871). Théorie du mouvement non-permanent des eaux, avec application aux crues des rivres et lintroduction des mares dans leur lit. *CR Acad Sci Paris*, *73*, 147–54.

Shi, Y., Ray, R. K., & Nguyen, K. D. (2013). A projection method-based model with the exact C-property for shallow-water flows over dry and irregular bottom using unstructured finite-volume technique. *Computers & Fluids*, *76*, 178–195.

Uh Zapata, M., Gamboa Salazar, L., & Nguyen, K. D. (2019). *An unstructured semi-coupled model for bed load sediment transport in shallow-water flows*. Preprint submitted.

Vidović, D., Segal, A., & Wesseling, P. (2006). A superlinearly convergent Mach-uniform finite volume method for the Euler equations on staggered unstructured grids. *Journal of Computational Physics*, *217*(2), 277–294.

Wu, W. (2004). Depth-averaged two-dimensional numerical modeling of unsteady flow and nonuniform sediment transport in open channels. *Journal of Hydraulic Engineering, ASCE*, *130*(10), 1013–1024.

Mathematical Model Research of the Siltation Downstream Estuary Floodgate Under the Effect of Float Mud

Xinzhou Zhang, Jian Jiao, Xiping Dou, Xiaodong Zhao and Weiyi Xia

Abstract The Jiao (Ling) River is a typical mountainous macrotidal river. The tidal current and runoff jointly guide sediment gathering in a specific section to form the turbidity maximum zone and develop fluid mud. This plays an important role in riverbed evolution. The construction of sluice in the mainstream of the Jiang (Ling) River will greatly change the original flow and sediment movement characteristics of the river channel, forming siltation downstream sluice and producing a big influence on flood control and drainage and navigation. The flow and sediment movement characteristics of Jiang (Ling) River are analyzed and the influence of fine-grained cohesive sediment movement characteristics and salinity considered. A flow and sediment mathematical model for sluice construction in the Jiang (Ling) River is established to simulate the hydrodynamic change and the temporal and spatial distribution characteristics of sedimentation after the sluice construction. The research results show that the sluice construction has an influence on the entire channel downstream sluice. The closer to the sluice site, the bigger the influence will be. At the initial stage of sluice construction, sediment is mainly deposited in a deep trench of 10 km downstream sluice. The siltation downstream sluice will elevate the flood level and low water level, thus affecting flood control and drainage. It will also decrease the water depth of the channel, thus reducing the navigation capacity of the Jiao (Ling) River. The research results have improved the simulation accuracy of sediment transport mathematical model in the estuary with sluice constructed and provided reference for similar sluice construction in estuaries.

Keywords Estuary with sluice constructed · Turbidity maximum zone · Siltation downstream sluice · Temporal and spatial distribution · Influence on flood control

X. Zhang (✉) · J. Jiao · X. Dou · X. Zhao · W. Xia
Nanjing Hydraulic Research Institute, Key Lab of Port, Waterway and Sedimentation Engineering of the Ministry of Transport, Nanjing 210024, China
e-mail: zhangxz@nhri.cn

J. Jiao
e-mail: jjiao@nhri.cn

K. D. Nguyen et al. (eds.), *Estuaries and Coastal Zones in Times of Global Change*, Springer Water,
https://doi.org/10.1007/978-981-15-2081-5_17

1 Introduction

Located in the middle sea area of Zhejiang, the Jiao (Ling) River Basin is the third largest river system in Zhejiang Province. With a basin area of 6603 km^2 and a total mainstream length of 209 km, it flows from the northwest to the southeast into Taizhou Bay. The Jiao (Ling) River Basin consists of the upstream tributaries (Yong'an Brook and Shifeng Brook), Ling River, Jiao River and Jiao River Estuary (Guo et al. 2007).

Yong'an Brook and Shifeng Brook converge in Sanjiang Village, the western suburb of Linhai City, and it is the main reach of Ling River to the Sanjiang Estuary of Huangyan. A tributary Yongning River flows into the Sanjiang Estuary. Its upstream is Changtan Reservoir. The reach downstream Sanjiang Estuary to the entrance (Niutoujing) is the Jiao River. After the Jiao River flows out of the entrance and enters the sea, its river channel expands outwards in a bell shape, known as the Jiao River Estuary. It flows into Taizhou Bay to the southeast. The sea area is wide to the east of Baisha and the Jiao River Estuary area shows a distinctive bell mouth shape (Sun 2006). Taizhou Bay has large shoals distributed under the water (see Fig. 1).

The Jiao (Ling) River is a typical mountainous macrotidal river. The fine sediment in the channel often forms the turbidity maximum zone, which moves back and forth under the two-way action of the runoff and the tidal current in the open sea and develops into fluid mud at the bottom of the channel (Wu et al. 2011). The movement laws of flow and sediment are extremely complicated. In recent years, human activities in the estuary become more frequent. In particular, the estuary reclamation has caused big changes in the hydrodynamic and boundary conditions of the estuary (Zhao et al. 1991). Moreover, the construction of upstream reservoir

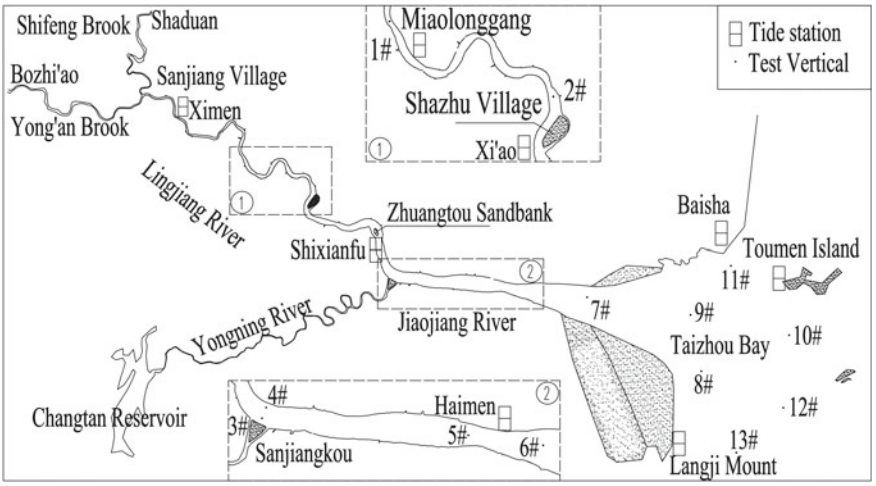

Fig. 1 Diagrammatic sketch of Jiaojiang river system

has reduced the runoff and peak discharge, in combination with the jacking function of tidal water, resulting in siltation and accretion in the channel and turbid river water, and showing a deteriorating trend (Tanaka et al. 1994). To alleviate the contradiction between the supply and demand of water resources in the Jiao (Ling) River Basin, and solve the problems of serious flood disasters and deteriorated ecological environment along the river, relevant units are planning to build a tidal barrage in the mainstream of the Jiao (Ling) River to block the upstream going of muddy water and salt water. The Jiao River Estuary has complex water and sediment conditions. Before construction, the movement laws of sediment must be grasped first, so as to reliably predict the siltation downstream sluice, thus providing a scientific basis for the selection of the sluice site.

The water and sediment movement characteristics of the channel before the sluice construction are analyzed according to the measured hydrological and sediment data of the Jiao (Ling) River Estuary (the test vertical line is shown in Fig. 1). Based on this, the simulation method of general sediment mathematical model is improved, and the sediment mathematical model of the estuary with sluice constructed is established to simulate the movement laws of the turbidity maximum zone in the Jiao (ling) River and the siltation process downstream sluice as well as the influence of sluice construction on flood control and drainage and navigation.

2 Natural Conditions

2.1 Runoff

The runoff in the Jiao River Basin is mainly formed by precipitation, and its annual distribution basically corresponds to precipitation. Affected by the plum rain and typhoon rain, the annual runoff distribution is extremely uneven, mainly concentrating in the flood season (April-September), accounting for 75% of the annual total; and the runoff in dry season (October to March of the following year) only accounts for 25% of annual total. The flood level in the basin rises and falls abruptly, the flood peak generally lasts 1–2 days and the runoff changes dramatically.

2.2 Tide

The Jiao River Estuary is a macrotidal estuary and its tidal type is irregular semidiurnal tide. The tidal wave is transmitted from the open sea to the Jiao River channel through the bell mouth-shaped estuary of the Jiao River. As the river width and water depth decrease, the tidal wave is affected by the friction resistance of shallow sea terrain, jacking of upstream runoff and constrained reflection of the two bank boundaries. It deforms intensely during the upstream movement. The duration of flood is

shortened and that of ebb elongated, and the waveform is asymmetrical and close to standing wave. Generally, the tidal current limit is located near Sanjiang Village, the mainstream entrance of Ling River, but moves downstream when the flood occurs in the basin. The measured data show that when the flood peak discharge reached 2500 m^3/s, the tidal current limit moved downstream and was only 20 km away from the entrance; when the peak discharge reached 7500 m^3/s, there was no flood current in the Jiao River Estuary; in case of a catastrophic flood, the freshwater plume could be washed away and reach 25 km beyond the entrance. According to the series of estuarine tide level data from 1959 to 2017, the highest tide level could reach up to 5.64 m, the lowest −2.88 m, and the extreme tide range more than 6 m. On the whole, the tidal wave moved upstream from east to west along the river via the open sea from Taizhou Bay to the Jiao River Estuary to the Ling River Reach, and the highest tide level, mean high tide level, and mean tide level showed a gradually increasing trend. The tidal range also tended to increase gradually, but rapidly decreased when above the tidal current limit.

2.3 Tidal Currents

The tidal current of the Taizhou Bay outside the Jiao River Estuary shows the characteristics of rotating flow, and it moves upstream to the Jiao River Estuary. The current in the river channel is mainly reciprocating flow. As indicated by the measured data of tidal current velocity along the channel from 2013 to 2017, the tidal current tended to increase gradually in Taizhou Bay-Jiao River-Ling River, and the flood strength was greater than the ebb strength. The maximum average vertical flood strength at the Jiao River Estuary was about 0.57–1.70 m/s, and the ebb strength about 0.51–1.45 m/s. The maximum average vertical flood strength of the Jiao River channel was 1.57–2.30 m/s, and the ebb strength 1.01–2.00 m/s. The maximum average vertical flood strength near Miaolong Port and Xi'ao of Ling River was about 1.42–2.28 m/s, and the ebb strength about 1.33–1.90 m/s. The changes in average vertical flow velocities at various stations along the channel of Jiao (Ling) River are shown in Fig. 2.

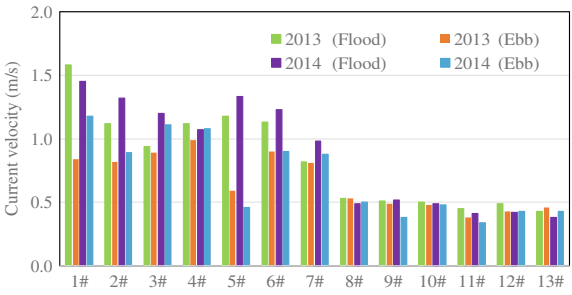

Fig. 2 Variation chart of various average vertical flow velocities

2.4 Sediment

(1) Sediment concentration

The sediment of the Jiao River Estuary comes from two directions: land area and sea area. According to the statistical measured data, the quantity of sediment carried by runoff is relatively small. The average sediment discharge from the Jiao River Basin in the past years was 1.22 million t/a, and the average sediment concentration was 0.236 kg/m^3.

According to the hydrological data from 2013 to 2014, the average vertical sediment concentration of Ling River and Jiao River was generally above 3.0 kg/m^3, while that of Taizhou Bay was generally below 0.3 kg/m^3. The plane distribution of sediment concentration showed a gradual decline trend from the Ling River channel-Jiao River channel-Jiao River Estuary to Taizhou Bay. The changes in sediment concentration are shown in Fig. 3. It can be seen that the maximum average vertical sediment concentration of the upstream Ling River channel is 18 kg/m^3 and that of Jiao River is 10 kg/m^3. The average vertical sediment concentration in the channel of the Jiao River Estuary is generally not more than 5 kg/m^3, and the sediment concentration in Taizhou Bay waters outside the Jiao River Estuary is relatively small, below 0.2 kg/m^3 on average.

(2) Sediment composition and grain size

Pursuant to the sediment grain size and composition in the Jiao (Ling) River, the suspended sediment median diameters of each vertical line are 0.005–0.0102 mm; the suspended sediment median diameters indicate the distribution characteristics of becoming gradually fined from Ling River channel to the downstream Jiao River channel. From the perspective of the distribution of suspended sediment and bottom sediment along the channel (as shown in Fig. 4), the Ling River reach is affected by the sediment transport in the upstream land area, and the bottom sediment is significantly thicker than Jiao River reach and the reach outside the estuary. The other reaches have small differences in the grain sizes of suspended sediment and

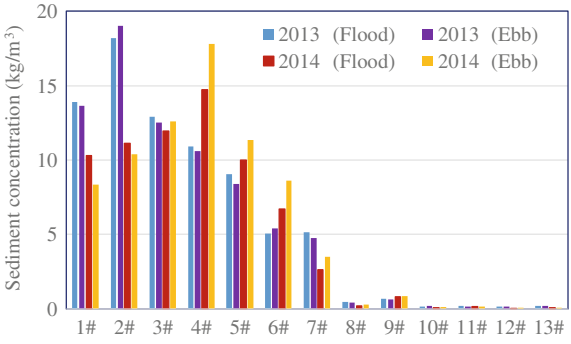

Fig. 3 Variation chart of average vertical sediment concentration in the river channel

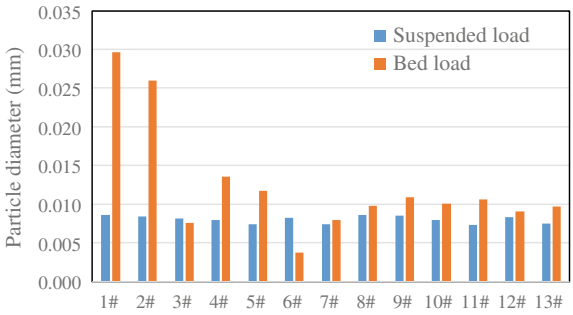

Fig. 4 Grain size of suspended sediment and bottom sediment in the channel

bottom sediment, indicating the rather frequent exchange between suspended load and bed load from the lower reaches of the Jiao River to the reach outside the estuary.

2.5 Movement Characteristics of the Turbidity Maximum Zone in the Jiao (Ling) River

The observational data show that in the dry season where the runoff is very small, the average vertical sediment concentration in the mainstream of Ling River reaches more than 20 kg/m^3, and the maximum sediment concentration at the bottom is about 60 kg/m^3, which occurs during the ebb slack period of spring tide. The spring tide has a high sediment concentration and the neap tide has a low one. The sediment content in the waters of Jiao River and Ling River is generally high, but that outside the Jiao River Estuary is relatively small. Under the action of flooding and ebbing tide, the sediment forms the movement characteristics of turbidity zone. Figure 5 is the movement process of turbidity zone observed during spring tide in June 2014.

It can be seen that the core part of the turbidity zone with the largest sediment content reciprocates under the action of the tidal current, moving downstream during ebb tide and upstream during flood tide. The spring tide migration reaches more than 30 km from Niutoujing to Xi'ao. The vertical distribution of sediment concentration shows the sediment concentration is large at the bottom and small at the surface; it gradually increases with the water depth and flood strength during the flood period, and the vertical gradient of sediment concentration is small; during the ebb period, as the water depth decreases and the ebb current weakens, the sediment accumulates to the bottom and the sediment content at the bottom is increased significantly and fluid mud is formed. Judging from the sediment conditions, there are abundant fine-grained sediments on the riverbed of the Jiao (Ling) River. As a result of the large-scale dredging activities in recent decades, the composition of riverbed sediment in Ling River and Jiao River has undergone great changes.

A large quantity of coarse sandy sediment has been taken away, and the sediment covering the entire river channel is fine-grained sediment, which has increased the sediment source formed by the turbidity zone with high sediment concentration.

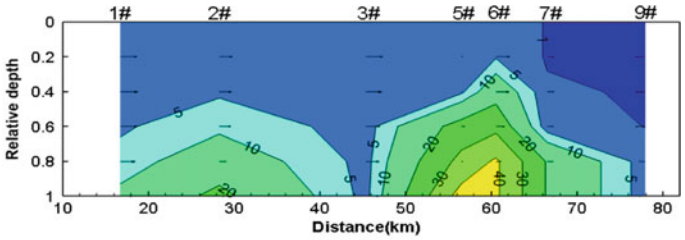

(a) Low tide level (Jun. 14 17:00)

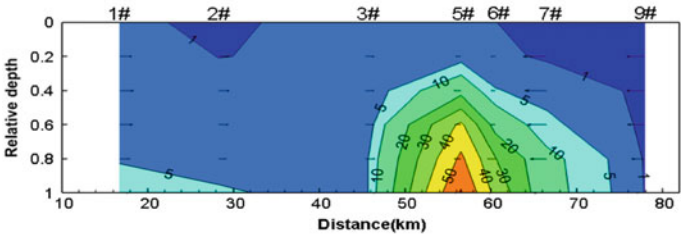

(b) Ebb slack period (Jun. 14 18:00)

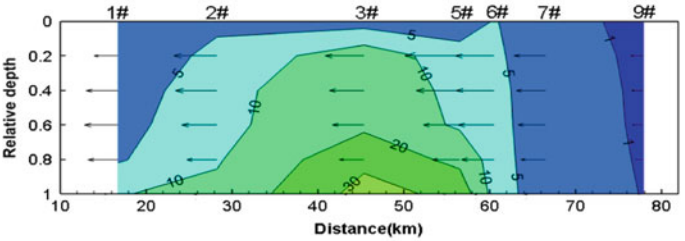

(c) Maximum flood period (Jun. 14 20:00)

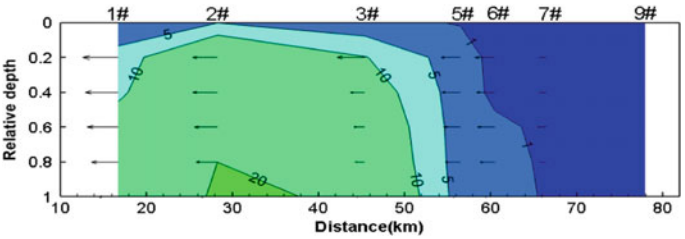

(d) High tide level (Jun. 14 20:00)

Fig. 5 Longitudinal profile of sediment concentration distribution at characteristic times of spring tide in June 2014 (Relative depth is the relative water depth; distance is the distance from Sanjiang Village)

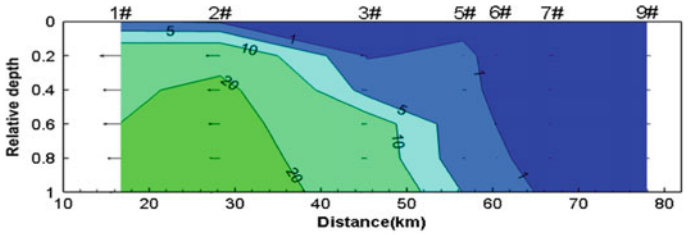

(e) Flood slack period (Jun. 14 23:00)

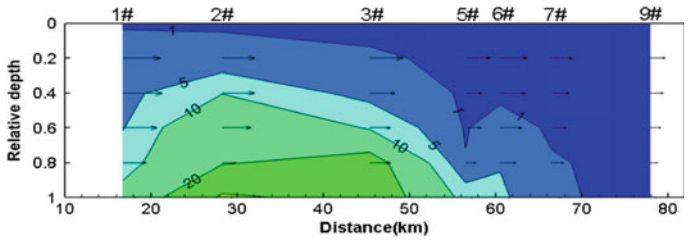

(f) Maximum ebb period (Jun. 15 1:00)

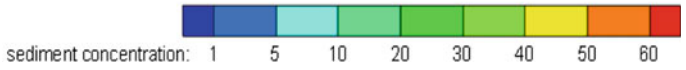

(g) Sediment concentration color scale

Fig. 5 (continued)

From the perspective of the dynamic mechanism, the tidal current and runoff jointly guide sediment gathering in a specific section. The Jiao (Ling) River has a small runoff in the dry period and the flood current can move upstream to Sanjiao Village and the upper reaches. The Jiao (Ling) River takes a plane shape of wide bottom and narrow top and tidal wave gradually deforms in the process of spreading to the estuary. The asymmetry of the ebb and flood tides causes Stokes transport and drives sediment to move upstream.

3 Establishment and Validation of Mathematical Model

3.1 Flow and Sediment Movement Equation

In the estuary area, the following control equation can be used for two-dimensional tidal wave movement:

(1) Continuity equation

$$\frac{\partial Z}{\partial t} + \frac{\partial Hu}{\partial x} + \frac{\partial Hv}{\partial y} = 0$$

(2) Momentum equation

$$\frac{\partial Hu}{\partial t}+\frac{\partial Huu}{\partial x}+\frac{\partial Huv}{\partial y}=-gH\frac{\partial \varsigma}{\partial x}-\frac{\partial H\overline{u'u'}}{\partial x}-\frac{\partial H\overline{u'v'}}{\partial y}+\frac{\tau_{sx}-\tau_{bx}}{\rho}+fHv$$

$$\frac{\partial Hv}{\partial t}+\frac{\partial Huv}{\partial x}+\frac{\partial Hvv}{\partial y}=-gH\frac{\partial \varsigma}{\partial y}-\frac{\partial H\overline{v'u'}}{\partial x}-\frac{\partial H\overline{v'v'}}{\partial y}+\frac{\tau_{sy}-\tau_{by}}{\rho}-fHu$$

Where u and v are the flow velocity components in x and y directions respectively; Z is the water level; H is the water depth; $f=2\omega\sin\varphi$ is the Coriolis force coefficient (ω is the rotational angular velocity of the earth); ($\tau_{sx,}$ τ_{sy}) is the surface wind stress term and ($\tau_{bx,}$ τ_{by}) is the bed resistance term at the bottom; g is the gravity acceleration.

The following formula can be used as the two-dimensional nonequilibrium transport equation of suspended load:

$$\frac{\partial HS}{\partial t}+\frac{\partial HuS}{\partial x}+\frac{\partial HvS}{\partial y}=\frac{\partial}{\partial x}\left(H\varepsilon_x\frac{\partial S}{\partial x}\right)+\frac{\partial}{\partial y}\left(H\varepsilon_y\frac{\partial S}{\partial y}\right)-F_s$$

Where α is the settlement probability of suspended sediment; ω is the settling velocity of suspended sediment; S is the sediment content; F_s is the erosion and deposition coefficient of suspended sediment on the bed surface; ε_x and ε_y are the sediment diffusion coefficients in the x and y directions of the coordinate system respectively.

The following formula can be used as the river bed level deformation equation:

$$\gamma_0\frac{\partial Z_b}{\partial t}=F_s$$

Where γ_0 is the dry bulk density of deposit and Z_b is the riverbed elevation.

3.2 Calculation Mode Improvement and Parameter Setting

Studies have shown that: tidal wave deformation is the basic driving force of siltation downstream sluice, marine sediment is the main source of siltation downstream sluice, and nonequilibrium sediment transport in the estuary is the basic mode of siltation downstream sluice. Based on the analysis of the mechanism of siltation downstream sluice, the estuary downstream sluice forms a deposition system on the riverbed surface under the action of tidal current which is composed of fine-grained cohesive suspended sediment, high sediment concentration layer, fluid mud and bottom sediment. The sediment coming from the sea area must undergo repeated tide rises and falls, transport, deposition, re-transport, and re-deposition as well as scouring and silting, exchange and transport of suspended load and bottom fluid mud

before reaching the downstream sluice. When the sluice gate is closed, the downstream sluice forms tidal estuary cecum channel and the flow velocity before the sluice is almost zero, similar to still water. Consequently, the flood current cannot transport large quantity of sediment to the sluice. However, the field observation data show that the siltation in the near area of the tidal sluice is the strongest at the initial stage of sluice construction in the estuary. It is difficult to reflect the movement characteristics of cohesive sediment downstream sluice and the sedimentation process using the existing sediment mathematical model and calculation mode, and the result of the gradually increasing siltation from the estuary to the downstream sluice cannot be obtained.

Based on the mechanism of siltation downstream sluice, and in comprehensive consideration of the combined action of incipient and depositing motion characteristics of fine cohesive sediment and salinity, new sediment calculation parameters are used to simulate the turbidity zone movement in the downstream of sluice, having accurately simulated the characteristics of siltation downstream sluice.

(1) Riverbed erosion and deposition function

With the change of flow intensity and sediment bed surface composition, sediment resuspension, erosion and flocculation sedimentation and deposition will occur on the bed surface of cohesive sediment. Generally, the bed surface erosion and deposition function can be expressed as:

$$F_s = D_b - E_b$$

Where D_b is the deposition flux on the riverbed interface; E_b is the sediment pick-up (resuspension) flux on the interface.

(2) Critical shear stress of incipient motion

Considering that shear stress is the main factor affecting sediment movement, many scholars determine the empirical relationships between sediment resuspension and flow shear stress, and critical shear stress of incipient motion through field or laboratory tests. Such relationships can be unifiedly written in the following form:

$$E = K\left(\frac{\tau_b - \tau_c}{\tau_c}\right)^n$$

Where K is the coefficient of scouring, indicating the anti-erosion performance of deposit; n is the coefficient that characterizes the sedimentation and consolidation characteristics; τ_b is the bottom shear stress; τ_c is the critical shear stress of sediment incipient motion. The coefficient of scouring varies with the change of bed sediment bulk density, generally ranging from 0.002 to 0.02.

With respect to the determination of the critical shear stress of sediment incipient motion, in the estuary area, after the fine-grained sediment is flocculated and settled on the bed surface, it will take a long time before it becomes relatively compacted. Before that, resuspension and incipient motion easily occur to the sediment just

settled on the bed surface, even with significant fluidity and forming fluid mud. When considering the resuspension of cohesive sand bed, the critical shear stress of sediment resuspension of the mud scum must be considered, which can be expressed using an empirical formula:

$$\tau_c = a(\gamma_w - 1)^b$$

Where: γ_w the wet bulk density of riverbed sediment, in t/m^3; a, b are the parameters to be determined. According to the results of field sediment incipient motion flume experiment, the above formula is calibrated and $a = 36.63$, $b = 2.27$ is obtained.

(3) Sedimentation flux of cohesive sediment

Krone's (1962) formula is used to calculate the sedimentation flux of cohesive sediment:

$$D = -\omega_s C P;\ P = \begin{cases} \left(1 - \frac{\tau_b}{\tau_d}\right), \tau_b < \tau_d \\ 0, \tau_b \geq \tau_d \end{cases}$$

Where ω_s is the settling velocity of cohesive sediment; C is the suspended sediment concentration near the bottom; P is the settlement probability of sediment; τ_b is the bottom shear stress; τ_d is the critical shear stress of sedimentation, which depends on the concentration and type of sediment, generally 0.06–0.1 N/m^2 pursuant to the field and laboratory experiments.

(4) Settlement of cohesive sediment

The suspended sediment in Jiao (Ling) River and Taizhou Bay are fine-grained, belonging to the category of cohesive sediment, with large sediment concentration. Flocculation, sediment content and changes in flow velocity must be taken into account in the calculation of sediment settling velocity, and Cao Zude's formula is adopted in its calculation:

$$\omega_s = \omega_0 K_f \frac{1 + 4.6S^{0.6}}{1 + 0.06V^{0.75}}$$

Where ω_0 is the settling velocity in still water; V is the flow velocity; K_f is the salt-fresh water mixing coefficient, $K_f = C_f C_d$, $C_f = 0.0017 D_{50}^{-1.82}$, $C_D = \left(1 + 0.12 \lg\left(\frac{0.03}{D_{50}}\right)\right) e^{\left(1.1 \times 10^5 D_{50}^2 - 99\right) s_t}$, S_t is the salinity of water body, K_f is 1.0 when the sediment grain size is bigger than 0.0307 mm.

3.3 Model Grid and Range

The upper boundary of the mathematical model calculation range is located at Shaduan Hydrological Station of Shifeng Brook and Baizhi'ao Hydrological Station of

Yong'an Brook. The east boundary of the open sea is at −30 m isobath, the north boundary at Qingzhishan Bapu Port, and the south boundary at Songmen Xieou Island. The model calculation domain grid adopts normal curve grid division, the grid number is 773 × 190 and the grid in the open sea is sparse, with a spacing of 300–1000 m. The grid in the channel area is dense, about 150 m along the river length direction and a spacing of 5–20 m mostly along the width direction. The spacing from the river channel to the estuary area is obtained by the interpolation of the latest measured topographic data of 2016, and the open sea terrain is obtained by the interpolation of the latest chart and local measured topographic data.

3.4 Model Verification

From 2013 to 2017, hydrology tests were performed in the project waters and a number of hydrological factors such as tide, tidal current, flow rate, sediment, water quality, weather, salinity, suspended sediment, and substrate particle were collected. The test station is shown in Fig. 1. The tidal current and sediment mathematical model is validated using these two large-scale measured data. The figures show that the calculated values of tide level, flow velocity, flow direction, and sediment concentration are consistent with the measured ones, indicating that the mathematical model has desirably reflected the flow and sediment movement characteristics of the Jiao (Ling) River and particularly well simulated the movement characteristics of turbidity zone with high sediment content.

4 Changes in Water Flow and Sediment Movement Caused by Sluice Construction

4.1 Construction Scheme and Calculation Conditions

The sluice site scheme of Miaolong Port is located in the middle of the mainstream of the Ling River, with a total net width of 250 m (10 holes × 25 m/hole). Miaolong Port is the flood discharge bottleneck in the Ling River. Sluice construction in this area in combination with barrier clearance, cutoff and local spur dredging can increase the flow sections as well as the flood discharge capacity; properly raise the water level in the Ling River and introduce clean water into Datian Plain and Yicheng Port, which is then discharged from the downstream of sluice through the Diaoyuting tunnel and Changshiling tunnel respectively, thus promoting the water circulation of the river network and improving the water environment of coastal cities.

According to the analysis of hydrological data in different years from 1957 to 2000, Year 1986 was a typical low flow year, Year 1976 was a typical normal year, and years from 1964 to 1968 were a series of continuous low flow years. Therefore,

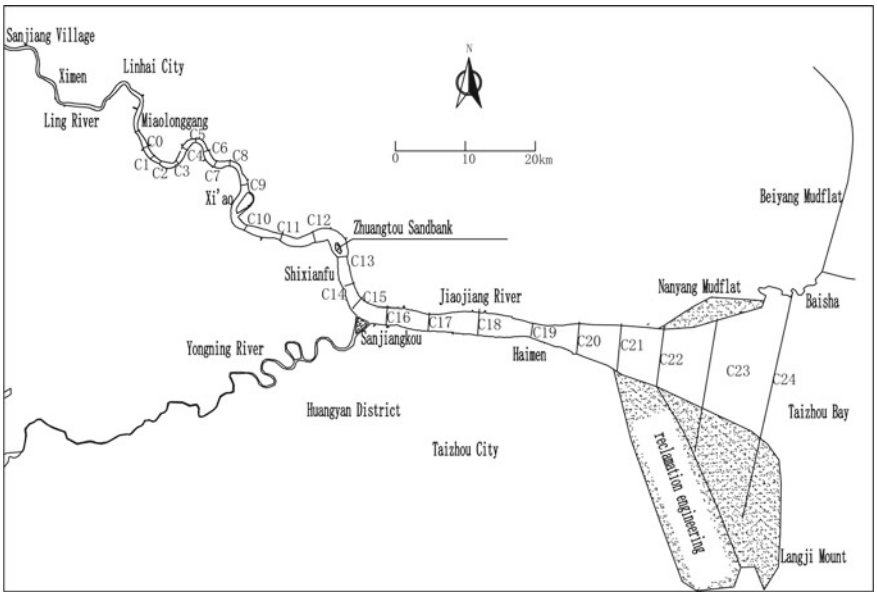

Fig. 6 Locations of the cross-sections

the hydrologic data of 1986 and 1964–1968 were used to calculate the siltation downstream sluice in a typical dry year and a series of low flow years, so as to grasp the influence of sluice construction under the most adverse conditions. The tidal level process in the open sea was obtained based on the combination of measured spring, middle and neap tide levels in the flood and dry seasons of 2013 and 2014.

To analyze the changes in water flow and sediment caused by the sluice construction, 25 sections (C0–C24sections) are taken along the Jiao (Ling) River, as shown in Fig. 6.

4.2 Tide Level Changes Caused by Sluice Construction

Figure 7 shows the tide level changes of various sections before and under the conditions of closed gate after sluice construction.

From the point of view of the changes in the tidal level processes at various stations, the tidal wave deforms more intensely in the near area downstream sluice than before sluice construction. The Miaolong Port station lies close to the downstream sluice. After the sluice is built, the maximum tide level is significantly raised (by more than 50 cm) during spring tide, the minimum tide level is reduced (by more than 20 cm), and the duration of rise is shortened by nearly 1 h. This will inevitably result in an increase in the ratio of flood strength to ebb strength compared with that before the construction. The changes in high and low tide levels in the estuary before and after

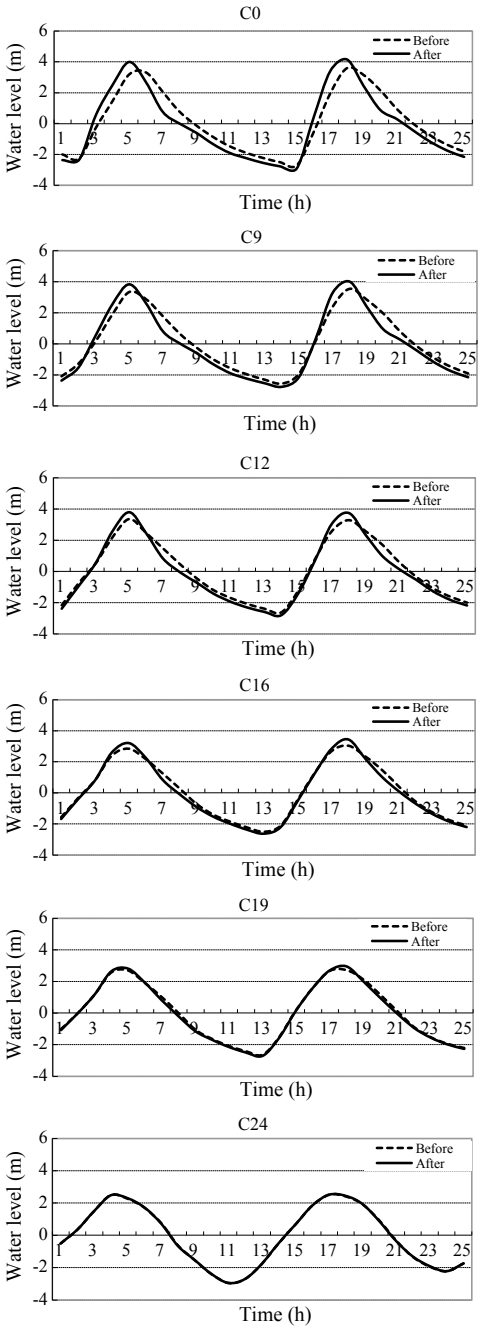

Fig. 7 Tide level changes before and after sluice construction Tidal current changes in low flow years

sluice construction are not more than 2 cm, less than 0.4% of the tidal range. The tidal level process basically has no changes before and after the construction from the estuary to Toumen Island and Langji Mountain outside the estuary.

Figure 8 shows the variation chart of flood and ebb strength process of the main sections before and after sluice construction at Miaolong Port.

From the perspective of the flow velocity process changes at each point, the flood and ebb strengths in the near area downstream sluice after the construction of sluice are reduced, and the closer to the sluice gate, the bigger the reduction will be. At the estuary section, the flow velocity hydrograph is basically not changed before and after sluice construction. This is consistent with the tide level changes before and after sluice construction. The influence of tidal wave deformation after sluice construction at Miaolong Port basically reaches the entrance of the Jiao River Estuary. From the comparison of the maximum velocities of flood and ebb tides before and after sluice construction, the maximum velocities of flood and ebb tides in the near area downstream sluice are rapidly reduced after sluice construction and the flood strength is reduced to 0.2 m/s, while the ebb strength to 0.1 m/s or less. The flood and ebb strengths are gradually increased towards the lower reaches. After sluice construction, the ratio of average flood strength to average ebb strength is generally increased. This indicates that the construction of sluice is helpful for the flood tide to carry sediment and enter the channel.

4.3 Tidal Volume Changes Caused by Sluice Construction

In order to analyze the changes in tidal volume caused by sluice construction at Miaolong Port, the changes in the flood and ebb tidal volume of sections along the line before and after sluice construction is calculated. The comparison of tidal volumes before and after sluice construction at Miaolong Port is listed in Table 1.

After sluice construction, the tidal wave downstream sluice is deformed, and from the sluice site to the downstream, the decrease of flood tidal volume tends to be small. The decrease in the flood tidal volume of several sections near the sluice is greater than the tidal prism upstream sluice before sluice construction and the flood tidal volume of the sections in the estuary reach does not decrease significantly, and even increases slightly. Among them, the tidal volume of Xi'ao section is reduced by about 50%, that of Sanjiang Estuary reduced by about 10% and that of Niutoujing reduced by about 1%.

4.4 Changes of Sediment Concentration

The changes in sediment concentration process at the section thalweg before and after sluice construction at Miaolong Port are shown in Fig. 9 and after construction means under the condition of gate closed.

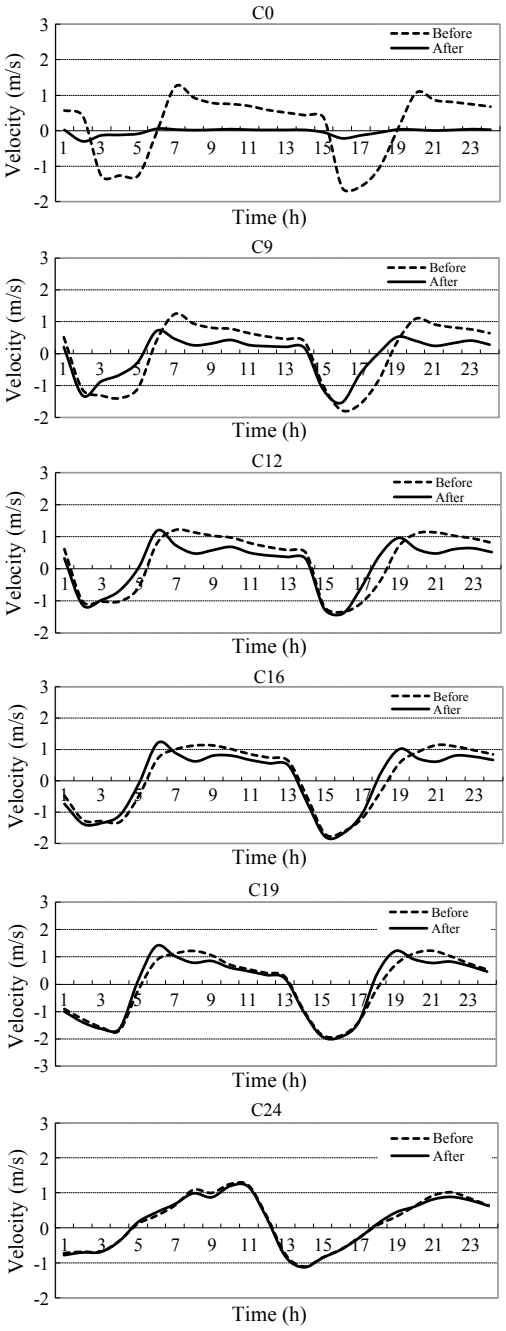

Fig. 8 Changes in the flood and ebb strength before and after sluice construction at Miaolong Port

Table 1 Comparison of flood and ebb tidal volumes before and after sluice construction at Miaolong Port (unit: 100 million m^3)

Section	Distance (km)	Before construction		After change	
		Flood tide	Ebb tide	Flood change (%)	Ebb change (%)
C0	1.35	0.567	0.567	−91.06	−92.82
C2	2.83	0.649	0.656	−74.89	−81.25
C4	5.16	0.773	0.729	−61.81	−69.51
C6	7.52	0.897	0.842	−53.10	−59.72
C8	9.67	0.996	0.957	−47.29	−51.93
C10	15.32	1.201	1.181	−37.91	−40.43
C12	20.43	1.499	1.543	−27.71	−27.40
C14	26.07	1.919	2.035	−16.01	−16.84
C16	29.53	2.345	2.333	−10.23	−8.97
C18	36.11	3.277	3.193	−3.28	−2.97
C20	43.31	4.229	4.172	0.40	−0.41
C22	49.34	5.883	5.949	2.66	2.20
C24	57.53	18.280	20.298	1.38	1.40

As the flood and ebb strengths are rapidly decreased and the tidal dynamic forces are weakened after sluice construction, the sediment concentration in the near area downstream sluice will be decreased. However, the sediment in the near area downstream sluice is generally new sludge that has just been deposited, with a low wet density and a small incipient velocity (0.15–0.3 cm/s). The flow velocity calculation results show that the flood strength of sections before the sluice still exceeds 0.2 m/s, and the flood strength of the downstream sections can reach the incipient velocity of the near-bottom sediment, thus the downstream sediment is transported to the front of the sluice.

The flood strength downstream has recovered to that before sluice construction to the 12# section and large quantity of sediment can still be carried to the front of the sluice. The sediment concentration change process is basically the same as that before sluice construction in the estuary area. After the sluice is built, the tidal current downstream sluice is weakened, resulting in a significant decrease in the sediment concentration in the river channel downstream sluice and downstream migration of turbidity zone movement interval. With reduced upstream and downstream movement length, the turbidity zone moves in the range from Sanjiang Estuary to Niutoujing of the Jiao River.

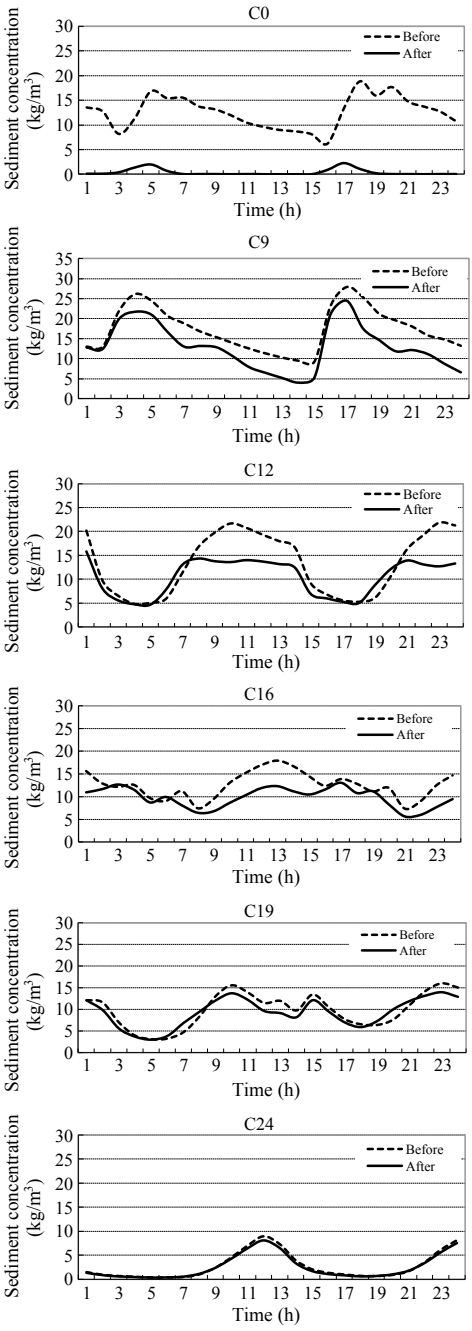

Fig. 9 Variation chart of sediment concentration process before and after sluice construction

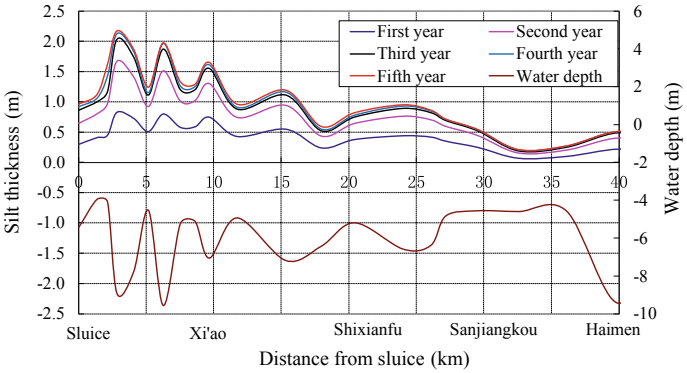

Fig. 10 Distribution of siltation downstream sluice in a series of low flow years (5 years)

4.5 Siltation Downstream Sluice

Years from 1964 to 1968 are a series of continuous low flow years and can be considered as the most unfavorable conditions of siltation downstream sluice. The average siltation thickness of each section during the series of low flow years is shown in Figs. 10 and 11.

In the case of continuous low flow years, the first two years belong to a period of accumulative rapid siltation, and the siltation intensity is increased exponentially, while after the third year, the siltation intensity downstream sluice slows down and tends to be in equilibrium. After the fourth year, siltation downstream sluice is basically in equilibrium, the sediment in the near area downstream sluice continues to advance toward the sluice, and the other areas are in the stage of dynamic equilibrium adjustment. After the dynamic equilibrium of scouring and silting through sediment mathematical calculation, sedimentation mainly concentrates within a range of 10 km downstream sluice, with the maximum average siltation thickness of 2.13 m, at the deep trench section of 2.8 km downstream sluice. The siltation intensity is gradually decreased in the further lower reaches, and in the estuary area, the average siltation thickness is reduced to 0.2–0.5 m. The siltation volume in the deep trench near Niutoujing is relatively large. The total siltation volume in the entire reach downstream sluice in the Jiao (Ling) River above Niujintou reaches up to 22.50 million m^3.

5 Influence of Siltation Downstream Sluice

The Jiao (Ling) River is a mountainous river, where flood water abruptly rises and falls. In order to analyze the influence of siltation downstream sluice on the flood

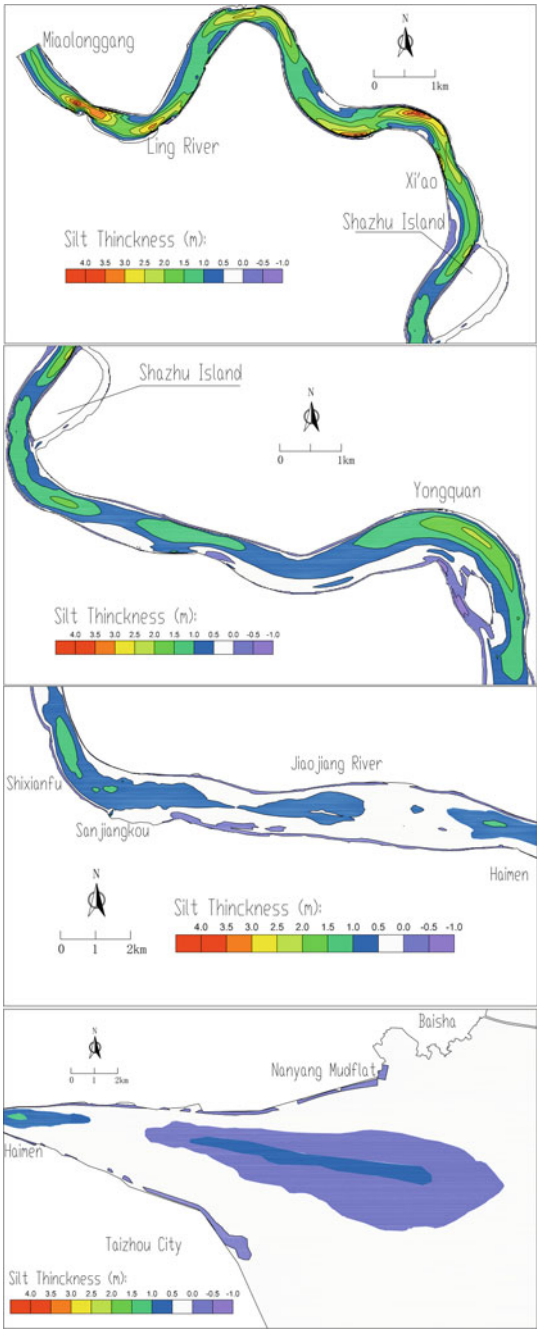

Fig. 11 Distribution of siltation downstream sluice after a series of low flow years (1964–1968)

control and drainage along the river, the mathematical model is used to calculate the changes in high and low water levels.

The results show that the riverbed near the sluice site is highly silted. The deposition body cannot be fully scoured during the flood, so the increase in flood level and minimum water level upstream sluice site is not significant, but the flood level and minimum water level near the sluice site are significantly raised. Among them, the flood level is raised by nearly 70 CM. In the estuary area, the flood water level rises slightly as a result of small quantity of sediment deposition, but the minimum water level still rises by 20 CM. Judging from the changes in flood level, siltation downstream sluice near the sluice site raises the riverbed, and the flood level rises dramatically, which is not conducive to flood discharge. From the perspective of the low water level, siltation downstream sluice reduces the low water level time required for self drainage of flood and the pump station is required for enhanced drainage, which affects the flood discharge efficiency. The significantly shortened duration of low water level at the drainage gate has an impact on the flood discharge efficiency, thus increasing the flooding time of the flood storage area.

Figure 12 shows the water depth changes in the channel after siltation downstream sluice. It can be seen that the water depth in the near area downstream sluice before sluice construction meets the design bottom elevation requirements of the channel, while the shallow section of the Jiao River reach in the estuary area with a length of approximately 7 km does not meet the requirements. After the sluice is built, the

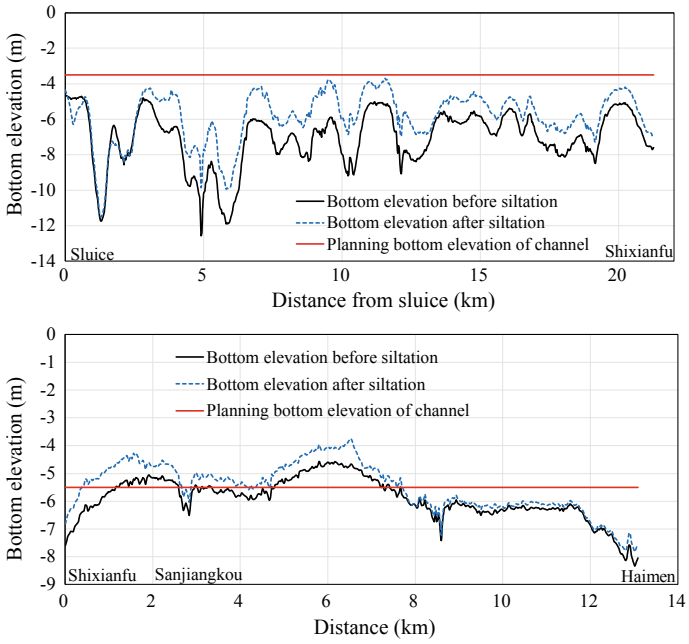

Fig. 12 Variation chart of water depth in the channel after siltation downstream sluice

position with serious siltation downstream sluice occurs in the range of 10 km in the downstream of sluice. The local channel water depth in the near area downstream sluice is decreased due to the impact of sedimentation and the average siltation thickness in the channel of the Jiao River Reach is about 0.4 m. The siltation volume is relatively high in the area with big local water depth. Thus the length that does not meet the design water depth is further increased. Therefore, the siltation downstream sluice decreases the water depth of the channel downstream sluice and reduces the navigation capacity of the channel.

6 Conclusions

(1) The Jiao (Ling) River is a typical mountainous macrotidal river, featured by strong tidal current dynamics, severe deformation of tidal wave in the process of propagation from the estuary to the upstream, obvious standing wave characteristics of the river reach, high sediment concentration, fine sediment particles, frequent exchange of suspended load and bed load, formation of turbidity maximum zone and development of fluid mud, which has a great impact on riverbed evolution.

(2) The sluice construction has greatly changed the original hydrodynamic characteristics of the channel. After the sluice is built, the high tide level downstream sluice is elevated and low tide level decreased, the closer to the sluice site, the bigger the change. The maximum tide level of spring tide downstream sluice in the dry season is raised by about 50 cm and the minimum tide level reduced by about 20 cm. The duration of rise is shortened by nearly 1 h and that of fall increased accordingly. After the construction of sluice, the flood and ebb strengths in the reach downstream sluice are reduced and the closer to the sluice, the greater the reduction. In the estuary, the change in flow velocity is small. After the construction, the tidal prism downstream sluice is decreased, and the closer to the sluice site, the greater the decrease, but the tidal volume does not change much in the estuary.

(3) The sluice construction has greatly changed the original sediment movement and riverbed evolution characteristics of the channel. After the sluice is built, the sediment concentration of flood and ebb tides in the near area downstream sluice is decreased, while that in the estuary does not change much before and after sluice construction. After the construction of sluice, the turbidity maximum zone still reciprocates in the channel downstream sluice. Nonequilibrium sediment transport results in sediment deposition downstream sluice. Such deposition mainly concentrates in a range of 10 km in the downstream of sluice gate, and the siltation thickness is relatively large.

(4) The siltation downstream sluice raises the riverbed and greatly increases the flood level, which is not conducive to flood drainage. The elevation of the low water level along the river has an influence on the drainage efficiency, thus further increasing the flooding time of the flood storage area. The siltation downstream

sluice reduces the water depth of the channel and port terminals in the reach downstream sluice, thus reducing the navigation capacity of the channel.

Acknowledgements The research work is supported by National Natural Science Foundation No. 51409163 and No. 51479122, National Key R&D Program of China (2017YFC0405402) and the National Natural Science Foundation of China (51479122).

References

Guo, L., & Chen, Z.-H. (2007). Remote sensing research on the distributed characteristics of suspended matter in Jiaojiang Estuary and Taizhou Gulf. *Journal of Wuhan University of Technology*, 49–52.

Liu, J., Cheng, H-F, Zhao De-Z., et al. (2013(11)). Spatial and temporal distribution of suspended sediment concentration in the Yangtze estuary 12.5 m deepwater channel. *Port & Water Engineering*, 49–54.

Sun, P.-F. (2006). *Study on 2-D mathematical model of tidal flow and sediment in Jiaojiang Estuary*. Hangzhou: Zhejiang University.

Wu, M.-Y., Xu J.-S., & Feng Y.-L. (2011(1)). Spacial-temporal distribution of suspended sediment concentration in Hangzhou Bay. *Journal of Sediment Research*, 33–37.

Zhao, L.-B., & Zhu Y.-K. (1991(4)). The preliminary analysis on the empirical relation of sediment transport capacity in Jiaojiang River Estuary. *Journal of Sediment Research*, 69–75.

Tanaka, H., & Sana, A. (1994). Numerical study on transition to turbulence in a wave boundary layer, In *Sediment transport mechanism in coastal environments and rivers* (pp. 14–25). Singapore: World Scientific.

Towards a Comprehensive Functionality Assessment of Estuaries: First Approaches in San Vicente de la Barquera Estuary (Cantabria, Spain)

M. Aranda, F. J. Gracia, G. Peralta and G. Flor-Blanco

Abstract Estuaries are complex systems, usually composed by connected subsystems (mostly beaches, dunes, saltmarshes and the main channel), resulting in a complex geomorphology and ecology that makes difficult its study from a comprehensive perspective. In this sense, characterizing the functionality of an estuary is a key element to develop adequate management tools for these environments. Unfortunately, very few studies have focused on the connectivity among their elements, mostly overlooking the derived interactions inherent to them. As an example, San Vicente de la Barquera estuary (Cantabria, Spain) has been selected for this first approach. Considering an estuary as a heterogeneous and continuous system, where system components and processes are interconnected, the present work proposes as methodology the combination of different detailed maps to identify links between morphosedimentary systems and related EU habitats of community interest. The combination of these types of maps allows to drawn up a table of equivalences to relate morphosedimentary units and habitat characteristics from a geographical point of view. In a second phase of this approach, it will be identified physical processes related to morphological systems (i.e., river discharges, water mixing, tidal currents, dynamosedimentary models) and biological processes related to ecological systems (i.e., presence and variation of plant communities). Additionally, induced anthropogenic processes will be considered as driving forces acting directly on the previous ones. With the aim of evaluate the global dynamic of the estuary, a set of geo-ecological indicators are proposed to describe the processes and the connectivity established in between their subsystems. The main results of this preliminary study are expected to provide a comprehensive first vision of the estuary functioning, together with the design of a new methodology to improve the environmental characterization of estuaries.

M. Aranda (✉) · F. J. Gracia
Department of Earth Sciences, University of Cádiz, Cádiz, Spain
e-mail: maria.aranda@uca.es

G. Peralta
Department of Biology, University of Cádiz, Cádiz, Spain

G. Flor-Blanco
Department of Geology, University of Oviedo, Oviedo, Spain

K. D. Nguyen et al. (eds.), *Estuaries and Coastal Zones in Times of Global Change*, Springer Water,
https://doi.org/10.1007/978-981-15-2081-5_18

Keywords Estuarine processes · Systems connectivity · Geomorphology · Ecology

1 Introduction

Coastal and estuarine landforms provide a physical support for numerous human activities (Murray et al. 2008), that benefit from ecosystem services, as buffering of erosion and flood risks (French et al. 2016). Human presence in coastal areas has increased in last decades, and is expected to keep increasing for the near future (de Andrés et al. 2018). This situation, together with the expected increase of coastal risks associated with climate change, supports the need for effective and comprehensive management tools that allow a correct assessment of coastal systems vulnerability.

Estuaries provide many ecosystem services including provision (i.e. fisheries, aquaculture or aggregates extraction), regulation (i.e. morphosedimentary processes, protection from flood and erosion risks or biological controls) and cultural services (i.e. tourism, leisure). They present high levels of complexity, and diverse morphosedimentary units and habitats (Borja et al. 2008) that make them complex from a management point of view. They are transition zones in between marine and terrestrial environments, where environmental gradients and adjacent system links favour the establishment of a mosaic of interrelated ecosystems with high environmental, tourist and commercial values (Pallero 2017).

According to Bridge and Demicco (2008), the connexions among beaches, dunes, sand channel bars and saltmarshes on estuarine zones are mainly made by means of tidal inlet dynamics. Tidal inlet deposits, like flood and ebb deltas, are commonly formed by washover processes active during coastal storms or by river flooding episodes. In the first case, flood-tidal deltas present on river mouths transport sand from the outer confining barrier (external beaches and dunes), mainly during energetic events when beaches and dunes are eroded, and move it into the estuary (Hayes 1979; Boothroyd 1985; Davis and Fitzgerald 2004). The deposits accumulate upstream and move to tidal channels, tidal flats and saltmarshes, along with nutrient dissemination. These particular characteristics and processes are decisive in the geomorphology and ecology of the system. As dynamic systems on constant change, its connectivity should be taken into account when applying measures and procedures in order to a better management and preservation of such environments and their influence areas. Unfortunately, most management tools overlook the estuarine connectivity, limiting our knowledge on the integral functionality of these complex systems and, therefore, limiting our capacity to preserve their ecosystem services.

The nature and dynamics of the substrate are the most important limiting factors in these systems. Under sedimentary deficit conditions, estuaries and all the associated systems (beaches, dunes and marshes) retreat and erode, and so it also happens with their respective habitats and biodiversity. An approach to the drivers of these changes and the resulting consequences can be obtained by analysing the historical changes recorded by estuaries, which according to Clark et al. (2001) is the only way to

establish future trends and priorities. In this sense, anthropic pressures have a crucial role on these studies by construction of hard structures which modify the natural morphodynamic and sediment dynamics of the estuarine systems.

The reconstruction and capacity to predict the evolution of estuaries from short to medium term needs the development of thematic maps, in order to integrate available historical information. Thus, we will improve our capacity to evaluate the resilience of the system but also to develop resources for effective management measures (FitzGerald and Knight 2005) to quantify processes on estuarine zones.

Increasing pressures and impacts affecting estuaries and coasts have led to the European Union (EU) to adopt several directives for coastal protection, specific for water and ecosystems management (Water Framework Directive, Directive on Marine Strategy, Habitat Directive and INSPIRE Directive, mainly). These EU Directives, mandatory for all EU member states, have the objective of bringing all European coasts to a 'Good Environmental Status' by 2020/21 moving towards its integrative management. All member states have made efforts to transpose these directives to national plans for habitat management; however, not all of them have used the same classification system, making difficult the sharing of the environmental information. This heterogeneity generates difficulties even to perform or implement measures for habitat conservation. Sharing environmental information is a European priority regulated by the INSPIRE directive, which specifies that habitats should be classify according to the EUNIS habitat classification, being also recommended to use on top the "habitat types" from the Annex I of the Habitats Directive and from the Marine Strategy Framework. Thus, equivalences between these two habitat classifications are already done (i.e. "*crosswalks*"), to facilitate the transition to a standard nomenclature for all the EU member states (European Environment Agency, 2017).

In Spain, some projects are looking towards these 'Good Environmental Status' (i.e.: *Preliminary ecological bases for conservation of Habitat of Community Interest in Spain*; Spanish Ministry of Environment and Rural and Marine Affairs, 2009; or Natura 2000 Network in Cantabria, developed by the Institute for Environmental Hydraulics (IH Cantabria) in 2010 for the study area). These projects propose a large number of coastal geo-ecoindicators to quantify the state of coastal areas. However, the high specificity of these methodologies hampers their applicability as general procedures necessary to provide a global view of the ecosystem (Pallero 2017).

In short, despite the accepted high relevance of the good functioning of the estuaries, most of the studies are not focused on a real comprehensive vision. To provide such perspective, it is still needed the development of integrative and easily replicable tools to assess ecosystem quality, both from scientific and stakeholder points of view. In particular, this preliminary study proposes a complementary methodology to the existing ones, simple and reliable, for the environmental characterization of mid latitude estuaries. The present study is the first stage of a larger project that will compare and validate the proposed methodology with other study zones. In a broad sense, this methodology evaluates morphosedimentary, oceanographic and ecological processes, together with the anthropogenic influence.

The aim of this preliminary study is to design a general, simple and reliable methodology for the environmental characterization of mid latitude estuaries. This

methodology seeks to characterize the estuarine subsystems and their connectivity. To cope with that, the characterization of the subsystems will combine thematic mapping with a selection of morphosedimentary, oceanographic and ecological variables, as well as an assessment of the anthropogenic pressures.

2 Study Area

The study area is located in the Cantabrian coast, at the North-Atlantic region of the Iberian Peninsula (Fig. 1a). San Vicente de la Barquera estuary is formed by two shallow estuary subsystems (Fig. 1b), constricted by a sand barrier at the mouth (Flor-Blanco et al. 2015). After discarding the upper channel (fluvial domain), which is out of this study, the estuary has been longitudinally divided in three sectors (Flor-Blanco 2007): mouth complex, sand bay and tidal flats, developing a set of morphodynamic units for each of them.

The main and largest tidal flat system is called *Rubín* (River Escudo), situated on the Eastern zone (approx. 200 ha, 4.38° W–43.37° N). It is the responsible for the development of most of the sedimentary units of San Vicente de la Barquera estuary. The second one, the *Pombo* system (River Gandarilla), is located on the left side of the valley (approx. 75 ha, 4.40° W–43.38° N).

The Cantabrian coast has an oceanic climate, with no dry season. Rainfall is very relevant and frequent throughout the year, with an average annual precipitation of 1021.74 l/m^2 during the period 2000–2015 (MeteoCantabria 2018). This region is considered a high energy area with strong and persistent winds from various directions (Flor-Blanco et al. 2015), but mainly blowing from WNW. On this sector of the Cantabrian coast, prevalent western winds produce a prevailing littoral drift to the East (Flor-Blanco 2007). Mean wind speed is about 2–3 m/s, with a frequency of almost 24% of the total (Fig. 2).

Regarding wave regime, predominant wave direction comes from NW (Fig. 3). The most frequent significant wave heights fluctuate between 0.5 and 1 m, and the peak period is higher than 9.0 s in most cases (with a frequency of 65%). Wind and wave data have been obtained from the SIMAR 3122034 (4.42° W–43.42° N) and provided by the Spanish National Port Authority (2018).

Tide is the most important dynamic factor in this area (Flor-Blanco et al. 2015). This is a mesotidal semidiurnal coast with tides ranging between 1.0 and 4.75 m, with an average of 2.84 m. The tidal flats extend upstream about 6.3 km from the mouth, favouring a broad development of large tidal flats in both, the *Rubín* and *Pombo* systems.

According to the classification of Simmons (1995), San Vicente de la Barquera is a hypersynchronous estuary. The tidal wave is higher up in the tidal flats areas than in the sand bay. This is due to a resonance phenomenon taking place around the bridge that separates both systems (Flor-Blanco et al. 2015).

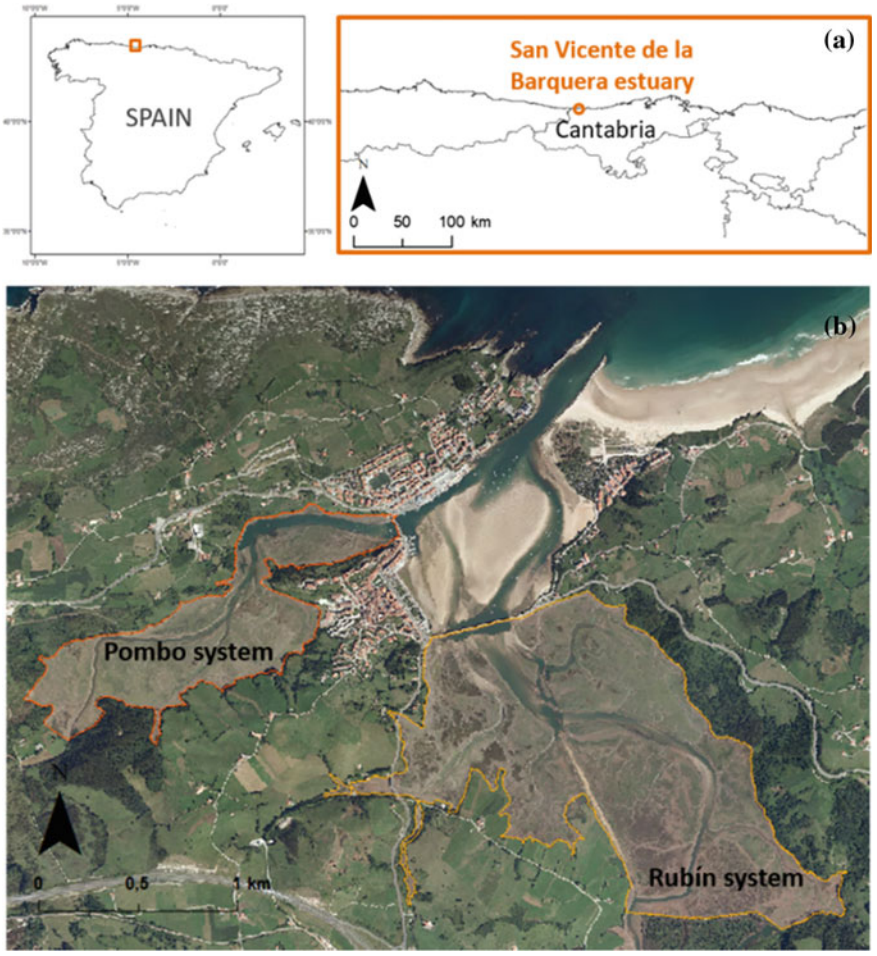

Fig. 1 Study area. **a** Location of San Vicente de la Barquera estuary. **b** Aerial photograph taken in 2010 (PNOA-IGN) with the names of the main systems

3 Methods

Estuarine conditions are assessed using a target-based-assessment form based on two main "work packages": (1) thematic mapping of the estuary and (2) a selection of indicators to define the environmental status of the system.

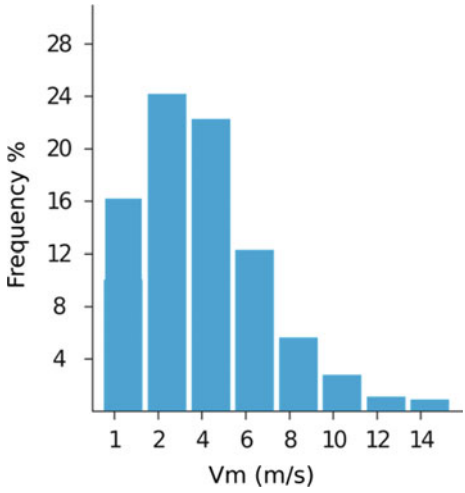

Fig. 2 Wind average velocity histogram during the period 1958–2011 (Spanish National Port Authority 2018)

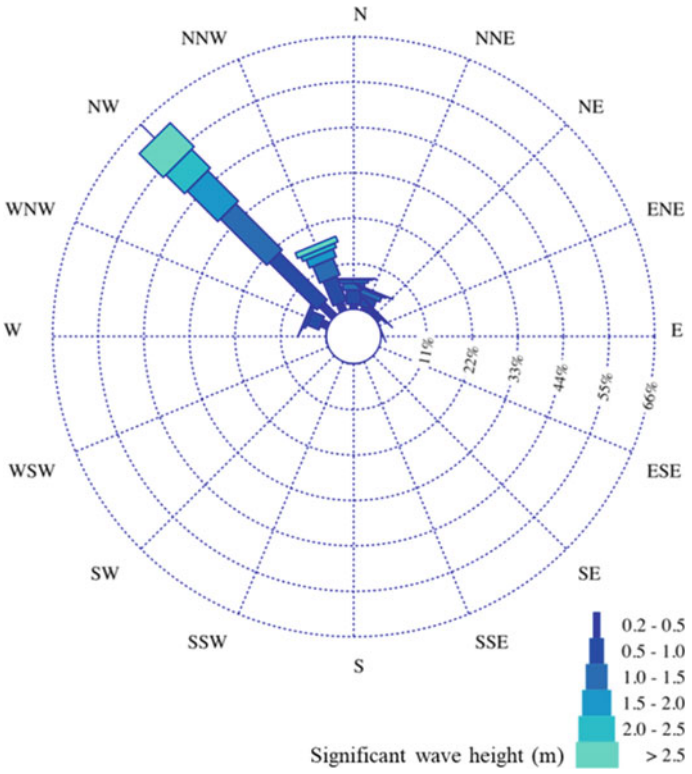

Fig. 3 Wave rose on the study zone during the period 1958–2011 (Spanish National Port Authority 2018)

3.1 Cartography

The thematic maps developed are: (a) map of main subsystems, (b) map of morphosedimentary units and (c) map of habitats.

An exhaustive revision of previous studies and maps has been done before elaborating the new ones, in order to complete and reuse existing information and adequate these resources to the requirements of the present work. Previous literature has given information about management actions and pressures in the area for a better understanding of its present state.

Once data collection is done, new maps have been elaborated to update the temporary series which will allow understanding changes and processes in the study zone and to set the system trend. The ortophotographs used to map all the elements have been collected from the National Plan of Aerial Ortophotography (PNOA). The ortophotographs must be on low tide in order to record all the submerged units and minimize errors. Unfortunately, not all the ortophotographs were made on low tide, so only years with these characteristics are selected. All the elements have been mapped with ArcGis 10.2 (© ESRI). When required, digital mapping has been combined with field campaigns to compare data in situ with the geomorphological maps and solve uncertainties from the ortophotographs.

For each element of the map, the attribute table contains fields with the same type of information for an easy comparison between different years and systems. The result gives a single database to define common standards to describe and share the spatial data according to INSPIRE Directive (2007). Once subsystems' area is calculated, changes intimately bound up with the evolution of each estuary can be established (López 2015).

The next step is to combine these maps to identify common areas and determine equivalences between subsystems (a) and habitats types (c). For this purpose, it was used the *Union* tool from ArcGis 10.2 (© ESRI), which calculates the geometric union of these two kind of maps. The output feature class contains polygons representing the geometric union of all the inputs. By combining them, equivalences are drawn up in order to relate both types of units from a geographical point of view. If there is any gap in the union between both features, it can be identified by doing an attribute query of all the input features FID fields that equal −1 ("no link").

The combination of these maps allows setting the connection between substratum (nature and dynamics) and plant communities, which is the main criterion to establish the habitat type according to EUNIS classification. Therefore, this combination of maps defines digitally the surface occupied by the different habitats, reducing efforts needed on in situ calibration.

Finally, habitat types from the Annex I of the Habitat Directive have been compared with habitats described by EUNIS classification to transpose maps into EUNIS classification. A first approach has been made using the Intertidal guide of the Natural Heritage of Cantabria (2010) together with the EUNIS habitats descriptions of fauna and flora (until level 4) in order to establish relationships between both classifications.

3.2 Selection of Variables for the Design of an Integrated Environmental Characterization Index (IEC)

In order to evaluate the integral functionality of the estuary, the present work focus on physical and biological variables relevant for processes and connectivity in between subsystems. Induced anthropogenic processes are considered, which are driving forces acting directly on the previous ones.

To design an integrated environmental characterization index (IEC) for estuaries, it has been performed a selection of geo-indicators, including those previously used in the literature and keeping in mind the feasibility and reliability of the method. The selected indicators should be sufficient to characterize morphosedimentary, ecological and management properties of the estuary and to understand the inter-connectivity between their connected subsystems. Biodiversity and physicochemical indicators have been reduced since they are usually included in methodologies used by official institutions (i.e. Spanish Royal Decree 817/2015, of 11 September 2011, establishing criteria for monitoring and evaluation of surface waters state and standards of environmental quality). Assuming that, it is proposed to reduce the list of indicators for the development of the cited index. They are selected, a priori, according to the studied subsystems (beaches, dunes, saltmarshes and mudflats, and main channel) and will be modified if necessary during the future study period.

4 Preliminary Results and Discussion

4.1 Cartography

A preliminary delimitation of (a) main subsystems, (b) morphosedimentary units and (c) habitat types from the Annex I of the Habitats Directive has been done.

There are four main subsystems identified, including beaches, dunes, saltmarshes & mudflats, and the main channel (Fig. 4). The surface covered by saltmarshes and mudflats is twice the area occupied by the other three subsystems together, supporting the importance of tides in this area.

To map the morphosedimentary units present on these subsystems (Fig. 5), the criteria of Flor-Blanco (2007) has been used. In total, 14 morphosedimentary units have been mapped, whose characteristics are described below within their corresponding subsystem.

1. Beaches
    a. Beach: sandy unit formed by supra and intertidal zones on the external confining barrier.
    b. Estuarine beach: unit located inside the estuary, with a small surface and strongly affected by sediment transport into the estuary.

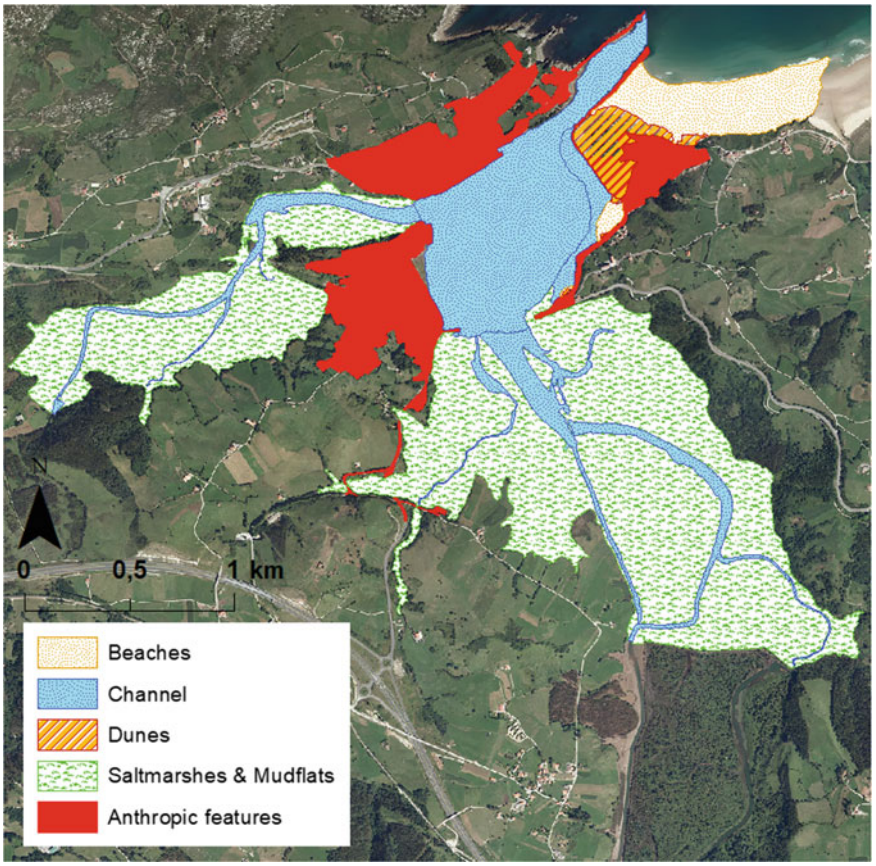

Fig. 4 Map of subsystems present on San Vicente de la Barquera estuary. Aerial photograph from 2010 (PNOA-IGN)

2. Dunes

    a. Dune: unit formed on the external confining barrier, on the upper part of the beach, and strongly affected by human activities (trampling, parking, etc.). There are also estuarine dunes on the top of the estuarine beaches.

3. Saltmarshes and Mudflats

    a. Saltmarshes: intertidal areas covered by saltmarsh vegetation.
    b. Mudflats: intertidal areas adjacent to saltmarshes with no saltmarsh plant presence.

4. Channel

    a. Main channel: principal water pathway connecting all the units on the estuary.

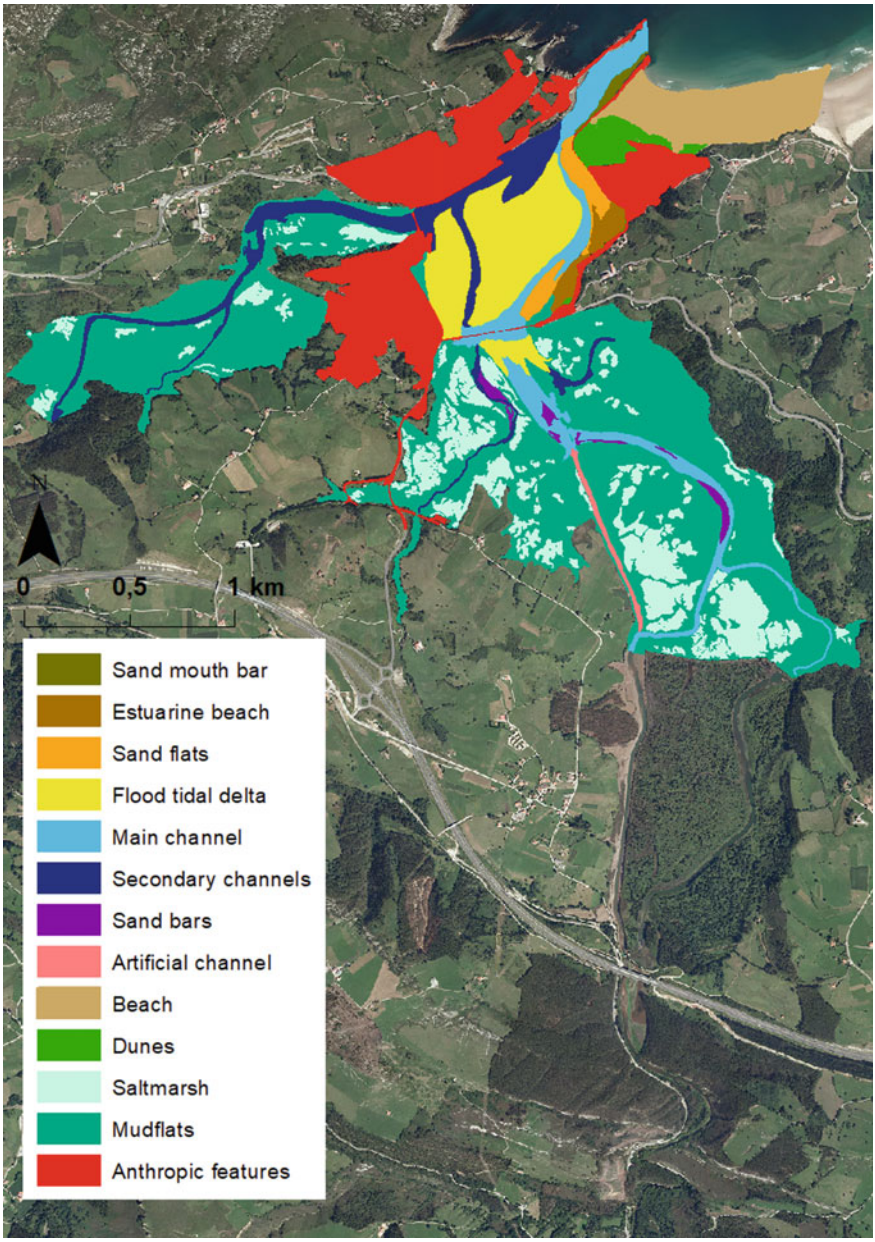

Fig. 5 Map of morphosedimentary units. Aerial photograph from 2010 (PNOA-IGN). Based on criteria used by Flor-Blanco (2007)

b. Secondary channels: set of minor channels connected to the main channel (Flor-Blanco et al. 2015). They regulate the water along the mudflats.
c. Artificial channel: built for navigation of recreational boats. It has a linear design protected by dikes.
d. Flood tidal delta: sand accumulation in the sand bay. It is the largest morphosedimentary unit located in the main channel.
e. Sand mouth bar: unit present at the river mouth. It requires periodic dredging to allow navigation.
f. Sand flats: units located at the margins on the wider part of the main channel. They are formed by high energy water movements (flux and reflux).
g. Sand bars: units formed at the margins of the channels in the southern part of the bridge due to sediment transport by the incoming flux.

5. Anthropic features

Anthropic features have introduced important changes on the estuarine zones and might be considered partly responsible on the estuarine behaviour. The actual geometry of the estuary here presented is partly result of the numerous human interventions done in this zone (i.e. dikes and dams' construction, human settlements on dunes, dredging, polluting discharges, estuarine beach nourishment, bridge construction, etc.). Therefore, these features have been included in all the thematic maps in order to highlight the importance of the human factors on this natural system.

Habitat types from the Annex I of the Habitat Directive have been mapped by modifying a pre-existing one (Natura 2000 Network in Cantabria, developed by the Institute for Environmental Hydraulics (IH Cantabria; Fig. 6). This map covers coastal habitats included in the EU Directive, except the habitat 1130 ("Estuaries"), which was excluded since it is so general that it would include any other habitat.

The habitats in the Beach subsystem, like *Annual vegetation of drift lines* (1210), are small and ephemeral (i.e. temporally variable), limiting the capacity for delimitation with aerial ortophotographs. Therefore, a consistent quantification of their extension will require in situ measurements.

The presence of seagrasses is considered as an ecological indicator of good-functioning on estuarine systems. In this study area, seagrasses are not mapped, but the seagrass *Zostera noltei* occupies large areas on the mudflats from saltmarsh and mud flat units. Its identification through aerial ortophotographs is a difficult task, consequently a good delimitation of the area occupied by them will also require field measurements.

The overlapping of subsystem and habitat type maps highlight their potential connections (Fig. 7). The most extensive subsystem (saltmarsh and mudflats, Fig. 4) covers 252.68 ha in total and it is mostly occupied by habitat 1140-*Mudflats and sandflats not covered by seawater at low tide* (195.72 ha on saltmarshes), and habitat 1110-*Sandbanks which are slightly covered by sea water all the time* that also occupies a wide area (25.22 ha on saltmarshes). Main channel is the second most extensive subsystem (96.22 ha in total) occupied mainly also by 1110 and 1140 habitats. Beach and dunes subsystems occupy a small area when compared with saltmarshes & mudflats, and the main channel, since they only appear on the external sector of the

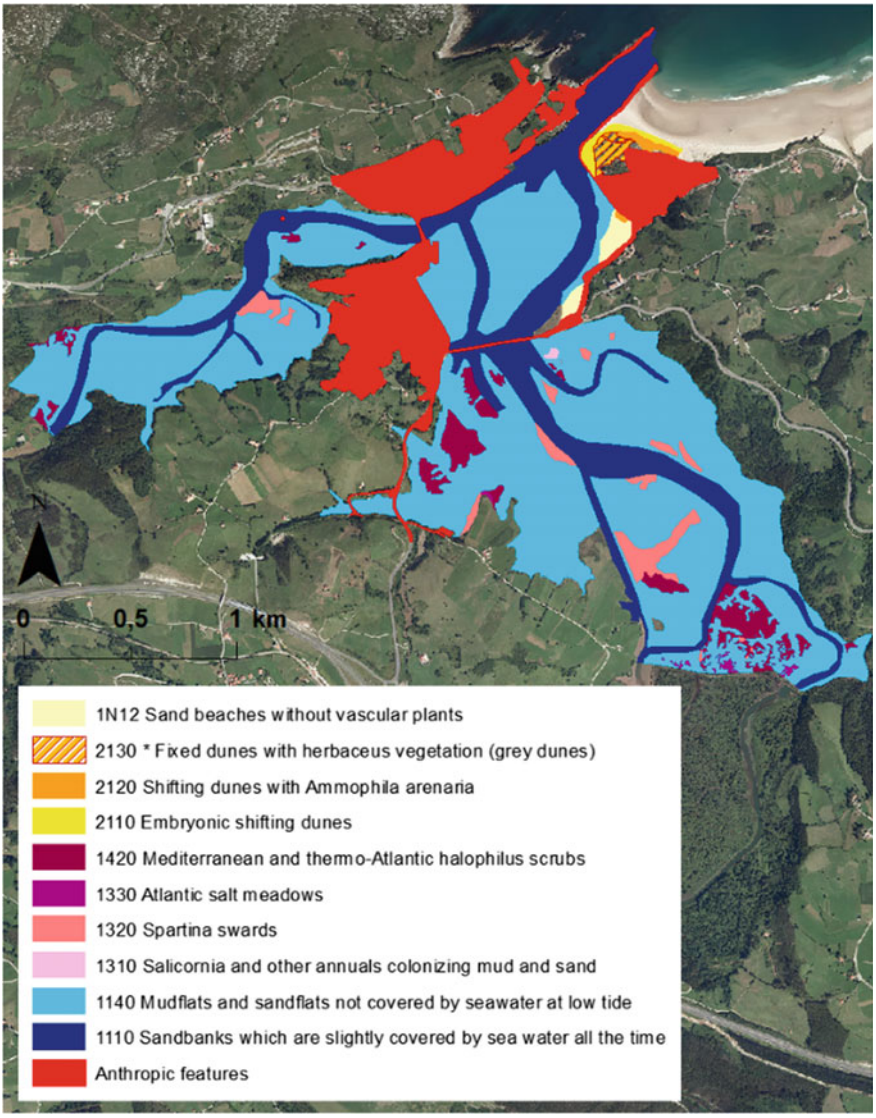

Fig. 6 Map of "Habitat types" from the Annex I of the EU Habitat Directive. Aerial photograph from 2010 (PNOA-IGN). Modified from Natura 2000 Network in Cantabria (http://rednatura2000cantabria.ihcantabria.com/lics/litorales/oyambre/)

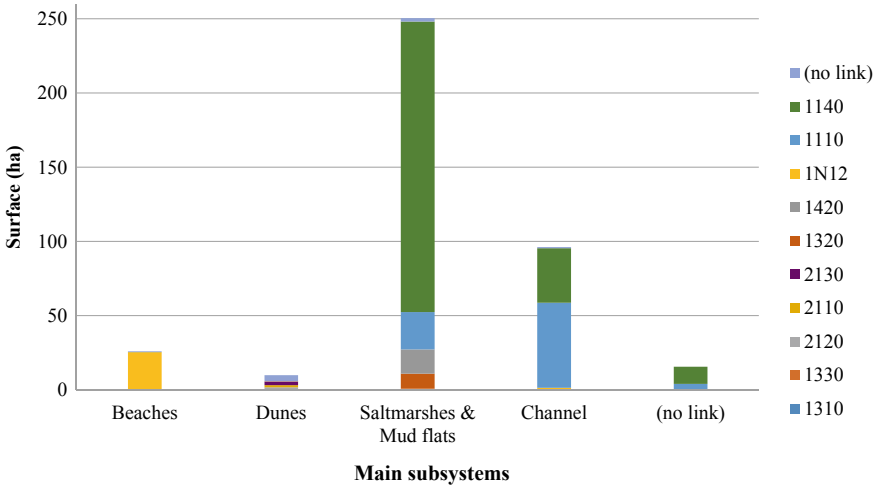

Fig. 7 Relationship between subsystems and habitat types surfaces (in ha) on San Vicente de la Barquera estuary. The "no link" class represent areas where subsystems and habitats do not overlap

estuary. In total, beach subsystem occupies 25.95 ha, presenting habitat 1N12-*Sand beaches without vascular plants* (24.59 ha), 1140—*Mudflats and sandflats not covered by seawater at low tide* (0.89 ha), 2110-*Embrionic shifting dunes* (0.33 ha), 2120-*Shifting dunes with Ammophila arenaria* (0.03 ha) and 2130-*Fixed dunes with herbaceous vegetation* (0.001 ha). Dunes occupy 9.89 ha, presenting habitats 1N12 (0.11 ha), 2110 (1.56 ha), 2120 (1.68 ha) and 2130 (2.11 ha). Finally, areas not linked to any subsystems or habitat types have been named as "no link" areas. However, the use of a more specific habitat description (e.g. EUNIS classification) would improve this type of analysis (i.e. Fig. 7).

Table 1 summarizes main equivalences between habitat types (Annex I of the Habitats Directive) and EUNIS classification. By comparing these equivalences with the occupied surface by each habitat type (Fig. 7), it is noted that habitats with greater surface are the ones the can be split in a larger number of EUNIS habitats (e.g. habitats 1110, 1140 and 1330 are related to more than 10 EUNIS habitats). Therefore, it is expected that the development of the corresponding EUNIS maps would improve accuracy on the definition of habitat presence/absence and will facilitate the transition to a standard nomenclature for all the EU member states.

Table 1 Equivalences between EU directive habitat types and EUNIS classifications on San Vicente de la Barquera estuary

Habitat types (EU directive)	EUNIS	
1110	A5.1 Sublittoral coarse sediment	A5.12 Sublittoral coarse sediment in variable salinity (estuaries)
	A5.2 Sublittoral sand	A5.22 Sublittoral sand in variable salinity (estuaries)
		A5.221 Infralittoral mobile sand in variable salinity (estuaries)
		A5.23 Infralittoral fine sand
		A5.231 Infralittoral mobile clean sand with sparse fauna
		A5.234 Semi-permanent tube-building amphipods and polychaetes in sublittoral sand
	A5.3 Sublittoral mud	A5.32 Sublittoral mud in variable salinity (estuaries)
		A5.323 *Nepthys hombergii* and *Tubificoides* spp. in variable salinity infralittoral soft mud
		A5.324 Infralittoral fluid mobile mud
	A5.4 Sublittoral mixed sediments	A5.42 Sublittoral mixed sediment in variable salinity (estuaries)
	A5.5 Sublittoral macrophyte-dominated sediment	A5.53 Sublittoral seagrass beds
		A5.533 *Zostera* beds in full salinity infralittoral sediments
1140	A2.2 Littoral sand and muddy sand	A2.21 Strandline
		A2.23 Polychaete/amphipod-dominated fine sand shores
		A2.24 Polychaete/bivalve-dominated muddy sand shores
	A2.3 Littoral mud	A2.31 Polychaete/bivalve-dominated mid estuarine mud shores
		A2.32 Polychaete/oligochaete-dominated upper estuarine mud shores

(continued)

Table 1 (continued)

Habitat types (EU directive)	EUNIS	
	A2.4 Littoral mixed sediments	A2.41 *Hediste diversicolor* dominated gravelly sandy mud shores
		A2.42 Species-rich mixed sediment shores
	A2.6 Littoral sediments dominated by aquatic angiosperms	A2.61 Seagrass beds on littoral sediments
1310	A2.5 Coastal saltmarshes and saline reedbeds	A2.54 Low-mid saltmarshes
		A2.55 Pioneer saltmarshes
1320	A2.5 Coastal saltmarshes and saline reedbeds	A2.55 Pioneer saltmarshes
1330	A2.5 Coastal saltmarshes and saline reedbeds	A2.52 Upper saltmarshes
		A2.521 Atlantic and Baltic brackish saltmarsh communities
		A2.53 Mid-upper saltmarshes and saline and brackish reed, rush and sedge beds
		A2.531 Atlantic upper shore communities
		A2.53B Mid-upper saltmarshes: sub-communities of *Festuca rubra* with *Agrostis stolonifera*, *Juncus gerardi*, *Puccinellia maritima*, *Glaux maritima*, *Triglochin maritima*, *Armeria maritima* and *Plantago maritima*
		A2.535 *Juncus maritimus* mid-upper saltmarshes
	A2.54 Low-mid saltmarshes	A2.541 Atlantic saltmarsh grass lawns
		A2.545 *Halimione portulacoides* low-mid saltmarshes
		A2.546 *Puccinellia maritima* low-mid saltmarshes
1420	A2.5 Coastal saltmarshes and saline reedbeds	A2.52 Upper saltmarshes
		A2.527 Atlantic salt scrubs
2110	B1.3 Shifting coastal dunes	B1.31 Embryonic shifting dunes

(continued)

Table 1 (continued)

Habitat types (EU directive)	EUNIS	
2120	B1.3 Shifting coastal dunes	B1.32 White dunes
2130	B1.4 Coastal stable dune grassland (grey dunes)	B1.42 Biscay fixed grey dunes
1N12	B2.2 Unvegetated mobile shingle beaches above the driftline	

4.2 Selection of Variables for an Integrated Environmental Characterization Index (IEC)

The physical, biological and anthropogenic variables selected to design an Integrated Environmental Characterization index (IEC) able to evaluate the integral functionality of the estuary are the following:

– **Beaches**

Considering beaches as very dynamic units, selected indicators will evaluate natural morphosedimentary processes (i.e. those favouring the establishment of plant communities) and also pressures and hazards on beach surface.

1. Morphosedimentary factors: beach geometry, energetic wave frequency, tidal regime, sediment texture, erosion/accretion (shoreline changes in the last 10 years) and beach slope.
2. Ecological factors: drift algae, presence/absence of fauna and flora characteristic of the beach and sublittoral zone.
3. Management factors: nourishment, occupancy rate in summertime, mechanic maintenance and cleaning, and hard structures on the beach.

– **Dunes**

To characterize dune units, the selected variables are:

1. Morphosedimentary factors: Dune geometry, erosion/accretion rates (changes in the last 10 years), sediment texture, dune system fragmentation (%) and erosive scarps on the foredune (%).
2. Ecological factors: Plant communities' succession, % of dunes with exposed roots, characteristic fauna and invasive exotic species.
3. Management factors: Access control, bridges and walkways, sand collectors, rubbish bins and informative panels of management actions.

– **Saltmarshes and Mudflats**

To characterize saltmarsh and mudflats units, the factors considered are:

1. Morphosedimentary factors: saltmarsh geometry, slope, structure and density of tidal creeks, tidal flood pattern and sediment texture.

2. Ecological factors: vegetated area, plant cover (%), plant zonation pattern, associated elevation, soil salinity, distance to nearest tidal creek.
3. Management factors: anthropogenic transformation (salterns), shellfish and landfill of waste.

– **Main channel and associated bars**

To characterize the main channel and structures associated to it, the following factors are considered:

1. Morphosedimentary factors: channel geometry, migration, narrowing, channel multiplicity, sediment texture and bar evolution.
2. Ecological factors: turbidity, fauna and diversity and salinity.
3. Management factors: dredging, dams (within the estuary and on the river basin), dikes and boat ramps.

These variables have been selected for their easy-to-apply character, reliable and representative of the state and quality of every subsystem. In addition, most of them do not require field measurements. The reduced number of variables for each subsystem facilitates their proper application and repeatability in time.

5 Conclusions

This work presents equivalences between morphosedimentary subsystems and main habitats in San Vicente de la Barquera estuary (North Spain). The morphosedimentary units forming the external confining barrier (beach and dunes) are relatively small and clearly related to specific habitats, whereas saltmarshes, mudflats and the main channel contain more ubiquitous habitats and, therefore, not site-specific. This results suggest the need to apply more detailed classifications and maps both to morphodynamic units and habitats for a more specific link between them.

In a broad sense, it seems easy to identify limits in between morphosedimentary units and it is feasible to define their corresponding habitat types. Therefore, this approach could be used to reduce efforts on field inspection when elaborating habitat cartography. Nevertheless, to apply the equivalences here presented, it is still necessary to validate them in other study zones to make them reliable.

Based on existing resources and comparison of morphosedimentary units with habitat types, this work also presents a preliminary selection of variables per subsystem considered useful to design an Integrated Environmental Characterization index (IEC) for estuaries.

This preliminary study reinforces the need for developing map series to characterize and evaluate estuarine zones. The combination of approaches here presented (morphosedimentary units and habitats types including human pressures), seems to have potential for characterizing the state of the functional integrity on estuaries, being a complement to provide missing information existing on actual methodologies that looks towards a ‘good environmental status’ on estuaries.

It is innovative to evaluate the connectivity between estuarine subsystems, through a combination of biotic and abiotic variables that inform on the functioning state of the estuary. The assessment of estuarine connectivity should include key dynamic processes to give a comprehensive perspective to the study of these complex littoral systems. Evaluating functional integrity on estuaries will improve our capacity to evaluate their resilience, favouring the efficiency of long-term management.

Acknowledgements We are grateful to Germán Flor Rodríguez for his field support, and to the Institute for Environmental Hydraulics (IH Cantabria) for the habitat cartography and information about the Nature 2000 Network in Cantabria.

This work is a contribution to the RNM328 and RNM214 groups of the Andalusian Research Plan (Junta de Andalucía).

References

Boothroyd, J. C. (1985). Tidal inlets and tidal deltas. In *Coastal sedimentary environments* (pp. 445–533). New York: Springer Verlag.

Borja, A., Bricker, S. B., Dauer, D. M., Demetriades, N. T., Ferreira, J. G., Forbes, A. T., et al. (2008). Overview of integrative tools and methods in assessing ecological integrity in estuarine and coastal systems worldwide. *Marine Pollution Bulletin, 56*(9), 1519–1537.

Bridge, J. S., & Demicco, R. V. (2008). *Earth surface processes, landforms and sediment deposits* (p. 815). Cambridge: Cambridge University Press.

Clark, J. S., Carpenter, S. R., Barber, M., Collins, S., Dobson, A., Foley, J. A., et al. (2001). Ecological forecast: an emerging imperative. *Science, 293,* 657–660.

Consejería de Medio Ambiente del Gobierno de Cantabria y Asociación Científica de Estudios Marinos (ACEM). (2010). Natural heritage of Cantabria. Intertidal guide. http://www.estudiosmarinos.com/patrimonio-litoral-cantabria/Patrimonio-litoral-Cantabria.pdf.

Council Directive 92/43/EEC, of May 1992, on the conservation of natural habitats and of wild fauna and flora. *Official Journal of the European Communities.*

Davis, R. A., & Fitzgerald, D. M. (2004). *Beaches and coasts*. Oxford: Blackwell.

De Andrés, M., Barragán, J. M., & Scherer, M. (2018). Urban centres and coastal zone definition: Which area should we manage? *Land Use Policy, 71,* 121–128.

Directive 2000/60/E of the European Parliament and of the Council, of 23 October 2000, establishing a framework for Community action in the field of water policy. *Official Journal of the European Communities*.

Directive 2007/2/EC of the European Parliament and of the Council, of 14 March 2007, establishing an Infrastructure for Spatial Information in the European Community (INSPIRE). *Official Journal of the European Union.*

Directive 2008/56/EC of the European Parliament and of the Council, of 17 June 2008, establishing a framework for community action in the field of marine environmental policy (Marine Strategy Framework Directive). *Official Journal of the European Union*.

European Environment Agency (EEA). (2017). An introduction to habitats. https://www.eea.europa.eu/themes/biodiversity/an-introduction-to-habitats.

FitzGerald, D. M., & Knight, J. (2005). Towards an understanding of the morphodynamics and sedimentary evolution of estuaries. In: FitzGerald, D. M. & Knight, J. (Eds.), *High resolution morphodynamics and sedimentary evolution of estuaries* (vol. 8, pp. 1–9). Springer.

Flor-Blanco, G. (2007). *Características morfosedimentarias y dinámicas y evolución ambiental de los estuarios de Tina Mayor, Tina Menor y San Vicente de la Barquera (Costa Occidental de Cantabria)* (Ph.D. Thesis). University of Oviedo. p. 477.

Flor-Blanco, G., Flor, G., Pando, L., & Abanades, J. (2015). Morphodynamics, sedimentary and anthropogenic influences in the San Vicente de la Barquera estuary (North coast of Spain). *Geologica acta, 13*(4), 279–295.

French, J., Payo, A., Murray, B., Oxford, J., Eliot, M., & Cowell, P. (2016). Appropriate complexity for the prediction of coastal and estuarine geomorphic behaviour at decadal to centennial scales. *Geomorphology, 256,* 3–16.

Hayes, M. O. (1979). Barrier island morphology as a function of tidal and wave regime. Leatherman, S. P. (Ed.), *Barrier Islands—From the Gulf of St. Lawrence to the Gulf of Mexico* (pp. 1–27). London: Academic Press.

Institute for Environmental Hydraulics (IH Cantabria). (2011). Nature 2000 Network in Cantabria. http://rednatura2000cantabria.ihcantabria.com/lics/litorales/oyambre/.

López, J. (2015). *Evolución morfosedimentaria e histórica de los estuarios asturianos de Navia, Nalón, Avilés, Villaviciosa y Ribadesella* (Ph.D. Thesis). University of Oviedo (Spain), p. 307.

MeteoCantabria. (2018). Territorial Delegation in Cantabria of the Spanish Meteorological Agency (AEMET). https://www.meteocantabria.es/meteocantabria/historico/filtrar.

Murray, A. B., Lazarus, E., Ashton, A., Baas, A., Coco, G., Coulthard, T., et al. (2008). Geomorphology, complexity, and the emerging science of the Earth's surface. *Geomorphology, 103,* 496–505.

Pallero, C. (2017). *Gestionando realidades naturales y sociales complejas: los estuarios*. (Ph.D. Thesis). University of Cádiz, p. 304.

Royal Decree 817/2015, of 11 September 2015, establishing criteria for monitoring and evaluation of surface waters state and standards of environmental quality (Spanish). Spanish Ministry of Agriculture, Feeding and Environment. *Official State Bulletin*, 219.

Simmons, H. B. (1995). Some effects of upland discharge on estuarine hydraulics. *Procedures of the American Society of Civil Engineering*, *81*, 729/1–729/20.

Spanish National Geography Institute. (2010). National aerial orthophotography plan. http://centrodedescargas.cnig.es/CentroDescargas/index.jsp.

Spanish National Port Authority. (2018). http://www.puertos.es/es-es/oceanografia/Paginas/portus.aspx.

Seasonal Morphodynamics and Sediment Transport in a Highly Turbid Meandering Estuarine Channel

Gubash Azhikodan, Kirana Somsook and Katsuhide Yokoyama

Abstract Intensive field surveys (longitudinal and transverse) in the upper region of the Chikugo River estuary (12–14.6 km landward from the river mouth), Japan were carried out in every three or four months during 2009–2011 using a digital sonar system equipped with a differential global positioning system. The primary concern of study was to investigate the spatial and temporal dynamics of bed morphology in relation to semidiurnal and fortnightly tidal variations, magnitude and movement of estuarine turbidity maximum (ETM), and seasonal variations in river discharge in a meandering estuarine channel. The results revealed that the estuary was dominated by tidal discharge for most of the year except for rainy season in which river flow dominates. During the low flow season (September to May), fine sediment was deposited near the inner bank during every semidiurnal tidal cycle and the depth of the inner bank becomes diminished. On the contrary, the outer bank was heavily eroded and becomes steep. As a result, ETM developed at the upstream of the estuary and the channel capacity reduced gradually during this period. However, in the rainy season (June to August), large flood events led to the breakdown of ETM and export the sediment in the upper reach of the estuary to the downstream tidal flat. The seasonal cyclic pattern of erosion and deposition processes were evident at the upstream meander. This cycle of morphological evolution of river bed continues based on the upstream sediment transport by the fortnightly tidal cycles and downstream sediment transport by the river discharge. Hysteretic effects between shear stress and SSC due to the asymmetrical flood and ebb tides as well as the seasonal variations in river discharge are the dominant factors that cause sediment transport and morphological changes in tide dominated estuaries.

Keywords Bed topography · Chikugo river estuary · Fluid mud · Sediment transport · Macrotidal estuary

G. Azhikodan (✉) · K. Somsook · K. Yokoyama
Department of Civil and Environmental Engineering, Tokyo Metropolitan University, 1-1 Minami Osawa, Hachioji, Tokyo 192-0397, Japan
e-mail: gubash@tmu.ac.jp

K. Yokoyama
e-mail: k-yoko@tmu.ac.jp

K. D. Nguyen et al. (eds.), *Estuaries and Coastal Zones in Times of Global Change*, Springer Water,
https://doi.org/10.1007/978-981-15-2081-5_19

1 Introduction

Estuaries are important regions for both human beings and wildlife. They are essential locally as well as internationally due to their high commercial, recreational and ecological values. Therefore, it is critical to understand the hydraulic conditions of estuaries, especially in the tide dominated estuaries, since they cause erosion, sediment transport, deposition, sedimentation, and formation of estuarine turbidity maximum (ETM) zone (Eysink 1990). The large suspended sediment load delivered by these estuaries can substantially alter the morphology of the river bed. This morphological evolution further have a significant impact on the coastal and estuarine environments (Moore et al. 2009). For example, the sediment deposition will reduces the water depth which will further leads to difficulties in navigation, fishing, etc. (Wolanski et al. 1992; Liu et al. 2002; Schrottke et al. 2006). Additionally, the cities located around the estuaries are susceptible to flood disasters due to the reduction in flood carrying capacity by the siltation. Also, the estuarine morphology is under pressure due to both natural forcing and anthropogenic activities. Therefore, an insight into the estuarine morphodynamic processes enables a better understanding of the physical and ecological changes of estuaries and is important in solving the managerial problems such as dredging, river channel maintenance, and to analyse the impact of ETM on the estuarine ecosystem.

The morphology of estuaries describes the gradual development of the estuarine bed over time as a result of nonlinear interaction between tidal flow, river flow, sediment transport, and bottom topography (Ahnert 1960; Hibma et al. 2004). Generally, a meandering channel is formed in the alluvial plain by the erosion of outer banks and deposition on the inner banks. Several studies have been carried out to analyse both the natural (Ralston et al. 2013; Kostaschuk et al. 1989) and anthropogenic impact (Wang et al. 2015; Du et al. 2016; Wei et al. 2016) on the estuarine morphology. Many researchers studied the formation of fluvial plain within a span ranging from 100 to 10,000 years and analysed the sediment layer structure with the horizontal changes in the river channel by using a combination of historical charts (Blott et al. 2006) and satellite remote sensing data (van der Wal et al. 2002) from a geological point of view. Based on the hydraulic perspective, there are many modelling studies, especially using one dimensional (1D) models (longitudinal), to estimate the sediment load and bed elevation changes (van Dongeren and de Vriend 1994; Lanzoni and Seminara 2002). They also investigated the erosion and deposition dynamics of non-cohesive sediments (sand and gravel) caused by the shear stress during flood events.

Additionally, field measurements and laboratory experiments were conducted to analyse the erosion and deposition of cohesive sediments (silt and clay) caused by the shear stress of tidal flow or wave (Tolhurst et al. 2000; Azhikodan and Yokoyama 2018). Although few 1D (vertical) models were proposed, they were inadequate to truly demonstrate the underlying process of the weakly consolidated mud generation. Furthermore, few studies have examined the relationship between the formation of the curving channel and flow field in an estuary. Yokoyama et al. (2011) calculated the

annual sediment budget in a river mouth estuary and demonstrated that the sediment transport by the ETM significantly affects the topography of tidal flat and estuarine channel. However, they did not considered the lateral sediment transport and the change in cross-sectional bed topography. Blanton et al. (2003) studied the transport of salt and suspended sediments in a curved channel of an estuary, but the lateral variation of suspended sediments and current distribution in the cross section were not measured.

Later, fine sediment transport by the ETM is well studied (Uncles 2002). However, the seasonal variation of erosion and deposition dynamics of cohesive sediments, and its relation to the movement of ETM is rarely studied. The studies related to the morphodynamic evolution of estuaries is still limited, because of the complex nature of evolution over a wide time span and space scale. The studies about the effect of river flow and tidal dynamics on the sediment transport and morphology are mostly based on analytical solutions but are still poorly quantified with real field observations.

Based on the above discussions, this study aims to analyse the morphological changes within estuaries over time by conducting in situ measurements of bottom elevation and suspended sediment concentration (SSC). The primary objective of our study is to investigate the spatial and temporal dynamics of bed morphology in relation to the (i) semidiurnal and fortnightly tidal variations, (ii) magnitude and movement of ETM, and (iii) seasonal variations in river discharge in a meandering estuarine channel even though the 3D morphodynamic analysis on anthropogenic activities is very much important.

2 Methods

2.1 Study Area

The study area (Fig. 1) is Chikugo River estuary, a highly turbid estuary located in the Kyushu district of south-western Japan. The Chikugo River ranks the 22nd largest river in Japan which drains from a watershed of 2860 km^2 to the Ariake Sea through the estuary. The total length of the river is approximately 143 km. The annual precipitation in the watershed is 2100 mm, reaching a maximum of 3000 mm from the upstream mountainous areas of the watershed. The Chikugo River estuary is one of the most productive estuarine systems in Japan, supporting many harvestable communities that are only found in this area (Azhikodan and Yokoyama 2016; Islam et al. 2006; Suzuki et al. 2012; Suzuki et al. 2009).

The mean river flow to the estuary during the dry and rainy seasons are 54 $m^3\ s^{-1}$ and 2800 $m^3\ s^{-1}$ respectively in which the major contribution was low flow during dry season while the storm discharge was dominant during rainy season. Consequently, the estuary receives a tidal discharge of nearly 2000 $m^3\ s^{-1}$ during spring tide and 500 $m^3\ s^{-1}$ during neap tide. Therefore, the estuary was found to be dominated by

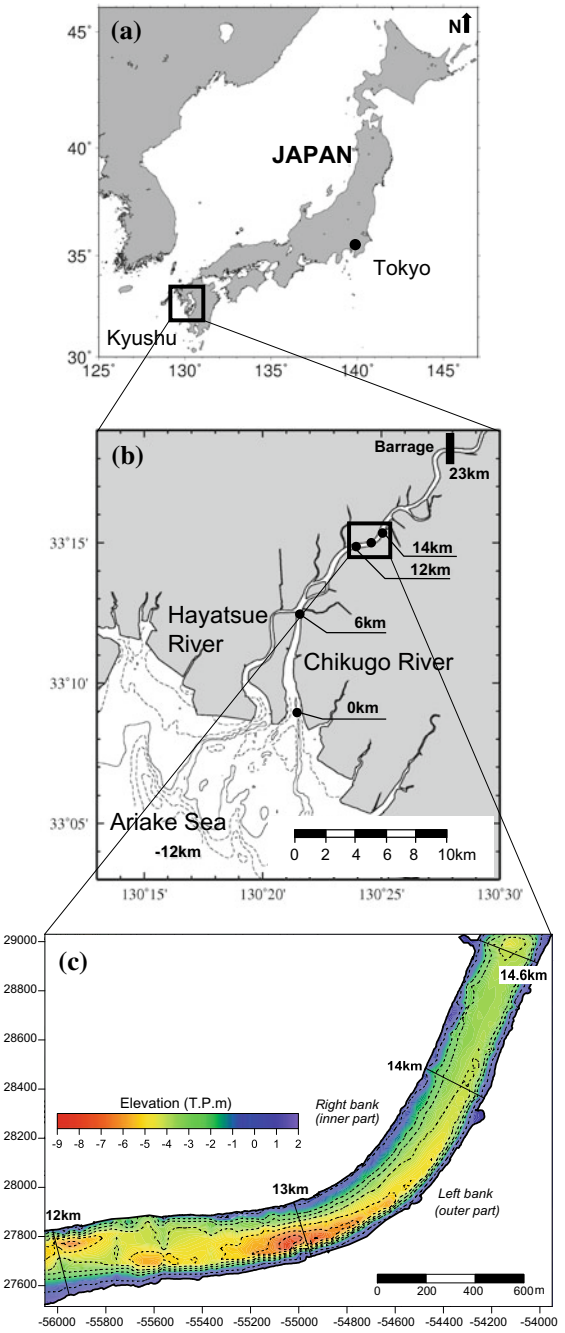

Fig. 1 Location map of the study area

tidal conditions during most of the year except in the rainy season (Azhikodan and Yokoyama 2015).

The salt water intrusion in the estuary reaches until the barrage which is located at a distance of 23 km upstream from the river mouth as shown in Fig. 1b. The width of the estuary varies from 1000 m at the river mouth (0 km) to 250 m at 23 km upstream. The bottom sediments in the tidal flat mainly consist of mud, whereas the section between the river mouth and 10 km from the mouth mainly composed of fine sand. The section between 10 and 20 km from the river mouth mainly consists of silt and clay whereas the region upstream of 20 km mainly composed of sand (Azhikodan and Yokoyama 2014, 2018).

2.2 Field Measurements

Field measurements were carried out at a location in the upper region of the Chikugo River estuary, Japan during 2009 to 2011. The field measurement methodology was comprised of (i) longitudinal and transverse survey at the meander (12–14.6 km landward from the river mouth) of the estuarine channel (Fig. 1c) in every three or four months using a digital sonar system equipped with a differential global positioning system (Eagle, Fishstrike-2000C), and (ii) continuous monitoring of the salinity (using ACTW-USB, JFE Advantech) and turbidity (using ATU75W-USB, JFE Advantech) at the bottom of the 14.6 km station in every 10 min interval. The transverse survey constitutes 17 cross sectional lines from 12 km station to 14.6 km station at intervals of 100–200 m, and the longitudinal survey was set at 4–6 alongside lines from 12 km station to 14.6 km station at intervals of 40–60 m. Water level data at the 14.6 km station was collected in every 10 min using a HOBO U20 water level logger (with a resolution of 2.1 mm). River discharge monitored at the gauge station located in the freshwater region (25.5 km from the river mouth) was collected from the Japanese Ministry of Land, Infrastructure, Transport, and Tourism.

2.3 Data Analysis

The turbidity measured by the turbidity sensor, ATU75W-USB (JFE Advantech) was related with the turbidity measured by an already calibrated turbidity sensor (Compact-CLW, JFE Advantech) at the same station during the same time and established a turbidity relationship with an R^2 value of 0.955. The turbidity of the Compact-CLW sensor was already calibrated for the SSC using the in situ collected sediment samples through the laboratory testing and a formula was developed to convert the turbidity to SSC ($R^2 = 0.97$) (Azhikodan and Yokoyama 2016). Subsequently, the turbidity relationship was substituted in the developed conversion formula in order to derive a new conversion formula (Eq. 1) for the SSC from the turbidity measured by the ATU75W-USB sensor (TB). Further, the SSC's computed from both the sensors

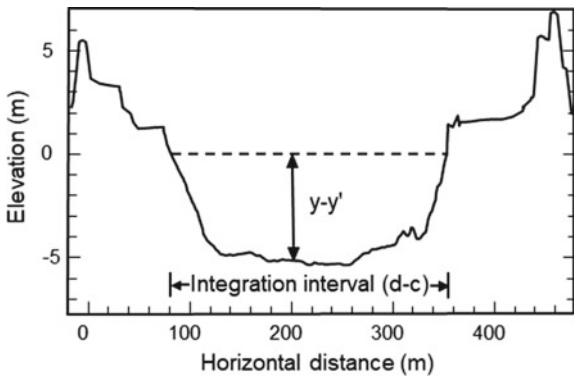

Fig. 2 Schematic representation of the cross section at 14 km from the river mouth

were related and the R^2 value of 0.92 showed an agreeable performance.

$$SSC = 0.95 \times TB + 3.25 \times 10^{-4} TB^2 + 3.58 \times 10^{-14} TB^5 \tag{1}$$

The river bed elevation was estimated from the water level data (collected by HOBO U20 water level logger during the field measurements as well as collected from Japan Water Agency) and acoustic image data. Latitude and longitude coordinates were converted to XY coordinates based on Japan geodetic system (Plane perpendicular coordinate system II) and expressed as the distance from the corresponding left bank reference point to the right bank (Fig. 2).

The cross sectional area of the estuarine channel at the 14 km station below the water surface (at elevation 0 m) during every field observation was estimated. For this purpose, the channel cross section (Fig. 2) was divided into very small sub sections and integrated these sub section areas between the interval d-c as shown in Eq. (2),

$$A = \int_c^d (y - y')dx \tag{2}$$

where A is the cross sectional area (m^2), y is the water level (m), y' is the riverbed elevation (m), c and d are the X coordinates (m) to the left and right banks respectively.

The percentage change in cross sectional area ($\%\Delta A$) of the estuarine channel at the 14 km station was calculated using the following Eq. (3),

$$\%\Delta A = \frac{A_t - A_{t-\Delta t}}{A_{t-\Delta t}} \times 100 \tag{3}$$

where A_t is the cross sectional area at time t, $A_{t-\Delta t}$ is the cross sectional area at time $t - \Delta t$, and Δt is the time interval between two consecutive field observations.

The bed shear stress is a fundamental variable in estuarine dynamics to link flow conditions to sediment transport (Biron et al. 2004). The bed shear stress (Chow et al.

1988) was estimated using the following Eq. (4) with the assumption of uniform flow near the bed,

$$\tau = \rho g R i \tag{4}$$

where τ is the bed shear stress (N m^{-2}), ρ is the density of water (kg m^{-3}), g is the acceleration due to gravity (m s^{-2}), R is the water depth (m), and i is the slope of the water surface.

3 Results and Discussion

3.1 Temporal Variations in Tidal and River Flow

The temporal variation of tides (at 14.6 km from the river mouth) during the years 2009, 2010, and 2011 was shown in Figs. 3a, 4a and 5a respectively. It is clear from Fig. 3a that the Chikugo River estuary is experiencing semidiurnal and fortnightly variations of tides. However, it shows some abnormal patterns during the beginning and end of July, 2009. Also during the subsequent years, the same abnormal behaviour of tidal pattern was observed which was during the middle of July in 2010 (Fig. 4a) and from the mid-June to mid-July in 2011 (Fig. 5a). The range of tidal amplitude was above 5 m and 1.5 m during the spring and neap tides respectively in all the considered periods. Therefore, the estuary can be classified as a mesotidal/macrotidal estuary as per the classification criterion proposed by Davies (1964) based on the tidal ranges.

Figures 3b, 4b, and 5b shows the temporal variation of freshwater discharge (at 25.5 km upstream from the river mouth) during the years 2009, 2010, and 2011 respectively. The river discharge observed during the dry period of all the considered years was below 50 m^3 s^{-1}. However, the discharge was very high and fluctuating during rainy season (June to August) in the study area. The Chikugo River estuary experienced severe floods with discharge of 3751.92 m^3 s^{-1} and 3531.40 m^3 s^{-1} in the beginning and end of July respectively in 2009 (Fig. 3b). During the year 2010, a peak discharge of 3392.90 m^3 s^{-1} was observed in July in addition to the peak discharge of 2139.26 m^3 s^{-1} in the end of May (Fig. 4b). Four flood events were noticed in the estuary from mid-June to mid-July of 2011 with the discharge ranging from 2450 to 2900 m^3 s^{-1} (Fig. 5b). Even though the peak storm discharge during the year 2011 was smaller in magnitude compared with the peak storm discharges in the previous years, it was close to the mean annual storm discharge of the estuary.

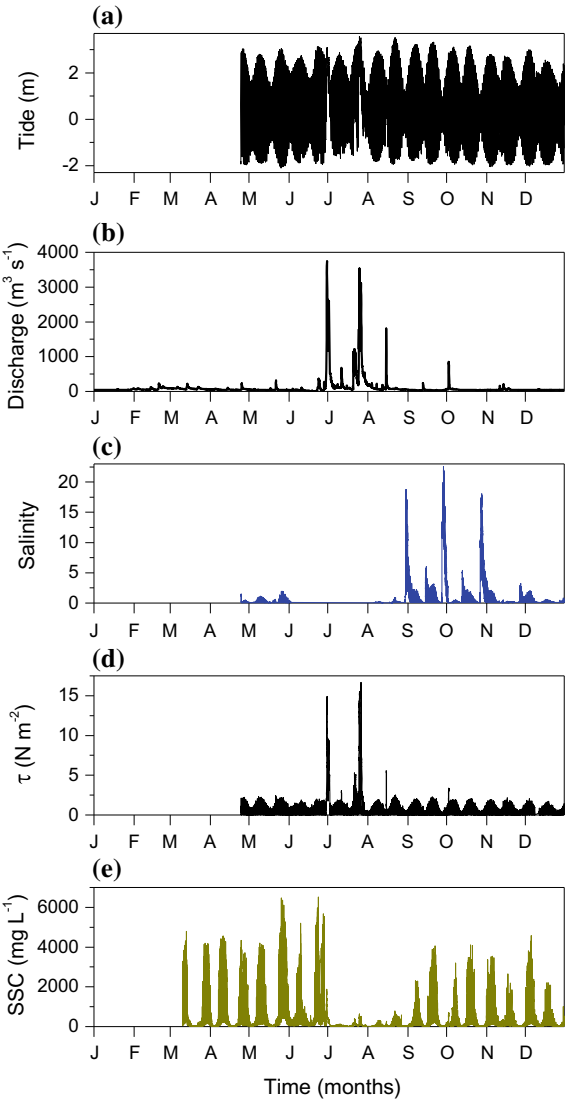

Fig. 3 Time series of **a** tide, **b** river discharge, **c** salinity, **d** shear stress (τ), and **e** SSC during January to December, 2009

3.2 Temporal Variations in Salinity Intrusion

The temporal variation of salinity near the bottom (at 14.6 km upstream from the river mouth) during the years of 2009, 2010, and 2011 was shown in Figs. 3c, 4c, and 5c respectively. The bottom salinity was recorded below 2 during the dry period of the year 2009. On the other hand, the maximum salinity ranging 18–22 was recorded during the neap tides from the end of August to end of November (Fig. 3c). The bottom salinity during the neap tide of year 2010 (Fig. 4c) was normally ranged

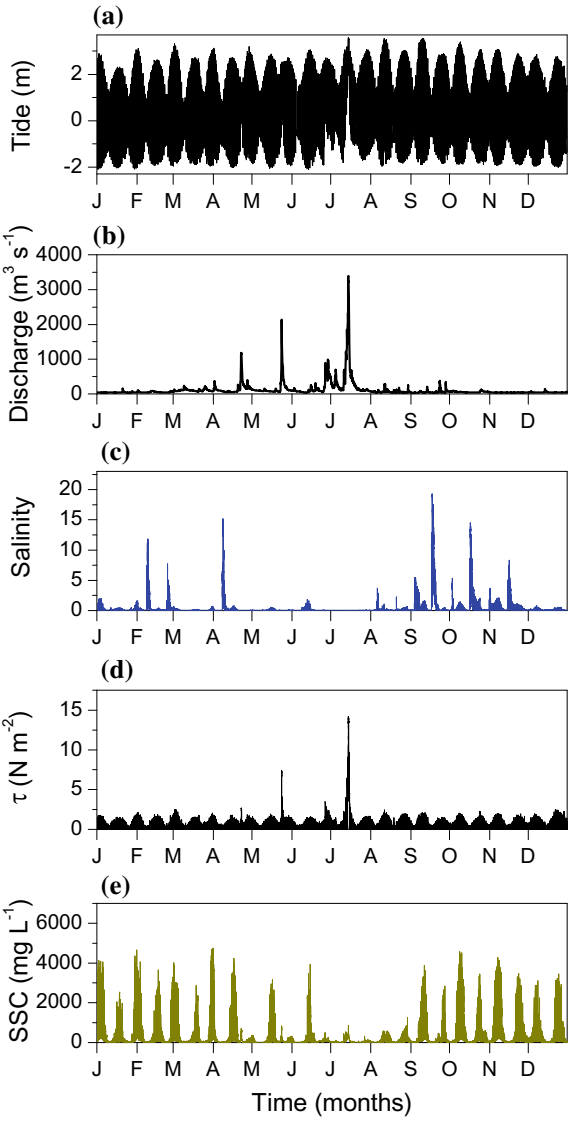

Fig. 4 Time series of **a** tide, **b** river discharge, **c** salinity, **d** shear stress (τ), and **e** SSC during January to December, 2010

between 8–19 except during May to August, while the same during the spring tide was below 2. The bottom salinity throughout the year of 2011 (Fig. 5c) was below 8 and 1 during the neap and spring tides respectively.

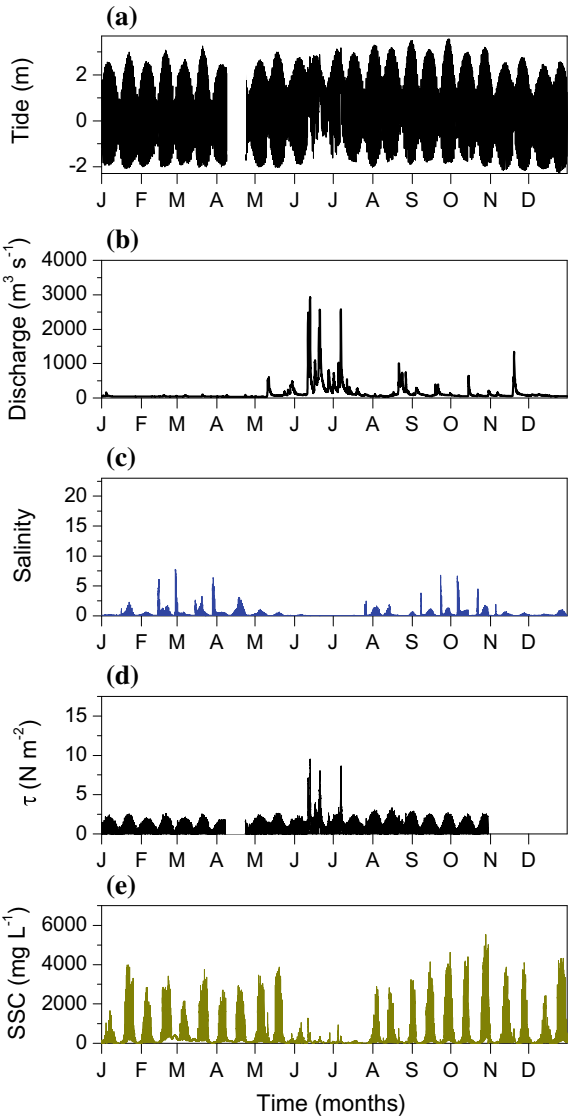

Fig. 5 Time series of **a** tide, **b** river discharge, **c** salinity, **d** shear stress (τ), and **e** SSC during January to December, 2011

3.3 Temporal Variations in Bed Shear Stress and SSC

The temporal variations of bed shear stress during the years 2009, 2010, and 2011 was depicted in Figs. 3d, 4d, and 5d respectively. The bed shear stress depicted a consistent pattern throughout the years except few rapid increases during the rainy season. The bed shear stress during the dry period of 2009 (Fig. 3d) was ranging between 1 and 2.25 N m^{-2} during the spring tide and was below 0.5 N m^{-2} during

the neap tide. The bed shear stress values associated with the neap tides for the year of 2010 during the dry season (Fig. 4d) was identical to that of observed during the year of 2009, while the same for the spring tide was quite distinct due to the difference in the upper range values. Subsequently, the range of observed shear stress during the dry periods of 2011 (Fig. 5d) increased to 2–3.2 N m^{-2} during spring tide comparing with that of previous years and the same during neap tide was remain unchanged from the previous years with values below 0.5 N m^{-2}. On the other hand, we noticed peak bed shear stress values ranges between 15 and 17 N m^{-2} during a short span in July which was the rainy season. However, the two peak shear stress values observed in 2010 were noticed in two months of May and July and it was 7.4 N m^{-2} and 14.1 N m^{-2} respectively which was small compared with the values of 2009. Multiple bed shear stress peaks were observed during 2011 which further reduced from the previous year values and it ranged between 7–9.5 N m^{-2}.

The SSC near the bed during March to end of June for the year 2009 was quite high with values ranging between 4000–6000 mg L^{-1} for the spring tide and was less than 100 mg L^{-1} at neap tides (Fig. 3e). There was a sudden drop in SSC values during the months of July and August and it was below 100 mg L^{-1} in both spring and neap tides. The SSC gradually gained momentum at the end of August and started to increase from September which was ranging between 2000–4000 mg L^{-1} during spring tides and was nearly 100 mg L^{-1} in the neap tides.

The SSC during January to June for the year 2010 (Fig. 4e) was slightly lower compared to that of the previous year (Fig. 3e) and it ranges between 3000–4700 mg L^{-1} at spring tides and was less than 100 mg L^{-1} at neap tides. The SSC diminished rapidly from June until the end of August and gradually increased from the beginning of September similar to that of previous year.

The bottom SSC during January to May for the year 2011 was ranging between 2000–4000 mg L^{-1} at spring tides and was below 100 mg L^{-1} at neap tides (Fig. 5e). The sudden decrease in SSC during June to July and its subsequent gradual increase were observed similar to that of previous years. The SSC during September to December was ranged between 3000–5500 mg L^{-1} at spring tides and below 100 mg L^{-1} at neap tides.

3.4 Seasonal Variations in Bed Topography

Morphological evolution of rivers and streams is the change of the shapes of rivers and streams with time and it is necessary to understand the detailed process of morphological evolution. Figure 6 shows the bed topography of the upstream meandering channel of the Chikugo River estuary (12–14.6 km landward from the river mouth) during the field surveys in 2009. During 23 April 2009, the meandering channel was deeper in the outer part of the meandering curve especially near the 13 km with shallow inner part of the meandering curve (Fig. 6a). A rapid increase in bed elevation

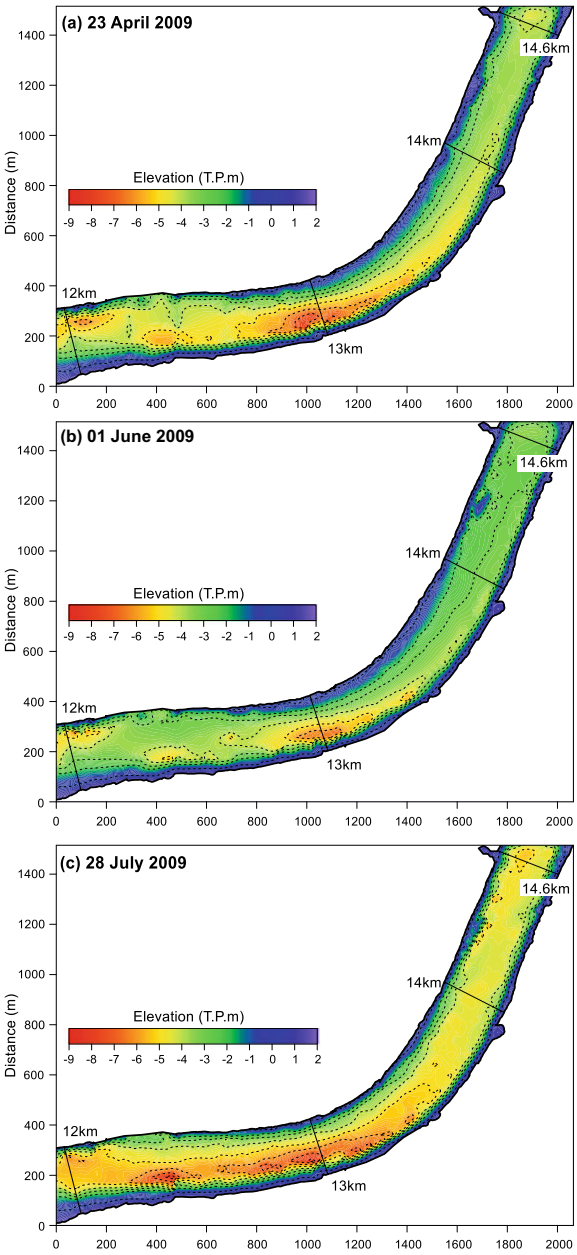

Fig. 6 Topographic data of the study area from 12 to 14.6 km during **a** 23 April 2009, **b** 01 June 2009, **c** 28 July 2009, and **d** 05 December 2009

Fig. 6 (continued)

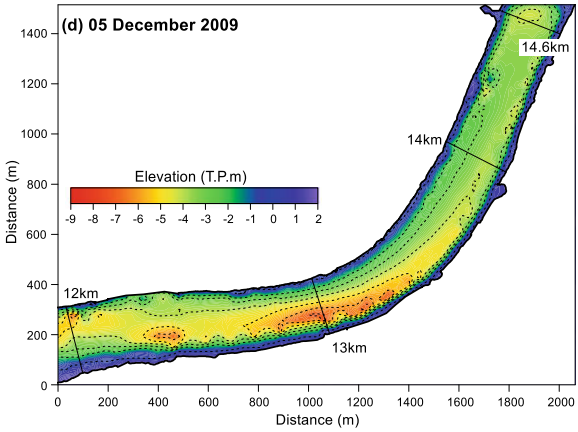

was found throughout the channel later in 1 June 2009 (Fig. 6b). The channel capacity was decreased drastically within a span of 5.4 weeks and the sediment deposition took place in the outer part of the meandering curve also.

From Fig. 6c, a drastic reduction in bed elevation of the meandering channel was observed during the field survey on 28 July 2009 which was immediately after the occurrence of two severe floods in the Chikugo River estuary as shown in Fig. 3b. The channel becomes very deep within a span of two months. Figure 6d further revealed that the channel bed elevation on 5 December 2009 was increased within a time span of four months from the previous observation on 28 July 2009. The inner part of the meandering curve became more shallower than the outer part of the meandering curve.

Figure 7 shows the temporal variations in cross section of the estuarine channel at 14 km from the river mouth during the years 2009–2011. Additionally, Table 1 shows the estimated cross sectional area of the 14 km station (Fig. 7) during 2009–2011. The symbol ↓represents the decrease in cross sectional area from the previous date of observation which means the occurrence of deposition. On the other hand, ↑represents the increase in cross sectional area from the previous date of observation which can be interpreted as the occurrence of erosion. The left and right banks (Fig. 7) are located at the outer and inner part of the meandering curve respectively (Fig. 1).

The cross section of the estuarine channel on 23 April 2009 resembles the shape of an inverted trapezoid with deep outer part and shallow inner part (Fig. 7a). The computed cross sectional area excluding the flood plain was 786.43 m^2 as shown in Table 1. A rapid decrease in the channel depth was observed on 1 June 2009 with a cross sectional area of 614.91 m^2 which further indicates that the channel capacity was decreased by 21.8% within a span of 5.4 weeks from the previous field survey. The cross sectional area of the estuarine channel on 28 July 2009 was increased as shown in Fig. 7a and having a uniform depth from left to right bank. It is clear from Table 1 that the area was 939.4 m^2 which was very high compared with the previous cross sectional area of 614.91 m^2 on 01 June 2009 that further implies that there is

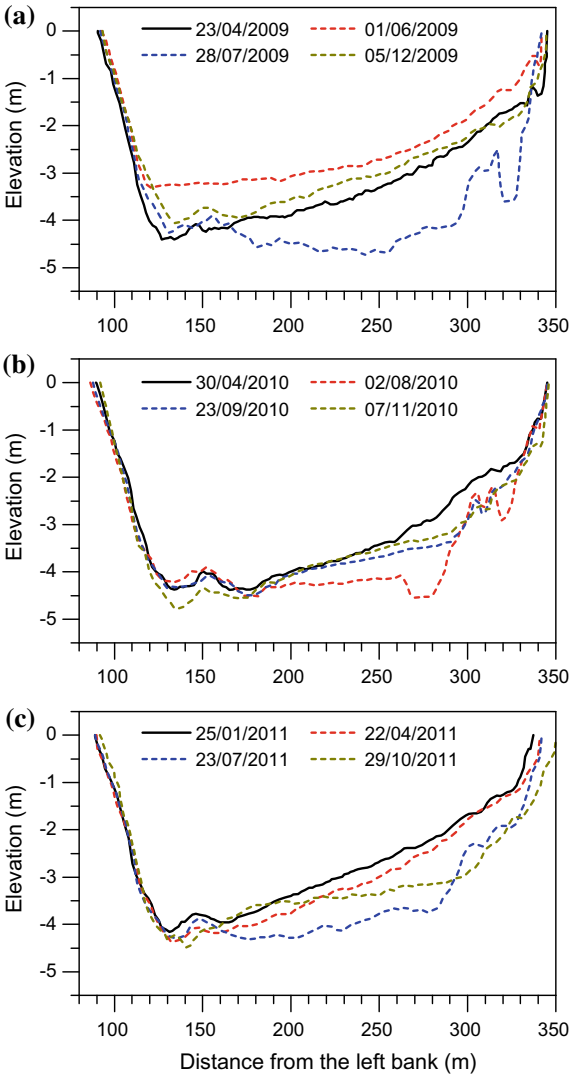

Fig. 7 Cross section of the measurement station at 14 km upstream from the river mouth during **a** 2009, **b** 2010, and **c** 2011

an increase in channel capacity by 52.8%. The cross sectional area of the estuarine channel on 5 December 2009 was found to be 719.33 m^2 which further indicates that the cross-sectional area was decreased by 23.4% from the previous one within a span of four months.

The same pattern of change in channel cross section was observed during the subsequent years of 2010 (Fig. 7b) and 2011 (Fig. 7c). Even though the changes in channel depth was observed during 2009–2011, the highest changes was observed during 2009 comparing to the other years. During 2009, the changes were observed in both outer and inner part of the curve. On the other hand, during 2010 and 2011,

Table 1 Cross sectional area and change in cross sectional area of 14 km station during 2009–2011

Date		Surveyed cross sectional area (m^2)	Peak river discharge ($m^3\ s^{-1}$)	Change in area, ΔA (%)
2009	23 April	786.43	-	-
	21 May	-	312.13	-
	01 June	614.91	-	-21.8↓
	30 June	-	3,751.92	-
	25 July	-	3,531.40	-
	28 July	939.40	-	52.8↑
	15 August	-	1,809.74	-
	05 December	719.33	-	-23.4↓
2010	22 April	-	1,178.76	-
	30 April	794.97	-	10.5↑
	23 May	-	2,139.26	-
	14 July	-	3,392.90	-
	02 August	904.21	-	13.7↑
	22 September		165.78	
	23 September	851.63	-	-5.8↓
	28 September	-	345.28	-
	07 November	858.88	-	0.9↑
2011	04 January	-	164.43	-
	25 January	669.19	-	-22.1↓
	20 March	-	104.37	-
	22 April	722.75	-	8.0↑
	12 June	-	2,923.93	-
	23 July	840.22	-	16.3↑
	21 August	-	1,010.50	-
	29 October	784.44	-	-6.6↓

☐ Intensive field survey
▒ Occurrence of peak river discharge

the greater variability in channel depth was observed only in the inner part of the curve.

4 Discussion

4.1 Estuarine Hydrodynamics

The abnormality pattern in tidal flow (Figs. 3a, 4a, and 5a) was exactly coincided with the occurrence of peak storm discharge during the whole period (Figs. 3b, 4b, and 5b). That means the strong storm discharge hinders the entry of tidal flow into the estuary and washout to the sea. The high abnormality was witnessed during the flood season of 2009 when the Chikugo River estuary faced two consecutive flood events with magnitudes 1.34 and 1.25 times higher than the mean annual storm discharge of the estuary. Hence, we can deduce that the abnormality of tides will increase with the increase in peak storm discharge.

It can be envisaged that the saltwater intrusion (Figs. 3c, 4c, and 5c) was influenced by the tidal (Figs. 3a, 4a, and 5a) and river discharges (Figs. 3b, 4b, and 5b). A salinity value of one was observed at the 14.6 km from the river mouth during spring tides of all the considered years, which further means that the freshwater saltwater interface was located near this 14.6 km during spring tide. However, saltwater intruded further to upstream during the neap tide. During the flood season, the saltwater intrusion was hindered by the storm discharge and the salinity in the water column rapidly diminishes to zero. High salinity intrusion was witnessed few weeks after the occurrence of flood events during the all considered years. Therefore, we can say that the tidal flow and salinity intrusion in the Chikugo River estuary is strongly influenced by the seasonal variations in river flow.

The bed shear stress during the years 2009–2011 was mostly exhibiting a harmonious behaviour which was induced by the fortnightly variations in tidal flow (Figs. 3d, 4d, and 5d). Additionally, there was some rapid variations in bed shear stress from the harmonious behaviour to high values ranging between 7 and 17 N m^{-2} which was simultaneous with the occurrence of peak storm discharges during the flood seasons. Therefore, it is clear that the estuary was mainly affected by the tide induced bed shear stress of 1–3 N m^{-2} during most of the periods of 2009–2011 except for the flood seasons.

Based on a fortnightly tidal perspective, high SSC during spring tide and low SSC during neap tide was seen at the station which is 14.6 km upstream from the river mouth throughout the period except during flood season (Figs. 3e, 4e, and 5e). Many studies suggest that the normal range of critical erosion threshold of the consolidated mud is 0.05–1 N m^{-2} (Gust and Morris 1989; Maa et al. 1998; Houwing 1999). Therefore, the high SSC during spring tide can be attributed to the observed high shear stress of 1–3 N m^{-2} during spring tide and the low SSC can be ascribed to the low shear stress below 0.5 N m^{-2} during neap tide (Figs. 3d, 4d, and 5d). The high

SSC in the upstream except during flood season can be explained as the erosion and transport of bottom sediments from the downstream tidal flat towards the upstream by the tide induced shear stress. High concentration of bottom sediments (Figs. 3e, 4e, and 5e) which corresponds to the ETM zone was located near the fresh and saltwater interface (Figs. 3c, 4c, and 5c). The location and magnitude of the ETM was driven by spring-neap transitions and concentration of suspended sediments in the water column (Dyer 1986; Uncles 2002, Azhikodan and Yokoyama 2012; Azhikodan et al. 2014).

During flood season, the near bed SSC at the upstream was diminishing rapidly and the bottom sediments were washed away to the downstream tidal flat by the strong bed shear stress generated by the storm discharge. The bed shear stress generated by the storm discharge was 4 -to 8 times higher than the tide induced shear stress (Figs. 3d, 4d, and 5d) and hence the ETM was moved to the downstream part of the estuary during flood season.

Overall, the Chikugo River estuary is exhibiting a fortnightly variations in tide, salinity intrusion, shear stress, SSC and location of ETM during most of the year with seasonal variations in river discharge. Even though the storm discharge is affecting only for a short period, its impact to the estuarine hydrodynamics is very high.

4.2 Morphological Evolution

A decrease in channel cross section at 14 km was observed on 1 June 2009 compared with the cross section on 23 April 2009. This may be due to the following reasons: (i) The freshwater saltwater interface was located near 14.6 km station with a salinity value close to 1 during spring tides. Generally, ETM zone in tidal estuaries is located near freshwater saltwater interface, where maximum deposition will takes place (Uncles 2002; Azhikodan and Yokoyama 2015); (ii) The river flow during this period was normally below 50 $m^3\ s^{-1}$ in most of the days with a maximum flow value of 312.13 $m^3\ s^{-1}$ (Fig. 3b, Table 1) which further indicates that the effect of river flow on ETM was negligible during this period. Hence, being a tidal estuary, erosion and upward transport of sediments from the downstream by the tide induced shear stress dominated during this period (Fig. 3d) which resulted in high near bed SSC of 4000–6000 mg L^{-1} at 14.6 km station (Fig. 3e). Azhikodan and Yokoyama (2018) reported that a mud layer of thickness 0.9 m was formed above the river bed at 14 km upstream of the Chikugo River estuary within a span of two weeks during low flow season. The bottom sediment consists of more than 99% fine silt and clay. Additionally, they found that the SSC at the inner part of the meandering curve was high compared to the SSC at the outer part of the curve. Therefore, if there is a prolonged dry period for more than two weeks, it can generate a fluid mud layer of more than 0.9 m in thickness which will further cause the reduction in the channel capacity.

On the other hand, the channel capacity increased by 52.8% during 1 June to 28 July 2009. This rapid increase in channel cross section can be attributed to the high rate of erosion due to the occurrence of two severe flood events within a span of one

month (from the end of June to the end of July, 2009). The channel bed layer with a thickness ranging from 1–2 m was scoured by the strong shear stress of 15–17 N m^{-2} generated by the storm discharge (Fig. 3d), and the deepest region was detected at the inner part of the meander. Hence we can deduce that the morphology of a river estuary changes rapidly during the period of flood and is dominated by the erosion and downstream sediment transport by the strong storm discharge.

The cross sectional area of the estuarine channel decreased by 23.4% from the previous one within a span of four months after the occurrence of two severe floods. The maximum height of sedimentation reached 1.8 m at the inner part of the meandering curve. During the period between the end of flood flow and 5 December 2009, which lasts for more than 3.5 months, the river flow was mainly contributed by low flow (50 m^3 s^{-1}) with a maximum flow value of 1809.74 m^3 s^{-1} (Fig. 3b).

The sedimentation at the upstream during the low flow periods indicate that the erosion, transport, and deposition dynamics of sediments were driven by the fortnightly and semidiurnal tidal cycle especially during spring tide. During spring tide, sediments at the downstream tidal flat are eroded by the tide induced shear stress of 1–3 N m^{-2} and transported upstream during flood tide. The transported sediments was deposited at the inner part of the meandering channel and a fluid mud layer was formed during high tide. This type of fluid mud layers are common features in highly turbid macrotidal estuaries and is associated with the occurrence of ETM (Sottolichio et al. 2011; Azhikodan and Yokoyama 2018). The deposited sediment was eroded again and transported seaward during ebb tide and re-deposited in downstream during low tide to restart their movement in the forthcoming tidal cycle. However, the sediment erodibility was reduced during ebb tide since the particles deposited during high tide was consolidated within a span of few hours. This will give a net positive upward sediment transport due to the hysteretic effects between shear stress and SSC during spring tides (Azhikodan and Yokoyama 2018) which is caused by the asymmetrical flood-ebb tides (Dronkers 1986). Hence sedimentation takes place during every semidiurnal tidal cycle which resulted in the rapid decrease in channel capacity.

The pattern of morphological changes at the upstream during the years of 2010 (Fig. 7b) and 2011 (Fig. 7c) was similar to that of in the previous year of 2009 (Fig. 7a). However, the rate of erosion during the flood season and deposition during the low flow period was low compared to that during the year 2009. The high rate of deposition occurred during 2009 can be attributed to the prevalence of long dry season resulted from delayed rainy season (April to June, 2009). On the contrary, two severe flood events (June to July, 2009) were happened after the long dry period whose magnitude was higher than the successive years which caused a high rate of erosion of bed sediments. The maximum increase in cross-sectional area of the estuarine channel during 2010 and 2011 was 13.7% and 16.3% respectively and that was very small compared with the drastic increase in channel cross-sectional area took place during the year 2009 within a short span of two months.

The river discharge patterns in the Chikugo River estuary varies seasonally with peak flows during June to August and low flow during dry season. Strong storm discharge (2800 m^3 s^{-1}) occurs approximately for one to two months per year. During

the rest of the months, the tidal discharge (500–2000 m^3 s^{-1}) was the predominant factor over the river discharge (54 m^3 s^{-1}) which controls the sediment transport and deposition process (Azhikodan et al. 2014; Azhikodan and Yokoyama 2015). On an annual scale, variations in river discharge significantly influence the formation, movement and breakdown of the ETM. Sedimentation occurs at the upstream of the meandering channel by the fortnightly tidal cycle with low river discharge during most of the year. These deposited sediments will be eroded and transported downstream by the strong storm discharge for a short period. Even though the high river flow occurs only for a very short period, the impact is very strong such that the sediment layer of 1–2 m can be scoured by the storm discharge. The cycle of morphological evolution of river bed continues based on the upstream sediment transport by the fortnightly tidal cycles and downstream sediment transport by the river discharge.

5 Conclusions

The spatial and temporal dynamics of bed morphology in relation to semidiurnal and fortnightly tidal variations, and seasonal variations in river discharge in a meandering estuarine channel were studied. Intensive field (longitudinal and transverse) surveys in the upper region (12–14.6 km landward from the river mouth) of the Chikugo River estuary, Japan were carried out in every three or four months during 2009–2011 using a digital sonar system equipped with a differential global positioning system.

The results revealed that the estuary was dominated by the fortnightly variations in tidal discharge for most of the year except for rainy season in which river flow dominates. Strong storm discharge occurs approximately for one to two months per year. During the rest of the months, the tidal discharge was the predominant factor over the low river discharge which controls the upward sediment transport and deposition process.

The sedimentation at the upstream during the low flow periods indicate that the erosion, transport and deposition dynamics of sediments were driven by the fortnightly and semidiurnal tidal cycle especially during spring tide. During these periods, fine sediment was transported from the downstream and deposited near the inner bank during every semidiurnal tidal cycle. As a result, the depth of the inner bank becomes diminished. On the contrary, the outer bank was heavily eroded and becomes steep. As a result, an ETM was developed at the upstream of the meandering channel and the channel capacity reduced gradually during this period. However, in the rainy season, large amount of deposited mud was washed away by the strong storm discharge to the downstream areas which results the rapid increase in channel capacity.

The seasonal cyclic pattern of erosion and deposition processes were evident at the upstream meandering channel. Even though the high river flow occurs only for a short period, the impact is very strong such that the sediment layer of 1–2 m can be scoured by the storm discharge. The cycle of morphological evolution of river bed continues based on the upstream sediment transport by the fortnightly tidal cycles

and downstream sediment transport by the river discharge. The study conclude that the hysteretic effects between shear stress and SSC due to the asymmetrical flood and ebb tides as well as the seasonal variations in river discharge are the dominant factors that causes sediment transport and morphological changes in tide dominated estuaries.

Acknowledgements The authors express special gratitude to the Tokyo Metropolitan Government for supporting the Doctoral study of second author Ms. Kirana Somsook through the Tokyo Human Resources Fund for City Diplomacy Scholarship. The authors are grateful to the Chikugo River Work Office, Ministry of Land, Infrastructure, Transport, and Tourism of Japan as well as to the Japan Water Agency for the data and cooperation. The authors also express sincere thanks to IDEA Consultants and all the members of Hydraulics laboratory, Department of Civil and Environmental Engineering, Tokyo Metropolitan University for their valuable support during the field surveys. The authors appreciate the reviewers for their positive feedback and constructive suggestions that substantially improved the structure and quality of our manuscript.

References

Ahnert, F. (1960). Estuarine meanders in the chesapeake bay area. *Geographical Review, 50*(3), 390–401.

Azhikodan, G., & Yokoyama, K. (2012, November 4–7). Influence of tidal mixing on suspended sediment transport and phytoplankton dynamics in the Chikugo River Estuary, Japan, in: Proceedings of the 10th International Conference on Hydroscience & Engineering (ICHE), Orlando, Florida, U.S.A. pp. 1–6. No. 40137245.

Azhikodan, G., & Yokoyama, K. (2014). Estuarine mixing and spatial distribution of phytoplankton in the Chikugo river estuary. *Journal of Japan Society of Civil Engineers Ser. B2 (Coastal Engineering)*, *70*, 1081–1085.

Azhikodan, G., & Yokoyama, K. (2015). Temporal and spatial variation of mixing and movement of suspended sediment in the macrotidal Chikugo river estuary. *Journal of Coastal Research, 313,* 680–689.

Azhikodan, G., & Yokoyama, K. (2016). Spatio-temporal variability of phytoplankton (Chlorophyll-a) in relation to salinity, suspended sediment concentration, and light intensity in a macrotidal estuary. *Continental Shelf Research, 126,* 15–26.

Azhikodan, G., & Yokoyama, K. (2018). Sediment transport and fluid mud layer formation in the macro-tidal Chikugo river estuary during a fortnightly tidal cycle. *Estuarine, Coastal and Shelf Science, 202,* 232–245.

Azhikodan, G., Yokoyama, K., & Morimura, Y. (2014). Effect of mixing on turbidity maximum movement during semilunar tidal cycle in the Chikugo river estuary. *Journal of Japan Society of Civil Engineers Ser. B1 (Hydraulic Engineering), 70*, 37–42.

Biron, P. M., Robson, C., Lapointe, M. F., & Gaskin, S. J. (2004). Comparing different methods of bed shear stress estimates in simple and complex flow fields. *Earth Surface Processes and Landforms, 29,* 1403–1415.

Blanton, J. O., Seim, H., Alexander, C., Amft, J., & Kineke, G. (2003). Transport of salt and suspended sediments in a curving channel of a coastal plain estuary: Satilla River, GA. *Estuarine, Coastal and Shelf Science, 57,* 993–1006.

Blott, S. J., Pye, K., van der Wal, D., & Neal, A. (2006). Long-term morphological change and its causes in the Mersey Estuary, NW England. *Geomorphology, 81*(1–2), 185–206.

Chow, V., Maidment, D., & Mays, L. (1988). *Applied hydrology, water resources and environmental engineering* (p. 572). New York: McGraw-Hill.

Davies, J. L. (1964). A morphogenetic approach to world shorelines. *Zeitschrift fur Geomorphologie, 8,* 127–142.

Dronkers, J. (1986). Tidal asymmetry and estuarine morphology. *Netherlands Journal of Sea Research, 20*(2–3), 117–131.

Du, J. L., Yang, S. L., & Feng, H. (2016). Recent human impacts on the morphological evolution of the Yangtze River delta foreland: A review and new perspectives. *Estuarine, Coastal and Shelf Science, 181,* 160–169.

Dyer, K. R. (1986). *Coastal and estuarine sediment dynamics* (p. 342). Chichester: Wiley.

Eysink, W. D. (1990). Morphologic response of tidal basins to changes. In *Proceeding 22nd Coastal Engineering Conference*, ASCE, Delft, vol. 2, the Dutch coast, Paper no. 8, pp.1948–1961.

Gust, G., & Morris, M. J. (1989). Erosion thresholds and entrainment rates of undisturbed in situ sediments. *Journal Coastal Research, 5,* 87–99.

Hibma, A., Stive, M. J. F., & Wang, Z. B. (2004). Estuarine morphodynamics. *Coastal Engineering, 51*(8–9), 765–778.

Houwing, E.-J. (1999). Determination of the critical erosion threshold of cohesive sediments on intertidal mudflats along the Dutch Wadden Sea Coast. *Estuarine, Coastal and Shelf Science, 49,* 545–555.

Islam, M. S., Ueda, H., & Tanaka, M. (2006). Spatial and seasonal variations in copepod communities related to turbidity maximum along the Chikugo estuarine gradient in the upper Ariake Bay, Japan. *Estuarine, Coastal and Shelf Science 68*(1–2), 113–126.

Kostaschuk, R. A., Church, M. A., & Luternauer, J. L. (1989). Bedforms, bed material, and bedload transport in a salt-wedge estuary: Fraser River, British Columbia. *Canadian Journal of Earth Sciences, 26*(7), 1440–1452.

Lanzoni, S., & Seminara, G. (2002). Long-term evolution and morphodynamic equilibrium of tidal channels. *Journal of Geophysical Research, 107,* 3001.

Liu, W. C., Hsu, M. H., & Kuo, A. Y. (2002). Modelling of hydrodynamics and cohesive sediment transport in Tanshui River estuarine system, Taiwan. *Marine Pollution Bulletin, 44*(10), 1076–1088.

Maa, J. P.-Y., Sanford, L., & Halka, J. P. (1998). Sediment resuspension characteristics in Baltimore Harbour, Maryland. *Marine Geology, 146,* 137–145.

Moore, R. D., Wolf, J., Souza, A. J., & Flint, S. S. (2009). Morphological evolution of the Dee Estuary, Eastern Irish Sea, UK: A tidal asymmetry approach. *Geomorphology, 103*(4), 588–596.

Ralston, D. K., Geyer, W. R., Traykovski, P. A., & Nidzieko, N. J. (2013). Effects of estuarine and fluvial processes on sediment transport over deltaic tidal flats. *Continental Shelf Research, 60,* 40–57.

Schrottke, K., Becker, M., Bartholoma, A., Flemming, B. W., & Hebbeln, D. (2006). Fluid mud dynamics in the Weser estuary turbidity zone tracked by high-resolution side-scan sonar and parametric sub-bottom profiler. *Geo Marine Letters, 26,* 185–198.

Sottolichio, A., Hurther, D., Gratiot, N., & Bretel, P. (2011). Acoustic turbulence measurements of near-bed suspended sediment dynamics in highly turbid waters of a macrotidal estuary. *Continental Shelf Research, 31,* 36–49.

Suzuki, K. W., Kasai, A., Nakayama, K., & Tanaka, M. (2012). Year-round accumulation of particulate organic matter in the estuarine turbidity maximum: comparative observations in three macrotidal estuaries (Chikugo, Midori, and Kuma rivers), southwestern Japan. *Journal of Oceanography, 68,* 453–471.

Suzuki, K. W., Nakayama, K., & Tanaka, M. (2009). Horizontal distribution and population dynamics of the dominant mysid Hyperacanthomysis longirostris along a temperate macrotidal estuary (Chikugo river estuary, Japan). *Estuarine, Coastal and Shelf Science, 83,* 516–528.

Tolhurst, T. J., Riethmuller, R., & Paterson, D. M. (2000). In situ versus laboratory analysis of sediment stability from intertidal mudflats. *Continental Shelf Research, 20,* 1317–1334.

Uncles, R. J. (2002). Estuarine physical processes research: some recent studies and progress. *Estuarine, Coastal and Shelf Science, 55,* 829–856.

van der Wal, D., Pye, K., & Neal, A. (2002). Long-term morphological change in the Ribble estuary, Northwest England. *Marine Geology, 189*(3–4), 249–266.

van Dongeren, A. R., & de Vriend, H. J. (1994). A model of morphological behaviour of tidal basins. *Coastal Engineering, 22*(3–4), 287–310.

Wang, Z. B., Van Maren, D. S., Ding, P. X., Yang, S. L., Van Prooijen, B. C., De Vet, P. L. M., et al. (2015). Human impacts on morphodynamic thresholds in estuarine systems. *Continental Shelf Research, 111,* 174–183.

Wei, W., Mei, X., Dai, Z., & Tang, Z. (2016). Recent morphodynamic evolution of the largest uninhibited island in the Yangtze (Changjiang) estuary during 1998–2014: Influence of the anthropogenic interference. *Continental Shelf Research, 124,* 83–94.

Wolanski, E., Gibbs, R. J., Mazda, Y., Mehta, A., & King, B. (1992). The role of turbulence in the settling of mud flocs. *Journal of Costal Research, 8,* 35–46.

Yokoyama, K., Suetsugi, T., & Kawano, K. (2011). Annual sediment budget in the Shirakawa river estuary, Japan. In *Proceedings of 6th International Symposium on Environmental Hydraulics* (pp. 893–898) Greece: IAHR.

Study on Sediment Transport Capacity of Different Flow Routes in the Yellow River Estuary

Chonghao Wang, Wenhong Cao, Chuansheng Guo and Xiongbo Chen

Abstract The sea-flow driven sediment transport capacity in the Yellow River Estuary is a complicated problem due to the dynamic interaction from river runoff, tidal current and waves. However, it is of a great significance for planning the flow routes into the sea. Two mathematical models for computing sediment transport and current are established based on the MIKE21 model in this chapter. The range of the large model covers the whole Bohai and the validity of the model is calibrated by the harmonic tidal components of observation data. Based on the open boundary conditions from the large model, the tidal currents and sediment transport processes in the Yellow River Estuary are studied by a small model with finer grids. The computational results show that three high tidal current zones exist with maximum current speed reaches 1.7 m/s. The alongshore current from Bohai Bay to Laizhou Bay is the dominant force to transport sediment. The analysis and calculated results show that net fluxes of sediment transported through both sides of 10 km width and into open sea in the routes of Diaokou River, Old Channel, current Qing8 Route, Maxinhe Route, Beicha Route and Shibahu Router are of about 51.04, 39.27, 29.94,17.75, 12.96 and 7.22%, comparing with the amount of sediment in the Lijin station, respectively. In the planning of the available flow routes, the DiaoKouhe Route has the largest sediment transport capacity. Interchangeable use of Qingshuigou routes including Qing8, Old channel and Beicha can be planned in the near future, Diaokou Route is a long-term consideration.

Keywords Yellow River Estuary (YRE) · Flow routes · Numerical modeling · Tidal flow · Sediment transport capacity · Alongshore flow

C. Wang (✉) · W. Cao · C. Guo
Department of Sediment Research, China Institute of Water Resources and Hydropower Research, Beijing, China
e-mail: 1124939065@qq.com

X. Chen
Yellow River Engineering Consulting Co., Ltd., Zhengzhou, China

K. D. Nguyen et al. (eds.), *Estuaries and Coastal Zones in Times of Global Change*, Springer Water,
https://doi.org/10.1007/978-981-15-2081-5_20

1 Introduction

The Yellow River is famous for its abundant sediment. A lot of sediment is transported to the estuarine area from different routes (see Fig. 1), resulting in the deposition and elevation of the tail channel and the extension of the mouth (Zeng et al. 1997; Wang et al. 2001; Hu and Cao 2003), which has seriously affected the flood control and economic development in the lower reaches of the Yellow River. Under the co-actions of river flow, tidal current and wave, sediments will be transported or diffused along-shoal and off-shoal, and part to the deep sea. However, the sediment dynamic transport in the Yellow River Estuary is a complex process, which is affected by many factors. Sediment transport capacity varies greatly in different flow routes and in different periods. The average annual amount of sediment transported into the open sea from the Shenxiangou Route was about 0.962 billion T and it was about 0.407 billion T from Diaokouhe Route. It was also realized that the sediment transport capacity by ocean dynamics during the Qingshuigou Route period is relatively stable, the average annual amount of sediment transported into the open sea is from 0.2 billion T to 0.24 billion T (Zhang, 1990).

At present, the understandings of tidal current and sediment transport processes in Yellow River Estuary are mainly based on the analysis of measured data. Because the measured data in the Yellow River Estuary are very limited and the mouth changes rapidly, the results of data analysis are often difficult to fully understand the characteristics of the sediment movement in the Yellow River Estuary. Therefore, it is also not satisfied with the practical needs. Due to the great quantities of sediment coming from the Yellow River, the current Qingshuigou Route elongates with sediment deposition, and the water level in the tail of the Yellow River Estuary increases gradually. For the safety of flood control in the Yellow River Estuary, how to arrange the flow routes scientifically is becoming a challenging problem. With the variation

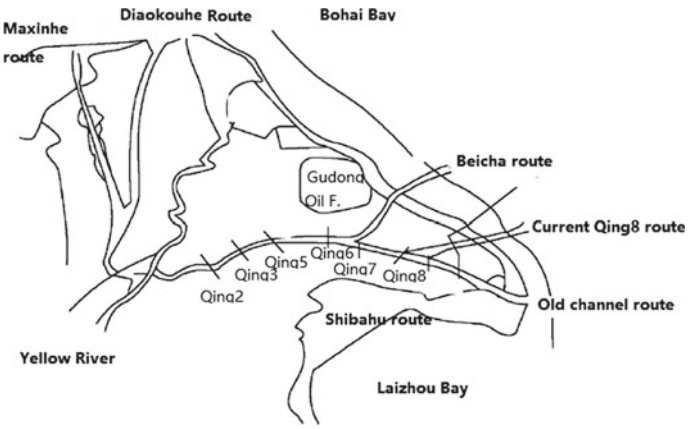

Fig. 1 Schemes of flow routes in the YRE

of water and sediment in the Yellow River and the evolution of the estuarine topography, the tidal flow field and the sediment transport capacity of driven by sea-flow are also bound to be adjusted. More in-depth study and discussions are needed to provide a scientific basis for the comprehensive control of the Yellow River Estuary. The planned flow routes are shown in Fig. 1.

2 Boundary Conditions and Model Validation

Two mathematical models for computing sediment transport and current are established based on the MIKE21 model in this paper. The domains are shown in Fig. 2. The range of the large model covers the whole Bohai and the validity of the model is calibrated by the harmonic tidal components of observation data. Based on the open boundary conditions from the large model, the tidal currents and sediment transport processes in the YRE are studied by the small model with finer grids.

The open boundary conditions are calculated for calculating the tidal waves in the large model of Bohai. Four sub-tidal boundaries of M2, S2, K1 and O1 are based

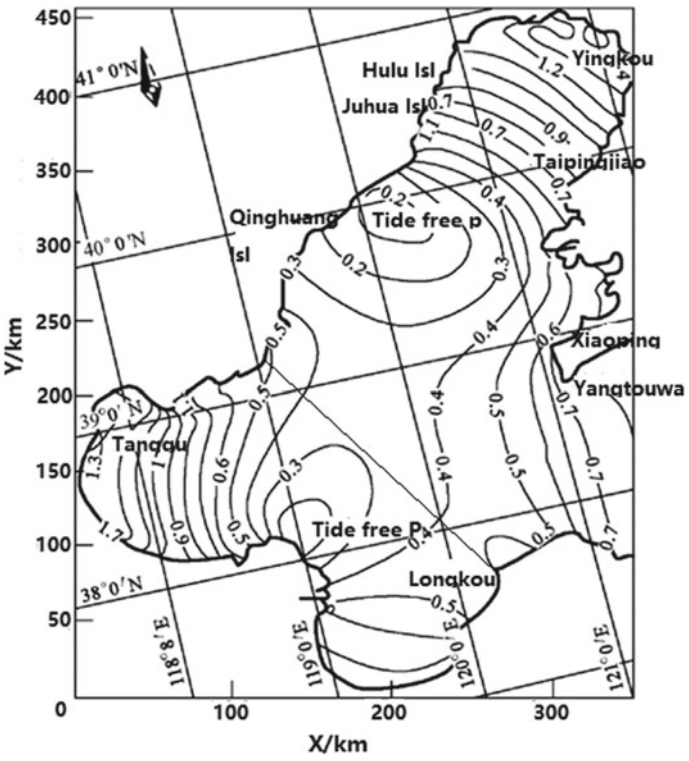

Fig. 2 Model domains and calculated Co-tide of M2

Table 1 Annual-averaged flow and sediment at Lijin (1976–2000)

	Flood season	Dry season	Yearly
Runoff (billion m^3)	14.41	7.75	22.16
Sediment load (billion T)	0.50	0.06	0.56

on the calculation of tidal wave propagation. The riverine boundary is set to the flow and sediment process of 1976 –2000 yearly-averaged values at Lijin station, which is the last control hydrologic station before the Yellow River flowing into the estuary, see Table 1.

Table 2 compares the measured values of the tidal amplitude and lag angle of the tidal stations along the Bohai coast. It can be shown that the calculated results are in good agreement with the analyzed values from measurements.

The calculated M2 co-tide chart, also be shown in Fig. 2, and the positions of two tide free points are in good agreement with that drawn from the previous measured data and the previous studies (Dou et al. 1979; Yin and Zhang 1983; Li 1988). It shows that M2 tidal wave from the outer sea spreads to Laizhou Bay, Bohai Bay and Liaodong Bay. Under the constraints of the terrain conditions, there form two "tide free points", one is near the abandoned Yellow River route, the other is in the northwest of Qinhuangdao waters.

3 Tidal Current

Figure 3 is the process of calculating the tidal level near the mouth of the current Qing8 Route. It can be seen that the tidal wave process outside the Yellow River mouth is an irregular semidiurnal tide with the lowest tide level of −0.72 m, the highest tide level of 1.10 m and the maximum tidal range of 1.82 m during the predicting period.

Figures 4 and 5 show the flooding and ebbing flow patterns during a spring tide in YRE under the action of four tidal components of M2, S2, K1 and O1. Here, the arrows indicate the magnitude and direction of the velocity, and the equivalent line is the tidal level. Figure 6 is the maximum flow velocity distribution during the spring tide. It can be seen from the maximum velocity distribution of the whole calculation sea area, the maximum flow velocity increases from the outer sea to the seashore, and reaches the maximum at the vertex of the Bohai Bay and Laizhou Bay. After then, and the maximum velocity decreased rapidly nearshore due to the resistance in shallow water. There are three high velocity regions in the YRE: one is about 10 km outside the Qingshuigou Old Channel, the maximum flow velocity is 1.7 m/s; the second one locates outside the Diaokouhe Route with the maximum velocity of about 1.2 m/s, and the third one locates outside the current Qing8 Route with the maximum velocity of about 1.0 m/s. Compared to the former two high speed flow regions, the flow velocity is slightly smaller near Qing8 Route. However, it can be

Table 2 Comparison of analyzed and calculated sub-tides

Stn		M2		S2		K1		O1	
		H (cm)	P (deg)	H (cm)	P (deg)	H (cm)	P (deg)	H (cm)	P (deg)
Xiao ping Isl	Anl.	87.0	295.0	26.0	344.0	21.0	10.0	14.0	326.0
	Cal.	80.4	298.5	24.1	347.5	22.6	12.6	15.0	328.6
Tai ping jiao	Anl.	89.0	111.0	23.0	173.0	36.0	86.0	27.0	35.0
	Cal.	89.2	111.8	23.0	173.8	31.2	86.2	23.4	35.2
Ying kou	Anl.	125.9	143.1	33.5	206.1	37.8	101.2	29.1	51.2
	Cal.	117.7	148.3	30.8	211.3	32.2	104.6	24.8	54.6
Yang Tou wa	Anl.	60.0	321.0	18.0	22.0	20.0	46.0	15.0	10.0
	Cal.	65.3	323.1	19.6	24.1	16.4	47.0	12.3	8.0
Tang gu	Anl.	117.2	90.3	33.8	164.5	35.6	153.8	26.9	98.7
	Cal.	113.0	100.0	29.9	174.0	31.8	162.0	24.4	17.0

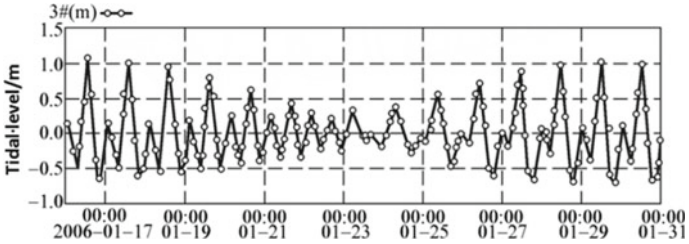

Fig. 3 Predicted tidal level near Qing8 route

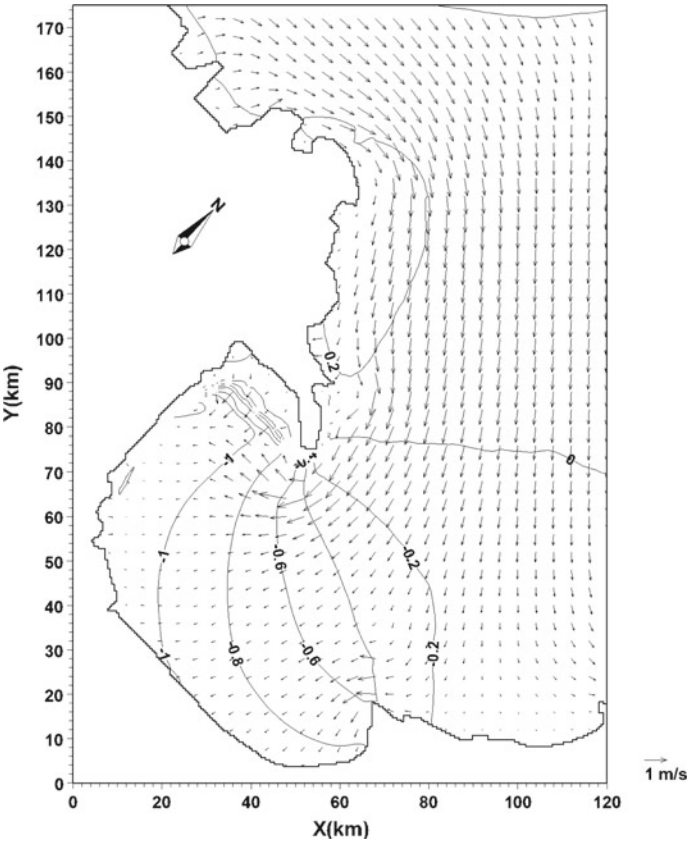

Fig. 4 Flooding flow pattern in a spring tide

foreseen that with the continued use of the current Qing 8 Route, sand mouth will continue to protruding into the sea, and the velocity of the high speed flow will also increase gradually, which will be beneficial to transport sediment into the deep sea.

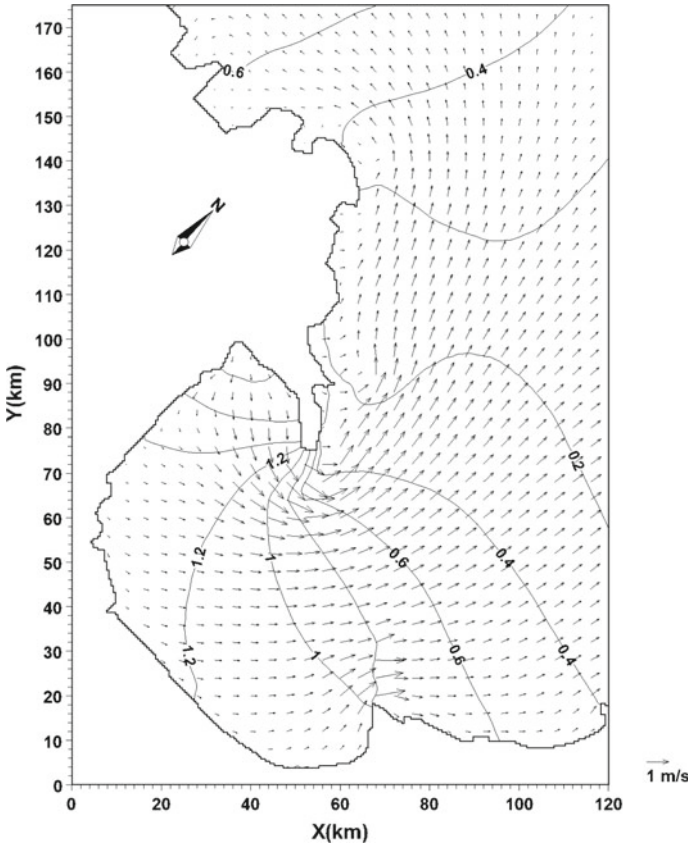

Fig. 5 Ebbing flow pattern in a spring tide

The flow process of the YRE has the following characteristics: (1) during flooding flow near the current Qing8 Route, the flow from the Bohai Bay is parallel to the direction of the coastline from the northwest to the southeastern direction, after bypassing the old channel in the Qingshuigou and moving to the Laizhou Bay. At this time, the water flow in the Laizhou Bay is in the initial stage of the flooding water; (2) during ebbing flow, part flow from the YRE and Laizhou Bay passes around the bend of the Zhuangxi oil field to the Bohai, and most of them flow directly to the open sea. There exists a large counter clockwise circulation.

4 Sediment Transport Capacity

In order to clearly describe the processes of tidal flow and sediment transport in the YRE, the enclosed section as shown in Fig. 7, is set to form a closed area for

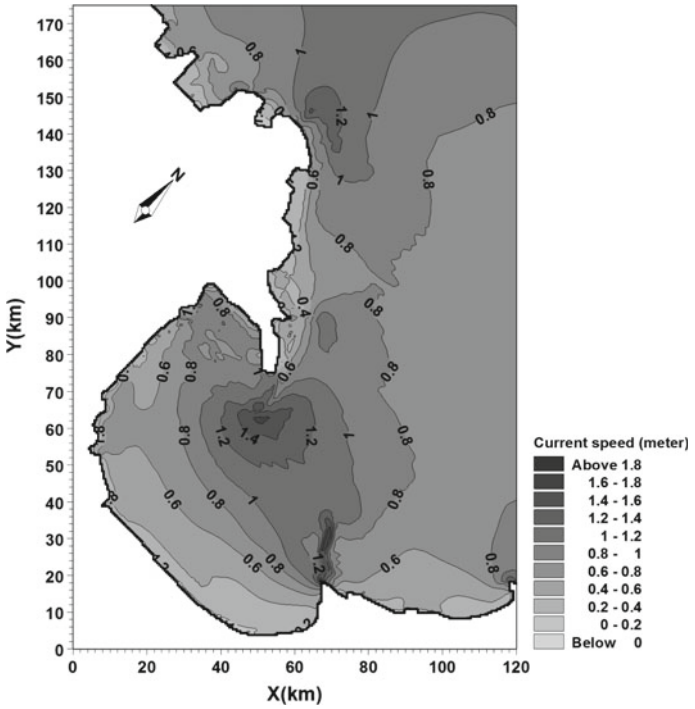

Fig. 6 Maximum flow velocity in a spring tide

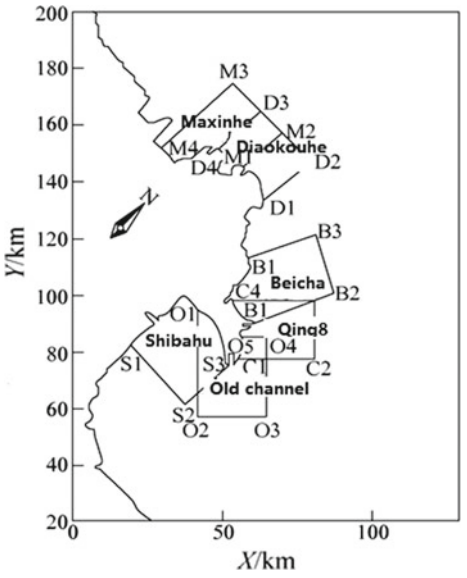

Fig. 7 Enclosed sections in each flow route

sedimentation. The sea outside in this enclosed area is regarded as the outer sea. The setting of the enclosed sedimentation area is generally in accordance with the sediment diffusion range and the maximum possible extension distance of each flow path (Jiao 2000). In longshore, the cross sections are about 12 km from the inlet of each route. In offshore, the cross sections are about at the −15 m isobath.

4.1 Characteristics of Sediment Transport

The followings focus on the characteristics of sediment transport from the Old Channel and current Qing8 Route. Under the action of runoff and tidal current, sediment transport near current Qing8 Route is dominated by southward longshore current, sediment transported through the C1–C2 section to southern Laizhou Bay accounts for more than 90%, the amount of sediment transported directly to the deep sea through the C2–C3 section is generally less than 10%, and little sediment transport through the C3–C4 section.

In the Old Channel of Qingshuigou route, the high speed flow outside the mouth can transport more than 70% of riverine sediment to the outer sea through the O2–O3 section during the spring tide, which is the main channel for sediment transport. The sediment discharge along the coastline is the secondary transport channel through O1–O2 and O3-O4, the amount of sediment transport through the two sections is roughly equivalent. The amount of sediment transported to the north through the O4–O5 section accounts for only about 1% of the total sediment discharged into the open sea.

Under the effect of the semi-diurnal tidal process, O2–O3 section is also the main channel for sediment transport accounting for about 50%. The sediment transport through the O1–O2 section to Laizhou Bay is the second channel of about 37% incoming sediment transported to the outer sea. The amount of sediment transported through O3–O4 and O4–O5 accounts for less than 10% of the total riverine sediment. During the neap tide, sediment diffuses evenly around the estuary.

4.2 Sediment Transport Capacity

The net sediment discharge through the closed sections of each flow route can be calculated statistically to analyze the effect of sea-flow dynamics on sediment transport capacity. Table 3 lists the percentage of sediment discharge to the open sea during the semi-diurnal tidal process.

It can be seen that the sediment transport capacities from strong to weak among the six flow routes are Diaokouhe, Old channel of Qingshuigou route, the current Qing8 Route, Maxinhe Route, Beicha Route and Shibahu Route, which can transport about 51.0, 39.3, 29.9, 17.8, 13.0 and 7.2% of incoming riverine sediment into the outer sea, respectively. According to the annual averaged incoming sediment of 0.556

Table 3 Ratio of sediment transported into outer sea to the incoming riverine sediment at Lijin station (in %)

Flow route	Flood season	Dry season	Averaged
Diaokouhe	53.13	47.74	51.04
Old channel	43.36	29.19	39.27
Qing8	34.33	24.62	29.94
Maxinhe	22.91	10.52	17.75
Beicha	16.60	0.35	12.96
Shibahu	10.45	6.83	7.22

billion T from the Yellow River, the tidal flow can transport about 0.30 billion T, 0.218 billion T, 0.166 billion T, 0.100 billion T, 0.07 billion T and 0.04 billion T to the outer sea through above flow routes in turn, respectively.

4.3 Comparative Analysis

In order to explain the reasonableness of the calculated tidal dynamic sediment transport capacity in the YRE, the characteristics of the sediment transport in different periods are analyzed based on the measured data. The amount of sediment transported to the outer sea reflects the capacity of the marine dynamic sediment transport in this period.

The tidal dynamics of the Yellow River Estuary is more stable, especially in the Old channel of Qingshuigou period, and the annually-averaged sediment discharge into the outer sea is 0.231 billion T, accounting for 34.9% of incoming sediment at Lijin station. From the whole period of the Qingshui Route (1976–2000), the annually-average sediment load to the outer sea is 0.20 billion T, which accounts for 35.4% of incoming riverine sediment. The calculated tidal dynamic sediment transport capacity from the Old channel of Qingshuigou route is 39.27%. Obviously, the calculated value is consistent with the measured data.

5 Discussions

The dynamic transport process of the YRE is very complex. The calculated tide-driven sediment transport capacity near the outside waters of each flow route is quite different. It is concluded that the capacity of marine dynamic sediment transport is mainly related to the amount of riverine water and sediment, the flow field outside the mouth, the topography and the extension of the sand mouth. The Diaokouhe Route has a high water depth, and there is a high velocity area. In addition, the route is in the acceleration area of the strong longshowl current in the direction of Bohai Bay to the Laizhou Bay. All these help the tidal current to bring the sediment from the Yellow River into the open sea. After using the Old channel of Qingshuigou

route, large amount of sedimentation had made the mouth sand spit more prominent. Consequently a high velocity area has also been produced there, which has strong ability to transport sediment into the outer sea. However, the current Qing8 Route is not very strong, and the high velocity area is in the process of formation, so the sediment transport capacity is relatively low, but with the continuous use of the flow path, the sand mouth will be more prominent, the high-speed flow area in the outside of the mouth is gradually forming, and the capacity of sediment transport will also be improved. The Maxinhe Route is mainly dominated by longshowl current. There is no high velocity area outside the mouth, and the two bays on both sides can allow sedimentation, which weakens the capacity of sediment transport to the open sea. With the effect of sedimentation from current Qing8 Route, the topography outside Beicha Route is shallow, and the coastal profile is also affected by the current Qing8 sands and Gudong oil field, the capacity of marine dynamic sediment transport in the initial stage of Beicha Route is obviously weaker. The Shibahu Route is located in the Laizhou Bay. There, the water depth is very shallow, and the longshowl current is blocked by the sand spit of the Old channel route. In result, the flow velocity is small and the sediment transport capacity is very weak. Therefore, Maxinhe and Shibahu routes can be excluded from consideration, it is reasonable to plan the recent use of Qingshuigou routes interchangeably, and long-term consideration of Diaokou Route.

6 Conclusions

Based on the above calculation and analysis, the conclusions are as follows: (1) the Yellow River flooding tidal current mainly comes from the Bohai Bay, and along shoal current to south-east, most of the ebbing flow flows through the Laizhou Bay to the outer sea, and there is a anticlockwise circulation; (2) there are 3 high velocity regions in the waters near routes in use and suspended. The first one is about 10 km outside Qingshuigou Route with the maximum velocity of 1.7 m/s. The second high velocity region of 1.2 m/s locates outside the DiaoKouhe Route. The third one is developing outside the current Qing8 Route, with the maximum velocity is 1.0 m/s; (3) longshore current is the dominant force driving sediment transport in the Yellow River Estuary; (4) the sediment transport capacity from strong to weak in turn of the compared 6 flow routes are Diaokouhe, Old Channel, current Qing8 Route, Maxinhe, Beicha and Shibahu Route, of about 51.0, 39.3, 29.9, 17.8, 13.0 and 7.2% incoming riverine sediment can be transported into the deep see, respectively. (5) Interchangeable use of Qingshuigou routes including Qing8, Old channel and Beicha can be planned in the near future, Diaokou Route is a long-term consideration.

Acknowledgements This study is supported by grants from the National Key Research and Development Program of China (2017YFC0405504), the special fund for transformation of science and technology achievements and the special projects for basic scientific research of China Institute of Water Resources and Hydropower Research (No. SE1003A02017, SC0145B172017).

References

Dou, Z. X., et al. (1979). Numerical calculation of tidal current and tidal residual current in Bohai. Report of *China Environmental Protection Institute affiliated to National Oceanic Bureau.*

Hu, C. H., & Cao, W. H. (2003). Variation and regulation of the water and sediment in the yellow river Estuary I: The basic law of the movement and evolution of water and sediment. *Journal of Sediment Research (in Chinese), 5,* 1–8.

Jiao, Y. L. (2000). The necessity and feasibility of the high water diversion in the Yellow River Estuary. Report of *Sandong bureau of Yellow River affairs affiliated to the Yellow River Water Conservancy Commission*.

Li, Z. G. (1988). Analysis of the basic situation and basic laws of the waters near the Yellow River Delta. Report of *Yellow River Institute of Hydraulic Research affiliated to the Yellow River Water Conservancy Commission*.

Wang, K. R., Yao, W. Y., Zhang, X. F., & Li, P. (2001). The present situation and its regulation of the yellow river Estuary. *Journal of Marine Science (in Chinese), 15*(1), 52–54.

Yin, X. L., Zhang, S. Q. (1983). Calculation of sediment transport and M2 sub-tide in the Yellow River Estuary. Report of *China Institute of Water Resources and Hydropower Research*.

Zeng, Q. H., Zhang, S. Q., & Hu, C. H. (1997). *Planning and regulation of the yellow river Estuary*. Zhengzhou, China: Yellow River Press.

Zhang, S. Q. (1990). Calculation of sediment transport and the variation of erosion and siltation in the yellow river Estuary. *Journal of Hydraulic Engineering (in Chinese), 1,* 23–33.

Numerical Modelling of Sediment Exchanges from the Gironde Estuary to the Continental Shelf: Hydrodynamic Model Validation and Sensitivity Analysis of Sediment Fluxes to Sediment Transport Parameters

Mélanie Diaz, Florent Grasso, Pierre Le Hir, Matthieu Caillaud and Bénédicte Thouvenin

Abstract Coastal environments are directly influenced by terrigenous inputs coming from rivers through estuaries. Quantifying the amount of nutrients and contaminants brought by sediment particles from the continental regions to the sea is of major interest for marine resource protection. Estuaries form a transition zone between river and maritime environments and therefore represent dynamic areas in terms of hydrodynamics, hydrology and sediment transport. The hydrodynamics is strongly dominated by asymmetrical tidal currents, modulated by neap and spring phasing. Moreover, the interaction between fresh and saltwater induces salinity gradients, and therefore density gradients, influencing the sediment dynamics. The complexity and the spatial variability of this interface area make it difficult to quantify the actual sediment transfers between the estuary and the ocean, either by in situ measurements, remote sensing or numerical simulation. This study is based on a 3D realistic hydrodynamic model of the Gironde estuary (South–West France) and the continental shelf seaward coupled with a multi-layer process-based sediment model accounting for sand and mud mixtures. In order to better understand the sediment dynamics between the estuary and the continental shelf, the objective is to provide a quantification of suspended sediment mass uncertainties associated with sediment transport parameters. The sensitivity analysis is conducted considering changes in the key sediment transport parameters, such as the settling velocity of the mud class and the sediment initial distribution. A better understanding of the uncertainties associated with simulated sediment transport will enhance the degree of confidence that can be placed in the quantification of the estuarine sediment exchanges with the sea. Such a quantification provides knowledge about the intra-estuarine exchanges with lateral intertidal mudflats, as well as sediment export to the sea, possible trapping in the subtidal muddy areas seaward of the mouth (e.g. the West Gironde Mud Patch) and dispersion along the adjacent coasts.

M. Diaz (✉) · F. Grasso · P. Le Hir · M. Caillaud · B. Thouvenin
IFREMER, Centre de Bretagne, ODE/DYNECO/DHYSED, ZI de la Pointe du Diable – CS 10070, 29280 Plouzané, France
e-mail: melanie.diaz@ifremer.fr

K. D. Nguyen et al. (eds.), *Estuaries and Coastal Zones in Times of Global Change*, Springer Water,
https://doi.org/10.1007/978-981-15-2081-5_21

Keywords Sensitivity analysis · sediment fluxes · Numerical modelling · Mud/sand · Gironde estuary

1 Introduction

During their transfer from continental area to the sea, pollutants, such as heavy metals and radionuclides, can be absorbed by fine suspended particles and trapped in the sediments. Hence investigating estuarine sediment dynamics, including fluxes to the open sea and residence time within the estuary is of major interest for coastal and estuarine resource protection.

Because of the influence of both tide and rivers, the transport of particles in estuaries is governed by complex processes in terms of hydrodynamics, hydrology and sediment dynamics. The hydrodynamics is strongly dominated by asymmetrical tidal currents, modulated by neap and spring phasing. The tidal wave is distorted as it propagates upstream and as the water becomes shallower. The tide crest travels faster than the trough, which induces stronger flood peak velocity and weaker ebb velocity (Allen et al. 1980). The flood phase tends to be shorter but more energetic than the ebb phase, with stronger currents and induced bed shear stresses, along with a longer-lasting high-water slack.

Large amount of mud is suspended during peak tidal currents and rapid settling occurs during slack water (Allen et al. 1980; Castaing and Allen 1981). Due to the tidal asymmetry, fine particles are more likely to be suspended during flood and to settle after low water slack. This "tidal pumping" of sediment is emphasized by the asymmetrical tidal mixing. During flood seawater tends to "repulse" the freshwater. The vertical mixing is then enhanced and the sediment concentration in the upper layer is higher. Conversely during ebb, stratification is restored and the vertical current shear is stronger, leading to reduced concentration of particles in the upper layer (Simpson et al. 1990; Burchard and Baumert 1998; Burchard and Hetland 2010). The combination of the two processes tends to emphasize the residual up-estuary sediment transport. Density circulation induced by the interaction between fresh and saltwater contributes to maintain the suspended particulate matter in the estuary and more precisely, around the limit of the salinity intrusion (Brenon and Le Hir 1999). Moreover, stratification increases from the upper estuary to the limit of the salinity intrusion, causing the suspended sediment trapping nearby the latter region (Geyer 1993).

The interaction between river discharge, residual upstream circulation and density gradients induces an accumulation of suspended sediment in an Estuarine Turbidity Maximum (ETM) (see for example Allen et al. 1976; Festa and Hansen 1978; Uncles and Stephens 1989; Geyer 1993; Burchard et al. 2018). In this area, Suspended Sediment Concentration (SSC) is high compared to upstream or downstream concentration in the estuary, which leads to stronger deposition of particulate matter and to the formation of a thick layer of fluid mud above the bed. These phenomena, including stratification, can be emphasized or, on the contrary, reduced by the

neap/spring phasing and can influence the ETM location (Allen et al. 1980; Uncles and Stephens 1989; Grasso et al. 2018)

This kind of key pattern including high turbidity levels and complex sediment dynamics can have dramatic implications for ecology and biology in case of particle contamination by pollutants (Roberts 2012). The residence time of sediment within an estuary is a key parameter to better understand the fate of contaminant and to protect coastal resources.

Many studies using in situ measurements and/or numerical modelling have focused on the ETM dynamics and attempted to figure out the main mechanisms involved in the ETM formation (Allen et al. 1980; Geyer 1993; Le Hir et al. 2001; Sottolichio et al. 2011; Jalon-Rojas et al 2015; Toublanc et al. 2016), but only a few took interest in quantifying the sediment fluxes at estuaries mouth (Schulz et al. 2018). As measurements are often isolated in time and/or in space and difficult to extrapolate, one of the best way to evaluate sediment budgets over long periods (seasonal to annual or even inter-annual) is to apply numerical models, once they are validated.

Based on a 3D realistic process-based numerical model, this study aims at quantifying uncertainties over these fluxes associated with different sediment transport parameters in order to better understand the sediment dynamics and better estimate the sediment fluxes between the Gironde Estuary (South–West France) and the continental shelf. The computed hydrodynamic model MARS3D is coupled to a multi-layer mud-sand transport module accounting for advection, diffusion and consolidation processes, forced by realistic boundary conditions (tide, wind, river flow and meteorological surge). It uses a curvilinear grid over a large domain including the Gironde Estuary and the continental shelf seaward. The mesh is refined in the upper estuary, in the river meandering and at the mouth. The hydrodynamics and hydrology are validated in terms of water elevation, velocity current and salinity measurements within the estuary.

In order to investigate sediment fluxes and to quantify the import and export of sediment from the estuary to the open sea, the first objective of this work is to determine the suspended sediment sensitivity to different parameters, and especially the main sediment transport parameters. To do so, the influence of changes in the following parameters is investigated: (i) the settling velocity of muddy particles (constant or variable in order to account explicitly for flocculation process) and (ii) the initial distribution of sediment bed cover.

For the study presented in this chapter, the sediment transport model has not yet been thoroughly calibrated but it does not impact the following sensitivity analysis. The model response in SSC is investigated for different values of these parameters. The parameter influence on the sediment suspended mass within the estuary and the net sediment fluxes at the mouth are examined over the simulated year.

2 Materials and Methods

2.1 Study Area

The Gironde Estuary is the largest estuary of Western Europe, with a total surface area of 635 km^2 (Jalon-Rojas et al. 2015). It is situated on the South–West coast of France on the Bay of Biscay (Figs. 1, 2 and 3), and it originates from the confluence of Garonne and Dordogne rivers at the location called "Bec d'Ambès". It is 170 km long from the mouth to the upper limit of tidal influence, 75 km long from the mouth to the confluence of the two rivers and it drains a basin surface of about 71,000 km^2 (Allen et al. 1980; Savoye et al. 2012; Fuentes-Cid et al. 2014). The Garonne River is the major tributary, supplying for two third of the water and particles introduced in the estuary, the Dordogne River bringing in the other third. The average total river discharge of both the Garonne and Dordogne rivers is about 700–800 m^3/s (Castaing

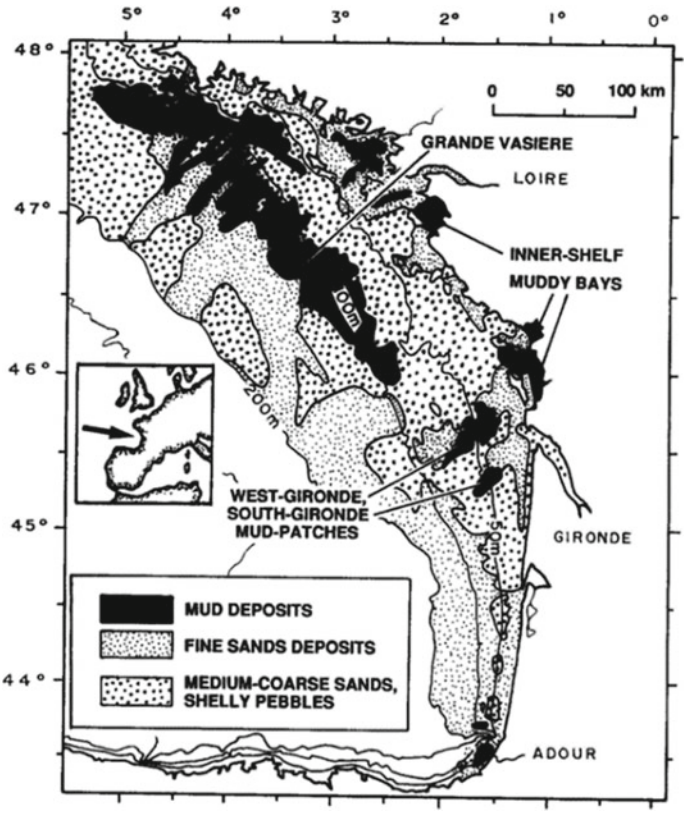

Fig. 1 Location map of muddy deposits and substrate distribution on the continental shelf of the Bay of Biscay, France (from Lesueur et al 1996, modified from Allen and Castaing 1977)

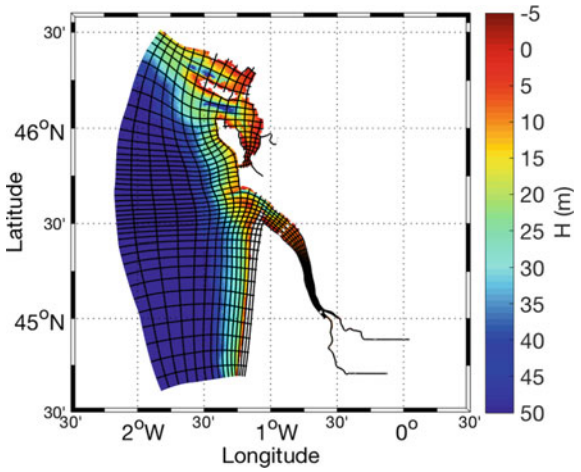

Fig. 2 Bathymetry (mean sea level chart datum) of the Gironde Estuary numerical model with the mesh grid (every 5 cells are represented)

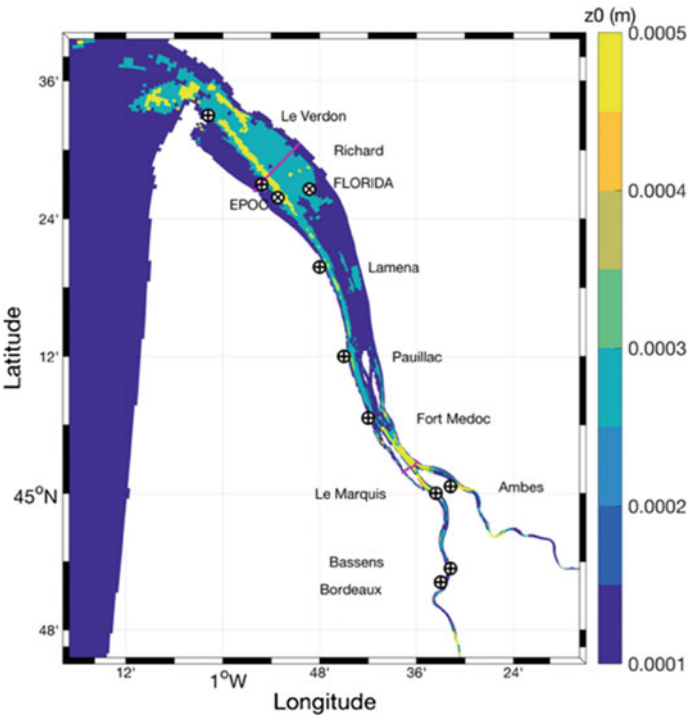

Fig. 3 Bottom roughness length of the Gironde Estuary numerical model. The markers represent the locations of the Grand Port Maritime de Bordeaux (GPMB) tidal gauges (pluses), and the EPOC and FLORIDA ADCPs (crosses) deployed in June 2015 for 6 months by the EPOC laboratory

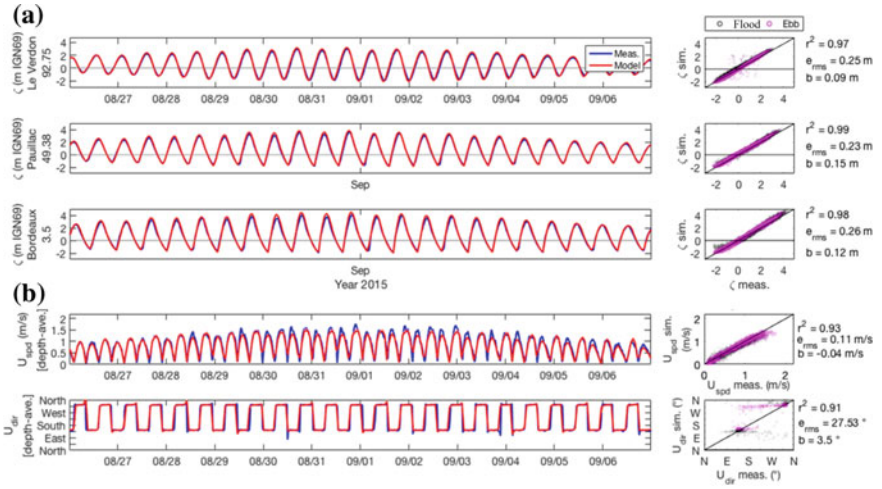

Fig. 4 **a** Water surface elevation at Le Verdon, Pauillac and Bordeaux (see locations in Fig. 3). **b** Depth-averaged current velocity (intensity and direction) at the FLORIDA ADCP location. Left panels: Measurements (blue) and simulation results (red) from August 26th to September 7th 2015. Right panels: Simulation results versus measurements during flood (black dots) and during ebb (pink dots), with the squared correlation coefficient r2, the root-mean-square error erms and the bias b

and Allen 1981). A well-defined seasonality in river flow occurs with a flood period from November to May (maximum values usually in January with 1500 m^3/s monthly mean) and a low flow period from June to October (less than 200 m^3/s in August). It is one of the two main estuaries on France's Atlantic Coast entering the Bay of Biscay (Jouanneau et al. 1999). The riverine sediment supply from the Gironde estuary to the continental shelf is about $1.5*10^6$ t/year, estimated to contribute for 60% of fine sediment input into the Bay of Biscay (Jouanneau et al. 1999).

As almost the entire French Atlantic coast, the Gironde estuarine system is macrotidal with tides ranging on average at the mouth from 1.5 m during neap tides to 5.5 m during spring tides (Castaing and Allen 1981). Following the classification of Le Floch (1961), the Gironde is considered as hypersynchronous (Allen et al. 1980). This means that the tidal wave amplitude reaches a maximum within the estuary as it propagates upstream. The effect of the upwards reduction of cross section is dominant over the energy loss by friction. As a consequence, the tidal wave amplifies along the lower estuary, while friction becomes dominant upwards. Together with the tidal range increasing, the ebb-flood asymmetry described in the introduction is strengthening. The accumulation of these phenomena along with the density circulation leads to the formation of an ETM. During high river flow, density gradient being well developed, the ETM is located at the density node (Allen et al. 1980). During low river discharge periods, the ETM spreads upstream on up to 40 km and reaches the limit of tidal influence.

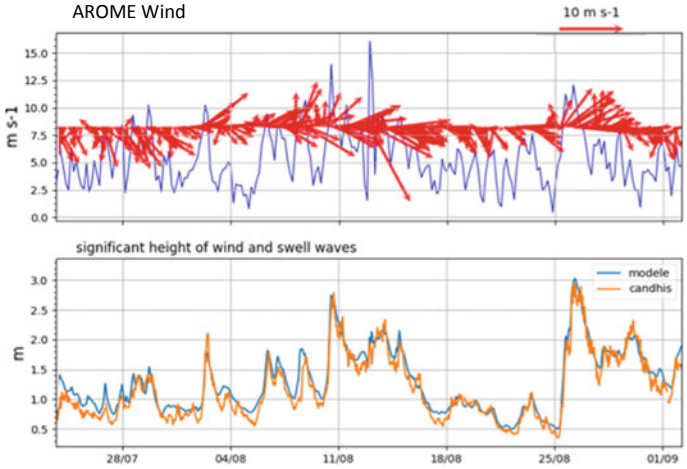

Fig. 5 Wind and wave conditions seaward of Oleron Island from late July to early September 2015. Upper panel: Wind velocity (blue) and direction (red arrows). Lower panel: significant wave height Hs (simulated in blue and measured in orange)

The Gironde ETM is one of the most developed in Europe and one of the most concentrated, with more than 1 kg/m^3 turbidity in surface waters (Castaing and Allen 1981; Doxaran et al. 2009). The dynamics of suspended sediment is particularly significant, with bottom values ranging from less than 0.1 up to 10 kg/m^3 (Sottolichio and Castaing 1999). Associated with the location of the ETM, the deepest and widest part of the channel are likely to trap large quantities of fine particles. These particulate matters remain in suspension above the bed in a thick layer of fluid mud, with concentrations up to 300 kg/m^3 (Allen 1971). Efficient deposition occurring in the middle estuary (near Pauillac, Fig. 3 and the station E in Fig. 6), can be associated with the existence of a narrow deep pit in the axis of the channel. This pattern act as a permanent source of easily erodible mud, maintaining a permanent secondary peak of turbidity (Sottolichio and Castaing 1999).

The superficial sediment map also exhibited the presence of two mud fields offshore the Gironde Estuary mouth, on the continental shelf (Fig. 1; Lesueur et al. 1996). The biggest one (40 km long) is called the "West-Gironde Mud Patch" and is located around 30 km westward of the mouth. The second one (25 km long) was observed at the south of the previous one and is referred as the "South-Gironde mud patch". They are located in front of the two channels of the Gironde mouth and are characterised by intermediate depths from 30 to 75 m. Fine particles accumulate in these areas when going out of the estuary. Indeed, most of the particles contributing to these muddy patches originate from the Gironde watershed (Lesueur et al. 2002).

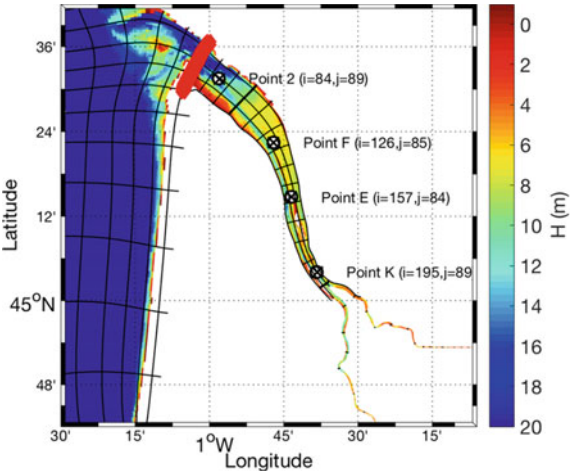

Fig. 6 Bathymetric map of the estuary and its tributaries. Black crosses represent the position of the measurement stations and black circles describe the grid cells selected to analyse the model outputs. The red line is the section where fluxes are calculated in Sect. 4.3

2.2 Numerical Model Set-up

2.2.1 Hydrodynamic Model

The MARS3D model, used to study hydrodynamics and sediment transport in the Gironde Estuary, solves the momentum equations using a finite difference scheme under the Boussinesq and hydrostatic hypothesis (Lazure and Dumas 2008).

The grid covers the Gironde Estuary with its tributaries, from the limit of tidal influence upstream (La Réole in the Garonne River and Pessac in the Dordogne River) to approximately the 100 m deep isobath offshore and from the Arcachon basin (southern limit) to Les Sables-d'Olonne (northern limit) (Fig. 2 and appendix). The domain is very large and includes the Marennes-Oléron bay. An orthogonal curvilinear grid was set up to better describe the particular shape of the estuarine mouth, the rivers meandering and the Marennes-Oléron system. The smallest cells are located upstream in rivers and are approximately 40 m $\times$ 350 m long against cells of 2 $\times$ 2 km^2 offshore. There are more than 400 cells from the 100 m isobath to the upstream limit of the domain and 220 cells in the South–North direction.

The model vertical grid is discretized in 10 equidistant sigma layers over the water column. The circulation is forced at the open (western and southern) boundaries by the main tidal components extracted from the CST France database (SHOM).

The model is also constrained by wind stresses and pressure gradients provided by the high-resolution meteorological AROME model (Meteo-France). Surges at the open boundaries are provided by another configuration of the MARS3D numerical model with a wider domain including the estuary and the continental shelf seaward. The realistic Garonne, Dordogne and Charente river flows are imposed at La Réole, Pessac and Rochefort, respectively (Fig. 2). Waves are simulated using the WAVEWATCH III® (WW3) numerical model (Roland and Ardhuin 2014). The simulation

is forced by the free surface elevation and the current velocity provided by the hydrodynamic model. For the purpose of this chapter, the wave-induced bed shear stress is not considered in the hydrodynamic and sediment transport module. The simulated significant wave height information was used for validation by comparison with measurements.

Ignoring wave effect in our case, the total bed shear stress corresponds to the current-induced shear stress only. It is calculated as

$$\tau_c = \rho u_*^2$$

where u_* is computed using the turbulent boundary layer theory

$$u(z) = \frac{u_*}{\kappa} \ln\left(\frac{z}{z_0}\right)$$

with u(z) the current velocity at elevation z, z_0 the bottom roughness length. The bottom roughness length is spatially varying over the domain based on the maximum current velocities and the associated sediment grain size distribution (Fig. 3b).

2.2.2 Sediment Model

The hydrodynamic model is coupled with a multi-class, multi-layer sediment transport module (MUSTANG) described in Le Hir et al. (2011), Grasso et al. (2015) and Mengual et al. (2017). The sediment bed is discretized with up to 100 layers of variable thickness (from 1 μm to 0.5 mm). This sediment transport model computes the spatial and temporal variations of sand and mud accounting for erosion, suspension and deposition processes as well as for consolidation. In the water column, it solves the 3-D advection-diffusion equation for different classes of particles. In our case, five classes of sediment were chosen, based on granulometry data available over the Gironde Estuary and offshore (over the West- and South-Gironde subtidal mudflats): one gravel (diameter $d = 3$ mm), three sands ($d = 400$ μm, $d = 250$ μm and $d = 100$ μm) and one mud ($d < 63$ μm). For each class, the grain density is 2600 kg/m^3.

The initial distribution of sediment classes over the domain is considered uniform with 10% of gravel, 20% of each sand classes and 30% of mud. The initial sediment concentration is forced at 1200 kg/m^3 and the initial sediment thickness is adjusted on the basis of this concentration, the initial distribution of each classes and the maximum volumetric concentration. This leads in our case to an initial thickness of 1.22 m.

The river sediment supplies are pure mud and are imposed at the same location as the river flows. Gravel and sand classes have fixed settling velocities which depend on their diameters (Soulsby 1997) and are advected as depth-averaged variables. To retrieve a distribution over the entire water column, the vertical concentration profile of these non-cohesive classes is assumed to follow a Rouse profile. The mud class is defined as a three-dimensional variable with a settling velocity that can either be

constant, or vary with the mud concentration and the turbulent shear rate, in order to explicitly account for flocculation process (Van Leussen 1994).

The erosion flux is based on Partheniades formulation (Partheniades 1965) that considers an erosion flux only when the bottom shear stress exceeds the critical erosion stress.

$$\begin{cases} \tau > \tau_e \Rightarrow E = E_0 \left(\frac{\tau}{\tau_e} - 1 \right)^n \\ \tau < \tau_e \Rightarrow E = 0 \end{cases} \quad (1)$$

In the case of mixed sediment, the behavior depends on cohesive and non-cohesive fraction. The mass fraction of mud (f_m) and the mean diameter of non-cohesive classes (d_{sand}) are used to distinguish a cohesive behavior from a non-cohesive one (Le Hir et al. 2008). In both cases, the erosion fluxes have the same formulations (1) but the parameters used can be different. For f_m greater than 0.7, the behavior is purely muddy, $E_0 = E_{0,mud}$, $n = n_{mud}$ and $\tau_e = \tau_{e,mud}$, the critical erosion stress of mud is expressed:

$$\tau_{e,mud} = \alpha_1 C_{relmud}^{\alpha_2}$$

with α_1 and α_2 empirical parameters (Table 1) and C_{relmud} the relative mud concentration (i.e. concentration in the space between non-cohesive classes). The variable C_{relmud} is linked to the consolidation state of the sediment. For $f_m < 1000 * d_{sand}$, the behavior is purely sandy. For the erosion flux formulation, this means that $n = n_{sand}$ (Table 1) and $\tau_e = \tau_{e,sand}$, computed following the Shields criteria for the critical erosion stress of sand (Soulsby 1997). Moreover, $E_0 = E_{0,sand}$ with

$$E_{0,sand} = \tau_{e,sand}^{n_{sand}} \min(0.27, 1000 * \langle d_{sand} \rangle - 0.01)$$

obtained from erodibility measurements (Le Hir et al. 2008). Finally, for a mixed behavior, the parameters are linearly interpolated between the purely sandy and purely muddy behaviors. A more detailed description of the sediment model is provided in Le Hir et al. (2011).

Table 1 Some parameters used in the 3D numerical model

Parameter		Symbol	Value
Muddy behavior	For the erosion rate of mud	$E_{0,\,mud}$	3.10^{-4}
		n_{mud}	1
	For the critical erosion stress	α_1	1.10^{-5}
		α_2	2
Sandy behavior		n_{sand}	1.6

3 Validation of the Hydrodynamic Model

The following numerical model results were obtained by running simulations over the year 2015. Over this period, tidal gauge measurements and wave height data were available as well as current velocity measurements from two ADCPs deployed in the estuary from June to November 2015 by the EPOC laboratory (Ross et al. 2017).

3.1 Water Elevation

The Gironde Estuary is a macrotidal environment where tidal currents are one of the dominant processes influencing the sediment dynamics. To properly reproduce the sediment transport within this type of environment, it is crucial to reproduce the tidal pumping induced by the propagation of tide upstream the estuary. In Fig. 4a the simulated water surface elevation is compared with the tidal gauge measurements at three distinct stations. Le Verdon is situated at the mouth, Pauillac in the central estuary and Bordeaux in the Garonne River upstream (Fig. 3). It is clearly readable that the tidal asymmetry increases, as well as the tidal range, as the tide propagates upstream. The simulated water levels were calibrated by adjusting the bottom roughness length (Fig. 3) and by taking into account meteorological surges at the offshore boundary of the domain. As a result, water levels are very well reproduced by the numerical model with a maximum root-mean-square error of 33 cm over the entire simulated period (one year) at Ambes station (see location in Fig. 3).

3.2 Current Velocity and Direction

Considering sediment dynamics, a particular attention must be paid to the current-induced bed shear stress. Current is the main forcing driving the sediment transport in our numerical model (as waves are not considered in this preliminary study). Figure 4b represents the depth-averaged current intensity (upper panel) and direction (lower panel) measured (blue) and simulated (red) at the FLORIDA ADCP location (Fig. 3). The vertical structure of the current has also been studied but is not shown in this chapter, as well as the currents at the EPOC ADCP location. The model provides a proper response regarding the direction as well as the intensity of the current. At the EPOC location, which lies close to the main channel, the root-mean-square error of the current intensity reaches 28 cm/s and the direction is very well reproduced by the simulation (not shown). The model tends to overestimate the current speed during ebb flows, which is emphasized for strong currents occurring during spring tides (maximum bias of 17 cm/s, not shown). At the FLORIDA point (Fig. 4b), nearby the Saintonge channel close to the right bank of the estuary, the root-mean-square error between measured and simulated current intensities is 11 cm/s.

However, the trend is reverse compared to the result at EPOC station. The model manages to reproduce flood and ebb currents with a good accuracy in general but during spring tides, the simulated currents are slightly underestimated (maximum bias of −4 cm/s). Nevertheless, the model is able to reasonably well simulate the current general characteristics with a satisfying accuracy.

3.3 Wave Dynamics

Local wind waves, generated by local winds in the estuary and swells coming from the Atlantic Ocean through the estuarine mouth may have strong influence on sediment resuspension. The wave-induced bed shear stress can be large when looking at shallow areas such as intertidal mudflats or during strong hydrodynamic or meteorological events. Even if, in this study, the wave effect is not considered in the sediment transport module, the hydrodynamic model outputs in terms of currents and water elevation have been used in the wave model WAVEWATCH III® to simulate the significant height of wind and swell waves. Wave heights are compared with buoy measurements (Fig. 5 lower panel) at a depth of 52 m provided by Candhis data center (National Center for Archiving Swell Measurements). The buoy recorded large waves reaching 3 m in late August 2015. The wave numerical model succeeds in reproducing correctly the significant wave height ($r^2 = 0.96$, $e_{rms} = 0.18$ m, mean bias = 0.15 m) with a slight overestimation during the second half of July (not shown in Fig. 5).

4 Results of the Sensitivity Analysis

Given that the ultimate purpose of this study concerns the suspended sediment dynamics of the Gironde Estuary and the behavior of potentially contaminated particles, the next chapter will focus on the cohesive sediment class simulated by the sediment transport model. The sediment model has not been thoroughly validated yet, the ETM mass is underestimated at the end of one year simulation and no equilibrium in achieved yet, but, as the aim of this chapter is to analyse the simulated suspended sediment sensibility to some key empirical parameters, the following study is still valid.

4.1 Sensitivity to the Mud Settling Velocity

Four constant settling velocities were tested (Ws = [0.3, 0.5, 1, 2] mm/s), falling in the range of common values that can be observed in such a type of estuary. Two variable settling velocities based on the Van Leussen's (1994) formula were analysed

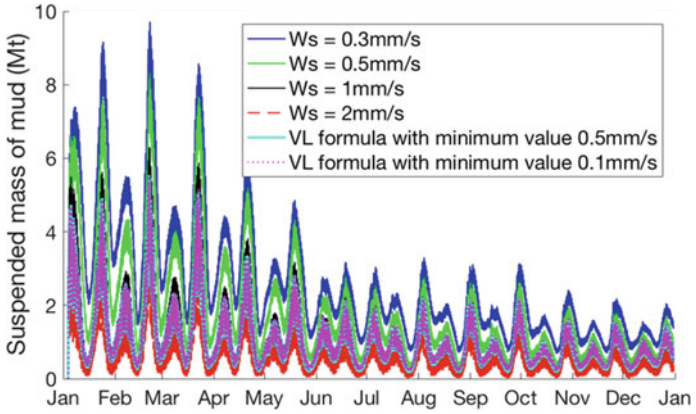

Fig. 7 Time series of total mass of mud in suspension within the estuary for different settling velocities, expressed in millions of tons

as well, bounded between a maximum value of 1.5 mm/s and two different minimum values: 0.5 mm/s and 0.1 mm/s.

When the settling velocity increases, the SSC generally decreases. A low settling velocity generally implies more suspended mud that could tend to be exported from the estuary more easily. In the long term, the ETM mass may not be conserved. The total mud in suspension integrated over the estuary (upstream of the mouth) is represented in Fig. 7 during the year of simulation.

First, it can be noted from Fig. 7 that the variable settling velocities seem to stand most of the time close to the maximum value, i.e. close to the 1 and 2 mm/s fixed settling velocity curves.

The suspended mass is clearly dependent on the neap-spring cycle, illustrating the influence of tidal currents on sediment erosion. However, the settling velocity does not drastically impact the tendency of mud to be exported or to be trapped in the sediment bed. The suspended mud mass decreases for all the settling velocities and a stabilisation occurs around June. This decrease could be a consequence of mud trapping in the intertidal flat, but it may also be due to the high river flow period that occurs from November to May. In order to analyse the "steady" state of the simulated results, only the second part of the year was considered in Fig. 8, from half June to the end of December.

Figure 8 shows the variability of the simulated surface SSC regarding the longitudinal current velocity. The tidal phase can be deduced from the current speed, with flood and ebb flows for positive and negative current, respectively. Colors represent the results for different mud settling velocities. Circles describe the mean SSC within fixed current speed ranges and standard deviations are represented by vertical bars. The same type of analyses was carried out for the bottom SSC with regards to the water surface elevation and the surface elevation gradient.

Figure 8 highlights the behavior of surface SSC with regards to the ebb and flood phases. The similarly analysed bottom SSC (not shown) revealed a much higher

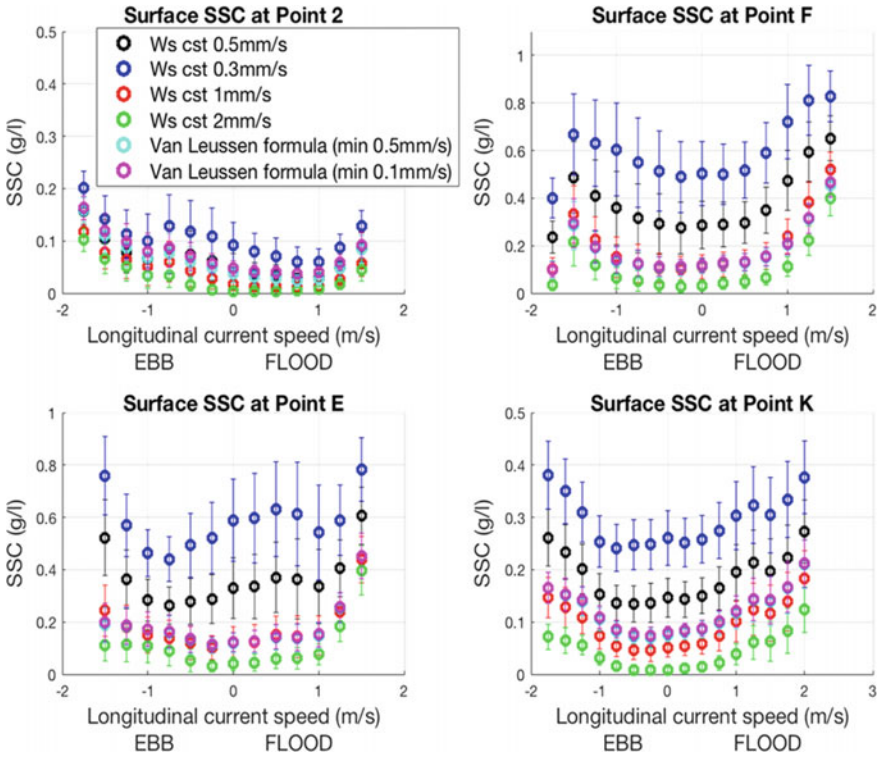

Fig. 8 Surface suspended mud concentration (SSC) versus surface longitudinal current velocity at 4 different stations (see locations on Fig. 6), for different mud settling velocities. Symbols and brackets represent average and standard deviation, respectively, associated with the hourly simulations between June and December 2015

turbidity than the surface one. We can see that SSC are generally higher at station F and E, which are most of the time within the ETM zone. The suspended matter is also higher during maximum ebb and flood currents, which occur during spring phases.

At station 2, situated close to the mouth downstream (Fig. 6), particles mostly remain in suspension when the tide is close to low water (not shown). It can clearly be seen on Fig. 8 that surface suspensions are predominant during ebb. This tendency is not observed at the bottom where no significant predominance was found. Indeed, close to the mouth, the tide is symmetrical and the surface suspended matter is mostly coming from the upper estuary during ebb.

As the tide propagates upstream (station F, Fig. 6), the tidal asymmetry develops and the flood predominance for surface suspended sediment strengthens. There is no significant preponderance of the tidal phase for the bottom suspended matter (not shown), but strong currents clearly contribute to sediment resuspension. The analysis

of SSC versus the water surface elevation (not shown) at station F revealed higher SSC values at low water slack.

A little further upstream (station E, Fig. 6), the flood predominance is maintained for high settling velocities, due to the increasing asymmetry of the tidal wave and the flood dominance of currents, but the ebb seems to strengthen for lower settling velocities. The analysis of SSC versus the water surface elevation (not shown) suggests a reverse tendency compared to further downstream for low settling velocities. SSC is higher during high water slack for Ws = 0.3 mm/s and 0.5 mm/s.

Finally, further upstream at station K (Fig. 6), no clear predominance of ebb/flood phase has been found. The suspended mud concentration is low compared to concentrations in the central estuary (stations E and F).

4.2 Sensitivity to Initial Sediment Distribution

To study the impact of sediment initial distribution on the simulated SSC, three different initial states were compared. The first one was defined in Sect. 2.2.2 and is uniform over the whole domain. The second one considers that the initial mud is only located in the estuary, the sediment over the continental shelf is composed of 10% of gravel and 30% of each sand.

The third distribution is the same than the second one with an additional initial layer of fluid mud in the upper estuary (Fig. 9). This layer is one meter thick and the mud initial concentration is 300 kg/m^3, which corresponds to the expected total mass of the ETM, after integration over the appropriate area (4 to 6 millions of tons (Allen 1973)).

Figure 10 describes the time evolution of the suspended mass of mud in the estuary over the simulated year. As in Fig. 7, the mass fluctuates with the neap-spring cycle and decreases drastically during the first half of the year, as the mud is exported off the estuary or trapped in the intertidal mudflats.

The initial distribution of sediment does not really impact the final mass. Even the simulation with an initial fluid mud layer of 4 millions of tons does not significantly increase the mass in suspension. The uniform initialisation is the one that ends up with the highest suspended mass, probably in relation with the larger initial mud quantity in the system.

Such considerations explain the choice of a uniform initialisation. The observation of the sediment final bed coverage (not shown) revealed that the mud is actually trapped on the intertidal mudflats and a signature of the subtidal mudflats seaward of the mouth is reproduced. However, the wave-induced bed shear stress being ignored in our study, the locations of the sedimentary structures are located too close to the shore than it should be.

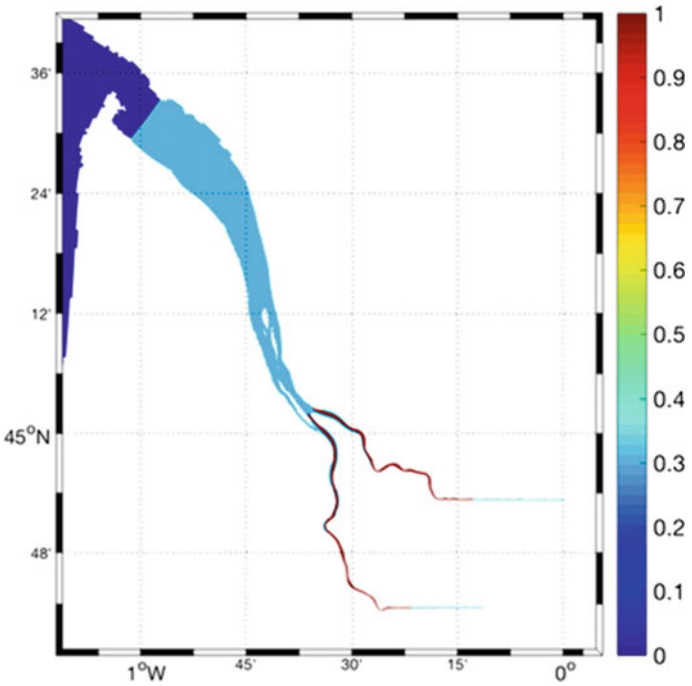

Fig. 9 Initial mud fraction in the 16 first millimeters of the sediment bed. There is no mud offshore and the red area in the upper estuary represents the fluid mud layer

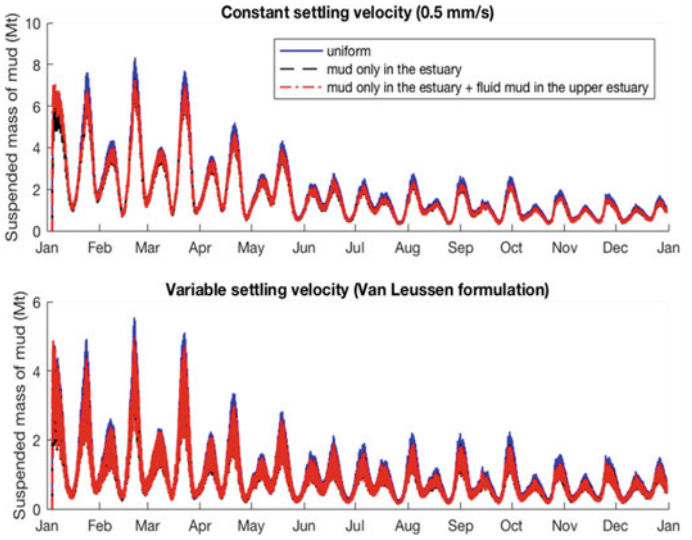

Fig. 10 Time series of total mass of mud in suspension expressed in millions of tons within the estuary for different initial distributions of sediment. Upper panel: constant mud settling velocity of 0.5 mm/s. Lower panel: variable mud settling velocity expressed with the Van Leussen formula

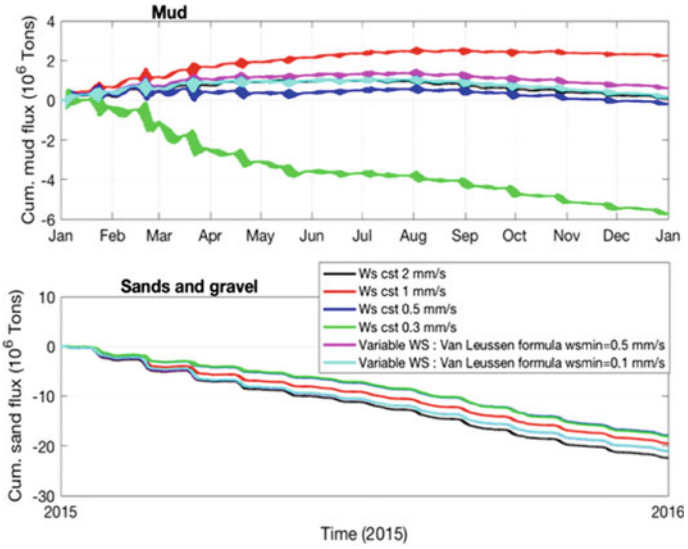

Fig. 11 Cumulative sediment fluxes (in millions of tons) through the cross-section described in Fig. 6, with regards to different mud settling velocities for the uniform initial sediment distribution. Upper panel: mud fluxes. Lower panel: sum of the fluxes for the non-cohesive classes. Positive values depict import into the estuary and negative values for export to the sea

4.3 Sensitivity on Sediment Fluxes

The sediment fluxes through the cross-section illustrated in Fig. 6 were calculated and represented in Figs. 11 and 12. In Fig. 11, the sensitivity to the mud settling velocity is analysed whereas in Fig. 12, the fluxes for different sediment bed initialisation are compared.

First, it can be seen on both figures that the non-cohesive classes export (lower panels) is much more significant than the mud one (upper panels) (up to 20 millions of tons versus up to 6 millions of tons for mud). This observation is in agreement with the fact that the initial distribution of sediment was composed of only 30% of mud and then, there is a larger quantity of non-cohesive sediment in the system initially. Moreover, the sand and gravel classes export is mostly due to the very fine ($d = 100$ µm) and fine ($d = 250$ µm) sand export (not shown).

Figure 11 reveals that the main mud import from the shelf to the estuary occurs for a mud settling velocity of 1 mm/s. Moreover, as was expected in part 4.2 but not exhibited on Fig. 7, the lower settling velocity (0.3 mm/s) suffers significant export offshore. Lastly, the figure exhibits the impact of the variable settling velocities. Both curves stand very close from each other but there is more mud import for the minimum value of 0.5 mm/s. Indeed, the minimum value is reached when the suspended concentration is low (and the flocculation process is reduced). Then a higher minimum value implies faster deposition in the case of low SSC, which tends

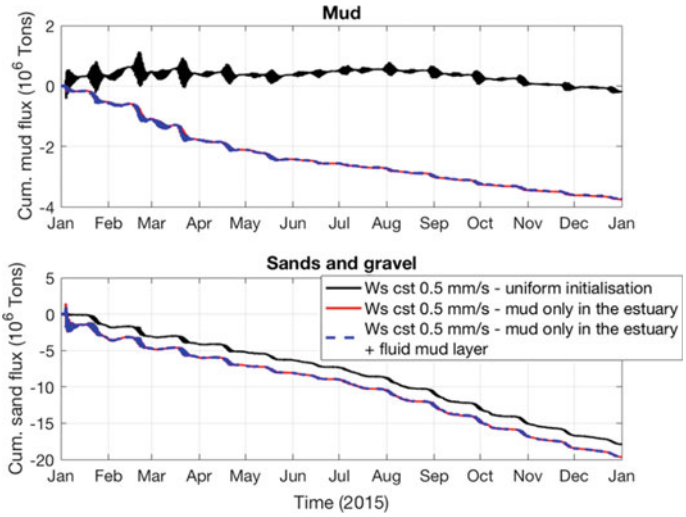

Fig. 12 Cumulative sediment fluxes (in millions of tons) through the cross-section described in Fig. 6, in relation to different initial sediment distributions. Upper panel: mud fluxes. Lower panel: sum of the fluxes for the non-cohesive classes. Positive values depict import into the estuary and negative values represent export to the sea

to limit horizontal advection. Another interesting point lies in the fact that the variable settling velocity with the minimum bound of 0.1 mm/s is almost mixed up with the constant value of 2 mm/s. Their values being rather different, this could be due to different behavior: the mud with the variable settling velocity may be easily exported when the settling velocity values are low, while the constant 2 mm/s settling velocity behavior may be due to a reduced horizontal advection. Indeed, the particles are likely to deposit quickly with a 2 mm/s value and do not remain suspended, which induces less import and less export as well.

Considering the sand and gravel behaviour, Fig. 11 lower panel suggests that it can be sensitive to the mud settling velocity. This is due to the mixed sediment erosion law, which depends on the superficial mud content. Therefore, changing the cohesive deposition dynamics through mud settling velocity impacts the non-cohesive erosion fluxes.

As for Fig. 12, it firstly suggests that the initial available mass of mud determines the sediment fluxes. If no mud is initially available over the continental shelf, the estuarine mud is exported to the sea. If there is enough mud over the whole domain, the export is compensated and even exceeded by mud import into the estuary. The resulting flux is directed towards the estuary, but it seems that at the end of the year, the tendency is reversed and the flux is directed seaward. This could be due to the high river flow period (November to May (Castaing and Allen 1981)) which tends to increase the mud export. Moreover, it can clearly be seen on Fig. 12 that the initial fluid mud layer of 4 millions of tons does not influence the sediment fluxes through the considered section. As for the sand and gravel fluxes, their analysis on Fig. 12

lower panel confirms what was observed before: their export is reduced when there is more mud within the estuarine system, at the beginning of the simulation.

5 Conclusions and Perspectives

In this chapter, the hydrodynamics and suspended sediment dynamics of the macrotidal Gironde Estuary were presented and a realistic 3D multi-class and multi-layer numerical model was implemented. This model, forced by winds, tides and river flow, fairly well reproduced the observed hydrodynamics. The sediment transport has not yet been calibrated and validated and the ETM mass at the end of one year simulation is underestimated.

A sensitivity analysis is conducted. The idea is to study the impact of key empirical sediment parameters on simulated suspended concentrations and on fluxes through the mouth of the estuary. The mud settling velocity and the initial sediment distribution were considered. The results confirm that mud particles with lower settling velocities tend to remain suspended longer, increasing the suspended sediment concentration. However, explicitly accounting for flocculation process in the settling velocity formulation (Van Leussen formulation) works the same way as increasing the settling velocity, which suggests that the maximum velocity boundary is reached most of the time. As expected, a lower settling velocity speeds up the particle export to the sea and when the settling velocity is high enough, the resulting flux at the mouth is directed towards the estuary. Another result stands in the sensitivity of the simulated sediment dynamics to the initial sediment bed distribution. Interestingly, the addition of 4 millions of tons of mud upstream, which is equivalent to the ETM mass, does neither impact the simulated ETM mass in the long term, nor the sediment fluxes through the mouth. This suggests that most of the fine sediments initially deposited in the estuary is trapped in the estuary, potentially in the intertidal lateral mudflats. Finally, the fluxes analysis revealed the sand and gravel transport is influenced by the mud content into the mixed sediment.

Results presented in this chapter are the first steps of a more integrated study. More parameters have to be analysed such as the erosion law formulation for mud and sand and the transition between a sandy and a muddy behavior (e.g. Mengual et al. 2017), which is currently linear. The wave-induced bed shear stress has to be accounted for as well. In addition, parameters for suspended sediment transport have to be calibrated in order to reproduce the expected ETM mass and the suspended sediment concentrations in the long term. Once the sediment model is calibrated and validated, it will be used to quantify sediment fluxes at the mouth under particular hydrometeorological events and to investigate the sediment accumulation and dispersion areas. The ultimate goal of this study is to better predict the transport and deposition of potentially contaminated particles, in the case of radionuclides pollution, not only in the Gironde estuary but also further offshore in the Bay of Biscay and along the adjacent coasts.

Acknowledgements This work has been done as part of the AMORAD project and received a state aid managed by the Agence Nationale de la Recherche (ANR) under the program Investissements d'avenir (AMORAD-ANR-11-RSNR-0002). The authors are thankful to the EPOC laboratory for providing the hydrodynamic measurements and the MAGEST data.

Appendices

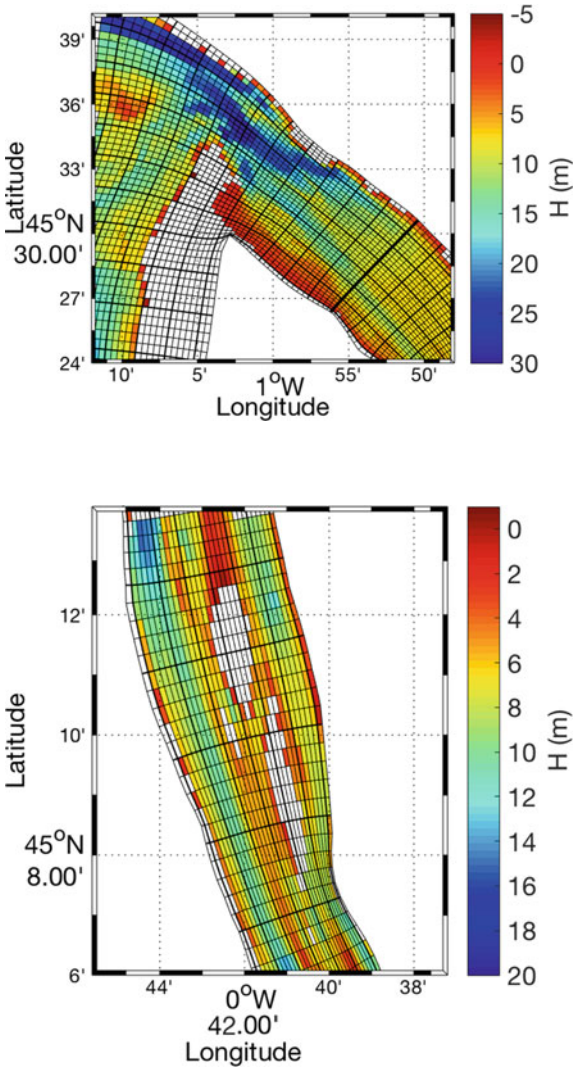

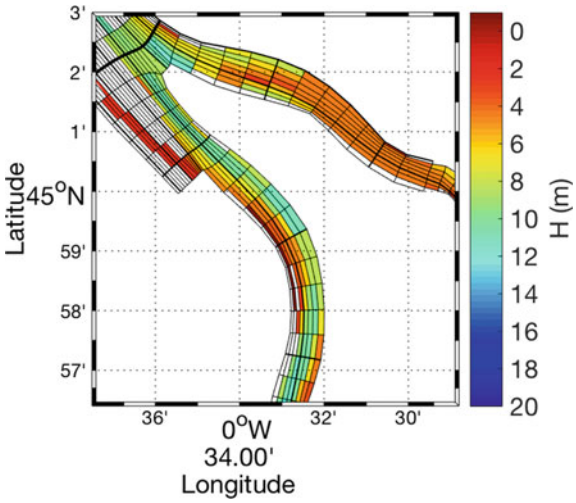

References

Allen, G.P. (1971). Déplacements saisonniers de la lentille de "crème de vase" dans l'estuaire de la Gironde*. C. R. Acad. Sci. Series D*: Vol. 273 (pp. 2429–2431). Paris.

Allen, G. P. (1973). *Etude des processus sédimentaires dans l'estuaire de la Gironde* (PhD Thesis). University Bordeaux I, p. 314.

Allen, G. P., & Castaing, P. (1977). Carte de répartition des sédiments superficiels sur le plateau continental du golfe de Gascogne. *Bulletin – Institut de Géologie du bassin d'Aquitaine (Bordeaux), 21,* 255–261.

Allen, G. P., Salomon, J. C., Bassoullet, P., Du Penhoat, Y., & de Grandpré, C. (1980). Effects of tides on mixing and suspended sediment transport in macrotidal estuaries. *Sedimentary Geology, 26*(1–3), 69–90.

Allen, G. P., Sauzay, G., Castaing, P. (1976). Transport and deposition of suspended sediment in the Gironde Estuary, France. In M. L. Wiley (Ed.), *Estuarine Processes* (pp. 63–81). New York: Academic Press.

Brenon, I., & Le Hir, P. (1999). Modelling the turbidity maximum in the Seine estuary (France): Identification of formation processes. *Estuarine Coastal and Shelf Science, 49*(4), 525–544.

Burchard, H., & Baumert, H. (1998). The formation of estuarine turbidity maxima due to density effects in the salt wedge. A hydrodynamic process study. *Journal of Physical Oceanography, 28*(2), 309–321.

Burchard, H., & Hetland, R. D. (2010). Quantifying the contributions of tidal straining and gravitational circulation to residual circulation in periodically stratified tidal estuaries. *Journal of Physical Oceanography, 40*(6), 1243–1262.

Burchard, H., Schuttelaars, H., & Ralston, D. (2018). Sediment Trapping in Estuaries. *Annual review of marine science, 10,* 371–395.

Castaing, P., & Allen, G. P. (1981). Mechanisms controlling seaward escape of suspended sediment from the Gironde: A macrotidal estuary in France. *Marine Geology, 40,* 101–118.

Doxaran, D., Froidefond, J.-M., Castaing, P., & Babin, M. (2009). Dynamics of the turbidity maximum zone in a macrotidal estuary (the Gironde, France): Observations from field and MODIS satellite data. *Estuarine Coastal and Shelf Science, 81,* 321–332.

Festa, J. F., & Hansen, D. V. (1978). Turbidity maxima in partially mixed estuaries: A two-dimensional numerical model. *Estuarine and Coastal Marine Science, 7,* 347–359.

Fuentes-Cid, A., Etcheber, H., Schmidt, S., Abril, G., De-Oliveira, E., Lepage, M., et al. (2014). Dynamics of coarse particulate matter in the turbidity maximum zone of the Gironde Estuary. *Comptes Rendus Geoscience, 346*(1–2), 28–36.

Geyer, W. R. (1993). The importance of suppression of turbulence by stratification on the estuarine turbidity maximum. *Estuaries, 16*(l), 113–125.

Grasso, F., Le Hir, P., & Bassoullet, P. (2015). Numerical modelling of mixed-sediment consolidation. *Ocean Dynamics, 65*(4), 607–616.

Grasso, F., Verney, R., Le Hir, P., Thouvenin, B., Schulz, E., Kervella, Y., et al. (2018). Suspended sediment dynamics in the macrotidal Seine Estuary (France): 1. Numerical modeling of turbidity maximum dynamics. *Journal of Geophysical Research Oceans, 123*(1), 558–577.

Jalon-Rojas, I., Schmidt, S., & Sottolichio, A. (2015). Turbidity in the fluvial Gironde Estuary (SW France) based on 10-year continuous monitoring: sensitivity to hydrological conditions. *Hydrology and Earth System Sciences Discussions, 12*(3), 2805–2819.

Jouanneau, J. M., Weber, O., Cremer, M., & Castaing, P. (1999). Fine-grained sediment budget on the continental margin of the Bay of Biscay. *Deep-Sea Research II, 46*(10), 2205–2220.

Lazure, P., & Dumas, F. (2008). An external-internal mode coupling for a 3D hydrodynamical model for applications at regional scale (MARS). *Advances in Water Resources, 31,* 233–250.

Le Floch, J. F. (1961). *Propagation de la marée dans l'estuaire de la Seine et en Seine-Maritime* (Ph.D. thesis). University of Paris, France, p. 507.

Le Hir, P., Cann, P., Waeles, B., Jestin, H., & Bassoulet, P. (2008). Erodibility of natural sediments: Experiments on sand/mud mixtures from laboratory and field erosion tests. *Proceedings in Marine Science, 9,* 137–153.

Le Hir, P., Cayocca, F., & Waeles, B. (2011). Dynamics of sand and mud mixtures: A multiprocess-based modelling strategy. *Continental Shelf Research, 31*(10), 135–149.

Le Hir, P., Ficht, A., Jacinto, R. S., Lesueur, P., Dupont, J.-P., Lafite, R., et al. (2001). Fine sediment transport and accumulations at the mouth of the Seine estuary (France). *Estuaries, 24*(6), 950–963.

Lesueur, P., Tastet, J. P., & Marambat, L. (1996). Shelf mud fields formation within historical times: Examples from offshore the Gironde estuary, France. *Continental Shelf Research, 16*(14), 1849–1870.

Lesueur, P., Tastet, J. P., & Weber, O. (2002). Origin and morphosedimentary evolution of fine-grained modern continental shelf deposits: the Gironde mud fields (Bay of Biscay, France). *Sedimentology, 49*(6), 1299–1320.

Mengual, B., Le Hir, P., Cayocca, F., & Garlan, T. (2017). Modelling fine sediment dynamics: Towards a common erosion law for fine sand, mud and mixtures. *Water, 9*(8), 1–15.

Partheniades, E. (1965). Erosion and deposition of cohesive soils. *Journal of the Hydraulics Division, 91*(1), 105–139.

Roberts, D. A. (2012). Causes and ecological effects of resuspended contaminated sediments (RCS) in marine environments. *Environment International, 40,* 230–243.

Roland, A., & Ardhuin, F. (2014). On the developments of spectral wave models: Numerics and parameterizations for the coastal ocean. *Ocean Dynamics, 64*(6), 833–846.

Ross, L., Valle-Levinson, A., Sottolichio, A., & Huybrechts, N. (2017). Lateral variability of subtidal flow at the mid-reaches of a macrotidal estuary. *Journal of Geophysical Research Oceans, 122*(9), 7651–7673.

Savoye, N., David, V., Morisseau, F., Etcheber, H., Abril, G., Billy, I., et al. (2012). Origin and composition of particulate organic matter in a macrotidal turbid estuary: The Gironde Estuary, France. *Estuarine Coastal and Shelf Science, 108,* 16–28.

Schulz, E., Grasso, F., Le Hir, P., Verney, R., & Thouvenin, B. (2018). Suspended sediment dynamics in the macrotidal seine Estuary (France): 2. numerical modeling of sediment fluxes and budgets under typical hydrological and meteorological conditions. *Journal of Geophysical Research Oceans, 123*(1), 578–600.

Simpson, J. H., Brown, J., Matthews, J., & Allen, G. (1990). Tidal straining, density currents, and stirring in the control of estuarine stratification. *Estuaries, 13*(2), 125–132.

Sottolichio, A., & Castaing, P. (1999). A synthesis on seasonal dynamics of highly-concentrated structures in the Gironde Estuary. *Comptes Rendus de l'Académie des Sciences, Serie IIa, Earth and Planetary Science, 329,* 795–800.

Sottolichio, A., Castaing, P., Etcheber, H., Maneux, E., Schmeltz, M., & Schmidt, S. (2011). Observations of suspended sediment dynamics in a highly turbid macrotidal estuary, derived from continuous monitoring. *Journal of Coastal Research, 64,* 1579–1583.

Soulsby, R. (1997). *Dynamics of marine sands: A manual for practical applications*. Thomas Telford.

Toublanc, F., Brenon, I., & Coulombier, T. (2016). Formation and structure of the turbidity maximum in the macrotidal Charente estuary (France): Influence of fluvial and tidal forcing. *Estuarine Coastal and Shelf Science, 169,* 1–14.

Uncles, R., & Stephens, J. (1989). Distributions of suspended sediment at high water in a macrotidal estuary. *Journal of Geophysical Research Oceans, 94*(C10), 14395–14405.

Van Leussen, W. (1994). Estuarine macroflocs and their role in fine-grained sediment transport, Ministry of Transport. In *Public Works and Water Management*, National Institute for Coastal and Marine Management (RIKZ).

Tidal Wave Propagation in the Flat Basin Under Wind Monsoon Climate

Hung M. Phan, Ad J. H. M. Reniers, Marcel J. F. Stive and Qinghua Ye

Abstract Tide is influenced due to not only mainly tide generating force but also local wind and weather patterns. The East Asian monsoons cause strong seasonal climatic variations in the Mekong Delta. A two-dimensional, barotropic numerical model was employed to investigate the dynamics of tidal wave propagation in the South China Sea with a particular interest for its characteristics along the Mekong deltaic coast under wind monsoon climate. The results reveal that wind monsoon climate could causes damped or amplified tidal amplitudes around Mekong deltaic coast approximately 2–3 cm due to the changing atmospheric pressure, the tangential stress of wind over the water surface, and wind enhanced bottom friction. The monsoon climate influences rather strongly on the M_2 semidiurnal tide system in the eastern Mekong deltaic coast, meanwhile the monsoon climate controls K_1 diurnal tide in the western region of Mekong delta.

Keywords Tidal wave propagation · Wind monsoon climate · Mekong deltaic coast · Delft3D

1 Introduction

Tide is the one of fundamental forces influencing hydrodynamic processes and morphology on numerous natural beaches in general as well as Mekong deltaic coast in particular (Fig. 1). Besides mainly tide generating force, tides can also be influenced by local wind and weather patterns. The wind driven contribution to flow and water level changes the tidal amplitude (Wijeratne et al. 2012). The monsoon winds in the South China Sea are caused by the influence of the trade winds and the seasonal change between the location of the earth and the sun. The East Asian monsoons cause strong seasonal climatic variations in the Mekong Delta (Hordoir et al. 2006).

H. M. Phan (✉) · A. J. H. M. Reniers · M. J. F. Stive
Hydraulic Engineering Department, Delft University of Technology, Delft, Netherlands
e-mail: m.h.phan@tudelft.nl

Q. Ye
Software Development Unit, Deltares, Delft, Netherlands

K. D. Nguyen et al. (eds.), *Estuaries and Coastal Zones in Times of Global Change*, Springer Water,
https://doi.org/10.1007/978-981-15-2081-5_22

Fig. 1 Mekong deltaic coast in Travinh province

Winds are coming mostly from north-east directions in the winter monsoon season from November to April and south-west winds prevail during the summer monsoon. Annual wind speeds have been recorded from 1999 to 2008 by the Southern Regional Hydro-Meteorological Center (Unverricht et al. 2014) at Vung Tau station ranging from 7 to 9 m/s and in Bac Lieu from 6 to 8 m/s. Under stormy conditions wind speeds can reach 20–30 m/s (Institute of Strategy and Policy on natural resources and environment ISPONRE 2009). The maximum wind stress prevails along the south-eastern coast of Vietnam in both monsoon seasons (Unverricht et al. 2014).

Although previous studies (e.g. Wyrtki 1961) agree that the circulation of the SCS is affected mostly by monsoon winds, these studies do not distinguish the different effects between the north east monsoon and the south west monsoon to tidal wave systems. Therefore, it is necessary to clarify the role of wind climate monsoon influencing the tidal wave propagation in the Mekong delta. The mechanisms of tidal wave propagation in the Mekong delta shelf are revealed with the aid of the high-resolution process based model Delft3D.

2 Method

2.1 Model Set up

The depth- averaged tidal dynamics model for the whole South China Sea has been constructed using Delft3D-FLOW, which includes the shallow water equations, the continuity equations and the transport equations for conservative constituents. This

model ranges from 96°–126°E and from 8°S to 24°N with flexible orthogonal mesh features with grid cell sizes nearly 22 km near the offshore boundaries and gradually reducing to 4 km around Mekong deltaic coast. The finer grids are necessary to resolve the topography needed for an accurate simulation. A total of 8 primary tidal constituents (O1, K1, P1, Q1, M2, S2, K2, N2) derived from 15 years of Topex-Poseidon and Jason-1 satellite altimetry (Gerritsen et al. 2003) adjusted to GMT 7 + have been applied for tidal simulations at 8 main boundaries, viz. Taiwan Strait, Luzon Strait, Celebes Zee, Flores Zee, Sape Strait, Lombok Strait, Sunda Strait and Andaman Zee.

The bathymetry data shown in Fig. 2a are obtained, from the General Bathymetric Chart of the Oceans (GEBCO) bathymetry database with 30 arc-second grid resolution. Higher resolution bathymetry data along Mekong deltaic coast are obtained by a bathymetry survey of the Mekong deltaic coast in 2009 and 2010 in the context of a Vietnam Government project (SIWRR 2010). The bed friction coefficient is 0.026 $m^{-1/3}$ s globally with some local values of n = 0.015 $m^{-1/3}$ s on the Vietnamese shelf and a value of n = 0.5 $m^{-1/3}$ s across the archipelagos separating the Sulu Sea from the South China Sea and the Celebes Sea accounting for the effect of partly unresolved islands and underwater ridges. As the model domain covers a large area and the water depth of several sections is relatively deep, TGF are included in this model and calculated including the equilibrium tide and the earth tide. In the model, the TGF of 10 tidal constituents (M2, S2, N2, K2, K1, O1, P1, Q1, MF, and MM) are considered. The six branches of the Mekong River are included as river boundaries with hourly discharges. The value for the horizontal eddy viscosity depends on the flow and the grid size used in the simulation. Because of the large area with grid sizes of kilometers, the horizontal eddy viscosity is specified at 250 m^2/s (Gerritsen et al. 2003). wind data available from NOAA.

2.2 Model Results Validation

The simulation is carried out for the whole year of 2014 using a time step of 5 min at zero initial conditions. In the whole South China Sea, along the coast of the Mekong Delta on the southern Vietnam shelf, 41 tidal stations were selected for model verification. Practical error measures for a tidal constituent k are the summed vector difference and root mean square error over selected observations:

$$\mathrm{SVD_k} = \sum_{s=1}^{s=s\max} \mathrm{VD_{k,s}}$$

$$\mathrm{VD_{k,s}} = \sqrt{(\mathrm{H_{c,k}cosG_{c,k}} - \mathrm{H_{o,k}cosG_{o,k}})^2 + \left(\mathrm{H_{c,k}sinG_{c,k}} - \mathrm{H_{o,k}\,sin\,G_{o,k}}\right)^2}$$

where $H_{c,k}, G_{c,k}, H_{o,k}, G_{o,k}$ are the computed and observed astronomical amplitude and phase of a tidal constituent k.

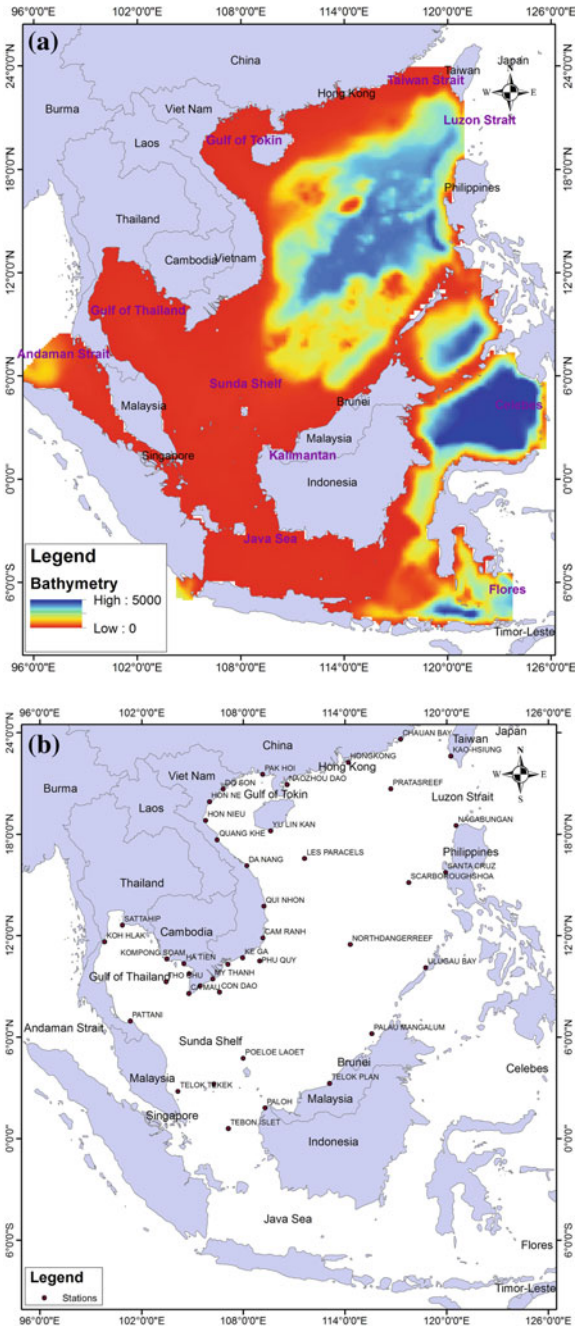

Fig. 2 **a** Bathymetry and **b** tidal data stations in the South China Sea

The RMSE of the complex amplitude is $\sqrt{\frac{1}{2N}\sum_{i=1}^{N}|H_{Si}-H_{Oi}|^2}$

where N is the number of the observation stations; H_{Si} and H_{Oi} are the model simulated and observation amplitude at station i, respectively.

Computed astronomical amplitudes and phases are analysed by a tidal harmonic analysis program called Delft3D-TIDE tool. The astronomical tide observed in oceans and seas is directly or indirectly the result of gravitational forces acting between the sun, moon, and earth. The influence of other celestial bodies is negligibly small. The observed tidal motion can be described in terms of a series of simple harmonic constituent motions, each with its own characteristic frequency l (angular velocity). The amplitudes A and phases G of the constituents vary with the positions where the tide is observed. The general formula for the astronomical tide is:

$$H(t) = A_0 + \sum_{i=1}^{k} A_i F_i \cos(w_i t + (V_0 + u)_i - G_i$$

Where: H(t): water level at time t; A_0: mean water level over a certain period; K: number of relevant constituents; I: index of a constituent; A_i: local tidal amplitude of a constituent; F_i: nodal amplitude factor; W_i: angular velocity; $(V_0 + u)_i$: astronomical argument; G_i: improved kappa number (=local phase lag).

The Delft3D-TIDE tool is formulated in terms of k relevant constituents, a total of (2 k +1) unknowns A0, Ai and Gi must be determined (or (2 k +2) unknowns, if Bt is included). This is realised by minimisation of the quantity: $\sum(W(t) - H(t))^2$ using a least—squares technique.

The harmonic constants of water level from 41 observation stations shown in Fig. 2b are collected from the International Hydrographic Organization (IHO) tidal dataset, published papers by Fang et al. (1999), Zu et al. (2008), permanent stations of Vietnam southern regional hydrometeorological center as well as the Global Tide Model. The Global Tide Model is developed by DTU Space (DTU10). The Global Tide Model is available on a 0.125 × 0.125 degree resolution grid for the major 10 constituents in the tidal spectra. This model is utilizing the latest 17 years multi-mission measurements from TOPEX/Poseidon, Jason-1 and Jason-2 satellite altimetry. The computed and observed harmonic constants are listed together for comparison (Fig. 3).

3 Results and Discussion

While climate seasonality is produced by the tilting of the Earth, monsoon climate systems are a consequence of the land-sea temperature differences affected by solar radiation (Huffman et al. 1997). The monsoon climate is an atmospheric flow over Asia and is variable greatly depending on the Siberian High and the Arctic Oscillation (Wang et al. 2012). The Southeast Asia countries are controlled by the monsoon climate, which is a large-scale seasonal reversals of the wind system (Serreze

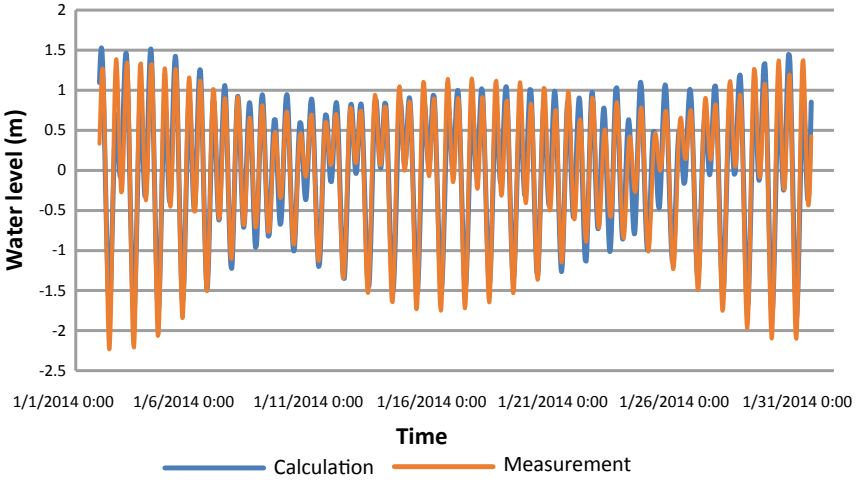

Fig. 3 Calculated and measured water level at Vungtau station

et al. 2010). The two main monsoon regimes are specifically named the northeast monsoon (winter monsoon) from November to April and the southwest monsoon (summer monsoon) from late May to September. Furthermore, October is the transition month from the southwest to northeast monsoon seasons (Cruz et al. 2012). The summer monsoon occurs when rainfall touches maximum during the boreal winter, whereas the winter monsoon takes place during boreal summer where rainfall reaches maximum.

Fluctuations of sea level are superimposed upon regular tidal oscillations. In addition to the temporary and often dramatic variations in sea level due to tsunamis, hurricanes and other storms, variations in the predicted sea level frequently occur in association with the regular path of cyclonic disturbances across the coastal waters. These changes in sea level may be attributed in part to modifications to the changing atmospheric pressure and in part to the build-up or reduction of water at the coast due to the tangential stress of wind over the water surface. The pressure gradients in the horizontal momentum equations for water of constant density (Deltares 2014) are computed by:

$$\frac{1}{\rho}P_x = g\frac{\partial \zeta}{\partial x}, \quad \frac{1}{\rho}P_y = g\frac{\partial \zeta}{\partial x}$$

where in ρ are the density of water, respectively, Px and Py are the horizontal pressure terms in the Cartesian horizontal x, y direction, ζ is water level above some horizontal plane of reference, g is acceleration due to gravity.

The steady state effect of wind stress on the free surface, wind is implemented as a uniform shear stress, based on the wind data available shown in Fig. 4 from NOAA included in the momentum equations. Wind stress magnitudes (Deltares 2014) are

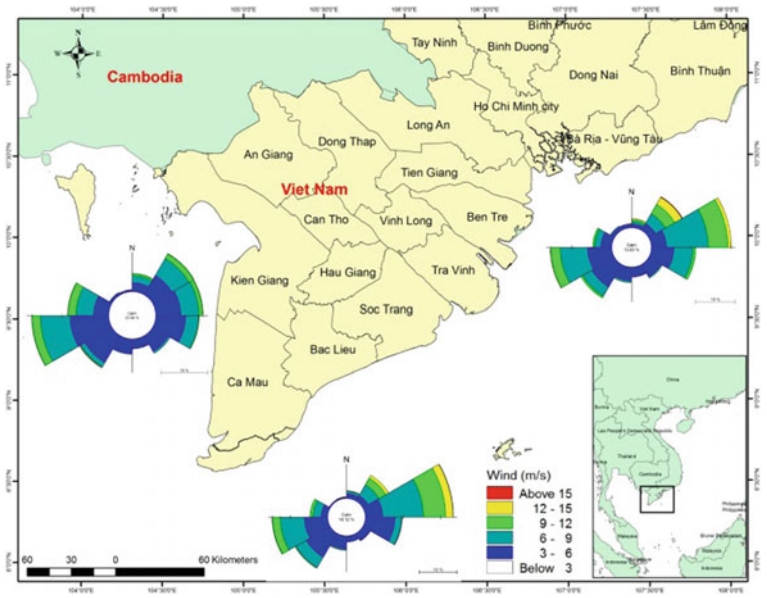

Fig. 4 Wind rose maps in Mekong deltaic coast

computed by:

$$\left|\overrightarrow{\tau_w}\right| = \rho_\alpha C_d U_{10}^2$$

where in ρ_α is the density of air (kg/m3), U_{10} the wind speed 10 m above the free surface (m/s) and C_d the wind drag coefficient.

Besides, Ruessink et al. (2006) showed that wind driven flow enhanced friction during the flood phase of a tidal cycle more than it reduced friction during the ebb flow, thereby increasing the friction over the tidal cycle and reducing the tide current range. Jones and Davies (2008) showed that changes in the bottom stress affect tidal elevations and currents in shallow sea during prevailing wind. The bed stress ((τ_b) $^{\rightarrow}$) is modeled as a quadratic friction based on the magnitude of the Eulerian velocity in the first layer above the bed ((u_b) $^{\rightarrow}$) (Deltares 2014):

$$\overrightarrow{\tau_b} = \frac{g\rho_0 \overrightarrow{u_b}\left|\overrightarrow{u_b}\right|}{C_{2D}^2}$$

where C2D is the 2D-Chézy coefficient (based on calibration of water levels), ρ_0is the density of water body.

Figure 5a, b show the difference of M2 semidiurnal tidal amplitudes and co-phase lines between original condition and wind climate monsoon condition. The results in the winter monsoon climate show that atmospheric forcing attenuates the M2 tidal amplitude up to 2.5 cm at Soc Trang province on the eastern Mekong deltaic coast,

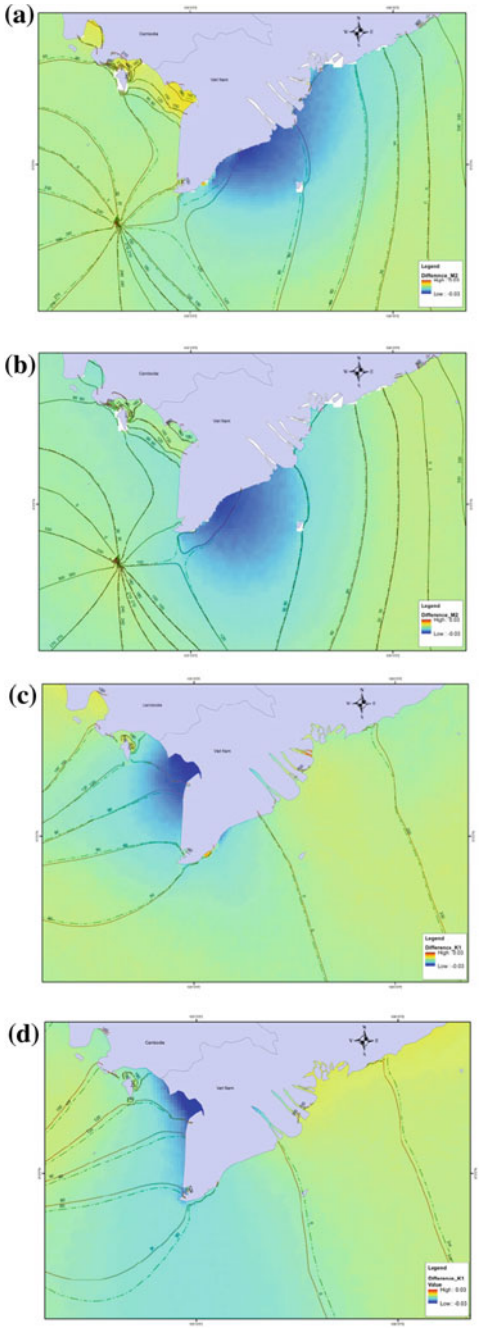

Fig. 5 Phase and amplitude difference of M2, K1 in case of wind climate monsoon in winter **a**, **c** summer **b**, **d**, brown and green lines represent the co-phase lines of case original condition and case of wind climate monsoon

meanwhile the difference of M2 tidal phase is insignificant only 3–4 min. In the summer monsoon, the M2 tidal amplitude is similarly damped until roughly 2 cm by wind forcing from a dominant southwest direction. The intensity of the M2 tidal amplitude attenuation in the summer monsoon moves southward compared with the winter monsoon as a result of distributive spatial difference of wind strength and atmospheric pressure in the climate monsoon.

Similarly, the change of the K1 semidiurnal tidal amplitudes and co-phase lines between the original condition and the wind climate monsoon condition are shown in Fig. 5c, d. Different from the M2 semidiurnal tide, the K1 diurnal tide is attenuated by an average of 1–2 cm in the western Mekong deltaic coast due to the distribution of tidal characteristic in around Mekong deltaic coast. The largest damped K1 diurnal amplitude amounts to 2.5–2.6 cm along the Kiengiang coast in both the winter and summer monsoon climate. Like for the M2 tide, the difference of K1 tidal phases is minor, i.e. only 8–10 min. Therefore, the influence of wind climate monsoon through the wind stress on the surface as well as the bed stress varies from region to region. The monsoon climate influences rather strongly on semidiurnal tide in the eastern Mekong deltaic coast, inversely the diurnal tide is affected quite considerably by the monsoon climate in the western region of Mekong delta.

4 Conclusion

A two-dimensional tidal model is constructed with a high resolution to allow the simulation of accurate tidal wave propagation in the South China Sea as well as along the Mekong deltaic coast under wind monsoon climate. The effect of the wind monsoon climate to the tidal wave system in this flat basin is investigated. The results reveal that atmospheric forcing in the monsoon climate could cause damped or amplified tides along the Mekong deltaic coast. The monsoon climate influences rather strongly on the M_2 semidiurnal tide system in the eastern Mekong deltaic coast, meanwhile the monsoon climate controls K_1 diurnal tide in the western region of Mekong delta.

References

Cruz, F. T., Narisma, T. G., Villafuerte, M. Q., Cheng, K. U. C., & Olaguera, L. M. (2012). A climatological analysis of the southwest monsoon rainfall in the Philippines. *Atmospheric Research, 122*(2012), 609–616.

Deltares (2014). User manual, Delft3D Flow, Deltares, Delft, the Netherlands.

Fang, G., Kwok, Y. K., Yu, K., & Zhu, Y. (1999). Numerical simulation of principal tidal constituents in the South China Sea, Gulf of Tokin and Gulf of Thailand. *Continental Shelf Research, 19,* 845–869.

Gerritsen, H., Schrama, E. J. O., Van der Boogaard, H. F. P. (2003). Tidal model validation of the seas of South East Asia using altimeter data and adjoint modelling. In *Proceedings of the 30th IAHR Congress*, Thessaloniki (Vol. D, pp. 239–246).

Hordoir, R., Polcher, J., Brun-Cottan, J.-C., & Madec, G. (2006). Towards a parametrization of river discharges into ocean general circulation models: A closure through energy conservation. *Climate Dynamics, 31*(7–8), 891–908.

Huffman, G. J., Adler, R. F., Arkin, P., Chang, A., Ferraro, R., Gruber, A., et al. (1997). The Global Precipitation Climatology Project (GPCP) combined precipitation dataset. *Bulletin of the American Meteorological Society, 78,* 5–20.

Institute of Strategy and Policy on natural resources and environment (ISPONRE). (2009). *Vietnam Assessment Report on Climate Change.* 127.

Jones, JE., Davies, AM. (2008) On the modification of tides in shallow water regions by wind effects. *Journal of Geophysical Research, 113* (C5).

Ruessink, B. G., Houwman, K. T., Grasmeijer, B. T. (2006) Modeling the nonlinear effect of wind on rectilinear tidal flow. *Journal of Geophysical Research-Oceans, 111*(C10002). http://dx.doi.org/10.1029/2006JC003570.

Serreze, R. G., Barry, R. G., and Chorley, R. J. (2010). *Atmosphere, Weather and Climate.* Routledge, Oxon.

Southern Institute of Water Resources Research (SIWRR). (2010). *Project for measurements of bathymetry, hydrodynamics in estuaries and coastal zone of Mekong delta from 2009 to 2010*. http://www.siwrr.org.vn/?id=nckh5 (in Vietnamese).

Unverricht, D., Nguyen, T. C., Heinrich, C., Szczucinski, W., Lahajnar, N., & Stattegger, K. (2014). Suspended sediment dynamics during the inter-monsoon season in the subaqueous Mekong Delta and adjacent shelf, southern Vietnam. *Journal of Ansian Earth Sciences, 79,* 509–519.

Wang, L., Li, J., Lu, H., Gu, Z., Rioual, P., Hao, Q., et al. (2012). The East Asian winter monsoon over the last 15,000 years: Its links to high-latitudes and tropical climate systems and complex correlation to the summer monsoon. *Quaternary Science Reviews, 32,* 131–142.

Wijeratne, E. M. S., Pattiaratchi, C., Eliot, M., & Haigh, I. D. (2012). Tidal characteristics in Bass Strait, south–east Australia. *Estuarine Coastal and Shelf Science, 114,* 156–165.

Wyrtki, K. (1961). *Physical oceanography of the Southeast Asian waters*. Scientific Results of Marine Investigations of the South China Sea and the Gulf of Thailand 1959–1961 (NAGA Report. 2). La Jolla, California: Scripps Institution of Oceanography, P. 195.

Zu, T., Gan, J., & Erofeeva, S. Y. (2008). Numerical study of the tide and tidal dynamics in the South China Sea. *Deep Sea Research I, 55,* 137–154.

Study on Sediment Test of the Physical Model at Pearl River Estuary

Chen Lu, Xiaozhang Hu, Yugui Yang and Yao Wu

Abstract Based on the analysis of hydrodynamics and sediment transport in the Pearl River Estuary, key techniques for modelling depositional and erosional patterns with physical model are detected. According to the exploration of distinct sediment characteristics and regional setting in Modaomen Estuary, Huangmao Sea and Lingding Bay, different modelling techniques were presented, which aids in the improvement of model results. Since the complex sediment transport process with fluvial and marine hydrodynamics in estuarine regions, key technologies in sediment experiments, including the synchronous simulation of tidal current and wave, automatic control of sediment adding system, were introduced. Additionally, by characterizing the sediment transport and key technical issues in the region, simulations and verifications of currents, waves, and sediments were carried out. Furthermore, the application of physical model in the simulation of sediment erosion and accretion with the impact of the Hong Kong-Zhuhai-Macao Bridge construction were displayed. The results indicated that the model can satisfy the similarity of flow movement and sediment siltation, which provides an important technical support for project construction.

Keywords Sediment experiment · Similarity scale · Physical model · Hong Kong-Zhuhai-Macau bridge

1 Introduction

The Pearl River Estuary, located in Guangdong Province, is the most prosperous region of southern China (Zhou et al. 2018). Three main tributaries of the Pearl River, the West River, the North River and the East River are characterized by multiple

C. Lu (✉) · X. Hu · Y. Yang · Y. Wu
Pearl River Hydraulic Research Institute, Pearl River Water Resources Commission, Guangzhou, China
e-mail: ganghangluchen@163.com

Key Laboratory of Estuarine Dynamics and Environment, The Ministry of Water Resources, Guangzhou, China

K. D. Nguyen et al. (eds.), *Estuaries and Coastal Zones in Times of Global Change*, Springer Water,
https://doi.org/10.1007/978-981-15-2081-5_23

avulsions, branching out into over 324 channels, which makes the Pearl River one of the most complex-structured river networks in the world (Wu et al. 2018). The Pearl River pours into the South China Sea through eight river mouths, including Humen estuary, Jiaomen estuary, Hongqimen estuary, Hengmen estuary, Modaomen Estuary, Jitimen estuary, Hutiaomen estuary and Yamen estuary (Fig. 1). Multiple fluvial and marine physical factors, including runoff, tide, wave, as well as salinity and bathymetry variations, controls the sediment erosion and deposition patterns (Wu et al. 2018).

Since the 1980s, the Pearl River Estuary has experienced highly economic development and rapid population growth. In 2016, the gross domestic product (GDP) of the Pearl River Delta was $1084 billion, accounting for about 10% of that of China.

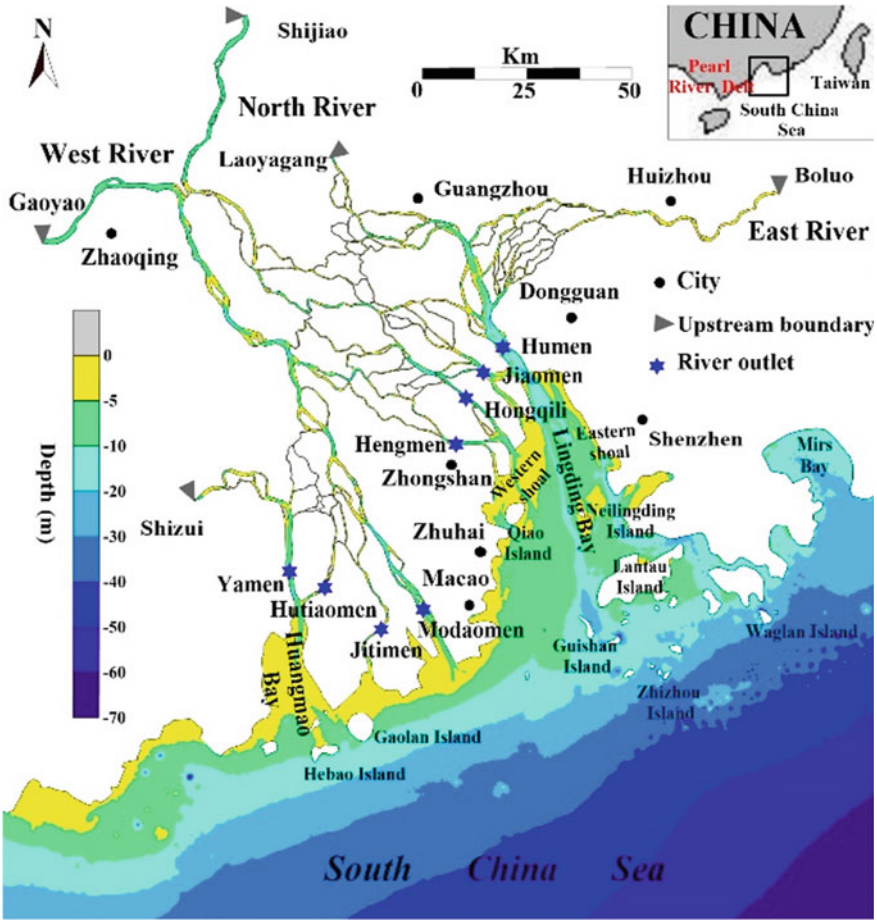

Fig. 1 The location of the Pearl River Estuary

Numerous anthropogenic engineering, such as reclamation, navigation channels, airports and bridges, have been constructed in the estuarine region in order to meet the social and economic demands. In 2017, the Guangdong-Hong Kong-Macao Greater Bay Area strategy was proposed, indicating more water-related projects would be implemented in the near future. Accordingly, human activities have exerted substantial influences on the hydrodynamics and sediment transport, which needs further researches.

Physical model has been proved to be an effective way to evaluated the changing regime of hydrodynamic and sediment transport, relating to different anthropogenic disturbances (Si et al. 2017; Wu et al. 2019). The global physical model of the Pearl River Estuary has been constructed in the early 21st century, which has played a significant role on studying the impacts of major projects on the hydrodynamic regime and the regulation of the estuary (Fagherazzi et al. 2015; Wolinsky et al. 2010). In order to meet the requirements of the controlling boundary of physical model, the global physical model of the Pearl River Estuary covers the river network of the Pearl River Delta and the shallow sea of the Pearl River Estuary. The length of the global physical model is about 150 m while the width is about 100 m. The upper boundary is at the confluence and bifurcation of West River and North River. The lower boundary covers eight river mouths and reaches −20 m isobath. The scope of the model is shown in Fig. 2.

Due to the expansive water area in the physical model, different water areas are characterized by distinct hydrodynamic pattern and sediment characteristics (Zhang et al. 2013, 2016). Thus, the key simulation techniques in estuarine regions is to meet the similarity requirement of horizontal distribution of water level and velocity. In the river network, similarity scale of flow process and water level also should be satisfied. According to the in situ hydrodynamic and sediment characteristics, the main parts of the Pearl River Estuary, the Lingding Bay, the Modaomen Estuary area and the Huangmao Sea were separated set up in the physical model. Moreover, the plane scale of the physical model is 700 and the vertical scale is 100. Thus, the distortion ratio of the model is 7, which is suitable for the modelling in estuarine region (Lazarus 2016). Based on the plane and vertical scale, other important scales of the physical model associated with experiment results were displayed in Table 1. In this study, the key technical problems in different parts of estuary in sediment experiments were presented. Correspondingly, key techniques in sediment experiments by the global physical model were introduced. Finally, the application of physical model on the large-scale project, called the HongKong-Zhuhai-Macao Bridge in the Pearl River Estuary is illustrated in detail.

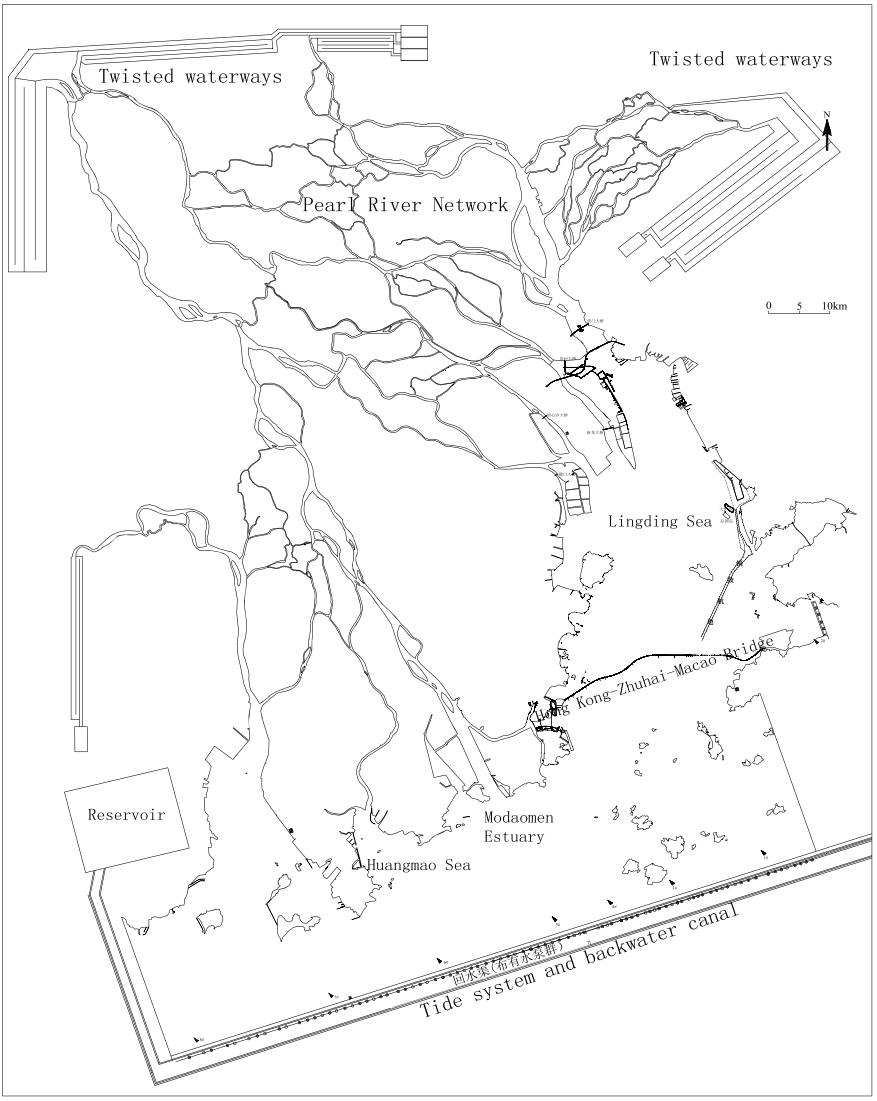

Fig. 2 The schematic diagram of the whole physical model of the Pearl River Estuary

Table 1 The scale of the physical model of Pearl River Estuary

Name	Plane scale	Vertical scale	Distortion ratio	Velocity scale	Roughness scale	Time scale	Flow scale
Symbol	λ_L	λ_H	η	λ_V	λ_n	λ_T	λ_Q
Value	700	100	7	10	0.814	70	700000

2 Regional Characteristics and Key Technical Problems in Sediment Experiments in the Pearl River Estuary

The sediment transport in different sub-estuaries of the Pearl River Estuary has distinct characteristics. In this study, the sediment characteristics relating to key technical problems in sediment experiments are respectively explained in three parts of estuary, the Modaomen Estuary, the Huangmao Sea and the Lingding Bay.

2.1 The Sediment Characteristics Relating to Experimental Techniques at Modaomen Estuary

The Modaomen Estuary is the outlet of the largest tributary of Pearl River, which shares most part of streamflow than other outlets, accounting for 28.3% of the whole discharge (Wu et al. 2018). The annual streamflow is about 92.3 billion m^3. The median size of the surficial sediment is about 0.010–0.160 mm on the shoal, which is larger than the median size of surficial sediment on the channel (0.003–0.009 mm).

The distribution of suspended sediment concentration in the Modaomen Estuary detected by remote sensing is shown in Fig. 3. The distributions of suspended sediment at wet season gradually decreases from the mouth to the open sea. The high sediment concentration concentrated in the main channel of West River, with the suspended sediment concentration more than 0.2 kg/m^3. When the streamflow with high suspended sediment transports to the river mouth, the sediment spreads to the surrounding region with the effect of the landform and the dilution of saltwater. As

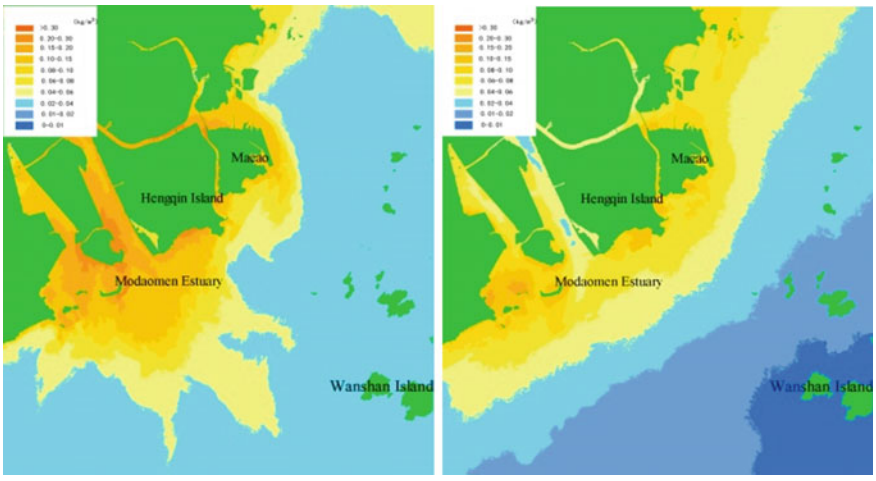

Fig. 3 The distribution of surface annual sediment concentration in Modaomen Estuary at flood (left) and dry (right) seasons

the plume flow with sediment further spreads seaside, the front edge extends to the -10 m isobaths, with the suspended sediment concentration ranging from 0.04 to 0.08 kg/m^3.

For the characteristic of suspended sediment concentration at dry season, the concentration is mainly influenced by wind and waves. The sediment distribution in the main channel of Hengzhou is characterized by "high west-low east", indicating the sediment concentration on the western shoal is higher than that on the eastern side. The suspended sediment close to the river outlet is mainly concentrated on the region near Jiaobeisha, Sisha, Sanzao Island, ranging from 0.10 to 0.20 kg/m^3.

The key technical problems in sediment experiment at Modaomen Estuary include that: (1) The wave impact plays a dominant role on the sediment transport in Modaomen, especially during the dry season, with few islands shielded. The sediment characteristic is thus mainly controlled by the wave power during the dry season. (2) Mouth bar is a typically morphological unit in the Modaomen Estuary (He et al. 2019). Significant sediment particle size sorting occurs in the vertical direction in the bar area. Different surficial sediment is found in the inner slope, outer slope and bar crest, which needs to be separately considered in the physical model. 3. Saltwater intrusion is a remarkable phenomenon in the Modaomen. The impact of saltwater associated with baroclinic influence on sediment transport should be payed attention in the sediment experiment.

2.2 The Sediment Characteristics Relating to Experimental Techniques at the Huangmao Sea

The Huangmao Sea locates at the western part of the Pearl River Estuary. It is characterized by tidal-dominated region while the streamflow maintains relatively low level. The median size of the surficial sediment is about 0.005–0.040 mm on the shoal, which is larger than the median size of surficial sediment on the channel (0.005–0.016 mm).

The distribution of suspended sediment concentration in the Huangmao Sea is displayed in Fig. 4. During the wet season, the distribution of suspended sediment in the Huangmao Sea is greatly affected by the streamflow. The suspended sediment distribution on the surface layer shows a decreasing trend from middle part of estuary to the lower part and from the northwest to the southeast. The high suspended sediment appears in the west shallow beach with the concentration more than 0.18 kg/m^3. As the results of the effect of runoff, the sediment are transported from the inside of bay to the outside. The suspended sediment concentration is below 0.04–0.06 kg/m^3.

In the dry season, the suspended sediment load from the upstream is much smaller than the wet season However, the distribution is roughly similar to that at wet season. The high suspended sediments in the bay appears in the west shallow beach, with the concentration more than 0.12 kg/m^3, which is mainly caused by the effect of the wind and waves lifting. Moreover, the water column in the southeast bay is affected

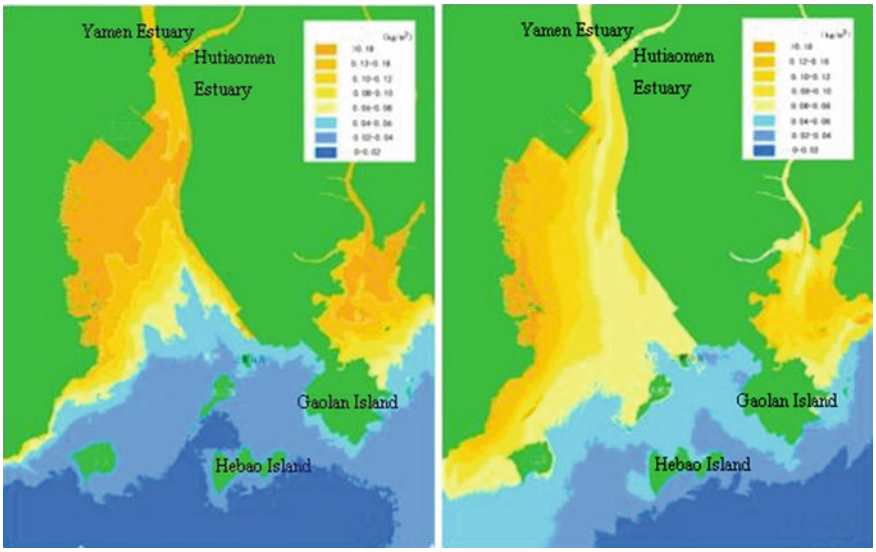

Fig. 4 The distribution of surface annual sediment concentration in Huangmao Sea at flood (left) and dry (right) seasons

by the high-salt and low-sediment waters in the open sea. The suspended sediment concentration relatively low, ranging from 0.04 to 0.06 kg/m^3, In the dry season, the resuspended sediment due to wind and wave on the shoal cannot be ignored. The suspended sediment concentration is even higher than that in the flood season.

The key technical problems in sediment experiment in the area of Huagmao sea include that: (1) The Gaolan Port in Zhuhai city is a large-scale project that affects the hydrodynamic regime. The embankment of the Gaolan Port has the potential to undermine the sediment-feeding channel from Jitimen estuary to the west. During the past 20 years, the Gaolan Port has been constructed and intermittently maintained. The boundary conditions of the water area thus constantly change, leading to enhancing the difficulty is the sediment experiment. (2) The Gaolan Port and its navigation channel are also important in sediment research. The water depth in this area is relatively large and several islands are found in the outlet of the Huangmao Sea, indicating the wave generally exerts relatively slight effect on the sediment movement. However, the Huangmao Sea area face the South China Sea where storm surge and typhoon waves are substantially responsible for sediment erosion and accretion.

2.3 The Sediment Characteristics Relating to Experimental Techniques at the Lingding Bay

The Lingding Bay locates at the eastern part of the Pearl River Estuary. It experiences relatively large tidal impact (Zhang et al. 2015). The median size of the surficial sediment is about 0.02–0.09 mm on the shoal, which is smaller than the median size of surficial sediment on the channel (0.03–0.38 mm) (Zhang et al. 2013).

The distribution of suspended sediment concentration in the Lingding Bay is displayed in Fig. 5. The distribution of suspended sediment in the Lingding Bay are high in the northwest but low in the southeast. Moreover, the suspended sediment in the upper part of estuary is higher than the lower part.

Based on the hydrological data collected since 1978, the sediment concentration in the Lingding Bay is between 0.12 and 0.2 kg/m^3. The sediment concentration in the west shoal is more than the east shoal. Additionally, the sediment concentration in the west shoal is larger than troughs. Larger sediment is found in the upper section of the west trough than the lower section, as well as the east trough. Moreover, the sediment concentration near the bay is between 0.04 and 0.08 kg/m^3.

There are two main sources of suspended sediment in the Lingding Bay. Apart from the fluvial sediment carried by the streamflow, another sediment source provided by wind and waves from the outer Lingding Bay is also remarkable. Therefore, the distribution of suspended sediment concentration is fundamentally limited by the multiple factors such as runoff, tide, wind wave and morphology (Wesselman et al. 2018) (Fig. 6).

The key technical problems in the sediment experiment in the Lingding Bay area are listed as follows: (1) Extensive shoal around the Lingding Bay has the potential

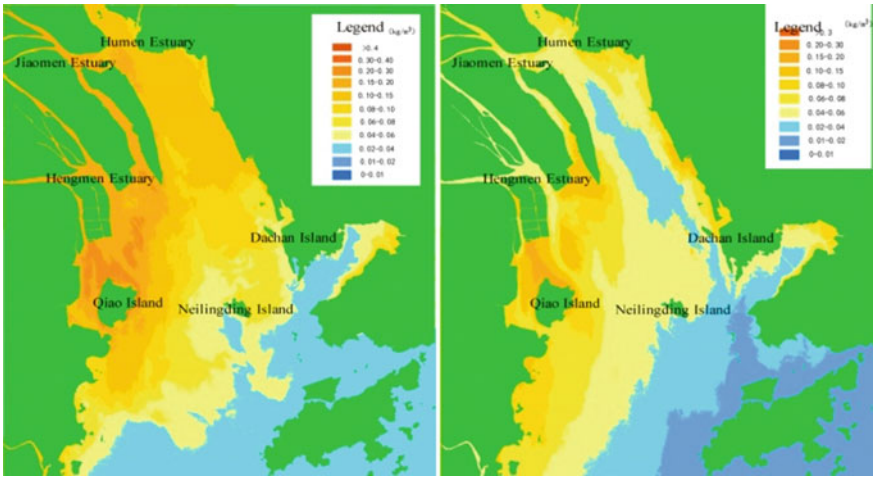

Fig. 5 The distribution of surface annual sediment concentration in Lingding Bay at flood (left) and dry (right) seasons

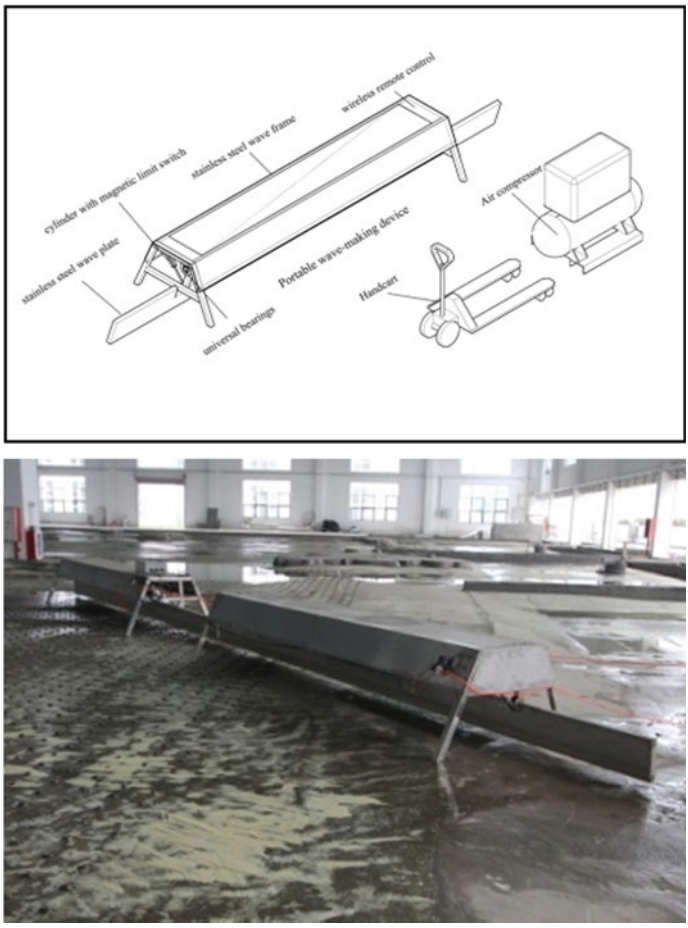

Fig. 6 Portable wave-making device

to be exposed during the intra-tidal process. The wave is an important driving force for sediment movement in shallow area, which needs to be considered in the physical model; (2) There are secondary transport of the sediment movement. So, it is difficult to choose the proper model parameters in the sediment experiment at present.

3 Key Techniques in Sediment Experiments in the Physical Model of the Pearl River Estuary

3.1 Main Practical Experiences in Sediment Experiments with the Physical Model

Based on the analysis of sediment characteristics and regional setting in the previous part, the sediment source and hydrodynamic mechanisms in different parts of the Pearl River estuary are distinct. Therefore, the sediment experiment with the global physical model could barely conduct a full-scale sedimentation test. According to the primary sediment characteristics in each part, the sediment experiment should be carried out in different subarea. The boundary condition of the three subareas, including the Lingding Bay, the Modaomen Estuary and the Huangmao Sea, can be separately controlled, which has been designed before the physical model construction. Correspondingly, the lower boundary of the model, more than 100 m, is divided into eight parts. The tidal level thus can be adjusted in different subarea in order to improve the accuracy of sediment experiment.

With plentiful researches about the influence of engineering construction on the estuarine region, a comprehensive analysis technique has been proposed and widely applied to explore the hydrodynamics and sediment movement in the Pearl River Estuary. Based on the historical remote sensing data and field measurement, the dynamic mechanism that drives the sediment transport is detected to capture the fundamental features. Then the numerical model is applied to compare the differences among multiple layout plans of the engineering. Finally, the physical model can be used to optimize the projects. Considering the limitations of the distortion ratio of the physical model of the Pearl River Estuary, a local amplification model is generally built at the same time. The global physical model and the small-scale local model are simultaneously performed and mutually verified.

Additionally, the model results must be the well validated based on effective in situ measurement, such as multiaxial velocity, salinity and suspended sediment concentration. Especially in the surrounding of coastal engineering, the model results should be consistent with the hydrodynamic characteristics. Then sediment experiment is conducted. Occasionally, an in-site trial-excavation for harbors or navigation channels construction is necessary. Its deposition processes are modelled to further meet the demand of experiment accuracy.

3.2 The Synchronous Simulation of the Tidal Current and Wave

Apart from the intra-tidal variations of reciprocating tidal current, wave also plays an vital role on the surficial sediment resuspension and transportation, especially during

the winter with high wind in the Pearl River Estuary. The sediment movement on the shoal near the coastal regions is subjected to the interaction of wave and periodic tidal current. Therefore, it is necessary to synchronously simulate the impacts of tidal current and wave, which is one of the technical difficulties in the sediment experiment through the physical model.

For an accurate simulation of waves in different areas, a set of flexible and movable wave-making devices are specifically designed for the global physical model. The wave-making device has the advantages of movable and flexible adjustment in wave direction, wave height, and wave period. Furthermore, it is also able to be elevated for the purpose of undermine the influence on the tidal current (Badulin 2014). As shown in Fig. 5, the wave making device consists of stainless-steel wave plate, stainless-steel wave frame, cylinder with magnetic limit switch, universal bearings, joint bearings, wireless remote control and air compression Machine. The wave direction is mainly adjusted by changing the orientation of the wave plate, While the wave frequency is controlled by changing the pressure limiting valve. Furthermore, the swing amplitude of the wave plate is changed by adjusting the limit position of the cylinder. Thus, the accurate wave height and wave period control can be achieved in the physical model.

3.3 Automatic Control of Sediment Feeding Devices

In order to accurately simulate the process of suspended sediment transport, automatic sediment feeding device with controlling system is designed, which has been equipped in the eight river mouths of the physical model. It mainly consists of on-line turbidimeters, electromagnetic flowmeters, frequency converters, sediment supply power systems, sediment deposition devices and sediment supply pipes (Fig. 7).

The on-line turbidimeter constantly collects the suspended sediment concentration in the flow. The signal then is fed back to the computer system of the controlling center. According to the real-time measured suspended sediment concentration from the model, the computer can calculate the demand of suspended sediment and order the feeding device in different part of estuary. On the other hand, if the sufficient suspended sediment is detected from the model, fresh water is supplied to prevent the hole for sediment feeding pipe from being blocked.

As shown in Fig. 7, a schematic diagram of the automatic sediment feeding device is displayed. It consists of four sediment pools and two fresh water pools. Firstly, the model sediment is soaked in the soaking pool to meet the requirements. The model sediment is then pumped to the stirring sediment pool with a stirrer equipped to prevent sedimentation. When the concentration satisfies the requirement, the sediment is pumped to the sediment adding pool. Similarly, the pool is equipped with a stirrer to prevent the settlement of sediment. An overflow port is set in the sediment adding pool to recycle the excess sediment laden flow to the sediment apportion pool, which makes sure that the water level in the pool is constant and is easy to control. The water flow is pumped to the sediment adding pipe through the pump controlled by the inverter after converging with the fresh water pipe. There are two fresh water

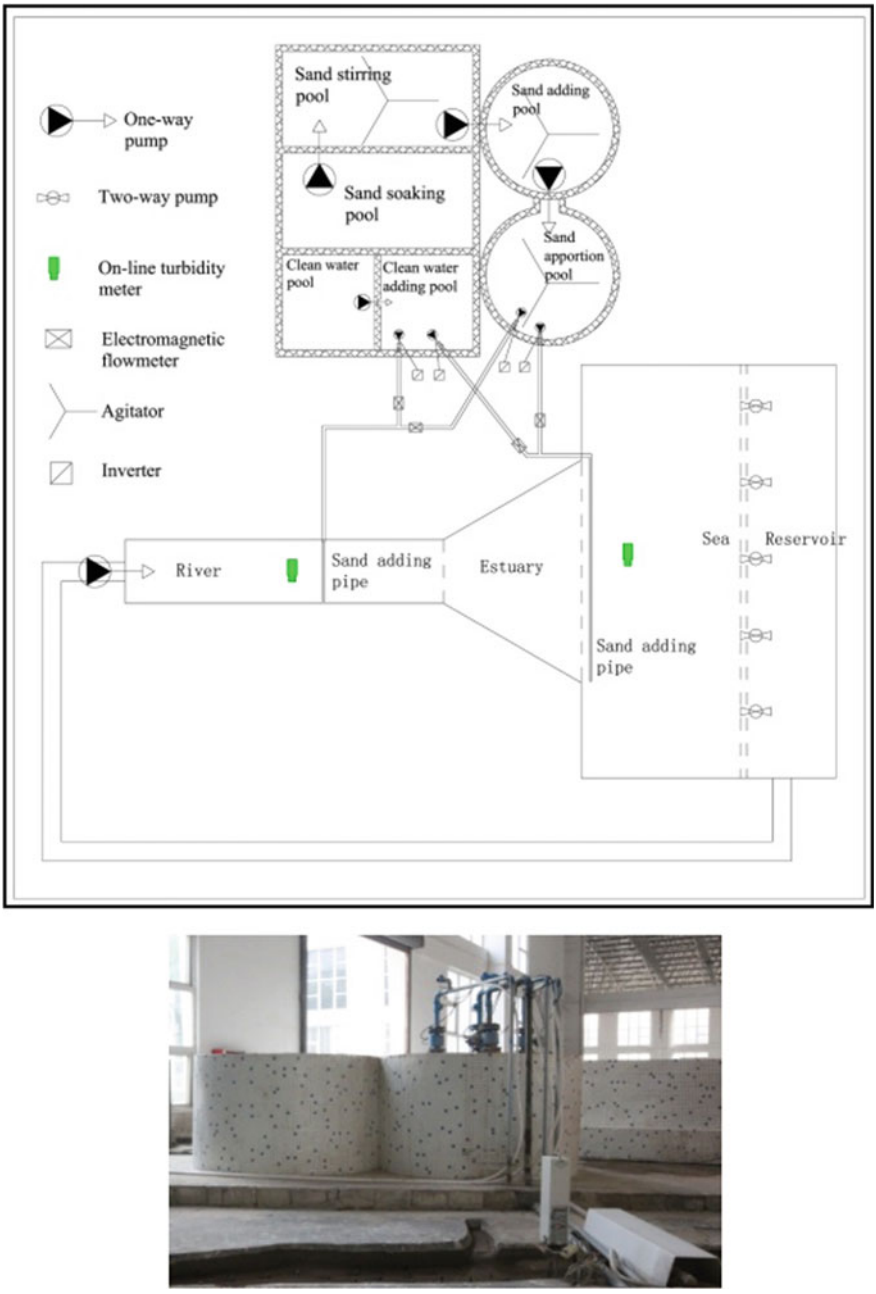

Fig. 7 The automatic sediment adding device of the physical model

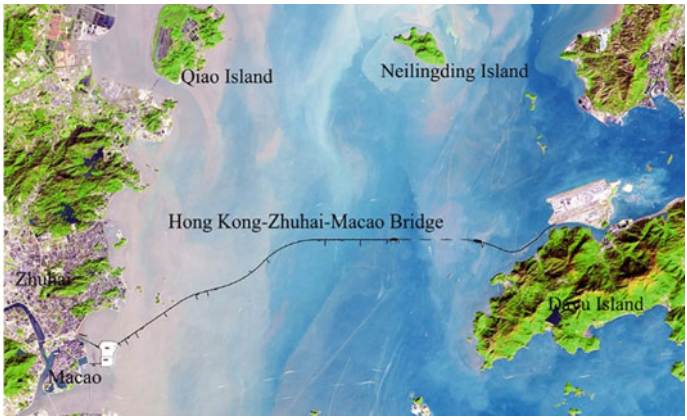

Fig. 8 The plan view of Hong Kong-Zhuhai-Macao Bridge

pools in the automatic sediment feeding system. One of that is a fresh water pool for reservation, which is responsible for supplying water to another water pool and recycling excess clean water. The other is the fresh water adding pool, which plays an important role on supplying the amount of fresh water and adjusting the sediment concentration on the sediment adding pipe. Finally, the sediment laden flow with appropriate concentration is supplied to the physical model (Fig. 8).

4 The Application of the Global Physical Model on the Sediment Experiments for the Hong Kong-Zhuhai-Macao Bridge

4.1 General Setting of the Hong Kong-Zhuhai-Macao Bridge

The Hong Kong–Zhuhai–Macao Bridge (HZMB) is located at the Lingding Bay of the Pearl River Estuary on the southeast of China. It links Hong Kong in the east with Zhuhai–Macao in the west. Actually, the project consists of two artificial islands, tunnel, and bridge with a total length of 55 km. A 6.7 km tunnel connects the two artificial islands (Lin and Lin 2017). The engineering has enhanced traffic conditions on the east and west sides of the Pearl River Estuary, which improves the communication, transportation, and economic integration of the Guangdong–Hong Kong–Macao Greater Bay Area (Zhu et al. 2019).

The Lingding Bay is prone to marine hydrodynamic and the streamflow injected from four eastern outlets of the Pearl River (Humen Estuary, Jiaomen Estuary, Hongqimen Estuary, and Hengmen Estuary). It is characterized by trumpet-shaped estuary with the direction of NNW-SSE. The upper part of bay is about 4 km width

(Humen Estuary). And the bay mouth is about 30 km width 72 km length, covering about 2110 km^2 water area. The transverse profile of topography is shallow in the west and deep in the east, while the longitudinal profile is narrow and deep in the upper part, wide and shallow in the middle part, wide and deep in the lower part.

Four primary sediments types are detected in the Lingding Bay and the adjacent region, including sandy clay, silty clay, clayey silt, and sand-silt-clay. Clayey silt and silty clay are the most dominant sediment types, accounting for 49 and 46% of the whole surficial sediment samples, respectively (Zhang et al. 2013). Furthermore, the region is characterized by a low energy micro-tidal estuary with a mean tidal range of 0.86–1.69 m. M2, S2, K1 and O1 are the four main tidal constituents. The tidal cycle in the Lingding Bay is a semidiurnal mixed tidal regime with daily inequality in range and time between highs and lows (Mao et al. 2004).

4.2 The Implement of the Sediment Experiment for Evaluating the Influence of HZMB

The Hong Kong-Zhuhai-Macao Bridge is one of the most important projects in the Pearl River Estuary, which undoubtedly exerts short-term and long-term impact on the Pearl River Estuary. Three important aspects on the sediment experiment are displayed below.

(1) The erosion of bridge piers and artificial islands: The construction of HZMB has the potential to be water-blocking, indicating the flow velocity between piers tends to increase. In the near future, it may cause the scouring impacts on the bridge piers and artificial islands to some extent. Accordingly, the eroded sediment will be transported and settle down in the surrounding region.
(2) The influence of dense piers in the west shoal on the sediment transport: The plane layout of the HZMB is curvilinear. Most part of bridge axis is perpendicular with the flow direction. However, in the west shoal, relatively obvious intersection angle between the axis of the bridge and the flow occurs, leading to more significant water-blocking effect by dense piers. At the same time, the pattern of sediment transport in the western part of estuary is also affected by the changing hydrodynamics.
(3) The potentially long-term evolution of the Lingding Bay: At present, the landform of the Lingding Bay is mainly suffered slight sediment deposition. Whether the deposited regime is changed or not by the construction of the HZMB in the further should be paid further attention.

Firstly, local erosion experiments for piers and artificial islands were conducted with a movable bed. The artificial islands and piers of the bridge may result in local erosion. It also can provide the terrain boundary for studying the long-term cumulative impact of the bridge on the hydrological and geomorphologic regime (Biria et al. 2015). Hence, the suitable model sediment for the movable bed needs to be chosen. According to the analysis of the surficial sediment particle size close

to the HZMB, the incipient velocity is set as 1.60 m/s. In the physical model, the incipient velocity of the model sediment is about 16.0 cm/s since the scale of flow velocity is 10. Additionally, a flume experiment was applied to determine the type of model sediment. Fine coal dust with a bulk density of 1.4 t/m^3 and a median particle diameter of 0.7 mm is selected as the model sediment for erosion experiments. The results of flume experiment found that the incipient velocity of the fine coal dust is 14.5–16.2 cm/s when the water depth is 5–13 cm, which generally meets the requirement of erosion experiment.

Furthermore, it is necessary to carry out the suspended sediment deposition experiment to explore the influence of HZMB construction on the geomorphologic evolution of the Lingding Bay. Based on the in-site hydrological surveys and the calculation of the similar scale, the settling velocity of the model sediment is determined as 0.028–0.035 cm/s. The incipient velocity should be 6–7 cm/s. Similarly, the flume experiment found that the wood powder is relatively suitable for the deposition experiment after the comparison of many kinds of model sediment. Wood powder with a specific gravity of 1.16 t/m^3 and settling velocity of approximately 0.03 cm/s was selected. Accordingly, the incipient velocity is approximately 5–7 cm/s. The wood powder is made by sycamore wood, which is relatively light and suitable for modelling the long-distance suspended sediment transport. The deposition experiment was validated by the bathymetric data. The silting sickness is accordant well with the annual sediment deposition of the Lingding Bay.

4.3 The Results of Sediment Experiment of the HZMB

A series of scouring experiments were implemented to evaluate the impacts of flow on the piers erosion (Wernette et al. 2018). In the western estuary, the scope of the movable bed is about 2 km upstream and 2.5 km downstream of the axis of bridge, while it is about 5 km upstream and 4 km downstream in the eastern part. The boundary conditions of the model are set as the discharge and tidal level in July 1997 and February 2001. Both of them cover spring tide, middle tide and neap tide, ranging about half a mouth.

The results of scouring experiment were displayed in Fig. 9. After the construction of the HZMB, the regions near the eastern and western artificial islands suffered obviously erosion. The deepest scour is about 2 m, which locates at the eastern side of the eastern artificial island. The region near the western artificial island experienced less scour. In the middle of eastern and western artificial islands, the magnitude of average erosion is about 0.3 m. The mild deepening of seabed might slightly improve the tidal prism of the Lingding Bay.

Moreover, the deposition experiment was conduct to explore the influence of the HZMB on the suspended sediment settling and deposited pattern. The results of deposition experiment were displayed in Fig. 10. The similar scale of suspended sediment is set to 0.22 while the depositional time scale is 726. Slight variations of tidal level, flow velocity and tidal prism were found between the pre and post

Fig. 9 The erosion results near the eastern (top) and western (bottom) artificial island

construction of the bridge. The increment of tidal level was less than 0.03 m. Besides, the largest increment of flow velocity occurred in the middle of eastern and western artificial islands, which was about 0.14 m/s. However, the tidal prism of Lingding Bay decreased about 0.5–0.7%. The deposited magnitude near the eastern and western artificial island is about 0.6 m and 0.8 m, respectively, covering about 5 km.

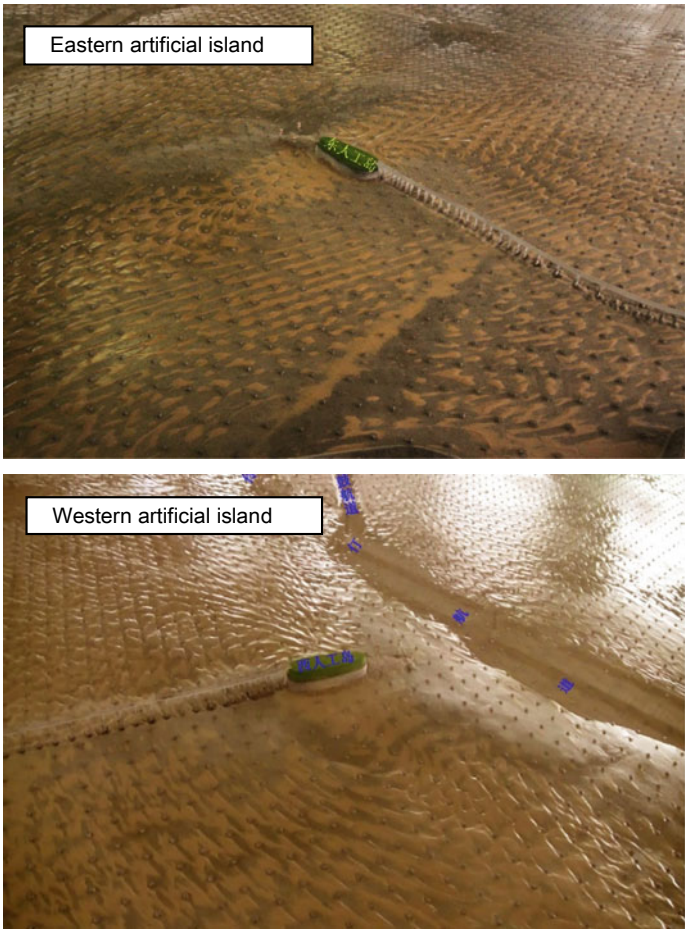

Fig. 10 The deposition results near the eastern (top) and western (bottom) artificial island

5 Conclusion

The global physical model of the Pearl River Estuary has been widely applied to explore the influence of engineering construction on the hydrodynamics and sediment transport. According to the regional differences of sediment characteristic relating to experimental techniques, three parts of estuary, including the Modaomen Estuary, the Huangmao Sea and the Lingding Bay, should be separately considered in the experiment. The main driving force in the Lingding Bay and Huangmao sea is tides. The primary sediment source consists of the fluvial sediment carried by the streamflow and the marine sediment resuspended by local tidal current. Nevertheless, wave plays an important role on the sediment transport for the shoal, especially during the dry season in the Huangmao Sea and the Modaomen Estuary. Moreover,

the mouth bar is characterized by a typically geomorphologic unit in the Modaomen Estuary. Significant sediment particle size sorting occurs in the vertical direction in the bar area, which needs to be taken into consideration in the model.

Additionally, key techniques in sediment experiments of the global physical model are introduced. Flexible and movable wave-making devices are specifically designed for the synchronous simulation of the tidal current and wave. Automatic sediment feeding devices with controlling system are equipped in the eight outlets of the Pearl River. The sediment experiment on studying the influence of HZMB construction is displayed as an example, including a deposition experiment and an erosion experiment for piers and artificial islands. The results found that the magnitude of average erosion is about 0.3 m while maximum erosion reaching 2 m near the artificial islands. However, the tidal prism of Lingding Bay has the potential to decrease about 0.5–0.7% after the HZMB construction. The slight decrease of tidal dynamic results in partial deposition with the magnitude about 0.6 and 0.8 m.

Acknowledgements This work was jointly supported by "National Natural Science Foundation of China" (NSFC, Project Nos. 51779280), "Guangdong provincial science and technology projects: Guangdong-Hong Kong-Macao Greater Bay Area Urban agglomeration ecosystem Observation and Research Station (Project Nos. 2018B030324002)" and "the Open Research Foundation of Key Laboratory of the Pearl River Estuarine Dynamics and Associated Process Regulation, Ministry of Water Resources" (Project Nos. [2017]KJ04, [2018]KJ05).

References

Badulin, S. I. (2014). A physical model of sea wave period from altimeter data. *Journal of Geophysical Research: Oceans, 119*(2), 856–869.

Biria, H. A., Neshaei, M. A. L., Ghabraei A, et al. 2015. Investigation of sediment transport pattern and beach morphology in the vicinity of submerged groyne (case study: Dahane Sar Sefidrood). *Frontiers of Structural and Civil Engineering, 9*(1), 82–90.

Fagherazzi, S., Edmonds, D. A., Nardin, W., et al. (2015). Dynamics of river mouth deposits. *Reviews of Geophysics, 53*(3), 642–672.

He, Y., Wu, Y., Lu, C., Wu, M. W., Chen, Y., & Yang, Y. G. (2019). Morphological change of the mouth bar in relation to natural and anthropogenic interferences. *Continental Shelf Research, 175,* 42–52.

Lazarus, E. D. (2016). Scaling laws for coastal overwash morphology. *Geophysical Research Letters, 43*(23), 12.

Lin, M., & Lin, W. (2017). The Hong Kong–Zhuhai–Macao Island and tunnel project. *Engineering, 3,* 783–784.

Mao, Q., Shi, P., Yin, K., et al. (2004). Tides and tidal currents in the Pearl River Estuary. *Continental Shelf Research, 24*(16), 1797–1808.

Moran, A. D. I. E., Abderrezzak, K. E. K., Mosselman, E., Habersack, H., Lebert, F., Aelbrecht, D., et al. (2013). Physical model experiments for sediment supply to the old Rhine through induced bank erosion. *International Journal of Sediment Research, 28*(4), 431–447.

Si, W., Bao, W., Jiang, P., et al. (2017). A semi-physical sediment yield model for estimation of suspended sediment in loess region[J]. *International Journal of Sediment Research, 32*(1), 12–19.

Wernette, P., Houser, C., Weymer, B. A., et al. (2018). Influence of a spatially complex framework geology on barrier island geomorphology. *Marine Geology, 398,* 151–162.

Wesselman, D., de Winter, R., Engelstad, A., et al. (2018). The effect of tides and storms on the sediment transport across a Dutch barrier island. *Earth Surface Processes and Landforms, 43*(3), 579–592.

Wolinsky, M. A., Edmonds, D. A., Martin, J. et al. (2010). Delta allometry: Growth laws for river deltas. *Geophysical Research Letters, 37*(21).

Wu, Y., He, Y., Wu, M. W., Lu, C., Gao, S. Y., & Xu, Y. W. (2018). Multifractality and cross-correlation analysis of streamflow and sediment fluctuation at the apex of the Pearl River Delta. *Scientific Reports, 8,* 1–11.

Wu, Z., Milliman, J. D., Zhao, D., et al. (2018). Geomorphologic changes in the lower Pearl River Delta, 1850–2015, largely due to human activity. *Geomorphology, 314,* 42–54.

Wu, C., Ji, C., Shi, B., et al. (2019) The impact of climate change and human activities on streamflow and sediment load in the Pearl River basin. *International Journal of Sediment Research*.

Zhang, W., Wu, Y., Wang, W. G., Xing, W. Q. (2016). Characterizing the seasonal changing patterns of hydrological variables in the East River, Southern China. *Journal of Hydrologic Engineering*, p. 05016031.

Zhang, W., Xu, Y., Hoitink, A. J. F., et al. (2015). Morphological change in the Pearl River Delta China. *Marine Geology, 363,* 202–219.

Zhang, W., Zheng, J., Ji, X. M., et al. (2013). Surficial sediment distribution and the associated net sediment transport pattern in the Pearl River Estuary South China. *Continental Shelf Research, 61,* 41–51.

Zhou, Q., Tian, L., Wai, O. W. H., et al. (2018). High-frequency monitoring of suspended sediment variations for water quality evaluation at Deep Bay, Pearl River Estuary, China: Influence factors and implications for sampling strategy. *Water, 10*(3), 323.

Zhu, Yongling, Lin, Ming, Meng, Fanchao, Liu, Xiaodong, & Lin, Wei. (2019). The Hong Kong–Zhuhai–Macao Bridge. *Engineering, 5*(1), 10–14.

Two-Phase CFD Modeling of Sediment Plumes for Dredge Disposal in Stagnant Water

S. N. Chan, Adrian C. H. Lai, Adrian W. K. Law and E. Eric Adams

Abstract Dredge spoil is commonly disposed in estuarine and coastal waters through submerged pipelines from a barge in the form of concentrated mixture of sediment and water. The discharge resembles a downward dense turbulent plume under the negative buoyancy of the sediment particles. Sediment discharge can increase the turbidity and suspended solid level of coastal water, causing damage the marine ecosystem. It is important to understand the mixing of a sediment plume with the ambient water in order to properly assess the environmental impact of disposal operation. This chapter presents a computational fluid dynamics (CFD) model of a sediment plume in a non-stratified stagnant ambient using the two-phase Eulerian approach. The axisymmetric two-phase continuity and momentum equations are solved with the drag force term accounting for the interaction between phases. The standard k-ε model is used for turbulence closure for sediment-water mixture. The radial turbulent dispersion of particles is modeled by a drift velocity term related to the concentration gradient of the particle phase. The model prediction is validated against experiments of a companion work and independent experimental data, with a wide range of particle sizes (68–1500 μm) and plume sediment volume fraction (maximum of 60%). The model predicted cross-sectional distribution of sediment concentration, plume fluid velocity and the slip velocity of particle to fluid can be well described by Gaussian profiles. The reduction of plume spreading rate with increasing particle size and settling velocity is also well predicted by the model. The CFD model results shed light on the development of a simple integral model for predicting the mixing of sediment plumes.

S. N. Chan (✉)
Department of Civil and Environmental Engineering and Institute for Advanced Study, The Hong Kong University of Science and Technology, Hong Kong, China
e-mail: treechansn@ust.hk

A. C. H. Lai · A. W. K. Law
Nanyang Environment and Water Research Institute and School of Civil and Environmental Engineering, Nanyang Technological University, Singapore, Singapore

E. Eric Adams
Department of Civil and Environmental Engineering, Massachusetts Institute of Technology, Cambridge, MA, USA

K. D. Nguyen et al. (eds.), *Estuaries and Coastal Zones in Times of Global Change*, Springer Water,
https://doi.org/10.1007/978-981-15-2081-5_24

Keywords Sediment plumes · CFD · Eulerian two-phase model · Volume fraction · Sediment disposal

1 Introduction

A particle plume is formed when buoyant (or dense) particles are discharged continuously into water. Particle plumes can be found in many engineering and natural processes. During land reclamation, sand can be discharged continuously into water, forming a sediment plume. In dredge disposal operations, dredge spoil or capping materials are placed to designated areas through continuous discharge from pipeline of a barge. Partially treated wastewater discharged from a submarine outfall in the form of buoyant jets often contains sediment and particulate matters; the settled sediment raises concern about its impact on the benthic ecology (Chan et al. 2014). Accurate predictions of the fate and transport of the particles in these flow processes are needed for their design, impact assessment and optimization.

The modeling of particle jets and plumes deals with the complexity of the particle-fluid interaction in a turbulent shear flow. Integral model, which assumes self-similarity of the flow as it progresses with its trajectory, is commonly used for single-phase turbulent jets and plumes to simplify the modelling effort yet capturing the key physics (e.g. Morton et al. 1956; Lee and Chu 2003). However, except for flows with very low particle concentration (<0.1%, Cuthbertson and Davies 2008), integral models based on entrainment hypothesis for single-phase plumes, cannot in general be used for multiphase plumes because particles affect plume entrainment and hence its mixing (Parthasarathy and Faeth 1987). An example of using the entrainment hypothesis for particle plumes can be found in Chan and Lee (2016), in which the transport of particles in the jet is predicted using a stochastic particle tracking equation coupled with a buoyant jet integral model. However the model is limited to cases with low particle concentration, in which particles have negligible effects on the fluid phase. Recently Lai et al. (2016) has developed an integral model of dense sediment plumes with a spreading hypothesis accounting for different sediment size and concentration. The model solves the integral equations of fluid and sediment momentum conservation, and sediment mass conservation. The model requires several assumptions: (1) the fluid velocity and sediment concentration follows self-similar Gaussian profile; (2) the local particle velocity is the sum of fluid velocity and settling velocity of particles in stagnant water; (3) the jet spreading rate of the fluid phase is constant and independent on the particle size and initial jet properties. The model achieves reasonable comparison with experimental data, yet some of the assumptions has to be confirmed.

Computational Fluid Dynamic (CFD) modelling is particularly useful for studying multiphase flows. Multiphase CFD modelling for sediment jets and plumes has been reported (e.g. Virdung and Rasmuson 2007; Azimi et al. 2011, 2012; Nguyen et al. 2012; Chan et al. 2014). Virdung and Rasmuson (2007) conducted CFD study on sediment plumes with a single particle size and a single jet flow rate, with particle

volume fraction less than 2%. Nguyen et al. (2012) studied finite volume sediment release through two-phase CFD modelling and laboratory experiments. Chan et al. (2014) studied on horizontal sediment-laden jets with sediment volume fraction less than 0.1%. While Azimi et al. (2012) provides a comprehensive study on particle plumes with different sediment sizes, concentrations and jet configurations, its CFD predictions mostly have not been validated, especially for cases with high plume sediment concentration.

This chapter presents a CFD study on sediment plumes with a wider range of sediment size and concentrations. The model predictions are validated with experimental data. The CFD results are used to confirm several important assumption of the integral model of Lai et al. (2016). In the chapter, the governing equations of the CFD model will be first introduced, followed by model validation with experimental measurements, and the analysis of CFD results to justify the assumptions of the integral model (Lai et al. 2016).

2 Problem Definition

Consider a dense sediment plume discharging downwards from a circular nozzle of diameter D into an otherwise quiescent ambient, with initial velocity U_0 and particle volume fraction (or concentration) α_0 (Fig. 1). Both plume and ambient fluid have the same density ρ_c. Spherical particles have uniform diameter d_d and density

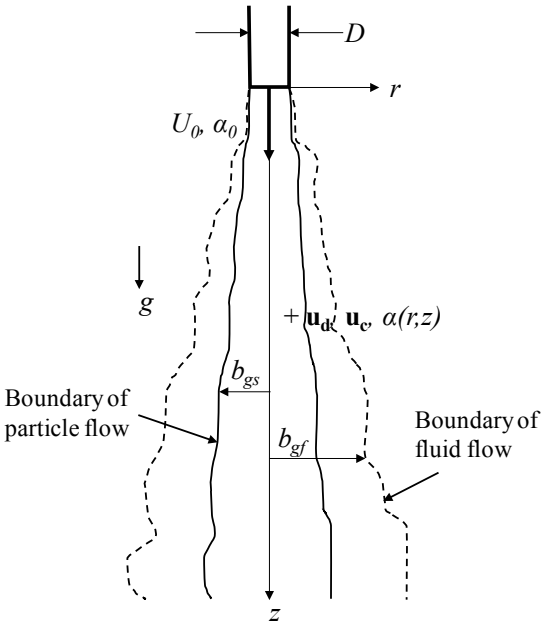

Fig. 1 Particle plume in quiescent ambient

ρ_d. A turbulent shear flow is generated by the initial fluid velocity difference and the descending motion of the solid particles. Sediment mixes with the ambient fluid though the turbulent eddies and its concentration decreases with downward distance. At the same time the fluid velocity also decreases due to the entrainment from the shear-induced turbulent eddies. The plume mixing characteristics is governed by the initial momentum from the plume flow, sediment concentration and its characteristics. The dynamics of sediment plume can be characterized by two non-dimensional parameters (Lai et al. 2016): the initial densimetric Froude number Fr and the plume number N_p

$$Fr = \frac{U_o}{\sqrt{\frac{(\rho_d - \rho_c)}{\rho_c} g \alpha_0 D}} \tag{1}$$

$$N_p = \frac{U_o}{w_s} \tag{2}$$

where $g = 9.81$ m/s^2 is the gravitational acceleration; w_s is the settling velocity of particles, determined by the particle size and fluid properties (density and viscosity). Fr represents the relative importance of the initial momentum of the plume flow to the particle-induced buoyancy; N_p affects the spreading rate of particle phase (Lai et al. 2016). The mixing and dynamics of the sediment plume is to be solved using a Eulerian two-phase CFD model to obtain the spatial distribution of fluid and particle velocity, and the sediment concentration.

3 Eulerian Multiphase CFD Model

The Eulerian multiphase model in ANSYS FLUENT (ANSYS 2013) is used for the prediction of the dynamics of sediment plumes. The Eulerian multiphase model allows the simulation of multiple separate, yet interacting phases. Unlike the mixture model where only the phase-averaged velocity for the sediment-water mixture are solved, the Eulerian two-phase model solves the velocity of each phases, allowing a better representation of the physics of sediment jets. The model solves the governing steady-state continuity and momentum equations of the solid and liquid phases. The continuity equations for the continuous (water, subscript c) and dispersed (particle, subscript d) phases are respectively:

$$\nabla \cdot (\alpha_c \rho_c \mathbf{u_c}) = 0 \tag{3}$$

$$\nabla \cdot (\alpha_d \rho_d \mathbf{u_d}) = 0 \tag{4}$$

where α is volume fraction; ρ is density; and $\mathbf{u}$ is the velocity of the individual phases. The volume fraction of the two phases is subjected to the volume fraction constrain:

$$\alpha_c + \alpha_d = 1 \tag{5}$$

The steady-state momentum equations of the water and particle phases are respectively:

$$\nabla \cdot (\alpha_c \rho_c \mathbf{u_c} \mathbf{u_c}) = -\alpha_c \nabla p + \nabla \cdot \boldsymbol{\tau}_\mathbf{c} + \alpha_c \rho_c \mathbf{g} + \mathbf{R_{dc}} \tag{6}$$

$$\nabla \cdot (\alpha_d \rho_d \mathbf{u_d} \mathbf{u_d}) = -\alpha_d \nabla p + \nabla \cdot \boldsymbol{\tau}_\mathbf{d} + \alpha_d \rho_d \mathbf{g} + \mathbf{R_{cd}} \tag{7}$$

where p is the total pressure; $\mathbf{g} = (0, 0, -9.81)$ is the gravitational acceleration. $\mathbf{R_{dc}} = -\mathbf{R_{cd}}$ is the interaction force between continuous and discrete phases; $\boldsymbol{\tau}_\mathbf{c}$ and $\boldsymbol{\tau}_\mathbf{d}$ are the turbulent shear stresses acting on the continuous (fluid) phase c and dispersed (solid) phase d respectively:

$$\boldsymbol{\tau}_\mathbf{c} = \alpha_c \mu_{T,c} \left(\nabla \mathbf{u_c} + \nabla \mathbf{u_c}^T \right) \tag{8}$$

$$\boldsymbol{\tau}_\mathbf{d} = \alpha_d \mu_{T,d} \left(\nabla \mathbf{u_d} + \nabla \mathbf{u_d}^T \right) \tag{9}$$

where $\mu_{T,c} = \mu_{T,d} = \mu_T$ are the turbulent viscosity of the fluid and particle phase respectively, assuming equal under the mixture turbulence model (see later discussion).

The interaction term with drag force is used for coupling the two phases

$$\mathbf{R_{cd}} = K_{cd}(\mathbf{u_d} - \mathbf{u_c}) = K_{cd}\mathbf{u_{dc}} \tag{10}$$

where $K_{cd} = \frac{\alpha_c \alpha_d \rho_d f}{t_d}$, $t_d = \frac{\rho_d d_d^2}{18 \mu_c}$ is the particle relaxation time; $f = \frac{C_D \mathrm{Re}_d}{24}$ is the drag function; μ_c is the dynamic viscosity of fluid. The drag coefficient C_D is determined from (Schiller and Neumann 1935; Crowe et al. 2012):

$$C_D = \begin{cases} \frac{24\left(1+0.15\mathrm{Re}_d^{0.687}\right)}{\mathrm{Re}_d} & \mathrm{Re}_d \leq 1000 \\ 0.44 & \mathrm{Re}_d > 1000 \end{cases} \tag{11}$$

where $\mathrm{Re}_d = \frac{\rho_c |\mathbf{u_{dc}}| d_d}{\mu_c}$ is the particle Reynolds number; $\mathbf{R_{cd}}$ is essentially the total drag force from the particle phase acting on the fluid phase in a control volume; $\mathbf{u_{dc}}$ is the relative velocity between phases.

In a turbulent flow, turbulence (velocity fluctuation) results in the dispersion of particles. The turbulent mixing is modeled by an additional "drift velocity" related to the gradient of volume fraction of the phases

$$K_{cd}\left(\mathbf{u_d'} - \mathbf{u_c'}\right) = K_{cd}\mathbf{u_{dr}} \tag{12}$$

where $\mathbf{u_d'}$ and $\mathbf{u_c'}$ are the turbulent velocity fluctuation of discrete and continuous phases. The drift velocity $\mathbf{u_{dr}}$ is modelled from the gradient of volume fraction of

the phases

$$\mathbf{u_{dr}} = -\frac{1}{\rho_m}\left(\frac{\mu_T}{\sigma_{cd}\alpha_d}\nabla\alpha_d - \frac{\mu_T}{\sigma_{cd}\alpha_c}\nabla\alpha_c\right) \tag{13}$$

where μ_T is the turbulent viscosity of the mixture, estimated by the turbulence model; $\sigma_{cd} = 0.75$ is a Prandtl number for turbulent diffusion of particles; $\rho_m = \alpha_c\rho_c + \alpha_d\rho_d$ is the density of particle-water mixture.

The mixture two-equation k-ε model is used for turbulence closure, where k is the turbulent kinetic energy and ε is the dissipation rate of the turbulent kinetic energy. A single set of k and ε equations are solved for the mixture of solid and liquid phases, where the mixture density and velocity are weighted using their volume fraction. The mixture turbulent viscosity is computed from the standard k-ε model (Launder and Spaulding 1974).

The governing Eqs. (3–7) and the turbulence model equations are casted in the axisymmetric form and solved numerically using a two-dimensional axisymmetric rectangular mesh of 10,000 cells in FLUENT code (ANSYS 2013). The domain of simulation is set as $75D$ radius $\times$ $200D$ height (Fig. 2) to minimize the influence of the open boundary conditions. The initial radius of the plume resolved by 5 cells. The inflow velocity is prescribed at the inflow boundary with $U_{c0} = U_{d0} = U_0$, with the sediment volume fraction of the inflow is α_0. The pressure outlet boundary with zero pressure is prescribed for the side and bottom; the top boundary is set as a solid wall. The steady-state solution is obtained by iteration from zero velocity and sediment volume fraction until convergence is declared with normalized residuals for all variables less than 10^{-4}.

4 Simulated Cases

A total of 11 cases were simulated using the conditions of different experimental studies (Table 1). The model simulations are validated against the experimental data in a companion study (Lai et al. 2016) and two independent studies (Hall et al. 2010; Virdung and Rasmuson 2007), covering a wide range of particle sizes (68–1500 μm) and plume sediment volume fraction (1.9–60%).

The experiments by Virdung and Rasmuson (2007) were conducted using glass particles with diameter 1.5 mm in an ambient fluid (benzyl alcohol and ethanol mixture) with density 951 kg/m^3 and viscosity 4.55×10^{-3} Pa/s, with index of refraction similar to the glass beads for Particle Imaging Velocimetry (PIV) measurement. Jet speed of about 1.5 m/s was used with particle volume fraction 0–1.9%. Both the fluid and particle velocities at $z = 0.2$–$11.2D$ were measured using PIV. Fr of the experiments was all above 20.2, indicating that they were momentum dominated jet flow cases.

The experiments by Hall et al. (2010) were conducted on slurry sand jets with volume fraction 5.5–60%. For experiments B1-B3, sand-water mixture was mixed

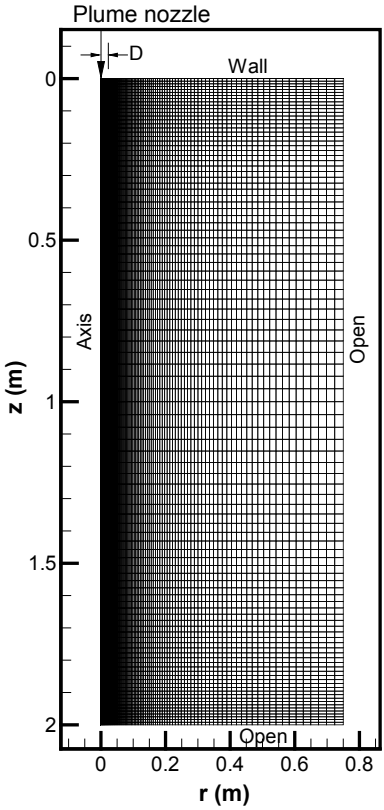

Fig. 2 Model mesh (axisymmetric) for CFD simulations of sediment plume

by mechanical stirrer and injected into the water with momentum. For experiments A1 and A2, particles were released from a funnel above the water surface with initial particle volume fraction assumed as 60%. The *Fr* for Hall's experiment was about 4–9, representing the transition between pure jet and pure plume. Silica sand particles were used in the experiments, with a measured average sand settling velocity of 3.3 cm/s, corresponding to an equivalent spherical particle diameter of 255 μm. Sand particle velocities and concentrations were measured by a calibrated fibre optical probe.

In experiments of Lai et al. (2016), the sediment was released underwater using a submerged hourglass to produce a steady efflux velocity ($U_0 = 11$–45 cm/s) of water-sediment mixture. Glass particles with density 2500 kg/m^3, and median diameters of 0.0675–0.725 mm were used ($w_s = 0.4$–10.8 cm/s). The initial sediment volume fraction was assumed to be 60%. The discharge had a low *Fr* of 0.3–1.0 which represented plume-like (buoyancy-dominated) discharge. The Gaussian half-width of sediment concentration was determined from video images of the experiments. Typical CFD predictions of sediment concentration field are shown in Fig. 3. Note

Table 1 Simulated sediment plume scenarios. D = jet diameter, U_0 = jet initial velocity, d_d = particle diameter, w_s = particle settling velocity, α_0 = initial particle volume fraction, Fr = jet densimetric Froude number (Eq. 1)

Case	D (mm)	U_0 (cm/s)	d_d (mm)	w_s (cm/s)	α_0 (%)	Fr
Lai et al. (2016)—ρ_d = 2.5 g/cm^3, ρ_c = 0.998 g/cm^3						
L-A	10.0	31.9	0.725	10.8	60	1.07
L-B	10.0	25.2	0.514	7.6	60	0.85
L-D	10.0	23.2	0.256	3.3	60	0.78
L-AE	15.0	17.4	0.120	1.0	60	0.48
L-AH	15.0	10.7	0.068	0.4	60	0.29
Hall et al. (2010)—ρ_d = 2.65 g/cm^3, ρ_c = 0.998 g/cm^3						
H-B1	15.5	100.0	0.206	2.5	5.5	8.93
H-B2	15.5	100.0	0.206	2.5	8.6	7.14
H-B3	15.5	98.0	0.206	2.5	12.2	5.87
H-A1	6.1	125.0	0.206	2.5	60	5.3
H-A2	10.3	127.0	0.206	2.5	60	4.2
Virdung and Rasmuson (2007)—ρ_d = 2.5 g/cm^3, ρ_c = 0.95 g/cm^3						
VR	19.2	145.0	1.50	13.9	1.9	20.2

that the radial sediment dispersion is relatively smaller for a larger particle size (Fig. 3a) compared to that of a small particle size (Fig. 3b).

5 Model Validation

The CFD model prediction is first validated with experimental measurements by independent studies of Hall et al. (2010) and Virdung and Rasmuson (2007). Figure 4 shows the comparison between predicted and measured centreline sediment velocity of three experiment cases (B1-B3) by Hall et al. (2010) with different initial sediment concentration but the same jet flow and jet diameter. It can be seen that the sediment velocity decreases with distance from the jet nozzle. The model predicts a slight increase in sediment velocity at $z \sim 5D$ (0.1 m), due to the accelerating sediment particles under gravity. At the same vertical location, the sediment velocity increases with increasing sediment concentration, reflecting the effect of sediment induced buoyancy.

Figure 5 shows the predicted centreline sediment concentration (volume fraction) compared with measurement of Hall et al. (2010), with a decaying trend of sediment concentration with distance from the jet nozzle due to turbulent mixing and dilution. Given that the measurement error of sediment concentration is about 15% (Hall et al. 2010), the CFD prediction of sediment concentration decay compares

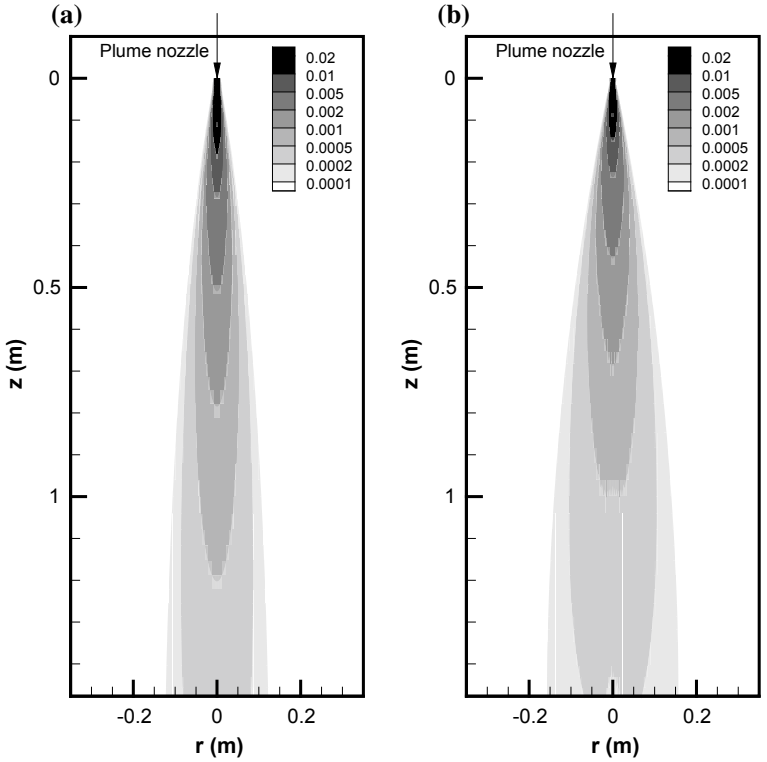

Fig. 3 CFD predicted sediment concentration for **a** Case L-A ($d_d = 0.725$ mm), **b** Case L-AH ($d_d = 0.068$ mm) of Lai et al. (2016). The prediction is mirrored against plume centerline

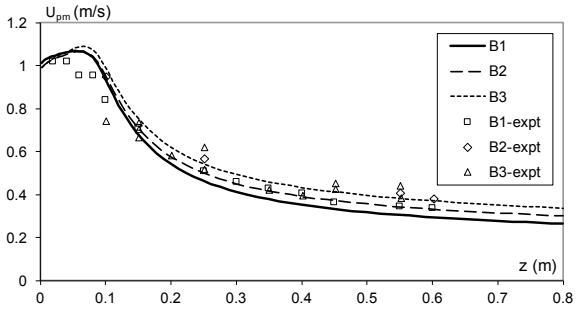

Fig. 4 Plume centerline particle velocity, Cases H-B1, B2, B3 (Hall et al. 2010)

favourably with the experimental measurement for a wide range of initial plume sediment concentration (5.5–60%), showing the two-phase Eulerian CFD model with a mixture turbulence model can be applied for the prediction of sediment plumes.

The CFD model prediction is also validated against the experiments of Virdung and Rasmuson (2007) with low particle concentration and a larger particle size. The

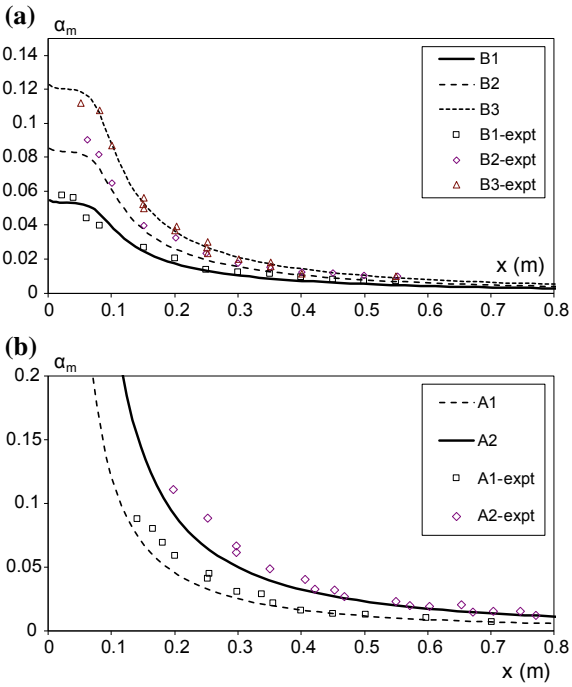

Fig. 5 Centerline sediment volume fraction, **a** Case H-B1, B2, B3, **b** Case H-A1, A2 (Hall et al. 2010)

predicted axial particle velocity profiles compare well with the measurement at $z = 8D$ (Fig. 6), however a lower fluid velocity is predicted at the centreline. A possible reason is that the highly turbulent jet flow results in fluctuating fluid forces counter-balancing the gravity. Since the present model only account for the drag force induced by the mean motion between particle and fluid, particle-turbulence interaction has not been well predicted at the initial jet region.

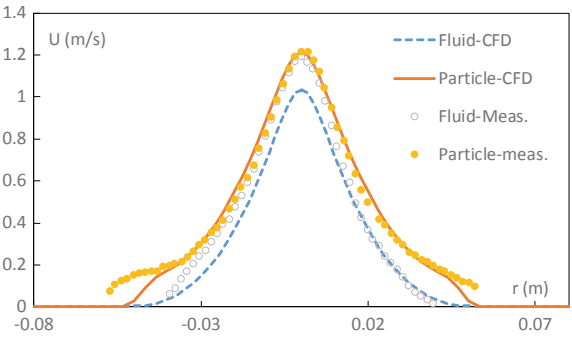

Fig. 6 Axial fluid and particle velocity for jet cross section $z = 8D$, Case VR (Virdung and Rasmuson 2007)

6 Velocity and Sediment Concentration Profiles

The validated CFD model revealed the sediment mixing characteristics of the experiments in Lai et al. (2016), which focuses on dense sediment plumes with volume fraction ~60% and particle sizes 68–725 μm. The assumptions in their integral jet model are verified. Figure 7 shows the predicted cross-sectional axial fluid velocity profile for experiment case L-A with sediment size of 0.725 mm. With normalization by the maximum fluid velocity and the Gaussian half width b_{gf} (defined as the radial location where $u_f/u_{fm} = e^{-1}$), the axial fluid velocity distribution follows a self-similar Gaussian profile and collapse into a single curve.

Figure 8 shows the CFD predicted radial particle velocity distribution for a case with large sediment size ($d_d = 0.725$ mm) at a cross section $z = 20D$ from the nozzle. The particle velocity is higher than that of the fluid velocity, and can be well approximated by the addition of the particle velocity with a constant stillwater settling velocity of the particle at the entire cross section ($U_s = 0.108$ m/s), confirming the assumption in the integral model of Lai et al. (2016).

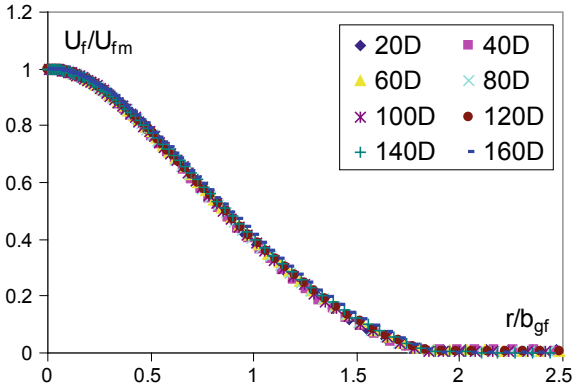

Fig. 7 Predicted cross-section fluid velocity profile, Case A (Lai et al. 2016)

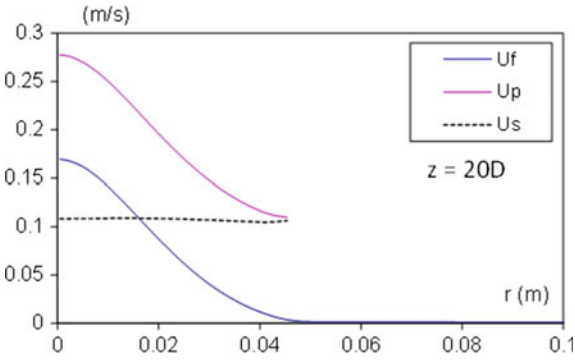

Fig. 8 CFD predicted fluid, particle and the relative velocity for Case L-A ($D =$ 1 cm, $d_d = 0.725$ mm, $U_0 =$ 31.8 cm/s, Lai et al. 2016), at cross-section z = 20D. $U_s = U_p - U_f$

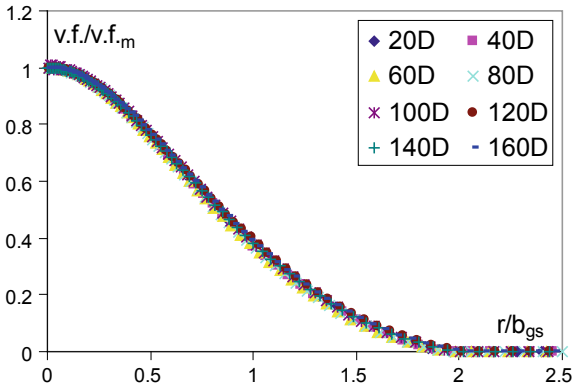

Fig. 9 Predicted cross-section sediment volume fraction profile, Case A (Lai et al. 2016)

Figure 9 shows the predicted radial sediment volume fraction distribution at various jet cross sections ($z = 20D$–$160D$), which follows a self-similar Gaussian profiles when they are normalized against the maximum sediment volume fraction at the centreline and the respective nominal half width of sediment concentration b_{gs}, defined as the radial location where $\alpha/\alpha_m = e^{-1}$. Note that the Gaussian half width of sediment concentration b_{gs} is in general not the same as the Gaussian half width of the fluid velocity b_{gf}, as larger particles tend to fall faster in the own settling velocity rather than being dispersed by the turbulent eddies in the plume, resulting in a smaller spreading of the particle concentration profile than the fluid velocity.

7 Jet Spreading Rate

The difference of the Gaussian jet width spreading rate in fluid and particles can be observed clearly from the CFD predictions in Fig. 10. While the fluid spreading rate $\beta_f = \mathrm{d}b_{gf}/\mathrm{d}z$ is approximately the same as that of a single phase plume of about 0.11, the spreading rate of sediment $\beta_s = \mathrm{d}b_{gs}/\mathrm{d}z$ decreases with increasing particle size. For a particle size of 0.725 mm, the sediment spreading rate is about 0.075 only, while for particles with size 0.12 mm, the sediment spreading rate is similar to that of the fluid. The predicted particle spreading rate is consistent with the experimental data and the prediction of an integral model developed previously (Lai et al. 2016), with a spreading hypothesis in the form of

$$\frac{db_{gs}}{dz} = \frac{db_{gf}}{dz}\left(\frac{U_f}{U_f + U_s}\right) \tag{14}$$

where U_f is the local average velocity of fluid assuming a top-hat profile and U_s is the settling velocity in stillwater.

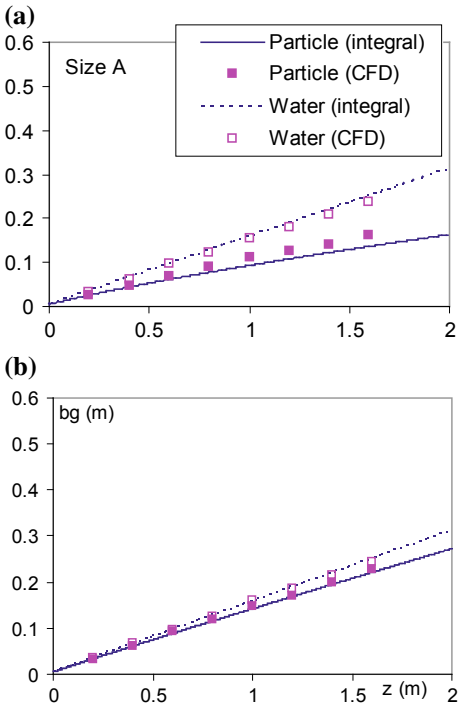

Fig. 10 Predicted Gaussian half width for sediment concentration with distance, using CFD and the spreading hypothesis in the integral model of Lai et al. (2016), **a** particle size 0.725 mm (Case L-A) and **b** 0.12 mm (Case L-AD) (Lai et al. 2016)

It is also worth-noting that a standard k-ε model for the particle-water mixture could predict the transverse dispersion of particles reasonably well, despite the complex turbulent interaction of particle and fluid. The model is relatively simple yet robust, compared to the more complex particle-turbulence interaction models used in other CFD studies (e.g. Parthasarathy and Faeth, 1987; Virdung and Rasmuson, 2007; Azimi et al. 2011; 2012). The turbulence closure model can be used for further exploring the physics of sediment discharge in more complex environmental conditions (with ambient flow and stratification, and different discharge directions).

8 Conclusions

A multiphase CFD model has been developed for sediment plumes with particle size of 68–1500 μm and initial sediment concentration of 0.2–60%. The Eulerian multiphase flow model solves the governing continuity and momentum equations for the interacting solid and fluid phases, with a mixture k-ε turbulence model. The model is validated against the experimental data of two independent studies. The assumptions in the integral model by Lai et al. (2016) is justified by the CFD results.

It is confirmed that in a particle plume, the fluid velocity and sediment concentration follows a self-similar Gaussian distribution. The particle velocity can be assumed as the addition of the fluid velocity with the settling velocity of the particle, as the particle slip velocity. The spreading rate of the plume fluid flow is a constant of about 0.1 and independent of the initial discharge and particle properties. The CFD model also predicts well the reduction of plume spreading rate with increasing particle size and settling velocity.

The numerical study sheds light on the development of a simple mathematical models for the prediction of mixing of sediment plumes for general engineering design and assessment of sediment discharge in the environment. It also demonstrates the applicability of Eulerian two-phase CFD model for predicting the mixing and dynamics of sediment plumes.

Acknowledgements This research was supported by the National Research Foundation Singapore through the Singapore-MIT Alliance for Research and Technology's Center for Environmental Sensing and Modeling interdisciplinary research program. The first author was partly supported by a research grant from the Institute for Advanced Study of the Hong Kong University of Science and Technology.

References

ANSYS FLUENT version 15.0 [Computer software]. (2013). Canonsburg, PA: ANSYS.

Azimi, A. H., Zhu, D. Z., & Rajaratnam, N. (2011). Effect of particle size on the characteristics of sand jets in water. *Journal of Engineering Mechanics, 137*(12), 822–834.

Azimi, A. H., Zhu, D. Z., & Rajaratnam, N. (2012). Computational investigation of vertical slurry jets in water. *International Journal of Multiphase Flow, 47,* 94–114.

Chan, S. N., & Lee, J. H. W. (2016). A particle tracking model for sedimentation from buoyant jets. *Journal of Hydraulic Engineering, 142*(5), 173–200.

Chan, S. N., Lee, K. W. Y., & Lee, J. H. W. (2014). Numerical modelling of horizontal sediment-laden jets. *Environmental Fluid Mechanics, 14*(1), 173–200.

Crowe, C. T., Schwarzkopf, J. D., Sommerfeld, M., & Tsuji, Y. (2012). *Multiphase flows with droplets and particles*. FL: CRC Press.

Cuthbertson, A. J. S., & Davies, P. A. (2008). Deposition from particle-laden, round, turbulent, horizontal, buoyant jets in stationary and coflowing receiving fluids. *Journal of Hydraulic Engineering Division of the American Society of Civil Engineers, 134*(4), 390–402.

Hall, N., Elenany, M., Zhu, D. Z., & Rajaratnam, N. (2010). Experimental study of sand and slurry jets in water. *Journal of Hydraulic Engineering*, pp. 727–738. https://doi.org/10.1061/(ASCE)HY.1943-7900.0000235.

Lai, A. C. H., Chan, S. N., Law, A. W. K., & Adams, E. E. (2016). Spreading hypothesis of a particle plume. *Journal of Hydraulic Engineering Division of the American Society of Civil Engineers, 142*(12), 04016065.

Launder, B. E., & Spalding, D. B. (1974). The numerical computation of turbulent flows. *Computer Methods in Applied Mechanics and Engineering, 3,* 269–289.

Lee, J. H. W., & Chu, V. H. (2003). *Turbulent jets and plumes: A Lagrangian approach*. New York: Springer.

Morton, B. R., Taylor, G. I., & Turner, J. S. (1956). Turbulent gravitational convection from maintained and instantaneous sources. *Proceedings of the Royal Society of London. Series A, 234*(1196), 1–23.

Nguyen, D. H., Levy, F., Bang, D. P. V., Guillou, S., Nguyen, K. D., & Chauchat, J. (2012). Simulation of dredged sediment releases into homogeneous water using a two-phase model. *Advances in Water Resources, 48,* 102–112.

Parthasarathy, R. N., & Faeth, G. M. (1987). Structure of particle-laden turbulent water jets in still water. *International Journal of Multiphase Flow, 13*(5), 699–716.

Schiller, L., & Naumann, Z. (1935). A drag coefficient correlation. *Z. Ver. Deutsch. Ing., 77,* 318.

Virdung, T., & Rasmuson, A. (2007). Hydrodynamic properties of a turbulent confined solid-liquid jet evaluated using PIV and CFD. *Chemical Engineering Science, 62,* 5963–5979.

Wave Transformation and Morphological Changes in Coastal Zones

This part, entitled "Wave Transformation and Morphological Changes in Coastal Zones", displays a panel of the studies on coastal processes. Those investigations rely on multiple approaches: numerical modelling, laboratory experiments, bathymetric/topographic surveys and aerial/satellite imagery. The common goal of these studies is to understand the past and present evolution of coastal areas in order to manage the environmental and human risks in future, in the context of decreasing sediment supply, more frequent and intense storms and high anthropogenic pressure. This part contains twelve chapters gathered into three groups.

The first three chapters are related to shoreline evolution studies, which have been based on aerial/satellite imagery and/or field surveys. *Bidorn et al.* analyse the shoreline change of a muddy coast in Thailand over the period 1953–2017 and investigate the role of different factors, such as mangroves, river sediment supply and aquaculture development. They show that (i) the shoreline evolution is mostly controlled by the changes in river sediment supply, by the local waves and coastal currents conditions and by the stabilisation of adjacent shorelines, and that (ii) the conversion of mangrove forest into agriculture and shrimp farming, has a negligible impact on the shoreline accretion. *Dornbusch* studies the growth and the break-up of a mixed sand-gravel spit, a coastal feature that has received little attention in the scientific literature. The study site is located in South-East England. The evolution of the spit was surveyed using multiple data. The large amount of data has permitted to describe various stages of the spit including growth, breaching and breakdown. This investigation allows us to understand the effect of coastal structures on the evolution of the spit. Furthermore, it is shown that, contrarily to many studies on sandy inlets, the increase in inlet channel length has a negligible impact on tidal exchange in the estuary. *Wang et al.* use a combination of shoreline model and field data to investigate the natural evolution of a sandy beach and its changes in response to the construction of a port. The studied site, named Lekki, is located along the Nigerian coast. The authors firstly show that the shoreline is relatively stable under natural conditions. Then, they note that the port will modify the littoral drift and induce a gradient in sediment transport. They also propose the measures, which could mitigate alleviate erosion, including beach nourishment and groynes system.

A second group of four chapters deals with the use of numerical models to simulate the interactions between currents, waves and sediment transport. This group presents the state of the art of current applications dedicated to engineering problems. *Do et al.* use a two-dimensional morphodynamic model to investigate the relative contribution of wave regime and river discharges to an estuary and its adjacent beach. The studied site is Cua Dai, Vietnam. Their simulations show that seasonal changes in wave regime strongly influence (i) the import of sediment into the estuary, and (ii) the sediment transport patterns in the adjacent coast. They also note that the river discharges play a major role in the sediment flux crossing the inlet, which has yet received little attention in the scientific literature. *Li et al.* use a two-dimensional current model coupled to a wave model (the wave model solves the steady-state wave-action balance and includes refraction, shoaling and breaking). Their study focusses on the interactions between currents and waves at the Tillamook inlet, Oregon, USA. Their main objective was to characterise the wave conditions affecting the boating operations. They find that ebb currents promote wave dissipations while flood currents weaken them. They also show that winter storms generate waves with great steepness and propose a safer passage of boats. *Jiao et al.* use a two-dimensional model to investigate the transport of cohesive and non-cohesive sediment and the associated morphodynamic changes in a waterway. The site of the application is Panjin Port, China. They underline the effect of storms on the deposition of sediment. Finally, *Tilai et al.* use a numerical sediment transport model to investigate the impact of engineering works on the transport of suspended sediment near a nuclear power station (Tianwan, China). They applied their model to determine the best conditions for dredging operations and for the excavation of a water intake and drainage channels.

Mitigating measures and warning systems are considered in the third group composed of five chapters. *Mury et al.* review different "ecogeosystems", which by attenuating the waves, permit the alleviation of coastal hazards. Existing studies on wave attenuation by natural systems are generally scattered and not harmonised. Here, the authors offer a comparative view of the ability of several natural systems to reduce wave energy. The studied site is the Bay of Mont-Saint-Michel (France), where numerous "ecogeosystems" are present encompassing saltmarshes, mudflats, seagrasses, shelly cheniers, oysters, honeycomb worms and sandworm reefs. *Sergent et al.* assess the efficiency of a new system dedicated to reduce beach erosion. The system, composed of nets, was deployed similarly to a groyne in the Authie estuary (France) in order to reduce the dune erosion by river meandering. The bathymetry around the system was monitored to assess the efficiency of the nets in trapping sediment. Numerical model was also used to optimise the dimensions of the system. The results showed that the nets successively reduce beach erosions and even promote the sediment deposition. *Abroug et al.* use measurements in a wave flume to characterise the transformation of a solitary wave propagating to shorelines. They measure wave characteristics over horizontal and slopping bottoms and compare their measurements according to theoretical laws on energy damping and wave height evolution in the shoaling/breaking zone. They also propose a new formula for the estimating run-up heights. *Zhang* studies the propagation of a solitary wave over a trench with

a 3D non-hydrostatic numerical model, in which the eddy viscosity is computed using the Spalart-Allmaras model. He investigates the effect of a trench on the flow separation, the boundary layer and the transport of suspended material. Finally, *Feng et al.* study historical documents and hydrological records to identify the conditions triggering co-oscillating tides (odd tides) in the South Yellow Sea (China). Their work aim at improving the defence against those events by more reliable predictions and warning systems. They show that most of odd tides originate from winter storms or by the wind-driven surges, caused by cyclones.

Jérôme Thiébot
LUSAC, University of Caen-Normandy, France

Evolution of Mangrove Muddy Coast in the Western Coast of the Upper Gulf of Thailand Over the Past Six Decades

Butsawan Bidorn, Nathamon Phanomphongphaisarn, Chaipant Rukvichai and Panida Kongsawadworakul

Abstract This study analyzed the shoreline change processes along the Phetchaburi intertidal mudflats with mangroves located on the western portion of the Upper Gulf of Thailand during the period 1953–2017. Historical shoreline positions along the coast were derived from the aerial photographs taken in 1953, 1967, 1976, 1994, 2002 and the satellite imagery in 2006, 2009, 2014, and 2017 using the Geographic Information System (ArcGIS) software. All imagery data were geo-referenced into Universal Transverse Mercator projection with the World Geodetic System 1983 (WGS1983) to eliminate distortion from the aerial photographs and satellite imagery. The shoreline positions along the study area were then digitized for each time period. The outer boundary of the mangrove forest was mainly used as a proxy to define shoreline positions of the muddy beach. The Digital Shoreline Analysis System (DSAS) version 4.4 was used to analyze the changes of shoreline positions in the study area. Results from this study revealed that about 26% of the 30 km Phetchaburi muddy shoreline in the mid portion of the study area had continuously retreated over the past sixty years with an average rate of -6.5 ± 1.8 m/y. The remaining, which was mainly located in the uppermost portion (near the major river mouths) and the lowermost portion (near a natural sandspit) had advanced seaward with the maximum and average rates of 30.0 ± 1.8 and 8.6 ± 1.8 m/y, respectively. Unlike mangrove muddy coasts in other regions, the results of this study suggested that the conversion of mangrove forest to agriculture and shrimp farming had not affected the rate of shoreline accretion of the study area. The variation of shoreline advanced rates likely reflected the changes in river sediment supply from the Phetchaburi River basin and in coastal sediment transport processes of the Phetchaburi coastal system. Meanwhile, the local wave and current conditions and the adjacent shoreline

B. Bidorn (✉) · N. Phanomphongphaisarn · C. Rukvichai
Department of Water Resources Engineering, Chulalongkorn University, Bangkok, Thailand
e-mail: butsawan.p@chula.ac.th

B. Bidorn
WISE Research Unit, Chulalongkorn University, Bangkok, Thailand

P. Kongsawadworakul
Department of Plant Science, Faculty of Science, Mahidol University, Bangkok, Thailand

K. D. Nguyen et al. (eds.), *Estuaries and Coastal Zones in Times of Global Change*, Springer Water,
https://doi.org/10.1007/978-981-15-2081-5_25

stabilization appeared to be the major factors dominating the shoreline recession of the Phetchaburi coast during the past six decades.

Keywords Shoreline change · Mangrove deforestation · Coastal erosion · Human activities

1 Introduction

Coasts are a highly dynamic landform that is continuously modified by natural processes and anthropogenic activities (Mujabar and Chandrasekar 2001; Saito et al. 2001). Shoreline change along deltaic coasts is a chronic problem in many regions such as the Yellow River and Pearl River deltas in China, Mekong River delta in Vietnam, and Chao Phraya River in Thailand (Li and Damen 2010; Saito et al. 2007; Uehara et al. 2010). Rapid industrialization and urbanization combined with improper coastal zone management can cause various coastal hazards, for example, land subsidence, beach erosion, flooding, storm impacts, seawater intrusion, and river channel siltation (Mujabar and Chandrasekar 2001; Hapke et al. 2006, 2009; Saito et al. 2007; Siripong 2010). Shoreline position is commonly used as a monitoring indicator of environmental change (Camfield and Morang 1996; Hapke et al. 2009). Therefore, information regarding past and present trends and rates of shoreline movement are vital for better understanding of coastal processes and for sustainable coastal planning and management including coastal environmental protection.

Even though shoreline movement processes in deltaic coasts have been documented by several studies (Blodget et al. 1991; Thanh et al. 2004; Thampanya et al. 2006; Chaverot et al. 2008; Yang et al. 2015; Anthony et al. 2017), the shoreline change studies of intertidal coasts in tropical regions are still erratic (Uehara et al. 2010). In Thailand, muddy coasts adjacent to several major rivers have undergone a significant shoreline retreat for decades, especially the deltaic coasts situated in the northern part of the Upper Gulf of Thailand, such as the Chao Phraya River, Tha Chin River, and Bang Pakong River deltas (Fig. 1) (Bidorn 2016; Natalaya et al. 1996; Uehara et al. 2010; Vongvisessomjai et al. 1996; Winterwerp et al. 2005). The recession of shoreline was reported as much as about 1 km during the past sixty years. The objective of this study is to quantitatively assess the shoreline changes of the Phetchaburi mangrove muddy coast located in the western portion of the Upper Gulf of Thailand. The evolution of the mangrove muddy coast during the period 1953–2017 was evaluated using geographic information system framework. Results of this study will facilitate future multidisciplinary studies on coastal environmental management and protection not only in the study area but hopefully also be useful in other similar low-lying areas.

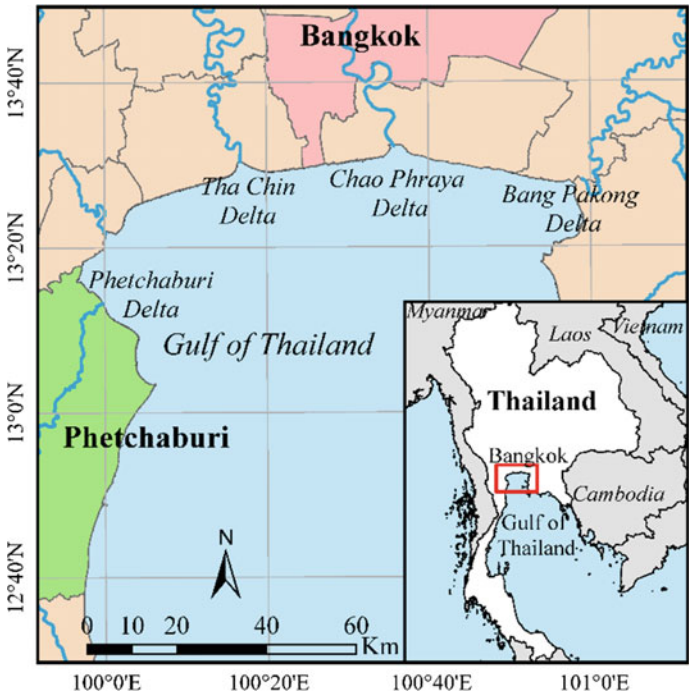

Fig. 1 Major deltas in the upper Gulf of Thailand

2 Study Area

The study area lies between 13° 02′–13° 16′ N latitude and 99° 57′–100° 07′ E longitude, and the coastline extends for approximately 30 km from Lam Phak Bia spit and Bang Ta Bun channel as a part of the coastal zone of Phetchaburi Province (Fig. 2). The coast is characterized by active tidal flats, estuaries, and mangrove forests with an average beach gradient less than 4° (Office of the Nation Economic and Social Development Board 1993; Office of Environmental Policy and Planning 2000). The Phetchaburi River delta is alluvial deposits formed during Quaternary period, and the coastal plain mostly comprises of silty clay. With the long period of delta development and the width of 500 m, the Phetchaburi River delta is considered as the oldest and largest river delta in Thailand (Office of the Nation Economic and Social Development Board 1993).

The Phetchaburi coast has a tropical monsoon climate characterized by the Southwest and Northeast monsoon seasons. The Southwest monsoon starting from May and ended in October brings moderate to heavy rains into the study area. The Northeast monsoon brings cold and dry air from the land between November and February; these winds generate high waves on the Phetchaburi coast. An annual rainfall in this

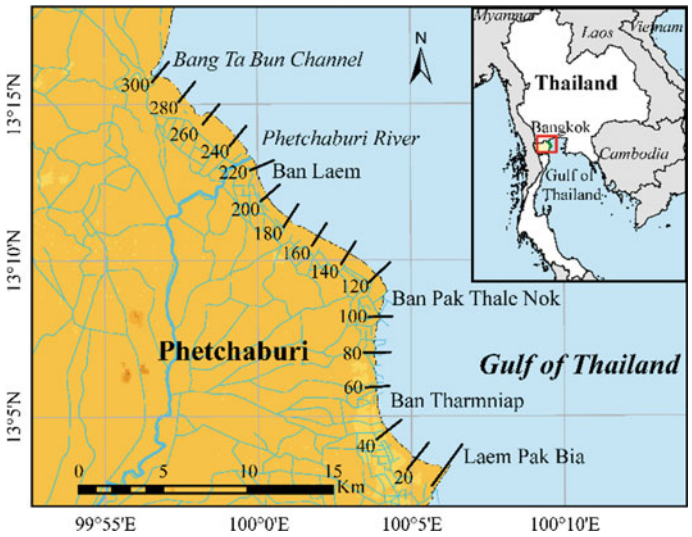

Fig. 2 Phetchaburi coast and the plot of transects used for evaluating shoreline change from Laem Pak Bia spit to Bang Ta Bun Channel

study averages about 1000 mm (Hydro and Agro Informatics Institute 2012). The major rivers of the study area are the Phetchaburi River and Bang Ta Bun Channel.

Astronomical tides in the Gulf of Thailand are diurnal or mixed and typically have a range of more than 2 m (Hydro and Agro Informatics Institute 2012), and the tidal current ranges between 0.25 and 0.40 m/s during the flood tide and between 0.1 and 0.15 m/s during the ebb tide. For wave climate in the study area, wave height less than 1.25 m is predominant (90%), and the wave period was between 4 and 5 s. Fishery and aquaculture farming in backwater are the major economic activities along this coast (Office of the Nation Economic and Social Development Board 1993; Hydro and Agro Informatics Institute 2012).

3 Materials and Methods

3.1 Data Sources and Geo-Referencing

Information on shoreline positions along the Phetchaburi coast from series of aerial photographs (1953, 1967, 1976, 1994, and 2002) and high-resolution satellite imagery (2006, 2009, 2014, and 2017) was used to quantify historical shoreline changes over the past six decades. All aerial photos were georeferenced to the 2002 georeferenced map and were rectified to remove image distortion due to changes in altitude along the flight lines (Alberico et al. 2012) using ArcGIS release 10.4.

Table 1 List of data sources used for assessing shoreline change along the Phetchaburi muddy coast

Year	Data source	Scale	RMSE (m)
1953	Aerial photo	1:42,000	9.2
1967	Aerial photo	1:15,000	9.5
1976	Aerial photo	1:50,000	3.4
1994	Aerial photo	1:50,000	4.5
2002	Orthophoto map	1:4000	Base map
2006	Satellite imagery[a]	1:1500	1.5
2009	Satellite imagery[a]	1:1500	1.7
2014	Satellite imagery[a]	1:1500	1.5
2017	Satellite imagery[a]	1:1500	1.0

[a]Downloaded in TIFF format at no cost from Google Earth Pro software. (https://www.google.co.th/intl/th/earth/download/gep/agree.html)

Satellite imagery data acquired from Google Earth Pro were also georeferenced with the map of 2002. The details regarding aerial photograph and satellite data including the errors associated the georeferencing procedure are listed in Table 1.

3.2 Shoreline Detection and Digitization

Nine shoreline positions during the period 1953–2017 along the Phetchaburi coast were digitized from georeferenced aerial photographs and satellite imagery using ArcGIS. Different descriptions of shoreline were used in the scientific literature (Alberico et al. 2012). As the coastline along the study area comprises of the natural muddy coast with mangrove at the fringe and urbanized coast, seaward edge of vegetation was used as shoreline proxy for the natural coast and as suggested by Zhang et al. (2014). Additionally, roads, bridges, dikes, seawalls, and structures were used to define the coastline of artificial or urbanized coasts.

3.3 Shoreline Change Rate Calculation

The rates of shoreline change along the coast were calculated using USGS Digital Shoreline Analysis System (DSAS) version 4.4, which is an extension of ArcGIS (Thieler 2011). To measure shoreline positions between 1953 and 2017 using DSAS, A total number of 300 transects were automatically generated perpendicular to the baseline at 100 m spacing as illustrated in Fig. 2. Then, the shoreline change for each time period corresponding to the baseline was calculated using either linear regression, endpoint rate, or weighted-linear regression rate. In this study, the analyses of

changes in shoreline position during the periods 1953–2017 and 2002–2017 were performed to determine the long-term and short-term coastline trends, respectively. The statistic of shoreline change rates was calculated with 90 percent of the confident interval.

4 Results and Discussion

Figure 3 shows the historical shoreline changes during the period 1953–2017. The long-term and short-term rates of the shoreline evolution are summarized in Table 2. It was revealed that about 26% of the 30 km Phetchaburi muddy shoreline in the mid portion of the study area had continuously eroded with an average rate of -6.5 ± 1.8 m/y during the past six decades. While the remaining coast had advanced seaward with the maximum and average rates of 30.0 ± 1.8 and 8.6 ± 1.8 m/y, respectively. To understand shoreline change in details, the study area was divided into four portions as Cell-1, Cell-2, Cell-3, and Cell-4 as depicted in Fig. 3. The Cell-1 extended from Laem Phak Bia Spit to Ban Tharmniap (transects 1–51) with the length of 5 km; Cell-2 had 6.3 km long started from Ban Tharmniap to Ban Pak Thale Nok (transects 52–115). The Cell-3 stretched from Ban Pak Thale Nok to the Phetchaburi River mouth (transects 116–228) with a 10.5 km long coastline, and Cell-4 was a 7.1 km long of coastline between the Phetchaburi River mouth and Bang Ta Bun Channel (transects 229–300). The major shoreline change trends are discussed in the following subsections.

4.1 Laem Pak Bia Spit Zone (Cell-1)

The 5 km coastline of Laem Pak Bia area (Cell-1 in Fig. 3), which accounts for 17% of the study are coastline located in the southernmost of the study area. This cell is characterized by fringe mangroves or tide-dominated mangroves. The results of this study indicated that the Cell-1 shoreline has continuously moved seaward owning to the colonization of the mangrove forest in this area (Fig. 3). Long-term and short-term shoreline changes were analyzed along 5 km of this portion as shown in Figs. 4 and 5, respectively. The long-term shoreline change rate for the Cell-1 was accretional with an average rate of 11.5 m/y. The highest shoreline advance rate of about 28 m/y was found in an area adjacent to the Laem Pak Bia spit, which functions as a natural groin trapping the southward sediment transport. The net area evolution of this cell over the past six decades was approximately 400 ha (6.3 ha/y).

Whereas many studies documented that aquaculture expansion was a major cause of mangrove destruction (Wolanski et al. 2000; Muttitanon and Tripathi 2005; Seto and Fragkias 2007; Ha et al. 2012; Hossain et al. 2013; Rahman et al. 2013; Ottinger et al. 2016), the analysis of shoreline evolution in this cell revealed that the conversion of mangroves to aquaculture which has been promoted in this section by

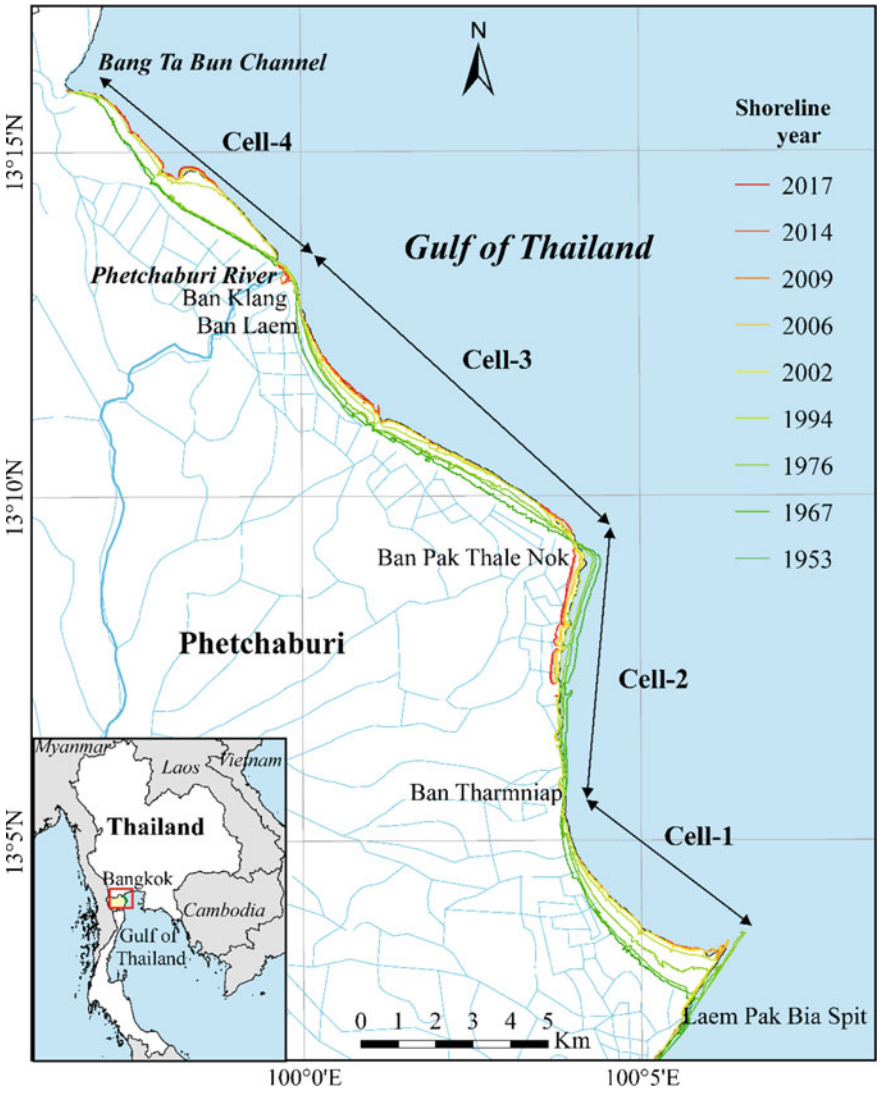

Fig. 3 Shoreline changes along the Phetchaburi coast from 1953 to 2017

1967 did not cause mangrove degradation in this area. In contrast, the highest rate of mangrove extension (14 m/y) occurred during the intensive agricultural expansion period (1976–1994).

In the short term (2002–2017), the rate of shoreline growth significantly decreased to less than 2 m/y, and the maximum shoreline advance near the Laem Pak Bia spit also reduced to 8 m/y during the past 25 years. Only 21 ha of land advanced seaward in this cell recently, and the land accumulation rate decreased more than 85% (less

Table 2 Shoreline change trends along the Phetchaburi muddy coast during the period 1953–2017

Zone	Transect no.	Shoreline change rate (m/y)			
		Long-term trend (±1.8 m/y)		Short-term trend (<±1.0 m/y)	
		Ave.	Max.	Ave.	Max.
Cell-1	1–51	11.5	28.4	1.9	18.0
Cell-2	52–115	−6.5	−11.9	−5.6	−18.8
Cell-3	116–228	6.3	2.6	2.7	14.2
Cell-4	229–300	9.6	30.0	2.9	30.0

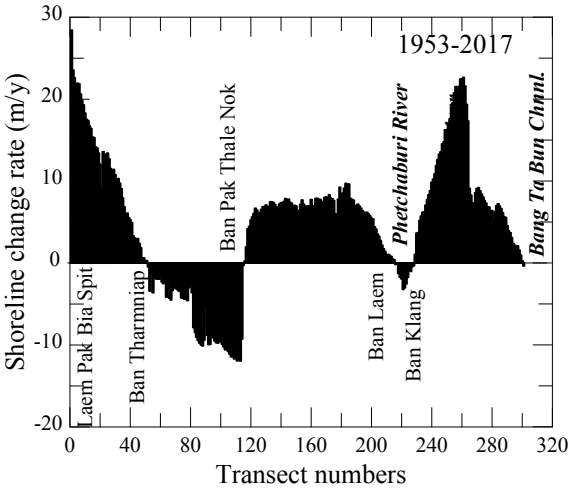

Fig. 4 Long-term shoreline changes along the Phetchaburi coast from 1953 to 2017

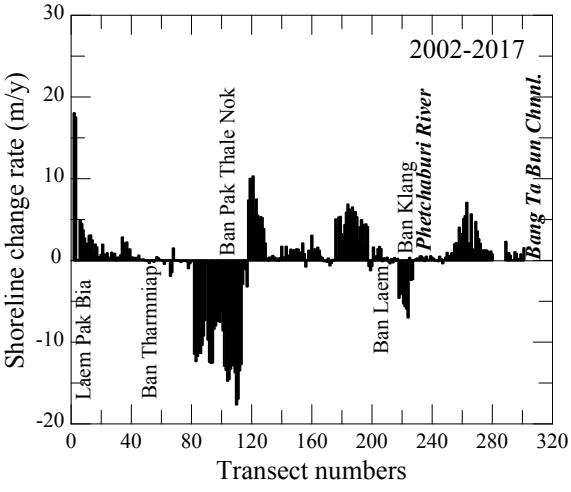

Fig. 5 Short-term shoreline changes along the Phetchaburi coast from 2002 to 2017

than 1 ha/y) compared to the long-term rate. This indicated the considerable reduction on the sediment transported southward during the past 15 years.

4.2 Ban Pak Thale Nok Zone (Cell-2)

The Ban Pak Thale Nok or Cell-2 section extends 6.3 km from the north of the Cell-1 to Ban Pak Thale Nok (Fig. 3). This section covers about 21% of the total muddy coastline of the Phetchaburi Province, and it is the only section that no fringe mangrove was found along the shoreline. Most of the coastline has been urbanized and developed for aquacultures by 1953. Results from the long-term shoreline change analysis indicated that the Cell-2 had a recessional trend, and the coastline of this cell had continuously retreated with an average erosion rate of −6.5 m/y. Along approximately 6.3 km of coastline between transects 52 and 115 has experienced a severe shoreline retreat with the erosion rate greater than −5 m/y. The highest rate of long-term shoreline retreat, −11.9 m/y, was found at Ban Pak Thale Nok (transects 111). The low rate of shoreline erosion was found in the remaining portion where the coast has been protected by coastal protection structures, such as seawalls and segment breakwaters.

The continuous erosion in this cell seemed to be shoreline adjustment in response to natural wave climate in the study area. Based on the short-term analysis, although, the average retreat rate slightly decreased to −5.6 m/y during the last 15 years, the highest short-term rate of shoreline retreat increased to about −19 m/y and occurred along Ban Thale Nok coast on which aquaculture farms have been intensively developed. Even though several studies suggested that severe shoreline erosion on muddy flat in Thailand may be caused by conversion of mangrove to aqua-culture ponds (Naohiro et al. 2012; Saito et al. 2001; Siripong 2010; Thampanya et al. 2006; Winterwerp et al. 2005), those aquaculture ponds just have accelerated the shoreline retreat rate. However, they seemed not to be a major cause of the coastal erosion along the Cell-2, since the pond dikes were devastated by wave action. The sea water rapidly encroached into those ponds and jumped up the rate of shoreline retreat in the area.

The sediment from the eroded coast along the Cell-2 were transported to the south during the Northeast monsoon and were trapped by the Laem Pak Bia spit resulting in the significant shoreline accumulation along the Cell-1 (as discussed in Sect. 4.1), even though the fringe mangrove forest in the Cell-1 had also been converted to salt pans and shrimp farms by 1960s. As mentioned above, the conversion of mangrove to aquaculture did not directly drive the shoreline recession in this region. From Table 2, it reveals that total land losses over the past 60 years in the Cell-2 was about 280 ha, and only 56 ha occurred during the last 15 years. The land losses from the Cell-2 to Cell-1 seemed to be accounted for 70 and 80% of the Cell-1's land accretion for the long-term and short-term, respectively.

4.3 Ban Laem Zone (Cell-3)

Ban Laem section (Cell-3) had about 11 km long of the coastline (about 35% of the total study coastline) stretching between Ban Pak Thale Nok and the Phetchaburi River mouth (from transects 116–228). Similar to the Cell-1, the Cell-3 coast is characterized by fringe mangrove. The comparison of shorelines between 1953 and 2017 showed that most of the Cell-3 coastline has constantly developed seaward by 6.3 m/y on average except the 1 km of coastline adjacent to the Phetchaburi River mouth (transects 216–228) that has eroded with the long-term rate of −1.3 m/y. The land accretion in this cell over the past six decades was totally about 415 ha. Because the location of the Phetchaburi River mouth directly confronts the northeasterly wave, the sediment discharged from the river transport separately in two directions, northward and southward of the river. The southward sediment transport plays a major role in land growth process along the Cell-3 coast as the major sediment source of the cell.

Similar to the Cell-1, the impact of aquaculture development along the Cell-3 was not significant during the past 60 years. The highest average rate of shoreline movement in this section was 14 m/y during the period 1967–1976. An expansion of mangrove forest (>6 m/y) was still observed even during the aquaculture blooming period (1976–1997). The amount of riverine sediment supplied from the Phetchaburi River and the network of irrigation channel (Fig. 3) seemed to be the dominant factor controlling the proliferation of mangrove in this cell.

However, based on the short-term analysis, the average rate of shoreline advance during the past 15 years in this cell significantly decreased to 2.7 m/y. Meanwhile, the rate of shoreline erosion adjacent the Phetchaburi River mouth rose to −2.3 m/y, and only 31 ha of land accumulation occurred during this period. Figure 5 revealed that 7% of the Cell-3 shoreline had the high short-term rate of shoreline accretion (>5 m/y). The low shoreline advanced rate (<2 m/y) was found along the 78% of total coastline in this section. Meanwhile, the remaining coastline had experienced shoreline recession during the last 15 years. The reduction of land accumulation combined with the extension of eroded coastline found along the Cell-3 clearly indicated a significant decline in riverine and longshore sediment supply to this coastal cell. The total land loss in this cell over the past 60 years was about 5 ha, and almost 58% of the loss took place during the last 15 years.

4.4 Ao Bang Ta Bun Zone (Cell-4)

The Ao Bang Ta Bun section (Cell-4) has approximately 7 km long of coastline extending from the Phetchaburi River to Bang Ta Bun Channel mouths (transects 229–300) as depicted in Fig. 3. In this section, the coast fringe was covered with mangrove belt as found in Cell-1 and Cell-3. The net long-term shoreline change rate for this cell was accretion with an average of almost 10 m/y. The maximum long-term rate of

shoreline accretion, almost 30 m/y, was found at transect 261 where the northward sediment transport from the Phetchaburi River and the southward sediment transport from the Bang Ta Bun Channel converged. Since this cell received sediment from those of river channels but different direction, this cell became an accretionary zone. Regarding its depositional environment, the fringe mangrove along the coast has rapidly colonized, and the Cell-4 shoreline has continued to grow seaward along most of its coastline, especially in the middle portion of the cell. Totally, the long-term land growth of this cell was approximately 360 ha over the past six decades. In a similar manner to the Cell-1 and Cell-3, even though mangrove deforestation for aquaculture along the Cell-4 coastline was intensive during the period 1976–1997, the mangrove forest expansion rate was about 11.6 m/y due to the high rate of sediment supplied from the Phetchaburi River, the Bang Ta Bun Channel and the irrigation channel network (Fig. 3).

Based on the short-term analysis of this cell, the results indicated that the shoreline advance rate considerably decreased during the recent 15 years with the average shoreline accretion rate of 2.9 m/y. The significant shoreline advance was found only along 2.5 km coastline at the mid of the cell. The reduction in shoreline growth and mangrove colonization rates in the Cell-4 indicated a significant change in coastal environment. The change possibly related to the change in riverine sediment supply due to the freshwater management for agricultural and tourism purposes during the past few decades. Another possible factor affected the rate of shoreline advance in this area is relative sea level change, which is responsible for severe shoreline retreat in some muddy beaches nearby the study area such as the Chao Phraya delta (Bidorn 2016).

5 Conclusion

In this chapter, the historical shoreline changes along the Phetchaburi muddy coast was assessed. Based on the long-term analyzes of 300 transects, the 30 km coastline of the study area had an accretional trend with the average net rate of long-term 3.1 m/y. Approximately 76% of the total coastline had continuously advanced with an average shoreline growth of 8.6 m/y, and the maximum shoreline advance of 30 m/y was found between the Phetchaburi River and Bang Ta Bun Channel mouths, which are the major sediment supply sources in the study area. Most of the accretion coastlines are characterized by fringe mangrove. Meanwhile, the remaining coastline has experienced shoreline recession, and the average shoreline retreat rate was about −6.5 m/y over the past six decades. The erosional trends were found along the 6.3 km coastline between Ban Tharmniap and Ban Pak Thale Nok; the highest rate of shoreline retreat was up to −12 m/y at the tip Ban Pak Thale Nok coast. In overall, the land loss and land growth along the Phetchaburi's coast during the period 1953–2017 were totally 287 ha and 1165 ha, respectively.

Results from the short-term analysis indicated that the majority of Phetchaburi muddy coast was still advancing seaward during the last 15 years, but the rate of

shoreline growth was significantly plummeted to less than 3 m/y. This trend can be implied that the Phetchaburi coastal environment has changed, and the changes are likely associated with the decrease in riverine sediment supply and relative sea level rise due to human activities. Meanwhile, the percentage of eroding beaches decreased to 14% as a result of coastal protection measures. However, the maximum rate of the shoreline recession in some unprotected areas rose to −18 m/y. As the long- and short-term shoreline retreat rates are slightly different, local coastal processes seem to be a major factor that controlled the pattern of shoreline retreat in this area. The results also suggested that the fringe mangroves can be only found in the area with the depositional environment. From 2002 to 2017, the total land loss and land growth were 58 ha and 118 ha, respectively.

Additionally, in contrast to the mangrove muddy coasts in other regions, such as Vietnam, Indonesia, Bangladesh, and even in the Southern part of Thailand, the population of mangrove along the Phetchaburi muddy coast had not affected by the conversion of mangrove to aquaculture. The results showed that if the river basin system can provide a sufficient sediment to maintain a depositional environment along the coast, the mangrove can naturally and rapidly proliferate. Therefore, the pattern of mangrove evolution possibly can be used as a proxy to indicate the changes in riverine sediment supply, which typically involves the changes in climate and human activities.

Acknowledgements The study was financially supported by the Grants for Development of New Faculty Staff, Ratchadaphisek-somphot Endowment Fund and Research Assistantship Fund, Graduate School, Chulalongkorn University.

References

Alberico, I., Amato, V., Aucelli, P., D'Argenio, B., Di Paola, G., & Pappone, G. (2012). Historical Shoreline change of the Sele Plain (Southern Italy): The 1870–2009 time window. *Journal of Coastal Research, 28,* 1638–1647. https://doi.org/10.2112/JCOASTRES-D-10-00197.1.

Anthony, E., Dussouillez, P., Dolique, F., Besset, M., Brunier, G., Nguyen, V., et al. (2017). Morphodynamics of an eroding beach and Foredune in the Mekong River Delta: Implications for deltaic Shoreline change. *Continental Shelf Research, 147,* 155–164. https://doi.org/10.1016/j.csr.2017.06.018.

Bidorn, B. (2016). *Causes of Shoreline recession in the Chao Phraya Delta*. (Ph.D. Dissertation). Florida State University, USA.

Blodget, H., Taylor, P., & Roark, J. (1991). Shoreline changes along the Rosetta-Nile Promontory: Monitoring with satellite observations. *Marine Geology, 99,* 67–77. https://doi.org/10.1016/0025-3227(91)90083-G.

Camfield, F. E., & Morang, A. (1996). Defining and interpreting shoreline change. *Ocean and Coastal Management, 32,* 129–151. https://doi.org/10.1016/S0964-5691(96)00059-2.

Chaverot, S., Héquette, A., & Cohen, O. (2008). Changes in storminess and Shoreline evolution along the Northern Coast of France during the second half of the 20 century. *Zeitschrift für Geomorphologie, Supplementary Issues, 52,* 1–20. https://doi.org/10.1127/0372-8854/2008/0052S3-0001.

Ha, T. T. T., van Dijk, H., & Bush, S. R. (2012). Mangrove conservation or shrimp farmer's livelihood? The devolution of forest management and benefit sharing in the Mekong Delta, Vietnam. *Ocean and Coastal Management, 69,* 185–193.

Hapke, C. J., Reid, D., & Richmond, B. M. (2009). Rates and trends of coastal change in California and the regional behavior of the beach and cliff system. *Journal of Coastal Research, 25,* 603–615. https://doi.org/10.2112/08-1006.1.

Hapke, C. J., Reid, D., Richmond, B. M., Ruggiero, P., & List, J. (2006). *National assessment of Shoreline change part 3: Historical Shoreline change and associated coastal land loss along sandy Shorelines of the California coast* (US Geological Survey Open-File Report). 1219, 27.

Hossain, M. S., Uddin, M. J., & Fakhruddin, A. N. M. (2013). Impacts of shrimp farming on the coastal environment of Bangladesh and approach for management. *Reviews in Environmental Science and Bio/Technology, 12*(3), 313–332. https://doi.org/10.1007/s11157-013-9311-5.

Hydro and Agro Informatics Institute. (2012). *Phetchaburi River Basin* (in Thai). http://www.thaiwater.net/web/attachments/25basins/19-petchaburi.pd.

Li, X., & Damen, M. C. (2010). Coastline change detection with satellite remote sensing for environmental management of the Pearl River Estuary, China. *Journal of Marine Systems, 82,* S54–S61. https://doi.org/10.1016/j.jmarsys.2010.02.005.

Mujabar, P. S., & Chandrasekar, N. (2001). Shoreline change analysis along the coast between Kanyakumari and Tuticorin of India using remote sensing and GIS. *Arabian Journal of Geosciences, 6,* 647–664. https://doi.org/10.1007/s12517-011-0394-4.

Muttitanon, W., & Tripathi, N. K. (2005). Land use/land cover changes in the coastal zone of Ban Don Bay, Thailand using Landsat 5 TM data. *International Journal of Remote Sensing, 26*(11), 2311–2323. https://doi.org/10.1080/01431160512331326666.

Naohiro, M., Putth, S., & Keiyo, M. (2012). Mangrove rehabilitation on highly eroded coastal Shorelines at Samut Sakhon, Thailand. *International Journal of Ecology, 2012,* 1–11. https://doi.org/10.1155/2012/171876.

Natalaya, P., Yong, R.N., Chumnankit, T., & Buapeng, S. (1996). Land subsidence in Bangkok during 1978–1988. In *Sea-level rise and coastal subsidence* (pp. 131–150). Springer. https://doi.org/10.1007/978-94-015-8719-8_6.

Office of Environmental Policy and Planning. (2000). *Mitigation of erosion problems along the coast from Phetchaburi River mouth, Phetchaburi Province, to Pranburi River mouth, Prachuap Kirikhan Province* (Master plan report) (in Thai).

Office of the Nation Economic and Social Development Board. (1993). *Potentiality of the Phetchaburi River Basin Development* (Report) (in Thai).

Ottinger, M., Clauss, K., & Kuenzer, C. (2016). Aquaculture: Relevance, distribution, impacts and spatial assessments–A review. *Ocean and Coastal Management, 119,* 244–266.

Rahman, A. F., Dragoni, D., Didan, K., Barreto-Munoz, A., & Hutabarat, J. A. (2013). Detecting large scale conversion of mangroves to aquaculture with change point and mixed-pixel analyses of high-fidelity MODIS data. *Remote Sensing of Environment, 130,* 96–107.

Saito, Y., Chaimanee, N., Jarupongsakul, T., & Syvitski, J. P. (2007). Shrinking Megadeltas in Asia: Sea-level rise and sediment reduction impacts from case study of the Chao Phraya Delta. *Inprint Newsletter of the IGBP/IHDP Land Ocean Interaction in the Coastal Zone, 2,* 3–9.

Saito, Y., Yang, Z., & Hori, K. (2001). The Huanghe (Yellow River) and Changjiang (Yangtze River) Deltas: A review on their characteristics, evolution and sediment discharge during the Holocene. *Geomorphology, 41,* 219–231. https://doi.org/10.1016/S0169-555X(01)00118-0.

Seto, K. C., & Fragkias, M. (2007). Mangrove conversion and aquaculture development in Vietnam: A remote sensing-based approach for evaluating the Ramsar convention on Wetlands. *Global Environmental Change, 17*(3–4), 486–500. https://doi.org/10.1016/j.gloenvcha.2007.03.00.

Siripong, A. (2010). Detect the coastline changes in Thailand by remote sensing. *International Archives of the Photogrammetry, Remote Sensing and Spatial Information Science, 38,* 992–996.

Thampanya, U., Vermaat, J., Sinsakul, S., & Panapitukkul, N. (2006). Coastal erosion and mangrove progradation of Southern Thailand. *Estuarine, Coastal and Shelf Science, 68,* 75–85. https://doi.org/10.1016/j.ecss.2006.01.011.

Thanh, T. D., Saito, Y., Van Huy, D., Nguyen, V. L., Ta, T., & Tateishi, M. (2004). Regimes of human and climate impacts on coastal changes in Vietnam. *Regional Environmental Change, 4,* 49–62. https://doi.org/10.1007/s10113-003-0062-7.

Thieler, E. (2011). *Digital Shoreline Analysis System (DSAS) version 4.0—An ArcGIS extension for calculating shoreline change* (US Geological Survey Open-File Report).

Uehara, K., Sojisuporn, P., Saito, Y., & Jarupongsakul, T. (2010). Erosion and accretion processes in a muddy dissipative coast, the Chao Phraya River delta, Thailand. *Earth Surface Processes and Landforms, 35,* 1701–1711. https://doi.org/10.1002/esp.2012.

Vongvisessomjai, S., Polsi, R., Manotham, C., Srisaengthong, D., & Charulukkana, S. (1996). Coastal erosion in the Gulf of Thailand. In J. D. Milliman, & B. U. Haq (Eds.), *Sea-level Rise and Coastal Subsidence: Causes, Consequences, and Strategies* (pp. 105–130). Springer. https://doi.org/10.1007/978-94-015-8719-8_7.

Winterwerp, J. C., Borst, W. G., & De Vries, M. B. (2005). Pilot study on the erosion and rehabilitation of a Mangrove Mud Coast. *Journal of Coastal Research*, pp. 223–230. https://doi.org/10.2112/03-832A.1.

Wolanski, E., Spagnol, S., Thomas, S., Moore, K., Alongi, D., Trott, L., et al. (2000). Modelling and visualizing the fate of shrimp pond effluent in a mangrove-fringed tidal creek. *Estuarine, Coastal and Shelf Science, 50*(1), 85–97.

Yang, Z., Wang, T., Voisin, N., & Copping, A. (2015). Estuarine response to river flow and sea-level rise under future climate change and human development. *Estuarine, Coastal and Shelf Science, 2*(156), 19–30. https://doi.org/10.1016/j.ecss.2014.08.015.

Zhang, X., Pan, D., Chen, J., Zhao, J., Zhu, Q., & Huang, H. (2014). Evaluation of coastline changes under human intervention using multi-temporal high-resolution images: A case study of the Zhoushan Islands, China. *Remote Sensing, 6,* 9930–9950. https://doi.org/10.3390/rs6109930.

Rapid Growth and Break-Up of a 'Dormant' Shingle Spit Across the Tidal Inlet of Pagham Harbour, Southeast England

Uwe Dornbusch

Abstract Little understanding on the growth and break-up of mixed sand and gravel spits exists, yet they are associated with estuaries and are often close to settlements and engineering structures, with potential impact and interactions with them. Understanding their behaviour can help manage the environmental and human risk in the future. This chapter reports on the growth, break-up, impact on tidal exchange and interaction with engineering structures of Church Norton Spit over the period 2001–2018 using over 50 topographic surveys, together with tide gauges inside and outside the estuary. During this time, the spit grew over 1100 m in 12 years during which time it rolled back through overwashing but only breached in 2016 due to a series of storms over a period of 3 months. Growth of the supratidal spit is controlled by sediment supply and the presence of an intertidal spit extension/ebb tide delta/intertidal shoals on which to advance. Final breaching results from the complex interaction of a shifting ebb-delta, a curved inlet channel that limits roll-back and a combination of storms and high tides to successively lower the crest through initial overwashing and eventual tidal scouring. Contrary to many studies on sandy inlets, the dramatic increase of the inlet channel length had no impact on tidal exchange in the estuary; this only occurred following breach and the breakdown of the spit. Understanding of the spit dynamics will improve the future management of other shingle spits and of Church Norton spit in case the increased sediment supply that started the growth in ~2003 is continuing and the spit will start to extend again.

Keywords Mixed sediment · Barrier breach · Roll-back · Church norton · Tidal exchange · Overwashing

1 Introduction

There is a considerable body of literature on the behaviour of tidal inlets on sandy, microtidal coasts that have attracted extensive classifications of processes of sediment

U. Dornbusch (✉)
Environment Agency, Worthing, UK
e-mail: uwe.dornbusch@environment-agency.gov.uk

K. D. Nguyen et al. (eds.), *Estuaries and Coastal Zones in Times of Global Change*, Springer Water,
https://doi.org/10.1007/978-981-15-2081-5_26

bypassing (e.g. Hayes and FitzGerald 2013; FitzGerald et al. 2000) or life-cycle models (Seminack and McBride 2018), particular in relation to the US East and Gulf coast. In contrast, the literature on tidal inlets in meso- or marcrotidal gravel and mixed sand and gravel (shingle) environments is much smaller (Burningham and French 2006, 2007; Burningham 2015). Equally, there is large body of literature on the evolution of sand barriers (e.g. Stripling et al. 2007) and the prediction of future behaviour (e.g. Plant et al. 2014) while for shingle beaches examples are scarce and are often confined to one or two storms and their impact (e.g. Orford 2011). Despite significant progress in short term progress understanding of pure gravel (McCall et al. 2015) and mixed sand and gravel beaches (Polidoro and Pullen 2016; Polidoro et al. 2014; Dornbusch et al. 2013) there is still the notion that "knowledge of gravel-barrier formation, general short-term barrier behaviour, and long-term barrier evolution under changing forcing scenarios are of growing concern" (Orford and Anthony 2011: 42).

Beaches on the south coast of England have predominantly formed from sediment moved onshore with sea level rise during the Holocene transgression (e.g. Mellett et al. 2012) and subsequently moved alongshore in an easterly direction (Bird et al. 2003). While "On some coasts wave action still moves sand and gravel from shallow sea-floor areas onto beaches […] the progressive reduction of offshore sediment volumes [means] that the seabed now supplies to the sediment budget only a small percentage of the previous amounts." (Bird et al. 2003, 208–9).

In the study area (Fig. 1) updrift cliff erosion at Selsey Bill was previously seen as a major sediment contributor "With annual cliff retreat in excess of 6 m a^{-1} between 1932 and 1951, the eastern cliffs at Selsey Bill were probably supplying about 9000 m^3 a^{-1} to the beach leading to Pagham." (May 2003: 280), however, May concludes that "Today the natural sediment supply [to the spit] has largely ceased as a result of anthropogenic influence" (2003: 281); the entire eastern frontage of the Selsey Bill peninsula has been protected by seawalls and a dense groyne field since the 1950s.

These conclusions in 2003 are the result of observations over the preceding ~35 years over which the coastal plan-shape had undergone virtually no changes. However, historic maps dating back to the 16th century show the changing positions of the harbour mouth within the ~2.5 km wide opening between raised ground (Robinson and Williams 1983; Scott and Townend 2017), and the present Lagoon traces the northward channel forced against the higher ground by the spit in the 1870s. None of these maps show the spit growing in front of the beach but rather the change in the mouth's position along the line of the barrier. It came as a surprise when the spit started prograding in 2003 and then in 2005 leading to the growth of the spit across the channel (Fig. 2).

Church Norton Spit (CNS), Pagham Harbour (PH) and parts of Pagham Beach (PB) have extensive national and international Nature designations predominantly for intertidal habitats, vegetated shingle habitat and birds. The often cited impact of the lengthening of inlet channels by reducing the hydraulic efficiency of the channel and thus reducing the tidal prism (FitzGerald et al. 2000; Hayes and FitzGerald 2013; Seminack and McBride 2018) is a concern in relation to the intertidal habitats inside

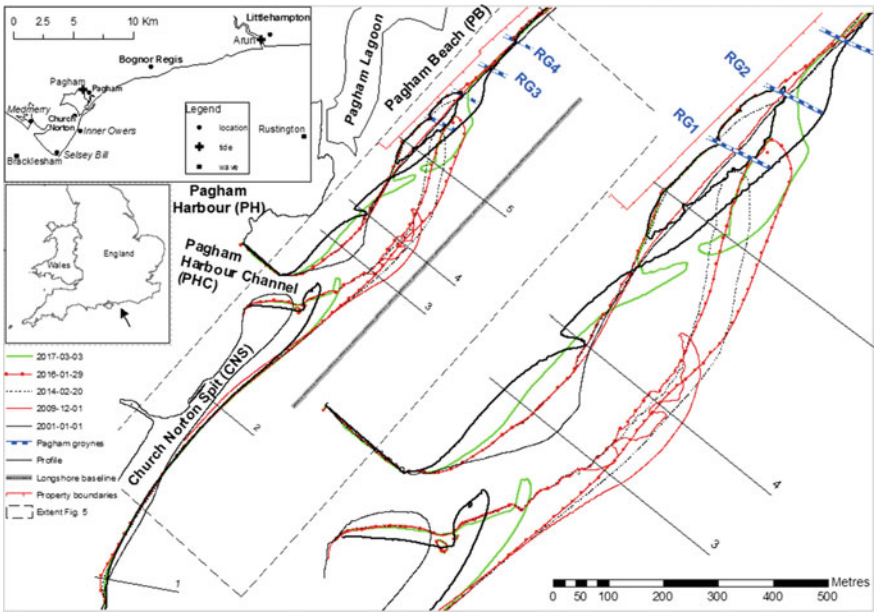

Fig. 1 Overview map showing locations and names mentioned in the text, MHW for selected surveys, location of profile lines and the baseline onto which the longshore profile in Fig. 4 is projected; the rectangle marks the area covered by the aerial photography in Fig. 5

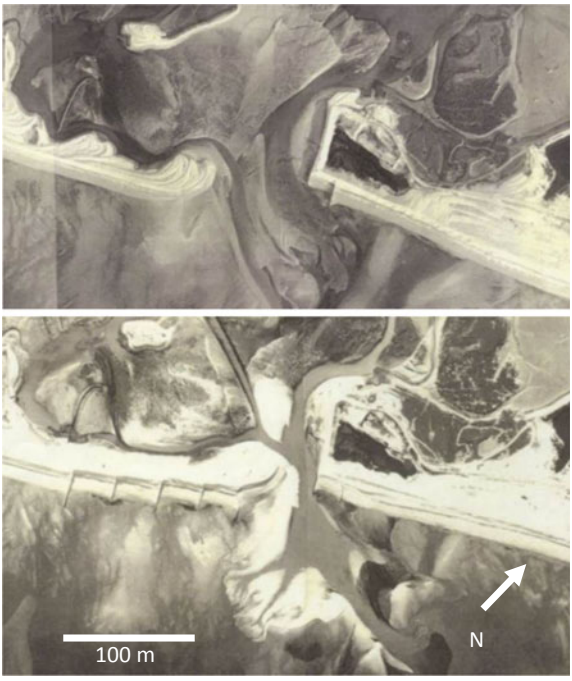

Fig. 2 Aerial photos showing spit growth and training arm in 1961 (top) and the artificially reshaped Church Norton Spit with five groynes in 1966

Fig. 3 Overwashing through area of lowered crest on 31-12-2015 at ~15:00 h as seen from PB. http://paghambeach.blogspot.co.uk/2015/12/

PH. The Site of Special Scientific Interest (SSSI) designation (Natural England 1980) includes specifically the geomorphology of the open coast. On the PB side, since the 1920s, beach huts made from disused railway carriages started to occupy the beach that had accumulated there only a couple of decades before, and over the years these huts have been converted and extended to permanent housing since the 1960s, coincident with the period of plan-shape stability.

The last attempt to stabilize the PH entrance was carried out in 1963 by replacing a range of training structures with a steel sheet pile wall (rebuilt after the failure of its seaward section through undermining and pushing-over by flood currents in 1986) on the PB side to stop the channel from migrating northwards and potentially threatening the growing beach community which was still >600 m to the northeast. In conjunction with this measure, the dominant threat was perceived to be a breach along CNS, and to this end timber groynes were installed in the 1960s (Fig. 2) and beach material was recycled by the Environment Agency (EA) and its predecessor organisations from the ebb-tide shoals southwest of the channel to the beach along CNS up to 2004, creating and maintaining an artificial—flat topped at 6 mOD—'drumstick' shaped barrier.

Following a brief description of the coastal environment and methodologies in Sects. 2 and 3, the paper describes the growth and disintegration of Church Norton Spit between 2001 and 2018 in Sect. 4 followed by a discussion of the observations in Sect. 5.

2 Coastal Environment

The area of Pagham Harbour is characterised by a mean tide range of just about 4 m (mean spring tidal range of 4.8 m) with MHWS at 2.55 mOD and MHWN at 1.25 mOD. Between 3 h before and 3 h after high tide, tidal currents flow in a southwesterly direction with peak velocities reached at high tide and an hour afterwards with speeds measured 1 m above the bed not exceeding 0.5 ms^{-1} (Barcock and Collins 1991). Flow direction over the ebb is more varied due to the bathymetry influence and flow speed is generally weaker. In both cases, tidal currents are insufficient

to mobilise gravel. The harbour entrance is somewhat sheltered from the dominant southwesterly waves (CCO 2017a, b) but south-southwesterly and southerly waves undergo less diffraction behind Selsey Bill and less refraction over the shallow subtidal bay where the −5 mOD (−10 mOD) contour is ~1 km (5–7 km) seaward of the beach. The average Hs exceedance during 0.05% of the year is 3.6 m and 3.8 m for Bracklesham and Rustington wave buoys (for location see Fig. 1) respectively (CCO 2017a, b). The study area experienced an unusual storm season over the winter 2013/2014 both in terms of wave conditions (Met Office 2014) and storm surges (Wadey et al. 2014) that created widespread coastal change along the English South Coast (Bradbury and Mason 2014) with particularly dramatic changes at Medmerry on the opposite side of the Selsey Peninsula (Dornbusch and Mylroie 2017).

3 Methodology

Bathymetry, aerial photography and topographic survey data have been collected since 2003 through the Coastal Monitoring Program (CCO 2017c) and also includes a small number of surveys carried out by the author. Topographic data pre-2003 was collected through photogrammetry by the Environment Agency (EA) and its predecessors and post-2002 was collected using GNSS surveys carried out on foot or with an all-terrain vehicle (Dornbusch 2010), in recent years combined with a mobile laser scanner. In addition, LIDAR data has been collected by the EA since 2004. Survey data since 2001 have been collected with a spatial density to allow for Digital Elevation Models (DEM) to be created from which contour lines and profiles shown in this chapter were derived. Finally a couple of Unmanned Aerial Vehicle surveys (UAV) have been carried out producing orthophotos on 23-10-2012 (not used in this chapter) and 26-09-2017 as well as a Google Earth scene collected on 22-04-2015.

Contours and profile data have been extracted from all available surveys. Profiles have been extracted at 2 m intervals along the coast and at 1 m distance across the study area perpendicular to the coastal alignment. For the longshore profiles in Fig. 4 the cross shore profiles have been cut at the beach toe of PB and the highest point extracted projecting the highest point onto a shore parallel line. This traces the advance of CNS along the shoreline and to the Northeast it reflects the highest point of any shoals. In both cases, the changes shown reflect both the alongshore and cross shore movement of the highest point. The cross shore dimension is shown for selected profiles in Figs. 6 and 7.

Bathymetry data for the wider bay was collected as single beam point survey at ~50 m interval in 2002 (Marine and Coastguard Agency 2002), through the Coastal Monitoring Programme in 2004/2006 (different areas with some overlap) as single beam profile survey (profile spacing ~150 m) across a 1 km strip seawards of MHW and in June 2016 as a swath bathymetry survey across an up to 3 km wide band. In addition, bathymetry and current data was collected using an EA Arc-boat (HR Wallingford 2014) along a small section of the inlet channel on 25-11-2014.

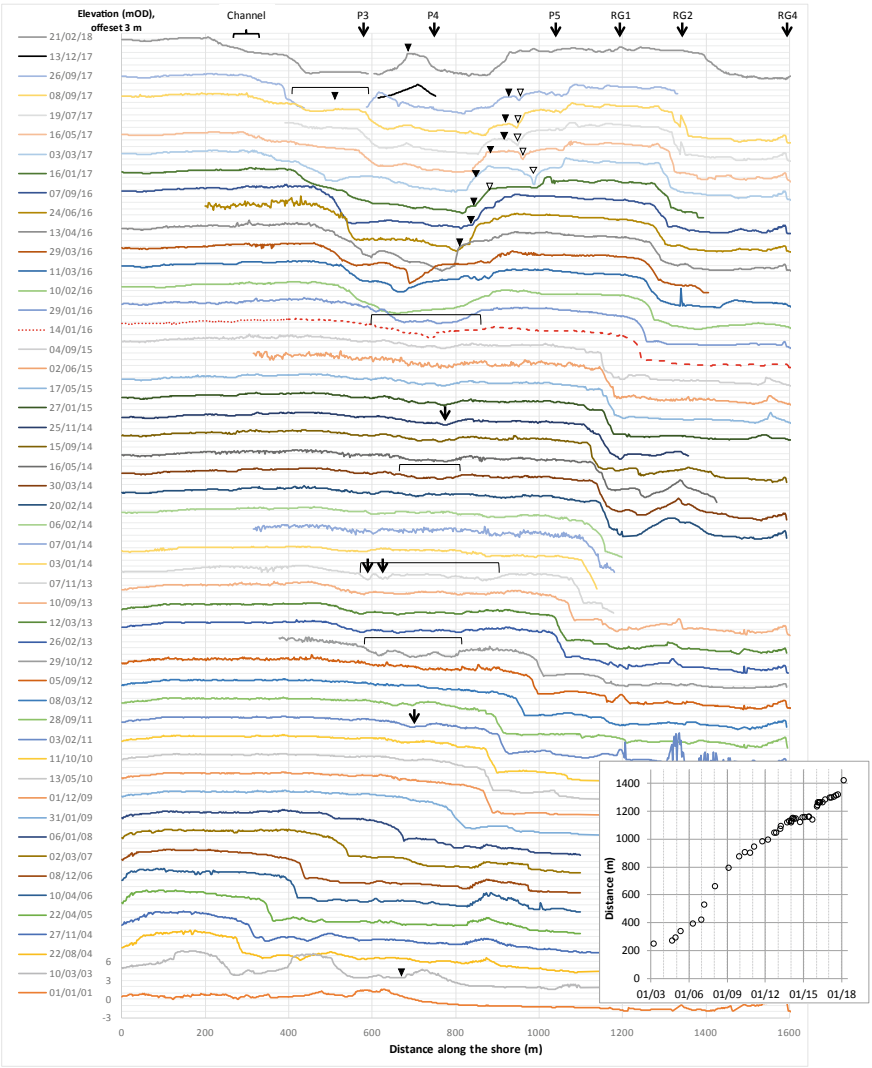

Fig. 4 Longshore profile along the highest points of CNS and the shoals to the north, seawards of PB. Arrows along the top indicate locations of the profiles in Figs. 6 and 7, the location of rock groynes and the position of the fixed channel exit at the training arm. Arrows and brackets within the graph highlight local or wider crest lowering. Triangles show projected position of centre of the inlet channel (closed for main channel and open for channel in CNL). Inset shows the position of the tip of CNS against time

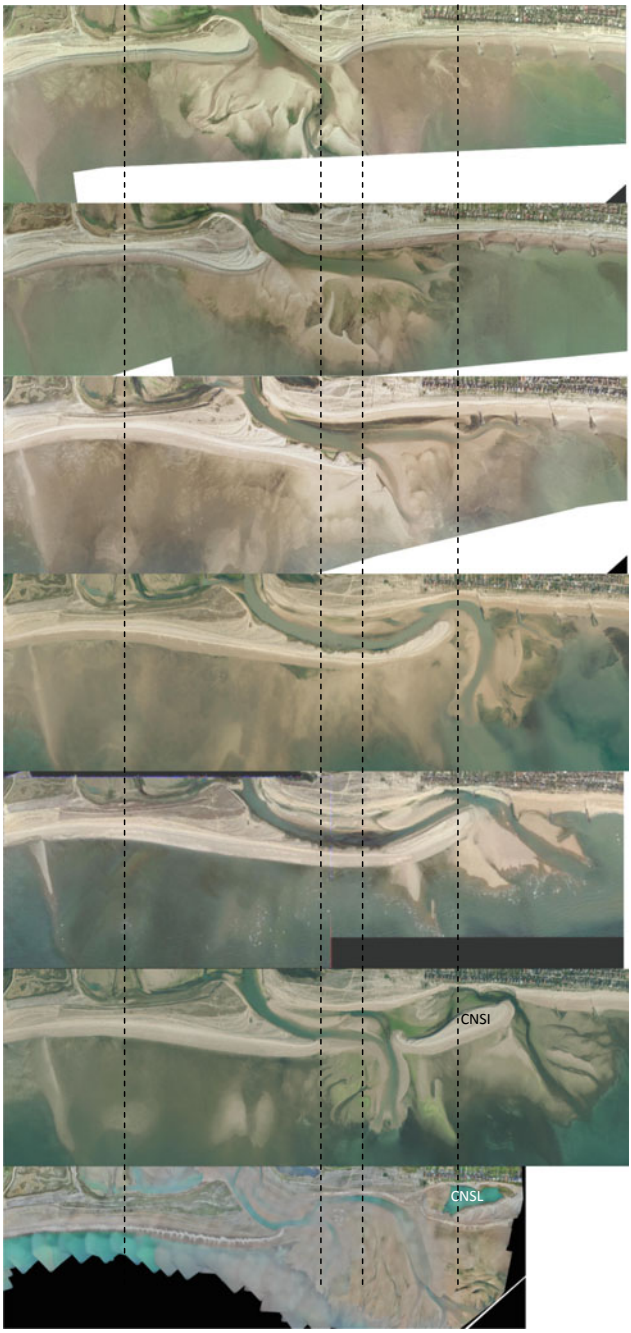

Fig. 5 Orthophotos sourced from aerial frame cameras (dates in normal font), satellite imagery (bold font) and UAV (underlined). Vertical lines show positions of P2 to P5. CNSI = Church Norton Spit Island, CNSL = Church Norton Spit Lagoon

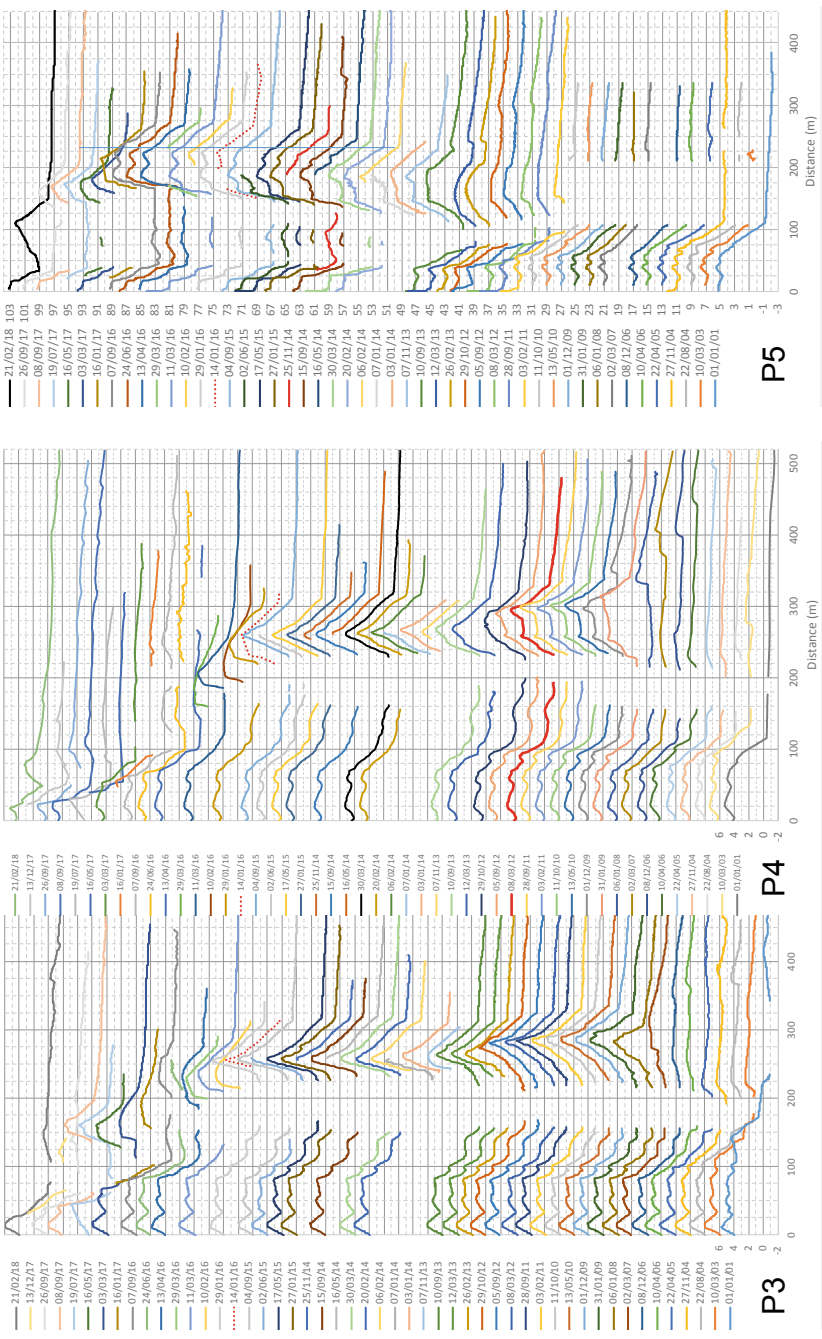

Fig. 6 Profile s P3, P4 and P5. distance in metres along the x-axis and elevation (mOD) on the y-axis with each profile offset by 1 m. For profile locations see Fig. 1

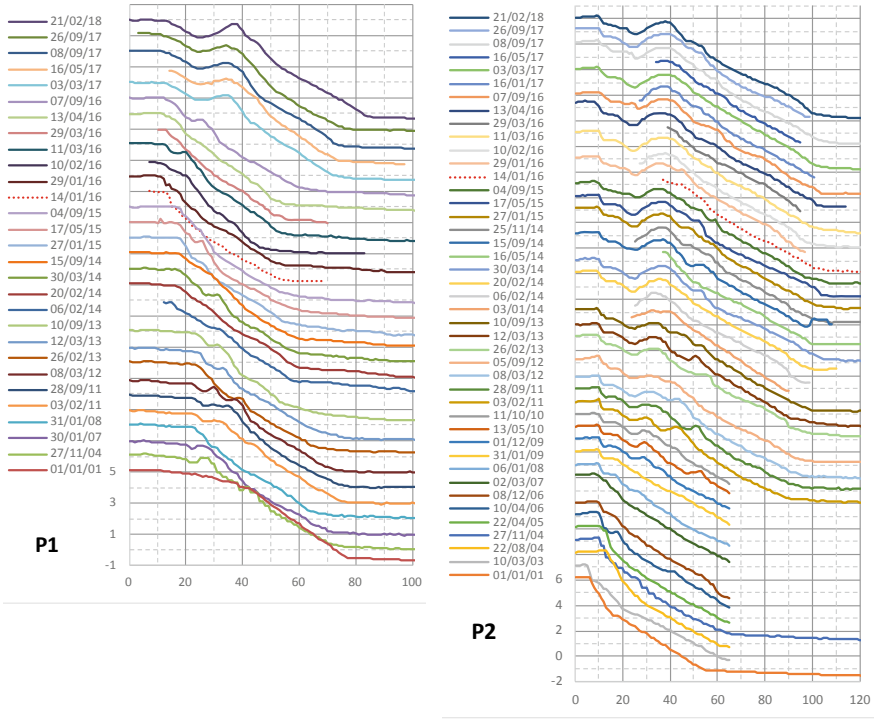

Fig. 7 Profiles P1 (root of CNS) and P2 showing distance in metres along the x-axis and elevation (mOD) on the y-axis with each profile offset by 1 m. For profile locations see Fig. 1

Tide gauge data comes from the EA gauges at the northern end of PH and within the mouth of the River Arun at Littlehampton (Fig. 1) recording at 15 min intervals.

Wave run-up was calculated using the Shingle Beach Run-up Tool (Polidoro et al. 2014) with wave data from Bracklesham wave buoy and water level data from the Littlehampton tide gauge. Wave run-up calculated by the tool is the maximum run-up and is only indicative of heights and frequencies because wave data was used directly from the buoy without modelling transformation to the vicinity of the CNS.

4 Growth and Disintegration

The evolution of CNS is shown using selected contour lines in Fig. 1, aerial photography in Fig. 5, a longshore profile along the highest point of CNS and the intertidal area in front of PB using all available surveys in Fig. 4 and representative cross shore profiles using all surveys in Figs. 6 and 7. An animation including all the surveys with complete coverage of the area up to February 2018 is provided by Adur and Worthing Council (2018).

4.1 1960s to 2001

Following a major breach in 1955 which opened the entire length between the root at Church Norton and the present training arm location, much of the broken-up spit was pushed into the harbour by wave action forming an island visible at the upper edge of the aerial photography shown in Fig. 2. By 1966, the CNS had reformed and groynes had been installed to stabilise the plan shape (Fig. 2).

Between 1966 and 2001, sediment was transported northeastwards along the Selsey East Beach and along CNS towards the Pagham Harbour Channel (PHC). In addition, sediment entered the frontage from the nearshore evidenced by sedimentary features persistent through time, i.e. the Inner Owers just south of the root of CNS (Fig. 1) or which are more flexible in position occurring along CNS and around the ebb delta. These are often delta shaped ramps pointing towards the coast with the highest point in the landward apex visible as individual (Figs. 2b and 5a, e and f) or joined up (Fig. 5b) landforms that migrate landwards, with the apex sometimes developing into a longer ridge. At the apex, these features can stand up to ~2 m above the surrounding intertidal area. In addition, shoreline orthogonal ridges described as transverse ridges and hypothesized in the past (Carter and Orford 1993; Orford et al. 1996) to aid landward transport of sediment, have been identified along the southern end of CNS. One of these ridges developed in 2003 and progressed along the coast at a rate of 10 m per year (Fig. 8 shows a shore perpendicular pattern of erosion and accumulation). It has been shown to act as a transport pathway for shingle (White 2016). Sediment reaching the tip of CNS was transferred through the ebb tidal current into the ebb delta from where wave transport processes pushed the material towards PB, aided by switching of the ebb channel across the delta similar to 'ebb-tidal delta breaching' and 'outer channel shifting' models by FitzGerald et al. (2000), also described for the mixed-sediment inlets at Woodbridge and Orford Haven by Burningham and French (2007). This has been illustrated in Barcock and Collins (1991) for the years 1977–1981.

4.2 2001 to December 2006—Building Up

The description of the evolution of the area is illustrated in Figs. 4, 5, 6, 7, 8 and 9 without specifically referencing them at every step.

The first DEM data for the area is available from a photogrammetric survey in the summer of 2001. In 2001, there is no sign (contour, longshore profile and aerial) of CNS being seaward of its position maintained over the previous decades. The ebb tide delta, reaching up to 1.3 mOD, extends for 810 m across the opening approximately half and half either side of the fixed channel (only about 700 m are shown in Fig. 4). By March 2003, the tip of the spit had accreted on the seaward side (chainage ~130–250 m) and a substantial shoal deflected the channel alongshore and closer to PB leading to a retreat at P3 of ~40 m.

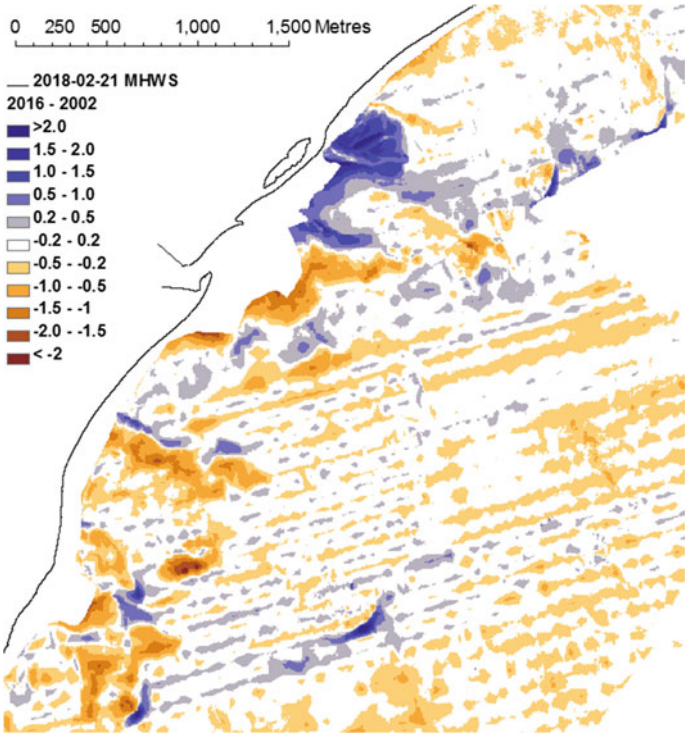

Fig. 8 Comparison of bathymetry collected in 2002 (point spacing ~50 m) and 2016 (swath bathymetry)

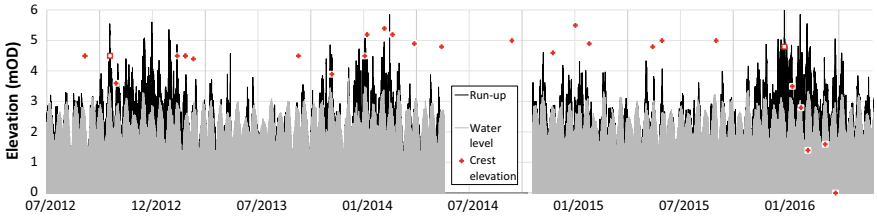

Fig. 9 Water level at Littlehampton, approximate maximum wave run-up elevation and lowest crest elevations for CNS; red squares highlight the two overwashing events discussed in more detail in the text

By the summer of 2005, CNS had continued to increase in length northeastwards, but also in the updrift direction, accompanied by an increase in maximum elevation of at least 0.5 m compared to March 2003. P3 and P4 together with the aerial photo show shoals moving landwards across the ebb-delta that was generally increasing in height across P3. The channel was pushed further against PB with an additional retreat of about ~20 m.

This gradual process of CNS extending northeast-wards and also building up updrift (indicated by the build-out of the beach toe in P2 by ~12 m) continued until December 2006. While CNS extended in size, it also grew in height with the area around chainage 200 increasing again by at least 0.4 m.

4.3 December 2006 to October 2010—Rapid Growth I

Over the next 36 months to December 2009, CNS advanced ~450 m along the coast on a slightly seaward trajectory, creating a number of discrete recurves (Fig. 1). The fastest advance appears to have occurred in the 3 months between December 2006 and March 2007 over which the CNS increased in length by ~110 m. However, it is not just the spit that advanced but also the shoals on the ebb-delta increased in elevation by up to 1.5 m and gained around 100 m^3 of sediment per metre of shoreline (P3). The shoal extending for ~160 m in front of CNS in March 2007 has an elevation of up 1.5 mOD, allowing for wave processes to push the sediment further landward and contribute to the further rapid growth up to December 2009 by providing a raised platform on which sediment - coming through longshore transport along CNS - can extend the supratidal feature.

The profiles from March 2007 to January 2009 in P3 show how the spit ridge 'springs' into existence using sediment from the shoal, that in turn lowers in this profile transformation, and then increases in elevation and builds out seaward. This is a general observation in relation to the maximum elevation longshore profile, that each newly created length of CNS is lower than the established sections and that, as the spit extends, maximum elevation increases.

By December 2009, advance of the supratidal CNS had outpaced the growth (northeastward extension and increase in elevation) of the ebb-delta and its shoals with all terrain lying ahead well below 0 mOD (Fig. 4). Because its trajectory had been slightly away from PB (Fig. 1), CNS started to swing towards PB during 2009. At the same time, the now more seaward part of CNS created in 2007/08 started to lose beach material from the front illustrated by the changes at P3 and in particular P4.

Over these 36 months, PB behind the advancing spit (P3, P4) as well as updrift (P2) and downdrift (P5) was unaffected, however, the root at P1 did experience some losses (though there are fewer surveys at this location than at the others).

The next 13 months (until October 2010) saw a period of consolidation with very little change in position of CNS or any of the profiles except that the ebb shoal built out and up again ahead of the CNS.

4.4 October 2010 to February 2014—Rapid Growth II

This preparatory work allowed for CNS to then again advance at a relatively constant rate for ~3.5 years until February 2014. Figures 1 and 5 clearly show that the trajectory was towards PB, aiming for the centre of the southernmost of the 4 rock groynes (RG1). During this progress, the ebb shoal initially advanced and rose with the spit but from 2012 shows in Fig. 4 to not to extend beyond the longshore position of RG1. The reason for this can be seen in the aerial photos of 2005, 2008 and 2013. While in the first two photos the main outflow channel is running essentially parallel to PB with some secondary channel(s) cutting across the ebb delta, the advance towards RG1 leads to a sharp 90° corner of the channel, forced by the presence of RG1. As a consequence, the sinuosity of the channel increased, leading to erosion of PB to the south of RG1 in front of the southernmost properties (P5) and the cutting away of the channel-facing side of CNS (P4 and to a lesser extent P3). At the same time, P4 shows the development of a shore-parallel in-channel shoal that separated the dominant flood current along PB from the dominant ebb current along the rear of CNS.

During this period, the first overwashing and crest lowering events became visible in the February 2011 survey around chainage 700, also affecting P3. The area self-healed over the summer and the subsequent winter. A more substantial event happened around 18-10-2012 (documented in the survey on 29-10-2012 for the longshore profile, P3 and particularly P4) which is shown to cover a length of CNS of more than 200 m, with lowering of up to 1.5 m down to a minimum level of ~3.6 mOD (Fig. 9) which is approximately 1 m above MHWS. Storms and water levels during this winter then led to crest build up again as documented with 4.5 mOD on 26-02-2013. However, P3 and P4 show that this was associated with the crest being rebuilt 21 m (P3) and 23 m (P4) further landwards. In particular at P4, the landward movement of the crest did not create any landward movement of the back of CNS into the inlet channel, thus creating a much narrower barrier. This level was maintained until a survey on 7-11-2013 which was preceded by high run-up together with high tides, creating two narrow overwash throats down to 3.9 mOD (P3) within a wider area ~ 300 m long. The following succession of storms over the winter 2013/14, in particular over Christmas 2013, raised the crest back up by the next survey on 03-01-2014 (together with some roll-back, see P4) to above 5 mOD, though by the end of the winter it was again below that level.

One of the fundamental changes along P3 is that the beach toe elevation decreased from 0.5 mOD in January 2007 to −1 mOD in February 2014 and further to -1.5 mOD in January 2016, thus allowing significantly higher waves to reach this segment of the beach.

At P2, and following mostly stability up to December 2010, this period saw the beach prograding with a wide storm ridge at 5.5 mOD established about 24 m seaward of the 2001 position. At P1 on the other hand, the beach toe and crest retreated by ~20 m. While the first suggests a healthy sediment supply towards CNS, the later could indicate some cannibalisation at the root, however, with a more southerly thane

average wave approach during the winter 2013/14, the retreat north of the last timer groyne of Chichester District Council could just be a subtle planform adjustment.

As the tip of CNS approached PB, the tidal inlet currents started to impact PB in an area with residential properties. P5 sits at the southern end of the main impact area, but the surveys covering this period nevertheless show how the PB side of the channel retreated in direct response to the channel being pushed toward it by the landward migrating ebb-shoal and later CNS. Owing to the potential risk to properties, an emergency rock revetment over the length of 130 m south of RG1 was started in mid-November and completed in early December 2013, shown first in the survey on 20-02-2014.

4.5 February 2014 to January 2016—Slow Changes

By mid-February 2014, the central part of RG1 had been undermined by the current forced through the 90° bend and breached, allowing the tidal flow through the gap in the rock groyne. As a consequence, the flow past the tip at the rear of CNS became straighter, leading to a gradual seaward erosion of the landward edge by ~20 m over this period. This widening of the channel provided the accommodation space for the in-channel shoal to migrate further north, visible by the increased width of dry land at low tide between the two channels in P5 (note that the survey on 25-11-2014 includes the Arc-boat bathymetry survey of this part of the channel). While the landward facing side retreated seawards, the seaward side prograded by ~35 m (P5), essentially rotating the last ~280 m of CNS seaward into a more shore parallel position (Fig. 1). The northern extent of CNS remained constant except for a brief cut-back over the summer in 2014; however, the forced channel between CNS and RG1 started to infill and a shoal built up to ~0 mOD. The same impact on PB as in 2013 started to occur in the groyne bay between RG1 and RG2 and additional rock, though not as a formal revetment, was placed along the PB in that groyne bay. In November/December 2015, CNS started to advance again over the shoal, passed RG1 on 23rd December 2015 and by 14-01-2016 had advanced 90 m from its September 2015 position and was now firmly between RG1 and RG2 with the outflow channel again turning almost 90° at RG2.

Over this period, P3 and P4 show stable profiles for CNS. Fluctuations of the crest level as seen in Fig. 9 continued until December 2015, though with a mix of data sources for the topographic surveys, changes in the range of ~±0.1 m are probably artefacts of the surveys.

P2 prograded slightly and P1 saw some erosion of the upper beach between September 2015 and January 2016.

4.6 January 2016 to February 2018—Breaching and Disintegration

A crest elevation of 5 mOD persisted until the end of December 2015 in the section prone to overwashing and roll-back, when over two successive high tides on 31-12-2015, the crest was lowered to a minimum of 3.5 mOD (Fig. 3) over a length of nearly 250 m as surveyed on 14-01-2016. P4 runs through this location.

During the next set of spring tides, which were slightly smaller, overwashing occurred again, widening and deepening the gap to just below 3 mOD as surveyed on the next day (29-01-2016). This level meant that during the following spring tides water could flow across CNS. The lowering was associated with a landward migration visible in Fig. 1.

By the time of the next survey on 10-02-2016 continuing storm activity and tidal water levels had lowered the gap to a minimum of 1.4 mOD, thus establishing tidal flows at high tides for all but lower neap tides. The lowering coincides with the landward displacement of the channel by ~30 m.

Over the following month (next survey on 11-03-2016), the area of lowering started to fill in again from both sides with the lowest 30 m long section around chainage 680 having risen to 1.7 mOD (see also P3 and P4). However, conditions over the next 18 days started to carve an ebb-dominated channel with a sill level at just over 0 mOD which meant that this new channel operated for most of the time, with the old channel at RG2 operating all the way through low tide.

By the next survey a fortnight later (13-04-2016), the role of both channels had changed, with the channel through the breach having become the dominant one operating even at low tide while the lower point in the sill to the old channel had risen to -0.4 mOD. Due to the obliquity of the channel in relation to the cross shore profiles from which the elevations in Fig. 4 were derived, and the growth of shoals in front of PB and landwards of the channel, the new channel through the breach section cannot be detected, but filled triangles mark the projected position of the centre of the new channel. Over the summer the width between CNS and the CNSI (Church Norton Spit Island) increased to over 300 m and the overall situation is captured in the July 2016 aerial photo showing the dramatic changes to the situation 15 months earlier (Fig. 5).

With PB no longer sheltered behind CNS, the recurves at the end of CNS and the southern end of CNSI bending landwards as well as the shoals in the breach lowering and pushing landwards too, PB, in particular in the vicinity of P4, underwent rapid erosion of 35 m (P4) and 50 m (P3) between April 2016 and July 2017. Some of this eroded material was transported south with the flood current towards the training arm and added to the sediment in the channel on the inside bend at the southern end of the training arm (still visible in the September 2017 aerial photo). During the ebb, sediment was moved northwards, where an oblique salient started to grow toward the southern end of the CNSI (see the 03-03-2017 MHW contour in Fig. 1).

This transport of sediment towards the north and to behind CNSI was aided by the still strong flow through the old channel for about half the tidal cycle. This flow

maintained the narrow channel between RG2 and the northern end of CNSI which had only moved ~50 m since February 2016 until it finally closed in February 2017. However, the main changes took place at the southern end of CNSI, where the end bent landwards and shortened with the sediment filling in the old channel. This can be seen in P5 where the April, June and September 2016 surveys connect CNSI and PB at levels of ~−1 mOD. The growth of the salient from PB towards CNSI and shown in an advanced stage by the contour and longshore profile for March 2017 created a connection that grew in elevation and helped to divert the inlet channel through the breach

As this connection grew in elevation, fed by sediment from PB and CNSI, a flood dominant channel was maintained into Pagham Spit Lagoon (PSL, Fig. 5) in shifting positions (marked in Fig. 4 with open triangles). While there where periods when this connection was at the same elevation (longshore profile on 16-01-2017), more often a flood channel was recut (longshore profile 03-03-2017 at chainage 980) which then migrated (longshore profiles 16-05 and 19-07-2017), but the lagoon has been fully closed since October 2017.

The widening of the breach resulted in the southward retreat of the northern end of CNS seen in the longshore profile and reflected in a lowering and/or landward migration of the highest point landwards at P3 between April 2016 and January 2017. Overwashing, lowering and roll-back of the northern end of the supratidal CNS was accompanied by northward growth again of the shoal up to September 2017 which can be seen both in the longshore profile and P3, where in the three surveys between May and September 2017 the elevation increases again to ~ 4 mOD. This growth against the outside curve of the inlet channel was then breached/the shoal in front of the supratidal CNS obliterated around 10-09-2017 and captured shortly after by the UAV survey collected on 26-09-2017. This shows the main inlet channel running still south of the CNSI and scattered shoals and minor channels spanning the >400 m wide gap to the CNSI. Near the centre of this gap, a small shoal was slightly higher just north of P3 in the longshore profile in that survey and which migrated north and landwards and had completely connected with PB by the survey in February 2018. In this process, the original inlet channel was closed and one main channel was draining the harbour again between chainage 680 or in very much the same location as in October 2003.

Over the 5 months between September 2017 and February 2018, roll-back encompassed all of CNSI illustrated by the February 2018 contour in Fig. 1 and the crest retreat of 50 m accompanied by a rise in elevation of 1 m at P5. CNSI also started to blend in with PB at its northern end (Fig. 4).

Over this period, P2's cross-sectional area remained stable though the crest retreated and slightly increased in elevation. In contrast, P1 saw a dramatic increase in cross-sectional area, in particular in the winter 2016/17, with the beach toe building out by >30 m and the crest by >20 m; the cross-sectional area in 2018 is larger than ever before.

Finally the head of the historic artificial part of CNS opposite the training arm, had seen retreat in the earlier years up to 2007 of ~20 m and had then stayed static through the breach and up to March 2017. Due to the movement of shoals to positions

on the inside bend around the training arm in spring 2017, the channel was pushed southwestwards and the area lost up to 30 m in 10 months (Fig. 1).

4.7 Bathymetric Changes

Changes up to 3 km seawards of the beach over the period 2002 to 2016 are shown in Fig. 8. Ignoring the striping associated with the 2002 data, most of the area beyond the intertidal zone shows no elevation changes. The changes in the intertidal zone and its proximity are the same as identified through the topographic surveys, that is, erosion of the ebb delta in front of the southern end of PB and growth of ebb delta in front of RG2 and RG3. In the Inner Owers, raised shingle features have been eroded while others have appeared, but overall the impression is one of fewer and smaller features.

4.8 Interaction with the Harbour

Changes to the outflow channel cross profile, plan shape and in particular length are thought to have an effect on the tide inside the harbour, and if that impact is maintained over longer periods of time could influence the intertidal habitats in the harbour. Tide gauges inside PH at its northern end and at the entrance at Littlehampton (~16 km apart, Fig. 1) have been operational over the period of the study. The gauge inside PH is located on the seaward side of the Pagham Rife river outfall where at low tide a shallow channel is maintained, so it only records a mid-tide series. Figure 10 shows the water levels for both gauges over one spring high and low tide in 2005, 2011, 2016, 2017 and 2018. Over the period 2005–2011, the observed pattern for the Pagham gauge in comparison to Littlehampton remains the same (Fig. 10):

(a) for the ~2 h of rising water after mid tide, Pagham water levels are rising at the same rate and only slightly delayed,
(b) on approaching high tide, Pagham reaches its peak 15–30 min later and generally falls a few decimetres short – this is in line with a general westward decrease in tidal range,

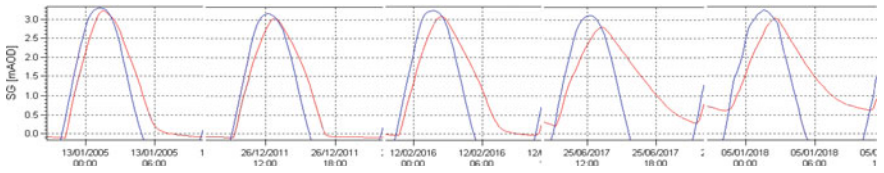

Fig. 10 Curves for comparable tides from the Littlehampton (blue) and Pagham (red) tide gauges

(c) the delay increasing on the ebb tide with a delay of ~1 h at the crossing of the 1 mOD level,
(d) for about 4 h, the water level at Pagham is around the 0 mOD level.

Following the initiation of the breach with flows through it at high tide, the example for 12 February 2016 shows a slightly longer delay during the flood, a slightly later peak still reaching the same levels, but a significant delay on the ebb with a delay of 2:10 h for crossing the 1 mOD level. However, the same ebb-slack water level was reached as before but for a shorter time before the flood was coming in again. By 25-06-2017, the main inlet channel was completely routed through the breach, i.e. a shortening of the channel by ~500 m, but the delay on the flood and ebb had increased (together with a slight reduction in the peak elevation) so that the 1 mOD level was crossed >3:10 h after Littlehampton, and was still emptying when the flood was coming in again, reaching only to about 0.4 mOD. A survey on 19-07-2017 encountered a minimum inlet channel elevation of

–0.3 mOD about 60 m upstream of P3. Following the second breach in September 2017 which shortened the channel by another ~ 300 m, the gauge comparison for 06-01-2018 shows a very similar pattern to that of June 2017 with the exception that the lowest water levels at Pagham only reached 0.6 mOD. The last comparison made on 04-03-2018 (not shown) suggests that the crossing delay at 1 mOD has decreased to <2:45 h and that the lowest levels reached are <0.3 mOD, i.e. that the efficiency of the channel appears to increase.

5 Discussion

Church Norton Spit has demonstrated growth and disintegration of a mixed sand and gravel spit at a scale not previously observed in the UK. The observations on the speed of growth and disintegration are particularly important when analysing past behaviour of coastal landforms from historic maps which are snap shots in time often several decades, if not centuries apart (e.g. Burningham 2015). It is often assumed that changes between two maps happened in a linear fashion and, for example, historic rates of spit growth for CNS have been calculated by Heron-Allen (1911) in that way. The observations presented suggest that such assumptions can be wrong. Transposing this rate of spatio-temporal change to the analysis of the subtidal area seawards of CNS with the aim to extract possible transport mechanisms of sediment onshore suggests that the bathymetry change shown in Fig. 8 based on surveys 12 years apart provides no basis for any interpretation of processes and transport. As such, the source of sediment that fuelled the growth is still elusive.

Growth of the supratidal spit is controlled by sediment supply alongshore (at least at the tip of the spit) and the presence of an intertidal spit extension/ebb tide delta/intertidal shoals on which to advance. This is very similar to the mechanisms of progression described by Aubrey and Gaines (1982:273) for the sand spit in the micro-tidal environment of Nantucket Sound where “Ebb-tidal flows build up a linear

channel-margin bar […] which becomes subaerial […], and finally lengthens the inlet throat parallel to the coast […], in a self-generative fashion". When this platform is missing or shrinking due to the subaerial spit extending faster, as seen in 2009/2010, spit advance is stalled or reduced; the same applies when the inlet channel current cuts across the tip of the spit (such as in 2013/2014) preventing this elevated ground to form.

There have been a number of overwashing events involving one or two successive high tides that led to crest lowering over lengths of more than 100 m, however, none of these managed to lower the crest to still water level. During that time the southeast coast experienced several storms with wave heights well in excess of 1 in 5 years (Bradbury and Mason 2014) suggesting that to create crest lowering that allows for tidal flows to commence, conditions with a return period much higher than that experienced are required for a single storm. Alternatively, it could be evidence to support Orford's hypothesis that "the self-limiting capacities of extreme events […] constrain the probability of barrier breakdown to that of crestal re-organisation only." (2011:1257). On all of these occasions, following storms led to crest build-up again, repairing the crest to the previous or even higher level, a process that was always associated with crest roll-back.

To create a full tidal breach several factors appear to be required:

(a) narrowing of the spit to a triangular shape through roll-back with over-steepening on the landward side by interaction with the tidal inlet channel,
(b) a succession of storm and high tide combinations that lower the crest to levels that allow tidal flow to go through the gap despite alongshore transport moving sediment into the gap, and
(c) sediment transport away from the gap by restricting the extent of overwash fans through a scouring inlet channel at the back and the creation of a new ebb-delta seawards of the gap.

The location of the breach, which is in the same location as all previous crest lowering events, seems to be related predominantly to a section of the CNS where through the removal of the original ebb-delta, beach toe and foreshore levels have fallen by from ~0 mOD to −1.5 m (P3 at about 340 m; 0.3 m between 2008 and 2009, 0.7 m between 2009 and 2010 and an additional 0.5 m between 2014 and 2015) thus allowing higher waves (change in water depth at MHWS from 2.6 to 4.1 m) to reach the spit than when it originally built up, driving it first back in 2013 and eventually leading to the breach.

Contrary to many studies on sandy inlets, the dramatic increase of the inlet channel length had no impact on tidal exchange in the estuary because the tidal currents had enough capacity to scour a sufficient channel either by scouring down or by landward displacement in response to spit roll-back. Only on establishing a tidal breach in spring 2016, which opened a second channel, thus spreading the flow over a larger cross-section and releasing large amounts of sediment both into the new breach location and into the previous inlet channel, did the exchange with PH become affected. This situation was exasperated through creation of a second breach in September that again released sediment that was driven into the semi fixed channel

with the training wall and even further into the Harbour as flood-delta. This inlet channel avulsion can be seen in the terminology or Hayes and FitzGerald (2013) as a switch from a 'tide-dominated' inlet that persisted over the spit extension to a 'wave-dominated' mode over the ~1.5 years following the breach; with the tidal signal inside PH showing signs of returning to its original state, the inlet is again switching back to a tide-dominated mode.

5.1 The Role of Engineering Structures

CNS is designated for its coastal geomorphology "as a classic shingle spit landform and for the links that have been demonstrated between the coastal near shore and offshore forms and sediments" (Natural England 1980). Given this description, the dynamic evolution observed over the last 17 years is of fundamental relevance to the interest feature of the site. There are two sets of engineering structures that have interacted with CNS: the rock groynes and the emergency rock revetment in front of properties on PB and the training wall at the southern end of PB.

It seems obvious to point to the presence of RG1 in attempting to explain why the advance of CNS came to a halt in the winter 2013/14, when it was only ~60 m away from the groyne. The funnelling of the tidal current through a 90° bend was forced by the groyne and meant that (a) there was no intertidal extension on which the spit could advance and (b) any sediment moved to the tip would have been carried far into the channel at the rising tide or far out to sea at low tide. No measurements of current speed or cross-sectional area in the gap between the tip of CNS and RG1 have been made, however, based on the cross-sectional area surveyed below 0 mOD at P5 on 25-11-2014 and the narrowest distance between CNS and RG1 in 2014-15 at the same elevation, the channel is likely to have extended to below −3 mOD at this point. The erosion of PB of up to 50 m in 15 months (P4) after the breach 2016 would suggest that without initial beach recycling into the beach southwest of RG1 and the construction of the emergency rock revetment in December 2013, CNS would have very likely pushed further landwards and outflanked RG1, which already was close to outflanking before December 2013. This would have most likely allowed the inlet channel to switch to a shore parallel route again which in turn would have allowed CNS to advance past RG1, similar to the advance once RG1 finally failed in February 2014, but along a path closer to the beach. That CNS only moved past RG1 nearly 2 years after the failure of RG1 is most likely due to an incomplete switch of the channel and the requirement for infilling the channel and building up an intertidal shoal structure over which CNS could start to advance again. It is debatable whether the hold-up of CNS at RG1 led to a delay in it breaching. P4 shows no change between 2014 and 2016 and it is questionable whether an advancing spit would have led to a thinning of the barrier at its narrowest point. Storm and water level conditions in that period were less severe, so that even a thinning spit may not have brought forward its breaching.

The role of the training wall as envisaged in the 1960s was to stabilise the entrance position by not allowing the entrance to shift northwards in response to pressure from CNS. It thus fulfilled a role similar to RG1 as CNS approached from the south by focussing the inlet currents. Similar to RG1 in 2013/2014, the training wall suffered undermining and partial collapse in 1986. Comparing the aerial photo from 1966 (Fig. 1) to that in 2001 (Fig. 5), the main change is that CNS had crept seawards in relation to the training wall which was even more pronounced in 2005, i.e. CNS prograded until the effect of the training wall diminished, so that it could grow seawards of it across the inlet mouth. Over a period of 40 years the training wall has therefore achieved its objective in an environment of low sediment supply. With higher sediment supply since 2004, it acted as a pivot point for the inlet channel by maintaining its seaward curvature which eventually contributed to the breach of CNS around the apex of the channel bend by limiting the opportunity for CNS to roll-back further in this location.

Acknowledgements The author would like to thank Julian Orford and Roger Spencer for discussions around Pagham, the Worthing Borough Council survey team lead by Dan Amos for their dedication to capture coastal change, the Environment Agency for access to data collected over the past decades and numerous people, including the local community, who took photos and videos on the ground or from the air to complete the picture. The views expressed in this chapter are those of the author and not of the Environment Agency.

References

Adur and Worthing Council. (2018). *Updated—Pagham Spit Evolution to February 2018*. 21 February 2018. https://www.youtube.com/watch?v=XwOzM-tCh3w.

Aubrey, D. G., & Gaines, A. G. (1982). Rapid formation and degradation of barrier spits in areas with low rates of littoral drift. *Marine Geology, 49*(3–4), 257–277. https://doi.org/10.1016/0025-3227(82)90043-3.

Barcock, N. W. S., & Collins, M. B. (1991). *Coastal erosion associated with a tidal inlet: Pagham, West Sussex. SUDO/TEC/91/3NC*. Southampton University Department of Oceanography.

Bird, E. C. F, Clayton, K. M., & Hansom, J. D. (2003). Chapter 5: Beaches, spits, barriers and dunes-an introduction. In V. J. May, & J. D. Hansom (Eds.), *Coastal geomorphology of Great Britain* (pp. 201–228). Geological Conservation Review Series 28. Peterborough: Joint Nature Conservation Committee.

Bradbury, A. P, & Mason, T. E. (2014). *Review of South Coast Beach response to wave conditions in the Winter of 2013–2014*. Southampton: Channel Coastal Observatory. http://www.southerncoastalgroup.org.uk/SR01_StormReport_2014.pdf.

Burningham, H. (2015). Gravel spit-inlet dynamics: Orford Spit, UK. In G. Randazzo, D. W. T. Jackson, & J. A. G. Cooper (Eds.), *Sand and gravel spits* (Vol. 12, pp. 51–65). Coastal Research Library. Cham: Springer International Publishing. http://link.springer.com/10.1007/978-3-319-13716-2.

Burningham, Helene, & French, Jon. (2006). Morphodynamic behaviour of a mixed sand–Gravel Ebb-Tidal Delta: Deben Estuary, Suffolk, UK. *Marine Geology, 225*(1), 23–44. https://doi.org/10.1016/j.margeo.2005.09.009.

Burningham, Helene, & French, Jon. (2007). Morphodynamics and sedimentology of mixed sediment inlets. *Journal of Coastal Research, Special Issue, 50,* 710–715.

Carter, R. W. G, & Orford, J. D. (1993). The morphodynamics of coarse clastic beaches and barriers: A short- and long-term perspective. *Journal of Coastal Research* (Special Issue) 15: 158–79.

CCO. (2017a). *Annual wave report 2016—Bracklesham Bay*. Southampton: Channel Coastal Observatory. http://coastalmonitoring.org/reports/index.php?link=&dla=download&id=749&cat=70/WaveReport2016_BkB.pdf.

CCO. (2017b). *Annual wave report 2016—Rustington*. Southampton: Channel Coastal Observatory. http://coastalmonitoring.org/reports/index.php?link=&dla=download&id=855&cat=79/WaveReport2016_Rst.pdf.

CCO. (2017c). "Channel Coastal Observatory." 2017. http://coastalmonitoring.org/.

Dornbusch, U. (2010). Ground survey methods for mixed sand and gravel beaches in intertidal environments: A comparison. *Journal of Coastal Research 26* (3), 451–64. https://doi.org/10.2112/08-1134.1.

Dornbusch, U., Bradbury, A., Curtis, B., Dane, A., Pitcher, A., & Polidoro, A. (2013). Design methodology and data improvements to facilitate regional gravel beach management. In *Coasts, Marine Structures and Breakwaters 2013 proceedings*. Edinburgh: ICE.

Dornbusch, U., & Mylroie, P. (2017). *Examples of coastal catch-up including barrier roll-back, marsh and brick-earth cliff erosion in Southeast England*. In *ICE Breakwaters*. Paper *20*: 1–10. Liverpool.

FitzGerald, D. M., Kraus, N. C., & Hands, E. B. (2000). Natural mechanisms of sediment bypassing at tidal inlets. *Coastal and Hydraulics Engineering Technical Note CHETN-IV-30*. Vicksburg, MS: US Army Engineer Research and Development Center.

Hayes, Miles O., & FitzGerald, Duncan M. (2013). Origin, evolution, and classification of tidal inlets. *Journal of Coastal Research, 69*(September), 14–33. https://doi.org/10.2112/SI_69_3.

Heron-Allen, E. (1911). *Selsey bill: Historic and prehistoric*. Duckworth & Company.

HR Wallingford. (2014). *ARC-Boat*. http://www.hrwallingford.com/expertise/arc-boat.

Marine and Coastguard Agency. (2002). *HI1003 Selsey bill to hooe bank*. UKHO INSPIRE Portal & Bathymetry DAC. http://aws2.caris.com/ukho/mapViewer/map.action.

May, V. J. (2003). Pagham harbour, West Sussex. In V. J. May, & J. D. Hansom (Eds.), *Coastal geomorphology of Great Britain* (pp. 278–281). Geological Conservation Review Series 28. Peterborough: Joint Nature Conservation Committee. http://jncc.defra.gov.uk/page-3012.

McCall, R. T., Masselink, G., Poate, T. G., Roelvink, J. A., & Almeida, L. P. (2015). Modelling the morphodynamics of gravel beaches during storms with XBeach-G. *Coastal Engineering, 103*(September), 52–66. https://doi.org/10.1016/j.coastaleng.2015.06.002.

Mellett, C. L., Hodgson, David M., Lang, A., Mauz, B., Selby, I., & Plater, A. J. (2012). Preservation of a drowned gravel barrier complex: A landscape evolution study from the North-Eastern English channel. *Marine Geology, 315–318,* 115–131. https://doi.org/10.1016/j.margeo.2012.04.008.

Met Office. (2014). A global perspective on the recent storms and floods in the UK. Reference February, 26 2014. http://www.metoffice.gov.uk/research/news/2014/uk-storms-and-floods.

Natural England. (1980). *Pagham Harbour*. SSSI—Citation. https://designatedsites.naturalengland.org.uk/PDFsForWeb/Citation/1000620.pdf.

Orford, J. D. (2011). Gravel-dominated coastal-barrier reorganisation variability as a function of coastal susceptibility and barrier resilience. In *Proceedings of the International Conference on Coastal Sediments 2011* (pp. 1257–1270). Miami: World Scientific Publishing.

Orford, J. D., & Anthony, Edward J. (2011). Extreme events and the morphodynamics of gravel-dominated coastal barriers: Strengthening uncertain ground. *Marine Geology, 290*(1–4), 41–45. https://doi.org/10.1016/j.margeo.2011.10.005.

Orford, J. D., Carter, R. W. G., & Jennings, S. C. (1996). Control domains and morphological phases in gravel-dominated coastal barriers of Nova Scotia. *Journal of Coastal Research, 12*(3), 589–604.

Plant, N. G., Flocks, James, Stockdon, H. F., Long, J. W., Guy, K., Thompson, D. M., et al. (2014). Predictions of barrier Island berm evolution in a time-varying storm climatology: Barrier-Island berm evolution. *Journal of Geophysical Research: Earth Surface, 119*(2), 300–316. https://doi.org/10.1002/2013JF002871.

Polidoro, A., & Pullen, T. (2016). *Modelling Shingle Beaches in bimodal seas*. CAS1227-RT002-R01-00. Wallingford: HR Wallingford. http://www.channelcoast.org/shingleb/Final_Report_CAS1227-RT002-R01-00.pdf.

Polidoro, A., Pullen, T., & Dornbusch, U. (2014). *Wave run-up on shingle beaches—A new method*. HR Wallingford. http://www.se-coastalgroup.org.uk/wp-content/uploads/2014/01/BMP_run-up_tool.zip. http://www.se-coastalgroup.org.uk/wp-content/uploads/2014/01/BMP_run-up_tool.zip.

Robinson, D. A, & Williams, R. B. G. (1983). The sussex coast past and present. In The Geography Editorial Committee (Ed.), *Sussex : Environment, landscape and society* (pp. 50–66). Gloucester: Alan Sutton. http://www.sussex.ac.uk/geography/researchprojects/coastview/Introduction_background/Sussex_blue_book_coasts.pdf.

Scott, C., & Townend, I. (2017). Pagham harbour: Managing a dynamic coast for people and the environment. In *ICE Breakwaters*. Paper 103, 1–20. Liverpool: ICE Publishing. http://www.ice-conferences.com/ice_events/media/bw2017/bw2017%20-%20day%202/1650-id-103_scott_paper.pdf.

Seminack, C. T., & McBride, R. A. (2018). A life-cycle model for wave-dominated tidal inlets along passive margin coasts of North America. *Geomorphology, 304*(March), 141–158. https://doi.org/10.1016/j.geomorph.2017.12.038.

Stripling, S., Bradbury, A., Brampton, A., & Cope, S. (2007). *Understanding barrier beaches*. Conference or Workshop Item FD1924/TR. R&D Technical Report. London: Defra.

Wadey, M. P., Haigh, I. D., & Brown, J. M. (2014). A century of sea level data and the UK's 2013/14 storm surges: An assessment of extremes and clustering using the Newlyn Tide gauge record. *Ocean Science, 10*(6), 1031–1045. https://doi.org/10.5194/os-10-1031-2014.

White, L. (2016). *An investigation into whether the welded bar at the Church Norton Spit Act as a sediment transport route from the sub-tidal to the beach*. (Undergraduate thesis). University of Sussex, Falmer, Sussex. http://www.scopac.org.uk/church-norton-spit.html.

Shoreline Evolution and Responses to Port Engineering at Lekki Coast, Nigeria

Yanhong Wang, Jie Shen and Si Zhao

Abstract The increasing coastal erosion associated with human activities and resulting negative environmental impacts have necessitated the need for improved understanding of the effects of coastal engineering works on coastal processes. Here, the proposed Port of Lekki, situated in the Gulf of Guinea 60 km east of Lagos, Nigeria, is investigated as a case study. Coastal surveys of cross shore profiles and sediment sampling were conducted. Based on investigations of coastal morphology, present erosion and deposition, longshore sediment transport, wave action, beach profile and sediment grain size, a sediment transport and shoreline evolution model was established to exam shoreline evolution and shoreline responses to the proposed port breakwaters. Results indicate that the Lekki coast is wave dominated. Swell waves from the south-southwest induce a longshore current travelling to the east, and leading to eastward longshore sediment transport. The capacities of eastward and westward sediment transport vary between 602,000 m^3 a^{-1} and 963,000 m^3 a^{-1}, and between 1000 m^3 a^{-1} and 18,000 m^3 a^{-1}, respectively. The eastward net sediment transport capacities were estimated to be between 584,000 m^3 a^{-1} and 962,000 m^3 a^{-1}. Under natural conditions, the shoreline near the proposed port is relatively stable. The model predicted that the shoreline to the west of the port will shift a maximum of 442 m, reaching the bend of the main breakwater in approximately 20 years. However, sediment bypassing will begin by approximately 6 years after construction leading to the shore shifting a maximum of 260 m due to longshore sediment transport in the lower surf zone. The shoreline to the east of the proposed port will retreat a maximum of 220 m by 20 years after construction. The maximum erosion is predicted to occur approximately 500 m to the east of the eastern breakwater, and not directly east, due to the effects of the main breakwater on wave propagation. Effective measures to

Y. Wang (✉)
State Key Laboratory of Hydrology-Water Resources and Hydraulic Engineering, Nanjing Hydraulic Research Institute, Nanjing, China
e-mail: yhwang@nhri.cn

J. Shen
Administrative Committee of the Lvsi Marine Economic Development Zone, Nantong, China

S. Zhao
Hainan Xinhai Science and Technology Company Ltd., Haikou, China

K. D. Nguyen et al. (eds.), *Estuaries and Coastal Zones in Times of Global Change*, Springer Water,
https://doi.org/10.1007/978-981-15-2081-5_27

alleviate erosion include the construction of groins and beach fill through dredged sands from the channel and basin.

Keywords Wave dominated coast · Shoreline evolution · Longshore sediment transport · Shoreline responses to engineering

1 The Study Area

The Lekki coast, Nigeria, faces the open sea area of the Gulf of Guinea, with a relatively straight coastline extended approximately east to west (Fig. 1). The site of the proposed Lekki port is situated 60 km east of Lagos city on a wave-dominated sandy coast, with obvious long-shore sediment transport from west to east under prevailing wave action from south-southwest. Over recent decades, the construction of jetties and channels near the entrance of Lagos Port has greatly impacted the evolution of the coastline. Presently, the coast to the east of the inlet of Lagos Port is mostly eroding, although groins have been constructed to protect some sections to the east.

The study area is located between two major rivers: the Niger River to the east and the Volta River (Ghana) to the west. Sediment carried by these rivers has played a major role in the evolution of the coast. Several inland water bodies such as lagoons and lakes have developed along the coast between the Volta River mouth and the proposed Lekki Port. Most of these water bodies are closed or maintain a small drainage channel for discharge of water from inland to the sea. Barrier islands have been formed in front of these lagoons and lakes during a geological period of high

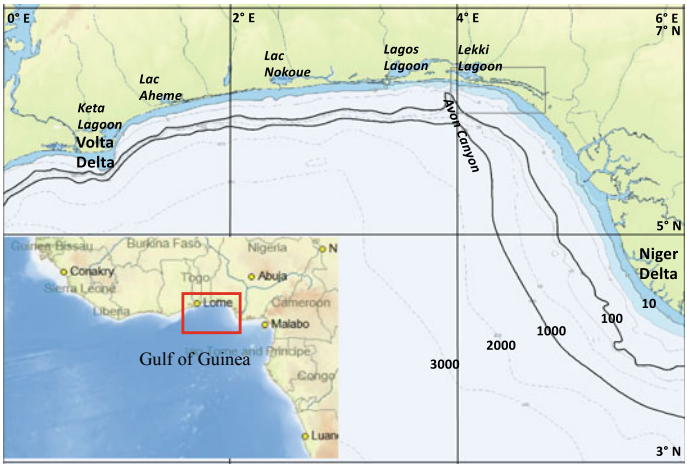

Fig. 1 The proposed site of the Port of Lekki, situated in the gulf of Guinea 60 km east of Lagos City, Nigeria

sediment supply. Due to reshaping by wave action, the barrier islands now form part of an almost continuously straight coast (Burke 1972) (Fig. 1).

2 Evolution of the Coast

2.1 Background to the Evolution of the Coastline

In geological timescales, the Lekki coastline is relatively young. The major features of the lagoon tidal system, such as the lagoon, the various channels and creeks and the older beach ridges, were formed during the Holocene period during which the level of the sea rose progressively to the current level. The presence of gullies is due to lower sea levels during the pre-Holocene period, during which rivers discharging into the Lagoon extended into Avon Canyon (Burke 1972).

A series of sand ridges are visible inland of the present beach to the east of Lekki, as shown by straight lines in the satellite image shown in Fig. 2. The ridge lines are indicative of the old beach and its historical evolution. The alignment of the ridge indicates that the rate of shoreline growth on the eastern area close to the Niger Delta is obviously higher than that on the western area close to the Lekki Coast. This indicates a higher historical accretion rate on the eastern area (near the Niger Delta) in relation to sediment supply from the eastward surf zone longshore sediment transport and sediment discharge of the Niger River.

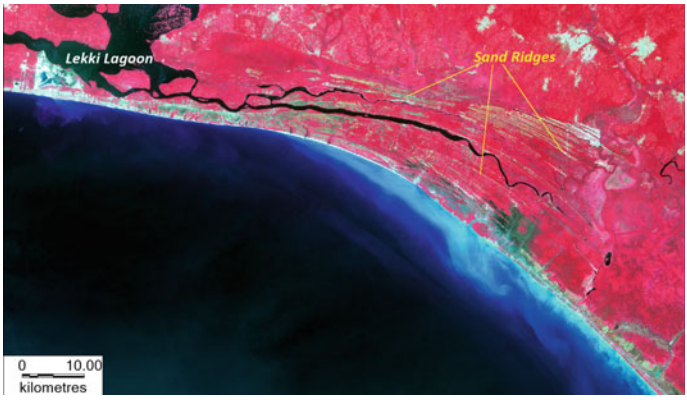

Fig. 2 The beach ridges near Lekki vegetation appears in shades of red. The barren sand ridges with vegetation appears in shades of light blue

2.2 Recent Shoreline Change

For investigation of the most recent shoreline evolution, Landsat images were acquired for 1984, 1999, 2005 and 2015. When compared to shorelines drawn from the images shown, the shoreline near the project site appears relatively stable. Notable change of the shoreline occurred on a 20 km stretch 30 km east of the project site, with shoreline growth of approximately 400 m from 1984 to 2015, averaging 13 m a^{-1}. The images in Fig. 3 indicated no obvious changes in the coastline west of the proposed site of the Lekki Port.

Recent shoreline evolution shows progradation on the curved section of coastline close to the Niger Delta, whereas the stretches of coastline near Lekki and Lagos are relatively stable as a whole. This observation corresponds with the historical evolution of the coastline discussed previously. Since the West-African coast between the Togo and Niger rivers is wave dominated, swells from the south-southwest induce an eastward longshore current. The rate of longshore sediment transport has decreased near the Niger Delta due to significant changes in shoreline orientation.

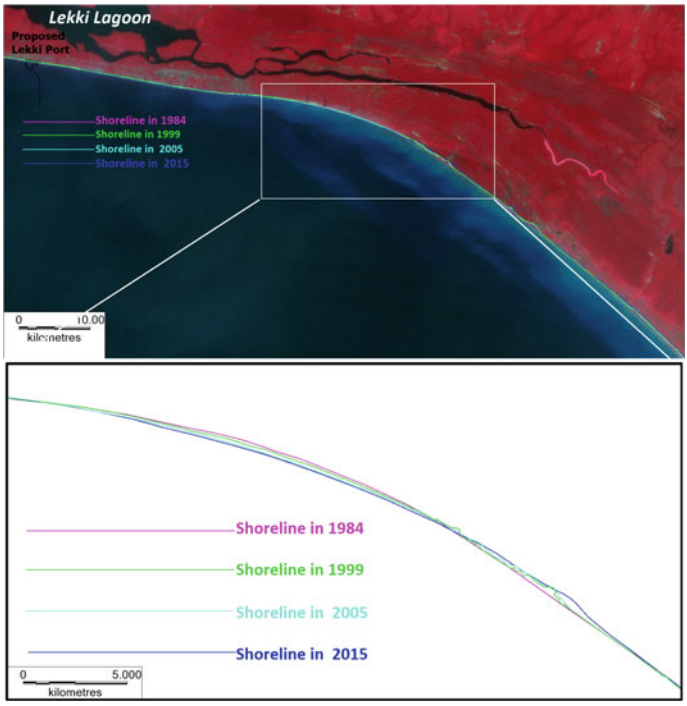

Fig. 3 Shoreline change from 1984 to 2015

3 Coastal Dynamics

3.1 Water Current

The coastal waters of Nigeria form part of the Atlantic Ocean, falling within the Gulf of Guinea, which starts at Cape Palmas, near Harper. The Guinea Current can be represented by Mariano Global Surface Velocity Analysis (MGSVA). Depending on the season, the primary source of water for the Guinea Current is either the Canary Current or the North Equatorial Counter Current (NECC). The Guinea Current, which travels from west–east, is the dominant ocean current affecting the Nigerian continental margin.

According to the simulation results of a hydrodynamic study for Lekki Port conducted by Muttray (2008), the nearshore currents in the project area are mostly induced by winds and tide. Tidal currents are mostly oscillating and travel parallel to the shoreline. Wind-induced currents tend to follow the wind direction and are transformed into currents moving in parallel to the shoreline as they approach the shoreline. The currents in the project area mostly head in an eastward direction.

At a distance of more than 5 km offshore, the prevailing current direction is north east. Again, the current rates are significantly reduced at Avon's Canyon (Fig. 1), with more variable current directions. At a distance of 2–4 km offshore, the prevailing current direction changes to parallel with the shoreline, in an eastward direction.

East of the site of the proposed port, the current is similarly mostly directed eastward; east-southeast currents occur less frequently and westward currents occur more frequently than at the other location (west of the port). Current rates are slightly higher and occasionally reach 0.25 m s^{-1}.

3.2 Waves

The wave action was analyzed using a hydrodynamic study based on wave data at time intervals of 3 h from 1997 to 2007 (Muttray 2008).

The prevailing (~90%) nearshore waves travel from south-southwest (186° to 208° from north). Operational offshore wave directions are plotted in Fig. 4. with a directional resolution of 5°.

Nearshore wave heights of Hs = 3.0 m are hardly exceeded; wave heights are typically between Hs = 0.75 m and 2.0 m. Significant wave heights of Hs = 0.5 m, 1.0 m, 1.5 m, 2.0 m and 2.5 m are exceeded approximately 99.5%, 77%, 29%, 5% and 0.3% of the time, respectively.

The project area is persistently exposed to a certain amount of wave action. Nearshore wave heights are seldom less than Hs = 0.5 m. Wave heights of Hs = 0.75 m are exceeded approximately 95% of the time.

The seasonal variation of nearshore wave heights is plotted in Fig. 5. The largest

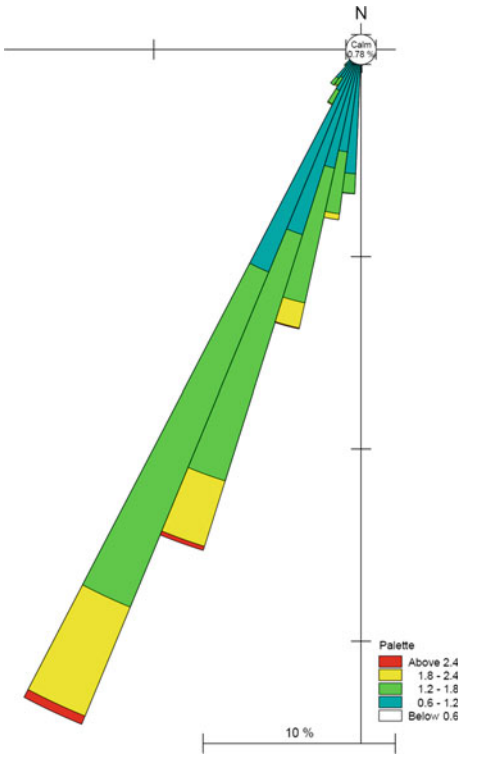

Fig. 4 Increase in nearshore wave height (depth = 10.9 m, period = 1997–2007)

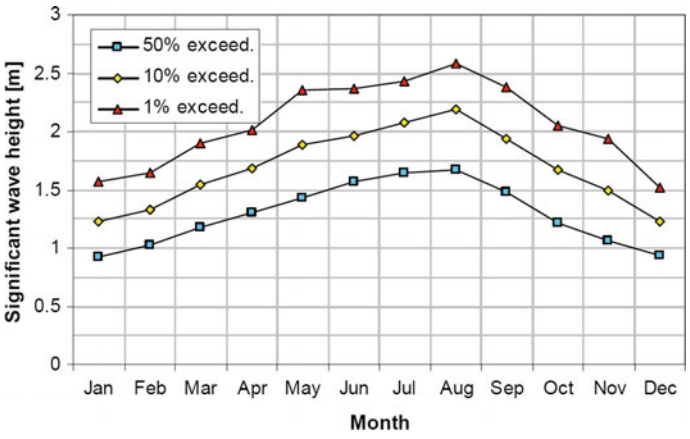

Fig. 5 Seasonal variation of wave heights

waves were observed in summer (June to August) with average wave heights exceeding Hs = 1.5 m. The nearshore wave height in summer is typically 1.0–2.0 m and is persistently larger than 0.7 m. The smallest nearshore wave heights were observed in winter (December to February) with average wave heights of approximately Hs = 0.9 m. The nearshore wave height in winter is typically 0.5–1.5 m and is persistently larger than 0.3 m.

3.3 Sediments

Little information is available for the characterization of the sediment near the study area. Sediment types making up the offshore seabed vary from very coarse sand to silty clay, and a large spatial variation is evident. Muddy material, mainly consisting of silt, is found on the Continental Shelf west of Lagos, whereas clay dominates the deeper parts (Allen 1965).

The stretch of sandy seabed, roughly 100 km long by 10 km wide, starts at the entrance to Lagos Harbor and ends at the OKLNG site. West of Lagos, the sandy bed is quite thin (approx. 500 m) and its width appears to start increasing at the entrance (Fig. 6) (Ballendux 2011).

Few past studies could be identified on the beach sediment distribution for the study area. In the present study, beach sediments were sampled at 12 sites along the study area, extending for 13 km. Site locations and the D50 (particle diameter representing the 50% cumulative percentile value) distribution along the shoreline is shown in Fig. 7. Among the sampling sites, W1, W2 and O2 are obviously effected by beach fill near the site W2. Sand colors are lighter than those at other sites, representing the sand originating from offshore.

Sediment grain size (D50) ranges between 0.424 mm at E5 and 0.613 mm at W5. No notable distribution trend could be identified along the 13 km stretch of beach near the project site. The present study found sediment grain size to be close to that measured by Titocan et al. (2011) for Okun-Mopo Beach, Ajah, approximately

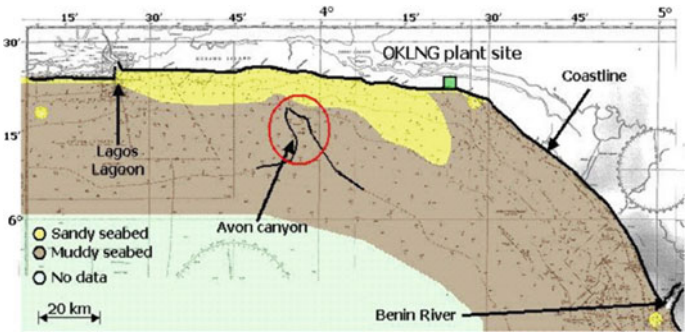

Fig. 6 Seabed sediment types (Ballendux 2011)

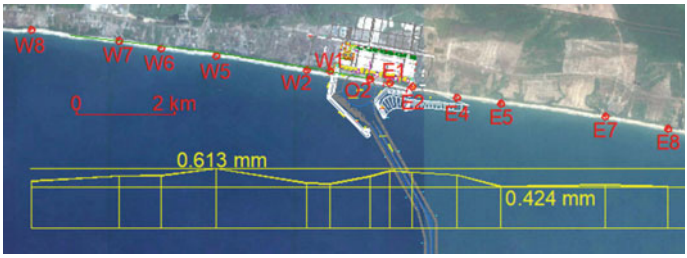

Fig. 7 Site locations and D50 (particle diameter representing the 50% cumulative percentile value) distribution along the shoreline

20 km west of the project site, with D50 ranging between 0.38 mm and 0.66 mm for 19 samples.

4 Sediment Transport Tendency

At a large spatial scale, the majority of sediment originates from the Volta, Benin and Niger rivers, as well as erosion of the West-African coast by waves and ocean currents.

The longshore sediment transport is related to the angle between the waves and the coast. The general wave direction in this region is from south-southwest, which results in eastward transport up to the point where the coastline is perpendicular to the wave direction, close to the OKNLG site shown in Fig. 6. Sediment originating from the Niger River is transported both in a westward and eastward direction. A build-up of sediment is expected near the OKLNG site where material from both the Niger River in the east and longshore transport from the west is deposited. It is unlikely that coarse sediment originating from the Niger River reaches the proposed port area via wave-generated longshore transport as the transport direction within this section is to the east. The sediment transport pattern (Fig. 8) has been reported by Pugh (1954), Sexton and Murday (1994) and Ballendux (2011).

Estimates of the littoral transport near Lagos Harbor range from 0.5 to 1.0 M m^3 a^{-1}, as estimated by Allersma and Tilmans (1993), or 0.6 to 0.7 M m^3 a^{-1}, as estimated by Bentum et al. (2012). Estimates of 0.7–1.3 M m^3 a^{-1} have been reported for the coast of the site of the proposed port by Muttray (2008). On the Dangote Permanent Jetty, approximately 10 km east of the project site, 0.5–0.8 M m^3 a^{-1} of sediment transport has been estimated by Royal Haskoning DHV (2016). Therefore, the longshore sediment transport rates vary from 0.5 to 1.3 M m^3 a^{-1} among the different sources.

With focused wave action, high longshore sediment transport capacity and highly-mobile sediments on the beach, the shoreline is very sensitive to changes of boundary conditions, even though it is relatively stable under present conditions. Small-scale

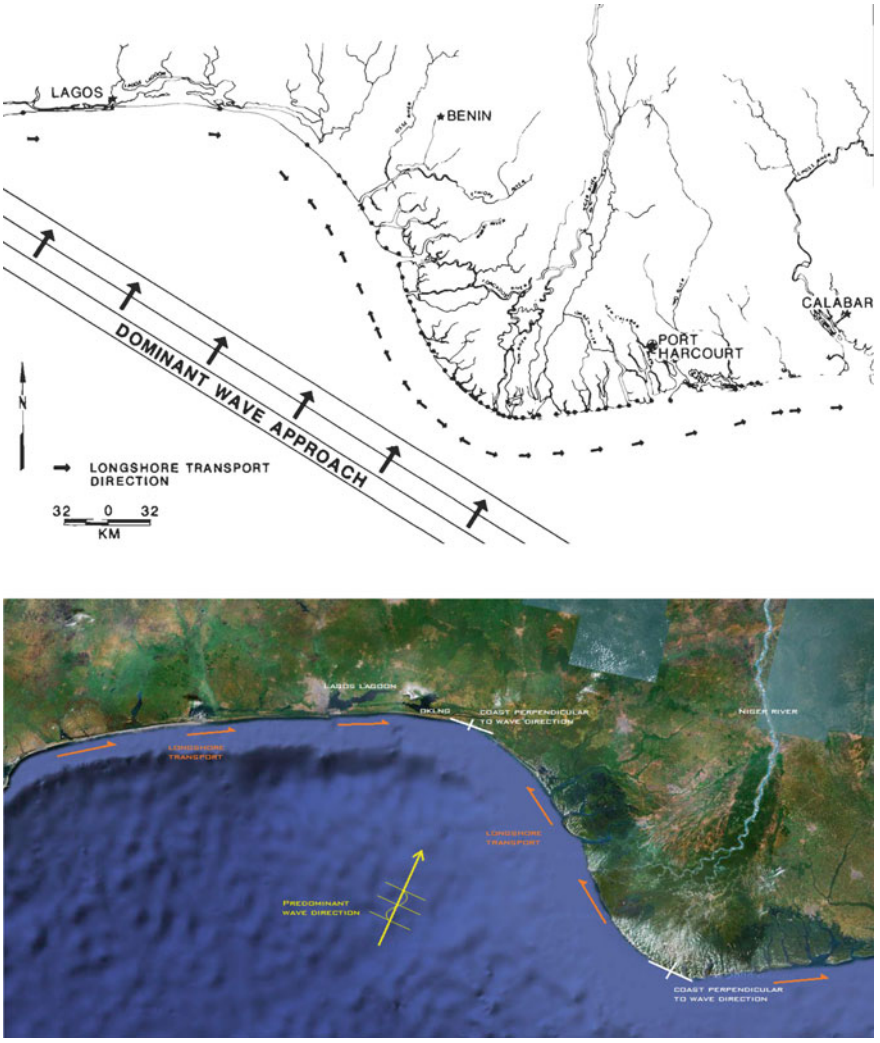

Fig. 8 The predominant wave approach on the shoreline is from the south-southwest, generating longshore currents in multiple directions [top panel from Sexton and Murday (1994); bottom panel from Ballendux (2011)]

structures, such as ship wreckage and steel pipes, may lead to notable erosion and deposition (Fig. 9).

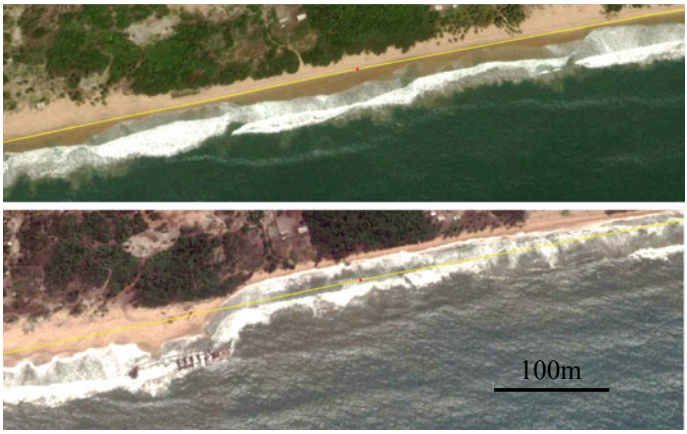

Fig. 9 A shipwreck situated to the west of Lekki, which has resulted in a 30 m retreat of the coastline (top panel from May 5, 2011; bottom panel from April 12, 2012)

5 Modeling of Shoreline Evolution

5.1 Method Introduction

Shoreline evolution was investigated using the LITtoral Processes And Coastline Kinetics (LITPACK) model suite, developed by DHI (2014). The model represents all relevant wave, sediment transport and morphological processes to calculate sediment transport in the surf zone.

The LITPACK model consists of two main modules; LITDRIFT, which calculates the cross-shore distribution of the littoral drift and LITLINE, which calculates the alongshore distribution of the littoral drift, and in turn, the coastline evolution over time. To calculate the coastline position for each time step, littoral transport at every grid point has to be known. The change in coastline position at a certain grid point is now determined by the difference in transport between two time steps; i.e., a negative value indicates erosion and a positive accretion.

5.2 Model Input

An associated program, LINTABL, calculates and tabulates transport rates as functions of the water level, wave period, wave height and wave direction relative to the coastline normal. The coastline, boundary conditions and the structures have to be defined.

To prevent the influence of boundaries on the evolution of the coastline of interest, the coastline profile should be extended beyond the primary study region. A 20 km

Table 1 Parameter values chosen for the LITtoral processes and coastline kinetics (LITPACK) application of Litline modeling of the proposed Lekki Port site

Parameter	Values
Tidal and meteorological currents included	No
Wind included	No
Sediment description	Uniform
Water temperature	25 °C
Sediment density	2.65 g cm^{-3}
Sediment porosity	0.4
Wave theory	Stokes
Wave spreading factor	0.5
Description of bed concentration	Deterministic

long section of coast was considered in the present study, with the site of the proposed port located at the center. The present shoreline position was extracted from the Landsat Image. The line was divided into 1000 grids at a grid resolution of 20 m.

The coastal cross-shore profile in the model domain was assumed to be uniform in a longshore direction. The applied cross-shore profile was extracted from the bathymetrical data. The profile extended for 5000 m, and was divided into 250 grids, with a resolution of 20 m.

The dominant forcing in this case mainly relates to waves. The wave data used for the calculation of the littoral drift originated from wave transformation modeling which used WANE2 data as boundary condition, as time series from 1 July 1997 to 31 December 2006 with a time step of 3 h, accompanied with water level data. Corresponding water level data were input into the model.

For the present study, no wind and/or currents were taken into account. The forcing of the littoral drift was related purely to waves.

Sediment samples were collected from near the modeled area and analyzed, as outlined in Sect. 3 of the current chapter. The average median grain size of all samples was approximately 0.5 mm. This value was uniformly applied across the entire model domain.

The parameter values applied for the model setup are shown in Table 1.

5.3 Alongshore Distribution of Littoral Drift

Sediment transport along the model domain was calculated using the local coastline orientation based on the coastline position in the absence of the proposed Lekki Port.

The yearly net littoral drift was calculated for the years 1998–2006, and is shown in Fig. 10.

The eastward sediment transport capacity varied between 602,000 m^3 a^{-1} and 963,000 m^3 a^{-1}, westward between 1000 m^3 a^{-1} and 18,000 m^3 a^{-1}, and a net

Fig. 10 Alongshore distribution of transport capacity ($m^3\ a^{-1}$)

transport capacity (eastward) between 584,000 $m^3\ a^{-1}$ and 962,000 $m^3\ a^{-1}$. Westward transport was calculated to be negligible.

The values of average net yearly sediment transport showed a decreasing trend eastward, corresponding to the coastline orientation along the domain. The average net yearly transport at the location of the port was calculated to be 652,000 $m^3\ a^{-1}$.

The volume and direction of sediment transport calculated in the present study corresponds with the results obtained from others studies along the Nigerian coast discussed in Sect. 4, which enhances confidence in the model setup and performance.

6 Shoreline Impact Assessment

The proposed port layout is schematized to include three groins and one breakwater as measures to alleviate sediment transport. The groins extend to the corner of the main breakwater, to the sea-most end of the eastern breakwater and to the sea-most end of the western breakwater, with offshore distances of approximately 460 m, 680 m and 440 m, respectively.

In the absence of the proposed port, a continuous flux of sediment would exist along the coast. However, the breakwaters resulting from the port construction would interrupt the littoral drift and cause a localized sharp gradient in sediment transport capacity. This change of transport capacity along the coast would result in a shift of the coastline position. The blocking of transport would result in a sedimentation to the west of the western breakwater, whereas the coastline to the east of the eastern breakwater would become eroded due to the increase of the sediment flux in an eastward direction. Figure 11 shows the projected coastline evolution as a result of the construction of the proposed port.

Figure 11. shows sedimentation over time directly west of the western breakwater of the proposed Lekki Port where the coastline advance is largest. The coastline west of the port is projected to reach the groin tip (the turning point of the main breakwater, at a cross-shore distance of 460 m) in approximately 20 years; however, it is emphasized that bypassing starts occurring much earlier. The accretion rate during the first 2 years after construction is projected to be 52 m a^{-1}, declining to less than 12 m a^{-1} after 10 years.

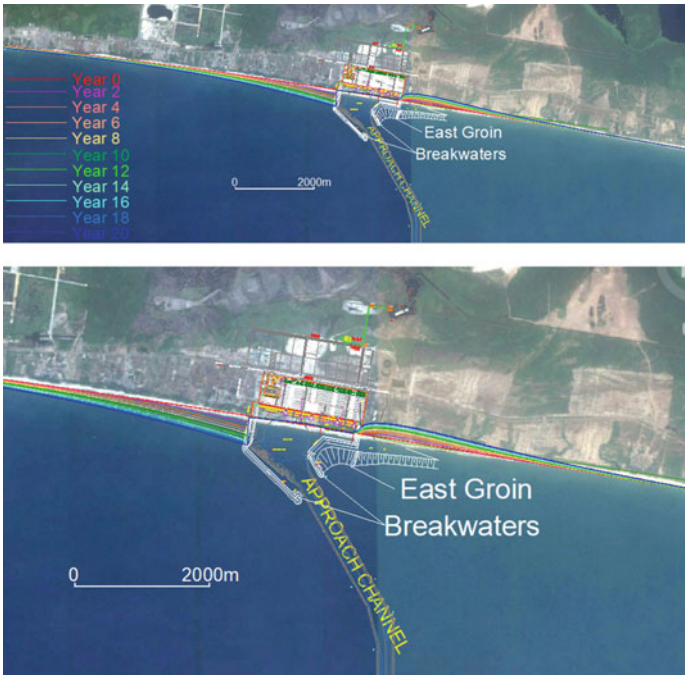

Fig. 11 Projected coastline evolution after the construction of the proposed port

After 6 years, 10 years and 20 years, the advance of the coastline to the west of the western breakwater is projected to equal approximately 215 m, 294 m and 442 m, respectively. Due to the fact that the total transport width is 250 m, bypassing of sediment starts after 6 years, initially at a small rate, but increasing rapidly over time, and the rate of coastline advance starts to decrease due to sand bypassing.

On the east side of the proposed Lekki Port, the coastline is projected to retreat by 220 m by 20 years after construction. The erosion rate during the first 2 years after construction is projected to be 22 m a^{-1}, reducing to approximately 10 m a^{-1} after 10 years. The maximum erosion point appears approximately 500 m east of the eastern groin, and not directly east due to the effects of the main breakwater on wave propagation.

If a noticeable effect of coastline retreat or erosion is defined as any value greater than 5 m, the effected stretches of shoreline after 2 years, 10 years and 20 years are projected to be 2220 m, 4580 m and 6800 m, respectively. In addition, 1860 m, 3960 m and 5840 m of shoreline is projected to retreat by more than 10 m after 2 years, 10 years and 20 years, respectively (Fig. 11 and Table 2).

Table 2 Length of shoreline projected to be effected by construction of the proposed Lekki Port

Time after construction	Erosional shoreline length (retreat >5 m)	Erosional shoreline length (retreat >10 m)
Year 2	2220 m	1860 m
Year 4	2960 m	2540 m
Year 6	3380 m	3080 m
Year 8	4080 m	3540 m
Year 10	4580 m	3960 m
Year 12	5000 m	4360 m
Year 14	5460 m	4740 m
Year 16	5900 m	5100 m
Year 18	6340 m	5480 m
Year 20	6800 m	5840 m

7 Mitigation Measures

7.1 Beach Fill by Sands from the Basin and Dredging the Channel

The yearly averaged net drift was calculated as 0.65 M m^3 for the present situation in absence of the proposed port. Sediment transport is projected to reduce to zero after construction of the breakwaters, resulting in the above-mentioned erosion and sedimentation patterns.

According to the general layout of the proposed Lekki Port, the basin and approach channel will be dredged to −16.5 m. The dredged sand could be utilized to fill in the beach between the eastern breakwater and the eastern groin, as well as the beach to the east of the eastern groin, thereby forming an artificial beach and providing a sediment source.

A projection of shoreline change after the construction was implemented based on the structures of the port and beach fill as follows: 2 mm^3 sand is used to fill the area between the eastern breakwater and the eastern groin to form an artificial beach, and an additional 10 mm^3 sand is used to fill the beach area east of the eastern groin for beach sand sustenance, during the initial period directly after the construction of the port.

As shown in Fig. 12, the beach fill measure and the artificial beach between the eastern breakwater and the eastern groin remain relatively stable, with protection of the structures on both sides. After the addition of 10 mm^3 of beach fill, the shoreline on the eastern side is projected to extend for 360 m from the present location, after which erosion is initiated. After 10 years, the extended shoreline is projected to retreat to the present location on the eastern side of the groin. In addition, the present beach will begin to erode. The maximum retreat distance is projected to be 106 m after

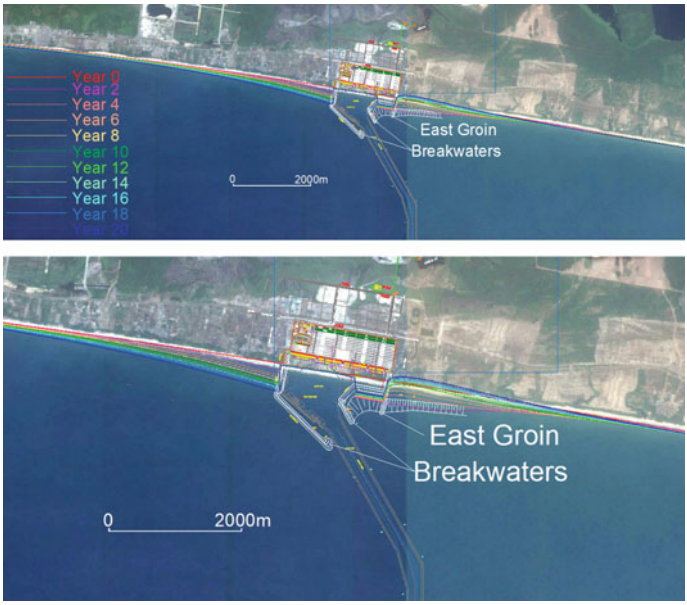

Fig. 12 Shoreline evolution after construction of the proposed Lekki Port. Sand from dredging the channel and basin is used as beach fill for the beach on the east side

20 years, with an additional 2.4 km of shoreline affected compared to the present shoreline location.

To the west of the western breakwater, the shoreline accretion is the same as that of the previous case in the absence of beach fill because the boundary condition of the west side does not change in this case. An obvious source of sand is the beach on the west side that is subject to significant siltation.

7.2 Beach Fill with Groin System

Based on the above-mentioned beach fill, a groin system is proposed. On the eastern side, four groins are placed from 1.0 to 2.5 km east of the port boundary, with 500 m spacing and extending 70 m from the present shoreline to protect the erodible beach section after construction of the port and beach fill. On the western side, 2 km from the root of the western breakwater, a groin extending for 200 m is installed to block eastward longshore sediment transport, thereby reducing deposition on the western side of the breakwater and channel siltation caused by bypassing.

The above result (Fig. 13) illustrates that the use of groins is favorable for shifting erosion sections eastward. Erosion of the present shore is projected to start after the port construction and beach fill. With the construction of groins, the maximum retreat of the shoreline is projected to decrease from 106 to 54 m, 20 years after construction

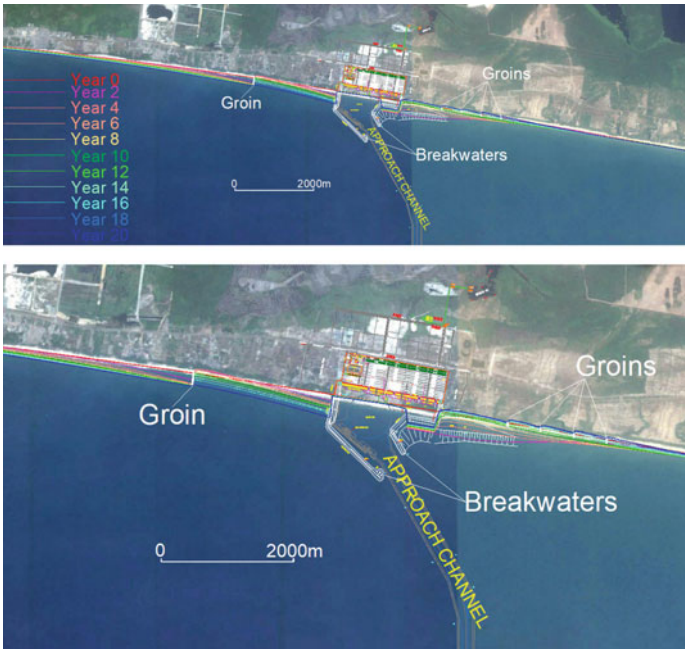

Fig. 13 Shoreline evolution after construction of the proposed Lekki Port with beach fill on the east side beach and groin system

of the port. However, the construction of groins is projected to extend the erosional section from 1.0 km eastwardly to 3.4 km.

Sediment originating from the west is partly blocked for the accretion section on the western side of the port by the placement of the groin 1 km west of the western breakwater. Accretion of the shoreline on the western side of the breakwater is slowed, particular between 4 years and 12 years after construction. Because there is sufficient sand to the east of the groin for transport and accretion during the beginning 4 years, local erosion on the eastern side of the groin is projected to be a maximum of 70 m. After 4 years, the western side of the groin is projected to be almost filled to capacity, and sediment originating from the western side begins to supply the section between the groin and the breakwater.

The maximum range of accretion on the western side of the breakwater is projected to be 350 m, with an approximate 100 m decrease compared with that in the absence of the groin. In addition, sediment bypassing begins 16 years after construction- a delay of 4 years compared to that in the absence of the groin.

7.3 Optimization of Mitigation Measures

With the erosion alleviation measures of beach fill and the groin system, beach erosion could be obviously reduced on the eastern side of the proposed port. However, beach accretion on the western side is inevitable, and projected channel siltation will be enhanced due to sediment bypassing during the latter years. Once sediment moves beyond the turning point of the main breakwater, it will be easily transported along the main breakwater toward the approach channel. The construction of a branch breakwater toward the southwest from the turning point of the main breakwater is considered as a sand blocker to prevent the transport of sand from eastward to the channel.

On the eastern side of the port, net sediment transport direction is projected to be eastward. The groin placed at the east end of the port (west end of the erosional beach) is not projected to play an effectively role in erosion alleviation caused by eastward longshore sediment transport. Due to the angle of erosion alleviation, the groin could be removed.

The optimization scheme is presented as follows:

(1) Remove the groin at the east end of the site of the proposed port.
(2) A branch breakwater (sand blocker) is placed at the turning point of the main breakwater, extending 300 m southwest.
(3) Four groins are placed between 1 and 2.5 km from the eastern end of the port, with a spacing of 500 m and length of 70 m.
(4) Sand totalling 12 mm^3 dredged from the basin and approach channel is use to fill the beach on the east side during the first year after construction.

The results (Fig. 14) show that the removal of the groin at the east end of the port does not lead to increasing erosion to the east. Instead, more artificially filled sand entered the erosional beach, rather than blocked between the removed groin and the east breakwater. The erosional section decreased from 3.4 to 2.5 km compared to the previous case, for 20 years after construction.

On the west side of the port, the shoreline evolution does not show a notable change caused by the sand blocker. However, the beach front remains > 300 m from the sea-most end of the sand blocker by 20 years after construction. Bypassing is not expected in 20 years under this condition.

8 Discussion and Conclusions

The site of the proposed Lekki Port is located on the west Nigerian coast on a sandy beach facing the Guinea Gulf. The beach is mainly composed of coarse sand with a mean grain size ranging between 0.4 and 0.6 mm. The sea current of site is generally weaker than 0.3 m s^{-1}, with a tidal range of approximately 1.0 m. The prevailing (90% of the time) nearshore wave direction is south-southwest (186° to 208° from north).

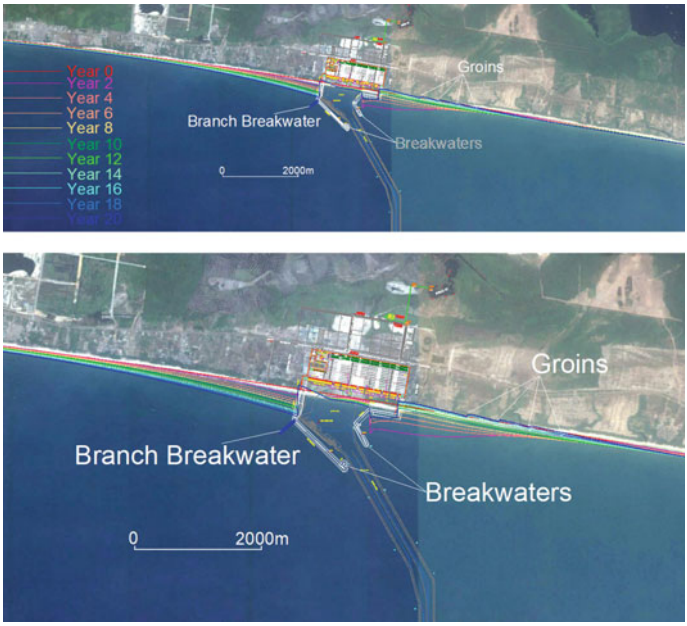

Fig. 14 Evolution of the shoreline after construction of the proposed port with erosion alleviation measures including beach fill on the east side beach and a sand blocker at the turning point of the main breakwater, replacing the groin at the eastern boundary of the port, and including four groins to the east

Nearshore wave heights of Hs = 3.0 m are hardly exceeded. Significant wave heights of Hs = 0.5 m, 1.0 m, 1.5 m, 2.0 m and 2.5 m are exceeded approximately 99.5%, 77%, 29%, 5% and 0.3% of the time, respectively. Wave action is the dominant force on near shore sediment transport.

The Lekki coast line has been relatively stable over recent decades near the project site, with the eastward net sediment transport rate ranging between 0.5 to 1.3 mm^3 a^{-1}, as reported by different sources. Approximately 0.65 mm^3 a^{-1} of sediment transport has been estimated at the project site of the current study. Due to a gradual varying of shoreline orientation, the eastward net sediment transport has decreased from the west section to the east section. This has resulted in beach accretion around the northeast turning area of the shoreline. The present condition of the coast has been affected by the dredging work to the southwest and beach fill to the west of the proposed port. Local erosion and accretion caused by temporary dredging work does not represent the natural condition of the relatively stable coastal evolution.

Simulations of shoreline evolution in absence of the proposed port show a continuous flux of sediment along the coast. However, the breakwaters resulting from the construction of the port would interrupt the littoral drift and result in a localized sharp gradient in sediment transport capacity. This change of transport capacity along the coast would result in a shift of the coastline. The blocking of transport would result

in sedimentation to the west of the western breakwater, whereas erosion would occur to the east of the eastern breakwater due to the increase of the sediment flux in an eastward direction. The maximum accretion of the shoreline on the west side of the main breakwater could reach a turning point in 20 years after construction. In addition, sand bypassing the turning point will occur in 12 years after construction. On the east side of the proposed Lekki Port, retreat of the coastline could reach 220 m, with the length of shoreline eroded reaching 6.8 km by20 years after construction.

Effective erosion alleviation measures to the east of the port include beach fill and a groin system. The effectiveness of beach fill depends on the volume of sand added. A volume of 12 mm^3 could ensure no erosion of the beach for approximately 12 years. With the alleviation measures of beach fill and the groin system, beach erosion could be obviously decreased on the east side of the proposed port. However, beach accretion on the west side is inevitable, and siltation of the approach channel will be enhanced due to sediment bypassing during the latter years.

The direction of net sediment transport is eastward. The groin placed at the east end of the port (west end of the erosional beach) would not play an effective role in erosion alleviation caused by eastward longshore sediment transport; therefore, the groin could be removed. Instead, a branch breakwater placed southwest of the turning point of the main breakwater could be considered as a sand blocker to prevent sand from being transported eastward to the channel.

According to model results, removal of the groin at the east end of the port does not lead to increasing erosion on the eastern beach. Instead, it is recommended that artificial sand filling be implemented on the erosional beach, rather than between the removed groin and the east breakwater. Using these methods, the model predicted a decrease in the erosional section from 3.4 to 2.5 km by 20 years after construction.

The evolution of the shoreline does not show notable changes caused by the sand blocker at the turning point of the main breakwater. However, the beach front remains >300 m away from the sea-most end of the sand blocker by 20 years after construction. As a result, bypassing at the tip of the sand blocker is not expected within 20 years.

It should be considered that the Dangote Permanent Jetty, approximately 10 km east of the site of the proposed Lekki Port, is under construction. The range of the accretion beach resulting from the Dangot Jetty will reach the erosional section caused by the proposed Lekki Port. That is helpful for erosion alleviation on the eastern side of the proposed Lekki Port.

References

Allermsa, E., & Tilmans, W. M. K. (1993). Coastal conditions in West Africa – A review. *Ocean and Coastal Management, 19,* 199–240.

Allen, J. R. L. (1965). Coastal geomorphology of eastern Nigeria. *Geologie en Mijnbouw, 44,* 1–21.

Ballendux, G. M. (2011). *On the morphodynamics of Lagos Harbour An exploratory study of the tidal system (MSc thesis).* TU Delft.

Bentum, K. M., Hoyng, C. W., Ledden, M. V. et al. (2012). The Lagos coast – investigation of the long-term morphological impact of the Eko Atlantic City project. In *Jubilee Conference Proceedings*, NCK-Days (pp. 207–212).

Burke, K. (1972). Longshore drift, submarine canyons and submarine fans in development of Niger Delta. *American Association of Petroleum Geologists, 56,* 1975–1983.

DHI. (2014). *LITPACK - An integrated modelling system for littoral processes and coastline kinetics, Short introduction and tutorial*. Copenhagen, Denmark, p. 64.

Muttray. (2008). Port@Lekki Detailed Design, Hydrodynamic Study, Delta Marine Consultants, pp. 25–44.

Pugh, J. C. (1954). A classification of the Nigerian coastline. *Journal West African Science Association, 1,* 3–22.

RHDHV. (2016). *Dangote permanent Jetty at KM9.8, numerical modelling Report* (P. 22).

Sexton, W. J., & Murday, M. (1994). The morphology and sediment character of the coastline of Nigeria-the Niger Delta. *Journal of Coastal Research, 10,* 959–977.

Titocan, M. I., Akinnigbagbe, E. A., Ibitola, P. M., et al. (2011). Numerical assessment and analysis of textural deposits of beach sediment: A case study of Ajah (Okun Mopo) Beach Lagos South West Nigeria. *Nature and Science, 9,* 165–174.

Hydrodynamics and Sediment Transport at a Seasonal Inlet and Its Adjacent Beach: Cua Dai, Vietnam

Anh T. K. Do, Sierd de Vries, Qinghua Ye, Marcel J. F. Stive and Trung Viet Nguyen

Abstract Cua Dai inlet is a typical microtidal, mixed energy-wave dominated inlet in a tropical monsoon regime in central Vietnam. Both the river flow regime and coastal processes such as induced by waves and tides influence Cua Dai Inlet and its adjacent coasts. Cua Dai Beach, the northern adjacent coast of Cua Dai inlet, has experienced severe erosion since 1995 due to an apparent non-periodic cyclic process, a decrease of sediment supply from the river, estuary and squeeze by coastal developments (Do et al. in J Coast Res 34(1):6–25, 2018). The inlet channel has shifted from North to South which served as an important controlling mechanism for the creation of a new ebb shoal. However, the role of the ebb-tidal delta in relation to the channel shifting and seasonal varying hydrodynamic conditions (river discharge and wave climate) remains poorly understood. Most studies have only considered the impact of waves and tides on the development of the ebb tidal delta. No study has included the impact of a varying river discharge on ebb shoal development and inlet migration. This chapter investigates the seasonal varying hydrodynamics and sediment transport of the inlet and adjacent coasts due to the seasonal varying river discharge and wave climate. The 2DH process-based morphodynamic numerical model (Delft3D) is applied using schematized wave conditions and river discharge. Six simulations with varying dominant wave conditions for the winter and for the summer are executed in combination with varying river discharge classes that corresponding to the dry, wet and flood seasons. There exists an East North East monsoon with a flood season from September to December, an East North East monsoon with

A. T. K. Do (✉) · S. de Vries · Q. Ye · M. J. F. Stive
Faculty of Civil Engineering and Geosciences, Delft University of Technology, Delft, The Netherlands
e-mail: dtkanh@dut.udn.vn

A. T. K. Do
Faculty of Water Resource Engineering, The University of Da Nang-University of Science and Technology, Da Nang, Vietnam

Q. Ye
Deltares, Delft, The Netherlands

T. V. Nguyen
Faculty of Civil Engineering, Thuy Loi University, Ha Noi, Vietnam

K. D. Nguyen et al. (eds.), *Estuaries and Coastal Zones in Times of Global Change*, Springer Water,
https://doi.org/10.1007/978-981-15-2081-5_28

a wet season from January to March, and a dry bidirectional South East/East North East monsoon from April to August. We investigate the effect of the seasonal wave climate and seasonal river discharges at Cua Dai inlet by analyzing the effects on the resulting hydrodynamics, sediment transports and potential morphological changes through the inlet and at the adjacent coasts. Primary results indicate that the seasonal variation in the wave climate has a strong influence on the sediment transport patterns in the adjacent coasts. The variation in the river flow dominates the magnitude of sediment transport through the inlet. The results of the simulations show that the inlet generally imports sediment into the estuary except in the case of the flood season. During the flood season the estimated sediment export is significant. Interestingly, the wave direction that varies during summer also influences the magnitude of sediment import into the estuary. Waves coming from the ENE contributes to larger sediment import than waves coming from the SE.

Keywords Seasonal inlet · Seasonal waves · Seasonal river discharge · Hydrodynamics · Sediment transport

1 Introduction

Cua Dai inlet is a typical microtidal, mixed energy- wave dominated inlet in a tropical monsoon regime and is strongly influenced by both river discharge and waves. Cua Dai Beach, the adjacent coast of Cua Dai inlet, located on the north side of Cua Dai Inlet, is experiencing severe erosion since 1995. To aid future management of this system, it is necessary to understand the factors that influence the existing morphology and that cause coastal retreat of the system. Do et al. (2018) reconstructed historical shoreline positions in combination with crude assumptions with respect to longshore sediment transport patterns and associated changes in sediment budgets over recent decades. In the study of Do et al. (2018), it is found that the long-term geomorphological development, and the decrease in sediment supply from the river and the estuary have put Cua Dai Beach under stress by causing the shoreline to erode.

The long-term geomorphological development of Cua Dai inlet appears to reflect a non-periodic cyclic process that takes place over several decades. It appears that the inlet channel shifted from North to South. Welding of the initial ebb shoal to the abandoned ebb-tidal delta and the development of a new ebb shoal were important primary controlling mechanisms. We propose two conceptual theories that represent the geomorphological development of the Cua Dai inlet. The first theory (A; Fig. 1a) is based on Landsat images in 1988 that depict the system in the past. The existing ebb shoal such as present in 1988 suggests that the system was rich in sediment. It is our hypothesis that the river flow was normally directed to the North and provided a large amount of sediment to the inlet gorge and to the ebb tidal delta, depending on the dry or wet season respectively. Hence, the wave driven alongshore sediment transport on the northern beaches, caused by the waves from ENE direction caused

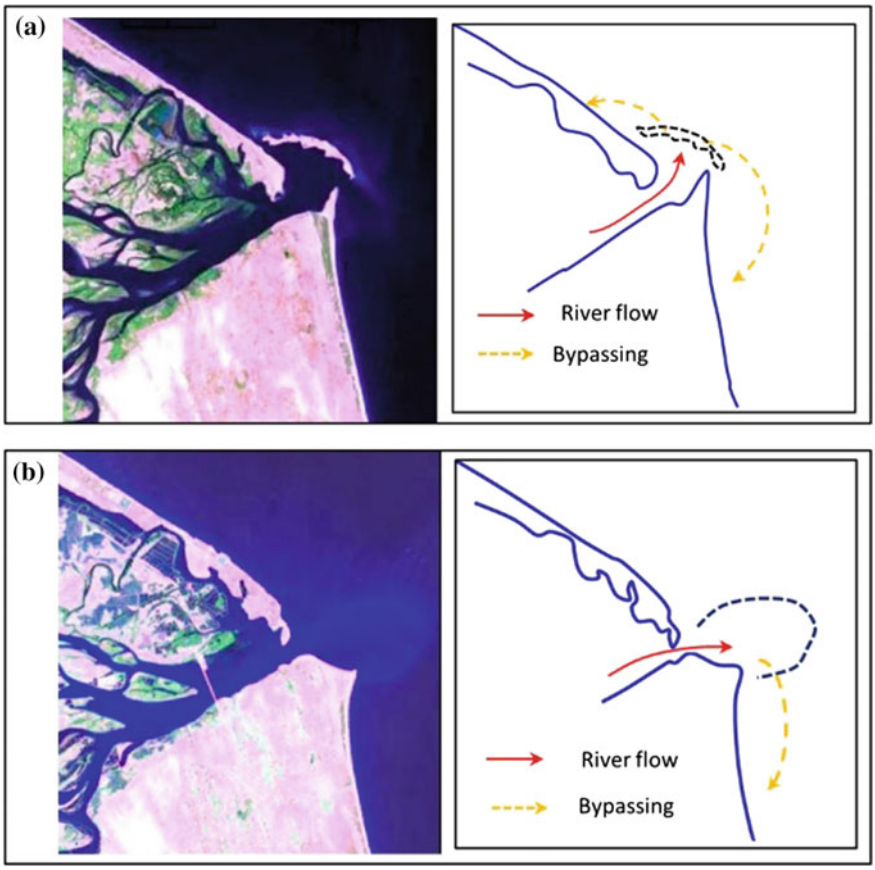

Fig. 1 Conceptual model description for the non-periodic cyclic process of Cua Dai inlet. **a** Scenario in the past, 1989 and **b** scenario at present, 2015

two important mechanisms. It builds a shoal such as present in 1988, preventing erosion of the Cua Dai near inlet shore and it also feds the more northern shore, annihilating the effect of divergence in transport. The second theory (B; Fig. 1b) based on Landsat images in 2015 depicts a more recent image. Due to storm Cecil (1989), the existing ebb shoal in 1988 was abandoned and it migrated landward until it attached to the beach due to bar welding process resulting in accretion at both adjacent coasts during the period 1988–1995 (Do et al. (2018). After the bar welding, a new ebb shoal started to develop further to the south than the previous ebb shoal. This process created a major sediment sink since formation of the new ebb shoal requires sediment to reach equilibrium. The new ebb shoal is also orientated more to the South. The northern beach is now not protected by the shoal and erosion continues due to the local divergence in longshore sediment transport, whereas the southern coast starts to accrete due to sand supply from bypassing.

Understanding the role of the ebb-tidal delta that interacts with the shifting channel and its associated seasonal behavior due to river discharge and wave climate is a remaining challenge. Inlets probably represent the most extreme level of difficulty in evaluating quantities of sediment transport related to the variety of acting physical forces (Komar 1996). The complexity of the interaction of tides, waves, and freshwater discharge, lead to very complex morphodynamic behavior observed in many inlets (Oertel 1972, 1988; Robinson 1975; Hubbard et al. 1979; Sha 1989; Komar 1996; FitzGerald 1984; and FitzGerald et al. 2000).

More recently, numerical modeling has been widely used and has been proved to be useful to study morphological behavior of complex coastal environments, including tidal inlets (e.g. Bertin et al. 2009; Cayocca 2001; Chen et al. 2015; Dissanayake et al. 2009; de Vriend et al. 1993; Herrling and Winter 2014; Nahon et al. 2012; Ridderinkhof et al. 2016; van Leeuwen et al. 2003). Today, medium to long-term coastal behavior can be investigated using process-based morphodynamic models (de Vriend et al. 1993; Roelvink and Reniers 2012; van der Wegen et al. 2010; Winter 2006). Such model simulates the non-linear interaction between currents; sediment transport and bed level changes at real world scales and may therefore overcome limitations of coastline models and flume experiments. Recent advances in numerical morphodynamics models allow simulations over very large spatial and temporal scales (Roelvink 2006; Dissanayake et al. 2009; van der Wegen et al. 2010). In the absence of sufficient observational data, systematic and schematic numerical simulations are assumed to be able to provide insight into medium to long-term coastal evolution (Daly et al. 2011).

Most studies have considered the impact of waves and tides to the development of ebb tidal deltas. Fewer studies have considered the impact of river discharge on the development of ebb shoals and inlet migration. This chapter investigates the seasonal varying hydrodynamics and sediment transport of the inlet and adjacent coasts due to a seasonal varying river discharge and wave climate. This study uses a 2DH process-based morphodynamic numerical model (Delft3D) and schematized wave conditions and river discharge.

2 Methodology

The investigation of the seasonal varying hydrodynamics and sediment transport of the inlet and adjacent coasts due to a seasonal varying river discharge and wave climate requires a comprehensive model. A 2DH process-based numerical morphodynamic model (Delft3D), which consists of Delft3D-WAVE and Delft3D-FLOW, is used to simulate hydrodynamics of river flows, tides, sediment transport at the inlet and its adjacent coasts simultaneously. In this section, the numerical model will first be introduced and then the details of the model setup and hydrodynamic settings will be discussed. An overview of the simulations is finally provided.

2.1 The Numerical Model

The modeling system Delft3D (Deltares 2014) solves the shallow water equations. The systems of equations consist of the equations of horizontal motion, with turbulence models to close the system of mean flow, the continuity equation, and the sediment transport equations. The details of the model have been described in e.g., Lesser et al (2004) and van de Wegen and Roelvink (2008). The spectral wave model SWAN in Delft3D-WAVE (Booij et al. 1999, and Ris et al. 1999) may run in stationary mode to simulate the wave propagation and deformation from offshore to nearshore. The hydrodynamics module (Delft3D-FLOW) is coupled to Delft3d-WAVE through the exchange of relevant parameters. The wave parameters and the forcing terms associated with the wave radiation stresses computed by Delft3D-WAVE module are used as input for the Delft3D-FLOW module to compute wave-driven currents, enhanced turbulence, bed-shear stress and sediment stirring by wave breaking. Then at each interval of one hour has been reached by FLOW, the water level, current velocities and bottom elevation from the Delft3D-FLOW are used as input to computation in Delft3D-WAVE.

The sediment transport formulation of van Rijn (1993) is used. The total sediment transport is calculated as the sum of both bed load and suspended load transport. Suspended sediment transport is treated above a reference height and calculated by a depth-average advection-diffusion equation, whereas the bed load is treated below that reference height.

2.2 Model Setup of Cua Dai Inlet

The computational domain of the model has been developed to represent the Cua Dai inlet which includes the open sea, the inlet and part of the river (Fig. 2). Three nested grids are used that range from a large regional model to Cua Dai inlet with decreasing spatial dimensions and increasing gird resolutions. The largest model with grid cell resolutions of 1500 m covers almost the entire central coast of Vietnam with 125 km in width and 190 km in length. This model was used to generate water level time series at the boundaries of the flow model. The wave model grid extends about 30 km in both northward (up to Son Tra mountain) and southward direction from the Cua Dai inlet to allow the proper development of waves in the domain of interest. The finest flow model extends to Nong Son hydrology station where the observed river discharge is available. Detailed bathymetry at the river area is derived from Vo (2015). Bathymetric data near the coast and inlet areas are collected in 2014 from measurement. The extended bathymetry at the open sea is derived from GEBCO.

The boundary conditions of the regional model are extracted from the global ocean tide model TPXO8.0. Thirteen tidal constituents (M2, S2, N2, K2, K1, O1, P1, Q1, MF, MN, M4, MS4 and MN4) are applied to generate tidal conditions at the boundaries of the regional model. This model is calibrated using the measured tide

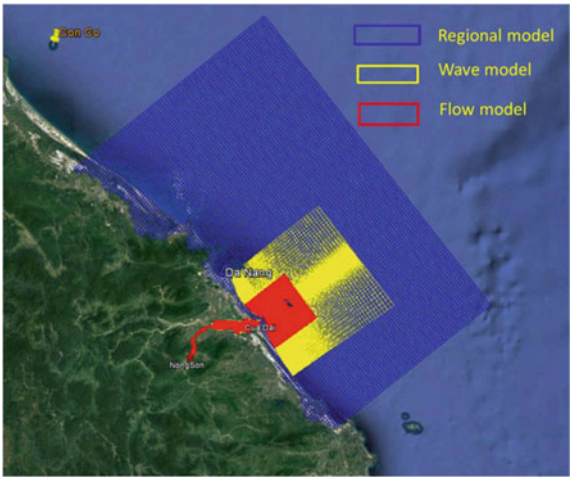

Fig. 2 Model domain including wave model domain and flow model domain

time series measured from the station at Da Nang near to Son Tra mountain. Then the regional model is nested to generate the boundary conditions for the flow model. The results of the flow model are validated with water level and velocity measured at Cua Dai inlet.

Wave forcing at the sea boundary in the wave model was extracted from the National Oceanic and Atmospheric Administration (NOAA) Wave Watch III archives at grid point (16.0°N, 109.0°E) in the period 2005–2013. Fresh water from Thu Bon River that flows into Cua Dai inlet was implemented at the river upstream boundary using the monthly average discharge during period 1977 to 2008. Measured discharge time series were obtained at the Nong Son station.

The sediment transport formulation of van Rijn (1993) is used for computing sediment transport by waves and currents. The simulations were performed with a median sediment diameter (D50) of 0.2 mm, a sediment density of non-cohesive sand of 2650 kg/m^3. A uniform value of 5 m of initial sediment layer thickness at bed is used as default in Delft3D.

2.3 Model Simulations

To test the influence of seasonal waves and seasonal river flow on hydrodynamics and sediment transport at the inlet and its adjacent coasts, this study choose to simulate 6 different conditions that represent winter and summer and one extreme flood event. Details can be found in Table 1. This selection is based on the integrated analysis based on both hydrology and wave climate from Do et al. (2018). For each condition the residual sediment transport patterns were computed and compared. The first five cases are simulated with the same duration of one month and the extreme flood event is simulated in 4 days representing the average time flood in this area.

Table 1 Overview of structure of the morphodynamic simulation considering seasonal waves and seasonal river discharges

Case		River discharge	Wave height	Wave period	Wave direction
		Q (m^3/s)	Hs (m)	Tp (s)	θ (°)
Winter season	Run 1	168	1.25	7.9	60 (ENE)
	Run 2	634	1.25	7.9	60 (ENE)
	Run 3	1037	1.25	7.9	60 (ENE)
Summer season	Run 4	88	0.75	6.42	60 (ENE)
	Run 5	88	0.75	6.4	135 (SE)
Extreme flood event	Run 6	10,600	1.25	7.9	60 (ENE)

3 Results and Discussion

This section firstly presents the results of the hydrodynamics (e.g. water level and velocity at the inlet). Secondly, the results of the alongshore sediment transport at the adjacent coasts are presented and discussed. Thirdly, the results of sediment transport through the mouth are presented and discussed. Fourth, the sediment transport pattern around the ebb tidal delta is presented and discussed. Finally, the morphological feedback around the ebb tidal delta and adjacent coast is presented and discussed.

3.1 Hydrodynamics Results

The regional model is calibrated with measurement of the water level at Da Nang station. Then flow model is also validated with observed data of water level and velocity that was measured in Cua Dai inlet. Figure 3 shows water levels computed by the model and measured data extract from global tides at Da Nang station during a one month period.

Figures 3, 4 and 5 show the comparison of observed and simulated water levels and velocities at Cua Dai inlet. Although the observed velocities are higher than compared to simulated data, the computed water level agrees well with observed data. These plots show that in general the level of agreement between observed and simulated data is quite good. Therefore the model is used to analyze the sediment transport pattern.

3.2 Longshore Sediment at Adjacent Coasts

The longshore sediment transports (LST) computed over one month for each condition during the summer months and the winter months are computed by defining 39

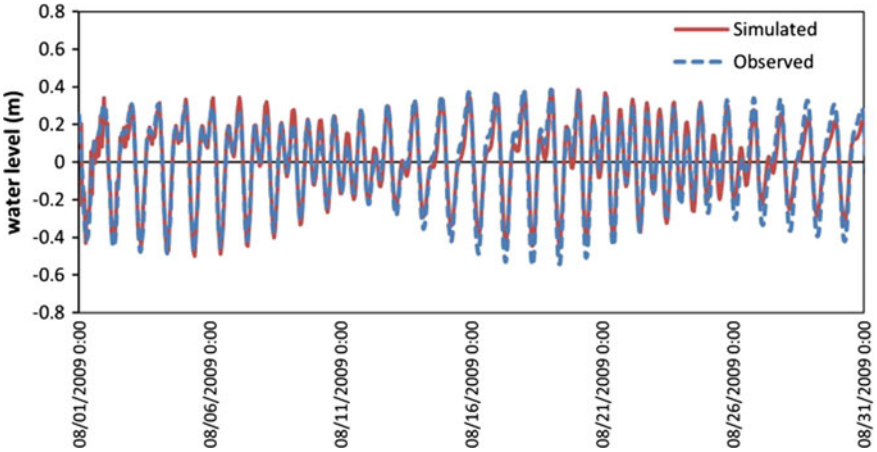

Fig. 3 Observed and simulated water level at Da Nang station

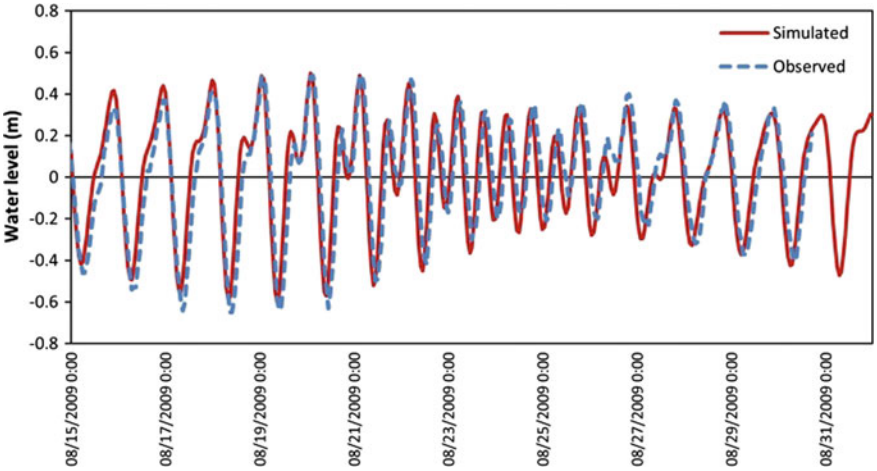

Fig. 4 Observed and simulated water level at Cua Dai inlet

transects in which 20 transects are at the north coast and the other 19 transects are at the south coast. These transects are chosen as the same position that were used to estimate LST induced by wave in Do, de Vries and Stive (2018). Positive values indicate southward transport whereas negative values indicate northward transport. The resulting sediment transports within one month are shown at the cross-sections for the different cases in Figs. 6 and 7.

In the case of ENE waves (60^o to north) during the winter (Fig. 6) and the summer (Fig. 7a) the LST at the northern coast, close to the inlet is generally directed to the south, whereas the LST is direct to the north father from the inlet. There is a transport

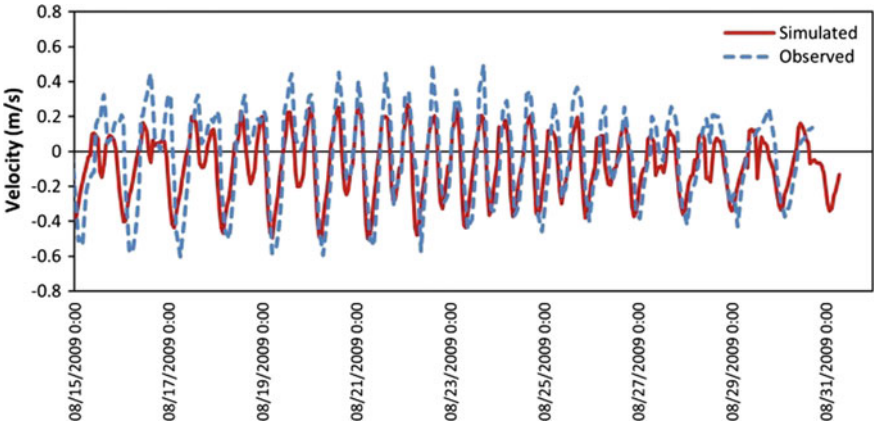

Fig. 5 Observed and simulated depth average velocity at Cua Dai inlet

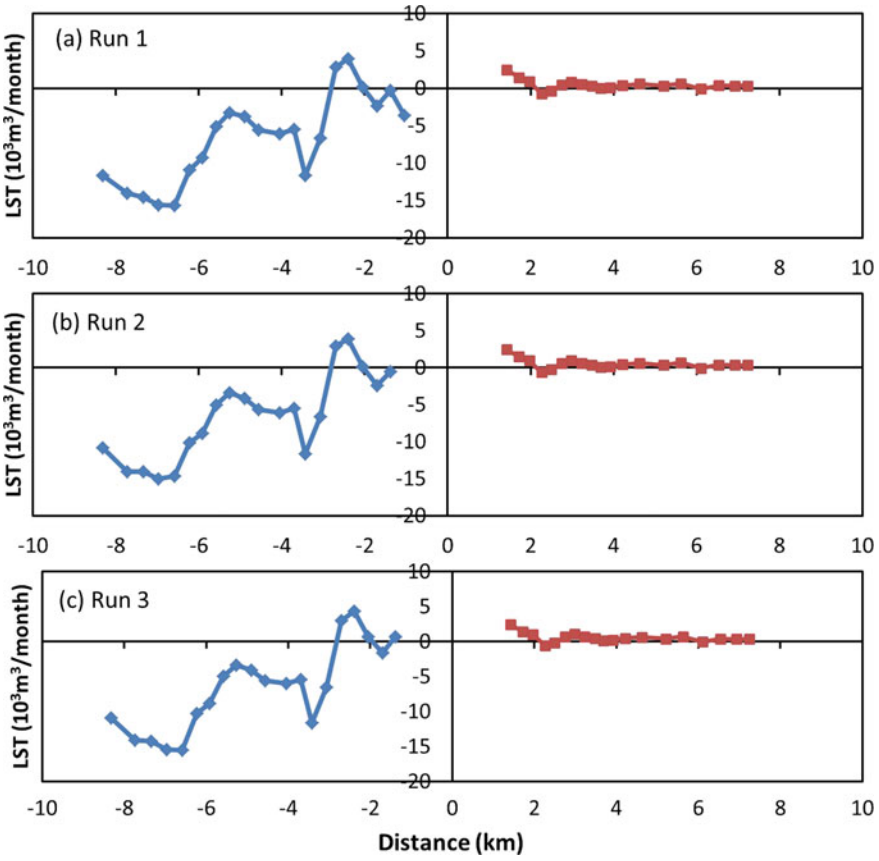

Fig. 6 Longshore sediment transport during the winter with different cases (Run 1, Run 2, and Run 3 as in Table 1)

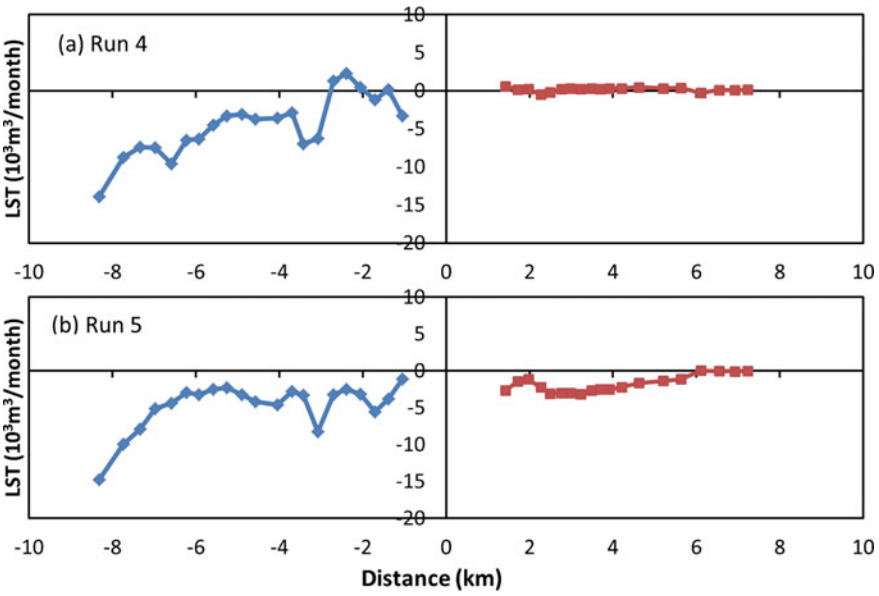

Fig. 7 Longshore sediment transport during the summer with different wave conditions (Run 4 and Run 5 as in Table 1)

diversion point at approximately 3 km to the north. Generally, at the northern coast the LST increase from the inlet to north, whereas at the southern coast the LST decrease from the inlet in the south direction.

For the offshore waves from the SE (135° to the north), the LST is generally towards the northern on both sides of the inlet (Fig. 7b). At the northern coast, the LST slightly increases from the inlet to the north, whereas at the southern coast the LST decreases significantly from the south in direction of the inlet. At around kilometer 6 at the northern coast, the LST significantly increase in the direction to the north. In general, the LST pattern induced by waves, tides and river discharge are similar when compared with the results calculated by Do, de Vries and Stive (2018) LST induced only by wave. The model results show that tides and river discharge do not impact directly on LST at the adjacent coasts.

The extreme flood event has strong impact on the sediment pattern at both southern and northern coast. At the northern coast there is a transport divergent point at approximately 3 km from the inlet to the north as ilustrated in Fig. 8. This phenomenon has found similar results of LST during the winter season when the ENE waves dominate (Do et al. 2018).

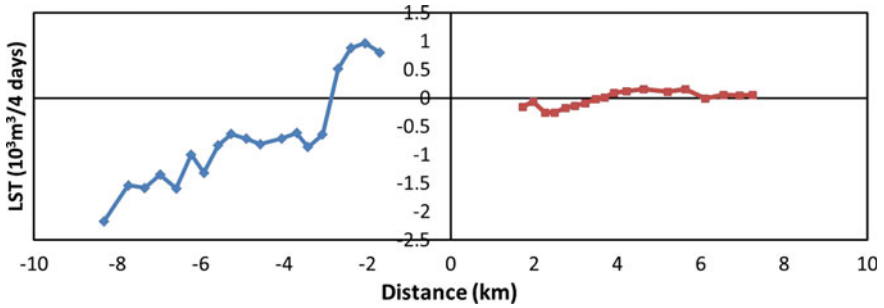

Fig. 8 Longshore sediment transport during the extreme flood event (Run 6 in Table 1)

3.3 Sediment Transport Through the Mouth

Sediment transport capacities through the inlet were investigated by comparing the cumulative sediment transport. Figure 9 shows the influence of different waves and river discharges on the sediment transport through the inlet within one month period. Negative values indicate export sediment whereas positive values indicate import sediment. Generally, the inlet experiences sediment import into the estuary, except in the case of the extreme flood event when the river discharge is extremely large. Run 1, 2 and 3 show clearly the impact of river discharge on sediment transport through the inlet. The increasing river discharge lead to less sediment import into estuary. This can be explained wave induced sediment supply to the inlet and the mainly tides and river discharges induced ebb flow capacity to transport the sediment from the

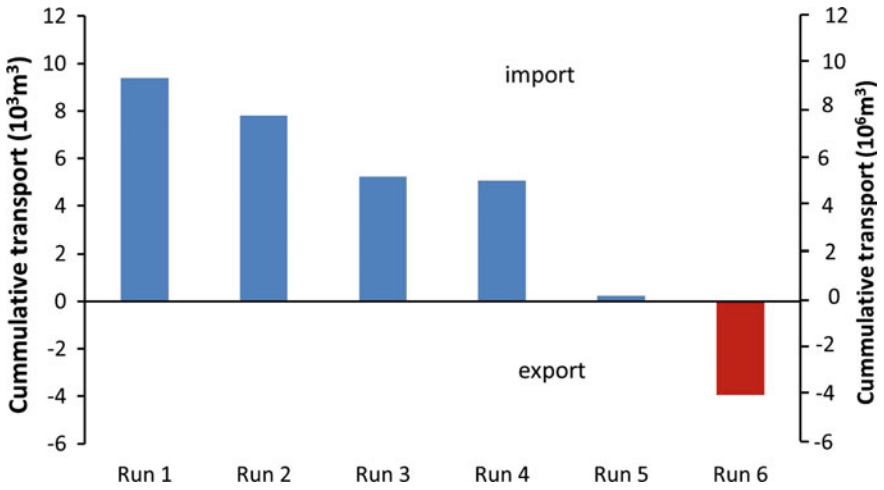

Fig. 9 Cumulative sediment transport through the inlet for varying waves conditions and river discharges

inlet. Therefore when the export sediment induced by tide and river is higher than the import sediment induced by waves the inlet is becoming export sediment.

Figure 9 also shows that waves approaching from both SE and ENE directions cause different magnitudes of sediment import into the estuary. Simulations show that waves coming from the ENE (run 4) contribute to larger sediment import than waves coming from the SE (run 5).

3.4 Sediment Patterns

Sediment transport patterns in the estuary and ebb tidal delta during difference cases in the winter and the summer are shown in Fig. 10. The pattern of sediment transport is quite complex because the flow responds to the combined forcing of tides, river flow, waves, and estuarine circulation. The influence of waves is particularly noticeable in the seaward side of the ebb tidal delta. For the waves coming from the ENE during the winter (Fig. 10a, b, and c), high sediment transport in landward direction can be found around the seaward side of the ebb tidal delta especially at the southward side. At the northward side of ebb tidal delta, the direction of sediment transport toward to the north however, the magnitude depends on the river discharge. The higher sediment transport to the north correspond to the larger river discharge (Fig. 10c) when the case of river discharge of 1037 m^3/s. For the lower river discharge during the summer season (Fig. 10d) the sediment transport is less than compare to other cases. At the landward side of ebb tidal delta there is an interaction between sediment import and sediment export due to river flow, tide and current induced by waves. At the northern side of the coast near the inlet the sediment transport toward to the inlet.

Sediment transport patterns in the estuary and ebb tidal delta during different cases in the summer are shown in Fig. 10d and e. When waves come from the southeast direction (Fig. 10d); sediment transport around ebb tidal delta is tending toward to the North especially at southern side of ebb tidal delta. This results support the results of LST induced by SE waves in the northern direction at the southern coast. Moreover, this result also explains why the sediment import into the estuary induced by SE waves is smaller (or nearly no import) than the import sediment induced by ENE waves. The sediment patterns induced by the ENE waves present the sediment transport in landward direction whereas the SE waves induce sediment in northern direction.

The flush of sediment through the inlet and even ebb shoal is clearly visible in the case of an extreme flood event (Fig. 10f). During the extreme flood event, large amount of sediment flush out from estuary and mainly sediment transport direct to the south. This pattern agrees to our 2nd hypothesis (Fig. 1b), the dominant flow is southwards thus the southern coast is benefiting from sediment bypassing.

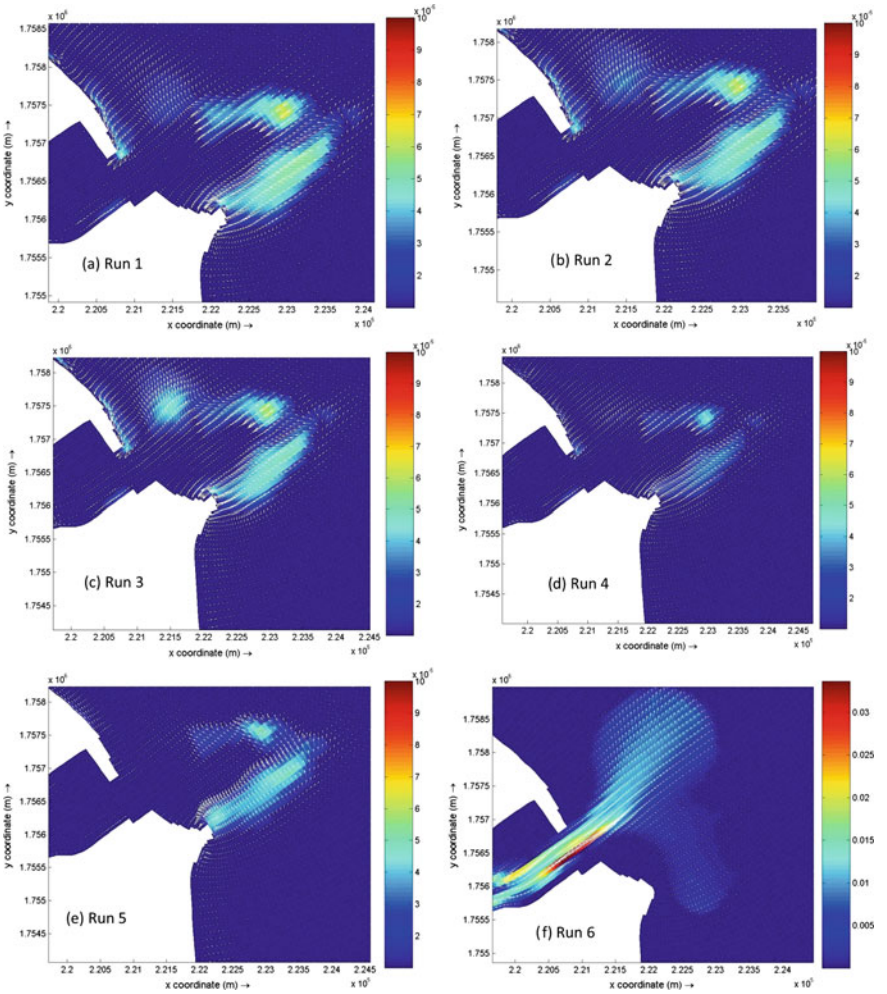

Fig. 10 Mean total sediment transport during one month for all the cases (vectors indicate direction and color map indicate the magnitude, scale on the right)

3.5 Pattern of Erosion and Deposition

Figure 11 shows the erosion/sedimentation pattern for the one month simulation period for the winter/summer cases and 4 days for extreme flood event. The first three cases during the winter exhibit similar erosion/sedimentation patterns. Outside of the ebb tidal delta erosion is shown whereas inside sedimentation is shown. The outside of the ebb tidal delta is affected by wave induced onshore sediment transport. At the inside of the ebb tidal delta, wave induced sediment transport diminishes and consequently erosion appears outside and deposition appear inside the ebb tidal

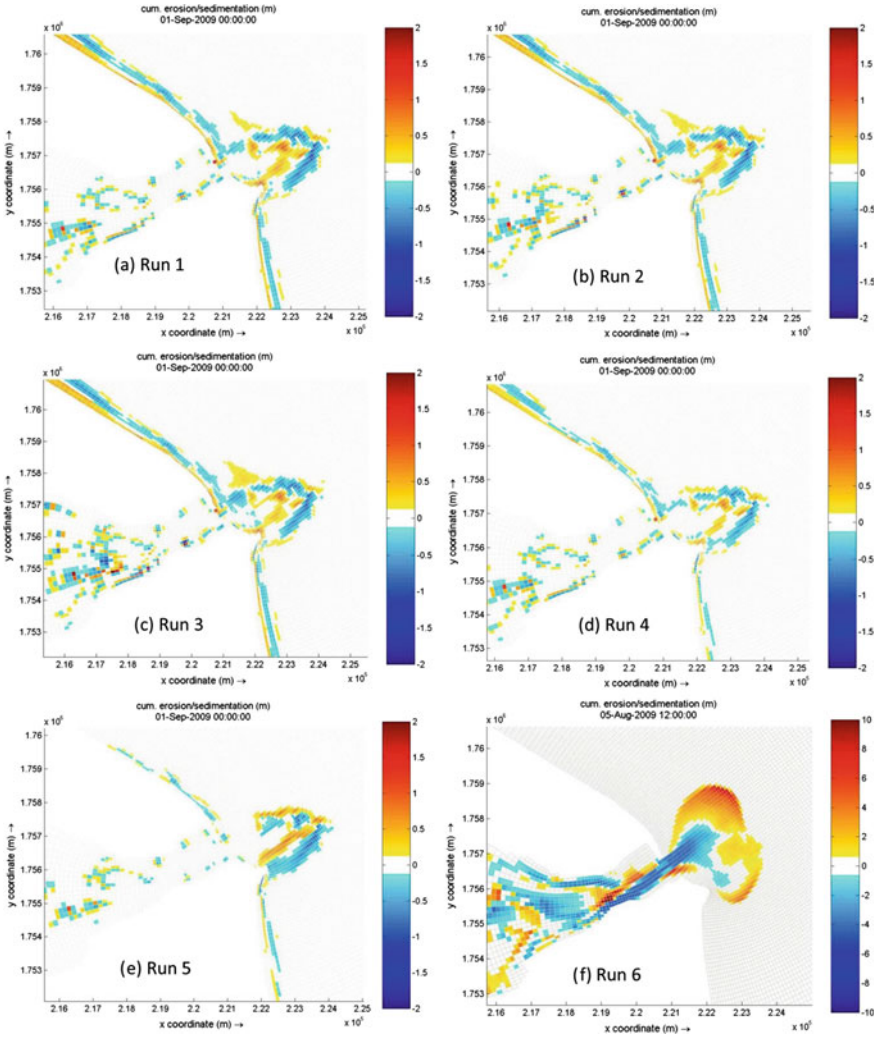

Fig. 11 Modelled erosion/deposition of ebb tidal delta and adjacent coast (negative values indicate erosion and positive values indicate sedimentation)

delta. The sedimentation inside of the ebb tidal delta may originate from the outside of the ebb tidal delta or from river supply. At the north of the ebb tidal delta, sedimentation occurs in all cases considering the winter season. The larger sedimentation corresponds to the larger river flood (Fig. 11c). During the summer, especially when waves are coming from SE and river discharge is very small, this area experiences no sedimentation. The morphology change of the inlet throat is less effected by variability in wave conditions because wave energy is dissipated at the shallow ebb-tidal shoals. There is only large sedimentation at the northern side of the inlet throat. The

littoral drift induced by waves and tides along the northern coast supplies sediment to the inlet throat leading to the sedimentation at the northern side to the inlet throat. This can explain the results of sediment import through the inlet in almost all cases in Fig. 9. In the deep part of the channel inlet, the river flow is strong enough to carry out and supply sediment to the ebb tidal delta. The results of the model simulations reveal that the morphological changes mainly occur on the ebb tidal delta during normal conditions in the winter and the summer. Only the extreme flood event has large influences on channel inlet morphology when the river discharge become dominant thus the inlet channel and ebb-tidal delta are scoured and the longshore sediment transport is interrupted.

4 Conclusions

Seasonal variations in river flow and wave climate, and long-term geomorphological developments make Cua Dai inlet a very complex seasonal varying tidal inlet. This study focused on understanding the effect of seasonal variations in wave conditions and seasonal river discharge. The effects of those on the resulting hydrodynamics and sediment transports through the inlet and at the adjacent coasts are investigated. Hydrodynamics and sediment transport at Cua Dai inlet and its adjacent coasts were simulated using Delft3D. Six scenarios with varying dominant wave conditions in the winter and the summer are executed in combination with various river discharge classes that correspond to the dry, wet and flood seasons.

The results from validation in hydrodynamics, e.g. water levels and velocities between simulated and observed indicate the model agree well.

The results from the alongshore sediment transports at adjacent coasts indicate that the seasonal variation in wave climate has a strong influence on the sediment transport pattern. Waves from the SE during the summer time generally induced alongshore sediment transport (LST) to the north, whereas the waves from the ENE create LST to the south. At the northern coast, the LST increase from the inlet to the north. At the southern coast, the LST decrease from the south in the direction of the inlet. The model shows that the patterns of LST are agree well with the LST induced only by waves from Do et al. 2018.

The simulated sediment transports through the mouth show clear variations due to seasonal variability of the river discharge and wave climate. Waves coming from the ENE at the northern coast induce longshore sediment toward the inlet and supply sediment to the inlet. The river flow helps to carry out and supplies sediment to the ebb tidal delta. When the river becomes dominant (extreme flood event) this leads to export of sediment. The results also indicate the influence of wave directions that influence the magnitude of sediment imported into the estuary. Waves coming from the ENE contribute to larger sediment import than waves coming from the SE.

The results from sediment patterns and morphological changes around the ebb tidal delta indicate that the influence of waves are particularly noticeable on the seaward side of the inlet and less in the landward side of the inlet due to the interaction

between the tides and river flow. Waves generally induce landward sediment transport. When the river flow is large during the flood season, river process are dominant leading to the system to flush out sediment through the estuary and even ebb tidal delta. Especially during the simulated flood event, sediment fluxes are large at the estuary and inner ebb tidal delta.

In a quantitative sense the simulation results are still insufficient to fully explain the channel shifting from north to south. In a qualitative sense however, the model results of this study show a large impact on the seasonal variation in waves and river discharge on sediment transports at Cua Dai inlet and its adjacent coasts. Especially the extreme flood event creates a large sediment export through the inlet and ebb tidal delta.

Acknowledgements This study is part of the PhD of the first author funded through an Erasmus Mundus Mobility Program with Asia (EMMAsia2014) and supported by Delft University of Technology. The authors gratefully acknowledge their co-author dr Nguyen Trung Viet of Thuy Loi University for providing bathymetry data in 2014 for this study.

References

Bertin, X., Fortunato, A. B., & Oliveira, A. (2009). A modeling-based analysis of processes driving wave-dominated inlets. *Continental Shelf Research, 29,* 819–834.

Booij, N., Ris, R. C., & Holthuijsen, L. H. (1999). A third generation wave model for coastal regions 1. Model description and validation. *Journal of Geophysical Research, 104*(04), 7649–7666.

Cayocca, F. (2001). Long-term morphological modelling of a tidal inlet: The Arcachon Basin, France. *Coastal Engineering, 42,* 115–142.

Chen, J. L., Hsu, T. J., Shi, F., Raubenheimer, B., & Elgar, S. (2015). Hydrodynamic and sediment transport modeling of New River Inlet (NC) under the interaction of tides and waves. *Journal of Geophysical Research: Oceans, 120*(6), 4028–4047.

Daly, C. J., Bryan, K. R., Roelvink, J. A., Klein, A. H. F., Hebbeln, D., & Winter, C. (2011). Morphodynamics of embayed beaches: the role of wave conditions. *Journal of Coastal Research, 64,* 1003–1007.

de Vriend, H. J., Zyserman, J., Nicholson, J., Roelvink, J. A., Pe´chon, P., & Southgate, H. N. (1993). Medium term 2DH coastal area modeling. *Coastal Engineering, 21,* 193–224.

Deltares. (2014). *User manual Defl t3D FLOW*. Online available from: https://oss.deltares.nl/documents/183920/185723/Delft3D-FLOW_User_Manual.pdf.

Dissanayake, D. M. P. K., Roelvink, J. A., & van der Wegen, M. (2009). Modelled channel patterns in a schematized tidal inlet. *Coastal Engineering, 56,* 1069–1083.

Do, T. K. A., de Vries, S., & Stive, M. J. F. (2018). Beach evolution adjacent to a seasonally varying tidal inlet in central Vietnam. *Journal of Coastal Research, 34*(1), 6–25.

FitzGerald, D. M. (1984). Interactions between the ebb-tidal delta and landward shoreline: Price Inlet, South Carolina. *Journal of Sedimentary Research, 54*(4), 1303–1318.

FitzGerald, D. M., Buynevich, I. V., Fenster, M. S., & McKinlay, P. A. (2000). Sand dynamics at the mouth of a rock-bound, tide-dominated estuary. *Sedimentary Geology, 131,* 25–49.

Herrling, G., & Winter, C. (2014). Morphological and sedimentological response of a mixed-energy barrier island tidal inlet to storm and fair-weather conditions. *Earth Surface Dynamics, 2,* 363–382.

Hubbard, D. K., Oertel, G. F., & Nummedal, D. (1979). The role of waves and tidal currents in the development of tidal inlet sedimentary structures and sand body geometry: Examples from North Carolina, South Carolina and Georgia. *Journal of Sedimentary Research, 49*(4), 1073–1092.

Komar, P. D. (1996). Tidal –inlet processes and morphology related to the transport of sediments. *Journal of Coastal Research, 23,* 23–45.

Lesser, G. R., Roelvink, J. A., van Kester, J. A. T. M., & Stelling, G. S. (2004). Development and validation of a three-dimensional morphological model. *Coastal Engineering, 51,* 883–915.

Nahon, A., Bertin, X., Fortunato, A. B., & Oliveira, A. (2012). Process-based 2DH morphodynamic modeling of tidal inlets: A comparison with empirical classifications and theories. *Marine Geology, 291–294,* 1–11.

Oertel, G. F. (1972). Sediment transport on estuary entrance shoals and the formation of swash platforms. *Journal of Sedimentary Petrology, 42*(4), 857–863.

Oertel, G. F. (1988). Processes of sediment exchange between tidal inlets, ebb deltas and barrier islands. In: D. G. Aubrey, L. Weishar (Eds.), *Hydrodynamics and sediment dynamics of tidal inlets*. *Lecture notes on coastal and estuarine studies* (Vol. 29, pp. 297–318). Berlin Heidelberg New York: Springer.

Ridderinkhof, W., de Swart, H. E., van de Wegt, M., & Hoekstra, P. (2016). Modeling the growth and migration of sandy shoals on ebb-tidal deltas. *Journal of Geophysical Research Earth Surface, 121,* 1351–1372.

Ris, R. C., Holthuijsen, L. H., & Booij, N. (1999). A third-generation wave model for coastal regions: 2. Verification. *Journal of Geophysical Research, 104*(C4), 7667–7681.

Roelvink, J. A. (2006). Coastal morphodynamic evolution techniques. *Coastal Engineering, 53,* 277–287.

Roelvink, J. A., & Reniers, A. (2012). A guide to modeling coastal morphology. *Advances in Coastal and Ocean Engineering, 12,* 274.

Robinson, A. H. W. (1975). Cyclical changes in shoreline development at the entrance to Teignmouth Harbour, Devon, England. In J. Hails & A. Carr (Eds.), *Nearshore sediment dynamics and sedimentation* (pp. 181–198). New York: Wiley.

Sha, L. P. (1989). Cyclic morphological changes of the ebb-tidal delta, Texel Inlet, The Netherlands. *Geology Mijnbow, 68,* 35–48.

van de Wegen, M., & Roelvink, J. A. (2008). Long-term morphodynamic evolution of a tidal embayment using a two-dimensional process-based model. *Journal of Geophysical Research: Oceans, 113,* C03016.

van der Wegen, M., Dastgheib, A., & Roelvink, J. A. (2010). Morphodynamic modeling of tidal channel evolution in comparison to empirical PA relationship. *Coastal Engineering, 57*(9), 827–837.

van Leeuwen, S. M., van der Vegt, M., & de Swart, H. E. (2003). Morphodynamics of ebb-tidal deltas: a model approach. *Estuarine Coastal and Shelf Science, 57,* 899–907.

van Rijn, L. C. (1993). *Principles of sediment transport in rivers, estuaries and coastal seas*. The Netherlands: Aqua publications.

Vo, N. D. (2015). *Deterministic hydrological modelling for flood risk assessment and climate change in large catchment. Application to Vu Gia Thu Bon catchment, Vietnam* (Ph.D. thesis), University Nice Sophia Antipolis.

Winter, C. (2006). Meseo-scale morphodynamics of the Eider Estuary: Analysis and numerical modelling. In *Journal of Coastal Research, SI 39 (Proceedings of the 8th International Coastal Symposium)* (pp. 498–503).

Interaction Between Waves, Current and Morphology Change at Tillamook Inlet

Honghai Li, Lihwa Lin, Zeki Demirbilek, Tanya M. Beck and Hans R. Moritz

Abstract The narrow jetty configuration of Tillamook Inlet functions to constrict tidal flow, increase current speed, and prevent sediment deposition. However, the interaction of strong currents with incoming ocean waves over the inlet's ebb shoal can amplify and complicate the wave environment at the inlet entrance. In this study, the Coastal Modeling System (CMS) was used to investigate time- and space-varying wave and current conditions affecting boating operations at Tillamook Inlet and quantify the effects of physical processes. Wave simulations with refraction, shoaling, and breaking provided estimates of wave-related parameters of interest to the navigable region at Tillamook. The simulation results showed the winter storms produced larger wave steepness and wave dissipation at the inlet complex, which were also closely associated with the bathymetry of ebb shoal. The flood currents weakened wave dissipation, while ebb currents increased wave dissipation over the ebb shoal and across the USCG recommended south passage in/out of the inlet. The effect of South Jetty shortening was localized to the immediate vicinity of the South Jetty. The calculated wave steepness and wave dissipation indicated that a south passage out of the inlet would be safer than a course straight out passing over the bar or a course turning to NW direction.

Keywords Numerical modeling · Waves · Current · Sediment transport · Channel infilling · Morphology change

1 Introduction

The Tillamook Inlet is located on the Pacific Northwest coast of Oregon, about 90 miles west of Portland. Five rivers drain into Tillamook Bay, a shallow estuary, which connects to the Pacific Ocean through the navigation channel that passes through a

H. Li (✉) · L. Lin · Z. Demirbilek · T. M. Beck
Coastal and Hydraulics Laboratory, US Army Corps of Engineers, Vicksburg, USA
e-mail: Honghai.Li@usace.army.mil

H. R. Moritz
US Army Corps of Engineers, Portland District, USA

K. D. Nguyen et al. (eds.), *Estuaries and Coastal Zones in Times of Global Change*, Springer Water,
https://doi.org/10.1007/978-981-15-2081-5_29

jetty-entrance and an ebb shoal, and joins with the open ocean at approximately the 80 m depth contour. The channel is well-defined from the entrance to Port of Garibaldi, the channel's termination point in Tillamook Bay (Fig. 1). The average depth in the Tillamook estuary is less than 2 m, and its dynamics is controlled by tide, wind, and surface water flows. Tillamook Bay has a mixed semi-diurnal tide with a mean tide range of 2 m and an extreme tidal range of 4.1 m (Komar 1997).

As shown in Fig. 1, the depth at the navigation channel entrance ranges between 8 and 13 m relative to mean lower low water (MLLW), which is comparatively deeper than in the middle and back bay (estuary). There are no markers defining the channel past beyond the tips of jetties over the ebb shoal and out in the ocean. As such, the width and depth of the unmarked channel seaward of the entrance over the entire ebb shoal and beyond are not specified. Consequently, there is no prescribed

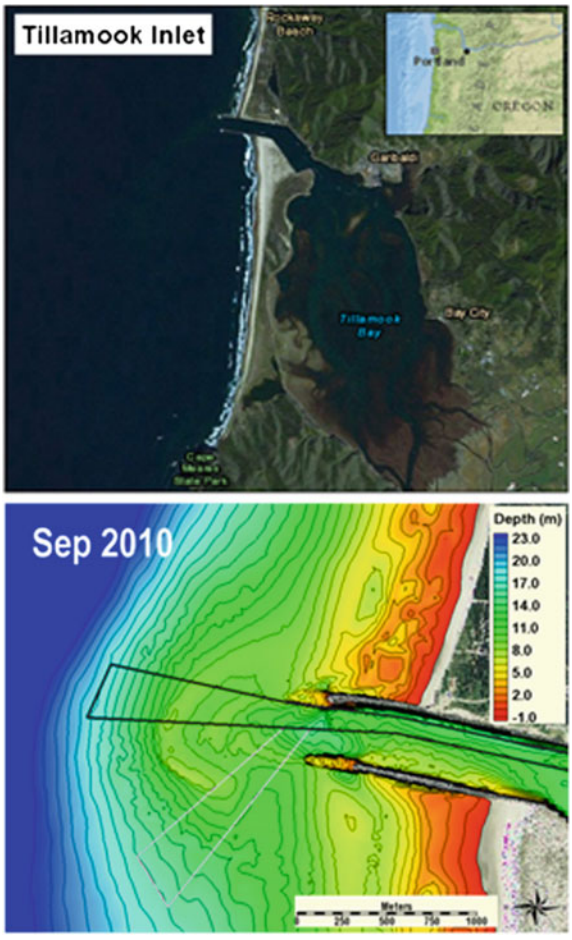

Fig. 1 Location map for Tillamook Inlet and Bay, Oregon, and Port of Garibaldi. The September 2010 bathymetry with authorized navigation channel (black polygon), and the USCG preferred south channel (grey polygon)

inbound/outbound vessel route for traffic moving over the ebb shoal, where depths vary between 8 and 15 m.

Because the Tillamook Inlet is naturally self-scouring, annual surveys indicate that the dual-jettied entrance has not shoaled to the 6 m MLLW depth limit to require dredging. Both jetty heads have degraded over the years, and as of 2010, the north and south jetties had receded landward approximately 160 m and 300 m, respectively. Thus, the knowledge of local wave severity, degradation of jetties, and change in the entrance channel morphology has led the U.S. Coast Guard (USCG) to reevaluate optimal approaches to the inlet. This resulted in a new turn in the channel direction that directed vessels abruptly toward a south-oriented navigation channel (the grey polygon in Fig. 1).

The narrow jetty configuration functions to constrict tidal flow and increase current speed, especially during the ebb tide. The spatial variation of waves and currents occurring over the ebb shoal is dependent partly on the morphology of the ebb shoal that changes year to year. Because of the dynamic nature of seasonally evolving ebb shoal geometry, the resulting wave and current magnitudes over the ebb shoal and in the entrance channel can vary rapidly year around. The interaction between waves and currents in these areas can develop dangerous conditions (large steep waves and strong currents) that may pose significant risks by endangering safety and stability of vessels which, approaching and exiting Tillamook Inlet entrance, must pass over the ebb shoal and into the Pacific Ocean (Demirbilek et al. 2013).

The present study was conducted with the goal to identify conditions that impact navigability in Tillamook Inlet. Consequently, the primary motivation behind this study was to investigate the time- and space-varying waves and currents affecting boating operations at Tillamook Inlet for summer and winter months and to better understand the cause-effect relationship between navigability conditions at Tillamook Inlet and characteristics of the ebb-shoal, hydrodynamics of entrance, role of the jetties, and interaction between the ebb shoal, entrance and estuary and between waves, current and morphology change.

2 Method

Coastal Modeling System

The Coastal Modeling System (CMS) was used in this investigation. As shown in Fig. 2, the CMS is an integrated suite of numerical models for waves, flows, and sediment transport and morphology change in coastal areas. This modeling system includes representation of relevant nearshore processes for practical applications of navigation channel performance, and sediment management at coastal inlets and adjacent beaches.

CMS-Wave model solves the steady-state wave-action balance equation on a non-uniform Cartesian grid to simulate spectral transformation of directional random waves and is designed to simulate wave processes with ambient currents at coastal

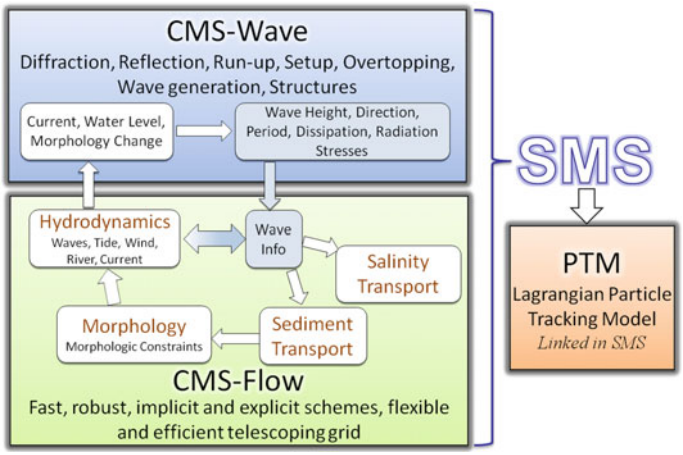

Fig. 2 The CMS framework and its components

inlets and in navigation channels. The model can be used either in half-plane or full-plane mode for spectral wave transformation (Lin et al. 2011). Wind wave generation and growth, diffraction, reflection, dissipation due to bottom friction, white-capping and breaking, wave-current interaction, wave runup, wave setup, and wave transmission through structures are the main wave processes included in CMS-Wave. The height and direction of waves approaching the Tillamook Inlet navigation channel change due to wave shoaling, refraction, diffraction, reflection, and breaking. Waves propagating through the entrance interact with bathymetry, surrounding land features, currents and coastal structures. These changes to waves affect bed shear stresses and sediment mobility around this inlet.

CMS-Flow solves the conservative form of the shallow water equations that includes terms for the Coriolis force, wind stress, wave stress, bottom stress, vegetation flow drag, bottom friction, wave roller, and turbulent diffusion. Governing equations are solved using the finite volume method on a non-uniform Cartesian grid. CMS-Flow calculates hydrodynamics (water level, depth-averaged circulation), sediment transport and morphology change, and salinity and temperature due to tides, winds, waves, and river inflows (Wu et al. 2011).

The coupled CMS-Flow and CMS-Wave models were used for investigation of wave-current interaction in Tillamook Inlet. This modeling includes effects of winds, waves, tides and river inflows. The calculated quantities of interest includes wave-related engineering parameters including significant wave height (H_s, m), spectral peak period (T_p, sec) and mean wave direction ($\overline{\theta}$, deg), wave steepness (H_s/L_p, where L_p is the spectral peak wavelength calculated at the local depth), wave dissipation (m^3/sec) (the wave energy loss in the wave propagation direction), and Ursell number ($H_s L_p^2/h^3$, where h is the local water depth) (Dally et al. 1985; Ursell 1953). Wave breaking intensity is expressed in terms of wave dissipation. Measured by significant wave height and water depth over wavelength ratio, the Ursell number helps

to identify the roles of wave "nonlinearity". These engineering parameters are used to assess wave and current conditions for safe navigation, and preferred entrance and exit courses for boating operations at Tillamook Inlet.

CMS-Flow modeling task includes specification of winds, tides and river flows (discharges) to the model. The effects of waves on the circulation are input to the CMS-Flow and have been included in the simulations performed for this study. The CMS-Flow modeling considers three wave heights (H_s = 2 m, 3 m, and 4 m) to investigate the effects of flow on these hypothetical wave conditions. These test runs were done in part for setting up the CMS-Flow for simulations using the actual field conditions in 2005 and 2010 for the months of August (summer) and December (winter).

Wave and Flow Model Setup

Three CMS-Wave grids were generated for wave modeling: (1) an asymmetric ebb shoal grid (based on September 2005 survey), (2) a symmetric ebb shoal grid (based on June 2010 survey), and (3) a shortened South Jetty grid. All three grids cover the same square domain of 17.6 × 17.6 km with varying cell sizes from 10 m spacing. The asymmetric ebb shoal grid (Fig. 3) was generated from the September 2005 survey that shows a crescent shape ebb shoal that extends seaward from the north jetty to the inlet outer bar. The symmetric ebb shoal grid was generated from the June 2010 survey, showing a symmetric, isolated ebb shoal seaward of the inlet entrance. The shortened South Jetty grid is a hypothetical case based on the June 2010 symmetric ebb shoal grid with a truncated South Jetty recessed landward by 230 m (750 ft). This hypothetical case was simulated to evaluate whether removing a section of the South Jetty would improve navigability of the channel. The offshore boundary of the grid domain is at the 80 m isobath. Figure 4 shows the symmetric ebb shoal grid domain and bathymetry. Figure 5 shows the local inlet entrance bathymetry contours for the shortened South Jetty grid.

A telescoping grid was used in the flow modeling that covered the same square domain as the wave grid (Fig. 6). The grid has finer resolution in areas of high interest such as the ebb shoal, entrance, inlet and Bay. The red circle denotes the location of NOAA's Garibaldi tide gage. Two red triangles denote the locations of the inlet entrance (Entrance Channel Station) and Kenchloe Point (Kenchloe Point Station) where high current were calculated. Three flow telescoping grids were generated corresponding to: (1) the asymmetric ebb shoal grid (based on September 2005 survey), (2) the symmetric ebb shoal grid (based on June 2010 survey), and (3) the shortened South Jetty grid.

The south jetty of the Tillamook Inlet has a recession rate of 40–80 ft/yr. Considering 15 years of the south jetty recession at a rate of 50 ft/yr, a third grid was developed using the symmetric ebb shoal bathymetry by shortening the South Jetty 230 m (750 ft). Existing and shortened South Jetty configurations are shown in Fig. 7.

Model Forcing

Simulations were conducted for a summer (August) and a winter (December) month for asymmetric ebb shoal (September 2005 bathymetry) and symmetric ebb shoal

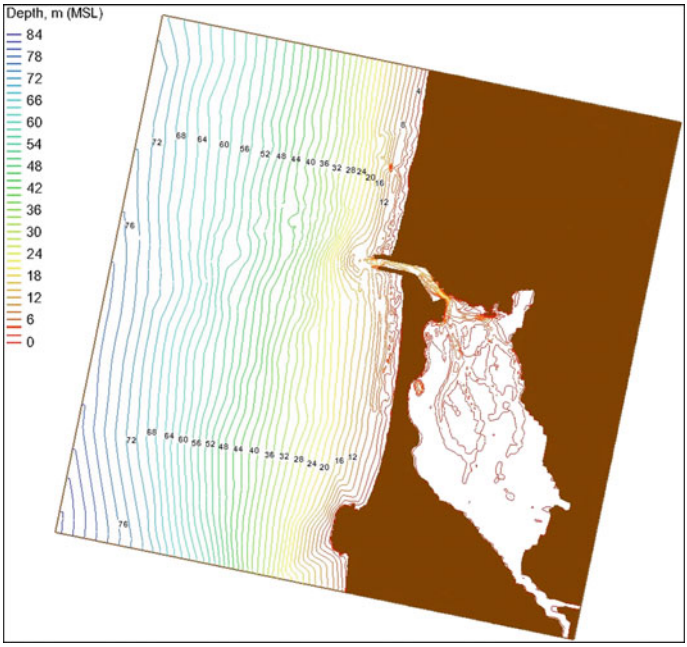

Fig. 3 CMS-Wave grid for asymmetric ebb shoal grid domain and bathymetry based on September 2005 survey, NGDC shoreline and GEODAS database

(June 2010 bathymetry). The shortened South Jetty was simulated only for the symmetric ebb shoal. In addition to the calculation of monthly mean and maximum parameters, four peak flood and ebb current scenarios were selected to show the strong current effects on wave-related parameters. A monthly maximum estimate could be due to maximum waves or maximum currents or both. These additional scenarios ensure that the peak flood and ebb current effects on wave-related parameters are included. For safety of navigation, the peak flood and ebb currents are of primary concern to boating operations.

Incident wave conditions were based on directional wave data collected by the National Data Buoy Center (NDBC, http://www.ndbc.noaa.gov) Buoy 46029, located approximately 60 miles northwest of Tillamook Inlet. The buoy wave data were transformed to the seaward boundary of the CMS-Wave grid using a simplified wave transformation for shore-parallel depth contours.

CMS-Flow was driven with the time-dependent water levels, winds, river discharges and waves. Water level data (Fig. 8) were obtained from NOAA coastal station (9435380) at South Beach, Yaquina River, Oregon, approximately 105 km south of Tillamook Inlet on the Oregon coast. To account for the distance between the South Beach Station and Tillamook Bay, tidal signals were phase-shifted by 30 min at the CMS-Flow open boundary. The data indicate no seasonal changes in tidal signals.

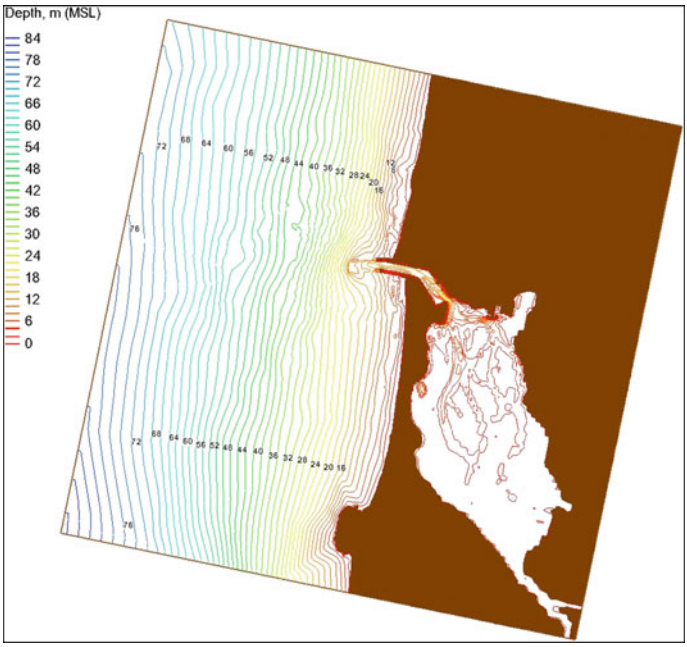

Fig. 4 Symmetric ebb shoal grid domain and bathymetry based on June 2010 survey, NGDC shoreline and GEODAS database

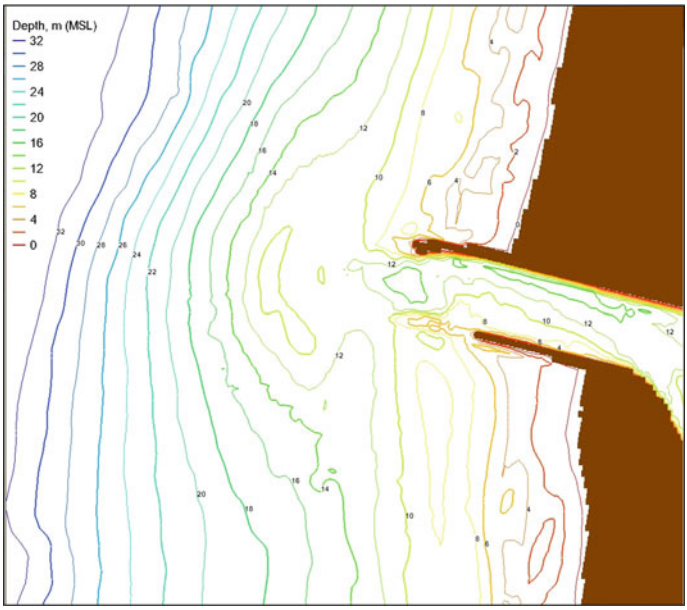

Fig. 5 Shortened south Jetty bathymetry contours

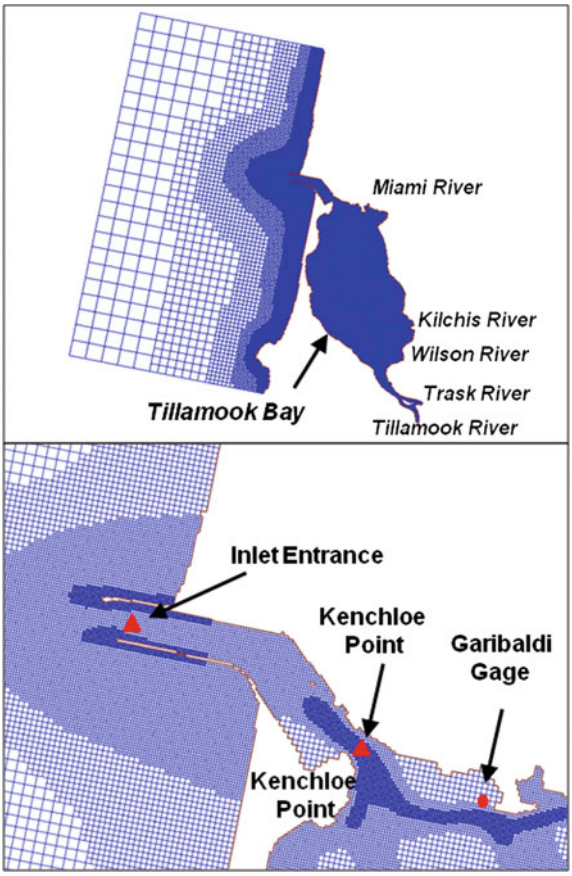

Fig. 6 CMS-Flow domain and telescoping grid

Wind data were obtained from the offshore NDBC Buoy 46029 as atmospheric input to flow modeling and river flow data were obtained from the USGS gages at the Trask and Wilson Rivers (Fig. 9). The flow discharge in summer is 1–2 orders of magnitude smaller than the winter. The flow discharges for three other rivers (Tillamook, Kilchis, and Miami Rivers) were estimated by a weighted drainage area approach.

3 Results

Simulations for Existing Jetty Condition

As an example, the calculated and the measured water surface elevations at Garibaldi for August 2010 are shown in Fig. 10. The calculated results show a good agreement with the measurements. Water levels at Garibaldi have a mixed signal that is mainly semi-diurnal tide. The mean tidal range (mean high water—mean low water) is

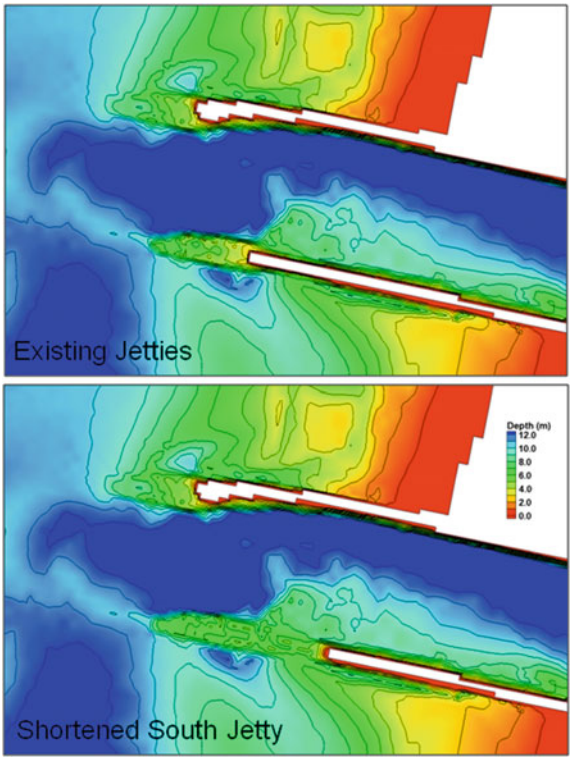

Fig. 7 Existing (top) and shortened (bottom) South Jetty configurations

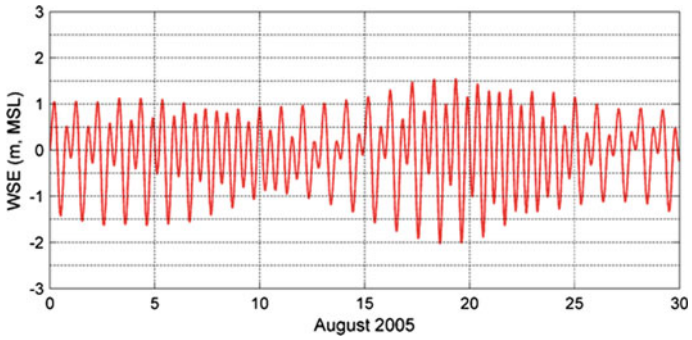

Fig. 8 Water level data for August 2005 at South Beach and Yaquina River, Oregon

1.9 m and the maximum tidal range (mean higher high water—mean lower low water (MLLW)) is 2.5 m. Considering the size of Tillamook Bay and the narrowness of the navigation channel through Tillamook Inlet, this tidal range is large enough to generate strong ebb and flood currents at the inlet channel.

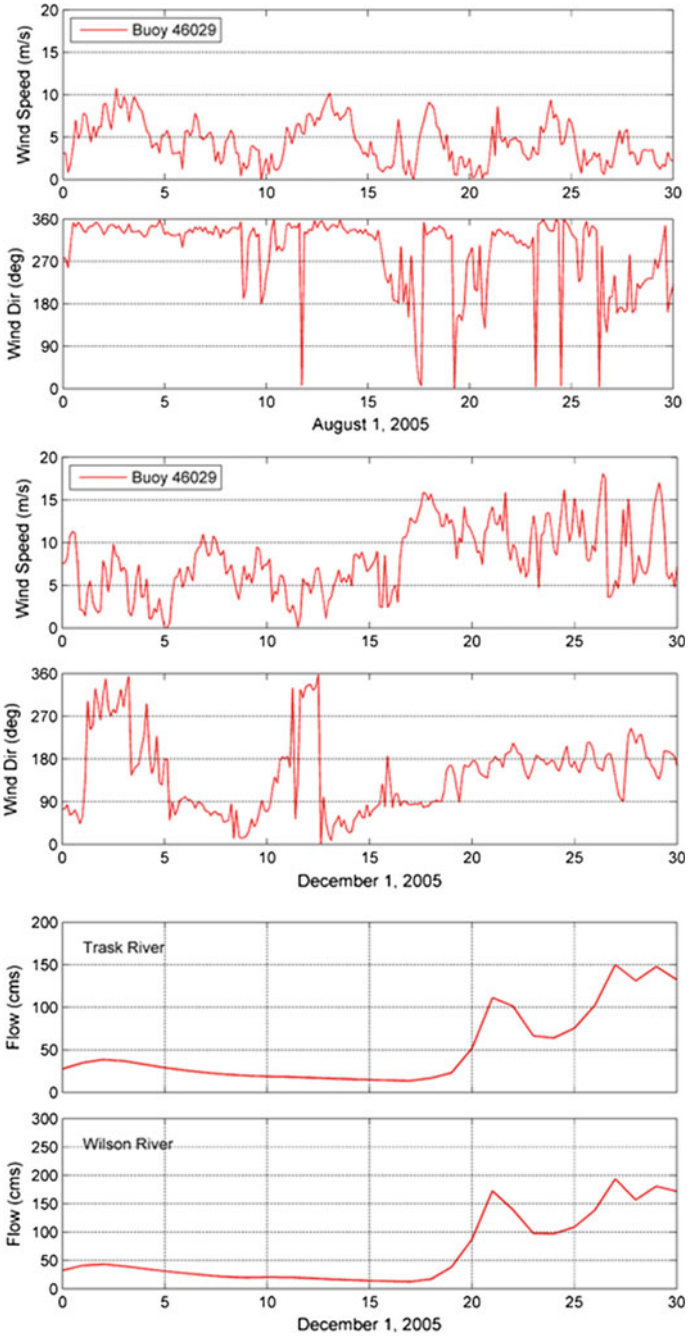

Fig. 9 Wind data for August and December 2005 at NDBC Buoy 46029 and river flow discharges for December 2005 and 2010 from USGS gages at Trask (#14302480) and Wilson (#14301500) Rivers, Oregon

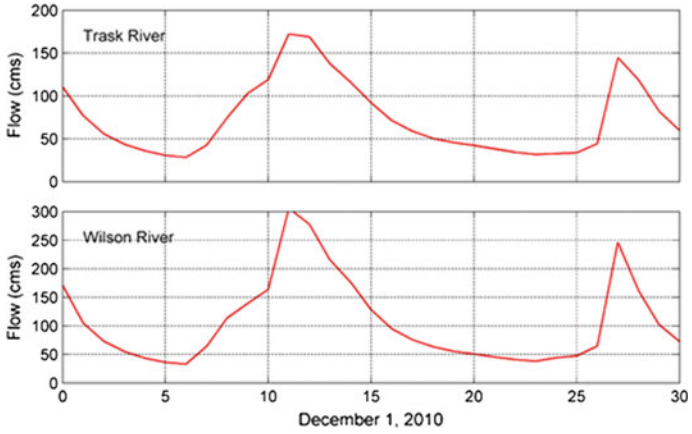

Fig. 9 (continued)

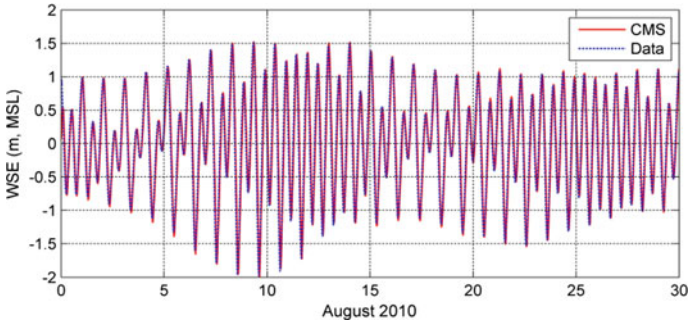

Fig. 10 Calculated water surface elevation at Garibaldi, August 2010

Example snapshots of calculated current fields on 12 August 2010 at 21:00 GMT, 13 August 2010 at 03:00 GMT, 27 December 2010 at 12:00 GMT, and 18:00 GMT, are shown in Figs. 11 and 12. In these examples, incident waves are from west-northwest (300 deg azimuth) in the summer cases, and west-southwest (260 deg azimuth) in the winter cases. The calculated current magnitude reaches 3.0 m/sec at the Kenchloe Point Station (Fig. 6). The current pattern at the ebb shoal is mainly controlled by wind, waves, and local bathymetry.

Calculated monthly mean and maximum wave steepness, wave dissipation, and Ursell number for August and December 2005 are shown in Figs. 13 and 14, respectively. Monthly mean and maximum wave steepness, wave dissipation, and Ursell number for August and December 2010 are shown in Figs. 15 and 16, respectively. The values of these parameters are small in summer but larger in winter as a result of higher waves in winter. For the summer month (August), calculated mean and maximum wave steepness, dissipation and Ursell number results show that stronger wave breaking and wave nonlinearity occur over the ebb shoal in August 2005 than August

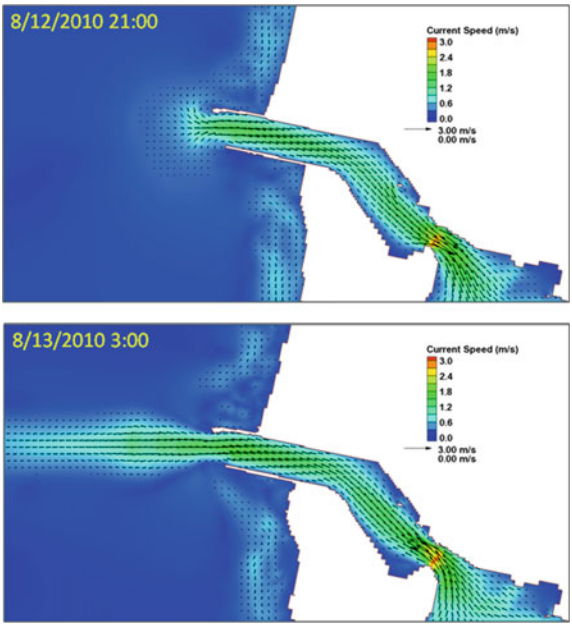

Fig. 11 Calculated current field on 12 August 2010 at 21:00 GMT (flood current) and on 13 August 2010 at 03:00 GMT (ebb current)

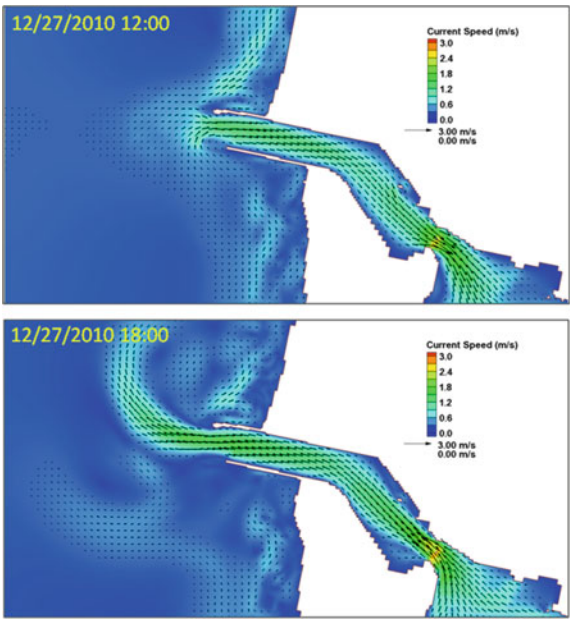

Fig. 12 Calculated current field on 27 December 2010 at 12:00 GMT (flood current) and 18:00 GMT (ebb current)

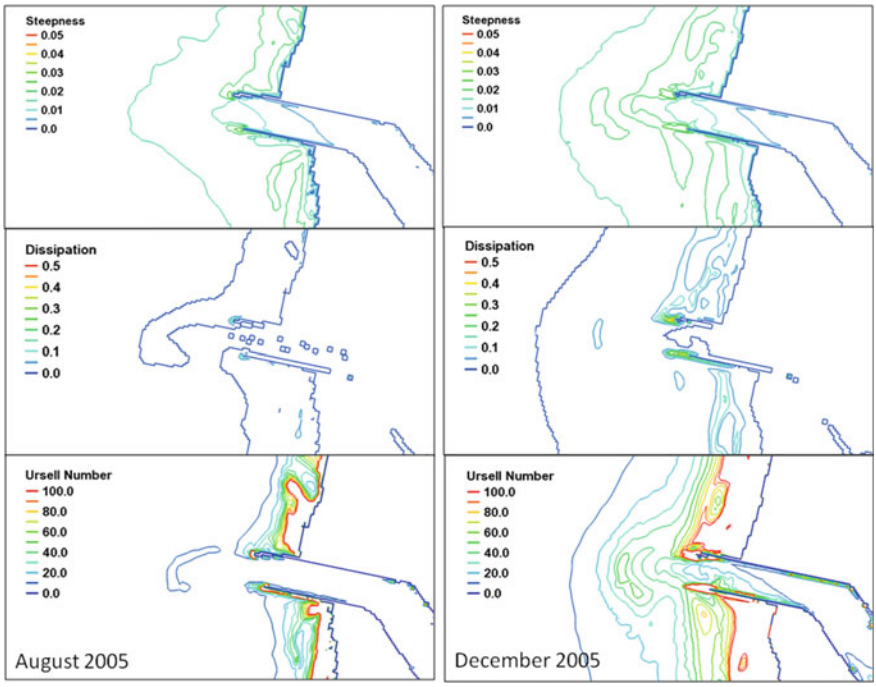

Fig. 13 Calculated monthly mean wave steepness (top), wave dissipation (middle), and Ursell number (bottom) for August and December 2005

2010. Calculated maximum dissipation and Ursell numbers are relatively small in the south entrance channel. For the winter month (December), calculated mean wave steepness, dissipation and Ursell number results show stronger wave breaking and wave nonlinearity occur over the ebb shoal in December 2005 than December 2010. The values of maximum wave steepness in December 2010 are higher than December 2005. The storm waves in December 2010 have shorter mean wave periods that produce waves with larger wave steepness.

Four scenarios of peak ebb and flood currents with large river inflows are used to show the current effects on waves. In these scenarios, the largest incident waves were around 2 m in August 2005 and 2010, and 3.4 m and 3.6 m in December 2005 and 2010, respectively. These waves came from northwest for the summer scenarios and southwest for the winter.

Figure 17 shows snapshots of calculated wave steepness, wave dissipation, and Ursell number fields for a peak flood current on 12 August 2010 at 21:00 GMT and for a peak ebb current on 13 August 2010 at 03:00 GMT. These incident waves are 2.0 m (9 s) from northwest (311 deg azimuth) and 2.1 m (9 s) from west-northwest (294 deg azimuth), respectively. The calculated current magnitudes at the Inlet Entrance Station (Fig. 6) are around 1.5 m/sec (Fig. 11). Calculated wave steepness and dissipation are higher for the peak ebb than the peak flood in the south entrance channel and

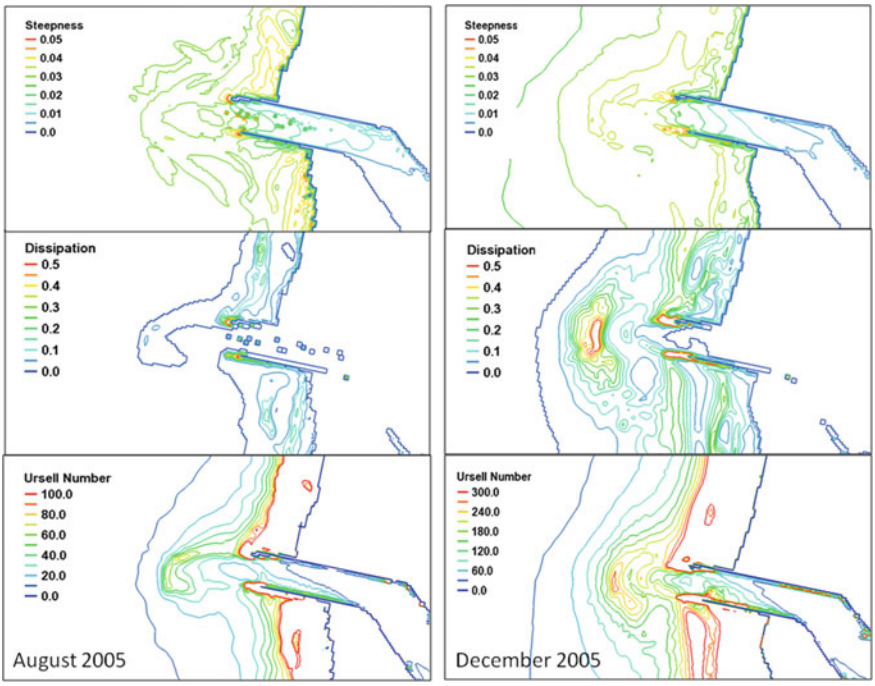

Fig. 14 Calculated maximum wave steepness (top), wave dissipation (middle), and Ursell number (bottom) for August and December 2005

ebb shoal. Calculated Ursell number fields are similar in both peak flood and ebb scenarios.

Figure 18 shows snapshots of calculated wave steepness, wave dissipation, and Ursell number fields for peak flood and ebb currents in 27 December 2010 at 12:00 GMT and in 27 December 2010 at 18:00 GMT, respectively. The incident waves at these times were 3.4 m (11 s) from west-southwest (259 deg azimuth) and 3.6 m (11 s) from west-southwest (264 deg azimuth). Calculated current magnitudes at the inlet entrance were around 1.4 m/sec (Fig. 12). The ebb current produced larger wave steepness, dissipation, and Ursell number over the ebb shoal and south entrance channel.

Figure 19 shows results for one more scenario for a peak ebb current on 24 December 2010 at 03:00 GMT. The incident waves were 3.2 m and 10 s from southwest (234 deg azimuth). The calculated ebb current magnitude at the inlet entrance was 1.7 m/sec. Compared to Fig. 18, this scenario, with a smaller wave height and a larger current, produced smaller values of wave steepness, dissipation, and Ursell number. These results show that waves may have a stronger role than the current at the inlet entrance and ebb shoal.

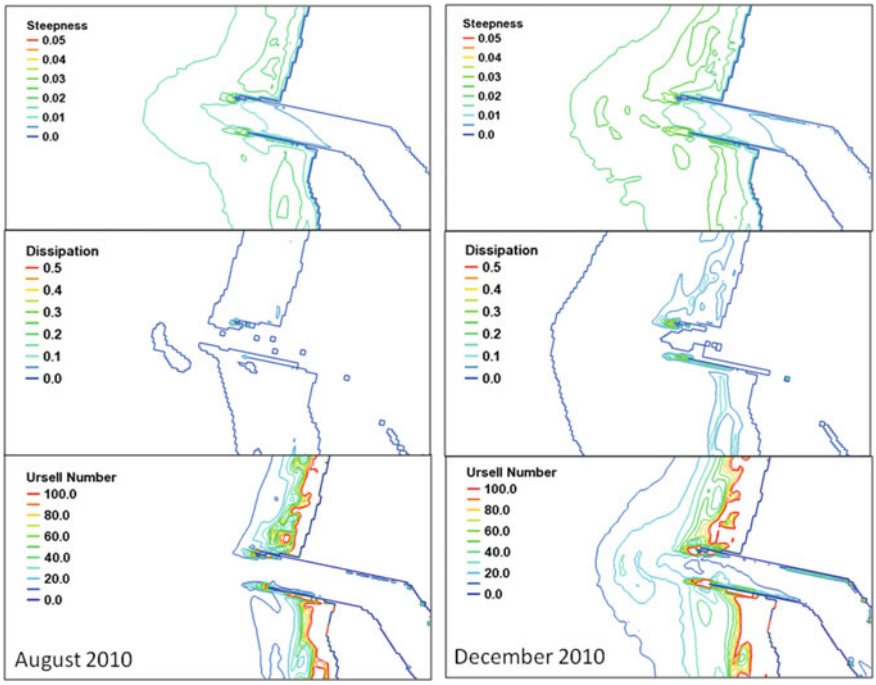

Fig. 15 Calculated monthly mean wave steepness (top), wave dissipation (middle), and Ursell number (bottom) for August and December 2010

Simulations for a Shortened South Jetty

For the shortened South Jetty, simulations were conducted only for August and December 2010 (symmetric ebb shoal). Figure 20 shows calculated current fields on 12 August at 21:00 GMT and 13 August at 03:00 GMT. Figure 21 shows the current fields on 27 December 2010 at 12:00 and 18:00 GMT. The peak flood and ebb current magnitudes at the Kenchloe Point (Fig. 6) remained unchanged between existing and shortened South Jetty simulations. With or without the South Jetty shortening, the currents at the entrance remained essentially unchanged during the ebb. The peak flood currents over the immersed section of the shortened South Jetty were reduced approximately by 0.2 m/sec (15% reduction) at the entrance. Results indicated that with the South Jetty shortening, the entrance becomes wider and this affects the flood current magnitude but not the ebb current magnitude.

Monthly mean and maximum wave steepness, wave dissipation, and Ursell number have similar patterns before and after the South Jetty shortening (Figs. 13, 14, 22 and 23). Both for summer and winter months, minor changes in wave breaking patterns occurred over the submerged section of the recessed South Jetty. Wave steepness, dissipation, and Ursell number increased and further extended into the main channel toward the Bay. This is much more noticeable for winter conditions. As we noted earlier for constant incident wave simulations, the peak values

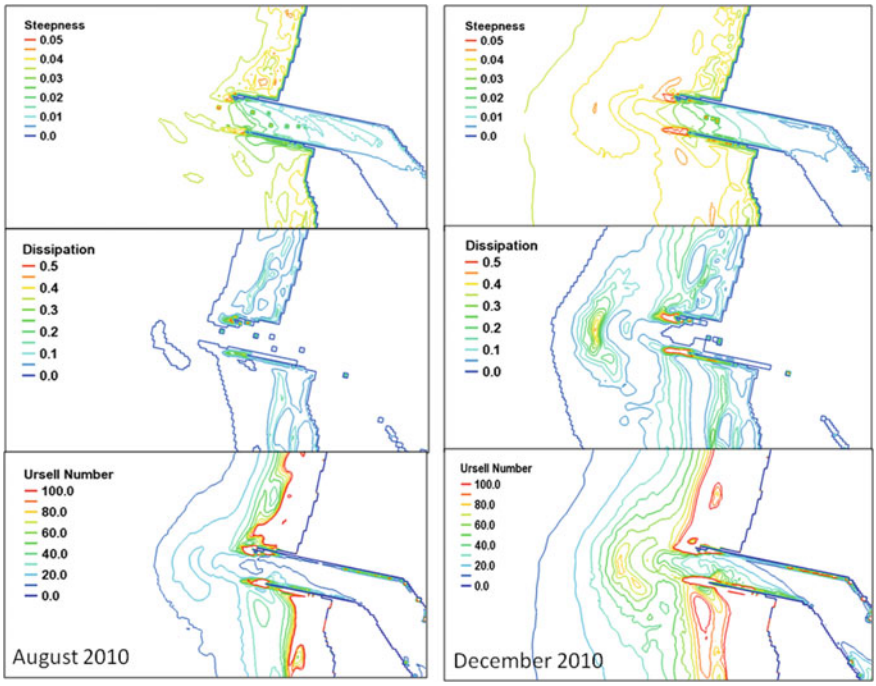

Fig. 16 Calculated maximum wave steepness (top), wave dissipation (middle), and Ursell number (bottom) for August and December 2010

of wave steepness, dissipation, and Ursell number for the shortened South Jetty occurred approximately at the same locations of the existing (full length) South Jetty configuration.

Figure 24 shows snapshots of wave steepness, wave dissipation, and Ursell number for the shortened South Jetty during a flood current on 12 August 2010 at 21:00 GMT and an ebb current on 13 August 2010 at 03:00 GMT. Figure 25 has snapshots of wave steepness, wave dissipation, and Ursell number for the shortened South Jetty during peak flood and ebb currents on 27 December 2010 at 12:00 GMT and on 27 December 2010 at 18:00 GMT, respectively. Comparing these to the cases of the existing jetty configuration (Figs. 17 and 18), we find that currents, wave heights, wave steepness, wave dissipation, and Ursell number have increased only over the submerged section of the shortened South Jetty. The snapshots in Fig. 25 correspond to an incident winter wave of 3.6 m from southwest, showing that waves propagate over the submerged South Jetty section to reach the navigation channel and penetrate further into the Bay.

Based on results shown in Figs. 22, 23, 24 and 25, the effect of South Jetty shortening was localized to the immediate vicinity of the jetty. It had little or no visible effect on waves or currents in the entrance and over the ebb shoal. For the 3 and 5 m waves with a recessed South Jetty, there was a slight increase in wave

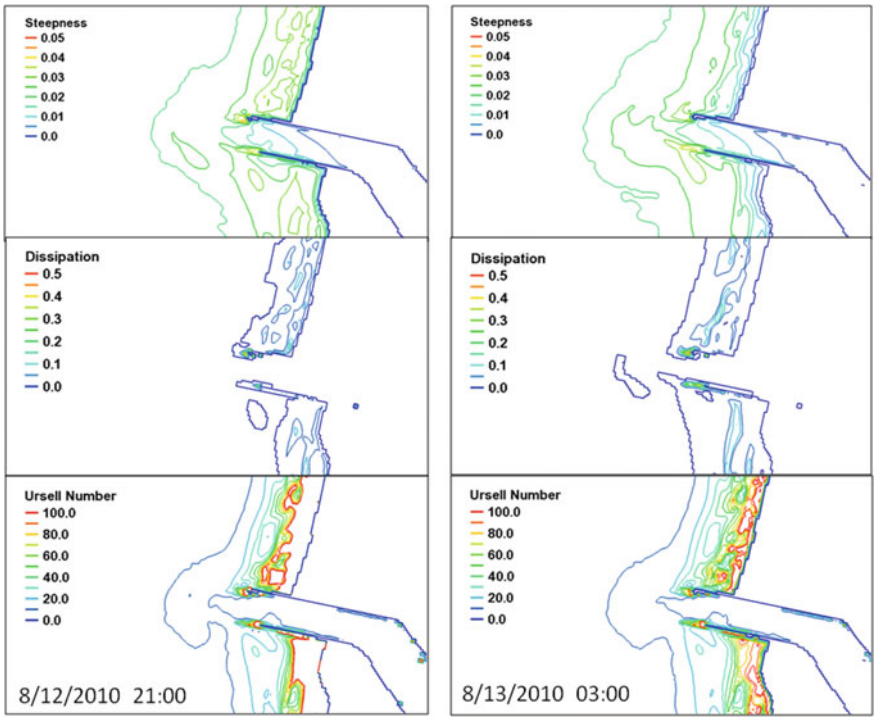

Fig. 17 Calculated wave steepness (top), wave dissipation (middle) and Ursell number (bottom) during a flood current on 12 August 2010 at 21:00 GMT and an ebb current on 13 August 2010 at 03:00 GMT

steepness and dissipation, and waves extended a little further into the main channel. With both jetty lengths, because the full South Jetty base was modified slightly, the peak values of wave steepness and dissipation occurred at the same locations.

4 Conclusions

Winds, waves, tides and river discharges were included in the combined wave and flow simulations described in this study. The simulations were performed with three telescoping grids corresponding to the 2005 asymmetric ebb shoal, the 2010 symmetric ebb shoal, and the 2010 shortened South Jetty. Three wave-related parameters (wave steepness, wave dissipation, and Ursell number) were calculated. The following observations were made.

Incident waves dominate the inlet system and wave heights could reach 6–8 m during winter storms, and 3.0 m/sec peak current occur in the main channel. The current direction outside the inlet over the ebb shoal and along north and south

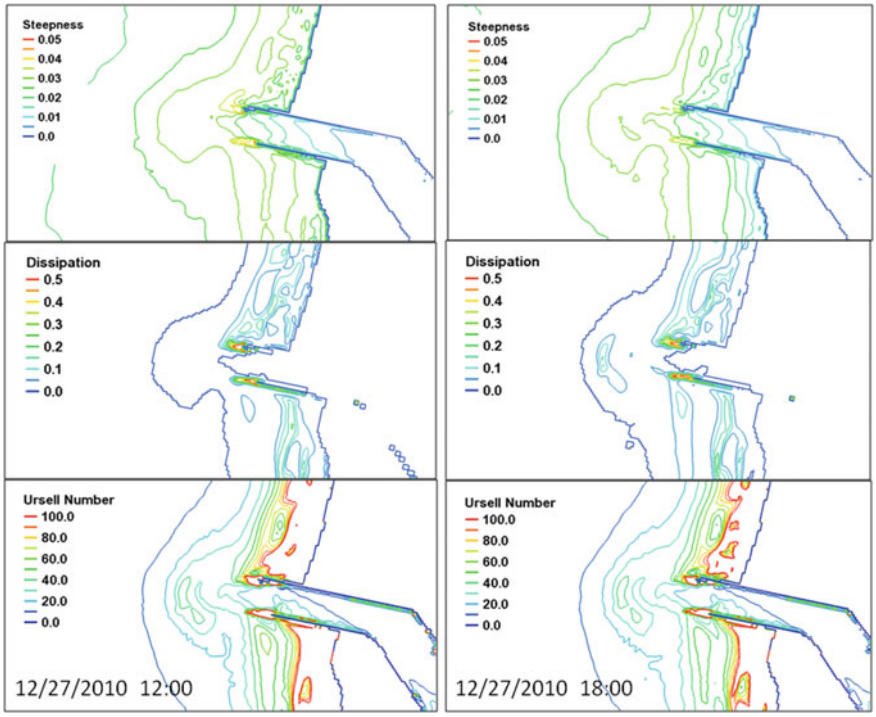

Fig. 18 Calculated wave steepness (top), wave dissipation (middle), and Ursell number (bottom) during a flood current on 27 December 2010 at 12:00 GMT and an ebb current on 27 December 2010 at 18:00 GMT

beaches is controlled mainly by local winds, wave actions and local bathymetry. The total freshwater discharges into Tillamook Bay can be as high as 28,000 cfs (800 m^3/sec) in the winter, and affect the ebb current.

Modeling results showed the winter storms produced larger wave steepness and wave dissipation at the inlet complex, which were also closely associated with the bathymetry of ebb shoal. The flood currents weakened wave dissipation, while ebb currents increased wave dissipation over the ebb shoal and across the USCG recommended south passage in/out of the inlet.

South Jetty shortening had a local effect in the immediate vicinity of the jetty and no discernible effect on wave steepness and dissipation at the entrance and over the ebb shoal. The shortened South Jetty reduced the flood current magnitude approximately by 0.2 m/sec (15%) at the entrance, but did not change the ebb flow pattern or current magnitude.

The calculated wave steepness and wave dissipation with the 2005 bathymetry indicated that a south passage out of the inlet would be safer than a course straight out passing over the bar or a course turning to NW direction.

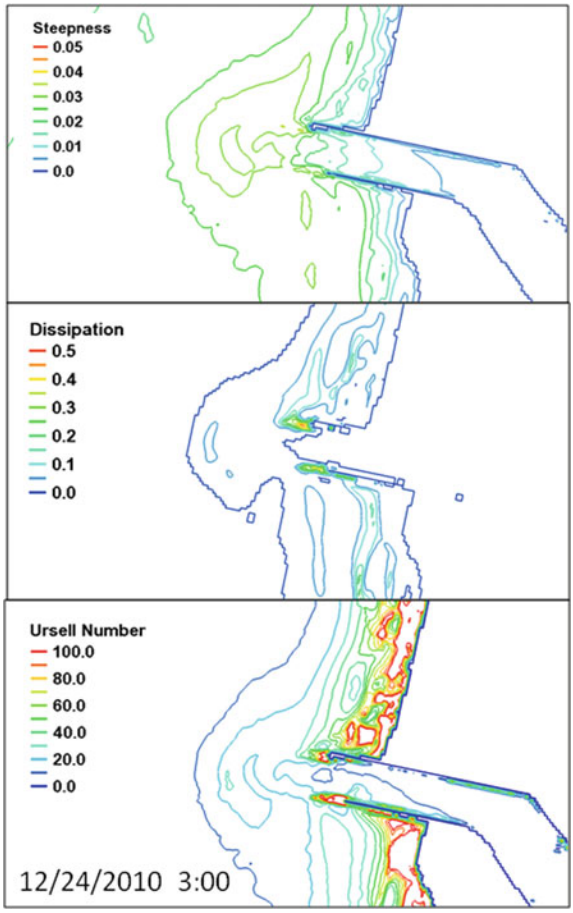

Fig. 19 Calculated wave steepness (top), wave dissipation (middle), and Ursell number (bottom) during an ebb current in 24 December 2010 at 03:00 GMT

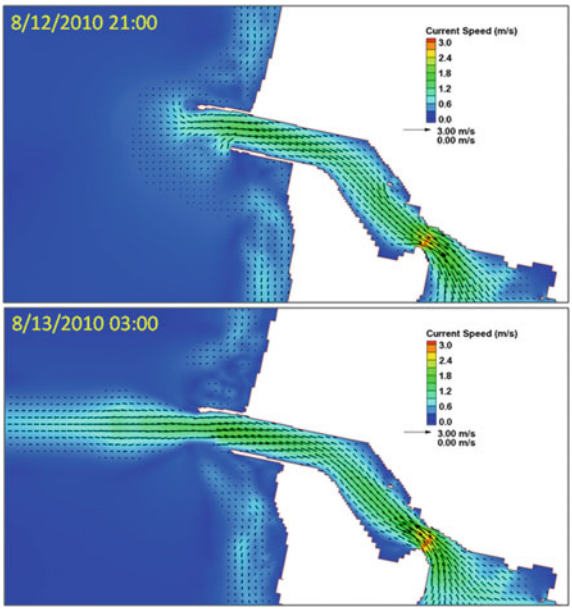

Fig. 20 Calculated current fields for the shortened South Jetty on 12 August 2010 at 21:00 GMT (flood current) and 13 August 2010 at 03:00 GMT (ebb current)

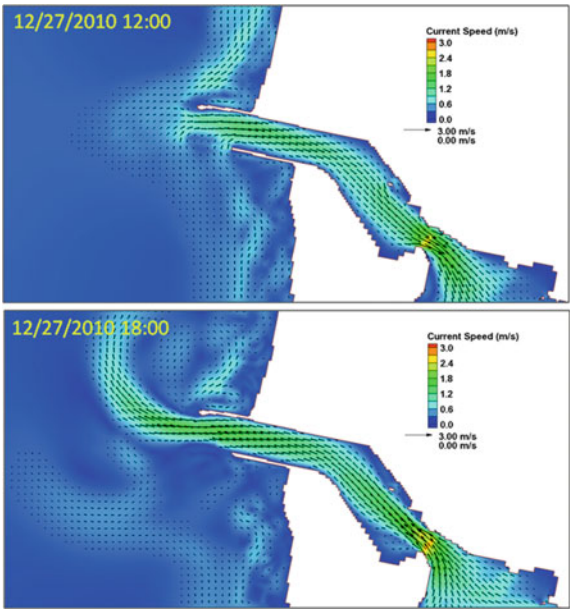

Fig. 21 Calculated current fields for the shortened South Jetty on 27 December 2010 at 12:00 GMT (flood current) and 18:00 GMT (ebb current)

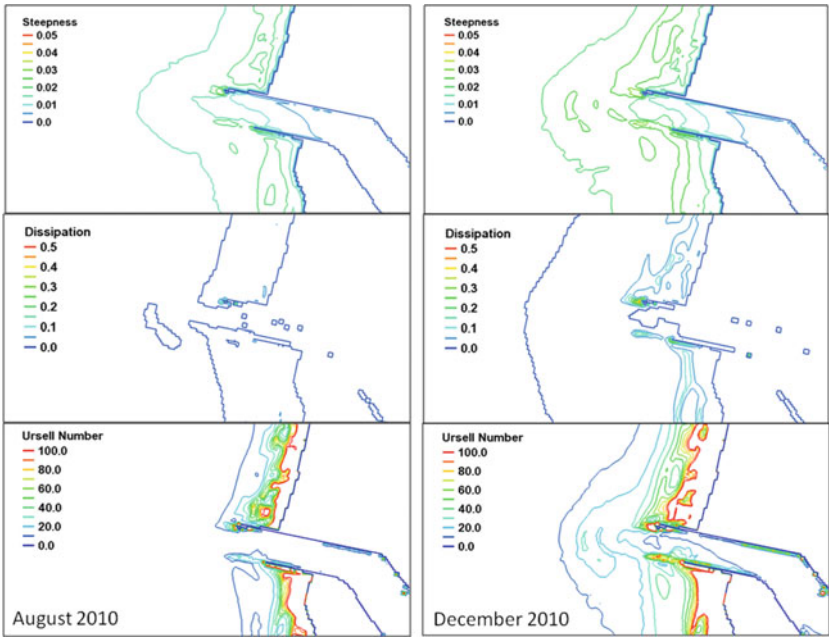

Fig. 22 Monthly mean wave steepness (top), wave dissipation (middle), and Ursell number (bottom) fields for the shortened South Jetty in August and December 2010

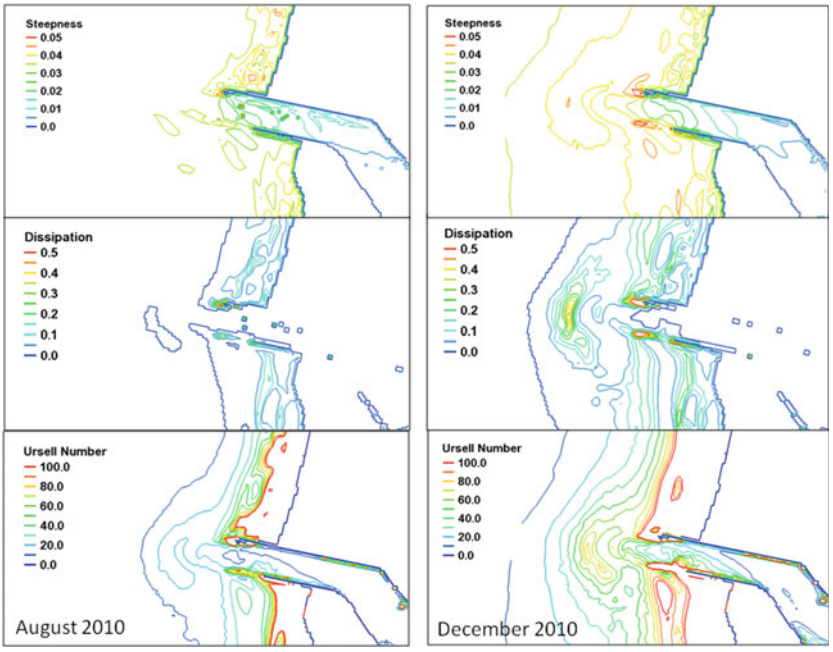

Fig. 23 Maximum wave steepness (top), wave dissipation (middle), and Ursell number (bottom) fields for the shortened South Jetty in August and December 2010

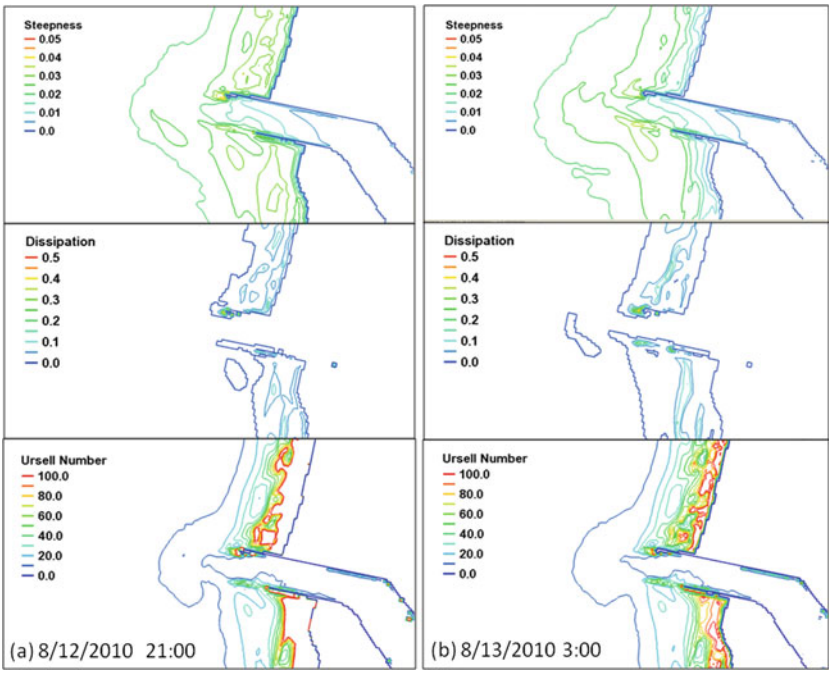

Fig. 24 Wave steepness (top), wave dissipation (middle), and Ursell number (bottom) for the shortened South Jetty: a) flood current in 12 August 2010 at 21:00 GMT and b) ebb current in 13 August 2010 at 03:00 GMT

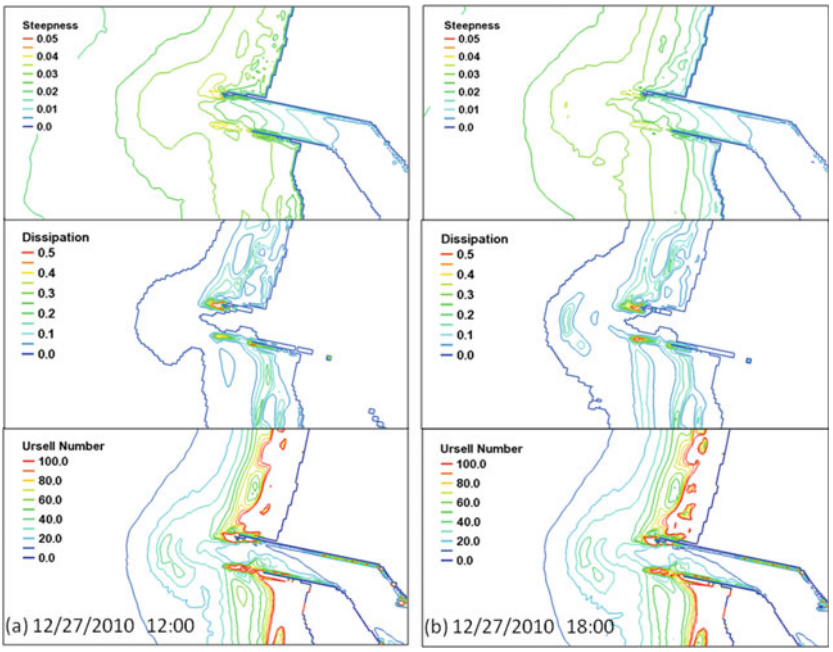

Fig. 25 Wave steepness (top), wave dissipation (middle), and Ursell number (bottom) for the shortened South Jetty: a) flood current on 27 December 2010 at 12:00 GMT and b) ebb current on 27 December 2010 at 18:00 GMT

Acknowledgements Permission was granted by the Chief, U.S. Army Corps of Engineers to publish this information.

References

Dally, W. R., Dean, R. G., & Dalrymple, R. A. (1985). Wave height variation across beaches of arbitrary profile. *Journal of Geophysical Research, 90*(C6), 11917–11927.

Demirbilek, Z., Li, H., Lin, L., Beck, T. M., & Moritz, H. R. (2013). *Preliminary analysis of morphology change, waves, and currents for navigation at tillamook inlet, Oregon*. Vicksburg, Mississippi: Army Engineer Research and Development Center, Coastal and Hydraulics Laboratory. (Report no. ERDC/CHL-TR-13-13).

Komar, P. D. (1997). *Sediment accumulation in Tillamook Bay, Oregon, a large drowned-river estuary*. Oregon: Report for the Tillamook Bay National Estuary Project.

Lin, L., Demirbilek, Z., & Mase, H. (2011). Recent capabilities of CMS-Wave: A coastal wave model for inlets and navigation projects. *Journal of Coastal Research, Special Issue, 59*, 7–14 (Proceedings, Symposium to Honor Dr. Nicholas Kraus).

Ursell, F. (1953). The long-wave paradox in the theory of gravity waves. *Proceedings of the Cambridge Philosophical Society, 49*(4), 685–694.

Wu, W., Sanchez, A., & Zhang, M. (2011). An implicit 2-D shallow water flow model on unstructured quadtree rectangular mesh. *Journal of Coastal Research, Special Issue, 59*, 15–26 (Proceedings, Symposium to Honor Dr. Nicholas Kraus).

Numerical Model Study of Navigation Channel Siltation

Jian Jiao, Xiping Dou, Xiangyu Gao, Lei Ding and Xinzhou Zhang

Abstract The 250,000 dwt Navigation Channel of the Panjin Port is planned to be constructed. Three layout schemes are designed in the project. The hydrodynamics, sediment transport and channel siltation before and after the project under different layout schemes are calculated by numerical model. The results show that for three schemes, the sediment concentration within the waterway show decrease after the construction of the waterway. The annual back-silting thickness is large near the port and small in the offshore area. The total deposition amount and average thickness of scheme 1 is larger than that of scheme 2. In addition, the channel of scheme 3 shows a significant sedimentation at the end of the channel because of the turn of the axis.

Keywords Panjin port waterway · Numerical model · Back silting · Storm surge

1 Introduction

Navigation channel is the waterway connecting the ocean and the port. After the completion of the waterway, the problem of sediment siltation always occurs due to the change of the original morphology (Zhang et al. 2015). Therefore, the prediction of channel siltation is of great significance to the comparison and selection of channel schemes and the future channel management before the implementation of the project (Xiao and Zheng 2003). Panjin Port 250,000 dwt navigation channel is taken as a case to study the waterway siltation.

Panjin Port is located in north of Bohai Bay, China (Feng et al. 2012) (Fig. 1). The existing channel of Panjin Port is 50,000 dwt (navigation width 179 m, design bottom standard height—12.6 m), which can meet the full load tidal navigation of 50,000 dwt oil tankers. The waterway is to be upgraded in two phases. In the near future, it is proposed to broaden its two sides to 100,000 dwt of waterway, according to meet the design of single line tide navigation of 100,000 dwt oil tankers (Jiao

J. Jiao (✉) · X. Dou · X. Gao · L. Ding · X. Zhang
State Key Lab of Hydrology-Water Resources and Hydraulic Engineering, Key Laboratory of Port, Waterway and Sedimentation Engineering of MOT, Nanjing Hydraulic Research Institute, Nanjing 210029, China

K. D. Nguyen et al. (eds.), *Estuaries and Coastal Zones in Times of Global Change*, Springer Water,
https://doi.org/10.1007/978-981-15-2081-5_30

Fig. 1 Location of the study area

et al. 2019). In the long term, the waterway is designed according to the single line tide navigation of 250,000 dwt oil tankers, the navigation width of the waterway is 350 m, the design bottom standard height is—21.2 and 22.6 m, and the total length is about 80 km.

There are three schemes of the waterway. The main differences between three schemes are the waterway direction and the length (Fig. 2). In scheme 1, the length is 80 km, the navigation span is 350 m and the design bottom elevation is—21.2 m. Compared with scheme 1, the waterway of scheme 2 has different direction and length, which is 62.1 km. The third scheme is derived from the scheme 1, the difference being that an additional turn is added to the mileage around 57 km (Table 1).

Liu et al. (2014) analyzed the mechanism of sediment hydrodynamics in Dandong Waterway and found that the sedimentation was characterized by wave lifted sediment and tidal transport sediment. Hou et al. (2012) analyzed the wave climate and bed load characteristics and the results showed that the high and rapid of back siltation appeared in the Yamen navigation channel in storm condition.

According to the hydrological survey data of Panjin Port, it is a semi-diurnal tide. The spring tide direction is basically NW-N, and the ebb tide direction is basically SSE-S. The flood and ebb tidal currents have a certain angle with the waterway near the port.

According to the field date of September to October 2006, the sediment concentration of the research area is less than 0.18 kg/m^3. During the whole year, winds above level 6 had the highest SSW, S, and SW directions, accounting for 55.05%, 15.77%, and 13.95% of the gale frequencies, respectively, accounting for 84.76% in

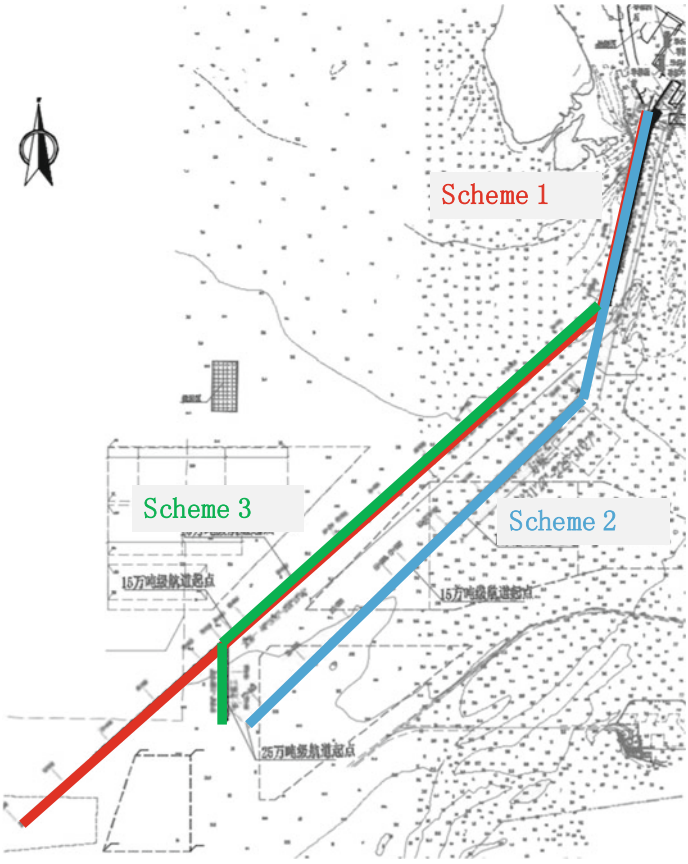

Fig. 2 Layout of different waterway schemes

Table 1 Design parameters of two schemes

Scheme	Grade	Length (km)	Navigation span (m)	Design bottom elevation (m)
1	250,000 dwt	80	350	−21.2 to −22.6
2		62.1	350	−21.2 to −22.6
3		62.5	350	−21.2 to −22.6

all three directions. The seasonal distribution of winds above level 6 was highest in spring.

This research aims at the back-siltation in normal year and under storm surges after the construction of the waterway in order to investigate the optimal scheme.

2 Methodology

A process-based numerical model is applied in this research for the waterway back-silting. The model was set up by Delft3D software. Delft3D is an open source software which can simulate hydrodynamics, sediment transport, morphological change, ecology and so on. A 2DH hydrodynamic-morphodynamic numerical model was built to simulate the channel back-silting after the construction of the waterway. In terms of the sediment transport, several sediment transport formulas are available in Delft3D. In this study, Van Rijn 93 Formula (Rijn 1993) is applied for the non-cohesive sediment transport and Partheniades-Krone Formula (Partheniades 1965) is adopted for calculation of erosion and siltation volume of cohesive sediment (grain size smaller than 0.064 mm). The model area and grids are shown in Fig. 3.

The water level condition is adopted at the open boundary in the north of the study area. The water level is derived from the East China Sea model. For the normal year back-siltation simulation, the hydrodynamic simulation time is 1 year.

According to the measured data, two sediment fractions (cohesive and non-cohesive sand) are employed in the model.

The water level, flow velocity, flow direction and sediment concentration of the numerical model are validated according to the measured date of 26th April to 4th May 2007. There are 6 water level stations and 15 velocity stations near the harbor. And the erosion/sedimentation of the waterway is validated according to the measured data of 2015–2016.

Due to space constraints, the specific verification diagram will not be described in detail. The RMS error and correlation factors of the model results and measured data

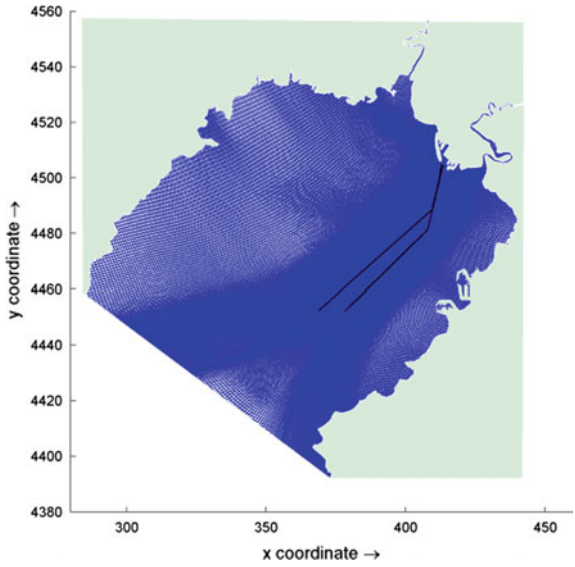

Fig. 3 Grids of the numerical model

showed that the model is reliable to predict the hydrodynamics, sediment transport and morphological change of the study area.

3 Results

3.1 Sediment Concentration

In order to statistic the sediment concentration before and after the project, observation points in and out of the channel were set.

In terms of the sediment concentration before and after the project, the average sediment concentration before engineering is larger than that after engineering for both scheme 1, 2 and 3. The average sediment concentration within channel before engineering is 0.02–0.46 kg/m^3 while after engineering is 0.01–0.44 kg/m^3 for three schemes.

Comparing the sediment concentration in and out of the channel, the results show that the average sediment concentration outside the channel is larger than that in the channel for three schemes. For scheme 1, the average sediment concentration outside the channel is 0.01–0.48 kg/m^3, and 0.01–0.39 kg/m^3 in the channel. The maximum difference between the sediment concentration in the channel and the sediment concentration in the beach appears at the 5 km, and the minimum difference appears at the end of the channel. The difference between the sediment concentration in the channel and the sediment concentration on the beach surface appears at—0.02–0.35 kg/m^3, and at the end of the channel. In the 5–31 km channel range, the difference between them is relatively large, more than 50%.

3.2 Bed Level Change

(1) Scheme 1

Figure 4 shows the morphological change of the study area 1 year after the construction of waterway scheme 1. Positive values represent silting, and negative values represent scouring. As can be seen from the figure, after the implementation of the project, the erosion and siltation in the near coast is greater than that in the offshore area. For the waterway, the deposition thickness near port is larger than that in the offshore area.

Table 2 shows the 1 year siltation thickness of the waterway. The siltation thickness of the channel outside the port entrance (channel mileage 0–5 km) is the largest, with an average siltation thickness of 2.2 m/a. The maximum siltation thickness can reach 2.68 m/a. From the channel mileage 5 km to the outer sea, the channel siltation decreases gradually. The normal annual back silting amount of option 1 is about 9.6313 million m^3.

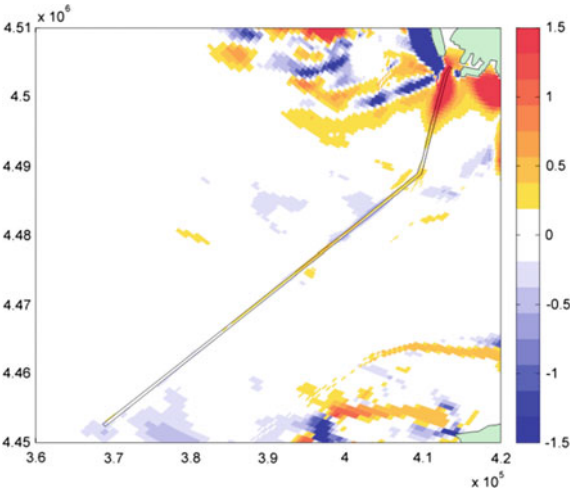

Fig. 4 Morphological change of numerical model results (Scheme 1)

Table 2 Annual back-silting thickness along the waterway (Scheme 1)

Mileage (km)	Maximum deposition thickness (m)	Average deposition thickness (m)	Total amount of deposition ($\times 10^4$ m^3)
0–5	2.68	2.20	385.79
5–10	1.74	0.84	147.12
10–15	0.33	0.18	31.66
15–20	0.34	0.27	47.42
20–25	0.32	0.28	48.89
25–30	0.44	0.37	64.88
30–35	0.47	0.41	71.32
35–40	0.40	0.33	57.52
40–45	0.23	0.22	38.69
45–50	0.20	0.19	33.72
50–55	0.18	0.12	20.24
55–60	0.04	0.02	3.91
60–65	0.06	0.03	4.97
65–70	0.05	0.02	3.21
70–75	0.02	0.01	2.18
75–80	0.01	0.01	1.62
0–80	2.68		963.13

(2) Scheme 2

Table 3 shows the siltation thickness of the channel along the channel under the normal condition of scheme 2. Figure 5 shows the morphological change of the study area. which is the same as that of scheme 1. The siltation thickness of the channel outside the port entrance (channel mileage 0–5 km) is the largest, with an average siltation thickness of 2.2 m/a. The maximum siltation thickness could reach 2.68 m/a; From the channel mileage 5 km to the outer sea, the channel siltation intensity decreases gradually. The annual siltation thickness of waterway is slightly larger than that of scheme 1. However, due to the short channel length of scheme 2, the normal annual back silting amount is slightly smaller than that of scheme 1, about 9.46 million m^3.

Compared with Scheme 1, most of the backfilling siltation intensity along the route of Scheme 2 is smaller than that of Scheme 1. At the same time, the length of Scheme 2 channel is 11 km shorter than that of Scheme 1, so the amount of backwashing at the 2nd year is less than that of Scheme 1.

(3) Scheme 3

Table 3 shows the siltation thickness of the waterway along the waterway under the normal condition of option 3. The excavation location and depth of the waterway in scheme 3 within 0–57 km are the same as that of scheme 1, so the amount of back silting after the project is almost the same as that of scheme 1. Outside the port gate (channel mileage 0–5 km), the channel siltation thickness is the largest, and the channel siltation intensity decreases gradually from the channel mileage 5 to 57 km. However, at 57–62 km, due to the inconsistency between the channel and

Table 3 Annual back-silting thickness along the waterway (Scheme 2)

Mileage (km)	Maximum deposition thickness (m)	Average deposition thickness (m)	Total amount of deposition ($\times 10^4$ m^3)
0–5	2.68	2.20	385.73
5–10	1.73	0.84	147.44
10–15	0.42	0.27	47.04
15–20	0.50	0.36	62.95
20–25	0.40	0.31	54.96
25–30	0.37	0.35	61.58
30–35	0.34	0.32	55.69
35–40	0.28	0.24	41.70
40–45	0.20	0.19	32.52
45–50	0.21	0.19	33.45
50–55	0.07	0.05	8.24
55–60	0.08	0.06	10.09
60–62	0.03	0.03	4.61
0–62	2.68		946.01

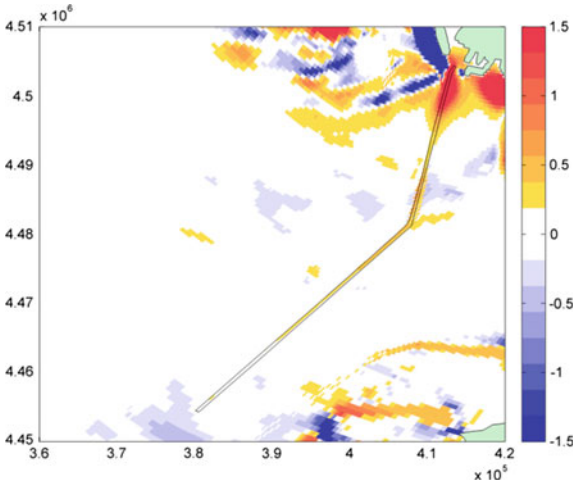

Fig. 5 Morphological change of numerical results (Scheme 2)

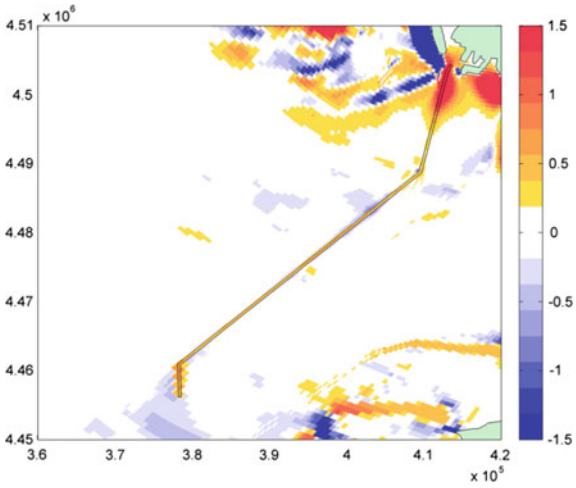

Fig. 6 Morphological change of numerical results (Scheme 3)

the flow direction, the amount of siltation increases slightly, and the average siltation thickness is 0.05 m/a. The normal annual back silting capacity of the channel is slightly less than that of scheme 1, which is 9.61 million m^3 (Fig. 6, Table 4).

4 Discussions

After construction of the waterway, the average sediment concentration inside the waterway decrease and sedimentation occurs along the waterway for three schemes.

Table 4 Annual back-silting thickness along the waterway (Scheme 3)

Mileage (km)	Maximum deposition thickness (m)	Average deposition thickness (m)	Total amount of deposition ($\times 10^4$ m^3)
0–5	2.68	2.20	385.79
5–10	1.74	0.84	147.12
10–15	0.33	0.18	31.66
15–20	0.34	0.27	47.42
20–25	0.32	0.28	48.89
25–30	0.44	0.37	64.88
30–35	0.47	0.41	71.32
35–40	0.40	0.33	57.52
40–45	0.23	0.22	38.69
45–50	0.20	0.19	33.72
50–55	0.18	0.12	20.24
55–60	0.04	0.03	5.48
60–62	0.07	0.05	8.32
0–62			961.04

This is mainly because the decrease of the average flow velocity then the sediment capacity decrease correspondingly.

After the construction of the waterway, the square of the cross-section increases. Assuming the tidal current is consistence before and after the project, the instantaneous discharge is consistence as well. The flow velocity decrease accordingly. According to the Van Rijn sediment transport formula, the shear stress decrease and less sediment will be eroded from the bed and more sediment will deposit. So the sediment concentration decrease and sedimentation occurs.

For three schemes, the back-silting thickness inside the waterway is large near shore and small off shore. This is because the deeper excavation in the near-shore area has resulted in a large change in sediment concentration, and there is a large difference in sediment concentration between inside and outside of the channel, so the backfilling is more obvious. Because of the quayside close to the shore, the amount of back silting is small.

For scheme 1, the average annual back-silting thickness along the waterway is slightly larger than scheme 2, and the total deposition amount is larger than scheme 2. The administrative authority should dredge the waterway regularly. There are obvious sedimentation of scheme 3 at the end of the channel. This is because the axis of the channel has a large angle with the flow direction. So the scheme 3 is not recommended.

5 Conclusions

The hydrodynamics, sediment transport and morphological change of Panjin Port 250,000 dwt navigation channel were simulated by Delft 3D numerical model and three schemes were compared. For three schemes, the sediment concentration within the waterway show decrease after the construction of the waterway. The annual back-silting thickness is large near the port and small in the offshore area.

The total deposition amount and average thickness of scheme 1 is larger than that of scheme 2. In addition, the channel of scheme 3 shows a significant sedimentation at the end of the channel because of the turn of the axis. So the scheme 3 is not recommended.

Acknowledgements This work is supported by the National Key R&D Program of China (2017YFC0405400), the National Natural Science Foundation of China (51479122)

References

Feng, Zhang, & Liu. (2012). Analysis on sediment environment and waterway siltation characteristics of Panjin port. *Applied Mechanics & Materials*, *212*, 205–210.

Hou, J. Y., Jie, H. E., & Xin, W. J. (2012). An analysis of sediment sudden siltationin Yamen waterway in storm condition. *Hydro-Science and Engineering*, 55–61.

Jiao, J., Dou, X. P., & Gao, X. Y. (2019). Numerical model study of Panjin Port Waterway Back-silting. *//APAC*, 2019.

Liu, H., Zhang, H., Zhang, H. Y., et al. (2014). Waterway siltation indicated by grain size distribution—Case study of Dandong waterway. *China Harbour Engineering, 191,* 14–21.

Partheniades, E. (1965). Erosion and deposition of cohesive soils. *Journal of the Hydraulics Division, ASCE 91* (HY 1): 105–139. 79, 329, 569.

van Rijn, L. C. (1993). *Principles of sediment transport in rivers, estuaries and coastal seas*. The Netherlands: Aqua Publications.

Xiao, X. U., & Zheng, J. Q. (2003). Tidal current experiment and siltation analysis on deep waterway engineering of Xiamen Harbor. *Journal of Oceanography in Taiwan Strait*, 92–101.

Zhang, W., Xiao, T. B., & Pang, L. (2015). Effect of encircled breakwater on waterway siltation in Lianyungang area. *Port & Waterway Engineering*, 93–99.

Mathematical Model of Sediment Diffusion During Construction Period of Extension Project in Tianwan Nuclear Power Station, China

Tilai Li, Xiangyu Gao, Liming Chen and Lei Ding

Abstract For extension project construction of Tianwan Nuclear Power Station (TNPS), China, the sediment suspension and diffusion will be caused in the process of blasting toe-shooting and dredging. The chapter analyzed the motion features of tides, waves, and sediment in engineering sea areas, established a 2-D tidal current and sediment mathematical model and conducted verifications through the actual measurements of tidal level, velocity and sediment concentration in accordance with nuclear safety guide rules and sea area use demonstration. Based on this, the advantageous tide types are selected, the source strength of blasting toe-shooting and mud dredging are determined, the mathematical model is used to study the suspended sediment diffusion scope caused by blasting toe-shooting and dredging respectively.

Keywords Mathematical model · Sediment · Nuclear power station · Diffusion

The site of Units No. 5 and 6 in Tianwan Nuclear Power Station (TNPS) Extension Project is located in Chuanshan in the northwest of Units No. 1–4 in TNPS, Lianyungang City, Jiangsu Province, China. Units No. 1 and 2 have been put into operation. Units No. 5 and 6 are Continued Construction Project of TNPT. The main works in the sea area of TNPS include water intake and drainage channels, shore protection engineering and other auxiliary buildings. Figure 1 is the geographic position for site of TNPS.

The water intake and drainage extension project in TNPS includes the construction of diversion dikes of water intake and drainage channels, excavation and dredging of water intake and drainage channels. The blasting toe-shooting construction method is mainly adopted for diversion dikes matched with dredging. The base slot excavation is conducted for open channels of water intake and drainage. Since the suspension and diffusion of mud will be caused in the process of blasting toe-shooting and excavation and dredging, it is necessary to study the effecting scope of sediment diffusion during the construction of the water intake and drainage project.

T. Li (✉) · X. Gao · L. Chen · L. Ding
Key Laboratory of Port, Waterway and Sedimentation Engineering of the Ministry of Transport, Nanjing Hydraulic Research Institute, Nanjing 210029, China
e-mail: ltli@nhri.cn

K. D. Nguyen et al. (eds.), *Estuaries and Coastal Zones in Times of Global Change*, Springer Water,
https://doi.org/10.1007/978-981-15-2081-5_31

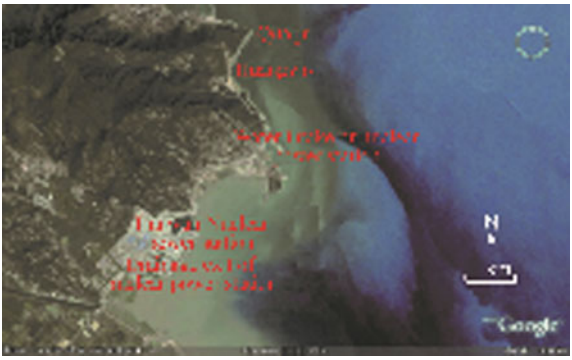

Fig. 1 Geographic position for site of TNPS

1 Natural Conditions in Lianyungang Sea Area

1.1 Tides and Currents

The site of the nuclear power station is located in the south of Lianyungang and the south bank of Haizhou Bay and lies in the influence range of standing wave system of the South Yellow Sea. The tides in Lianyungang sea area are irregular semi-diurnal tides, medium intensity, average high tide level of 2.01 m, average low tide level of −1.87 m, average flood tidal range of 3.91 m, average ebb tidal range of 3.85 m, highest tide level of 2.83 m, lowest tide level of −2.92 m, average duration of tidal rise of 5 h and 38 min, and average duration of tidal fall of 6 h and 47 min.

The tidal current in Lianyungang sea area is a counter-clockwise rotation. The major axis direction of tidal current ellipse is NW-SE in the south of Lianyungang, parallel to the coast, while the top of Haizhou Bay to the north of Lianyungang is NE-SW, basically perpendicular to the coast. The velocity of flood tidal current is greater than that of ebb, and the ratio of the velocities is generally 1: 1.3. The phases of tidal level and velocity are obviously different in the south and the north area. In the south area, the currents are close to advancing wave, and the maximum velocity appears in the high and low slack water levels. In the north, the phase is the standing wave, and the maximum value of the flood and ebb tidal currents appears near the middle level.

According to the measured velocity analysis of 11 gauge stations in July 2004, the average velocities of the measured points are not more than 0.50 m/s.

1.2 Waves

According to the measured wave data of Lianyungang station from 1962 to 2003, the $H_{1/10}$ is 0.5 m. The average wave height of each month is 0.4–0.6 m, and the wave height in autumn and winter is slightly higher than that in spring and summer. The

maximum wave height of $H_{1/10}$ is 5.0 m, which is NNE direction. The maximum wave height of $H_1\%$ is 6.0 m. The largest average period of each direction is 4.3 s in the direction of NNE, followed by 4.1 s in NE direction, the wave period of NW-N direction and ENE direction is between 3.0–3.8 s and the remaining wave period is below 3.0 s. The largest maximum period of each direction is 8.5 s in the direction of NE, followed by 8.2 s in NNE direction, the wave period of W-N direction, ENE-SE direction and SW direction is between 5.0 and 7.8 s, and the remaining wave period is below 3.5 s.

1.3 Sediment

1.3.1 The Source of Sediment

Haizhou Bay is an open bay near the Yellow Sea, which is the convergence zone of bedrock-sandy coast and muddy coast. When the lower reaches of the Yellow River was diverted into the sea from Lijin, Shandong Province in 1855, the sediment transport along the Haizhou Bay was greatly reduced. Additionally reservoirs were built in most of the upper and middle reaches of the seagoing rivers along the coast, so the sediment into the sea was greatly reduced. Coastal erosion matters become the main source of sediment.

1.3.2 Sediment Concentratio

According to the large-scale hydrographic survey data of Lianyungang sea area in the winter and summer of 2005, the sediment concentration in vertical near the coast is higher than that far from the coast due to the influence of typhoon during the spring tide. The maximum sediment concentration is 0.233 kg/m^3 in summer and 0.371 kg/m^3 in winter. The maximum mean-depth sediment concentration is between 0.100 and 0.210 kg/m^3 in summer, and between 0.061 and 0.287 kg/m^3 in winter.

1.3.3 Surface Sediment

Based on the measuring data, the median particle diameter of suspended sediment in the vertical line is 0.005–0.019 mm, the maximum surface particle diameter is 0.062–0.125 mm and mainly silt sand. The median particle diameter of bed sand is about 0.02 mm.

2 2D Mathematical Model of Tidal Current and Sediment

2.1 Establishment of the Mathematical Model

2.1.1 Basic Equation of Two-Dimensional Tidal Current Movement

Under the orthogonal curvilinear coordinate system $\xi - \eta$, the basic equation of two-dimensional tidal current movement can be expressed as follow:

Continuity equation

$$\frac{\partial \zeta}{\partial t} + \frac{1}{g_\xi g_\eta}\frac{\partial}{\partial \eta}\left(Hvg_\xi\right)\frac{1}{+g_\xi g_\eta}\frac{\partial}{\partial \xi}\left(Hug_\eta\right) = 0 \tag{1}$$

Momentum equation

$$\begin{aligned}&\frac{\partial u}{\partial t} + \frac{u}{g_\xi}\frac{\partial u}{\partial \xi} + \frac{v}{g_\eta}\frac{\partial u}{\partial \eta} + \frac{uv}{g_\xi g_\eta}\frac{\partial g_\xi}{\partial \eta} - \frac{v^2}{g_\xi g_\eta}\frac{\partial g_\eta}{\partial \xi} + g\frac{u\sqrt{u^2+v^2}}{C^2 H}\\ &\quad - fv + \frac{g}{g_\xi}\frac{\partial \varsigma}{\partial \xi} = E\left(\frac{1}{g_\xi}\frac{\partial A}{\partial \xi} - \frac{1}{g_\eta}\frac{\partial B}{\partial \eta}\right)\end{aligned} \tag{2}$$

$$\begin{aligned}&\frac{\partial v}{\partial t} + \frac{u}{g_\xi}\frac{\partial v}{\partial \xi} + \frac{v}{g_\eta}\frac{\partial v}{\partial \eta} + \frac{uv}{g_\xi g_\eta}\frac{\partial g_\eta}{\partial \xi} - \frac{u^2}{g_\xi g_\eta}\frac{\partial g_\eta}{\partial \xi} + g\frac{v\sqrt{u^2+v^2}}{C^2 H}\\ &\quad + fu + \frac{g}{g_\eta}\frac{\partial \varsigma}{\partial \eta} = E\left(\frac{1}{g_\xi}\frac{\partial B}{\partial \xi} + \frac{1}{g_\eta}\frac{\partial A}{\partial \eta}\right)\end{aligned} \tag{3}$$

where

$$\left.\begin{aligned}A &= \left[\frac{\partial}{\partial \xi}\left(ug_\eta\right) + \frac{\partial}{\partial \eta}\left(vg_\xi\right)\right]/g_\xi g_\eta\\ B &= \left[\frac{\partial}{\partial \xi}\left(vg_\eta\right) - \frac{\partial}{\partial \eta}\left(ug_\xi\right)\right]/g_\xi g_\eta\\ g_\xi &= \sqrt{x_\xi^2 + y_\xi^2}\\ g_\eta &= \sqrt{x_\eta^2 + y_\eta^2}\end{aligned}\right\}$$

u and v are the velocity components in ξ and η directions respectively; ζ is the water level and H is the total water depth; C is the Chezy coefficient, $C = \frac{1}{n}H^{1/6}$; n is the roughness coefficient; $f = 2\omega \sin\phi, f$ is the Coriolis force coefficient; ω is the rotation angular velocity; ϕ is the latitude; g_ξ and g_η are the Lami coefficient; E is the flow turbulent viscosity coefficient.

2.1.2 Suspended Load Non-equilibrium Sediment Transport Equation

In the orthogonal curvilinear coordinate system, the two-dimensional suspended sediment transport equation is:

$$\frac{\partial(HS)}{\partial t}+\frac{1}{g_\xi g_\eta}\left[\frac{\partial\left(HuSg_\xi\right)}{\partial\xi}+\frac{\partial\left(HvSg_\xi\right)}{\partial\eta}\right]+\alpha\omega(S-S_*)-\frac{S_m}{g_\xi g_\eta}$$
$$=\frac{1}{g_\xi}\frac{\partial}{\partial\xi}\left(D_\xi\frac{H}{g_\xi}\frac{\partial S}{\partial\xi}\right)+\frac{1}{g_\eta}\frac{\partial}{\partial\eta}\left(D_\eta\frac{H}{g_\eta}\frac{\partial S}{\partial\eta}\right) \tag{4}$$

where H is the total water depth and u and v are the velocity components in ξ and η directions respectively g_ξ and g_η are the Lami coefficient; S is the vertical average sediment concentration; α is a coefficient to be determined by verification calculation; ω is the sediment settling velocity or the flocculating settling velocity under the flocculating condition; S_m is the suspended solids source intensity; S_* is the sediment carrying capacity of flow, and according to the DOU Guoren's formula, under the combined action of tidal currents and waves it can be expressed as follows:

$$s_*=\alpha_0\frac{\gamma\gamma_s}{\gamma_s-\gamma}\left[\frac{\left(u^2+v^2\right)^{3/2}}{C^2H\omega}+\beta_0\frac{H_w^2}{HT\omega}\right] \tag{5}$$

where γ_s and γ are the unit weight of water and sediment particles respectively; H_w and T are the mean wave height and period respectively. Based on the measuring data in some sea areas, $\alpha_0=0.023$, $\beta_0=0.004\ f_w$, f_w is the wave friction coefficient.

2.1.3 Calculate Area and Model Terrain

The calculation range of the model is from the north latitude of 34° 24′ in the south to the north latitude of 35° 24′ in the north; from the east longitude of 119° 10′ in the west to the east longitude of 120° 04′ in the east. The orthogonal curvilinear grid is used and the number of grids is $274\times260=71240$. The grids are refined near the water intake and outlet of the nuclear power station, with the size between 20 and 1800 m.

The model topography is based on the topographic map of Lianyungang sea area measured in July 2004 (1: 5000), the large-scale topographic map of Lianyungang sea area measured in September 2005 (1: 50000) and the sea chart of Lianyungang sea area measured in 2004 (1: 12000).

2.2 Verification of the Mathematical Model

2.2.1 Verification Data

The verification data is based on the hydrological and sediment concentration measurement data of 8 vertical lines in Lianyungang sea area in July 2004 (Fig. 2 and Table 1).

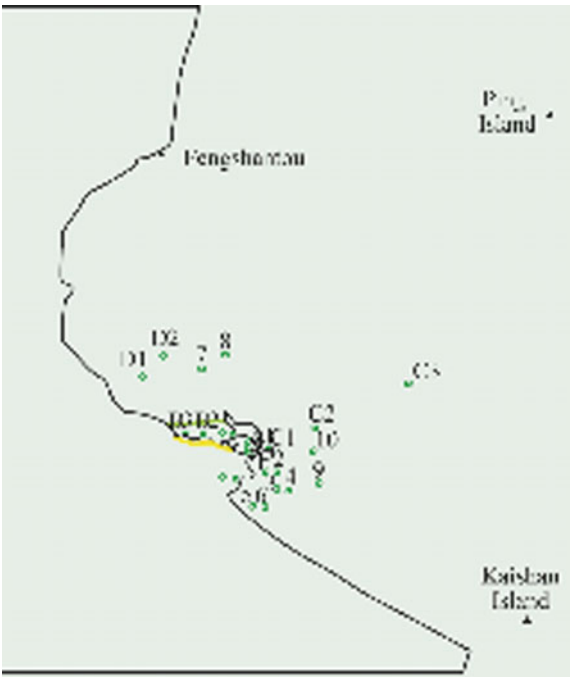

Fig. 2 Position of hydrographic data measured in 2004

Table 1 Hydrographic data in 2004

Tidal pattern	Measuring time	Station
Spring tide	2004.7.1(23:00)–7.3(2:00)	Tide station: oil wharf, coal wharf, Xugou wharf; Velocity and sediment concentration station: A1, A2, A3, B1, B2, B3
Medium tide	2004.7.6(15:00)–7.7(18:00)	
Neap tide	2004.7.9(17:00)–7.10(20:00)	
Spring tide	2004.7.17(12:00)–7.18(15:00)	Velocity and sediment concentration station: C1, C2, C3, D1, D2
Medium tide	2004.7.8(4:00)–7.9(7:00)	
Neap tide	2004.7.11(6:00)–7.12(9:00)	

2.2.2 Boundary Condition and Parameter Determination

The open boundary of the sea of the model is controlled by the tide level process provided by the East China Sea model established by Hohai University, China, and the intake and drainage are controlled by flow discharges.

The parameters are determined by the verification of tidal level and velocity. The roughness is obtained by linear interpolation from the open sea to the coastline using $n = 0.012 + \frac{0.01}{H} \sim 0.022 + \frac{0.01}{H}$, the turbulent viscosity coefficient E is 50 m^2/s. The calculation time steps of the tidal current model and sediment model are 1.5 and 30 s respectively.

According to the relevant data of Lianyungang sea area, the flocculation settling velocity of suspended sediment is 0.0005 m/s, the dry unit weight of sediment is 640 kg/m^3, the median particle diameter of sediment is 0.007 mm, the settling probability of sediment is 0.1, the average wave height is 0.6 m, and the average wave period is 3.1 s.

2.2.3 Verification Result

From the comparison of calculated and measured values, it can be seen (Figs. 3 and 4) that the tidal level process at the tidal station is basically the same as that of the measured one. The calculated and measured values of velocity and direction are also in good agreement with each other. The process verification result of the sediment concentration of spring tide shows that the calculated and measured values are almost the same except for several individual measuring points. Through the verification of

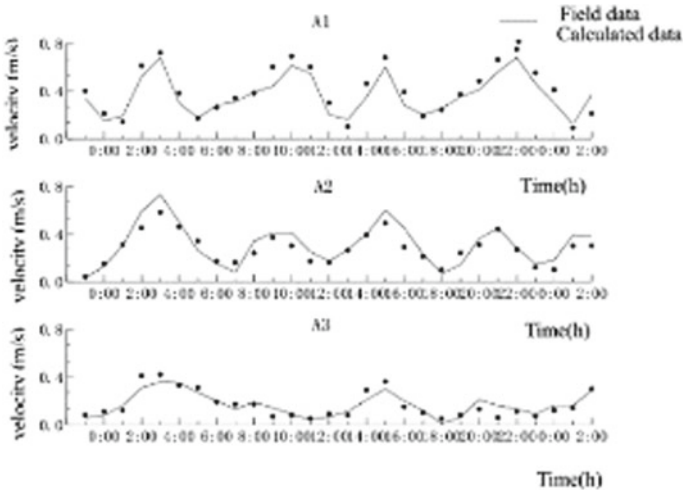

Fig. 3 The verification of the spring tide velocities

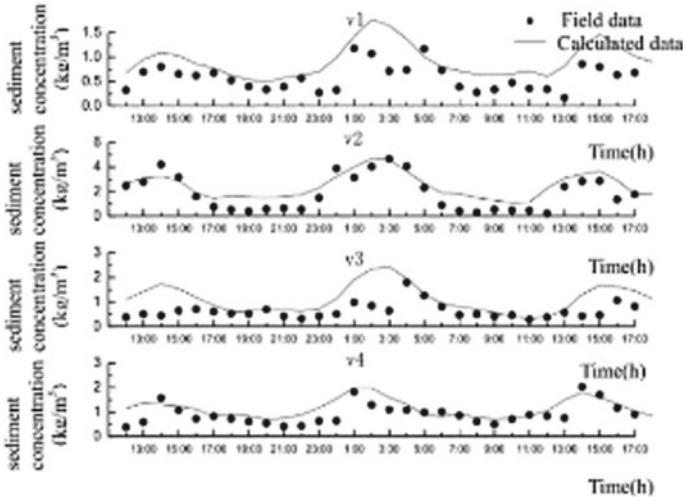

Fig. 4 The verification of the spring tide concentration

tidal current and sediment concentration field, the verification results are good, which provides a basic condition for the calculation of suspended sediment diffusion caused by construction.

3 Sediment Diffusion During Construction Period

3.1 Project Overview

The diversion dike of the intake channel is divided into two phases to be constructed. For the first phase, the length of the southern dike is 1542 m, and the length of the northern dike is 2063 m. Both the south and north diversion dikes of the second phase are 2063 m long. The distance between the axis of the north and south dike is 320 m. The drainage channel was excavated to −9.5 m.

There are two schemes for the drainage channel construction (Fig. 5). Scheme I: the diversion dike shall be commenced from the end of the built northern diversion dike of nuclear power units No. 1 and 2 with the overall length of 1220 m; Scheme II: the diversion dike shall be located in the south of outfalls in units No. 5–8 and the dike end shall be 100 m from the outfall with the length of diversion dike for 990 m. The drainage channel shall be excavated to −3.5 m.

Fig. 5 Two schemes for the drainage channel construction and representative operation points

3.2 Construction Process

3.2.1 Construction Sequence of Diversion Dike

The north and south dikes are constructed with land area filling and blasting toe-shooting method, the north dike shall be filled with Huangwo Shore as the starting point to the sea while the south dike shall be filled with the south dike end of open channel of the intake in the first-phase and second-phase project as the starting point to the sea. The south dike and the north dike have the difference of 724.5 m in the length. To reduce the influence for water quality, dislocation construction and stagger time blasting shall be adopted for the construction of the north and south dike.

3.2.2 Construction Sequence of Intake Channel Dredging

Excavation and blasting toe-shooting construction shall be conducted at intervals. When the south dike and north dike are extended to form open channel with the length of 1000 m, grab dredgers are arranged to enter into the channel. The dredging construction shall be conducted from inside to outside from the root position of the south dike to ensure excavation not to affect the dike head blasting toe-shooting construction to promote.

3.3 Computation Conditions

3.3.1 Controlling Tide Type

According to the actually measured tide level process, the accumulation proportion of spring tide range is no less than 10% and the accumulation proportion of mean

neap range is no more than 90% through tide difference assurance rate are used as typical spring and neap tide to model sediment diffusion. Through the comparison of the maximum envelope line of sediment diffusion under the condition of the typical tide types, the disadvantage tide type adopted in suspended sediment diffusion of construction period shall be confirmed.

3.3.2 Source Strength Confirmation

(1) *Confirmation of transient source strength*

Blasting toe-shooting is for transient source strength. The blasting shall be conducted once every two days for transient source strength according to construction flow process. There is no measured data for suspended sediment amount caused by blasting toe-shooting. According to the research of transient source strength in Fuqing Harbor, China, the suspended sediment quantity occurred in blasting toe-shooting is 162 m^3. In the model, the sediment concentration of water is computed according to the suspended sediment quantity and blasting toe-shooting operation position and treated as the initial value of sediment concentration of the sea area. The computation formula of sediment concentration in transient source strength: $S_{blasting} = 162\Upsilon_{silt\ volume\text{-}weight}/V_{water\ volume}$ and the average natural unit weight of silt is about 15.8 KN/m^3.

(2) *Confirmation of continuous source strength*

The dredger shall continuously work for 12 h every day. The suspended sediment caused by dredging is treated as succession. According to the research of dredging source strength in Fuqing Harbor, the continuous dredging source strength is confirmed to be 1.48 kg/s.

3.3.3 Representative Operation Points

The representative operation points for blasting and toe-shooting are selected at A, C, E, G, and I points of south diversion dike and B, D, F, H and J points of north diversion dike; Diversion dikes of drainage channel is at K, L, and M points in Scheme I and T, U, and V points in Scheme II.

The representative dredging operation points is N, O, P and Q points of intake channel and R and S points in Scheme I and W and X points in Scheme II of drainage channel (Fig. 5).

Table 2 Calculation combinations I

Position	Blasting point	Blasting and dredging point	Open channel dredging point
South diversion dike for water intake channel	A	A	
North diversion dike for water intake channel	B	B	
Scheme I Drainage channel diversion dike	K	K	
Scheme II Drainage channel diversion dike	T	T	

Table 3 Calculation combinations III

Position	Blasting point	Blasting and dredging point	Open channel dredging point
Water intake channel south diversion dike to be promoted for 1500 m	E	E	N, O
Water intake channel north diversion dike to be promoted for 1800 m	F	F	
Scheme I Drainage channel diversion dike to be completed	M	M	
Scheme II Drainage channel diversion dike to be completed	V	V	

3.4 Hydrodynamic Field Computation

Typical spring and neap tide is adopted to calculate currents of during the construction period and provide hydrodynamic conditions for sediment diffusion. Total six combinations for currents calculation and only three are listed in Tables 2, 3 and 4 due to page limitation.

3.5 Suspended Sediment Diffusion Scope

Table 5 shows the most possible influenced area of sediment diffusion under the conditions of typical spring tide and neap tide. Through comparison, it can be seen that the influencing area for sediment diffusion in spring tide is larger than that of neap tide. The spring tide condition is selected to simulate the sediment diffusion.

Table 4 Calculation combinations V

Position	Blasting point	Blasting and dredging point	Open channel dredging point
Water intake channel south diversion dike to be completed	I	I	(Depth dredging of water intake channel in front of point P)
Water intake channel north diversion dike to be promoted for 4000 m	J	J	
Drainage channel to be completed			

Table 5 The Highest possible influenced area of sediment diffusion under typical spring and neap tide (Unit: km^2)

Construction situation		Blasting toe-shooting	Blasting heap dredging	Intake channel excavation and dredging
Typical spring tide (sediment concentration)	>10 ml	0.59	0.66	0.12
	>100 ml	0.3	0.03	0.05
	>150 ml	0.22	0.02	0.04
Typical neap tide (sediment concentration)	>10 ml	0.29	0.52	0.1
	>100 ml	0.18	0.02	0.04
	>150 ml	0.13	0.01	0.03

3.5.1 Suspended Sediment Diffusion Scope Caused by Blasting Slot-Shooting

The suspended sediment diffusions, caused by blasting slot-shooting at flood tides and ebb tides, are simulated when computing the suspended sediment diffusion scope. The area of influence by suspended sediment diffusion caused by blasting slot-shooting construction at representative operation points of diversion dikes in water intake channels are given due to page limitation.

During flood tides and ebb tides, the maximum influence areas are respectively 0.41 km^2, 0.24 km^2 and 0.23 km^2 with the sediment diffusion concentration more than 10 mg/L, 100 mg/L and 150 mg/L caused by blasting slot-shooting at representative points. The highest possible influence areas are respectively 4.79 km^2, 3.39 km^2 and

2.88 km^2 with the sediment diffusion concentration more than 10 mg/L, 100 mg/L and 150 mg/L caused by blasting slot-shooting construction of the south diversion dike of water intake channel. The highest possible influence areas are respectively 3.0 km^2, 2.18 km^2 and 1.77 km^2 with the sediment diffusion concentration more than 10 mg/L, 100 mg/L and 150 mg/L caused by blasting slot-shooting construction of the north diversion dike of water intake channel.

3.5.2 Suspended Sediment Diffusion Scope Caused by Dredging

The dredging project of water intake and drainage channels includes two parts: sediment heap caused by blasting toe-shooting and base slot excavation. According to the operation position, the maximum influenced scope of suspended sediment diffusion after continuously dredging for 12 h at representative points is calculated. The largest possible influence scope of suspended sediment diffusion, caused by dredging in water intake and drainage channels, is obtained.

Diffusion Scope Caused by Blasting Heap Dredged

The highest possible influence areas are respectively 0.66 km^2, 0.06 km^2 and 0.04 km^2 with the sediment diffusion concentration more than 10 mg/L, 100 mg/L and 150 mg/L for dredging blasting heap at the points of diversion dikes of water intake channels. For water drainage channels Scheme I, the highest possible influence areas are respectively 0.74 km^2, 0.1 km^2 and 0.06 km^2 with the sediment diffusion concentration more than 10 mg/L, 100 mg/L and 150 mg/L for dredging blasting heap at the points of diversion dikes. For water drainage channels Scheme II, the highest possible influence areas are respectively 0.34 km^2, 0.07 km^2 and 0.04 km^2 with the sediment diffusion concentration more than 10 mg/L, 100 mg/L and 150 mg/L for dredging blasting heap at the points of diversion dikes.

The highest possible influence areas are respectively 5.6 km^2, 4.29 km^2, 1.98 km^2 and 0.78 km^2 with the sediment diffusion concentration more than 10 mg/L, 0.62 km^2, 1.03 km^2, 0.73 km^2 and 0.33 km^2 with the concentration more than 100 mg/L and 0.41 km^2, 0.7 km^2, 0.55 km^2 and 0.22 km^2 with the concentration more than 150 mg/L caused in the whole construction process of dredging at blasting heap on diversion dikes of Scheme I and II of drainage channel and south and north diversion dikes of intake channels.

Suspended Sediment Diffusion Scope Caused by Base Slot Excavation for Intake and Drainage Channels

The maximum influenced areas are respectively 0.33 km^2, 0.06 km^2 and 0.04 km^2 with the suspended sediment diffusion concentration more than 10 mg/L, 100 mg/L and 150 mg/L caused by base slot excavation at operation points of the intake channel. In Scheme I, the maximum influenced areas are respectively 0.27 km^2, 0.04 km^2 and 0.03 km^2 with the concentration more than 10 mg/L, 100 mg/L and 150 mg/L caused by base slot excavation at the points of drainage channel. In Scheme II, the maximum influenced areas are respectively 0.27 km^2, 0.04 km^2 and 0.03 km^2 with

the suspended sediment diffusion concentration more than 10 mg/L, 100 mg/L and 150 mg/L caused by base slot excavation at the points of drainage channel.

The highest possible influenced areas are respectively 1.32 km^2, 0.47 km^2 and 0.4 km^2 with the suspended sediment diffusion concentration more than 10 mg/L, 0.64 km^2, 0.18 km^2 and 0.11 km^2 with the suspended sediment diffusion concentration more than 100 mg/L, and 0.34 km^2, 0.1 km^2 and 0.07 km^2 with the suspended sediment diffusion concentration more than 150 mg/L caused by the base slot excavation in the intake channel and Scheme I and II of drainage channels.

4 Conclusion

Through analysis for hydrodynamic and sediment transport in Lianyungang coast area, a 2D mathematical model is established for tidal current and sediment diffusion to verify the measured tide levels, current velocities and directions and sediment concentration and some relevant parameters in the model are be determined. Typical spring tide and neap tide are designed and the model is adopted to study suspended sediment diffusion scope caused by blasting toe-shooting and dredging. Typical spring tide is selected as adverse condition for calculation and some results are obtained:

(1) The highest possible scopes of influence with the suspended sediment diffusion concentration less than 10 mg/L are respectively 0.52 km^2 for flood tide and 0.43 km^2 for ebb tide caused by blasting toe-shooting and the influence at flood tide is slightly larger than that at ebb tides; the highest possible influence areas with the suspended sediment diffusion concentration less than 10 mg/L are respectively 4.79 km^2 and 3.0 km^2 for the south and north diversion dikes of water intake channels, 1.83 km^2 and 0.78 km^2 for the diversion dike Scheme I and II of drainage channel in the blasting toe-shooting construction process. The influence scope of diversion dikes construction of intake channels is larger than that of the drainage channel.
(2) For water intake channel, the highest possible influence scope is 0.33 km^2 with the suspended sediment diffusion concentration of less than 10 mg/L caused by the dredging of base slot excavation at the representative operation points and that is less than 1.32 km^2 caused by base slot excavation.
(3) For scheme I and II of water drainage channel, the highest possible influence scopes are both 0.27 km^2 with the suspended sediment diffusion concentration less than 10 mg/L caused by base slot excavation at representative operation points; the highest possible influence scopes are respectively 0.47 km^2 and

0.4 km^2 with the suspended sediment diffusion concentration less than 10 mg/L caused by the dredging of base slot excavation. The influence of Scheme I with a longer diversion dike is slightly larger than that of Scheme II with a shorter diversion dike.

Acknowledgements This work is supported by the National Key R&D Program of China (2017YFC0405400), the National Natural Science Foundation of China (51479122), Fundamental Research Fund of Nanjing Hydraulic Research Institute (Y217010).

Wave Attenuation Service by Intertidal Coastal Ecogeosystems in the Bay of Mont-Saint-Michel, France: Review and Meta-Analysis

Antoine Mury, Antoine Collin, Samuel Etienne and Matthieu Jeanson

Abstract The wave attenuation service (WAS) literature review over the Bay of Mont-Saint-Michel encompasses saltmarshes, mudflats, seagrasses, shelly cheniers, oyster, honeycomb worm and sandworm reefs, which all together will be named "ecogeosystems" in this review due to their combination of biogenic systems, ecological systems and geomorphological systems (Mury et al. in Geophys Res Abstr 20:2044, 2018). It provides a comparative meta-analysis of the various measurements of wave attenuation induced by "ecogeosystems" across different studies focusing on wave height monitoring. The array of "ecogeosystems" included in this review was firstly identified through a fine-scale mapping of the Bay of Mont-Saint-Michel, then literature research was led using several keywords related to ecosystem services and coastal protection. A total of 32 studies was compiled over six countries. The majority of studies was located on North-Atlantic Ocean coastlines. According to their specificities, "ecogeosystems" were synthetically split into two categories, surface (saltmarshes, mudflats, seagrasses and oyster reefs) and punctual (shelly cheniers), for the sake of the WAS comparability. WAS associated with surface saltmarshes, mudflats, seagrasses, and oyster reefs ranged from 0.25 to 7.86%/m, from 0.01 to 4%/m, from 0.03 to 0.77%/m, from 1 to 64%/m, respectively. The punctual shelly chenier was monitored from 70 to 98%. Honeycomb worm and sandworm reefs have no data about WAS according to our literature review.

Keywords Protection ecosystem service · Coastal hazards · Coastal management · Mega-tidal environment

A. Mury (✉) · A. Collin · S. Etienne
Ecole Pratique des Hautes Etudes (EPHE), PSL Université Paris, CNRS LETG, Dinard, France
e-mail: antoine.mury@etu.ephe.psl.eu

M. Jeanson
Ecole Pratique des Hautes Etudes (EPHE), PSL Université Paris, EA CHart, Paris, France

K. D. Nguyen et al. (eds.), *Estuaries and Coastal Zones in Times of Global Change*, Springer Water,
https://doi.org/10.1007/978-981-15-2081-5_32

1 Introduction

A consequence of global change might be an increase in coastal risks (Temmerman et al. 2013). Indeed, sea-level rise conjugated with spring tides, can lead to hazardous sea-levels, in worldwide coastal areas subject to unprecedented demographic densification (exposure), thus risks. Coastal "ecogeosystems" such as tropical coral reefs, have the potential to alleviate hazards by reducing wave energy due to their topographic complexity (drag coefficient, Harris et al. 2016, 2018). However, studies focusing on the wave attenuation service (WAS) of natural barriers remain spatially discrete and scattered, as well as not harmonized. Moreover, the WAS of some barrier types remains poorly known, or even unknown.

A comprehensive view of the ensemble of coastal "ecogeosystems" is needed to help stakeholders tasked with coastal risk reduction and coastal protection. The Bay of Mont-Saint-Michel (BMSM, France) suitably matches this objective, given its mega-tidal regime and the large panel of natural barriers (Collin et al. 2018a) facing hazards and protecting human assets.

The WAS literature review over the BMSM encompasses saltmarshes, mudflats, seagrasses, shelly cheniers, oyster, honeycomb worm and sandworm reefs. It offers a comparative view of the various values of wave attenuation by "ecogeosystems" observed across different studies through wave height monitoring. Ecological parameters acting as wave height attenuation factors have also been evaluated. Beyond the comparative results, the main objective of the study is to give an overview of the existing knowledge of WAS evaluation and identify the gaps hindering an efficient implementation of ecogeosystem-based solution to sustainably cope with coastal risks. Therefore, this work will be an opportunity to bring new data on the WAS of shelly cheniers, honeycomb worm and sandworm reefs, three types of "ecogeosystems" still under-considered for their role in coastal protection (only two studies: Jeanson et al. 2016; Mury et al. 2018).

2 Methods

The first step of this review work consists in the identification of the various "ecogeosystems" of the intertidal environment, which may take part in the wave mitigation process and thus which have to be considered in an integrated vision towards the management of coastal risks.

In so doing, five different "ecogeosystems" of the intertidal domain, which can possibly take part of the WAS, were able to be identified from a mapping of the BMSM (saltmarshes, mudflats/sandflats, shelly cheniers, honeycomb worm and sandworm reefs) (Figs. 1, 2 and 3), and two others were identified in the literature (seagrasses, and oyster reefs) to have a more complete view of the intertidal "ecogeosystems" of temperate coastal areas.

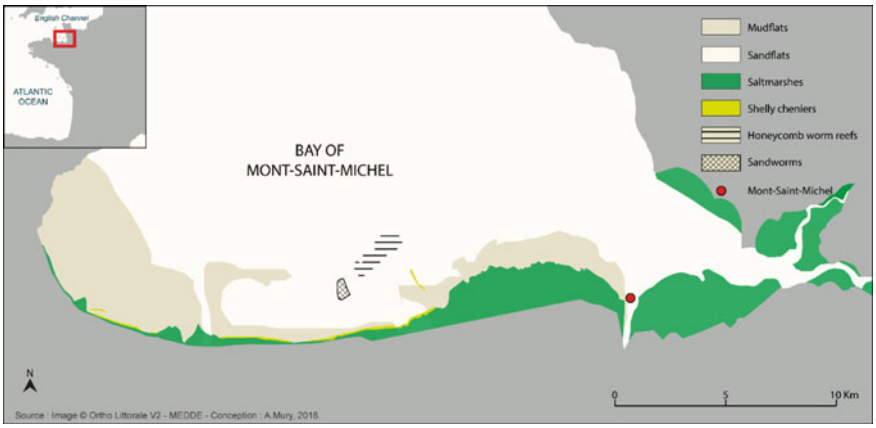

Fig. 1 Location map of the "ecogeosystems" observed in the Bay of Mont-Saint-Michel, France

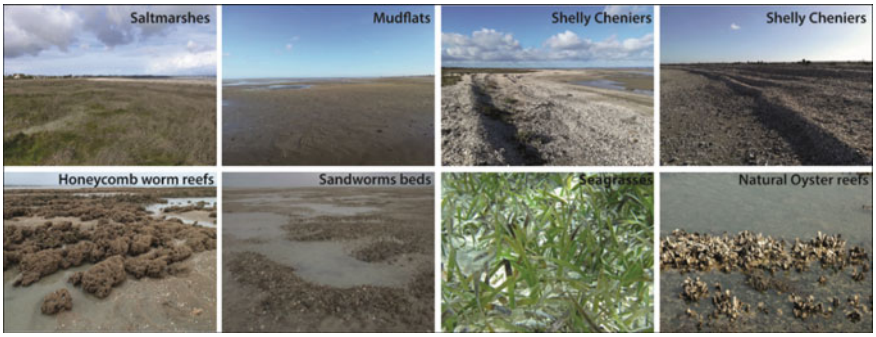

Fig. 2 Illustration of the "ecogeosystems" concerned by the WAS review

These "ecogeosystems" can be separated in three categories depending on their nature: (1) plant ecosystems (saltmarshes, seagrasses), (2) geomorphological structures (mudflats/sandflats, shelly cheniers), and (3) biogenic structures (honeycomb worm, oyster and sandworm reefs).

Concerning the screening method for scientific papers on WAS by coastal "ecogeosystems", the attention was focused specifically on the wave attenuation through the wave height attenuation data (WHA) (neither the velocity nor flow), due to its recognized representativeness of the submersion hazards. We examined the temperate intertidal natural features (what excluded the mangroves and coral reefs, which are tropical ecosystems as well as artificial seagrasses). We searched for the literature using research portals like Google Scholar, Web of Sciences and BibCnrs (Database of CNRS research teams) to target papers dealing with coastal protection, wave attenuation, ecosystem services and nature-based solutions for wave mitigation.

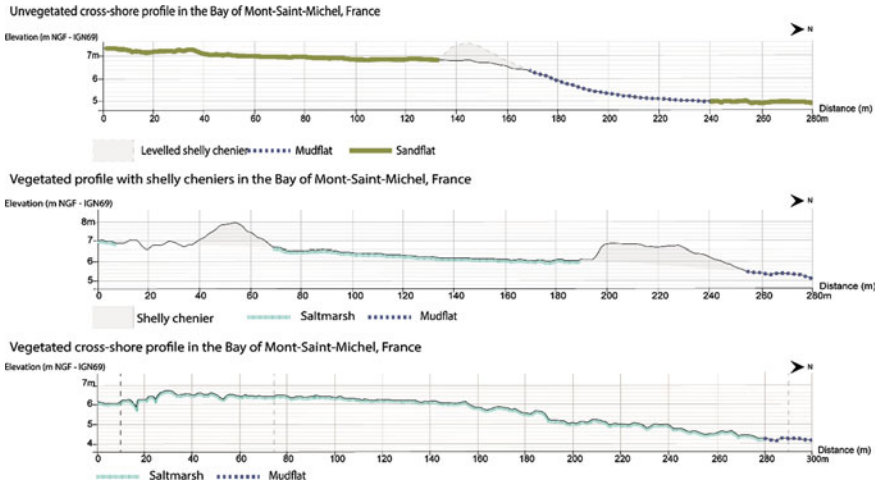

Fig. 3 Cross-shore profiles in the Bay of Mont-Saint-Michel, France

To achieve this literature review, several keywords were used, from generic keywords (i.e., ecosystem services, coastal protection service, coastal protection) to more detailed terms, in the form of *feature* + wave attenuation (or mitigation or reduction) or *feature* + wave height attenuation or *feature* + protection service (e.g., saltmarsh wave attenuation, saltmarsh wave height attenuation, saltmarsh protection service). Subsequently, were selected papers mentioning a percentage of attenuation by the whole selected features or a percentage per unit of distance (%/m) for the sake of data comparisons.

3 Results

A suite of 33 papers corresponded to the mentioned research criteria: 15 concerned saltmarshes WAS, 7 mudflats/sandflats, 5 seagrasses, 4 oyster reefs, 2 shelly cheniers, 0 dealt with honeycomb and sandworm reefs WAS. Some of the identified "ecogeosystems" like honeycomb worm reefs were not considered for their WAS yet, thus were not mentioned in the literature (Fig. 4). Some "ecogeosystems", such as oyster reefs, are well known to act as natural breakwaters, but their WAS is seldom assessed. Most studies, extracted in this literature review, took place on the margins of the Atlantic Ocean, especially along the European and North-American coastlines (Fig. 5).

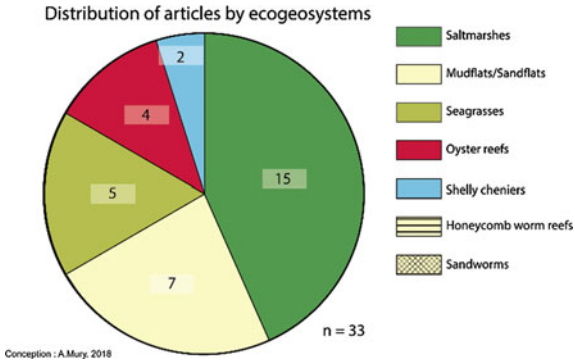

Fig. 4 Diagram of the distribution of the papers

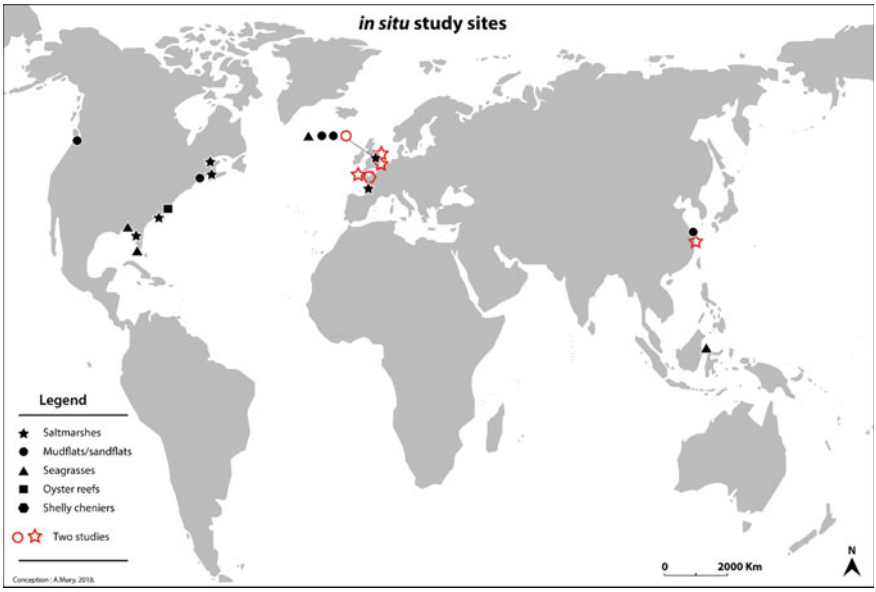

Fig. 5 Location map of the in situ study sites, from the review

3.1 Saltmarshes

About the saltmarsh review, fourteen studies dealing with the WAS were selected (Table 1). Considering the diversity across the different sites and the discrepancy in measurement methods in the literature dataset, we had to implement methodological choices to analyse the distinct study results. First, we decided to compare the studies by using the wave height attenuation (WHA) value, expressed as a percentage of attenuation per meter, to obtain a common unit between studies. When the WHA value was not directly provided by the authors, we calculated it (see shaded boxes). Even though the influence of the distance from the shore, of the foreshore and

Table 1 Synthesis table of Saltmarshes wave attenuation service studies (WHA: Wave Height Attenuation; WEA: Wave Energy Attenuation; * grey literature, PS.: pressure sensors)

References	Study location	Tidal category	Materials	Site characteristics		Wave attenuation			
						WHA		WEA	
						Whole	%/m	Whole	%/m
Wayne (1976)	Adams Beach, Florida, USA	Micro-tidal	NC	*S. alterniflora*		71%/20 m	3.6	92%/20 m	4.6
				T. testudinum		42%/20 m	2.1	67%/20 m	3.4
Knutson et al. (1982)	Chesapeake Bay, Virginia, USA	Micro-tidal	Wave gage	*S. alterniflora*		40%/2.5 m 57%/5 m 65%/10 m 87%/20 m 94%/30 m	3.1	64%/2.5 m 72%/5 m 88%/10 m 98%/20 m 100%/30 m	3.33
Moller et al. (1996)	North Norfolk, UK	Macro-tidal	PS.	North-West European mixed Saltmarsh		53.6%/180 m	0.3	79%/180 m	0.44
Moller et al. (1999)	North Norfolk, UK	Macro-tidal	PS.	North-West European mixed Saltmarsh		60.96%/180 m 63%/200 m	0.34	82%/180 m	0.45
Moller and Spencer (2002)	Dengie Peninsula, Essex, UK	Macro-tidal	PS.	North-West European mixed Saltmarsh	Shallow slopping edge	87.37%/163 m	0.54	98.92%/ 163 m 99%/310 m (whole transect)	0.61 – 0.3 (whole transect)
					Cliffed edge	43.81%/10 m	4.38	79.13%/ 10 m	7.91
Cooper (2005)	The Wash, Eastern England, UK	Macro-tidal	Buoy and PS.	Wrangle flats transect		90.7%/ 300 m	0.3	97.1%/300 m	0.32
				Butterwick Low transect		63.5%/ 250	0.25	71.9%/ 250 m	0.29

(continued)

Table 1 (continued)

References	Study location	Tidal category	Materials	Site characteristics	Wave attenuation			
					WHA		WEA	
					Whole	%/m	Whole	%/m
				Breast Sand transect	78%/110 m	0.7	91.3%/ 110 m	0.83
Moller (2006)	Dengie Peninsula, Essex, UK	Macro-tidal	PS.	North-West European mixed salt marsh	2–7%/10 m	1–1.8	/	/
Yang et al. (2008)	Eastern Chongming, China	Macro-tidal	Wave recorder/PS.	*S. mariqueter*, *S. alterniflora*	16%/16.5 m	0.95	29%/16.5 m	1.80
Lambert (2009)	Saint Laurent Estuary, Canada	NC	PS.	*S. alterniflora, S. patens*	/	/	37–88%/ 566 m	0.7–0.16
Morgan et al. (2009)	Northern New England, USA	NC	/	*S. alterniflora*	55%/7 m	7.86	/	/
				S. patens, J. gerardii, D. spicata and *P. maritima*	52%/7 m	7.43	/	/
Yang et al. (2012)	Eastern Chongming, China	Macro-tidal	PS.	*S. alterniflora*	30%/7.5 m 51%/20 m 79%/51 m	2.34	/	/
Moller et al. (2014)	Ex situ	/	PS.	Mixed saltmarsh of *E. athericus, P. maritima, A. prostrata*	20%/40 m (high energy conditions)	0.5	/	/

(continued)

Table 1 (continued)

References	Study location	Tidal category	Materials	Site characteristics	Wave attenuation			
					WHA		WEA	
					Whole	%/m	Whole	%/m
Lechevalier (2016)*	Moëze, France	Macro-tidal	Wave sensors/PS.	*S. maritima*	/	1.9	/	/
				H. portulacoides	/	5.6	/	/
Collin et al. (2018b)	Bay of Lancieux, France	Mega-tidal	PS.	Lower marsh of *S. anglica* and *S. europaea*	5–10%/100 m	0.05–0.1	/	/
				Medium marsh of *H. portulacoides* and *T. maritima*	10–20%/100 m	0.1–0.2	/	/
				Upper marsh of *H. portulacoides, T. maritima, P. maritima* and *F. rubra*	>20%/100 m	>0.2	/	/
Mury et al. (2018)	BMSM, France	Mega-tidal	PS.	North-West European mixed Salt marsh	>78%/100 m	>0.78	/	/

seabed characterization, the hydrodynamic conditions and water depth, underlying the studies was not accounted for, the calculated values offer a first-level comparison set. Second, we carried out a classification based on ecological criteria and more specifically on the plant length, to compare the WAS across the studies. In this way, we retrieved plant communities with a higher length range (*Spartina alterniflora, Spartina maritima, Scirpus mariqueter, Spartina patens*), which corresponded to the fringing marsh of the lower mixed marsh communities (North-West European mixed saltmarsh*, Elymus athericus, Puccinellia maritima, Salicornia, Suaeda maritima*, etc.).

Regarding the higher plant community studies (Wayne 1976; Knutson et al. 1982; Morgan et al. 2009; Yang et al. 2008, 2012; Lechevalier 2016), the WHA ranged from 0.95 to 7.86%/m (mean: 3.3%/m).

These findings differed considerably from those observed for the lower mixed saltmarshes (Moller and Spencer 2002; Moller 2006; Moller et al. 1996, 1999, 2014; Cooper 2005; Collin et al. 2018b). Indeed, the WHA measured bottomed at 0.3 and topped at 1.8%/m (mean: 0.52%/m) range.

3.2 Mudflats/Sandflats

The second part of the review work was dedicated to the WAS of mudflats and sandflats, in which seven studies were selected (Table 2). The majority of these studies indirectly dealt with the wave attenuation process by mudflats or sandflats. Indeed, mudflat transect measurements were mainly used as samples for comparison with the other "ecogeosystems" WAS (only Houser and Hill 2010, focused on the mudflat WAS).

The WHA recorded in these various studies were generally found between 0.23%/m (modest increase) and 0.2%/m (with the exception of the Morgan et al. 2009, study data that reached 4%/m, a relatively high percentage due to the low distance between recording stations).

3.3 Seagrasses

Concerning the review work allocated to seagrasses WAS, an important methodological choice has been made by excluding all studies dealing with artificial seagrasses (Table 3). Indeed, considering the relative fragility of seagrasses in their natural environment, a plethora of studies focused on artificial seagrasses. The exclusion of artificial seagrasses from this review is justified by primarily targeting the natural components of the intertidal domain and their responses to meteorological and wave forcing. Considering the studies dealing with WHA, a great variability has been recorded, from 0.03%/m to 0.77%/m. This variability in results can be explained by the fragility of this kind of ecosystem and his dependence on the experimental

Table 2 Synthesis table of Mudflats and Sandflats wave attenuation service studies

References	Study location	Tidal category	Materials	Site characteristics	Wave attenuation			
					WHA		WEA	
					Whole	%/m	Whole	%/m
Moller et al. (1996)	North Norfolk, UK	Macro-tidal	PS.	/	13.5%/197 m	0.07	26%/197 m	0.13
Moller et al. (1999)	North Norfolk, UK	Macro-tidal	PS.	/	15.29%/197 m	0.08	29%/197 m	0.15
Moller and Spencer (2002)	Dengie Peninsula, Essex, UK	Macro-tidal	PS.	Marsh edge: shallow slopping	20.57%/147 m	0.14	35.25%/147 m	0.24
				Marsh edge: cliffed edge	+23.91%/102 m (	+0.23	+55.06%/102 m	+0.54
Cooper (2005)	The Wash, Eastern England, UK	Macro-tidal	Buoy/PS.	Wrangle flats transect	10.1%/330 m	0.03	15.9%/330 m	0.05
				Butterwick Low transect	23%/390 m	0.06	35.8%/390 m	0.09
				Breast Sand transect	36.4%/180 m	0.2	56.2%/180 m	0.31
Yang et al. (2008)	Eastern Chong-ming, China	Macro-tidal	Wave-tide recorder/PS.	/	11%/185 m	0.06	21%/185 m	0.11
Morgan et al. (2009)	Northern New England, USA	NC	NC	/	28%/7 m	4.0	/	/
Houser and Hill (2010)	Fraser River Delta, Canada	NC	Current profiler/PS.	/	42%/4500 m	0.01	62%/4500 m	0.014

WHA Wave Height Attenuation; *WEA* Wave Energy Attenuation; *Grey literature, PS.: pressure sensors)

Table 3 Synthesis table of Seagrasses wave attenuation service studies

References	Study location	Tidal category	Materials	Site characteristics		Wave attenuation			
						WHA		WEA	
						Whole	%/m	Whole	%/m
Fonseca and Cahalan (1992)	Ex situ—wave flume	/	Wave flume	*Halodule wrightii, Syringodium filiforme, Thalassia testudinum, Zostera marina*		/	/	20–76%/1 m (mean 40%)	
Prager and Halley (1999)	Calusa Key, Florida Bay, USA	NC	PS.	*Thalassia testudinum*		/	/	>80%/2500 m	0.03
Paul and Amos (2011)	Ryde Sand, Isle of Wight, UK	Macro-tidal	PS.	*Zoster-a noltii*	High shoot density	20%/30–95 m	0.66–0.21	/	/
					Low shoot density	<10%/30–95 m	0.33–0.11	/	/
Bradley and Houser (2009)	Santa Rosa Island, Florida, USA	Micro-tidal	PS.	*Thalassia testudinum*		+20%/5th m then decrease of 30%/39 m	0.77 (39 m)	/	/
Christianen et al. (2013)	Derawan Island, Indonesia	NC	PS.	*Halodule uninervis*		18%/667 m 30%/450 m 11%/200 m	0.03–0.07	/	/

WHA Wave Height Attenuation; *WEA* Wave Energy Attenuation; *Grey literature, PS.: pressure sensors)

conditions. Furthermore, another explanatory factor of this variability is the diversity of the morphological characteristics (e.g., root system, leaf morphometry) of the various species.

3.4 Oyster Reefs

Oyster reefs are deemed as natural breakwaters since several centuries and are currently utilized in ecosystem restoration programs. Their value as a protective ecosystem is attested, but there are surprisingly not so many studies, which aimed at quantifying their WAS value. Among the retained studies, three out of four are ex situ studies (Table 4). Data from these studies were difficult to harmonize because of the discrete shape of the oyster reefs, thus an attenuation percentage per meter (i.e., surface metrics) could be inappropriate to estimate it. A punctual metric would be more likely to capture the WAS of these reefs. The only value we could find stemmed from Garvis (2012): 23% attenuation for a three-metre transect, that is to say 7.6%/m. Noteworthy was the absence of consideration of the non-linearity of the attenuation and the possible shoaling effect.

3.5 Shelly Cheniers

The capacity of shelly cheniers to alleviate wave energy is also accepted, although it is little documented. Shelly cheniers are besides relatively rare geomorphic structures worldwide, resulting in a few studies about their WAS. To date, we listed only two papers about this attenuation aspect (Table 5). The first study showed a very high WEA rate, around 98% for healthy cheniers, whilst the second study, focused on the WHA, showed a rate around 61% for the whole well-developed chenier, and around 39% for the degraded one. It is also advocated to use a global punctual rate for the whole reef, since the attenuation percentage per meter looks inappropriate (discrete aspect).

3.6 Honeycomb Worm and Sandworm Reefs

To our knowledge, WAS of honeycomb worm (*Sabellaria alveolota*) and sandworm (*Lanice conchilega*) reefs were not studied yet. Nevertheless, literature references evoke a potential mitigation process by the honeycomb colonies, which might significantly increase the surface roughness (Collin et al. 2018a) and so reduce wave energy. This lack of consideration of engineer-ecosystems into their protective role could be explained for several reasons. These biogenic structures are overall poorly known due to their relative rarity in comparison with some others features like saltmarshes

Table 4 Synthesis table of Oyster Reefs wave attenuation service studies

References	Study location	Tidal category	Materials	Site characteristics	Wave attenuation			
					WHA		WEA	
					Whole	%/m	Whole	%/m
Garvis (2012)*	Ex situ	/	PS.	Dead reef	<1%/3 m		/	/
				Natural reef	23%/3 m		/	/
				Restored reef	25%/3 m		/	/
Taube (2013)*	Delmarva Peninsula, Virginia, USA	Micro-tidal	Wave recorder—Acoustic Doppler	*Crassostrea virginica* reef	/	/	49%	/
Manis et al. (2015)	Ex situ	/	PS.	Newly deployed oyster shell	10.3%	/	18.7%	/
				1-year established oyster	10.5%	/	44.7%	/
Godfroy (2017)*	Ex situ	/	Model	/	9–64%	/	/	/

WHA Wave Height Attenuation; *WEA* Wave Energy Attenuation; *Grey literature, PS.: pressure sensors)

Table 5 Synthesis table of Shelly Cheniers wave attenuation service studies

Reference	Study location	Tidal category	Materials	Site characteristics	Wave attenuation			
					WHA		WEA	
					Whole	%/m	Whole	%/m
Jeanson et al. (2016)	BMSM, France	Mega-tidal	PS.	Well-developed shelly cheniers	/	/	98%	/
				Degraded shelly cheniers	/	/	70%	/
Mury et al. (2018)	BMSM, France	Mega-tidal	PS.	Well-developed shelly cheniers	61.1%/100 m	0.61	/	/
				Degraded shelly cheniers	39.3%/100 m	0.39	/	/

WHA Wave Height Attenuation; *WEA* Wave Energy Attenuation; *Grey literature, PS.: pressure sensors)

or seagrasses. In addition, their location at the bottom of the intertidal zone (remote from the coastline) drives scientists to consider them as some marginal elements in the WAS of the entire intertidal zone, especially in a mega-tidal environment.

4 Discussion

This review of the existing literature about the WAS of the intertidal "ecogeosystems" in temperate areas allowed us to highlight several elements.

Indeed, it appears that WAS of some "ecogeosystems" are well documented, as it is the case for saltmarshes (Table 1). Contrariwise, some features, rarer worldwide or located lower in the intertidal zone, are poorly known, particularly shelly cheniers, honeycomb worm and sandworm reefs.

Thus, by a quantitative and qualitative analysis of the different papers, we can deduce one pattern: the more we go away from the coastline, the more we observe gaps in the WAS knowledge. The distribution of the reviewed papers along a cross-shore transect could be used to illustrate this finding (Fig. 6).

Another element we drew from this review is the difficulties to harmonize the various data across studies. These difficulties are due to several factors. The first one is about the structural heterogeneity of study sites and "ecogeosystems": their shape (punctual features as cheniers versus surface features as saltmarshes), and their inherent composition (i.e., different vegetation communities for saltmarshes studies, various length measurement transects and various measurement conditions: weather, seasons, tidal category, water levels). The second reason is about the published datasets: some technical information might miss; foreshore and seabed morphometry and features backing the natural barriers, hydrodynamic regime and distance from the coastline are often not specified, thus introducing biases in the data harmonization due to the ignorance of the influence of these elements on the WAS. The third reason concerns the heterogeneity of measurement methods between the different studies

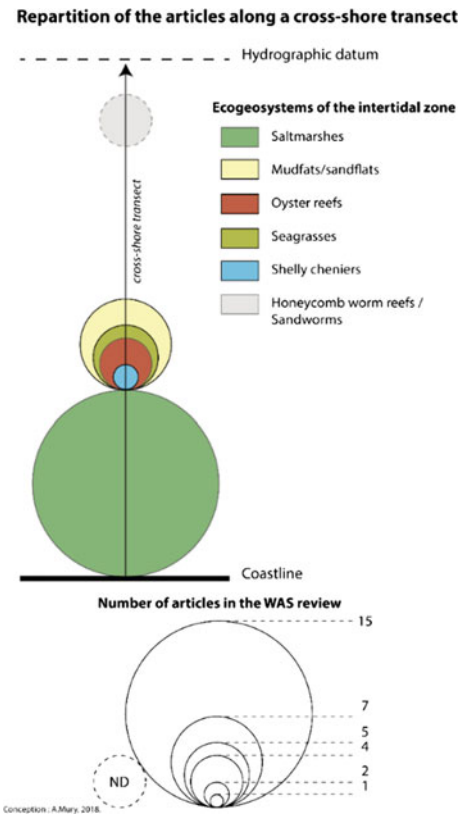

Fig. 6 Scheme of papers' distribution along a conceptualized cross-shore transect

(pressure sensor, buoy, wave recorder), which complexify and even impede the comparison between studies. Moreover, significant wave height calculation methods are overshadowed, because of the absence of specifications in papers.

As a single variable based on significant wave height WHA might appear as a simplistic methodological choice in this review. Not considered in this review were the characteristics linked to the tidal regime (infragravity waves) and the flow velocity, taking probably part of the marine flood hazards. Moreover, in most cases, WHA is mathematically approached as a linear process along the study section while it is obviously a non-linear process in the complex real world (Koch et al. 2009). The wave reduction decreases from the start to the end of the section, i.e., the shoaling effect, which is rarely investigated in the research studies. This simplified linear approach of the mitigation process could be explained by the methodological and material contingencies. Indeed, frequently the data used for the calculation of the wave attenuation arise from punctual and fixed stations, at the beginning and the end of the study section. This approach does not allow to observe the process in its entirety. Several technical processes, in on-going development, should correct for

Table 6 Synthesis table of WAS from the meta-analysis

Shape	Ecogeosystems	WHA
Surface	Saltmarshes	0.05–7.86%/m
	Mudflats	0.01–4%/m
	Seagrasses	0.03–0.77%/m
Punctual	Oyster reefs	1–64% (whole reef)
	Shelly Cheniers	70–98% (whole transect)*

WHA Wave Height Attenuation, *Wave energy attenuation data were used for Shelly Cheniers

this problem, in particular by the contribution of the high-resolution satellite imagery (Collin et al. 2018b).

Table 6 synthetizes results obtained from the papers reviewed. Despite its plain design, the table gives a first overview of the WAS value for every studied "ecogeosystem".

To conclude, a work of harmonization of the results of the different studies is recommended by insisting on the transparency in the methods used. To leverage a generic model adaptable for all coastlines with their diversity of "ecogeosystems" and specificities, we propose to improve the knowledge about all the potential "ecogeosystems" WAS worldwide. To solve the problem of harmonization, a robust approach would be to either find generic metrics across all "ecogeosystems" or ranking them through a table showing both range, mean and standard deviation values. This synoptic product holds great promise to be integrated into toolboxes of stakeholders tasked with nature-based mitigation of coastal risks.

References

Bradley, K., & Houser, C. (2009). Relative velocity of seagrass blades: Implication for wave attenuation in low-energy environments. *Journal of Geophysiscal Research*, *114*(F1).

Christianen, M. J. A., van Belzen, J., Herman, J., van Katwijk, M. M., Lamers, L. P. M., van Leent, P. J. M., et al. (2013). Low-canopy seagrass beds still provide important coastal protection services. *PLoS ONE, 8*(5), e62413.

Collin, A., Dubois, S., Ramambason, C., & Etienne, S. (2018a). Very high-resolution mapping of emerging biogenic reefs using airborne optical imagery and neural network: The honeycomb worm (*Sabellaria alveolata*) case study. *International Journal of Remote Sensing*, 1–16.

Collin, A., Lambert, N., James, D., & Etienne, S. (2018b). Mapping wave attenuation induced by salt marsh vegetation using WorldView-3 satellite imagery. *Revista de investigación Marina, 25*(2), 67–69.

Cooper, N. J. (2005). Wave dissipation across Intertidal surfaces in the wash tidal inlet, Eastern England. *Journal of Coastal Research, 21*(1), 28–40.

Fonseca, M. S., & Cahalan, J. A. (1992). A preliminary evaluation of wave attenuation by four species of seagrass. *Estuarine, Coastal and Shelf Science, 35,* 564–576.

Garvis, S. K. (2012). *Quantifying the impacts of oyster reef restoration on oyster coverage, wave attenuation and seagrass fragment retention in Mosquito Lagoon, Florida* (M.sc. thesis, p. 2284). University of Central Florida, Electronic These and dissertations.

Godfroy, M. (2017). *Quantifying wave attenuation by nature based solutions in Galveston bay* (M.sc. thesis, p. 145). Delft University of Technology.

Harris, D. L., Rovere, A., Casella, E., Power, H., Canavesio, R., Collin, A., et al. (2018). Coral reef structural complexity provides important coastal protection from waves under rising sea levels. *Science advances*, *4*(2), eaao4350.

Harris, D. L., Rovere, A., Parravicini, V., Casella, E., Canavesio, R., & Collin, A. (2016). Healthy coral reefs may assure coastal protection in face of climate change related sea level rise. In *American Geophysical Union Fall Meeting*, GC11D-1167.

Houser, C., & Hill, P. (2010). Wave attenuation across an intertidal sand flat: Implication for mudflat development. *Journal of Coastal Research, 26*(3), 403–411.

Jeanson, M., Etienne, S., & Collin, A. (2016). Wave attenuation and Coastal Protection by Shelly Ridges: Mont-Saint-Michel Bay, France. *Journal of Coastal Research, 75,* 398–402.

Knutson, P. L., Brochu, R. A., Seelig, W. N., & Inskeep, M. (1982). Wave damping in spartina alterniflora. *Wetlands, 2,* 87–104.

Koch, E. W., Barbier, E. B., Siliman, B. R., Reed, D. J., Perillo, G. M. E., Granek, E. F., et al. (2009). Non-linearity in ecosystem services: Temporal and spatial variability in coastal protection. *Frontiers in Ecology and the Environment, 7,* 29–37.

Lambert, N. (2009). *Modélisation de la dissipation de l'énergie des vagues par la végétation de marais littoral* (Ph.D. thesis, p. 97). Rimouski, Québec, Université du Québec à Rimouski, Institut des sciences de la mer de Rimouski.

Lechevalier, A. (2016). *Etude de l'atténuation des vagues par un champ de végétation composé de Spartina maritima et Halimione portulacoides* (M.sc. thesis, p. 34). Université de La Rochelle,

Manis, J. E., Garvic, S. K., Jachec, S. M., & Walters, L. J. (2015). Wave attenuation experiments over living shorelines over time: A wave tank study to assess recreational boating pressure. *Journal of Coastal Conservation, planning and management, 19*(1), 1–11.

Moller, I. (2006). Quantifying saltmarsh vegetation and its effect on wave height dissipation: Result from a UK East coast saltmarsh. *Estuarine Coastal Shelf Science, 69,* 337–351.

Moller, I., Kudella, M., Rupprecht, F., Spencer, T., Paul, M., van Wesenbeeck, B. K., et al. (2014). Wave attenuation over coastal salt marshes under storm surge conditions. *Nature Geoscience, 7,* 727–731.

Moller, I., & Spencer, T. (2002) Wave dissipation over macro-tidal saltmarshes: Effects of marshes edge typology and vegetation change. *Journal of coastal research*, 506–521.

Moller, I., Spencer, T., & French, J. R. (1996). Wind wave dissipation over saltmarshes surfaces: Preliminary results from Norfolk, England. *Journal of Coastal Research, 12*(4), 1009–1016.

Moller, I., Spencer, T., French, J. R., Leggett, D. J., & Dixon, M. (1999). Wave transformation over salt marshes: a field and numerical modelling study from North Norfolk, England. *Estuarine, Coastal and Shelf Science, 49,* 411–426.

Morgan, P. A., Burdick, D. M., & Short, F. T. (2009). The functions and values of fringing salt marshes in Northern New England, USA. *Estuaries and Coasts, 32,* 483–495.

Mury, A., Collin, A., & Etienne, S. (2018). Wave attenuation service of saltmarshes and shelly cheniers: A spatio-temporal study in Mont-Saint-Michel Bay, France. *Geophysical Research Abstracts, 20,* 2044.

Paul, M., & Amos, C. L. (2011). Spatial and seasonal variation in wave attenuation over Zostera noltii. *Journal of Geophysical Research, 116,* C08019.

Prager, E. J., & Halley, R. B. (1999). The influence of seagrass on shell layers and Florida Bay mudbanks. *Journal of Coastal Research, 15*(4), 1151–1162.

Taube, S. R. (2013) *Impact of fringing oyster reefs on wave attenuation and marsh erosion rates* (M.sc. thesis). University of Virginia.

Temmerman, S., Meire, P., Bouma, T.J., Herman, P. M., Ysebaert, T., De Vriend, H. J. (2013). Ecosystem-based coastal defence in the face of global change. *Nature, 504*(7478), 79–83.

Wayne, C. J. (1976). The effects of sea and marsh grass on wave energy. *Coastal Research Notes, 14,* 6–8.

Yang, S. L., Li, H., Ysebaert, T., Bouma, T. J., Zhang, W. X., Wang, Y. Y., et al. (2008). Spatial and temporal variations in sediment grain size in tidal wetlands, Yangtze Delta: On the role of physical and biotic controls. *Estuarine, Coastal and Shelf Sciences, 77,* 657–671.

Yang, S. L., Shi, B. W., Bouma, T. J., & Ysebaert, T. (2012). Wave attenuation at a salt marsh margin: A case study of an exposed coast on the Yangtze Estuary. *Estuaries and Coasts, 35,* 169–182.

Large Scale Demonstrator of Fishing Nets Against Coastal Erosion of Dunes by Meanders in Authie Estuary (Côte D'Opale—France)

Philippe Sergent, Nicolas Huybrechts and Hassan Smaoui

Abstract A device that is composed of nets is experimented to reduce the erosive currents on estuary banks. A porous environment that generates turbulent dissipation is created by several nets that are assembled in several inverted V in a tepee configuration. The sediments are trapped inside the different layers near the sea bed. The nets are maintained by chains and anchors, whereas the deployment for rising and falling tide is assured by floating buoys. This geometry is completed by vertical nets in order to obtain significant height for the damping of currents behind the nets. The nets were set in November 2014 along the right bank of Authie in a position of groyne. The initial length was 150 m and the initial height was 1 m. The height was raised to 2 m in March 2016. The Bay of Authie is characterised by meanders of the estuary that regularly threaten the right bank in front of dunes in the site named Fir wood. During the last severe erosion in 2011 the meander approached and eroded the dunes so that many trees fell on the beach and were carried away by the flow of the estuary. After a theoretical analysis of the shielding effect of the nets, the sensitivity of the sediment deposit to the net height concludes that it is useless to raise the nets more than 2 m. The monitoring consists in comparing the bathymetry around the nets before and after the last raising and in measuring velocity currents and water height. A deposit of sediment of 1 m due to sand trapping was observed after the last raise in the area around the nets. The results of modelling confirm that the combination of nets is an efficient option regarding the head loss if the inter-nets distance is sufficient. The vertical profiles of current velocity show that the wake effect is observed on a distance of 25 cm downstream and that the reduction of current velocity behind the net can reach 15% up to 5 m downstream.

P. Sergent (✉) · N. Huybrechts · H. Smaoui
Cerema, Direction Technique Eau, Mer et Fleuves, 134 rue de Beauvais, CS 60039, Margny-lès-Compiègne 60280, France
e-mail: philippe.sergent@cerema.fr

N. Huybrechts · H. Smaoui
FRE 2012 Roberval, CNRS, Centre de recherche Royallieu, Sorbonne Université, université de technologie de Compiègne, CS 60319, Compiègne cedex 60203, France

K. D. Nguyen et al. (eds.), *Estuaries and Coastal Zones in Times of Global Change*, Springer Water,
https://doi.org/10.1007/978-981-15-2081-5_33

Keywords Nets · Sediment transport · Groyne · Meander · Estuary · Dune · Sand trapping

1 Introduction

A device composed of nets and developed by the company S-Able (Michon, 2017) was first tested in a wave tank (Boucher et al. 2014a, b) in order to assess its impact for beaches eroded by wave actions. This device was then experimented to reduce the erosive currents on river banks in Saint-Brévin les Pins (Boucher et al. 2014a, b) in small estuary Boivre. It is here experimented in the larger estuary of Authie River in a specific position of groyne in order to prevent dune erosion by river meandering. Monitoring is done in order to study two effects: firstly a shielding effect that consists in deviating partially the flow and secondly a local effect of sand trapping. This new technique of coastal engineering is in competition with sand bypassing or rock groyne. It combines partially the objectives of these two solutions while working more with nature. The reduction in flow velocity downstream of a fishing net is assessed with a CFD code and is compared qualitatively with experimental investigation (Bi et al. 2013).

2 Erosion of Dunes by Meandering of the Estuary

At the limits of the Somme and the Pas-de-Calais in a macro tidal environment, the Bay of Authie is characterised near Berck sur Mer by meanders of the river Authie that regularly threatens the right bank of the dunes on the site named Fir wood in Groffliers. The last severe erosion occurred in 2011. The meander approached and eroded the dunes with the combined action of currents and waves. During this event many fir trees fell on the beach and were then carried away by the flow of the river. The South-North longshore sand drift pushes sand banks and the river near the coast as long as the river flow does not cut the banks (see Fig. 1). An equilibrium is found between this longshore drift and the sediment transport in the estuary due to tide and river discharge. During some winters, the equilibrium is lost and the river takes a previous bed with flows and erosion along the coastline.

The dunes represent a natural coastal defence for the hinterland that mainly lies below the mean seal level. Except the erosion by the meanders of the river, there is also a standard evolution of beach profile and movements of sandbars (Ouahsine et al. 2013) due to waves. Big bags in geotextile fabrics have been recently placed on the top of the dunes and filled with sand in order to prevent the sea from overflowing the low areas.

If the flood risk is controlled by these sand bags, the erosion risk has not been yet treated and dunes erosion threatens the present efforts against submersion.

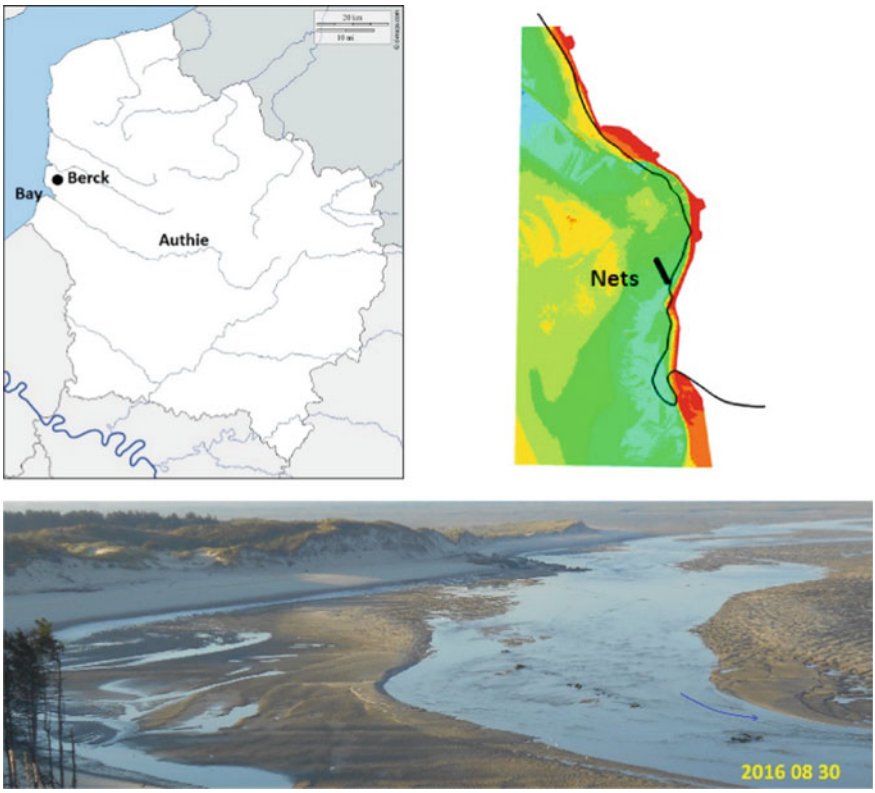

Fig. 1 Location of nets in Bay of Authie

3 Characteristics of the Nets

A device that is composed of nets is experimented to reduce the erosive currents on river banks. This device (Fig. 2a) is developed by the company S-Able (Michon,

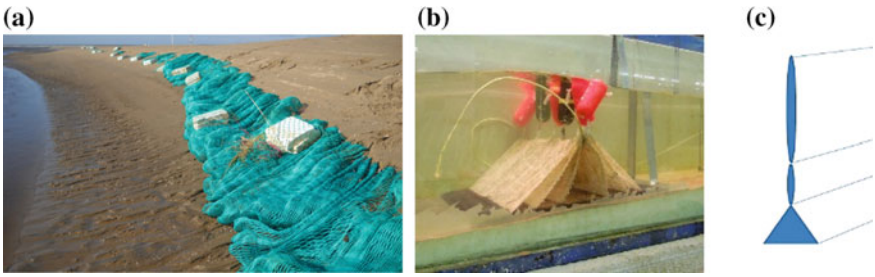

Fig. 2 Design and action of the nets in sea water

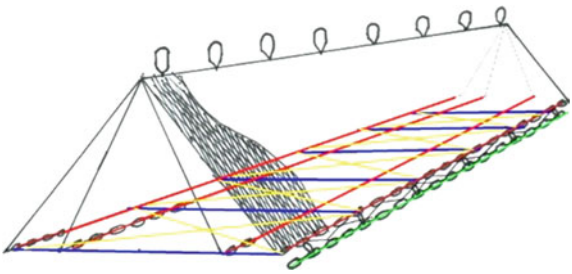

Fig. 3 Nets assembled in several inverted V according to the patent of Michon (2017)

2017), which applied for the patent. A porous environment that generates turbulent dissipation is created by several nets that are assembled in several inverted V (Figs. 2b and 3). The sediments are trapped inside the different layers near the sea bed. The nets are maintained by chains and anchors, whereas the deployment on rising and falling tide is assured by floating buoys. Dimensions are assured:

– on the length, by chains designed for load of 12 tonnes and fixed by adapted anchorages.
– on the width, by spacer bars that maintain the toe width. The internal nets are spaced from 0.75 m.
– on the height, by floating buoys.

The net solidity describes the ratio between the projected area of a plane net and the total area enclosed by the plane net. This geometry can be completed by vertical nets in order to obtain a significant height for the damping of currents behind the nets (Fig. 2c). After several months, sand deposit occurs around the nets with the creation by tidal flow of a sandy groynes in the estuary. The nets were set in November 2014 along the right bank of Authie as a demonstrator. The initial length was 150 m and the initial height was 1 m. The height was raised to 2 m in March 2016. Very quickly after only several weeks sand deposit was observed behind the nets (Fig. 4). The height of the nets was raised of 3 m again in May 2017.

The diameter of ropes is 4 mm and the maximal distance between two adjacent ropes is 5 mm (see Fig. 5). The solidity of nets are therefore assessed between 80% and 90%. The dimension of knots is around 1 cm.

Fig. 4 Sand deposit behind the nets after several weeks

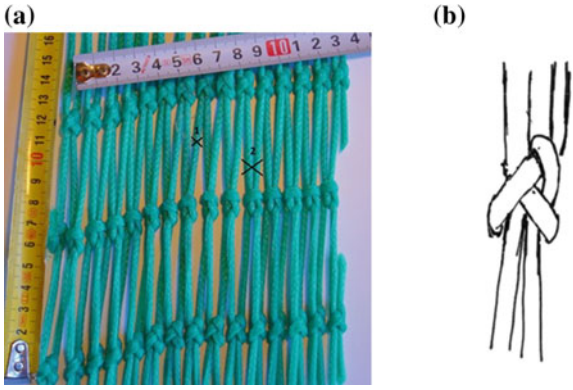

Fig. 5 **a** Solidity of the net and **b** knot

4 Shielding Effect

The nets have a primary effect that consists in partially closing a branch (branch 2) of the meanders of the Authie River and favouring the flow in the other branch (branch 1) as it is presented in Fig. 6. The nets can also be considered as a permeable groyne.

The head loss ΔH across the nets conditions the flow in the diverted branch. The stationary momentum equation in each branch is indeed (Thual 2010):

$$\frac{\mathrm{d}h}{\mathrm{d}s} = \frac{I - J}{1 - F_r^2} \tag{1}$$

where F_r is the Froude number, h is the water depth and I is the bottom slope with Z_f the bottom height:

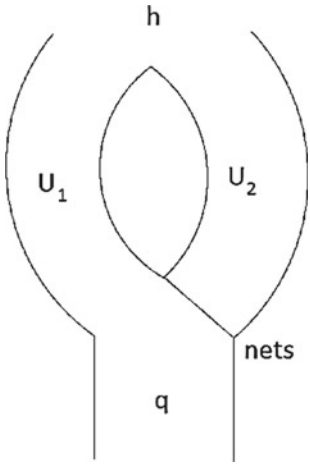

Fig. 6 Schematic view of the shielding effect of the nets

$$\mathrm{I} = \frac{\mathrm{d}Z_f}{\mathrm{d}s} \tag{2}$$

J is the linear head loss parameterized by the Manning–Strickler formula $U = K_s h^{\frac{2}{3}} J^2$ with K_s the Strickler coefficient related with the bottom roughnes. It is defined as follows.

$$J = I\left(\frac{h}{h_n}\right)^{-\frac{10}{3}} \quad h_n = \left(\frac{q^2}{I K_s^2}\right)^{\frac{3}{10}} \tag{3}$$

with h_n the normal water height that depends on the bottom slope I. The Froude number is defined as follows.

$$F_r^2 = \left(\frac{h_c}{h}\right)^3 \quad h_c = \left(\frac{q^2}{g}\right)^{\frac{1}{3}} \tag{4}$$

with h_c the critical water height that does not depend on the bottom slope. With these definitions, the stationary momentum equation is finally:

$$\frac{\mathrm{d}h}{\mathrm{d}s} = \mathcal{F}(h, q) = I\frac{1 - \left(\frac{h}{h_n}\right)^{-\frac{10}{3}}}{1 - \left(\frac{h}{h_c}\right)^{-3}} \tag{5}$$

In the branch 1, we find the upstream water height h* as function of the downstream water height h and of the water discharge q_1 in the branch 1:

$$\mathrm{h}* = \mathcal{M}(h, q_1) \tag{6}$$

In the branch 2, we find the upstream water height h* with ΔH the head loss through the nets:

$$\mathrm{h}* = \mathcal{M}(h, q_2) + \frac{\Delta H}{1 - F_r^2} \tag{7}$$

The continuity of water height and the conservation of the water discharge at the entrance of the two branches give:

$$\mathcal{M}(h, q - q_2) = \mathcal{M}(h, q_2) + \frac{\Delta H}{1 - F_r^2} \tag{8}$$

This Eq. (8) enables to find the discharge, the current velocity and the water height in the branch 2 and in consequence in branch 1. That shows clearly that, if we want to increase the shielding effect of the nets, we must increase the head loss and therefore increase the solidity of the nets and increase the height of the nets.

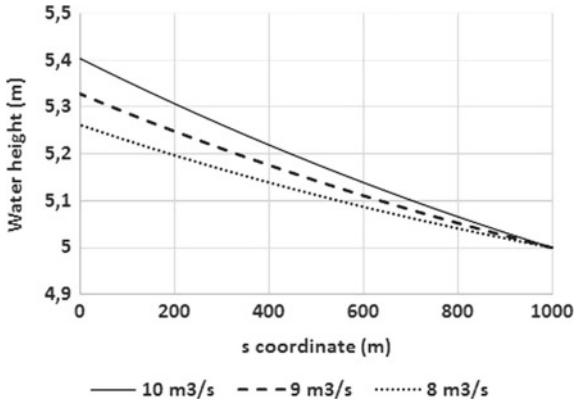

Fig. 7 Water height in function of water discharge

An application is done with a water depth h of 5 m, a bottom slope I of 1/1000, a branch length of 1 km and a Strickler coefficient of 40. Since the Froude number is small compared to 1, the Fig. 7 shows that a head loss of 10 cm that is observed in situ corresponds approximately to a reduction of the water discharge of 10%.

5 Sand Trapping

Another effect of the nets is sand trapping. Due to the deceleration of the flow through the nets, a sand deposit occurs behind the net that is considered as a porous medium.

Figure 8 shows results of simulation of the flow through an aquaculture cage that is also considered as a porous medium in presence of fishes. The view is inverted vertically in order to correspond to the case of the nets.

We observe clearly that the presence of a porous medium reduces the current velocity at the bottom. This reduction is all the stronger when the net height is large.

Let us note $q_s^1(\mathrm{t})$ and $q_s^2(\mathrm{t})$ the solid discharge per width unit upstream and downstream of the nets. Considering ebb flow, then $q_s^1(\mathrm{t}) > q_s^2(\mathrm{t})$. Part of the sediment transport will deposit downstream. The instantaneous deposit $D(\mathrm{t})$ per width unit is proportional to $q_s^1(\mathrm{t}) - q_s^2(\mathrm{t})$.

$$D(t) \propto q_s^1(\mathrm{t}) - q_s^2(\mathrm{t}) \tag{9}$$

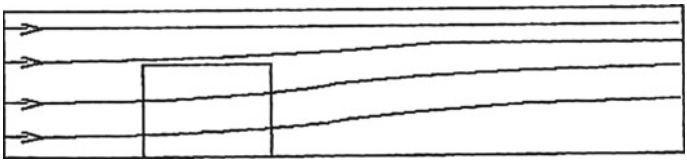

Fig. 8 Schematic view of the deceleration through a porous medium (from Poizot et al. 2016)

This expression is rewritten in function of the relative variation of solid discharge through the nets $\frac{\Delta q_s}{q_s}$:

$$D(t) \propto q_s^1(\mathrm{t}) \frac{\Delta q_s}{q_s} \tag{10}$$

Engelund and Hansen law (1972) said «EH» was, initially a bed load sediment transport law but it can be used to assess total load sediment transport. It was validated for relatively fine sediments with diameters between 0.2 mm and 1 mm. The total load sediment transport is written from following parameters:

- Water depth H
- Channel width B
- Average current velocity V_e
- Gravity g
- Bottom roughness k_{sc}
- Average sediment diameter d_{50}
- Water density γ_w
- Sand density γ_s.

$$s = \frac{\gamma_s}{\gamma_w}$$

$$q_s = \frac{0.05}{(s-1)^2 g^2 d_{50}} \frac{V_e^5}{7.83 \ln\left(\frac{11H}{k_{sc}}\right)} \tag{11}$$

$$Q_s = B q_s \tag{12}$$

From (10) and (11), we deduce that the deposit is proportional to the relative difference of current velocity. Since the current velocity is not homogeneous (see Fig. 8), we replace V_e by V the current velocity in the lowest part of the water height that contributes the most to the sediment transport. We obtain then:

$$D(t) \propto q_s^1(\mathrm{t}) \frac{\Delta V}{V} \tag{13}$$

Considering that the dissipation rate of kinetic energy is proportional to the net height $h_{net}(t)$ we deduce that:

$$D(t) \propto q_s^1 h_{net}(t) \tag{14}$$

Solid deposit is therefore considered proportional to the total load sediment transport and to the height of the nets.

After raising the nets, the new instantaneous height is noted $h^*_{net}(t)$.

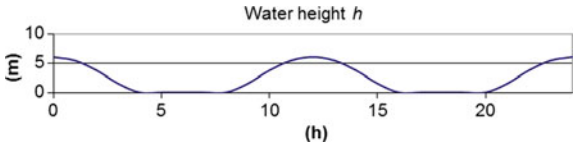

Fig. 9 Schematic evolution of water height for a spring tide

Averaged efficiency η of the raising of the nets, over a tidal cycle of period T, is assessed from the ratio of deposit calculated before and after the raising:

$$\eta = \frac{\int_0^T q_s h_{net}^* dt}{\int_0^T q_s h_{net} dt} \tag{15}$$

We consider in Fig. 9 a schematic spring tide in Bay of Authie with a tide amplitude of 9 meters in front of the nets and with a maximal water height of 6 meters.

We assess the variations of current velocities in Fig. 10 in front of the nets as the gradient of the water height in adjusting the amplitude to observations and in setting the current velocity to zero when the nets lye on the bottom.

We calculate the evolution of the height of the nets $h_{net}(t)$ for spring tide in Fig. 11 in function of water height $h(t)$ and of the maximal height of the net $h_{net}^{\max}$:

$$h_{net}(t) = \min\left(h(t), h_{net}^{\max}\right) \tag{16}$$

Two values of maximal height of the net $h_{net}^{\max}$ are considered: 2,1 m before raising noted $h_{net}^{\max}$ and 5.1 m after raising noted $h_{net}^{*\max}$.

The expression $q_s h_{net}$ that is used in equation [14] is proportional to $V^5 h$ using EH law presented in (11). We name here this expression as the instantaneous efficiency of the nets for sand trapping. We neglect here the variations of the denominator i.e. the effects of the water depth on the roughness in Eq. (11).

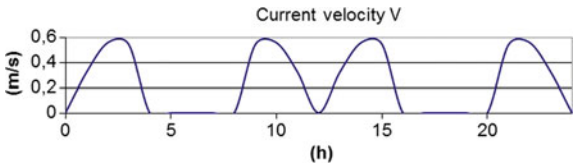

Fig. 10 Schematic evolution of current velocity for a spring tide

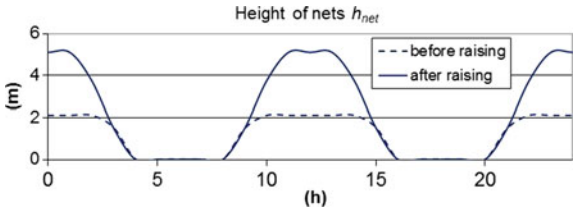

Fig. 11 Schematic evolution of height of the nets for a spring tide

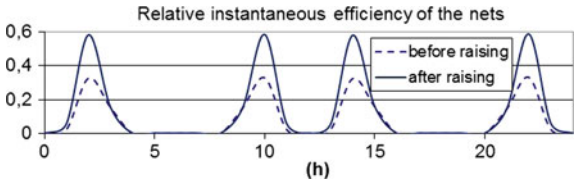

Fig. 12 Schematic evolution of instantaneous efficiency for a spring tide

Table 1 Efficiency of the raising of the nets for spring tide

	Raising of the nets	1 m (%)	2 m (%)	3 m (%)	4 m (%)
Initial height of the nets	h = 2.1 m	32	55	57	58
	h = 1 m	73	138	190	194
	h = 0.5 m	199	309	445	485

Table 2 Efficiency of the raising of the nets for neap tide

	Raising of the nets	1 m (%)	2 m (%)	3 m (%)	4 m (%)
Initial height of the nets	h = 2.1 m	13	14	14	14
	h = 1 m	73	106	107	107
	h = 0.5 m	197	306	313	313

The figure below represents this instantaneous efficiency that is normed with the maximum of efficiency (with $V_{\max}$ and $h_{net}^{*\max}$). Hypotheses for the nets are the same (i.e. $h_{net}^{\max} = 2.1$ m and $h_{net}^{*\max} = 5.1$ m).

In Fig. 11 we observe that the nets are in action during 8 h at each tide and that the raising has an effect only during 6 h. We need simultaneously water height and current velocity for a good efficiency. Since the peak of current velocity is out of phase with high tide, the instantaneous efficiency of raising is observed during 2 h only in Fig. 12.

We assess the efficiency of raising from Eq. (15) with four hypothesis for the raising and three hypothesis for the initial height for a spring tide of tide amplitude of 9 m. The first hypothesis corresponds to the real nest height (2.1 m). The two other hypothesis take into account a possible burial of nets under a layer of sand. The active net height is then reduced. Table 1 presents results.

The same assessment is done for neap tide of tide amplitude of 4 m. Table 2 presents results.

6 Monitoring

Coming along with the raising of the nets, a monitoring has been set up in May 2017.

Fig. 13 Current sensor on a tripod

A current sensor Aquadopp Profiler was mounted on a tripod and was placed behind the nets in the Authie bed for a duration of 90 days (cycle of spring and neap tides) (Fig. 13).

Because of the height of tripod, the sensor measures in air at low tide. The signal is filtered in order to measure only the water height and the sea current velocities. Figure 14 shows during 90 days the evolution of water height that varies between 4 and 6.5 m.

Average current velocities in Fig. 15 on the water depth reach maxima between 0.75 and 1.5 m/s for neap tide and spring tide respectively. The direction varies

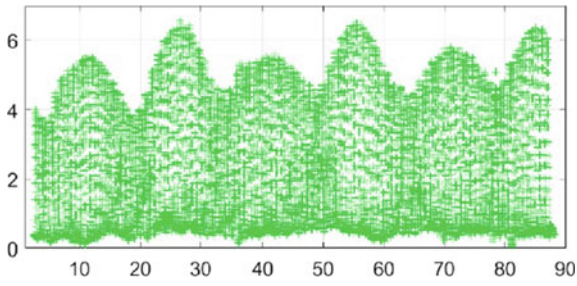

Fig. 14 Water height in m during 90 days

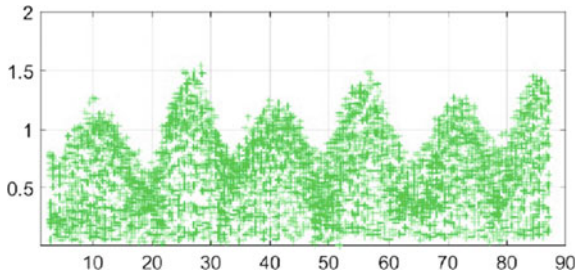

Fig. 15 Current velocity in m/s during 90 days

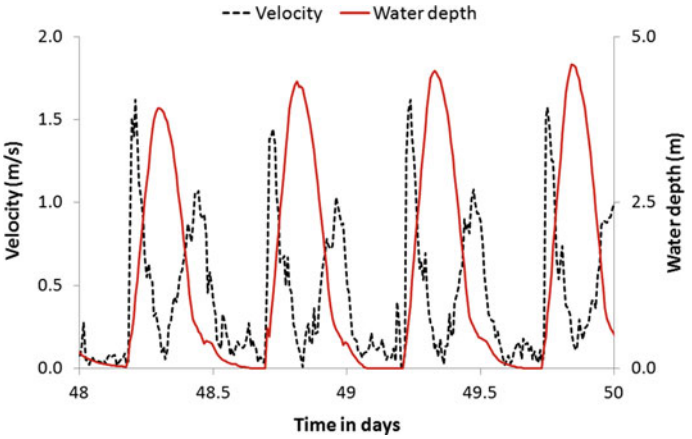

Fig. 16 Water height in m and current velocity during 2 days (zoom for spring tides)

between 200° in flow et 30° in ebb. Flows are generally stronger than ebbs except at certain times where both are almost equal.

Considering spring tides only, we present in Fig. 16 the evolution of water height during two days.

In Sect. 5, computations are done with schematic tides. To be closer to the real case, the same method is applied to real data of water height and current velocity. Efficiency is applied with two hypothesis for initial net height (0.5 and 1 m). The net heights are chosen lower than in Sect. 5 because the analysis of measurements in Fig. 16 shows that the peaks of current velocity and therefore of sediment transport occur between 0.5 and 1 m.

Figures 17 and 18 show the evolutions of the efficiency on a cycle of spring and neap tides for two options of raising of the nets:

– Initial height of 1 m and final height of 2 m (after raising) in Fig. 17.
– Initial height of 0.5 m and final height of 1 m (after raising) in Fig. 18.

For option 1 in Fig. 17, efficiency is small and around 30% for spring tides. The average efficiency on 20 days is 9%. Efficiency is more important for option 2 with the initial height of 0.5 m. Table 3 sums up the average efficiency for different configurations of initial and final net heights. Results show that it is not necessary to use a net higher than 2 m.

The differences between our analytical calculation and the calculation based on the measurements result essentially from tidal currents. The analysis of the measurements shows that the peaks of velocities and thus of sediment transport occur when the water level is situated between 0.5 and 1 m. Thus the observations of currents are of a precious help to examine finely the interest of the raising of the nets.

Increase of deposit if therefore assessed between 10 and 100%. Uncertainty remains large because:

– The burial of nets is unknown;

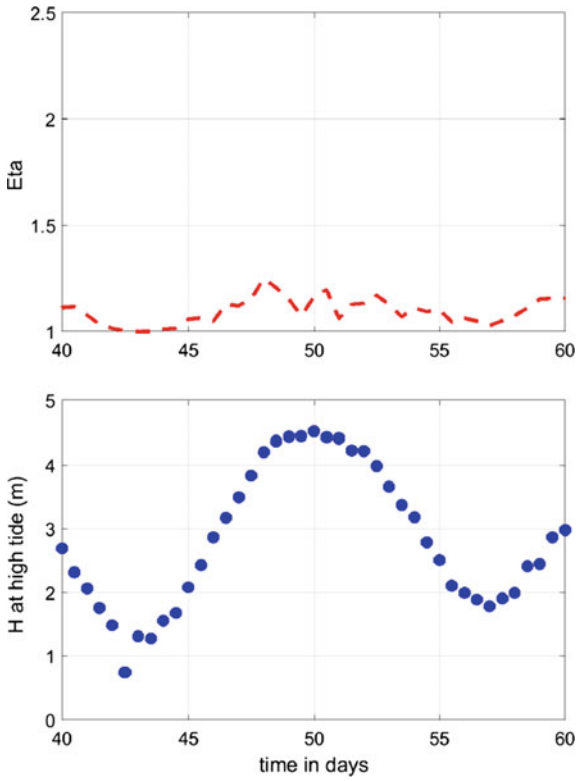

Fig. 17 Efficiency and water height for option 1

– Measured currents maybe do not represent accurately the currents in front of nets;
– The EH formula remains approximate.

The observation of bathymetry is done with a depth sensor that is mounted on a floating support with a GPS. The zone is covered in two hours with a boat on a rectangular grid of 300 m by 200 m. Two surveys were carried out: 11th of May 2017 before the last raising of the nets and 10th of August 2017 three months after.

Figure 19 shows the bathymetry of 11th of May 2017. The difference between the two bathymetries in Fig. 20 presents a clear trend of deposit, in particular in the West of nets. Other zones of evolutions are observed, in particular zones of erosion in the vicinity of the deposit.

The survey is completed by pictures that show a stability of the intertidal zone during this period of three months.

The cross-shore profiles show during a longer period a general trend of erosion that is slightly reduced in the zone behind the nets.

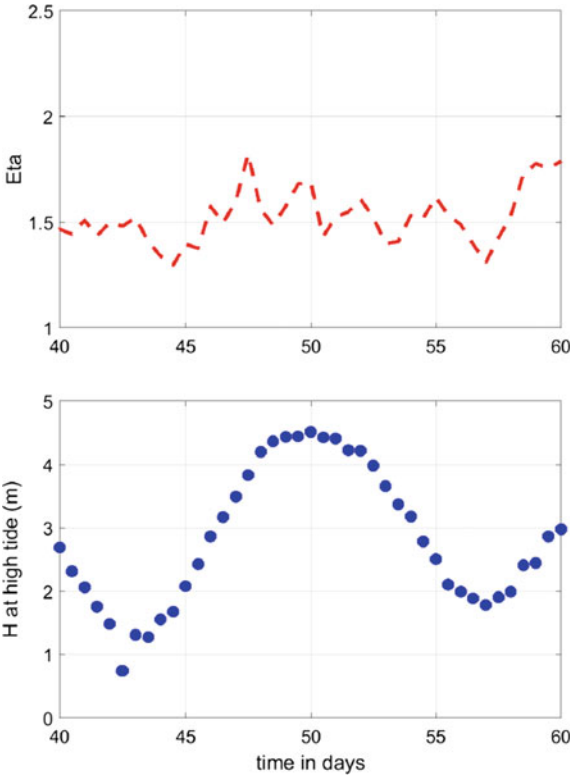

Fig. 18 Efficiency and water height for option 2

Table 3 Efficiency of the raising of the nets with real data

	Final height of the nets	1 m (%)	2 m (%)	3 m (%)	4 m (%)
Initial height of the nets	h = 1 m	–	9.24	9.84	9.95
	h = 0.5 m	51.24	65.54	66.47	66.65

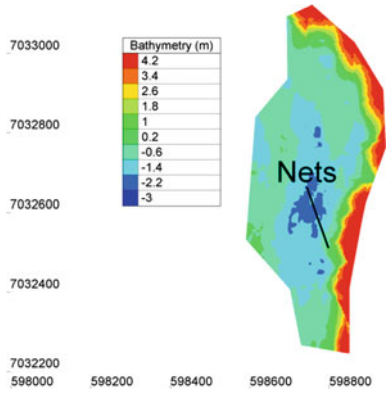

Fig. 19 Bathymetry in m NGF IGN 69 (general levelling of France) on 11th of May 2017 before the last raising of the nets

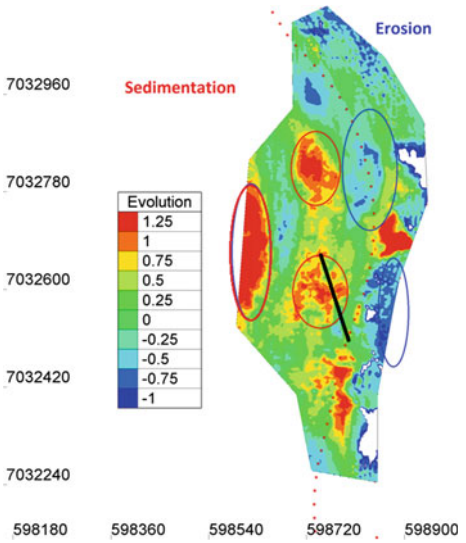

Fig. 20 Difference of bathymetry in m between 10th of August 2017 and 11th of May 2017

7 Modelling

The modelling of the effects of nets on the flow and sediment transport must be done on three different scales:

- The local scale of the knots inside the nets with observation of individual drag forces and wake effects of the knots and ropes on the flow;
- The medium scale around the nets with observation of the vertical profile of current velocities and the process of sand trapping;
- The large scale with introduction of the head loss due the nets and the process of shielding effect.

On local scale, the RANS Fluent model of ANSYS is used with a non-compressible fluid without volumic forces except gravity. The free fluid surface is supposed to be fixed. The input current velocity and the input pressure are imposed. We consider firstly that the top of the net is at the free surface.

The configuration of nets is as follows.

The diameter of rope is around 0.6 mm and the maximal distance between two adjacent ropes is 2 mm (see Fig. 21). The solidity is around 60% and is therefore smaller than in situ.

In order to analyse the effect of two or three successive nets, a wake study is necessary in order to maximise the head loss.

Three horizontal velocity lines are selected in order to study the effect of wake behind ropes and knots. The wake zone corresponds to the distance for which the current velocity comes back to the initial velocity after the nets. The wake dimension is in Fig. 22 of 25 cm. The following net must therefore be placed at a distance superior to 25 cm in order to maximise the total head loss.

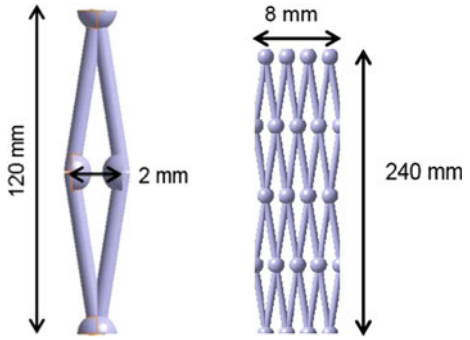

Fig. 21 Configuration of nets

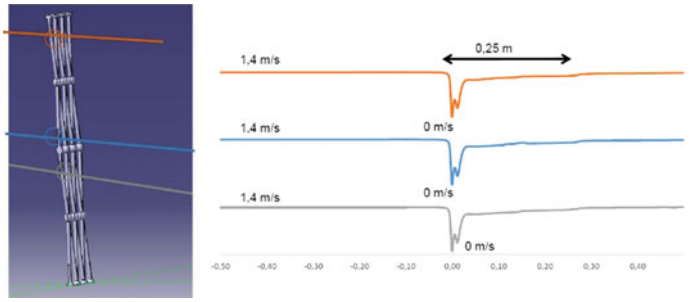

Fig. 22 Wake zone behind the nets

To assess the singular head loss coefficient through the net, the following formula is used:

$$\Delta P = \frac{1}{2} k \gamma_w V^2 \tag{17}$$

ΔP is the difference of pressure between the input and the output (in Pa) and k is the coefficient of head loss.

We show in Table 4 that the coefficient of head loss increases with the number of nets if the successive nets are not in the wake zone. This result confirms the experimental investigation of Bi et al. (2013) with 4 parallel nets. It has been shown also with another configuration that the solidity plays an important role in the head

Table 4 Coefficients of head loss for vertical nets

Number of nets	Position of nets	Coefficient of head loss
1	–	2.2
2	Out of wake zone	6.4
3	In wake zone	3.9
3	Out of wake zone	8.8

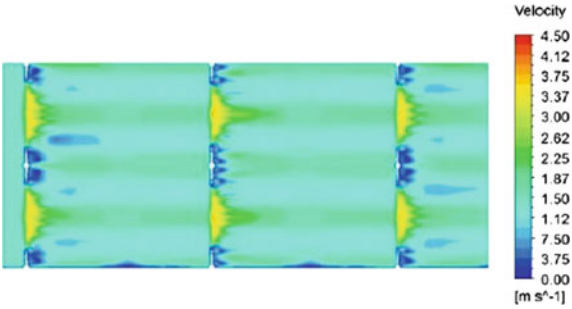

Fig. 23 Wake zone with three nets with d = 0.18 m

Table 5 Coefficients of head loss for the "tepee" shape

Number of nets	Position of nets	Coefficient of head loss
3	Tepee	3.9

loss. Figure 23 with three nets shows that the velocity increases by a factor three in the holes and that the chosen distance d = 0.18 m is not sufficient to suppress totally the wake effect.

In situ the shape of the nets is the "tepee". We have therefore studied the impact of the angle of the nets on the head loss. The tepee is made by linking three nets at the top (Table 5).

We observe that the head loss is superior to that of a simple net, but lower than the modelling with three nets out of wake zones. This is due to the fact that at the top of the tepee, the distance of wake is not respected and thus the head loss in this area remains reduced. We can see in Fig. 24 that the wake zones appear again, however they are perturbed by the geometry.

We test now the effect of a hole in the outer net of the tepee. Figure 25 presents the net with a hole in a loose configuration (left) and in the tight configuration (right) that is chosen is this work.

As we suppress a surface of nets, we observe a slight reduction of the coefficient of head loss that will decrease the shielding effect of the system. On the other hand, we see in Fig. 26 that we increase the flow at the bottom. This flow will bring a large volume of sediments that will then be trapped by the two other nets. The vertical position of the hole is still in discussion because a low hole is efficient for pulling

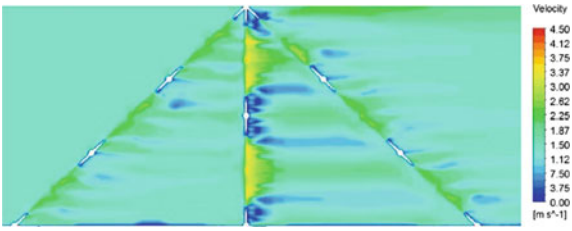

Fig. 24 Wake zone with the tepee

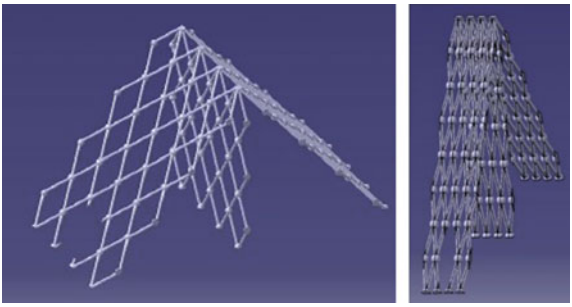

Fig. 25 Tepee with a hole in a loose configuration (left) and in the tight configuration (right)

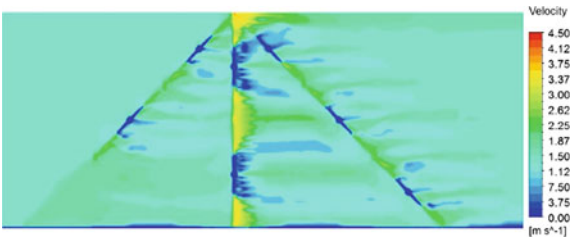

Fig. 26 Wake zone with the tepee and a hole

Table 6 Coefficients of head loss for the "tepee" shape with a hole

Number of nets	Position of nets	Coefficient of head loss
3	Tepee with a hole	3.5

the sediments inside the tepee but a high hole will also increase the vertical gradient of current velocity (Table 6).

This work is completed by a study at a medium scale. There is now water above the nets. That means that the net height (2 m) is smaller than the water height (3 m).

With a net solidity around 0.25 Bi et al. (2013) have observed a flow reduction downstream from a fishing net around 10% that approximately remains the same in different currents.

We present here the results with a higher solidity of 0.60 with an upstream velocity of 1.2 m/s. The general pattern of wakes is presented in Fig. 27. We observe first in Figs. 28 and 29 that wakes provoke oscillations of velocities downstream of 0.7 m/s of amplitude around the average velocity on the profile 0.05 m downstream. This amplitude decreases rapidly to 0.4 m/s (0.10 m downstream), 0.2 m/s (0.25 m downstream) and almost 0 m/s (0.50 m downstream).

We observe also in particular in Fig. 29 that the current velocity above the bottom is the input velocity of 1.2 m/s and that it decreases linearly up to the top of the net to 1.0 m/s i.e. a maximal reduction of current velocity of 15%. Just above the net, an acceleration of the flow is observed that decreases slightly up to the free surface.

These results confirm the possibility of sand trapping through the nets with the reduction of current velocity that can be increased by two means: multiplying the nets and increasing the net solidity.

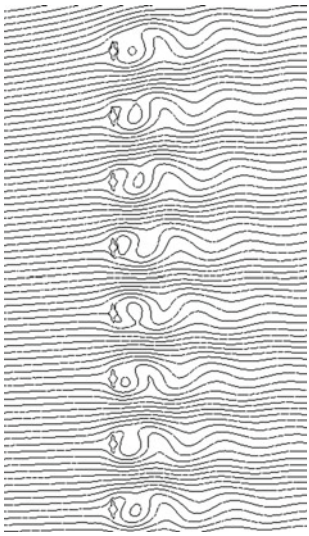

Fig. 27 Wakes behind the nets

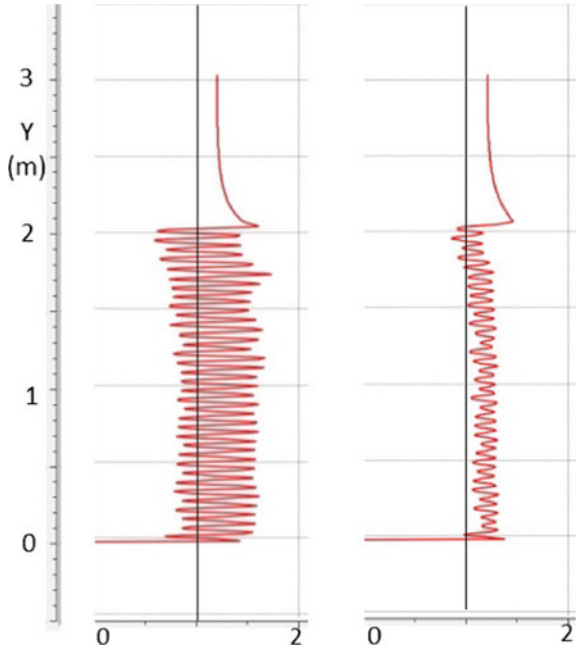

Fig. 28 Horizontal component of current velocity along a vertical profile with 0.1 m downstream (left) and 0.25 m downstream (right)

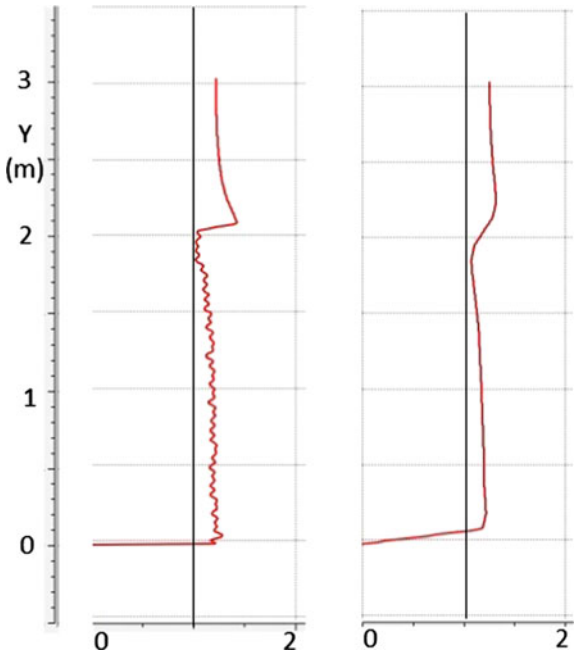

Fig. 29 Horizontal component of current velocity along a vertical profile with 0.5 m downstream (left) and 5 m downstream (right)

8 Conclusion

A device composed of nets and developed by the company S-Able has been experimented in the estuary of Authie River in a specific position of groyne in order to prevent dune erosion by river meandering.

We have shown firstly that, if we want to increase the shielding effect of the nets, we must increase the head loss and therefore increase the solidity of the nets and increase the height of the nets.

Sand trapping is secondly an additional effect of the net. Due to the deceleration of the flow through the nets, a sand deposit occurs behind the net that is considered as a porous medium. We have shown that the influence of the net height is limited for sand trapping.

The observations of two bathymetries in May and August 2017 indicates a clear trend of deposit in the vicinity of the nets.

The results of modelling confirm that the combination of nets is an efficient option regarding the head loss if the inter-nets distance is sufficient. The tepee configuration remains an interesting configuration even if the head loss is slightly reduced.

The vertical profiles show that the wake effect is observed on a distance of 25 cm downstream and that the reduction of current velocity behind the net can reach 15% up to 5 m downstream.

Acknowledgements We thank Jean-Claude Borger, Jean-Bernard Loiseau and Stéphane Brimeux for the data of DDTM 62, François-Xavier Clerc and Patrick Queval for the pictures and their help for the installation of the current sensor. Floccari Kevin, Youcef Medelfef, Quentin Royo, Clément Guillaume and Julien Avril have also brought their help to this work.

References

Bi, C. W., Zhao, Y. P., Donga, G. H., Xua, T. J., & Guib, F. K. (2013). Experimental investigation of the reduction in flow velocity downstream from a fishing net. *Aquacultural Engineering, 57,* 71–81.

Boucher, O., Pham Van Bang, D., Sergent, P., & Michon D. (2014a). Etude en modèle réduit de l'impact de filets 3D sur la dynamique sédimentaire en zone côtière. In *Proceedings of 13th Journées Génie Civil Génie Côtier, Dunkerque*.

Boucher, O., Sergent, P., & Michon D. (2014b). Défense de berge par un dispositif de filets. In *Proceedings of Small Scale Morphological Evolution of Coastal, Estuarine and River Systems, Local Processes, Bank Erosion and Meandering, Nantes*.

Engelund, F., & Hansen E. (1972). A monograph on sediment transport in alluvial streams. In *TEKNISKFORLAG Skelbrekgade 4 Copenhagen V, Denmark.*

Michon, D. (2017). Dispositif et système de protection contre l'érosion du littoral. In *European Patent EP 2585640 B1 2017-09-06*.

Ouahsine, A., Smaoui, H., Meftah, K., Sergent, P., & Sabatier, F. (2013). Numerical study of coastal sandbar migration, by hydro-morphodynamical coupling. *Environmental Fluid Mechanics, 13–2,* 169–187.

Poizot, E., Verjus, R., Nguyen, H. Y., Angilella, J. R., & Méar, Y. (2016). Self contamination of aquaculture cages in shallow water. *Environmental Fluid Mechanics, 16–4,* 793–805.

Thual O. (2010). Hydrodynamique de l'environnement (2010). In éditions de l'Ecole Polytechnique.

Physical Modeling of Extreme Waves Propagating from the Open Sea to the Coastal Zone

Iskander Abroug, Nizar Abcha, François Marin and Armelle Jarno

Abstract The evolution of solitary wave along the flume is investigated. Experiments were conducted in a smooth, rectangular sloping flume. Solitary waves are generated using a piston-type wave maker. These type of waves are generated by impulsive mechanism, close to the generation zone, their profile contains both elevation and depression components. These depressions are attached to the main solitary wave along the flume during the propagation. The main hydraulic parameters investigated are: energy damping along the flat bottom, wave height evolution on the slope (shoaling), breaking process and runup heights. It was found that experimental results are almost in good agreement with earlier studies. An empirical formula for runup heights determination is suggested. A good way for tracking the evolution of a solitary wave on flat and sloping bottom is presented thanks to spatiotemporal diagram. It is noted that for better accuracy, especially when investigating breaking, it is better to use camera.

Keywords Extreme waves · Solitary waves · Shoaling · Energy damping · Breaking waves · Runup

Notation

A_0	Amplitude of solitary wave 3 m form the wave maker, m
A_1, A_2	Wave heights in water depths h_1 and h_2, m
A_b	Breaking height, m
A_s	solitary wave amplitude, m
A_t	Amplitude of solitary wave at the toe of the beach, m
$C_{gr} = {}^{d\omega}/_{dk}$	Group velocity corresponding to the main solitary wave, m.s^{-1}

I. Abroug (✉) · N. Abcha
Normandie Université, UNILEHAVRE, CNRS, UMR 6294 LOMC, 76600 Le Havre, France
e-mail: iskander.abroug@unicaen.fr

F. Marin · A. Jarno
Normandie Université, UNICAEN, UNIROUEN, CNRS, UMR 6143 M2C, 14000 Caen, France

K. D. Nguyen et al. (eds.), *Estuaries and Coastal Zones in Times of Global Change*, Springer Water,
https://doi.org/10.1007/978-981-15-2081-5_34

E	Energy on a unit length in the direction transversal in the direction of wave propagation, J
g	Acceleration of gravity, m.s^{-2}
h_0	Stillwater depth, m
h_b	Breaking depth, m
L_0	Wave length scale, m
R	Runup height, m
S_0	Slope parameter
T	Duration of impulse, s
$\beta = 0.04$	Slope, rad
$\varepsilon = A_0/h_0$	Non linearity parameter (1)
$\varepsilon' = A_t/h_0$	Non linearity parameter (2)
η	Free surface elevation, m
$<\eta>$	Mean water level, m
ρ	Water density, 1 g.cm^{-3}

1 Introduction

Giant waves or extreme waves correspond to waves of very high amplitude, appearing mainly on high seas (Kharif and Pelinovsky 2003). These waves may be accompanied by deep troughs that may appear before or after the highest peak. This type of wave has been a mythical phenomenon in the marine environment for centuries. Extreme waves occur in basins of different depths (deep and shallow) with and without current. One of the first people who observed this phenomenon was the captain and naval officer of an expedition in 1826 Dumont d'Urville. He said that he saw waves of 30 m high and he was ridiculed at that time. These waves with abnormally high amplitude occur not only on high seas, but also in the coastal zone. If these waves have been studied in open ocean, they are little studied in the coastal zone. One of the possible mechanisms for the appearance of unusually high waves at the littoral level is associated with the transformation of theses waves propagating from the open ocean to the shore. The study of such a mechanism is an important issue as these waves can notably have a significant impact on sediment transport and erosion of the seabed in the coastal zone (Strusińska-Correia and Oumeraci (2012).

These waves are due to a large variety of physical mechanisms (Kharif and Pelinovsky 2003). Among others, one may cite solitary waves. The first description of this non-linear wave phenomenon was made by John Russel (1845) who observed a boat trained rapidly by a pair of horses in a channel at Hermiston. When the boat suddenly stopped, Russel noted that a wave having the shape of a lonely high altitude is continuing its course along the channel apparently without a change in shape (Russel 1845). Boussinesq (1871) derived a mathematical expression for the solitary wave profile generated on a horizontal, rectangular channel. Therefore, solitary

waves are traditionally used as tsunami waves approximations because of the hydrodynamic similarity between them (e.g. Hsiao and Lin (2010)). For instance, there exist several laboratory modeling which investigated Shoaling (Camfield and Street (1969), Kishi and Saeki (1966)) and runup of solitary waves (e.g. Synolakis (1987), Li and Raichlen (2001), Zelt (1991)). Gradual damping was investigated by Keulegan (1948) and Daily and Stephan (1952). Synolakis and Skjelbreia (1993) investigated the amplitude evolution of breaking solitary waves on a plane beach. They found that the complete amplitude evolution can be divided into four regions (especially in the case of smooth slopes). Synolakis (1991) confirmed mathematically that, the solitary wave amplitude before breaking, can be perfectly modelled by green's law.

The chapter is organized as follows. Section 1 describes the experimental set-up. Section 2 is devoting to present results for solitary wave: Shoaling, energy dependence, Breaking and runup. Discussions and conclusions are presented in Sect. 3.

2 Experimental Set-up

Experiments were carried out in a wave flume of the coastal and continental morphodynamics Laboratory at Caen University, France. The flume is 20 m length and 0.8 m width. An Edinburgh designs Ltd piston-type paddle was used to generate waves. Waves propagate through uniform water depth to a 1/25 sloping beach, at the other end of the flume.

Its side walls are made of glass. The beach toe is located 9.5 m from the wave maker. Flume bottom is elevated 1.15 m from the ground to ease the visualizations from sides. Free surface elevations were measured by resistance waves gauges. Mainly three wave gauges have been used. Gauges 1 and 2 have been used to plot the space-time diagram DST (more details in next section) and gauge 3 is used for measuring free surface elevation at the toe of the beach. Waves of different spectrum and amplitudes are generated in the flume under conditions of deep water and shallow water. To generate surface waves in the flume, a computer controlled wavemaker is used. A schematic sketch of this experimental setup is shown in Fig. (1).

In order to confirm repeatability, surface elevation measurements at the same location have been conducted. Differences were less than 2%. However, tests are less repeatable once the wave breaks down due to the entrapped compressed air present during the breaking process.

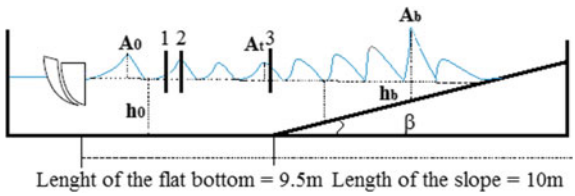

Fig. 1 Sketch of experimental setup

The governing parameters include the Stillwater depth h_0, the local water depth h, the initial solitary wave amplitude A_0, the local solitary wave amplitude A, the free surface elevation η, the wave amplitude at breaking A_b, the corresponding water depth h_b and run-up height R.

A high-speed camera was used for tracking the wave features, such as breaking process and run-up. The camera was operated with a 30 Hz acquisition frequency.

3 Results

3.1 Wave Profile

To test the ability to generate experimentally steep solitary waves, a comparison with a nonlinear solution obtained theoretical by Boussinesq approximation is shown in Fig. 2 for $\varepsilon = A_0/h_0 = 0.24$. One can observe an excellent agreement between the experimental and theoretical solutions. Note that, the experimental profile presents a very weak dispersive tail.

To generate solitary waves, Goring (1979) used derived Boussinesq's first order solution (Eq. 1)

$$\eta(\xi) = \eta(x - Vt), \tag{1}$$

$$\eta(\xi) = A_s \cosh^{-2}\left(\sqrt{\frac{3A_s}{4h_0^3}}(x - Vt)\right)$$

$$V_s = V_0\left(1 + \frac{A_s}{2h}\right), with V_0 = \sqrt{gh} \tag{2}$$

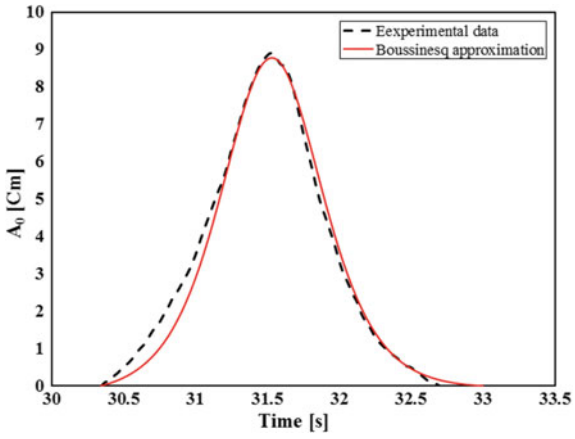

Fig. 2 Comparison between theoretical and experimental solitary wave form

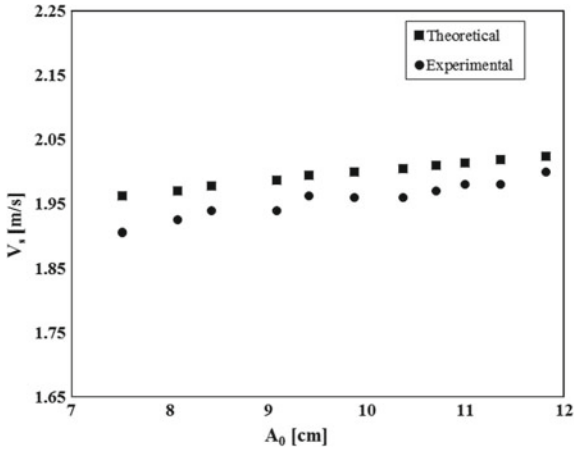

Fig. 3 Comparison between theoretical and experimental solitary velocity

where η is free surface displacement A_s is solitary wave amplitude, V_s is theoretical solitary wave velocity, and A_0, A_t the amplitude of solitary wave 3 m from the wave maker and at the toe of the beach respectively.

Comparison between theoretical (Eq. 2) and experimental solitary wave velocities have been also obtained (Fig. 3).

3.2 Shoaling and Energy Dependence

Shoaling

The free surface elevations at different locations along the flume were recorded thanks to capacitance wave gauges (gauge 1 and 2, figure). Indeed, free surface instantaneous components can be overlaid chronologically at regular time intervals in order to obtain space-time diagrams. After having processed all the signals corresponding to the acquisition points along the entire length of the channel, they are put together in a matrix which will constitute the source file describing the evolution of free surface elevation along the flume.

An example of this diagram is shown in Fig. (4). In this diagram, the evolution of the amplitude of the wave $A_0/h_0 = 0.28$, and the width of the solitary wave along the channel are well described. A very weak dispersive tail observed behind the main solitary wave.

The solitary wave has a symmetric profile along the flat bottom. When it reaches the slope, the wave height increases and the shape became more and more asymmetric (Fig. 5).

Synolakis and Skjelbreia (1993) addressed that the wave amplitude evolution of a breaking solitary wave on a sloping beach can be divided into four zones for both plunging or spilling breakers. They termed the zones of gradual shoaling and

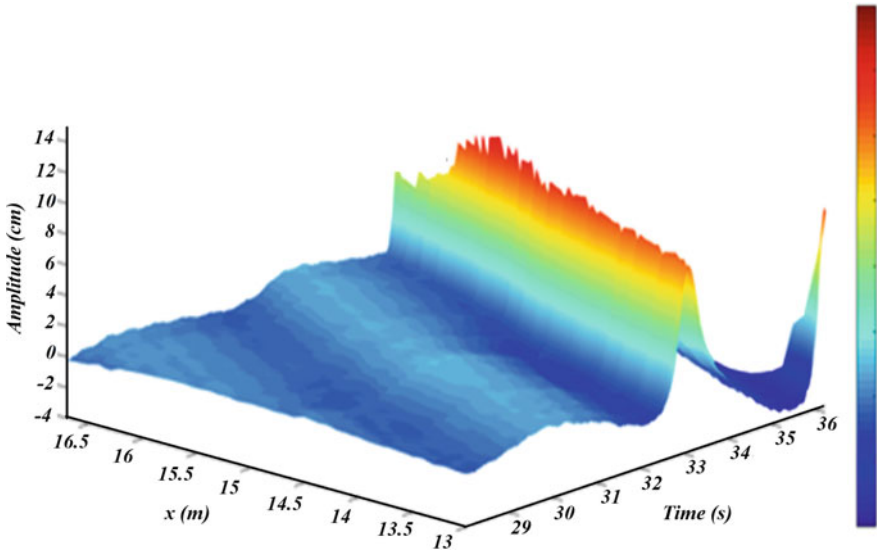

Fig. 4 Zoom in on main solitary wave; $A_0/h_0 = 0.28$

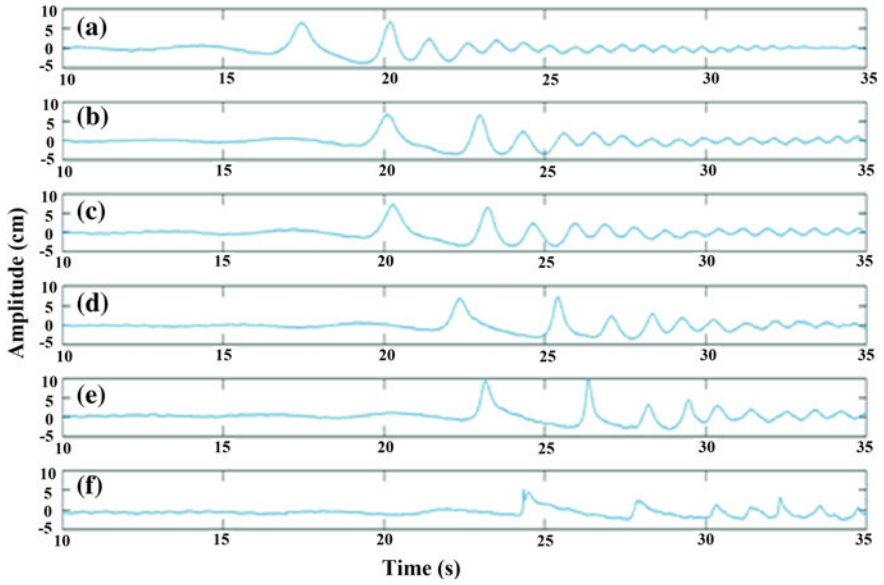

Fig. 5 Solitary wave form evolution: instantaneous signals at different distances from the wave maker; **a** 6 m; **b** 8 m; **c** 10 m; **e** 12 m; **f** 14 m

rapid shoaling before the breaking point, and named the zones of rapid decay and gradual decay inside the surf zone. In particular, in each zone the maximum local wave elevation can be adequately described by a simple power-law-type formula as a function of absolutely spatial location with a normalization of breaking water depth for convenience (Synolakis and Skjelbreia 1993).

In this study experimental amplitudes amplifications were compared to the following shoaling relationship based on linear long waves (Green's law):

$$\frac{A_1}{A_2} = \left(\frac{h_1}{h_2}\right)^{-1/4} \tag{3}$$

where A_1 and A_2 is wave heights respectively in water depths h_1 and h_2.

Figure 6 shows that Green's law describes quite good amplitude evolution on the slope.

When the crest velocity overtakes the solitary wave celerity, the wave breaks. By zooming in on the DST, position and height of breaking can be identified. In practice it is better to zoom in as much as possible and detect the brutal change

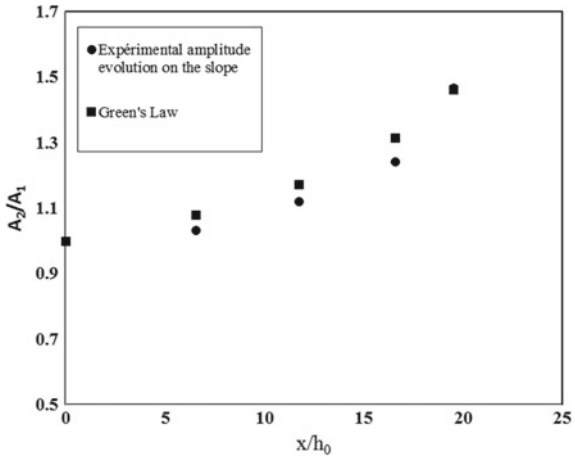

Fig. 6 Amplitude evolution on the slope for $A_t/h_0 = 0.26$ and comparisons with Green's Law

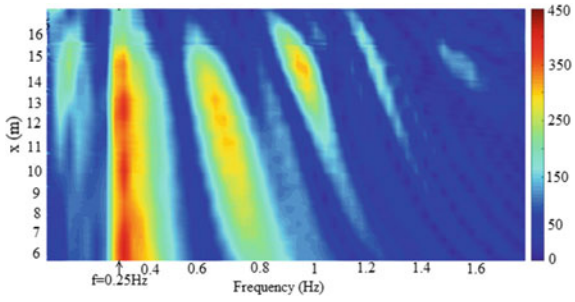

Fig. 7 Spectrogram of complete solitary wave signal; $A_0/h = 0.28$

Table 1 Height and distance of breaking; comparisons between DST and camera measurement

A_t/h_0	X_b (Camera)	X_b (DST)	A_b (Camera)	A_b (DST)
0.21	587	[580; 590]	9.32	8.91
0.24	558	[540; 550]	10.31	10.01
0.27	532	[530; 540]	11.15	10.70
0.31	514	[510; 520]	11.66	11.15

in amplitude (Fig. 4). The DST is a good way to get a better overview of what is happening along the flume, before and after shoaling. On the other hand, the video visualization gives a good resolution of locally water surface elevation. Therefore, when investigating breaking height and distance, the camera is a better solution. Table 1 summarize comparisons between DST and video visualization results. One can see that, breaking heights are slightly underestimated when DST is used.

Energy dependence

Energy dependence have been investigated on the flat bottom and on the slope. Indeed, for this, Eq. 4, given by Tian et al. (2010), have been used to calculate the energy of the solitary wave on the flat bottom and in a given abscissa.

$$E = \frac{\rho g}{2} C_{gr} \int \left((\eta - < \eta >)^2 dt \right) \tag{4}$$

where $C_{gr} = \frac{d\omega}{dk}$ is the group velocity corresponding to the main solitary wave, g for acceleration of gravity, ρ water density, T duration of impulse, η and $<\eta>$ are free surface displacement and mean water level, respectively.

The experimental analysis of the damping of solitary waves, shows that the experimental coefficient of damping depends on the amplitude of the crest.

Indeed, it is shown in Fig. (8) that dissipation factor decreases linearly from 17% for lower solitary wave amplitude up to 4% for higher wave amplitude. This has been proved also experimentally by Ippen and Kulin (1954). When the solitary wave reaches the slope and before breaking, the celerity decreases, the height of the crest increases and the total energy is approximately conserved. (Li and Raichlen 2002). Beyond breaking point, kinetic and potential energy decrease. This energy loss ends when the runup process starts. The spectrogram (Fig. 7) shows that the spectrum density ($f_{excitation} = 0.25$ Hz) of the main solitary wave ($A_0/h_0 = 0.28$) is conserved up to breaking which occurs in approximately x = 15 m. One can see a second band around 0.7 Hz which correspond to the spectrum density of the wave generated by the piston pullback. In term of intensity this band and small bands which come after (1 and 1.25 Hz) are less important when compared to the main band. Therefore, '' super harmonics" waves do not have an impact on the shoaling phenomenon and on the runup of the main solitary wave. Moreover, higher frequency waves travel slower than lower frequency waves and reaches the shore after the solitary wave (Orszaghova et al. (2014). This band is a little bit inclined when compared to the

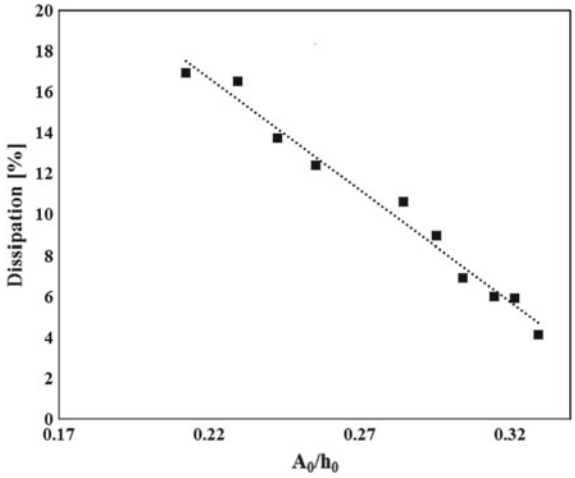

Fig. 8 Dissipation factor decrease

main spectrum. When propagated along the flume, this band tends to get closer to the solitary wave spectrum. This inclination is due to the instable form of the wave generated by the pullback of the piston. On the other hand, it is also shown that a band around 0.15 Hz, which correspond to low frequency waves, appeared especially when the slope starts. These subharmonic waves are present along the flume. They are amplified when arriving on the slope (Shoaling). However, in term of spectral density intensity they are approximately three times less energetic than the main solitary wave. Therefore, we consider that subharmonic wave effect is not significant, and is neglected in this study.

Breaking

Grilli et al. (1997) and Synolakis (1987) have defined a breaking criterion. Indeed, they suggested two thresholds (Eqs. 5 and 6 respectively) that predict if the incident solitary wave is a breaking wave or not.

$$\varepsilon' = \frac{A_t}{h_0} = 16.9\beta^2 = 0.027 \tag{5}$$

$$\varepsilon' = \frac{A_t}{h_0} = 0.818\beta^{\frac{10}{9}} = 0.023 \tag{6}$$

where $\beta = 0.04$ is defined as the inclination of beach slope, $\varepsilon' = A_t/h_0$ is nonlinearity parameter. Nonlinearity parameter of solitary waves generated during this study are between $\varepsilon = 0.15$ and $\varepsilon = 0.35$. Therefore, all waves generated are breaking waves.

Nonlinearity parameters (ε) have been used to predict breaking characteristics such as breaker type. Indeed, Grilli et al. (1997) and Yasuda et al. (1992) suggested empirical parameters of breaking type (Eqs. 7 and 8 respectively):

$$S_0 = \frac{sL_0}{h_0} = 1.521\frac{\beta}{\sqrt{\varepsilon}} \tag{7}$$

$$With : L_0 = \frac{2h_0}{3\varepsilon'/4} ar\tanh\frac{\sqrt{3}}{3}$$

$$S_0 = \frac{\beta}{\varepsilon^{0.4}} \tag{8}$$

where S_0 is slope parameter, L_0 is the wave length. Breaking in this study is considered as plunging breaking for all solitary wave amplitudes.

Using a speed camera of high resolution, we followed the evolution of the free surface in space and identified the position of the wave breaking point. Figure 9 illustrates the snapshots of Breaking process of a solitary wave $A_0/h_0 = 0.28$. The vertical tangent to the free surface corresponds to the spatial position of the breaking wave.

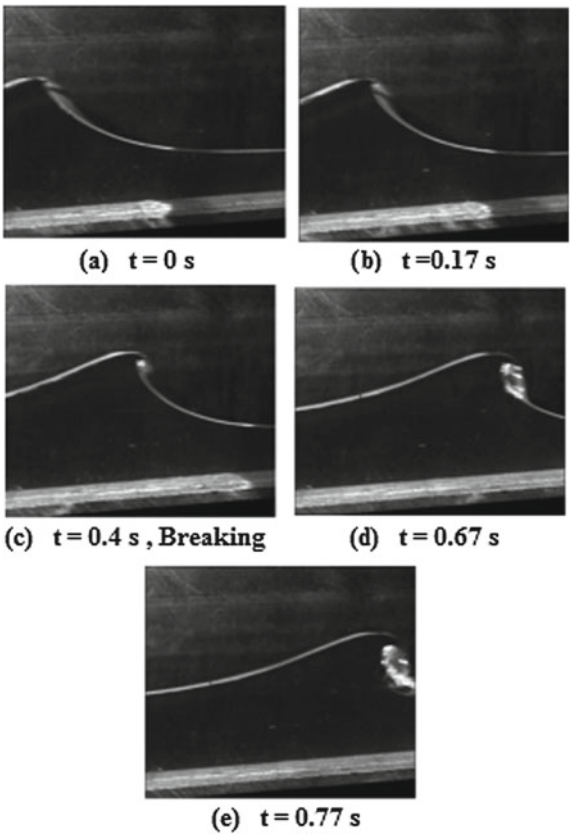

Fig. 9 Snapshots of Breaking process of a solitary wave $A_0/h_0 = 0.28$

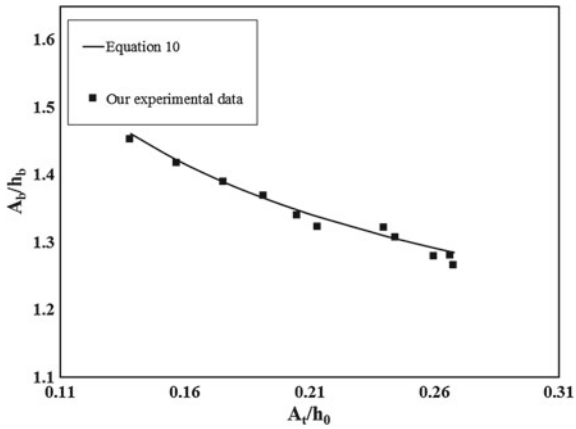

Fig. 10 Breaking height evolution

Figure 10 illustrates the breaking height evolution, A_b/h_b ratio tends to increase with the decrease of A_t/h_0 and this is more pronounced when the slope is large. The dispersion of the points describing the evolution of the ratio A_b/h_b versus A_t/h_0 is greater when the slope increases (Ippen and Kulin 1954).

$$\frac{A_b}{h_b} = 0.75 + 25\beta - 112\beta^2 + 3.870\beta^3 \tag{9}$$

$$\frac{A_b}{h_b} = 0.841\mathrm{e}^{6.421S_0} \tag{10}$$

Grilli et al. (1997), Ippen and Kulin (1954) have suggested empirical formulas based on an average of their experimental results concerning breaking height determination. In Fig. 10, Eq. 10 is also plotted. It is shown that breaking heights in this study matches quiet good with Grilli et al. predictions.

For a given slope and depth, waves of smaller amplitude grow relatively higher and break in lower depths than higher amplitude waves. In Fig. 11, ratio h_b/h_0 versus A_t/h_0 has been plotted. In the same plot, Eqs. 11 and 12 suggested by Grilli et al. (1997) and Hafsteinsson et al. (2017) respectively have been plotted.

$$\frac{h_b}{h_0} = \frac{0.149}{\left(\frac{S_0}{\varepsilon'}\right)^{0.523}} \tag{11}$$

$$\frac{h_b}{h_0} = -0.25\left[1 + \ln\left(\varepsilon'^{-1}\tan\beta\right)\right] \tag{12}$$

It is shown in Fig. 11 that experimental data are in good agreement with Grilli's predictions using Eq. 11 (curve with solid line). On the other hand Hafsteinsson predictions using Eq. 12 (curve with dotted line) underestimate clearly breaking depths.

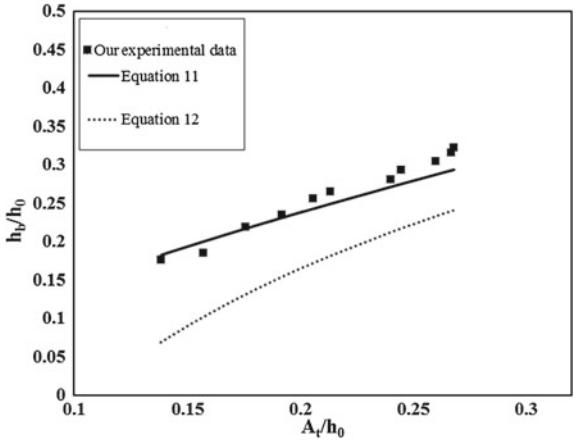

Fig. 11 Breaking distance evolution

3.3 Runup

Measured Runup heights were compared with literature. Figure 12 shows that the steeper slope is, the highest runup bring about on the same wave. The experimental obtained data shows that when $\varepsilon' = A_t/h_0$ increases, run-up height increases, this is due to larger energy content of large solitary wave amplitudes.

There are quite a few semi-empirical formulas. Synolakis (1987) suggested the following empirical formula:

$$\frac{R}{h_0} = 1.0957\varepsilon'^{0.5816} \tag{13}$$

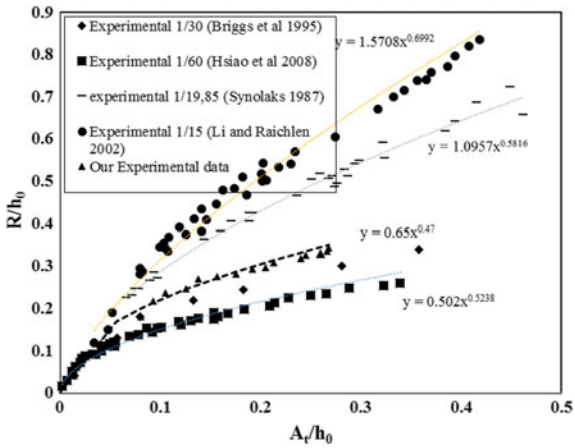

Fig. 12 Runup evolution for different slopes

where R is the maximal run-up amplitude. This formula is exclusively for the slope that Synolakis used (β = 1:19.85).

Many studies have suggested several empirical formulas similar to that of Synolakis (the same form).

$\frac{R}{h} = a\varepsilon'^{b}$, a and b are parameters that vary according to the slope. For our study, an empirical formula is suggested for estimating runup heights for 1:25 slope:

$$\frac{R}{h_0} = 0.65\varepsilon'^{0.47} \tag{14}$$

Hughes (2004) employed the momentum flux parameter to predict maximum runup:

$$\frac{R}{h_0} = (1.39 - 0.027\cot(\beta))\left(\frac{M_F}{\rho g h_0}\right)^{1/2} \tag{15}$$

where $M_f/\rho g h_0$, is the wave momentum flux parameter (This parameter is easily determined in Hughes (2004)). He noted that this equation gives reasonable predictions as far as the slopes are between 1/10 and 1/30 and for $\varepsilon < 0.25$.

Hsiao et al. in 2008 suggested a simple predictive model based on the nonlinear least-square algorithm:

$$\frac{R}{h_0} = 7.712\cot(\beta)^{-0.632}\left(\sin\left(\varepsilon'\right)\right)^{0.618} \tag{16}$$

Equations 15 and 16 predict well maximum runup amplitude for low waves (up to $\varepsilon' = 0.15$)), whereas they over estimate it for ε' higher than 0.2 (Fig. 13). It was mentioned in Hsiao et al. (2008) that Eq. 16 contains no physical meaning, but it

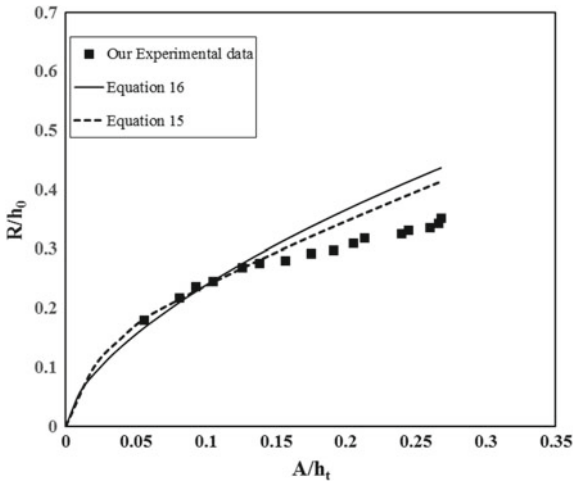

Fig. 13 Maximal run-up amplitude comparisons with Eqs. 15 and 16

gives reasonable maximum runup predictions for a wide range of slopes. It is the case when Eq. 16 is compared to Briggs (1993) who have worked with a 1/30 slope. Agreements are less good when ε' becomes higher than 0.20.

Figure 14 shows that waves with greater amplitude reach runup saturation later than lower wave amplitudes. For this, time for runup saturation is plotted versus solitary wave amplitude (Fig. 15).

Runup velocity was determined by high speed camera. Indeed, a video recording of 30 Hz acquisition frequency was used for each solitary wave. Furthermore, each solitary wave is identified by an only runup saturation height.

Briggs (1993) have plotted the maximal run-up amplitude versus an energy-based parameter using runup speed to reach the associated runup saturation. They suggested a linear relationship that can be used to predict the runup saturation for a known runup velocity.

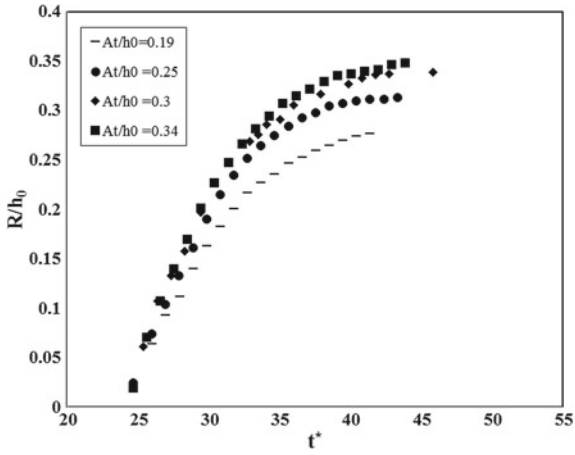

Fig. 14 Runup evolution versus time for 4 different waves

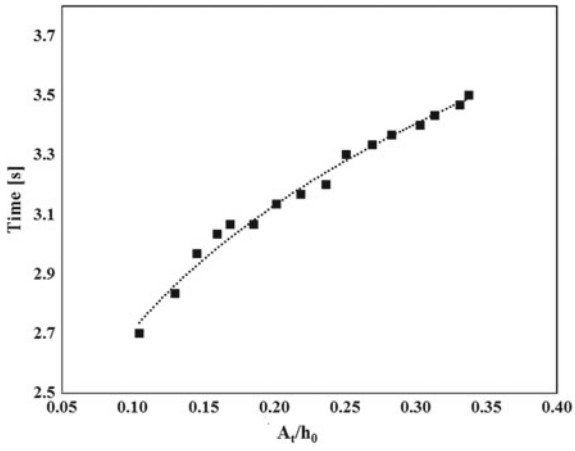

Fig. 15 Time of runup saturation

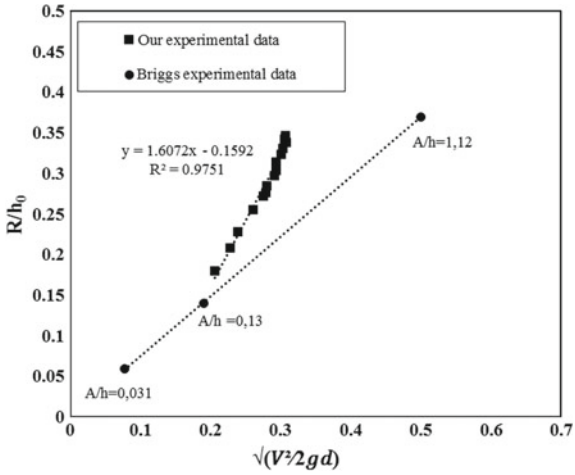

Fig. 16 Runup velocity evolution

$$\frac{R}{h_0} = 0.0013 + 0.7755 \times V \tag{17}$$

In Fig. (16), maximal run-up amplitude versus runup velocities have been plotted. Runup speed for 1:25 slope is greater than that which corresponds to 1:30 slope. This is not true for small wave amplitudes (mainly non-breaking waves). This is due to the energy dissipation which is more important for low amplitudes.

4 Discussions and Conclusions

Variations in wave characteristics for solitary wave in shallow water were discussed. A general idea of the behavior of the solitary wave in both flat and sloping bottom have been given. We found that energetic dissipation of the solitary wave on the flat bottom is related to non-linearity (ε) parameter. In term of energetic intensity, low and high frequency components due to generation mode, are negligible when compared to main solitary wave spectrum. It was found that experimental results are in good agreement with literature. Concerning breaking, it has been shown that empirical formulas given by Hafsteinsson et al. (2017) slightly underestimate breaking distances. This is mainly due to different experimental setup. Indeed, in Hafsteinsson et al. (2017) study, wavemaker was situated at the toe of the beach ($V_s = 0$ m.s^{-1}). When compared to this study, solitary wave reaches the slope with a non-null velocity. Therefore, solitary waves breaks in shallower water in Hafsteinsson et al. (2017) studies.

This present study on the propagation of individual solitary wave representing the main component of a tsunami waveform should be extended to include other experimental generation mode. Indeed, future research needs to be focused on laboratory

investigations of waveforms composed of group focused waves. The challenge is to compare these two types of generation.

References

Boussinesq, M. H. (1871). Théorie de l'intumescence liquide, appelée onde solitaire ou de translation, se propageant dans un canal rectangulaire. *C. –R. Academic Science Paris*, 72 p.

Briggs, J. M. (1993). Laboratory measurements of Tsunami Run-up. In *Conference: IUGG/IOC International Tsunami '93 Symposium, At Wakayama, Japan* (Vol. 1).

Camfield, F. E., & Street, R. L. (1969). Shoaling of solitary waves on small slopes. *Journal of Waterway and Harbor Division, ASCE, 1,* 1–22.

Daily, J. W., & Stephan, S. C. (1952). The solitary wave: Its celerity, profile, internal velocities and amplitude attenuation in a horizontal smooth channel. In *Proceedings of 3rd Conference of Coastal Engineering* (pp. 13–30).

Goring, D. G. (1979). *Tsunami-the propagation of long waves onto a shelf,* (*Ph.D. thesis*). California Institute of Technology, Pasadena, Calif.

Grilli, S. T., Svendsen, I. A., & Subramanya, R. (1997). Breaking criterion and characteristics for solitary waves on slopes. *Journal of waterway, Port, Coastal, and Ocean Engineering, 123*(3), 102–112.

Hafsteinsson, J. H., Evers, M. F., & Hager, H. (2017). Solitary wave run-up: Wave breaking and bore propagation. *Journal of Hydraulic Research, 55*(6), 787–798.

Hsiao, S. C., & Lin, T. C. (2010). Tsunami-like solitary waves impinging and overtopping an impermeable seawall: Experiment and RANS modeling. *Journal of Coastal Engineering, 57*(1), 1–18.

Hsiao, S. C., Lin, T. C., & Chang, Y. H. (2008). On the evolution and run-up of breaking solitary waves on a mild sloping beach. *Coastal Engineering, 55*(12), 975–988.

Hughes, S. A. (2004). Estimation of wave run-up on smooth, impermeable slopes using the wave momentum flux parameter. *Coastal Engineering, 51,* 1085–1104.

Ippen, A. T., & Kulin, G. (1954). The shoaling and breaking of the solitary wave. In *Coastal Engineering Proceedings*.

Keulegan, G. H. (1948). Gradual damping of solitary waves. *Part of the Journal of Research of the National Bureau of Standards, 40,* 487–498.

Kharif, C., & Pelinovsky, E. (2003). Physical mechanisms of the rogue wave phenomenon. *European Journal of Mechanics B, 22,* 603–635.

Kishi, T., & Saeki, H. (1966). The shoaling, breaking and runup of the solitary wave on impermeable rough slopes. In *Proceedings of the 10th Conference on Coastal Engineering,* (I, pp. 322–348).

Li, Y., & Raichlen, F. (2001). Solitary wave runup on plane slopes. *Journal of Waterway, Port, Coastal, and Ocean Engineering, 127*(1), 33.

Li, Y., & Raichlen, F. (2002). Non-breaking and breaking solitary wave runup. *Journal of Fluid Mechanics, 456,* 295–318.

Strusińska-Correia, A., & Oumeraci, H. (2012). Nonlinear behavior of Tsunami-like solitary wave over submerged impermeable structures of finite width. *Coastal Engineering Proceedings*, ICCE, Vol. 33, Currents.6

Orszaghova, J., Taylor, H. P., Borthwick, A. G. L., & Raby, A. C. (2014). Importance of second-order wave generation for focused wave group run-up and overtopping. *Journal of Coastal Engineering, 94,* 63–79.

Russel, J. S. (1845). Report on waves. In *Proceedings 14th Meeting British Association for the Advancement, 1845* (pp. 311–390).

Synolakis, C. E. (1987). The runup of solitary waves. *Journal of Fluid Mechanics, 185,* 523–543.

Synolakis, C. E. (1991). Green's law and the evolution of solitary waves. *Journal of Physics of Fluids A: Fluid Dynamics, 3*(3), 490–491.

Synolakis, C. E., & Skjelbreia, J. E. (1993). Evolution of maximum amplitude of solitary waves on plane beaches. *Journal of Waterway, Port, Coastal, and Ocean Engineering, 119*(3), 323–342.

Tian, Z., Perlin, M., & Choi, W. (2010). Energy dissipation in two-dimensional unsteady plunging breakers and eddy viscosity model. *Journal of Fluid Mechanics, 655*(217–257), 2010.

Yasuda, T., Sakakibara, Y., & Hara, M. (1992). BIM simulation on deformation up to breaking of solitary waves over uneven to bottoms. In W. R. Blain, & E. Cabrera (Eds.), *Proceedings, 4th International Conference on Hydraulic Engineering Software, Fluid Flow Modelling* (pp. 523–535). Southampton, U.K: Elsevier.

Zelt, J. A. (1991). The runup of nonbreaking and breaking solitary wave. *Coastal Engineering, 15*(3), 205–246.

Investigation of Solitary Wave Over a Trench Using a Non-hydrostatic Numerical Model

J. X. Zhang

Abstract A three-dimensional non-hydrostatic model was presented to simulate solitary wave propagation. A one equation turbulent model (Spalart-Allmaras model) was used to calculate the eddy viscosity. To simulate the bottom boundary layer flow, a high grid resolution was used within the boundary layer. The bottom shear stress was directly calculated using the turbulent model. The model was validated by means of comparing the calculated water elevation with analytical results. Taking a stable solitary wave being simulated in a long numerical flume as the initial condition, we simulated the solitary wave propagation over a trench. The wave profile skewness, the velocity distribution, the local flow separation, and the dissolved mass transportation were elaborately analysed.

Keywords Solitary wave · Boundary layer · Non-hydrostatic model · Trench

1 Introduction

Offshore trench is commonly dug in order to lay pipelines or immersed tube for submarine tunnel. In estuaries, a trench-type channel is often maintained to promote the channel navigation condition. The complex interaction of the fluid flow with trench consists of flow separation at the trench crest, the water deep-going into the trench, and the evolution of shear flow passing the trench. There are numerous studies about steady incident flow passing over a trench (Balachandar et al. 2002; Yue et al. 2005, 2006; Zhang et al. 2014). Compared with steady flow, in offshore engineering, the ocean environment is much complex due to the combined wave-current (Duan et al. 2017). Besides the sinusoidal wave, the solitary wave attracts a lot of studies. The solitary wave is a permanent progressing wave form consisting of a single elevation above the undisturbed surface. In some circumstances, the solitary wave is used to

J. X. Zhang (✉)
Key Laboratory of Hydrodynamics, Ministry of Education, Shanghai 200240, China
e-mail: zhangjingxin@sjtu.edu.cn

School of Naval Architecture, Ocean and Civil Engineering, Shanghai Jiao Tong University, Shanghai 200240, China

K. D. Nguyen et al. (eds.), *Estuaries and Coastal Zones in Times of Global Change*, Springer Water,
https://doi.org/10.1007/978-981-15-2081-5_35

present tsunami waves. This study focuses on the investigation of a solitary wave over a fixed trench.

There are numerous studies of the solitary wave using analytical method (Peregrine 1967; Grimshaw 1970, 1971). The potential theory is significantly popular in dealing with wave dynamics, in which the viscous effect has been ignored. Although the analytical method is successful in predicting the wave form, the shear stress on solid wall cannot be successfully calculated. However, the shear stress on bottom or solid wall (e.g. a bridge pier), is critical to determine the dynamic forces. For sand bed deposition or erosion, it is very important to accurately calculate the shear stress on the bottom.

In order to consider the viscous effects on solitary wave propagation, Liu and Orfila (2004) and Liu and Orfila (2004) proposed a method considering the viscous effects by integrating the wall boundary layer flow, and developed depth-averaged Boussinesq-type equations. Dutykh and Dias (2007) proposed a potential flow model considering the fluid viscous effects. Compared with a full three-dimensional Navier-Stokes equation model, the Boussinesq equation model is efficient and economical in computational costs, but lower accurate because of some simplification. A three-dimensional non-hydrostatic model is feasible in presenting complex flow structures compared with depth-averaged model. Meanwhile, the non-hydrostatic model is much more efficient than the Navier-Stokes equations using VOF method to capture the free surface, especially for flow with a large spatial scale.

Casulli (1999) and Casulli and Zanolli (2002) reported on a model that used the hydrodynamic pressure terms. Jankowski (1999) presented the details of a predictor-corrector method for calculation of the non-hydrostatic pressure. Similar numerical schemes were developed by variants of the non-hydrostatic models (Li and Fleming 2001; Kocyigit et al. 2002; Chen 2003; Fringer et al. 2006; Ma et al. 2012; Zhang et al. 2014, 2015, 2016). The present study proposed a non-hydrostatic model to simulate solitary wave propagating over a trench.

The chapter is organized as follows. In Sect. 2, a brief overview of the model employed in this work is presented. In Sect. 3, the dynamics of waves over a trench are discussed. The general conclusions are in Sect. 4.

2 Numerical Formulation

2.1 Mathematical Model

The non-hydrostatic model splits the pressure gradients into the hydrostatic and non-hydrostatic parts, which is the extension of the traditional shallow water equations (SWE). The present model adopts a σ coordinate transformation in the vertical direction, which is efficient in fitting the free surface and uneven bottom. The governing equations are summarized,

$$\frac{\partial \zeta}{\partial t} + \frac{\partial q_x}{\partial x} + \frac{\partial q_y}{\partial y} + \frac{\partial q_\sigma}{\partial \sigma} = 0 \tag{1}$$

$$\frac{\partial q_x}{\partial t} + \frac{\partial q_x u}{\partial x} + \frac{\partial q_x v}{\partial y} + \frac{\partial q_x \tilde{\omega}}{\partial \sigma} = -gD\frac{\partial \zeta}{\partial x} - \frac{D}{\rho_0}\frac{\partial p_n}{\partial x} + \frac{\partial}{\partial x}\left(\upsilon_t \frac{\partial q_x}{\partial x}\right) + \frac{\partial}{\partial y}\left(\upsilon_t \frac{\partial q_x}{\partial y}\right) + \frac{1}{D}\frac{\partial}{\partial \sigma}\left(\frac{\upsilon_t}{D}\frac{\partial q_x}{\partial \sigma}\right) \tag{2}$$

$$\frac{\partial q_y}{\partial t} + \frac{\partial q_y u}{\partial x} + \frac{\partial q_y v}{\partial y} + \frac{\partial q_y \tilde{\omega}}{\partial \sigma} = -gD\frac{\partial \zeta}{\partial y} - \frac{D}{\rho_0}\frac{\partial p_n}{\partial y} + \frac{\partial}{\partial x}\left(\upsilon_t \frac{\partial q_y}{\partial x}\right) + \frac{\partial}{\partial y}\left(\upsilon_t \frac{\partial q_y}{\partial y}\right) + \frac{1}{D}\frac{\partial}{\partial \sigma}\left(\frac{\upsilon_t}{D}\frac{\partial q_y}{\partial \sigma}\right) \tag{3}$$

$$\frac{\partial q_z}{\partial t} + \frac{\partial q_z u}{\partial x} + \frac{\partial q_z v}{\partial y} + \frac{\partial q_z \tilde{\omega}}{\partial \sigma} = -\frac{1}{\rho_0}\frac{\partial p_n}{\partial \sigma} + \frac{\partial}{\partial x}\left(\upsilon_t \frac{\partial q_z}{\partial x}\right) + \frac{\partial}{\partial y}\left(\upsilon_t \frac{\partial q_z}{\partial y}\right) + \frac{1}{D}\frac{\partial}{\partial \sigma}\left(\frac{\upsilon_t}{D}\frac{\partial q_z}{\partial \sigma}\right) \tag{4}$$

where $q_x = Du$, $q_y = Dv$, $q_z = Dw$, $q_\sigma = D\tilde{\omega}$, u, v, w are the respective velocities in x, y, z directions. $\tilde{\omega}$ is the vertical velocity in the σ coordinate framework, $D = h+\zeta$ is the total water depth, h is the still water depth, and ζ is the free surface elevation. p_n is the non-hydrostatic pressure. g is the gravitational acceleration. The molecule viscous coefficient is υ, and the eddy viscosity is υ_t. Correspondingly, the velocity along the σ coordinate is calculated as,

$$q_\sigma = \frac{q_z}{D} - \frac{q_x}{D}\left(\sigma\frac{\partial D}{\partial x} + \frac{\partial \zeta}{\partial x}\right) - \frac{q_y}{D}\left(\sigma\frac{\partial D}{\partial y} + \frac{\partial \zeta}{\partial y}\right) - \left(\sigma\frac{\partial D}{\partial t} + \frac{\partial \zeta}{\partial t}\right) \tag{5}$$

The eddy viscosity υ_t is determined using the one-equation Spalart-Allmaras (S-A) turbulence model (Spalart 2000), in which an advection and diffusion equation for an auxiliary variable $\tilde{\upsilon}$ is given by,

$$\frac{D\tilde{\upsilon}}{Dt} = c_{b1}\tilde{S}\tilde{\upsilon} - c_{w1}f_w\left[\frac{\tilde{\upsilon}}{\tilde{d}}\right]^2 + \frac{1}{\tilde{\sigma}}\left\{\nabla\cdot\left[(\upsilon+\tilde{\upsilon})\nabla\tilde{\upsilon}\right] + c_{b2}(\nabla\tilde{\upsilon})^2\right\} \tag{6}$$

where $\chi \equiv \tilde{\upsilon}/\upsilon$, $f_w = g\left[(1+c_{w3}^6)/(g^6+c_{w3}^6)\right]^{1/6}$, $g = r + c_{w2}\left(r^6 - r\right)$, $r \equiv \tilde{\upsilon}/(\tilde{S}\kappa^2 d^2)$, $\tilde{S} = \left|\bar{S}\right| + f_{v2}\tilde{\upsilon}/(\kappa^2 d^2)$, $f_{v1} = \chi^3/(\chi^3 + c_{v1}^3)$, $f_{v2} = 1 - \chi/(1+\chi f_{v1})$, $\bar{S}_{ij} = \left(\partial u_i/\partial x_j + \partial u_j/\partial x_i\right)/2$. The model constants are $c_{b1} = 0.1355$, $\sigma = 2/3$, $c_{b2} = 0.622$, $\kappa = 0.41$, $c_{w1} = c_{b1}/\kappa^2 + (1+c_{b2})/\sigma$, $c_{w2} = 0.3$, $c_{w3} = 2.0$, $c_{v1} = 7.1$.

2.2 Numerical Scheme

A predictor–corrector scheme is widely used as a numerical method for the non-hydrostatic model. In summary, the flow driven by the hydrostatic pressure is calculated in the predictor step, and the flow driven by the non-hydrostatic pressure is further resolved in the corrector step. For numerical simulations of free surface flows in rivers, oceans, and coasts, the predicted flow field under hydrostatic pressure is very accurate, and the updated process in the corrector step is efficient based on the predicted flow. Compared with the traditional numerical scheme SIMPLE, the numerical scheme is highly efficient because only one numerical iterative process is done to uncouple the flow velocity and pressure. Especially, for cases of the non-hydrostatic pressure being predominant in a local zone, for example, solitary wave propagating over a flat bottom, a zonal non-hydrostatic model is feasible to promote the numerical efficiency (Zhang et al. 2018). In the present model, the grid system consists of unstructured horizontal grids and multi-layers through the water depth. The governing equations are discretised based on the finite volume method (FVM). A 2nd order total variation diminishing (TVD) scheme (OSHER scheme) is adopted. The in-house codes (HydroFlow®) are paralleled by the OpenMP library.

2.3 Simulation Implementation

In the present work, the solitary wave was generated by specifying the initial solitary wave profile and the velocities using theoretical expressions given by Grimshaw (1971). During the solitary wave propagation, a series of small waves are commonly dispersed, and gradually departed away from the main wave. Because the viscous effect was considered in the present numerical model, the solitary wave height decreased all the way. When the series of wake waves departing fully from the main solitary wave, the single solitary wave was considered to be stable. The instantaneous flow field was saved as initial incident solitary wave for investigation of solitary wave over a trench.

The stable solitary wave was obtained by numerical simulating solitary wave propagation in a flume of 200 m length, and 1 m still water depth. The present work focused on the solitary wave propagating over a two-dimensional trench, so the width of the numerical flume was ignored. In the study, only one grid in the span wise direction (e.g. channel width) was used, meanwhile, the slip wall boundary condition was specified at the side walls. The horizontal grid size was $\Delta x = 0.1m$, which was chosen by aid of the grid convergence validation. Within the bottom boundary layer, the flow eddy viscosity is vigorous. However, both the molecular and eddy viscosity are ignored in the potential models. Neglecting viscosity leads to zero shear stress on the bottom. To simulate the boundary layer flow using models with considering viscosity, a fine grid resolution near the bottom is necessary. In the present work, a non-slip boundary condition was used, which demanded a normal

grid size of $\Delta_{\perp}^{+} = O(1)$ at the first grid points to the bottom. Near the free surface, the vertical grid was refined to about 1% of the total water depth. The same grid resolution was used to simulate solitary wave propagation over a trench. The schematic diagram of the computational domain and grid system is presented in Fig. 1. A symmetric trench with a height of 0.18 m and a bottom length of 0.3 m was symmetric about x = 0.0 m. The side slope was specified as the response angle of sands ($\beta = 32°$). The flows were recorded at 5 locations, which is shown in Fig. 2. In the present work, five solitary waves of relative wave amplitudes ($\varepsilon = a_0/h_0$): 0.2, 0.3, 0.4, and 0.5 were generated.

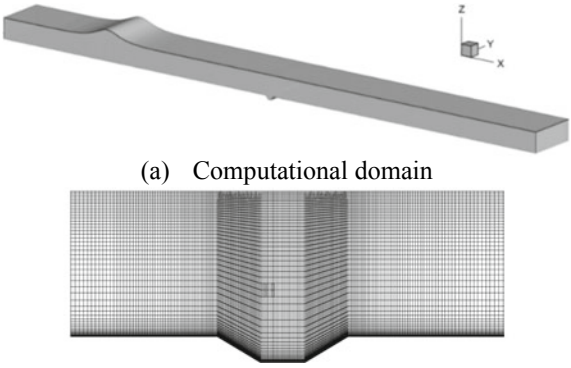

(a) Computational domain

(b) Local mesh

Fig. 1 Schematics of the computational domain and mesh

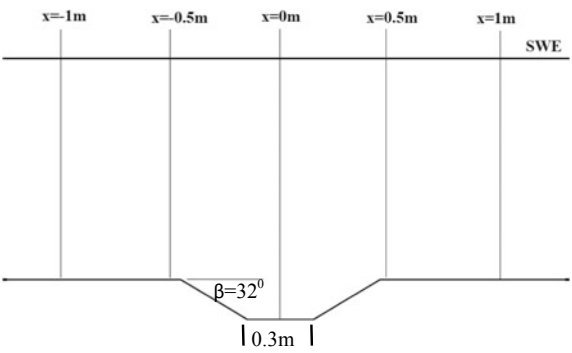

Fig. 2 Geometry of the trench and measured locations

3 Results and Analysis

3.1 Model Validation

The simulated solitary wave was stable over a long distance on a flat bottom. The simulated free surface profiles were compared with the analytical solutions of the third order solitary wave theory by Grimshaw (1971). Figure 3 reveals the comparisons of the calculated solitary wave profiles and the analytical results, where the x coordinate has been shifted in order to make the wave peak at x = 0.0 m. The numerical results were well coincided with the theoretical solutions although the discrepancy increased where away from the main wave peak.

The solitary wave amplitude is damped by viscous effects, so there is no constant wave profile over a long distance. Liu and Orfila (2004) proposed an analytical expression for solitary wave damping in a flume,

$$\left(\frac{a}{a_0}\right)^{-1/4} = 1 + 0.08356\left(1 + \frac{h_0}{W}\right)\left(\frac{\upsilon_t}{h_0\sqrt{gh_0}}\right)^{1/2}\left(\frac{a_0}{h_0}\right)^{1/4}\left(\frac{x}{h_0}\right) \tag{7}$$

where $2W$ is the flume width, a is the wave height at arbitrary x, a_0 and h_0 are the wave height and the still water depth at reference point, and υ_t is the eddy viscosity. In formula (7), the ratio of the water depth to the flume width is sensitive, which means that the effect of the side wall increases with the water depth increasing. For experiments, the water depth in a channel is limited by a critical ratio in order to reduce the side wall blocking. In the present work, the flow was considered as two-dimension in the vertical plane, and the side wall effect was neglected by aid of a

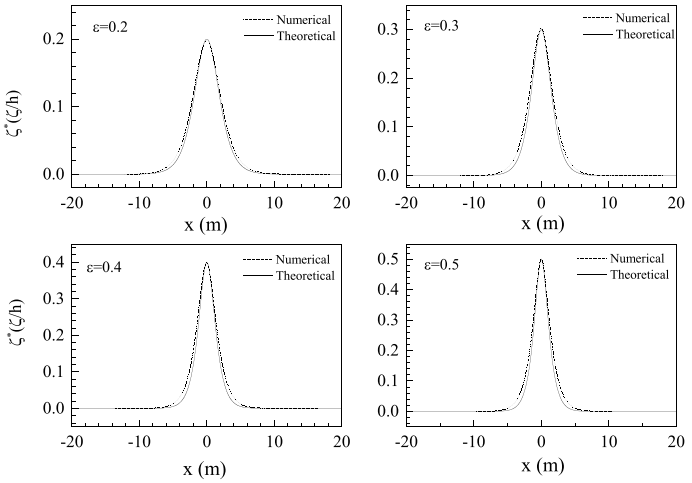

Fig. 3 Theoretical and numerical solitary wave profile

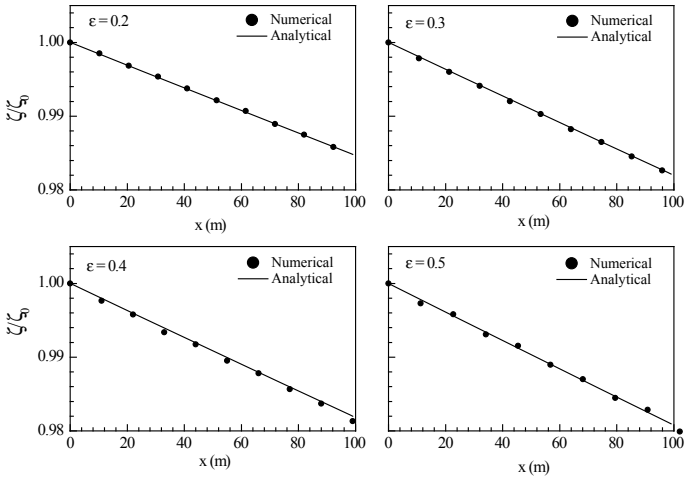

Fig. 4 Analytical and numerical wave amplitude over the plane

slip boundary condition. A zero value of h_0/W was substituted into formula (7) to meet the numerical simulation. The eddy viscosity is another critical parameter in formula (7). In the present work, the calculated eddy viscosity was substituted into formula (7) to calculate the wave damping ratio. Figure 4 reveals a well agreement of the wave damping between calculated and analytical results. The validation of the model reveals a good simulation of the viscous effects on the solitary wave propagation over a long flat bottom.

3.2 Solitary Wave Over a Trench

The present work focused on the evolution of the solitary waves over a trench. Figure 5 reveals the time histories of the free surface elevation at the recorded sites (marked in Fig. 3). A little skewness of the wave profile was observed for different incident waves when the solitary wave propagating over the trench. The solitary wave was damped over a distance due to the fluid viscous effects. However, the wave height was slightly amplified over a trench, which was definitely due to the sharp local topography. Figure 6 presents the wave heights over the trench where the wave heights were normalized by that at x $= -1.0$ m, i.e. in front of the trench. At the front crest of the trench, the relative wave heights were amplified about 0.4% for different incident waves. The amplification of the wave amplitude increased with the incident wave amplitude decreasing. The wave amplification increased over the trench until the back crest, i.e. x $= 0.5$ m. Over the trench, the amplification of the wave amplitude for different incident waves revealed a reversal characteristics compared with that at x $= -0.5$ m. With the incident wave height increasing, the

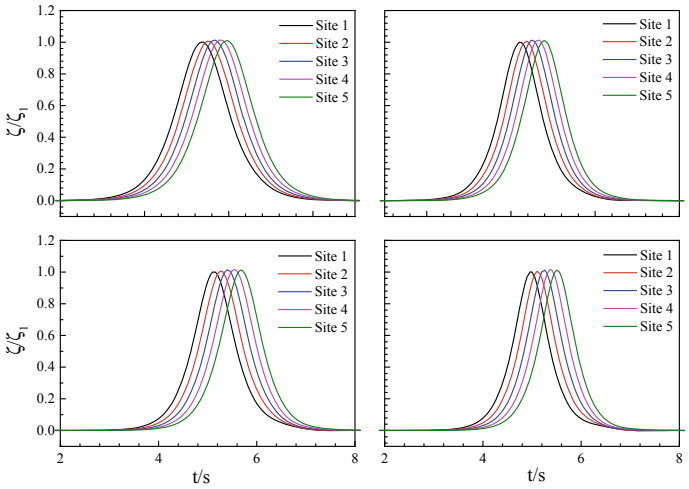

Fig. 5 Solitary wave evolution over the trench

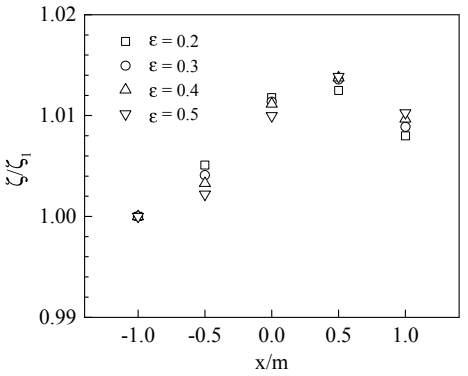

Fig. 6 Amplification of solitary wave amplitude over the trench

relative amplification factor increased until approaching to the position x = 0.5 m. Downstream of the trench, the solitary wave was continually damped (Fig. 6). When a solitary wave propagates over a trench, the trench topography induces wave reflection and complex interactions between waves and solid walls (Jung et al. 2008; Xie and Liu 2012).

The analytical method presents a vertical velocity profile. The present simulation revealed a similar velocity distribution through the most water depth beyond the bottom boundary layer. Within the bottom boundary layer, the fluid viscosity needs to be considered to calculate the bottom shear stress. Although the bottom boundary layer is very thin, it is key to the bed sediment deposition or erosion. The instantaneous horizontal velocities under the solitary wave peak were extracted and compared. Figure 7 reveals the vertical profile of the horizontal velocities at selected positions.

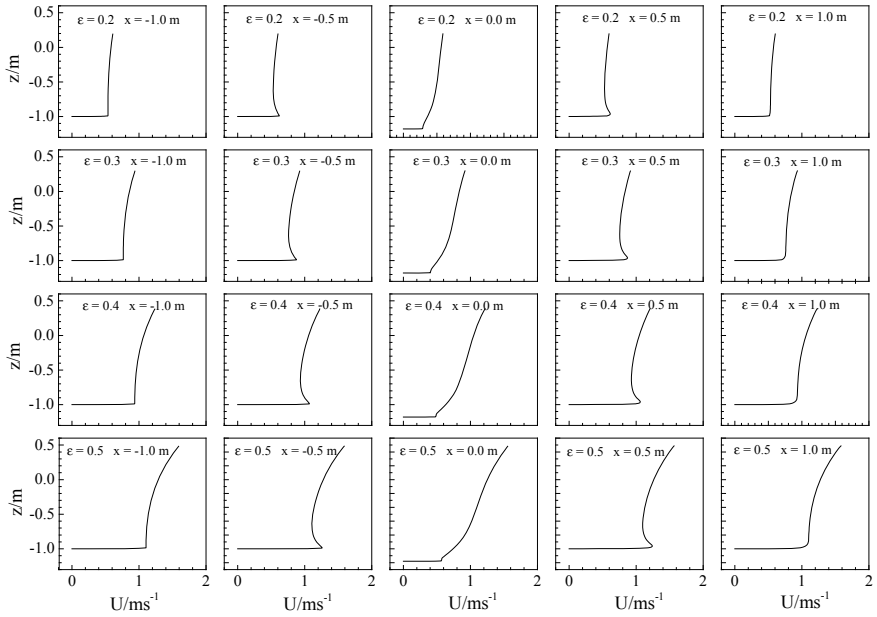

Fig. 7 Velocity profiles over the trench

In front of the trench, i.e. $x = -1.0$ m, the velocity profile consisted of a small part covering the boundary layer and a big part above the bottom boundary layer. At the front crest of the trench, the flow within the boundary layer was distinctly accelerated. A jet-like velocity profile occurred at the upper edge of the bottom boundary layer. At the trough of the trench, the velocity decreased near the bottom. The vertical profile of the velocity deviated obviously from the normal velocity distribution under solitary wave. At the back crest, i.e. $x = 0.5$ m, the velocities recovered approximately to those at the front crest, but with a bit mild gradient across the upper bottom boundary layer edge.

The velocity distribution within the bottom boundary layer is important to calculate the bottom shear stress. Figure 8 reveals the time histories of the bottom shear stress at selected positions for different incident solitary waves. At the front crest of the trench ($x = -0.5$ m), the sharp increasing of the velocity within the boundary layer induced a maximum bottom shear stress (see Fig. 8). Although the velocity profiles were similar between positions at $x = 0.5$ m and -0.5 m, the bottom shear stress at $x = 0.5$ m decreased significantly to approximate 20% of that at $x = -0.5$ m. The bottom shear stress at the trench trough decreased obviously due to the velocity decreasing within the boundary layer. The negative bottom shear stress was induced by a reversal flow near the bottom when a solitary wave propagating over the trench. Comparisons shown in Fig. 8 reveals that the relative negative bottom shear stress decreased with the incident wave height increasing.

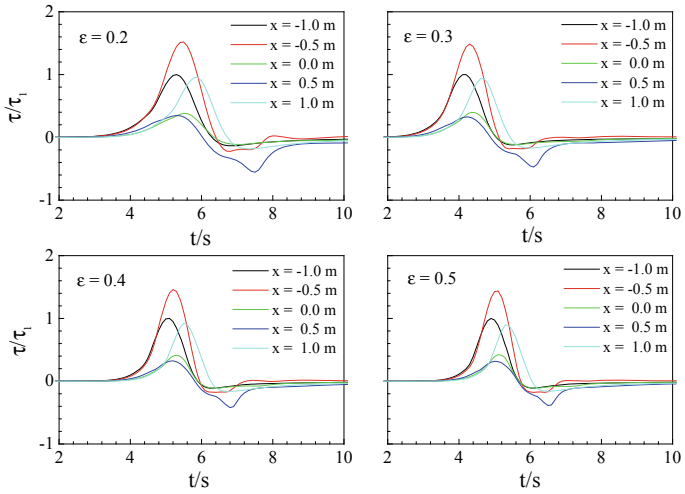

Fig. 8 Bottom shear stress over the trench

The flow field structures are clearly presented by the instantaneous streamlines in Fig. 9 where four snapshots are shown for different incident waves, respectively. The out-of-plane vorticity contoured by red present clockwise flow circulations, and contoured by blue present counter-clockwise flow circulations. At t = 5.0 s, the solitary wave peak was justly in front of the trench. At t = 5.7 s, the wave peak was approximately over the trench trough. The solitary wave was away from the trench after t = 8.0 s. During the first half phase of a solitary wave, the upward flows induced hardly boundary layer flow separation at the front crest of the trench. Meanwhile, the favourable pressure gradient forced the boundary layer flows accelerating, which induced hardly flow separation. However, when the wave peak passing the front crest, i.e. during the second half phase of a solitary wave, the water dipped into the

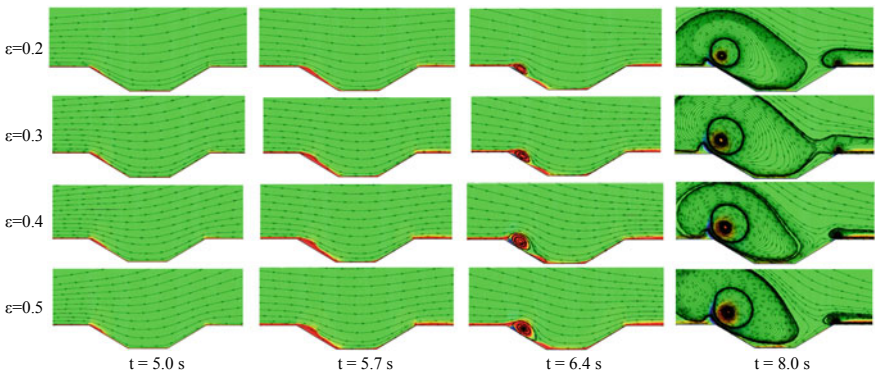

Fig. 9 Velocity field of solitary wave over the trench

trench, and flowed reversely near the bottom. The adverse pressure gradient boosted the boundary layer flow separation. With the incident wave height increasing, the local flow separation became stronger at the front crest of the trench. After t = 8.0 s, the solitary wave went far away from the trench. In the local trench domain, the eddy viscosity decayed sharply, and the flow circulation structures enlarged distinctly due to the weaker viscous dissipation. The analysis of the flow structures contributes to investigate the sediment transportation induced by solitary waves.

3.3 Analysis of Dissolved Mass Transportation

Compared with sinusoidal wave, the solitary wave is nearly unidirectional at an arbitrary wave phase. The flow near the bottom is significantly accelerated compared with open channel flow, which provides a much powerful energy to transport mass. The process of mass transportation was investigated by means of numerical solving the governing equation of mass concentration. The initial mass concentration was specified as $C = 1.0$ within the trench, and $C = 0.0$ outside the channel water (Fig. 10). Figure 11 shows the instantaneous snapshots of the concentration under different incident solitary waves. The dissolved mass was directly advected downstream over the trench. The downstream distance of the mass advection increased with the incident wave amplitude increasing. Although there was reversal flows within the bottom boundary layer, the reversal net mass flux was limited due to the very thin

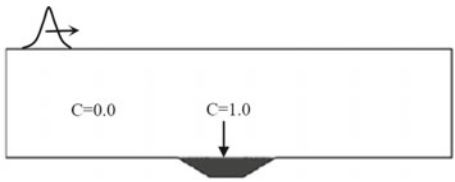

Fig. 10 Initial dissolved mass concentration

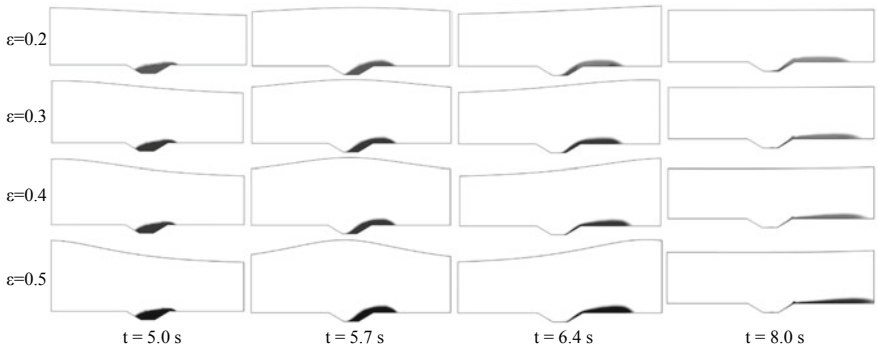

Fig. 11 Dissolved mass transportation under solitary wave

boundary layer height. After the solitary wave propagating across the trench, most of the dissolved mass was advected outside the trench, especially for a higher incident wave amplitude.

4 Conclusions

A non-hydrostatic numerical model has been developed, and used to simulate the solitary wave propagating over a flat bottom. The viscous effect was considered to accurately simulate the bottom boundary layer flow. The simulations of solitary wave over a trench highlight a clear flow field structure including the wave profile skewness, bottom shear stress, and local flow separation. The model considering the fluid viscous effect can contribute to investigate the turbulent flows in the very thin bottom boundary layer.

Acknowledgements This work was supported by the National Natural Science Foundation (No. 11572196) and the National Basic Research Programme (973 programme) of China (No. 2014CB046200).

References

Balachandar, R., Polatel, C., Hyun, B.-S., Yu, K., Lin, C.-L., Yue, W., et al. (2002). LDV, PIV and LES investigation of flow over a fixed dune. In *Proceeding of the Symposium Held in Monte Verità: Sedimentation and Sediment Transport* (pp. 171–178). Dordrecht: Kluwer Academic.

Casulli, V. (1999). A semi-implicit finite difference method for non-hydrostatic, free-surface flows. *International Journal for Numerical Methods in Fluids, 30,* 425–440. https://doi.org/10.1002/(SICI)1097-0363(19990630)30:4%3c425:AID-FLD847%3e3.0.CO;2-D.

Casulli, V., & Zanolli, P. (2002). Semi-implicit numerical modeling of nonhydrostatic free-surface flows for environmental problems. *Mathematical and Computer Modeling, 36,* 1131–1149. https://doi.org/10.1016/S0895-7177(02)00264-9.

Chen, X. J. (2003). A fully hydrodynamic model for three-dimensional, free-surface flows. *International Journal for Numerical Methods in Fluids, 42,* 929–952. https://doi.org/10.1002/fld.557.

Duan, L. L., Liao, C. C., Jeng, D. S., & Chen, L. (2017). 2D numerical study of wave and current-induced oscillatory non-cohesive soil liquefaction around a partially buried pipeline in a trench. *Ocean Engineering, 135,* 39–51. https://doi.org/10.1016/j.oceaneng.2017.02.036.

Dutykh, D., & Dias, F. (2007). Viscous potential free-surface flows in a fluid layer of finite depth. *Comptes Rendus Mathematique, 345*(2), 113–118. https://doi.org/10.1016/j.crma.2007.06.007.

Fringer, O. B., Gerritsen, M., & Street, R. L. (2006). An unstructured-grid, finite-volume, non-hydrostatic, parallel coastal ocean simulator. *Ocean Modeling, 14,* 139–173. https://doi.org/10.1016/j.ocemod.2006.03.006.

Grimshaw, R. (1970). The solitary wave in water of variable depth. *Journal of Fluid Mechanics, 42*(3), 639–656. https://doi.org/10.1017/S0022112070001520.

Grimshaw, R. (1971). The solitary wave in water of variable depth. Part 2. *Journal of Fluid Mechanics, 46*(3), 611–622. https://doi.org/10.1017/s002211207100739O.

Jankowski, J. A. (1999). A non-hydrostatic model for free surface flows. Ph.D. Dissertation, University of Hannover, Germany.

Jung, T. H., Suh, K. D., Lee, S. O., & Cho, Y. S. (2008). Linear wave reflection by trench with various shapes. *Ocean Engineering, 35,* 1226–1234. https://doi.org/10.1016/j.oceaneng.2008.04.001.

Kocyigit, M. B., Falconer, R. A., & Lin, B. (2002). Three-dimensional numerical modeling of free surface flows with non-hydrostatic pressure. *International Journal for Numerical Methods in Fluids, 40,* 1145–1162. https://doi.org/10.1002/fld.376.

Li, B., & Fleming, C. A. (2001). Three-dimensional model of Navier-Stokes equations for water waves. *Journal of Waterway, Port, Coastal and Ocean Engineering, 127*(1), 16–25. https://doi.org/10.1061/(ASCE)0733-950X(2001)127:1(16).

Liu, P. L.-F., & Orfila, A. (2004). Viscous effects on transient long-wave propagation. *Journal of Fluid Mechanics, 520,* 83–92. https://doi.org/10.1017/S0022112004001086.

Liu, P. L.-F., Simarro, G., Vandever, J., & Orfila, A. (2006). Experimental and numerical investigation of viscous effects on solitary wave propagation in a wave tank. *Coastal Engineering, 53,* 181–190. https://doi.org/10.1016/j.coastaleng.2005.10.008.

Ma, G. F., Shi, F. Y., & Kirby, J. T. (2012). Shock-capturing non-hydrostatic model for fully dispersive surface wave processes. *Ocean Modelling, 43–44,* 22–35. https://doi.org/10.1016/j.ocemod.2011.12.002.

Peregrine, D. H. (1967). Long waves on a beach. *Journal of Fluid Mechanics, 27*(4), 815–827. https://doi.org/10.1017/S0022112067002605.

Spalart, P. R. (2000). Strategies for turbulence modelling and simulations. *International Journal of Heat Fluid Flow, 21,* 252–263. https://doi.org/10.1016/S0142-727X(00)00007-2.

Xie, J. J., & Liu, H. W. (2012). An exact analytic solution to the modified mild-slope equation for waves propagating over a trench with various shapes. *Ocean Engineering, 50,* 72–82. https://doi.org/10.1016/j.oceaneng.2012.05.014.

Yue, W., Lin, C. L., & Patel, V. C. (2005). Large eddy simulation of turbulent open-channel flow with free surface simulated by level set method. *Physics of Fluids, 17,* 1–12. https://doi.org/10.1063/1.1849182.

Yue, W., Lin, C. L., & Patel, V. C. (2006). Large-eddy simulation of turbulent flow over a fixed two-dimensional dune. *Journal of Hydraulic Engineering, 132*(7), 643–651. https://doi.org/10.1061/(ASCE)0733-9429(2006)132:7(643).

Zhang, J. X., Sukhodolov, A. N., & Liu, H. (2014). Non-hydrostatic versus hydrostatic modelings of free surface flows. *Journal of Hydrodynamics, 26*(4), 840–847. https://doi.org/10.1016/S1001-6058(14)60058-5.

Zhang, J. X., Wang, X. K., Liang, D. F., & Liu, H. (2015). Application of detached-eddy simulation to free surface flow over dunes. *Engineering Applications of Computational Fluid Mechanics, 9*(1), 556–566. https://doi.org/10.1080/19942060.2015.1092269.

Zhang, J. X., Liang, D. F., & Liu, H. (2016). An efficient 3D non-hydrostatic model for simulating near-shore breaking waves. *Ocean Engineering, 140,* 19–28. https://doi.org/10.1016/j.oceaneng.2017.05.009.

Zhang, J. X., Liang, D. F., & Liu, H. (2018). A hybrid hydrostatic and non-hydrostatic numerical model for shallow flow simulations. *Estuarine, Coastal and Shelf Science, 205*, 21–29. https://doi.org/10.1016/j.ecss.2018.03.012.

Characteristics of Storm-Induced Odd-Tide in the South Yellow Sea Radial Sand Ridges

Xi Feng and Xiao Xu

Abstract Co-oscillating tide, also called odd-tide is a kind of abnormal phenomenon of high tide. It usually comes with storms or big waves, and the associated flood roars on, swifts and clashes on the shore violently. The South Yellow Sea Radial Sand Ridges are featured by a broad beach and large tidal amplitude. The odd-tide happens frequently here. This study tends to find the storm-induced odd-tide in the South Yellow Sea Radial Sand Ridges, with a focus on the historical record analysis. It starts from collecting historical documents, hydrological records, and measured data to identify the storm-induced odd-tides in this area. It parameterizes the waveform and kinematics characteristics of the storm-induced odd-tides. It compares the tropical storms and the winter storm-induced odd-tides, as well as the variations in the south and north wings of the Radial Sand Ridges. Factor tests are operated to find out the sensitivity of the odd-tides to a variety of external elements. Multidimensional regression models will be built to interpret the correlations between the external motivation factors and the characteristic parameters of odd-tide. The investigation tries to make a summary of the local characteristics of space and time, as well as the exploration of the factors and generation mechanisms for the odd-tides.

Keywords Odd-tides · South Yellow Sea · Radial Sand Ridges · Winter-storminess · Extra-tropical storm · Storm surge · Cold front

1 Introduction

Odd-tides, also known as "eccentric tides", are an abnormally-high tidal phenomenon frequently happened on the mudflat of the South Yellow Sea. It usually appears as

X. Feng (✉) · X. Xu
Key Laboratory of Coastal Disaster and Defence, Hohai University, Ministry of Education, 1 Xikang Road, Nanjing 210098, China
e-mail: xifeng@hhu.edu.cn

X. Feng
College of Harbor, Coastal and Offshore Engineering, Hohai University, Nanjing 210098, China

K. D. Nguyen et al. (eds.), *Estuaries and Coastal Zones in Times of Global Change*, Springer Water,
https://doi.org/10.1007/978-981-15-2081-5_36

a fast rising tidal level ahead of the astronomic tide. Without any prediction, its occurrence has no symptoms, as it comes and goes rapidly, a period of which usually lasts from a few minutes to a few hours. Ever since the late 1950th, odd-tide has become the most destructive and dreadful coastal disasters along the Jiangsu Coast. According to statistical result from the Nantong Hydrological Bureau, a total of 53 disasters caused by the odd-tide happened along Nantong Coast from 1998 to 2008, with a death toll of 150. Table 1 lists all the potential odd-tide related marine perils with the earliest available records. Among them, those with detected locations were spread on the tidal flats, and there existed a few in the tidal channels near the edge of the Radial Sand Ridges and near the submerged sand ridges. Winds associated with these events were found along with most of the perils, though constant or slightly varied in space and in time. On March 25, 1959, a large disaster occurred in Lusi Fishery; with 1300 people drown and dozens of boat destroyed. Along the South Yellow Sea coast, City of Haian, Rudong, Nantong, Haimen and Qidong (Fig. 1) all have reported the potential peril events related to odd-tide, and currently more than 400 thousand people were engaged in the aquaculture on the tidal flat of the South Yellow Sea, making it most vulnerable area to the odd-tides.

There are multiple terms to describe odd-tides. Xiu (1985) referred odd-tide phenomenon as 'co-oscillating tide', implying the sudden rise of tidal level is triggered by topographically related resonances. For instance, 'harbor resonances', an abnormally high tide origins from atmospheric disturbances, the wave height of which is enlarged in harbors which is often found along the China Yellow Sea (Wu and Wang 1999; Cao et al. 2001). Such resonances were also explained by edge wave theories (Zhang and Sheng 2013; Chen et al. 2004). Other scholars deemed odd-tide approximate to 'riptide' (e.g. Xiu et al. 2004; Liu et al. 2002; Liu 2015), which often was related to a sudden rise in oceanic current. Liu (2015) assumed that the odd-tide can be regarded as either a tidal bore or a riptide and he also mentioned both of the hydraulic phenomena are related to the complex tidal channels in the South Yellow Sea. However, he failed to provide the evidence of the correlation of the riptide to high tidal anomalies as observed from odd-tide witness. Xie et al. (2016) pointed out that it is the surge-tide-topography tri-interaction that ends up with the abnormally high in tidal level. Tide-surge interactions were also found in other places around the world. Feng et al. (2016) reported that the semidiurnal perturbation to surges were frequently found in nearshore region of the South Atlantic Bight. The perturbation is mainly due to the interactions between surge and semidiurnal tide in the central space of the Bight. Whereas, different to Xie et al. (2016)'s findings in the South Yellow Sea of China and abnormal sea level behavior showed a slow varying oscillation. High-frequency sea oscillation phenomenon triggered by atmospheric disturbances were not rare around the world, these oscillations in different names were now often categorized into one term "meteo-tsunamis". The wave height associated with meteo-tsunamis could be reach multiple meters and the oscillation period is in a band between several minutes and several hours (Lamb 1932; Proudman 1929; Vennell 2010; Olabarrieta et al. 2017), which is quite similar to the reported occurrence of "odd-tide". These types of oscillations are usually induced by atmospheric gravity waves, pressure jumps, frontal passages, squalls, and etc. (Monserrat et al.

Table 1 Marine perils observed in Rudong area from 1959 to 2010

Order	Date	Position	Reason	Consequence
1	03/25/1959	Tidal channel	Improper aquaculture operation	1300 dead
2	09/27/1962	Tidal flat	Improper aquaculture operation	18 dead
3	02/18/1972	Tidal flat	Improper aquaculture operation	61 dead
4	11/21/1983	Tidal flat	Improper aquaculture operation	59 dead
5	09/01/1990	Tidal flat	Improper aquaculture operation	18 dead
6	02/02/1996	Rudong nearshore area	Stranding	13 dead
7	09/29/1996	Rudong nearshore area	Stranding	
8	04/12/1997	Rudong nearshore area	Fire	2 dead
9	03/20/1998	Rudong nearshore area	Wind (steady)	
10	05/24/1998	Rudong nearshore area	Wind (change gradually)	
11	06/01/1998	Rudong nearshore area	Wind (change suddenly)	12 dead
12	01/02/1999	Rudong nearshore area	Wind (steady)	
13	01/15/1999	Rudong nearshore area	Unspecified	
14	01/18/1999	Rudong nearshore area	Stranding	
15	05/03/1999	Rudong nearshore area	Fire	
16	06/11/1999	Rudong nearshore area	Unspecified	
17	06/14/1999	Rudong nearshore area	Unspecified	1 dead
18	11/11/1999	Rudong nearshore area	Wind (steady)	
19	11/25/1999	Rudong nearshore area	Wind (steady)	
20	03/19/2000	Rudong nearshore area	Wind (change gradually)	
21	04/10/2000	Rudong nearshore area	Stranding	8 dead
22	06/03/2000	Rudong nearshore area	Wind (cyclone)	
23	07/12/2000	Rudong nearshore area	Fire	
24	10/12/2000	Rudong nearshore area	Colliding	
25	10/13/2000	Rudong nearshore area	Unspecified	1 dead
26	10/26/2000	Rudong nearshore area	Unspecified	4 dead
27	10/31/2000	Rudong nearshore area	Unspecified	
28	11/16/2000	Rudong nearshore area	Wind (change gradually)	
29	11/17/2000	Rudong nearshore area	Unspecified	1 dead
30	11/30/2000	Rudong nearshore area	Stranding	
31	12/23/2000	Rudong nearshore area	Colliding	9 dead
32	09/22/2001	Tidal channel	Improper aquaculture operation	5 dead

(continued)

Table 1 (continued)

Order	Date	Position	Reason	Consequence
33	11/12/2001	Sand ridge	Improper aquaculture operation	10 dead
34	12/21/2002	Tidal channel	Unspecified	11 dead
35	02/01/2003	Rudong nearshore area	Unspecified	
36	09/15/2003	Rudong nearshore area	Colliding	
37	09/26/2003	Sand ridge	Improper aquaculture operation	7 dead
38	01/11/2004	Sand ridge	Improper aquaculture operation	
39	08/29/2004	Rudong nearshore area	Wind (steady)	
40	09/05/2004	Tidal channel	Wind (steady)	
41	05/12/2005	Sand ridge	Swell	13 dead
42	05/20/2005	Rudong nearshore area	Unspecified	1 dead
43	12/14/2005	Tidal flat	Shipwreck	9 dead
44	11/17/2006	Rudong nearshore area	Wind (steady)	4 dead
45	12/27/2006	Rudong nearshore area	Stranding	
46	03/05/2007	Rudong nearshore area	Wind (steady)	2 dead
47	04/15/2007	Sand ridge	Improper aquaculture operation	19 dead
48	11/12/2007	Rudong nearshore area	Swell	
49	01/20/2008	Tidal channel	Wind (change gradually)	9 dead
50	01/07/2009	Rudong nearshore area	Wind (steady)	1 dead
51	01/14/2009	Rudong nearshore area	Unspecified	1 dead
52	09/16/2010	Rudong nearshore area	Shipwreck	1 dead

2006) and holds a similar wave shape to seismic induced tsunamis, along with the similar unpredictability. The odd-tide is obviously not related to landslides or seismic activities, as there are no geologic conditions to excite the above two in the South Yellow Sea. Atmospheric disturbances then remain the only dynamic sources for odd-tide. Whereas, the genesis of the meteo-tsunamis also needs to satisfy multiple conditions specifically places to trap the wave energy. Coincidently, the Radial Sand Ridges in the South Yellow Sea with interlaced tidal channels and submerged sand ridges provide the conditions for wave repeated reflection and wave energy concentration. The odd-tide perils often occurred during calm weather without fierce winds, in which people without warning usually remained in normal operation on the tidal flat and failed to escape. As meteo-tsunamis is atmospheric pressure wave dominated, question arouses: could odd-tide be categorized as a type of meteo-tsunamis?

As a summary, this phenomenon has received little systematic studies. The potential origins of odd-tides remained blur and they could be explained by the following:

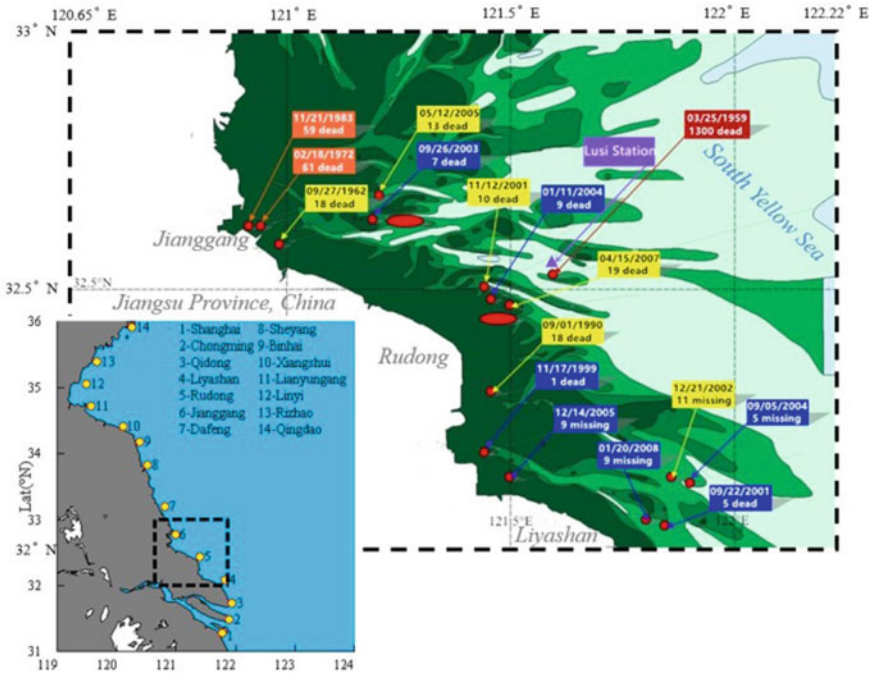

Fig. 1 The most vulnerable region of odd-tide induced marine perils in the South Yellow Sea, the scale of which is shown in the inserted dashed box in the small figure showing the Yellow Sea and the coastal area; the alongshore dots indicate the locations of which the meteorological conditions are explored during odd-tide events

1. Topographic resonances, e.g. harbor resonances, seiches
2. Meteo-tsunami or Atmospheric disturbance induced sudden sea level jump
3. Tide-storm surge interaction
4. Riptide or tidal bore by tidal channel contraction.

Nevertheless, the odd-tides generally come from marine perils, verbal statement and visual observations make the atmospheric of the odd-tide in the South Yellow Sea remains unclear. From Xie et al. (2016) and Liu's investigation (2015), the odd-tide could also be a delayed surge response in the tidal flats for far-distance storm surge happened days before and out of Radial Sand Ridges. Whether it is wind-dominated or atmospheric pressure dominated therefore needs further investigation. In this study, we adopted the methodology for extracting the meteo-tsunami signals from tidal residuals for determination of the odd-tide as the two share similar perturbation periods, while an exploration on meteorological sources was also conducted to determine the main triggers of this phenomenon.

2 Methodology

Water-level records at Lusi Station (Fig. 1a) inside the Radial Sand Ridges of the South Yellow Sea were obtained from Hawaii Sea Level Center archives to analyze the occurrence of storm-induced odd-tide and their statistics. The analysis considered over 22 years of water level records from year 1975 to year 1996, with a sampling interval of 60 min. The total water level oscillation contains water level oscillations from multiple bands of frequencies. The odd-tide usually comes with a spur of high tidal level that can flood within multiple time of minutes and the period of which falls into the high frequency band (<6 h). The tidal residuals with the odd-tide event are more analogous to a train of high-frequency wave than a surge perturbation with a period inherited by the main tidal constituents. Besides, when the odd-tide occurs, the relevant tidal shape follows with a rapid flooding velocity and a higher water level than prediction, meaning an advanced tidal shape along with a positive surge. Whereas after the protruding of high tidal oscillation, the tidal level also goes back to normal condition. In order to detect such tidal behavior, we creates the following framework: (1), a low-pass filter (Beardsley et al. 1985) with a cutoff period of 6 h (approximates to that of the quarter-diurnal tidal constituents) was applied in order to completely exclude the astronomic tides and lower varying oscillations such as surge signal; (2), we then calculated the wave height of the high-frequency tidal residuals, and defined the threshold of a significant odd-tide event, of which the peak wave height is larger than 0.5% of the spring tidal amplitude and a duration with the starting and ending point of the wave heights larger than 2 times of the standard deviation of the high-frequency tidal residuals over the entire time span; (3), as shown in Fig. 2b, c, we selected only the events coincident with either an

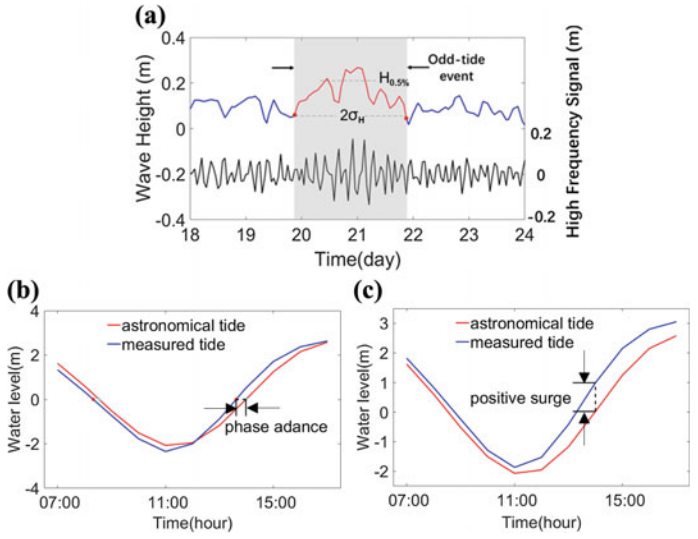

Fig. 2 **a** Duration of odd-tide; **b** phase advance; **c** positive surge

advanced tidal phase or with a positive surge, as compared to the astronomic tidal level, in the observed water level records; (4), storm surges were extracted from tidal residuals with a cutoff period of 25 h assuming that odd-tide has a positive storm surge; 4), the time gap between two neighboring events was defined as larger than 24-h to ensure the independence of each event. The above thresholds were chosen with trials with visual detection to ensure the truncated tidal levels can characterized the observed odd-tidal behaviors.

In the following sections, to quantify the characteristics of the storm-induced odd-tides: we first investigated the temporal variations of the occurrences of storm-induced odd-tide events; then an analysis of characteristics of the tidal behavior during odd-tide events is conducted; next, we analyzed the atmospheric conditions associated with each odd-tide event in order to diagnose the main atmospheric triggers of the tide. Measured atmospheric measurements are not available at Lusi station and sources from assimilated dataset from HYCOM oceanic current modeling system are used as a substitute. The importance of the investigation is to predict when and how fast the abnormal high tide would come the tidal flat. To quantify the characteristics of the abnormal high tide, we considerred the main physical aspects, including the intensity and duration of the odd tide phase advancement of high tide, the maximum differences between the measurement and astronomical tide. To quantify the intensity of odd-tide, we made use of the maximum wave energy ($\varepsilon = \frac{1}{8}\rho g H^2$) of the high-frequency tidal residuals, where ρ is seawater density and H is the maximum wave height of odd-tide oscillations. For each storm-induced odd tide event detected with the free-surface elevation time series, we manually checked that pressure and/or wind speed disturbances during the timespan of each event. The atmospheric conditions were mainly separated into constant or low-varying wind field and highly-evolutional wind field. The first type of the wind field is commonly observed during a winter-storm event. It comes often with a large area of cold air mass on top of the South Yellow Sea. The second type of the wind field usually comes with a passing-by cyclone or anti-cyclone and it is more dynamic.

3 Results

A total number of 180 odd-tide events during the period year 1975–1996 was detected in Rudong from water level records gathered at Lusi Station (Fig. 3a). Among them 51 were observed during the year 1992–1996, a period that has associated meteorological dataset. On average, around 10 odd-tide events were detected per year, while the occurrences during the year 1995 abnormally reached 25. Detailed discussion on this odd-tidal year is given in the later text. Figure 3b shows the annually-accumulative wave energy ($\sum_i^n \varepsilon_i$), where n is the number of events of each year and ε is the wave energy of each event and the yearly distribution reveals no decadal trend and the variation generally goes with the occurrences distribution.

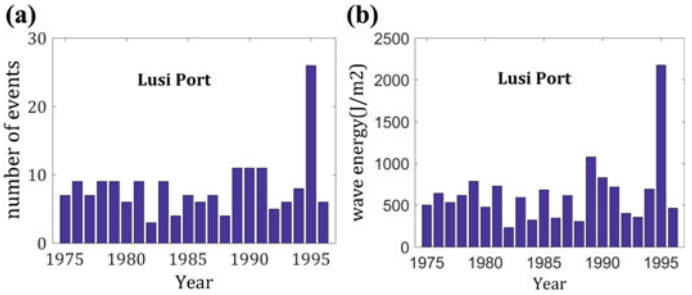

Fig. 3 **a** Yearly distribution of the number the odd-tide events observed at Lusi Station; and **b** yearly distribution of the accumulative maximum wave energy observed at Lusi Station; all the samples are from water level records along the year 1975–1996

Temporal Distribution of Occurrences and Duration of the Odd-Tide Events

The annual distribution of odd-tide events were bimodal at Lusi Station, with the maximum number of events happened in the local winter-storm season (November–March) and summer-storm season (July–October). The monthly occurrences of odd-tide with a short-period sample from the year 1992–1996 showed a similar trend (Fig. 4a, b). Most of the events lasted no more than 24 h, and the monthly-averaged ones were slightly higher during a summer-storm season (Fig. 5a, b). The longest events (lasting over 48 h) happened in either winter-storm season or summer-storm season. Events that were induced by summer-storms were longer than the ones related to winter-storms (Fig. 5c, d).

Temporal Distribution of the Wave Energy of the Storm-Induced Odd-Tide Events

Most events have mild sea level oscillations with high-frequency wave energy less than 100 $\left(\mathrm{J/m^2}\right)$, which approximates to the wave energy purely induced by atmospheric disturbances related meteo-tsunamis detected in the other places. The accumulative wave energy of events counting both single event intensity and occurrences reveal a bimodal pattern, which peaks during both the summer-storm season and winter storm season. Whereas, considering the monthly-average wave energy, the most

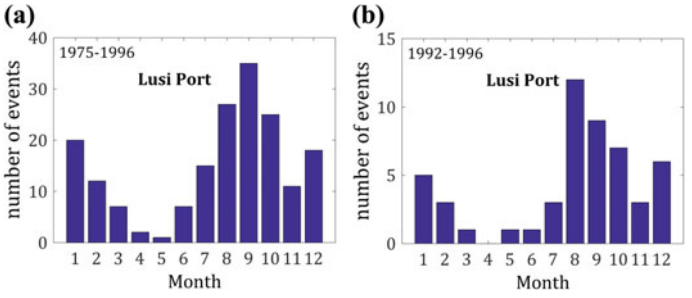

Fig. 4 Annually distribution of the total number of the odd-tide events observed at Lusi Station from water level records along **a** the year 1975–1996 and **b** the year 1992–1996

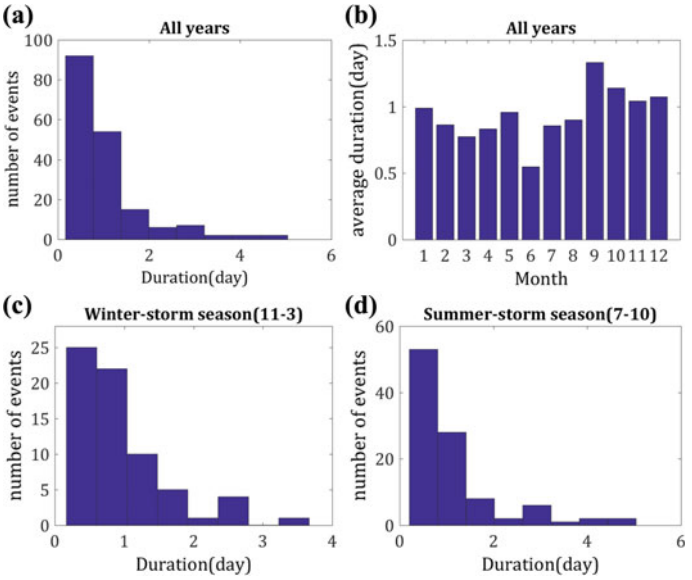

Fig. 5 **a** Distribution of the duration of the total odd-tide events observed at Lusi Station; **b** annually distribution of the average duration of the odd-tides; **c** distribution of the duration of the odd-tide events during winter-storm season; **d** distribution of the duration of the odd-tide events during summer-storm season; all the samples are from water level records along the year 1975–1996

energetic events occurred in January, March, and April, making winter and early spring the vulnerable months for odd-tides. A short-period of wave energy annually distributions during the year 1992–1996 were also detected (Fig. 6 right column). The probability of the single event intensity and the accumulated wave energy shows similar distributions compared to the 22-yearly long sampling distributions. The monthly averaged wave energy peaks in January and March.

Tidal Characteristics of the Storm-Induced Odd-Tide Events

Among the 180 detected events, a number of 171 events were observed with higher tidal level, revealing a positive surge dominated odd-tidal events. Most of the odd-tide events detected in this chapter can be regarded as storm-induced odd-tide events. The analysis of water level records showed that the tendency for odd-tide to occur most frequently on the rising tide which matched to visual observation from odd-tides. The statistics show that a short period sampling from the year 1992–1996 has similar patterns in tidal residual levels and phase differences from year 1975 to 1996 (Fig. 7). The tidal residual peaks around 0.75 m, which is about 20% of the tidal amplitude of the Rudong shallow water areas (upper panel in Fig. 7). The mode of tidal residual occurrence is 15–20 min before the nearest high water (lower panel in Fig. 7). (surge > 2.0 m).

Because the above data analysis show that the characteristics of the odd-tides hold no significant decadal variation nor yearly trend, which implying neither the

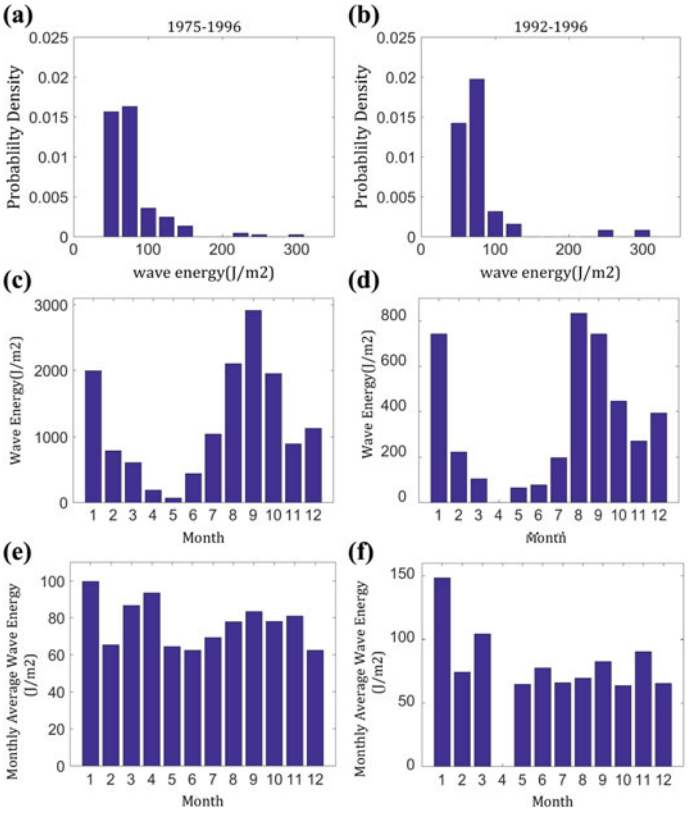

Fig. 6 Probability density distribution of the maximum wave energy of each odd-tide event observed at Lusi Station from water level records along **a** the year 1975–1996 and **b** the year 1992–1996; annually distribution of the accumulative maximum wave energy of the odd-tide events during **c** the year 1975–1996 and **d** the year 1992–1996; the monthly-average maximum wave energy of the odd-tide events during **e** the year 1975–1996 and **f** the year 1992–1996

global climate trend nor the sampling size may influence the odd-tides. Therefore, the available meteorological conditions from the short period (the year 1992–1996) are used here to explore the potential atmospheric triggers for the odd-tides. The top 10 energetic events and the top 10 durable odd-tide events during year 1992–1996 are shown in the following sections to explore the potential triggers and temporal evolution of the odd-tides, respectively. For the analysis, we considered the wave height of the high-frequency tidal residuals, the pressure anomaly relative to the mean sea level atmospheric pressure (Pa = 1013.25 hpa) and the wind field along the Yellow Sea coast (locations for plotting the meteorological conditions are shown in Fig. 1) (Figs. 8 and 9).

Top10 Longest Events

Most of the longest events happened during August to October and the rest existed in the winter-storm season (Fig. 8). A further investigation of these events coincident

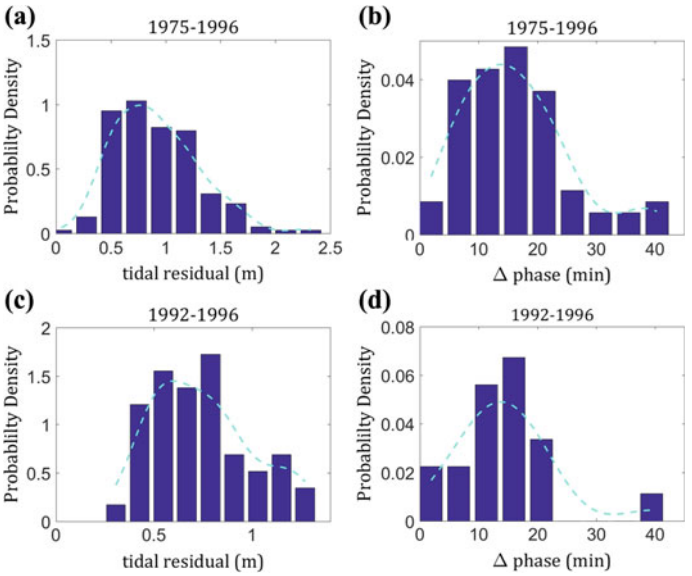

Fig. 7 Probability density distribution of the maximum tidal residual (calculated as the differences between the observed water level and the predicted water level, positive value indicating storm surge) of each odd-tide event observed at Lusi Station from water level records along **a** the year 1975–1996 and **b** the year 1992–1996; probability density distribution of the maximum tidal phase shift (calculated as the differences between observed water level and predicted water level, positive value indicating advanced tidal phase) of each odd-tide event observed at Lusi Station from water level records along **c** the year 1975–1996 and **d** the year 1992–1996

with the tropical and extra tropical events in these summer seasons, whereas the most interesting aspect of these extra-tropical cyclones is they never falled in the Rudong coastal regions. Basically, they curved away from the edge of the Radial Sand Ridges. However, we found among the top 10 longest events, the perturbation maximized when wind came from east and in most cases the east wind lasted continuously more than 12 h. Besides, the east winds were steadily strong between Qidong and Liyashan channel, two major tidal channels in the South Yellow Sea. The secondary major wind direction is parallel to Xiyang Channel, the largest northern tidal channel of the Radial Sand Ridges and it is generally meridian. Atmospheric shift with an absolute anomaly larger than 2 hpa were found in nine of the ten events. The wave height of odd-tide usually peaked at the fronts when an atmospheric jump or fall happened. Furthermore, anti-cyclones and regional tornadoes were also found among these events. It needs to mention more than half of the events happened during year 1995.

Top10 Most Intense Events

The top 10 largest events happened with more uncertainty (Fig. 9). The occurrences show a half-half probability between winter-storm season (Nov–March) and summer storm season (July–October). The largest event with wave height ~0.5 m happened

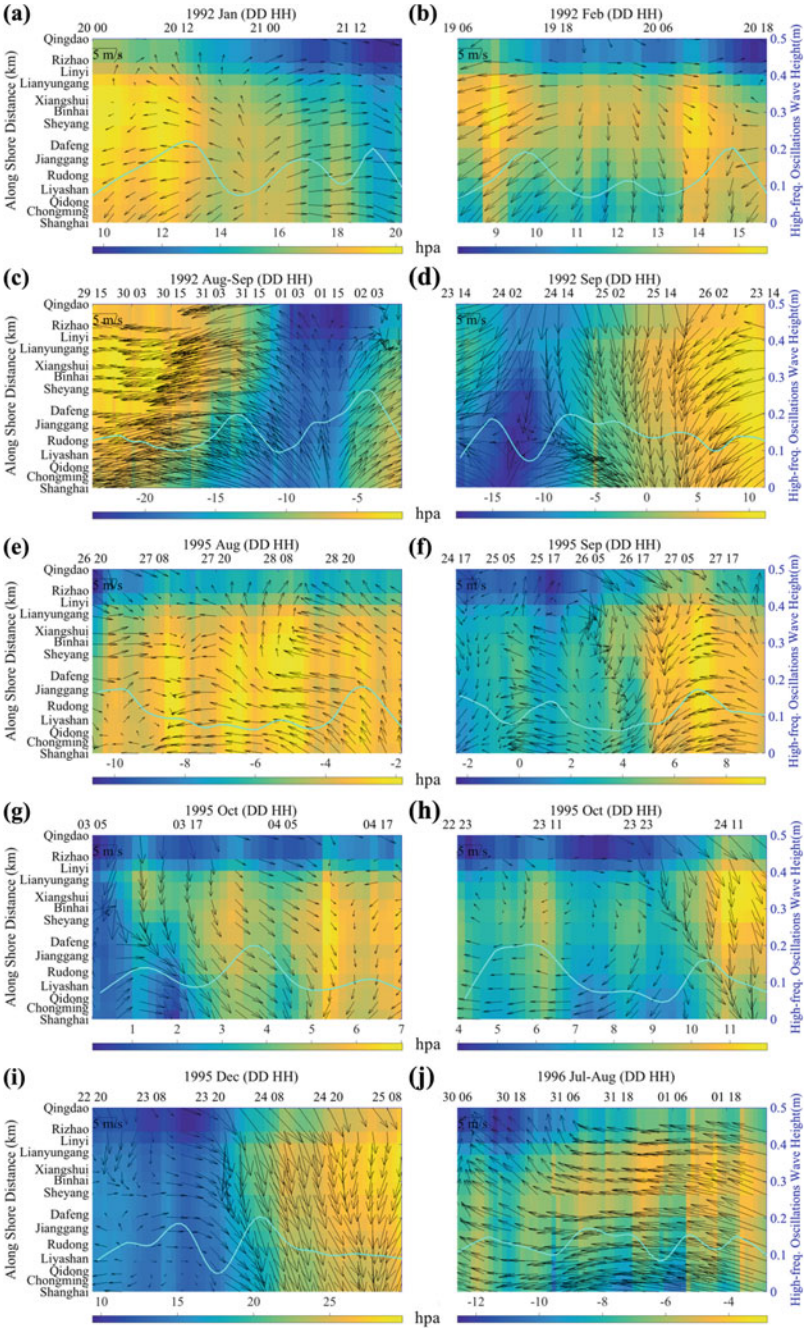

Fig. 8 Hovmöller diagram of the top 10 longest events during the year 1992–1996. The right axis stands form the wave height of the odd-tide and the left axis stands for the distance along the shore and the zero point is set at Shanghai (refer to Fig. 1)

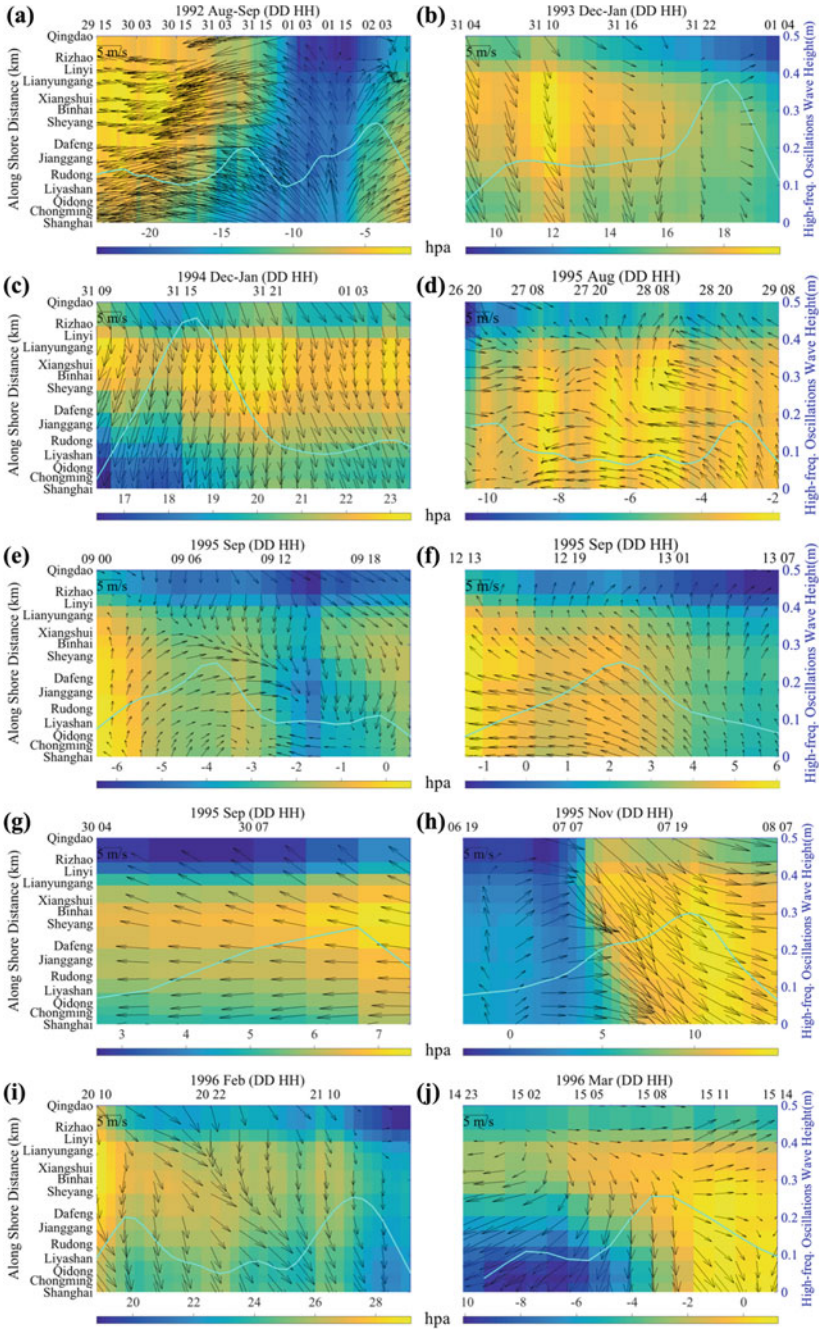

Fig. 9 Hovmöller diagram of the top 10 largest (maximum wave height) events during the year 1992–1996. The right axis stands for the wave height of the odd-tide and the left axis stands for the distance along the shore and the zero point is set at Shanghai (refer to Fig. 1)

across the year 1994 to the year 1995, in which an apparently southwarding cold front can be observed and the winter-storm also induced north winds blowing constantly over the entire Yellow Sea coast. For the rest of the events, they are associated with various meteorological conditions: including atmospheric pressure shift, anti-cyclones, extra-tropical induced onshore winds. Among the top 10 extreme events, 5 of them happened in the year 1995, except for the across-yearly events.

4 Discussion

Odd-Tides in the Storm-Intense Year 1995

The odd-tide events are most active in the year 1995, a year also characterized by the exceptionally storm-heavy season. A total of 25 odd-tides happened in 1995 (Table 2) with 14 of them in the summer-storm season and rest in the winter-storm season, particularly during November to December. An exploration of the typhoons during

Table 2 Odd-tide events in year 1995

Order	Start time	End time	Type[a]	hrangmax (m)	Δsurge (m)	Δphase (min)
1	07/15 19:00	07/15 10:00	1	0.22	0.51	
2	07/25 19:00	07/26 0:00	3	0.22	0.54	15.82
3	08/03 0:00	08/03 13:00	3	0.26	0.58	1.89
4	08/03 20:00	08/04 7:00	1	0.22	0.47	
5	08/26 20:00	08/29 8:00	3	0.29	0.64	11.43
6	08/07 6:00	08/08 7:00	1	0.22	0.59	
7	08/13 0:00	08/14 10:00	1	0.26	0.61	
8	08/29 8:00	08/29 15:00	1	0.23	0.52	
9	08/29 21:00	08/30 3:00	2	0.22		8.42
10	09/02 0:00	09/02 7:00	2	0.25		17.45
11	09/09 0:00	09/09 21:00	3	0.28	0.70	8.49
12	09/12 13:00	09/13 7:00	3	0.27	0.60	9.45
13	09/24 17:00	09/28 3:00	1	0.24	0.81	
14	09/30 4:00	09/30 11:00	1	0.26	0.64	
15	10/03 5:00	10/04 20:00	1	0.23	0.92	
16	10/08 6:00	10/08 18:00	1	0.22	0.54	
17	10/22 23:00	10/24 15:00	1	0.23	0.71	
18	11/06 19:00	11/08 7:00	1	0.32	1.19	
19	11/22 20:00	11/29 19:00	1	0.25	0.92	
20	11/25 22:00	11/26 3:00	1	0.23	0.46	

(continued)

Table 2 (continued)

Order	Start time	End time	Type[a]	hrangmax (m)	Δsurge (m)	Δphase (min)
21	12/03 2:00	12/03 20:00	1	0.21	0.45	
22	12/06 22:00	12/07 8:00	1	0.20	0.52	
23	12/08 15:00	12/09 3:00	3	0.26	0.31	3.28
24	12/19 3:00	12/19 14:00	1	0.24	0.44	
25	12/22 20:00	12/25 11:00	1	0.25	0.81	

[a]Type refers to associated surge level and tidal phase to odd-tide events with: 1-positive surge only; 2-advanced tidal phase only; 3-positive surge + advanced tidal phase

the year 1995 is surprising, that includes 24 tracks and spreading throughout the year. The relationship between the typhoon and odd-tide needs further exploration as the typhoons were not making landfalls in Rudong and thus no direct contribution to the genesis of odd-tide. Whereas, it is highly possible that the offshore surges induced by these storms can via a series wave transformation through the Radial Sand Ridges and finally produced the odd-tide.

Potential Meteor-Triggers Associated with the Storm-Induced Odd-Tide Events

The bimodal distribution of the annual occurrence of odd-tides observed in Rudong area is largely related to the seasonality of the storminess in the area. Results showed storm-induced odd-tide are dominated among all the odd-tide events. The main triggers, though not directly, contained 3 types of storms: (a) cold front induced winter storm (basically north winds) over the Yellow Sea Coastal area, (b) offshore cyclone triggered positive onshore wind-driven surge. Whereas, a further exploration on the mesoscale convective system should be explored. The mesoscale convective system's overall cloud and precipitation pattern of each odd-tidal weather systems such as extra-tropical cyclones, squall lines, and Siberian cold front, is generally formed near weather fronts which were often observed on the South Yellow Sea coasts during both winter-storm season and summer storm season.

5 Summary

Odd-tide is an integrated sea level oscillation detected in the South Yellow Sea Radial Sand Ridges. It is in need to explore the space and temporal distribution of the odd-tide events, as well as to understand the associated meteorological conditions in order to provide better predictions of occurrences for use in odd-tide hazard defense. In this study, we draw attention to the existence of critical time and space scales for odd-tide development. Using data from Lusi tide gauge, which located in the center of the most vulnerable area of odd-tides and has the longest available water level records in the Yellow Sea, China, we show that the storm dominated odd-tide events.

The mode of odd-tide occurrence is usually 15–20 min before the nearest high water and most of the events are accompanied with a positive surge. The duration of the odd-tides usually lasts no more than one day. High frequency oscillation of the tidal signal combined with a positive low-frequency surge, which could possibly relate to the passage of cold front or curved extra tropical cyclone outside of the Radial Sand Ridges, provides a good description of the odd-tidal behavior. We show that the wave shape and wave energy distribution of the odd-tide are larger than, but close to meteo-tsunami detected in other places such as the ones on the west coast of Florida, US. Atmospheric disturbances with anomalies larger than 2 hpa, a threshold for triggering meteo-tusnami, are also found in most of the odd-tide events. For dynamic mechanism detection of the odd-tides, coastal numerical models are inquired in the future work to reproduce the odd-tide formation and evolutional process.

Acknowledgements This work is also supported by National Natural Science Foundation of China [No. 51709091]; Jiangsu Natural Science Foundation of China [No. BK20170874]; State Key Laboratory of Satellite Ocean Environment Dynamics (SOED) [No. SOED1609] and the Fundamental Research Funds for the Central Universities [No. 2017B00514].

References

Beardsley, R. C., Limeburner, R., Rosenfeld, L. K. (1985). Introduction to the CODE-2 moored array and large-scale data report. In R. Limeburner (Ed.), *CODE-2; Moored array and large-scale data report: Woods Hole Oceanographic Institution technical report*. WHOI v.85–35.

Cao, C. M., Guo, K., Li, K., & Chen, Z. (2001). Synoptic analyses for the formation of large-amplitude seiche in the main harbors along the coasts of Bohai Sea and the Huanghai Sea. *Acta Oceanological Sinica, 23*(5), 24–32.

Chen, G. Y., Chien, C., Su, C., & Tseng, H. M. (2004). Resonance induced by edge waves in Hua-lien Harbor. *Journal of Oceanography, 60*(6), 1035–1043.

Feng, X., Olabarrieta, M., & Valle-Levinson, A. (2016). Storm-induced semidiurnal perturbations to surges on the US Eastern Seaboard. *Continental Shelf Research, 114*(2016), 54–71.

Lamb, H. (1923). *Hydrodynamics* (6th edn). Cambridge: Cambridge University Press.

Liu, K. F. (2015). *Demonstration and research on the disaster monitoring and warning technology of the odd-tide in the shoal of Jiangsu Coast*. China Ocean Press.

Liu, A. J., Xiu, R. C., Zhang, Z. L., & Yin, X. F. (2002). Coastal rapids along Jiangsu Coast. *Acta Oceanologica Sinica, 24*(6), 120–126.

Monserrat, S., Vilibic, I., & Rabinovich, A. B. (2006). Meteotsunamis: Atmospherically induced destructive ocean waves in the tsunami frequency band. *Natural Hazards and Earth System Sciences, 6*, 1035–1051.

Olabarrieta, M., Valle-Levinson, A., Martinez, C. J., Pattiaratchi, C., & Shi, L. (2017). Meteotsunamis in the northeastern gulf of Mexico and their possible link to el niño southern oscillation. *Natural Hazards, 88*(6),1325–1346.

Proudman, J. (1929). The effects on the sea of changes in atmospheric pressure. *Monthly Notices of the Royal Astronomical Society, 2*(4), 197–209.

Vennell, R. (2010). Resonance and trapping of topographic transient ocean waves generated by a moving atmospheric disturbance. *Journal of Fluid Mechanics, 650*, 427–442.

Wu, S. H., & Wang, X. N. (1999). Preliminary study on the characteristics and causes of false tides in the gulf. *Marine Science Bulletin, 3*(3), 1–6.

Xie, D., Tan, Y., Chu, A., & Zhang, C., 2016. Analysis on the cause of the specific high tides in the South Yellow Sea. In *The 26th International Ocean and Polar Engineering Conference*. International Society of Offshore and Polar Engineers.

Xiu, R. C. (1985). Propagation of tide wave in a basin with variable cross sectional area. *Acta Oceanological Sinica, 4*(1), 1–8.

Xiu, R. C., Zhang, Z. L., & Liu, A. J. (2004). Observations and analysis of oceanic riptide. *Acta Oceanologica Sinica, 26*(2), 118–124.

Zhang, H., & Sheng, J. (2013). Estimation of extreme sea levels over the eastern continental shelf of North America. *Journal of Geophysical Research: Oceans, 118*(11), 6253–6273.

Experimental Studies on Sediment Transport and Geophysical Flows

The increasing amount of computational studies as compared to experimental studies would suggest that physical modelling is passé. However, there are a number of strong arguments against this perception. Despite scale effects and laboratory effects when transferring the laboratory results to the prototype, scale model experiments will not only remain a desirable and viable approach but also inevitable for improving process understanding and generating data for the validation of numerical models. This part, which includes four chapters related to various hydro-morphodynamic topics using laboratory experiments, may be viewed in this context as a contribution to support the statements above for the case of coasts and estuaries.

The first chapter by Vah et al. is focused on dunes and ripples under limited sediment supply conditions, which have received much less attention than those under unlimited sediment supply conditions. For dunes under the latter conditions, the results confirm that both dune heights and lengths at the equilibrium state are essentially determined by the mean water depth so that both formulae proposed by Allen (1968) can be applied as a reference to account for the effect of limited sediment supply. For dune heights, it is found that (i) this effect is noticeably independent on flow velocity and sediment size so that the exponential formulation by Tuijnder et al. (2009) can be applied, and (ii) no clear relationship of this effect with dune lengths could be observed. For ripples under unlimited sediment supply, the results show that the formulae in Soulsby et al. (2012) can be applied as a reference case to account for the effect of limited sediment supply on ripple heights and lengths, which is found to increase with increasing sediment availability. Prediction formulae are finally provided by adjusting and extending the aforementioned exponential formulation for ripple length and height, respectively.

The second chapter by Truong et al. is dedicated to the shallow flow in compound vegetated channels with gentle transverse slopes. It shows clearly that large horizontal coherent structures (LHCSs) emerge as a result of the shear layer dynamics, rather like in a vegetation field than due to the difference in water depths. These LHCSs are shown to be determinant for the transverse exchange processes which may affect the flow in the main channel as well as the flow in the vegetation area. These results might have important implications for the requested forest width, for the sediment transport

processes and the river bank stability. Though the study is related to compound vegetated channels in the Mekong Delta, the results are generally applicable for any compound vegetated channel and might represent a good database for the validation of a CFD model which can be deployed to perform a more comprehensive parameter study.

The third chapter by Yuan et al. may be viewed in the context of the revival of laboratory experiments for alluvial fan research in recent years. In contrast to previous studies which rather addressed the long-term evolution of alluvial fans as affected by changes in water and sediment supply, this laboratory study attempts to focus on the short-term response of alluvial fans to abrupt changes in river flow discharge and sediment supply under lateral confinement with due consideration of sediment accumulation and river evolution. As a result, a delayed response of the fan to the external disturbance is obtained which depends on the disturbance intensity, the state of the fan prior to disturbance and the alluvial fan's response pattern. This may result in a regime shift corresponding to a new equilibrium state of the fan after disturbance. A reduction in the sediment supply by half may result in a river evolution cycle alternating between straight channels and braided channels. With the further reduction in the flow discharge until clear water scour conditions, only a straight channel is observed. Overall, the results, even if limited, contributed to improve the knowledge of alluvial fan response to abrupt changes in river flow discharge and sediment supply.

The fourth chapter by Namaee et al. is concerned with large-scale model experiments. As ice covers impose an additional boundary layer on channel flow conditions and may thus affect sediment transport in the channel, this study aims at determining the effect of such an additional boundary on bridge scour in a non-uniform sand bed by considering both smooth and rough ice covers. The fact that, in general, only very few studies have yet considered the effect of ice covers on bridge scour volume and area and, in particular, that this study is unique in the sense that such an effect is considered for scour around a group of bridge-supporting piles in a non-uniform sand bed using large-scale model testing underlines the relevance of this study. It is found that this effect on both scour volume and scour area is significant as compared to open channel flow and that this effect is larger under rough than smooth ice cover conditions and for finer bed sediments. Finally, empirical formulae relating scour volume and area under open channel flow and ice-covered flow conditions are proposed.

Hocine Oumeraci
TU Braunscheig, Germany

Experimental Study on Sediment Supply-Limited Bedforms in a Coastal Context

Mélanie Vah, Armelle Jarno, François Marin and Sophie Le Bot

Abstract Experiments are carried out in a flume without slope. Tests are performed for different unidirectional steady flow conditions, varying the initial sediment thickness and recirculating the sediment to ensure a constant supply condition, from an extremely limited sediment supply to an unlimited sediment supply condition. The formation of ripples and dunes is considered from an initially flat bed. The growth rate of the mean wavelength of ripples depends on the sediment supply, whether it is extremely limited or not. In spite of a rapid initial growth when sediment supply is extremely limited, the growth rate is much higher when sediment availability increases. As far as the equilibrium dimensions of the sedimentary structures are concerned, an increase of mean heights of ripples and dunes is pointed out when the sediment availability increases. The similar trend is found for mean ripple lengths but no clear trend is exhibited for dunes which are few and irregular. The empirical law proposed by Tuijnder et al. (2009) in a fluvial context for relative dune heights in the case of sediment limited supply conditions can be used for dunes in a coastal context. However, this formulation cannot be extended to ripple heights for which a dependence with flow conditions is noted. Ripple equilibrium lengths can be described with a relation suggested by Tuijnder et al. (2009) for dunes if an adaptation factor is considered.

Keywords Ripples · Dunes · Coastal bedforms · Sediment supply limitation · Sediment dynamics · Physical modeling

M. Vah (✉) · A. Jarno · F. Marin
Normandie Univ, UNIHAVRE, UMR 6294, CNRS, LOMC, 76600 Le Havre, France
e-mail: melanie.vah@univ-lehavre.fr

S. Le Bot
Normandie Univ, UNIROUEN, UNICAEN, UMR 6143, CNRS, M2C, 76000 Rouen, France

K. D. Nguyen et al. (eds.), *Estuaries and Coastal Zones in Times of Global Change*, Springer Water,
https://doi.org/10.1007/978-981-15-2081-5_37

Nomenclature

d	water depth (m)
D_{xx}	grain size for which XX percent is finer
D_*	dimensionless grain size
g	gravitational acceleration (m/s^2)
h	height (m)
I_e	slope energy level
Re	Reynolds number
s	sediment relative density
U	mean velocity (m/s)
u_*	shear stress velocity (m/s)
x	position in the flume (m)
α, α_T, α''_T, β, β_T, γ_T	dimensionless parameters
γ_p	growth exponent
δ	layer thickness (m)
θ	Shields parameter
λ	wavelength (m)
ρ	water density (kg/m^3)
σ_g	standard deviation
ν	kinematic viscosity (m^2/s)
’	grain related
c	threshold
eq	equilibrium
eq_inf	equilibrium value without supply-limitation

1 Introduction

The study of bedforms is of major importance as they affect the bottom roughness, flow conditions and sediment transport. Ripples and dunes are mainly discriminated according to their dimensions, dunes being typically about one order of magnitude higher than ripples and characterized by a length to water depth ratio which is much lower for ripples than for dunes (Kennedy 1963; Flemming 2000). It was also reported that no ripples can form for grains of median diameter greater than 0.6 mm (Coleman and Nikora 2011; Soulsby et al. 2012).

In the last decades, much work was devoted to understanding the processes of emergence of bedforms and of their development, in fluvial and coastal contexts. Some review papers have reported on this abundant literature (Engelund and Fredsøe (1982), Blondeaux (2001), Seminara (2010) among others). A unified description of bedform growth and saturation was proposed by Colombini and Stocchino

(2011) and Charru et al. (2013) under steady unidirectional flows. Equilibrium time of bedforms development has also been considered (Baas 1993; Coleman et al. 2005). Equilibrium bedforms morphologies have been considered by Allen (1963, 1968), Yalin (1964), van Rijn (1984), Flemming (1988), van Landeghem et al. (2009), Soulsby et al. (2012).

Sediment-supply limited bedforms have received little attention when compared to the extended literature dedicated to bedforms under unlimited sediment-supply conditions. However, the in situ conditions of a limited movable sediment stock are not so uncommon both in river and coastal contexts. Sediment limitation can be due to an unerodible bottom or partially immobile sediments. For example, Carling et al. (2000) described large sandy barchans migrating over an armor layer in the Rhine (Germany) downstream of a dam. Also, in the coastal context of the Channel, the sedimentary layer is highly heterogeneous in grain size and shape, leading sometimes to a significant sedimentary gradient between immobile zones and regions rich in movable sediments (Le Bot and Trentesaux 2004). Tuijnder et al. (2009) studied the relationship between dune geometry and the amount of movable sediments on an immobile gravel layer in an inclined 30 m flume. They found a strong relationship between the mobile volume of sediment and dune geometry. The supply-limited bedforms have lower lengths and heights than the bedforms observed in alluvial conditions according to these authors. They also pointed out that dunes become more irregular when sediment supply is increased. Empirical relationships between dune dimensions and supply limitation were proposed in the form of an exponential relation. Although the experimental conditions for Dréano et al. (2010) were different from Tuijnder et al. (2009), with a closed channel of very small dimensions and glass beads to simulate sediments, their results are in good agreement with those of Tuijnder et al. (2009). Another type of experimental installation—a divergent flume—was used by Rauen et al. (2009) to study the influence of supply limitation under non-uniform flow. Kleinhans et al. (2002) worked on the occurrence of bedforms in sediment supply-limited conditions with experiments in flume and in the field (river Allier, France and river Waal, The Netherlands).

The objectives of this chapter are to extend the exploration of the effect of sediment supply on ripple growth and equilibrium state and to compare new data for dune bedforms measured in a flume designed for coastal studies (no slope) with results from Tuijnder et al. (2009).

2 Setup and Experimental Conditions

Experiments are carried in a current flume. This flume is 10-m-long, 0.49-m-wide without slope (Fig. 1). The current is generated by a recirculating pump. The flow rate can be adjusted in the range 0–100 L/s. The mean water depth d is measured above the flat sand layer at the beginning of each experiment. A carriage system above the flume allows the motion of the experimental device at a controlled speed. Traps at the downstream part of the flume are used to collect the transported sand. A

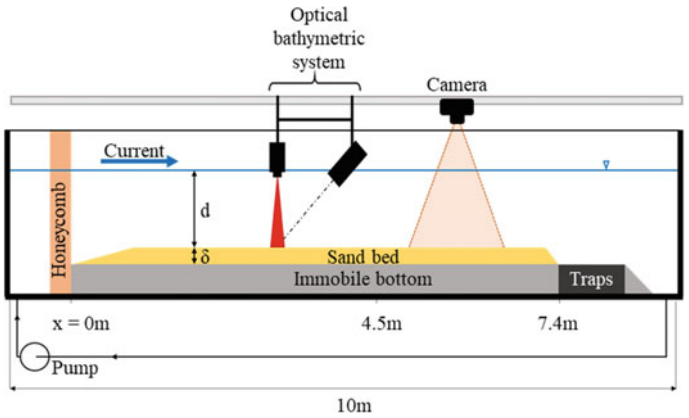

Fig. 1 Schematic view of the flume with measurement equipment

length of 7.4 m between the honeycomb, installed in the upstream part of the flume, and the traps is used for experiments.

The bottom of the flume is made of Polyvinyl Chloride (PVC). A sanding hand machine equipped with a coarse sand abrasive disk is used to adjust the roughness level to a homogeneous micro-surface roughness.

Velocity profiles without sediment have been performed as preliminary tests and have shown an established logarithmic velocity profile 4.5 m downstream of the honeycom. The flow is in the turbulent regime (Re $\gg$ 5000, where Re is the Reynolds number). The sandy part located in the region 4.50 m < x < 7.4 m is investigated for the development of bed forms.

For present experiments, two different natural types of sand were selected. These sands are composed of quartz and come from a quarry. Their relative density is s = 2.65 (where $s = \rho_s/\rho$ with ρ_s the sand density and ρ the fluid density in clear water). One of the two sand type is of medium grain size with a median diameter D_{50} = 328 μm and the second sand type is a coarse sand with D_{50} = 617 μm which may form dunes (D_{50} > 600 μm, Coleman and Nikora 2011; Soulsby et al. 2012). Both sands are well-sorted according to Soulsby criterion, with the geometric standard deviation defined by $\sigma_g^2 = D_{84}/D_{16}$ equal to 1.5 and 1.4 respectively, where D_{84} and D_{16} are the grain diameter such as 84 and 16% in grain mass are smaller.

All the tests are conducted according to the same experimental protocol. First, the sand bed is flattened to reach a height noted δ (Fig. 1). During the tests, the current was regularly stopped, after fifteen minutes to one hour according to the current velocity, till a steady state is reached. At each stop, the sand accumulated in the downstream traps is spread in the upstream region (0 m < x < 2.5 m). This sediment transfer fulfills the quasi-constant sediment supply condition.

Each time the current is stopped, top view photos of a 1.50 long extended region (5 m < x < 6.5 m) are taken with a high resolution camera (0.1 mm per pixel). Positions

of the bedforms crests are manually extracted. Each wavelength is calculated as the mean value of the crest-to-crest distance.

Several times in each experiment, optical bathymetries measured on a 2.3 m field length (4.5 m < x < 6.8 m) are performed with a laser beam coupled to a camera with a spatial resolution of 0.05 mm per pixel (Marin and Ezersky 2008). Post-processing is performed to detect position of crests and troughs. Individual structure heights are estimated from the elevation differences between the crest levels and the mean of the upstream and downstream associated trough levels. Then, mean wavelength and height are calculated.

The wavelengths were regularly measured from photos from the beginning of the experiment (flat bed) to the bedforms equilibrium state. Tests were carried out for different sediment thickness (Table 1), from a very thin sediment layer, approximately three grains diameters height, to unlimited sediment supply conditions, that is for a 5.5 cm sand thickness for present conditions. The height was measured about 5 times during growth phase of bedforms.

Test conditions are given in Tables 1 and 2. Set M1 and Set M2 are performed with the medium sand whereas the other sets are carried out with the coarse one. For

Table 1 Dimensional parameters

	Set M1	Set M2	Set C1	Set C2	Set C3
D_{50} (μm)	328	328	617	617	617
d (m)	0.25	0.25	0.195	0.25	0.25
U (m/s)	0.35	0.45	0.45	0.45	0.55
u'_* (m/s)	0.016	0.021	0.024	0.023	0.029
δ (cm)					
3 grains diameters	×	×	×	×	
0.5	×	×	×	×	×
1	×	×	×	×	×
2	×	×	×	×	×
3.5	×	×	×	×	×
5.5	×	×	×	×	×
Type of bedform	Ripple	Ripple	Dune	Dune	Dune

M = medium sand
C = coarse sand

Table 2 Dimensionless parameters

	Set M1	Set M2	Set C1	Set C2	Set C3
Re	87,500	112,500	87,500	112,500	137,500
θ'	0.050	0.084	0.059	0.055	0.084
θ_c	0.036	0.036	0.030	0.030	0.030
D_*	8.3	8.3	15.6	15.6	15.6

each set, 6 different tests are performed with different sediment supply conditions (except for Set C3: 5 thicknesses).

The main dimensionless parameters involved in this study are the Reynolds number (Re), the Shields parameter (θ), and the grain dimensionless diameter (D_*).

The flow Reynolds number is defined as follows:

$$\mathrm{Re} = \frac{Ud}{\nu} \tag{1}$$

where:
U = mean flow velocity (m/s)
d = mean water depth (m)
ν = the fluid kinematic viscosity, $\nu = 1.10^{-6}$ m^2/s

The Shields parameter is defined as follow:

$$\theta = \frac{u_*^2}{(s-1)gD_{50}} \tag{2}$$

where:
u_* = bed shear stress velocity (m/s)

The critical value of the Shields parameter for the sediment incipient motion θ_c is estimated using Soulsby's (1997) relation:

$$\theta_c = \frac{0.3}{1+1.2D_*} + 0.055(1-\exp(-0.02D_*)) \tag{3}$$

where:

$$D_* = \left\{\frac{(s-1)g}{\nu^2}\right\}^{1/3} D_{50} \tag{4}$$

g = the acceleration due to gravity (m/s^2).

The type of identified bedforms observed at the equilibrium state, when the amount of sand is unlimited, is indicated in Table 1 (Colombini and Stocchino 2011; Fourrière et al. 2010; Charru et al. 2013).

3 Qualitative Description

Figure 2 illustrates the equilibrium bedforms for sediment supply conditions varying from very limited to unlimited, for Set M1. Mature ripples can be observed at the equilibrium state. The sediment supply limitation clearly impacts the bed morphology. An increase of the mean ripple length is induced by a sediment thickness increase.

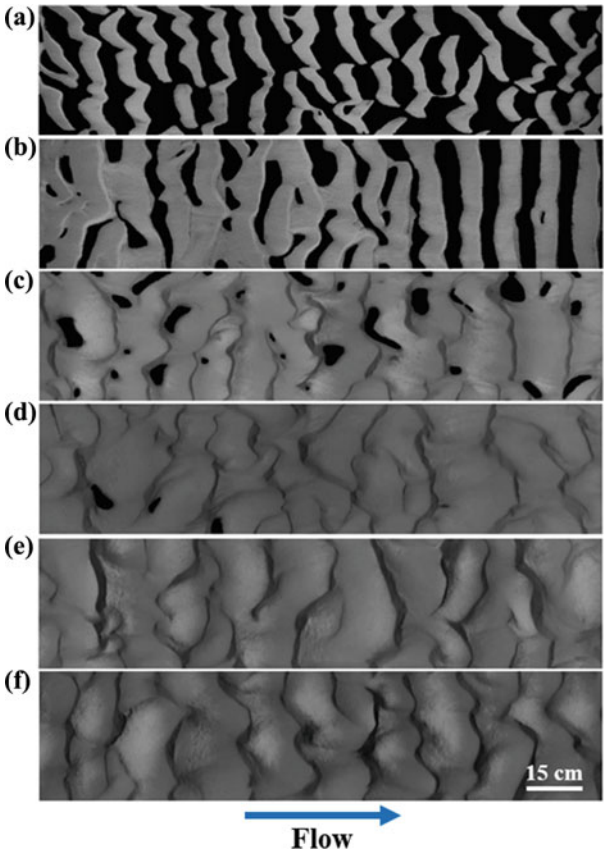

Fig. 2 Top view photos at equilibrium state for each initial sediment thickness. Set M1. **a** 3 grains diameters, **b** 0.5 cm, **c** 1 cm, **d** 2 cm, **e** 3.5 cm and **f** 5.5 cm. The bottom of the flume appears in black

Three distinct bed states can be identified according to sediment supply. Indeed, for very small initial sediment height ($\delta \approx 3$ grains diameters and $\delta = 0.5$ cm), we observe an alternation of ripples and uncovered zones. Starved ripples are separated from each other by large immobile zones since the beginning of pattern formation until it reaches equilibrium. When sediment supply is increased but remains limited ($\delta = 1$ cm and $\delta = 2$ cm), only some patches of immobile uncovered bottom are still visible at the end of the tests. For large sediment supply ($\delta = 3.5$ cm and $\delta = 5.5$ cm), the influence of supply limitation cannot be detected just by an observation of the bed surface.

4 Time Evolution as a Function of the Supply Limitation

Set M1 was conducted under the weakest shear stress conditions for grains. In this case, the bedforms dynamics is relatively slow. It is therefore the best candidate set to analyze the influence of sediment supply on the growth of mean pattern geometric parameters. The wavelength growth is reported from the flat bottom to steady-state conditions. It is clear that the first bed-profile measured after 15 min cannot be used to identify directly an initial wavelength. In fact the initial wavelength corresponds to the first length that appear in the first instant of an experiments. However, the growth phase of bedforms can be accurately analyzed. Figure 3 shows that the impact of the sediment thickness on the temporal evolution of the bedforms wavelength is significant.

For a very limited sediment supply ($\delta \approx 3$ grains diameters), the first wavelength detected corresponds approximately to 70% of the equilibrium wavelength, whereas it corresponds approximately to 45% for an important or even unlimited sand supply ($\delta = 5.5$ cm). In addition, although the wavelength is rapidly of a great value for a very limited sediment supply, the remaining 30% of growth to reach equilibrium state requires a longer time than the one required to increase the mean length by 65% for unlimited sediment supply conditions. It can be concluded that the growth rate is much higher when sediment availability increases and that the processes of formation of the two equilibrium bedforms cannot be the same.

Two different formulations have been proposed to characterize bedform growth for unlimited supply. According to Nikora and Hicks (1997), the growth of average sediment geometric characteristics can be written in the form of a power law (Eq. 5). Then, Coleman and al. 2005 proposed an exponent adjusted to a large collection of experimental data for ripples and dunes. For length of ripples and dunes,

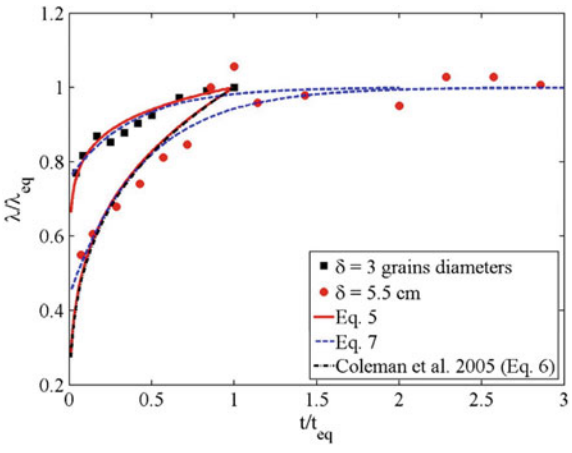

Fig. 3 Time evolution of wavelength for two tests of Set M1 ($\delta = 3$ grains and $\delta = 5.5$ cm). Best fit of power law (Eq. 5) and exponential law (Eq. 7) are plotted for both tests as well as Coleman et al. 2005 predicted power law (Eq. 6)

$$\frac{\lambda(t)}{\lambda_{eq}} = \left(\frac{t}{t_{eq}}\right)^{\gamma_p} \text{ for } 0.01 < \frac{t}{t_{eq}} < 1 \tag{5}$$

where:
λ = bedforms length, (m)
λ_{eq}, = bedforms equilibrium length, (m)
t = time, (s)
t_{eq} = the time to achieve equilibrium state, (s)
γ_p = the growth exponent

Coleman et al. 2005 defined the growth exponent as:

$$\gamma_p = 0.14 D_*^{0.33} \tag{6}$$

The second proposed evolution law for unlimited supply is an exponential law (Eq. 7). This kind of development equation was proposed by Baas (1993).

$$\frac{\lambda}{\lambda_{eq}} = 1 - \beta \exp\left(\frac{-t}{\alpha t_{eq}}\right) \tag{7}$$

where:
α and β = dimensionless parameters.

The two equations were used to fit our data. For each test, t_{eq} was adjusted to generate the best fit with both the power law and the exponential law. Mean wavelength at equilibrium was estimated by its mean value for $t > t_{eq}$.

For unlimited supply ($\delta = 5.5$ cm), the growth law fits with the power law proposed by Coleman et al. (2005) with the same exponent ($R^2 = 0.89$) but the high slope of the curve leads to a deviation with the equilibrium wavelength when t/t_{eq} is approaching 1. The regression coefficient of the exponential law is lower ($R^2 = 0.83$) but insures the convergence towards the equilibrium state. For strong limited supply ($\delta \approx 3$ grains diameters), the power law with Coleman exponent does not match and has to be adjusted ($\gamma_p = 0.089$, $R^2 = 0.92$). The exponential law has also to be adjusted in strong supply limitation to fit experimental data ($\alpha = 0.38$, $\beta = 0.24$, $R^2 = 0.94$).

Finally, the different sediment heights of Set M1 are analyzed to find the best fit. The two tests with very low sand supply fit the same exponential law or power law with the same adapted coefficient. The other four sediment heights corresponding to an intermediate ($\delta = 1$ cm; $\delta = 2$ cm) or infinite sediment supply ($\delta = 3.5$ cm; $\delta = 5.5$ cm) (Table 3) behave like the infinite sediment supply test plotted on Fig. 3. The power law with Coleman exponent still works with present tests conducted with a small supply limitation. Under strong supply limitation conditions ($\delta \approx 3$ grains diameters; $\delta = 0.5$ cm), the physical processes are different and the time evolution of the bottom cannot be supported by the same equation.

Equilibrium time for ripple length found by Coleman et al. (2005) for unlimited supply conditions are in the same order than the one measured in Set M1 with both

Table 3 Best fit dimensionless laws coefficient

	Strong supply limitation	Small or no supply limitation
Power law ($0.01 < t/t_{eq} < 1$)	$\gamma_p = 0.07$ $R^2 = 0.72$	$\gamma_p = 0.28$ (Coleman et al. 2005 exponent) $R^2 = 0.86$
Exponential law	$\alpha = 0.37$; $\beta = 0.2$ $R^2 = 0.75$	$\alpha = 0.41$; $\beta = 0.56$ $R^2 = 0.74$

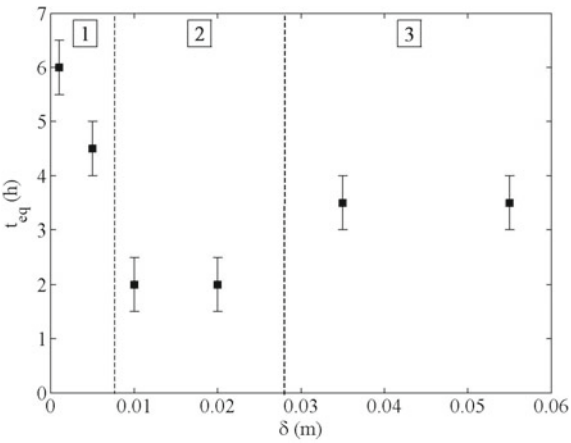

Fig. 4 Evolution of the equilibrium time (t_{eq}) with the sediment height (Set M1). 1: Strong supply limitation; 2: Small supply-limitation; 3: Unlimited supply

limited and unlimited supply. However, significant different times of formation were measured according to sediment supply conditions (Fig. 4).

Tests conducted with a very limited sediment supply (Fig. 4, range 1) are characterized by a long time to achieve the steady state. This can be explained by the small height of ripples in this case with small recirculation zones generated. This leads to limited exchange of sediment between ripples and consequently a long time to reach equilibrium. Range 2 of Fig. 4 corresponds to a small supply limitation with mobile ripples whose troughs can reach the immobile bottom. For range 2, all the grains contribute to the movement and belong to ripples. The equilibrium time is lower in this zone. When an unlimited supply condition is simulated (range 3), the equilibrium time is intermediate. In this case, intense recirculation vortices are generated (Stoesser et al. 2008). The active layer is fully developed and it can be assessed that the equilibrium time is the necessary time for grains to organize in the whole active layer.

We obtain the same equilibrium time for wavelengths and heights for each sediment supply condition, as previously obtained by Baas (1993) and Coleman et al. (2005) for unlimited sediment supply.

5 The Equilibrium State Under Limited Sediment Supply

1. Variation of bedform dimensions with supply limitation: results

Equilibrium is reached when mean geometric dimensions of bedforms become invariable in time. Let us consider the evolution of bedforms lengths and heights at the equilibrium state when the sediment availability is varied.

Figure 5 shows that the bedforms heights at the equilibrium state increase for increasing values of the initial sediment thickness δ. The standard deviation for bedform heights is approximately 10% for all the tests.

Tests for thick initial sediment layers (δ > 3.5 cm; Fig. 5) simulate unlimited supply conditions. For these conditions, present results show that bedforms heights depend on the flow conditions: an increase of the bottom shear stress leads to higher bedform heights. For example, for ripples (Sets M1 and M2, Fig. 5a), the skin friction Shields parameter equals to 0.050 and 0.084 for Set M1 and Set M2 respectively and

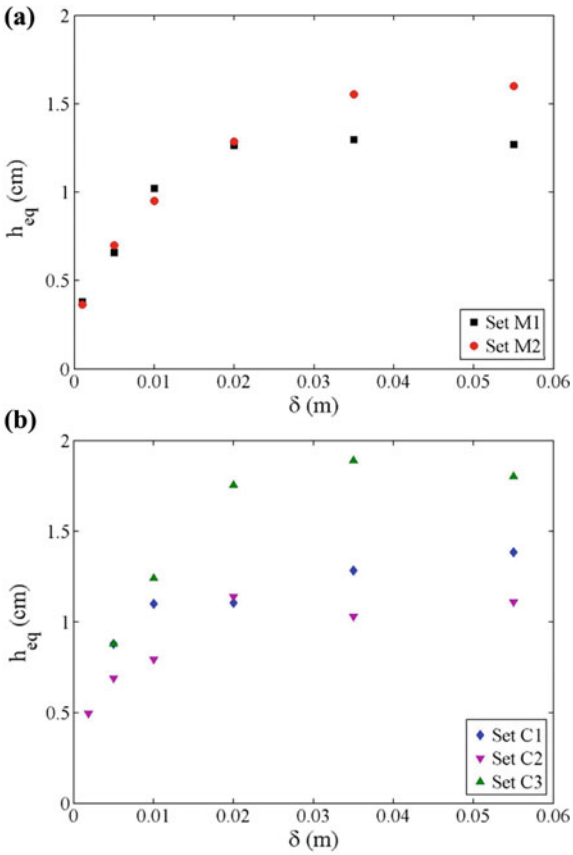

Fig. 5 Variation of the bedforms heights at the equilibrium state with the initial sediment thickness. **a** Ripples; **b** dunes

leads to an increasing of 0.3 cm in the value of the equilibrium ripples heights under unlimited sediment supply.

When the sediment supply is limited ($\delta < 3.5$ cm), dunes and ripples do not show the same dependence with respect to the flow conditions (Fig. 5). For Set M1 and Set M2, ripples heights are similar for a fixed δ-value (Fig. 5a). As the 2 sets have been conducted with two different flow velocities [$U = 0.35$ m/s and $U = 0.45$ m/s for Set M1 and Set M2 respectively (Table 1)], ripple heights do not depend on the bed shear stress in this case. This behavior is not found for dunes (Sets C1, C2 and C3, Fig. 5b) where a dependence with flow conditions is pointed out.

Dune lengths (Sets C1, C2 and C3) at the equilibrium state do not exhibit a clear evolution with the sediment supply height (Fig. 6b). This can be partly due to the few number of dunes formed in the flume for the involved tests, because of the relatively high dune length (approximately 60 cm (Fig. 6b)). This can also be attributed to the irregular nature of dunes formed with a standard deviation of about 40%. The same irregularity of dunes was reported by Tuijnder et al. (2009) in a longer channel.

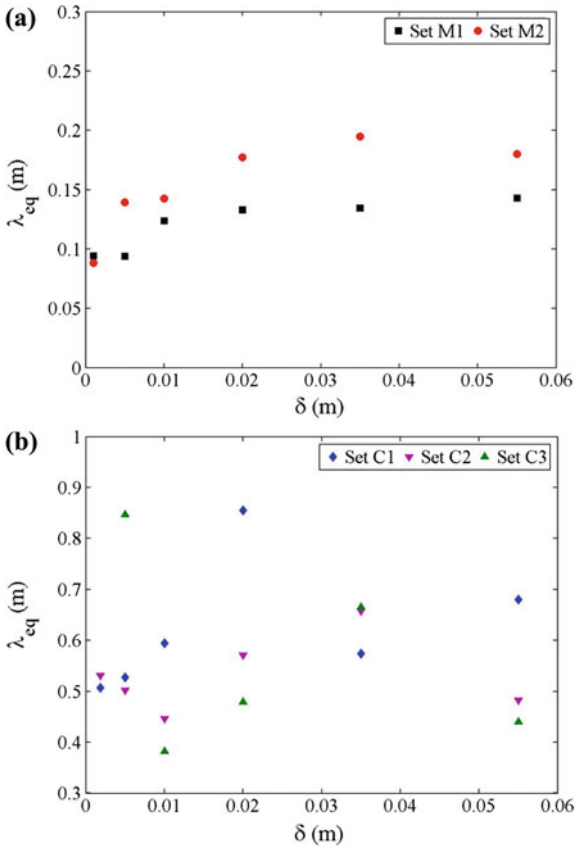

Fig. 6 Variation of the bedforms wavelength at the equilibrium state with the initial sediment thickness. **a** Ripples; **b** dunes

For ripple length (Sets M1 and M2), numerous ripples with small lengths are formed and the mean length can be accurately estimated. The standard deviation for ripple length is about 20%; ripple lengths are less irregular than dune lengths. A clear increase of ripple lengths for increasing sediment supplies is shown in Fig. 6a.

For unlimited conditions ($\delta > 3.5$ cm), the ripple lengths depend on the hydrodynamic conditions as for ripples heights but for supply-limited conditions ripple lengths seem also to depend on the applied bottom shear stress (Fig. 6a).

2. **Comparison with unlimited supply studies**

Values for large initial sediment layers are supposed to simulate no supply limitation conditions. Thus, a comparison with previous empirical laws for unlimited sediment supply can be performed.

For ripples, the formulations that gives the closest value for length and height, with the experimental data under unlimited sediment supply, are the one proposed by Soulsby et al. (2012) for $1.2 < D_* < 16$:

$$h_{eq\_inf} = 202 D_{50} D_*^{-0.554} \tag{8}$$

$$\lambda_{eq\_inf} = D_{50}\left(500 + 1881 D_*^{-1.5}\right) \tag{9}$$

where:
h_{eq_inf} and λ_{eq_inf} = respectively the height and length at the equilibrium state for unlimited sediment supply conditions (m).

According to Eqs. 8 and 9, ripple dimensions depend only on the grain density and diameter. Equation 8 predicts a ripple wavelength of 0.19 m for Sets M1 and M2 which is in the same order of magnitude than the values experimentally found. For ripple heights, Eq. 7 gives a value of 2 cm which in good agreement with Set M2 under unlimited sediment supply ($\left(h_{eq\_inf}(\mathrm{M2}) = 1.6\,\mathrm{cm}\right)$ while it slightly overestimates h_{eq_inf} for Set M1 $\left(h_{eq\_inf}(\mathrm{M1}) = 1.3\,\mathrm{cm}\right)$ in the same condition. In other words, it appears that the flow condition is a significant parameter for the estimation of ripples dimensions which is not the case in these formulations.

Equations 10 and 11 present the estimation of dune heights and wavelengths at the equilibrium state, for unlimited sediment supply, according to Allen (1968):

$$h_{eq\_inf} = 0.086 d^{1.19} \tag{10}$$

$$\lambda_{eq\_inf} = d^{0.6} \tag{11}$$

Equation 9 gives theoretical values for height of 1.2 cm and 1.65 cm for d = 19.5 cm and d = 25 cm respectively. The percentage of error obtain are 5% for Set C1, 23% for Set C2 and 13% for Set C3.

For dune wavelengths, we obtain under unlimited sediment supply a good agreement with Eq. 11.

In other words, the mean water depth is the most significant parameter for the estimation of dune lengths and heights.

3. Formulation for bedform dimensions in the case of sediment supply limitation

Tuijnder et al. (2009) proposed empirical laws to describe the evolution of equilibrium dunes lengths and heights with the sediment availability. These formulations were fitted with experiments conducted with coarse mobile sand ($D_{50} = 800$ μm) on an immobile bottom composed of pebbles. The flume was covered with dunes at the equilibrium state. In the fluvial context of Tuijnder et al. (2009) experiments, the slope of the flume was adjusted to simulate the required flow ($-2.2 < I_e < -0.5$, where I_e is the slope energy level). The objective is to determine if these formulae can be applied to present experiments for dunes and ripples formation, carried on in a coastal context with a nearly smooth immobile bottom. The range of velocities are of the same order than Tuijnder et al. (2009) but the grain size is smaller even for experiments with dunes.

Dune and ripple heights

Dune heights may be estimated at the equilibrium state for sediment supply limited conditions with Eq. 12, according to Tuijnder et al. (2009):

$$\frac{h_{eq}}{h_{eq\_inf}} = 1 - \exp\left(\frac{-\delta}{\alpha_T h_{eq\_inf}}\right) \tag{12}$$

where:

α_T = a dimensionless coefficient ($\alpha_T = 0.39$).

Figure 7 shows that dune heights at the equilibrium state for present tests (Sets C1, C2, C3) are in good agreement with Eq. 12, despite a difference in grain size

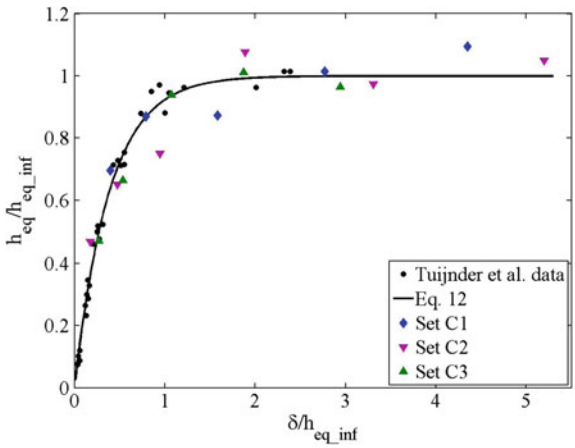

Fig. 7 Variation of the relative dune height with the relative initial layer thickness

(617 μm for present Sets C1, C2, C3) and 800 μm for Tuijnder et al. (2009) tests), and a strong difference in the immobile bottom roughness conditions. Then, in the range of parameters tested, the initial roughness of the bed and the sediment diameter do not seem to play a dominant role in dune height at equilibrium even for extremely limited sediment availability. We validate with present data Tuijnder hypothesis that relative dune heights can be related to relative thickness layer without dependence on flow velocity and sediment diameter. Furthermore, in spite of an additional force induced by the slope in Tuijnder experiments that may have a stabilizing effect on the bed structures (Fredsøe 1974), no significant differences with present tests (no slope) on the dune steady state is noticed.

For ripples, as pointed out on Fig. 5, the influence of flow conditions is only noted for unlimited sediment supply conditions. Thus, the relative ripple height cannot be related to the relative sediment thickness layer with Eq. 12. We propose an adaptation of Eq. 12 suggested by Tuijnder et al. (2009) for dune heights in order to take into account the effect of flow conditions on bedforms heights in the case of ripples:

$$\frac{h_{eq}}{h_{eq\_inf}} = 1 - \exp\left(\frac{-\delta}{\alpha''_T \theta' h_{eq\_inf}}\right) \tag{13}$$

where:
α''_T = a dimensionless parameter fixed to $\alpha''_T = 8.24$
θ' = the Shields parameter calculated without bedforms or skin friction Shields parameter.

The substitution of α_T parameter by a linear function depending on the Shields parameter applied on the initial bottom significantly improves the agreement with present results (Fig. 8; $R^2 = 0.94$). The bed shear stress influences ripple heights for sediment supply limited conditions.

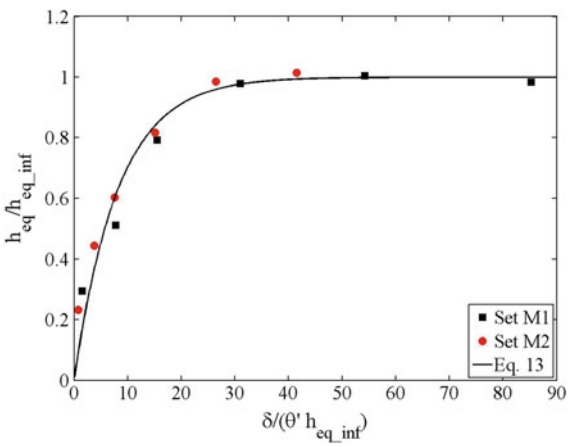

Fig. 8 Variation of the relative ripple height with the relative initial sediment thickness

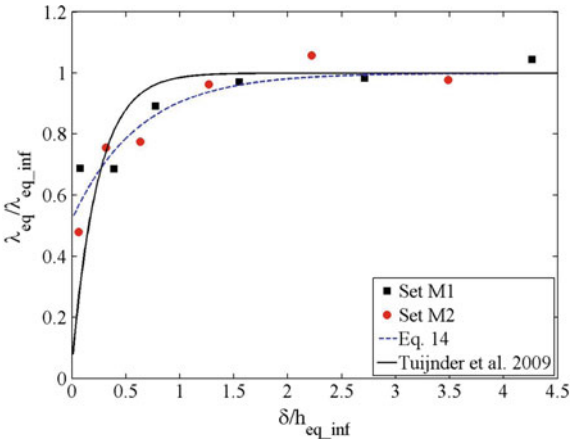

Fig. 9 Variation of the relative ripple wavelength with the relative initial sediment thickness

Ripple lengths

Let us consider the ripples case. Concerning the equilibrium wavelengths, Tuijnder et al. (2009) dune model is applied to Set M1 and Set M2 (Eq. 14). In this equation, the calculation of the equilibrium wavelength depends on the bedform equilibrium heights for unlimited sediment supply conditions:

$$\frac{\lambda_{eq}}{\lambda_{eq\_inf}} = 1 - \beta_T \exp\left(\frac{-\delta}{\gamma_T h_{eq\_inf}}\right) \tag{14}$$

where:
β_T and γ_T = dimensionless parameters.

Tuijnder et al. (2009) suggested to use $\beta_T = 0.96$ and $\gamma_T = 0.24$ for dunes. These values induce a poor agreement for ripples (Fig. 9; $R^2 = 0.76$). A best fit is obtained for $\beta_T = 0.48$ and $\gamma_T = 0.62$ ($R^2 = 0.89$). However, more data are needed to confirm the coefficients adjustments in the case of ripples.

While ripple height seems to depend on the Shields parameter calculated on the flat bottom, no dependence with this parameter was detected for ripple length.

6 Conclusions

The main conclusions about this experimental study on dunes and ripples formation under supply limitation are the following ones.
For dunes:

– The heights and lengths at the equilibrium state under unlimited supply conditions agree with the relations suggested by Allen (1968).

– Heights at equilibrium increase when the sediment availability increased.
– The formulation proposed by Tuijnder et al. (2009) for dune heights in a fluvial context can be applied in a coastal context. It confirms that flow conditions and sediment diameter do not impact noticeably the relative dune height evolution versus relative thickness layer.
– No clear evolution with the sediment availability is found for dunes lengths.

For ripples:

– Heights and lengths at the equilibrium state in unlimited sediment supply conditions are in good agreement with the relation proposed by Soulsby et al. (2012).
– The time to reach the equilibrium state depends on the sediment supply limitation.
– The impact of the supply limitation on the ripple length growth is shown. For unlimited sediment supply conditions, the temporal variation of ripple length can be described by a power law (Eq. 4; Coleman et al. (2005)).
– Lengths and heights increase for increasing sediment availability.
– New coefficients are given to adjust the model of Tuijnder et al. (2009) to ripples length evolution versus the sediment supply availability.
– An adaptation of the relation initially proposed by Tuijnder et al. (2009) for dunes heights at the equilibrium state under sediment supply limitation is suggested in the case of ripples, introducing a coefficient involving the skin friction Shields parameter.

This experimental study shows differences between dunes and ripples evolution of dimensions at equilibrium when varying the sediment supply-limitation. More tests should be performed to validate new present results for ripples.

Future studies may consider the sediment transport and the migration speed of bedforms in sediment limited supply conditions.

Acknowledgements The authors express their sincere thanks to the Normandy region (SCALE Research Network) for funding this work. The help of master student C. El Hadi for the flume experiments was greatly appreciated.

References

Allen, J. R. L. (1963). The classification of cross-stratified units. With notes on their origin. *Sedimentology, 2*(2), 93–114.

Allen, J. R. L. (1968). Sand waves: A model of origin and internal structure. *Sedimentary Geology, 26*(4), 281–328.

Baas, J. H. (1993). *Dimensional analysis of current ripples in recent and ancient depositional environments*, Faculteit Aardwetenschappen.

Blondeaux, P. (2001). Mechanics of coastal forms. *Annual Review of Fluid Mechanics, 33*(1), 339–370.

Carling, P. A., Golz, E., Orr, H. G., & Radecki-Pawlik, A. (2000). The morphodynamics of fluvial sand dunes in the River Rhine, near Mainz, Germany. I. Sedimentology and morphology. *Sedimentology, 47*(1), 227–252.

Charru, F., Andreotti, B., & Claudin, P. (2013). Sand ripples and dunes. *Annual Review of Fluid Mechanics, 45,* 469–493.

Coleman, S. E., Zhang, M. H., & Clunie, T. (2005). Sediment-wave development in subcritical water flow. *Journal of Hydraulic Engineering, 131*(2), 106–111.

Coleman, S. E., & Nikora, V. (2011). Fluvial dunes: Initiation, characterization, flow structure. *Earth Surface Processes and Landforms, 36*(1), 39–57.

Colombini, M., & Stocchino, A. (2011). Ripple and dune formation in rivers. *Journal of Fluid Mechanics, 673,* 121–131.

Dreano, J., Valance, A., Lague, D., & Cassar, C. (2010). Experimental study on transient and steady-state dynamics of bedforms in supply limited configuration. *Earth Surface Processes and Landforms, 35*(14), 1730–1743.

Engelund, F., & Fredsøe, J. (1982). Sediment ripples and dunes. *Annual Review of Fluid Mechanics, 14*(1), 13–37.

Flemming, B. W. (1988). Zur Klassifikation subaquatischer, strömungstransversaler Transportkörper. *Bochumer geologische und geotechnische Arbeiten, 29,* 44–47.

Flemming, B. W. (2000). The role of grain size, water depth and flow velocity as scaling factors controlling the size of subaqueous dunes. In T. Garlan, & A. Trentesaux (Eds.), *Marine Sandwave Dynamic, International Workshop* (Vol. 1, pp. 55–60). Université de Lille.

Fourrière, A., Claudin, P., & Andreotti, B. (2010). Bedforms in a turbulent stream: Formation of ripples by primary linear instability and of dunes by nonlinear pattern coarsening. *Journal of Fluid Mechanics, 649,* 287–328.

Fredsoe, J. (1974). On the development of dunes in erodible channels. *Journal of Fluid Mechanics, 64*(1), 1–16.

Kennedy, J. F. (1963). The mechanics of dunes and antidunes in erodible bed channels. *Journal of Fluid Mechanics, 16,* 521–544.

Kleinhans, M. G., Wilbers, A. W. E., De Swaaf, A., & Van den Berg, J. H. (2002). Sediment supply-limited bedforms in sand-gravel bed rivers. *Journal of Sedimentary Research, 72*(5), 629–640.

Le Bot, S., & Trentesaux, A. (2004). Types of internal structure and external morphology of submarine dunes under the influence of tide- and wind-driven processes (Dover Strait, northern France). *Marine Geology, 211*(1–2), 143–168.

Marin, F., & Ezersky, A. B. (2008). Formation dynamics of sand bedforms under solitons and bound states of solitons in a wave flume used in resonant mode. *European Journal of Mechanics-B/Fluids, 27*(3), 251–267.

Nikora, V. I., & Hicks, D. M. (1997). Scaling relationships for sand wave development in unidirectional flow. *Journal of Hydraulic Engineering, 123*(12), 1152–1156.

Rauen, W. B., Lin, B., & Falconer, R. A. (2009). Modelling ripple development under non-uniform flow and sediment supply-limited conditions in a laboratory flume. *Estuarine, Coastal and Shelf Science, 82,* 452–460.

Seminara, G. (2010). Fluvial sedimentary patterns. *Annual Review of Fluid Mechanics, 42,* 43–66.

Soulsby, R. (1997). *Dynamics of marine sands: a manual for practical applications*. Thomas Telford.

Soulsby, R. L., Whitehouse, R. J. S., & Marten, K. V. (2012). Prediction of time-evolving sand ripples in shelf seas. *Continental Shelf Research, 38,* 47–62.

Stoesser, T., Braun, C., Garcia-Villalba, M., & Rodi, W. (2008). Turbulence structures in flow over two-dimensional dunes. *Journal of Hydraulic Engineering, 134*(1), 42–55.

Tuijnder, A. P., Ribberink, J. S., & Hulscher, S. J. (2009). An experimental study into the geometry of supply-limited dunes. *Sedimentology, 56*(6), 1713–1727.

van Landeghem, K. J. J., et al. (2009). Post-glacial sediment dynamics in the Irish Sea and sediment wave morphology: Data–model comparisons. *Continental Shelf Research, 29,* 1723–1736.

van Rijn, L. C. (1984). Sediment transport, part III: Bed forms and alluvial roughness. *Journal of Hydraulic Engineering, 110*(12), 1733–1754.

Yalin, M. S. (1964). Geometrical properties of sand wave. *Journal of the Hydraulics Division, 90*(5), 105–119.

A Laboratory Study of the Shallow Flow Field in a Vegetated Compound Channel

S. H. Truong, K. L. Phan, Marcel J. F. Stive and W. S. J. Uijttewaal

Abstract The significant defensive role of vegetation in general and mangroves in particular for coastal and estuarine regions has been increasingly recognized. However, understanding the shallow flow field in and around the region of vegetation is still limited. In order to gain more insight, a laboratory experiment of a vegetated compound channel was conducted. The emerged circular cylinders are a representative model for the emergent mangrove forest. Scenarios of different widths and densities of vegetation were considered. Data acquired from Acoustic Doppler Velocimetry (ADV) and force sensors have been analysed. The influences of vegetation on the shallow flow field were clarified by comparing different scenarios with and without vegetation. Furthermore, the results confirm the presence of the large horizontal coherent structures (LHCSs). The large coherent structures formed in the mixing layer at the vegetation interface emerge, promoting the transverse momentum exchange toward the forests. The LHCSs has not only boosted flow penetration into the vegetated floodplain area but also strongly disturbed the flow inside the forest. As the LHCSs move, they cause the fluctuation of the force on the cylinders. The fluctuations are largest at the vegetation edge. Negative values of stream wise forces were also recorded.

Keywords Vegetation · Laboratory study · Turbulent flow · Forces on vegetation · Compound vegetated channel

S. H. Truong (✉) · K. L. Phan · M. J. F. Stive · W. S. J. Uijttewaal
Hydraulic Department, Faculty of Civil Engineering and Geosciences, Delft University of Technology, Delft, The Netherlands
e-mail: s.truonghong@tudelft.nl; truong@kict.re.kr

S. H. Truong · K. L. Phan
Hydraulic Department, Faculty of Civil Engineering, Thuyloi University, Ha Noi, Viet Nam

S. H. Truong
Department of Land, Water and Environment Research, Korea Institute of Civil Engineering and Build Technology, Goyang-si, South Korea

K. D. Nguyen et al. (eds.), *Estuaries and Coastal Zones in Times of Global Change*, Springer Water,
https://doi.org/10.1007/978-981-15-2081-5_38

1 Introduction

Vegetation in general and mangroves in particular play an important role for the protection of coastal and estuarine regions. The complex systems of strong and dense mangrove roots, stems and canopies provide an effective tool to damping the attacking waves and the strong currents along banks. In recent decades, this topic has withdrawn increasingly more attention, especially in the context of increasing coastal and river bank erosion and sea level rise.

Numerous studies, mostly based on experimental results have been published, focusing on understanding the hydrodynamic processes in and around forests and the defensive role of vegetation in coastal and estuarine regions (Ikeda et al. 1991; Nadaoka and Yagi 1998; Nezu and Onitsuka 2001; Van Prooijen et al. 2005; White and Nepf 2007, 2008). However, the knowledge obtained is limited. For example, what is the required forest width to avoid the squeeze effect and to ensure a sustainable protection and development? it is not clear to what distance the mangrove forest should be remained so that their sustainable development can be ensured.

Along the Mekong Delta Estuary, mangrove forests usually dominate the floodplain region with a gentle slope of 1:10. In the last three decades they have been strongly destroyed because of the construction of fish-farms in this region. As a result, only a narrow strip of mangrove of about 50 to 100 m is usually left, and river banks are eroding with the rate of about 3 myr^{-1} (see Fig. 1). In this condition, the estuarine mangroves can be studied as vegetation in a floodplain channel (Truong

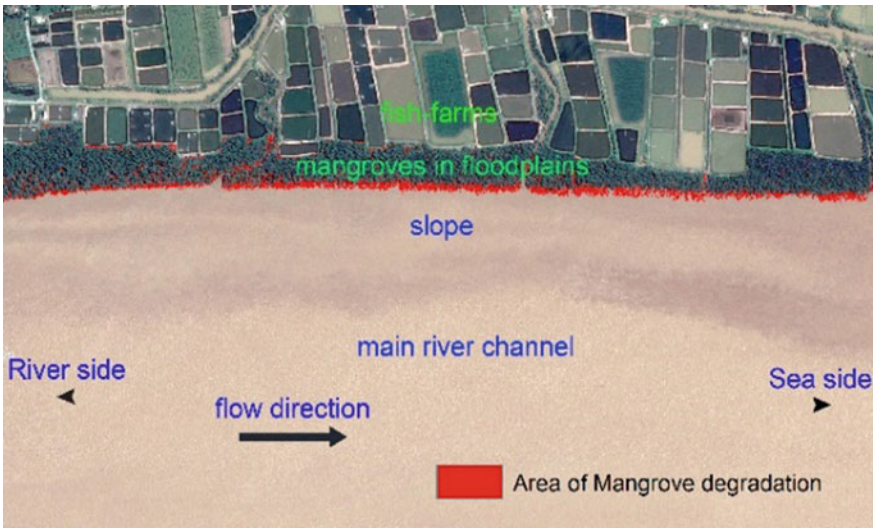

Fig. 1 Representative mangrove distribution along the dai estuary in the mekong delta

et al. 2019; Truong et al. 2017) in which, the hydrodynamics in and around the vegetation is the key factor determining the sustainable growth of the whole ecological system.

2 Experimental Set-up and Measurement

In order to obtain more insight in this topic, a physical model, mimicking the estuarine mangrove in the Mekong Delta Estuary was set up and performed in scenarios with different mangrove densities, discharge and water levels. The top view of the experiment can be seen in Fig. 2.

The experiment profile includes a floodplain, a transition slope (1:10) and an open flow channel. Cylinder arrays was installed in the floodplain area. The density of cylinder arrays was determined based on the solid volume fraction of *S. Alba*,

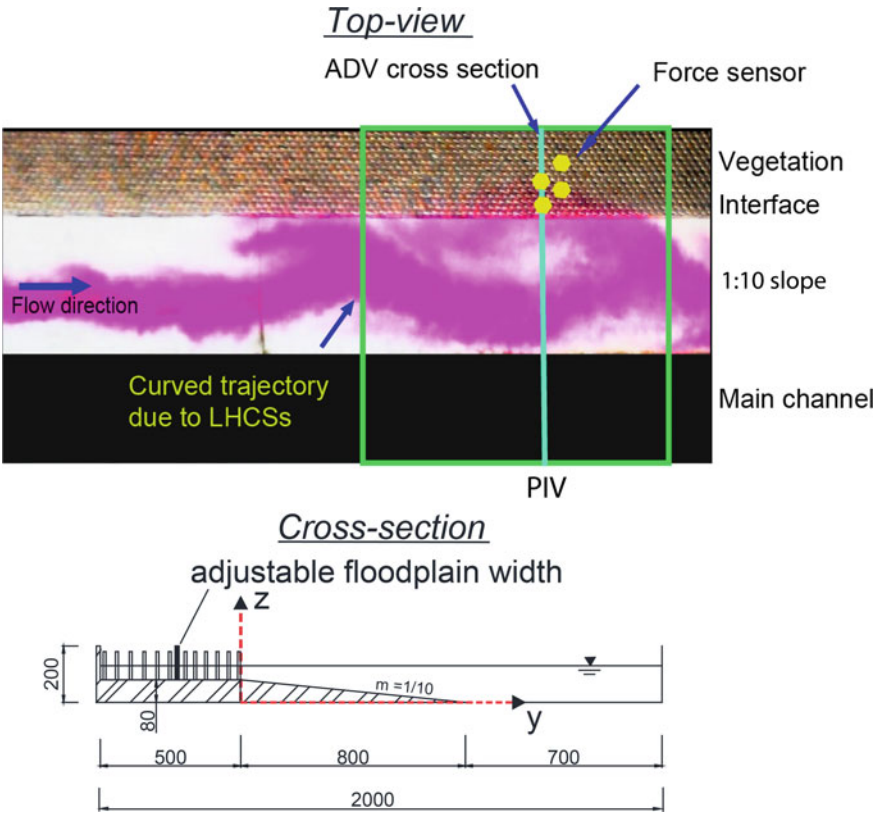

Fig. 2 Experimental set-up including top view and cross section of the experiment and measured techniques

which is the typical type of mangroves along the Mekong estuarine (Truong et al. 2017). In this way, two densities of cylinder arrays (139 and 556 cylinder/m^2) were considered. The input discharge and the water level could be changed by means of a pump upstream and a downstream crested weir, respectively.

It is noted that the flow over the shallower floodplain is much slower than in the deeper main channel because of the water depth difference inside the vegetation and adjacent open channel. Consequently, a mixing layer develops between the vegetated floodplain and the channel. In the present experiment, the measurements were taken at 10 m from the beginning of the flume, where the mixing layer can be safely assumed to be fully developed.

A Nortek Acoustic Doppler Velocity meter (ADV) was used to measure the depth-averaged velocity (mid-depth). The quality of the ADV signal was significantly improved by an electrolyzer with 0.1 mm thick wires placed in front of the ADV (see Fig. 3). Moreover, four sensitive force sensors were mounted under the bottom of the metal cylinders located at different locations inside the vegetation region. In this way, the direct streamwise force on a single cylinder can be obtained and the drag coefficient can be determined.

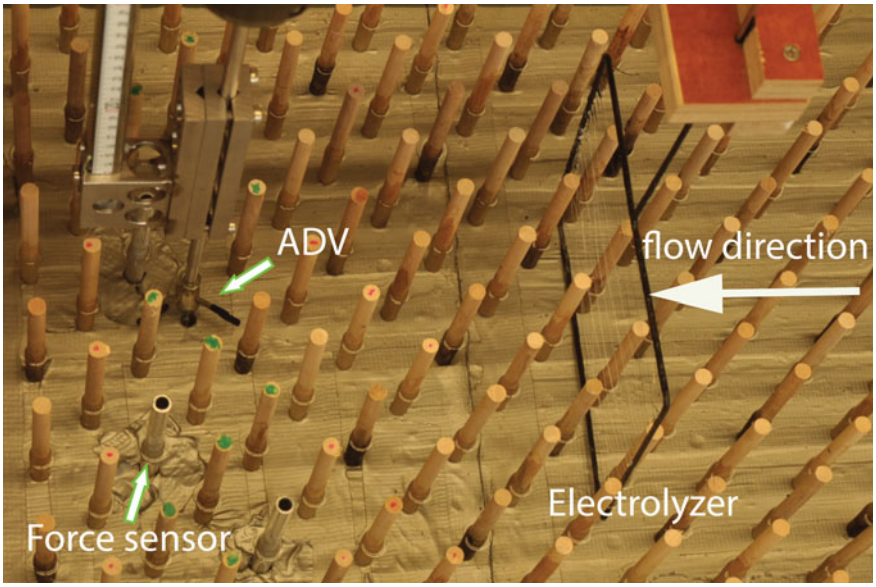

Fig. 3 Velocities and forces measurement

3 Mean Stream Wise Velocity

Velocity measurements were taken over a time interval of 10 min (sampling rate of 25 Hz). After that, it was time-averaged to obtain the depth and time-averaged velocity at the corresponding location. Figure 4 illustrates the representative velocity profile in scenarios with different cylinder densities (floodplain width = 50 cm; discharge = 80 l/s; water depth = 14 cm).

First, it can be clearly observed that for the cases with vegetation, the depth and time-averaged streamwise velocity inside the floodplain region was damped significantly (about 2 and 8 cm/s in dense and sparse cases compared to 35 cm/s in cases without vegetation). As a result, in the cases with vegetation, the velocity gradient between the vegetation area and the main open channel greatly increases. Furthermore, it can be seen that the profile of the mean streamwise velocity in the dense case can decrease and reach an uniform value in the floodplain region after a distance of about 10 cm (Fig. 4). In other words, the penetration of the flow into the cylinder arrays is about 10 cm. It is noticed that this penetration of the flow into the vegetation region appears to be larger than that in cases with sparse vegetation

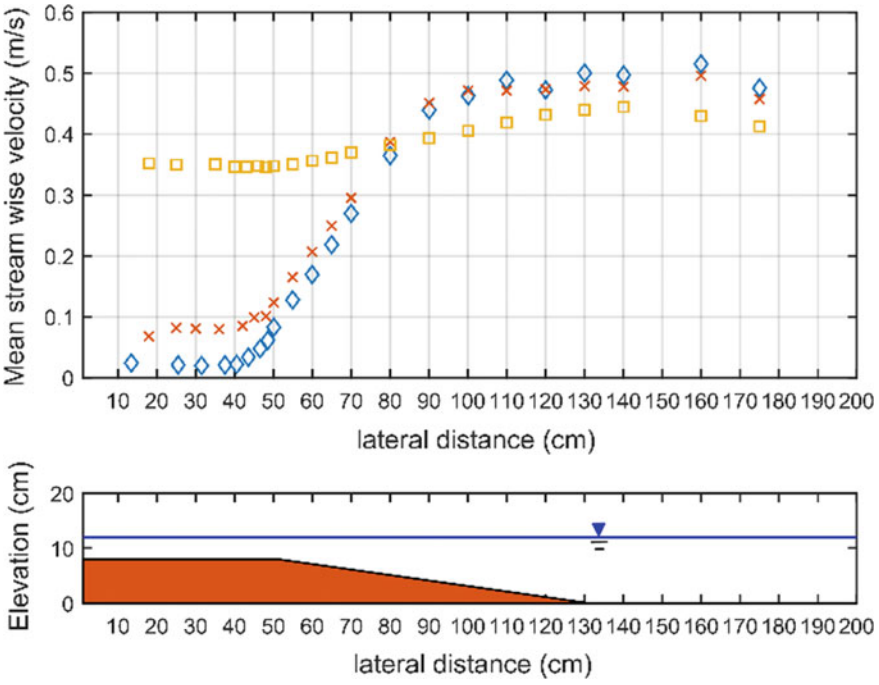

Fig. 4 Mean streamwise velocity in scenarios with different densities (squares: no cylinder; crosses: sparse density; rhombuses: high density), floodplain width = 50 cm; discharge = 80 l/s; water depth = 14 cm

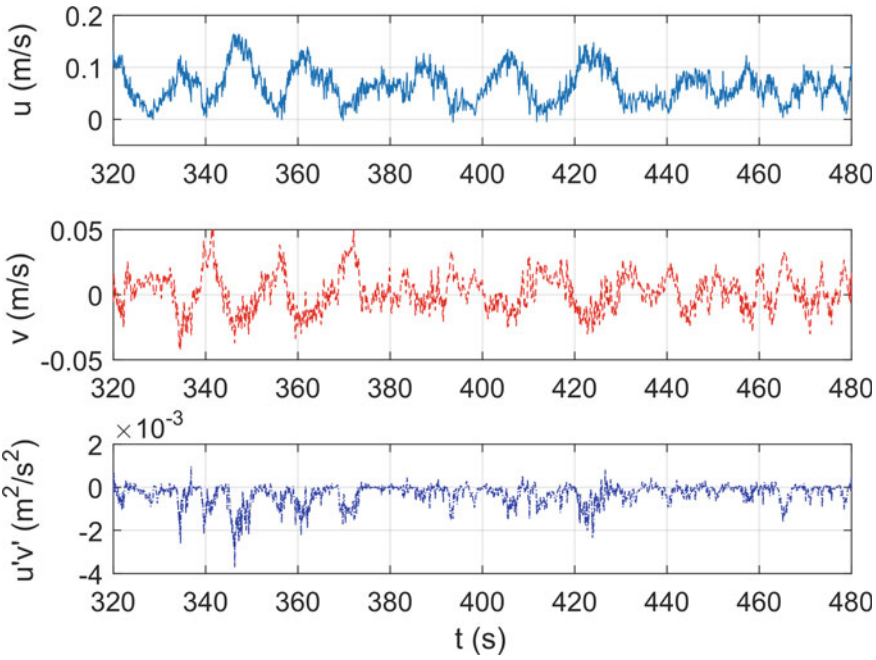

Fig. 5 Mean streamwise and transverse velocities and the corresponding Reynold's stresses at the vegetation interface, in a scenario with floodplain width = 50 cm; discharge = 80 l/s; water depth = 14 cm

and in cases without vegetation. In this sense, the presence of vegetation appears to boost the flow penetration into the vegetated floodplain area.

In order to obtain further insight, the data measured from the ADV can be analysed in more detail. Figure 5 shows the time series of the mean streamwise velocities (u), lateral velocities (v) and their corresponding shear stresses ($u'\ v'$) which were obtained from the ADV at the vegetation interface.

First, it can be clearly seen that there is a fluctuation in the time signal of the streamwise (u) and transverse velocity (v) (period T = 15–20 s). This is caused by the presence of quasi-two dimensional structures which is termed large horizontal coherent structures (LHCSs). In the literature, these large coherent structures were recognized because of the Kelvin-Helmholtz (K-H) instability triggered by the parallel shear flows between the floodplain and adjacent open region (Bousmar 2002; White and Nepf 2008; Adrian and Marusic 2012).

The peaks in the corresponding turbulence shear stresses ($u'\ v'$) can also be observed. These peaks are associated with the flow events i.e. sweeps and ejections (White and Nepf 2018). As the transverse exchange of momentum is directly related to the Reynold shear stresses, these flow events are of primary importance for the exchange processes in the vegetation (Truong et al. 2019).

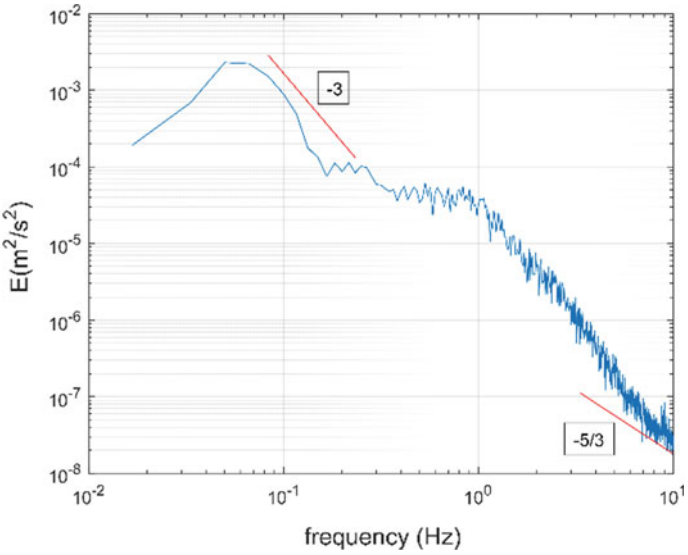

Fig. 6 Power density spectra of lateral velocity fluctuations at location 46.5 cm distance from the wall—dense scenario, 50 cm width, discharge = 45 l/s, water level = 12 cm

4 Power Density Spectra (PDSs)

The presence of LHCSs can be studied in more detail by analysing the power density spectra (PDSs) of the fluctuating transverse velocity (v') (Figs. 6 and 7). The quasi-two dimensional eddy structures can be recognized through the −3 slope at the low-frequency side of the PDS (Uijttewaal and Booij 2000). The decrease in energy density at the high-frequency side of the PDSs almost follows a slope −5/3 which is indicative of flows with a large inertial subrange.

Figure 7 shows the PDS of the lateral velocity fluctuations along the cross-section of the flume in cases with different floodplain widths (50 and 25 cm). In the main channel, the −3 slope at the low-frequency side of the PDSs cannot be observed. Moreover, when reducing the floodplain width from 50 to 25 cm, clear differences in the PSDs can be observed. The definite peak regions (yellow regions) in the power density spectrum with slope −3 in case 25 cm is more spread and less concentrated as in cases of 50 cm floodplain width. This implies that the LHCSs are less regular when the floodplain width is reduced.

5 Forces Induced by the LHCSs

As the LHCSs move they causes the velocity fluctuation, resulting in the fluctuation of the forces. Figure 8a shows the distribution of measured stem forces by box plots

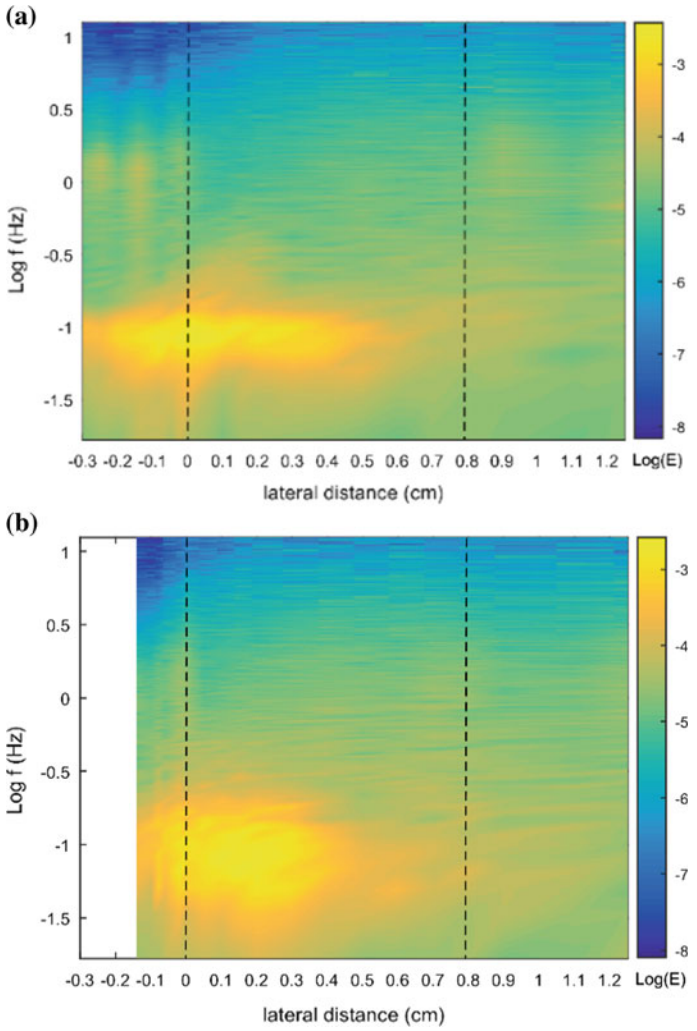

Fig. 7 Power density spectra of lateral velocity fluctuations along the cross-section of the flume, dense scenario, 50 cm width (**a**) and 25 cm width (**b**), discharge = 45 l/s, water level = 12 cm

at different locations. The mean value is given by red line with the box indicating the 25th and 75th percentiles. The fluctuation is strongest at the floodplain edge (location 4). Because the effects of LHCSs become weaker further inside the vegetation, the fluctuation and the magnitude of the streamwise forces also become smaller. It is noticed that the negative values of the streamwise forces can be observed in this figure. This is possibly caused by the backward motions induced by the LHCs (Truong et al. 2019).

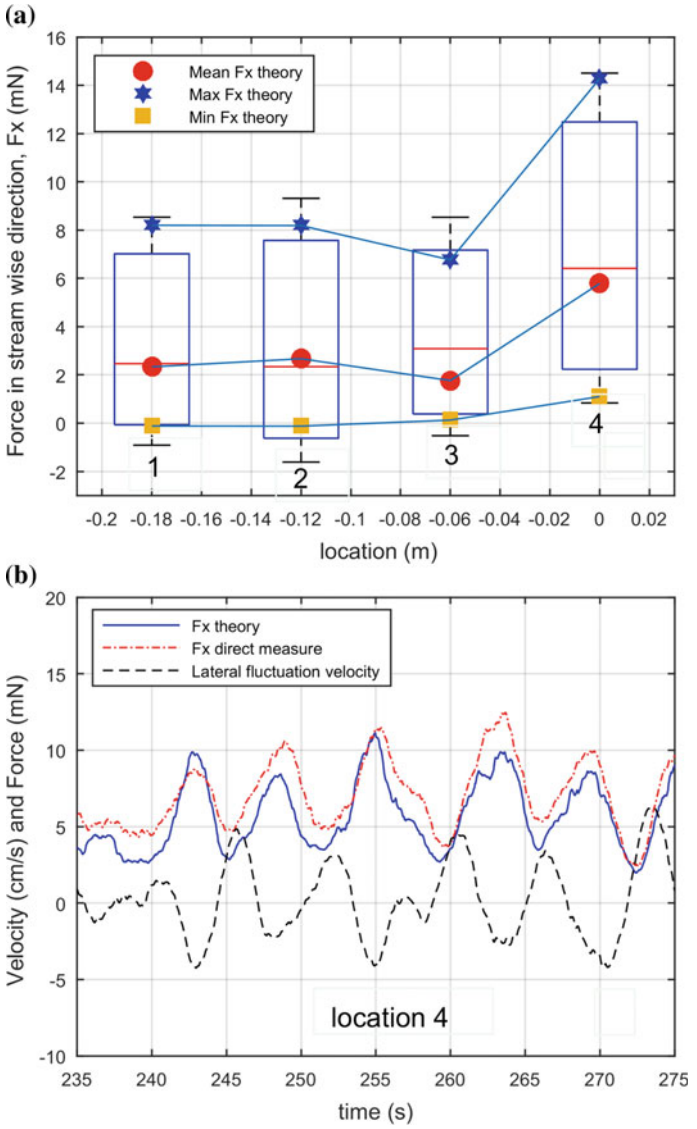

Fig. 8 Distribution of measured stem forces on cylinders, including the corresponding values determined from the theory (**a**). Directly measured streamwise force, F_x on cylinder 4 (at the edge of the vegetation), compared with the estimated forces, $F_{x,theory}$ from the theory (Cd = 1; correlation 55%) and corresponding lateral velocity fluctuation (**b**)

Figure 8b shows the time series of the streamwise force (F_x) measured on cylinder 4 together with the predicted one ($F_{x,theory}$) and the lateral fluctuation velocity (v'). It is suggested that the force reaches its maximum value together with the minimum lateral fluctuation velocity ($v' < 0$). This indicates that the force on the cylinder is largest during the inflows (sweeps) and smallest during the outflows (ejections).

6 Conclusions

This chapter introduces some initial results of a laboratory experiment of a vegetated floodplain channel, mimicking the estuarine mangrove forests in the Mekong Delta, Vietnam. The experimental results confirm the capability of the vegetation in damping the flow inside the forests. The presence of vegetation significantly increases the velocity gradient, boosting the development of the LHCSs, and thereby also causes more mixing into the vegetation. The LHCSs then creates flow events, contributing a large part to the total transverse momentum exchange. These flow events cause velocity fluctuations. As a result, the forces acting on the vegetation also fluctuate and apparently reach the maximum values during the ejections. Future work will focus on a further interpretation of the data acquired and the validation of a numerical model using the experimental data.

References

Adrian, R. J., & Marusic, I. (2012). Coherent structures in flow over hydraulic engineering surfaces. *Journal of Hydraulic Research*, *50*(5), 451–464.

Bousmar, D. (2002). Flow modelling in compound channels. *Unire de Genie Civil et Environnemental*.

Ikeda, S., Izumi, N., & Ito, R. (1991). Effects of pile dikes on flow retardation and sediment transport. *Journal of Hydraulic Engineering, 117*.

Nadaoka, K., & Yagi, H. (1998). Shallow-water turbulence modeling and horizontal large-eddy computation of river flow. *Journal of Hydraulic Engineering, 124*(5), 493–500.

Nezu, I., & Onitsuka, K. (2001). Turbulent structures in partly vegetated open channel flows with LDA and PIV measurements. *Journal of Hydraulic Research*, *39*(6), 629-642. https://doi.org/10.1080/00221686.2001.9628292.

Truong, S. H., Uijttewaal, W. S. J., & Stive, M. J. F. (2019). Exchange processes induced by large horizontal coherent structures in floodplain vegetated channel. *Water Resources Research, 55,* 2014–2032. https://doi.org/10.1029/2018WR022954.

Truong, S. H., Ye, Q., & Stive, M. J. F. (2017). Estuarine mangrove squeeze in the Mekong delta, Vietnam. *Journal of Coastal Research*, 747–763.

Uijttewaal, W. S. J., & Booij, R. (2000). Effects of shallowness on the development of free-surface mixing layers. *Physics of Fluids, 12*(2), 392–402.

Van Prooijen, B. C, Battjes, J. A., & Uijttewaal, W. S. J. (2005). Momentum exchange in straight uniform compound channel flow. *Journal of Hydraulic Engineering, 131*(3), 175–183.

White, B. L., & Nepf, H. M. (2007). Shear instability and coherent structures in shallow flow adjacent to a porous layer. *Journal of Fluid Mechanics, 593*, 1–32. https://doi.org/10.1017/S0022112007008415.

White, B. L., & Nepf, H. M. (2008). A vortex-based model of velocity and shear stress in a partially vegetated shallow channel. *Water Resources Research*, *44*(1).

Laboratory Study of Short Term Response of Alluvial Fans to Changes in Input Water Flow and Sediment Supply Under Lateral Confinement

Yuan Yuan, Jingqiong Zhao, Xue Luo, Yanchen Zhou and Siqiang Wang

Abstract In this chapter, the autogenic process of alluvial fan under various discharges and sediment feed rates were studied. Meanwhile, the discharge and sediment feed rate were suddenly changed during some experiments to analyze alluvial fan's delayed response to external disturbances. The results demonstrate that progradation processes both slow down when water discharge or sediment feed rate is halved separately. When reducing both water discharge and sediment feed rate simultaneously, progradation process become even slower. Widening process of alluvial fan is less sensitive to change of discharge and sediment concentration than progradation process. When sediment feed rate is reduced by half, alluvial fan aggradation processes along flow path slows down obviously. When water discharge is reduced by half, upstream aggradation processes accelerate while downstream aggradation processes decelerate. The alluvial fan fluvial cycle and the channel morphology react to discharge reduction differently with sediment concentration reduction. The rate law can be employed to describe the actual response process of the deposition thickness. Calculated results demonstrate that the response rate of the upper-fan siltation layer is higher than that of the mid-fan and lower-fan. The response rate of the fine-sand alluvial fan is higher than that of coarse-sand. The response of the deposition layer to discharge increase is faster than that of discharge decrease. Alluvial fan development is influenced by both fan reaction mode and the status of fan development.

Keywords Alluvial fan · Lateral confinement · Laboratory study · Sedimentation · Delayed response

Y. Yuan (✉) · J. Zhao · X. Luo · Y. Zhou
Key Laboratory of River Regulation and Flood Control of MWR, Wuhan, Hubei Province, China

S. Wang
Changjiang Limited Liability Company of Survey, Design and Research Planning, Wuhan, Hubei Province, China

K. D. Nguyen et al. (eds.), *Estuaries and Coastal Zones in Times of Global Change*, Springer Water,
https://doi.org/10.1007/978-981-15-2081-5_39

1 Introduction

Alluvial fan is formed by sediment deposition from sediment-laden flow (Nemec and Steel 1988). The continuous expansion of alluvial fans is an important mechanism for the formation of alluvial plains. The essence of this process is the symbiotic development of alluvial rivers and surrounding sedimentary geomorphology. The plain landforms formed by continuous development of alluvial fans can be divided into two types. The first type is characterised by the deposition which area is wide and the development of alluvial plan which is not restricted laterally. The other type is characterised by its development in narrow river valleys, which is subject to obvious lateral constraints. Many research studies focused on the development of the first type of alluvial fan, including geological field surveys, physical model tests, numerical simulations and so on (Hashimoto et al. 2011; Dirszowsky and Desloges 2004; Van Dijk et al. 2012; Caldwell and Edmonds 2014). Due to the appearance of boundary wall constraints, the development process of the laterally constrained alluvial fan is more complex. Most studies are concentrated on geological field surveys, while less attention is paid to the symbiotic development of sediment accumulation and river evolution (Ravazzi et al. 2013; Taha and Anderson 2008).

Zhang et al. (2016) studied the development of an alluvial fan under lateral confinement, as well as the evolution process of river pattern on the fan, based on a flume experiments with a total duration of 183 h. In order to shorten the experiment duration, a series of tests are carried out in a small experiment tank. Multiple sets of input water and sediment conditions were designed to study the influence of upstream boundary conditions on the alluvial fan autogenic process. The short term response of alluvial fans to changes in input water flow and sediment supply under lateral confinement was mainly discussed.

With the increase of human activities in the valley plain, the geomorphic evolution in the region is more closely related to human production and life. Landforms change frequently due to human activities, not only interferes with the normal evolution process of alluvial fans, but also increases the probability of natural disasters. Therefore, the research on the development process of alluvial fans under the lateral confinement can help to improve the understanding of the evolution law of alluvial fans and provide effective guidance for disaster risk management in the region.

2 Experimental Methods

2.1 Experiment Setup and Materials

Given that the experimental model has a long history in alluvial fan research and provides a range of advantages unavailable to other methods of scientific investigation, it was used in this chapter to study the autogenic process of alluvial fan under various discharges and sediment feed rates (Clarke 2015).

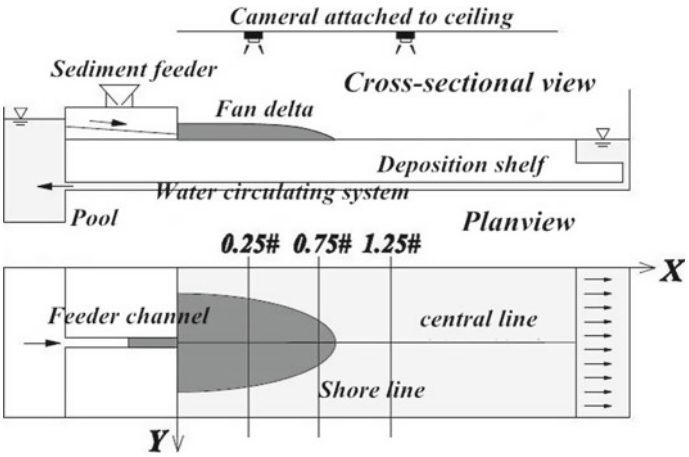

Fig. 1 Sketch of the experiment tank. The layout of the cross sections is arranged as above. Cross Section 0.25#, 0.75#, and 1.25# are 0.25,0.75, and 1.25 m away from the feeder channel, respectively

This experiment was conducted in the experimental tank at Wuhan University. The experimental setup of the small tank is shown in Fig. 1. The tank also includes three regions: an inlet region, a deposition shelf (3 m × 0.7 m) with an adjustable gradient and a narrow sediment feeder channel (0.5 m × 0.05 m × 0.26 m). The depth was controlled by an overflow weir. The slope of deposition shelf is 0. The downstream water depth is 0.

2.2 Data Collection

One camera was fixed on the ceiling to take photographs simultaneously every 2 min in order to record planform and fluvial morphology of the fan. The fan topography was measured using a stylus profilometer with a vertical measuring resolution of 0.6 mm and a lateral measuring resolution of 10 mm. The measurement of flow velocity used the buoy method and a LH-1 water level meter developed by Wuhan University was utilized to measure water level. The geometric parameters of the tank can be extracted from the photograph or measured directly in the experiment.

Three kinds of sediment were adopted in the experiments, which are the coarse sediment, the median sediment and the fine sediment. The median size was 0.4, 0.3 and 0.17 mm correspondingly. The density of the sediment is 2600 kg/m^3.

Table 1 Parameters in each test

Case study	Discharge Q_w ($\times 10^{-4}$ m^3/s)	Sediment feeding rate Q_s ($\times 10^{-6}$ m^3/s)	Sediment type	Remarks
W2S2	1.7	1.1	Coarse	Clear water scouring after 6.2 h
W1S2	0.85	1.1	Coarse	
W2S1	1.7	0.55	Coarse	Clear water scouring after 10.2 h
W1S1	0.85	0.55	Coarse	
W1S1-moderate	0.85	0.55	Moderate	Clear water scouring after 17.9 h
W1S1-Fine	0.85	0.55	Fine	Clear water scouring after 23.3 h
W3S1	0.56–1.11	0.55	Coarse	0–3.3 h, $Q_w = 0.56 \times 10^{-4}$ m^3/s; 3.3–9.2 h, $Q_w = 1.11 \times 10^{-4}$ m^3/s 9.2 h,$Q_w = 0.56 \times 10^{-4}$ m^3/s

2.3 Test Conditions

7 sets of experiments were conducted in this study. Parameters in each test are shown in Table 1.

3 Influences of Water Discharge and Sediment Supply on Alluvial Fan Development

3.1 Influences of Upstream Boundary Conditions on the Sedimentation

The progradation process curve of the alluvial fan is shown in Fig. 2. When the upstream flow discharge and the sediment amount are halved separately, the progradation process of the alluvial fan slows down significantly, and the progradation curves after the slowing down are very close to each other. When the amount of

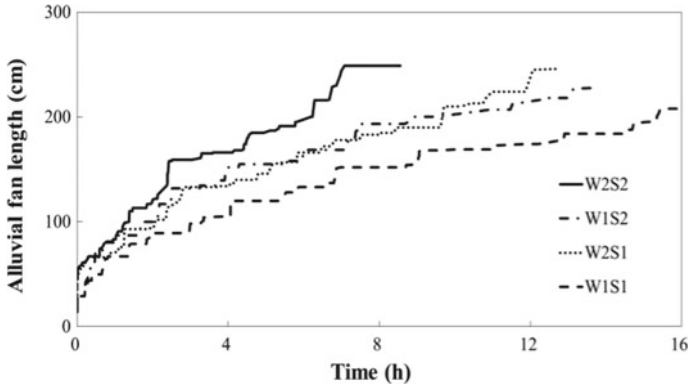

Fig. 2 The progradation process curve of the alluvial fan

water and sand in the upstream is halved at the same time, the progradation process of alluvial fan slows down further than that of water and sand separately halved.

The change process curve of alluvial fan width over time is shown in Fig. 3. The widening process of alluvial fan is less affected by the change of water and sand conditions. When the amount of sediment is halved solely, the lateral advancing speed of the alluvial fan slows down slightly due to insufficient sediment supply. When the flow is halved solely, the broadening speed increases slightly. This is because halving the flow increases the lateral flow rate by increasing the transverse slope. In addition, halving the flow rate reduces the water depth in the tank and the lateral spreading of sediment is less impeded. When the flow and the sediment are halved at the same time, the expansion speed of the alluvial fan is also slowed down, and its broadening process is very similar to that of sand halved solely. Comparing the above three situations, it can be found that when the sediment amount is small, the impact of flow change can be ignored. However, when the flow is small to a

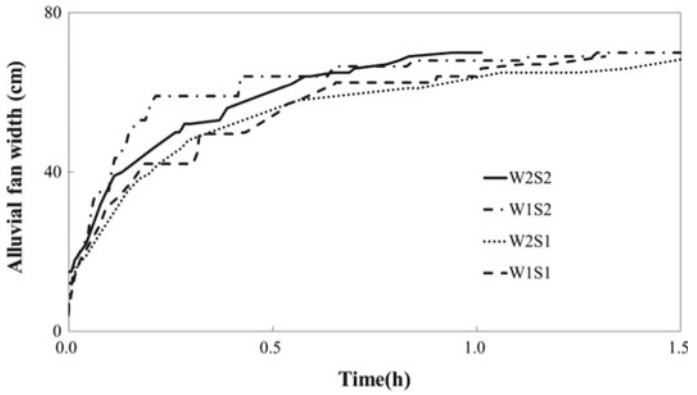

Fig. 3 The change process curve of alluvial fan width over time

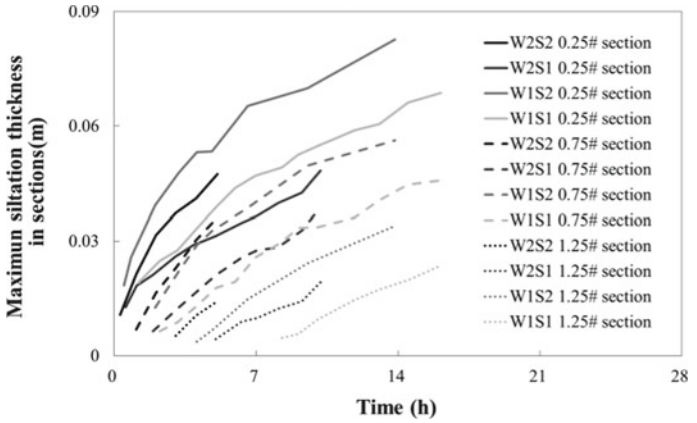

Fig. 4 The aggradation process of alluvial fans under different boundary conditions

certain extent, the impact of reducing the amount of sand is even greater. It can be seen that the influence of sediment on the expansion of the alluvial fan is greater than that of the flow discharge.

Figure 4 shows the aggradation process of alluvial fans under different boundary conditions. When the sediment discharge is reduced by half, the aggradation processes of cross sections along the alluvial fan are obviously slowed down. When the flow is reduced solely, the upstream aggradation process is accelerated and the downstream aggradation process may be slowed down. When water and sand are reduced simultaneously, the aggradation process becomes more complicated. This is because halving water flow and halving sediment have different effects on the sediment accumulation process of alluvial fans. Halving sediment concentration directly reduces sediment deposition, while halving sediment concentration only changes the spatial distribution of sediment.

3.2 Influences of Upstream Boundary Conditions on the Fluvial Cycle

Table 2 shows the fluvial cycle and river channel geometry parameters under different conditions. When the upstream sediment amount is halved separately, the fluvial cycle duration of the river channel on the alluvial fan becomes longer. On the one hand, the reduction of sediment volume makes the water carrying sediment stronger and the river channel can be eroded more deeply. As the flow does not increase, the width of the channel does not change significantly. As a result, the channel morphology is more mature, the width-depth ratio is smaller. The narrow and deep channel makes the straight channel more stable and its proportion in the river pattern cycle increases. All these make the fluvial cycle to have the tendency of getting longer. On the other

Table 2 Parameters of channel morphology and fluvial cycle in each test

	W2S2	W1S2	W2S1	W1S1	W3S1
The average river width (cm)	12.8	10.1	12.3	9.9	8.8
The average *Fr*	1.54	1.77	1.05	1.89	2.05
The water depth (mm)	4.9	3.9	6.2	3.8	3.6
The average longitudinal slope	0.033	0.053	0.031	0.042	0.046
The average transverse slope in the upstream	0.06	0.069	0.054	0.057	0.057
The average transverse slope in the middle reach	0.049	0.024	0.03	0.041	0.027
The average transverse slope in the downstream	0.022	0.02	0.019	0.021	0.023
The fluvial cycle (h)	0.47	0.28	0.62	0.38	0.43
The proportion of straight channel	0.41	0.54	0.5	0.59	0.62

hand, the decrease in sediment has resulted in a slight decrease in the longitudinal slope. This causes the flow rate to decrease, which in turn reduces the Froude number *Fr*. These factors make the backsilt of the river easier to occur, and the fluvial cycle tends to decrease. The influence of the increase of the water depth on the river cycle is dominant, which makes the river cycle longer and causes the proportion of the straight channel to increase.

When the flow discharge is halved solely, the duration of the river cycle becomes shorter. This is also the result of a combination of two factors. The decrease of flow rate makes the longitudinal slope of alluvial fan larger. The steeper terrain makes retrogressive deposition more difficult. On the other hand, the decrease of flow makes the flow rate and water depth smaller. The sediment propulsion dynamics is weaker and more prone to silting in river channels. This tends to reduce the fluvial cycle. Finally, the effect of reducing the flow rate on the river cycle is dominant. However, due to shorter fluvial cycle, the proportion of straight channel increases.

Since halving the flow rate is contrary to the effect of halving sediment amount on the fluvial cycle, the fluvial cycle on the surface of alluvial fan changes slightly when the flow rate and sediment are halved at the same time. However, because the amount of water and sand is smaller and the energy of incision and advancing is weaker, the fluvial cycle is still slightly smaller than before. The reduced cycle length is between the values that prevail when the flow and sediment are halved separately. The proportion of the straight channel becomes greater when the amount of water and sand is halved and bigger than the value after the flow and sediment are halved separately. This is partly because the longitudinal slope of alluvial fan has increased, which makes the straight channel more sustainable. On the other hand, due to the shorter fluvial cycle of river pattern, the proportion of straight channel increases greatly. The influence of water and sediment conditions on the fluvial cycle is similar to that of Straub and Wang (2013).

4 Delayed Response of Alluvial Fan to Sudden Change of Discharge and Sediment Condition

4.1 Delayed Response of Alluvial Fan to Scour

The incoming flow and sediment conditions of natural rivers are constantly changing in natural environment. When the river system is disturbed by external changes, it will always develop towards a new equilibrium state in order to adapt to the new boundary condition, which reflects the equilibrium tendency of the alluvial system. However, the change of flow and sediment conditions is often faster, while the corresponding riverbed erosion and deposition are slower. The self-adjustment process of flow and sediment condition always falls behind the change of external conditions, which is called delayed response (Wu et al. 2007). The changing process is shown in Fig. 5. The delayed response process is divided into three phases, which are the reaction stage, the adjustment stage, and the equilibrium stage. Under some conditions, the system response is so quickly, that the reaction stage can be ignored.

After the sand feeding rate is reduced to zero, the river bed was scoured in the upstream and the sediment was accumulated in the downstream above the alluvial fan. The sediment in the upstream channel was transported to the downstream. On the one hand, the longitudinal profile of the sediment accumulation body was flatter and the slope was decreased. On the other hand, the length of the fan was increased, which caused the progradation process to accelerate. However, the acceleration was short-lived. When the upstream scour was weakened, the sediment deposition in the downstream decreased gradually. Finally, the progradation process of the alluvial fan is gradually stopped because the upstream is no longer supplied with sediment. The progradation process of alluvium fan was accelerated firstly and then stabilized under the erosion of clear water, which corresponds to the adjustment stage of delayed response.

The delayed response of fluvial fan is quantitatively analyzed by the rate law taking example of the thickness of sediment accumulation.

$$\mathrm{d}y/\mathrm{d}t = \beta(y_e - y) \tag{4.1}$$

where:

y the characteristic variable.
y_e the equilibrium value of the characteristic variable;
t time.

β is a coefficient which is positive, whose dimension is $1/T$. When β is larger, the adjustment rate of riverbed characteristic variable is faster, therefore it is called the adjustment speed parameter of river course.

According to the calculation condition and characteristic, three patterns are put forward in the solution of the rate law of delayed response, which are the universal integration pattern, the single step analytic pattern, and the multistep recursive

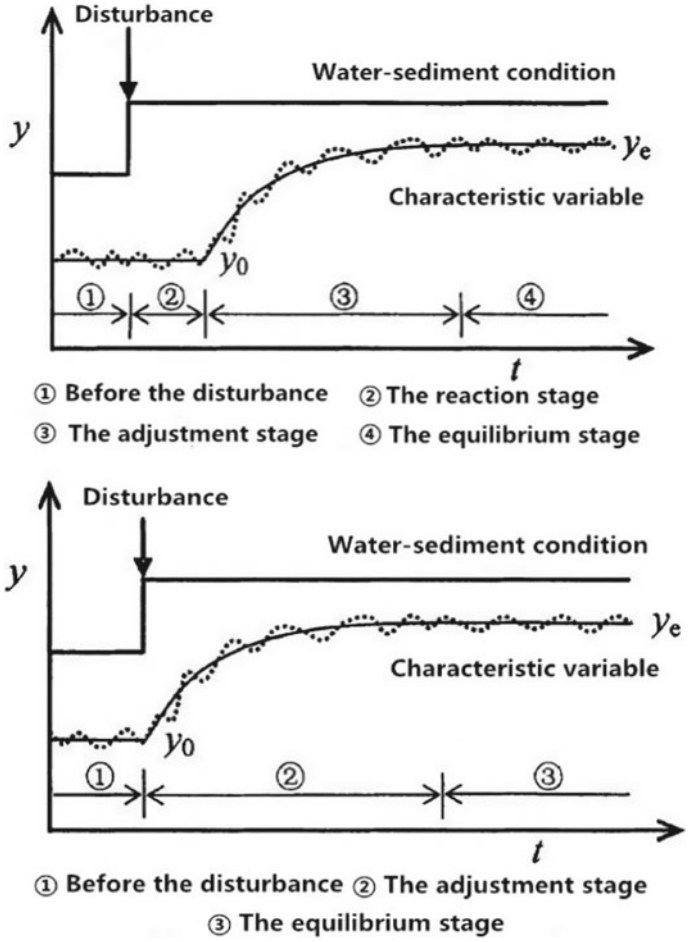

Fig. 5 Schematic diagram of adjustment process of river system characteristic variable after disturbance (Knighton 1998)

pattern. In this study, the flow and sediment remained unchanged after they were changed abruptly, until the alluvial fan reaches a new equilibrium. The reaction of the fan had only one period, so the single step analytic pattern was applied to solve the rate law of delayed response.

The single step analytic pattern can be computed as:

$$y_1 = \left(1 - e^{-\beta \Delta t}\right) y_{e1} + e^{-\beta \Delta t} y_0 \tag{4.2}$$

where:

y_1 the computed value of characteristic variable after a time interval

y_{e1} the equilibrium value of characteristic variable after a time interval
y_0 the initial value of characteristic variable before the disturbing
Δt the duration of the time interval.

Take the siltation thickness as the characteristic variable, y_1 is siltation thickness after a time interval, y_0 is the initial siltation thickness, $y_{e1}$is the equilibrium value of the siltation thickness, Δt is the time interval between the adjacent measurements of topography, β is the adjustment parameter for siltation thickness.

For the alluvial fan test in a small tank, we selected all three sections of the upstream, middle, and downstream of the alluvial fan for sediment thickness statistics ($x = 0.25$ m section, $x = 0.75$ m section and $x = 1.25$ m section) for each working condition. In the midstream and downstream sections, we calculate the average siltation thickness of the section. In the upstream section, we calculate the siltation thickness of the channel bed.

The comparison between measured results and simulated results of sediment thickness response process is in Fig. 6. It can be seen that by choosing appropriate parameters, we can use the rate law to better describe the actual response process

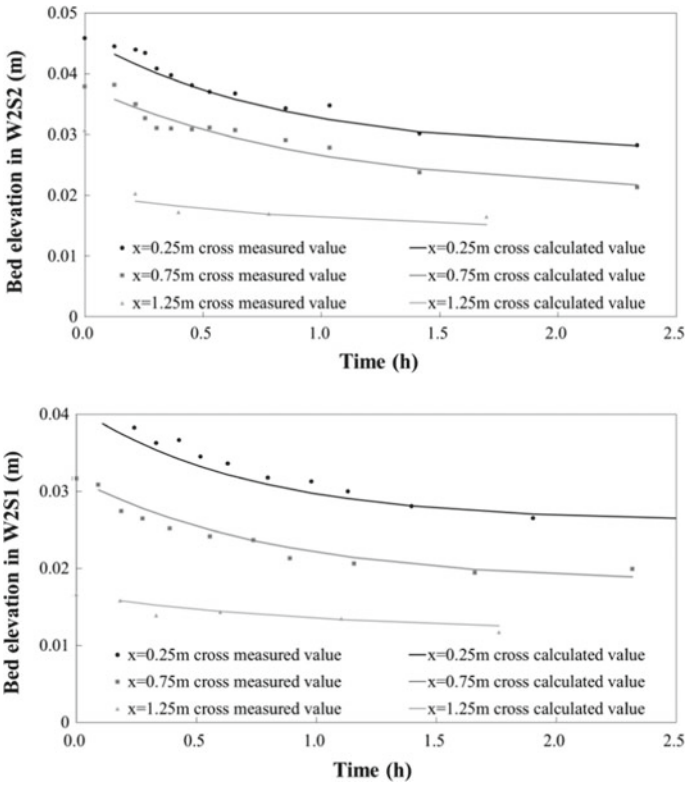

Fig. 6 Comparison between measured results and simulated results of sediment thickness response process

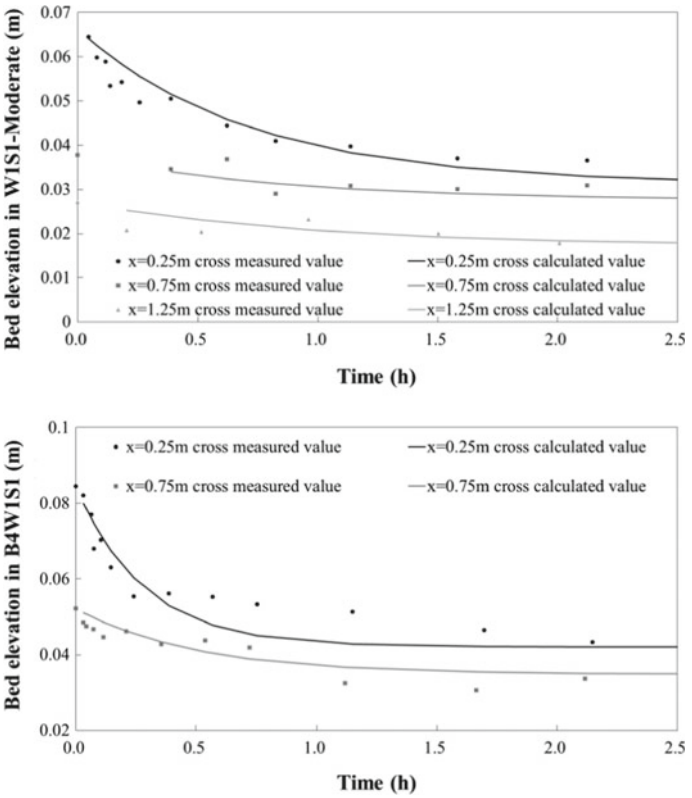

Fig. 6 (continued)

of the deposition thickness. The β value of the upstream section is often larger than that of the middle and lower reaches, indicating that the adjustment rate of the upstream deposition thickness is greater. This is because the flushing caused by clear water in the upper reaches is the most severe, and the river bed needs to be adjusted more to reach a new equilibrium form. Further downstream, the sediment content of the flow recovers. The resulting erosive intensity gradually weakens and the bed response process becomes slower.

4.2 Delayed Response of Alluvial Fans to Discharge Variation

In the small sink operating conditions W3S1 (Q_s halved, Q_w periodically changing), the upstream flow rate periodically varies between 1.11×10^{-4} and 0.56×10^{-4} m^3/s. Through this design, we studied the continuous response process of the deposition thickness after continuous discharge changes. Two changes in upstream discharge

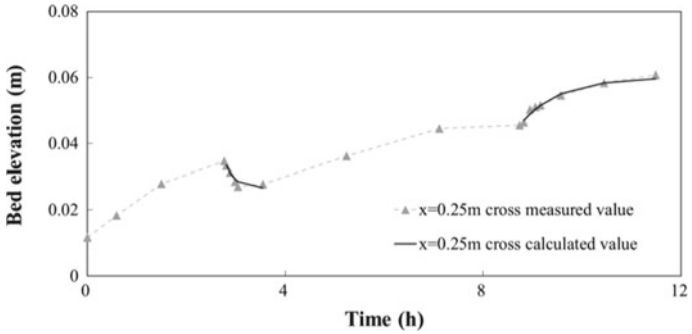

Fig. 7 Simulation of delayed response of deposition thickness after flow change

are generalized into two separate response periods. The solution to the variability equation still uses the single step analytic pattern. At the $x = 0.25$ m section, the sedimentation thickness of the riverbed surface over time is shown in Fig. 7. We use the rate law to simulate the two stages of the delayed response process, and the calculated results agree well with the measured data.

Simulation of delayed response of deposition thickness after flow change is in Fig. 7. The calculation results show that the two delayed response speeds of the alluvial fan thickness are significantly different when the upstream discharge rate changes continuously. At the first mutation, when the discharge increased from 0.56×10^{-4} to 1.11×10^{-4} m^3/s, the bed surface response speed is very fast, β value is about 5. At the second mutation, the discharge decreased from 1.11×10^{-4} to 0.56×10^{-4} m^3/s, and the riverbed response speed slowed down significantly. The β value is only 1.3. On the one hand, this is related to the response of alluvial fans. When the discharge suddenly increases, the bed is flushed and undercut. The undercut area is concentrated in the channel, making the bed thickness more variable. When the discharge suddenly drops, the channel is quickly filled with sediment. The water flow covers most of the alluvial fan area, making the sediment deposition range significantly larger and the deposition thickness change naturally smaller. On the other hand, this may be related to the different state of the alluvial fan before the two discharge mutations. Before the first discharge mutation, the alluvial fan has a smaller size and a larger vertical slope. The evolution process is more sensitive to changes in water and sediment conditions. Before the second discharge mutation, the alluvial fan slope became very small and the velocity was slow. This means that alluvial fans encounter more terrain resistance when responding, and are more resilient to changes in the external environment.

5 Conclusions

In this chapter, the influence of water discharge and sediment concentration on the alluvial fan autogenic process is studied experimentally. Besides, alluvial fan's delayed response to external disturbances is demonstrated by changing discharge and sediment feed rate during experiments. Conclusions are as follows:

(1) Fan progradation process becomes slower when either discharge or sediment feed rate is reduced. When discharge and sediment feed rate are reduced simultaneously, the process is much slower. The widening process of alluvial fans is less sensitive to water discharge and sediment feed rate variation.
(2) When sediment discharge is reduced, aggradation processes slows down along the fan. When discharge is reduced, spatial distribution of sediment varies along the fan, while the overall sedimentation amount stays the same. The upstream aggradation process accelerates while downstream aggradation process slows down.
(3) The reaction of the fluvial cycle and channel morphology to water discharge reduction is the opposite of that to sediment reduction. When sediment is reduced, the water depth in the river channel increases and the velocity decreases, the river cycle becomes longer and the proportion of straight channel increases. When discharge is reduced, the river cycle becomes shorter. Although the duration of straight channel doesn't increase, the proportion of straight channel increases. When discharge and sediment feed rate decrease simultaneously, the longitudinal slope of alluvial fans and flow velocity increases, while the river cycle becomes slightly shorter. The duration of straight channel is longer, which makes its proportion in the river cycle increase greatly.
(4) The rate law can be employed to describe the actual response process of the deposition thickness. Calculated results demonstrate that the response speed of upper-fan siltation thickness is bigger than that of mid-fan and lower-fan. The response speed of fine-sand alluvial fan is larger than that of coarse-sand fan. The response speed of deposition thickness to water discharge increase is larger than that associated with the decrease of the water discharge. The fan response rate to external disturbance is not only related to the response mode of alluvial fans, but also related to the different state of the alluvial fan before the disturbance.

Acknowledgements The authors wish to thank Xi Wu, Shun Xu, Zhang yong Li for their group effort to make this experiment possible. We also thank Shi Ren, Wenting Yang, Yi Hu, Mengji Qi for their language help that greatly improved the readability of the chapter. This study was supported by the National Key R&D Program of China (2016YFC0402305, 2016YFC0402309, 2017YFC0405304, 2017YFC0405306), the Special fund for basic scientific research business of central public research institutes (Grant No. CKSF2017010/HL, CKSF2015049/HL), Scientific scheduling research project of Three Gorges Reservoir (SXSN/4277), the National Natural Science Foundation of China (Grant No. 51,609,009).

References

Caldwell, R. L., & Edmonds, D. A. (2014). The effects of sediment properties on deltaic processes and morphologies: A numerical modeling study. *Journal of Geophysical Research: Earth Surface, 119*(5), 961–982.

Clarke, L. E. (2015). Experimental alluvial fans: advances in understanding of fan dynamics and processes. *Geomorphology, 244*, 135–145.

Dirszowsky, R. W., & Desloges, J. R. (2004). Evolution of the moose lake delta, british Columbia: Implications for Holocene environmental change in the Canadian Rocky Mountains. *Geomorphology, 57*(1), 75–93.

Hashimoto, M., Fukushima, Y., & Fukahata, Y. (2011). Fan-delta uplift and mountain subsidence during the Haiti 2010 earthquake. *Nature Geoscience, 4*(4), 255–259.

Knighton, D. (1998). *Fluvial forms and processes: A new perspective [M]*. New York: Wiley.

Nemec, W., & Steel, R. J. (1988). What is a fan delta and how do we recognize it. *Fan Deltas: Sedimentology and Tectonic Settings*, 3–13.

Ravazzi, C., Marchetti, M., Zanon, M., et al. (2013). Lake evolution and landscape history in the lower Mincio River valley, unravelling drainage changes in the central Po Plain (N-Italy) since the Bronze Age. *Quaternary International, 288,* 195–205.

Straub, K. M., & Wang, Y. N. (2013). Influence of water and sediment supply on the long-term evolution of alluvial fans and deltas: Statistical characterization of basin-filling sedimentation patterns. *Journal of Geophysical Research: Earth Surface, 118,* 1602–1616.

Taha, Z. P., & Anderson, J. B. (2008). The influence of valley aggradation and listric normal faulting on styles of river avulsion: a case study of the Brazos River, Texas, USA. *Geomorphology, 95*(3), 429–448.

Van Dijk, M., Kleinhans, M. G., Postma, G., et al. (2012). Contrasting morphodynamics in alluvial fans and fan deltas: effect of the downstream boundary. *Sedimentology, 59*(7), 2125–2145.

Wu, B. S., Wang, G. Q., & Xia, J. Q. (2007). Case study: Delayed sedimentation response to inflow and operations at sanmenxia dam. *Journal of Hydraulic Engineering ASCE.*

Zhang, X. F., Wang, S. Q., Wu, X., Xu, S., & Li, Z. Y. (2016). The development of a laterally confined laboratory fan delta under sediment supply reduction. *Geomorphology, 257,* 120–133.

Effects of Ice Cover on Local Scour Around Bridge Piers—An Experimental Study

Mohammad Reza Namaee, Yuquan Li and Jueyi Sui

Abstract Local scour around bridge piers can cause significant damage or bridge failure and lead to excessive repairs, loss of accessibility, traffic disruption or even life-threatening incidents. The scouring phenomenon is quite complex and high degrees of uncertainties are associated with the parameters describing this event. Accurate determination of the scour volume and scour area is important in practical decision-making for the control of local scour and the safe design of countermeasures. In the present study, by using three non-uniform sands, a series of large-scale flume experiments have been carried out to investigate the local scour process around four pairs of side-by-side cylindrical bridge piers under conditions of open channel, smooth ice-covered and rough ice-covered flows. Results showed that, under condition of rough ice-covered flow, the scour extent (described by scour areas, scour volumes) is the highest, compared to those under conditions of open channel and smooth ice-covered flows. Finally, empirical relationship between scour area and scour volume have been developed which might be useful for the design of bridge piers.

Keywords Bridge pier · Local scour · Scour area · Scour volume

1 Introduction

Local scour is considered as one of the major reasons for failure of hydraulic structures especially bridge foundation. Bridge failure may result in the loss of lives and financial costs for reconstruction and restoration. Difficulties in perceiving the clear interaction between the geometries of bridge piers with scouring mechanisms make the prediction of local scour depth around bridge piers difficult. The foremost feature of the flow around bridge foundations is the large-scale eddy structure, or system of vortices (Breusers et al. 1977). The vortex system around bridge piers and abutments

M. R. Namaee · Y. Li · J. Sui (✉)
Environmental Engineering Program, University of Northern British Columbia, Prince George, BC, Canada
e-mail: jueyi.sui@unbc.ca

K. D. Nguyen et al. (eds.), *Estuaries and Coastal Zones in Times of Global Change*, Springer Water,
https://doi.org/10.1007/978-981-15-2081-5_40

removes the erodible bed materials and may result in the failure of bridge foundation. Numerous studies have been conducted with the purpose of predicting scour depth of scour holes, and various equations have been developed (e.g. Laursen and Toch 1956; Liu et al. 1961; Shen et al. 1966; Jain and Fischer 1980; Raudkivi and Ettema 1983; Melville and Sutherland 1988; Froehlich 1989; Melville 1992; Abed and Gasser 1993; Richardson and Richardson 1994; Heza et al. 2007). Most of these empirical equations were developed based either on laboratory results or field data. These empirical equations were different from each other in terms of the factors considered in the scour model, parameters used in the equation, laboratory or site conditions, flow condition, grain sizes of bed material, etc. For instance, Raudkivi and Ettema (1983) studied relationship between local scour depth and particle size distribution of bed sediment and developed an equation to estimate the maximum depth of local scour hole. Although numerous studies have been conducted to investigate local scour around bridge foundation, this challenging phenomenon has been remained as one of the main issues in terms of bridge pier design. Local scour process around bridge pier gets more complicated when the water surface is covered by ice. In this situation, the presence of ice cover leads to a different set of geomorphological conditions comparing to those under open flow conditions (Hicks 2009). The characteristics of flow under ice cover affects the process of sediment transport, traverse and vertical mixing and mean flow velocity (Andre and Thang 2012). It has been proved that the formation of a stable ice cover effectively doubles the wetted perimeter compared to that under open channel condition, alters the hydraulics of an open channel by imposing an extra boundary to the flow, causing velocity profile to be shifted towards the smoother boundary (channel bed) and adding up to the flow resistance (Sui et al. 2010; Wang et al. 2008). However, up to date, there is still very limited research work regarding local scour around bridge infrastructures under ice covered condition, and this issue is one of the major concerns in bridge foundation design field. Using non-uniform sediments, Wu et al (2013) carried out experiments to investigate scour morphology around bridge abutment under ice cover. It was found that that under ice cover, at different locations of the abutment, the sediment sorting process were observed. Wu et al. (2014a, b) assessed the impacts of ice cover on local scour around a semi-circular bridge abutment. It was found that the average scour depth under ice-covered condition was always greater compared to that in open flow condition. The average scour depth under rough ice cover was 35% greater than that under smooth ice cover. Wu et al. (2014a, b) studied the incipient motion of bed material and shear stress distribution around bridge abutments under ice-covered condition. They claimed that the average scour angle around a semi-circular abutment is around 10° larger than that around the square abutment. Wu et al (2015) compared the scour profile under an ice-covered condition with previous studies by considering the role of relative bed coarseness, flow shallowness, and pier Froude number. It was found that the scour depth under ice-covered condition is larger compared to that under open flow condition. Besides, the presence of an ice cover results in a greater scour depth in flow with a shallower flow depth, and with the increase in flow depth, the impact of ice cover decreases.

In terms of protection against possible undermining caused by local scour process around bridge infrastructure, riprap is the most commonly employed countermeasure (Lauchlan and Melville 2001). The most suitable countermeasure for avoiding local scour process around hydraulic structure depends on the relative effectiveness, cost, maintenance, and ability to detect failures (Deng and Cai 2009). Having an accurate and precise estimation of scour area and scour volume is crucial for the safe design of bridge piers and abutments. Very few studies have thoroughly investigated scour volume and scour area around bridge piers, especially under condition of ice-covered flow. In this case, Wu et al. (2014a, b) found that there was a linear correlation between scour depth and volume of scour hole around bridge abutments under ice covered condition. Khwairakpam et al. (2012) developed two equations to estimate scour volume and scour area around a vertical pier under clear water condition in terms of approach flow depth and pier diameter. Hirshfield (2015) found that scour area and volume increase with pier size. The aim of this study is to thoroughly investigate scour volumes and scour areas based on a series of large-scale flume experiments using non-uniform natural sediment under conditions of open channel and ice-covered flow around four pairs of side-by-side cylindrical bridge piers and also to investigate how different scour volume and scour area are under ice-covered flow compared to those of open flow conditions.

2 Methodologies and Experimental Setup

Experiments were carried out in a large-scale flume at the Quesnel River Research University of Northern British Columbia. The flume was 40-m long, 2-m wide and 1.3-m deep. The longitudinal slope of the flume bottom was 0.2 percent. A holding tank with a volume of nearly 90 m^3 was located at the upstream end of the flume and provides a constant head in the experimental zone. At the end of the holding tank, water overflowed from a rectangular weir into the flume section for experiments. A flow diffuser was placed downstream of the rectangular weir to maintain the flow uniform. Two sand boxes with the depth of 0.30 m were spaced 10.2 m. Three natural non-uniform sediments were used in this experimental study. The median grain sizes of these sands (D_{50}) were 0.58, 0.50 and 0.47 mm, and the geometric standard deviation (σ_g) was 2.61, 2.53 and 1.89, respectively. For all the three sediments, the geometric standard deviation (σ_g) was larger than 1.4, which can be treated as non-uniform sediments (Barbhuiya and Dey 2004). The first sand box was 5.6-m long and the second sand box was 5.8-m in length. Four pairs of bridge piers with diameter of 6, 9, 11 and 17 cm were used in this study. Bridge piers were made of PVC circular plumbing pipe. A pair of side-by-side bridge piers were placed inside each sand box. The distance between the central lines of these side-by-side bridge piers was 50 cm. Each pier was offset from the centre line by 25 cm, as illustrated in Fig. 1a. Water depth in the flume was adjusted by adjusting the tailgate. In front of the first sand box, a SonTek Incorporated 2D flow meter was installed to measure the approaching flow velocity and water depth during each experiment. A staff gauge

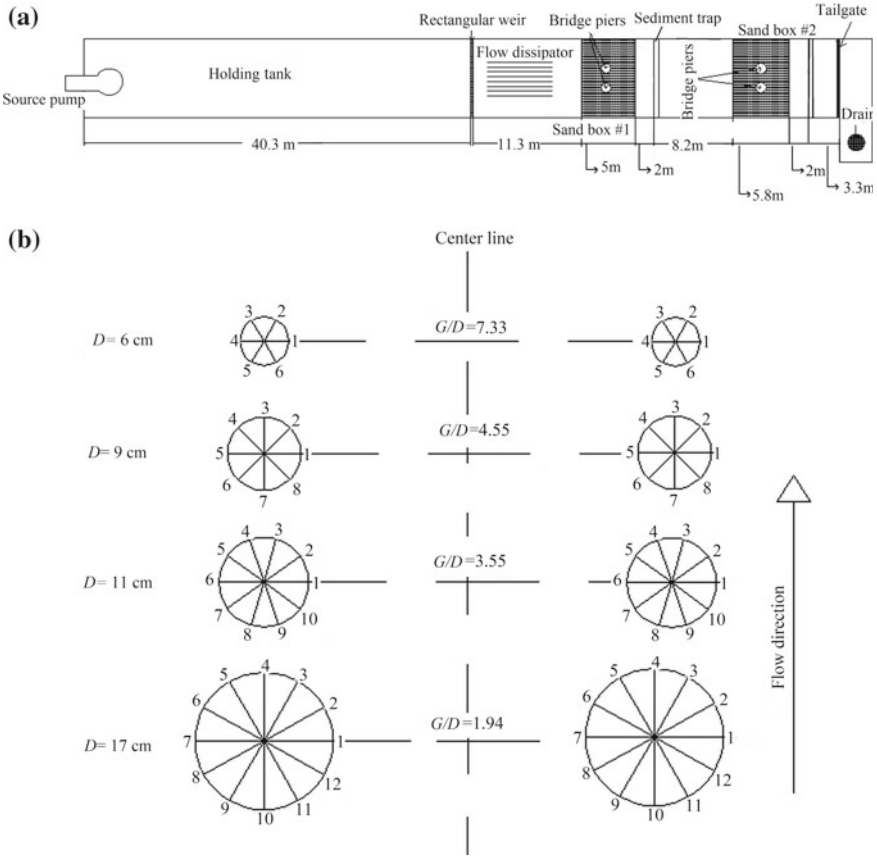

Fig. 1 **a** Plan view and vertical view of experiment flume, **b** measuring points around the circular bridge pier

was also installed in the middle of each sand box to manually verify water depth. The scour hole velocity field was measured using a 10-MHz Acoustic Droppler Velocimeter (ADV) by SonTek. The ADV is a high-precision instrument used to measure 3D water velocity in a wide range of environments including laboratories, rivers, estuaries, and the ocean (Cea et al, 2007). The Styrofoam panels were used to simulate ice cover. Styrofoam density was 0.026 gr/cm^3 and was floatable on water surface during the experimental runs. In the present study, two types of model ice cover were used, namely smooth cover and rough cover. The smooth ice cover was the surface of the original Styrofoam panels while the rough ice cover was made by attaching small Styrofoam cubes to the bottom of the smooth cover. The dimensions of Styrofoam cubes were 2.5 cm × 2.5 cm × 2.5 cm and were 3.5 cm spaced apart. For the "Concrete Trowel finish", according to Mays (1999), the roughness coefficient is suggested to be 0.013. Therefore, for the relatively smooth concrete-like surface of the Styrofoam panel, the roughness of the modeled smooth ice-cover is suggested to

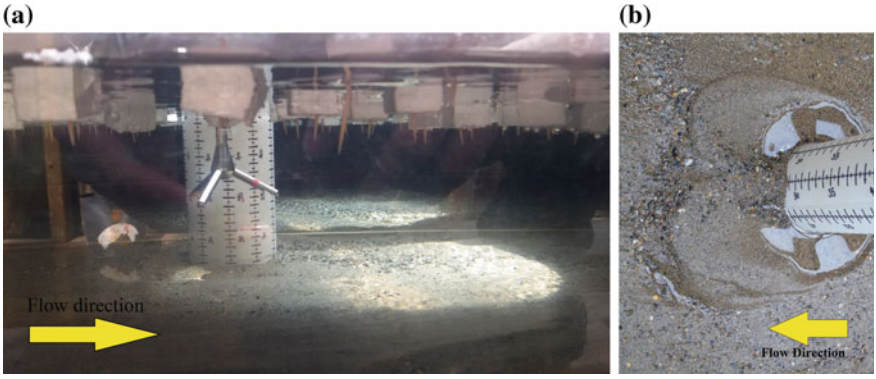

Fig. 2 **a** Side view of scour hole around the 11-cm-bridge pier under rough ice-covered condition, **b** top view of the local scour pattern around the 9-cm-bridge pier under rough ice-covered condition ($D_{50} = 0.50$ mm)

be 0.013. In terms of rough ice-covered flow condition, Li (2012) reviewed several methods for calculating the Manning's coefficient for rough ice cover, the following equation can be used depending on the size of the small cubes:

$$\frac{n_i}{k_S^{1/6}} = \frac{(8g)^{-1/2}\left(R/K_S\right)^{1/6}}{0.867\ \ln\left(12R/K_S\right)} \tag{1}$$

In which, K_s is the average roughness height of the underside of ice cover and R is the hydraulic radius. Figure 2a shows the side view of local scour around 11 cm bridge pier under condition of rough ice-covered flow, and Fig. 2b shows the top view of local scour around the 9-cm-bridge pier in sand bed of for $D_{50} = 0.50$ mm under rough ice-covered condition. Each experimental run lasted 24 h, and this allowed the local scour process to reach to an equilibrium condition. After 24 h, the flume was gradually drained. The scour depth was manually measured along the outside lines of the circular bridge piers. In terms of scour depth measurement, the outside perimeter of each bridge pier was equally divided into numbered measuring point in order to accurately read the scour depth at different locations to draw scour hole contours, as shown in Fig. 1b. The scour hole around bridge piers were measured at proper increments from numbered measuring point along each bridge pier.

In total, 108 Experiments were conducted to investigate scour area and scour volume. For each sediment type, 36 experiments were carried out under different flow conditions, namely, open channel, smooth ice-covered and rough ice-covered. It should be mentioned that the range of Froude number in the first sand box was higher than the second sand box. This is because of the longitudinal slope of the channel and dissipation of momentum of flow due to friction. The flow Froude number in the first sand box ranges from 0.072 to 0.270, and in the second sand box ranges from 0.054 to 0.177. In this study, four pairs of bridge piers were placed in

sand boxes to do experiments, namely, 6-cm-diameter piers, 9-cm-diameter piers, 11-cm-diameter piers, and 17-cm-diameter piers. Throughout the calibration stage of the experiments, the depth of scour holes around bridge piers was carefully measured hourly for any changes. It was observed that after approximately a period of 6 h, no significant change in scour depth was observed. To make sure that the scour process achieves an equilibrium state, each experiment lasted for 24 h. Note: a limited number of experiments were also extended to 38 h and there was not any particular scour depth change between 24-h and 38-h experiments.

In this study, the critical velocity for incipient motion (V_c) is calculated using following equation which is proposed by Gao et al. (1993):

$$V_c = 3.28\left(\frac{y_0}{D_m}\right)^{0.14}\left(8.85D_m + 6.05E^{-7}\left[\frac{10 + 0.3048y_0}{(0.3048D_m)^{0.72}}\right]\right)^{0.5}$$

In which V_c is critical shear velocity, D_m is the medium grain size and y_0 is the approaching flow depth.

Results indicated that the typical value of V_c/V is approximately equal to 0.43. Thus, all experiment runs were done under clear water condition.

3 Results and Discussions

Table 1 shows experimental results regarding series B ($D_{50} = 0.47$ mm). To compute scour hole volume and area for each run, all measured data for scour hole were entered into the Surfer 12 which is a surface and contour mapping program. The planar area defined in the Surfer 12 is computed by projecting the cut and fill portions of the surface onto a plane and calculating the area of the projection where positive planar area represents the projection of the cut (map areas where the upper surface is above the lower surface) onto a horizontal plane and negative planar area represents the projection of the fill (map areas where the upper surface is below the lower surface) onto a horizontal plane. In terms of scour volume, the cut and fill volumes section of the grid volume report display the positive volume (cut) and the negative volume (fill). The cut portion is the volume between the upper and lower surface when the upper surface is above the lower surface while the fill portion is the volume between the upper and lower surfaces when the upper surface is below the lower surface (Yang et al. 2004; Surfer on-line manual). For instance, Fig. 3a, b display the scour volume and scour area associated with the 11-cm-bridge pier under smooth ice-covered condition for sediment of $D_{50} = 0.47$ mm. As Fig. 3b shows, the blue regions are the planar areas which are needed to be filled while the red regions are the planar areas needed to be cut off. It is important to know that planar area is independent of the depth of scour hole. Besides, it should be mentioned that among a pair of piers, the one which shows the highest scour volume and scour area was selected in order to investigate the most critical case in terms of bridge pier design. Figure 3b shows

Table 1 Experimental results regarding D_{50} = 0.470 mm

Run #	Cover	D (mm)	D_{50} (mm)	θ (degrees)	y_0 (mm)	y_{max} (mm)	U (m/s)	U^* (m/s)	U/U^*	Q (m^3/s)
1B	Open flow	60	0.47	11.83	250	22	0.11	0.20	0.56	0.056
2B	Open flow	60	0.47	11.62	110	35	0.18	0.14	1.30	0.040
3B	Open flow	60	0.47	11.45	280	25	0.17	0.21	0.81	0.094
4B	Open flow	90	0.47	11.83	200	35	0.13	0.18	0.74	0.054
5B	Open flow	90	0.47	11.62	90	60	0.25	0.13	1.96	0.045
6B	Open flow	90	0.47	11.45	230	68	0.20	0.19	1.05	0.093
7B	Open flow	110	0.47	11.50	242	25	0.12	0.19	0.60	0.058
8B	Open flow	110	0.47	11.83	100	71	0.28	0.13	2.09	0.056
9B	Open flow	110	0.47	11.72	253	75	0.20	0.20	1.05	0.101
10B	Open flow	170	0.47	11.50	250	24	0.12	0.20	0.59	0.059
11B	Open flow	170	0.47	11.83	100	45	0.18	0.13	1.35	0.036
12B	Open flow	170	0.47	11.72	270	48	0.16	0.20	0.77	0.084
13B	Smooth	60	0.47	11.62	250	29	0.12	0.15	0.82	0.061
14B	Smooth	60	0.47	11.59	110	35	0.17	0.10	1.68	0.037
15B	Smooth	60	0.47	11.55	260	42	0.17	0.15	1.16	0.090
16B	Smooth	90	0.47	11.62	200	31.2	0.15	0.13	1.13	0.060
17B	Smooth	90	0.47	11.59	100	64	0.23	0.10	2.40	0.046
18B	Smooth	90	0.47	11.55	240	68	0.20	0.14	1.38	0.096
19B	Smooth	110	0.47	11.59	243	42	0.10	0.14	0.68	0.048
20B	Smooth	110	0.47	11.10	90	78	0.21	0.09	2.29	0.038
21B	Smooth	110	0.47	11.57	255	80	0.20	0.15	1.44	0.102

(continued)

Table 1 (continued)

Run #	Cover	D (mm)	D_{50} (mm)	θ (degrees)	y_0 (mm)	y_{max} (mm)	U (m/s)	U^* (m/s)	U/U^*	Q (m^3/s)
22B	Smooth	170	0.47	11.59	260	29	0.09	0.15	0.63	0.049
23B	Smooth	170	0.47	11.10	105	48	0.15	0.10	1.55	0.032
24B	Smooth	170	0.47	11.54	250	49	0.18	0.15	1.20	0.089
25B	Rough	60	0.47	11.48	220	47	0.16	0.14	1.18	0.072
26B	Rough	60	0.47	11.45	100	55	0.17	0.10	1.76	0.034
27B	Rough	60	0.47	11.59	250	57	0.22	0.15	1.48	0.109
28B	Rough	90	0.47	11.48	220	67	0.14	0.14	0.99	0.061
29B	Rough	90	0.47	11.45	100	73	0.23	0.10	2.38	0.046
30B	Rough	90	0.47	11.59	230	85	0.20	0.14	1.37	0.090
31B	Rough	110	0.47	11.58	240	80	0.12	0.14	0.86	0.058
32B	Rough	110	0.47	11.61	90	92	0.20	0.09	2.22	0.037
33B	Rough	110	0.47	11.62	220	93	0.19	0.14	1.39	0.085
34B	Rough	170	0.47	11.58	220	49	0.12	0.14	0.86	0.053
35B	Rough	170	0.47	11.61	110	58	0.16	0.10	1.61	0.036
36B	Rough	170	0.47	11.62	280	61	0.17	0.16	1.08	0.093

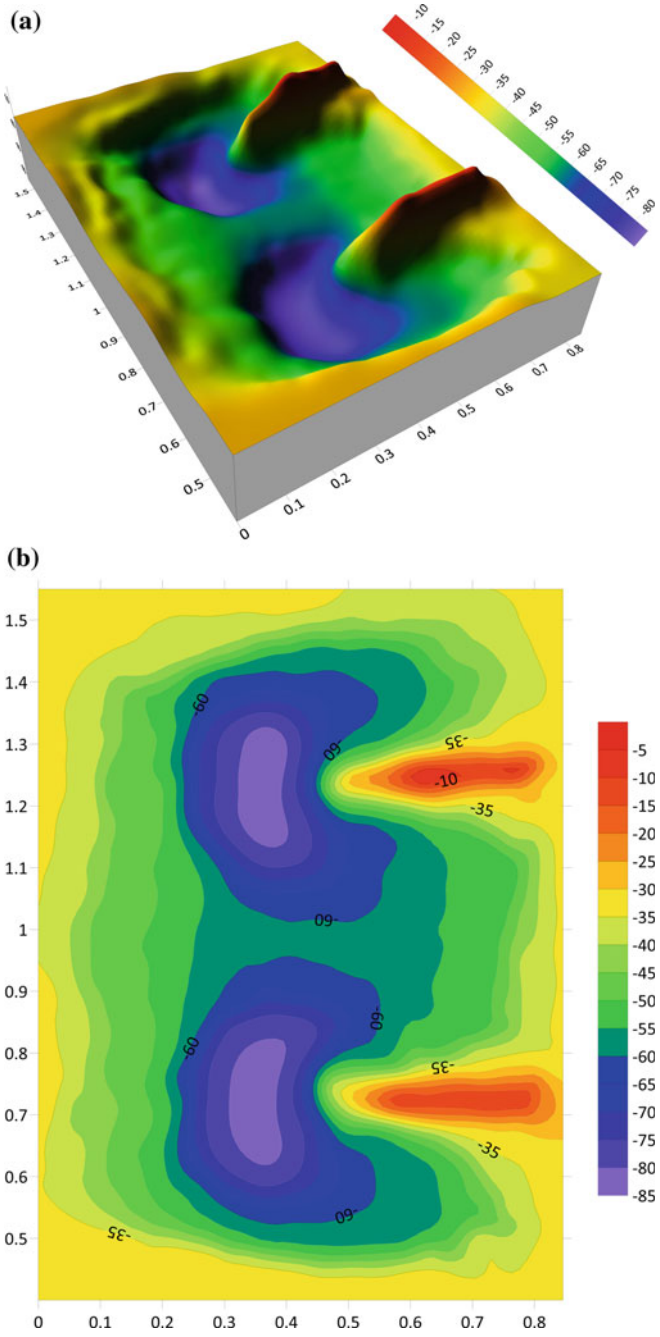

Fig. 3 **a** 3-D scour volume view for the 11-cm-bridge pier under smooth ice-covered flow condition for sediment of $D_{50} = 0.50$ mm, **b** top view of cut and fill scour area for the 11-cm-bridge pier under smooth ice-covered flow condition for sediment of $D_{50} = 0.50$ mm

the scour hole contour around the bridge piers along with the turbulence that the obstruction of pier placement has caused in the bed morphology.

Figure 4 shows the changes in scour volume with respect to pier size and grain size of sediment under different flow conditions (open channel, smooth ice-covered and rough ice-covered flows). In Fig. 4, for each type of sediment, the first three experiments, the second three experiments, the third three experiments and the last three experiments are associated with different pier diameters of 6 cm, 9 cm, 11 cm and 17 cm, respectively. One can see from Fig. 4 that for sediment of $D_{50} = 0.50$ mm, the volumes of scour hole under rough ice-covered condition are the highest and the volumes of scour hole under open flow condition are the lowest. The mean scour volume under open flow, smooth ice-covered and rough ice-covered flow conditions is 459.96 cm^3, 661.81 cm^3 and 1069.24 cm^3, respectively. The difference between the mean scour volume under rough ice-covered flow condition and that under open flow condition is 56.98%, and the difference between the mean scour volume under smooth ice-covered flow condition and that under open flow condition is 35.10%. These differences indicate that, under nearly the same flow condition with the same bed material, the presence of rough ice cover and smooth ice cover resulted in an increase in scour volume of 56.98% and 35.10% respectively compared to those under the open channel flow condition. The reason for an increase in the scour volume under ice-covered condition compared to that under open flow condition is the modification of flow velocity distribution caused by ice cover. As stated by Sui et al (2010), the maximum flow velocity under ice-covered flow condition is located between channel bed and ice cover, depending on the roughness of ice cover

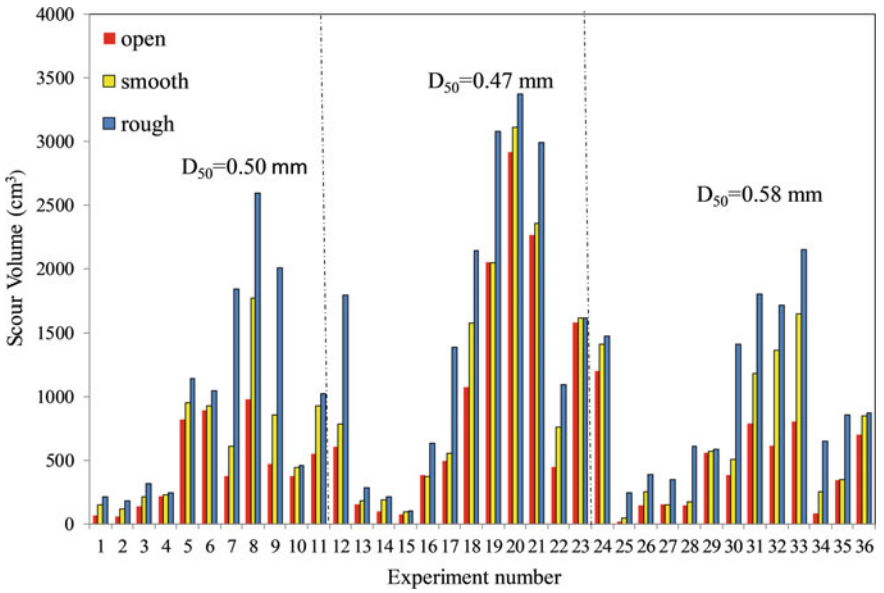

Fig. 4 Variation of scour volume around bridge pier

and channel bed. The near bed flow velocity under ice-covered conditions is higher than that under open flow conditions. As the near bed velocity increases, the kinetic energy exerted on the bed material also increases, implying more sediment transport (Sui et al. 2010). In terms of scour volume for sediment of $D_{50} = 0.47$ mm, similar to results for sediment of $D_{50} = 0.50$ mm, the volume of scour hole under rough ice-covered flow condition is the highest and the volume of scour hole under open flow condition is the lowest. Besides, under ice-covered condition, the volume of scour hole for sediment of $D_{50} = 0.47$ mm has significantly increased compared to that for sediment of $D_{50} = 0.50$ mm. This reveals the fact that under the same flow condition, the impact of ice cover on local scour process is significant for finer sediment type. The mean scour volume under open flow, smooth ice-covered and rough ice-covered conditions is 1059.66 cm^3; 1187.77 cm^3 and 1529.95 cm^3, respectively. Namely, under the same flow condition and with the same sand bed, compared to the scour volumes under the open channel flow and smooth-ice-covered flow conditions, the presence of rough ice cover resulted in an increase in the scour volume of 30.72% and 22.35%, respectively. In terms of scour volume for sediment of $D_{50} = 0.58$ mm, similar to those of $D_{50} = 0.50$ mm and $D_{50} = 0.47$ mm, the volume of scour hole under rough ice-covered condition is the highest and the volume of scour hole under open channel condition is the lowest. However, the difference between volume of scour hole around same bridge pier in bed sand of $D_{50} = 0.58$ mm and that in bed sand of $D_{50} = 047$ mm has relatively decreased. This result shows that, regardless of the flow cover, as the grain size of bed sediment increase, the volume of scour hole decrease. For sediment of $D_{50} = 0.58$ mm, the mean scour volume under open flow, smooth ice-covered and rough ice-covered conditions is 392.58 cm^3; 610.72 cm^3 and 965.76 cm^3, respectively. Therefore, under the same flow condition and with the same sand bed, compared to the scour volumes under the open channel flow and smooth-ice-covered flow conditions, the presence of rough ice cover resulted in an increase in the scour volume of 36.82% and 58.1%, respectively. The grain size of sediment plays a key role on the volume of scour hole. For instance, regardless of flow cover, for sediment of $D_{50} = 0.47$ mm, the mean scour volume around the 11-cm-bridge pier is 2684.5 cm^3 with the highest scour volume of 3366.72 cm^3. However, for sediment of $D_{50} = 0.50$ mm, the average volume of scour hole around the 11-cm-pier is 1275.5 cm^3. It is worth mentioning that there is a tremendous difference of 52.49% between the mean volume of scour hole around the 11-cm-bridge pier for bed sand of $D_{50} = 0.47$ mm and that for bed sand of $D_{50} = 0.50$ mm. Results also showed that it takes slightly shorter time for the scour hole to reach to the equilibrium state for the finer sediment. In contrast, for the coarser sediment, it takes longer time for the scour hole to reach an equilibrium state.

Figure 5 shows the scour area with respect to sediment types under different flow conditions (open channel, smooth ice-covered and rough ice-covered flows). Similar to Fig. 4, for each type of sediment, the first three experiments, the second three experiments, the third three experiments and the last three experiments are associated with different pier diameters of 6 cm, 9 cm, 11 cm and 17 cm, respectively. Unlike the volume of scour hole, the scour area is not dominantly highest for flow under rough ice-covered condition comparing to those under smooth ice-covered and open

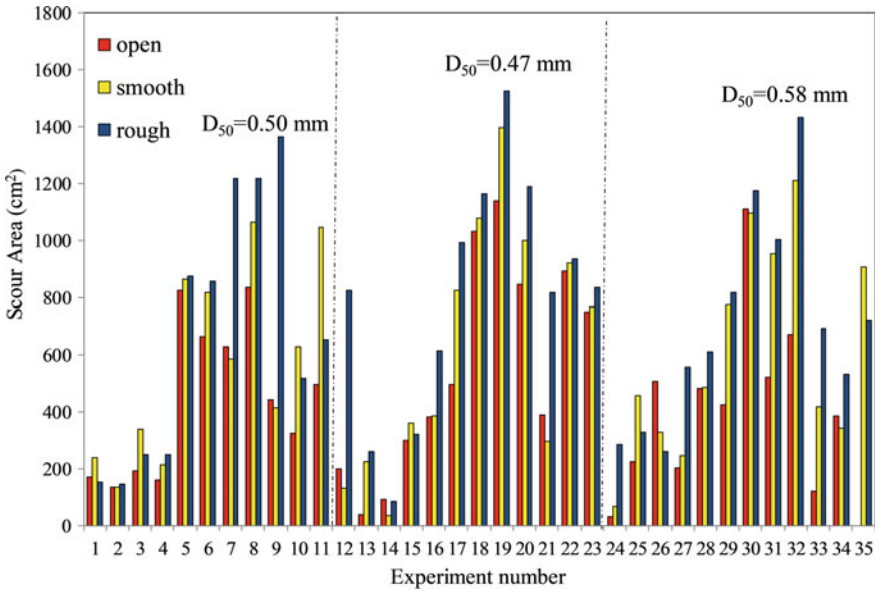

Fig. 5 Variation of scour area around bridge pier

channel flow conditions. In terms of scour area for sediment of $D_{50} = 0.47$ mm, in most cases, the scour area under rough ice-covered condition is the highest and the scour area under open channel condition is the lowest. However, under the same flow condition and with the same sand bed, compared to the scour area under the smooth-ice-covered flow condition, the presence of rough ice cover didn't result in a clear increase in the scour area. This means that the impact of smooth ice-covered flow on scour area is nearly the same as that of rough ice-covered flow. This is partly due to the method that surfer uses to calculate the planar scour area without considering the corresponding depth of the cut surfaces. For sediment of $D_{50} = 0.47$ mm, the mean scour areas under open flow, smooth ice-covered and rough ice-covered conditions are 546.09 cm^2; 618.40 cm^2 and 796.77 cm^2, respectively. Therefore, under the same flow condition and with the same sand bed, compared to the scour area under the open channel flow and smooth-ice-covered flow conditions, the presence of rough ice cover resulted in an increase in the mean scour area of 31.46% and 22.39%, respectively.

In terms of scour area for sediment of $D_{50} = 0.50$ mm, the mean scour areas under open flow, smooth ice-covered and rough ice-covered conditions are 443.54 cm^2; 585.44 cm^2 and 714.85 cm^2, respectively. Therefore, under the same flow condition and with the same sand bed, compared to the scour area under the open channel flow and smooth-ice-covered flow conditions, the presence of rough ice cover resulted in an increase in the mean scour area of 37.95% and 18.10%, respectively.

In terms of scour area for sediment of $D_{50} = 0.58$ mm, in most cases, the scour area under rough ice-covered condition is the highest and the scour area under open

channel condition is the lowest. For sediment of $D_{50} = 0.58$ mm, the mean scour areas under open flow, smooth ice-covered and rough ice-covered conditions are 426.10 cm^2, 607.19 cm^2 and 700.78 cm^2, respectively. So, under the same flow condition and with the same sand bed, compared to the scour area under the open channel flow and smooth-ice-covered flow conditions, the presence of rough ice cover resulted in an increase in the mean scour area of 13.40% and 15.39%, respectively. The grain size of sediment plays a key role on the scour area. For instance, regardless of flow, for sediment of $D_{50} = 0.47$ mm, the mean scour area around the 11-cm-bridge pier is 1151.70 cm^2 with the highest scour area of 1524.94 cm^2. However, for sediment of $D_{50} = 0.50$ mm, the average scour area around the 11-cm-pier is 881.47 cm^2 with the highest scour area of 1216.82 cm^2. It is worth mentioning that there is a tremendous difference of 52.49% between the mean scour area around the 11-cm-bridge pier for bed sand of $D_{50} = 0.47$ mm and that for bed sand of $D_{50} = 0.50$ mm.

Figure 6 shows the relationships between scour volume (V) and scour area (A) under condition of both ice-covered flows and open channel flows. These relationships can be described as follows:

Under condition of open channel flow:

$$V = 0.2288(A)^{1.2557} \tag{2}$$

Under condition of ice-covered flow

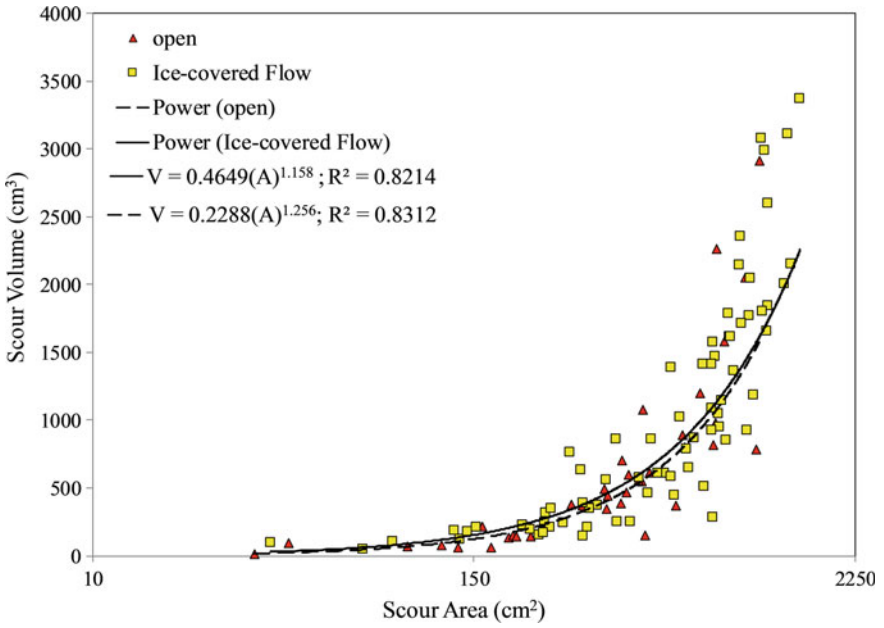

Fig. 6 Scour volume (V) versus scour area (A)

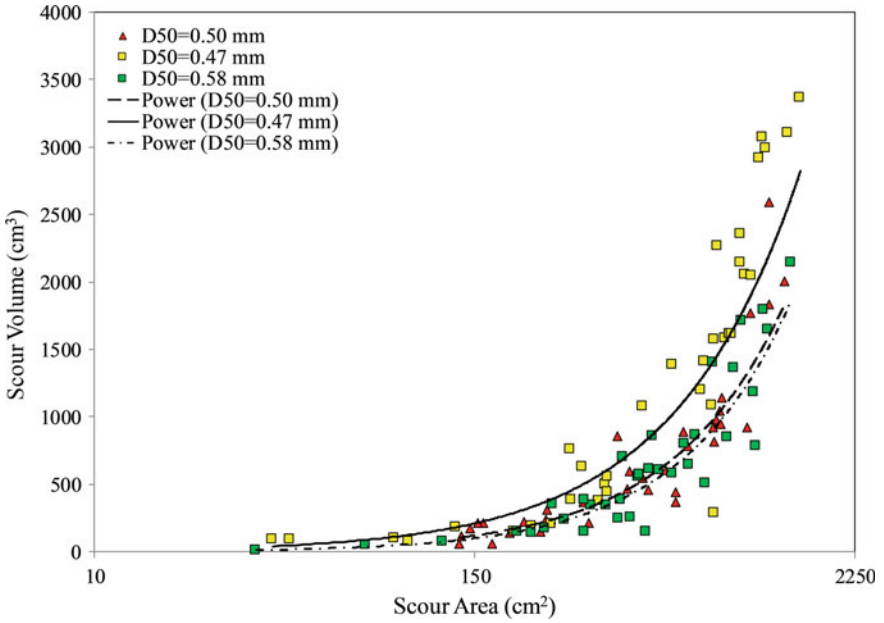

Fig. 7 Relationship between scour volume and scour area in terms of sediment type

$$V = 0.4649(A)^{1.158} \tag{3}$$

where:
V = volume of scour (cm^3)
A = area of scour (cm^2).

According to Eqs. 2 and 3, the coefficient factor of regression equation under ice-covered flow is larger than that under open channel flow, implying that the flow under ice-covered condition has led to higher amount of scour volume and scour area. Figure 7 gives the relationship between scour volume and scour area in terms of grain size of sediment. One can see from Fig. 7 that the largest amount of scour volume and scour area occurs in the finest sand of $D_{50} = 0.47$ mm.

4 Conclusion

In the present study, the main objective was to thoroughly investigate the correlation between scour volume and scour area under conditions of ice-covered and open channel flow in flume with non-uniform sediment. In this study, three natural non-uniform sediment mixtures with median grain size of 0.58, 0.50 and 0.47 mm were used. Besides, two types of artificial ice cover namely rough and smooth ice cover were used to simulate ice-covered flow conditions. Totally, 108 Experiments were

conducted in a large-scale flume to study scour area, scour volume around four pairs of side-by-side cylindrical bridge piers. The following are the major conclusions of this study:

(1) In terms of grain size of sediment, under the same flow condition, the finest sediment size of $D_{50} = 0.47$ mm yielded the largest scour volume and scour area. The impact of ice cover on local scour volume and area is more significant for finer sediment type. On the other hand, under the same flow conditions, the coarsest sediment of $D_{50} = 0.58$ mm yielded the smallest scour volume and scour area.
(2) In terms of flow cover, it was found that the rough ice-covered flow has led to the maximum amount of scour volume and scour area. Besides, under the same flow condition, the flow turbulence caused by high velocities and lower flow depths occurring around bridge piers with smaller pier spacing is more significant for finer sediment. It was also found that, regardless of the flow cover, the scour volume decreases with the increase in bed sediment size.
(3) Finally, two empirical equations were developed to predict scour volume and scour area under conditions ice-covered flow and open channel flow.

Acknowledgements This work is partially supported by UNBC Research Project Award. Physical experiments were conducted at Quesnel River Research Center (QRRC), Likely, BC. We gratefully acknowledge the help provided by QRRC staff.

References

Abed, L., & Gasser, M. M. (1993). Model study of local scour down-stream bridge piers. In *Proceedings of the 1993 National Conference on Hydraulic Engineering* (pp. 1738–1743). San Francisco: American Society of Civil Engineers.

Andre, R., & Thang, T. (2012). Mean and turbulent flow fields in a simulated ice-cover channel with a gravel bed: Some laboratory observations. *Journal of Earth Surface Processes and Landforms, 37*(9), 951–956.

Barbhuiya, A. K., & Dey, S. (2004). Local scour at abutments: A review. *Academy Proceedings in Engineering Sciences, Sadhana, 29*(5), 449–476. https://doi.org/10.1007/BF02703255.

Breusers, H. N. C., Nicollet, G., & Shen, H. W. (1977). Local scour around cylindrical piers. *Journal of Hydraulic Research, 15*(3), 211–252 (I.A.H.R.).

Cea, L., Puertas, J., & Pena, L. (2007). Velocity measurements on highly turbulent free surface flow using ADV. *Experiments in Fluids, 42*(3), 333–348.

Deng, L., & Cai, C. S. (2009). Bridge scour: Prediction, modeling, monitoring, and countermeasures. *Practice Periodical on Structural Design and Construction, 15*(2), 125–134.

Froehlich, D. C. (1989). Local scour at bridge abutments. In *Proceedings of the 1989 National Conference on Hydraulic Engineering* (pp. 13–18), New Orleans, LA, USA.

Gao, D., Posada, G., & Nordin, C. F. (1993). Pier scour equations used in China. In *Hydraulic engineering* (pp. 1031–1036). ASCE.

Heza, Y. B. M., Soliman, A. M., & Saleh, S. A. (2007). Prediction of the scour hole geometry around exposed bridge circular-pile foundation. *Journal of Engineering and Applied Science, 54*(4), 375.

Hicks, F. (2009). An overview of river ice problems. *Journal of Cold Regions Science and Technology, 55*(2), 175–185.

Hirshfield, F. (2015). *The impact of ice conditions on local scour around bridge piers*, Doctoral dissertation, University of Northern British Colombia.

Jain, S. C., & Fischer, E. E. (1980). Scour around bridge piers at high flow velocities. *Journal of the Hydraulics Division, 106*(11), 1827–1842.

Khwairakpam, P., Ray, S. S., Das, S., Das, R., & Mazumdar, A. (2012). Scour hole characteristics around a vertical pier under clear water scour conditions. *ARPN Journal of Engineering and Applied Sciences, 7*(6), 649–654.

Lauchlan, C. S., & Melville, B. W. (2001). Riprap protection at bridge piers. *Journal of Hydraulic Engineering, 127*(5), 412–418.

Laursen, E. M., & Toch, A. (1956). *Scour around bridge piers and abutments*. Bull. No. 4, Iowa Highways Research Board, Ames, Iowa.

Li, S. S. (2012). Estimates of the Manning's coefficient for ice-covered rivers. *Proceedings of the Institution of Civil Engineers-Water Management, 165*(9), 495–505.

Liu, H. K., Chang, F. M., & Skinner, M. M. (1961). *Effect of bridge constriction on scour and backwater*. Rep. No. CER60HKL22, Dept. of Civil Engineering, Colorado State Univ., Fort Collins, Colo.

Mays, L. W. (Ed.). (1999). *Hydraulic design handbook*. McGraw-Hill Professional Publishing.

Melville, B. W. (1992). Local scour at bridge abutments. *Journal of Hydraulic Engineering, 118*(4), 615–631.

Melville, B. W., & Sutherland, A. J. (1988). Design method for local scour at bridge piers. *Journal of Hydraulic Engineering, 114*(10), 1210–1226.

Raudkivi, A. J., & Ettema, R. (1983). Clear-water scour at cylindrical piers. *Journal of Hydraulic Engineering, 109*(3), 338–350.

Richardson, J. R., & Richardson, E. V. (1994). Practical method for scour prediction at bridge piers. *Journal of Hydraulic Engineering*, 1–5.

Shen, H. W., Schneider, V. R., & Karaki, S. S. (1966). *Mechanics of Locar Scour*. U.S. Department of Commerce, National Bureau of Standards, Institute for Applied Technology.

Sui, J., Wang, J., He, Y., & Krol, F. (2010). Velocity profiles and incipient motion of frazil particles under ice cover. *International Journal of Sediment Research, 25*(1), 39–51.

Wang, J., Sui, J., & Karney, B. (2008). Incipient motion of non-cohesive sediment under ice cover—An experimental study. *Journal of Hydrodynamics, 20*(1), 117–124.

Wu, P., Hirshfield, F., & Sui, J. (2013). Scour morphology around bridge abutment with non-uniform sediments under ice cover. In *Proceedings of 2013 IAHR Congress*, Beijing: Tsinghua University Press.

Wu, P., Hirshfield, F., & Sui, J. (2014a). Further studies of incipient motion and shear stress on local scour around bridge abutment under ice cover. *Canadian Journal of Civil Engineering*, *41*(10), 892–899.

Wu, P., Hirshfield, F., Sui, J., Wang, J., & Chen, P. P. (2014b). Impacts of ice cover on local scour around semi-circular bridge abutment. *Journal of Hydrodynamics, 26*(1), 10–18.

Wu, P., Hirshfield, F., & Sui, J. (2015). Local scour around bridge abutments under ice covered conditions-an experimental study. *International Journal of Sediment Research, 30*(1), 39–47.

Yang, C. S., Kao, S. P., Lee, F. B., & Hung, P. S. (2004). Twelve different interpolation methods: A case study of Surfer 8.0. In *Proceedings of the XXth ISPRS Congress* (Vol. 35, pp. 778–785), Istanbul, Turkey.

Effect of Human Activities on Morphology of Estuaries and Deltaic Coasts

90% of the world's population is located along the coasts. This leads to river and coastal developments such as rived bed modifications, reservoirs, hydroelectric dams, water uses, sediment mining and agriculture. Thus, the human activities induce a modification of estuaries and coastal zones. Such modifications could have an impact on the river functioning or on the coastline erosion. This part presents three chapters relating to the impact of human activities on the evolution of estuaries and deltas.

The first chapter by Han and Lu studies the effect of the human activities on the Yangtze estuary during the last 20 years. Estuaries are a natural interface between the sea and human land-based activities. Then, they concentrate a large number of human constructions like ports, waterways, dredging, bridges and reservoirs. The authors have studied the evolution of the Yangtze estuary and the effects of these developments on the estuary functioning for a period of 20 years using a collection of monitoring data. They concluded that the human activities have some local impacts, which can be positive such as, for example, the stabilisation of the estuary by stopping some continuous erosion of shoal ridge. However, they do not have large-scale effects on estuary morphologies.

The second chapter by Shou-Long and Mei-Qiong presents a study on the impact of the reconstitution of riverbed depths in an estuary after upstream hydropower dam constructions. Hydropower dams are used to produce electricity and to storage freshwaters. However, the river downstream of the dam has other uses like shipping. A minimum depth is necessary. The authors propose to use a combination of a physical and a depth-average model coupled with a sediment transport model to study the sediment and water transport in the Minjiang Estuary from the sea up to the Shuikan Dam.

The third chapter by Chuansheng et al. proposes a study of the impact of river narrowing on flows and sediment transport in a river delta. In the area with a dense population, the need to gain ground on the estuary is great. Such human activities could have impacts at more large scale by changing the flow regime of the river network and produce a modification of sediment displacement and deposition. The authors study the real case of the Changjiang River Delta (between Shanghai and Jiangsu) where the North Channel was narrowing. They used a 3D model to simulate

flows and sediment transport and to analyse the modifications dues to the estuary changes. The results show that the general flow characteristics remain unchanged with the channel bank modifications. Moreover, the concentration of suspended sediment in the north branch reduces after the project construction, whereas the impact on the south branch of the Changjiang river is estimated as small.

The fourth chapter by Zhao et al. presents the impacts of the construction of tide gate at Yongding New River Estuary on the transportation of water, sediment and pollutant. These impacts will be different under different operation mode, which also in turn restricts the scheduling plan. In order to provide a basis for the selection of tide gate operational modes, the 1D mathematical model for unsteady flow-sediment-water quality in channel with a sluice has been established, which was used to study the impact of tide gate operation of Yongding New River. The result shows that, comparing with the operation mode, which only stores freshwater, the water quality will be better with the operation mode, which stores seawater. The water quality has been gradually improved with higher storage water level. However, there will be more deposition in upstream and downstream of the tide gate.

Sylvain S. Guillou
LUSAC, University of Caen-Normandy, France

Effects of Human Activity on the Evolution of the Yangtze Estuary During the Last 20 Years

Yufang Han and Chuanteng Lu

Abstract The Yangtze River Estuary has been the scene of intense human activity in the past two decades. A large number of projects have been implemented to develop waterways and ports, construct bridges, reclaim land, and build reservoirs. During this time, an abundance of monitoring data has been collected. Human activity in natural estuaries often have two major consequences: (1) the dynamic features of the estuary undergo transformation; and (2) engineering activities will change the natural morphology of the ecosystem, harming the integrity of the estuary. Consequently, human activity may lead to the development of a different ecosystem, including the complete filling of waterways with silt, causing serious environmental impacts. This study focuses on the process of the morphological evolution of the Yangtze Estuary. The goal of the present study is to improve our fundamental knowledge of small-scale processes around navigation channels of this estuary, increase our understanding of the large-scale response of estuaries, and explain some complex phenomena, such as the high level of siltation occurring in the North Passage of the Yangtze Estuary. Managers will find the results useful in developing appropriate management plans for the estuary.

Keywords Yangtze Estuary · Morphological evolution process · Human activity · Qingcaosha Reservoir · Yangtze Estuary Deep-Draft Channel Project

1 Background

The Yangtze Estuary, located on the north side of Shanghai, China, is about 160 km long and about 90 km at the downstream entrance. This estuary has formed on a delta characterized by ample flow and sediment with obvious tidal influence. These conditions have created a basic estuary regimen characterized as having a three-stage bifurcation, four-river mouth division, shoal development an alternative navigable channel, sandbars and an extensive submerged delta (Fig. 1).

Y. Han (✉) · C. Lu
Department of River & Harbor, Nanjing Hydraulic Research Institute, Nanjing, China
e-mail: yfhan@nhri.cn

K. D. Nguyen et al. (eds.), *Estuaries and Coastal Zones in Times of Global Change*, Springer Water,
https://doi.org/10.1007/978-981-15-2081-5_41

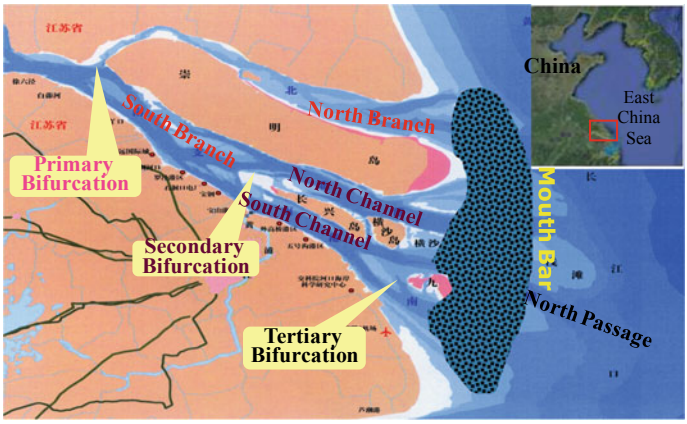

Fig. 1 Layout of Yangtze Estuary with an inset map of the location along the East China Sea, showing three riverine bifurcations and various channels

After centuries of morphological evolution combined with human modification, the Yangtze Estuary has formed a stable basic regimen with a three-stage bifurcation and four-river mouth divisions; namely, the North Branch, North Channel, North Passage, and South Passage. At the mouth of the river where fresh and salt water mix, the current meets the tides, forming a large and complicated hydrodynamic circulation system where fine sediment is easily flocculated and re-suspended. As a result, a 40–60 km-long shallow sandbar has come into being at the river mouth. The navigable water was only 7 m (theoretically lowest tide level, the same blow) deep prior to dredging operations. Obviously, the river system cannot meet the current demands for ocean-going cargo transportation in support of social and economic development, in part because of the low-efficiency of river traffic along the Yangtze River.

2 The Main Projects of the Yangtze Estuary in the Last 20 Years

From the standpoint of human activity, the Yangtze Estuary has been the most active estuary worldwide in the past two decades. A large number of projects have been implemented to develop waterways and ports, construct bridges, reclaim land, build reservoirs and so on, and an abundance of monitoring data has been collected (Wan et al. 2014; Han et al. 2013). The most famous projects involved the development of Qingcaosha Reservoir and the Yangtze Estuary Deep-Draft Channel Project (Fig. 2).

The Yangtze Estuary deep-draft channel improvement project began in 1998. A 7-m deep channel (under Theoretical Lowest Tidal Level) was dredged to 8.5, 10, and 12.5 m deep in various locations. The regulating structures include two training

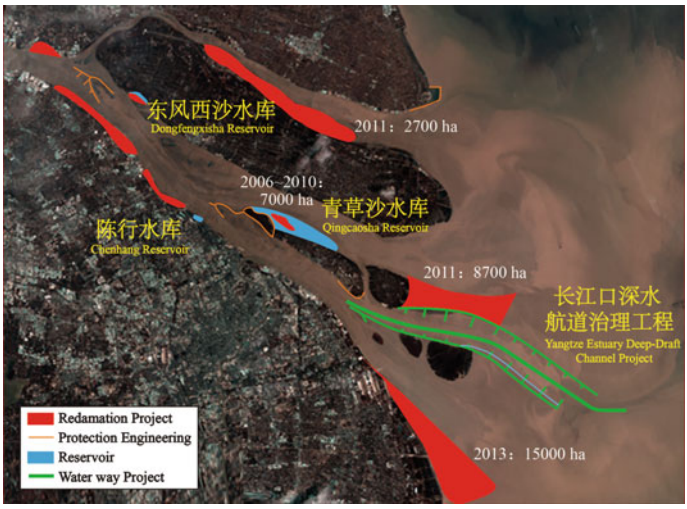

Fig. 2 Locations of engineering projects in the Yangtze River Estuary in recent years, including the development of the Qingcaosha Reservoirs and the Yangtze Estuary Deep-Draft Channel Project

dikes, one set of flow control work at the division point between the North and South passages, and 19 groynes along the two dikes (Chen et al. 1995; Chen and Chen 2005).

The improvement project was carried out under the principle of "planning at very beginning, phased construction for phased benefits" (Le and Chen 2005); as a result, the project was completed in three phases. In March 2000, the first-phase project, the 8.5-meter-deep waterway, was completed ahead of schedule and was accepted by the National Completion Acceptance Meeting in 2002. Phase II of the project started in April 2002, and the period target of 9-meter-depth was achieved in May 2004. On March 2005, the 10-meter-deep waterway was completed. Phase III of the project started in April of 2009, and a channel depth of 12.5 m was achieved in 2010.

Construction of the Qingcaosha Reservoir, located northwest of Changxing Island, began in 2006 and was completed in 2010. In June 2011, the original water project of Qingcaosha Reservoir was completed, including three main projects; specifically, (1) the Qingcaosha Reservoir and the water transfer pump gate, (2) the Yangtze River raw water transmission tunnel, and (3) land line and booster pump station. The water of Qingcaosha Reservoir covers nearly 70 km^2 and is held by a 43-km long dam. The maximum effective reservoir capacity of 553 million m^3, the design of usable capacity of 435 million m^3, the scale of water supply of 7.19 million m^3 is more than 50% of the total scale of the raw water supply in Shanghai.

3 Large-Scale Morphological System Response to Human Development

Tidal wave deformation and the tidal storage effects in the tidal river cause the general plane shape of the tidal estuary to form a bell-shaped mouth that gradually widens toward the sea, with exceptions of the present general characteristics of the river, such as bends and branching. The average widening rate of the South Branch is 12% in the Yangtze Estuary.

Based on 2016 data, several typical sections were chosen from Nanjing to downstream, and statistics related to some parameters were analyzed, such as cross-section area, average water depth, and average tidal ebb flow volume. The location of sections show in Fig. 3.

Figure 4 summarizes the variation in these parameters from the upstream to downstream regions along the river.

The red line in Fig. 4 shows the variation in the average ebb flow based on the mathematical model; we can see the change of average ebb flow steadily increased from upstream to downstream. There is no great fluctuation along the path of the

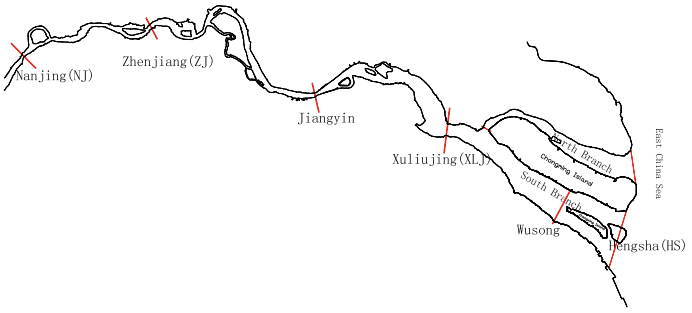

Fig. 3 Locations of sections of the Yangtze River Estuary from upstream to downstream

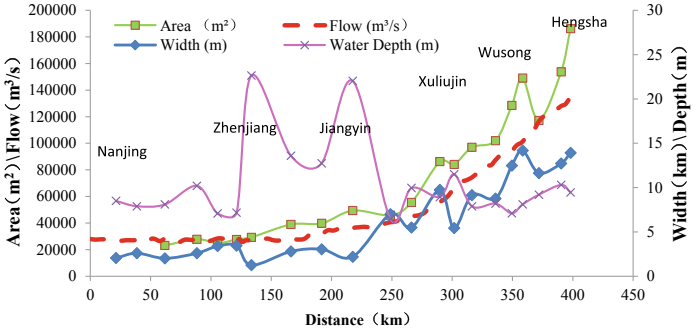

Fig. 4 Variation of area, flow, width, and water depth of the Yangtze River Estuary from upstream to downstream

width of the channel. The green line in Fig. 4 shows the change of cross-sectional area along the river; its relative change in amplitude is greater than that of the river width (blue line). This occurs because the resistance to flow of the wide shallow reach is larger than that of the narrow section of the river. Therefore, the larger cross-section is needed to adapt to the dynamic flow and sediment conditions.

The regularity of runoff and tide shows that the flow of the Yangtze River Estuary moves from upstream to downstream. The changes in riverbed morphology are more complex, because in addition to the incoming water and sediment conditions, riverbed morphology was more influenced by the varied relative stability and nature of the bank slope and bottom. Wide and narrow areas of the river flow near to each other; in addition, the water depth varied in different parts of the river. All of these phenomena are a reflection of this factor, especially the average depth of each section and the distribution of the deep groove, which is mainly modified by the effects of the level of resistance in the bottom of the river.

Many factors influence riverbed stability, but from the above analysis, we can see that in the case of ensuring steady increase of ebb flow, as well as a small change in average water depth, that narrowing the width of the river provides the most effective method of enhancing the stability of the shoreline and thalweg of the river. Especially for the river shoals, the stability of the channel associated along with a ford can be enhanced; at the same time the stability of the entire riverbed can also be improved (Han and Chen 2004; Chen and Chen 2005). In Fig. 4, there are two relative stable river sections, namely, Zhenjiang and Jiangyin, which is narrower than other river sections in river width.

Figure 5 shows the large scale morphological evolution of the Yangtze Estuary from 1998 to 2016. This figure shows the basic regimen of three-stage bifurcation and how the four-river mouth of the Yangtze Estuary came into being under specific boundary conditions; currently, the general river regimen is expected to remain stabilize for a long time.

The regulating structures at the area where the South and North channels divide and the reclamation works along the North Channel will provide a favorable boundary for the channel regulation works. These structures will stabilize the present regimen. River managers believe it is desirable to maintain the ratio of flow and sediment for the main division of the bifurcated channels. From the point of view of controlling the river regimen, when regulating the North Channel, it is important (1) to block the gullies connecting to the North Branch, (2) to stabilize the boundary in the mouth bar area, and to minimize the water/sand interchange between the shoals and channels.

By comparing the different evolution models of the three main passages in the Yangtze Estuary, we can say the effects of navigation works are mainly limited to the North Passage, and the effects on the large-scale morphological development is little on the other passages in estuaries.

During the long-term evolution of the Yangtze River Estuary, the estuary has experienced significant changes in morphology and hydrodynamic conditions. During the history of the limits of tidal effects, with the outward migration of the estuary this limit has moved downstream about 200 km from Wuhu in Anhui Province to near the

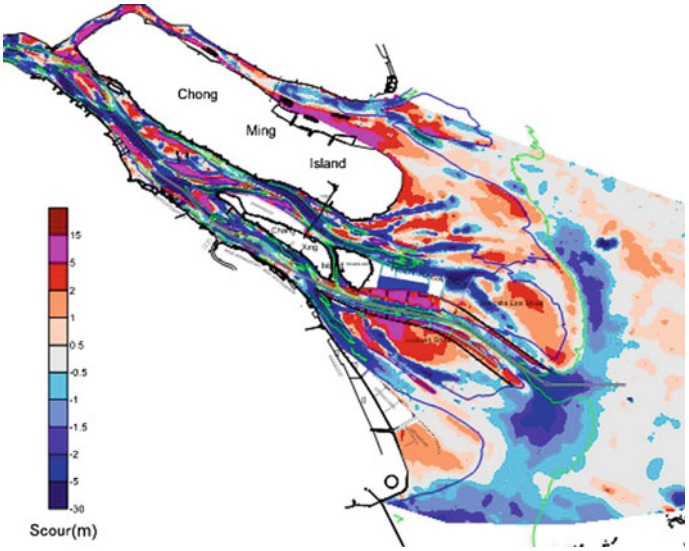

Fig. 5 Large-Scale Morphological Evolution of the Yangtze Estuary from 1998 to 2016 (red color means sedimentation, blue color means erosion)

city of Jiangyin in Jiangsu Province. In the past two decades, large-scale development and reclamation of the Yangtze River Estuary has been carried out, especially after the Three Gorges Project was completed. The comprehensive responses of the Yangtze River Estuary to human activity and changes in upstream runoff conditions included a decrease in estuarine area and an increase of riverbed volume and area.

In order to analyze the influence of these changes, the terrain boundary conditions of 2003 and 2014 were calculated, respectively. Table 1 provides different section's statistics of related to the volume, area, average depth, and average river width of the riverbed. The location of different sections show in Fig. 3. From this table we can see the general trend of large scale morphological evolution is: the river width was

Table 1 Statistics related to area and volume of the Yangtze River Estuary in the study area

Section	Area (km^2)		Volume (Bm^3)	
	2003	2014	2003	2014
ZJ-XLJ	941.6	881.4	8.92	9.21
XLJ-HS	1056.3	945.8	7.54	8.20
NB	273	168	0.96	0.61
Total	2271	1995	17.4	18.0
Change	***−0.12***		***0.03***	

Bold indicates data difference between years 2003 and 2014
Note HS—Hengsha; NB—North Branch; XLJ—Xuliujing; ZJ—Zhenjiang

narrowed with increased water depth, but the total increase of the riverbed volume was less than that of the estuary area. This means that the tidal prism of the Yangtze estuary has decreased.

The evolution of the South Branch seriously influences the morphological processes of the North Channel. According to the measured data, the upstream point of each shoal in the South Branch was slowly and continuously moving downstream. In recent years, although the thalweg in the South Branch moved with the recession of the shoals, the thalweg in the lower reach of South Branch has remained stable with little movement. This will provide good conditions, if the point of division between the South and North channels is stabilized with engineering structures.

During the period from 1998 to 2016, the volume of the South Branch of the Yangtze River Estuary was gradually increasing, and the trend of channel volume erosion was maintained for 12.5 m channel maintenance in the third stage (Fig. 6). Compared to the past years, the river volume has increased slightly.

After 1998, the change in volume of the South Channel was directly related to the evolution of Ruifeng Shoal in this river (Fig. 7). The change in the volume of the river channel continued to increase after 2012. The erosion trend of the South Channel

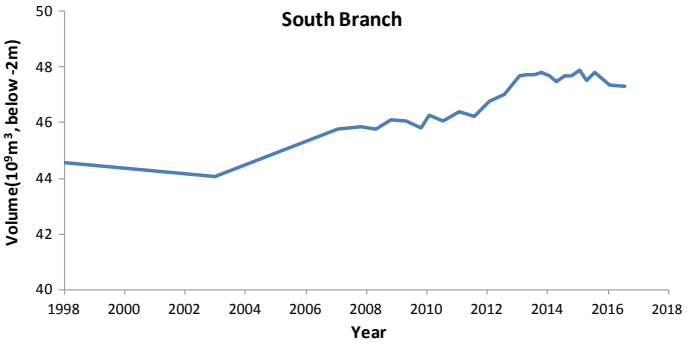

Fig. 6 Volume changes of the South Branch of the Yangtze River over time

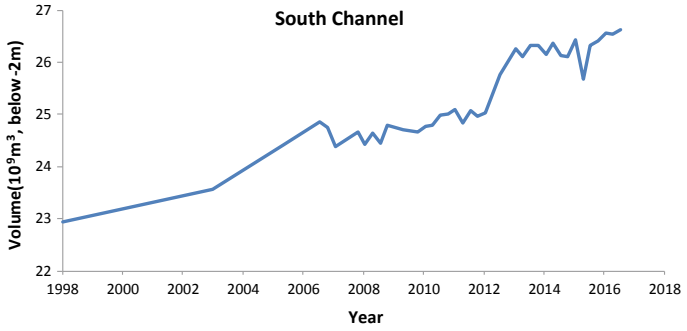

Fig. 7 Volume changes of the South Channel of the Yangtze River over time

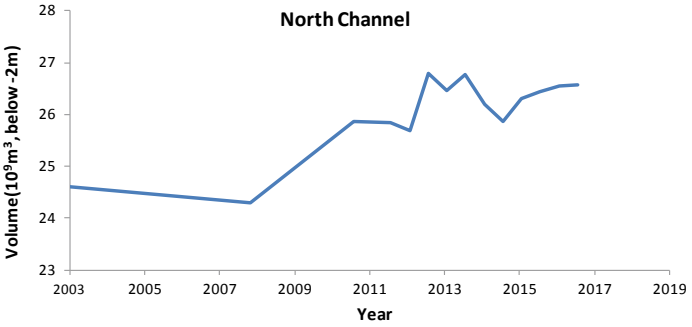

Fig. 8 Volume changes of the North Channel of the Yangtze River over time

was beneficial to the maintenance of the river channel, but the erosion provided some part of the sand source to the downstream river areas.

From 1998 to 2012, the volume of the North Channel generally increased (Fig. 8). However, due to the creation of the Qingcaosha Reservoir, the area of the high beach decreased between 2007 and 2010. There was no obvious change in the diversion ratio between the North and South channels, and the volume below 5 m to 10 m increased. The riverbed reached a narrow channel.

4 Small-Scale Evolution Processes in the Yangtze Estuary

4.1 Evolution of the Mouth Bar in the North Passage of the Yangtze Estuary

Analyses of the change in the riverbed after the construction of the first and second phase regulation works show that river regulation has changed the natural morphology of the Yangtze Estuary. For example, the general effects of the regulation work in the North Passage are shown in Figs. 9 and 10.

The construction of the flow control work at the point of division between the North and South passages stabilized the central shoal and stopped the continuous erosion and recession of the shoal ridge, which provides a favorable boundary for the distribution of runoff and sediment transport.

The two training dikes now provide a stable boundary for the North Passage; these dikes block the water and sediment interchange between the shoals and channel as well as provide an effective barrier for sediment transport from shoal to channel during the typhoon season or winter storms.

Before the project, an ebb channel was located at the south of Passage and the flood channel was closed to the north of Passage; between the ebb and flood channels a mouth bar (sand bar or sill) formed due to the complex morph-dynamic conditions

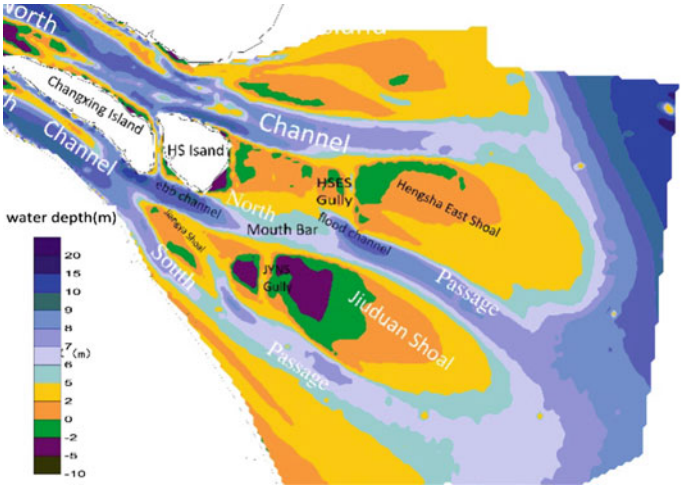

Fig. 9 Topography of the Yangtze Estuary (1998) with isobaths in meters

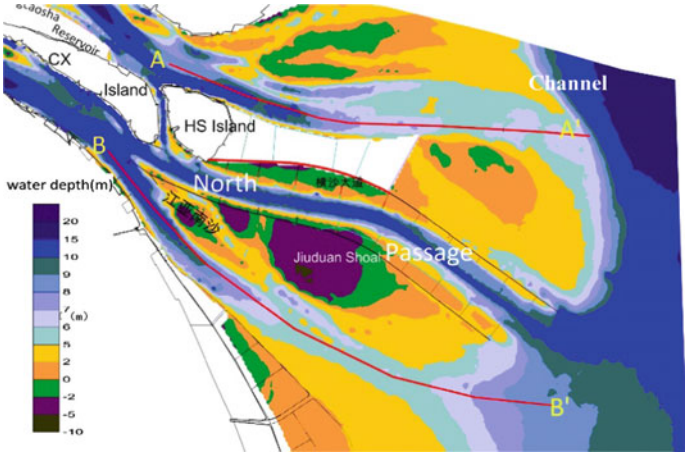

Fig. 10 Topography of the Yangtze Estuary (2016) with isobaths in meters. The alignments A–A′ and B–B′ are the thalwegs of the North Channel and South Passage, respectively

and sediment flocculation in the maximum turbidity area (the same area as mouth bar).

After the project, which created the regulating line along the groyne heads as well as adjusted the flow fields, deepened the mouth bar area, and merged the ebb channel with flood channel, a faintly-curved channel was obtained in the North Passage.

In the groyne fields, sedimentation occurred because the flow velocity decreased in these areas. The channel transferred from a wide-shallow river pattern to a narrow-deep pattern, which is favorable for channel maintenance.

At the entrance of the North Passage, sedimentation occurred and the cross-section area decreased due to the fact that the distribution of runoff from the South Channel declined; this was caused by the friction increasing in the North Passage of the river. In addition, near the division point, the south training dike blocked the gully that previously had been used to discharge some of the runoff from North Passage to South Passage, which was also reduced the hydrodynamic conditions near the entrance to these passages. Nevertheless, in this area the water is still deep enough to maintain the development and equilibrium of the North Passage.

In the middle bend area, a gully previously connected the North Passage with the North Channel. After construction the north training dike blocked the water and sediment interchange between the two channels; thus in this area, the flow velocity decreased and siltation of suspended sediments occurred.

After the project, the flow field of the lower reach of the North Passage changed from a rotating to an alternating tidal current; as a result the hydrodynamics increased, causing erosion of the sea bed.

With the morphological adjustment inside the North Passage, some sediments were eroded and transported outside of the regulating structure. Outside of the regulating structures, the channel was becoming wider. In this area, the channel is relatively deep and the strong rotating velocity field will help to prevent sedimentation.

In summary, the regulation works in the North Passage have successfully modified the river channel. The combination of regulating works and channel dredging can be adopted for managing the other passages in the Yangtze River Estuary.

Since the implementation of the Yangtze River Estuary deep-draft channel project, the North Passage of the riverbed has shown main channel erosion and dam site deposition.

The total volume of North Passage has generally declined from 1998 to 2016 (Table 2), while the 5 m isobaths have been increasing continuously.

Table 2 Volume variation of the North Passage of the Yangtze River over time

Time	Volume	
	Total	Below-5 m
1998	3.9	6.6
2007	27.9	6.7
2010	28.6	8.2
2013	28.5	8.5
2016	28.7	9.0
1988–2015 (10^8 m^3/year)	−0.13	0.14
2007–2010 (10^8 m^3/year)	0.27	0.53
2010–2013 (10^8 m^3/year)	−0.04	0.12
2013–2016 (10^8 m^3/year)	0.07	0.20

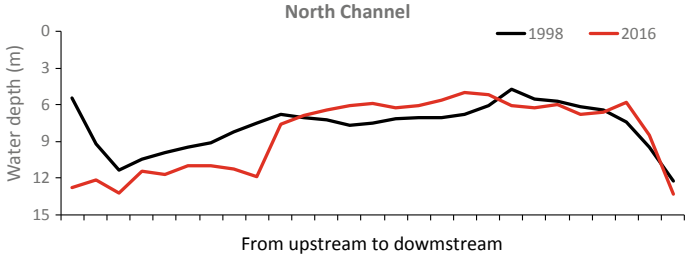

Fig. 11 Water depth in the North Channel of the Yangtze River (from upstream (point A) to downstream (point A′) in Fig. 10, 2016)

4.2 Evolution of Mouth Bars in Another Two Passages of the Yangtze Estuary

As a faintly curved channel was obtained in the North Passage, mouth bar terrain has been disappearing after the Deep-draft Channel Regulation Project. At the same time, the mouth bars still persist in other channels without the regulation project, such as in the South Passage and in the North Channel (Figs. 10 and 11), the water depth is also shallow than 6 m.

The North Channel is 90 km long and is located between the islands of Chongming, Changxing, and Hengsha. the North Channel is an important and convenient channel for ships from the northern coastal ports that are entering and leaving the mouth of the Yangtze River; therefore, the North Channel is important for economic development and foreign exchange in the Chongming, Changxing, and Hengsha island coastal areas.

Currently, the North Channel is a naturally deep channel, with water up to 10 m deep; the water depth over sand bar segments is less than 5.5 m making sandbars only navigable to some of the fishing boats, passenger ferries, and small cargo ships. The future management of the North Channel should include a study of the engineering measures; the outer section of the flow constraints need to be closely integrated with other projects.

Before 1998, the shallowest depth of water in the mouth bar of the North Channel was about 5 m, which is almost same with the depth in 2014 (Fig. 11).

The South Passage is about 86 km long; the main diversion from the South Channel provides the main passageway for small ships from the Yangtze River Estuary to enter the sea. In 2013, the South Channel was dredged locally. The scope of the dredging project lies 19.2 km downstream from the Jiuduansha warning area. The effective width here is 250 m and the design depth of the channel is 5.5 m. This can meet the needs of the full load of the 5000-ton bulk carrier for two-way navigation with tide and the reduction of the load of the 20,000-ton bulk carrier for two-way navigation with tide.

The erosion and deepening of the deep channel in the North Passage has increased in recent years. The South Channel has been affected by the North Passage project

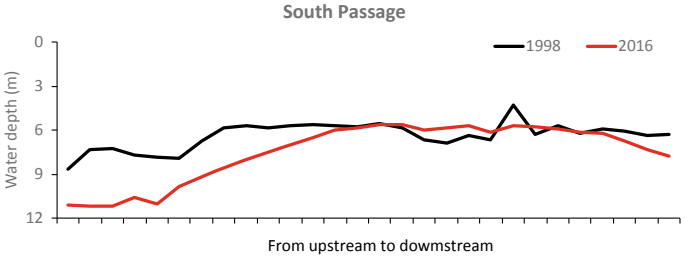

Fig. 12 Water depth in the South Passage of the Yangtze River (from upstream (point B) to downstream (point B′) in Fig. 10, 2016)

obviously. However, there are different influences to the South Passage: (1) the entrance of the passage in upstream part was eroded, (2) however the change of the terrain of the barrier was small, which the Shallowest water depth of the mouth bar in the South Passage remained similar before and after the regulation works in the North Passage (Fig. 12).

The erosion rate has become larger in the upper part while the barrier area of the mouth has changed small. The total volume of the South Passage increased before 1998–2003, but this volume declined from 2004 to 2013; during 2014–2016 increasing trend of channel volume has accelerated.

5 Conclusion

Human activity have caused more relatively stable regimen of the Yangtze River Estuary in present than in the history period that drastic change occurred between the shallow shoal and deep channel. The construction of the flow control work, located at the division point of three-stage bifurcations, stabilized the central shoal and stopped the continuous erosion and recession of the shoal ridge, which provides a favorable boundary for the distribution of runoff and sediment transport. In the future, maintaining the current division of flow and sediment into the main bifurcated channels is desirable. The past work has affected the natural morphology of the river system only within certain local areas but has not had a large-scale effect on the morphological development in estuaries and has not changed the long-term development of the inter-tidal flats. However, we should also note that the comprehensive impact of all water control work in the last 20 years is the gradual decrease of the estuarine tidal prism; the comprehensive impact of this on the evolution of estuaries requires further study. In particular, the effects on the safety of different estuary projects will be different. There are various demands on estuaries, and different requirements in different areas will lead to different practical problems.

Acknowledgements We thank LetPub (www.letpub.com) for its linguistic assistance during the preparation of this manuscript.

References

Chen, Z.-C., & Chen, J.-Z. (2005). Regulation principle of Yangze River estuary deep channel. *Hydro-Science and Engineering, 1*, 1–7.

Chen, Z.-C., Gu, P.-Y., Zhu, Y.-S., & Zhao, X.-D. (1995). Research on deep water channel of Yangtze estuary. *Hydro-Science and Engineering, 3*, 210–220.

Han, Y., & Chen, Z. (2004). Effects of spur dikes in adjustment of bed topography of wide-shallow river. *Hydro-Science and Engineering, 2,* 23–28.

Han, Y.-F., Chen Z-C., & Luo X-F. (2013). Physical model research on the improvement project of the deep-draft channel of the Yangtze Estuary. In *Proceedings of the Seventh International Conference on Asian and Pacific Coasts (APAC)*, September 2013 Bali Indonesia (APAC-2013), pp. 209–213.

Le, J.-Z., & Chen, Z.-H. (2005). Selection and training principle of deep channel in the Yangze River estuary. *Hydro-Science and Engineering, 2*, 1–8.

Wan, Y., Roelvink, D., Li, W., Qi, D., & Gu, F. (2014). Observation and modeling of the storm-induced fluid mud dynamics in a muddy-estuarine navigational channel. *Geomorphology, 217,* 23–36.

The Impact of Replenishing Flow and Sediment on the Riverbed Repairing of Minjiang Estuary and Water Level Rising Under Shuikou Dam

Shou-long Yang and Mei-qiong Huang

Abstract Since the completion of Shuikou hydropower station, the process of flow and sediment has undergone profound changes in Minjiang estuary. Under the combined action of hydrodynamic force and sand dredging, the riverbed of Minjiang estuary was cut down sharply. The water level under the hydropower station dam which was 110 km away from Guantou section of Minjiang estuary decreased from 8.80 m in October 1991 to 5.40 m in April 2009, and it also caused shipping suspend during the dry season. Due to the fact that the tail water can not meet the suction height requirement of turbine, the normal operation of the unit has been affected. In addition, the decline of the water level has also led to salinity intrusion, which threatens the safety of urban water intake. The measure presented in this chapter is to replenish flow and sediment of the estuary by means of discharging flood through the combined use of the bottom hole and the surface hole of the hydropower station, so as to restore the riverbed and raise the water level under the dam of Shuikou hydropower station. The flow and sediment numerical model shows that under the condition of 3570 m^3/s discharge flow, 2-day duration, and using synchronous measurement of tide level process in the estuary, when the sediment concentration of the discharge is 0.625, 6.25 and 28 kg/m^3, the riverbed elevation under the dam of the hydropower station will rise by 0.26–0.32, 0.99–2.16 and 4.71–8.24 m, but as the distance is longer than D20 section which is 7.38 km away from Shuikou hydropower station, the riverbed elevation is of no obvious change. This means that the short-term measure of replenishing flow and sediment only has the repairing effect on the short-distance riverbed of the downstream of the hydropower station. Under the condition of 10-day duration, 6.25 kg/m^3 sediment concentration and 308 m^3/s basic discharge flow, the lowest water level under the dam of the hydropower station will rise by 7.77 m. Meanwhile, within the distance of about 12.62 km which is located at D1 section to D33 section of the downstream of the hydropower station, the lowest water level will rise by 1.91–7.77 m; among the section of about 27.44 km, which is located at D1 section to D64 Hongwei section, the average riverbed elevation will rise by 4.72 m.

S. Yang (✉) · M. Huang
Fujian Provincial Investigation Design and Research Institute of Water Conservancy and Hydropower, Fujian, China
e-mail: yangshoulong2010@163.com

K. D. Nguyen et al. (eds.), *Estuaries and Coastal Zones in Times of Global Change*, Springer Water,
https://doi.org/10.1007/978-981-15-2081-5_42

The results show that the water level under the dam of Shuikou hydropower station can be restored to the original design level through the measures of replenishing flow and sediment with 0.625 kg/m^3 sediment concentration, 3570 m^3/s discharge flow, and 4.38-day discharge duration.

Keywords River evolution · Replenishing flow and sediment · Numerical model calculation · Physical model test

1 Statement of Problem

Minjiang river is the largest river in Fujian Province, the basin area is only 8.1% of Yellow river which basin area is 752,443 km^2, but, in the "6.23", flood of the Minjiang river in 1998, the peak discharge of the Zhuqi hydrometric station reached 33,800 m^3/s, which was close to the historical maximum flow of the Yellow river. Shuikou hydropower station is a large I(1) type hydrojunction for power generation, shipping and crossing, which is 117 km away from Changmen estuary of Minjiang river section, the maximum dam height is 101 m, the discharge capacity is 48,800 m^3/s, and the total installed capacity of the power station is 7 × 200 MW. It is the largest conventional hydropower station in east china. The shipping structure of the hydrojunction on the right bank of the dam has a 2 × 500 t first line three grade ship lock and a 2 × 500 t grade two barges joint crossing dam vertical ship lift, which annual freight design volume is 4 million tons. The construction of Shuikou project has greatly improved 100 km shipping from Nanping to Shuikou hydropower station, expanded the river's water transport capacity, and created conditions for opening inland river container routes. The design of the navigable terminal takes the 9.82 m water level of the power station base-load flow 308 m^3/s as the lowest navigable design water level, which is also the lowest level of power generation. However, under the combined action of hydrodynamic force and sand dredging, the water level under the hydropower station dam was 8.80 m in October 1991, to 6.67 m in December 2004. According to the shuikou hydropower station dam's tail water level records, it reduced to 5.72 m in December 2007 and even to 5.40 m in April 30, 2009 (at this time, the discharge of Shuikou hydropower station was 344 m^3/s). The water level under the dam was 4.42 m lower than the lowest navigable water level originally designed, and the bottom of the ship lock had exposed 1.42 m above the water surface. As the water level under the dam continues declining, Shuikou hydropower station is increasing annual discharge volume in order to shipping. The original design of 308 m^3/s basic discharge flow for achieving shipping is also increasing year by year, 800 m^3/s in 2000, 1500 m^3/s in 2004, and 2000 m^3/s in 2005. In 2006, the basic discharge flow reached 2350 m^3/s, which was 7.63 times that of the original design required minimum navigable flow. Fujian Shuikou Power Generation Co., Ltd. made the best efforts to increase the outflow rate in the shipping day, but the reservoir capacity was limited. If the downstream water level control is

not carried out, the downstream of hydrojunction will be faced with the possibility of shipping suspension during the dry season. The original design of the lowest plant tail water level is also 9.82 m, so the current plant tail water level is 4.42 m lower than the original design when the base-load flow is 308 m^3/s. Moreover, the lowest tail water level is still decreasing. The suction height of turbines does not meet the original design requirements, which causes the normal operation of the unit to be affected. Recently, the unknown reason has been found in the Shuikou power plant. The continuous decline of water level under the dam has seriously affected the shipping function of the hydrojunction and the normal operation of the power station. Not only that, the severe cutting of natural river bed has caused profound changes in hydrodynamic conditions, and has brought great damage and potential safety hazard to downstream public safety. River bank collapsed, ancient bridge was destroyed, new bridge has constantly potential safety hazard. Shunli pier collapsed due to serious erosion, and Xintong pier has serious siltation that affected Changle's flood control and drainage. The salinity intrusion drove straight in, and the chloride ion once exceeded 10 times at the water intake of Changle Hua'neng thermal power plant. Therefore, how to raise the river bed through replenishing flow and sediment for restoring the natural flow conditions of the Minjiang estuary has become a focus of all parties concerned.

2 The Establishment and Verification of Numerical Model

2.1 Control Equation and Numerical Method

Continuity equation:

$$\frac{\partial \xi}{\partial t} + \frac{\partial p}{\partial x} + \frac{\partial q}{\partial y} = \frac{\partial h}{\partial t} \tag{1}$$

x-direction hydrodynamic control equation:

$$\begin{aligned} &\frac{\partial p}{\partial t} + \frac{\partial}{\partial x}\left(\frac{p^2}{H}\right) + \frac{\partial}{\partial y}\left(\frac{pq}{H}\right) + gH\frac{\partial \xi}{\partial x} + \frac{gp\sqrt{p^2+q^2}}{C^2H^2} \\ &- \frac{1}{\rho}\left[\frac{\partial}{\partial x}(H\tau_{xx}) + \frac{\partial}{\partial y}\left(H\tau_{xy}\right)\right] - fq - f_w|W|W_x = 0 \end{aligned} \tag{2}$$

y-direction hydrodynamic control equation:

$$\frac{\partial q}{\partial t} + \frac{\partial}{\partial y}\left(\frac{q^2}{H}\right) + \frac{\partial}{\partial x}\left(\frac{pq}{H}\right) + gH\frac{\partial \xi}{\partial y} + \frac{gp\sqrt{p^2+q^2}}{C^2H^2}$$

$$-\frac{1}{\rho}\left[\frac{\partial}{\partial y}\left(H\tau_{yy}\right)+\frac{\partial}{\partial x}\left(H\tau_{xy}\right)\right]-fq-f_w|W|W_Y=0 \tag{3}$$

In the equation: H is water depth, $H = h + \xi$, ξ, h are the water level and depth respectively; p, q are fluxes in the direction of x and y respectively; C is chezy coefficient; g is Gravitational acceleration; y is Coriolis coefficient; ρ is water density; W, W_x, W_y are the components of wind speed on x, y; f_w is wind resistance coefficient; τ_{xx}, τ_{xy}, τ_{yy} are effective shear force component.

Suspended sediment transport equation:

$$\begin{aligned}&\frac{\partial(h\bar{c})}{\partial t}+\frac{\partial(p \bmod \bar{c})}{\partial x}+\frac{\partial(q \bmod \bar{c})}{\partial y}-\frac{\partial}{\partial x}\left(k_{xx}h\frac{\partial\bar{c}}{\partial x}\right)-\frac{\partial}{\partial y}\left(k_{yy}h\frac{\partial\bar{c}}{\partial y}\right)\\&-\frac{\partial}{\partial x}\left(k_{xy}h\frac{\partial\bar{c}}{\partial y}\right)-\frac{\partial}{\partial y}\left(k_{yx}h\frac{\partial\bar{c}}{\partial x}\right)=w_s\Phi_0(\eta_0)(\overline{c}_e-\bar{c})\end{aligned} \tag{4}$$

In the equation: $\overline{c_e}$ is average sediment concentration of the vertical line in the state of non scour and non siltation, $\bar{c}$ is average sediment concentration of the vertical line, w_s is suspension settling velocity, $k_{xx}, k_{xy}, k_{yx}, k_{yy}$ are suspension diffusion coefficient.

Numerical solution method is used to integrating the differential equations on the control volume with the finite volume method, using the coordinate rotation invariance of flux to convert two-dimensional problem into a series of partial one-dimensional problem, and using the flux difference splitting format to calculate water and momentum flux for each unit. The solution is characterized by the conservation of water and momentum in the flow model even in the case of coarse mesh. According to the measured flow data, the river roughness is 0.018–0.035, and the sediment median diameter is 0.23–0.65 mm.

2.2 Numerical Model Range, Verification and Working Condition

The total length of the river numerical model is about 185 km, including 93 km from Shuikou hydropower station to Baiyantan by Fuzhou south river, 34 km of Fuzhou north river, 35 km from Baiyantan to Meihua estuary, and 23 km from Tingjiang to Guantou estuary. The two-dimensional mesh is in the form of an unstructured triangular mesh with 34,420 nodes and 64,992 elements. The upper boundary of the model is flow, that is the discharge process of the Shuikou hydropower station, and the lower boundary is water level, that is the typical daily water level process of Guantou hydrological station. The numerical model is validated by flood, middle and low water level processes of Xiapu hydrological station, Zhuqi hydrological station, Wenshanli hydrological station, Jiefang bridge upstream hydrological station, Jiefang bridge downstream hydrological station, and Xianan hydrological station.

The hydrological stations and important analysis sections are shown in Fig. 1. The sediment concentration is validated by the measured water and sediment process of Zhuqi hydrometric station, and the topography of the riverbed is validated by the river evolution before and after flood. In addition, the corresponding verification has been carried out on the physical model which covering an area of about 20 acres, and received good results. The range of physical model is as large as that of numerical model, the horizontal scale is 1:540 and the vertical scale is 1:80, as shown in Fig. 2.

The working condition used 3570 m^3/s discharge of Shuikou power station, and typical daily tide level of Guantou hydrological station. The discharge sediment concentration were 0.625 kg/m^3, 6.25 kg/m^3, 28.00 kg/m^3 and 62.5 kg/m^3 respectively, and the discharge duration were 2-day, 10-day, 50-day and 100-day. A total of 259 analysis sections were set up, of which 125 sections were from Shuikou hydropower station to Huai'an diversion port, 59 sections were in Fuzhou south river, 56 sections were in Fuzhou north river, and 17 sections were in the lower reaches of Sanjiang confluence.

3 Effect of the Discharge Sediment Concentration and Duration on the Riverbed Repairing of Minjiang Estuary

3.1 Discharge Duration and Riverbed Deformation

The general topography of Minjiang estuary presents the shape features of "six-curves, two-diversions, and one confluence", that is Minqing Anrenxi—Beixi curve, Minqing bridge curve, Minhou Tangyuan curve, Minhou Damucheng curve, Minhou Shangqi curve, Minhou Shadi curve, Huai'an diversion port, Tingjiang diversion port, and Sanjiang confluence. Under the condition of 3570 m^3/s discharge flow, 2-day duration, and 0.625 kg/m^3 sediment concentration, the river within the distance of about 4 km from D1 section under the dam of the hydropower station to D13 Daxicun section in the middle of Minqing Anrenxi—Beixi curve will silt up 0.2–0.92 m. The change is not obvious. However, the river within the distance of about 0.8 km from D15 Daruocun section to D17 Beixi section will silt up 3.12–8.13 m, the impact of riverbed repairing is obvious. The riverbed topography within the distance of about 47.38 km from D20 Xiaoruoxiang section to D123 Houguan section is steady, the scour and siltation is about −0.41 m ~+0.67 m. The riverbed topography of Minjiang north river, south river, and entrance passages to the sea are basically unchanged.

When the discharge duration increases from 2 to 10 days, the siltation of riverbed from D1 section to D13 section increases by 0.12–1.97 m than before. With the width of the river gradually widens from 150 m (D15 section) to 595 m (D33 section), the obvious area of riverbed repairing is extended 6.62 km. The siltation height of the riverbed from Shuikou hydropower station to D33 Minqing water plant section is 5.10–12.87 m, and it increases by 4.80–7.74 m than before. The lower reach of

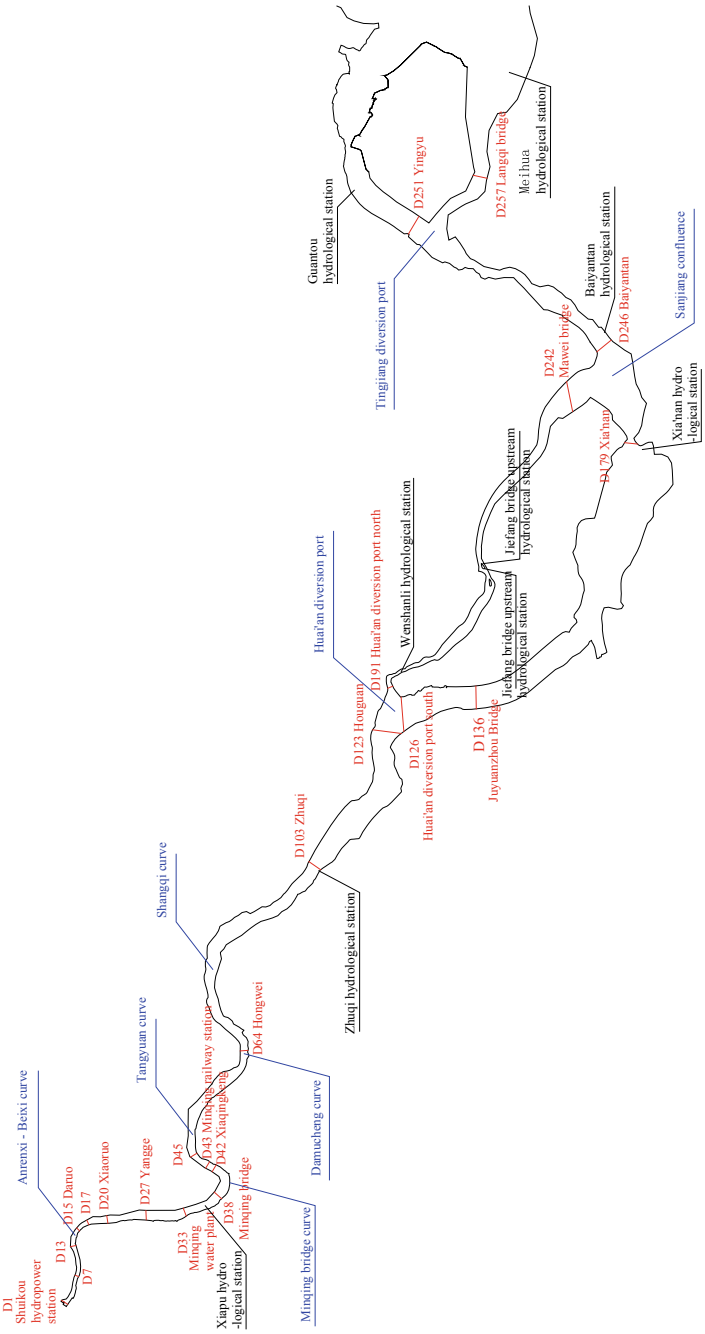

Fig. 1 The hydrological stations and numerical analysis sections

(a) Minhou Tangyuan - Damucheng Curve **(b) Huai'an diversion port**

Fig. 2 Minjiang river physical model

Minqing water plant section is not obviously deformed, except for D64 Hongwei section of which silts 3.9 m in the middle of Minhou Damucheng Curve.

When the discharge duration increases to 50 days, the section under the dam of Shuikou hydropower station silts up 14.02 m. The obvious deformation range is moved from D33 Minqing water plant section to D64 Hongwei section. It continues to advance 14.82 km downstream compared with 10-day duration working condition. The siltation height of the riverbed is 6.42–12.52 m, and the maximum changes little. When the discharge duration is 10-day, the river within the distance of about 12.30 km from D38 section to D64 section isn't silted up basically. However, when the duration increases to 50 days, the river silts up 6.42–8.59 m obviously. The south river is relatively wide, and the maximum width can reach to 3540 m, but the river width of D179 Xia'nan section is only 874 m which as the important control section in Fuzhou south river. When the discharge duration is 50-day, the section silts up 3.19 m. When the discharge duration increases to 100 days, the riverbed does not change much, except for a few sections. The results are shown in Fig. 3. When the discharge sediment concentration increases to 6.25, 28 and 62.5 kg/m^3, the rive evolution is similar.

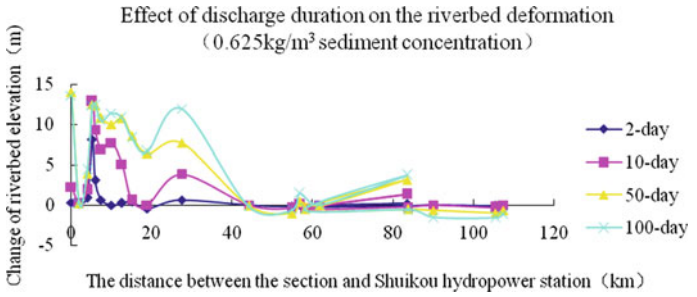

Fig. 3 Effect of discharge duration on the riverbed deformation

3.2 *Sediment Concentration and Riverbed Deformation*

When the discharge lasts for 2 days, the sediment concentration is 0.625 kg/m^3, 6.25 kg/m^3, and 28 kg/m^3 respectively, and the riverbed deformation shows three obvious characteristics. Firstly, when the sediment concentration is low, the riverbed topography of D1 section under Shuikou hydropower station dam has little change, but when the sediment concentration iincreases to 28 kg/m^3, the riverbed of D1 section silts up 8.24 m obviously, as shown in Fig. 4a. Secondly, the great impact of sediment concentration is concentrated on the area within the distance of about 0.8 km from D15 section to D17 section, which silts up 1.90–8.13 m, and the sediment concentration increases from 0.625 to 28 kg/m^3, the influence range and riverbed deformation are little. For example, in D17 section, the riverbed deformation is only 0.22 m, as shown in Figs. 4b, c. Thirdly, the change of sediment concentration has little effect on the downstream riverbed of D20 section, basically no more than 1 m, as shown in Fig. 4d.

When the discharge duration increases to 10 days, the riverbed deformation is similar to that of 2 days, but the extremum and range are different. Firstly, the riverbed siltation of the D1 section under Shuikou hydropower station dam is more obvious. When the discharge sediment concentration is 6.25 kg/m^3, the riverbed of D1 section silts up 13.49 m obviously. When the discharge sediment concentration is 28 kg/m^3, the riverbed of D1 section silts up 16.55 m obviously. Secondly, the impact range of sediment concentration is more wide, and it is concentrated on the area within the distance of about 7.41 km from D15 section to D33 section, which silts up 1.36–12.87 m. Thirdly, the change of sediment concentration has little effect on the downstream riverbed of D38 section, basically no more than 1 m.

When the discharge duration increases to 50 days, the extremum and range of riverbed deformation

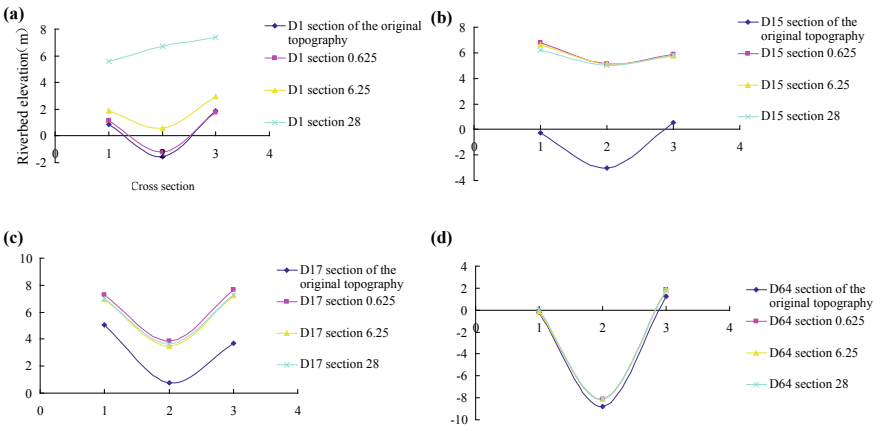

Fig. 4 Influence of sediment concentration on the riverbed deformation (2-day duration)

increases obviously. Firstly, When the sediment concentration is 0.625 kg/m^3, the riverbed siltation of the D1 section under Shuikou hydropower station dam is 14.02 m. Secondly, the great impact of sediment concentration is concentrated on the area within the distance of about 22.23 km from D15 section to D64 section, which silts up 1.19–16.46 m. Thirdly, the change of sediment concentration has little effect on the downstream riverbed of D103 section, basically no more than 1 m.

4 Water Level Variation Caused by Replenishment Sand Flow Under the Base-Load Flow

4.1 Sensitivity Analysis of Influence of Discharge Duration and Sediment Concentration on Raising Water Level Under the Dam

Under the condition that the discharge lasts for 10 days unchangeably, when the sediment concentration increases from 0.625 to 6.25 kg/m^3, increasing 10 times, the water level under Shuikou hydropower station dam rises from 12.85 to 13.39 m, only rising by 0.54 m. When the sediment concentration increases from 6.25 to 28.00 kg/m^3, keeping increasing 4.48 times, the water level under Shuikou hydropower station dam rises from 13.39 to 15.91 m, rising by 2.54 m. When the sediment concentration increases from 28.00 to 62.50 kg/m^3, keeping increasing 2.23 times, the water level under Shuikou hydropower station dam rises from 15.91 to 16.17 m, only rising by 0.26 m. Increasing the sediment concentration has an obvious effect on raising the downstream water level in a certain range, and if it continues to be increased, the lifting effect decreases, as shown in Fig. 5. The results show that if the water level under the dam is to rise by 1 m, the sediment concentration should increase from 0.625 kg/m^3 by 11.68 times to 7.30 kg/m^3 under the condition of 10-day duration.

Under the condition that the sediment concentration is 0.625 kg/m^3 unchangeably, when the discharge duration increases from 2 to 10 days, increasing 5 times, the water

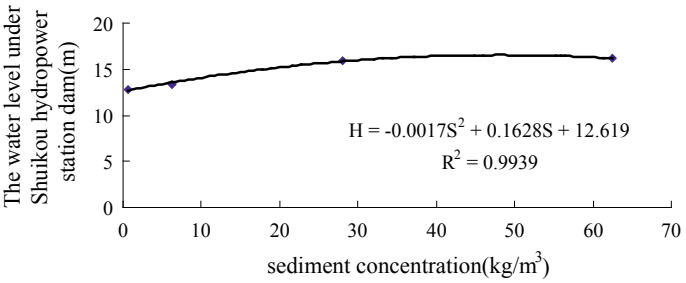

Fig. 5 Effect of sediment concentration on the water level under Shuikou hydropower station dam

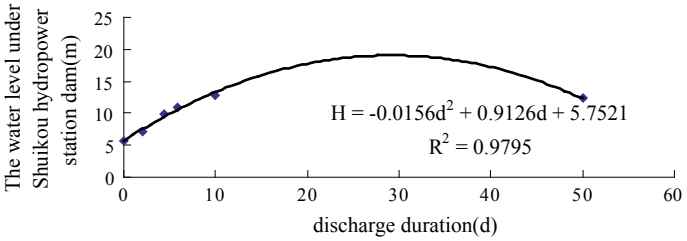

Fig. 6 Effect of discharge duration on the water level under Shuikou hydropower station dam

level under Shuikou hydropower station dam rises by 5.72 m. When the discharge duration increases to 100 days, increasing 50 times, the water level under the dam rises by 7.48 m, only 1.76 m higher than the 10-day duration working condition. It is similar to the sediment concentration condition that increasing the discharge duration has an obvious effect on raising the downstream water level in a certain range, and if it continues to be increased, the lifting effect decreases, as shown in Fig. 6. The results show that if the water level under the dam is to be raised to a peak value of 19.99 m, the discharge duration should increase to 29.2 days under the condition of 0.625 kg/m^3 sediment concentration. Based on the current 5.62 m water level under Shuikou hydropower station dam, when the discharge duration is 0.97-day and the sediment concentration is 0.625 kg/m^3, the water level under the dam is to rise by 1 m. It indicates that prolonging discharge duration is more effective than increasing sediment concentration on raising water level under the dam.

4.2 Water Level Variation and Tidal Limit

Under the current topography condition, the water level amplitude is 0 m, the water level value is 5.45–5.62 m, and the water surface gradient is 2.30/100,000 in each section within the distance of about 7.38 km from D1 Shuikou hydropower station section to D20 Xiaoruo section, and the tidal limit is in the D20 section. Then, the water level amplitude in the lower reaches gradually increases. It rises from 0.35 m to 1.91 m within the distance of about 46.73 km from D27 Yangge section to Huai'an diversion port section. The water level amplitude of D179 Xia'nan section reaches 3.33 m through south river 26.91 m, and it is similar to 3.26 m of D251 Yingyu section and 3.44 m of D257 Langqi bridge section in the estuary. It shows that the river is completely controlled by the tide in the dry season. The variation of the minimum water level and the water level difference in each section after replenishing flow and sediment are shown in Fig. 7.

Under the condition that the sediment concentration is 0.625 kg/m^3 unchangeably, when the discharge duration is 2-day, the tidal limit is 7.38 km away from Shuikou hydropower station. When the discharge duration increases to 10 days and 50 days, the tidal limit is 12.62 km and 18.90 km away from Shuikou hydropower station

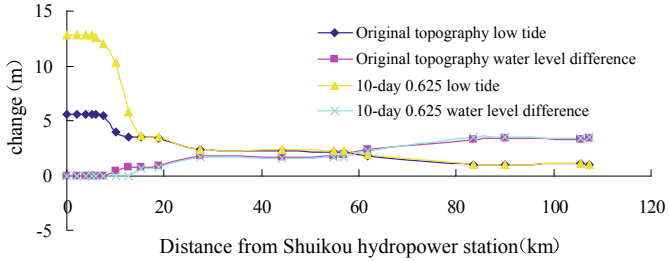

Fig. 7 The variation of the minimum water level and the water level difference in each section after replenishing flow and sediment

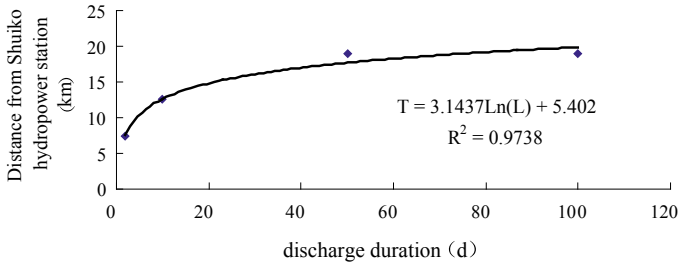

Fig. 8 Discharge duration and tidal limit

respectively. When the discharge duration increases to 100 days, the tidal limit is basically unchanged, as shown in Fig. 8.

Under the condition that the discharge lasts for 10 days unchangeably, when the sediment concentration is 0.625 kg/m^3, the tidal limit moves from D20 Xiaoruo section down to D33 Minqing water plant section, moving 5.24 km. When the sediment concentration increases to 6.25, 28, and 62.5 kg/m^3, the tidal limit is basically unchanged. The above studies further confirm that the effect of discharge duration on the tidal limit is greater than that of the sediment concentration (Chen 2017).

5 Repair Measures and Effects in Estuary

5.1 Repair Measures

The statistics of the average annual sediment concentration from 1993 to 2008 showed that, during the 16 years, the total sediment transportation was 39.572 million tons, of which the average annual sediment concentration in 2005 and 2006 were 0.107 kg/m^3 and 0.097 kg/m^3 respectively, and the rest were less than 0.1 kg/m^3. According to the statistics of daily sediment concentration for 731 days in 2005–2006, the maximum

was 0.652 kg/m^3, while there were only 34 days more than 0.1 kg/m^3, accounting for 4.65%, indicating that Minjiang river was a typical "Clear River". The dam of Shuikou hydropower station has been built for 20 years, making full use of the reservoir siltation and the two bottom holes with maximum discharge up to 2030 m^3/s. It is possible to replenish flow and sediment by means of discharging flood through the combined use of the bottom holes and the surface holes of the hydropower station. The results show that the water level under the dam of Shuikou hydropower station can be restored to the original design level through the measures of replenishing flow and sediment with 0.625 kg/m^3 sediment concentration, 3570 m^3/s discharge flow, and 4.38-day discharge duration (Zeng 2016; Hu et al. 2011).

5.2 *Main Characteristics of Riverbed Deformation Before and After Repair*

After the implementation of the repair measures in 5.1, some characteristics of the riverbed deformation under the hydropower station dam are presented as follow: The area with obvious change is from D1 section to D33 section about 12.62 km, which silts up 0.50–4.50 m. The area with transitional change is from D33 section to D64 section about 15.00 km, which silts up −0.50 to +0.50 m. The stable area is from D64 section to the estuary, which remains basically unchanged before and after repair. The topography amplitude before and after repair are shown in Figs. 9 and 10, and Table 1.

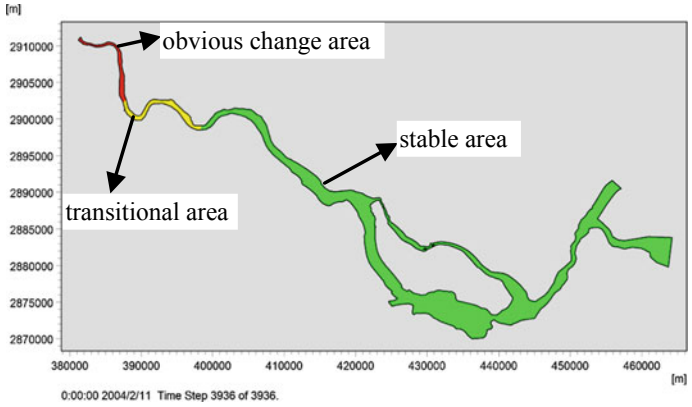

Fig. 9 Divisions of topography amplitude

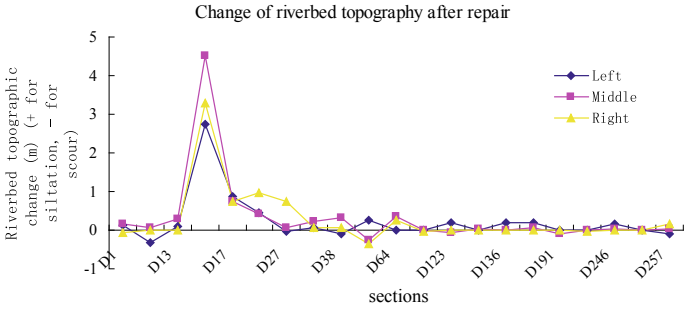

Fig. 10 The topography changes of sections before and after repair

5.3 Change of Flow Condition Before and After Repair

After the implementation of the repair measures in 5.1, some characteristics of the flow condition under the hydropower station dam are presented as follow: After repair, the tidal current limit moves from D42 Xiaqingkeng section to D43 Minqing railway station section about 0.50 km, and the flow of the area changes from periodic variation with the tide to one-way along the river. In the obvious change area, because the water level increases with siltation and water drop increases along the river, the flow velocity between the D15-D33 sections increases obviously, but the flow field is well-distributed. in the stable area. The flow changes periodically with the tide, the velocity increases slightly, and the flow field is stable. Flow velocity changes before and after repair are shown in Fig. 11 and Table 2.

After the implementation of the repair measures in 5.1, some characteristics of the water level under the hydropower station dam are presented as follow: After repair, the water level under the dam obviously rises, and decreases gradually and then tends towards stability. The tidal limit moves from D20 Xiaoruo section to D27 Yangge section. The obvious area of water level change is from D1 section to D20 section about 7.38 km, and the water level rises by 3.02–4.33 m. The transitional area is from D20 section to D27 section about 2.62 km, and the water level rises by 1.09–1.44 m. The stable area is from D33 section to Minjiang estuary, and the water level amplitude is very small and does not exceed 0.1 m. The changes in the 24-hour water level of three areas before and after repair also show that repair measure can raise the water level under Shuikou hydropower station dam obviously. The changes of water level before and after repair are shown in Figs. 12, 13, and Table 3.

6 Conclusion

The replenishing fow and sediment is very effective for repairing the riverbed of Minjiang estuary, especially for raising the water level under Shuikou hydropower

Table 1 The topography changes of typical section before and after repair

Condition	Topo-graphy	Under Shuikou hydropower station dam section	Obvious change area	Xiaoruo section	Yangge section	Huai'an diversion port	The middle of North river	The middle of South river	Sanjiang confluence	Tingjiang diversion port
Original	Left	0.87	−0.29	4.91	1.35	3.71	4.43	−2.20	−5.56	−8.27
	Middle	−1.55	−3.00	3.33	1.10	−1.46	−7.84	−16.58	−8.79	−5.02
	Right	1.86	0.56	3.74	5.50	3.68	−0.28	−2.08	−10.01	−5.32
After repair	Left	1.01	2.44	5.36	1.31	3.71	4.43	−2.02	−5.41	−8.28
	Middle	−1.38	1.51	3.74	1.17	−1.56	−7.85	−16.50	−8.77	−5.02
	Right	1.78	3.86	4.72	6.25	3.68	−0.32	−2.08	−10.00	−5.32

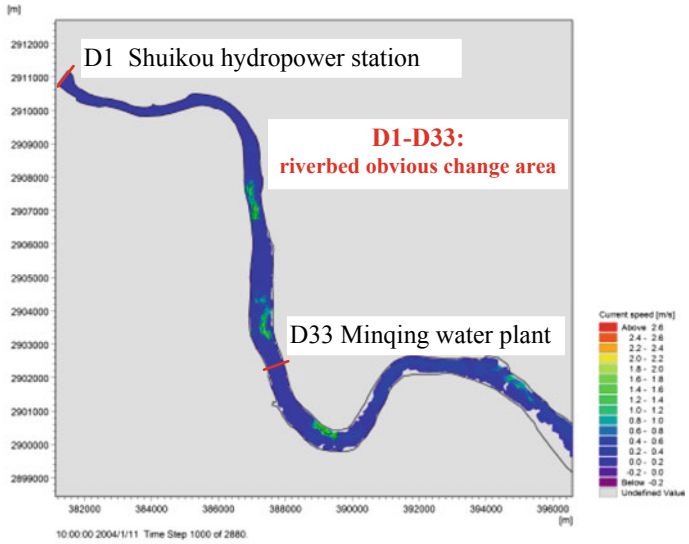

flow velocity (before repair)

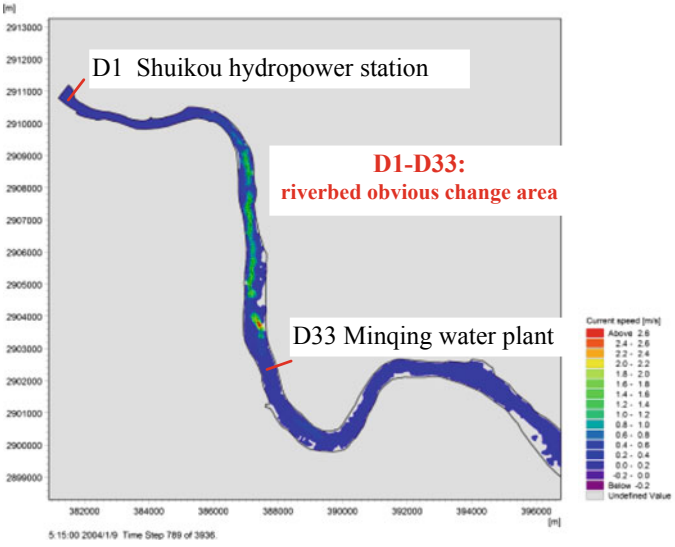

flow velocity (after repair)

Fig. 11 Flow velocity before and after repair of obvious change area

Table 2 Maximum velocity of flood tide and ebb tide after repair

Condition	Velocity	Under Shuikou hydropower station dam section	Obvious change area	Xiaqing-keng section	Minqing station section	Huai'an diversion port	The middle of North river	The middle of South river	Sanjiang confluence	Tingjiang diversion port
Original	Flood tide	–	–	0.02	0.04	0.64	2.31	1.41	2.63	2.55
	ebb tide	0.14	0.20	0.25	0.38	0.52	0.70	0.75	0.86	0.77
After repair	Flood tide	–	–	–	0.04	0.44	2.31	1.43	2.62	2.56
	ebb tide	0.08	0.72	0.25	0.45	0.79	0.80	1.08	1.07	0.97

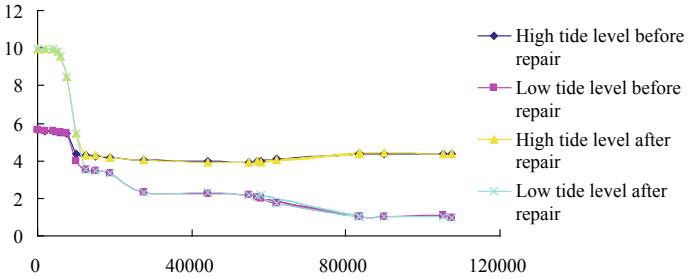

Fig. 12 Change of water level eigenvalues along the river

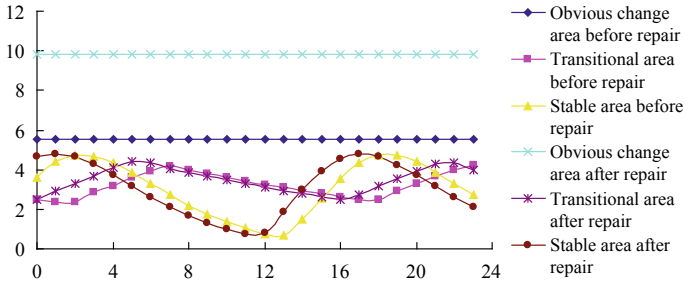

Fig. 13 Change in the 24-hour water level

station dam. Studies show that under the condition that the discharge flow and the tide level in the estuary remain unchanged, the effect of the discharge duration on the river evolution is obviously greater than that of the sediment concentration. The results show that the water level under the dam of Shuikou hydropower station can be restored to the original design level of 9.92 m through the measures of replenishing flow and sediment with 3570 m^3/s discharge flow, 0.625 kg/m^3 sediment concentration, 4.38-day discharge duration, 1351 million m^3 water, and 844.4 thousand tons sediment.

Table 3 Water level change before and after repair

Condition	Water level	Under Shuikou hydropower station dam section	Obvious change area	Xiaoruo section	Yangge section	Huai'an diversion port	The middle of north river	The middle of south river	Sanjiang confluence	Tingjiang diversion port
Original	High	0.87	−0.29	4.91	1.35	3.71	4.43	−2.20	−5.56	−8.27
	Low	−1.55	−3.00	3.33	1.10	−1.46	−7.84	−16.58	−8.79	−5.02
	Difference	1.86	0.56	3.74	5.50	3.68	−0.28	−2.08	−10.01	−5.32
After repair	High	1.01	2.44	5.36	1.31	3.71	4.43	−2.02	−5.41	−8.28
	Low	−1.38	1.51	3.74	1.17	−1.56	−7.85	−16.50	−8.77	−5.02
	Difference	1.78	3.86	4.72	6.25	3.68	−0.32	−2.08	−10.00	−5.32

Acknowledgements Grateful acknowledgement is made to my colleagues who gave me considerable help by means of suggestion, comments and criticism. Without their illuminating instruction, this thesis could not have reached its present form. In addition, I deeply appreciate the contribution to this thesis made in various ways by my friends and families.

References

Chen, Y. (2017). On water surface line caculation of some river channel project based on HEC-RAS software. *Shangxi Architecture*, pp. 207–208.

Hu, X., Jiang, J., & Yu, Q. (2011). Design study on construction scheme of water level regulation project for Shuikou downstream hydro-junction. *Dam and Safety*, pp. 3–6, 10.

Zeng, J. (2016). Construction scheme analysis of water level control project under Shuikou hydropower station dam. *Hydraulic Science and Technology*, pp. 64–67.

Numerical Analysis on Impacts of the Project of North Branch Narrowing on Sediment Distribution at the North Branch in the Changjiang River Estuary

Guo Chuansheng, Tang Liqun, Wang Chonghao, Zhao Huiming, Wang Yuhai and Liu Dabin

Abstract To analyze the effect of the project of North Branch Narrowing at Changjiang River on hydrodynamic and sediment transport, a 3D numerical model for Changjiang Estuary was established. The verification of the models shows that they are effectively for simulating tidal current and suspended sediment distribution. The model were then used to simulate the hydrodynamic and distribution of sediment after the north branch narrowing. The results show that, after the narrowing-project, the new shoreline direction conforms with the main current direction of tide, the characteristics of flooding and ebbing tide basically remains unchanged; the project narrows the estuary width of north branch. After the north branch narrowing, the channel and the mouth of the north branch would be narrowed significantly, and tide would be weakened and water level would also be reduced, and tide current would be increased due to the narrowing of channel in the north branch. The concentrations of suspended sediment in the north branch would be reduced along with the reduce of tide level and current speed. The concentrations of suspended sediment reduce 0 to −14.9% after the project construction. It has little impact on the tidal level, current speed and suspended sediment concentration in the south branch in the Changjiang River.

Keywords Suspended sediment transport · Tidal shear front · Sediment siltation · Tidal current · Sediment · Numerical modeling

1 Introduction

With the development of numerical simulation methods and the improvement of computational facilities, three-dimensional mathematical models have been widely used in the solution of many real-life engineering problems and applied to study the

G. Chuansheng (✉) · T. Liqun · W. Chonghao · Z. Huiming · W. Yuhai · L. Dabin
State Key Laboratory of Simulation and Regulation of Water Cycle in River Basin, China Institute of Water Resources and Hydropower Research, Beijing, People's Republic of China
e-mail: guoliu1982@126.com

K. D. Nguyen et al. (eds.), *Estuaries and Coastal Zones in Times of Global Change*, Springer Water,
https://doi.org/10.1007/978-981-15-2081-5_43

effect of land reclamation on the hydrodynamics involving sediment transport by tidal currents and waves in estuaries, erosion and sedimentation in river channels and reservoirs.

The Changjiang Estuary is located in the East China Sea and the Changjiang River is one of the largest rivers in the world. It is more than 6300 km in length and its catchment area is approximately 1.94×10^6 km^2 (Xie et al. 2013). The annual average total suspended sediment discharge of the Changjiang River is about 4.245×10^8 t, and large quantity sediments are transported to the East China Sea. The Chongming Island separates the main channel into two parts: the North Branch and the South Branch of the Changjiang River Estuary. Due to the human impacts and channel changes in the Changjiang River Estuary over the past half century, the main water and sediment discharge of the Changjiang River has moved to the South Branch, and runoff into the North Branch decreasing rapidly. The phenomenon of "salt tide inversion" is another problem to the estuary. In order to delay the natural siltation of the North Branch and resolve the problem of "salt tide inversion" in the Changjiang River Estuary, Shanghai and Jiangsu Province implemented a narrowing project on the North Branch of the Changjiang River Estuary (Fig. 1).

The North Branch of the Changjiang River Estuary is mainly controlled by East China Sea tidal system. The tides of the North Branch are irregular semidiurnal. The characteristic values of tidal stages can be summarized as follows: the mean high tidal level is 3.84 m, the mean low tidal level is 1.13 m and the mean tidal range is 2.68 m. The tidal current is the primary dynamic force for maintaining the stability of the seabed and the sediment transport. The averaged flood current velocity is about 0.64–1.01 m/s and the averaged ebb is about 0.56–1.25 m/s; the current speed of flood

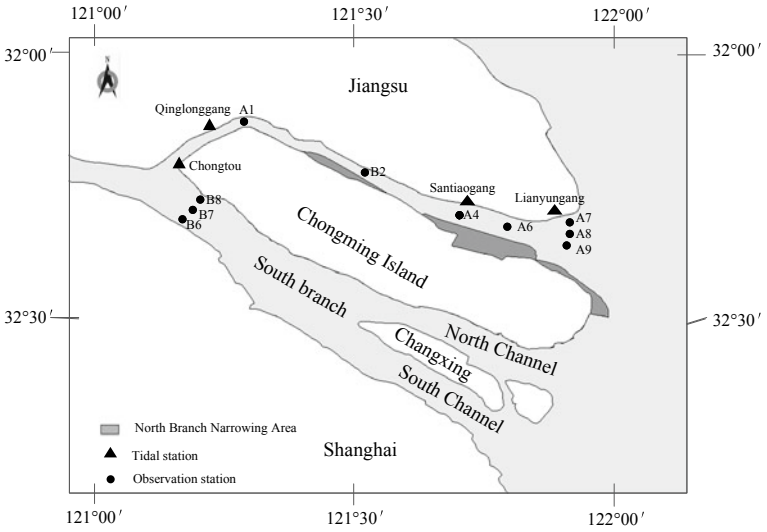

Fig. 1 The location of the project of North branch narrowing

tide is less than that of the ebb tide. And the currents are reversing with directions of WNW-ESE. Under the condition of current dynamics and sediment transport is the Changjiang River, the suspended sediment concentration (SSC) in the North Branch is high. Based on the data of A1–A9 station (Fig. 1), the maximum SSC is over 6.0 kg/m^3 at the bottom and the maximum vertical average SSC is 2.98 kg/m^3. The yearly-averaged SSC near the surface is over 0.8 kg/m^3 in this area. The sediment in the North Branch is mostly from the local high SSC layer near the bottom, besides the suspended sediment transport of the Cahngjiang River. The high SSC is mainly interacted by the local sediment and flow transport.

In this chapter, the sediment transport model in the Changjiang River Estuary is established based on the three-dimensional tidal current sediment model, and numerical simulation analysis is conducted on the change of sediment transport in the north branch after the implementation of the narrowing project, which provides a reasonable and comprehensive implementation of the renovation project.

2 Mathematic Model

The three-dimensional equation involving the effect of waves are based on the circulation model FVCOM in the sigma (σ) coordinates (Chen et al. 2003). Where the baroclinic terms are neglected and the horizontal diffusion terms are replaced with those in the present forms, and the wave radiation stress terms are added.

The model is written as follows:

$$\frac{\partial Du}{\partial x} + \frac{\partial Dv}{\partial y} + \frac{\partial w}{\partial \sigma} + \frac{\partial \eta}{\partial t} = 0 \tag{1}$$

$$\frac{\partial Du}{\partial t} + \frac{\partial Du^2}{\partial x} + \frac{\partial Duv}{\partial y} + \frac{\partial uw}{\partial \sigma} = fDv - gD\frac{\partial \eta}{\partial x} + \frac{\partial}{\partial \sigma}\left(\frac{K_M}{D}\frac{\partial u}{\partial \sigma}\right)\frac{gD}{\rho_0}\left[\frac{\partial}{\partial x}\left(D\int_\sigma^0 \rho d\sigma'\right) + \sigma\rho\frac{\partial D}{\partial x}\right] + DF_x \tag{2}$$

$$\frac{\partial Dv}{\partial t} + \frac{\partial Duv}{\partial x} + \frac{\partial Dv^2}{\partial y} + \frac{\partial vw}{\partial \sigma} = fDu - gD\frac{\partial \eta}{\partial y} + \frac{\partial}{\partial \sigma}\left(\frac{K_M}{D}\frac{\partial v}{\partial \sigma}\right)\frac{gD}{\rho_0}\left[\frac{\partial}{\partial y}\left(D\int_\sigma^0 \rho d\sigma'\right) + \sigma\rho\frac{\partial D}{\partial y}\right] + DF_y \tag{3}$$

$$\frac{\partial P}{\partial z} + \rho Dg = 0 \tag{4}$$

where u, v and w are the velocities in the x, y and σ directions, respectively, the vertical coordinate σ ranges from $\sigma = 0$ at the free surface to $\sigma = -1$ at the bottom, t is the time, η is the free surface elevation, D is the total water depth, f is the Coriolis

parameter, p is the pressure, ρ is the water density, g is the gravitational acceleration, K_x, K_y, K_z are the mixing coefficients under waves and currents in the x, y and σ directions, respectively. In the present study, the mixing coefficients depend on the bed shear velocities under waves and currents, which are relevant to the wave-current bottom shear stress. Hence, the horizontal mixing coefficients (Pham et al. 2009) are adopted as follows

$$K_x = K_y = \alpha_x u_* D \tag{5}$$

Where α_x =5.93, u^* is the bed frictional shear velocity due to the combined actions of waves and currents and $u_* = \sqrt{2\tau_{cw}/\rho}$, τ_{cw} is the bottom shear stress in the wave-current and is calculated according to a non-linear formula (Wang and Kang 2015) as follows

$$\tau_{cw} = \tau_c \left[1 + 1.2 \left(\frac{\tau_w}{\tau_c + \tau_w} \right)^{3.2} \right] \tag{6}$$

where τ_c is the current bottom shear stress, τ_w is the wave bottom shear stress.

The model includes transport of both suspended load and bedload. The suspended load model uses a concentration-based approach subject to the following evolution equation

$$\frac{\partial C_i}{\partial t} + \frac{\partial u C_i}{\partial x} + \frac{\partial v C_i}{\partial y} + \frac{\partial (w - w_i) C_i}{\partial z} = \frac{\partial}{\partial x}\left(A_H \frac{\partial C_i}{\partial x} \right) + \frac{\partial}{\partial y}\left(A_H \frac{\partial C_i}{\partial y} \right) + \frac{\partial}{\partial z}\left(K_H \frac{\partial C_i}{\partial z} \right) \tag{7}$$

where C_i is the concentration of sediment i, A_h is the horizontal eddy viscosity and K_h is the vertical eddy viscosity. The settling velocity w_i is prescribed by the user for each sediment type in the input parameter file. At the surface, a no-flux boundary condition is used for the sediment concentration

$$K_h \frac{\partial C_i}{\partial z} = 0, \quad z = \zeta \tag{8}$$

At the bottom, the sediment flux is the difference between deposition and erosion

$$K_h \frac{\partial C_i}{\partial z} = E_i - D_i, \; z = -D \tag{9}$$

The erosion rate is calculated as

$$E_i = \Delta t \, Q_i (1 - P_b) F_{bi} \left(\frac{\tau_b}{\tau_{ci}} - 1 \right) \tag{10}$$

where Q_i is the erosive flux, P_b is the bottom porosity, F_{bi} is the fraction of sediment is in the bottom, τ_b is the bottom shear stress, and τ_{ci} is the critical shear stress of sediment i.

3 Model Verification and Application

Tidal current calibration is the basis of the tidal current and suspended sediment transport model. It is necessary to simulate the tidal level and flow velocities, and directions in the North Branch.

Using the data of December 2012, the computational results for the water-surface elevation, velocity, flow direction and suspended sediment concentration can be in good agreement with the field data. Four tidal level stations (Chongming, Qinglonggang, Santiaogang and Lianxinggang) and five tidal current stations (A1, B2, A4, A8 and B7) are chosen to validate the hydrodynamic model. As shown in Figs. 2 and 3, the model results capture the observed tidal characteristics and well reproduce the tidal speed and direction at each station. The absolute error of the tide current speed and direction is 0.24 m/s and 15°, respectively.

The measured and calculated sediment concentration at six station (see Fig. 1 for their locations) are compared in Fig. 4. The result shows that the distributions of suspended sediment concentration under the combined effects of tidal currents and waves are consistent with the measured values. The computed values match well with the observations. So the model would be combined to the simulations of flow motion, sediment transportation and bed-form reworking.

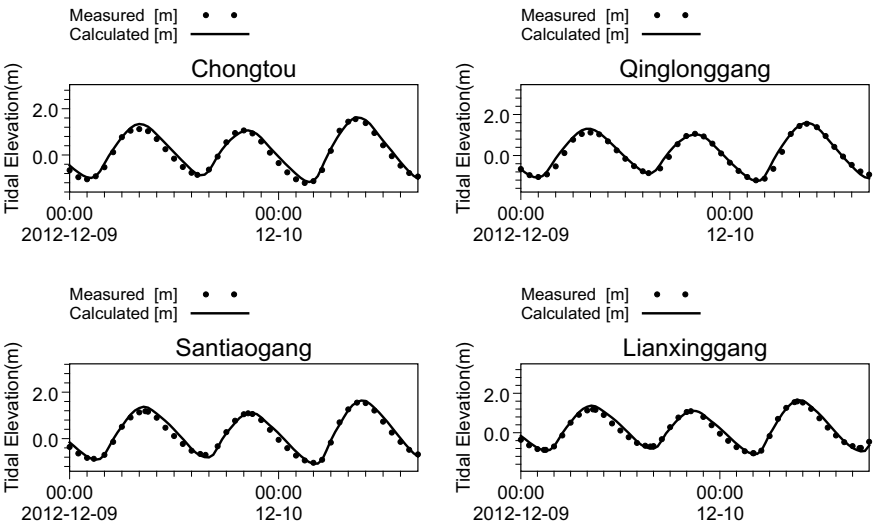

Fig. 2 Comparison between the measured and simulated tidal elevation at stations

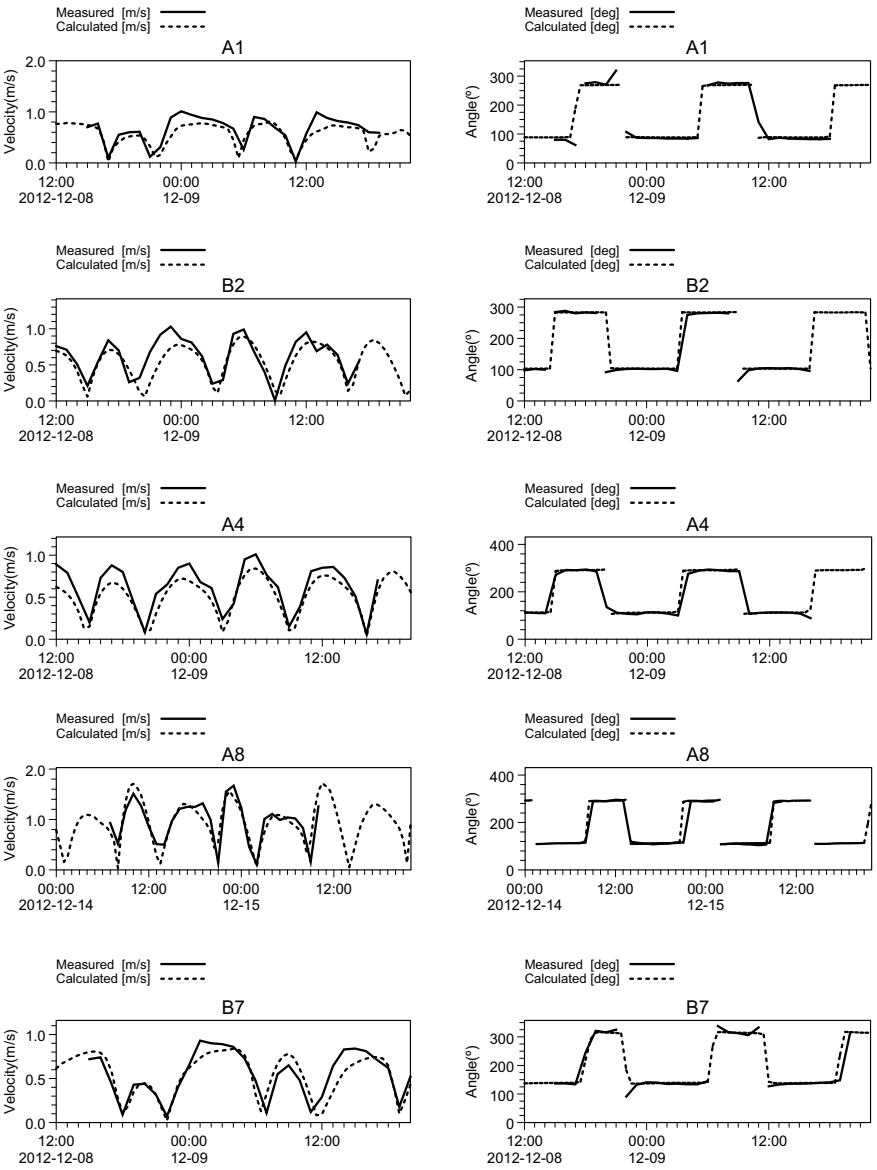

Fig. 3 Comparison between the measured and simulated velocities

In the process of high tide in the Changjiang River Estuary, tidal waves are first fluxed from the open sea to the North Branch. When the high tide begins near the northern branch gate and the tide of Lianxinggang, the middle and upper sections of the North Branch and the entire South Branch are falling. Although the tide of the North Branch was earlier than the South Branch, due to the bending of the North

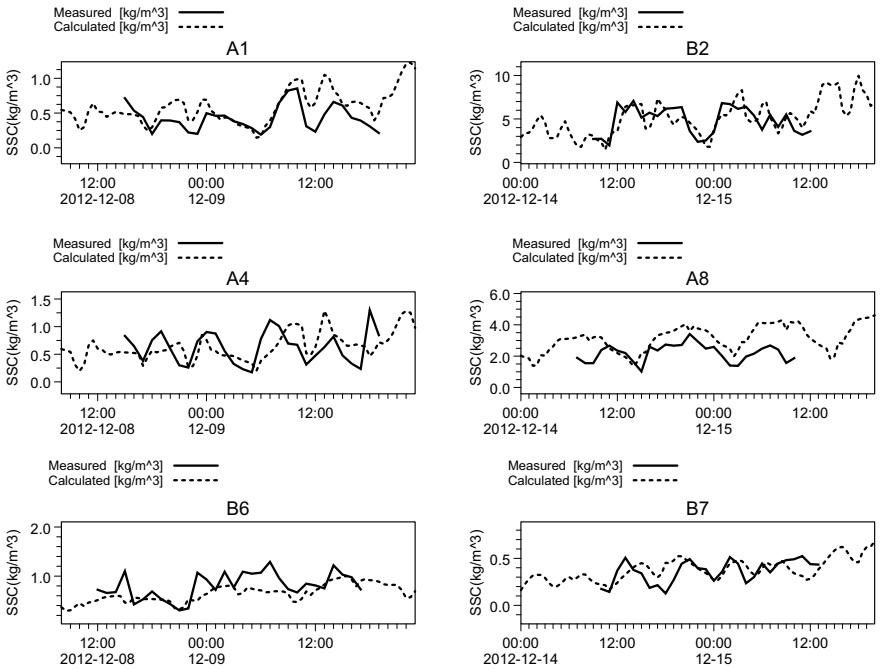

Fig. 4 Comparison between the measured and simulated sediment concentration

Branch, the resistance was greater than that of the South Branch. When tide in the South Branch rose to the point where it reached the diversion opening of the North and South branches, the Chongtou in the upper part of the North Branch was still a down trend. Tidal water flows into the North Branch (Fig. 5). As a result, the vicinity of Chongtou in the upper part of the North Branch is a weak flow area, and silt is easy to be deposited. When the South Branch is a downtrend, the north branch is still high tide near Chongtou, the water level is higher than the South Branch, the North Branch of the water flow to the South Branch, which is the driving force intruded in the South Branch from the North Branch.

After the north branch narrowing project, the significant change of the flow field appears in the north branch channel. The new shoreline direction conforms with the main current direction of tide, the characteristics of flooding and ebbing tide basically remains unchanged. But, the tide would be weakened and water level would also be reduced, and tide current would be increased due to the narrowing of channel in the north branch.

Figure 6 shows the sediment concentration fields after the north branch narrowing. The narrowing of the north branch river channel reduced the intrusion of tidal water carrying sand in the open sea, which contributed to the decrease of sediment concentration in the north branch channel. But the north branch is also the high concentration zone in Changjiang River Estuary.

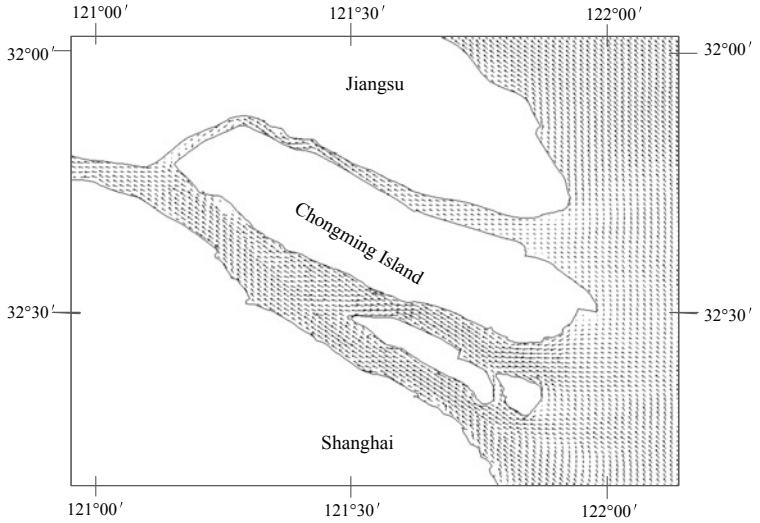

Fig. 5 Current velocity field during maximum flood

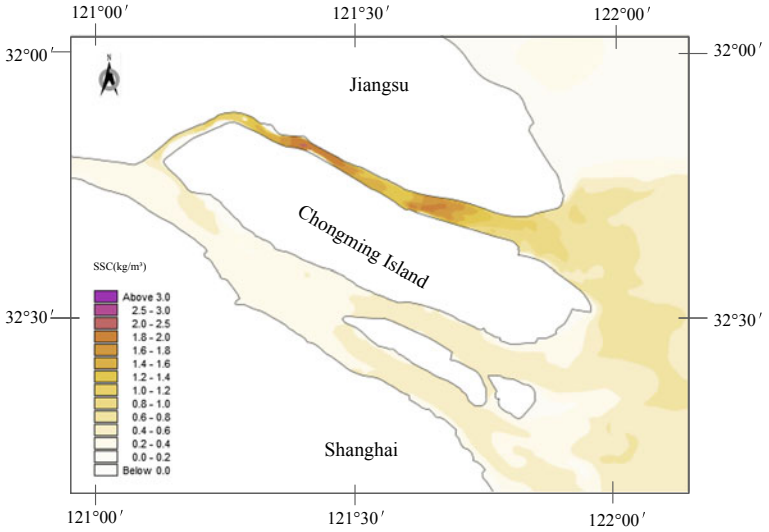

Fig. 6 Suspended sediment distribution in the Changjiang Estuary

Table 1 and Fig. 7 show the changes of sediment concentration at the north branch of the project before and after the project. It can be seen from the figure that the sediment concentration at different sites after the project has been reduced to varying degrees. Due to the fact that the narrowing of the north branch changed the north branch river to a greater degree, narrowing the river channel and the concentration of

Table 1 Changes of suspended sediment after the north narrowing

Location	SSC(kg/m^3)	SSC(kg/m^3)	The percent of changes (%)
	Before the north branch narrowing	After the north branch narrowing	
Chongtou	1.892	1.601	−14.84
Qinglonggang	1.795	1.524	−15.01
Santiaogang	1.586	1.673	5.52
Lianxinggang	1.213	1.059	−12.68

sediment in the northern branch waters decreased. At the same time, after the implementation of the project, the tidal level of the North Branch was reduced, resulting in a reduction in the amount of sediment transported by the tidal current to the north branch and the flow rate did not increase significantly. This was also the reason that the sediment concentration in the northern branch decreased. The concentrations of suspended sediment reduce 0 to −14.9% after the project construction.

The narrowing of the north branch river channel resulted in a lower tidal level and also reduced the intrusion of tidal water carrying sand in the open sea, which contributed to the decrease of sediment concentration in the north branch channel. The southern branch and the mouth area are basically unaffected, and there is no significant change in sediment concentration.

4 Conclusions

Based on the characteristics of the tidal currents and sediments in the Changjiang River Estuary, a 3D integrated current-sediment field model considering the combined effects of tidal currents and sediment is developed in the present study. The results show that, after the narrowing-project, the new shoreline direction conforms with the main current direction of tide, the characteristics of flooding and ebbing tide basically remains unchanged. After the north branch narrowing, the channel and the mouth of the north branch would be narrowed significantly, and tide would be weakened and water level would also be reduced. The concentrations of suspended sediment in the north branch would be reduced along with the reduce of tide level and current speed. The concentrations of suspended sediment reduce 0 to −14.9% after the project construction. It has little impact on the tidal level, current speed and suspended sediment concentration in the south branch in the Changjiang River.

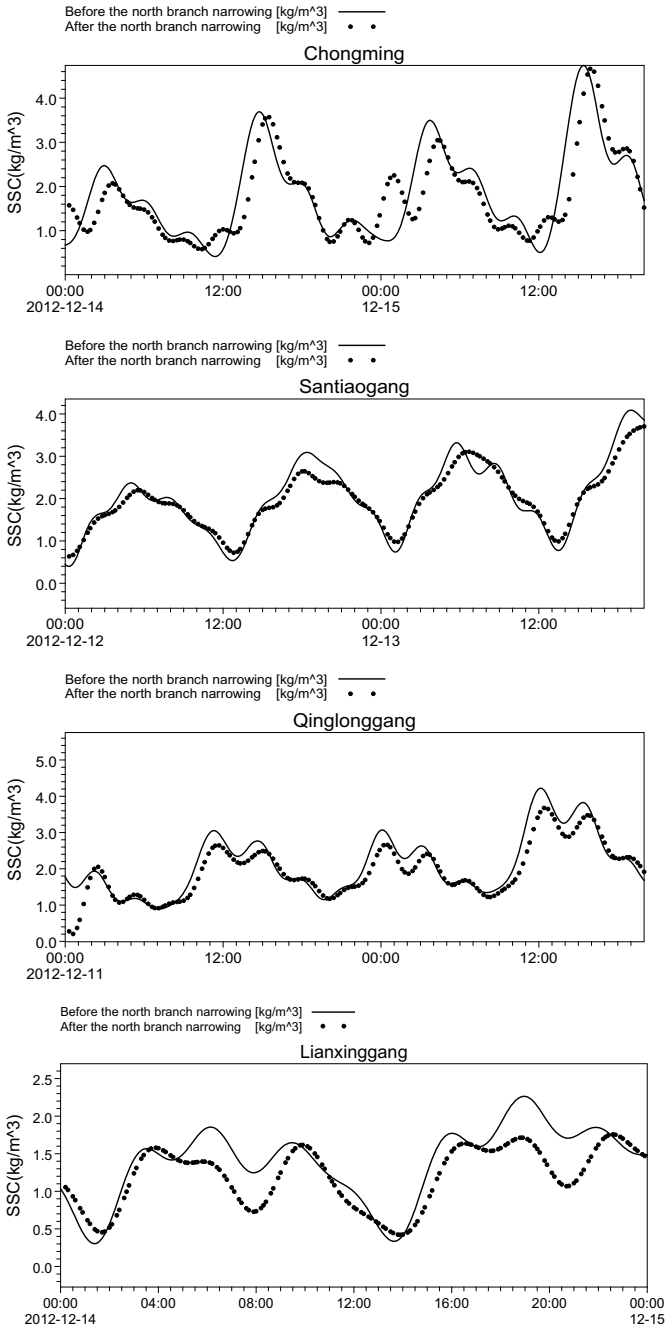

Fig. 7 Comparison of SSC before and after the north branch narrowing

Acknowledgements This research was supported financially by the National Key Research and Development Program of China (2018YFC0407503) and IWHR Research and Development Support Program (SE0145B142017). The author would like to thank FVCOM developer for the open access of the source code.

References

Xie, L., Zhang, Z. K., Zhang, Y. F., Wang, Y. P., & Huang, X. J. (2013). Sedimentation and morphological changes at Yuantuojiao Point, estuary of the North Branch, Changjiang River. *Acta Oceanologica Sinica, 32*(2), 24–34.

Chen, C. S., Liu, H. D., & Robert, C. B. (2003). An unstructured grid, finite-volume, three-dimensional, primitive equations ocean model: Application to coastal ocean and estuaries. *Journal of Atmospheric Oceanic Technology, 20*(1), 159–186.

Pham, T. S., Larson, M., Hanson, H., et al. (2009). A numerical model of nearshore waves, currents and sediment transport. *Coastal Engineering, 56*(11–12), 1084–1096.

Wang, Q., & Kang, H. (2015). A three-dimensional modeling of the morphological change in the Liaodong Bay. *Frontiers of Earth Science, 9*(3), 509–520.

Impact of Tide Gate Operation on Sediment and Water Quality of Yongding New River

Zhao Jinqiong, Yuan Yuan and Luo Xue

Abstract The construction of tide gate at Yongding New River estuary will influence the transportation of water, sediment and pollutant, and these changes at upstream/downstream of sluice will be different under different operation mode, which also in turn restricts the scheduling plan. In order to provide a basis for the selection of tide gate operational modes, the 1-D mathematical model for unsteady flow-sediment-water quality in channel with a sluice has been established, which was used to study the impact of tide gate operation of Yongding New River. The result shows that, comparing with the operation mode which only storing fresh water, the water quality will be better with the operation mode which storing sea water. And the water quality gradually improved with higher storage water level. However, there will be more deposition upstream & downstream of tide gate.

Keywords Tidal reach · Water lock · Sedimentation · Pollutant transportation · Yongding new river

1 Introduction

The sluice constructed at the estuary has changed the condition of water flow motion and the change of sediment deposition and water quality in the river channel upstream/downstream the sluice will be different under different sluice scheduling mode, which also in turn restricts the selection of final scheduling mode for the sluice. In this chapter, in order to provide a basis for the selection of tide gate operational modes, the 1-D mathematical model for unsteady flow-sediment-water quality in channel with a sluice has been established, taking Yongding New River as an example.

Yongding New River (Fig. 1) is located in the north of the urban areas of Tianjin, with its west start from Qu Jiadian in Beichen District and east to Beitang Street in Tang-gu District where it flows into the Bohai Sea. The overall length of the river is 63 km. It passes Airport Drainage River, Beijing Sewage River, New Chaobai

Z. Jinqiong (✉) · Y. Yuan · L. Xue
Key Laboratory of River Regulation and Flood Control of MWR, Wuhan, Hubei Province, China

K. D. Nguyen et al. (eds.), *Estuaries and Coastal Zones in Times of Global Change*, Springer Water,
https://doi.org/10.1007/978-981-15-2081-5_44

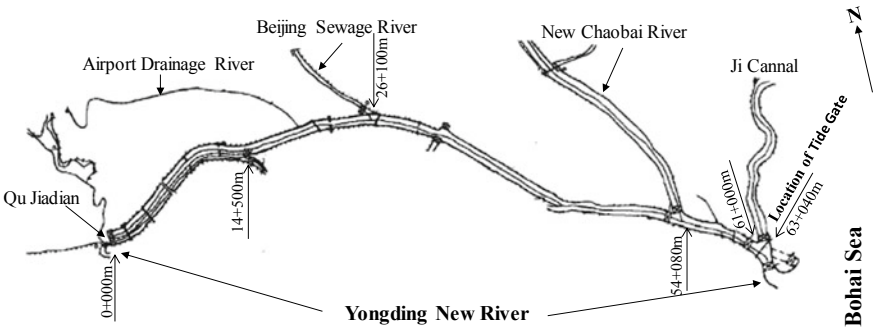

Fig. 1 The sketch map of Yongding new river

River and Ji Cannal along the way, which is not only the common estuary trail channel for Yongding River, North Canal, Chaobai River and Ji Cannal of north system in Haihe River, but also the northern defense of flood control for Tianjin. Since the establishment of Yongding New River, the sediment coming from sea area deposits in river channel constantly and the flood discharge capacity has decreased dramatically. Besides, the water quality in this river reach is relatively poor. The general planning of governance for Yongding New River is desilting plan by means of sluice construction. In this chapter, the author selects this river reach as the object of study.

The one-dimensional water-sediment calculation of unsteady flow in the river channel takes the sample from Qu Jiadian to estuary, the overall length of which is 66 km. All the pattern of cross section are mainly compound channels for flood discharging in deep channel, the river width is 500–600 m and the bottom width of the deep channel is 130–200 m. Among them, the location of 63 + 041 is the cross section where sluice locates.

2 The Establishment of Mathematical Model

2.1 Basic Equation and Solving Method

The basic approaches to describe motion of sediment in one-dimensional water flow involve water flow continuity equation, water flow motion equation, sediment continuity equation and river bed deformation equation etc. The establishment of model and solving method of the basic equation refer in the book of Yang (1993).

2.2 Handling of Some Problems that Exist in the Model

① Boundary inside the sluice

Based on above mentioned model of river channel, the water flow model for non tidal river channel with sluice is established after introducing the inside boundary condition of sluice. The water flow upstream and downstream of sluice shall be handled specially, as shown in Fig. 2.

Take the calculation cross Sect. 1-1 in the sluice upstream, and take the calculation cross Sect. 2-2 at normal depth in sluice downstream to make a list of two internal boundary condition respectively (Zhu et al. 2001): In the future, the flow rate must maintain:

$$Q_1^{J+1} = Q_2^{J+1} \tag{1}$$

The relation between water level and flow rate in sluice upstream/downstream shall be determined by mean of orifice outflow or weir formula, namely:

$$Q_1^{J+1} = Q_1(Z_1^{J+1}, Z_2^{J+1}) \tag{2}$$

The water flow continuity equation can be treated after discrete:

$$\Delta Q_2 = \Delta Q_1 + Q_1^J - Q_2^J \tag{3}$$

The motion equation of water flow can be expanded by use of Taylor expansion:

$$Q_1^J + \Delta Q_1 = Q_1(Z_1^J, Z_2^J) + \frac{\partial Q_1}{\partial Z_1}\Delta Z_1 + \frac{\partial Q_1}{\partial Z_2}\Delta Z_2 \tag{4}$$

Equations (3) and (4) constitute an equation set to solve water flow upstream and downstream the sluice, which replaces de Saint-Venant system of equations in local area of sluice, simplifies the simulation of phenomena of complicated water flow in local area of sluice and also maintains the consistency of water flow calculation. The problem can be solved being supplemented with overflowing calculation of sluice.

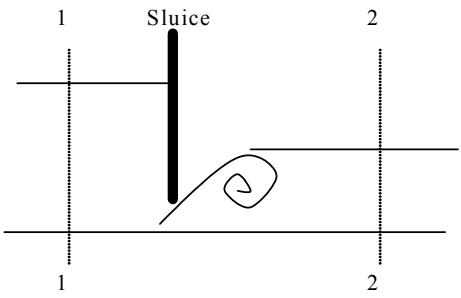

Fig. 2 The schematic diagram for cross section calculation of sluice

② Calculation mode of local scouring and silting of sluice

After the local opening of sluice has been put into use, the water will flow from outlet of the building towards broad river channel downstream with bigger flow velocity owing to artificial narrowing of the water flow. The plane back flow caused by transversal flow velocity gradient of the water flow will be formed in the area where the water flow becomes broaden suddenly. In the process of calculation, the handling of back flow area must also be considered. Owing to some built-in defects in the two-dimensional mathematical simulation on local water flow, with the addition of complicated calculation, empirical model (Cao 1998) of local erosion-deposition in the sluice has been introduced into the model.

The exchange relation of sediment in main back flow area is shown in Fig. 3, the equation of sediment transportation in local river reach can be obtained after theoretical derivation. As for the local back flow presented in sluice upstream, the longitudinal flow velocity in back flow area is smaller in comparison with flow velocity of main flow, and the influence on main flow is too minor that can be ignored. Therefore, the back flow area plays a role of water storage with regard to main flow, which can be handled by use of simplified calculation mode for swale. Conduct the uncoupled solution by calculation, namely, divide main back flow area according to Fig. 4, calculate each hydraulic element according to mode of swale and then calculate the change of local erosion-deposition by use of sediment motion equation and river bed deformation equation after deducting. The basic equation

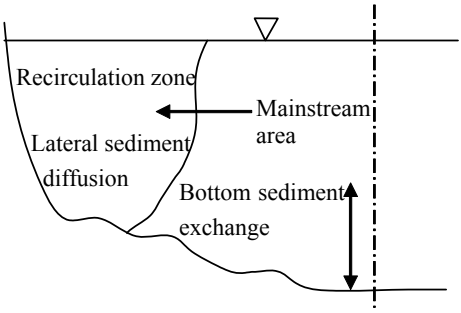

Fig. 3 Schematic diagrams for local cross section of sediment exchange

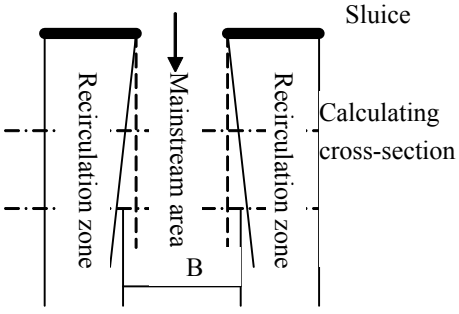

Fig. 4 The division of main back flow zone and the determination of cross section width

reflecting mathematical model for local erosion-deposition as follows (Yang 1993):

$$B_s \frac{\partial Z}{\partial t} + \frac{\partial Q}{\partial X} = 0 \tag{5}$$

$$\frac{\partial Q}{\partial t} + \frac{\partial}{\partial x}\left(\alpha \frac{Q^2}{A}\right) + gA\frac{\partial Z}{\partial x} + g\frac{n^2 Q|Q|}{AR_h^{4/3}} = 0 \tag{6}$$

$$\frac{\partial (QS)}{\partial x} + \frac{\partial (AS)}{\partial t} + \alpha\omega B(S - S_*) = -g_l \tag{7}$$

$$\frac{\partial (QS)}{\partial x} + \frac{\partial (AS)}{\partial t} + \rho' \frac{\partial A_0}{\partial t} = -g_l \tag{8}$$

Complementary equations:

$$g_l = g_s H = 0.0168 U_m H(S_m - S_{r*}) \tag{9}$$

$$S_{r*} = K\left(\frac{U_{r\omega}^3}{gB_0\omega}\right)^m \tag{10}$$

$$B_0 = L = \frac{13.66 c_0 H \ln \frac{A}{A-A'}}{2 + c_0^2 \frac{H}{D} \ln \frac{B}{B-D}} \tag{11}$$

where x represents flow path; Q represents main flow rate; R_h represents hydraulic radius of main flow area; Z represents water level; B_s represents river width involving back flow area; t represents time; A represents the area of cross-section of river for main flow; n represents roughness coefficient; α represents hydrodynamic correction coefficient; g represents acceleration of gravity. Among them, $S_m = S$ represents the average sediment concentration in the cross section of the main flow, and S_* represents sediment-carrying capacity of the main flow, S_{r*} represents the sediment-carrying capacity of back flow, U_m represents the flow velocity of main flow with regard to back flow area for a certain cross section and a certain water depth, and g_l represents sediment diffusing capacity of cross section per unit time. In the equation, $U_{r\omega}$ represents the transversal flow velocity of back flow, B_0 represents the length of whole back flow interface, ω represents sediment settling velocity; k, m are coefficients for sediment-carrying capacity. c_0 represents dimensionless Chézy coefficient calculated from vertical water depth, $c_0 = \frac{c}{g}$, where g represents acceleration of gravity, D represents the dam length, H represents depth of water, $(A - A')/A$ represents constriction rate of area, $(B - D)/B$ represents the constriction rate of river width.

The one-dimensional unsteady flow fundamental equation to describe transportation and diffusion of matter in water body as reference of Xie (1996).

Table 1 The scheduling mode of sluice

Scheduling plan		Open sluice	Close sluice
Fresh water storage	Drainage	$Z_1 > L_1$ and $Z_1 < Z_2$	$Z_1 < Z$ or $Z_1 > L_2$
Sea water storage	Drainage	$Z_1 > L_1$ and $Z_1 > Z_2$	$Z_1 < Z$ or $Z_1 < L_3$
	Diversion	$Z_1 <= L_3$ and $Z_1 < Z_2$	$Z_1 > Z$ or $Z_1 > L_2$

3 Impact of Tide Gate Operation

3.1 Scheduling Plan

There are two kinds of utility pattern in discussion in terms of tidal sluice in the estuary of Yongding New River: one is the fresh water storage plan which can fully reject the tidal wave at sluice downstream and change the river channel upstream into the river channel that is similar to reservoir. It will release water from sluice in due time. The other is the seawater storage plan, which means introduce a certain amount of seawater with preferable water quality into the river channel at first and then release water from sluice after the accumulated water level of fresh water is excessively high. In allusion to these two proposals, the author conducts generalizational calculation respectively and analyzes the influence of sediment deposition on the environment comparatively. The specific sluice scheduling criteria is shown in Table 1.

Remarks Z_1 represents water level in the sluice; Z_2 represents water level outside the sluice; L_1 represents maximum water level in the sluice, which is set as 1.0 m; L_2 represents normal water storage level, which is set as 0.4 m; L_3 represents the minimum water level in the sluice, which is set as −0.5 m.

3.2 The Change of Scouring and Silting

To satisfy the requirements of safe operation of sluice and stability of river channel, the opening of sluice requires reasonable scheduling in the process of calculation to make flow velocity passing the sluice generally less than starting flow velocity. As for fresh water storage, since there are fewer sediments transported from tributaries streams and it is very hard to move the sediment of fine particle in the river bed, therefore, scouring and silting deformation happens infrequently and the development situation of scouring and silting in each frictional cross section in sluice downstream within 10 years as shown in Fig. 5. Since the discharging clear water from sluice upstream has taken away part of deposited sediment, the deposition rate of sluice downstream will slow down and the average accretion in the first year is

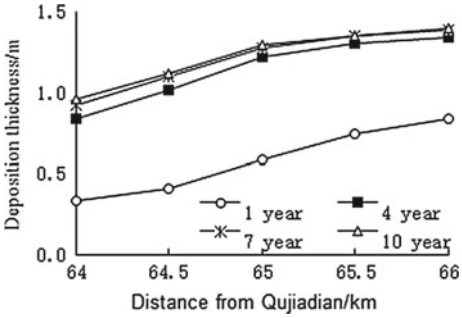

Fig. 5 The change of sediment erosion and siltation in the outside of sluice in fresh water storage plan

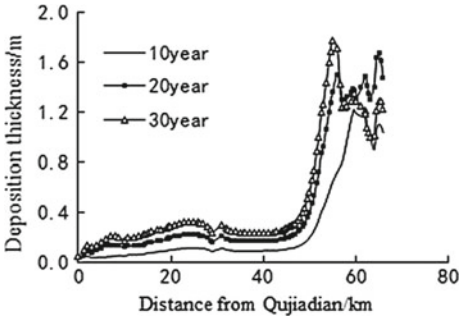

Fig. 6 The change of silt and siltation in the inside and outside of the gate in seawater storage plan

0.58 m. In this plan, the scouring and silting has reached an equilibrium state in the sluice downstream within 10 years and the maximum thickness of deposition is 1.4 m. It also demonstrates that the method of hydraulic scouring and silting by means of opening the sluice for discharging at regular intervals will have some effects on restraining the deposition of sediment in sluice downstream.

Figure 6 demonstrates the change of scouring and silting in each frictional cross section within 30 years after adopting seawater storage plan. A large amount of sediment coming from the sea has been introduced inside the sluice after opening the sluice for diversion and then deposits in the river channel. It is very hard for the sediment of fine particle move again after deposition and the maximum deposition thickness is 1.78 m. The annual average deposition amount is about 230,000 m3, which is considerably larger than deposition amount in fresh water storage plan of the same period. Viewed from desilting, the dredging amount in this plan is more difficult than that of the fresh water storage plan.

3.3 Change of Water Quality

After the construction of sluice in Yongding New River, the average change of COD concentration of different scheme in the river channel within the year is shown in

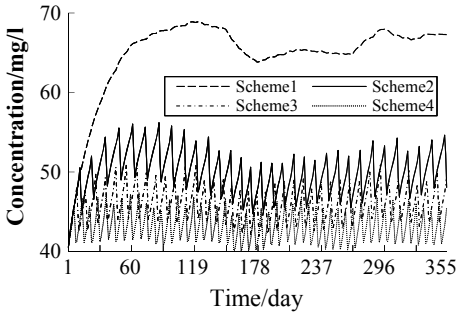

Fig. 7 Daily mean change of COD concentration of different schemes

Fig. 7. Scheme 1 is the fresh water storage plan; Scheme 2, 3 and 4, respectively, for the storage of sea water to 0.4, 0.6 and 0.8 m.

The pollutant coming from tributaries inflow shows up certain change rule in one year and the pollutant concentration will be lower if the tributary inflow is bigger. The pollutant concentration inside the sluice has decreased in a certain degree. In comparison with fresh water storage plan, introducing sea water to improve water quality inside the sluice proposed by seawater storage plan plays an obvious role. Besides, introducing the seawater until the water level has reached 0.4 m can basically control the COD concentration lower below 55 mg/L. However, the initial water quality inside the sluice has already been classified as grade V and the receiving sewage in the river channel will lose the way out after construction of sluice, which leads to further deterioration of water quality inevitably. In the mean time, intensive discharging of a great deal of sewage will have negative influence on marine environment and also marine products environment in estuary.

In order to further analyze the improvement effects of seawater introduced on the water environment inside the sluice, two cases in the seawater storage plan have been calculated respectively–stored sea water has reached 0.6 and 0.8 m. With the rise of control water level, the amount of diverted water will increase and the water quality of water body will be further improved. However, the frequency of opening sluice has increased and the diversion/drainage period has been shortened from 13 days at the level of 0.4 to 7 days at the level of 0.8 m. Meanwhile, due to the rise of water level during the course of diversion, the containable volume of water inside the sluice has decreased and the salt content in the water body has increased, which is unfavorable for domestic water supplying the residents living in river banks and agricultural production.

4 Conclusion

In order to provide a basis for the selection of tide gate operational modes, the 1-D mathematical model for unsteady flow-sediment-water quality in channel with a

sluice has been established, which was used to study the impact of tide gate operation of Yongding New River. The following conclusions are drawn:

(1) Based on existing mathematical model for one-dimensional unsteady flow and non-uniform water-sediment, the inside boundary condition of sluice has been introduced to establish mathematical model for sediment and water quality which is suitable for non-tidal river channel with sluice of Yongding New River, in combination with local erosion-deposition empirical model and water quality mathematical model.
(2) comparing with the operation mode which only storing fresh water, the water quality will be better with the operation mode which storing sea water. And the water quality gradually improved with higher storage water level. However, there will be more deposition upstream and downstream of tide gate.

Acknowledgements This work was supported by the National Key R&D Program of China (2016YFC0402309),the National Natural Science Foundation of China (Grant No. 51779014), the public industry research special funding projects of Ministry of Water resources (Grant No. 201501002-1), the Special fund for basic scientific research business of central public research institutes (Grant No. CKSF2015049/HL).

References

Cao, Z. F. (1998). *Research and Application of the one-dimensional and two-dimensional mathematical model* (pp. 47–49). Wuhan: Wuhan University of Hydro-electric Engineering.

Xie, Y. M. (1996). *Introduction to environmental water quality model* (pp. 52–53). Beijing: China Science and Technology Press.

Yang, G. L. (1993). *River mathematical model* (pp. 76–77). Beijing: Ocean Press.

Zhu, Y. L., Yan, Y. X., Jia, L. W., & Mao, L. H. (2001). Numerical model of unsteady flow and suspended-sediment transport in river networks with junction control method. *Journal of Hydrodynamics, 16,* 503–510.

Monitoring Field Surveys and Remote Sensing

Integrated management of water and erosion risks always need sufficient meteo-hydrological and hydro-sediment data. This requires monitoring systems and advanced measurement techniques. Advances in remote sensing, satellite data, revisit times, computing capacity and processing speed are on their way to introduce a revolution in the monitoring and management of coastal erosion owing to systematic remote sensing of the shoreline from space.

This part includes four chapters and focuses on data measurements by monitoring systems, particularly by using remote sensing and satellite image treatment.

The first chapter by Verpoorter et al. demonstrates that the synergy between multispectral remote sensing images may be suitable for generating both reliable sedimentary and primary productivity budgets, at least for on-surface sediments. The application site, Authie Estuary, which is located at the eastern part of the English Channel, is of environmental, ecological, economic and societal importance. With the intention to better understand sediment dynamics, it is important to correctly assess the role of sediment dynamics including erosion, stabilization and sediment reworking processes which is challenging in such complex environments. It is also important to consider biogenic components such as the microphytobenthos (MPB) distribution, as the primary productivity may play an important role with the bio-stabilization process. Consequently, there is a crucial need to provide a synoptic overview of inherent bio-physical characteristics of sediments in estuarine environments by generating precise quantitative maps to predict in a second step estuarine evolution by including sediment transport, sedimentation rates, coastal flows processes and sea-level rise caused by climate change. The use of the remote sensing technology is increasingly used for mapping estuarine and coastal environments by providing a synoptic overview of bio-physical characteristics of sediments. In that sense, the combination between remote sensing imaging, topographic data (LiDAR) and *in situ* measurements is suitable for improving our understanding of sediment dynamics with respect to physical and biological forcing.

The second chapter by Valette et al. presents major progress on a far greater scale than the current state of the art. European public satellites of the Sentinel Constellation (Sentinel-1 and Sentinel-2) of the COPERNICUS program currently offer a

revisit time of (i) five days with four satellites under the same viewing conditions, for bathy-topography investigation of the shoreline, i.e. from the continental shelf-break to the foreshore, (ii) a few days at mid-latitudes but from different points of view and (iii) almost daily at higher latitudes. New tools in open source like the SNAP toolbox or interfaces like Coastal Thematic Exploitation Platform allow public labs and companies to benefit from this breakthrough in data acquisition, rapid processing or database collection. Via remote sensing techniques, time series of seafloor bathymetry and suspended sediment in the water column can be derived from optical (spectral analysis) and SAR imagery (correlation between radar cross-sectional changes and Bragg scattering of the water-foreshore surface for the assessment of the errors). It complements, when required, very high resolution (VHR) surveys made on order with commercial imagery (or dug out from archives), aeriallight detection and ranging (LiDaR) with planes or drones, or depths sounders (on launches) and topographic instrumentation for beach profiling. Yet, the current swarms of nanosatellites such as Planet/Doves give access to systematic VHR cover of the earth.

The third chapter by Menuge et al. presents a study, the objective of which is to determine sediment transport trends in the Authie estuary (North of France) using Sentinel-2 data for different periods. This estuary is marked by a critical erosion of the northern shore due to a prograding sandy spit and a general sand filling. In order to analyse seasonal variations, a set of four images were analysed for a period between 2016 and 2018, two during summer and two during winter. A new methodology was developed for mapping sediment transport trend based on grain-size parameters (mean, sorting and skewness) determined from remote sensing data. The resulting transport vectors were spatially coherent with sedimentary bedforms (i.e. megaripple) and consistent with known transport directions. Maps of potential sediment transport show spatial variation between summer and storm periods. Our results suggest changes according to the period and some changes in direction following the formation of new structures or channel deviations. This study demonstrates that remote sensing combined to grain-size trend analysis can be a useful approach for sediment transport trends determination with a high spatial resolution. Further investigations are needed to identify the role of topographic variations and to obtain a long-term transport trend in order to understand the spatial variability in sand filling and erosion processes in the estuary.

In the last chapter, Nguyen Ngoc Tran analyses the historical hourly water level data during 29 years, from 1988 to 2016, to determine annual mean water level, annual highest high water level, annual lowest low water level, annual maximum range of tide and some others levels at coastal hydrological stations of the Mekong Delta. Results show that at these stations, the annual mean water level and the volume of sea water entering in the delta with tide are increasing; the volume of inland water evacuated to the sea with tide tends to decrease. Evolution of the annual lowest low water level shows an increasing trend, faster in the last 14 years at most of the coastal stations. During 1988–2016, the annual maximum range of tide increases in the eastern coast stations, decreases at Năm Căn, and in the western coast stations except Xẽo Rô, but decreases at most of the stations during 2003–2016 except Bình Đại, Xẽo Rô and Rạch Giá. The changes of the water levels at the estuarine areas

reported in this paper are informative for the planning of water regulation works in the Mekong Delta, especially relating to the construction of the sluicegates Cái L´ơn and Cái Bé currently under study and the planned ones on the Ti`ên River branches such as Hàm Luông and Cổ Chiên. Whether and how the changes of water levels at Năm Căn station are relevant to the confluence and interaction between the tides of the East Sea (South China Sea) and the West Sea (Gulf of Thailand) in the context of global climate change, sea level rise, is an open issue.

Kim Dan Nguyen
Laboratory for Hydraulics Saint-Venant, Université de Paris-Est, France

Synergy Between Hyperspectral (HYSPEX), Multispectral (SPOT 6/7, Sentinel-2) Remotely Sensed Data and LiDAR Data for Mapping the Authie Estuary (France)

Charles Verpoorter, Benoit Menuge, Patrick Launeau, Vona Méléder, Arnaud Héquette, Adrien Cartier and Vincent Sipka

Abstract The Authie estuary, located at the eastern part of the English Channel is of environmental, ecological, economic and societal importance. With the intention to better understand the sediment dynamic it is important to better assess the role of sediment dynamics including erosion, stabilization and sediment reworking processes which is challenging in such complex environment. It is also important to consider biogenic components such as the microphytobenthos (MPB) distribution, as the primary productivity may play an important role with the bio-stabilization process. As a consequence, there is a crucial need to provide a synoptic overview of inherent bio-physical characteristics of sediments (i.e., composition, water content, grain-size, and biomass) in estuarine environment by generating precise quantitative maps for predicting in a second step estuarine evolution by including sediment transport, sedimentation rates, coastal flows processes and sea level rise caused by climate change for instance. The use of the remote sensing technology is increasingly used for mapping estuarine and coastal environments by providing a synoptic overview of bio-physical characteristics of sediments. In that sense, the combination between remote sensing imaging, topographic data (LiDAR) and *in situ* measurements is suitable for improving our understanding of sediment dynamics with respect to physical and biological forcings. The main objective of this study is to demonstrate

C. Verpoorter (✉) · B. Menuge · A. Héquette · A. Cartier · V. Sipka
LOG, Laboratoire D'Océanologie et de Géosciences, Univ. Littoral Côte D'Opale, Univ. Lille, CNRS, UMR 8187, 62930 Wimereux, France
e-mail: charles.verpoorter@univ-littoral.fr

P. Launeau
Université de Nantes, UMR 6112 CNRS, Laboratoire de Planétologie et Géodynamique de Nantes, 2 Chemin de La Houssinière, BP 92208, 44322 Nantes, France

V. Méléder
Université de Nantes, EA 2160 MMS, Laboratoire Mer Molécule Santé de Nantes, 2 Chemin de La Houssinière, 44322 Nantes, France

A. Cartier
Géodunes, 19 Rue Maurice Ravel, 59240 Dunkirk, France

K. D. Nguyen et al. (eds.), *Estuaries and Coastal Zones in Times of Global Change*, Springer Water,
https://doi.org/10.1007/978-981-15-2081-5_45

that the synergy between multispectral (i.e., SPOT 6–7 [1.5 m/pixel]; Sentinel-2, 10–60 m/pixel, 5–10 days)", hyperspectral [Hyspex, 70 cm/pixel, 160 spectral bands] remote sensing images may be suitable for generating both reliable sedimentary and primary productivity budgets; at least for surficial sediments. All presented data were acquired during the same day (09/21/2017) in the framework TéléEST, CPER MARCO and CNRS-OMPBI projects.

Keywords Remote sensing · Hyperspectral · Multispectral · LiDAR · Physical properties mapping · Morphology · Bay of authie

1 Introduction

With the intention to improve our understanding of sediment dynamics within estuarine environments such as the Bay of Authie (North of France) it is crucial to generate precise quantitative maps of physical and biological properties of the sediment deposits. Inherent sedimentary parameters such as grain-size, moisture content, biological content, topography as well as physical forcing conditions (e.g. tidal conditions and wave currents) are needed for retrieving environmental changes over time and therefore to be able to generate reliable sedimentary budgets prior to define any management strategies or any decisions which may help to overcome erosion or sandfilling issues. Sedimentary trend predictions are generally based on field data such as samples sediments, in situ measurements but also any precise quantitative maps. In that sense remotely sensed products, maps of sedimentary parameters, may be assimilated by models such as transport models, erosion/stabilization models and thus for computing those predictions under various scenario. Even hydrodynamic condition knowledge is needed for fully assessing the general sedimentary trend, in this study, we decided to only focus on inherent sedimentary parameters mapping. Grain-size maps are important for fully assessing sediment transport trend, erodibility of sediment surfaces, etc. It is also important to consider moisture content both in sedimentology aspects as it influences the cohesiveness behavior of sediments and in ecology aspects for mapping habitats or evaluating hydration stress conditions for example. Microphytobenthos (MPB), a photosynthetic benthic microalga, is in partly responsible of the bio-stabilization process. Consequently, mapping of MPB biomass is important for fully assessing the reworking sediment processes.

Remote Sensing is now considered as an useful tool for mapping physical properties of sediments (Rainey et al. 2003; Deronde et al. 2008; Adam et al. 2010; Small et al. 2009; Verpoorter et al. 2014) or biophysical properties (Combe et al. 2005; Méléder et al. 2010; Launeau et al. 2018). While remote sensing tool presents the advantage to get a synoptic overview of coastal zones with wide swaths, scenes analyzed for mapping are only restricted to few millimeters of sediment surfaces limiting our understanding of sedimentary processes over time to approximately one or several tidal cycles. Nevertheless several processes such as erosion, stabilization, bio-stabilization, transport and deposition can be assessed over time using imagery

Table 1 Spatial and spectral resolutions of sensors used

Hyspex 1600 VNIR		SPOT 6/7		S2	
Spatial resolution (m/pixel)	Spectral bands	Spatial resolution (m/pixel)	Spectral bands (nm)	Spatial resolution (m/pixel)	Spectral bands (nm)
0.7	160 bands between 400 and 1000 nm	6	450–520	10	425–555
			530–590		525–595
			625–695		635–695
			760–890		
		1.5	450–745		727–957

at high spatial resolution (SPOT 6/7, 1.5 m/pixel; Sentinel-2 (S2), ~10 m/pixel). The high spatial SPOT 6/7 multispectral satellite is well designed for that purpose. Although SPOT 6/7 multispectral data enable us to precisely map sedimentary and geomorphic structures (e.g, ridges and runnels, mega-ripples, spit, waterline, shoreline, etc.) at various scales of observation, S2 sensor presents the benefit to have a very high repetitive time over the same scene (3–5 days with the S2A and S2B configuration) allowing to generate homogenous time-series. Multispectral data contain few spectral channels (Table 1) compared to hyperspectral data. When spatial resolution of hyperspectral sensors which are generally mounted onboard an aircraft are maximized, hyperspectral images are well-suited for deriving accurate quantitative maps with respect to spectral models used. It is explain by the fact that hyperspectral sensor is the only one allowing the collection of a contiguous reflectance spectrum per pixel in numerous narrow spectral bands. In this study, we proposed to use the synergy between various optical sensors operated onboard satellites (SPOT 6/7 and S2) and airborne platforms (HySpex 1600 VNIR) for mapping sedimentary parameters variability at low tide and thus during the same day (09-21-2016).

The main objective of this study consists in 1) mapping sediment properties by tacking the advantage of the synergy between remotely sensed data (SPOT 6/7, S2, and hyperspectral image termed HySpex) and LiDAR data. Bedform dynamics will be examined by calculating topography changes with two sets of LiDAR data between 2013 and 2016.

2 Study Site

The Authie estuary (50° 22′ 25″ N, 1° 37′ 52″ E, Fig. 1a is located on the French coast of the Eastern English Channel (EEC), and it is characterized by a semi-diurnal and macrotidal regime. The Authie estuary is a “picard” type-estuary according to the Briquet (1930) study. The Authie estuary forms a shallow elongated embayment oriented SE/NW (N120). It is affected by a general sandfilling and it presents a typical geomorphology structures, in accretion to the south zone such as ‘la pointe

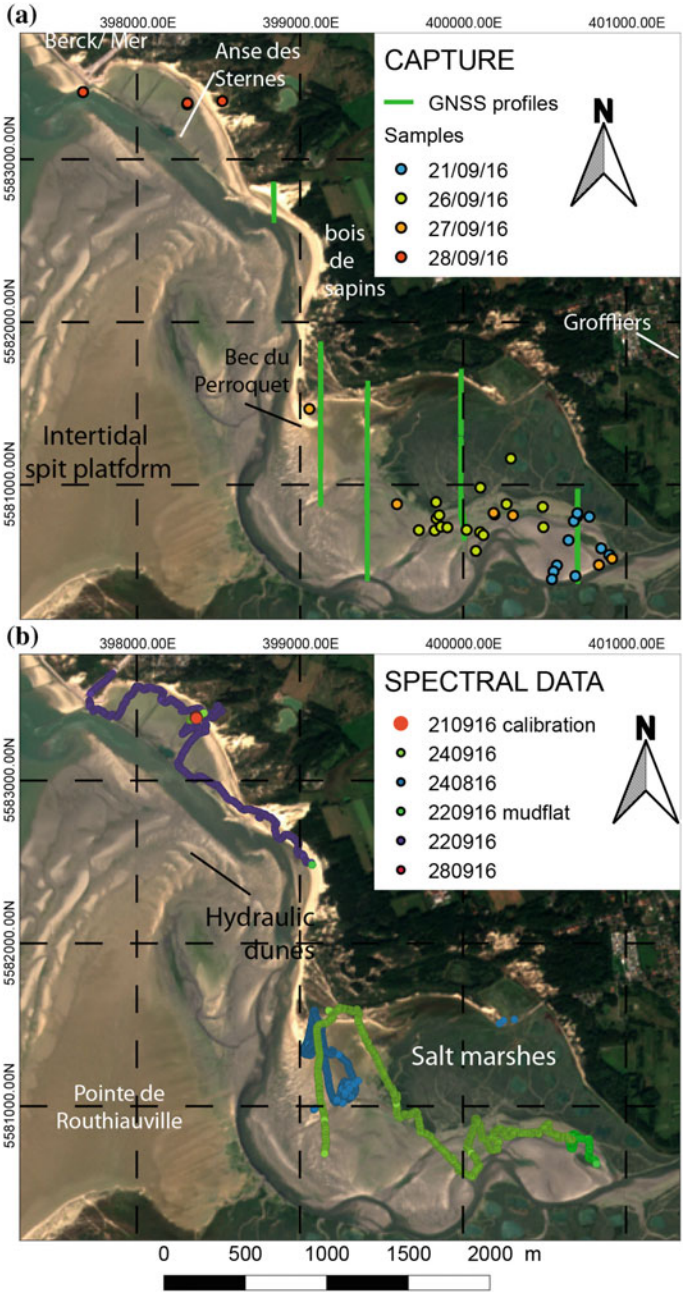

Fig. 1 In situ investigations in the Authie Bay. **a** Sediment samples and GNSS cross-shore profiles, **b** radiometric measurements acquired between the 21th of September 2016 and the 21st of September 2016

de Routhiauville' spit which reflect a northward progradation (~6.1 m/an between 2005 and 2012; Dobroniak 2005; Sogreah 2009; Hesp et al. 2016) in contrast with the northern part which is affected by a local erosion. The Authie sea-chenal deviates to the North as a response of the spit accretion and the sandfilling. As a consequence, the northern coastal line is affected by erosion of the secondary sediment cells such as 'la Grande dune' (sand-dune), 'Bois de Sapins' (pine forest) and the 'Anse des Sternes' (a well-protected area) with an erosion rate of 50.000 m^3/an (Sogreah 2009). All reworked sand sediments participate to the general infilling of the inner bay. In the medium estuary, a secondary spit structure (a cuspate foreland) was in accretion, termed the 'Beck du Perroquet' testifies to this sandy transport until the salt-marches. It is a southward prograding system (Hesp et al. 2016). The sediment coverage is highly controlled by the tidal conditions with a general decrease in particle-size from the marine estuary to the low estuary. Along the marine side, the morphology is marked by the presence of ridges and runnels (sedimentary bars) which is a particular characteristic of the EEC macrotidal coastal system. It is composed by coarse to medium sizes of sand-deposits. Upper and middle part of the estuary are mainly composed by intertidal sand flats and sandy bars ranging from fine sizes (D50 = 0.1 mm) to medium sizes (D50 = 0.6 mm) including a shelly debris component. Low estuary is mainly composed by silty sediments. Mudflats and salt-marches occur mainly in the inner estuary (Deloffre et al. 2007) as well as in the Anse des Sternes as these zones are relatively well-protected from wave-current by breakwater and groynes. Whatever the sites considered MPB, mainly diatoms, can form biofilm patches on muddy sediments. Due to the described overall sandy-transport pattern, it is not rare that during a tidal cycle some sand sediment might recover the existing muddy surfaces within the salt marshes and mudflats.

3 Materials and Methods

As mentioned before, here it is proposed to map sediment parameters by integrating the synergy between a MultiSpectral Instrument (MSI) on Sentinel-2 (S2) platform, a high spatial resolution image (SPOT 6/7), high spectral resolution images called hyperspectral images (HySpex) and LiDAR topographic data. In the framework of the 'Défi littoral OMPBI' project the Authie Bay was imaged on September 21th 2016 between 9:07 and 09:58 (UTC) by a hyperspectral/LiDAR campaign at low tide.

Sediments samples (Fig. 1a) and cross-shore elevation profiles were also collected using a GNSS (Leica TPS Syst1200) with vertical and horizontal accuracy of ±2.5 cm and ±1.5 cm respectively (Fig. 1a, in green line) at the same day for further assessments and validations. Radiometric measurements were also performed using an ASD Fieldspec 4 FR4 [2500 spectral bands]) in order to calibrate hyperspectral images and also have a reliable atmospheric correction (Fig. 1b, red spot). The in situ survey was conducted during one week, where further samples and radiometric data were collected (Fig. 1). A total of 65 surficial sediment samples were collected across

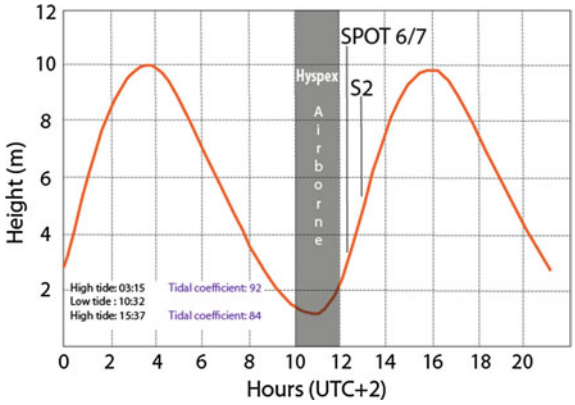

Fig. 2 Tidal condition and airborne-satellites overpass configuration in 21st of September 2016

the intertidal and supratidal domains during one week and at low tide (Fig. 1a). Conditions for further investigation in grain-size, chlorophyll-a concentration (10 samples).

In situ and laboratory dataset were used for validation of spectral models. Then sediment samples were analyzed under laboratory conditions. Chlorophyll-a contents were measured using a spectrophotometer on a set of 10 samples acquired during the overflight. Grain-sizes analyses were performed using LS230 laser particle-sizer (© Beckman Coulter). Grain size parameters (mean, sorting and skewness), sedimentary facies and classes were calculated using the GRADISTAT software (Blott and Pye 2001) following the Folk and Ward (1957) methods.

Multispectral remotely sensed data (SPOT 6/7 and S2) were acquired more or less 30–60 min after the airborne overpass (Fig. 2). While LiDAR data were acquired simultaneously with the hyperspectral images (HySpex'sensor) we can assume that topography and main geomorphic structures did not affected by significant changes from an image to another one, at least in the inner estuary. Such as multi-sensors configuration is judged to be really rare and it offers us the opportunity to map sedimentary facies under topographic controlled during the immersion time.

SPOT6/7 image was ordered in the frame of the GEOSUD program. Initially the multispectral bands (6 m/pixel) were pan-sharpened to the panchromatic one (1.5 m/pixel) for enhancing the spatial resolution of all spectral bands to 1.5 m/pixel using the Gram –Schmidt pan-sharpening technique (Laben and Bower 2000). Then, raw images were calibrated and corrected from atmospheric effects using the FLAASH method. With a spatial resolution of 1.5 m/pixel (Table 1), the spatial resolution is sufficient to discriminate accurately sedimentary structures of bedforms such as sedimentary bars, mega-ripples, creeks, sea-channel, etc.

Sentinel-2 sensor was operated belong ESA (European Spatial Agency) and delivered throughout the THEIA platform into a L2A format following the MAJA method (Hagolle et al. 2010). MAJA is an evolution of MACCS (Multi-sensor Atmospheric Correction and Cloud Screening), in which a couple of methods inspired by ATCOR

software have been added. With a spatial resolution of 10–20 m per pixel, the resolution is not sufficient to discriminate accurately all sedimentary structures at fine-scale such as some of the mega-ripples. However, S2 is well-suite for mapping meso-scale structures such as sandy spit, main channel, ridges and runnels, some of the mega-ripples, etc.

Hyperspectral images were acquired with a HySpex Visible Near InfraRed (VNIR) 1600 camera having a spectral resolution of 4.5 nm in 160 spectral channels between 400 and 1000 nm. Simultaneously, topographic data were acquired with the LiDAR platform of Nantes-Rennes universities with a spatial resolution of 1 m/pixel. Fly conditions was set-up for maximizing the spatial resolution of hyperspectral data at 0.7 m per pixel. Atmosphere correction was performed with the ATCOR 4/ MODTRAN. A Minimum Noise Fraction (MNF) transformation (Green et al. 1988) was applied to images to reduce noise from signal.

A digital terrain model (DTM) was generated with a spatial resolution of 1 m per pixel (Fig. 3). In addition, GNSS data (2273 ground control points) were used for minimizing error in areas covered dense vegetation. DTM correction was performed based on a linear regression approach between LiDAR data and GNSS ground control

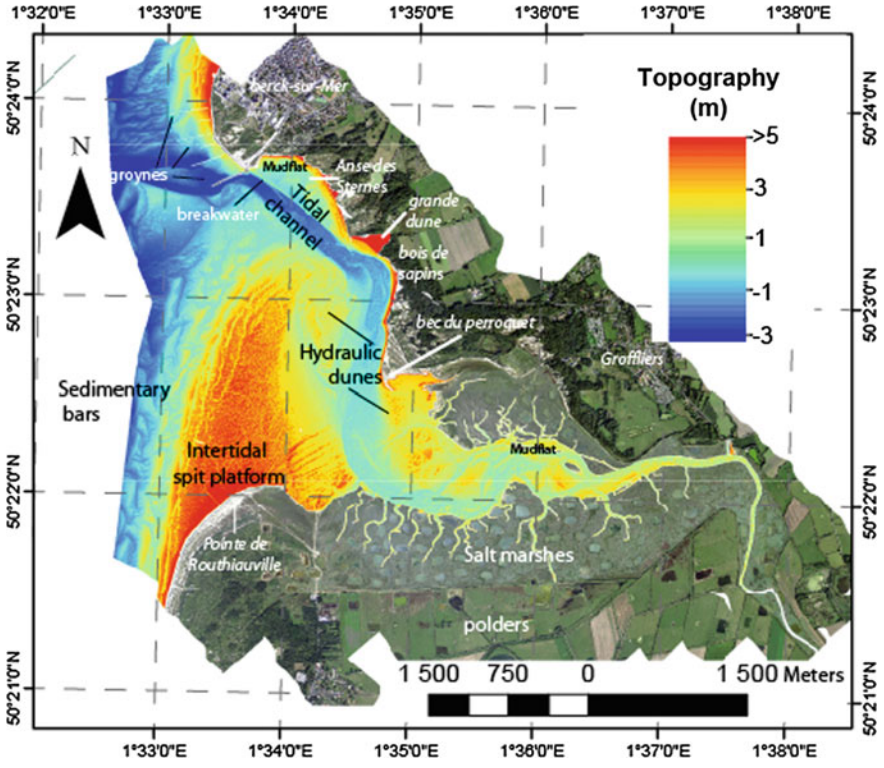

Fig. 3 Morphology map of the Authie estuary generated from LiDAR data, 21st of September 2016

points (y = 1.005–0.39, R^2 = 0.99, RMSE = 0.386). Figure 3 displays the bay morphology including ridge and runnels, crest of sedimentary bars, hydraulic dunes, salt marshes, etc. In addition, in the framework of the SNO DYNALIT previous a LiDAR topographic data (ALS60 LiDAR, © Leica Geosystems) was acquired in December 2013 by the Circle operational teams. The planimetric position accuracy of the data points range from ±0.10 to 0.17 m with a vertical accuracy b ± 0.10 m as verified by several ground control points. In this study we only compare the 2016 LiDAR data to the 2013 one. Topographic discrepancies were computed for interpreting the morpho-sedimentary dynamics and characteristics of the sea-bed estuary.

With the intention to derive maps of sediment parameters, several spectral models were used according to the spectral resolution. When mapped with multispectral sensors, biomass is usually expressed in NDVI (Normalizes Differential Vegetation Index, Tucker 1979) values. Another spectral index called MPBI index was proposed by Méléder et al. (2010) to distinguish MPB from macrophytes. In this study, two methods were tested. Combe et al. (2005) developed a non-linear unmixing model for hyperspectral data based on MGM (Modified Gaussian Model) continuum removal. Even if this model is recognized to be well-appropriate for very high spectral resolution data, we tested a similar approach designed for multispectral data. Basically the developed approach stills the same except that we didn't perform any continuum removal prior to derive biomass and it is based on a linear unmixing approach. For simplicity, this method was called LMM for Linear Mixing Method. Compared to spectral indices methods, LMM has the advantage to integrate sandy and muddy surfaces into the mixing itself.

However, when mapped with hyperspectral resolution, advanced spectral model may be used allowing to analyze the full shape of continuous reflectance spectra and narrow absorption bands characteristics with respect to different MPB groups (Combe et al. 2005). In the framework of the OMPBI project, a radiative transfer algorithm called MPBOM (MicroPhytobenthos Optical Model) was applied with hyperspectral data (Launeau et al. 2018). While many biomass products could derived from this model, here the latter was only used to retrieve the biofilm absorption coefficient α which was linearly related to biomasses. Then, MPBOM outputs were briefly compared to the unmixing algorithm outputs.

With the intention to compare maps of grain-size and water content parameters for each of sensors used, we decided to apply a simple multispectral algorithm (see *more detailed in appendices*) based on spectral features and in situ measurements of collocated sediment surfaces. Basically, algorithms consisted in confronting in situ measurement (mean grain-size) to reflectance value of the images. For such as comparison, hyperspectral images were resampled to the SPOT 6/7 spectral resolution.

4 Results

4.1 Morphology of the Seabed

Surface elevation evolution can be retrieve using LiDAR data acquired at different periods. Topographic differences enable us to quantify precisely the relative sedimentary budget trend. Crapoulet (2015) calculated a positive budget for the overall Authie estuary from LiDAR data acquired between 2008 and 2011 about 827,162 m^3 (+0.08 m^3/m^2). Conversely, they calculated a negative budget for the overall Authie estuary from LiDAR data acquired between 2011 and 2013 about −569,529 m^3 (−0.05 m^3/m^2). As a consequence, between 2008 and 2013 there is a volumetric gain of +111,191 m^3 (+0.01 m^3/m^2).

We propose here to revise the budget number by integrating new LiDAR data acquired during the OMPBI survey from 2013 to 2016. Basically DTMs relative map differences were computed exhibiting a sea-bed dynamics allowing to identify erosion (blue-yellow-orange) and accretion (in red) zones. The relative sedimentary budget remains negative over the overall estuary (Mean = −0.41 ± 0.859 m^3/m^2) which is consistent with Crapoulet (2015) study. Indeed, a negative budget for the overall Authie estuary from LiDAR data acquired between 2011 and 2013 about −219,239 m^3 (−0.04 m^3/m^2). As a consequence, between 2008 and 2016 there is a volumetric loss of −108,048 m^3 (−0.02 m^3/m^2). Consequently the net changes in elevation surface between 2008 and 2016 reveals a significant loss of volume on the overall estuary.

Because ridge and runnels (sedimentary bars) and mega-ripples systems are highly dynamics from a tidal cycle to another one, they are not representative of the sedimentary budget for such a long period ~3 years. Intentionally we do not consider them into our sedimentary budget and we restricted our calculations to several representative zones within the inner estuary ('Bois de Sapins', mudflats, 'Anse des Sternes', 'Bec du Perroquet', middle estuary and spit platform).

Observations (Fig. 4) are consistent with literature as the 'Bois de Sapins' is affected by strong erosion (blue color) with a decrease of elevation ranging from −9 to 3 m (Mean = −1.2 ± 1.3 m^3/m^2). This is explains by the fact that the estuary mouth is largely blocked by the prominent sand spit platform, and this has forced the Authie channel of the estuary to flow along the northern shore. As the consequence, this zone concentrates a maximum of energy. Despite that the anthropic area called 'Anse des Sternes' is well protected from waves and currents with breakwater and groynes structures, the sedimentary budget is slightly negative with an elevation ranging from −6 to 0.8 m (Mean = −0.5 ± 0.2 m^3/m^2). The eastern part of the 'Bec du Perroquet' presents slight negative elevation variations with an elevation surface ranging from −2.3 to 1.5 m (Mean = −0.23 ± 0.27 m^3/m^2). Natural mudflats located along the northern salt-marches are affected by a slight erosion (yellow color) with a decrease of elevation ranging from −2 to 0.65 m (Mean = −0.3 ± 0.3 m^3/m^2). The spit platform budget is slightly negative with an elevation ranging from −1.6 to 1.0 m (Mean = −0.41 ± 0.01 m^3/m^2). Negative budgets observed in mudflats, spit and

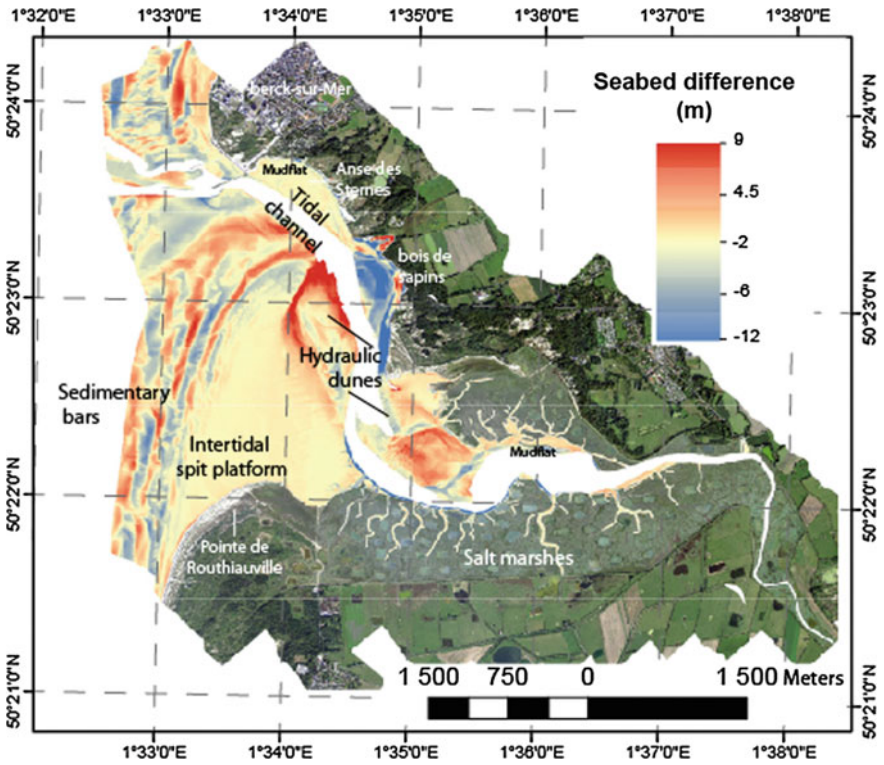

Fig. 4 Net changes in surface elevation between December 2013 and September 2016 based on LiDAR topographic data

anywhere else can be explained by the fact that the sediment supply may decrease over time explaining that there is less deposits or that the sediment compaction processes might more efficient.

While the overall estuary presents a negative budget, several zones are clearly affected by accretion such as the middle estuary and the north of the backside part of the spit. In the middle estuary, there is a positive elevation (in red) variation ranging from -1.3 to 1.3 m (Mean $= 0.25 \pm 0.30$ m^3/m^2). This positive budget can be explained by the fact that the allochthonous sediments coming from the maritime side and autochthonous sediments coming from erosive sites may increase over time due to high sedimentary transit during the flood-tide and thus until their deposits. To conclude some sediment accumulations occurred downdrift to the south, but only took place at middle estuary. The backside of the spit platform budget presents a positive budget (in red) mainly in the northern part with an elevation ranging from -0.83 to 2.8 m (Mean $= 1.0 \pm 0.6$ m^3/m^2). This may be explained by the fact that the spit is prograding toward the N–W part of the bay. In addition, reworking sediments coming from the erosion sites may contribute of some sediment accumulations downdrift to the south, but only took place at tip of northern spit.

Finally, regarding the supratidal domain, 'la Grande Dune', a parabolic dune seems to be in accretion at the top due to Aeolian deflation inputs which may coming from intertidal sandy bars, generally drier than the rest of intertidal sediments. The bottom part of this dune is in erosion. With a ranging from −10 to 9 m (Mean = −0.65 ± 2.40 m^3/m^2) the overall budget is slightly negative.

4.2 MPB Spatial Distribution Mapping

As mentioned before a LMM spectral model was applied at multispectral resolution sensors allowing to compare biomass output products together (Fig. 5). Whatever the sensor used MPB generally occurs over fine sediment substrates such as very fine-sands or silts. High MPB concentrations are mainly present on mudflat sediments ('Anse des Sternes' and along salt-marshes). In details, MPB was locally observed at the bottom of mega-ripples with respect to the spatial resolution of the sensors. This is explained by the fact that grain-size may slightly decrease and that moisture content is generally higher compare to mega-ripple crests. Surprisingly, MPB also occurs on most part of the spit. Despite that the spit structure is mainly composed by sandy sediments (135 ± 40 μm; HySpex), it is possible to observed a very thin layer composed by muddy sediment covering the sand substrates. This might appear when tide energy becomes lower during low tide. However, it is well-known that MPB distributions are not only a function of the sediment cover-type (sand or mud), it may also vary in time and space as a function of numerous factors like: time of emersion, solar energy, and nutrients inputs, etc. Because images were acquired at various times of acquisitions at the same day, sensors synergy offers us a unique opportunity for mapping the evolution of the MPB distribution during a tidal cycle especially at the emersion time. Figure 5 exhibits strong spatial variation in biomass concentrations which means that MPB migration is highly dynamic at short time during aerial exposure. It seems that the MPB concentration spatially decrease from 10:00 to 13:00 UTC+2 which means that the maximum of MPB production is observed with a mean value of 27 ± 19 $mg.m^{-2}$ during the HySpex overpass (Fig. 5a) while the minimum of MPB production (Fig. 5b) is observe during the S2 overpass (Fig. 5c) with a mean value of 17 ± 13 mg m^{-2}. Intermediate values are observed during the SPOT 6/7 overpass (Fig. 5b) with a mean value of 21 ± 18 mg m^{-2}. Note that the MPB variability was correlated to the PAR (Photosynthetically Active Radiation) values. Although these general patterns reveal a decrease in biomass coverages, in details some patches do not follow this trend. Clearly the S2 image reveals some patches with higher chlorophyll-a content than the SPOT6/7 or HySpex ones.

Although MPB production seems to be correlate to the solar radiation changes as a first order, other parameters may have a significant influence on it. Indeed, it is known that MPB migration may be influenced by the tidal range. For example, we denote that during the S2 overpass, the flood-tide coming back in the western part of the upper estuary, as a consequence it may induce an impact in our estimates. On the other hand, spatial resolution may also have a significant impact on MPB estimates due to

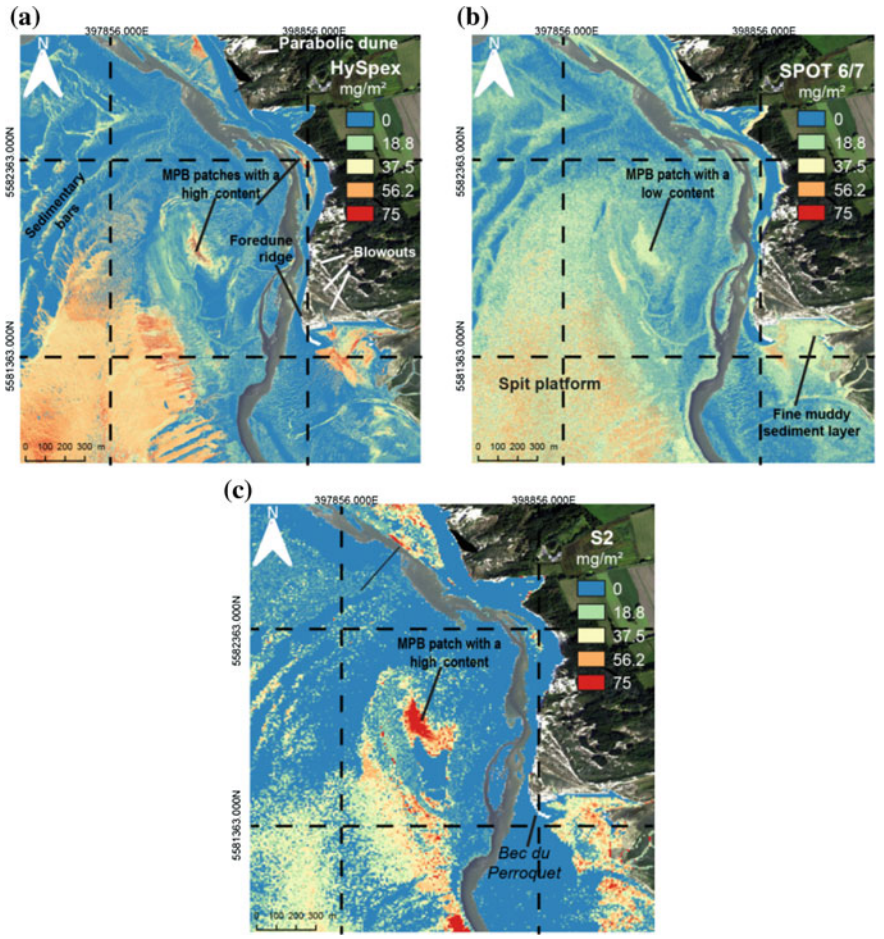

Fig. 5 Maps representing the net primary production (in mg m^{-2}) at low tide (09/21/2016) from **a** HySpex VNIR; **b** SPOT 6/7 and **c** S2 data and by applying the Liner Mixing Model (LMM)

non-linear mixing between natural surfaces within a pixel. Because, S2' resolution is coarser than SPOT 6/7 (with a factor ~3) and HySpex ones (with a factor ~14), the probability that MPB covers are mixed with abiotic surfaces (e.g. sand or mud) is pretty high. As a result, biomasses may be underestimated. It is one of the reasons why more advanced methods such as non-linear unmixing model (Combe et al. 2005) or none-scale dependent approaches such as the MPBOM (Kazemipour et al. 2012) still desirables. However, those methods cannot be applied on multispectral data.

MPBOM was applied to hyperspectral HySpex images in the framework of the 'Défi littoral OMPBI' project. Among biomass products (coefficient of absorption, peak of the Chl-a, biomass of the MPB) the distribution of the absoption coefficient peak at 673 nm was analyzed. Figure 6 display the total chlorophyll-a distribution

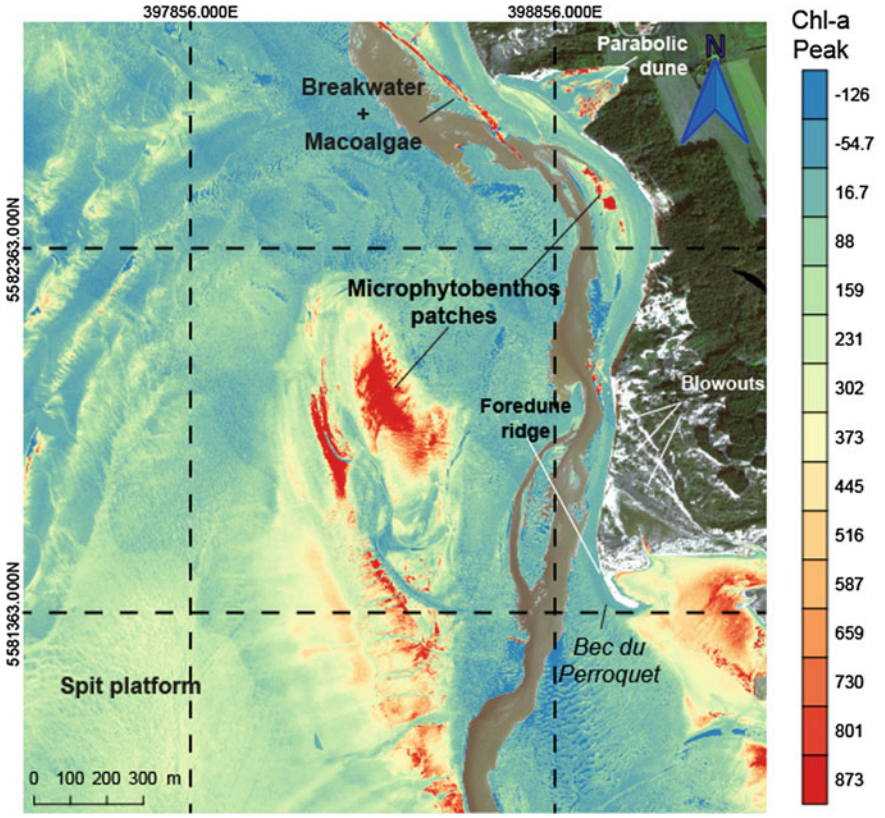

Fig. 6 Map representing the peak of the absorption coefficient at 673 nm during low tide (09/21/2016) from HySpex VNIR data and by applying the MPBOM in the framework of the 'Défi littoral OMPBI' project

deriving from the absoption coefficient peak at 673 nm. High absorption contents are observed on the breakwater. High chlorophyll contents composed by microphytobenthos are generally observed in the backside of the spit platform and muddy sites. As mentioned before, during the airborne campaign 10 samples were collected for calculating the chlorophyll-a concentration and compared them at the pixel location of the HySpex data. MPBOM pixels are positively correlated with these samples ($R^2 = 0.57$). However, for better assessment more samples are needed. MPBOM product (Fig. 6) exhibits clearly strong discrepancies with the LMM (Fig. 5a), especially over the spit whereas similar trend is observed with S2 data especially over some patches (Fig. 5c).

Because MPBOM take into account non-linear mixing effects, we can assume that non-linear effects may induce an overestimation of the biomass with multispectral models used here.

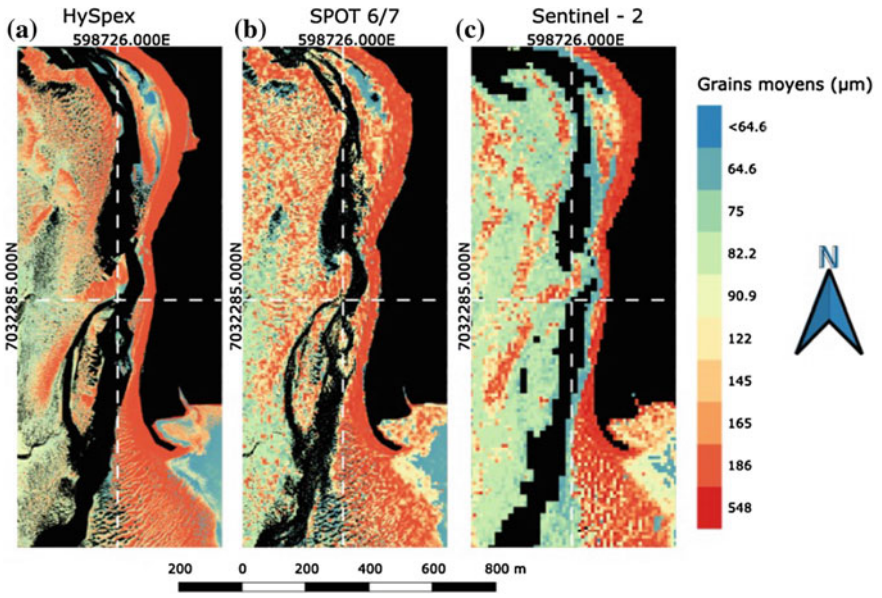

Fig. 7 Maps representing the grain-size distribution (in µm) at low tide (09/21/2016) from A) HySpex VNIR; B) SPOT 6/7 and C] S2 data and by applying experimental spectral model

4.3 Physical Properties of Surficial Sediments

As mentioned before an experimental spectral model was applied at multispectral resolution sensors allowing the comparison of physical properties (grain-size and moisture content) products together. Whatever the sensor used, grain-size (Fig. 7) and moisture content (Fig. 9) display similar patterns with a high spatial correlation.

Grain-size product validations were performed using true field data as reference. During the airborne campaign among the overall collected samples, 26 samples were analyzed using Coulter LS230 laser particle-sizer for calculating the mean grain-size and compared them at the pixel location of the satellite images. RMSE calculations ($RMSE_{HySpex} = 52$ µm; $RMSE_{SPOT\ 6/7} = 40$ µm and $RMSE_{S2} = 44$ µm) reveals that the range of variation between pixel values and true field data is quite low providing reasonable estimates for differencing sediment surface fraction sizes.

In Fig. 7, coarse sediments (red color) are observed on beaches, on the crest of mega-ripples, on sediment sandy bars, spit, and dunes where topography values are relative higher than the rest of the slikke (green-blue color). Locally, coarse sediments are present in shell beds deposit. The intertidal domain is mostly composed by fine sand and very fine sand sediments (~85%). Silty sediments are particularly observed on mudflat (blue color) where hydrodynamic conditions are low in energy. Mean grain-size of the Authie Bay reaches an average of 120 ± 50 µm of 170 ± 70 µm of 160 ± 70 µm at the HySpex, SPOT 6/7 and S2 resolutions. S2 image displays a large amount of fine-sediments pixels (in green) in comparison with the HySpex

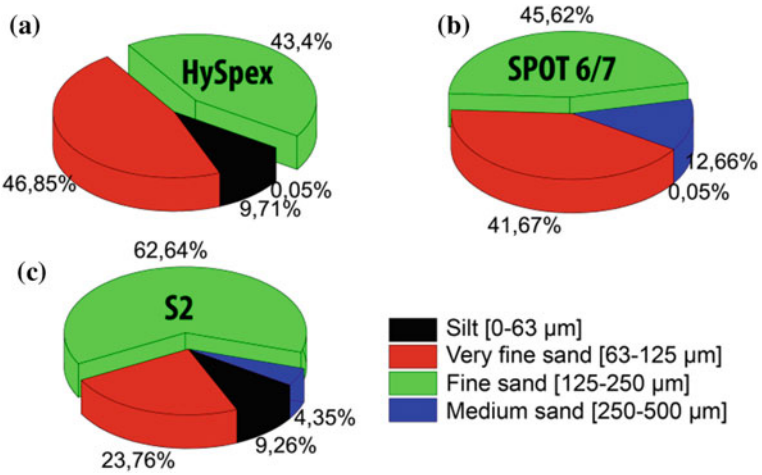

Fig. 8 Pie diagrams representing the grain-size distribution (in %) for each sensor: A) HySpex VNIR; B) SPOT 6/7 and C] S2 images

image which display coarser sediment pixels (in red). The SPOT 6/7 image displays intermediate values (in orange). With respect of the spatial resolution used, grain-size products display some major discrepancies. Indeed the coarser the spatial resolution is, the coarser the grains-size is (Fine sand + medium sand).

Whatever the sensor used (Fig. 8), fine sand sediments represent the grain-size fraction which is thee more abundant (HySpex: 43%, SPOT 6/7: 45% and S2: 62%) followed by very fine sands (HySpex: 46%, SPOT 6/7: 41% and S2: 23%) silts (HySpex: 9%, SPOT 6/7: 45% and S2: 62%) an medium sands (SPOT 6/7: 12% and S2: 9%).

Accordingly, grain-size products are impacted the spatial resolution of the sensors which might lead to an overestimate or an underestimate in the final products. Again, this explained by the non-linear unmixing effect which is not taking into account with experimental spectral model developed. Contrary to microalgae surfaces which are highly dynamic over time, grain-size fractions should not exhibit strong changes during the low tide, even slightly reworking may locally appear (e.g. grazing, feeding). As a consequence, we can assert that spectral resolutions and scale factors are respectively main factors explaining those discrepancies.

In Fig. 9, dry sediments (red color) are observed on beaches, on crests of mega-ripples, on sediment sandy bars, spit, and dunes where topography is relative higher than the rest of the slikke (green-blue color). Very moist-sediments are observed in mudflats. It is not rare to observe a thin surficial water layer over sediment substrates. Water content is widely influenced by the porosity of sedimentary structures as well as time of aerial exposure during a tidal cycle. It is clear that grain-size patterns are spatially correlated to water content patterns. This is simply explained by the fact that coarser sediments are drier than silty sediments due to the higher efficiency in the percolation process. Water content products are also influenced spectral resolutions of

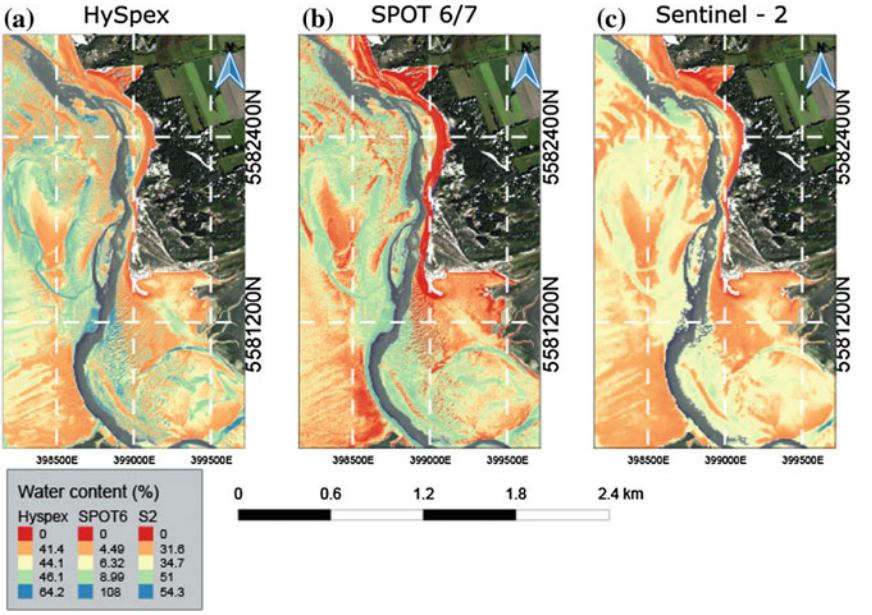

Fig. 9 Maps representing water content (in %) at low tide (09/21/2016) from **a** HySpex VNIR; **b** SPOT 6/7 and C] S2 data and by applying experimental spectral model

sensors used. Some of the S2 water-pixels seems to be underestimated in comparison with the HySpex and SPOT 6/7 ones.

5 Conclusions and Perspectives

The following conclusions may be made from this study:

i. Net changes in surface elevation between December 2013 and September 2016 based on LiDAR topographic data were computed allowing to revise formal sedimentary budgets. We demonstrated that the Authie Bay is affected by a relative loss of volume between 2008 and 2016 with a sediment loss of −108,048 m^3 (−0.02 m^3/m^2) over the overall Authie estuary. Based on LiDAR data acquired between 2013 and 2016, a significant loss of volume was calculated about −219,239 m^3 (−0.04 m^3/m^2). To summarize, the sedimentary budget was highly positive between 2008 and 2011, negative between 2011 and 2013 (Crapoulet 2015) and remains negative between 2013 and 2016 (this study). The remaining question is what mechanisms control the sediment supply within the Authie Bay? It might be driven by the fact that there is less sediments inputs likely due to a decrease of the Holocene stocks in the subtidal domain or it might be a response of the spit extension which protects the inner estuary from natural

sediment supply. Consequently the bay infilling might be caused by a decrease of tidal energies or currents within the estuary resulting with an increase of mud deposits along salt marshes, an infilling of the secondary channels across the salt-marches and a salt-marches prograding.

ii. In details all domains present negative sediment budgets except in the middle estuary and in the tip of the spit. However, it is well-known that the Authie bay is affected by a general infilling while locally some sites appear to be eroded between 2013 and 2016 such as the '*Bois de sapins*' site. However, it is reasonable to mention that such as analyze is relative as the morphology of the bay may drastically change with storm impacts for example. It is difficult to calculate an absolute budget at high frequency using few LiDAR data following a longer time serie. In that sense, UAV acquisitions combined to photogrammetry analysis may help to fill the gap of information.

iii. We demonstrated that is possible to map sediment bio-physical properties using both hyperspectral and multispectral data (HySpex, SPOT 6/7 and S2). We proposed to use LMM with multispectral data and MPBOM with hyperspectral data. Whatever the approach used, spatial patterns of bio-physical properties exhibited are spatially consistent with field observations and laboratory measurements and our knowledge of sedimentary processes. Whatever the sensor used, grain-size distributions and water content reveal similar patterns. Grain-size and water content are spatially highly correlated with topography. However, further investigation still needed for fully understand the role of the geomorphic structures on sediment deposits as well as the net primary production. As perspectives, grain-size maps may be used as inputs of transport models (like GSTA, 3D models, etc.) and thus for computing transport trends. Moisture content is also an important parameter to consider as the latter may be used for improving our knowledge about the cohesive behavior, the role of the Aeolian deflation over the intertidal sandy bars towards dunes in accretion for instance, etc. Finally, it is crucial to assess the distribution of microphytobenthos as the latter influence the bio-stabilization processes and thus the reworking of intertidal sediments.

iv. Regarding the biomass products, data generated from LMM may be overestimated particularly on the spit compared to MPBOM product. As a consequence, spectral algorithm choice differs from the sensor used. This may be explained by the fact that both non-linear mixing effects and scale factors are not taking into account with multispectral models.

v. Multispectral experimental models were developed with the intention to compare images each other. Developed algorithms were based on a learning dataset approach by confronting spectral behaviors directly to physical properties of the sampled sediments. Although we do not demonstrated that these algorithms are not reproducible to other coastal domains, in the frame of this study they remain useful for improving our understanding of the estuary evolution during a low tide cycle. In that sense, the synergy between various sensors presents some interesting advantages. For instance, it seems possible to predict net primary budget over time by analyzing data at various time of acquisitions. However,

with the intention to determine the impact of the non-linear mixing effect on products more similar assessments are needed.

vi. To conclude, when a long time serie is available such as the multispectral S2-MSI or Landsat-OLI images, it becomes possible to better understand some processes like erosion and sandfilling interactions over time. With a high revisiting time over the same scene (5–10 days), Sentinel-2 data would be particularly well-adapted for assessing effects of seasonal variation or storm events and their respective geomorphic variations. L8 have a temporal resolution of 16 days per scene acquired. Note that Landsat serie is known to be the longest time-serie available in remote sensing starting from 1972 with Landsat-1 platform to now with Landsat-8 platform. It would be interesting to process such as data for better assessing the infilling of picard estuaries.

Acknowledgements We would like to thank the CPER-MARCO and the BQR-ULCO-TéléEST for their funding supports allowing some of the field investigations within the Bay of Authie.

Some of the image computations were performed on resources provided by the SCOSI/ULCO (Service Commun du Système d'Information de l'Université du Littoral Côte d'Opale) Infrastructure for Computing through CALCULCO platform under the TéléEST project.

This work was supported by public funds received in the framework of GEOSUD, a project (ANR-10-EQPX-20) of the program "Investissements d'Avenir" managed by the French National Research Agency which allow us to collect SPOT 6/7 images.

Hyperspectral and 2016 LiDAR data were acquired in the frame of the Défi Littoral 2016 de la Mission pour l'interdisciplinarité du CNRS. The 2013 LiDAR data were obtained through the interregional program CLAREC funded by the Regional Councils of Normandy, Picardie and Nord-Pas de Calais and by the French Centre National de la Recherche Scientifique (CNRS).

Appendice 1: Grain-Size Algorithm Used for Mapping

With the intention to derive map grain-size properties from remotely sensed data, a spectral algorithm was computed based on the matching technique between field sampling (grain-size value) and spectral information (reflectance values) for each of sampling pixels. Mean grain-size is computed such as (Eqs. 1 and 2):

$$Coarse = 215.30 * \log\left(\frac{R_{red} - R_{green}}{R_{NIR} - R_{bleue}}\right) + 290.69 \quad (1)$$

$$Fine = \left|-121.17 * \left(\frac{R_{red} - R_{green}}{R_{NIR} - R_{bleue}}\right) + 290.69\right| \quad (2)$$

where:

R_X Reflectance values for a spectral channel.

These two resulting maps (fine fraction and coarse fraction maps) were merges for obtaining a mean grain-size map. Merging criteria was defined by the following

ratio (Eq. 3):

$$Ratio = \frac{R_{red} - R_{green}}{R_{NIR} - R_{red}} > X \tag{3}$$

where:

X Muddy/Sandy ratio, empirically fixed by the operator. (for this study, X range from 0.20 to 0.25).

Appendice 2: Water Content Algorithm Used for Mapping

With the intention to derive maps of water content from remotely sensed data, a spectral algorithm was computed based on laboratory measurements flowing the Verpoorter et al. (2014) approach. It consists in measuring reflectance response during dehydration process from representative sediments. Then, the resulting spectral behavior was modelled using an exponential regression function by selecting the red wavelength channel which is known for responding well to the water content changes ($R^2 = 0.77$; $P < 0.0001$). Finally, the resulting model was applied at the remotely sensed images following the Eq. (4):

$$[H_2O]\% = 87.42 * \exp^{\left(-R_{red}/0.07\right)} - 3.61 \tag{4}$$

References

Adam, S., De Backer, A., De Wever, A., Sabbe, K., Toorman, E. A., Vincx, M., et al. (2010). Biophysical characterization of sediment stability in mudflats using remote sensing: A laboratory experiment. *Continental Shelf Research*. https://doi.org/10.1016/j.csr.2009.12.008.

Blott, S. J., & Pye, K. (2001). GRADISTAT: a grain-size distribution and statistics package for the analysis of unconsolidated sediments. *Earth Surf. Processes Landforms, 26,* 1237–1248.

Briquet, A. (1930). Le littoral du nord de la France et son évolution morphologique, suivi d'un appendice, l'évolution du rivage du Nord de la France et l'activité de l'homme, Revue du Nord, 16, N°64, 313–319, ISSN: 0035–2624

Crapoulet, A. (2015). Evolution du trait de côte, bilan sédimentaire et évaluation des zones à risques sur le littoral du Nord-Pas-de-Calais: Analyse multiéchelles par LiDAR aéroporté. *These de doctorat en Geographie Physique. Wimereux: Universite du Littoral Cote d'Opale*.

Combe, J. P., Launeau, P., Carrere, V., Despan, D., Meleder, V., Barillé, L., et al. (2005). Mapping microphytobenthos biomass by non-linear inversion of visible-infrared hyperspectral images. *Remote Sensing of Environment, 98,* 371–387. https://doi.org/10.1016/j.rse.2005.07.010.

Deloffre, J., Verney, R., Lafite, R., Lesueur, P., Lesourd, S., & Cundy, A. B. (2007). Sedimentation on intertidal mudflats in the lower part of macrotidal estuaries: Sedimentation rhythms and their preservation. *Marine Geology, 241,* 19–32. https://doi.org/10.1016/j.margeo.2007.02.011.

Deronde, B., Houthuys, R., Henriet, J.-P., & Lancker, V. V. (2008). Monitoring of the sediment dynamics along a sandy shoreline by means of airborne hyperspectral remote sensing and LIDAR: A case study in Belgium. *Earth Surface Processes Landforms, 33,* 280–294. https://doi.org/10.1002/esp.1545.

Dobroniak, C. (2005). Morphological evolution and management proposals in the Authie Estuary, northern France. *Proceeding Dunes and Estuaries, 2205,* 537–545.

Folk, R. L., & Ward, W. C. (1957). Brazos river bar: A study in the significance of grain-size parameters. *Journal of Sedimentary Petrology, 27,* 3–26.

Green, A. A., Berman, M., Switzer, P., & Craig, M. D. (1988). A transformation for ordering multispectral data in terms of images quality with implications for noise removal. *IEEE Transactions on Geoscience and Remote Sensing, 26*(1), 65–74.

Hagolle, O., Huc, M., Villa Pascual, D., & Dedieu, G. (2010). A multi-temporal method for cloud detection, applied to FORMOSAT-2, VENμS, LANDSAT and SENTINEL-2 images. *Remote Sensing of Environment, 114*(8), 1747–1755.

Hesp, P. A., Ruz, M.-H., Hequette, A., Marin, D., & Miot da Silva, G. (2016). Geomorphology and synamics of a travelling cuspate foreland, Authie estuary France. *Geomorphology, 254,* 104–120. https://doi.org/10.1016/j.geomorph.2015.11.015.

Kazemipour, F., Launeau, P., & Méléder, V. (2012). Microphytobenthos biomass mapping using the optical model of diatom biofilms: Application to hyperspectral images of Bourgneuf Bay. *Remote Sensing of Environment, 127,* 1–13.

Launeau, P., Méléder V., Verpoorter, C., Barillé, L. Kazemipour F., Giraud, M., et al. (2018). Microphytobenthos biomass and diversity mapping at different spatial scales with hyperspectral optical model. *Remote Sensing, 10*(5), 716.

Laben, C. A., & Bower, B. V. (2000). Process for enhancing the spatial resolution of multispectral imagery using pan-sharpening. US Patent 6.011875.

Méléder, V., Launeau, P., Barillé, L., Combe, J. P., Carrère, V., Jesus, B., et al. (2010). Hyperspectral imaging for mapping microphytobenthos in coastal areas. In M. Maanan & M. Robin (Eds.), *Geomatic solutions for coastal environments* (pp. 71–139). New York: Nova Science Publishers Inc.

Rainey, M. P., Tyler, A. N., Gilvear, D. J., Bryant, R. G., & McDonald, P. (2003). Mapping intertidal estuarine sediment grain size distributions through airborne remote sensing. *Remote Sensing of Environment, 86,* 480–490. https://doi.org/10.1016/S0034-4257(03)00126-3.

Small, C., Steckler, M., Seeber, L., Akhter, S. H., Goodbred, S., Jr., Mia, B., et al. (2009). Spectroscopy of sediments in the Ganges-Brahmaputra delta: Spectral effects of moisture, grain size and lithology. *Remote Sensing of Environment, 113,* 342–361. https://doi.org/10.1016/j.rse.2008.10.009.

Smith, G. M., Thomson, A. G., Moller, I., & Krompkamp, J. C. (2004). Using hyperspectral imaging for the assessment of mudflat surface stability. *Journal of Coastal Research*, *20*(4), 1165–1175. West Palm Beach (Florida). ISSN 0749-0208.

Sogreah, (2009). Diagnostic, étude d'opportunité et de faisabilité pour l'aménagement de la rive Nord de l'Authie. *Rapport provisoire. Communauté de Communes Opale Sud*.

Tucker, C. J. (1979). Red and photographic infrared linear combinations for monitoring vegetation. *Remote Sensing of Environment, 8,* 127–150. https://doi.org/10.1016/0034-4257(79)90013-0.

Ubertini, M., Lefebvre, S., Gangnery, A., Grangeré, K., Gendre, R. L., & Orvain, F. (2012). Spatial variability of benthic-pelagic coupling in an estuary ecosystem: Consequences for microphytobenthos resuspension phenomenon. *PLoS ONE, 7,* e44155.

Verpoorter, C., Carrère, V., & Combe, J. P. (2014). Visible, near-infrared spectrometry for simultaneous assessment of geophysical sediment properties (water and grain size) using the Spectral Derivative–Modified Gaussian Model. *Journal of Geophysical Research : Earth Surface, 119*, 2098–2122. hal- 01130379.

New Perspectives in the Monitoring of Marine Sedimentary Transport by Satellites—Advantage and Research Directions

Vallette Anne, Jackson Jan, Mangin Antoine, Jaegler Thomas and Martin-Lauzer François-Régis

Abstract Advances in satellite data, revisit times, computing capacity and processing speed are on their way to deliver a revolution in the monitoring and management of coastal erosion due to systematic remote sensing of the shoreline from space. This represents, and enables further, major progress on a far greater scale than the current state of the art. European public satellites of the Sentinel Constellation (Sentinel-1 and Sentinel-2) of the COPERNICUS program currently offer a revisit time of (i) five days with four satellites under the same viewing conditions, for bathy-topography investigation of the shoreline, i.e. from the continental shelf-break to the foreshore, (ii) a few days at mid latitudes but from different points of view, and (iii) almost daily at higher latitudes. The low resolution (5-to-20 m) of the radar & VNIR components of the time-series is mitigated by high spectral density that allows a true spectral analysis of the earth surface and waters, after appropriate corrections, i.e. removal of atmospheric scattering, sun glint and white caps effects, geometric configuration due to the anisotropic bidirectional soils & waters reflectance distribution function (BRDF). New tools in open source like the SNAP toolbox or interfaces like Coastal Thematic Exploitation platform allow public labs and companies to benefit from this breakthrough in data acquisition, rapid processing or database collection. Via remote

V. Anne (✉)
French Branch of ARGANS Ltd., 260 route du Pin Montard, BP234, 06904 Sophia Antipolis Cedex, France
e-mail: avallette@argans.eu

J. Jan · M.-L. François-Régis
ARGANS Ltd., Chamberlain House, 1 Research Way, Devon, Plymouth PL6 8BU, UK

M. Antoine
ACRI-EC, Casa Abdelmoumen Business Centre, Immeuble Atrium, n374 lotissement Manazyl ALMaymoune Boulevard Abdelmoumen, 20100 Casablanca, Morocco

J. Thomas
ARCTUS Inc., 24 rue des Pins Sud, Sainte-Pétronille, QC GOA4C0, Canada

M.-L. François-Régis
AdwäisEO, 11, Rue Pierre Werner, L-6832 Betzdorf, Luxembourg

ACRI-ST 260 route du Pin Montard, BP234, 06904 Sophia Antipolis Cedex, France

K. D. Nguyen et al. (eds.), *Estuaries and Coastal Zones in Times of Global Change*, Springer Water,
https://doi.org/10.1007/978-981-15-2081-5_46

sensing techniques, time series of seafloor bathymetry and suspended sediment in the water column can be derived from optical (spectral analysis) and SAR imagery (correlation between radar cross section changes and Bragg scattering of the water-foreshore surface for the assessment of the errors). It complements, when required, Very High Resolution (VHR) surveys made on order with commercial imagery, (or dug out from archives), aerial LiDaR (Light Detection and Ranging) with planes or drones, or depths sounders (on launches) and topographic instrumentation for beach profiling. Yet, the current swarms of nanosatellites such as Planet/Doves give access to systematic VHR cover of the earth. Such work can be carried out in the frame of national programs such as LITTO3D or regional/local programs.

Keywords Earth observations by satellites (EO) · Shoreline · Sediment load · Satellite-Derived bathymetry · Sentinel-1 & 2 · Erosion-Accretion

1 Introduction

To characterise coastal erosion, or accretion phenomenon, we need not only to extract an accurate shoreline area from datasets, but also assess the volume of materials involved in the spatio-temporal changes, and to describe the phenomena. The first indicator is the shoreline containing a number of different measurement parameters within it, from the high water mark to the low astronomical tide. In a critical review of 45 scientific papers, 28 different definitions of the shorelines indicator were reported (Boak and Turner 2005): from the bluff/cliff top (Moore et al. 1999) to mean lower water line (Fisher and Overton 1994). Most authors define the shoreline as the position of the land-water interface at one instant time, i.e. the waterline. But, in case of zones subject to tidal cycle, the position of the waterline varies between centimetres to hundreds of meters, depending on the beach slope, tidal range, and meteorological conditions (e.g. pressures, waves). Boak and Turner (2005) categorized shoreline indicators in three groups: visible discernible features, tidal datum-based indicators and indicators based on the processing technique to extract the shoreline. For the first group, the high water line is the preferred indicator for photo interpretation. For the second, the tidal datum-based shoreline indicator is determined by the intersection of the coastal profile with a specific vertical elevation, defined by the tidal parameters such as mean high water (MHW), mean sea level or mean lower low water. The MHW indicator requires the use of digital elevation models generated by stereo optical imagery or LiDaR techniques.

The origin of the definition is generally lacking, e.g. in France, the High Astronomical Tide defines the edge of the *Domaine Public Maritime* and in New Zealand and United States, the legal shoreline is defined by using the MHW. Finally, the third group of shoreline indicators is based on the application of image-processing techniques to extract proxy shoreline features from digital coastal images, such as the wet/dry line.

According to the available data, the choice of the shoreline indicator can vary, depending on the use of aerial photography, beach surveys, remote sensing or video images (Gens 2010). By exploiting Earth Observations (EO) data (multispectral, hyperspectral, microwaves), acquired from different sensors (e.g. resolution, precision), the shorelines delineation can be based on the use of visually discernible coastal features, digital image-processing analysis or specified tidal datum. The main limitations of this data source are the pixel resolution and costs (Cracknell 1999). It is reminded that the horizontal accuracy, which actually determines the shoreline location, is typically of the same order of magnitude as the spatial resolution of its source data. Secondary factors—such as the mineralogy and grain size of sediments, the solar zenith angle, the tide and the beach profile—can also impact the results (Gens 2010).

After a critical review of methods to detect coastal erosion and its elements, cf. Sects. 2–6, the novelty and impact of the advances in public satellite missions, i.e. systematic global cover at high spatial resolution (3-to-20 m) and increased revisit times (1-to-6 days), cf. Sect. 7. The new computing capacity and software, made available by the European Space Agency (ESA), offers an improved service for data processing, useful for detecting coastal erosion trends, cf. Sect. 8. The conclusion stresses on novelties and advantages of satellite data to overcome gaps in monitoring of marine sedimentary transport.

2 Detection of Waterline from Satellites Images

For more than 20 years, remote sensing by one-time snapshots has been used for the shorelines delineation and to detect and monitor the trends despite a crude sampling rate which creates aliasing in estimates (Boak and Turner 2005).

a. To extract the shoreline, from optical mode images, the scientific community mainly uses the following indicators: the Normalized Difference Vegetation Index (NDVI) (Muttitanon & Tripathi 2005), Normalized Difference Water Index (NDWI) (Hagenaars et al. 2017), an indicator combining NDVI and NDWI (Maglione et al. 2014) or a derived index named Modified Normalized Difference Water Index (Ghosh et al. 2015). To date, the difficulties such as making the difference between a dry sand and a wet sand, have hampered the use of these techniques by the Ordnance Survey Agencies.

Infra-red (IR) observations were tested by survey teams working on Satellite-Derived Bathymetry with low success (ACRI-IN internal communication). Zhang et al. (2013) also used an automated method based on edge detection, named object-based region growing integrating edge detection (OBRGIE) in which an object merging index is applied on the near-IR (NIR) bands of SPOT and Landsat satellites: it gives visually good results for the artificial coast, but it failed to capture the real coastline position in coastal areas having large tidal ranges. In the case of tidal flats, especially during the ebb tide, the short-wave IR band is too sensitive to the water remaining on the exposed tidal flat and the NIR band is also affected by the high

turbidity of ebb tide water, causing alterations in the shoreline detection (Ryu et al. 2002).

Pardo-Pascual et al. (2012) used subpixel analysis and tested their method on artificially and permanently stabilised coasts to evaluate the accuracy and limits of the method. The identified limitations of automatic extraction of the shoreline are: (i) the form of the shoreline, as strong curvature or thin pier; (ii) the land cover and (iii) the impact of the tide—particularly for the ebb tide phase in areas with macro-tide although their training area is located in a micro-tidal coast.

Sekovski et al. (2014) used unsupervised classification, such as the ISODATA algorithm, and have supervised the classification to compare the accuracy of the methods for the shorelines extraction, based on the wet/dry line. The study concluded that there are larger discrepancies between coasts with heterogeneous geomorphological characteristics and homogeneous areas. They also, applied this method to an area with a micro-tidal regime.

In most cases, the main hurdles were (i) the lack of time-series of EO from satellite allowing the sampling of all events that move the waterline then a shoreline, e.g. storms, floods, preventing proper statistics, and its use to precisely study coastal erosion for engineering, and (ii) the lack of precision for legal matters.

b. The Synthetic Aperture Radar images (SAR) have two main attributes: (i) sensors can "operate" under any weather conditions, and (ii) by day and night (Buono et al. 2014). However, SAR measures either the backscatter of "hard" materials or the Bragg scattering of liquids which are two different phenomena, and it is also affected by speckle, a multiplicative noise that gives the images a grainy appearance and makes the interpretation of SAR images a challenging task compared to optical image processing (some filters to smooth the signal are applied to solve this problem). Moreover, if the sea is roughened by wind, it shows heterogeneous radar backscattering sectors (Silveira and Heleno 2009) although the extraction of shorelines from SAR imagery is facilitated by the large contrast in the backscatter signal, as received from sea and land areas (Van Der Sanden and Ross 2001). Numerous image processing methods—such as edge detection, canny edge detection, clustering, thresholding, wavelets and active contour, filters or segmentations—have been used by scientists. E.g. the algorithm proposed by Silveira and Heleno (2009) or the method proposed by Shu et al. (2017) are able to accurately delineate the shoreline at the tide moment and with the spatial accuracy as long as the seafloor is not too flat.

3 Geometry—Need of Terrain Model, Tide Gauges Record or Tide Models, Wave Buoys Records or Wave Models

The shoreline is the intersection between two surfaces, the water surface and the land surface. Because of the ebb and rise of the sea surface (e.g. tides and atmospheric pressure), and the average dynamic slope of the sea-surface due to waves landing on the

shore, instantaneous observations by satellites need be corrected to retrieve a virtual line—such as the MHW; corrections make use of nearshore/foreshore bathymetric models, i.e. cross-shore profiles. Surveys are needed because it is not yet possible to predict on empirical grounds, let alone theoretical grounds, the shape of a beach after it was subjected to given wave conditions. To go beyond the use of the sounding pole, the French Navy, for instance, tried to get beach profiles from Unmanned Aerial Vehicles with multispectral sensors similar to satellite borne sensors (trials in 2014–2016). In all cases, the issue is the concurrence between the bathy/topography survey and the shoreline observation(s) at the scale of a stable period in coastal systems' self-organization. The best results come from using the shoreline, a 1D feature, and the terrain model, a 2D feature, from the same observations. Currently, French governmental agencies delineate the shoreline from concurrent measurements of the tide and bathy/topography, i.e. surveys by aerial blue-green and IR LiDaR surveys (e.g. Litto3D programme) every 3 to 5 years.

Because LiDaR surveys are expensive, the organizations to whom the authors belong have carried out numerous satellite remote sensing surveys since 2014 (Fig. 1) for various governments, agencies and companies using various empirical methods (Lyzenga 1985; Stumpf et al. 2003) and semi-empirical methods (Lee et al. 1998; Hedley et al. 2012) of Satellite-Derived Bathymetry (Figs. 12 and 13), including for the delineation of legal shorelines, territorial waters, contiguous zones and Exclusive Economic Zones to be presented to courts, using images at 15–30 m of spatial resolution from Landsat, 10 m from Sentinel-2 or SPOT, 5 m from RapidEye, 1 m

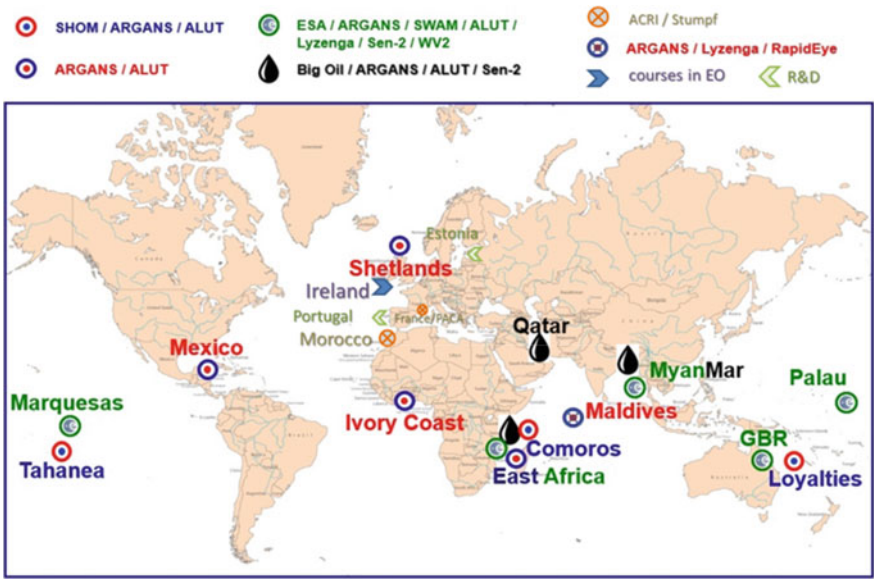

Fig. 1 Satellite-Derived bathymetry surveys by ARGANS UK

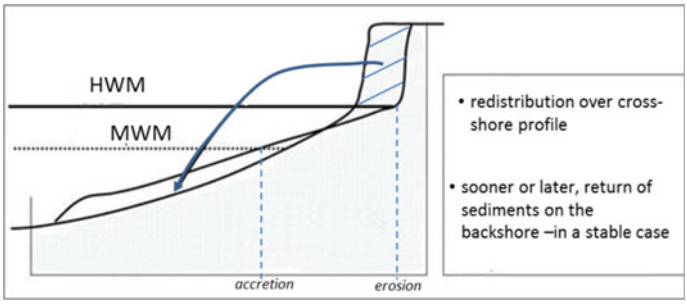

Fig. 2 Rate of recession vs. rate of erosion, or the ambiguities of shoreline characterization (HWM: High Water Mark; MWM: Mean Water mark)

from Ikonos, QuickBird, SPOT & Pleiades, and a sub-metric spatial resolution with WorldView2.

4 Impact of Surface and Volumes

To quote http://www.coastalwiki.org by the Flanders Marine Institute, Coastal erosion is "*the process of wearing away material from the coastal profile due to imbalance in the supply and export of material… It takes place in the form of scouring in the foot of the cliffs or in the foot of the dunes. Coastal erosion takes place mainly during strong winds, high waves and high tides and storm surge conditions, and results in coastline retreat*".

Although the erosion rate is often confused with coastline retreat, and, for instance expressed in m/year, it shall be correctly enunciated in volume/length/time, e.g. m3/m/year, the time scale being counted in years for structural erosion (deficit in the littoral drift budget or long-shore mode, and days/weeks/months for incidental erosion (cross-shore processes, usually reversible). Assessment of profiles then volumes under the 'shoreface', i.e. the shore surface, is key to assess the rate of erosion (Fig. 2).

5 Land and Seafloor Materials Transport

Materials eroded from the mainland during storm and flood events settle in deeper water, through cross-shore transport and longshore sediment transport, before being potentially transported back to the mainland. It is most important to track the flow of suspended sediments from the sea surface by remote sensing, even if the flow of bed sediments is masked by the water column. Three examples are given herein below, in the Saint-Laurent River (Fig. 3), at the mouth of the Seine River (Fig. 4),

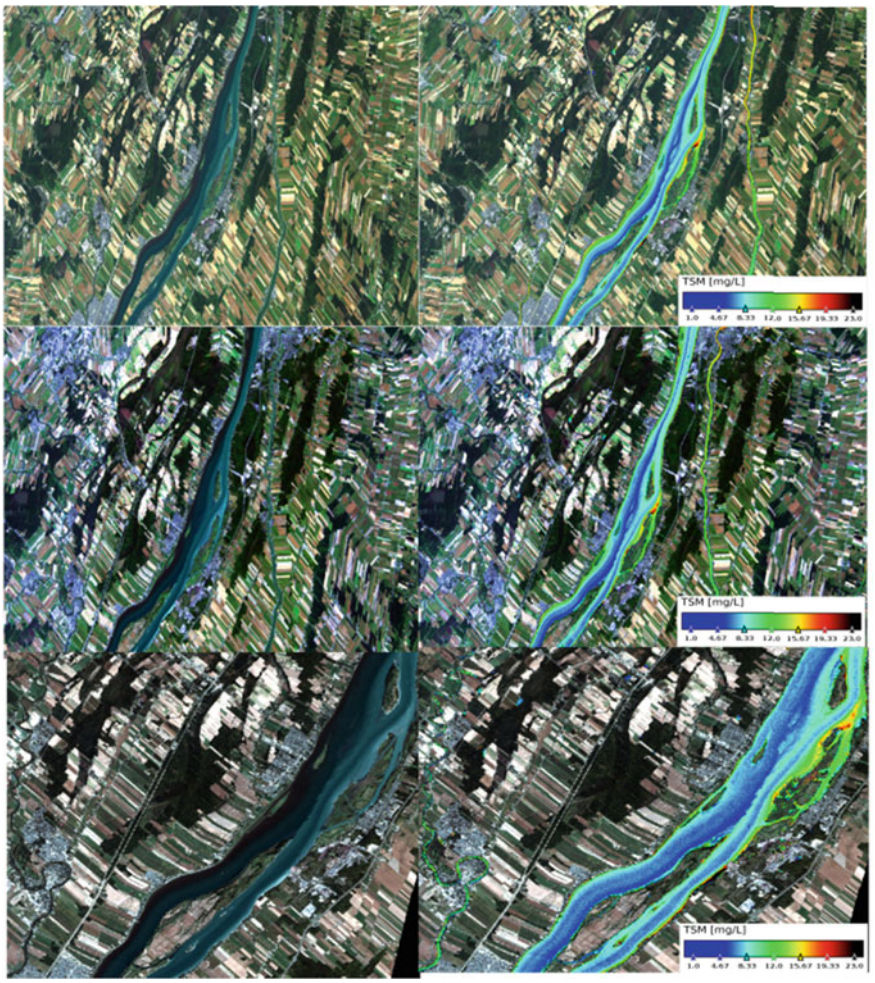

Fig. 3 Total suspended matter map of the fluvial section of the Saint-Lawrence for **a** Landsat 8 (30 m resolution, 2017-10-02), **b** Sentinel 2 (10 m resolution, 2017-10-03) and **c** PlanetScope (3 m resolution, 2017-10-01)—by ARCTUS 2017

and in French Guyana (Fig. 5). The use of the snapshots from the swarm of Dove nanosatellites of Planet at 3 m resolution were tested on the Saint-Laurent, as it may provide standardly high-resolution daily surveys of the world coastlines though with less sensitivity that Sentinel-2 sensors at 10 m resolution with weekly revisits. There are trade-offs to be made in the choice of satellite missions based on spatial resolution, temporal resolution, spectral density and Signal/Noise amplitude among others.

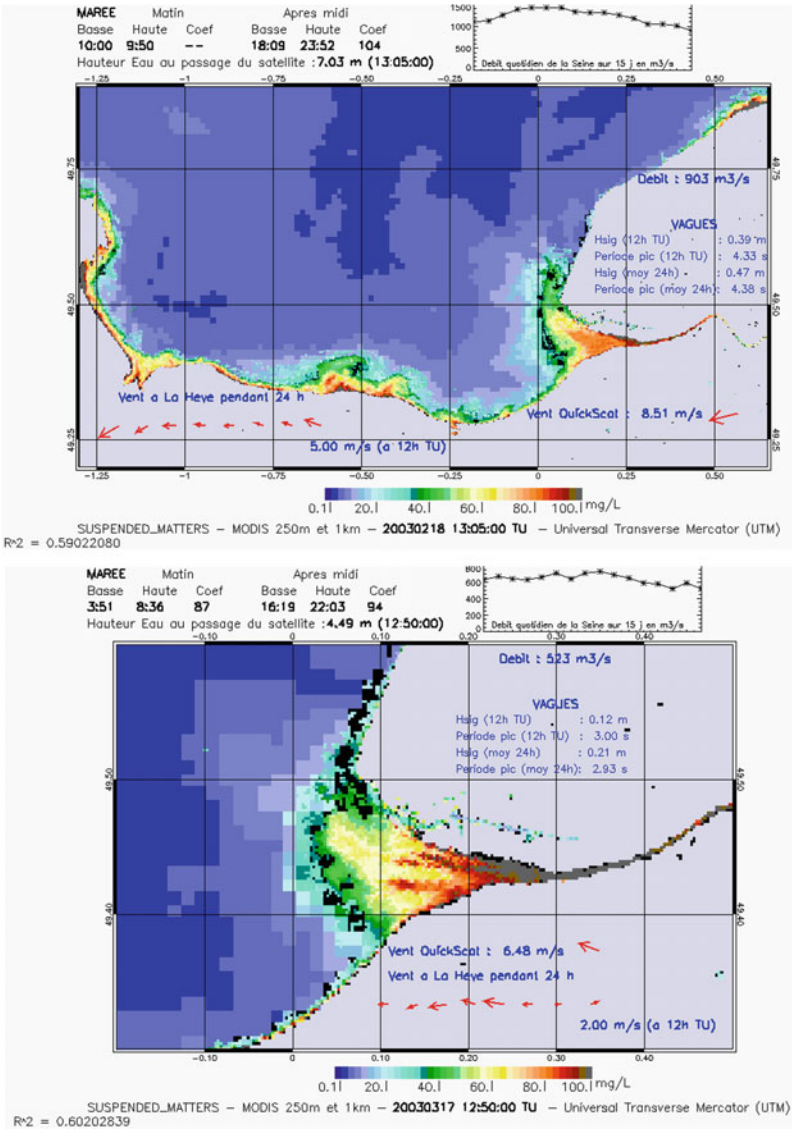

Fig. 4 Total suspended matter map of the Seine river 2003-02-18, from a time series 2003–2009 using MODIS—by ARGANS France

The images over Guyana and Normandy are at low resolution, i.e. 300 m, compared to the Sentinel-2's and Doves'—if they do not help provide the shoreline, they inform on sediment transport.

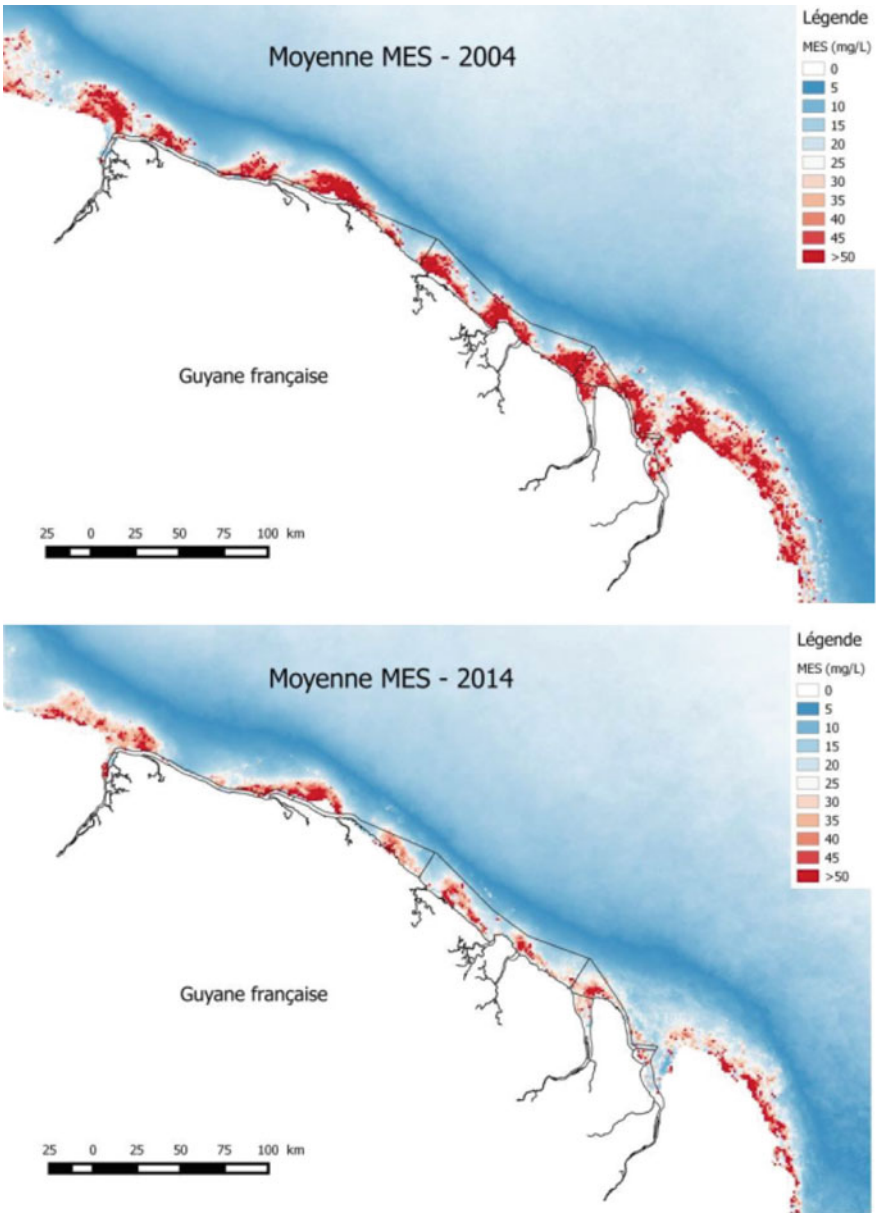

Fig. 5 Total suspended matter map of Guyana in a 2003–2014-time-series using MODIS, MERIS, and VIIRS—by IFREMER & ARGANS France

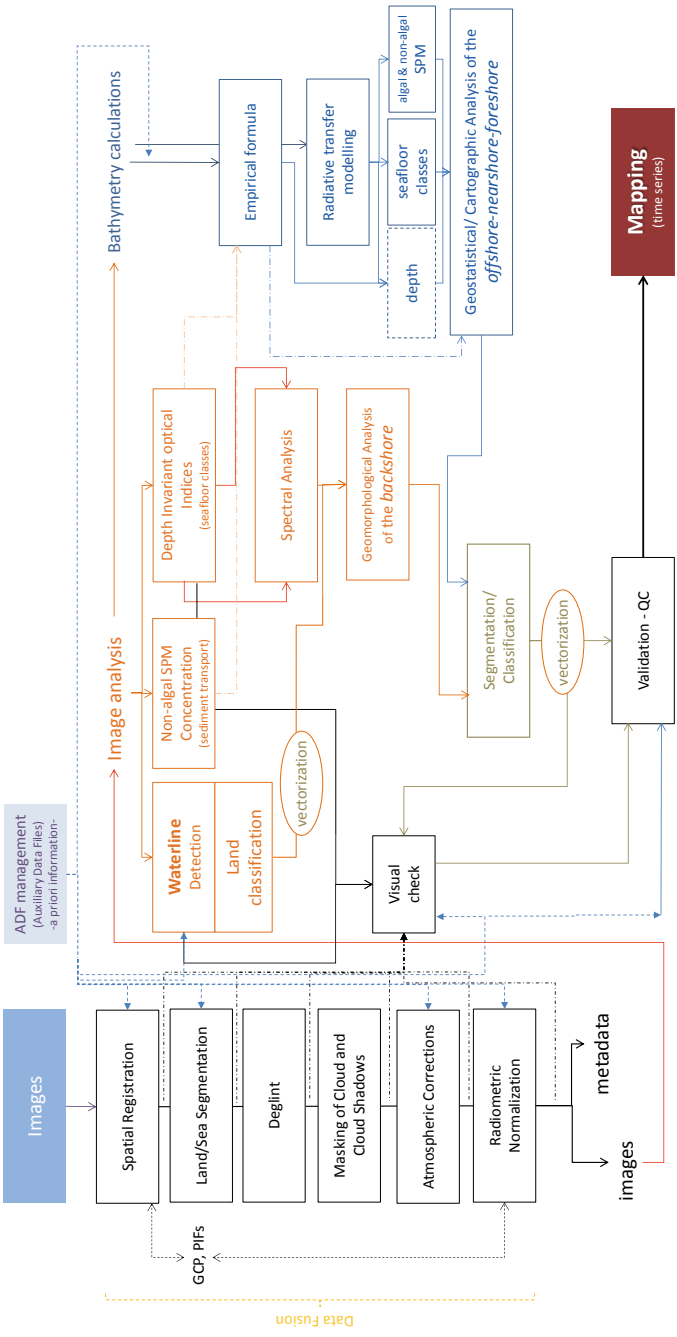

Fig. 6 Data processing chain for the build-up of time series that merge data from various sensors from landsat to WorldView3 through Sentinel-2, Rapid Eye, SPOT, Pleiades—by ARGANS France—(GCP = Ground Control Points, PIF = Pseudo Invariant Features, QC = Quality Control, ADF = Auxiliary Data)

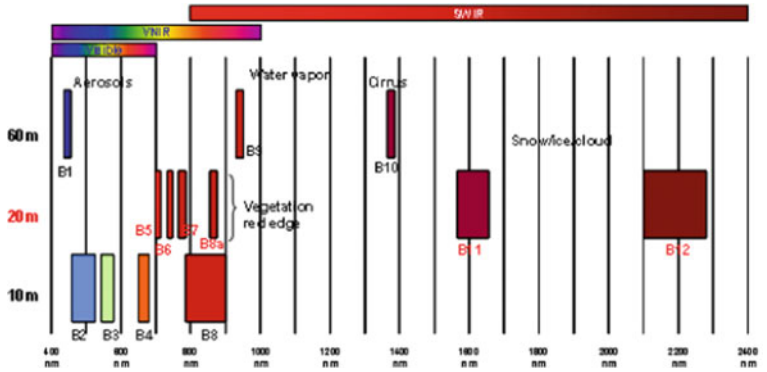

Fig. 7 Density of spectral bands of the multispectral instrument sensor on-board Sentinel-2 A & B at various spatial resolution. *Courtesy* CESBIO

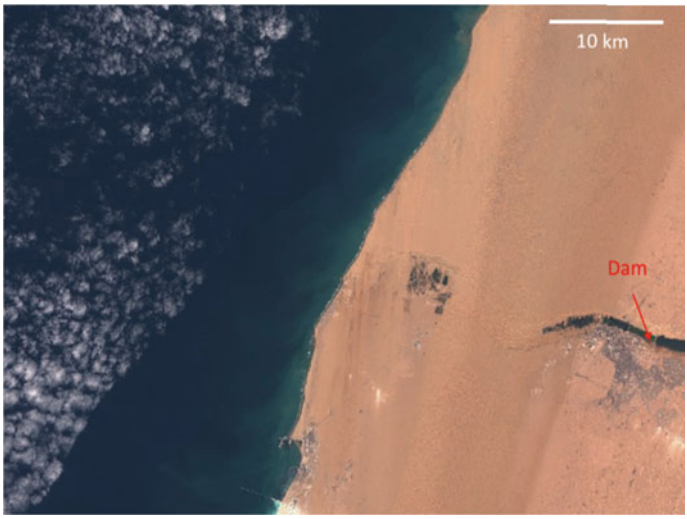

Fig. 8 Foum el Oued, 20th October 2016—before the flood of Oued Sakia El Hamra

6 The Shoreline & Coastline Change Detection

a. For the detection of change, the traditional methods are (i) Principal Component Analysis, image classification, post-classification comparison, image ratio (Muttitanon and Tripathi 2005; Ghosh et al. 2015) applied to surfaces, and (ii) vector analysis in GIS Software of the vectorised shorelines, e.g. Digital Shoreline Analysis System, an extension module of ArcGIS 10 (Sekovski et al. 2014).
b. For the lines' change analysis and the deduction of a trend (sea-surface dynamics and erosion/accretion regime), there is still a need (i) to correct the water-land

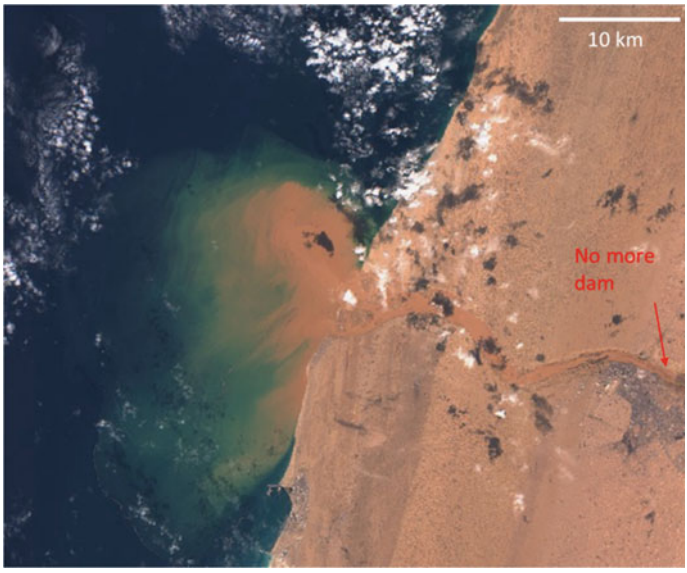

Fig. 9 Foum el Oued, 30th October 2016—just after the flood of 29 October 2016

edge taking into account the foreshore profile, tides, waves and barometric pressure (Thieler & Danforth 1994) and, when studying long-term erosion, (ii) to have enough samples to correct for seasonal influences such as alternating phases of erosion and accretion (Moore 2000) even if the active coastal zone always tends to a state of dynamic equilibrium.

Nota: the changes' time-scale is driven by the resistance of structures to erosion, e.g. hard outcrops/cliffs or loose sediments.

As a reminder, nothing is static: the beach state in dynamic equilibrium fluctuates around an equilibrium state in response to fluctuations in hydrodynamic factors and sediment supply. The pixel accuracy of coastlines derived from low-resolution satellite imagery may not be of sufficient accuracy to capture small changes along the coast. Sub-pixel mapping approaches may provide good alternatives under these situations, but these methods were only tested on short coastline sectors (Zhang et al. 2013), or on micro-tidal regime coast (Pardo-Pascual et al. 2012).

7 Novelty: New Perspectives of Missions Sentinel-1 & Sentinel-2

The COPERNICUS program of the European Union and the European Space Agency (ESA) introduces a new order in coastal surveys. Whereas before, geographers were stuck with rare snapshots at high spatial resolution or daily snapshots at 300 m

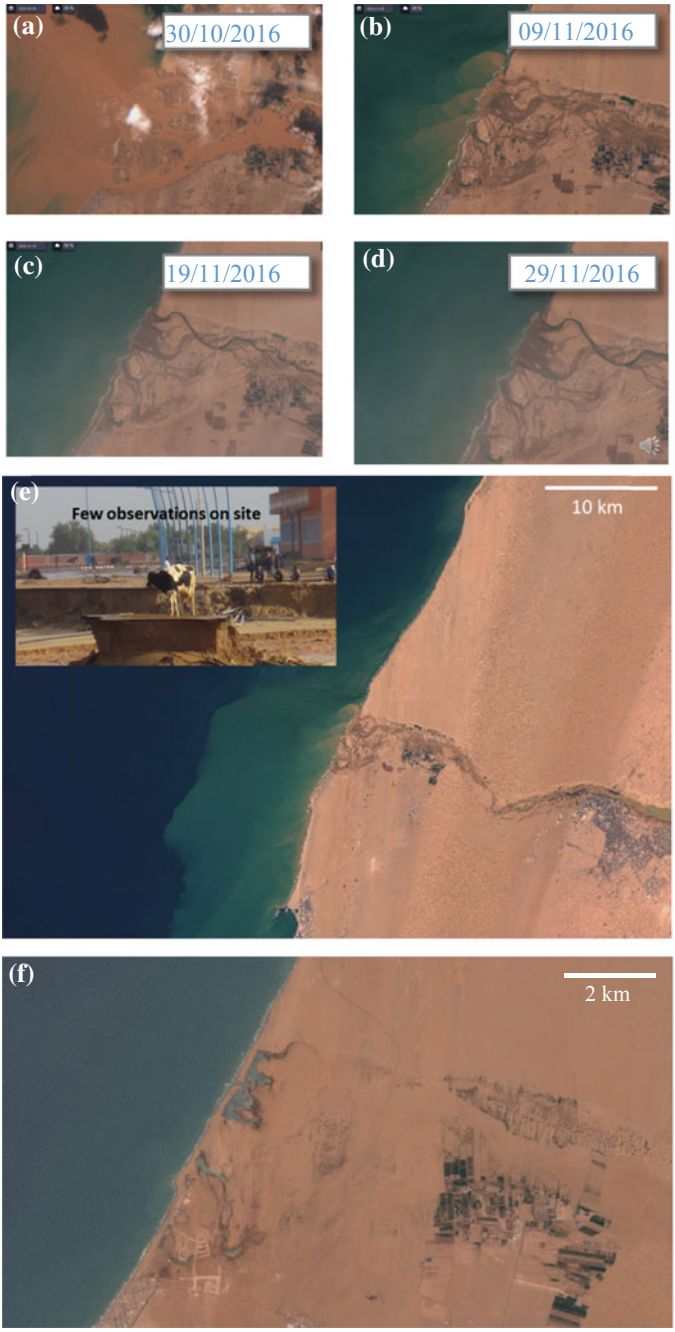

Fig. 10 Foum el Oued, from 30 October 2016 **a** to 29 Nov 2016 **d** with a plain image for 9 November 2016 **e** and the stabilization by May 2018 **f**

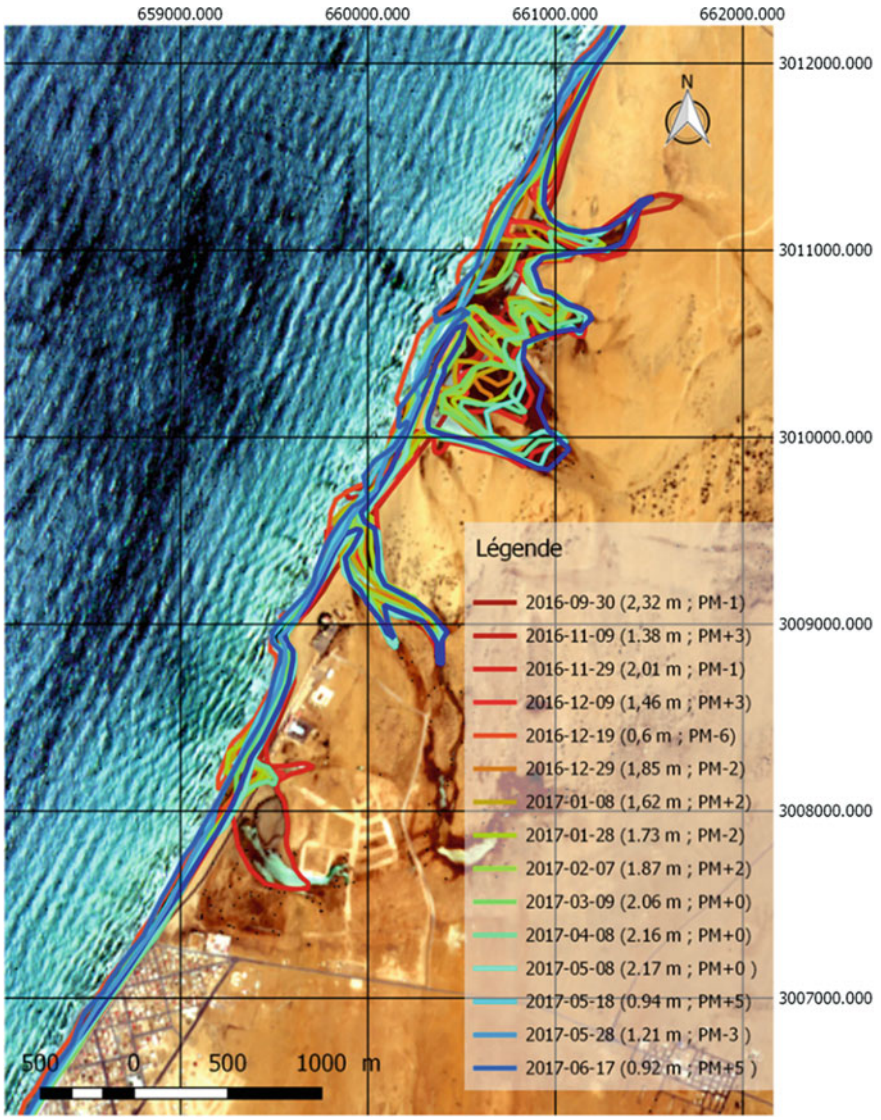

Fig. 11 Foum el Oued, coast delineation, from 30 Sep 2016 (first day of the flood) to 17 Jun 2017—drawn with Sentinel-2 data sets—by ACRI-EC

resolution, Sentinel-2A & B satellites and Sentinel-1A & B satellites supply users with an optical and radar snapshot in the region of every week at the Equator, and a few per week at mid-latitudes, and with resolution of 5-to-10 m, which is still insufficient for a precise instant drawing of the shoreline but may be adequate if performing proper statistics.

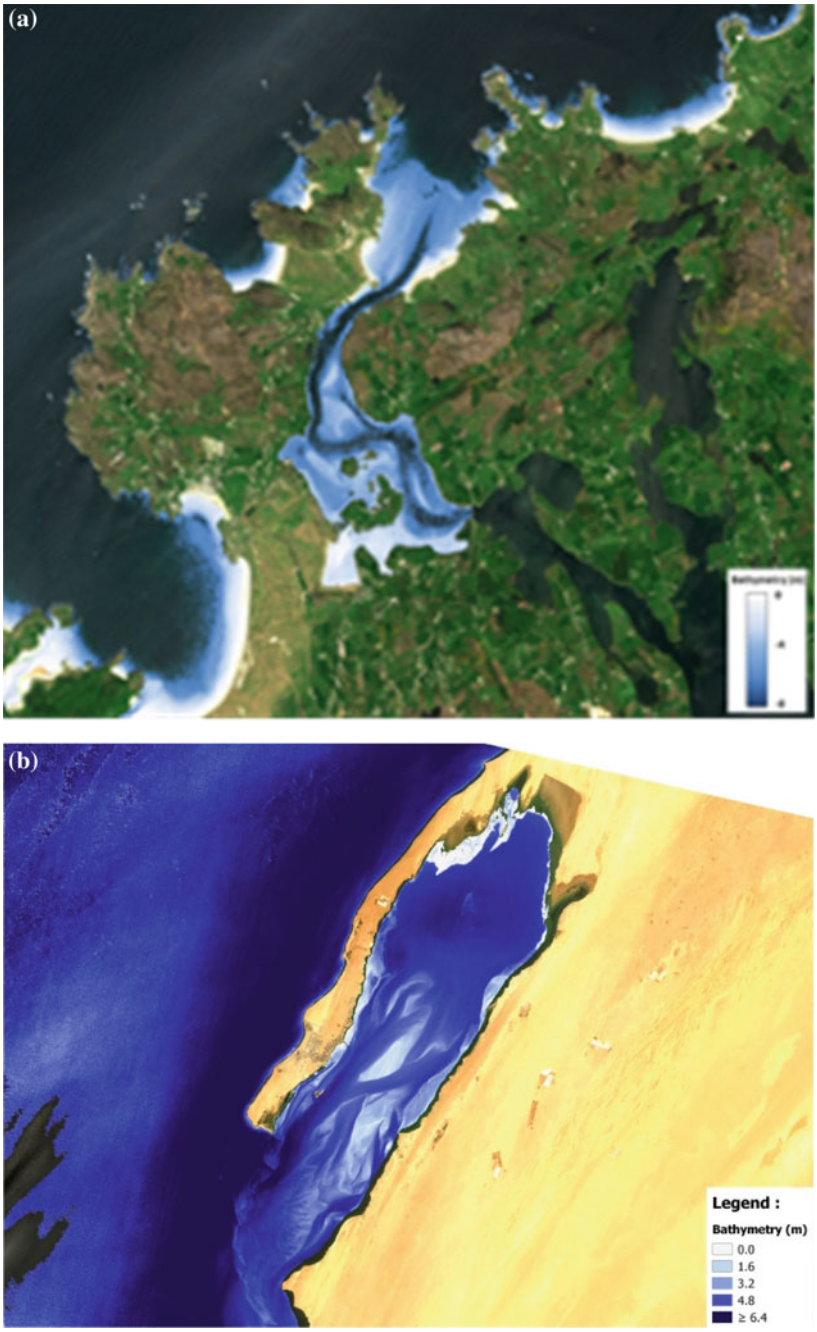

Fig. 12 Derived bathymetry from satellite image **a** Mulroy Bay (Ireland) by ARGANS UK **b** Dakhla by ARGANS France

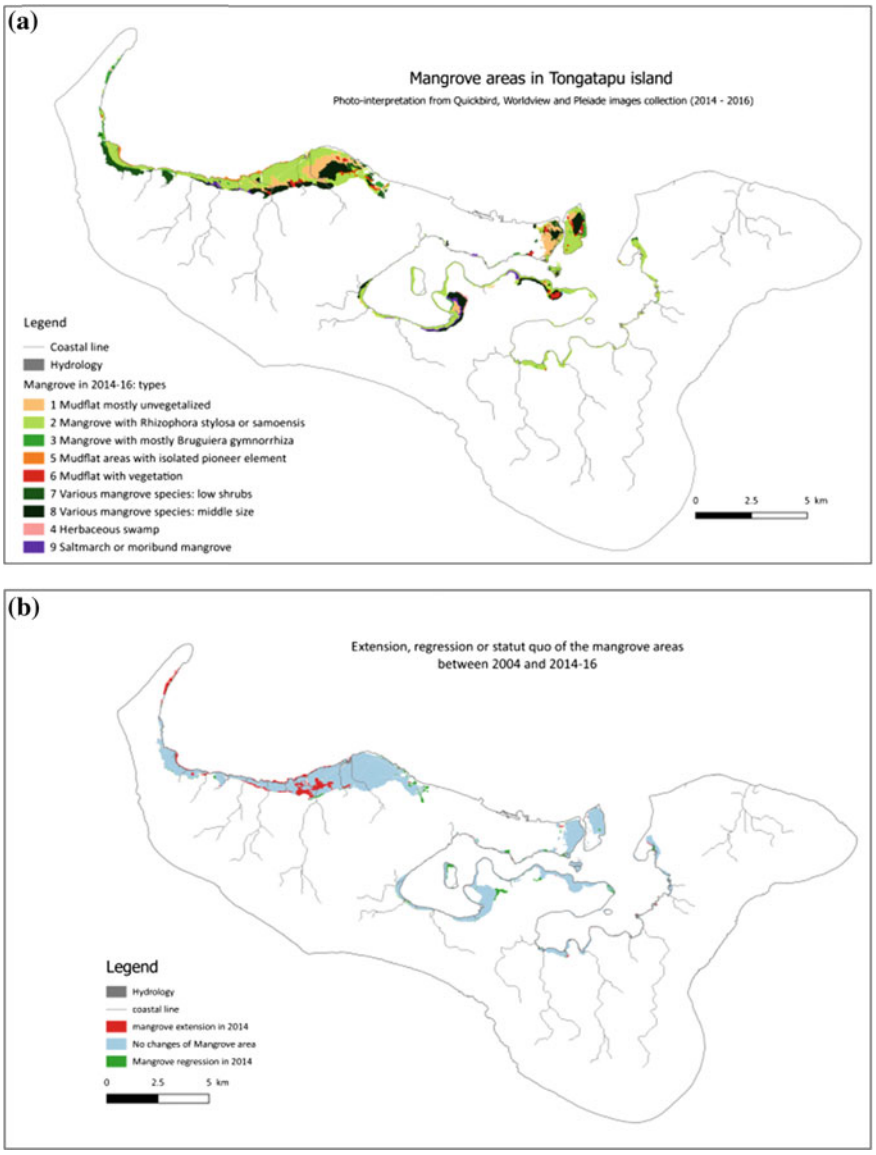

Fig. 13 Tongatapu Island, **a** Photointerpretation of VHR images; **b** change analysis of the mangrove land cover and coastline between 2004 and 2014

The spectral density of Sentinel-2 (Fig. 7) allows the use of good atmospheric corrections avoiding the reliance upon empirical assumptions for the conservation of bands ratio from the Top of the Atmosphere to the Bottom of the Atmosphere that are traditionally accepted by remote sensing scientists because they are not verifiable on commercial data sets such as SPOT or Pleiades:

One issue is the lengthy data processing to get the accurate data for the parameters retrieval (Fig. 6), what NASA and ESA refer to as "Level-4 products". With Sentinel-1 data, i.e. SAR data, we need to use a different polarization signal to characterize the terrain as well as the water content near the sea surface.

Following paragraphs give examples of Sentinel-2 use.

7.1 Monitoring of a Flood Impact on the Coast Line

Further to the dam burst in Laayoune caused by the flood of Oued Sakia El Hamra, we have monitored the evolution of the shoreline and the backshore, where a technopole was under construction (Figs. 8, 9, 10 and 11). It was the first attempt to use Sentinel-2 data for engineering planning (restoration of coastal defence and land area).

7.2 Monitoring of Stilting

The inversion of data from satellites such as Sentinel-2 (Fig. 12a) or a mix of Sentinel-2 & Landsat8 (Fig. 12b) gives access to time series of bathymetry with seasons' sampling.

7.3 Monitoring Coastal Changes in a Mangrove Area

If the monitoring of the changes in a mangrove area is best done from EO data at Very High Resolution (VHR, < 1m) but with a sampling of one map every 5 years (Fig. 13), Sentinel 2 weekly data combines to improve the vegetation delineation in a swamp area (Fig. 14). The Sentinel-2 results match with the analysis of the VHR images (Worldview2, Quickbird, Ikonos, Pleiades), except, obviously in cloud shadows and in areas affected by tides.

8 The Necessary Computing Capacity

To analyse weekly or daily data sets in time-series of a few years, one needs efficient software on powerful computing platforms. Examples of such software are in the

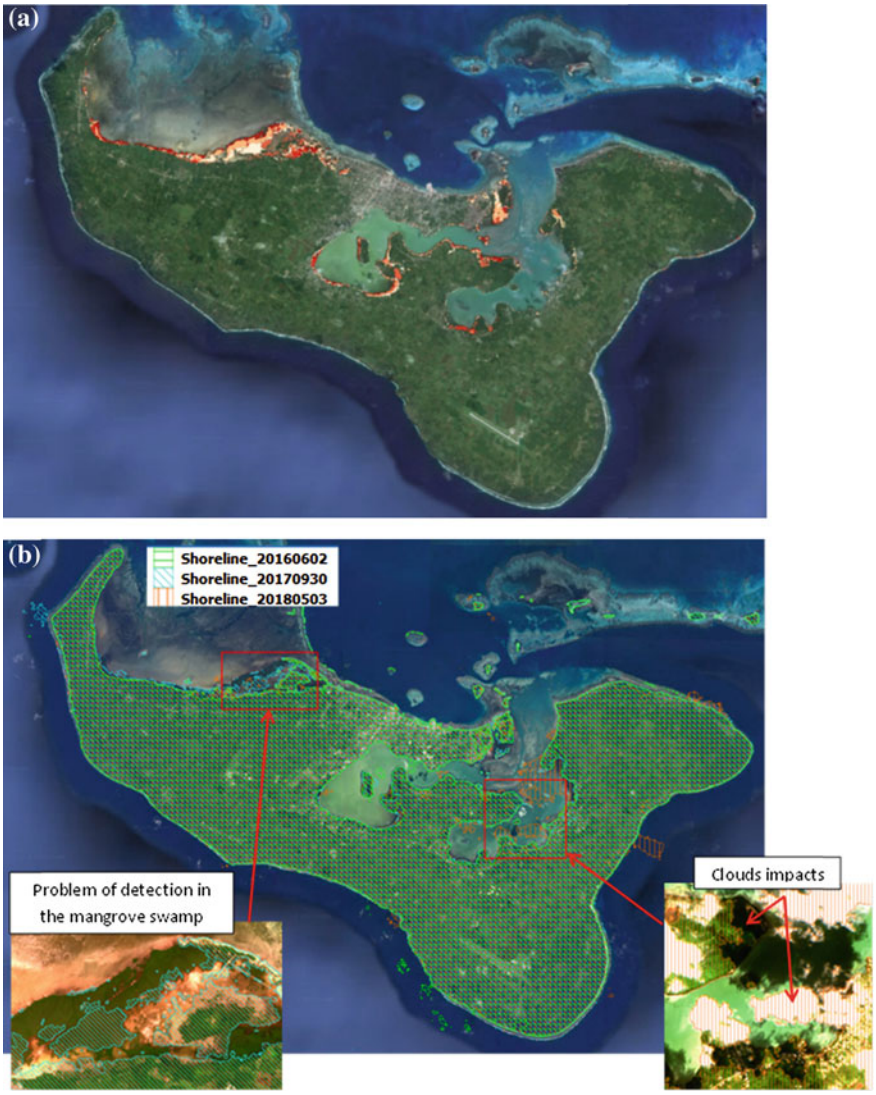

Fig. 14 Automatic detection of mangrove **a** and coastline **b** from Sentinel-2 image—the second figure represents the changes from 02/06/2016 to 03/05/2018

SNAP toolbox of ESA (http://step.esa.int/), an open source library which will already include atmospheric correction processors and soon include the SDB processor. To run such software, whose functional organization is described in Fig. 6, a platform such as the Coastal Thematic Exploitation Platform by ESA (C-TEP: https://coastal-tep.eo.esa.int/) facilitates data handling if it has access to a worldwide cover of data. Such a database is developed by the Luxembourg Ministry of Economy under

the name of LU CollGS in the framework of the Sentinel Collaborative Ground Segments' program of ESA. The C-TEP is currently implemented on this platform, enabling for the first time, the systematic remote sensing of the shoreline. It includes a geographic information system, QGIS.

9 Conclusion

The COPERNICUS program, with its four HR satellites equipped with radar and optical/infra-red sensors, and the complementary constellations of nanosatellites such as Planet's, trigger a revolution in coastal erosion management by local communities and governmental agencies, and environmental protection & coastal defence design. Another critical component of the success is the advance capabilities in data access and computing, allowing the management and monitoring of coastal erosion for multiple stakeholders.

Acknowledgements This work compiles results obtained by companies of the ACRI-group for numerous customers, incl. the Phosboucraa Foundation, the port of Montreal, the Asian development Bank. The R&D could not have been performed without the support of ESA on numerous contracts.

References

Boak, E. L., & Turner, I. L. (2005). Shoreline definition and detection: A review. *Journal of Coastal Research, 21*(4), 688–703.

Buono, A., Mascolo, L., Nunziata, F., & Migliaccio, M. (2014). A multipolarization analysis of coastline extraction using X-Band COSMO-skymed SAR data. *IEEE Journal of Selected Topics in Applied Earth Observations and Remote Sensing, 7,* 2811–2820.

Cracknell, A. P. (1999). Remote sensing techniques in estuaries and coastal zones-an update. *International Journal of Remote Sensing, 19*(3), 485–496.

Fisher, J. S., Overton, M. F. (1994). Interpretation of shoreline position from aerial photographs. In *Proceedings of the 24th International Conference on Coastal Engineering* (Kobe, Japan) (pp. 1998–2003).

Gens, R. (2010). Remote sensing of coastlines: detection, extraction and monitoring. *International Journal of Remote Sensing, 31,* 1819–1836.

Ghosh, K. M., Kumar, L., & Roy, C. (2015). Monitoring the coastline change of Hatiya Island in Bangladesh using remote sensing techniques. *SPRS Journal of Photogrammetry and Remote Sensing, 101,* 137–144.

Hagenaars, G., Luijendijk, A., De Vries, S., & De Boer, W. (2017). Long term coastline monitoring derived from satellite imagery. *Coastal Dynamics, 122,* 1551–1562.

Hedley, J., Roelfsema, C., Koetz, B., & Phinn, S. (2012). Capability of the Sentinel 2 mission for tropical coral reef mapping and coral bleaching detection. *Remote Sensing of Environment, 120*, 145–155.

Lee, Z., Carder, K. L., Mobley, C. D., Steward, R. G., & Patch, J. S. (1998). Hyperspectral remote sensing for shallow waters. I. A semianalytical model. *Applied Optics, 37*(27), 6329–6338.

Lyzenga, D. R. (1985). Shallow-water bathymetry using combined lidar and passive multispectral scanner data. *International Journal of Remote Sensing, 6,* 115–125.

Maglione, P., Parente, C., & Vallario, A. (2014). Coastline extraction using high resolution WorldView-2 satellite imagery. *European Journal of Remote Sensing, 47,* 685–699.

Moore, L. J. (2000). Shoreline mapping techniques. *Journal of Coastal Research, 16*(1), 111–124.

Moore, L. J., Benumof, B. T., & Griggs, G. B. (1999). Coastal erosion hazards in Santa Cruz and San Diego. *Journal of Coastal Research, 28,* 121–139.

Muttitanon, W., & Tripathi, N. K. (2005). Land use/land cover changes in the coastal zone of Ban Don Bay, Thailand using Landsat 5 TM data. *International Journal of Remote Sensing, 26*(11), 2311–2323.

Pardo-Pascual, J. E., Almonacid-Caballer, J., Ruiz, L. A., & Palomar-Vazquez, J. (2012). Automatic extraction of shorelines from Landsat TM and ETM + multi-temporal images with subpixel precision. *Remote Sensing of Environment, 123,* 1–11.

Ryu, J.-H., Won, J.-S., & Duck Min, K. (2002). Waterline extraction from landsat TM data in a tidal flat a case study in Gomso Bay, Korea. *Remote Sensing of Environment, 83,* 442–456.

Sekovski, I., Stecchi, F., Mancini, F., & Del Rio, L. (2014). Image classification methods applied to shoreline extraction on very high resolution multispectral imagery. *International Journal of Remote Sensing, 35,* 3556–3578.

Shu, Y., Li, J., & Gomes, G. (2017). Shoreline extraction from RADARSAT-2 intensity imagery using a narrow band level set segmentation approach. *Marine Geodesy, 33,* 187–203.

Silveira, M., & Heleno, S. (2009). Separation between water and land in SAR images using region-based level sets. *IEEE Geoscience and Remote Sensing Letters, 6*(3), 471–475.

Stumpf, R. P., Holderied, K., & Sinclair, M. (2003). Determination of water depth with high-resolution satellite imagery over variable bottom types. *Limnology Oceanography, 48*(1, part 2), 547–556.

Thieler, E. R., & Danforth, W. W. (1994). Historical shoreline mapping (I): Improving techniques and reducing positioning errors. *Journal of Coastal Research, 10*(3), 549–563.

Van Der Sanden, J. J., Ross, S. G. (2001). *Applications potential of RADARSAT-2: A preview*. (Unpublished report). Canada Centre for Remote Sensing.

Zhang, T., Yang, X., Hu, S., & Su, F. (2013). Extraction of coastline in aquaculture coast from multispectral remote sensing images: Object-based region growing integrating edge detection. *Remote Sensing, 59,* 4470–4487.

Mapping of Estuarine Transport from Spatial Remote-Sensing Products: Application to Authie Bay (France)

Benoit Menuge, Charles Verpoorter, Arnaud Héquette and Vincent Sipka

Abstract In many domains of application such as sedimentology, remote sensing may be used to fill the gap of field sampling. This gap is often due to unavailable logistics or inaccessible areas. It is recognized that sediment transport directions can be assessed from grain-size parameters of sediment samples, but the determination of transport trend patterns from grain-size remote sensed products has still not been carried out. The main objective of this study was to determine sediment transport trends in the Authie estuary (North of France) using Sentinel-2 data for different periods. This estuary is marked by a critical erosion of the northern shore due to a prograding sandy spit and a general sandfilling. In order to analyse seasonal variations, a set of 4 images were analysed for a period between 2016 and 2018, two during summer and two during winter. A new methodology was developed for mapping sediment transport trend based on grain-size parameters (mean, sorting and skewness) determined from remote sensing data. Three sectors of the estuary were selected according to their main morphodynamics characteristics (e.g. critical erosion and sandfilling sectors). The resulting transport vectors were spatially coherent with sedimentary bedforms (i.e. megaripple) and consistant with known transport directions. Maps of potential sediment transport show spatial variation between summer and storm periods. Our results suggest a changes according the period and some vectors demonstrate a change in direction following the formation of new structures or channel deviations. This study demonstrates that remote sensing combined to grains-size trend analysis can be a useful approach for sediment transport trends determination with a high spatial resolution. Further investigations are needed to identify the role of topographic variations and to obtain a long-term transport trend in order to understand as the spatial variability in sandfilling and erosion processes within the estuary.

Keywords Remote sensing data · Grain-size trend · Sediment transport · Spatial changes · Estuary

B. Menuge (✉) · C. Verpoorter · A. Héquette · V. Sipka
LOG, Laboratoire D'Océanologie et de Géosciences, Université de Littoral Côte D'Opale, Université de Lille, CNRS, UMR 8187, 62930 Wimereux, France
e-mail: Benoit.Menuge@univ-littoral.fr

K. D. Nguyen et al. (eds.), *Estuaries and Coastal Zones in Times of Global Change*, Springer Water,
https://doi.org/10.1007/978-981-15-2081-5_47

1 Introduction

Determination of sediment transport permits to better understand estuarine dynamics. Generally field sampling is necessary to assess the sediment transport. However field sampling could be limited by logistics meaning or difficult access of some area (i.e. mudflat) during the low tide. Giving a synoptic information, remote sensing tool can overcome to these issues by mapping the overall estuary at various time of acquisition. Depending on the algorithm applied, each pixel of the processed image should correspond to a sediment parameter such as grain-size, water content, and biomass, etc. However the resulting map is restricted to surficial sediments structures.

In term of coastal remote sensing applications, different methods were used to map sediment properties such as supervised or unsupervised classifications (Adam et al. 2006), statistical models (Small et al. 2009) or inverted bio-optical models from hyperspectral data (e.g. Smith et al. 2004; Deronde et al. 2007). Yang et al. (1999) *combined* remote sensing to Geographic Information System (GIS) techniques for assessing delta evolutions using automated time-serie analyses. However, their study revealed some variations following environmental fluctuations (e.g. vegetation seasonal cycle, tidal range and soil moisture).

Rainey et al. (2003) used an airborne sensor to retrieve the type of sediment in estuarine environment. Authors used statistical models from pixels and field samples in order to determinate microphytobenthos abundance, mud/sand coverages and moisture content. Although they successfully retrieved the type of sediment they were unable to map grain-size fractions.

Small et al. (2009) presented a methodology to map sedimentary properties from hyperspectral data. Their methodology was decorrelating soil moisture and grain-size effects using principal component analysis. Even if this distinction was possible, they were unable to identify specific spectral features to determinate well-known differences of sediment (i.e. soil moisture and grain-size).

In term of sediment transport, McLaren (1981) and McLaren and Bowles (1985) demonstrated that grain-size properties composing sediment deposits were controlled by grain-size distribution and sedimentary processes (i.e. transport and deposition). Sediment surfaces undergoing erosion process exhibit a high probability for some grains to go into transport. When sediments are deposed, they noticed a case characterised by a diminution of the mean grain-size, a better sorting with a negative skew called FB- (case 1). The lag remaining after erosion is coarser, well sorted and positively skew is called CB+ (case 2). In the case of sediment transport lead to a selective deposit, sediment grain-size trend become finer or coarser, with a positive skew and a well sorted case named respectively FB + (case 3a) and CB + (case 3b).

Gao and Collins (1992) highlighted other potential cases like FB− and CB+ cases. The latter could occur without any net-transport process. In case of "no transport", six possible cases were added diminishing the probability to one eighth to retrieve one of these two cases. McLaren's method was based on one spatial dimension whereas Gao and Collins' method took into account two dimensions following a critical distance (Dcr) defined as mean sample spacing. As a consequence, it produced more

significant results and it reduced some bias in the selection of the sampling line. They purposed a comparison for each sample with its neighbouring one. The three grain-size parameters were taken into account applying the two cases where vectors are summed. In order to reduce the "noise" a filtering step was used to organise vectors.

Leroux (1994) reduced sediment transport trend at four cases (FB + , FB−, CB + and CB−) by considering that the sorting systematically improve following the transport which is not the case for mean grain-size and skewness parameters. Smoothing operation still used as suggested in the Gao and Collins (1992) *study.*

Based on variogram analysis, Poizot et al. (2006) defined a new critical distance called the geostatistical distance (Dg). According to the authors, vector transport are spatially better organised with Dg compared to Dcr as it consider eventual obstacle occurrences. Following this methodology the smoothing step is not required.

2 Methodology

2.1 Study Area: Authie Bay

'Picard estuaries' (Canche, Authie and Somme) is a local denomination characterising specific morphologies of estuaries. They located in front of the Eastern English Channel. These estuaries are characterised by the presence of a prograding sand spit, local bank erosions and affected by a general sandfilling. (Dobroniak 1999; Dobroniak 2005). Picard estuaries are described as macrotidal systems with a wave-tidal influence. The mean tidal range is comprised between 4.5 m (neap tide) and 8.5 m (spring tide). Among estuaries, this study focused on the Authie bay (Hauts-de-France, North of France).

Authie estuary is localised between Canche and Somme estuaries (50° 22′ 15, 344″ N; 1° 35′ 4592″ E). The spit namely "Pointe de Routhiauville" (Fig. 1) is prograding following the long-shore drift (Orientation South-North). The forming spit is in partly responsible of the northern bank erosion situated along the Berck beaches and pine forest sector (Hesp et al. 2016). This long-shore drift causes a sediment supply estimated to 20,000/30,000 m^3 per year (Thullie 2016). Spit and main channel evolutions are considered to be main factors inducing the observed erosion while other secondary factors such as storm events may also cause drastic environmental changes.

The sedimentary dynamics is widely influenced by physical forcings such as waves, wind and tides currents. Authie river forcing is considered to have a minor effect with a discharge of 10 $m^3\ s^{-1}$ (Deloffre et al. 2007). Authie bay is mostly filled by sand, even if there is locally some silty to muddy patches where hydrodynamic energy is low. They are located along salt marshes, back to the internal-spit and within well-protected zones such as the 'Anse des Sternes' (i.e. anthropised zone).

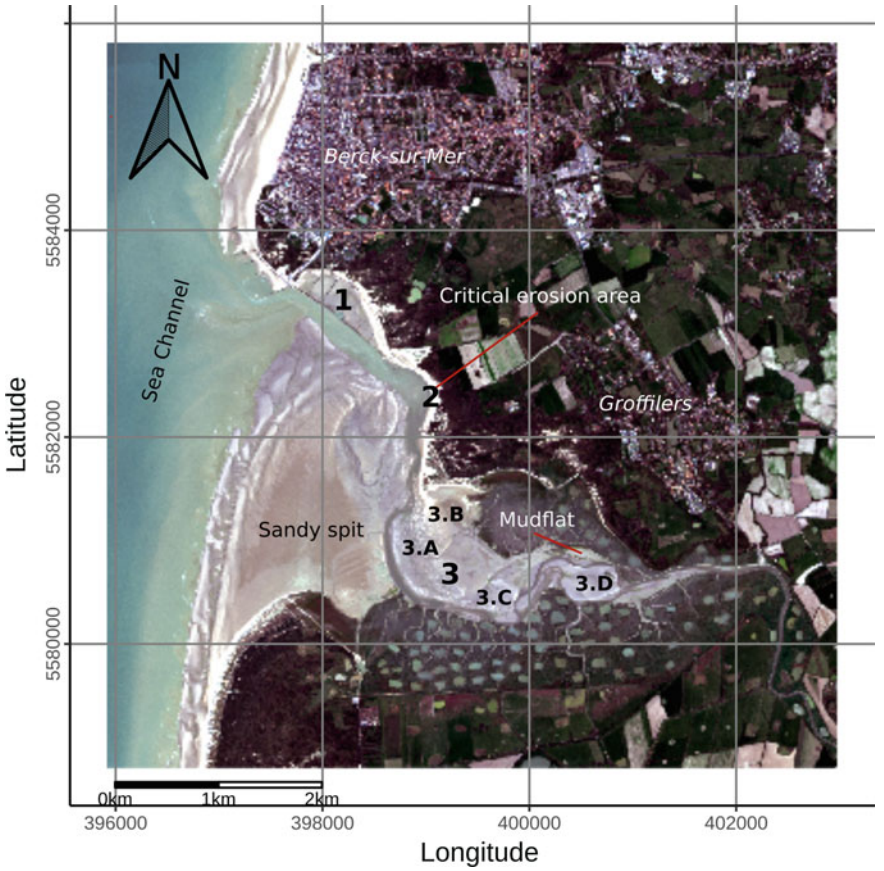

Fig. 1 Studied site representing the Authie bay. Image was acquired with the Sentinel-2 MSI sensor of 09/21/16 (WGS84-UTM31 N). Numbers represent remarkable area for this study

Mean grain-size of downstream-estuary is ranging from 200 to 250 μm. Upstream-estuary denotes a decreasing in grain-size following a long-shore gradient. Close to the Authie channel, mean grain-size (200–250 μm) decreases toward salt marshes domain below 100 μm (Deloffre et al. 2007; Dobroniak 2005).

3 Datasets

Because the main objective of this study was to map spatial and temporal changes of the sediment transport, the multispectral Sentinel-2 (S2) satellite data were perfectly designed for it with a high revisited time over the same scene. S2 sensors (Sentinel-2a and Sentinel-2b) were operated belong ESA (European Spatial Agency).

Table 1 Table representing S2 selected scenes of Authie bay and date of acquisition a period 2016–2018 and main tidal characteristics

Date of acquisition	Tidal Coefficient	Water height (m)	Tidal state	Notable event
21/09/16	70	2.24	Low tide	/
19/01/17	54	2.83	Low tide	After Ergon/Nanette
18/07/17	55	3.67	Low tide	After Leiv/Kurt
25/02/18	48	3.79	Low tide	After succession of storm (5)

The synergy between two similar satellites characteristics, Sentinel-2a and Sentinel-2b, allow to considerably increase the revising time (one image per 5 days) compared to only one satellite platform. With a spatial resolution of 10 meters per pixel, the resolution is not sufficient to discriminate accurately sedimentary structures at low-scale like small ridge marks or punctual spot of vegetation. However, this spatial resolution is suitable for high-scale structures such as sandy spit, main channel, and some megaripples, etc.

Raw images are downloaded from the PEPS platform for free. For this temporal study, among the Sentinel-2 archive, four scenes were selected during a period between September 2016 and February 2018. Each acquisition was captured during the ebb tides in order to maximise the emerged surface. Prior to derive grain-size parameters products using a developed spectral algorithm, images had to be corrected from atmospheric effects. The SEN2COR algorithm (Muller-Wilm et al. 2013) was applied for that purpose. The algorithm used an auto-determination of atmospheric parameters (WINTER/SUMMER and RURAL/MARITIME aerosol) (Table 1).

3.1 Sediment Transport Trend Retrieval

The first step procedure consisted in retrieving from reflectance values grain-size parameters (i.e. mean, sorting, skweness) in each pixel of the image. With this intention, a multi-spectral algorithm was generated directly from spectral features of the sediment surfaces (*more detailed in appendices*). Basically, the algorithm consists in confronting in situ measurement to reflectance value of the images (Fig. 2). Field samples (n = 120) were collected during the S2 overpass at low tide. An hexagonal mesh spacing fixed to 12 m was applied to extract values from grain-size images to the mesh points. The choice of the mesh spacing is constrained by the sentinel-2's spatial resolution. In that sense, there was one node per pixel. Finally the generated grid from remote sensing data was composed by a total of n = 14,534 nodes.

The high spatial sampling window that offer the S2 satellite image resolution presented a serious advantage compared to traditional in situ sampling methods for making sediment trend transport analysis. The grid generated by remote sensing

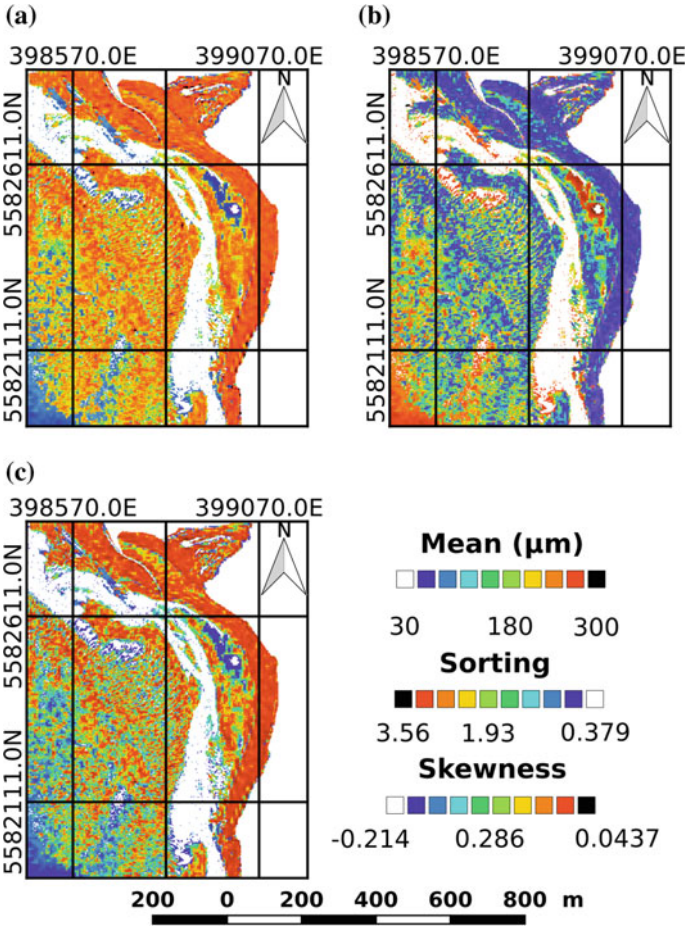

Fig. 2 Example of grain-size properties mapping in Authie estuary (Area 2). **a** represent mean grain-size (µm), **b** Sorting and **c** Skewness. Mapping from algorithm applied to SPOT 6/7 (1.5 m). (WGS84-UTM31 N)

techniques is regularly distributed with a high spatial resolution whereas data are in often unevenly distributed and sparse using traditional sampling strategies. Mean, Sorting and Skewness grid were generated (Fig. 2) with a characteristic distances fixed to 15 m, corresponding to the average spacing of the mesh after remove No-available (NA)-value nodes.

The second step consisted in implementing these extracted values as inputs of the GSTA analysis. Here the GSTA- plug-in used was developed by Poizot et Méar (2010). This extension is freely available on QGIS software. In term of transport trend, the eight potential cases defined in Gao and Collins (1992) were used.

After the second step applied, among the transport vectors pool, some of them did not follow the best transport case or were not significant. The third step was to

select only representative vectors with a determined case. The selection was based on vector-modules (significance of the transport vector) included in the interquartile range.

At that step procedure, maps may display disorganised transport trends. That is the reason why, Gao and collins (1992) applied a filtering step to limit the noise response and reorganize vectors. The last step was smoothing angle value of vectors by operating an interpolation procedure, the inverse distance weighting under the GRASS-GIS 7.0 software. Note that this step was recommanded since the Dcr was retained in this study. Finally a better interpretation of the sedimentary transport pattern was observed. Indeed, following each step of the overall procedure presented here, transport patterns may be highlight and discuss according to sedimentary processes and with respect to sedimentary structures throughout the overall bay

As mentioned before, the Authie bay presents 3 interesting areas, (Fig. 1). The first selected zone (1) is located close to the town of Berck, it is the most anthropic area of the inner estuary with seven embankments (six groins and one long-shore embankement) and one riprap close to the upper beach. The second selected zone (2) is located in front of a pine woods, this area is characterised by a high erosion rate (Hesp et al. 2016) and the last one is located close to the salt marsh in the middle estuary. This is a prograding domain which indirectly affected by the general sand-filling. This last area was sub-divided into four sub-areas following their structures and/or hydrological characteristics: megaripple, east of western intertidal/subtidal platform, middle mudflat and east mudflat area (cf. Fig. 1a–d).

4 Results

4.1 Embankment Sector: Anthropogenic-Influenced Area

This sector is characterised by the presence of embankments. Figure 3 corresponds to a simplified map of sediment transport trend. The scene shows few morphological variations. Whatever the period of acquisition considered transport vectors are south-oriented. In details, Fig. 3b and d (storm season) reveals similar patterns whereas 3a and c reveals discrepancies notable at the south and at the east of the scene.

Rose diagram representation is usually used to summarise transport orientation. For realising this diagram, all vectors of the selected sectors are used ($n = 2673$ nodes). Mean and standard deviation (sd $\pm$ mean) are represented by points and the colour code is the same as Fig. 2 one.

Whatever the period considered, Fig. 4 demonstrates the main transport trend is south-south-east-dominated. A mean change are observed for 01/17 and 09/16. Figure 4 may presented a change concerning the sediment transport trend for this area.

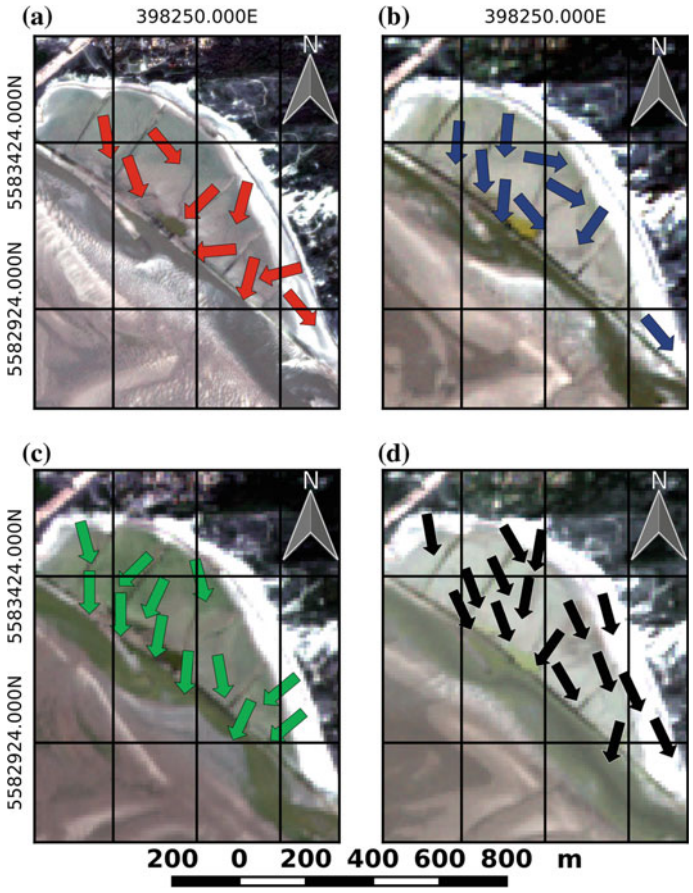

Fig. 3 Transport evolution for the embankment sector corresponding to **a** 09/16, **b** 01/17, **c** 07/17 and **d** 02/18. For a suitable reading some vectors were represented

4.2 Pine Forest: Erosion Area This Sector Presents a High Erosion Rate

At the east of the scene (Fig. 5), it demonstrates the progression of the sandy spit and the deviation of the main channel toward east sector. Figure 5 displays a sediment transport trend mainly south-oriented with a strong spatial and temporal variation. At the North, vectors indicate two transport behaviours: (1) close to channel, sediment transport vectors are oriented toward channel except for Fig.5b whereas (2) close to pine-forest zone vectors are oriented toward upper beach. Figure 5c (07/17, in green) shows in the southern part a sediment transfer from West to East.

Figure 6 demonstrates a temporal changing in vectors orientation trend. East transport frequency vector increases whereas West transport frequency vectors increases

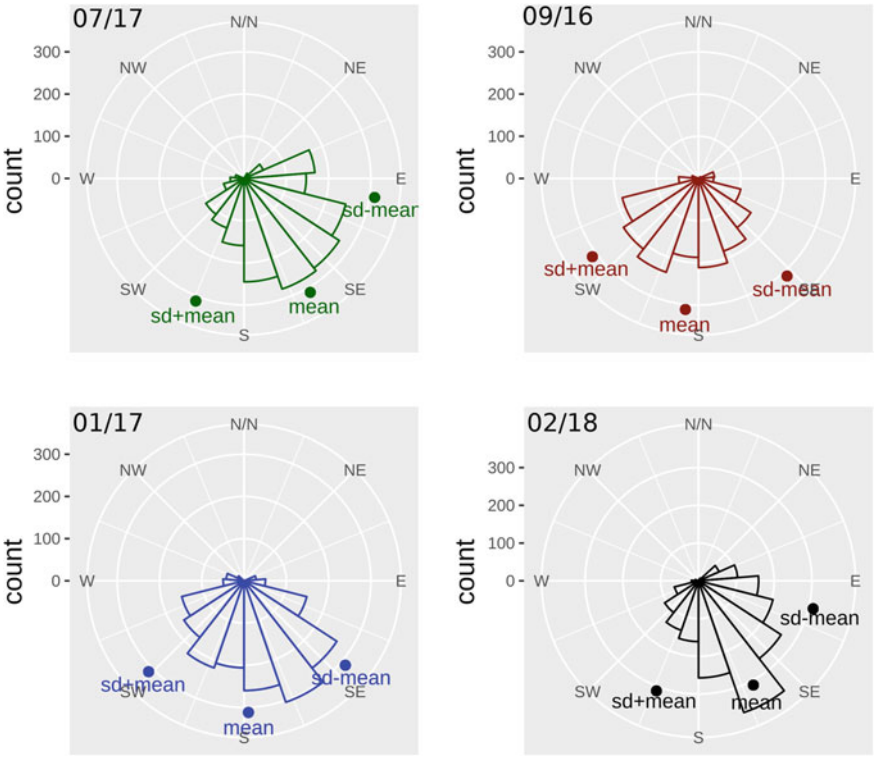

Fig. 4 Rose diagram showing main azimuthal trend of vectors transport in the embankment sector. Frequency of the transport orientations are represented by the coloured boxes and the points represent standard deviation and the mean of transport orientation. In red 09/16, blue 01/17, in green 07/17 and in black 02/18. Rose diagram suggests a change of mean transport trend for this area from 07/17

then diminishes. It is notably true for 02/18 period. 09/16 is considers as a period where transport towards channel is the most substantial. 01/17 and 07/17 demonstrate a sediment transport trend toward south places. 02/18 period displays a shift in comparison with 09/16 one

4.3 Middle Estuary

4.3.1 Megaripples Area

Megaripples usually describe a sector with a highly dynamics caused by strong tidal currents. Within this sector, megaripples are formed by flood tidal current. Figure 7

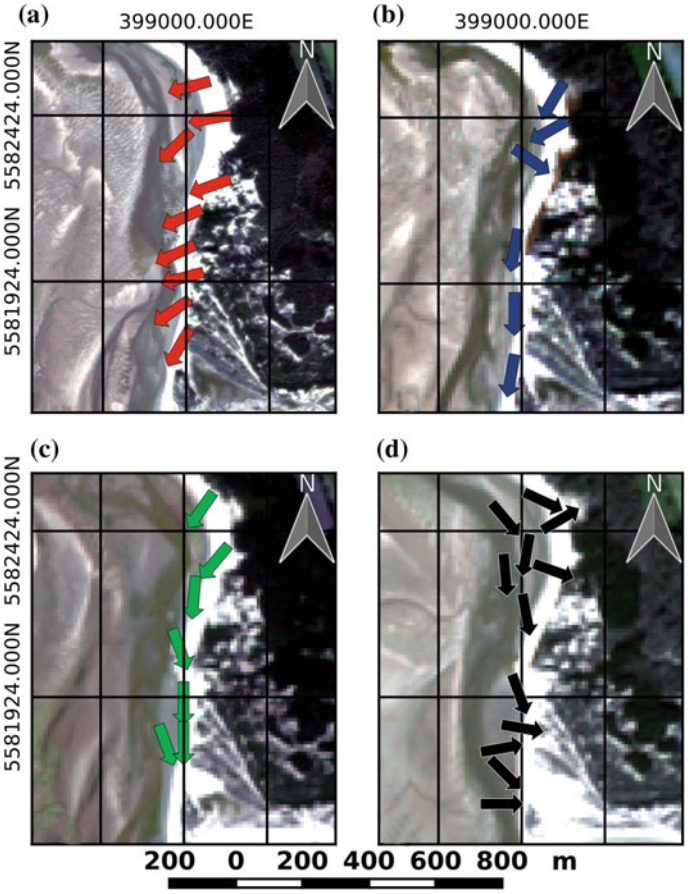

Fig. 5 Transport evolution for the pine forest sector corresponding to **a** 09/16, **b** 01/17, **c** 07/17 and **d** 02/18. For a suitable reading some vectors were represented. For a suitable reading some vectors were represented

displays a strong spatial variability over time. Vector transport trends switch preferably oriented toward south-south east with the time. Maps show a sandy bank progressing toward south. Close to the Authie channel, the different figure display transport vector orientations follwing the main channel. Everywhere else vectors follow the sandy bank progression which is consistent with sedimentology knowledges, notably Fig. 7d.

Figure 8 also shows a changes of the transport trend in this area. Mean transport seems to oscillate between S–SE and South. Green and black rose demonstrate a transport mode mainly oriented toward east (middle estuary and mudflat). Red and blue rose diagram diagram are similar and show a transport mode mainly oriented toward the Authie channel.

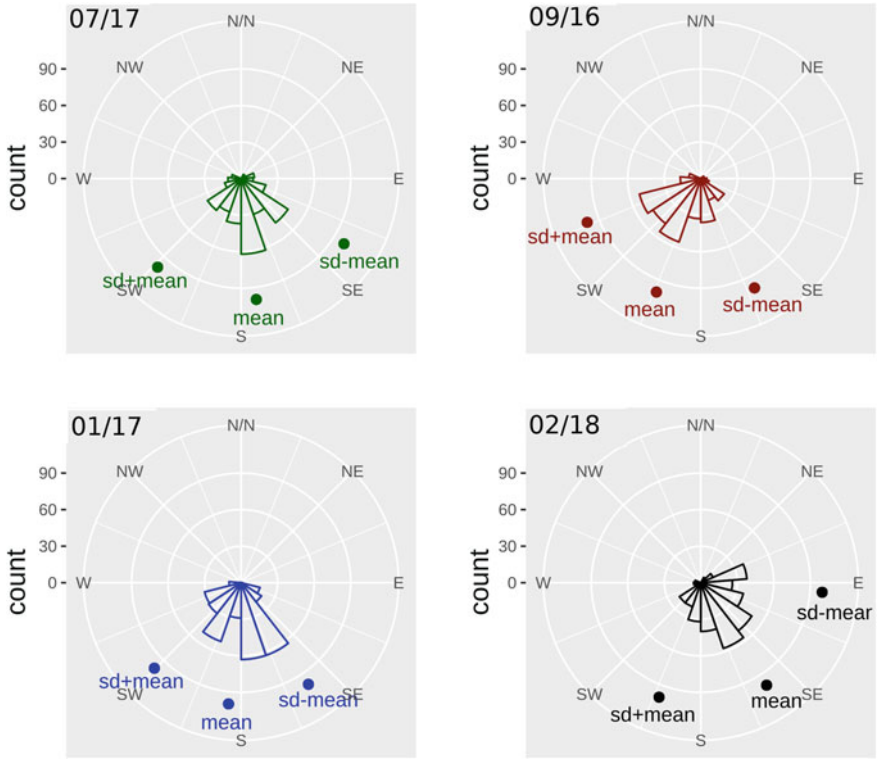

Fig. 6 Rose diagram showing main azimuthal trend of vectors transport in the high erosion rate sector. Frequency of the transport orientations are represented by the coloured boxes and the points represent standard deviation and the mean of transport orientation. In red 09/16, blue 01/17, in green 07/17 and in black 02/18. Notice a difference of mean transport between 02/18 (in red) and the others periods. The erosion behavior seems to diminish

4.3.2 Internal Western Platform

This area is characterised by silty sediment due to a low hydrological energy. Maps presented in Fig. 9 permits to detect important changes in geomorphological structures.

The first observed change correspond to segmentation of the point of the spit from its basis by an overwash effect which is probably caused by the channel east-deviation. The second change results from this segmentation and correspond to a drastic change of sedimentary facies. Indeed, the forming overwash causes a clear modifications in term of sediment transport trend, in particular at the North of this sector. Figure 9d displays potential transport of sediment from the overwash to the south. Other figures seem to demonstrate a sediment transport trend characterising this sector of "closed system". At the East of the images, except for Fig. 9a and b,

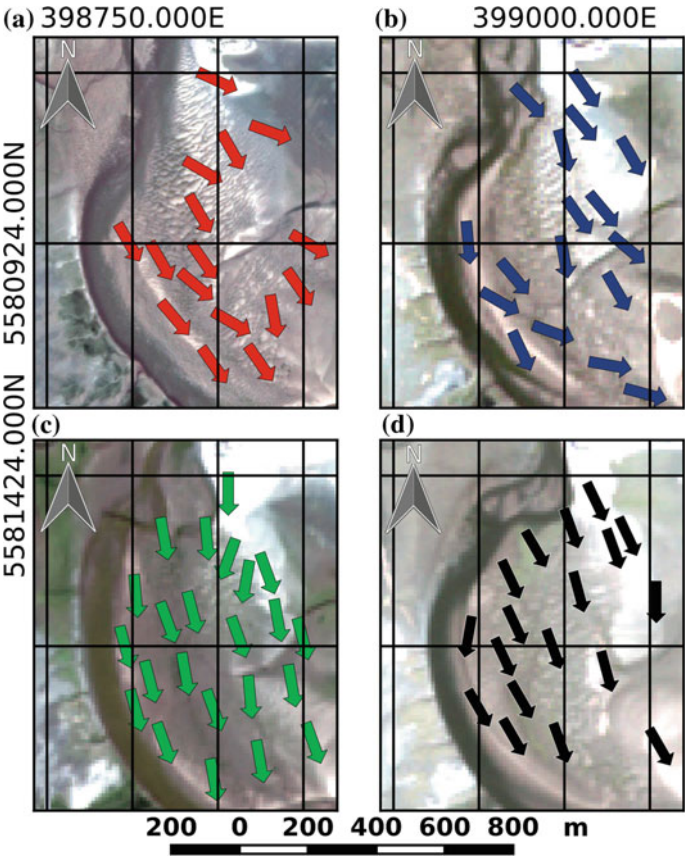

Fig. 7 Transport evolution for the megaripples sector corresponding to **a** 09/16, **b** 01/17, **c** 07/17 and **d** 02/18. For a suitable reading some vectors were represented. For a suitable reading some vectors were represented

data indicate a transport orientation vectors are consistent with the building of a new coastal dunes.

Rose diagram in Fig. 10 displays a strong changing in transport trend. East transport becomes important whereas West transport becomes lower. SE orientation has increased since 07/17 (green and black). Black rose diagram (02/18) seems to demonstrate a increasing of frequency of west and south-oriented vectors and an increasing of south and east-south oriented one.

4.3.3 Middle Mudflat

The acquisitions of middle mudflat sector in Fig. 11 shows a sediment transport trend quite uniform and a cross-shore oriented with variation between SSO and SSE.

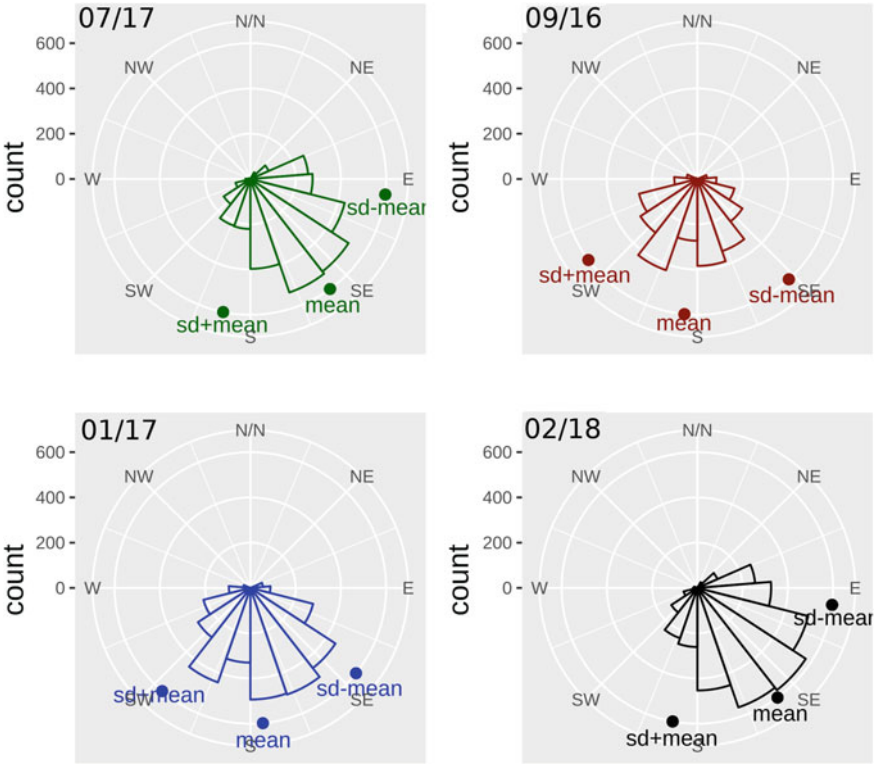

Fig. 8 Rose diagram showing main azimuthal trend of vectors transport in the megaripples sector. Frequency of the transport orientations are represented by the coloured boxes and the points represent standard deviation and the mean of transport orientation. In red 09/16, blue 01/17, in green 07/17 and in black 02/18. Mean frequencies describes a shift from S-SW to S-SE

Transport trend seems to follow secondary channels. Close to the mudflat (North of the map), transport trend are quite constant and display a transport trend toward Authie channel. These maps display a secondary channel at the centre part of the zone, vectors, close to it, seems to follow the draining flux. After 01/17 (green) a shift is noticed at the east of the transport trend maps.

Rose diagram for this sector (Fig. 12) seems to confirm the changing transport trend toward South and West. SSE and East-oriented transport trend decrease. In term of variability, red and green rose diagrams (09/16 and 07/17) possess a higher variability than the two others.

4.3.4 East Mudflat

For this sector, strong spatial variation of the channel variation are observed in the northern part (Fig. 13). Figure 13c reveals two well-formed channels. Transport

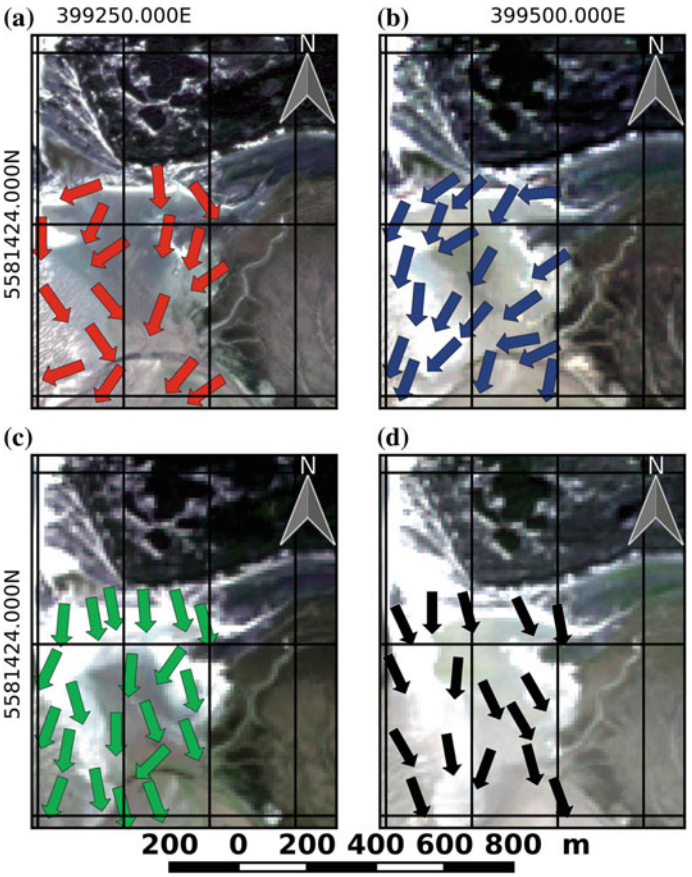

Fig. 9 Transport evolution for the platform sector corresponding to **a** 09/16, **b** 01/17, **c** 07/17 and **d** 02/18. For a suitable reading some vectors were represented

vector representation in Fig. 13 display a sediment transport trend along the Authie channel. However, the cross-shore transport trend variates. Indeed, Fig. 13a (09/16) and c (07/16) show an orientation toward the downstream. Figure 13b and c seem to demonstrate a converging pattern. Figure 13d (02/08) display a east-deviation pattern.

Rose diagram, Fig. 14, confirms the shift of transport trend toward east. Indeed, means of transport trend show a progressive shifting from south to SSE. East sediment transport trend becomes stronger whereas west becomes lower. Rose diagrams are similar with presented one in Fig. 12.

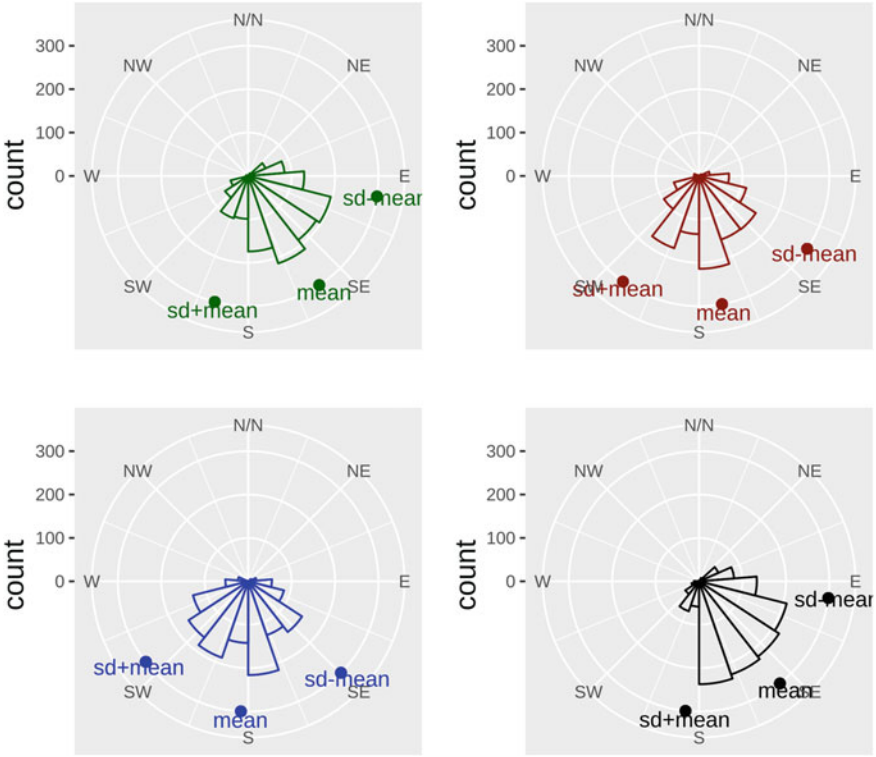

Fig. 10 Rose diagram showing main azimuthal trend of vectors transport in the internal side of plateform sector. Frequency of the transport orientations are represented by the coloured boxes and the points represent standard deviation and the mean of transport orientation. In red 09/16, blue 01/17, in green 07/17 and in black 02/18. Frequencies of south-east-oriented vector increase and mean seems to display the influence of the secondary spit segmentation

5 Discussion

5.1 Embankment Sector: Effects of the Construction

In the embankment sector, sediment transport trend is strongly marked by ebb tide, explaining south-oriented vectors. It is important to notice that evacuation of water is locally possible by a breach within the embankment. Figure 4 shows a temporal variation of the transport trend and it is difficult to differentiate summer profile from storm profile due to embankment. The rose diagram representation also shows a decreasing west-oriented transport. A local transport is notice due to alteration by the wave current or channel deviation, which do not permit a sedimentary retention. Some associations (e.g. *SOS Baie d'Authie*) notified construction alterations notably

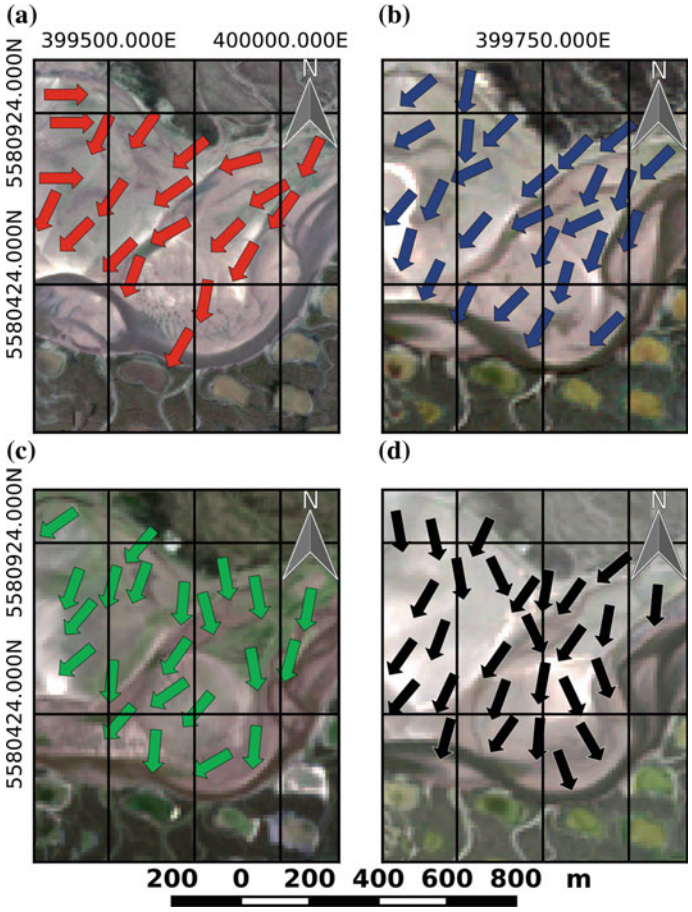

Fig. 11 Transport evolution for the middle mudflat sector corresponding to **a** 09/16, **b** 01/17, **c** 07/17 and **d** 02/18. For a suitable reading some vectors were represented

for the distal part. A variation of frequencies of SE-oriented vectors and a decreasing of west-oriented vectors may affect the supply of sediment in the pine forest sector.

5.2 Pine Forest: Sector Undergoing a Critical Erosion

This sector is marked by a long-shore flux, the rose diagram (Fig. 6) indicates a transport trend toward a secondary spit. It also demonstrates a reversal of erosion trend in 02/18. However upper beaches can be affected by a variables sandy supply as shown in Fig. 5. The transport trend display a change from long-short to cross-shore, notably at the south of this sector. This change of transport orientation can be

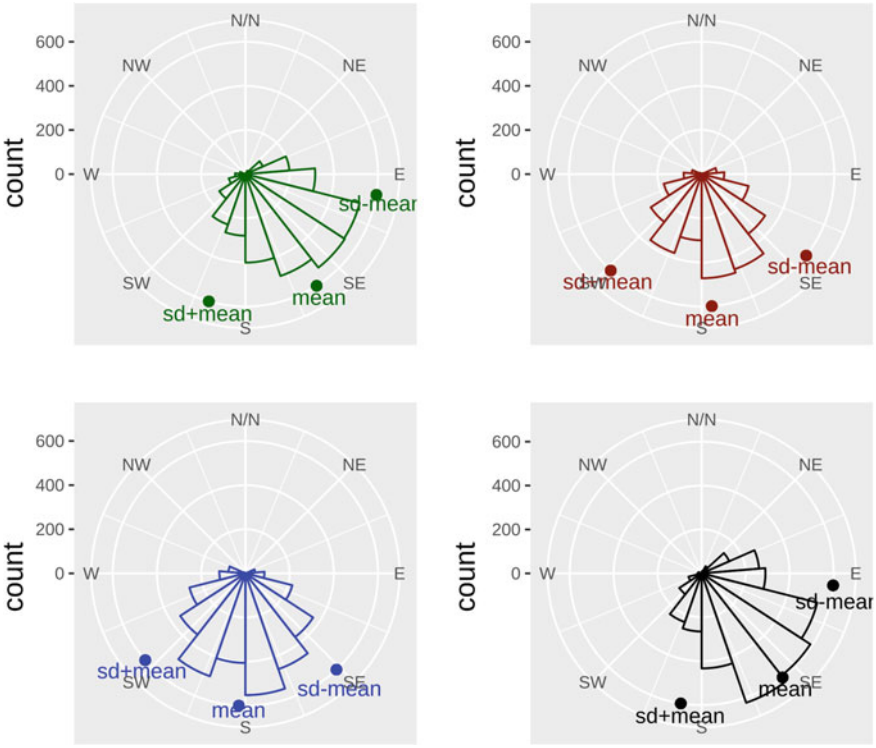

Fig. 12 Rose diagram showing main azimuthal trend of vectors transport in the middle mudflats sector. Frequency of the transport orientations are represented by the coloured boxes and the points represent standard deviation and the mean of transport orientation. In red 09/16, blue 01/17, in green 07/17 and in black 02/18. Frequencies display a change of transport trend

explained by the formation of an overwash. The overwash changes the narrow upper-beach into a larger one that makes cross-shore transport possible. An explanation of the formation of this overwash is the emergence of a former embankment deviating the channel toward the secondary spit. The channel deviation provokes a weakening of the upper-beach which induces an exposure of the dunes to the wave effects especially during storm periods. The presence of this natural breach influences the internal secondary spit and its sediment transport. For future studies, it could be interesting to realise a time serie analysis on this sector in order to obtain characteristic transport for each sub-area.

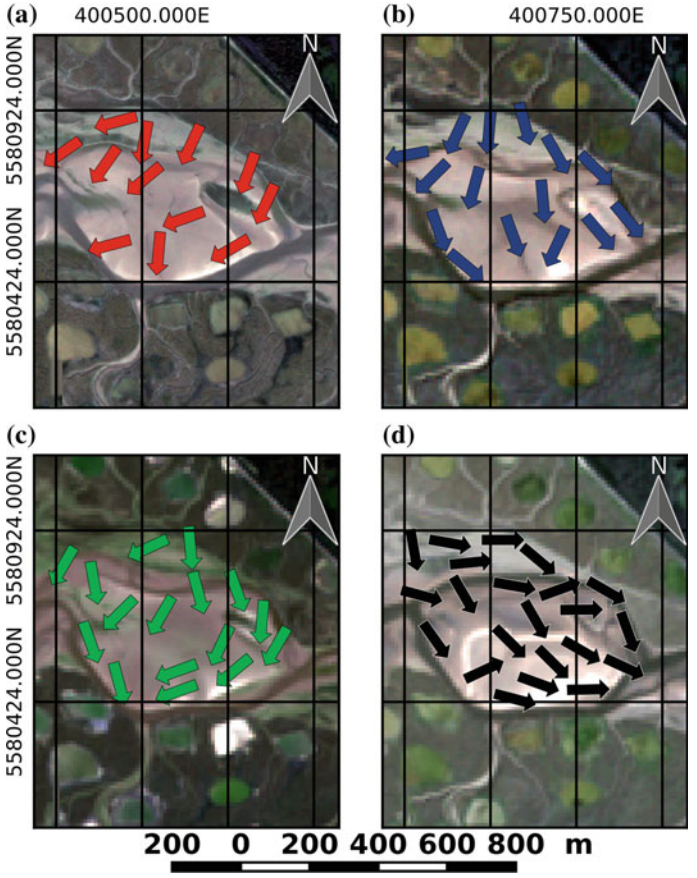

Fig. 13 Transport evolution for the east mudflat sector. corresponding to **a** 09/16, **b** 01/17, **c** 07/17 and **d** 02/18. For a suitable reading some vectors were represented. For a suitable reading some vectors were represented. During storm period (**b** and **d**), shifting of sediment transport vectors are observed

5.3 Middle Estuary: Progradation of the Mudflat

This sector is mainly marked by a decreasing east transport, mainly in middle and east sectors (Figs. 11, 12 and 13). This diminution suggests a potential changes of the sandfilling trend. Middle and east sectors are mostly similar. However a possible influence of ebb tides can overestimates the representation of some vectors. For a better interpretation, ebb tides influence must be defined in order to determine the cross-shore transport trend.

For the internal side of secondary spit, from 09/16 to 07/17, the transport is characterised by a «semi-closed circuit». Some vectors follow the south-progressing of the sandy structure which is appeared after Leiv and Kurt storms (03-05 February

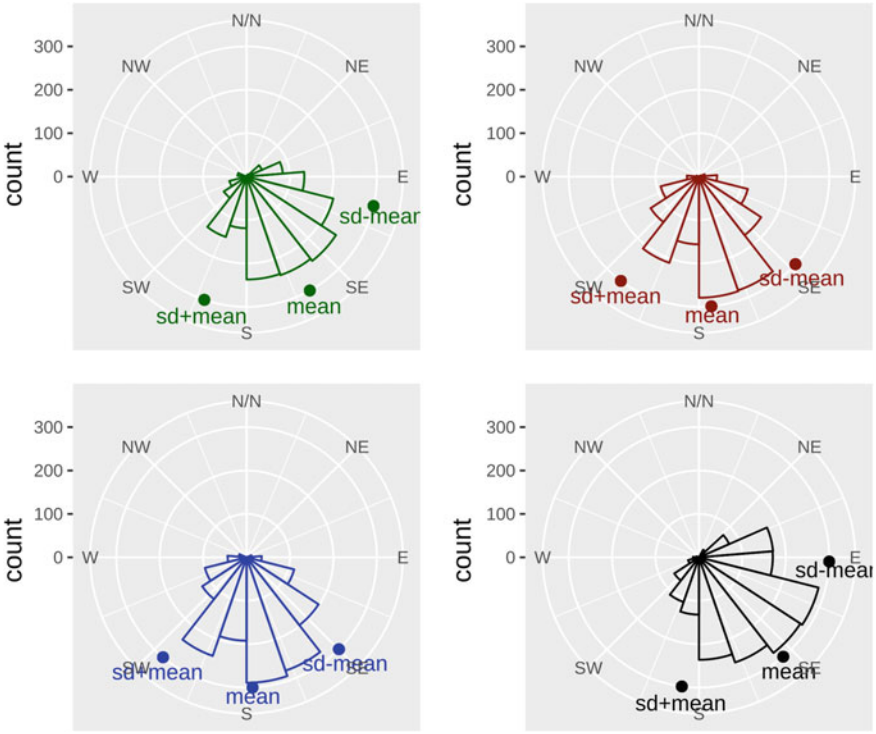

Fig. 14 Rose diagram showing main azimuthal trend of vectors transport in the eastern part mudflat sector. Frequency of the transport orientations are represented by the coloured boxes and the points represent standard deviation and the mean of transport orientation. In red 09/16, blue 01/17, in green 07/17 and in black 02/18. Means of vector orientation demonstrate a progressive change toward S–SW. An increasing in frequency is observed for S–SE and E- oriented vector. For S–SW oriented vector, frequencies diminish with the time

2017). Figure 9c and d shows the consequences of separation of the top of the spit from its basis due to the overwash event. Transport trend describes an open system with a sediment supply from the external side of the spit to the internal one. Sandy structure still progresses and some vectors follow this progression. Rose diagram for this sector. Figure 10 confirms the change of transport from «semi-closed circuit» to open system. It is possible to distingish this discruption taking acount mean of tansport trend. This deviation is due to an increasing frequency of S–SE oriented vectors occurrence which is explained by the formation of the overwash.

Middle and east sectors present some similar characteristics such as decreasing of the occurrence of east-oriented vector and a strong response of the ebb tide (rose diagram of Figs. 12 and 14). However, the observation of the map in the middle part (Fig. 11) demonstrates that the transport turn to be long-shore while Fig. 13 show a reversing transport trend from East to West. This shifting seems to be less marked in middle part of the estuary. This observation noticed in east part could be justified

by the formation of new channel showed in Fig. 13d which deviates the transport of sediment and the water evacuation effect during ebb tide seem to be strengthened. It is possible to consider prevalence between tidal and river forcing to understand transport trend variability.

Megaripples sectors are noticed by a strong spatial and temporal variation (Figs. 7 and 8). This sector is characterized by a high hydrodynamic. Moreover most of vectors are oriented in the same direction as megaripples one. These structures are formed by flood current. Transport trend follow the formation of sandy structure. It is possible to notice a sandfilling of an secondary channel (Fig. 7). Vector describing draining flux (S and SSW-oriented) are less represented.

6 Conclusion

This study demonstrates that the developed approach based on remote sensed grain-size products combined to a GSTA is a useful technique for mapping sediment transport trends. Such as results are important for observing long-term events such as sandfilling, erosion/accumulation patterns. The purposed study displays a possible change of some described event (i.e. sandfilling, erosion). However many vectors may be influenced by last short-term event (i.e. ebb tide currents), a correction would be operated to obtain responses masked by the ebb tidal effects one. Such as results are important for observing short-term events such as storm events and their consequences on drastic changes in sediment deposits.

Observations assume the influence of estuarine dynamics on transport trend. For example the formation of an overwash in secondary spit sector causes the opening of internal side on external side. This variation justifies a reworking of the sectoring of the estuary in order to observe accurately local variation. It is necessary to validate transport vectors generated by comparing azimuthal vectors with well-known sedimentary structures and *a fortiori* topographical analyses. Similarly transport vectors may be confronted with current measurements, while erosion effects may be link to shore-line variations.

Acknowledgements E. Poizot for his advises and for making the software GSTA available. ESA and PEPS/THEIA platform for sharing the L1 Sentinel-2 Data. We would like to thank the CPER-MARCO and the BQR-ULCO-TéléEST for their funding supports allowing field some investigations within the Authie Bay.

Appendices: Grain-Size Parameters Algorithm Introducing

In order to map grain-size properties, algorithm was applied. This algorithm is based on the synergy between field sampling and spectral information (Reflectance) for a pixel. Mean grain-size is computed such as:

$$\left\{ \begin{array}{l} Coarsefraction = 215.30 \times \log\left(\dfrac{R_{\text{red}} - R_{\text{green}}}{R_{\text{green}} - R_{\text{blue}}}\right) + 290.69 \\ Finefraction = \left| -121.17 \times \left(\dfrac{R_{\text{green}} - R_{\text{blue}}}{R_{\text{blue}}}\right) + 112.20 \right| \end{array} \right\} \quad (1)$$

where:

RX Reflectance values for a spectral channel.

These two resulting maps are merges to obtain a mean grain-size map. Merging criteria is defined by the following ratio:

$$Ratio = \frac{R_{\text{red}} - R_{\text{green}}}{R_{\text{Infra - red}} - R_{\text{red}}} > X \quad (2)$$

where:

X Muddy/Sandy ratio, empirically fixed by the operator. (for this study X = 0.20–0.25).

The sorting parameter is computed such as:

$$\sigma = 0.002 \times D_{90} - 0.013 \times D_{10} - 0.004 \times D_{50} + 3.642 \quad (3)$$

where:

D10 0.59047(mean grain-size)
D50 1.68(mean of coarse grain-size) and 0.90227(mean of fine grain-size)
D90 1.21(mean grain-size) + 69.71.

The skewness parameter is applied such as:

$$S = \frac{\left(9.1.10^{-4}\ D_{50} + 1.5.10^{-3}\ D_{10}\right)^2 - (0.23\log(D_{50}) + 1.3)^2}{2} \quad (4)$$

References

Adam, S., Vitse, I., Johannsen, C., & Monbaliu, J. (2006). Sediment type unsupervised classification of the Molenplaat, Westerschelde estuary, the Netherlands. *EARSeL eProceedings, 5,* 146.

Deloffre, J., Verney, R., Lafite, R., Lesueur, P., Lesourd, S., & Cundy, A. B. (2007). Sedimentation on intertidal mudflats in the lower part of macrotidal estuaries: Sedimentation rhythms and their preservation. *Marine Geology, 241,* 19–32. https://doi.org/10.1016/j.margeo.2007.02.011.

Deronde, B., Houthuys, R., Henriet, J.-P., & Lancker, V. V. (2008). Monitoring of the sediment dynamics along a sandy shoreline by means of airborne hyperspectral remote sensing and LIDAR: A case study in Belgium. *Earth Surface Processes Landforms, 33,* 280–294. https://doi.org/10.1002/esp.1545.

Dobroniak, C. (1999). Les progrès de la sédimentation dans un estuaire de type picard: L'estuaire de l'Authie (Nord-Pas-de-Calais). *Méditerranée, 93,* 65–68. https://doi.org/10.3406/medit.1999.3134.

Dobroniak, C. (2005). Morphological evolution and management proposals in the Authie Estuary, northern France. *Proceeding Dunes and Estuaries, 2205,* 537–545.

Gao, S., & Collins, M. (1992). Net sediment transport patterns inferred from grain-size trends, based upon definition of "transport vectors". *Sedimentary Geology, 81,* 47–60. https://doi.org/10.1016/0037-0738(92)90055-V.

Hesp, P. A., Ruz, M.-H., Hequette, A., Marin, D., & Miot da Silva, G. (2016). Geomorphology and dynamics of a traveling cuspate foreland. *Authie estuary, France, Geomorphology, 254,* 104–120. https://doi.org/10.1016/j.geomorph.2015.11.015.

Leroux, J. P. (1994). Net sediment transport patterns inferred from grain-size trends, based upon definition of "transport vectors". *Sedimentary Geology, 90,* 153–156. https://doi.org/10.1016/0037-0738(92)90055-V.

Mclaren, P. (1981). An interpretation of trends in grain size measures. *Journal of Sedimentary Research, 51*. https://doi.org/10.1306/212F7CF2-2B24-11D7-8648000102C1865D.

McLaren, P., & Bowles, D. (1985). The effects of sediment transport on grain-size distributions. *Journal of Sedimentary Research, 55*(4), 457. https://doi.org/10.1306/212F86FC-2B24-11D7-8648000102C1865D.

Muller-Wilm, U., Louis, J., Richter, R., Gascon, F., Niezette, M.: Sentinel-2 Level 2A Prototype processor: Architecture, algorithms and first results. *ESA Living Planet Symposium*, 2013, 722, ESA Special Publication, 98.

Poizot, E., Mear, Y., Thomas, M., & Garnaud, S. (2006). The application of geostatistics in defining the cheractristic distance or grain-size trend analysis. *Compute and Geosciences, 32,* 360–370. https://doi.org/10.1016/j.cageo.2005.06.023.

Poizot, E., & Méar, Y. (2010). Using a GIS to enhance grain size trend analysis. *Environmental Modelling and Software, 25,* 513–525. https://doi.org/10.1016/j.envsoft.2009.10.002.

Rainey, M. P., Tyler, A. N., Gilvear, D. J., Bryant, R. G., & McDonald, P. (2003). Mapping intertidal estuarine sediment grain size distributions through airborne remote sensing. *Remote Sensing of Environment, 86,* 480–490. https://doi.org/10.1016/S0034-4257(03)00126-3.

Small, C., Steckler, M., Seeber, L., Akhter, S. H., Goodbred, S., Jr., Mia, B., et al. (2009). Spectroscopy of sediments in the ganges-brahmaputra delta: Spectral effects of moisture, grain size and lithology. *Remote Sensing of Environment, 113,* 342–361. https://doi.org/10.1016/j.rse.2008.10.009.

Smith, G. M., Thomson, A.G., Moller, I., & Krompkamp, J. C. (2004). Using hyperspectral imaging for the assessment of mudflat surface stability. *Journal of Coastal Research*, *20*(4), 1165–1175. West Palm Beach (Florida). ISSN 0749-0208.

Thulie, A. (2016). Côte & Mer, *La lettre du Réseau d'Observation du Littoral Normand et Picard*.

Yang, X., Damen, M., & van Zuidam, R. (1999). Satellite remote sensing and GIS for the analysis of channel migration changes in the active Yellow River Delta, China. *International Journal of Applied Earth Observation and Geoinformation, 1,* 146–157. https://doi.org/10.1016/S0303-2434(99)85007-7.

Evolution of Water Levels at Coastal Hydrological Stations of the Mekong Delta

Ngọc Trân Nguyễn

Abstract From the historical hourly water level data during 29 years, from 1988 to 2016, annual mean water level, annual highest high water level, annual lowest low water level, annual maximum range of tide and some others levels at coastal hydrological stations of the Mekong delta are computed. Results show that at these stations, the annual mean water level and the volume of sea water entering in the delta with tide are increasing; the volume of inland water evacuated to the sea with tide tends to decrease. Evolution of the annual lowest low water level shows an increasing trend, faster in the last 14 years at most of the coastal stations. During 1988–2016 the annual maximum range of tide increases in the eastern coast stations, decreases at Năm Căn, and in the western coast stations except Xẽo Rô, but decreases at most of stations during 2003–2016 except Bình Đại, Xẽo Rô and Rạch Giá. The changes of the water levels at the estuarine areas reported in this chapter are informative for the planning of water regulation works in the Mekong Delta, especially relating to the construction of the sluicegates Cái Lớn and Cái Bé currently under study and the planned ones on the Tiền River branches such as Hàm Luông and Cổ Chiên. Whether and how the changes of water levels highlighted at Năm Căn station are relevant to the confluence and interaction between the tides of the East Sea (South China Sea) and the West Sea (Gulf of Thailand) in the context of global climate change, sea level rise, is an open issue.

Keywords Mekong delta · Coastal hydrological station · Estuaries · Tide · Water levels · River and marine processes · Sea level rise

1 Introduction

Every river delta in the world is a place where the sea and the river interact. The estuarine area is the interface of this interaction.

The formation of the Mekong Delta has been well researched. Studies have agreed that the delta has been built during the last 6000 years since the sea receded by the

N. T. Nguyễn (✉)
University of Ho Chi Minh City, Ho Chi Minh City, Vietnam

K. D. Nguyen et al. (eds.), *Estuaries and Coastal Zones in Times of Global Change*, Springer Water,
https://doi.org/10.1007/978-981-15-2081-5_48

sediment transport and deposition process of the Mekong (Tamura et al. 2012). The delta is being affected by climate change, sea level rise, and by upstream water uses (Nguyễn 2010). Does the Mekong delta be starting an inverse process? In this chapter, the author proves that sea level rise is a reality by assessing the changes of water levels monitored at the river mouths in the delta between 1998 and 2008.

The effective sea level rise in a delta depends also on the local human activities (Ericson et al. 2006). River sand mining (Bravard et al. 2013; Anthony et al. 2015) and groundwater extraction (Erban et al. 2014) are quite important in the delta, especially along Tiền river branches. These facts, added to the changes of water level monitored closely at the stations at Tiền River's mouths up to 2013, show that the Mekong Delta is facing the danger of sinking and erosion (Nguyễn 2015).

Given the increasingly serious coastal erosion along the eastern coast and the western coast of the delta, this report examines the changes in water levels at all the coastal hydrological stations in the delta from January 1, 1988 to December 31, 2016. The water levels examined include annual mean water level, annual highest high water level, annual lowest low water level, annual mean daily high water level, annual mean daily low water level, and annual maximum range of tide.

2 The Main River Channels Connected to the Sea

The Tiền River is connected to the East Sea through 5 channels spanning approximately 200 km of the coast, including Cửa Tiểu, Cửa Đại, Ba Lai, Hàm Luông, Cổ Chiên (which divides into Cổ Chiên and Cung Hầu before pouring into the sea). The Hậu River has 2 main mouths namely Định An and Trần Đề. Other channels such as Mỹ Thanh, Gành Hào, and Bồ Đề are also flowing into the East Sea.

Formerly, the Tiền and the Hậu Rivers used to flow into the East Sea through a total of nine distributaries including Cửa Tiểu, Cửa Đại, Ba Lai, Hàm Luông, Cổ Chiên, Cung Hầu, Định An, Bassac (Ba Thắt), and Trần Đề. The Bassac channel disappeared due to natural sediment deposition while the Ba Lai channels has been blocked since 2003 with a salinity control sluicegate.

In the Ca Mau peninsula, the main channels connected the delta to the sea are Mỹ Thanh, Gành Hào, and Cửa Lớn—Bồ Đề running from the east coast to the west coast. The main channels flowing into the West Sea including Cửa Lớn, Bảy Háp, Ông Đốc, Cái Lớn, Cái Bé, Cái Sắn which runs from the Hậu River to the West Sea.

In Cà Mau province, there is a total of 27 channels of different sizes connected to the West Sea. All the major channels are blocked by salinity control sluicegates. In An Minh and An Bien districts, there are 10 channels connected to the sea spanning a long stretch of coastal mudflat.

3 The Coastal Hydrological Stations

There are 9 coastal hydrological gauging stations in the Mekong Delta, listed clockwise, including Vàm Kênh, Bình Đại, An Thuận, Bến Trại, Mỹ Thanh, Gành Hào, Sông Đốc, Xẽo Rô, and Rạch Giá. The Năm Căn station on the Cửa Lớn River running from the East Sea to the West Sea is additionally examined. The locations of the stations are presented in Fig. 1.

The stations can be categorized into (1) the Tiền river mouth stations including Vàm Kênh, Bình Đại, An Thuận, and Bến Trại, (2) the Cà Mau peninsula stations on the eastern coast including Mỹ Thanh and Gành Hào, (3) the Năm Căn station in between the East Sea and the West Sea, and (4) the West Coast stations including Sông Đốc, Xẽo Rô, and Rạch Giá.

4 Water Level Data at the Coastal Hydrological Stations

The data used in this report are historical hourly water level measured at the 10 stations mentioned above. As regulated by the hydro-meteorological sector, the data are first sent to the Southern Regional Hydro meteorological Center. After being checked and adjusted if necessary, the data are disclosed and considered official. The data from Vàm Kênh station, one of the five stations in the Mekong Delta and the only automatic coastal station, installed by the Mekong River Commission, are sent directly to the provincial center and the Southern Regional Hydro meteorological Center.

With the help of the Regional Center and the provincial centers namely Tiền Giang, Bến Tre, Sóc Trăng, Bạc Liêu, Cà Mau, and Kiên Giang, we obtained water level data from January 1, 1988 to December 31, 2016. The data series at My Thanh stopped on December 31, 2008 and the data from Song Doc began on January 1, 1996.

A river delta is a place of interaction between the river and the sea processes in which the river mouths are the interface. When the annual mean water level increases, the inundation risk increases. It is the same with the annual highest high water level and the volume of sea water pouring into the delta through the river mouths. When the annual lowest low water level increases, the drainage of water from the delta by tide into the sea decreases.

For these reasons, annual mean water level, annual highest high level, annual lowest low water level, and annual maximum range of tide in the 29 year period (1988–2016) and the 14 year period (2003–2016) at the river mouth's stations will be examined.

Trạm	Địa danh	Sông	Vĩ độ	Kinh độ	Loại trạm
Vàm Kênh	Tiền giang - Gò Công Đông - Tân Thành	Cửa Tiểu	10°16'	106°44'	I
Bình Đại	Bến Tre - Bình Đại - Bình Thắng	Cửa Đại	10°11'	106°42'	I
An Thuận	Bến Tre - Ba Tri - An Thủy	HàmLuông	9°58'	106°36'	I
Bến Trại	Bến Tre - Thanh Phúc - An Thuận	Cổ Chiên	9°52'	106°31'	I
Mỹ Thanh	Sóc Trăng - Long Phú -Trung Bình 7	Mỹ Thanh	9°25'	105°10'	I
Gành Hào	Bạc Liêu - Giá Rai -Thị trấn Gành Hào	Gành Hào	9°02'	105°24'	I
Năm Căn	Cà Mau - Ngọc Hiển - Ngọc Hiển	Cửa Lớn	8°46'	105°01'	III
Sông Đốc	Cà Mau - Cà Mau -Thị trấn Ông Đốc	Ông Đốc	9°02'	104°50'	I
Xẻo Rô	Kiên Giang - An Biên - Tây Yên	Cái Lớn	9°52'	105°06'	I
Rạch Giá	Kiên giang - Rạch Giá - P.Vĩnh Thanh	Kiên	10°00'	105°05'	I

Nguồn: Quyết định số 16/2007/QĐ-TTg Quy hoach tổng thể mạng lưới quan trắc TNMTQG đến năm 2020)
http://cmh.com.vn/article/199-Danh-sach-cac-tram-thuy-van.html

Fig. 1 Coastal hydrological stations in the Mekong delta

5 Results

(1) *The trend of annual mean water level*

The changes of annual mean water level during the 29 year period (1988–2016) and the 14 year period (2003–2016) at Bình Đại station are presented in Fig. 2 with the linear trend line, average mean increase (Δ, mm/yr) and R^2. Table 1 provides Δ and R^2 values of the annual mean water level at the coastal stations during the two periods.

The second line in the table indicates the distance from Vũng Tàu station. The third line shows the value of the annual mean water level at each station (in cm).

The increasing trend of the annual mean water level is highest at the Bình Đại (11.4/10.1 mm) among the Tien River's mouth stations, at Gành Hào (13.3/20.1 mm), and at Sông Đốc on the west coast (10.7/16 mm) during the two periods.

(2) *Evolution of the annual highest high water level*

The data from stations show that the annual highest high water level (HHW) is reached once or more per year at each station.

The moment and the number of the annual HHW appearances during the 29 year period (1988–2016) are shown in Table 2.

In the table, the lines indicate the stations and the columns, the moments (shown briefly by months). The intersections are the times of appearance of the annual HHW

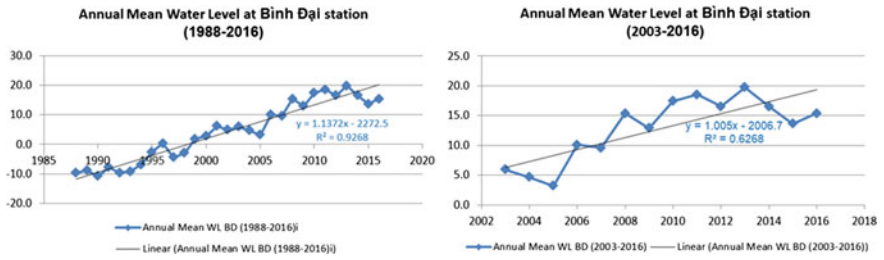

Fig. 2 Change of the annual mean water level at Bình Đại station

Table 1 Annual evolution rate of the mean water level change at stations **a** during (1988–2016) (top); **b** during (2003–2016) (down)

	VT	Vàm Kinh	Bình Đại	An Thuận	Bến Trại	Gành Hào	Năm Căn	Sông Đốc	Xẻo Rô	Rạch Giá
1988-2016	0	42	50	83	111	271	331	421	520	539
Average		-6.0	4.2	4.1	4.2	9.7	14.7	3.9	-0.9	3.7
Annual	Δ	6.7	11.4	5.8	5.5	13,3	13.8	10.7	5.7	5.7
Water Level	R^2	0.797	0.927	0.787	0.744	0.833	0.884	0.835	0.728	0.709

	VT	Vàm Kinh	Bình Đại	An Thuận	Bến Trại	Gành Hào	Năm Căn	Sông Đốc	Xẻo Rô	Rạch Giá
2003-2016	0	42	50	83	111	271	331	421	520	539
Average		-1.4	12.8	8.5	8.0	18.6	24.2	6.8	3.2	7.5
Annual	Δ	5	10.1	5.5	6.9	20.1	9.4	16	6	5.97
Water Level	R^2	0.377	0.627	0.365	0.574	0.762	0.691	0.939	0.411	0.502

Table 2 Moment and number of the annual HHW appearances at coastal stations

HHW	1	2	3	4	5	6	7	8	9	10	11	12	Tổng	Lặp
Vàm Kênh	0	1	3	0	0	0	0	0	1	16	9	3	33	4
Bình Đại	0	1	0	0	0	0	0	0	0	11	13	4	29	0
An Thuận	5	2	0	0	0	0	0	0	0	11	13	6	37	8
Bến Trại	1	1	0	0	0	0	0	0	0	17	8	6	33	4
Gành Hào	0	2	1	1	0	0	0	0	0	17	11	6	38	9
Năm Căn	2	0	0	0	0	0	0	0	0	4	18	8	32	3
Sông Đốc	2	0	0	0	0	2	1	0	1	0	7	8	21	0
Xẻo Rô	0	0	0	1	3	4	5	7	3	2	5	1	31	2
Rạch Giá	0	0	0	1	2	1	5	1	4	7	6	2	29	0

reached during the period (1988–2016). The two last columns represent the sum of appearances and the additional times, if any.

On the eastern coast, the annual HHW are reached essentially during October, November, and December (end of the rainy season and beginning of the dry season). Meanwhile in the western coast, the annual HHW spans a 9 months (3 months in the dry season and 6 months in the rainy season).

At Năm Căn station, most of the annual HHW are observed in November and December.

The graphs of the annual HHW in the 29 year period (1988–2016) and the 14 year period (2003–2016) at Gành Hào are presented in Fig. 3 with the linear trend line, the annual increase (Δ, mm) and the R^2. Table 3 presents Δ and R^2 at the coastal stations.

The annual HHW increases along the eastern coast from Vàm Kênh to Gành Hào from 176 to 221 cm.

At Năm Căn station, the annual HHW declines to 169 cm. On the western coast, from Sông Đốc to Rạch Giá, the annual HHW declines to 101–110 cm.

The annual HHW in the two periods (29 yr fig./14 yr fig.) shows an increasing trend. The highest increases were observed at Bình Đại (18/21.1 mm), Gành Hào (15.4/18.8 mm), Năm Căn (24.2/20.6 mm), and Sông Đốc (13.2/13.6 mm).

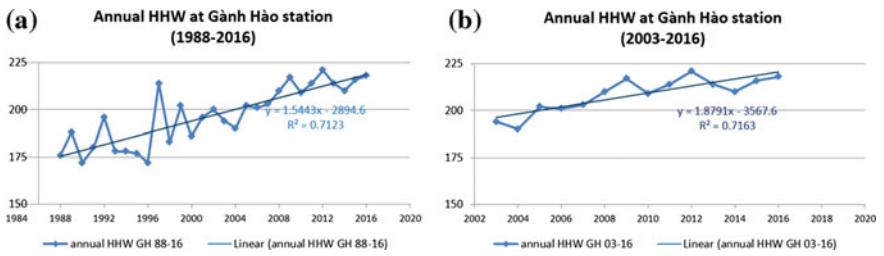

Fig. 3 Graphs of the annual HHW at Gành Hào station. **a** during (1988–2016) (left); **b** during (2003–2016) (right)

Table 3 Annual evolution rate of the annual HHW change at coastal stations **a** during (1988–2016) (top); **b** during (2003–2016) (down)

	VT	Vàm Kinh	Bình Đại	An Thuận	Bến Trại	Gành Hào	Năm Căn	Sông Đốc	Xẻo Rô	Rạch Giá
1988-2016	0	42	50	83	111	271	331	421	520	539
Annual		176	184	188	190	221	169	103	101	110
Highest	Δ	7.2	18.0	13.3	7.4	15.4	24.2	13.2	5.9	3.5
High WL	R^2	0.435	0.893	0.758	0.484	0.712	0.906	0.576	0.321	0.124

	VT	Vàm Kinh	Bình Đại	An Thuận	Bến Trại	Gành Hào	Năm Căn	Sông Đốc	Xẻo Rô	Rạch Giá
2003-2016	0	42	50	83	111	271	331	421	520	539
Annual		170	184	188	187	221	169	103	101	110
Highest	Δ	7.7	21.1	11.8	11.9	18.8	20.6	13.6	4.2	9.2
High WL	R^2	0.404	0.812	0.535	0.762	0.716	0.706	0.445	0.101	0.266

(3) ***Evolution of the annual mean of daily high water level***

At each station, the annal mean of daily high water level is calculated. The graphs of this water level over the two periods (1988–2016) and (2003–2016) at Vàm Kênh station are presented in Fig. 4 with the linear trend line, the annual mean of daily high water increase (Δ, mm) and the R^2. Table 4 presents Δ and R^2 at the coastal stations.

The increase of the annual mean of the daily high water level confirmed the increase of the annual HHW.

(4) ***Evolution of the annual lowest low water level***

The data from stations show that the annual lowest low water level (LLW) is reached once or more per year at each station.

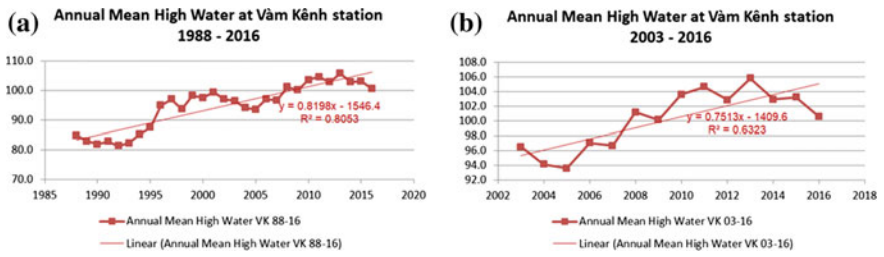

Fig. 4 Graphs of the annual mean of daily high water level at Vàm Kênh station. **a** during (1988–2016) (left); **b** during (2003–2016) (right)

Table 4 Annual evolution rate of the annual mean of daily high water levels at coastal stations

		Vàm Kinh	Bình Đại	An Thuận	Bến Trại	Gành Hào	Năm Căn	Sông Đốc*	Xẻo Rô	Rạch Giá
1988-2016		42	50	83	111	271	331	421	520	539
Annual	Δ	8.2	14.4	8.4	5.4	14.2	16.6	10.4	5.7	4
Mean HW	R^2	0.8053	0.9414	0.8637	0.691	0.9381	0.952	0.8716	0.6508	0.5528
		Vàm Kinh	Bình Đại	An Thuận	Bến Trại	Gành Hào	Năm Căn	Sông Đốc*	Xẻo Rô	Rạch Giá
2003-2016		42	50	83	111	271	331	421	520	539
Annual	Δ	7.5	15.2	5.7	5.5	20.7	14.3	11.7	3.6	4.5
Mean HW	R^2	0.6323	0.7857	0.3987	0.5178	0.9542	0.8038	0.8567	0.1601	0.2749

Table 5 Moment and number of the annual LLW appearances at coastal stations

LLW	1	2	3	4	5	6	7	8	9	10	11	12	Tổng	Lặp
Vàm Kênh	0	0	0	0	0	3	17	9	0	0	0	0	29	0
Bình Đại	0	0	0	0	2	5	16	7	0	0	0	0	30	1
An Thuận	0	0	0	0	1	12	13	5	0	0	0	0	31	2
Bến Trại	0	0	0	0	2	12	15	4	0	0	0	0	33	4
Gành Hào	0	0	0	0	4	22	9	2	0	0	0	0	37	8
Năm Căn	0	0	0	0	7	14	8	0	0	0	0	0	29	0
Sông Đốc	0	0	0	0	5	16	2	0	0	0	0	0	23	2
Xẻo Rô	6	9	1	4	5	5	3	1	0	0	0	0	34	5
Rạch Giá	3	6	1	2	6	9	2	0	0	0	0	0	29	0

The moment and the number of the annual LLW appearances during the 29 year period (1988–2016) are shown in Table 5.

In the table, the lines indicate the stations and the columns, the moments (shown briefly by months). The intersections are the times of appearance of the annual LLW reached during the period (1988–2016). The two last columns represent the sum of appearances and the additional times, if any.

On the eastern coast, the annual LLW are reached essentially during May, June, July, August (first half of the rainy season). Meanwhile in the western coast, the annual LLW occur from January to August, except at Sông Đốc. At this station and at Năm Căn, most of the annual LLW are observed in May to July, especially in June.

The graphs of the annual LLW during the two periods (1988–2016) and (2003–2016) at Gành Hào are presented in Fig. 5 with the linear trend line, the annual increase (Δ, mm) and the R^2. Table 6 presents Δ and R^2 at the coastal stations.

The annual LLW decreases then increases along the eastern coast from Vàm Kênh to Gành Hào, valued −220 cm at Năm Căn and −71 cm from Sông Đốc to Rạch Giá.

The annual LLW in the two periods (29 yr fig./14 yr fig.) show an increasing trend, faster in the second period at most of the coastal stations.

(5) ***Evolution of the annual mean of daily low water level***

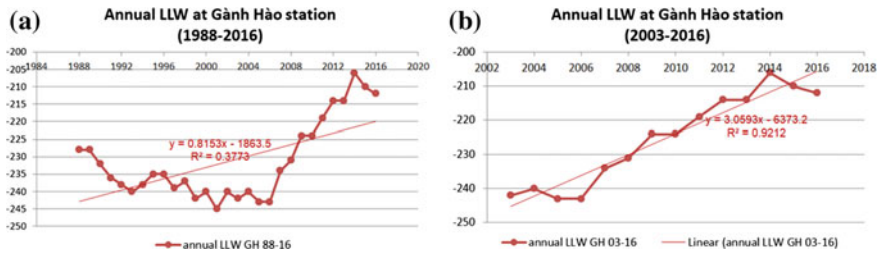

Fig. 5 Graph of the annual LLW at Gành Hào station. **a** during (1988–2016) (left); **b** during (2003–2016) (right)

Table 6 Annual evolution rate of the annual LLW change at coastal stations **a** during (1988–2016) (top); **b** during (2003–2016) (down)

	VT	Vàm Kinh	Bình Đại	An Thuận	Bến Trại	Gành Hào	Năm Căn	Sông Đốc	Xẻo Rô	Rạch Giá
1988-2016	0	42	50	83	111	271	331	421	520	539
Annual		-268	-246	-238	-257	-245	-220	-72	-71	-72
Lowest	Δ	7.1	9.4	4.4	11.8	8.2	16.4	12.8	3.9	8.8
Low WL	R^2	0.277	0.446	0.149	0.54	0.377	0.717	0.65	0.481	0.883

	VT	Vàm Kinh	Bình Đại	An Thuận	Bến Trại	Gành Hào	Năm Căn	Sông Đốc	Xẻo Rô	Rạch Giá
2003-2016	0	42	50	83	111	271	331	421	520	539
Annual		-248	-223	-238	-242	-243	-195	-67	-68	-59
Lowest	Δ	12.5	7.3	18.3	27.5	30.6	15.5	17.5	6.4	13.2
Low WL	R^2	0.374	0.173	0.549	0.715	0.921	0.603	0.608	0.436	0.884

At each station, the annual mean of daily low water level is computed. The graphs of this water level over the two periods (1988–2016) and (2003–2016) at An Thuận station are presented in Fig. 6 with the linear trend line, the annual mean of daily low water increase (Δ, mm) and the R^2. Table 7 presents Δ and R^2 at the coastal stations.

The increase of the annual mean of the daily low water level during (2003–2016) is faster than during (1988–2016), and confirmed the increase of the annual LLW.

(6) ***Evolution of the annual maximum range of tide***

The evolution of the annual maximum range of tide during (1988–2016) and (2003–2016) periods at Bình Đại station is presented in Fig. 7 with the linear trend, the annual increase (Δ, mm) and the R^2. Table 8 presents Δ và R^2 of the annual maximum range of tide at the coastal stations.

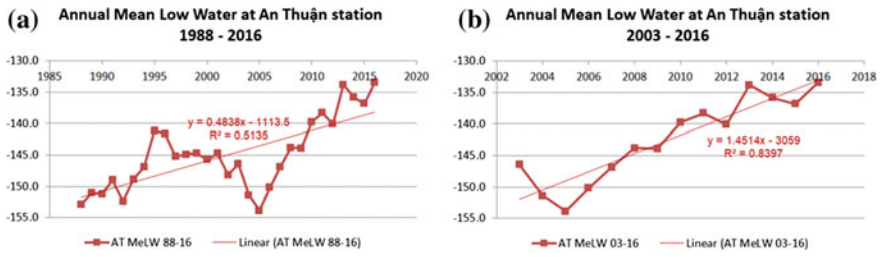

Fig. 6 Graphs of the annual mean of daily low water level at An Thuận station. **a** during (1988–2016) (left); **b** during (2003–2016) (right)

Table 7 Annual evolution rate of the annual mean of daily low water levels at coastal stations

		Vàm Kinh	Bình Đại	An Thuận	Bến Trại	Gành Hào	Năm Căn	Sông Đốc*	Xẻo Rô	Rạch Giá
1988-2016		42	50	83	111	271	331	421	520	539
Annual	Δ	4.6	9.3	4.8	9.7	11.1	16.5	12.1	5.3	6.7
Mean LW	R^2	0.3446	0.8366	0.5135	0.7352	0.7074	0.8685	0.8209	0.6508	0.695

		Vàm Kinh	Bình Đại	An Thuận	Bến Trại	Gành Hào	Năm Căn	Sông Đốc*	Xẻo Rô	Rạch Giá
2003-2016		42	50	83	111	271	331	421	520	539
Annual	Δ	8.9	12.0	14.5	20.6	29.1	17.8	18.7	6.1	6.2
Mean LW	R^2	0.4345	0.7336	0.8397	0.876	0.9522	0.8172	0.9342	0.4969	0.5151

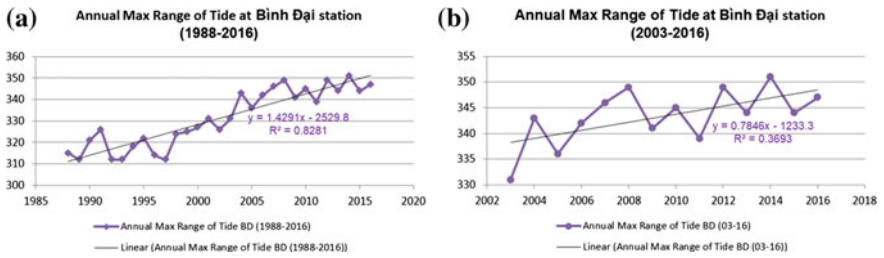

Fig. 7 Graphs of the annual maximum of the range of tide at Bình Đại station **a** (1988–2016) (left); **b** (2003–2016) (right)

Table 8 Annual evolution rate of the annual maximum range of tide at coastal stations

1988-2016		Vàm Kênh	Bình Đại	An Thuận	Bến Trại	Gành Hào	Năm Căn	Sông Đốc**	Xẻo Rô	Rạch Giá
Annual max R. of Tide	Δ	8.2	14.3	13.3	1.7	7.7	-3.8	-2.3	2.7	-3.7
	R^2	0.524	0.828	0.609	0.022	0.421	0.114	0.013	0.088	0.101
2003-2016		**Vàm Kênh**	**Bình Đại**	**An Thuận**	**Bến Trại**	**Gành Hào**	**Năm Căn**	**Sông Đốc****	**Xẻo Rô**	**Rạch Giá**
Annual max R. of Tide	Δ	-1.1	7.8	-5.9	-17.9	-7.3	-8.4	-10.4	3.3	4.8
	R^2	0.013	0.369	0.116	0.505	0.244	0.224	0.145	0.043	0.042

The annual maximum range of tide increases in the East Sea stations, decreases at Năm Căn, and West Sea stations except Xẽo Rô during (1988–2016), but decreases at most of stations during (2003–2016) except Bình Đại, Xẽo Rô and Rạch Giá. The strongest decreases are at Bến Trại (−17.9 mm/year) and at Sông Đốc (−10.4 mm/year).

6 Discussion

(1) The analysis of the water levels observed at the coastal stations in the Mekong delta has shown meaningful results:

- The annual mean water level along 539 km of the coast of the delta, from Vũng Tàu to Rạch Giá, increased with the most rapid rate observed during the last 2 decades;
- With the annual highest high water level increased, the volume of sea water level flows into the delta from the sea with the tide through the river mouth increased, especially at Bình Đại, Gành Hào, Năm Căn, and Sông Đốc.
- With the annual lowest low water level increased, with the highest increase in 2003–2016, the drainage of water from the delta inland into the sea become more difficult.
- In the 14 year period (2003–2016), the annual maximum range of tide declined at most of stations except Bình Đại, Xẽo Rô, and Rạch Giá, with the strongest decreases at Bến Trại and Sông Đốc.

(2) The increasing or decreasing trends of the annual mean water level in the two periods are merely derived from the observed water levels at the stations. The relevant provinces were consulted on the results of the analysis. However, the results remain to be explained.

During 29 years (1988–2016), especially from 2003 to 2016, the mean rates of evolution of the water levels show the interaction between the sea and the river at the river mouth leaning toward the sea factor.

The fact that the interaction between the sea and the river processes tended to become more dominated by the sea, beside the climate change, sea level rise, arises also from the weakening of the river process due to the water uses from upstream, especially the construction of hydropower dams on the mainstream, and in the delta itself.

The weakening of the river processes differed among the mouths of the Tiền River shows in the differences in the changes among the stations at Vàm Kênh, Bình Đại, An Thuận, and Bến Trại.

The Landsat 8 satellite imagery[1] on September 18, 2014, Fig. 8, as compared to images in the previous years show that the mainstream flow on the Tiền River had changes from Tân Châu, from Vĩnh Long and from Mỹ Tho downstream.

(3) Except sudden events, the interaction of the sea and the river is a continuous iterated process. In the context of the Mekong delta, this chapter used the annual cycle with consecutive wet and dry seasons as the basis for examination.

After each year, the interaction sea—river reshaped the morphology of the river, in particular at the estuaries. The reformed river morphological changes then determined the water levels in the next years. Therefore, the water levels

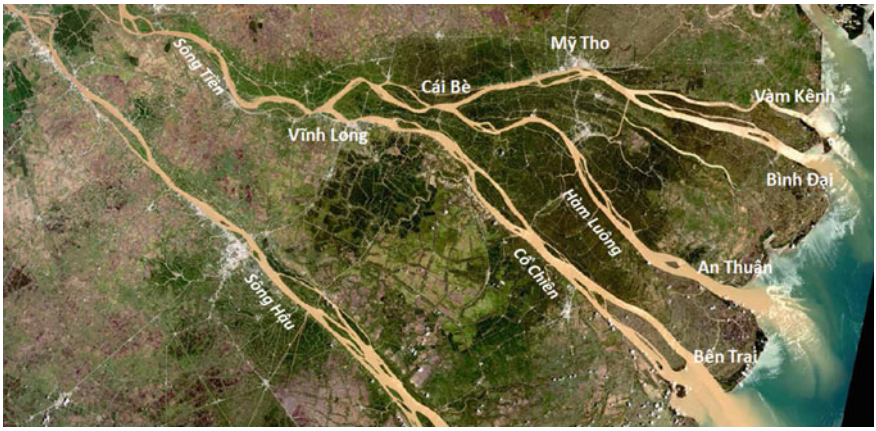

Fig. 8 Hậu River, Tiền River, its branches and Vàm Kênh, Bình Đại, An Thuận, Bến Trại stations (Landsat 8, September 18, 2014)

[1]Landsat Satellite Imagery https://earthexplorer.usgs.gov/.

analysed in this chapter at the coastal stations are synthetic, real expressions of this interaction.

(4) The water levels highlighted in this chapter include implicitly the effects of natural and the accelerated human-induced land subsidence at the coastal hydrological gauging stations because the hourly water level is measured continuously and directly in situ. However how are the contributions of these effects remains an open issue.

(5) The changes of the water levels at the interfaces of the river and the sea reported in this chapter provides useful informations for the planning of water regulation works in the Mekong Delta, especially relating to *the construction of the sluice-gates* such as the *Cái Lớn and Cái Bé* curently under study, and the planned ones on *Hàm Luông* and *Cổ Chiên* branches of Tiền River.

These informations are also needed for the study on coastal erosion and the engineering projects planned for the protection of the coast of the delta.

(6) We included the Năm Căn station in the list of coastal stations because it is not so far from the East and West Seas and strongly influenced by both the uneven semidiurnal tidal regime from the East and the uneven diurnal tidal regime from the West.

At Năm Căn, the rates of increase of the annual mean water level, the annual highest high water level, and the annual lowest low water level are rather high compared to other stations in the eastern and the western coasts, while the annual maximum range of tide decrease during 1988–2016 and faster during 2003–2016 (Cf. Tables).

Whether, and how these phenomena are relevant to the confluence and interaction between the two tides, of the East Sea and the West Sea, in the context of global climate change, sea level rise? This open question is still a simplified version because it does not take into account the interaction with the Hậu River given the water from Cà Mau flowing through Bảy Háp and Kênh Tắt to Năm Căn.

These are follow up studies needed for the master development planning for the Ca Mau Peninsula, a young, rich and complex part of the Mekong delta.

Acknowledgements The author would like to thank warmly the Southern Regional Hydrometeorological Center and the Hydrometeorological Center of Tiền Giang, Bến Tre, Trà Vinh, Sóc Trăng, Bạc Liêu, Cà Mau and Kiên Giang Provines for their precious support.

References

Anthony, E. J., Brunier, G., Besset, M., Goichot, M., Dussouillez, P., &Nguyen, V. L. (2015). Linking rapid erosion of the Mekong River delta to human activities. *Scientific Reports, 5*, 14745. https://doi.org/10.1038/srep14745.

Bravard, J. P., Goichot, M., & Gaillot, S. (2013). Geography of sand and gravel mining in the lower mekong river. *First Survey and Impact Assessment, EchoGeo, 26*(10–12), 2013.

Decision 16/2007/QĐ-TTg. (2007). *Quy hoạch tổng thể mạng lưới quan trắc TNMTQG đến năm 2020)* (Master Plan for the National Ressources and Environment Monitoring up to year 2020) http://cmh.com.vn/article/199-Danh-sach-cac-tram-thuy-van.html.

Erban, L. E., Gorelick, S. M., & Zebker, H. A. (2014). Groundwater extraction, land subsidence, and sea-level rise in the Mekong Delta Vietnam. *Environmental Research Letters*, *9*, 084010 (6 pp).

Ericson, J. P., Vorosmarty, C. J., Dingman, S. L., Ward, L. G., & Meybaeck, M. (2006). Effective sea-level rise and deltas: Causes of change and human implications. *Global and Planetary Change*, *50* (1–2), 63–82.

Tamura, T., Saito Y., Nguyen, V. L., Oanh Ta, T. K. Bateman, M. D., Matsumoto, D., & Yamashita S. (2012). Origin and evolution of interdistributary delta plains; Insights from Mekong River delta. *GEOLOGY, 40,* (4), 303–336.

Nguyễn, N. T. (2010). The vietnamese mekong delta facing the double challenge of the climate change. In *Proceedings of the 78th annual meeting, international symposium of the international commission on large dams*, Hà Nội 25/5/2010.

Nguyễn, N. T. (2015). The Mekong Delta is facing the danger of sinking and erosion, Keynote Speech. In *Proceedings of the international conference on multiphysical interaction and environment*, 2015, March 9th–10th. pp. 1–14. https://drive.google.com/file/d/0BxMiCNS4rqGxUElLakpiU0VveVk/view.